DEFENSE DOCUMENTATION CENTER

FOR

SCIENTIFIC AND TECHNICAL INFORMATION

CAMERON STATION ALEXANDRIA. VIRGINIA

Fourth Symposium on

NAVAL HYDRODYNAMICS

PROPULSION HYDROELASTICITY

Sponsored by the

OFFICE OF NAVAL RESEARCH

and the

WEBB INSTITUTE OF NAVAL ARCHITECTURE

August 27–31, 1962

Washington, D.C.

ACR-92

OFFICE OF NAVAL RESEARCH—DEPARTMENT OF THE NAVY

Washington, D.C.

Statements and opinions contained herein are those of the authors and are not to be construed as official or reflecting the views of the Navy Department or of the naval service at large.

FOREWORD

The field of Naval Hydrodynamics covers many problems of great concern to ship design and to naval strategy and tactics. Substantial improvements in ship performance, in general, depend critically on successful research in hydrodynamics.

The prime objective of the Symposia on Naval Hydrodynamics has been to present the latest research results on central themes of timely interest and significance. The First Symposium[1] was devoted to critical surveys of the state-of-the-art in various important areas. The Second Symposium[2] concentrated on noise and cavity flows, while the Third Symposium[3] explored aspects of high-performance ships. In accordance with this pattern, the two topics covered in this Fourth Symposium are (a) Propulsion of Ships and (b) Hydroelasticity.

Although the Navy has used propellers for over 100 years for developing thrust for its ships, at this date there is no completely satisfactory analytical means available to the designer to predict propeller characteristics. Existing mathematical models involve some oversimplifying assumptions that require large semi-empirical corrections. The interaction of the ships flow field and the propeller is only qualitatively understood. The unsteady pressure field and the unsteady thrust and torque developed by a propeller behind a ship provide forces and moments that excite ship vibration. In addition to these areas, there are many ship applications where the conventional propeller is not adequate. For these applications, the ship designer and operator should have available sufficient information on ducted propellers, cycloidal propellers, supercavitating propellers, jet propulsion, etc.

The subject of hydroelasticity, which is an extension to denser media of the classical aeroelastic phenomena encountered in airplane and missile applications, is a relatively new category. The obvious hydroelastic counterpart of aeroelasticity is the determination of the unsteady loads, divergence and flutter

[1] "First Symposium on Naval Hydrodynamics," National Academy of Sciences - National Research Council, Publication 515, 1957, Washington, D. C.; $5.00.
[2] "Second Symposium on Naval Hydrodynamics," Office of Naval Research, Department of the Navy, ACR-38, 1958; Superintendent of Documents, U. S. Government Printing Office, Washington, D. C., Catalog No. D210.15:ACR-38; $4.00.
[3] "Third Symposium on Naval Hydrodynamics," Office of Naval Research, Department of the Navy, ACR-65, 1960; Superintendent of Documents, U. S. Government Printing Office, Washington, D. C., Catalog No. D210.15:ACR-65; $3.50.

of lifting surfaces, such as rudders and hydrofoils. However, for the purposes of this symposium, the concept of hydroelasticity is broadened to encompass all problems in which the flow field and the hydrodynamic forces and moments are significantly affected by the structural deflections. Thus, many rather diverse subjects are included, such as cavity resonance, the slamming of ships and the interaction of ships' structure with wave-induced forces and underwater explosions.

The program of this and the previous symposia have emphasized that substantial improvements in ship performance can be obtained only when the fundamental physics is understood. With this basic knowledge in hand, parametric studies can be made that will give the designer meaningful tools on which to base his design. Thus, the papers herein are concerned with the entire gamut from basic research to design methods.

This single volume is substantially the same as the Preprints initially issued in three volumes by the Office of Naval Research as ACR-73 several weeks before the symposium. However, eight papers which were not available for printing with the Preprints are now included.

Technical organization of the program was under the direction of the Fluid Dynamics Branch of the Office of Naval Research. In this connection, I would like to express sincere appreciation to the members of the informal committee which helped develop the format. This group consisted of:

Mr. Jacques Hadler	David Taylor Model Basin
Mr. David Jewel	David Taylor Model Basin
Mr. James Schuler	Bureau of Ships
Dr. Bennett Silverstein	Office of Naval Research

The able assistance of Webb Institute of Naval Architecture, in solving both technical and administrative problems that have arisen, has been instrumental in assuring the smooth progress of this symposium. Thanks are gratefully extended to Professor E. V. Lewis and Mr. Robert Zubaly.

The burden of detailed administration of this symposium has been borne capably by Bennett Silverstein of the Office of Naval Research. As editor of these proceedings, he has meshed together the thousand-and-two jigsaw pieces that comprise the operation of this large symposium. For this I offer my deep appreciation. His persistent pressure to meet deadlines resulted in the early publication of the Preprints, which this volume supersedes, and also incurred authors' wrath; for the latter, I offer my sympathy.

The flow of necessary information between authors, chairmen, and the symposium administrators has been kept steady and timely through the efforts of Mrs. Yetta Hassin and Miss Eunice Harrison of this Office.

Grateful appreciation is extended to Dr. W. P. A. van Lammeren of the Netherlands Ship Model Basin who considerately merged his plans for a meeting on ship propulsion into this symposium.

I am especially appreciative of the excellent cooperation afforded this symposium by the David Taylor Model Basin. Special thanks are extended to the Commanding Officer, Captain J. A. Obermeyer, to Dr. Karl E. Schoenherr the

Technical Director of the Hydrodynamics Laboratory, and to Dr. Alfred Keil, Technical Director of the Structural Laboratory. The research conducted by their scientific staff provides a very important segment of the papers.

To the chairmen of the various sessions, I would like to express my sincere admiration for their willingness to take on the often thankless job of confining authors to the allotted time and of guiding discussers into brief, cogent remarks.

Above all, I would like to thank the most important people, the authors, without whose efforts there would be no Symposium on Naval Hydrodynamics.

RALPH D. COOPER, Head
Fluid Dynamics Branch

CONTENTS

. Monday, August 27

Morning Session

PROPULSION

Chairman: Shiro Kan

Transportation Technical
Research Institute
Tokyo, Japan

1

ON THE THEORY OF SCREW PROPELLERS

R. Yamazaki
Kyushu University
Fukuoka, Japan

INTRODUCTION

The theory of screw propellers based on the vortex theory was proposed and developed by A. Betz and later by other researchers. In the previous paper [1], the same theory was developed further for the propellers working steadily in the uniform flow on the basis of the lifting surface theory, taking into account the effects of the variation of the principal dimensions more precisely. In actual cases, however, the screw propeller is usually working with pulsation in a non-uniform flow such as a wake of the ship, and further sometimes in heavy load conditions.

In this paper, therefore, we attempt to develop a hydrodynamical theory of the screw propeller so as to include these cases. In section 1, general expressions are presented for the performance characteristics of the propeller working unsteadily in a non-uniform flow on the basis of the lifting surface theory. And details of them are pursued for specific cases of nearly steady state in section 1 and also of quite steady state in section 2. The theory is also developed for the case of heavy load conditions including a separated flow based on the non-linear wing theory in section 2. In section 3, the approximate method of calculations is presented for the case of steady state by means of the linear theory, and some numerical results obtained theoretically are compared with the experimental values. And it is shown that these two results almost agree with each other when the flow around the blade are considered not to be separated. However, the numerical calculations for the non-linear effect referred to the separated flow and also the performance characteristics in unsteady state are postponed to later works.

1. THEORY OF PROPELLERS IN UNSTEADY STATE

In this section the hydrodynamical characteristics of a screw propeller working unsteadily in a non-uniform flow are studied by using the vortex theory. In this treatment the propeller blades are assumed to be very thin, and therefore it may be presumed that the mean surfaces of them can be replaced by

3

bound vortex sheets and the free vortices springing from the bound vortices recede freely from the blade retaining their strength. And the disturbed velocity induced by the boss is neglected since it is considered to be very small.

We consider the case of the screw propeller with N blades, denoting the propeller radius by r_o and the boss radius by r_B. Cylindrical coordinates (x, r, θ) fixed in space are chosen so that the x-axis coincides with the axis of rotation of the propeller. The propeller is assumed to advance along the negative direction of the x-axis, while rotating around x-axis in the negative direction of θ (vid. Fig. 1).
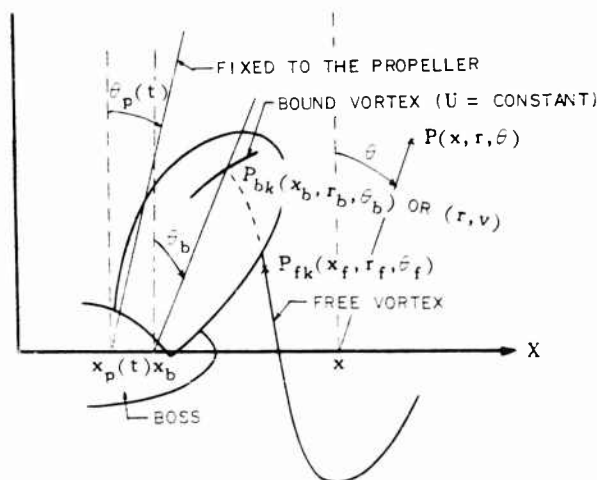
Fig. 1 - Sketch of propeller

While the orientation of the propeller at time t is represented by $(x_p(t), 0, \theta_p(t))$, the position of a point fixed on the mean surface of a blade is represented by the parameters (u, v), which are coordinates fixed to the blade, and here we take $u = r$. Then the space coordinates of a fixed point $P_{bk}(x_b, r_b, \theta_b)$ on the mean surface of the k-th blade can be expressed as

$$\left.\begin{aligned} x_b &= x_b(r, v) - x_p(t) , \\ r_b &= r , \\ \theta_b &= \theta_b(r, v) - \theta_p(t) + 2\pi(k-1)/N . \end{aligned}\right\} \tag{1.1}$$

where $x_b(r, v)$ and $\theta_b(r, v)$ are functions of r and v, and obviously

$$v_L(r) \lessgtr v \lessgtr v_T(r) , \quad r_B \lessgtr r \lessgtr r_o .$$

$$k = 1, 2, \ldots, N ,$$

4

the suffix b refers to quantities related to the blade and the suffixes L and T refer to the leading and trailing edges of the blade.

Then the bound vortices are assumed to be arranged along the lines of v = constant on the mean surface (1.1) of the blade. And the strength of the bound vortices contained in the elemental width dv on the k-th blade at a time τ is represented by $\gamma_k(r, v, \tau)\, dv$, and also the space coordinates at the time t of a point $P_{fk}(x_f, r_f, \theta_f)$ fixed on the free vortices at the time t sprung from these bound vortices at the point $P_{bk}(r, v)$ at the past time τ are expressed as

$$\left.\begin{aligned}
x_f &= x_{fk}(r, v, \tau, t), \\
r_f &= r_{fk}(r, v, \tau, t), \\
\theta_f &= \theta_{fk}(r, v, \tau, t),
\end{aligned}\right\} \tag{1.2}$$

where the suffix f represents values related to the free vortices. From the definitions (1.1) and (1.2) it follows

$$x_b = [x_f]_{\tau = t}, \quad r_b = [r_f]_{\tau = t}, \quad \theta_b = [\theta_f]_{\tau = t}. \tag{1.3}$$

And the velocity components of the general flow at a point (x, r, θ) are represented by v_x, v_r and v_θ in the x-, r- and θ-directions respectively, and these are functions of x, θ, r and t.

If the fluid is considered to be non-viscous and incompressible, the systems of the bound and free vortices can be represented by the superposition of elemental horse-shoe vortices, and the velocity potential ϕ_p at the point (x, r, θ) is expressed as follows:

$$\phi_p = -\frac{1}{4\pi} \sum_{k=1}^{N} \int_{r_B}^{r_o} dr' \int_{v_L(r')}^{v_T(r')} dv' \int_{-\infty}^{t} \gamma_k(r', v', \tau) \left\{ \left(\frac{r_f' \partial \theta_f'}{\partial \tau} \frac{\partial r_f'}{\partial r'} - \frac{r_f' \partial \theta_f'}{\partial r'} \frac{\partial r_f'}{\partial \tau} \right) \frac{\partial}{\partial x_f'} \right.$$

$$\left. + \left(\frac{\partial r_f'}{\partial \tau} \frac{\partial x_f'}{\partial r'} - \frac{\partial r_f'}{\partial r'} \frac{\partial x_f'}{\partial \tau} \right) \frac{\partial}{r_f' \partial \theta_f'} + \left(\frac{\partial x_f'}{\partial \tau} \frac{r_f' \partial \theta_f'}{\partial r'} - \frac{\partial x_f'}{\partial r'} \frac{r_f' \theta_f'}{\partial \tau} \right) \frac{\partial}{\partial r_f'} \right\} \frac{1}{R_f} d\tau, \tag{1.4}$$

where

$$R_f = \sqrt{(x_f' - x)^2 + r_f'^2 + r^2 - 2r_f' r \cos(\theta_f' - \theta)},$$

and x_f', r_f' and θ_f' represent the values of x_f, r_f and θ_f respectively as referred to the point (r', v', τ) in (1.2), respectively. Using ϕ_p, the axial, radial and tangential components of induced velocity, w_x, w_r and w_θ, at a point (x, r, θ) are expressed by

$$w_x = \frac{\partial \phi_p}{\partial x}, \quad w_r = \frac{\partial \phi_p}{\partial r}, \quad w_\theta = \frac{\partial \phi_p}{r \partial \theta}. \tag{1.5}$$

5

When the blade has a moderate angle of attack, Kutta-Joukowsky condition must be satisfied at the trailing edge of the blade, that is, the load function $\gamma(r,v,t)$ vanishes there. And the boundary condition must be so satisfied that the relative velocity normal to the surface of the blade is zero, that is, at the point (r,v) on the first blade we have

$$
\frac{\partial\theta_b(r,v)}{\partial v}\left(\frac{dx_p(t)}{dt} + \left[v_x\right]_{(b)} + \left[w_x\right]_{(b)}\right) - \frac{\partial x_b(r,v)}{r\,\partial v}\left(r\frac{\partial\theta_p(t)}{\partial t} + \left[v_\theta\right]_{(b)} + \left[w_\theta\right]_{(b)}\right)
$$
$$
- \left(\frac{\partial x_b(r,v)}{\partial r}\frac{\partial\theta_b(r,v)}{\partial v} - \frac{\partial x_b(r,v)}{\partial v}\frac{\partial\theta_b(r,v)}{\partial r}\right)\left(\left[v_r\right]_{(b)} + \left[w_r\right]_{(b)}\right) = 0, \quad (1.6)
$$

or using (1.5),

$$
\left[\left\{\frac{\partial\theta_b(r,v)}{\partial v}\frac{\partial}{\partial x} - \frac{\partial x_b(r,v)}{r\,\partial v}\frac{\partial}{r\,\partial\theta} - \left(\frac{\partial x_b(r,v)}{\partial r}\frac{\partial\theta_b(r,v)}{\partial v} - \frac{\partial x_b(r,v)}{\partial v}\frac{\partial\theta_b(r,v)}{\partial r}\right)\frac{\partial}{\partial r}\right\}\varphi\right]_{(b)}
$$
$$
= \frac{\partial x_b(r,v)}{r\,\partial v}\left(r\frac{d\theta_p(t)}{\partial t} + \left[v_\theta\right]_{(b)}\right) - \frac{\partial\theta_b(r,v)}{\partial v}\left(\frac{dx_p(t)}{dt} + \left[v_x\right]_{(b)}\right)
$$
$$
+ \left(\frac{\partial x_b(r,v)}{\partial r}\frac{\partial\theta_b(r,v)}{\partial v} - \frac{\partial x_b(r,v)}{\partial v}\frac{\partial\theta_b(r,v)}{\partial r}\right)\left[v_r\right]_{(b)}, \quad (1.7)
$$

where $[\ ]_{(b)}$ means the value obtained by substituting $(x_b, r_b, \theta_b)_{k=1}$ in (x, r, θ). The equations similar to (1.6) or (1.7) hold for the other blade k, too.

It is noted that, even though the radius of the boss is finite, the boundary conditions on the surface of the boss can be neglected in this treatment as its effect is considered to be very small [2].

Then we shall examine further the condition of the free vortices. Since the position of the free vortices drifts inevitably by the force of a flow, the following equations are obtained for the point on the free vortices:

$$
\left.\begin{aligned}
\frac{\partial x_f}{\partial t} &= \left[\frac{\partial\varphi}{\partial x}\right]_{(f)} + \left[v_x\right]_{(f)}, \qquad \frac{\partial r_f}{\partial t} = \left[\frac{\partial\varphi}{\partial r}\right]_{(f)} + \left[v_r\right]_{(f)} \cdot \\
r_f\frac{\partial\theta_f}{\partial t} &= \left[\frac{\partial\varphi}{r\,\partial\theta}\right]_{(f)} + \left[v_\theta\right]_{(f)} \cdot
\end{aligned}\right\}
\quad (1.8)^*
$$

_____

*In the case of a propeller working steadily in an uniform flow, taking
$$
x_f = x_b + x_{fo}(r,v,\theta), \quad dx_p(t)/dt = \overline{V}, \quad v_x = 0,
$$

where θ is a function of $t - \tau$, we have
$$
\frac{\partial x_f}{\partial t} = \frac{\partial x_b}{\partial t} + \frac{\partial x_{fo}(r,v,\theta)}{\partial t} = -\overline{V} + \frac{\partial x_{fo}(r,v,\theta)}{\partial\theta}\frac{\partial\theta}{\partial t}.
$$

Substituting this expression in the first equation of (1.8), we had the equation (1.4) in the previous paper [1]. The similar equations for the r- and θ-directions are to be obtained in the same manner.

6

where $[\ ]_{(f)}$ means the value at the point on the free vortices. We shall consider now a point $P_{fk}(\tau = t - \Delta t)$, which is placed on the free vortex sprung from the bound vortex at a point P_{bk}, receding from it by the infinitesimal time interval Δt, and denote the differences of the x-, r- and θ-coordinates between these two points, i.e., $P_{fk}(\tau = t - \Delta t)$ and P_{bk}, by Δx_f, Δr_f and $\Delta \theta_f$, respectively. Then using (1.3), we can obtain for Δ_f, for instance,

$$\Delta x_f = \left[x_f\right]_{\tau=t} - \left[x_f\right]_{\tau=t-\Delta t} \doteqdot - \left[\frac{\partial x_f}{\partial \tau}\right]_{\tau=t} \Delta t .$$

On the other hand we have

$$\left[\frac{\partial x_f}{\partial \tau}\right]_{\tau=t} = \frac{\partial \left[x_f\right]_{\tau=t}}{\partial t} - \left[\frac{\partial x_f}{\partial t}\right]_{\tau=t} .$$

Hence, using the first equation of (1.8), we can obtain

$$\Delta x_f = \left(\frac{dx_p(t)}{dt} + \left[v_x\right]_{(b)} + \left[w_x\right]_{(b)}\right) \Delta t .$$

In the same manner we have

$$\Delta r_f = \left(\left[v_r\right]_{(b)} + \left[w_r\right]_{(b)}\right) \Delta t ,$$

$$\Delta \theta_f = \left(\frac{d\theta_p(t)}{dt} + \frac{1}{r} \left[v_\theta\right]_{(b)} + \frac{1}{r} \left[w_\theta\right]_{(b)}\right) \Delta t .$$

Substituting these Δx_f, Δr_f and $\Delta \theta_f$ in (1.6), the following equation is obtained:

$$\frac{\partial \theta_b(r,v)}{\partial v} \Delta x_f - \frac{\partial x_b(r,v)}{\partial v} \Delta \theta_f$$

$$- \left(\frac{\partial x_b(r,v)}{\partial r} \frac{\partial \theta_b(r,v)}{\partial v} - \frac{\partial x_b(r,v)}{\partial v} \frac{\partial \theta_b(r,v)}{\partial r}\right) \Delta r_f = 0 . \quad (1.9)$$

Since the equation (1.9) represents the tangential plane of the blade surface (1.1), the free vortices sprung from the bound vortices are seen to follow initially along the blade surfaces.

It is in general a very complicated problem to solve (1.1) - (1.8) for a given propellers working in unsteady state, where the "strength" and the "positions" of the bound and free vortices are fluctuating with time unlike to the case of steady state. However, when the working condition does not deviate so far from the steady state, as in the case of the steady state superposed by small fluctuations of the movement of the propeller and the outer flow, we may safely neglect the time fluctuation of the geometrical positions of the free vortices, for the variation of the pitch of the helical free vortices is generally proved to have little effect upon the performance characteristics of the propeller working steadily [1]. We may also neglect the contraction of the free vortices [2] and the

7

effect of an oblique flow, because these effects are considered to be very small in the case of steady state. In these circumstances the position of the free vortices is approximated by

$$
x_f = x_b(r,v) - x_p(t) + \tilde{x}(r,\varphi) ,
$$

$$
r_f = r ,
$$

$$
\theta_f = \theta_b(r,v) - \theta_p(t) + \varphi + 2\pi(k-1)/N ,
$$

where $\varphi = \varphi_o(t-\tau)$ and φ_o is a constant to be determined hereafter. Taking

$$
\dot{x}_p = \frac{dx_p(t)}{dt} , \qquad \dot{\theta}_p = \frac{d\theta_p(t)}{dt} ,
$$

(1.4) is re-expressed by

$$
\varphi_p = \frac{1}{4\pi} \sum_{k=1}^{N} \int_{r_B}^{r_o} dr' \int_{v_L(r')}^{v_T(r')} dv' \int_{0}^{\infty} \gamma_k \left(r',v',t - \frac{\varphi}{\varphi_o} \right) \left[\left\{ r' \frac{\partial}{\partial x} - \frac{\partial\tilde{x}(r',\varphi)}{r'\partial\varphi} \frac{\partial}{\partial\theta} \right. \right.
$$
$$
\left. \left. + r' \left(\frac{\partial x_b(r',v')}{\partial r'} - \frac{\partial\theta_b(r',v')}{\partial r'} \frac{\partial\tilde{x}(r',\varphi)}{\partial\varphi} + \frac{\partial\tilde{x}(r',\varphi)}{\partial r'} \right) \frac{\partial}{\partial r_f'} \right\} \frac{1}{R_{f'}} \right]_{r_f'=r'} d\varphi, \quad (1.10)
$$

where

$$
R_{f'} = \sqrt{ \left[\tilde{x}(r',\varphi) + x_b(r',v') - x - x_p(t) \right]^2 + r_f'^2 + r^2 }
$$
$$
\overline{ - 2r_f'r \cos \left[\varphi + \theta_b(r',v') - \theta - \theta_p(t) + 2\pi(k-1)/N \right] } .
$$

And the boundary condition (1.6) or (1.7) for first blade is re-expressed by

$$
\left(\dot{x}_p + \left[v_x \right]_{(b)} + \left[w_x \right]_{(b)} \right) - \left(\frac{\partial x_b(r,v)}{r\partial v} \middle/ \frac{\partial\theta_b(r,v)}{\partial v} \right) \left(r\dot{\theta}_p + \left[v_\theta \right]_{(b)} + \left[w_\theta \right]_{(b)} \right)
$$
$$
- \left(\frac{\partial x_b(r,v)}{\partial r} - \frac{\partial x_b(r,v)}{\partial v} \frac{\partial\theta_b(r,v)}{\partial r} \middle/ \frac{\partial\theta_b(r,v)}{\partial v} \right) \left(\left[v_r \right]_{(b)} + \left[w_r \right]_{(b)} \right) = 0 , \quad (1.11)
$$

or

$$
\frac{1}{4\pi r} \sum_{k=1}^{N} \int_{r_B}^{r_o} dr' \int_{v_L(r')}^{v_T(r')} dv' \int_{0}^{\infty} \gamma_k \left(r',v',t - \frac{\varphi}{\varphi_o} \right) \left[\left\{ r \frac{\partial}{\partial x} - \left(\frac{\partial x_b(r,v)}{r\partial v} \middle/ \frac{\partial\theta_b(r,v)}{\partial v} \right) \frac{\partial}{\partial\theta} \right. \right.
$$
$$
\left. \left. - r \left(\frac{\partial x_b(r,v)}{\partial r} - \frac{\partial x_b(r,v)}{\partial v} \frac{\partial\theta_b(r,v)}{\partial r} \middle/ \frac{\partial\theta_b(r,v)}{\partial v} \right) \frac{\partial}{\partial r} \right\} \left\{ r' \frac{\partial}{\partial x} - \frac{\partial\tilde{x}(r',\varphi)}{r'\partial\varphi} \frac{\partial}{\partial\theta} \right. \right. \quad \begin{matrix} (1.12) \\ (\text{Cont.}) \end{matrix}
$$

$$+ \; r'\left(\frac{\partial x_b(r,v')}{\partial r'} - \frac{\partial \theta_b(r',v')}{\partial r'} \; \frac{\partial \tilde{x}(r',\varphi)}{\partial \varphi} + \frac{\partial \tilde{x}(r',\varphi)}{\partial r'}\right)\frac{\partial}{\partial r'_f}\Biggr\}\frac{1}{R_{f'}}\Biggr]_{\substack{r'_f = r' \\ x = x_b \\ \theta = [\theta_b]_{k=1}}} \; d\varphi$$

$$= \left(\frac{\partial x_b(r,v)}{r\,\partial v}\,\middle/\,\frac{\partial \theta_b(r,v)}{\partial v}\right)\left(r\dot{\theta}_p + \left[v_\theta\right]_{(b)}\right) - \left(\dot{x}_p + \left[v_x\right]_{(b)}\right)$$

$$+ \left(\frac{\partial x_b(r,v)}{\partial r} - \frac{\partial x_b(r,v)}{\partial v} \; \frac{\partial \theta_b(r,v)}{\partial r}\,\middle/\,\frac{\partial \theta_b(r,v)}{\partial v}\right)\left[v_r\right]_{(b)}. \tag{1.12}$$

Similar equations as (1.11) or (1.12) can be obtained for the k-th blade, too.

Then we shall consider the forces acting on the propeller. Since the pressure difference between upper and lower surfaces of the propeller blade is equal to the product of the strength of the vortex and the component of the velocity normal to the vortex, we can derive the following expressions for those forces. Letting the density of fluid be ρ, the force due to the component of the bound vortex in the r-direction can be expressed as

$$\rho\left(\dot{x}_p + \left[v_x\right]_{(b)} + \left[w_x\right]_{(b)}\right)\gamma_k(r,v,t)\,dv\,dr\,,$$

$$-\rho\left(r\dot{\theta}_p + \left[v_\theta\right]_{(b)} + \left[w_\theta\right]_{(b)}\right)\gamma_k(r,v,t)\,dv\,dr$$

in the θ- and the x-component respectively, and that due to the component of the bound vortex in the x-direction as

$$\rho\left(r\dot{\theta}_p + \left[v_\theta\right]_{(b)} + \left[w_\theta\right]_{(b)}\right)\gamma_k(r,v,t)\,\frac{\partial x_b(r,v)}{\partial r}\,dv\,dr\,,$$

$$-\rho\left(\left[v_r\right]_{(b)} + \left[w_r\right]_{(b)}\right)\gamma_k(r,v,t)\,\frac{\partial x_b(r,v)}{\partial r}\,dv\,dr$$

in the r- and the θ-component respectively, and also that due to the component of the bound vortex in the θ-direction as

$$\rho\left(\left[v_r\right]_{(b)} + \left[w_r\right]_{(b)}\right)\gamma_k(r,v,t)\,\frac{r\partial \theta_b(r,v)}{\partial r}\,dv\,dr\,,$$

$$-\rho\left(\dot{x}_p + \left[v_x\right]_{(b)} + \left[w_x\right]_{(b)}\right)\gamma_k(r,v,t)\,\frac{r\partial \theta_b(r,v)}{\partial r}\,dv\,dr$$

in the x- and the r-component respectively. By means of these expressions, we obtain the expressions for the thrust T_o and the torque Q_o due to the pressure differences, that is,

9

$$T_o = \rho \sum_{k=1}^{N} \int_{r_B}^{r_o} dr \int_{v_L(r)}^{v_T(r)} \gamma_k(r,v,t) \left\{ r\dot{\theta}_p + \left[v_\theta\right]_{(b)} + \left[w_\theta\right]_{(b)} \right.$$
$$\left. - \frac{r\partial\theta_b(r,v)}{\partial r} \left(\left[v_r\right]_{(b)} + \left[w_r\right]_{(b)} \right) \right\} dv,$$

$$Q_o = \rho \sum_{k=1}^{N} \int_{r_B}^{r_o} dr \int_{v_L(r)}^{v_T(r)} \gamma_k(r,v,t) \left\{ \dot{x}_p + \left[v_x\right]_{(b)} + \left[w_x\right]_{(b)} \right.$$
$$\left. - \frac{\partial x_b(r,v)}{\partial r} \left(\left[v_r\right]_{(b)} + \left[w_r\right]_{(b)} \right) \right\} r\,dv. \tag{1.13}$$

On the other hand, in realistic conditions we must take into account the effect of surface tractions caused by viscosity which was neglected in the above derivations. Using the local drag coefficient C_D, the thrust T_D and the torque Q_D due to the surface tractions can be expressed in parallel with (1.13) as

$$T_D = -\frac{1}{2}\rho \sum_{k=1}^{N} \int_{r_B}^{r_o} dr \int_{v_L(r)}^{v_T(r)} C_D \left\{ 1 + \left(\frac{\partial x_b(r,v)}{r\,\partial v} \middle/ \frac{\partial\theta_b(r,v)}{\partial v} \right)^2 \right\}$$
$$\times \left(r\dot{\theta}_p + \left[v_\theta\right]_{(b)} + \left[w_\theta\right]_{(b)} \right) \left(\dot{x}_p + \left[v_x\right]_{(b)} + \left[w_x\right]_{(b)} \right) r\,dv,$$

$$Q_D = \frac{1}{2}\rho \sum_{k=1}^{N} \int_{r_B}^{r_o} dr \int_{v_L(r)}^{v_T(r)} C_D \left\{ 1 + \left(\frac{\partial x_b(r,v)}{r\,\partial v} \middle/ \frac{\partial\theta_b(r,v)}{\partial v} \right)^2 \right\}$$
$$\times \left(r\dot{\theta}_p + \left[v_\theta\right]_{(b)} + \left[w_\theta\right]_{(b)} \right)^2 \cdot r^2\,dv. \tag{1.14}$$

Then adding (1.13) and (1.14) we obtain the expressions for the total thrust T and torque Q acting on the propeller, and also for the efficiency η:

$$T = T_o + T_D, \quad Q = Q_o + Q_D, \quad \eta = (\dot{x}_p T)/(\dot{\theta}_p Q). \tag{1.15}$$

Thus we obtain in general the performance characteristics of a given propeller working under an unsteady state.

Then we shall consider the case where the movement of the propeller is quasi-steady, i.e., $\dot{x}_p \doteq \bar{V}$, $\dot{\theta}_p = \Omega$, whereas the outer flow $[v_x]_{(b)}$, $[v_r]_{(b)}$ and $[v_\theta]_{(b)}$ is oscillating. The coordinates fixed to the propeller (ξ, τ, ζ) is defined by $\xi = x - \bar{V}t$, $\tau = r$ and $\zeta = \theta - \Omega t$. However, we shall use hereunder the notation (x, r, θ) in place of (ξ, τ, ζ). In this case averaging (1.12) with respect to time, we obtain

10

$$\frac{1}{4\pi r} \sum_{k=1}^{N} \int_{r_B}^{r_o} dr' \int_{v_L(r')}^{v_T(r')} \gamma(r',v')\ dv' \int_0^{\infty} \left[\left\{ r\ \frac{\partial}{\partial x} - \left(\frac{\partial x_b(r,v)}{r\,\partial v} \bigg/ \frac{\partial \theta_b(r,v)}{\partial v} \right) \frac{\partial}{\partial \theta} \right. \right.$$

$$- r \left(\frac{\partial x_b(r,v)}{\partial r} - \frac{\partial x_b(r,v)}{\partial v}\ \frac{\partial \theta_b(r,v)}{\partial r} \bigg/ \frac{\partial \theta_b(r,v)}{\partial v} \right) \frac{\partial}{\partial r} \right\} \left\{ r'\ \frac{\partial}{\partial x} - \frac{\partial \tilde{x}(r',\varphi)}{r'\partial \varphi}\ \frac{\partial}{\partial \varphi} \right.$$

$$\left. + r' \left(\frac{\partial x_b(r',v')}{\partial r} - \frac{\partial \theta_b(r',v')}{\partial r'}\ \frac{\partial \tilde{x}(r',\varphi)}{\partial \varphi} + \frac{\partial \tilde{x}(r',v)}{\partial r'} \right) \frac{\partial}{\partial r_f'} \right\} \frac{1}{R_{f2}} \right]_{\substack{r_f'=r' \\ x=x_b(r,v) \\ \theta=\theta_b(r,v)}} d\varphi$$

$$= \left(\frac{\partial x_b(r,v)}{r\partial v} \bigg/ \frac{\partial v_b(r,v)}{\partial v} \right) \left(\Omega r + \left[\tilde{v}_z \right]_{(b)} \right) - \left(\overline{V} + \left[\tilde{v}_x \right]_{(b)} \right)$$

$$+ \left(\frac{\partial x_b(r,v)}{\partial r} - \frac{\partial x_b(r,v)}{\partial v}\ \frac{\partial v_b(r,v)}{\partial r} \bigg/ \frac{\partial \theta_b(r,v)}{\partial v} \right) \left[\tilde{v}_r \right]_{(b)}, \tag{1.16}$$

where

$$R_{f2} = \sqrt{ (\tilde{x}(r',z) + x_b(r',v') - x)^2 + r_f'^2 + r^2 - 2r_f'r\ \cos(z + \theta_b(r',v') - \varphi + 2\pi(k-1)/N)},$$

and $\gamma(r,v)$, $[\tilde{v}_x]_{(b)}$, $[\tilde{v}_r]_{(b)}$ and $[v_z]_{(b)}$ represent the time averages of $\gamma(r,v,t)$, $[v_x]_{(b)}$, $[v_r]_{(b)}$ and $[v_z]_{(b)}$ at a constant radius respectively. On the other hand, in the procedure of calculations of T and Q from (1.13), (1.14) and (1.15), we may also safely obtain the average values under the approximation neglecting the terms of higher order of fluctuations in these expressions. Averaging further (1.10), the velocity potential $\overline{\varphi}_p$ can be expressed as

$$\overline{\varphi}_p = \frac{1}{4\pi} \sum_{k=1}^{N} \int_{r_B}^{r_o} dr' \int_{v_L(r)}^{v_T(r)} \gamma(r',v')\ dv' \int_0^{\pi} \left[\left\{ r'\ \frac{\partial}{\partial x} - \frac{\partial \hat{x}(r',z)}{r'\partial z}\ \frac{\partial}{\partial z} \right. \right.$$

$$\left. + r' \left(\frac{\partial x_b(r',v')}{\partial r'} - \frac{\partial \theta_b(r',v')}{\partial r'}\ \frac{\partial \tilde{x}(r',z)}{\partial z} + \frac{\partial \tilde{x}(r',z)}{\partial r'} \right) \frac{\partial}{\partial r_f'} \right\} \frac{1}{R_{f2}} \right]_{r_f'=r'} dz . \tag{1.17}$$

Then we shall here examine the form of the bound vortices, which is determined by the expressions (1.1) through the functions $x_b(r,v)$ and $\theta_b(r,v)$. For the purpose, we shall consider now the two ways of approximation for $\theta_b(r,v)$. At first, we take the form

$$\theta_b(r,v) = \frac{1}{2} \left[\theta_L(r) + \theta_T(r) \right] + \frac{1}{2} \left[\theta_T(r) - \theta_L(r) \right] v , \tag{1.18}$$

where $\theta_L(r)$ and $\theta_T(r)$ correspond to the leading and trailing edges of the blade respectively, hence

11

$$\theta_L(r) \;\lesseqgtr\; \theta_b(r,v) \;\lesseqgtr\; \theta_T(r), \quad -1 < v < 1.$$

In this case, using a parameter $a(r)$, we can express $x_b(r,v)$ in the approximate form

$$x_b(r,v) \;\doteqdot\; x_0(r) + \frac{1}{2} a(r) \left[\theta_T(r) - \theta_L(r)\right] v. \tag{1.19}$$

The expression (1.19) means physically that the vortex sheets bounded to the propeller blades are placed in the helical surface with radially varying pitch $2\pi a(r)$, and further that these vortices are lying along equi-chord lines on the surfaces of the blades.

Next, if we take the angular coordinate θ as v, then

$$\theta_b(r,v) = \theta, \tag{1.20}$$

where

$$\theta_L(r) \;\lesseqgtr\; \theta \;\lesseqgtr\; \theta_T(r).$$

In this case we obtain

$$x_b(r,\theta) \;\doteqdot\; x_0(r) + a(r) \left\{\theta - \frac{1}{2}\left[\theta_L(r) + \theta_T(r)\right]\right\}. \tag{1.21}$$

This is the form adopted in the previous paper [1].

2. THEORY OF PROPELLER IN STEADY STATE

In this section we shall examine further the performance characteristics of the propeller working in steady state. Since the velocity potential φ does not generally contain the variable t explicitly in this case, the expression (1.10) or (1.17) is re-expressed as follows:

$$\bar{\varphi}_p = \int_{r_B}^{r_0} dr' \int_{v_L(r')}^{v_T(r')} \gamma(r',v') \, Q(x,r,\theta; r',v') \, dv', \tag{2.1}$$

where

$$Q(x,r,\theta; r',v') = \frac{1}{4\pi} \sum_{k=1}^{N} \int_0^\infty \left[\left\{r' \; \frac{\partial}{\partial x} - \frac{\partial \widetilde{x}(r',\varphi)}{r'\partial\varphi} \; \frac{\partial}{\partial\varphi}\right.\right.$$

$$\left.\left. + r'\left(\frac{\partial x_b(r',v')}{\partial r'} - \frac{\partial \theta_b(r',v')}{\partial r'} \; \frac{\partial \widetilde{t}(r',\varphi)}{\partial\varphi} + \frac{\partial \widetilde{x}(r',\varphi)}{\partial r'}\right)\frac{\partial}{\partial r'_f}\right\} \frac{1}{R_{f^2}}\right]_{r'_f=r'} d\varphi, \tag{2.2}$$

$$R_{f^2} = \sqrt{\left[\widetilde{x}(r',\varphi) + x_b(r',v') - x\right]^2 + r_f'^2 + r^2 - 2r_f'r\cos\left[\varphi + \theta_b(r',v') - \theta + 2\pi(k-1)/N\right]}.$$

12

Then the boundary condition (1.16) can be re-expressed as

$$\frac{1}{r} \int_{r_B}^{r_o} dr' \int_{v_L(r')}^{v_T(r')} \gamma(r',v') \ S(r',v'; r,v) \, dv'$$

$$= \left(\frac{\partial x_b(r,v)}{r \partial v} \middle/ \frac{\partial \theta_b(r,v)}{\partial v} \right) \left(\Omega r + \left[\bar{v}_\theta \right]_{(b)} \right) - \left(\overline{V} + \left[\bar{v}_x \right]_{(b)} \right)$$

$$+ \left(\frac{\partial x_b(r,v)}{\partial r} - \frac{\partial x_b(r,v)}{\partial v} \ \frac{\partial \theta_b(r,v)}{\partial r} \middle/ \frac{\partial \theta_b(r,v)}{\partial v} \right) \left[\bar{v}_r \right]_{(b)}, \tag{2.3}$$

where

$$S(r',v'; r,v) = \left[\left\{ r \frac{\partial}{\partial x} - \frac{a(r,v)}{r} \ \frac{\partial}{\partial \theta} - r \left(\frac{\partial x_b(r,v)}{\partial r} \right. \right. \right.$$

$$\left. \left. - a(r,v) \ \frac{\partial \theta_b(r,v)}{\partial r} \right) \frac{\partial}{\partial r} \right\} Q(x,r,\theta; r',v') \right]_{\substack{x=x_b(r,v) \\ \theta=\theta_b(r,v)}}, \tag{2.4}$$

$$a(r,v) = \frac{\partial x_b(r,v)}{\partial v} \middle/ \frac{\partial \theta_b(r,v)}{\partial v} \ .$$

On the other hand, from (1.5) and (2.1) the components of the induced velocity $\bar{w}_x$, $\bar{w}_r$ and $\bar{w}_\theta$ are re-expressed as

$$\left.\begin{array}{l} \bar{w}_x = \displaystyle\int_{r_B}^{r_o} dr' \int_{v_L(r')}^{v_T(r')} \gamma(r',v') \ \frac{\partial}{\partial x} \ Q(x,r,\theta; r',v') \, dv', \\[2.5em] \bar{w}_r = \displaystyle\int_{r_B}^{r_o} dr' \int_{v_L(r')}^{v_T(r')} \gamma(r',v') \ \frac{\partial}{\partial r} \ Q(x,r,\theta; r',v') \, dv', \\[2.5em] \bar{w}_\theta = \displaystyle\int_{r_B}^{r_o} dr \int_{v_L(r')}^{v_T(r')} \gamma(r',v') \ \frac{\partial}{r \partial \theta} \ Q(x,r,\theta; r',v') \, dv'. \end{array}\right\} \tag{2.5}$$

Finally (1.13), (1.14) and (1.15) are re-expressed as follows:

$$\left.\begin{array}{l} T_o = \ \partial N \displaystyle\int_{r_B}^{r_o} dr \int_{v_L(r)}^{v_T(r)} \gamma(r,v) \left\{ \Omega r + \left[\bar{v}_\theta \right]_{(b)} + \left[\bar{w}_\theta \right]_{(b)} \right. \\[2em] \left. \qquad - \frac{r \partial \theta_b(r,v)}{\partial r} \left(\left[\bar{v}_r \right]_{(b)} + \left[\bar{w}_r \right]_{(b)} \right) \right\} dr \ , \end{array}\right\} \begin{array}{l} (2.6) \\ (\text{Cont.}) \end{array}$$

13

$$Q_o = \rho N \int_{r_B}^{r_o} dr \int_{v_L(r)}^{v_T(r)} \gamma(r,v) \left\{ \overline{V} + \left[\overline{v}_x\right]_{(b)} + \left[\overline{w}_x\right]_{(b)} \right.$$

$$\left. - \frac{\partial x_b(r,v)}{\partial r} \left(\left[\overline{v}_r\right]_{(b)} + \left[\overline{w}_r\right]_{(b)} \right) \right\} r dr ,$$

$$T_D = -\frac{1}{2} \rho N \int_{r_B}^{r_o} dr \int_{v_L(r)}^{v_T(r)} C_D \left\{ 1 + \left(\frac{\partial x_b(r,v)}{r \partial v} \middle/ \frac{\partial \phi_b(r,v)}{\partial v} \right)^2 \right\}$$

$$\times \left(\Omega r + \left[\overline{v}_\phi\right]_{(b)} + \left[\overline{w}_\phi\right]_{(b)} \right) \left(\overline{V} + \left[\overline{v}_x\right]_{(b)} + \left[\overline{w}_x\right]_{(b)} \right) r dr , \qquad (2.6)$$

$$Q_D = \frac{1}{2} \rho N \int_{r_B}^{r_o} dr \int_{v_L(r)}^{v_T(r)} C_D \left\{ 1 + \left(\frac{\partial x_b(r,v)}{r \partial v} \middle/ \frac{\partial \phi_b(r,v)}{\partial v} \right)^2 \right\}$$

$$\times \left(\Omega r + \left[\overline{v}_\phi\right]_{(b)} + \left[\overline{w}_\phi\right]_{(b)} \right)^2 r^2 dr ,$$

$$T = T_o + T_D , \quad Q = Q_o + Q_D , \quad \eta = (\overline{V}T)/(\Omega Q) .$$

When principal dimensions of the propeller and a velocity of the outer flow are given, we can calculate the value of $\gamma(r,v)$ using (2.3) and (2.4), and therefore the induced velocity on the blade $\left[\overline{w}_x\right]_{(b)}$, $\left[\overline{w}_r\right]_{(b)}$ and $\left[\overline{w}_\phi\right]_{(b)}$ using (2.5). Thus we can obtain the performance characteristics in this case from (2.6).

Then we shall compare the expressions (2.5) with the formulas deduced from the law of Biot-Savart. At first, putting, for convenience,

$$X = \tilde{x}(r',v) - x_b(r',v') - x ,$$
$$\Theta = v + \phi_b(r',v') - \phi + 2\pi(k-1)/N . \qquad (2.7)$$

and calculating the integrand of (2.5) by means of (2.2), we obtain the following expressions:

$$\frac{\partial}{\partial x} Q(x,r,\phi:r',v') = \frac{1}{4\pi} \sum_{k=1}^{N} \left(\frac{\partial}{\partial r'} \int_0^\pi \frac{r'(r'-r\cos\Theta)}{R_2^3} dv \right.$$

$$\left. - \left[\frac{r\sin\Theta - r'(r'-r\cos\Theta)\frac{\partial\Theta}{\partial r'}}{R_2^3} \right]_{v=0} \right) . \qquad (2.8)$$
$$\text{(Cont.)}$$

14

$$\frac{\partial}{\partial r} Q(x, r, \theta; r', v') = \frac{1}{4\pi} \sum_{k=1}^{N} \left(\frac{\partial}{\partial r'} \int_0^{\infty} \frac{\frac{\partial \tilde{x}(r', \varphi)}{\partial \varphi} r' \sin \Theta - r'X \cos \Theta}{R_2^3} d\varphi \right.$$
$$\left. - \left[\frac{X \sin \Theta - r' \sin \Theta \frac{\partial X}{\partial r'} + r'X \cos \Theta \frac{\partial \Theta}{\partial r'}}{R_2^3} \right]_{\varphi=0} \right),$$

$$\left. \frac{\partial}{r \partial \theta} Q(x, r, \theta; r', v') = \frac{1}{4\pi} \sum_{k=1}^{N} \left(\frac{\partial}{\partial r'} \int_0^{\infty} - \frac{\left\{ Xr' \sin \Theta + \frac{\partial \tilde{x}(r', \varphi)}{\partial \varphi} (r' \cos \Theta - r) \right\}}{R_2^3} d\varphi \right.$$
$$\left. - \left[\frac{-X \cos \Theta + (r' \cos \Theta - r) \frac{\partial X}{\partial r'} + r'X \sin \frac{\partial \Theta}{\partial r'}}{R_2^3} \right]_{\varphi=0} \right) \right\} \quad (2.8)$$

where

$$R_2 = \sqrt{X^2 + r'^2 + r^2 - 2r'r \cos \Theta}.$$

Then, substituting (2.8) in (2.5), and integrating (2.5) by parts, we can prove that the integrals corresponding to the first and second terms of the right hand side of (2.8) agree with the components of the induced velocities obtained by integrating the free and bound vortices by means of the law of Biot-Savart respectively.

Then, in order to simplify the calculations, we shall adopt the expressions (1.20) and (1.21), which means $a(r, v) = a(r)$ in (2.4), and assume further

$$a(r) = a, \qquad x_b(r, \tau) = a\tau \qquad (2.9)$$

for the form of the bound vortices, and

$$\frac{\partial \tilde{x}(r, \tau)}{\partial \tau} = h(\tau), \qquad \frac{\partial \tilde{x}(r, \tau)}{\partial r'} = 0 \qquad (2.10)$$

for the form of the free vortices. The expressions (2.9) and (2.10) mean that the surfaces of the bound and free vortex sheets are replaced by the helical surfaces which have constant pitches over the radial direction respectively. Introducing further the variables ε_x and ε_φ by

$$\left. \begin{array}{c} x_b(r, \tau) - x = a\tau - x = h(\tau)\varepsilon_x, \\ \tau' - \tau = \varepsilon_\varphi. \end{array} \right\} \qquad (2.11)$$

(2.1) and (2.2) will be re-expressed as

15

$$\overline{\varphi}_p = \int_{r_B}^{r_o} dr' \int_{\theta_L(r')}^{\theta_T(r')} \gamma(r',\theta') \, Q(x,r,\theta;r',\theta') \, d\theta', \tag{2.12}$$

where

$$Q(x,r,\theta;r',\theta') = -\frac{1}{4\pi} \sum_{k=1}^{N} \int_0^{\infty} \left[\left(\frac{r'}{h(\varphi)} \frac{\partial}{\partial \varepsilon_x} - \frac{h(\varphi)}{r'} \frac{\partial}{\partial \varepsilon_\theta} \right) \frac{1}{R_3} \right]_{\substack{\varepsilon_x = \frac{1}{h(\varphi)}(a\theta'-x) \\ \varepsilon_\theta = \theta'-\theta}} d\varphi \quad ,$$

$$R_3 = \sqrt{h(\varphi)^2 (\varphi+\varepsilon_x)^2 + r'^2 + r^2 - 2r'r \cos(\varphi + \varepsilon_\theta + 2\pi(k-1)/N)} \quad . \tag{2.13}$$

And also neglecting the higher order terms in (2.3) and (2.4), we obtain

$$\frac{1}{r} \int_{r_B}^{r_o} dr' \int_{\theta_L(r')}^{\theta_T(r')} \gamma(r',\theta') \, S(r',\theta';r,\theta) \, d\theta'$$

$$= \frac{\partial x_b(r,\theta)}{r \partial \theta} \left(\Omega r + \left[\overline{v}_\theta \right]_{(b)} \right) - \left(\overline{V} + \left[\overline{v}_x \right]_{(b)} \right) , \tag{2.14}$$

where

$$S(r',\theta';r,\theta)$$

$$= \frac{1}{4\pi} \sum_{k=1}^{N} \int_0^{\pi} \left[\left(\frac{r}{h(\varphi)} \frac{\partial}{\partial \varepsilon_x} - \frac{a}{r} \frac{\partial}{\partial \varepsilon_\theta} \right) \left(\frac{r'}{h(\varphi)} \frac{\partial}{\partial \varepsilon_x} - \frac{h(\varphi)}{r'} \frac{\partial}{\partial \varepsilon_\theta} \right) \frac{1}{R_3} \right]_{\substack{\varepsilon_x = \frac{a}{h(\varphi)}(\theta'-\theta) \\ \varepsilon_\theta = \theta'-\theta}} d\varphi \quad . \tag{2.15}$$

Furthermore, approximating $\gamma(r,\theta)$ by

$$\gamma(r,\theta) \doteqdot \frac{2}{\pi \left[\theta_T(r) - \theta_L(r) \right]} \sqrt{\frac{\theta_T(r) - \theta}{\theta - \theta_L(r)}} \, \Gamma(r) . \tag{2.16}$$

then multiplying the equation (2.14) by the operator

$$\frac{2}{\pi \left[\theta_T(r) - \theta_L(r) \right]} \int_{\theta_L(r)}^{\theta_T(r)} d\theta \sqrt{\frac{\theta - \theta_L(r)}{\theta_T(r) - \theta}} \quad . \tag{2.17}$$

and calculating the integral of the left hand side by means of the formula of approximation [3]

16

$$\frac{1}{\pi} \int_{-1}^{1} \sqrt{\frac{1+x}{1-x}} \, f(x) \, dx \doteq f\left(\frac{1}{2}\right), \tag{2.18}$$

where $f(x)$ is an arbitrary function, we obtain finally

$$\frac{1}{r} \int_{r_B}^{r_o} \Gamma(r') \, S\left[r', \theta_{1/4}(r'); r, \theta_{3/4}(r)\right] dr' = a(r)\left(\Omega + \left[\bar{v}_\theta\right]_{(b)}\Big/r\right) - \left(\overline{V} + \left[\bar{v}_x\right]_{(b)}\right), \tag{2.19}$$

where

$$a(r) = \frac{2}{\pi \left[\theta_T(r) - \theta_L(r)\right]} \int_{\theta_L(r)}^{\theta_T(r)} \frac{\partial x_b(r,\theta)}{r\partial\theta} \sqrt{\frac{\theta - \theta_L(r)}{\theta_T(r) - \theta}} \, dr, \tag{2.20}$$

$$\left. \begin{aligned}
\theta_{1/4}(r') &= \frac{3\theta_L(r')}{4} + \frac{\theta_T(r')}{4}, \\
\theta_{3/4}(r) &= \frac{\theta_L(r)}{4} + \frac{3\theta_T(r)}{4},
\end{aligned} \right\} \tag{2.21}$$

and $\left[\bar{v}_x\right]_{(b)}$ and $\left[\bar{v}_\theta\right]_{(b)}$ are taken as average values of $\left[\bar{v}_x\right]_{(b)}$ and $\left[\bar{v}_\theta\right]_{(b)}$ with respect to the chord direction instead of the more correct values of them, i.e., those on the 3/4-chord lines $\theta = \theta_{3/4}(r)$, because $\left[\bar{v}_x\right]_{(b)}$ and $\left[\bar{v}_\theta\right]_{(b)}$ generally vary very little along the x-axis. Equation (2.20) means that $2 \pi a(r)$ is the pitch of the zero lift line of the blade section and a in (2.9) is taken so as to coincide with $a(r)$ at the equivalent section $r = r_1$ of the blade.

From (2.9), (2.16) and (2.6) we can obtain

$$\left. \begin{aligned}
T_o &= \rho N \int_{r_B}^{r_o} \Gamma(r) \left\{ \Omega r + \left[\bar{\bar{v}}_\theta\right]_{(b)} + \left[\bar{\bar{w}}_\theta\right]_{(b)} \right\} dr, \\[2ex]
Q_o &= \rho N \int_{r_B}^{r_o} \Gamma(r) \left\{ \overline{V} + \left[\bar{\bar{v}}_x\right]_{(b)} + \left[\bar{\bar{w}}_x\right]_{(b)} \right\} r \, dr, \\[2ex]
T_D &= -\frac{1}{2} \rho N \int_{r_B}^{r_o} C_D \left[\theta_T(r) - \theta_L(r)\right] \left(1 + \frac{a^2}{r^2}\right) \left(\Omega r + \left[\bar{\bar{v}}_\theta\right]_{(b)} + \left[\bar{\bar{w}}_\theta\right]_{(b)}\right) \\[1ex]
&\qquad\qquad\qquad\qquad\qquad \times \left(\overline{V} + \left[\bar{\bar{v}}_x\right]_{(b)} + \left[\bar{\bar{w}}_x\right]_{(b)}\right) r \, dr, \\[2ex]
Q_D &= \frac{1}{2} \rho N \int_{r_B}^{r_o} C_D \left[\theta_T(r) - \theta_L(r)\right] \left(1 + \frac{a^2}{r^2}\right) \left(\Omega r + \left[\bar{\bar{v}}_\theta\right]_{(b)} + \left[\bar{\bar{w}}_\theta\right]_{(b)}\right)^2 r^2 \, dr,
\end{aligned} \right\} \begin{matrix} (2.22) \\ (\text{Cont.}) \end{matrix}$$

17

$$T = T_o + T_D, \quad Q = Q_o + Q_D, \quad \eta = \bar{V}T/(\Omega Q), \qquad \left.\right\} \quad (2.22)$$

where $[\bar{\bar{w}}_x]_{(b)}$ and $[\bar{\bar{w}}_\theta]_{(b)}$ represent the values of the components of the induced velocity $[\bar{w}_x]_{(b)}$ and $[\bar{w}_\theta]_{(b)}$ on the 1/4-chord lines, and $[\bar{\bar{v}}_x]_{(b)}$ and $[\bar{\bar{v}}_\theta]_{(b)}$ are the same as those defined above. From (2.5), (2.13), (2.16) and (2.18), we have

$$\left[\bar{\bar{w}}_x\right]_{(b)} = \int_{r_B}^{r_o} \Gamma(r') \left[\frac{\partial}{\partial x} Q(x, r, \theta; r', \theta_{1/4}(r'))\right]_{\substack{x = a\theta_{1/4}(r) \\ \theta = \theta_{1/4}(r)}} dr',$$

$$\left[\bar{\bar{w}}_\theta\right]_{(b)} = \int_{r_B}^{r_o} \Gamma(r') \left[\frac{\partial}{r\partial\theta} Q(x, r, \theta; r', \theta_{1/4}(r'))\right]_{\substack{x = a\theta_{1/4}(r) \\ \theta = \theta_{1/4}(r)}} dr',$$

and after some deductions we obtain

$$\left[\bar{\bar{w}}_x\right]_{(b)} = \frac{r}{r^2 + h^2} \int_{r_B}^{r_o} \Gamma(r') \, S_T(r', r) \, dr' \qquad \left.\right\}$$

$$\left[\bar{\bar{w}}_\theta\right]_{(b)} = -\frac{h}{r^2 + h^2} \int_{r_B}^{r_o} \Gamma(r') \, S_T(r', r) \, dr' \qquad \left.\right\} \quad (2.23)$$

where

$$S_T(r', r) = \left[S(r', \theta'; r, \theta)\right]_{\theta' = \theta}.$$

At this stage it remains to determine the pitch of the free vortices. For this purpose, we shall consider the simpler case of a wing placed in an uniform flow [4,5]. When angle of attack of the wing is small, the free vortices sprung from the bound vortices follow along surface of the wing and separate from it at the trailing edge, and the linear theory holds in this case. On the other hand, when the angle of attack is increased, the free vortices are separated at an intermediate position on the wing in front of the trailing edge, and when the angle of attack is further increased, a stall is caused at last, the condition of which depends largely on the form of the camber line of the wing. Furthermore, when the leading and side edges of the wing are very sharp, the flow is separated at these edges irrespective of the angle of attack. In these cases a non-linear effect on the lift coefficient of the wing becomes important, and this effect is particularly appreciable when the aspect ratio of the wing is small. Contrary to the cases, when the aspect ratio of the wing is very large, the non-linear effect becomes negligible even if the leading and side edges are very sharp or the wing is heavily loaded. And for these cases the well known linear theory can be applied. These considerations for the single wing can be also applied for the case of the propeller in which the following three cases are distinguished:

18

a. a flow without separation at the leading edge,
b. a flow separated all over the leading edge,
c. a flow separated partially at the leading edge.

a. In this case, in order to calculate the average effect of the system of the free vortices, we shall now introduce an assumption for the path of the free vortices that the free vortices sprung from the bound vortices on the blade follow initially along the helical surface with constant pitch as described by (1.21) or (2.9), leaving the blade at the line $\theta = \theta_1(r)$ instead of the trailing edge, and receding along the helical surface with another pitch. In this case we can take

$$\tau' = \tau + \theta_b(r,v) - \theta_1(r),$$

$$\tilde{x}(r,\tau) = a(r)\tau', \quad \text{for} \quad \theta_b(r,v) - \theta_1(r) < \tau' < 0 \quad (2.24)$$

$$= h(r)\tau', \quad \text{for} \quad 0 < \tau' < \infty$$

or using (2.9), for equivalent section $r = r_1$ of the blade

$$\tau' = \tau + \bar{\theta} - \theta_1(r),$$

$$h(\tau) = a, \quad \text{for} \quad \bar{\theta} - \theta_1(r) < \tau' < 0$$

$$= h, \quad \text{for} \quad 0 < \tau' < \infty.$$

On the other hand, since the equation (2.19) means that the bound vortices concentrate on the $1/4$-chord lines of the propeller blades, we may deduce that the free vortices are carried away with the velocity nearly equal to that in the neighbourhood of the concentrated vortices when the width of the blade is not large. Hence, using (2.24), the condition (1.8) for the free vortices can be replaced by

$$\overline{V} - \left[\bar{\bar{v}}_x\right]_b + \left[\bar{\bar{w}}_x\right]_{(b)} = h(r)\tau_0,$$

$$\Omega r + \left[\bar{\bar{v}}_\theta\right]_b + \left[\bar{\bar{w}}_\theta\right]_{(b)} = r\tau_0.$$

where $\left[\bar{\bar{w}}_x\right]_{(b)}$ and $\left[\bar{\bar{w}}_\theta\right]_{(b)}$ are used for approximation in place of $\left[w_x\right]_{(f)}$ and $\left[w_\theta\right]_{(f)}$ in (1.8), and the second equation of (1.8) can not hold since the contraction of the free vortices is neglected. From the above equations we have

$$h(r) = \frac{\overline{V} - \left[\bar{\bar{v}}_x\right]_{(b)} + \left[\bar{\bar{w}}_x\right]_{(b)}}{\Omega + \left[\bar{\bar{v}}_\theta\right]_b / r + \left[\bar{\bar{w}}_x\right]_{(b)} / r}.$$

Furthermore, for the equivalent section $r = r_1$ of the blade we have

$$h = \frac{\overline{V} + \left[\bar{\bar{v}}_x\right]_{(b)(r_1)} + \left[\bar{\bar{w}}_x\right]_{(b)(r_1)}}{\Omega + \left[\bar{\bar{v}}_\theta\right]_{(b)(r_1)} / r_1 + \left[\bar{\bar{w}}_x\right]_{(b)(r_1)} / r_1}. \quad (2.25)$$

19

where $[\bar{\bar{v}}_x]_{(b)(r_1)}$, $[\bar{\bar{w}}_x]_{(b)(r_1)}$, etc., represent the values of $[\bar{\bar{v}}_x]_{(b)}$, $[\bar{\bar{w}}_x]_{(b)}$, etc., at the equivalent section. For the lightly loaded propeller, we can assume $a = h$. In the previous paper [1] the theory is developed along this idea.

b. In this case we may avail the method used by Gersten [4] in this treatment of the single wing which has large chord length and arbitrary plan form. He represented a flow separated all over the back of the wing by appropriate systems of free vortices, in which the free vortices are assumed to leave the wing with half an angle of the angle of attack of the wing, thus he showed that the calculated values coincide with the experimental rectangular ones, delta or swept back wings in the range where the wings do not stall. The similar assumptions can be used in our case, that is, we assume that the free vortices springing from the points all over the blades recede forming the helices of constant pitch and retaining their strength without following the surface of the blade. In this case the pitch of the free vortices can be determined by using the following expressions:

$$\tilde{x}(r, \varphi) = h(r)\varphi,$$

$$h(r) = \frac{\sqrt{\left[r^2 + a(r)^2\right]\left[r^2 + h_o(r)^2\right]} - \left[r^2 - a(r)\,h_o(r)\right]}{a(r) + h(r)},$$

$$h_o(r) = \frac{\bar{V} + \left[\bar{\bar{v}}_x\right]_{(b)}}{\Omega + \left[\bar{\bar{v}}_\varphi\right]_{(b)}/r}.$$

From these expressions we have for the equivalent section $r = r_1$

$$\left.\begin{array}{c}h(\varphi) = h,\\[2mm]h = \dfrac{\sqrt{(r_1^2 + a^2)(r_1^2 + h_o^2)} - (r_1^2 - ah_o)}{a + h_o},\\[3mm]h_o = \dfrac{\bar{V} + \left[\bar{\bar{v}}_x\right]_{(b)(r_1)}}{\Omega + \left[\bar{\bar{v}}_\varphi\right]_{(b)(r_1)}/r_1}.\end{array}\right\} \qquad (2.26)$$

Then neglecting the higher order terms of $(a - h)$, we obtain

$$S(r', \varphi' : r, \varphi) \doteq \left[S(r', \varphi' : r, \varphi)\right]_{a=h} + (a-h)\left[\frac{\partial}{\partial a}S(r', \varphi' : r, \varphi)\right]_{a=h}. \qquad (2.27)$$

For simplicity, taking

$$\Gamma(r) \doteq \left\{a\left(\Omega + \left[\bar{\bar{v}}_\varphi\right]_{(b)(r_1)}/r_1\right) - \left(\bar{V} + \left[\bar{\bar{v}}_x\right]_{(b)(r_1)}\right)\right\}\left\{\Gamma_o(r) - (a-h)\,\Gamma_1(r)\right\}. \qquad (2.28)$$

and substituting this in (2.19), the following equations are obtained:

20

$$\frac{1}{r} \int_{r_B}^{r_o} \Gamma_o(r') \left[S(r', \theta_{1/4}(r'); r, \theta_{3/4}(r)) \right]_{a=h} dr'$$

$$= \frac{a(r) \left(\Omega + \left[\bar{\bar{v}}_\theta \right]_{(b)} / r \right) - \left(\bar{V} + \left[\bar{\bar{v}}_x \right]_{(b)} \right)}{a \left(\Omega + \left[\bar{\bar{v}}_\theta \right]_{(b)(r_1)} / r_1 \right) - \left(\bar{V} + \left[\bar{\bar{v}}_x \right]_{(b)(r_1)} \right)} \,,$$

$$\frac{1}{r} \int_{r_B}^{r_o} \Gamma_1(r') \left[S(r', \theta_{1/4}(r'); r, \theta_{3/4}(r)) \right]_{a=h} dr'$$

$$= - \frac{1}{r} \int_{r_B}^{r_o} \Gamma_o(r') \left[\frac{\partial}{\partial a} S(r', \theta_{1/4}(r'); r, \theta_{3/4}(r)) \right]_{a=h} dr \,.$$

$$(2.29)$$

The first equation of (2.29) coincides with the fundamental integral equation of the linear theory, and the second one is nothing but the equation determining the non-linear term $\Gamma_1(r')$. Hence solving (2.29) and using (2.28), the total $\Gamma(r')$ can be obtained. Substituting this $\Gamma(r')$ in (2.21), the induced velocity $[\bar{\bar{w}}_x]_{(b)}$ and $[\bar{\bar{w}}_\theta]_{(b)}$ can be obtained. Thus the performance characteristics can be obtained from (2.22).

c. This is the intermediate case between a. and b., and is difficult to be dealt with theoretically without using further assumptions.

3. NUMERICAL EXAMPLE IN STEADY STATE

In this section we shall examine further the approximate method to calculate the performance characteristics of a screw propeller in steady state. Taking into account the various numerical examples studied in the previous paper [1], we shall start our calculations using the expression as the appropriate form of $\Gamma(r)$

$$\Gamma(r) = \Gamma \frac{2}{r_o^2 - r_B^2} \sqrt{(r_o^2 - r^2)(r^2 - r_B^2)} \,. \tag{3.1}$$

where Γ is a circulation of the blade at the equivalent section $r = r_1$ and

$$r_1 = \sqrt{(r_o^2 - r_B^2)/2} \,. \tag{3.2}$$

Then multiplying both the sides of (2.19) by the operator

$$\frac{16}{\pi(r_o^2 - r_B^2)^2} \int_{r_B}^{r_o} dr\, r \sqrt{(r_o^2 - r^2)(r^2 - r_B^2)} \,. \tag{3.3}$$

21

we have

$$\Gamma \frac{32}{\pi(r_o^2 - r_B^2)} \int_{r_B}^{r_o} \sqrt{(r_o^2 - r^2)(r^2 - r_B^2)} \, dr \int_{r_B}^{r_o} \sqrt{(r_o^2 - r'^2)(r'^2 - r_B^2)}$$

$$\times \, S\left[r', \theta_{1/4}(r'); r, \theta_{3/4}(r)\right] dr' = a(\Omega + q_z) - (\overline{V} + q_x), \tag{3.4}$$

where

$$a = \frac{16}{\pi(r_o^2 - r_B^2)^2} \int_{r_B}^{r_o} a(r) \sqrt{(r_o^2 - r^2)(r^2 - r_B^2)} \; rdr \, .$$

$$q_x = \frac{16}{\pi(r_o^2 - r_B^2)^2} \int_{r_B}^{r_o} \left[\bar{\bar{v}}_x\right]_{(b)} \sqrt{(r_o^2 - r^2)(r^2 - r_B^2)} \; rdr \, .$$

$$q_z = \frac{16}{\pi(r_o^2 - r_B^2)^2} \int_{r_B}^{r_o} \frac{a(r)}{a} \left[\bar{\bar{v}}_z\right]_{(b)} \sqrt{(r_o^2 - r^2)(r^2 - r_B^2)} \; dr \, .$$

$$\doteq \frac{16}{\pi(r_o^2 - r_B^2)^2} \int_{r_B}^{r_o} \left[\bar{\bar{v}}_z\right]_{(b)} \sqrt{(r_o^2 - r^2)(r^2 - r_B^2)} \; dr \, .$$

$$\left. \right\} \tag{3.5}$$

and $2-a(r)$ is the pitch of the zero lift line of the blade section. Substituting (3.1) in (3.22) and (2.23), and performing the integrations, we have

$$T_o = \rho \frac{\pi(r_o^2 - r_B^2)}{8} N\Gamma(\Omega + q_z + u_z\Gamma) \, .$$

$$Q_o = \rho \frac{\pi(r_o^2 - r_B^2)}{8} N\Gamma(\overline{V} + q_x + u_x\Gamma) \, .$$

$$\left. \right\} \tag{3.6}$$

where

$$u_x = \frac{32}{\pi(r_o^2 - r_B^2)^3} \int_{r_B}^{r_o} \sqrt{(r_o^2 - r^2)(r^2 - r_B^2)} \; dr \; \frac{r^2}{r^2 - h^2}$$

$$\times \int_{r_B}^{r_o} S_T(r', r) \sqrt{(r_o^2 - r'^2)(r'^2 - r_B^2)} \; dr' \, . \tag{3.7}$$
<div style="text-align:right">(Cont.)</div>

22

$$u_\theta = \frac{32}{\pi(r_o^2 - r_B^2)^3} \int_{r_B}^{r_o} \sqrt{(r_o^2 - r^2)(r^2 - r_B^2)} \ dr \ \frac{h}{r^2 + h^2}$$

$$\times \int_{r_B}^{r_o} S_T(r',r) \sqrt{(r_o^2 - r'^2)(r'^2 - r_B^2)} \ dr' . \qquad (3.7)$$

Then assuming

$$C_D \left[\theta_T(r) - \theta_L(r) \right] (1 + a^2 r^2) \left(\Omega r + \left[\bar{v}_\theta \right]_{(t)} + \left[\bar{w}_\theta \right]_{(t)} \right)$$

$$\doteq \frac{2}{r_o^2 - r_B^2} \left[C_D r \left(\theta_T(r) - \theta_L(r) \right) (1 + a^2 r^2) \right]_{r=r_1} (\Omega - q_\theta - u_\theta^-) \sqrt{(r_o^2 - r^2)(r^2 - r_B^2)} .$$

T_D and Q_D are calculated approximately as

$$T_D = -N \left(\frac{\pi}{16} \right) (r_o^2 - r_B^2) \left[C_D r (\theta_T(r) - \theta_L(r)) (1 + a^2 r^2) \right]_{r=r_1}$$

$$\times (\Omega + q_\theta - u_\theta^-) (\bar{V} - q_x - u_x^-) .$$

$$Q_D = N \left(\frac{\pi}{32} \right) (r_o^4 - r_B^4) \left[C_D r (\theta_T(r) - \theta_L(r)) (1 + a^2 r^2) \right]_{r=r_1}$$

$$\times (\Omega + q_\theta - u_\theta^-)^2 . \qquad (3.8)$$

Finally we obtain

$$T = T_o - T_D . \quad Q = Q_o - Q_D . \quad \eta = (\bar{V}T)/(\Omega Q) . \qquad (3.9)$$

Defining the non-dimensional quantities as follows,

$$\Omega = 2\pi n . \qquad r_o = D/2 . \qquad T = \rho n^2 D^4 C_T . \qquad Q = \rho n^2 D^5 C_Q .$$

$$\Gamma = \Omega r_o^2 G . \qquad \bar{V} = \Omega r_o \nu . \qquad q_x = \bar{V} \bar{q}_x . \qquad q_\theta = \Omega \bar{q}_\theta .$$

$$u_x = (\bar{V}/\Omega r_o^2) \bar{u}_x . \qquad u_\theta = (1/r_o^2) \bar{u}_\theta . \qquad r = r_o \xi . \qquad r_B = r_o \xi_B .$$

$$r_1 = r_o \xi_1 . \qquad a(r) = r_o \odot (\xi) . \qquad a = r_o \alpha . \qquad h = r_o \iota_1 . \qquad \left. \right\} \quad (3.10)$$

and putting

$$\xi^2 = \frac{1 + \xi_B^2}{2} + \frac{1 - \xi_B^2}{2} t ,$$

$$S\left[r', \theta_{1/4}(r'), r, \theta_{3/4}(r)\right] = - \frac{4}{\pi(1 - \xi_B^2)} \frac{\xi' \xi}{(t' - t)^2} \left[F_o^B(t', t, \nu) + F_o^T(t', t, \nu_1)\right] , \tag{3.11}$$

where $F_o^B(t', t, \nu)$ and $F_o^T(t', t, \nu)$ are defined in the previous paper, (3.4) and (3.5) are re-expressed by

$$G = \left[\nu(1 - \bar{q}_z) - \nu_o(1 + q_x)\right] k_2 .$$

where

$$k_2 = - \frac{2}{\pi^2} \int_{-1}^{1} \sqrt{1 - t^2} \, dt \int_{-1}^{1} \sqrt{1 - t'^2} \left[F_o^B(t', t, \nu) + F_o^T(t', t, \nu_1)\right] \frac{dt'}{(t' - t)^2} . \tag{3.12}$$

$$\nu = \frac{2}{\pi} \int_{-1}^{1} \odot (\xi) \sqrt{1 - t^2} \, dt .$$

$$\bar{q}_x = \frac{2}{\pi} \int_{-1}^{1} \frac{\left[\bar{v}_x\right]_{b}}{\bar{V}} \sqrt{1 - t^2} \, dt . \tag{3.12}$$

$$\bar{q}_z = \frac{2}{\pi} \int_{-1}^{1} \frac{\left[\bar{v}_z\right]_{b}}{\bar{v}} \sqrt{1 - t^2} \, dt$$

and also (3.6), (3.7), (3.8) and (3.9) by

$$C_{T_o} = \frac{-3}{32} N(1 - \xi_B^2) G(1 - \bar{q}_z - \bar{q}_z G) .$$

$$C_{C_o} = \frac{-3}{64} N(1 - \xi_B^2) G \nu_o (1 - \bar{q}_x - \bar{q}_x G) .$$

$$C_{TD} = \frac{-3}{64} N(1 - \xi_B^2) C \nu_o (1 - \bar{q}_z - \bar{q}_z G)(1 - \bar{q}_x - \bar{q}_x G) \tag{3.14}$$

$$C_{OD} = \frac{-3}{256} N(1 - \xi_B^4) C(1 - \bar{q}_z - \bar{q}_z G)^2$$

$$C_T = C_{T_o} - C_{TD} . \quad C_Q = C_{C_o} - C_{OD} . \quad - = \bar{V}T \quad (3.0)$$

where

$$C = \left[C_D \xi + F_T(\xi) - F_L(\xi)(1 - t^2 \xi^2)\right]_{t = \xi_2} \tag{3.15}$$

24

$$\bar{u}_x = -\frac{2}{\pi^2 \nu_o} \int_{-1}^{1} \sqrt{1-t^2} \, dt \, \frac{\xi^2}{\xi^2 + \nu_1^2} \int_{-1}^{1} \sqrt{1-t'^2} \, F_o^T(t',t,\nu_1) \, \frac{dt'}{(t'-t)^2} \, ,$$

$$\bar{u}_\theta = -\frac{2}{\pi^2} \int_{-1}^{1} \sqrt{1-t^2} \, dt \, \frac{\nu_1}{\xi^2 + \nu_1^2} \int_{-1}^{1} \sqrt{1-t'^2} \, F_o^T(t',t,\nu_1) \, \frac{dt'}{(t'-t)^2} \, . \tag{3.16}$$

Furthermore for a given ν_o, ν_1 can be determined approximately from (2.26), we get

$$\nu_1 = \frac{\sqrt{(\xi_1^2 + \nu^2)(\xi_1^2 + \nu_o'^2)} - (\xi_1^2 - \nu \cdot \nu_o')}{\nu + \nu_o} \, .$$

$$\nu_o' = \nu_o \frac{1 - \bar{q}_x}{1 + \bar{q}_z} \, . \tag{3.17}$$

Using (3.17) we can obtain the value of ν_1 for a given ν_o.

For a given outer flow, for instance, in the case of open water $\bar{q}_x = \bar{q}_z = 0$ and for a given propeller for which $②(\xi)$, $\hat{s}_L(\xi)$ and $\hat{s}_T(\xi)$ and accordingly ν and $F_o^B(t',t,\nu)$ are given, we can calculate ν_1 from (3.17) and therefore $F_o^T(t',t,\nu)$ for a given ν_o. Then using (3.12) and (3.16), we obtain k_2 and G, and also $\bar{u}_x$ and $\bar{u}_z$. On the other hand, if C_D is assumed, we can calculate C from (3.15). Thus using these G, C, $\bar{u}_x$ and $\bar{u}_z$, we can calculate C_T and C_Q from (3.14). On the contrary, if C_T and C_Q for a given ν_o are known from experiments, we can calculate C and G from (3.14), using ν_1, $\bar{u}_x$ and $\bar{u}_z$ evaluated from (3.16) and (3.17) for the given ν and ν_o.

As examples, we shall compare the values of G calculated theoretically from (3.12) and (3.17) with those obtained by experiments using (3.17), (3.16) and (3.14). The propellers adopted are shown in the Table 1, and the results calculated are shown in Figs. 2-5. In this case, the results calculated theoretically from (3.12) is based on the linear theory. The discrepancy between the theory and the experiments is considered to be attributed to the non-linear effect. As shown in Figs. 2-5, when the pitch ratio is small, the non-linear effect is small. On the other hand, when the pitch ratio is large, the non-linear effect is very large, especially for the Gawn type in which the shape of the blade section is ogival. On the contrary, for the shape of the blade section of the B_5 - 50 type (T.T.R.T.) which is airfoil in main part excepting the place near the tips where the shape is ogival, the non-linear effect is not so large. The reason for this phenomenon can be explained from the standpoint mentioned in the last part of section 2 [6,7].

ACKNOWLEDGMENT
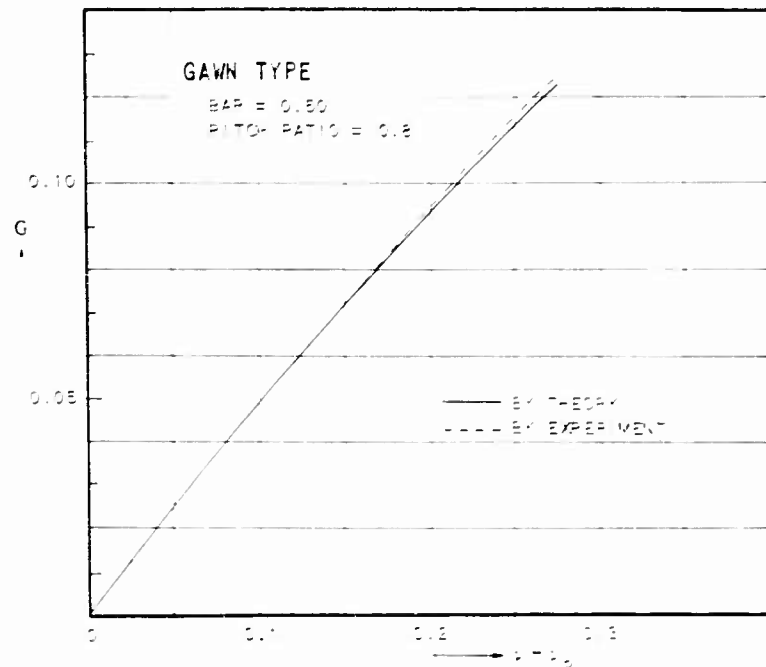
Fig. 2 - Comparison of G

Fig. 3 - Comparison of G

26
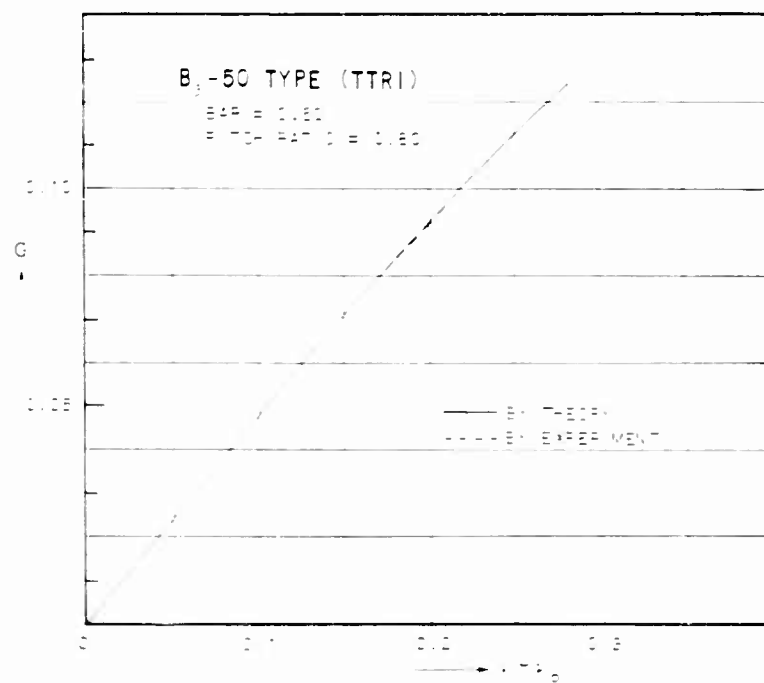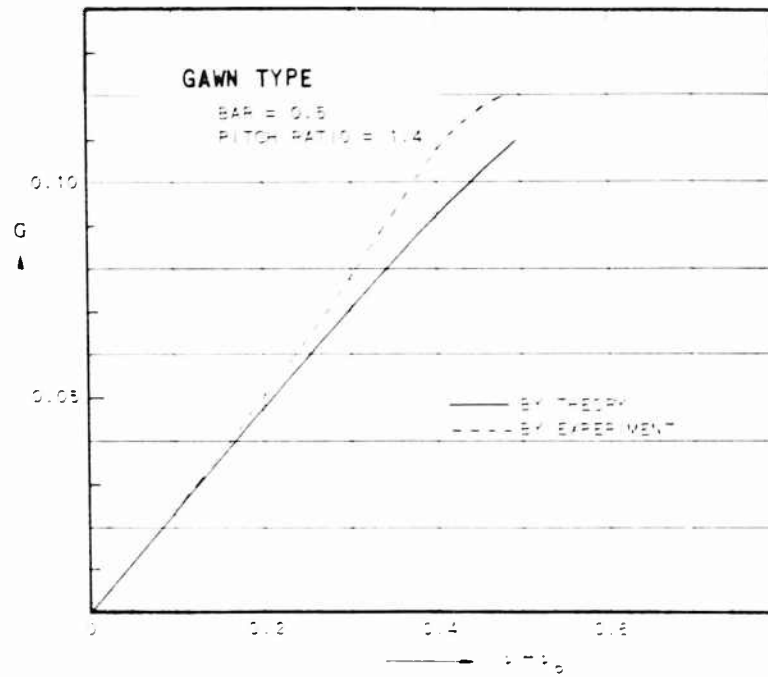
Fig. 4 - Comparison of G
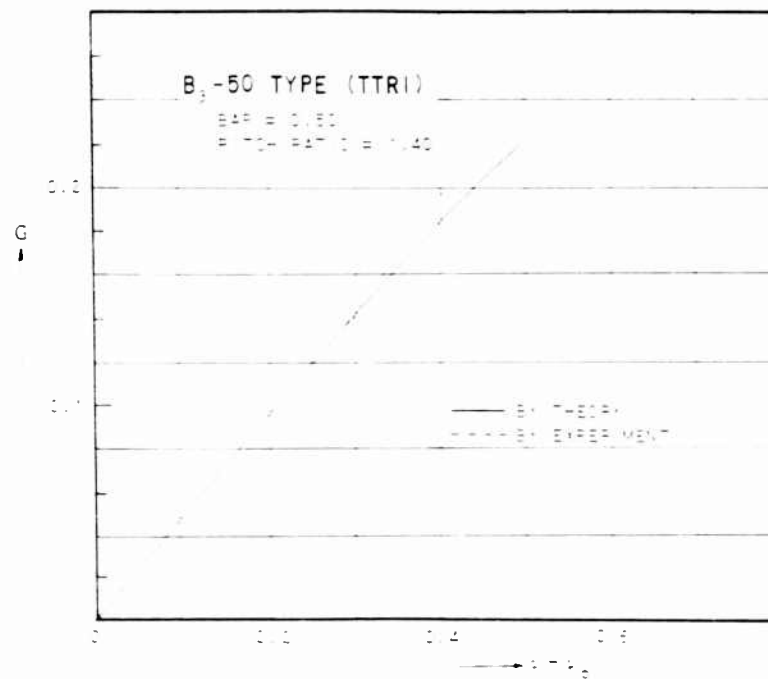
Fig. 5 - Comparison of G

Table 1

Experimenter	Gawn	Tsuchida (T.T.R.I.)
Type		B_3 - 50
Number of blade	3	3
Boss ratio	0.2	0.2
Blade area ratio	0.50	0.50
Blade thickness ratio	0.060	0.050
Rake	0	10° - 18°
Face pitch ratio	0.8, 1.4	0.8, 1.4
Blade section shape	ogival	airfoil (ogival at tips)
Developed blade outline	Elliptical	

in writing this paper, and also thanks to the Assistants Sunao Hasegawa and Kunio Ryū for their cooperation in the numerical calculations.

REFERENCES

1. R. Yamazaki, "A Study on Screw Propellers," Memoirs of the Faculty of Engineering, Kyushu University, Vol. 19, No. 1 (1960), p. 1

2. M. Iwasaki, "Vortex Theory of an Airscrew, in which Contraction or Expansion of Slip stream and Variation of Pitch of Vortex Sheets in it are taken into Consideration," Doctor Thesis of Kyushu University (1960)

3. J. Weissinger, "Neuere Entwicklungen in der Tragflügeltheorie bei inkompressibler Strömung," Z. Flugwiss. 4(1956), p. 225

4. K. Gersten, "Nichtlineare Tragflächentheorie für Rechteckflügel bei inkompressibler Strömung," Z. Flugwiss, 5(1957), p. 276

    K. Gersten, "Tragflügeltheorie bei Unterschallgeschwindigkeit," Jahrbuch 1958 der WGL, p. 25

5. G.E. Bartlett and R.J. Vidal, "Experimental Investigation of Influence of Edge Shape on the Aerodynamic Characteristics of Low Aspect Ratio Wings at Low Speeds," Jour. Aeron. Sci., Vol. 22 (1955), p. 690

6. R.W.L. Gawn, "Effect of Pitch and Blade Width on Propeller Performance," Trans. INA, Vol. 95 (1953), p. 157

7. K. Tsuchida, "Open Water Tests of 3-Blade Propellers," Journal of the Society of Naval Architects of Japan, No. 79 (1951), p. 1

*   *   *

COMPARISON OF PROPELLER DESIGN TECHNIQUES

C.-A. Johnsson
Swedish State Shipbuilding Experimental Tank
Göteborg, Sweden

ABSTRACT

In the present paper some propeller design methods, based on vortex theory, are discussed and compared. Using different combinations of lifting line and lifting surface theories propellers for two non-optimum loading cases have been designed. According to the resulting designs for one of the loading cases model propellers have been manufactured and submitted to open water and cavitation tunnel tests in homogeneous flow. The effective pitch and cavitation properties thus determined are compared with those theoretically predicted. In the cavitation tunnel also the axial component of the induced velocity behind the propeller has been measured at different radii and the values obtained compared with calculated values. For comparison also an optimum propeller has been designed, manufactured and tested.

Some of the conclusions drawn from the results are summarized at the end of the paper.

INTRODUCTION

In an earlier report [1] the author presented the results of a comparison between the application of different propeller theories all based on vortex theory, on an extreme loading case, characterized by a rather low advance ratio and an appreciable unloading of root and tip. Lifting line theories of Goldstein (λ-method), Guilloton, Lerbs (induction factor method) and Strscheletzky (induction factor method) were compared together with lifting surface theories developed by Ludwieg and Ginzel, Guilloton and Strscheletzky.

The theories were used for the design of three-bladed propellers of a given blade form for a loading case defined by the condition that a prescribed non-optimum circulation distribution should be obtained at an advance ratio, $J = 0.45$ in homogeneous flow.

29

According to some of the methods model propellers were manufactured and submitted to cavitation tunnel and open water tests.

The present investigation is a continuation of the investigation referred to. A new loading case is treated, some of the methods mentioned omitted and some new added. The experimental part of the investigation also includes measurement of the axial component of the induced velocity behind the propeller.

For comparison some calculations are performed for a corresponding case of optimum circulation distribution. Also for this case a propeller has been manufactured and tested.

Finally some comparative lifting line and lifting surface calculations for a loading case originally published by Pien [17] are presented and discussed.

LIFTING LINE THEORIES USED IN THE PRESENT COMPARISON

Among the lifting line theories available those of Goldstein, Guilloton, Lerbs and Strscheletzky were presented in [1]. In the present comparison Guilloton's theory is omitted, being applicable only to three-bladed propellers. In the following some limitations in application of and approximations involved in the different theories are discussed. For a more thorough description of the methods is referred to [1] and to the original papers.

Goldstein's $\mathscr{K}$-Theory

In its original version [2,3] this theory is only applicable to the case of a propeller with maximum induced efficiency or minimum kinetic losses and hub diameter zero. Thanks to this limitation of the problem the relation between the bound circulation Γ_b and the tangential component of the induced velocity can be expressed by the simple equation

$$z \Gamma_b = 2 \pi r \mathscr{K} \, 2u_T \tag{1}$$

where $\mathscr{K}$ is a function of u_i and x only.

As the induced velocity component u_N in Fig. 1 can be proved to be perpendicular to V in this case the remaining component u_A, the hydrodynamic pitch angle and the lift can be calculated from pure geometrical considerations. In [3] diagrams are given of u_i, making it possible to calculate u_i and $\tan \beta_i$ directly from the equation

$$u_i = \frac{u}{u_i} = x \tan \beta_i \tag{2}$$

Later $\mathscr{K}$- and u_i-values for the case of an optimum propeller with finite hub were deduced [4,5].

30
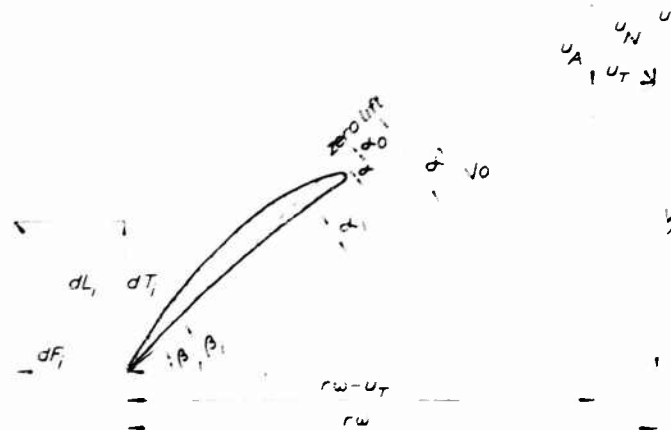
Fig. 1 - Velocities and forces at a blade section in ideal flow

In spite of what has been said above, the $\mathscr{U}$-method is often used also for calculating propellers with non-optimum circulation distributions. The hydrodynamic pitch angle and lift for each section is thereby determined independently from the others by a trial and error procedure.

The Induction Factor Method as Put Forward by Lerbs

The calculation of the relation between the circulation distribution $G_L(x)$ and the distribution of induced velocities $u_T(x)$, $u_A'(x)$ and $u_R'(x)$ according to the induction factor method starts from the equation

$$\frac{u_A}{V_A} = \frac{1}{2} \int_{r_i}^{1} i_A \frac{dG_L}{dx} \frac{dx}{x' - x} \tag{3}$$

for the axial component of the induced velocities at the blades and corresponding equations for the other components.

The only difference between Eq. (3) and the corresponding expression for the induced velocity at a wing is the presence of the induction factor i_A in the former equation. The induction factors i_A and i_T representing the free vortex system from the propeller to infinity downstream were calculated by Lerbs in an analytical manner [6,7], calculations which were later refined by Wrench [8,9].

The factors i remain finite when $x' \to x$. Again Eq. (3) $\to \infty$ when this is the case. This difficulty is overcome by Lerbs [6,7] in the same way as is common when treating the case of a three-dimensional wing, i.e., the dimensionless

31

circulation distribution $G_L(x')$ is represented by a Fourier series

$$G_L = \sum_{m=1}^{\infty} G_m \sin(m t')$$ (4)

with

$$x' = \frac{1}{2}(1 + x_h) - \frac{1}{2}(1 - x_h) \cos t'.$$ (5)

Further the values of the induction factors $i(x/x', \beta_i)$, as calculated or read off in diagrams are resolved into an even Fourier series with respect to t

$$i = \sum_{n=0}^{\infty} I_n(t') \cos(nt).$$ (6)

Equation (3) is then transformed into

$$\frac{u_A}{V_A} = \frac{1}{1 - x_h} \sum_{m=1}^{\infty} \pi G_m h_m^a(t').$$ (7)

where the coefficient h_m^a (and the corresponding coefficient h_m^t for the tangential component) is made up of trigonometric expressions deduced in [6] and [7].

The Induction Factor Method as Put Forward by Strscheletzky

The induction factor method developed by Strscheletzky in [10] differs in some respects from that of Lerbs. Thus, by introducing the transformation in (4) and (5), Eq. (3) is transformed into

$$\frac{u_A}{V_A} = \frac{1}{1 - x_h} \int i_A \frac{\sum_{n=1}^{\infty} G_n n \cos nt}{\cos t - \cos t'} dt.$$ (8)

The evaluation of this integral is performed by dividing the blade in radial direction into three parts and integrating

$$\int = \int - \int - \int .$$

The first and third integral are evaluated by using Simpson's rule. For the small region 2ϵ around the section considered, where the expression passes through infinity, the residual

$$-\frac{2\epsilon}{\sin t'} \left(\frac{i i}{t t} \frac{t G_t}{t t} - \frac{t^2 G_t}{t t^2} \right)$$ (9)

was deduced in [10].

Regarding the induction factors i_A, i_T and i_R (also the radial component is considered by Strscheletzky) they are obtained by numerical integration of the fundamental equations. The results, only covering three-bladed propellers, are given in [11]. In addition also induction factors Δi_A, Δi_T and Δi_R for three-bladed propellers, corresponding to small parts Δs of the free helical lines, are given in [11]. These induction factors were obtained by stepwise integration of the fundamental equations and are given on the basis of the hydrodynamic pitch angle β_i and the ratio x/x' for the values $\Delta \varphi$ shown in Table 1, $\Delta \varphi$ being the angle, corresponding to an element Δs of the free helical vortex, projected in the disc plane.

Table 1

Length of Element $\Delta \varphi$	Position of Element $\varphi_{n-1} - \varphi_n$
° 16	0 - ° 16 ° 16 - - ° 8
° 8	° 8 - ° 4 ° 4 - 3° 8 3° 8 - ° 2
° 4	° 2 - 3° 4 .... 7° 4 - 2°
° 2	2° - 2.5° .... 4.5° - 5.0°
°	5° - 6°. 6° - 7°
3°	7° - 10°

These diagrams can for instance be used for calculating the contraction of the slip stream and the variation of the pitch of the free vortex lines with the distance from the blades. They are also used by Strscheletzky in his approximate lifting surface theory [10,11].

CONSIDERATION OF SOME APPROXIMATIONS INVOLVED IN THE LIFTING LINE THEORIES PRESENTED

Pitch of Free Vortices

In the way they are normally used the Goldstein $\varkappa$-theory and the induction factor methods are equal in the respect that the hydrodynamic pitch angle β_i of the free vortices is regarded as constant from their starting point at the blades to infinity downstream. The values β_i used when reading off in the $\varkappa$-diagrams or i -diagrams are normally defined from the expression

$$\tan \beta_i = \frac{1 - \dfrac{u_A}{V_A}}{\dfrac{x}{} - \dfrac{u_T}{V_A}}. \tag{10}$$

33

where u_T/V_A and u_A/V_A are defined according to Eq. (3), i.e., the pitch at the blades is regarded as representative for the whole vortex. As is well known the magnitude of the induced velocities at infinity downstream is twice that at the blades in ideal flow. The significance of this approximation is illustrated by the diagram in Fig. 2. In this diagram some values $\Sigma \Delta i_A$ are shown on the basis of $\Delta \theta$, one curve based on the β_i-values at the blades and one curve based on the β_i-values at infinity downstream. The β_i-values correspond to $x = 1$, $x' = 0.2$ for Loading Case 1 of Table 1, the Δi_A-values, however, being applicable to a three-bladed propeller. It is evident that the parts of Δi_A corresponding to $\Delta \theta$-values far from the blades are more sensitive to changes in β_i than those corresponding to $\Delta \theta$-values close to the blades, indicating that the assumption $\beta_i \approx \beta_{i\infty}$ when calculating the induction factors i_A may be a better approximation than the one normally used.
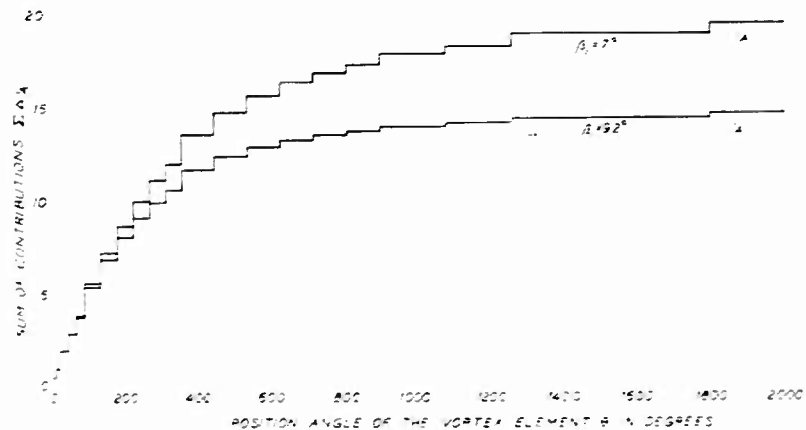
Fig. 2 - Contributions $\Sigma \Delta i_A$ to the total induction factor i_A from different parts of a free vortex: $x \, x' = 5$

In these calculations the influence of the contraction of the slipstream on the β_i- and $x \, x'$-values was neglected, being small in the present case.

The Introduction of the Transformation $z = f(x)$
  into the Calculations

By introduction of the transformation of Eq. (5) for x and x' the representation of an arbitrary circulation distribution by a Fourier series according to Eq. (4) is made possible and the calculations facilitated. In Lerbs' method also the induction factors are represented by a similar expression. Eq. (6).

When representing a circulation distribution by a Fourier series of the kind of Eq. (4) it is generally recommended to include three or five terms in the expansion. In fact the accuracy is very good with both three and five terms
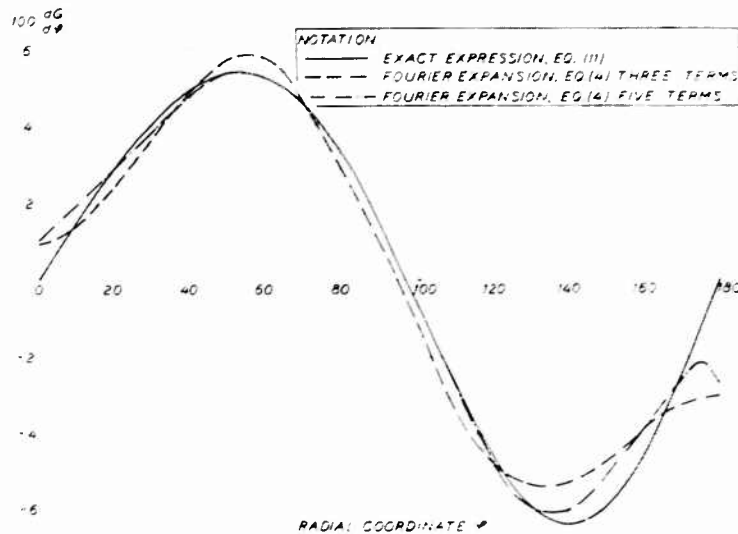
Fig. 3 - Illustration of the accuracy of the
Fourier expansion of the derivative $dG/d\tau$

included except at the endpoints where the discrepancies are appreciable and of
the same order in both cases. The intensity of the free vortices is, however,
defined by dG_L/dx or $dG_L/d\tau$ which are related to each other through the
expression

$$\frac{dG_L}{d\tau} = \frac{dx}{d\tau}\frac{dG_L}{dx} = 0.5 \ (1 - x_h) \ \sin \tau \ \frac{dG_L}{dx} . \tag{11}$$

It is evident that, when starting from a circulation distribution $G_L = f(x)$,
the derivative $dG_L/d\tau$ deduced from Eq. (11) will always $\to 0$ at the endpoints
$\tau = 0$, $\tau = \pi$, corresponding to root and tip. On the other hand, when starting
from $G_L = f(\tau)$, dG_L/dx will always $\to \infty$ at the endpoints. The former case is
illustrated in Fig. 3, where, for the circulation distribution defined by Eq. (15),
with $k = 0.2073$, the direct transformation of the exact expression for dG/dx is
compared with the corresponding derivatives of the three- and five-term expan-
sions. The agreement between the approximate curves and the curve repre-
senting the exact expression is not very good in the vicinity of the endpoints. In
the diagram in Fig. 4 the influence of these discrepancies on the calculated
values of the hydrodynamic pitch angle β_i is illustrated. This influence is
evidently restricted to the vicinity of the blade tip. It must however, be remem-
bered that the curves given in Fig. 4 represent results obtained when using the
same β_i-values for all the calculations. When repeating the calculations with
the new β_i-values of the respective curves new induction factors are obtained
resulting in new β_i-values, thus increasing the discrepancies between the results.
As the induction factor i_A is very much affected by changes in β_i, especially
for great values of x/x', the approximation discussed here is less accurate than
the similar approximation used when calculating wings of finite span.

35
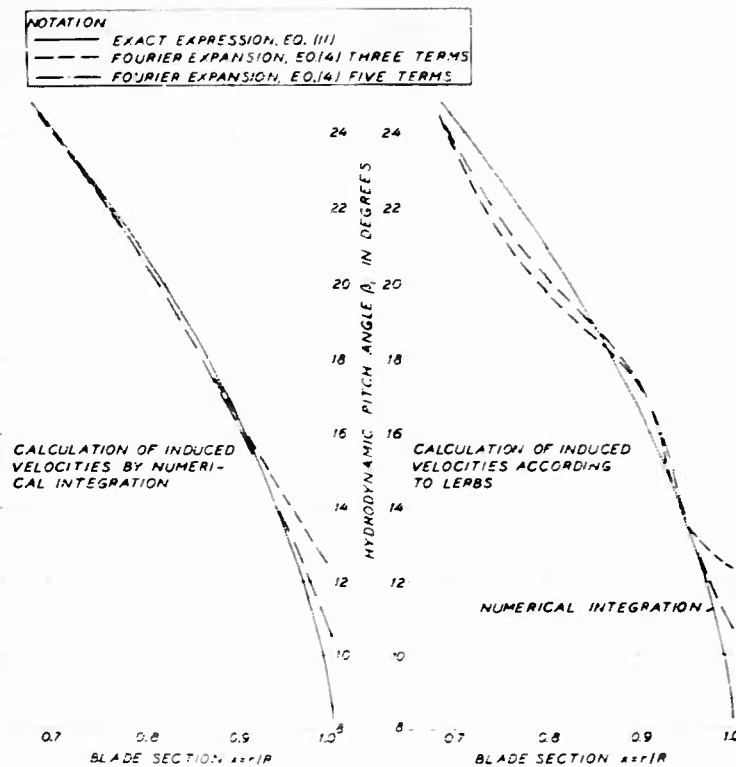
Fig. 4 - Hydrodynamic pitch angles for the outer part of the blade, calculated according to different procedures

Numerical Procedure Used when Calculating the Induced Velocities

Earlier in this paper two different procedures for evaluating the induced velocities, both using the induction factor concept, were introduced. Lerbs proceeds in an analytical manner and succeeds, by using l'Hospital's rule in deducing expressions for the induced velocities also for the endpoints $x = 0$ and $x = \pi$. When the calculations are performed in the way proposed by Strscheletzky the basic expression, Eq. (8), is integrated numerically. An application of l'Hospital's rule to this expression leads to $u_A = u_T = \pi$ at the endpoints and the values for these points must be obtained by extrapolation from the values obtained for the other sections x'.

A comparison of results obtained for the outer part of the blade, when applying the two methods to the circulation distributions of Fig. 3, is shown in Fig. 4, the same β_i-curve being used for all the cases when determining the induction factors i_A and i_T. From the diagram it can be seen that the influence of the numerical method is small when the same β_i-values are used as starting point.

36

When the calculations are repeated in the way proposed by Strscheletzky using new β_i-values the fact that the β_i-value at $x = 1$ must be obtained by extrapolation will delay the convergence of the procedure. Using Lerbs' method the β_i-value at $x = 1$ is calculated directly and will not differ very much from that obtained in the first attempt. Thus the final results can be expected to differ more than the results shown in Fig. 4.

Modified Procedure for Induction Factor Calculations

Regarding what has been said above it seems natural to try to evaluate the original expression for the induced velocities, Eq. (3) by numerical or analytical methods, without introducing the transformation according to Eq. (5). A drawback when using such a procedure is that generally it is more laborious to represent an arbitrary circulation distribution by a polynomial expression than to use a Fourier expansion, if the same degree of accuracy is desired.

In the present report some results obtained by numerical integration of Eq. (3) for two different loading cases are given. The calculations were performed on a FACIT electronic computer using a program for integration with 22 unequally spaced ordinates, the ordinates being determined by the following formulas:

$$x_r = x' - 0.005 - \left(\frac{n}{10}\right)^2 (x' - 0.005 - x_h)$$

$$x_n = x' + 0.005 + \left(\frac{n}{10}\right)^2 (1 - x - 0.005)$$

for the inner and outer part of the blade respectively, n going from 0 to 10. To the values thus integrated the remaining rectangles between $x' - 0.005$ and $x' - 0.005$ were added.

LIFTING SURFACE THEORIES USED IN THE PRESENT COMPARISON

The lifting surface theories available today for calculating the induced curvature and pitch angles can be divided into two main groups:

1. Lattice methods. In these methods the continuous vortex system covering the blade is replaced by a system of concentrated radial and helical vortex lines, forming a lattice, from which free vortices are shed downstream. Methods belonging to this group are those of Guilioton [13], Strscheletzky [10,11] and Kerwin [14].

2. Methods where the continuous system of bound vortices is represented analytically and the result obtained by numerical integration of expressions deduced by the law of Biot-Savart. This approach was used by Ludwieg and Ginzel [15,16] and Pien [17].

When using the former type of methods, the spacing of the vortices forming the lattice is affecting the accuracy of the results considerably. This point has been thoroughly discussed by Kerwin [14].

Also if reasonable simplifications are introduced into the equations lifting surface calculations are always laborious. From the designer's point of view it is therefore desirable that the equations are programmed into a computer or that results of calculations showing the influence of circulation distribution, blade form and other important parameters are available in diagrams. Up to now camber corrections for streamline curvature have normally been determined from diagrams based on some calculations performed by Ludwieg and Ginzel. In the present paper some of these Ginzel factors are compared for two cases with results obtained by calculations according to Guilloton's method which is the most simple and least laborious of those mentioned above. In one of the cases also results according to Pien's method as calculated in (17) are included in the comparison.

The Ludwieg and Ginzel Theory

By this theory the geometric camber is obtained from the equation

$$f_{geom} = f_{eff} - f_{ind} = \frac{f_{eff}}{k} . \tag{12}$$

where f_{geom} = the geometric camber at the midpoint of the profile. The values of k are obtained by Ludwieg and Ginzel by calculating the slope of the streamline in the midpoint of the sections

$$\tan z = \frac{u_-}{V} . \tag{13}$$

where V = inflow velocity including induced velocities (see Fig. 1), and

u_m = induced velocity at the midpoint, perpendicular to V.

The expressions for u_m are obtained by using the law of Biot-Savart. The calculations are performed for circular arc mean lines but to facilitate the calculations the bound circulation in chordwise direction, which for this type of mean line is elliptic, is replaced by an equivalent rectangular distribution extending over a length $l' = 0.707$. This simplification introduced, the vortex system from the propeller blade to infinity can be proved to be equivalent to a "remain" vortex system consisting of a closed vortex line along the blade outline and a set of "remainder" chordwise vortices connecting the leading and trailing edges. By introducing the well-known expression for the radius of curvature for a function and putting into it the expressions of u_- and du_- ds deduced an approximate expression for f_{ind} is obtained. By relating this to values of f_{eff} obtained by lifting line calculations, k-values are obtained for some loading cases which are given in diagrams in [15] and [16]. The results cover only three-bladed propellers of zero hub diameter with symmetrical blades (i.e., blade forms having no skew back) having circular arc mean lines, working at shock free entry. Two

38

different circulation distributions were investigated in combination with different blade forms, firstly the optimum case, secondly propellers having the circulation distribution

$$\Gamma_b = Ax(1 - x^2). \tag{14}$$

More extensive calculations for the optimum case, also covering the case of finite hub diameter was later performed by Cox [13].

The practical use of the values calculated for the optimum case is complicated by the fact that $k \to 0$ when $x \to 1$, resulting in infinite camber at the tip.

For a long time the above-mentioned method was the only one available for calculating curvature corrections. Individual calculations according to this method were however too laborious in the pre-computer era. Because of this the original calculations, the results of which were accounted in diagrams in [15] and later on in [16], were accomplished for a few loading cases only. To get the material underlying the diagrams in [19], [20] and [21], which are intended for general use, a certain amount of interpolation and extrapolation work was necessary. Thus the k-values obtained from these diagrams can only be regarded as "Approximate Ginzel" camber correction factors. In the values given in [21] also a viscosity correction is included which is removed when these values are accounted in the present paper.

The Theory of Pien

A similar approach as that of Ludwieg and Ginzel was used by Pien when evaluating his lifting surface theory [17]. From the fundamental equations he deduces expressions liable to numerical integration by the use of which the induced velocities can be calculated for different points along the chords of the blade sections. Thus calculations according to this method give a more complete result than that obtained when using Ludwieg and Ginzel's equations. To reduce the integration work, however, only the effect of the part of the free vortex system is calculated which is located between the leading and trailing edges of the blades. This means that the results from the calculations give only the additional velocities relative to those obtained by the preceding lifting line calculations.

In [17] is mentioned that the rather laborious equations have been programmed into the high-speed computer IBM 709, this program being applicable to propellers with blade sections having uniform chordwise loading distribution (NACA $a = 1$ mean lines or, if the approximation according to Ludwieg and Ginzel is accepted, also circular arc mean lines).

In the present paper numerical results for one case (named Loading Case 2 in present paper) published by Pien himself in [17] are compared with results obtained with other lifting surface methods.

39

The Guilloton Theory

A lattice method simple enough to make calculations by hand possible for individual cases is that of Guilloton [13]. When using this method the bound vortex system is replaced by 5 radial vortex lines having a dividing angle of $20°$ to which the circulation is concentrated in proportion to the chordwise load distribution. Each radial vortex line is then divided into 5 steps, within each step assuming the bound circulation to be constant, thus giving rise to six free vortices of helical form. The free vortices emanating from the different vortex lines add to each other resulting in a circulation $-d\Gamma_b/dr$ behind the propeller. The induced velocity component perpendicular to the inflow velocity V_o (see Fig. 1) due to this system of free vortices, in excess of the corresponding component calculated by lifting line theory was determined by Guilloton by the use of the law of Biot-Savart for all the 30 points mentioned above. For general use the results are given in tables in [13], covering pitch ratios between 0.416 and 1.25. In these coefficients the influence from the bound and free vortices from two other blades of a three-bladed propeller are included.

A drawback when using the tables mentioned above for calculating camber corrections for propeller blades is that the dividing angle as well as the number of vortex lines of the vortex system is fixed. For narrow-bladed propellers the number of vortices covering the blades is insufficient near the tip, while for broad-bladed propellers the same is true near the hub.

Discussion of the Different Lifting Surface Methods

An approximation introduced when deducing the final equations of the different methods referred to above is the excluding of the free vortices in the region behind the blades. By limiting the aim of the calculations in this way only the induced velocities in excess of those resulting from the lifting line calculations are obtained. This means that the pitch of the free vortex lines from a certain blade section is assumed to be constant from the starting point to infinity downstream of the propeller. A further step towards greater accuracy would be to extend the lifting surface calculations downstream to the point where the total induced velocities are twice those calculated by lifting line theory. The lifting line calculations should then be repeated using induction factors of the type i mentioned earlier, thereby considering the pitch variation and contraction of the free vortices. Such a procedure was proposed by Strscheletzky in [10].

In the present comparison the three lifting surface methods referred to above appear as representing three different stages of lifting surface calculations.

To represent "Approximate Ludwieg and Ginzel Method," k-values obtained from diagrams in [19], [20] and [21] are used. It did not seem justified to include results obtained by calculations according to this method for the individual cases as the complexity of such calculations is of the same order as when the calculations are performed according to Pien's method, the latter giving a more complete result.

40

Guilloton's method represents an approximate way of estimating the influence of circulation distribution and blade form by individual calculations. The necessary calculations are relatively simple.

Pien's method represents the stage at which the aid of an electronic computer is necessary.

PROPELLER CALCULATIONS

Starting Points for the Calculations

The different lifting line and lifting surface theories referred to earlier were applied to two non-optimum loading cases characterized in first hand by different circulation distributions. See Fig. 5.
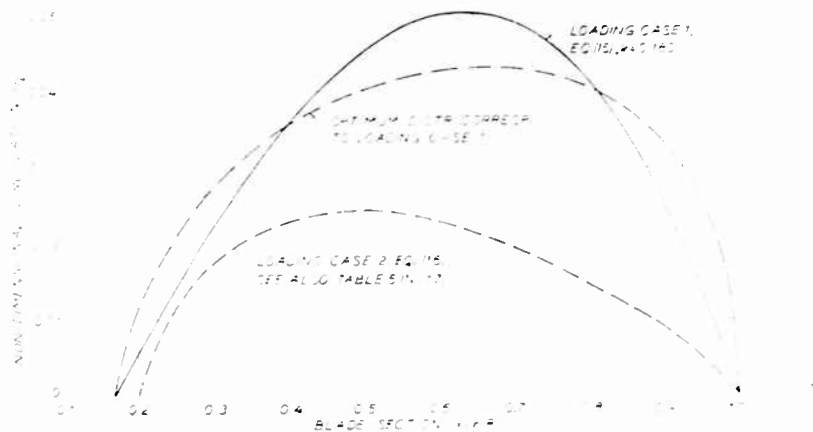
Fig. 5 - Circulation distributions used in present paper

The J-K_T-combination of Loading Case 1 represents an ordinary merchant ship propeller. The circulation distribution can be expressed by the equation

$$G_L = k (x - 0.167) (1 - x^2) . \tag{15}$$

which is similar to Eq. (14), the only difference being zero circulation at the hub for the distribution of Eq. (15). Other data for Loading Case 1 are given in Table 2.

Loading Case 2 is the case treated by Pien in [17] and was included in the present report primarily to make possible a comparison between Pien's lifting surface theory and other lifting surface theories without performing the very laborious calculations involved with the former method. For data of this case, see Table 2.

41
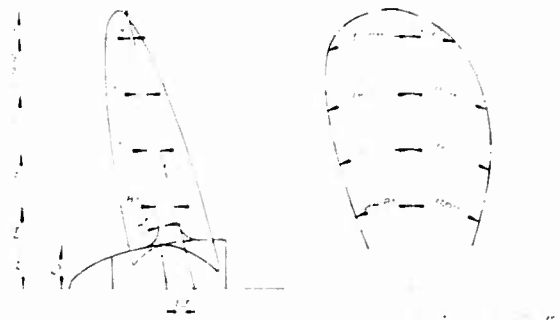
Fig. 6 - General appearance of the model propellers in the present investigation (Loading Case 1)

Table 2
Data of Loading Cases 1 and 2

	Loading Case 1	Loading Case 2
Design advance number J	0.637	0.840
Preliminary design K_T	0.193	0.137
Number of blades z	4	5
Circulation distribution	Eq. 15) (k = 0.180)	Eq. (16)
Hub radius x_h	0.167	0.2
Section mean lines	NACA a = 0.8	NACA a = 1
Blade form	Fig. 6	Fig. 4 of Ref. [17] (no skew back)

The circulation distribution used by Pien is shown in Fig. 5. By the use of a computer program intended for analytical representation of ordinates of bodies of revolution [12] this curve was represented by an eighth-degree polynomial

$$G_L = -0.199899 - 2.185379x - 9.022462x^2 - 18.848083x^3 - 15.542070x^4$$

$$- 6.557301x^5 - 26.585941x^6 - 20.826257x^7 - 5.52844x^8 \qquad (16)$$

the maximum deviation in G_L from the values given in [17] being less than $\pm 1\%$.

The Results of the Lifting Line Calculations

The induced velocities u_A and u_T calculated according to some of the methods mentioned earlier, the hydrodynamic pitch angle ϵ_i can be determined from Eq. (10) and the pitch ratios in ideal flow from the equation

42

$$P_i/D = \pi x \tan \beta_i . \tag{17}$$

Further the lift $C_L \ell/D$ can be calculated from

$$\frac{C_L \ell}{D} = 2\pi G_L \frac{\cos \beta_i}{\dfrac{\pi x}{J} - \dfrac{u_T}{V_A}} \tag{18}$$

finally giving for a prescribed blade form the effective camber $f_{eff} \ell$ of the different sections.

The values of P_i/D obtained when applying different lifting line theories to Loading Case 1 are shown in the diagram in Fig. 7. Results from the following lifting line calculations are included in the diagram:

1. Goldstein's $\varkappa$-method with $\varkappa$-values taken from [4]. The influence of the hub considered.

2. The induction factor method as put forward by Lerbs. The β_i-values at the blades used when determining the induction factors.

3. The induction factor method, the induced velocities calculated by direct integration of Eq. (3) in the way described earlier. The β_i-values at the blades used when determining the induction factors.

4. Same as 3. but the $\beta_{i\infty}$-values at infinity downstream used when determining the induction factors.

The induction factors used were calculated directly from the equations in [9] using a FACIT electronic computer.

Fig. 7 - Pitch ratio curves in ideal flow, calculated according to different lifting line theories (Loading Case 1)

In Fig. 8 the values of P_i/D resulting from calculations according to 2. and 4. for Loading Case 2 are shown. In this case the results representing Lerbs' method were taken directly from [17].

From the diagram in Fig. 7 it can be seen that the pitch distribution obtained with the $\mathscr{H}$-method differs from those obtained with the induction factor methods, the differences between the latter methods being of moderate order for Loading Case 1. The differences between the results from different induction factor calculations for Loading Case 2 as visualized in Fig. 8 are very small except at the endpoints.
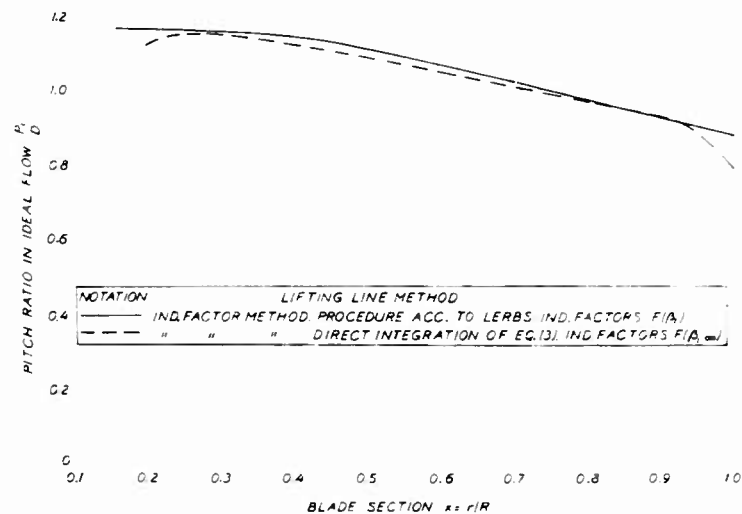
Fig. 8 - Pitch ratio curves in ideal flow, calculated according to the induction factor method using different numerical procedures (Loading Case 2)

The Results of the Lifting Surface Calculations

The geometric camber f_{geom} for the different blade sections x as calculated according to different lifting surface methods are given in Fig. 10 (Loading Case 1) and Fig. 12 (Loading Case 2) together with the effective camber obtained by lifting line calculations. The corresponding values of the camber correction factor k as defined in Eq. (12) are given in Fig. 9 and Fig. 11.

As f_{geom} of a section is used the ordinate at the midpoint relative to a line connecting the endpoints. This is not entirely correct as the induced curvature as calculated by some of the methods is not symmetrical around the midpoint. The differences in form between the mean line used when determining f_{eff} and the induced curvature f_{ind} are, however, small in the cases accounted in the present report.

44

Fig. 9 - Camber correction factors calculated according to different lifting surface methods (Loading Case 1)

Fig. 10 - Geometric camber calculated according to different lifting surface methods (Loading Case 1)

45

Results from calculations according to the following methods are included in the diagrams:

1. "Approximate Ludwieg and Ginzel" method with k-values according to [20].

2. "Approximate Ludwieg and Ginzel" method with k-values according to [21]. As mentioned earlier these values include a correction for viscosity which was omitted in the calculations presented here.

3. "Approximate Ludwieg and Ginzel" method with k-values according to [19] (only Loading Case 1).

4. The method of Guilloton.

5. The method of Pien (only Loading Case 2).

When performing the calculations for Loading Case 2 a symmetrical blade form was assumed. In Figures 11 and 12 where the results from these calculations are visualized also the corresponding results from Pien's calculations for a non-symmetrical blade form [17] are reproduced.

When applied to non-symmetrical blade forms both Guilloton's and Pien's methods give rise to a pitch correction if the pitch angle is defined relative to a line connecting the leading and trailing edges of the mean lines. The magnitude of this correction for different blade sections x, as obtained with Guilloton's method for Loading Case 1 and Pien's method for Loading Case 2 is shown in Fig. 13, which shows the correction in percent pitch relative to the pitch curve obtained with Lerbs' induction factor method.

From the diagram in Fig. 9 it can be seen that, of the different k-values based on Ludwieg and Ginzel's theory, those from [20] differ from the two other sets. This can be explained by the fact that the former values are based on Ginzel's calculations for the non-optimum circulation distribution of Eq. (14) rather than the corresponding results for the optimum case from which the two other sets originate.

As the circulation distribution of Loading Case 1 is similar to that of Eq. (14), the k-values of [20] could be expected to be the more proper ones for this case when Ludwieg and Ginzel's calculations are used as basis. It is therefore interesting to notice the good agreement between these k-values and those calculated according to Guilloton. The discrepancies at the blade tip might be due to inaccuracies in the latter method, an idea which is supported by the existence of a similar, although less marked deviation between results from this method and Pien's method, as shown in Fig. 11 for Loading Case 2. In this comparison Pien's method must be looked upon as the most reliable of the two.

The predominant influence of the circulation distribution on the k-values is illustrated by the result of the comparison for Loading Case 2 shown in the diagram in Fig. 11. In this case there is good agreement between the results obtained with the methods of Guilloton and Pien, both methods considering this influence. The two "Approximate Ginzel" curves which originate from other
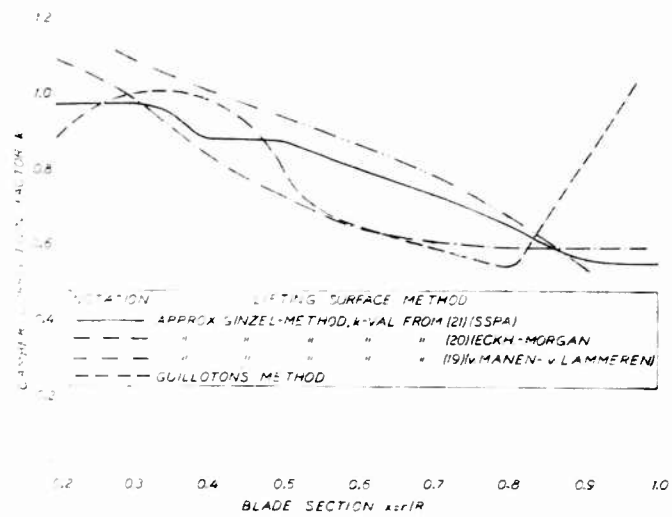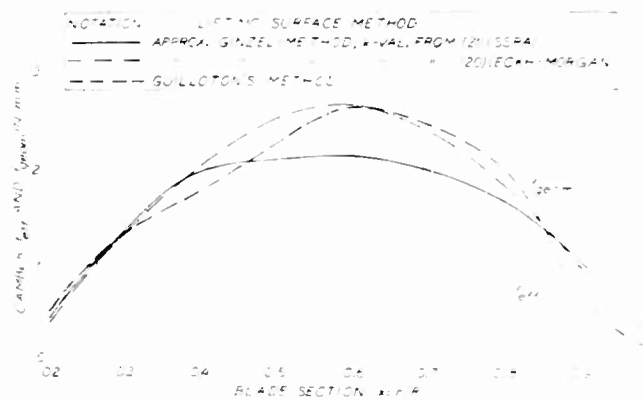
46
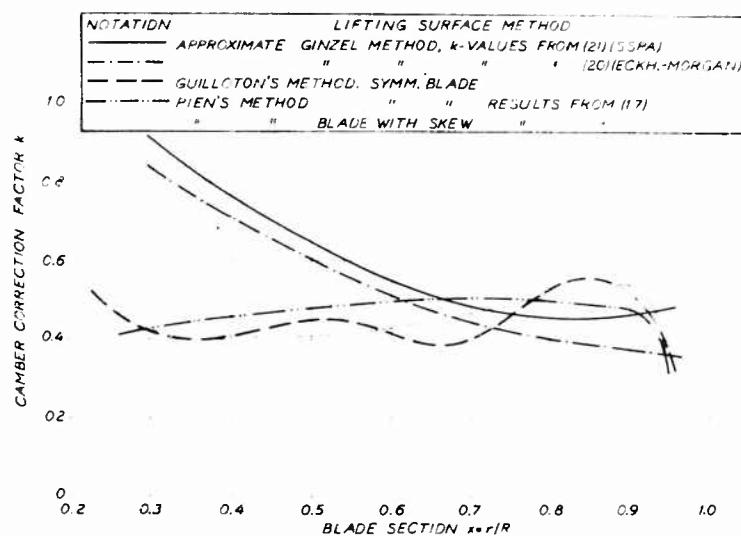
Fig. 11 - Camber correction factors calculated according
to different lifting surface methods (Loading Case 2)
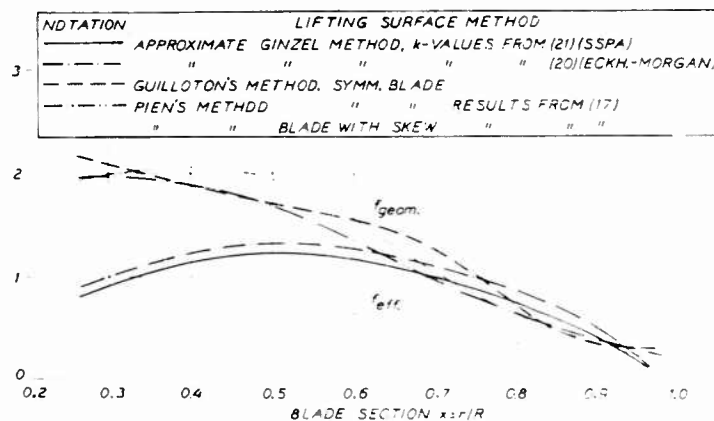
Fig. 12 - Geometric camber calculated according to
different lifting surface methods (Loading Case 2)

47
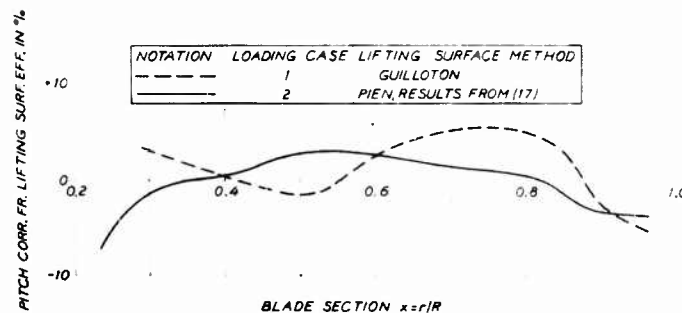
Fig. 13 - Induced pitch corrections from lifting surface effect. Loading Case 1 and 2. Blades with skew back.

circulation distributions give entirely different k-values for the blade sections near the hub.

From the results of Pien's calculations, as reproduced in Fig. 11, it is evident that the influence of skew back on the k-values is small so much the more as the present case is one of extreme skew back. As mentioned above the influence of skew back, however, manifests itself as a pitch correction.

Complete Propeller Calculations for the Design of
  Model Propellers

For some combinations of lifting line and lifting surface theories complete propeller calculations were performed and model propellers having a diameter $D = 250$ mm manufactured according to the resulting designs. The starting points for the calculations are given in Table 3, the design values corresponding to Loading Case 1 for three of the propellers. Propeller No. P1017 is an equivalent propeller designed to have optimum circulation distribution.

In order to get propellers being as equal as possible what regards effective pitch, the k-value in Eq. (15) was not chosen exactly the same for all the propellers.

Of the different applications of the induction factor method discussed earlier only that of Lerbs was tested as the difference between the pitch curves obtained with the different procedures mentioned earlier is of moderate order. See Fig. 7. The intention is, however, to complete the investigation later on in this respect.

RESULTS OF OPEN WATER TESTS PERFORMED WITH
  MODEL PROPELLERS

With the propeller models of diameter $D = 0.250$ m manufactured according to the different designs shown in Table 3 open water tests were performed at a

Table 3
Particulars of Calculations for Model Propellers

Common Starting Points and Equations Used in the Calculations	
Design advance ratio	$J = 0.637$
Hub diameter	$x_h = 0.167$
Blade area ratio	$A_D/A_O = 0.53$
Number of blades	$z = 4$
Blade form, rake, blade section thickness	Fig. 6
Mean line of blade sections	NACA $a = 0.8$
Thickness distribution of blade sections	NACA 66 modif. [20]
Ideal angle of attack	$\alpha_i = 1.54\, C_L$ degrees
Friction loss correction (when applied as pitch correction)	$\alpha_f = 1.61\, C_L$ degrees ($\mu = 0.85$)

Circulation Distribution and Further Data				
Propeller No.	P1017	P1018	P1040	P1052
Circulation distr.	Optimum	Eq. (15), $k = 0.180$	Eq. (15), $k = 0.180$	Eq. (15), $k = 0.153$
Lifting line theory	Goldstein, $\varkappa$-values from [4]. Hub considered		Induction factor method acc. to Lerbs, i_A and i_T from [9]	
Lifting surface theory: Camber corr.	"Approximate Ginzel," k-values from [21], viscous part omitted			Guilloton
Lifting surface theory: Pitch corr.	None			Guilloton Faired values from Fig. 13
Viscosity corr.	Pitch correction		2/3 on camber 1/3 on pitch	

constant number of revolutions $n = 12.2$ r/s, corresponding to a Reynolds number $R_{n\,0.75R} = 4.5 \times 10^5$ at the design advance ratio $J = 0.637$.

The results of the open water tests are given in the diagram in Fig. 14 and in Table 4.

In Table 4 the experimental values of K_T and τ_o are compared with those calculated according to the equations

49
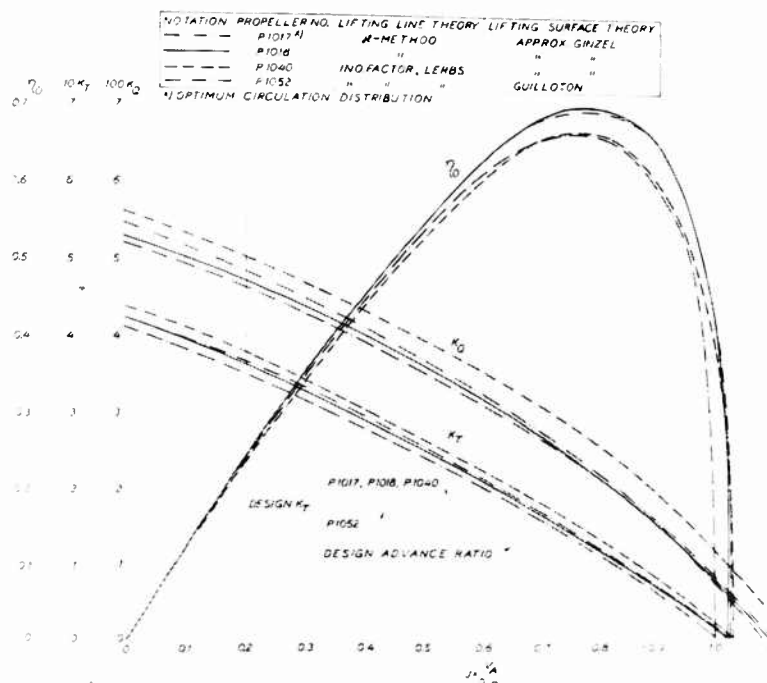
Fig. 14 - Results from open water tests with model propellers. Circulation distribution acc. to Eq. (15).

Table 4

Propeller No.	P1017	P1018	P1040	P1052
Circulation distribution	Optimum	Eq. (15)	Eq. (15)	Eq. (15)
K_T calculated at design advance ratio $J = 0.637$	0.197	0.194	0.194	0.167
K_T measured at design advance ratio $J = 0.637$	0.196	0.192	0.207	0.184
$100 \left(\dfrac{K_{T\,meas.}}{K_{T\,calc.}} - 1 \right) \%$	-0.5	-1.0	+6.7	+10.0
η_o calculated at design advance ratio, $C_D = 0.008$	0.677	0.668	0.629	0.649
η_o calculated at design advance ratio, $C_D = 0.006$	0.690	0.682	0.643	0.663
η_o measured at design advance ratio	0.660	0.660	0.634	0.638
Peak efficiency	0.696	0.702	0.670	0.667
Lifting line method	$\varkappa$-method hub considered		Ind. factor	Lerbs
Lifting surface method	"Approx. Ginzel," Ref. [21]			Guillo-ton

$$K_T = \frac{z\pi J^2}{2} \int_{x_h}^{1} G_L \left(\frac{\pi x}{J} - \frac{u_T}{V_A} \right)(1 - \epsilon \, \tan \, \beta_i) \, dx ,\tag{19}$$

$$K_Q = \frac{z\pi J^2}{4} \int_{x_h}^{1} G_L \left(1 + \frac{u_A}{V_A} \right)\left(1 + \frac{\epsilon}{\tan \, \beta_i} \right) x dx ,\tag{20}$$

$$\eta_o = \frac{J}{2\pi} \frac{K_T}{K_Q} .\tag{21}$$

When calculating the efficiency, both $C_D = 0.008$ and $C_D = 0.006$ were used while the K_T-values were calculated only for the case $C_D = 0.008$, the influence of C_D on K_T being very small.

From Table 4 it can be seen that the two propellers based on lifting line calculations using Lerbs' induction factor method delivered 7 to 10% more thrust at the design advance ratio than calculated while while the thrust delivered by the propellers designed according to the $\mathcal{H}$-method agreed very well with that predicted.

Replacing the k-values obtained with "Approximate Ginzel Method" by a combined curvature and pitch correction calculated according to Guilloton's method does not influence the effective pitch and efficiency very much.

From the results given in Table 4 it might be concluded that calculations according to Lerbs' induction factor method result in propellers having greater effective pitch than predicted. As can be seen from the pitch curves in Fig. 7 this state of things is not changed essentially in the present case by using any of the alternative induction factor procedures discussed earlier.

In this connection the inaccuracy of the friction loss correction must, however, be emphasized. In the calculations presented here a viscosity correction on pitch angle

$$\alpha_f = 1.61 \, C_L \text{ degrees}$$

was used, corresponding to a friction loss coefficient $\kappa = 0.85$, a value normally used at SSPA for all mean lines.

In [7] and [20] the value $\kappa = 1.05$ is proposed for the NACA $a = 0.8$ mean line. Using this value the correction

$$\alpha_f = -0.39 C_L$$

is obtained resulting in 2 to 3% decrease in local pitch values.

What regards efficiency the values calculated assuming $C_D = 0.008$ agree well with those measured for all the propellers. It is interesting to notice that, when the $\mathcal{H}$-method is used, the experimentally determined efficiency is almost

the same for the optimum propeller P1017 and the non-optimum propeller P1018.
The two other propellers show a somewhat lower efficiency. For the non-
optimum propellers the latter result is more reasonable as the circulation dis-
tribution presumed at the calculations differs considerably from the optimum.
See Fig. 5.

CAVITATION TESTS PERFORMED WITH MODEL
PROPELLERS IN HOMOGENEOUS FLOW

Carrying Out of the Tests

With the four model propellers designed according to the principles shown
in Table 3 cavitation tests were performed in uniform flow in the SSPA cavita-
tion tunnel [22] using a test section $0.5 \, m \times 0.5 \, m$, the water velocity being
3.5 -4 m/sec. during the tests. The water velocity in the tunnel was measured
by means of a pitot tube placed between the propeller and the tunnel wall. The
measured values of speed and static pressure were corrected according to
equations given by Lerbs [23] and good agreement was obtained between pro-
peller characteristics from the tunnel at atmospheric pressure and the corre-
sponding results from open water tests.

The air content ratio of the water was kept low during the tests.

The tests included observations of the inception of different kinds of cavi-
tation at different advance ratios.

Results of the Tests

The results of the observations on the different propellers are given in the
diagrams, Figs. 15 and 16.

In Fig. 15 incipient cavitation curves σ_i for different kinds of cavitation are
plotted for the different propellers with the design advance ratio J as basis.

In Fig. 16 the cavitation properties of the propellers are compared at the
design advance ratio $J = 0.637$. The diagrams show the extension of different
kinds of cavitation over the blades.

In the diagrams in Fig. 16 also theoretical curves are given, representing
the incipient cavitation number

$$\sigma_i = \frac{\Delta p}{\frac{\rho V_A^2}{2}} \tag{22}$$

for different blade sections, where Δp = the maximum pressure drop in ideal
flow at the profile considered, calculated by the use of profile data given in [20].
For an approximate estimate of the inception of tip vortex cavitation the well
known formula for the pressure p_c in the centre of a vortex
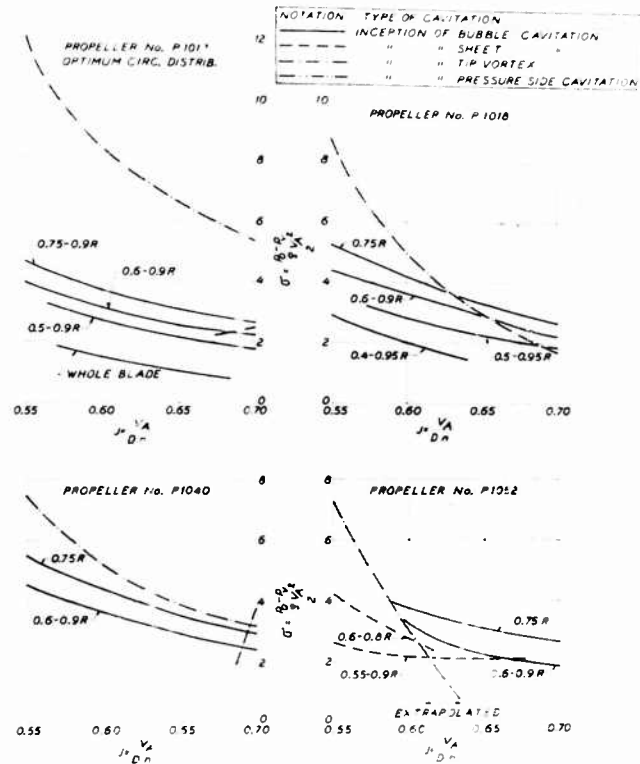
Fig. 15 - Incipient cavitation curves for model propellers. Circulation distribution acc. to Eq. (15). Data of propellers in Table 3.

$$p_c = p_b - \frac{\Gamma^2}{8\pi^2 a^2}$$ (23)

was used in [1], where

p_b = pressure at the boundary of the vortex,

Γ = circulation round the vortex, and

a = radius of the vortex.

Assuming the tip vortex to start immediately behind the blade, the intensity of this vortex will be equal to that calculated by lifting line theory and in Eq. (23) the approximation
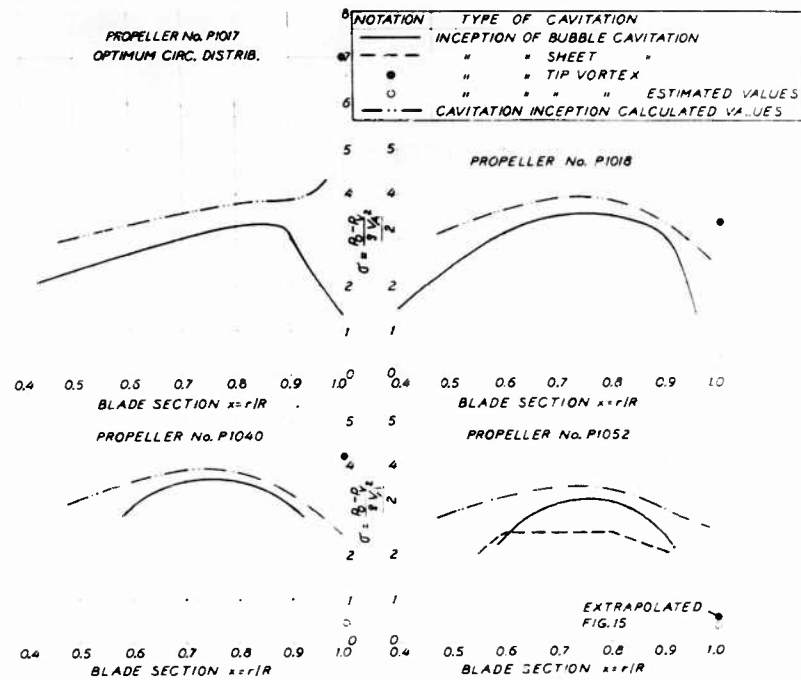
Fig. 16 - Comparison between the cavitation properties of
the model propellers at the design advance ratio $J = 0.637$.
Circulation distribution acc. to Eq. (15).

$$\frac{\Gamma}{a} \approx 2 \left[\frac{d\Gamma_b}{dr}\right]_{tip}$$

can be made, giving for the pressure drop

$$\frac{\Delta p_1}{\frac{\rho V_A^2}{2}} = \frac{p_b - p_c}{\frac{\rho V_A^2}{2}} = 4 \left[\frac{dG}{dx}\right]_{tip}^2 \tag{24}$$

For the pressure drop Δp_2 at the edge of the tip vortex relative to the undisturbed flow Bernoulli's equation gives

$$\frac{\Delta p_2}{\frac{\rho V_A^2}{2}} = \frac{u_T^2 + u_A^2}{V_A^2} \tag{25}$$

54

if the radial component of the induced velocity is neglected. Values calculated according to Eqs. (24) and (25) are included in the diagrams in Fig. 16. For the optimum case Eq. (24) gives $\sigma_i = \infty$.

It is evident from the diagrams in Fig. 16 that, what regards bubble cavitation, the measured values of cavitation inception σ_i are lower than those calculated, the greatest difference occurring at the blade tips. For the optimum propeller P1017 this difference is considerable, indicating that the desired circulation distribution was not realized for this propeller.

In the region $0.6 < x < 0.9$ of the blades the experimental values of bubble cavitation inception are 85 to 95% of those calculated at the design advance ratio. Part of this difference may be due to the fact that Eq. (22) assumes static conditions, another explanation being that values of $\triangle p$ calculated for ideal flow may not hold for viscous flow.

Regarding tip vortex inception only the results from propeller No. P1052 (Lerb's induction factor method + Guilloton's lifting surface method) show good agreement between calculated and measured values. The experimental values for this propeller must, however, be regarded as approximate as they have been obtained by extrapolation of data given in Fig. 15 for other J-values than the design value.

From the diagrams in Fig. 16 it is evident that the cavitation properties of the propellers P1018 and P1040 are very similar at the design advance ratio, the former being a little better what regards tip vortex cavitation. On the other hand the latter propeller delivers 8% more thrust at this advance ratio. Thus no essential change in the cavitation properties was resulting when, in combination with approximate Ginzel camber correction, the $\varkappa$-method was replaced by Lerbs' induction factor method. When, however, the latter method was combined with a curvature and pitch correction calculated according to Guilloton's method the cavitation number of tip vortex inception was lowered from 4.2 to 0.5, the latter value being close to the value predicted by Eqs. (24) and (25).

The only propeller showing sheet cavitation at the design advance ratio is P1052.

MEASUREMENT OF THE AXIAL VELOCITIES INDUCED BEHIND THE PROPELLER

A way of checking if the calculated load distribution along the blades has been realized is to measure the velocity in the wake behind the propeller. If ordinary pitot tubes are used for this purpose, the total velocity component is obtained. In the present case calculation of the inflow angle by using theoretical values of u_T and u_A result in very small corrections to these values and thus a fairly good estimation of the magnitude of the axial component can be made from these measurements. Results of this kind are shown in Fig. 17. In this figure diagrams are given showing values of the axial component of the induced velocity at the design advance ratio $J = 0.637$, measured in the cavitation tunnel 200 mm downstream of the propeller. For comparison curves are
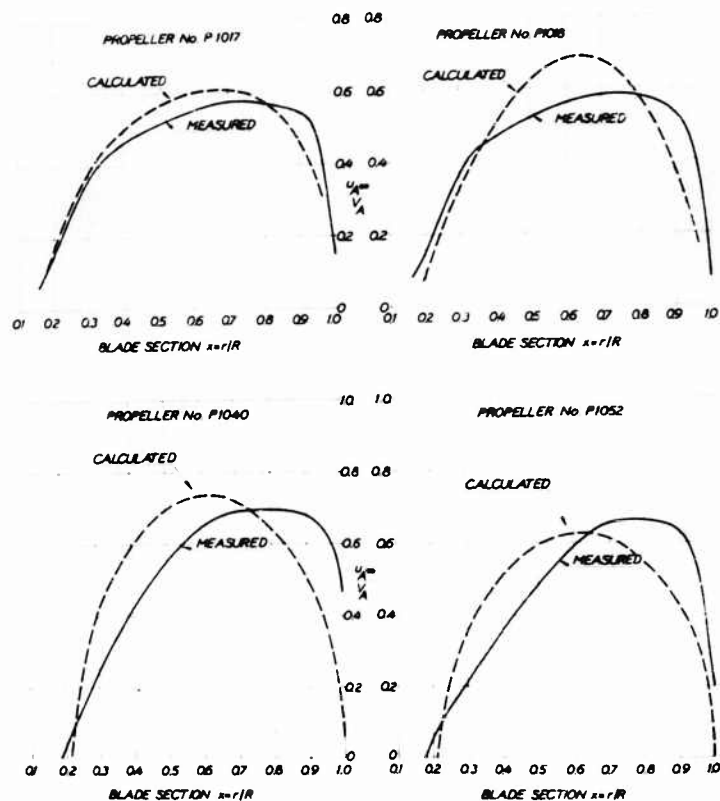
Fig. 17 - Axially induced velocity
behind model propellers

included in the diagrams, showing the corresponding theoretical values
$(u_A/V_A)_\infty = 2u_A/V_A$ calculated according to the lifting line theory applied to the
propeller considered.

The values measured have been shifted radially in proportion to the con-
traction, the latter being determined by measuring the diameter of the wake
when running the tunnel at a pressure at which a thin tip vortex was visible
behind the propeller. The contraction R_{200}/R measured in this way was for the
different propellers

	P1017	P1018	P1040
R_{200}/R	0.89	0.86	0.82

For P1052 no tip vortex was visible and the value 0.82 was used.

Almost identical values of induced velocity and contraction were obtained when for propeller P1017 the measurements were repeated at a distance 100 mm downstream of the propeller.

Using results of theoretical calculations by Lerbs given in tables in [23] for a propeller working in a water tunnel $R_\infty/R = 0.85$ is obtained for the actual disc area/tunnel area ratio.

Calculations according to an equation deduced by Theodorsen in [24] for a propeller in open water give $R_\infty/R = 0.83$.

Considering what has been said above the results in Fig. 17 may be said to give an idea of the variation in radial direction of the induced axial velocity behind a propeller in homogeneous flow. As is illustrated by the diagram in Fig. 17 there are rather large discrepancies between calculated and experimental values for all the propellers except the optimum propeller P1017.

For the other propeller calculated according to the $\mathscr{X}$-method, P1018, the two curves in Fig. 17 agree well except in the region $0.5x - 0.7x$ where the calculated values are greater than those measured.

For the two other propellers, P1040 and P1052, the measured values are greater than those calculated at the outer part of the blades, the reverse occurring at the inner part.

From the results in Fig. 17 it may be expected that the propellers P1017 and P1018 should deliver less thrust than predicted. As is shown in Table 4, however, the measured values of K_T at the design advance ratio agree very well with those calculated.

For the propellers P1040 and P1052 the measured values of K_T are greater than those calculated. Together with the results of Fig. 17 this would indicate too great loading of the outer sections which, however, is contradicted by the good cavitation properties for these propellers as shown in Fig. 16.

CONCLUSIONS

From the results of calculations and experiments presented here the following conclusions may be drawn:

1. Some of the approximations involved in the lifting line and lifting surface theories applied in the present paper requires further investigation.

2. For the non-optimum circulation distribution investigated the pitch distribution obtained in ideal flow with the $\mathscr{X}$-method differs considerably from those obtained with different applications of the induction factor method. See Fig. 7.

3. Different applications of the induction factor method to two non-optimum loading cases result in rather similar pitch distributions except at the tip and root of the blades. See Figs. 7 and 8.

4. For the two loading cases investigated "Approximate Ginzel" camber correction factors obtained by interpolation in and extrapolation from Ludwieg and Ginzel's original diagrams result in geometrical cambers differing considerably from those obtained with more thorough lifting surface methods. See Figs. 9-12.

5. Calculations of the camber correction factors by the relatively simple lifting surface method of Guilloton seem to give realistic results over the greater part of the blade.

6. The influence of skew back on the camber correction factors, as calculated by Pien according to his lifting surface method [17], is very small but instead a pitch correction is obtained. See Figs. 11 and 13.

7. The effective pitch of the propellers is in the present case not changed essentially if the "Approximate Ginzel" camber correction factors are replaced by correction factors calculated according to Guilloton's method together with the pitch correction obtained with the latter method. Compare propellers Nos. P1040 and P1052 in Table 4.

8. The results of the open water tests show that in the optimum as well as in the non-optimum case investigated the delivered thrust at the design advance ratio agrees well with that calculated for the propellers calculated according to the $\mathscr{H}$-method (influence of hub considered). The propellers calculated according to the induction factor method of Lerbs for the non-optimum case deliver 7 to 10% more thrust than predicted. When judging the error in effective pitch the uncertainty of the friction loss correction must, however, be considered.

9. The calculated and measured values of the efficiency agree well for all the propellers if $C_D = 0.008$ is used at the calculations. See Table 4.

10. When starting from the same non-optimum circulation distribution the measured efficiency at the design advance ratio is 0.66 when the $\mathscr{H}$-method is used for the propeller calculations and 0.64 when the propeller calculations are performed according to Lerbs' induction factor method. The former value is exactly the same as that obtained with the corresponding optimum propeller. As the circulation distribution in this case differs considerably from the optimum distribution a certain decrease in efficiency could be expected.

11. No essential differences between the cavitation properties are observed when, for the same non-optimum circulation distribution, the lifting line calculations are performed according to the induction factor method of Lerbs or when the $\mathscr{H}$-method is used. "Approximate Ginzel" camber correction factors are used in both cases. See Fig. 16.

12. If the "Approximate Ginzel" camber correction factors are replaced by those deduced with Guilloton's method together with the pitch correction thereby obtained the cavitation number for incipient tip vortex decreases from 4.2 to 0.5, the latter value being close to the one resulting from an approximate prediction. See Fig. 16.

58

13. For all the propellers except P1017 the results of the measurements of the axial component of the induced velocity at different radii x behind the propeller differ considerably from the predicted values. See Fig. 17.

ACKNOWLEDGMENT

NOMENCLATURE

$$C_D = \frac{dD}{\frac{\rho}{2} \ell \, db \, V^2} = \text{drag coefficient}$$

$$C_L = \frac{dL}{\frac{\rho}{2} \ell \, db \, V^2} = \text{lift coefficient}$$

D = propeller diameter

dD = drag of profile

dL_i = lift of profile in ideal flow

f = camber

$G_L = \Gamma_b / \pi \times D V_A$ = non-dimensional circulation coefficient according to Lerbs

G_m = Fourier coefficients of G_L

i_A, i_T, i_R = induction factors of the induced velocities

$J = V_A / nD$ = advance ratio of propeller

k = camber correction coefficient according to Ludwieg and Ginzel. See Eq. (12).

$K_T = T / \rho D^4 n^2$ = thrust coefficient

$K_Q = Q / \rho D^5 n^2$ = torque coefficient

ℓ = length of blade section

n = number of revolutions

p_o = static pressure

59

p_v = vapour pressure

$P_i/D = \pi x \operatorname{tg} \beta_i$ = propeller pitch ratio in ideal flow

Q = torque

r, r' = radius of blade section

r = radius of helical vortex

$R = D/2$

$R_{n0.75R} = \dfrac{\ell_{0.75R}}{\nu} \sqrt{V_A^2 + (0.75\pi nD)^2}$ = Reynolds number of propeller

u_T, u_A, u_R, u_N = components of the induced velocity at the propeller

V_A = advance velocity of propeller

V = inflow velocity to propeller blade section including induced velocities

V_o = inflow velocity to propeller blade section excluding induced velocities

x, x' = r/R and r'/R

x_h = non-dimensional hub radius

α = angle of attack of blade section

β = advance angle of blade section

β_i = hydrodynamic pitch angle of free vortex at the blades

$\beta_{i\infty}$ = hydrodynamic pitch angle of free vortex at infinity downstream of propeller

Γ_b = circulation of bound vortex

Γ_f = circulation of free vortex

Δi = induction factor corresponding to a vortex element $\Delta\varphi$

$\Delta\varphi$ = angular length of vortex element projected in the disc plane

Δp = pressure drop at profile

ε = drag/lift ratio

η_o = propeller efficiency

60

Comparison of Propeller Design Techniques

η_i = ideal propeller efficiency

$\varkappa$ = Goldstein function

$\lambda = J/\pi$

$\lambda_i = x \tan \beta_i$

ν = kinematic viscosity

ρ = density

$\sigma = \dfrac{P_o - P_v}{\dfrac{\rho}{2} V_A^2}$ = test cavitation number

$\sigma_i = \dfrac{\Delta p}{\dfrac{\rho}{2} V_A^2}$ = inception cavitation number

REFERENCES

1. Johnsson, C.-A., "An Examination of Some Theoretical Propeller Design Methods," Publ. No. 50 of the Swedish State Shipb. Exp. Tank, Göteborg, 1962.

2. Goldstein, S., "On the Vortex Theory of Screw Propellers," Proc. Royal Soc. London, Series A, Vol. 123, 1929.

3. Kramer, K.N., "Induzierte Wirkungsgrade von Best-Luftschrauben endlicher Blattzahl," Luftfahrtforschung, Bd. 15, 1938.

4. Tachmindji, A.J. and Milam, A.B., "The Calculation of the Circulation Distribution for Propellers with Finite Hub Having Three, Four, Five and Six Blades," DTMB Rep. No. 1141, 1957.

5. Schultz, J.W., Jr., "The Ideal Efficiency of Optimum Propellers having Finite Hubs and Finite Number of Blades," DTMB Rep. No. 1148, 1957.

6. Lerbs, H.W., "Moderately Loaded Propellers with a Finite Number of Blades and an Arbitrary Distribution of Circulation," Trans. SNAME, Vol. 60, 1952.

7. Lerbs, H.W., "Ergebnisse der angewandten Theorie des Schiffspropellers." Jahrb. STG, Bd. 49, 1955.

8. Morgan, W.B., "Propeller Induction Factors," DTMB Rep. No. 1183, 1957.

9. Wrench, J.W., "The Calculation of Propeller Induction Factors," DTMB Rep. No. 1116, 1957.

10. Strscheletzky, M., "Hydrodynamische Grundlagen zur Berechnung der Schiffsschrauben," Verlag G. Braun, Karlsruhe, 1950.

11. Strscheletzky, M., "Berechnungskurven für dreiflügelige Schiffsschrauben," Verlag G. Braun, Karlsruhe, 1955.

12. Williams, Å., "Mathematical Formulation of Bodies of Revolution by Use of a Digital Computer," Publ. No. 51 of the Swedish State Shipb. Exp. Tank, Göteborg, 1962.

13. Guilloton, R., "Calcul des vitesses induites en vue du tracé des helices," Schiffstechnik 4. Bd., 1957.

14. Kerwin, J.E., "The Solution of Propeller Lifting Surface Problems by Vortex Lattice Methods," prepared under Contract No. Nonr.-1841 (63), Bureau of Ships, U.S. Dep. of the Navy. MIT, Cambr., Mass., June 1961.

15. Ludwieg, H. and Ginzel, J., "Zur Theorie der Breitblattschraube," Bericht 44/A/08, V.M. 3097 der Aerodynamische Versuchsanstalt Göttingen, 1944 (see also ibid 45/H/3 Strassl, H., "Berechnung der Wölbungskorrektur von Schiffsschraubenpropellern").

16. Ginzel, I., "Theory of the Broad-Bladed Propeller," ARC Current Paper No. 208, London, 1955.

17. Pien, P.C., "The Calculations of Marine Propellers Based on Lifting-Surface Theory," Journal of Ship Research, Vol. 5, 1961.

18. Cox, G.G., "Corrections to the Camber of Constant Pitch Propellers," Trans. INA, Vol. 103, 1961.

19. van Manen, J.D. and van Lammeren, W.P.A., "The Design of Wake Adapted Screws and their Behaviour Behind the Ship," Int. Shipb. Progr., Vol. 2, 1955.

20. Eckhardt, M.K. and Morgan, W.B., "A Propeller Design Method," Trans. SNAME, Vol. 63, 1955.

21. Lindgren, H. and Johnsson, C.-A., "Propellerberäkning enligt virvelteorien. Räkneexempel och diagram" (Propeller Calculations using Vortex Theory. Diagrams and Example of Calculation), Allmän Rapport No. 2 of the Swedish State Shipb. Exp. Tank (SSPA), Göteborg, 1956.

22. Lindgren, H., "The Cavitation Laboratory of the Swedish State Shipbuilding Experimental Tank," Publ. No. 43 of the Swedish State Shipb. Exp. Tank, Göteborg, 1958.

23. Lerbs, H.W., "Untersuchung der Kavitation an Schraubenpropellern," 131. Mitteilung der Hamburgischen Schiffbau-Versuchsanstalt, 1936.

24. Theodorsen, T., "Theory of Propellers," McGraw-Hill, N.Y., 1948.

*   *   *

NUMERICAL RESULTS OF SPARENBERG'S LIFTING SURFACE THEORY FOR SHIP SCREWS

J. D. van Manen* and A. R. Bakker⁺
Netherlands Ship Model Basin
Wageningen, The Netherlands

SUMMARY

Sparenberg's lifting surface theory for ship screws was programmed for the digital computer X 1 of the Netherlands Ship Model Basin. The results of systematic calculations for symmetric blades and pressure distributions can be interpreted as "lifting line to lifting surface correction" factors. These factors were plotted in a diagram for different pitch ratios, numbers of blades, blade area ratios and three types of radial load distributions.

Also the effect of skew back and asymmetric chordwise pressure distributions has been considered.

INTRODUCTION

After Lerbs' excellent review in 1955 of the progress made in propeller theory [1] the impression was established that completeness of this theory had been approached.

Test results of the N.S.M.B. published in 1958 gave rise to doubt as to this completeness, in particular with respect to the effect of the number of blades [2].

In the U.S.A., England, Japan and The Netherlands attempts were made during the last years to develop lifting surface theories for ship propellers [3-7]. In the present paper numerical results of Sparenberg's lifting surface theory [7] for ship screws are discussed.

---

*Assistant Director N.S.M.B.
⁺Head of Computer Department N.S.M.B.

Sparenberg assumed the blades to be infinitely thin and the influences of the ship's hull and propeller hub negligible.

He started from the basic equations of hydrodynamics and showed that a pressure dipole layer can represent the screw blades. His theory results into two equivalent expressions each of which can be chosen for determining the shape of the propeller blades for a given pressure distribution.

1.   Sparenberg's Equations

Sparenberg considers a rotating helicoidal surface

[2.1] $H(x, r, \varphi, t) \overset{def}{=} \varphi + \omega t - ax = 0, \quad a = \frac{\omega}{U},$

where t represents the time and x, r and φ form a system of cylindrical co-ordinates. The domain of x and r can be described by

[2.2] $x_\ell(r) \leq x \leq x_t(r), \qquad r_i \leq r \leq r_o.$

The functions $x_\ell(r)$ and $x_t(r)$ determine respectively the leading edge of the trailing edge of the blade, r_i and r_o are the inner and the outer radius of the blade. For $a = \omega/U$ [2.1], the rotating surface $H = 0$ does not disturb the incoming uniform flow.

Next is considered a screw blade $F = 0$, which lies in the neighbourhood of $H = 0$,

[2.3] $F(x, r, \varphi, t) \overset{def}{=} \varphi + \omega t - ax - \varepsilon f(x, r) = 0.$

The function $f(x, r)$, which is a measure for the deviation of the screw blade from the helicoidal surface, is some reasonable smooth function, ε being a small constant. This deviation (angle of attack and camber) induces disturbances of the uniform flow, which are supposed to be small with respect to U.

Sparenberg's first expression is the integral equation for the distribution of pressure dipoles:

$$4\pi\varepsilon\rho U^2 r \frac{\partial f}{\partial x} = \lim_{\delta \to 0} \left[\left(\int_{r_i}^{r-\delta} - \int_{r-\delta}^{r_o} \right) \int_{x_\ell(\xi)}^{x_t(\xi)} \right.$$

$$\left. \times\ S(\xi, \zeta) \sum_{n=0}^{N-1} K\left(x, r, \xi, \zeta, \frac{2\pi n}{N}\right) d\xi\, d\zeta - \frac{4\sqrt{1 - a^2 r^2}}{\delta} \int_{x_\ell(r)}^{x} S(\xi, r)\, d\xi \right]$$

$$(1.1)$$

64

where

$$K\left(x, r, \xi, \rho, \frac{2\pi n}{N}\right) = \int_{-\infty}^{x-\xi}\left[\frac{3\left\{a\rho\tau - r\sin\left(a\tau + \frac{2\pi n}{N}\right)\right\}\left\{ar\tau - \rho\sin\left(a\tau + \frac{2\pi n}{N}\right)\right\}}{\left\{\tau^2 + r^2 + \rho^2 - 2r\rho\cos\left(a\tau + \frac{2\pi n}{N}\right)\right\}^{5/2}}\right.$$
$$\left. - \frac{a^2 r\rho + \cos a\tau}{\left\{\tau^2 + r^2 + \rho^2 - 2r\rho\cos\left(a\tau + \frac{2\pi n}{N}\right)\right\}^{3/2}}\right]d\tau , \tag{1.2}$$

where

    ρ = mass density, .

    U = speed of advance,

x, r, z = ordinates,

ξ, ρ, τ = ordinates of the pressure dipoles,

    S = pressure dipole strength, and

    N = number of blades.

For further details reference is made to Sparenberg's original work [7].

    The second expression is the integral equation for the distribution of bound vortices

$$4\pi\rho U^2 r \frac{\partial f}{\partial x} = \lim_{\delta \to 0}\left\{\left(\int_{r_1}^{r-\delta} - \int_{r+\delta}^{r_o}\right)\int_{\xi_f(z)}^{\xi}\right.$$

$$\times S(\xi, z)\sum_{n=0}^{N-1}\frac{\left\{ar^2\sin\left[a(x-\xi) - \frac{2\pi n}{N}\right] - (x-\xi)\cos\left[a(x-\xi) - \frac{2\pi n}{N}\right]\right\}}{\left\{(x-\xi)^2 + r^2 + z^2 - 2rz\cos\left[a(x-\xi) - \frac{2\pi n}{N}\right]\right\}^{3/2}} d\xi\,dz$$

$$- \left(\int_{r_1}^{r-\delta} - \int_{r+\delta}^{r_o}\right)\int_{\xi_f(z)}^{\xi}\frac{\partial S(\xi, z)}{\partial z} M(x, r, ax, \xi, z)\, d\xi\,dz$$

$$+ \left(\int_{r_1}^{r-\delta} - \int_{r+\delta}^{r_o}\right)S\left[\xi_f(z), z\right] M\left[x, r, ax, \xi_f(z), z\right]\left(\frac{d\xi_f(z)}{dz}\right)dz \tag{1.3}$$
(Cont.)

65

$$- \int_{r_i}^{r_o} S\left[\xi_t(\rho),\rho\right] M\left[x, r, ax, \xi_t(\rho),\rho\right] \left(\frac{d\xi_t(\rho)}{d\rho}\right) d\rho \Bigg\} \tag{1.3}$$

in which

$$M(x, r, \sigma, \xi, \rho) = \int_{-\infty}^{(x\cdot\xi)} \sum_{n=0}^{N\cdot1}$$

$$\times \frac{\left\{(1 - a^2r^2)\sigma\cos\left[a(\tau-x) + \sigma + \frac{2\pi n}{N}\right] + a\sigma\tau\sin\left[a(\tau-x) + \sigma + \frac{2\pi n}{N}\right] - r(1 - a^2\sigma^2)\right\}}{\left\{\tau^2 + r^2 + \sigma^2 - 2r\sigma\cos\left[a(\tau-x) + \sigma + \frac{2\pi n}{N}\right]\right\}^{3/2}} d\tau. \tag{1.4}$$

2. Remarks About the Numerical Calculation

For a numerical calculation of Sparenberg's lifting surface theory either (1.1) or (1.3) may be used. For a propeller with a given load distribution no differential equation has to be solved, since Eqs. (1.1) and (1.3) are then multiple integrals only.

In the case of a one-bladed screw with a uniform load distribution the numerical difficulties are about equal for both methods. For this case the calculation has been carried out for both approaches. The results show only a maximum difference of half a percent.

Formula (1.1) leads to the numerical calculation of a Hadamard principal value. This calculation requires a lot of analytical preparatory work for a non-uniform load distribution. For a constant pressure distribution this is reduced considerably. In order to obtain an acceptable accuracy special series expansions are required in the neighbourhood of the singularities of high order at $\sigma = r; x = \xi; n = 0$.

At the point $\sigma = r$, $x = \xi$, $n = 0$ formula (1.3) renders less difficulties, since only a Cauchy principal value has to be calculated. However, now square root singularities are found at the inner and the outer radius for many types of blades.

The asymptotic behaviour of the integral of the function $M(x, r, \sigma, \xi, \rho)$ leads to a convergence worse than that of $K(x, r, \xi, \sigma, 2\pi n/N)$. Nevertheless the formula (1.3) was used for a more bladed screw with a non-uniform load distribution.

The right-hand side of (1.3) was calculated for a number of values of the radius r, and for each value of r a number of points x on the chord was chosen.

To save computing time all variables in Sparenberg's formulas were made dimensionless by multiplication by a.

66

If $B = \min \left| x - \xi_t(\rho) \right|$ for all values of x at one radius, the value of $M(B + \xi,$ $r, ax, \xi, \rho)$ may be used in the calculation of (1.3) for all x at that radius. The asymptotic behaviour of the integrand of $M(x, r, ax, \xi, \rho)$ is of the type 1^{-2}.

To obtain an oscillating integrand the function

$$\frac{- r (1 - z^2)}{\left\{ z^2 + r^2 + z^2 \right\}^{3/2}}$$

was subtracted and integrated exactly.

By a simple transformation the integral may be written as

$$\int_{B - \tau}^{B} \sum_{i=0}^{z} \sum_{n=0}^{N-1} \left[\frac{(1 - r^2) z \cos\left(\tau + \frac{2\pi n}{N} \right) + z(\tau + 2\pi i) \sin\left(\tau + \frac{2\pi n}{N} \right) - r(1 - z^2)}{\left\{ (\tau + 2\pi i)^2 + r^2 + z^2 - 2rz \cos\left(\tau + \frac{2\pi n}{N} \right) \right\}^{3/2}} \right.$$

$$+ \frac{r(1 - z^2)}{\left\{ (\tau + 2\pi i)^2 + r^2 + z^2 \right\}^{3/2}}$$

$$- \frac{(1 - r^2) z \cos\left(\tau + \frac{2\pi n}{N} \right) + z(\tau + 2\pi i + \tau) \sin\left(\tau + \frac{2\pi n}{N} \right) - r(1 - z^2)}{\left\{ (\tau + 2\pi i + \tau)^2 + r^2 + z^2 - 2rz \cos\left(\tau + \frac{2\pi n}{N} \right) \right\}^{3/2}}$$

$$\left. + \frac{r(1 - z^2)}{\left\{ (\tau + 2\pi i + \tau)^2 + r^2 + z^2 \right\}^{3/2}} \right] d\tau. \tag{2.1}$$

Formula (2.1) gives an expression that is quickly convergent for small values of z and r, but also for moderate values the convergence is sufficient. It is possible to estimate the remainder term if the infinite series is cut off, so that a prescribed accuracy may be obtained.

The integration is performed by use of the Gauss five point rule. In general it is sufficient to cut the region $B - \tau \leq \tau \leq B$ into two equal parts, and to apply this rule to each part. An accuracy of five decimal places is then obtained for all cases considered. This accuracy is checked by variation of the number of times the Gauss rule was used.

All terms containing this tail of the infinite integral are integrated in radial direction by a special integration rule, being exact for square root singularities in both end points and also for polynomials of the degree equal to the number of points in this rule minus two. The rule is of a type analogue to the integration rules of Newton Cotes of the open type.

67

$$\int_{a}^{a+h} f(x)\,dx \;=\; h \sum_{i=0}^{N-1} C_{Ni}\; f\left(a + \frac{2i+1}{2N}\,h\right).\tag{2.2}$$

For the derivation of these and other integration rules see Ref. [8].

At the point $z = r$ with $n = 0$ singularities are found in $M(x, r, ax, \xi, z)$ for $\xi < x$. These singularities are of the type $1/(z-r)$ and $\log |z-r|$. Moreover at the inner and outer radius root singularities generated by

$$\frac{d\xi_\ell(z)}{dz} \quad \text{and} \quad \frac{d\xi_t(z)}{dz}$$

must be expected.

The integration in radial direction is performed by an integration rule of the open type, being exact for logarithmic singularities at one and square root singularities at the other endpoint. The Cauchy principal value is calculated by combination of the function values for $r + z$ and $r - z$. It turns out that a sufficient accuracy is obtained if an eight-point rule is used three times.

Since only the integration boundary varies, for a given set of values (r, z) the integrand of $M(x, r, ax, \xi, z)$ is the same for all x corresponding to that value of r. Therefore it is possible to calculate these function values only one time. To use these function values also for the calculation of the double integral

$$\int_{\xi_\ell(z)}^{\xi_t(z)} \frac{\partial S(\xi, z)}{\partial z} \; M(x, r, ax, \xi, z)\,d\xi$$

integration formulas of the following type have been derived:

$$\int_{a-h}^{a+h} (x-a)^{p+2} \left\{ \int_{a+h}^{x} f(y)\,dy \right\} dx \;=\; h^p \sum_{i=0}^{N-1} D_{Nip}\, f\left(a + \frac{2i-N+1}{N}\,h\right).$$

If it is possible to approximate $\partial S(\xi, z)/\partial z$ locally by a polynomial in ξ. These rules together with the normal integration rule of Newton Cotes of the open type offer the possibility to calculate the required integrals for all values of x at that radius starting from one set of values of the integrand of $M(x, r, ax, \xi, z)$.

It is necessary to use such type of tricks to get an acceptable computing time unless a very fast computer is available. For application of the calculation method in ship screw design it will be necessary to improve the programme.

At present about two hours are needed for the calculation of one screw on an X1 digital computer (16,000 basic cycles per second).

The accuracy has been checked by variation of the order of the integration rules, and the maximum step size in these rules.

The accuracy of the integration in radial direction is found to be the greatest difficulty when Sparenberg's formula (1.3) is used. When (1.1) is used, the convergence found by improvement of the order of the integration rule is better.

The obtained accuracy for analytical load distributions is better than 1 percent, in the middle of the blade. If the boundaries are approached the errors may be somewhat larger. The calculation for the load distributions $a = 0.6$ and $a = 0.2$, is not very accurate since the function $\partial S(\xi, a)/\partial a$, can not very well be approximated by a polynomial in the neighbourhood of the point where the derivative is discontinuous.

3. Discussion of Numerical Results

The numerical results according to Sparenberg's equations for ship screws are given as values for

$$r(\partial f/\partial x)$$

representing the derivative of the camber lines for the different radii.

In Fig. 1 such a derivative is given for a four-bladed propeller. The integration of this curve results in direct information about the camber line and its pitch angle.

Fig. 1 - The function $r(\partial f/\partial x)$, which is representative for the derivative of the camber line
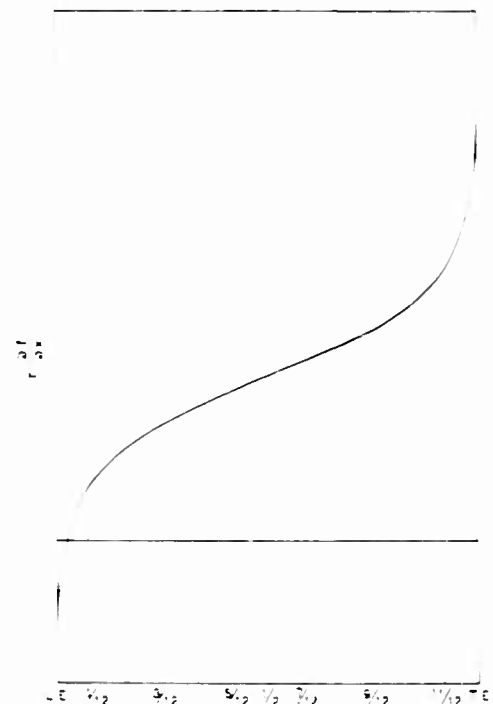
In the case of symmetric blade contours and uniform chordwise pressure distributions the following facts could be proved:

a. From geometrical considerations for vortex line elements on a helicoidal surface it follows that the value of $r(\partial f/\partial x)$ at midchord represents the corresponding lifting line value, i.e., the downwash at the location of the lifting line.

b. The curves of $r(\partial f/\partial x)$ are antisymmetric relative to midchord.

c. Analysis of the numerical results shows that for elliptical blades within the calculation accuracy the computed values of $r(\partial f/\partial x)$ may be obtained by multiplying the derivative of the camber line of the corresponding two dimensional profile by a constant factor.

From these facts it follows for the outlined symmetric case:

1. That no pitch angle correction is needed for lifting surface effects;

2. That a three dimensional $a = 1$ camber line for a section of a screw propeller is identical to the $a = 1$ camber line for two-dimensional profiles;

3. That the camber correction factor, that is the ratio between the three dimensional geometrical camber f_{geo} and the two dimensional effective camber f_{eff}, is constant along the chord.

For the two dimensional profile the effective camber ratio is determined by the relation: $f/1 = 0.05515\ C_L$* for an $a = 1$ camber line [9].

The following systematic calculations were carried out in order to get an idea about the effect of the different variations. For all calculations a hub-diameter ratio $d_h/D = 0.2$ was applied.

For a symmetric elliptic blade contour and a both radially and chordwisely uniform pressure distribution the camber correction factors

$$k = \frac{f_{geo}}{f_{eff}}$$

were calculated for 1-, 2-, 3-, 4- and 5-bladed propellers for two different radii ($x = r/R = 0.60$ and 0.76) and four different chord-diameter ratios l/D. The advance ratio $\lambda = v_a/nD$ was kept constant in these calculations. The results are given in Table 1 and Fig. 2.

In Table 2 and Fig. 3 the results are plotted of similar calculations for four-bladed propellers over a wider range of chord-diameter ratios.

*For the symbols of section 3 see the list at the end of the paper.

70

Fig. 2 - Camber correction as a function of number of blades and blade width for two different radii

Table 1
Camber Correction Values f_{geom} f_{eff} for Symmetric Elliptic Blade Contour
Uniform Pressure Distribution Both Radially and Chordwise

$\cdot = 0.167$

z	$1 = D = 0.20$	$1 = D = 0.258$	$1 = D = 0.264$	$1 = D = 0.317$
x = 0.60				
1	1.20	1.31	1.32	1.42
2	1.19	1.30	1.31	1.40
3	1.18	1.28	1.29	1.37
4	1.16	1.24	1.25	1.31
5	1.13	1.19	1.20	1.24
x = 0.76				
1	1.26	1.39	1.40	1.52
2	1.26	1.38	1.39	1.51
3	1.25	1.36	1.38	1.49
4	1.24	1.34	1.35	1.45
5	1.22	1.31	1.32	1.40

71

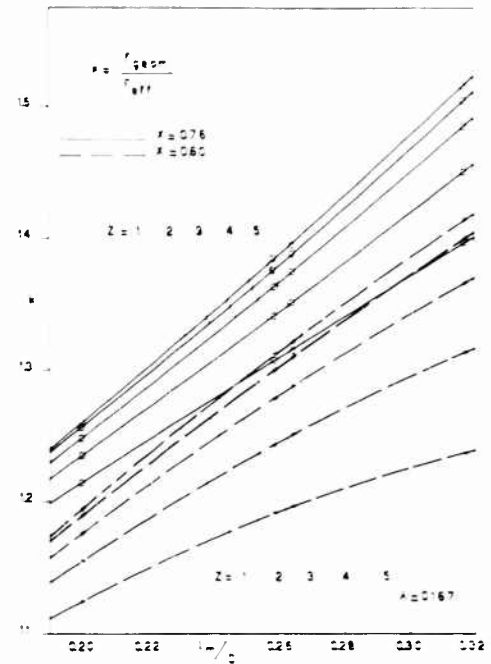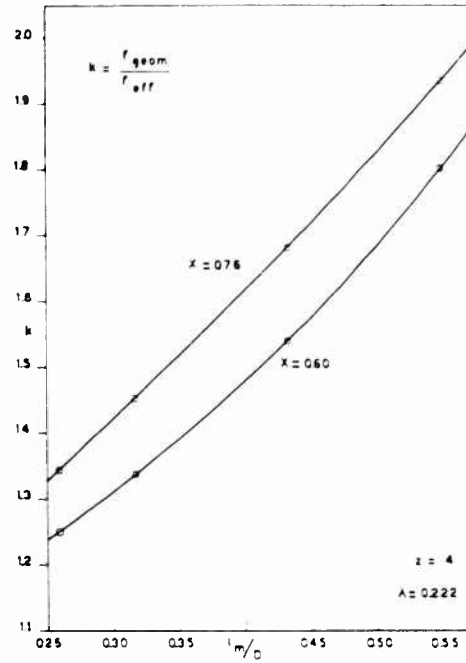Fig. 3 - Camber correction for four-bladed screws as a function of blade width for two different radii

Table 2
Camber Correction Values f_{geom} / f_{eff} for Symmetric Elliptic Blade Contour
Uniform Pressure Distribution Both Radially and Chordwise

$\lambda = 0.222; \ z = 4$

x	$lm/D = 0.258$	$lm/D = 0.317$	$lm/D = 0.433$	$lm/D = 0.550$
0.60	1.25	1.34	1.54	1.80
0.76	1.34	1.45	1.68	1.94

In Table 3 and Fig. 4 camber correction factors are given for a four-bladed propeller over a range of advance ratios.

These results are plotted on basis of the advance ratio λ instead of λ_i because they are independent of the induced velocities.

In Table 4 and Fig. 5 these factors are given for 1-, 2-, 3-, 4- and 5-bladed screws at five different radii for one chord-diameter ratio $lm/D = 0.317$. Advance ratio $\lambda = 0.222$.

The results of calculations for a symmetric blade contour and chordwisely uniform pressure distribution have been given for three variations in the radial pressure distribution in Table 5 and Fig. 6.
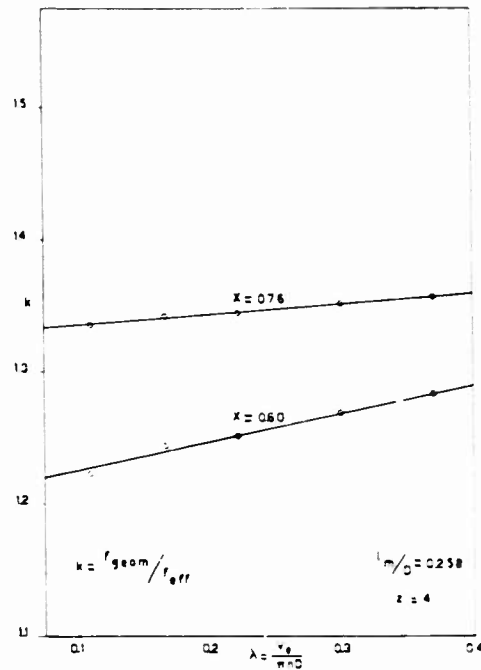
72

Fig. 4 - Camber correction as a function of the advance ratio for two different radii
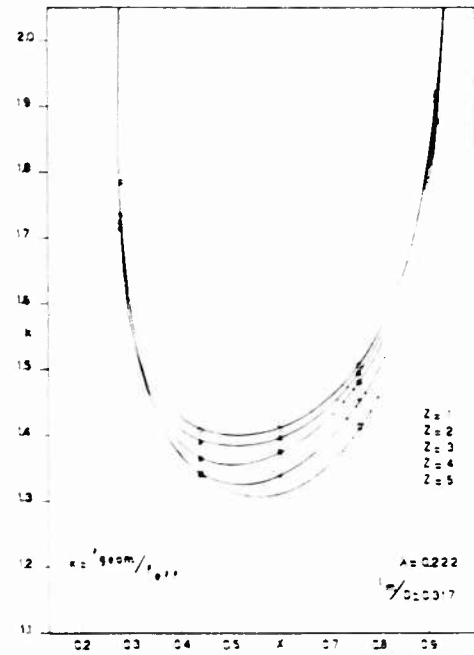
Fig. 5 - Camber correction as a function of the radius and the number of blades

Table 3
Camber Correction Values f_{geom} f_{eff} for Symmetric Elliptic Blade Contour
Uniform Pressure Distribution Both Radially and Chordwise

1m D = 0.258; z = 4

x	= 0.111	= 0.167	= 0.222	= 0.300	= 0.370
0.60	1.22	1.24	1.25	1.27	1.28
0.76	1.34	1.34	1.34	1.35	1.36

Table 4
Camber Correction Values f_{geom} f_{eff} for Symmetric Elliptic Blade Contour
Uniform Pressure Distribution Both Radially and Chordwise

= 0.222; 1m D = 0.317

z	x = 0.28	x = 0.44	x = 0.60	x = 0.76	x = 0.92
1	1.73	1.41	1.41	1.51	1.92
2	1.72	1.39	1.40	1.50	1.92
3	1.71	1.37	1.37	1.48	1.91
4	1.73	1.34	1.34	1.45	1.90
5	1.78	1.34	—	1.41	1.88

73

Fig. 6 - Effect of radial load distribution on the camber correction

In Table 6 the values of $r(\partial f / \partial x)$ for four different values of the skew back are given for a four-bladed screw with a chord-diameter ratio $1_m/D = 0.258$ and an advance ratio $\lambda = 0.222$ at $x = 0.6$
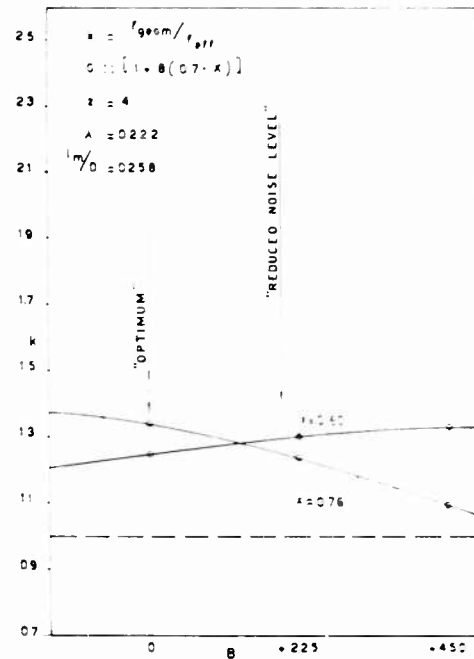
For all skew back values the projected midchord points are situated on straight lines. For $x = 0.6$ the chord situation is equal for all cases.

From Table 6 it appears that the effect of skew back on the derivative $r(\partial f / \partial x)$ and thus on the camber correction factor is small.

In Fig. 7 the results are presented for $a = 0.6$ and 0.2 camber lines. These results were calculated for a four-bladed propeller with a chord-diameter ratio $1_m/D = 0.258$ and an advance ratio $\lambda = 0.222$.

From Fig. 7 it seems that the derivative of the camber line of a three dimensional screw section with an

Table 5

Camber Correction Values $f_{geo} - f_{eff}$ for Symmetric Elliptic Blade Contour and Uniform Chordwise Pressure Distribution

$$G :: \left[1 + B (0.7 - x)\right]; z = 4; \lambda = 0.222; 1_m/D = 0.258$$

x	B = 0	B = 2.25	B = 4.5
0.60	1.25	1.30	1.33
0.76	1.34	1.24	1.10

Table 6

$r(\partial f / \partial x)$ -Values for Systematic Skew Back Variations for a Uniform Pressure Distribution

Percentage of the Chord	$\dfrac{Skew}{D} = 0$	$\dfrac{Skew}{D} = 1/12$	$\dfrac{Skew}{D} = 1/6$	$\dfrac{Skew}{D} = 1/4$
3.33	4.43	4.17	3.61	2.65
25	7.63	7.57	7.47	7.48
41.67	9.53	9.61	9.59	9.36
58.33	11.22	11.35	11.54	11.82
75	13.12	13.18	13.38	13.74
91.67	16.32	16.30	16.51	16.94

Fig. 7 - $r(\partial f/\partial x)$ values for $a = 0.6$ and $a = 0.2$ pressure distributions
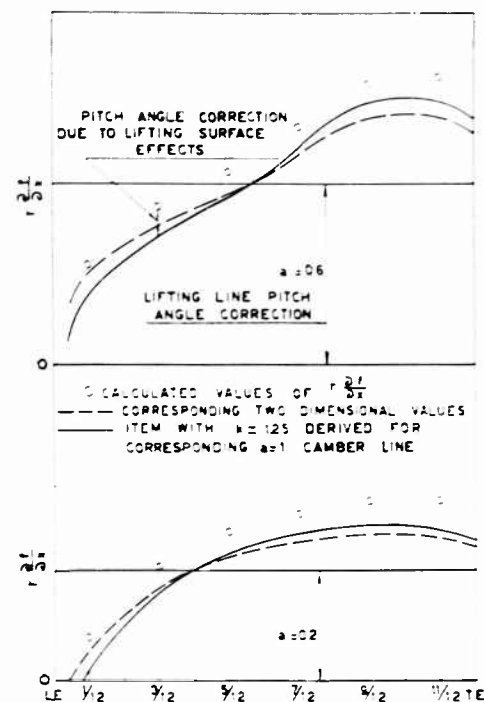
$a = 0.8 - 0.6 - 0.4$ or 0.2 camber line can be obtained by superposing on the lifting line pitch angle correction the two dimensional corresponding "a" - camber line corrected in camber with a k-value calculated for the $a = 1$ camber line and an extra pitch angle correction, which is small compared with the lifting line pitch angle correction.

4. Conclusions

For a uniform pressure distribution along the chord ($a = 1$ camber line) the three dimensional camber line of a propeller blade section is identical to the camber line of the two dimensional profiles. As a consequence the camber correction factor is constant along the chord.

In the case of a symmetric blade contour and a uniform chordwise pressure distribution ($a = 1$ camber line) no extra pitch angle correction apart from the lifting line pitch angle correction is needed.

The effect of the number of blades on the camber correction factor is almost zero at the hub and the blade tip for equal blades but more pronounced in the middle of the blades.

The effect of the radial load distribution on the camber correction factors is not very pronounced.

75

The effect of skew back on the camber correction factor is practically negligible, especially in the middle of the blades.

If non-uniform chordwise pressure distributions such as $a = 0.8$ camber lines are applied, the k-values found for the $a = 1$ camber line can be used. However, an extra pitch angle correction, which is small compared with the lifting line pitch angle correction, has to be applied.

Though due to differences in blade contour it is difficult to make comparisons the impression is established that the presented curvature correction values

$$k = \frac{f_{geom}}{f_{eff}}$$

are larger than those published by Ludwig, Ginzel and Kerwin, and comparable in magnitude with some values published by Cox.

The tendencies given in this paper will be used in practical screw design. However, it still must be investigated whether the effect of the hub and thickness of the blades must also be introduced in the theory. Especially for the higher numbers of blades this might be necessary.

Finally it must be considered which is the best way of using the results of lifting surface theory in practice:

a. To optimize the computer programme in order to be able to calculate each propeller design individually with the lifting surface theory; and

b. To carry out a large systematic series of calculations, resulting in a scheme of camber corrections dependent on the propeller design data, which can be applied in combination with a lifting line theory.

REFERENCES

1. Lerbs, H., "Ergebnisse der Angewandten Theorie des Schiffspropellers," Jahrbuch S.T.G., 1955.

2. Manen, J. D. van and Crowley, J. D., "Some Aspects of Circulation Theory Design of Screw Propellers," Int. Shipb. Progress, 1959.

3. Kerwin, J. E., "The Solution of Propeller Lifting Surface Problems by Vortex Lattice Methods," Massachusetts Inst. of Techn., Dept. of Naval Arch. and Mar. Eng., 1961.

4. Pien, P. C., "The Calculation of Marine Propellers Based on Lifting Surface Theory," D.T.M.B., 1961.

5. Nishiyama, T., "Lifting Surface Theory of the Widely Bladed Marine Propellers"; Nakajima, Y., "Theory of the Wide-Bladed Propellers and its Application," Journal of Zosen Kiokai (The Soc. of Naval Arch. of Japan), Vol. 109, 1961 (Japanese).

6. Cox, G. G., "Corrections to the Camber of Constant Pitch Propellers," Trans. R.I.N.A., 1961.

7. Sparenberg, J. A., "Application of Lifting Surface Theory to Ship Screws," Proc. K.N.A.W., Ser. B, 1959; Int. Shipb. Progress, 1960.

8. Bakker, A. R., "Numerical Computation of Sparenberg's Lifting Surface Theory to Ship Screws," N.S.M.B. Report (to be published).

9. Abbott, I. H., Doenhoff, A. E. von and Stivers, L. S., "Summary of Airfoil Data," N.A.C.A. Report No. 824, 1945.

LIST OF SYMBOLS
(Section 3)

C_L = lift coefficient

D = diameter

$f/1$ = camber ratio

G = non-dimensional circulation at radius x

$k = f_{geom}/f_{eff}$ = camber correction factor

lm/D = maximum chord-diameter ratio

$x = r/R$ = non-dimensional radius

z = number of blades

$\lambda = v_e/-nD$ = advance ratio

* * *

HYDRODYNAMICS OF AN OSCILLATING SCREW PROPELLER

T. Hanaoka
Transportation Technical Research Institute
Tokyo, Japan

INTRODUCTION

The development of methods for calculating the hydrodynamic forces acting on the blade of a screw propeller in non-uniform flow has occupied the attention of numerous investigators. Theoretical developments and calculations have been presented for an infinite number of blades, or for high aspect ratio blades, by Isay [1], Loewy [2], Timman and van de Vooren [3], and others. However, the writer has been unable to find any reference to the subject of nonsteady helical fluid field for a screw propeller with a finite number of blades.

The present paper is concerned with the problem of the oscillating screw propeller with finite blades, within the frame of the linearized lifting-surface theory (we may apply the present theory to the case that the surrounding fluid oscillates, instead of the blade itself). The scope of the present work may briefly be described as follows. The starting point of the work is a formulation of the helical velocity field. The velocity potential can simply be derived by means of the conception of acceleration potential [4]. The boundary-value problem can be converted to the integral equation that relates a prescribed downwash distribution to an unknown lift distribution for harmonically oscillating blades. The integral equation appears as a singular integral equation. The kernel function is reduced to a form that can be accurately evaluated by numerical procedures. The form and order of all its singularities are determined. We shall be able to solve the integral equation by means of a completely numerical method. Application of this method awaits the numerical evaluation of the kernel function.

SYMBOLS

We discuss the fluid field disturbed by an oscillating screw propeller which moves with a constant linear velocity V along the negative x-axis rotating with a constant angular velocity Ω about the axis in clockwise.

t   time

$r, \theta, x;$ cylindrical coordinates. The x-axis coincides with the
r', θ', x' propeller axis, the ' denoting that these quantities are
related to the point on the blade.

V   velocity of advance

Ω angular velocity of rotation

ν circular frequency of oscillation

ρ fluid density

p   fluid pressure

$\varpi = \varpi_o e^{i\nu t}$ acceleration potential

$\Phi = \Phi_o e^{i\nu t}$ velocity potential

$\mu', \mu = \mu'/\Omega$ Rayleigh's frictional coefficient

ϖ_u, ϖ_ℓ the acceleration potentials at the upper and lower sides of
the blade, respectively

$\delta n'$ line-element normal to the surface of chord, positive in the
direction contrary to the lift direction

r_o radius of the propeller

ℓ number of blades

$\varepsilon = 2p\pi/\ell$ phase difference of oscillation between each blade

$H = -iH_o e^{i\nu t}$ displacement of the blade, normal to the datum plane (heli-
cal surface), positive in the direction contrary to the lift
direction

$$h = \frac{V}{\Omega}, \qquad p = \frac{\nu}{\Omega}, \qquad \xi = \frac{r}{h}, \qquad \xi' = \frac{r'}{h}, \qquad \xi_o = \frac{r_o}{h},$$

$$\varphi = \theta - \frac{x}{h}, \qquad \bar{\varphi} = \theta + \frac{x}{h}, \qquad \varphi' = \theta' - \frac{x'}{h}, \qquad \bar{\varphi}' = \theta' + \frac{x'}{h},$$

$$W = \sqrt{V^2 + \Omega^2 r^2} = V\sqrt{1 + \xi^2}, \qquad W' = V\sqrt{1 + \xi'^2}.$$

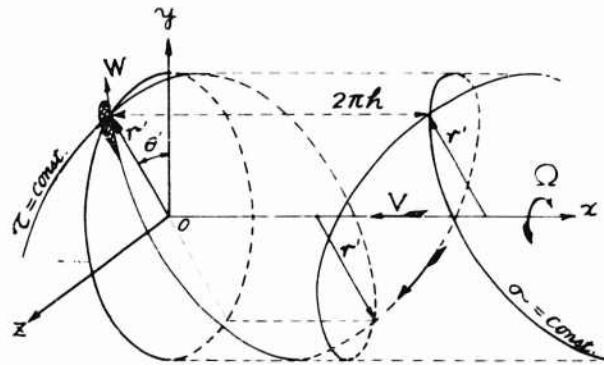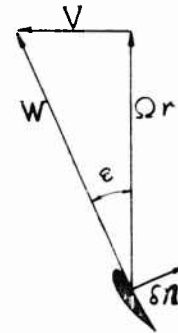$$c(\varpi_u - \varpi_\ell) = \pi = \pi_o e^{i\nu t}.$$

80

Figure 1

Figure 2

1. SYMMETRIC OSCILLATION OF A SYMMETRIC PROPELLER

When each blade of propeller oscillates arbitrarily in frequency, phase, or mode, the evaluation of the lift distribution of the blade is very complicated, because we must carry out the evaluation on all the blades. But on the case of the actual oscillations of marine propellers, there is often a simple relationship among frequency ν, phase difference ε of oscillation between each blade, and angular velocity of rotation.

The helical velocity field becomes symmetric and the complex amplitude of the lift distribution on the blades coincides with each other, if the propeller oscillates under the condition such that:

a. The propeller has symmetric blades.

b. The frequency, mode, amplitude of the oscillation does not differ on each blade.

c. The phase angle between each blade is equal to $2p\pi/\nu$ or zero, where p is an integer.

$\varepsilon = 2p\pi/\nu$ corresponds to $p = \nu/\Omega$, because $\varepsilon = 2p\pi/\nu$ implies that each blade oscillates p times in the course of one rotation. We may call such an oscillation "a symmetric oscillation." As a typical example, we can find the "symmetric oscillation" in the velocity field due to the propeller rotating in non-uniform flow.

2. FUNDAMENTAL EXPRESSION OF VELOCITY POTENTIAL

We regard the fluid as an inviscid and incompressible medium and neglect the effect of gravity. If σ denotes the acceleration potential, the equation of motion is written in the form

81

$$c = -\frac{p}{\rho} + f(t) . \tag{2.1}$$

When the propeller is lightly loaded, it may be permitted that the fluid velocity disturbed by the motion of the propeller is so small compared with the velocity of the blade elements themselves that the square term in Euler's equation of motion may well be taken negligible with impunity. Moreover, we may avail ourselves of an artifice due to Rayleigh, and assume that the deviation of any particle of the fluid from the state of uniform flow is resisted by a force proportional to the relative velocity. This law of friction has the great mathematical convenience that it does not interfere with the irrotational character of the motion. In such a case, we have a linearized relation

$$c = \frac{\partial\Phi}{\partial t} + V\frac{\partial\Phi}{\partial x} + \Omega\frac{\partial\Phi}{\partial\varsigma} + \mu'\Phi = \frac{\partial\Phi}{\partial t} + 2\Omega\frac{\partial\Phi}{\partial\tau} + \mu'\Phi , \tag{2.2}$$

regarding a point which moves along a helical path with constant velocity V and Ω in a constant phase relative to the propeller, and c satisfies Laplace's differential equation $\Delta c = 0$, as well as Φ.

The acceleration field does not present any discontinuity except at the surfaces of the lifting system, being connected with the pressure by the linear relation (2.1). The discontinuity of the acceleration potential may be supposed to occur on the projected area of an actual blade upon the helical surface which is the locus of the moving blade, within the limitations of the linearized theory. We may call it "a datum plane." Hence, for the acceleration potential due to a lifting system whose thickness is negligible, we have

$$c(\tau, \varsigma, \varpi; t) = -\frac{1}{4\pi}\int\int(c_u - c_\ell)\frac{\partial}{\partial n'}\left(\frac{1}{R}\right)dS' . \tag{2.3}$$

where the surface integral extends over the whole datum plane and

$$R = h\sqrt{(\tau - \tau' - \varsigma + \varsigma')^2 4 + \varpi^2 + \varpi'^2 - 2\varpi\varpi'\cos\{(\tau - \tau' + \varsigma - \varsigma')\,2\}} .$$

If we regard (2.2) as a differential equation with respect to Φ, the solution is

$$\Phi(\tau, \varsigma, \varpi; t) = \frac{1}{2\pi}\int_{-\infty}^{\tau} e^{-\frac{\mu'}{2\Omega}(\tau - T)} c\left(T, \varsigma, \varpi; t - \frac{\tau - T}{2\Omega}\right)dT . \tag{2.4}$$

Putting $c_u - c_\ell = c_o e^{i\nu t} c$ in (2.3) and then substituting (2.3) in (2.4), we obtain the complex amplitude of the velocity potential in the form

$$\Phi_o(\tau, \varsigma, \varpi) = -\frac{1}{8\pi\Omega\varsigma}\sum_{m=0}^{\ell-1}\int\int c_o(\tau', \varpi') e^{-i2pm\pi^{-\ell}}dS'$$

$$\times \int_{-\infty}^{\tau} e^{-(\mu + ip)(\tau - T)\,2}\frac{\partial}{\partial n'}\left(\frac{1}{R}\right)dT . \tag{2.5}$$

82

where the surface integral extends over the datum plane of one blade, and

$$R = h\sqrt{(T - \tau' - \sigma + \sigma')^2/4 + \mu^2 + \mu'^2 - 2\mu\mu' \cos \{(T - \tau' + \sigma - \sigma' - 4m\pi/\ell)/2\}} \quad . \qquad (2.6)$$

Let the angle between the plane of rotation and the datum plane of the blade by ϵ', it follows from the geometric relationship that

$$\sin \epsilon' = \frac{V}{W'} , \qquad \cos \epsilon = \frac{\Omega r'}{W'}$$

and

$$\frac{\partial}{\partial n'} = \cos \epsilon' \frac{\partial}{\partial x'} - \sin \epsilon' \frac{1}{r'} \frac{\partial}{\partial \theta'}$$

$$= \frac{1}{h\sqrt{1 + \mu'^2}} \left\{ - \left(\mu' + \frac{1}{\mu'} \right) \frac{\partial}{\partial \sigma'} + \left(\mu' - \frac{1}{\mu'} \right) \frac{\partial}{\partial \tau'} \right\} . \qquad (2.7)$$

Equation (2.5) is a fundamental expression of the velocity potential of the fluid field disturbed by an oscillating screw propeller.

3. VORTEX THEORY

As stated above, we could derive the velocity potential purely analytically by means of the conception of acceleration potential. But in the field of propelier hydrodynamics, the vortex theory has been adopted as an ordinary conception, and we are accustomed to attribute the induced velocity field to the effect produced by the vortex system.

It does not only afford an intuitive concept of the real circumstances, but also it will be quite within the bounds of possibility to progress into the non-linear theory. In the following analysis, the readers will see the vortex system created by propeller in the velocity field expressed by (2.5).

When we put $\mu = 0$, (2.5) is written

$$\Phi_0(\tau, \sigma, \mu) = - \frac{1}{8\pi^2} \sum_{m=0}^{\ell-1} \int_0^{r_0} dr' \int_{s_1}^{s_2} \gamma_0(s' . r') e^{-i 2pm\pi i} ds'$$

$$\times \int_{-\infty}^{\tau} e^{-\frac{ip}{2}(\tau - T)} \frac{\partial}{\partial n'} \left(\frac{1}{R} \right) dT . \qquad (3.1)$$

where s denotes the distance measured along the helical locus of the blade, and s_1, and s_2 denote the positions of leading and trailing edges of the blade respectively. We have

83

$$ds = W \, d\tau/(2\Omega) = h\sqrt{1 + \mu^2} \; d\tau/2 \tag{3.2}$$

from the geometric relationship.

Writing $\mathbf{T} = \tau + \tau' - \mathbf{T}'$ in the integral of (3.1), we get

$$\Phi_o(\tau, \sigma, \mu) = -\frac{1}{8\pi\Omega\rho} \sum_{m=0}^{\ell-1} \int_0^{r_o} dr' \int_{s_1}^{s_2} \pi_o(s', r') \; e^{-i2pm\pi/\ell} \; ds'$$

$$\times \int_{\tau'}^{\infty} e^{-\frac{ip}{2}(\mathbf{T}'-\tau')} \; \frac{\partial}{\partial \mathbf{n}''} \left(\frac{1}{R}\right) d\mathbf{T}' \; , \tag{3.3}$$

where $\partial/\partial\mathbf{n}''$ means the operation writing $\partial/\partial\mathbf{T}'$, in place of $\partial/\partial\mathbf{T}$ in (2.7). When $\mu = 0$, φ is written in the form

$$\varphi = \frac{\partial\Phi}{\partial t} + W \frac{\partial\Phi}{\partial s}$$

by (3.2) and so

$$\frac{\tau(s, t)}{\varphi} = \frac{\partial}{\partial t}(\Phi_u - \Phi_\ell) + W\left(\frac{\partial\Phi_u}{\partial s} - \frac{\partial\Phi_\ell}{\partial s}\right). \tag{3.4}$$

When we write

$$\frac{\partial\Phi_u}{\partial s} - \frac{\partial\Phi_\ell}{\partial s} = \gamma(s, t) = \gamma_o(s) \; e^{i\nu t}, \tag{3.5}$$

$\gamma(s, t)$ means the circulation density and it disappears in front of the leading edge of the blade.

Therefore, (3.4) is written in the form

$$\frac{\tau(s, t)}{\varphi} = \frac{\partial}{\partial t} \int_{s_1}^{s} \gamma(s', t) \; ds' + W \frac{\partial}{\partial s} \int_{s_1}^{s} \gamma(s', t) \; ds'. \tag{3.6}$$

Integrating the linear differential Eq. (3.6), we obtain the circulation distribution

$$\int_{s_1}^{s} \gamma(s', t) \; ds' = \frac{1}{\varphi W} \int_{s_1}^{s} \tau\left(s', t - \frac{s - s'}{W}\right) ds'$$

$$= \frac{e^{i\nu t}}{\varphi W} \int_{s_1}^{s} e^{-\frac{i\nu}{W}(s - s')} \tau_o(s') \; ds'. \tag{3.7}$$

84

Changing the variable from $\mathbf{T}'$ to s in the integral of (3.3) by (3.2), we have

$$\frac{1}{2\Omega\rho} \int_{s_1}^{s_2} \pi_0(s')\, ds' \int_{\tau'}^{\infty} e^{-\frac{ip}{2}(\mathbf{T}'-\tau')} \frac{\partial}{\partial \mathbf{n}''}\left(\frac{1}{R}\right) d\mathbf{T}'$$

$$= \frac{1}{\rho W'} \int_{s_1}^{s_2} \pi_0(s')\, ds' \int_{s'}^{\infty} e^{-\frac{i\nu}{W'}(\tilde{s}-s')} \frac{\partial}{\partial \mathbf{n}''}\left(\frac{1}{R}\right) d\tilde{s} .$$

Reversing the order of integration by virtue of Dirichlet's transform, and substituting (3.7), we obtain

$$= \frac{1}{\rho W'} \int_{s_1}^{\infty} \frac{\partial}{\partial \mathbf{n}''}\left(\frac{1}{R}\right) d\tilde{s} \int_{s_1}^{\tilde{s}} \pi_0(s')\, e^{-\frac{i\nu}{W'}(\tilde{s}-s')}\, ds'$$

$$= \int_{s_1}^{\infty} \frac{\partial}{\partial \mathbf{n}''}\left(\frac{1}{R}\right) d\tilde{s} \int_{s_1}^{\tilde{s}} \gamma_0(s')\, ds' .$$

Therefore, (3.3) is written in the form

$$\Phi_0(\tau,\sigma,\mu) = -\frac{1}{4\pi} \sum_{m=0}^{\ell-1} e^{-i2pm\pi/\ell} \int_0^{r_0} dr' \int_{s_1}^{\infty} \int_{s_1}^{\tilde{s}} \gamma_0(s')\, ds' \frac{\partial}{\partial \mathbf{n}''}\left(\frac{1}{R}\right) d\tilde{s} . \tag{3.8}$$

This is the potential of the velocity field induced by the vortices lain on the helical surfaces along which the blades have traveled, and its circulation density is $\gamma_0(s)$.

Differentiating (3.7) with respect to s, we at once get

$$\gamma(s,t) = \frac{\tau(s,t)}{W} - \frac{1}{W^2} \int_{s_1}^{s} \frac{\partial \tau}{\partial t}\left(s',t - \frac{s-s'}{W}\right) ds' . \tag{3.9}$$

In right-hand member, the first and second terms imply the circulation density of the bound and the free vortices respectively. This is "the Prandtl's principle of vortex conservation." When we put $-(\tau w) = \tau^*$, (3.9) satisfies Prandtl's relation

$$\frac{\partial \gamma^*}{\partial t} + \frac{\partial \gamma}{\partial t} - w\frac{\partial \gamma}{\partial s} = 0 .$$

When the lifting system is oscillating harmonically, the complex amplitude of the circulation density is written

$$\gamma_o(s) \;=\; \frac{\pi_o(s)}{\rho W} \;-\; \frac{i\nu}{\rho W^2} \int_{s_1}^{s} \pi_o(s') \; e^{-\frac{i\nu}{W}(s-s')} \; ds' . \tag{3.10}$$

Consequently, we see that the velocity field (2.5) derived by the method of acceleration potential is converted into the velocity field induced by a vortex system. The linearization of the Euler's equation of motion corresponds with the assumption in the vortex theory that the trailing vortices are lying on the locus of the advancing blades.

4. APPLICATION OF GREEN'S FUNCTION TO THE EXPRESSION OF VELOCITY POTENTIAL

There is no difficulty in realizing the general nature of the disturbance represented by the equation (2.5), as shown in section 3. But if we use the Green's function and perform such the integration that appears in (2.5), the derived expressions will serve for us to realize the nature of the velocity field analytically and also it will be suitable for the development.

Green's function in whole space is written

$$\frac{1}{R} = \frac{1}{h\sqrt{(\tau-\tau'-\sigma+\sigma')^2/4 + \mu^2 + \mu'^2 - 2\mu\mu' \cos\{(\tau-\tau'+\sigma-\sigma')\,2 - 2m\pi/\ell\}}}$$

$$= \frac{1}{\pi h} \sum_{n=-\infty}^{\infty} \int_{-\infty}^{\infty} e^{\frac{i}{2}(\lambda+n)(\tau-\tau') - \frac{i}{2}(\lambda-n)(\sigma-\sigma') - i2nm\pi/\ell} \, I_n(\lambda\mu) \cdot K_n(\lambda\mu') \, d\lambda ,$$

where $\mu' > \mu$ and I_n, K_n denote the modified Bessel functions. Since we at once obtain

$$\frac{\partial}{\partial n'} \int_{-\infty}^{\tau} e^{-(\mu+ip)(\tau-T)/2} \frac{1}{R} \, dT \;=\; \frac{-2}{-h^2\sqrt{1-\mu'^2}} \sum_{n=-\infty}^{\infty} \int_{-\infty}^{\infty} \frac{\mu'\lambda - n\mu'}{\lambda + p + n - i\mu}$$

$$\times \; I_n(\lambda\mu) \cdot K_n(\lambda\mu') \, e^{\frac{i}{2}(\lambda+n)(\tau-\tau') - \frac{i}{2}(\lambda-n)(\sigma-\sigma') - i2nm\pi/\ell} \, d\lambda .$$

the velocity potential (2.5) is written in the form

$$\Phi_o(\tau,\sigma,\mu) \;=\; \frac{1}{4\pi^2 \Omega h^2 \sigma} \sum_{m=0}^{\ell-1} \iint \frac{\pi_o(\tau',\mu')}{\sqrt{1-\mu'^2}} \; e^{-i2pm\pi/\ell} \, dS'$$

$$\times \sum_{n=-\infty}^{\infty} \int_{-\infty}^{\infty} \frac{\mu'\lambda - n\mu'}{\lambda + p + n - i\mu} \, I_n(\lambda\mu_<) \cdot K_n(\lambda\mu_>)$$

$$\times \; e^{\frac{i}{2}(\lambda+n)(\tau-\tau') - \frac{i}{2}(\lambda-n)(\sigma-\sigma') - i2nm\pi/\ell} \, d\lambda \tag{4.1}$$

86

or

$$\Phi_o(\tau,\sigma,\mu) = \frac{\ell}{4\pi^2\Omega h^2\rho}\iint \frac{\pi_o(\tau',\mu')}{\sqrt{1+\mu'^2}}\,dS'$$

$$\times \sum_{k=-\infty}^{\infty}\int_{-\infty}^{\infty}\frac{\mu'\lambda - (\ell k - p)/\mu'}{\lambda + \ell k - i\mu}\,I_{\ell k-p}(|\lambda|\mu_<)\cdot K_{\ell k-p}(|\lambda|\mu_>)$$

$$\times e^{\frac{i}{2}(\lambda+\ell k-p)(\tau-\tau')-\frac{i}{2}(\lambda-\ell k+p)(\sigma-\sigma')}\,d\lambda \tag{4.2}$$

by virtue of

$$\sum_{m=0}^{\ell-1} e^{-\frac{i2m\pi}{\ell}(p+n)} = \begin{cases} 0, & p+n \neq k\ell \\ \ell, & p+n = k\ell \end{cases} \quad (k; \text{ integer, included zero}), \tag{4.3}$$

where $\mu_>$ and $\mu_<$ imply the major and minor quantities of μ and μ' respectively. When $\mu \to 0$, we obtain

$$\Phi_o(\tau,\sigma,\mu) = \frac{1}{4\pi^2\Omega h^2\rho}\sum_{m=0}^{\ell-1}\iint \frac{\pi_o(\tau',\mu')}{\sqrt{1+\mu'^2}}\,e^{-i2pm\tau/\ell}\,dS'$$

$$\times \sum_{n=-\infty}^{\infty}\oint_{-\infty}^{\infty}\frac{\mu'\lambda - n/\mu'}{\lambda + p + n}\,I_n(|\lambda|\mu_<)\cdot K_n(|\lambda|\mu_>)$$

$$\times e^{\frac{i}{2}(\lambda+n)(\tau-\tau')-\frac{i}{2}(\lambda-n)(\sigma-\sigma')-i2nm\pi/\ell}\,d\lambda$$

$$- \frac{i}{4\pi\Omega h^2\rho}\sum_{m=0}^{\ell-1}\iint \frac{\pi_o(\tau',\mu')}{\sqrt{1+\mu'^2}}\,e^{-i2pm\pi/\ell}\,dS'$$

$$\times \sum_{n=-\infty}^{\infty}\left\{\mu'(p+n)+n/\mu'\right\}I_n(|p+n|\mu_<)\cdot K_n(|p+n|\mu_>)$$

$$\times e^{-\frac{ip}{2}(\tau-\tau')+\frac{i}{2}(p+2n)(\sigma-\sigma')-i2nm\pi/\ell} \tag{4.4}$$

When $p + n = 0$, we have

$$\lim_{p+n\to 0} I_n(|p+n|\mu_<)\cdot K_n(|p+n|\mu_>) = \frac{1}{2p}\left(\frac{\mu_<}{\mu_>}\right)^p.$$

87

Hanaoka

since $I_n = I_{-n}$, $K_n = K_{-n}$, and the asymptotic expansions are

$$I_n(x) \sim \frac{1}{n!}\left(\frac{x}{2}\right)^n, \qquad K_n(x) \sim \frac{(n-1)!}{2}\left(\frac{2}{x}\right)^n \tag{4.5}$$

for $x \sim 0$, $n \geq 1$.

From (4.4), we derive the velocity potential in the region infinitely far behind the propeller.

The integral of λ can be transformed into the integral along the imaginary axis by considering the integral

$$\frac{1}{2\pi i}\int \frac{\mu' z - n/\mu'}{z + p + n}\, I_n(z\mu_<) \cdot K_n(z\mu_>)\, e^{\frac{i}{2}(\tau - \tau' - \sigma + \sigma')z}\, dz , \tag{4.6}$$

taken round suitable contours.

When $\tau - \tau' - \sigma + \sigma' > 0$, the contour is chosen with a loop as shown in Fig. 3, and then there are no poles inside the contour; and the integral round the large quadrant tends to zero as the radius tends to infinity. The integral round the indentation at $z = -(p+n)$ tends to the half of the residue. We thus have
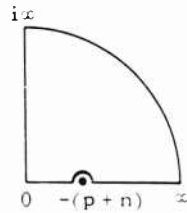

Figure 3

$$\oint_0^\infty \frac{\mu'\lambda - n/\mu'}{\lambda + p + n}\, I_n(\lambda\mu_<) \cdot K_n(\lambda\mu_>)$$

$$\times\, e^{\frac{i}{2}(\tau - \tau' - \sigma + \sigma')\lambda}\, d\lambda = -\frac{i\pi}{2}\int_0^\infty \frac{i\mu'\lambda - n\mu'}{\lambda - i(p+n)}$$

$$\times\, J_n(\lambda\mu_<) \cdot H_n^{(2)}(\lambda\mu_>)\, e^{-\frac{1}{2}(\tau - \tau' - \sigma + \sigma')\lambda}\, d\lambda$$

$$-i\pi\epsilon_n\{\mu'(p+n) + n\mu'\} \cdot I_n\{-(p+n)\mu_<\} \cdot K_n\{-(p+n)\mu_>\}\, e^{-\frac{i}{2}(\tau - \tau' - \sigma + \sigma')(p+n)} \tag{4.7}$$

where

$$\epsilon_n = \begin{cases} \dfrac{1}{2}, & p+n = 0 \\[2mm] 1, & p+n \neq 0 \end{cases}$$

and the second term vanishes when $p+n > 0$.

In like manner, the integral of λ along negative axis can be transformed into the integral along the imaginary axis. Consequently, we have

88

$$\oint_{-\infty}^{\infty} \frac{\mu'\lambda - n/\mu'}{\lambda + p + n} \; I_n(|\lambda|\mu_<) \cdot K_n(|\lambda|\mu_>) \cdot e^{\frac{i}{2}(\tau - \tau' - \sigma + \sigma')\lambda} \; d\lambda$$

$$= -i\pi \int_0^{\infty} \frac{i\mu'\lambda - n/\mu'}{\lambda - i(p+n)} \; J_n(\lambda\mu_<) \cdot J_n(\lambda\mu_>) \cdot e^{-\frac{1}{2}(\tau - \tau' - \sigma + \sigma')\lambda} \; d\lambda$$

$$-i\pi\{\mu'(p+n) + n/\mu'\} \cdot I_n(|p+n|\mu_<) \cdot K_n(|p+n|\mu_>) \; e^{-\frac{i}{2}(\tau - \tau' - \sigma + \sigma')(p+n)} \, , \qquad (4.8)$$

for $\tau - \tau' - \sigma + \sigma' > 0$. When $\tau \to \infty$, the first term of (4.8) vanishes. Therefore, the velocity potential in the region far behind the propeller becomes

$$\Phi_{o\,\infty}(\tau,\sigma,\mu) \;=\; -\frac{i}{2\pi\,\Omega h^2 \rho} \sum_{m=0}^{\ell-1} \iint \frac{\pi_o(\tau',\mu')}{\sqrt{1 + \mu'^2}} \; e^{-i2pm\pi/\ell} \; dS'$$

$$\times \sum_{n=-\infty}^{\infty} \left\{\mu'(p+n) + n/\mu'\right\} \cdot I_n(|p+n|\mu_<) \cdot K_n(|p+n|\mu_>)$$

$$\times \; e^{-\frac{ip}{2}(\tau - \tau') + \frac{i}{2}(p + 2n)(\sigma - \sigma') - i2nm\pi/\ell} \, . \qquad (4.9)$$

We see that the velocity field harmonically varies along the helical surface in the region far behind the propeller.

5. INTEGRAL EQUATION

If $H = -iH_o e^{i\nu t}$ denotes the displacement of the blade, normal to the datum plane, the boundary condition

$$\frac{dH}{dt} \;=\; \frac{\partial H}{\partial t} + W \frac{\partial H}{\partial s} \;=\; \frac{\partial\Phi}{\partial n} \qquad (5.1)$$

may be satisfied on the datum plane, within the limit of the linearized theory. Therefore, it is also written in the form

$$\nu H_o - i2\Omega \frac{\partial H_o}{\partial \tau} \;=\; w_o \;=\; \frac{\partial\Phi_o}{\partial n}\bigg|_{\sigma=\sigma'} \, . \qquad (5.2)$$

By using (4.1) and (2.7), we get

$$w_o(\tau,\mu) \;=\; \frac{i}{4\pi^2\,\Omega h^3 \rho \sqrt{1 + \mu^2}} \sum_{m=0}^{\ell-1} \iint \frac{\pi_o(\tau',\mu')}{\sqrt{1 + \mu'^2}} \; e^{-i2pm\pi/\ell} \; dS' \qquad \begin{array}{r}(5.3)\\ (\text{Cont.})\end{array}$$

89

$$\times \sum_{n=-\infty}^{\infty} \int_{-\infty}^{\infty} \frac{(\mu'\lambda - n/\mu') \, (\mu\lambda - n/\mu)}{\lambda + p + n - i\boldsymbol{\mu}} \; I_n(\,|\lambda|\mu_<) \cdot K_n(\,|\lambda|\mu_>)$$

$$\times \; e^{\frac{i}{2}(\lambda+n)(\tau-\tau') - \frac{i}{2}(\lambda-n)(\sigma-\sigma') - i\,2nm\pi/\ell} \Bigg|_{\sigma=\sigma'} . \tag{5.3}$$

This is the integral equation that relates oscillatory lift and downwash distribution on a blade.

6. BOUNDARY CONDITION AND DOWNWASH

In the linearized theory, the downwash distribution on the blade is directly related with the motion of the blade as shown in (5.2). In this section we show the various kinds of the downwash distribution on the blade.

Oscillation of Blades

For flexural oscillation of a blade, the normal displacement of the blade is given by

$$H = -iH_o(r)\,e^{i\nu t}$$

and so

$$w_o = \nu H_o(r) .$$

For torsional oscillation of a blade, the normal displacement of the blade is given by

$$H = -is\,\alpha_o(r)\,e^{i\nu t} = -\frac{i}{2}\,\alpha_o(r)\,h\sqrt{1 + \mu^2}\; \tau e^{i\nu t}$$

and so

$$w_o = \alpha_o(r)\sqrt{1 + \mu^2}\;(\nu h\tau/2 - iV) , \tag{6.1}$$

where $\alpha_o(r)$ denotes the amplitude of torsion.

The amplitude of the blade oscillation should become maximum when $k\Omega$ (k: integer) coincides with the frequency of the natural oscillation, because the frequency of the oscillatory hydrodynamic force acting on the moving blade in non-uniform flow often becomes $k'\Omega$ (k: integer) as shown below. And we can analyse the velocity field as the symmetric oscillation. But we need not apply the above theory to the oscillating blade probably, because the blades of marine propellers are very rigid in general.

90

Non-uniform Flow

We regard the axial inflow velocity at the center of the propeller as the advance velocity V of the propeller. If u and v denote the axial and tangential components of difference of linear inflow velocity to the propeller in non-uniform flow, these are given, in general, by

$$u = \sum_{k=0}^{\infty} \left\{ a_k(r) \sin k\theta + b_k(r) \cos k\theta \right\},$$
$$v = \sum_{k=0}^{\infty} \left\{ c_k(r) \sin k\theta + d_k(r) \cos k\theta \right\}. \tag{6.2}$$

We must put $\theta - \Omega t$ in place of θ in (6.2) in order to express u and v in connection with the point which moves along a helical path with constant velocities V and Ω in a constant phase relative to the propeller.

If all terms vanish except for b_1, c_1, in (6.2), u and v at the blade $(\sigma = \sigma' = 0)$ are given by real parts of

$$u = b_1(r)\, e^{i\nu t - i\tau/2},$$
$$v = i\, c_1(r)\, e^{i\nu t - i\tau/2}, \tag{6.3}$$

since $\nu = \Omega$ for $k = 1$ and $\theta = (\tau + \sigma)/2$.

The normal components of u and v to the blade is $u \cos \epsilon - v \sin \epsilon$, where $\epsilon = \tan^{-1} V/\Omega r$. As the downwash must be equal to $-u \cos \epsilon + v \sin \epsilon$,

$$w_o = -\frac{e^{-i\tau/2}}{\sqrt{1 + \mu^2}} \left\{ b_1(r)\, \mu - i\, c_1(r) \right\}. \tag{6.4}$$

When $b_1(r) = br$ (b: const.), u gives a linear non-uniform flow. When $c_1 = $ const., v implies the side-ship velocity of the propeller. For an arbitrary shape of non-uniform flow, we must solve the integral equation with regard to the respective value of $p = k$.

Oscillation of the Propeller Overall

Now consider the propeller oscillating overall, in connection with the ship hull. We take the positive y-axis in downward direction and the positive z-axis to starboard. When the propeller makes a translating oscillation along the - axis and a pitching oscillation about the z-axis with frequency γ, the linear displacements of the point on the plane of rotation of the propeller are given by $\delta x = \beta_o r \cos \theta \cos \gamma t$ in axial direction and $\delta(r\theta) = y_o \sin \theta \sin \gamma t$ in tangential direction where y_o and β_o are the amplitude of the translating and pitching oscillations respectively. We must write $\theta - \Omega t$ instead of θ in order to express them with respect to a rotating point. We thus obtain

91

Hanaoka

$$\delta x = -\frac{i\beta_o r}{2} \left\{ e^{i(\gamma-\Omega)t+i\tau/2} + e^{i(\gamma+\Omega)t-i\tau/2} \right\},$$

$$\delta(r\theta) = -\frac{y_o}{2} \left\{ e^{i(\gamma-\Omega)t+i\tau/2} - e^{i(\gamma+\Omega)t-i\tau/2} \right\}. \qquad (6.5)$$

Since the displacement of the blade is given by $H = -\delta x \cos \epsilon + \delta(r\theta) \sin \epsilon$, we have

$$H = \frac{1}{2\sqrt{1+\mu^2}} (i\mu\beta_o r - y_o) e^{i\tau/2+i(\gamma-\Omega)t}$$

$$+ \frac{1}{2\sqrt{1+\mu^2}} (i\mu\beta_o r + y_o) e^{-i\tau/2+i(\gamma+\Omega)t}. \qquad (6.6)$$

If we substitute (6.6) in (5.2), we obtain the downwash distribution.

In this case, we must solve two integral equations separately, because the downwash has two kinds of frequencies, $\gamma-\Omega$ and $\gamma+\Omega$. When $\gamma = k\Omega$ (k: integer), we can analyse the velocity field as the symmetric oscillation.

7. REVERSE FLOW THEOREM

We may say that reverse flow theorem is the same relation with "principle of reciprocity" [5] in potential flow. von Karman appears [6] to have been the first to point out such a relationship in the field of linearized wing theory. Reverse flow theorem gives relations between the hydrodynamic properties of lifting system of the same planform in forward and reverse flows. It has been developed for various kinds of flow by a number of investigators. Now we derive the relation in the velocity field of propeller.

Now we consider two kinds of fluid fields around a blade, which are the fields disturbed by the propeller moving along a helical path with constant velocities $-V$ and $-\Omega$, or V and Ω. We may say the former direct flow and the latter reverse flow. When the frequencies are equal in both fields, there are the relations

$$\varphi_o = i\nu\Phi_o + 2\Omega \frac{\partial\Phi_o}{\partial\tau},$$

$$\tilde{\varphi}_o = i\nu\tilde{\Phi}_o - 2\Omega \frac{\partial\tilde{\Phi}_o}{\partial\tau}, \qquad (7.1)$$

where the "~" denotes the corresponding quantities for the reverse flow.

In section 3 we know that Φ_o and $\tilde{\Phi}_o$ are continuous and $\Delta\Phi_o = 0$, $\Delta\tilde{\varphi} = 0$ in whole space except for the helical surface along the locus of blades. By virtue of Green's theorem, we have

92

$$\iint \left(\Phi_o \frac{\partial \tilde{\phi}_o}{\partial n} - \tilde{\phi}_o \frac{\partial \Phi_o}{\partial n} \right) dS = 0 , \tag{7.2}$$

where the surface integral is taken over both the sides of the helical surface and δn denotes an element of the outwardly directed normal to the helical surface.

Substituting (7.1) in (7.2), we have

$$\frac{\nu}{2\Omega} \iint \sqrt{1+\mu^2} \left\{ \Phi_o \frac{\partial}{\partial n} \left(i\nu\tilde{\Phi}_o - 2\Omega \frac{\partial \tilde{\Phi}_o}{\partial \tau} \right) - \tilde{\phi}_o \frac{\partial \Phi_o}{\partial n} \right\} d\tau \ dr = 0 . \tag{7.3}$$

Performing a partial integration, we get

$$\sum_m \int_0^{r_o} \int_{-\infty}^{\infty} \sqrt{1+\mu^2} \left(\pi_o \frac{\partial \tilde{\Phi}_o}{\partial n} - \tilde{\pi}_o \frac{\partial \Phi}{\partial n} \right) d\tau \ dr = 0 .$$

π_o and $\tilde{\pi}_o$ disappear outside the datum plane.

The summation with respect to the blades may be dropped, since the field is helically symmetric. Consequently, we get

$$\int_0^{r_o} \sqrt{1+\mu^2} \ dr \int_{\tau_1}^{\tau_2} \pi_o \tilde{w}_o d\tau = \int_0^{r_o} \sqrt{1+\mu^2} \ dr \int_{\tau_1}^{\tau_2} \tilde{\pi}_o w_o d\tau \tag{7.4}$$

as the reverse flow theorem of an oscillating propeller.

If the integral equation of both fields are written in the forms,

$$w_o = \iint_\sigma \pi_o \Re(\tau, \tau'; \mu, \mu') \ dS \tag{7.5}$$

$$\tilde{w}_o = \iint_\sigma \tilde{\pi}_o \tilde{\Re}(\tau, \tau'; \mu, \mu') \ dS , \tag{7.6}$$

it is verified that the kernel of the integral equation in reverse flow is the mathematical adjoint of the kernel appropriate to the direct flow. The adjoint relationship between direct and reverse flows leads immediately to the reverse flow theorem (7.4).

8. VARIATION PRINCIPLE AND LIFTING-LINE TECHNIQUE

Flax [7] derived a variation principle for lifting surface and this principle provides a direct systematic way of reducing the two-dimensional integral equation to a finite set of one-dimensional integral equations.

The following analysis is performed along a similar course to Flax's work. If a function I is given by

93

$$I = \iint_\sigma \sqrt{1 + \mu^2} \ (\pi_o \widetilde{w}_o + \widetilde{\pi}_o w_o) \, d\tau \, dr$$

$$- \frac{h}{2} \iint_\sigma \sqrt{1 + \mu^2} \ \widetilde{\pi}_o(\tau, r) \, d\tau \, dr \iint_{\sigma'} \sqrt{1 + \mu'^2} \ \pi_o(\tau', r') \, \Re \, d\tau' \, dr' \, ,$$

the first variation of this function is written

$$\delta I = \iint_\sigma \sqrt{1 + \mu^2} \ (\delta\pi_o \widetilde{w}_o + \delta\widetilde{\pi}_o w_o) \, d\tau \, dr$$

$$- \frac{h}{2} \iint_\sigma \sqrt{1 + \mu^2} \ \delta\widetilde{\pi}_o \, d\tau \, dr \iint_{\sigma'} \sqrt{1 + \mu'^2} \ \pi_o \, \Re \, d\tau' \, dr'$$

$$- \frac{h}{2} \iint_\sigma \sqrt{1 + \mu^2} \ \widetilde{\pi}_o \, d\tau \, dr \iint_{\sigma'} \sqrt{1 + \mu'^2} \ \delta\pi_o \, \Re \, d\tau' \, dr' \, , \tag{8.1}$$

where $\iint_\sigma d\tau \, dr$ denotes the surface integral extending over the datum plane of one blade. Using the reverse flow theorem, we obtain, from (8.1)

$$\delta I = \iint_\sigma \sqrt{1 + \mu^2} \left[\widetilde{w}_o - \frac{h}{2} \iint_{\sigma'} \sqrt{1 + \mu^2} \ \widetilde{\pi}_o \widetilde{\Re} \, d\tau' dr' \right] \delta\pi_o \, d\tau \, dr$$

$$+ \iint_\sigma \sqrt{1 + \mu^2} \left[w_o - \frac{h}{2} \iint_\sigma \sqrt{1 + \mu'^2} \ \pi_o \Re \, d\tau' dr' \right] \delta\widetilde{\pi}_o \, d\tau \, dr \, . \tag{8.2}$$

Therefore,

$$\delta I = 0 \tag{8.3}$$

is equivalent to the integral equations (7.5) and (7.6). This is Flax's variation principle.

When the planform of a blade is symmetric about a radial axis and has relatively high aspect ratio, the lift distribution in radial direction is given by [8]

$$\pi_o(s, r) = A_1 u_1(r) \sqrt{\frac{\frac{\hat{c}}{2} - s}{\frac{\hat{c}}{2} + s}} + A_2 u_2(r) \sqrt{1 - (2s/\hat{c})^2}$$

$$+ A_3 u_3(r) (2s/\hat{c}) \sqrt{1 - (2s/\hat{c})^2} + \cdots . \tag{8.4}$$

Reversal of flow direction involves only a replacement of s by $-s$ in (8.4). The first variation of π_o is written

$$\delta\pi_o(\tau, r) = u_1(r) \sqrt{\frac{\frac{c}{2} - \tau}{\frac{c}{2} + \tau}} \; \delta A_1 + u_2(r) \sqrt{1 - (2\tau/c)^2} \; \delta A_2 + \cdots, \qquad (8.5)$$

where $c = 2\Omega\hat{c}/W$. Substituting (8.4) and (8.5) in (8.2), we have

$$\delta\widetilde{A}_1 \iint_\sigma \sqrt{1 + \mu^2} \; \widetilde{u}_1(r) \sqrt{\frac{\frac{c}{2} + \tau}{\frac{c}{2} - \tau}} \left[w_o - \frac{h}{2} \iint_\sigma \sqrt{1 + \mu'^2} \; \Re\pi_o d\tau' dr' \right] d\tau \, dr$$

$$+ \; \delta\widetilde{A}_2 \iint_\sigma \sqrt{1 + \mu^2} \; \widetilde{u}_2(r) \sqrt{1 - (2\tau/c)^2} \left[w_o - \frac{h}{2} \iint_\sigma \sqrt{1 + \mu'^2} \; \Re\pi_o d\tau' dr' \right] d\tau \, dr$$

$$+ \; \cdots = 0 \, .$$

Since $\delta\widetilde{A}_1$ and $\delta\widetilde{A}_2$ are independent, the term multiplied by $\delta\widetilde{A}$ are equal to zero. Since $\widetilde{u}_1$ and $\widetilde{u}_2$ are arbitrary functions, the integration along the radius may be dropped. We thus obtain a finite set of one-dimensional integral equations,

$$\left.\begin{array}{l} \displaystyle\int_{\tau_1}^{\tau_2} \sqrt{\frac{\frac{c}{2} + \tau}{\frac{c}{2} - \tau}} \; w_o d\tau = \frac{h}{2} \int_{\tau_1}^{\tau_2} \sqrt{\frac{\frac{c}{2} + \tau}{\frac{c}{2} - \tau}} \; d\tau \iint_\sigma \sqrt{1 + \mu'^2} \; \Re\pi_o d\tau' dr' \\[4mm] \displaystyle\int_{\tau_1}^{\tau_2} \sqrt{1 - (2\tau/c)^2} \; w_o d\tau = \frac{h}{2} \int_{\tau_1}^{\tau_2} \sqrt{1 - (2\tau/c)^2} \; d\tau \iint_\sigma \sqrt{1 + \mu'^2} \; \Re\pi_o d\tau' dr' \end{array}\right\} \; . \quad (8.6)$$

If these equations are solved with respect to $A_1 u_1(r)$, $A_2 u_2(r)$ simultaneously, we obtain the lift distribution by using (8.4). If a suitable approximation for the lift distribution is given by the first term of (8.4), the integral equation is written in the form

$$k(r) = \int_0^{r_o} U_1(r') \; \Re(\mu, \mu') dr', \qquad (8.7)$$

where

$$\left.\begin{array}{l} \displaystyle k(r) = \int_{\tau_1}^{\tau_2} \sqrt{\frac{\frac{c}{2} + \tau}{\frac{c}{2} - \tau}} \; w_o(\tau, r) \, d\tau \\[6mm] U_1(r) = A_1 u_1(r) \\[4mm] \pi_o = U_1(r) \sqrt{\dfrac{\frac{c}{2} - \tau}{\frac{c}{2} + \tau}} \end{array}\right\} \quad \begin{array}{l}(8.8)\\(\text{Cont.})\end{array}$$

95

$$\mathfrak{R}(\mu,\mu') = \frac{h}{2}\sqrt{1+\mu'^2} \int_{\tau_1}^{\tau_2} \sqrt{\frac{\frac{c}{2}+\tau}{\frac{c}{2}-\tau}} \, d\tau \int_{\tau'_1}^{\tau'_2} \sqrt{\frac{\frac{c'}{2}-\tau'}{\frac{c'}{2}+\tau'}} \, \mathfrak{R}(\tau,\tau';\mu,\mu') \, d\tau' . \qquad (8.8)$$

This is the lifting-line technique of an oscillating screw propeller.

9. THE AVERAGE WORK DONE BY A PROPELLER

Let us consider the mean rate of work done against the surrounding fluid by a propeller. If $\hat{H}$ denotes the instantaneous normal displacement of a point on the blade from the datum plane, $\hat{H}$ is written

$$\hat{H} = H_s - iH_o e^{i\nu t} \qquad (9.1)$$

and the whole lift density is written

$$\hat{\pi} = \pi_s + \pi_o e^{i\nu t}. \qquad (9.2)$$

where suffix "s" implies that the quantities are related to steady state. The amounts of resistance and lift acting on an advancing blade element in unit of time are given by

$$\begin{aligned}
\hat{R} &= \frac{\nu}{2\pi} \int_0^{2\pi/\nu} dt \int_{s_1}^{s_2} \frac{\partial\hat{H}}{\partial s} \hat{\pi} \, ds \\
&= \int_{s_1}^{s_2} \frac{\partial H_s}{\partial s} \pi_s ds - \frac{\nu}{2\pi} \int_0^{2\pi/\nu} dt \int_{s_1}^{s_2} \mathfrak{Re}\left(i \frac{\partial H_o}{\partial s} e^{i\nu t}\right)\cdot\mathfrak{Re}\left(\pi_o e^{i\nu t}\right) ds \\
L &= \frac{\nu}{2\pi} \int_0^{2\pi/\nu} dt \int_{s_1}^{s_2} \hat{\pi} \, ds = \int_{s_1}^{s_2} \pi_s ds .
\end{aligned} \qquad (9.3)$$

Non-steady term appears only in resistance, as

$$\overline{R} = -\frac{\nu}{2\pi} \int_0^{2\pi/\nu} dt \int_{s_1}^{s_2} \mathfrak{Re}\left(i \frac{\partial H_o}{\partial s} e^{i\nu t}\right) \cdot \mathfrak{Re}\left(\pi_o e^{i\nu t}\right) ds . \qquad (9.4)$$

On the other hand, mean rate of the work done against the fluid by the blade element is given by

$$\overline{p} = \frac{\nu}{2\pi} \int_0^{2\pi/\nu} dt \int_{s_1}^{s_2} \frac{\partial\hat{H}}{\partial t} \hat{\pi} \, ds + \frac{\nu W}{2\pi} \int_0^{2\pi/\nu} dt \int_{s_1}^{s_2} \frac{\partial\hat{H}}{\partial s} \hat{\pi} \, ds .$$

Therefore,

96

Hydrodynamics of an Oscillating Screw Propeller

$$\bar{p} = \frac{\nu}{2\pi} \int_0^{2\pi/\nu} dt \int_{s_1}^{s_2} \Re\left(\nu H_o e^{i\nu t}\right) \cdot \Re\left(\pi_o e^{i\nu t}\right) ds + W \int_{s_1}^{s_2} \frac{\partial H_s}{\partial s} \pi_s ds$$

$$+ \frac{\nu W}{2\pi} \int_0^{2\pi/\nu} dt \int_{s_1}^{s_2} \Re\left(i \frac{\partial H_o}{\partial s} e^{i\nu t}\right) \cdot \Re\left(\pi_c e^{i\nu t}\right) ds . \tag{9.5}$$

Introducing (5.2) or (9.4) in (9.5) and leaving out the steady term, we obtain

$$\bar{p} = \frac{\nu}{2\pi} \int_0^{2\pi/\nu} dt \int_{s_1}^{s_2} \Re\left(w_o e^{i\nu t}\right) \cdot \Re\left(\pi_o e^{i\nu t}\right) ds \tag{9.6}$$

or

$$\bar{p} = \frac{\nu}{2\pi} \int_0^{2\pi/\nu} dt \int_{s_1}^{s_2} \Re\left(\nu H_o e^{i\nu t}\right) \cdot \Re\left(\pi_o e^{i\nu t}\right) ds + W\bar{R} . \tag{9.7}$$

Integrating $\bar{p}$ all over the blades, we obtain

$$\bar{P} = \sum_m \int_0^{r_o} \bar{p} \, dr = P^* + \sum_m \int_0^{r_o} W\bar{R} \, dr , \tag{9.8}$$

where

$$P^* = \frac{\nu}{2\pi} \int_0^{2\pi/\nu} dt \sum_m \int_0^{r_o} dr \int_{s_1}^{s_2} \Re\left(\nu H_o e^{i\nu t - i2pm\pi/\ell}\right)$$

$$\times \Re\left(\pi_o e^{i\nu t - i2pm\pi/\ell}\right) ds . \tag{9.9}$$

P^* implies the amount of work done against the fluid by the oscillation of blades in unit of time and the second term of (9.8) implies mean rate of the work done against the resistance of advancing blades.

If R_a and R_t denote the axial and tangential components of $\bar{R}$,

$$\bar{R} = R_t \cos \epsilon + R_a \sin \epsilon$$

$$= \frac{\Omega r}{W} R_t + \frac{V}{W} R_a . \tag{9.10}$$

If we take the average, all the non-steady hydrodynamical forces acting on the blade disappear except for $\bar{R}$, as shown (9.3). Therefore the average thrust and torque are derived from $\bar{R}$. We thus have

97

$$\sum_m \int_0^r W\overline{R}\,dr \;=\; \Omega \sum_m \int_0^{r_o} r\,R_t\,dr \;+\; V\sum_m \int_0^{r_o} R_a\,dr$$

$$=\; \Omega\overline{Q} + V\overline{D}\,, \tag{9.11}$$

where $\overline{D}$ and $\overline{Q}$ denote the average resistance and torque of an oscillating screw propeller. Substituting (9.11) in (9.8), we obtain

$$\overline{P} \;=\; P^* + \Omega\overline{Q} + V\overline{D}. \tag{9.12}$$

In the above analysis, we except the "suction" force at the leading edge of blade [9]. The effect of the force is explained in section 11.

We shall now derive the expression of $\overline{P}$ by using the velocity potential. Integrating $\bar{p}$ of (9.6) all over the blades, we obtain

$$\overline{P} \;=\; \frac{\nu}{2\pi}\int_0^{2\pi/\nu} dt \sum_m \int_0^{r_o} dr \int_{s_1}^{s_2} \Re\left(w_o\,e^{i\nu t - i2pm\pi/\ell}\right)$$

$$\times\; \Re\left(\pi_o\,e^{i\nu t - i2pm\pi/\ell}\right) ds\,. \tag{9.13}$$

$\overline{P}$ is equal to ℓ times of the amount of work done by a blade, since $\overline{P}$ implies the average work with respect to time. But we use (9.15), for the convenience of the development of analysis.

When we put

$$\left.\begin{aligned} w_o\,e^{-i2pm\pi/\ell} &= w_r + i\,w_i \\ \pi_o\,e^{-i2pm\pi/\ell} &= \pi_r + i\,\pi_i \end{aligned}\right\}, \tag{9.14}$$

(9.13) is written in the form

$$\overline{P} \;=\; \frac{h}{4}\sum_m \int_0^{r_o} \sqrt{1+\omega^2}\;dr \int_{\tau_1}^{\tau_2} (w_r\,\pi_r + w_i\,\pi_i)\,d\tau$$

$$=\; \frac{h}{4}\sum_m \int_0^{r_o}\sqrt{1+\omega^2}\;dr \int_{\tau_1}^{\tau_2}\Re\left(w_o\,e^{-i2pm\pi/\ell}\right.$$

$$\times\; \bar{\pi}_o\,e^{i2pm\pi/\ell}\right)d\tau\,, \tag{9.15}$$

where $\bar{\pi}_o$ denotes a conjugate complex of π_o and so

$$\bar{\pi}_o\,e^{i2pm\pi/\ell} \;=\; \pi_r - i\,\pi_i\,.$$

98

If we write $\tau + 2m\pi/\ell$ for τ and $\sigma + 2m\pi/\ell$ for σ in (5.3) and then put $\sigma = \sigma'$, we obtain the expression of $w_o\, e^{-i2pm\pi/\ell}$

$$
\begin{aligned}
w_o\, e^{-i2pm\pi/\ell} \;=\;& \frac{i}{8\pi^2\,\Omega h\rho\,\sqrt{1+\mu^2}}\;\sum_{m'=0}^{\ell-1}\int_0^{\mu_o} d\mu' \int_{\tau_1'}^{\tau_2'} \pi_o'\, e^{-i2pm'\pi/\ell}\, d\tau' \\
&\times \sum_{n=-\infty}^{\infty} \oint_{-\infty}^{\infty} \frac{(\mu'\lambda - n/\mu')(\mu\lambda - n/\mu)}{\lambda + p + n}\, I_n(|\lambda|\mu_<)\cdot K_n(|\lambda|\mu_>) \\
&\times\; e^{\frac{i}{2}(\lambda+n)(\tau-\tau') + \frac{i2n\pi}{\ell}(m-m')}\, d\lambda \\
&- \frac{1}{8\pi\,\Omega h\rho\,\sqrt{1+\mu^2}}\;\sum_{m'=0}^{\ell-1}\int_0^{\mu_o} d\mu' \int_{\tau_1'}^{\tau_2'} \pi_o'\, e^{-i2pm'\pi/\ell}\, d\tau' \\
&\times \sum_{n=-\infty}^{\infty}\{\mu'(p+n) + n/\mu'\}\{\mu(p+n) + n/\mu\}\, I_n(|p+n|\mu_<) \\
&\times\; K_n(|p+n|\mu_>)\cdot e^{-\frac{ip}{2}(\tau-\tau') + \frac{i2n\pi}{\ell}(m-m')}. \qquad (9.16)
\end{aligned}
$$

For the simplicity, we use the symbols

$$
\left.
\begin{aligned}
\sum_{m'=0}^{\ell-1}\int_0^{\mu_o} d\mu' \int_{\tau_1'}^{\tau_2'} d\tau' \;&=\; \int^* dS' \\
\sum_{m=0}^{\ell-1}\int_0^{\mu_o} d\mu \int_{\tau_1}^{\tau_2} d\tau \;&=\; \int^* dS
\end{aligned}
\right\} . \qquad (9.17)
$$

$$
\left.
\begin{aligned}
\Pi_1 \;=\; \sum_{n=-\infty}^{\infty} \oint_{-\infty}^{\infty} d\lambda\; \frac{(\mu'\lambda - n/\mu')(\mu\lambda - n/\mu)}{\lambda + p + n}\, I_n(|\lambda|\mu_<)\cdot K_n(|\lambda|\mu_>) \\
\Pi_2 \;=\; \sum_{n=-\infty}^{\infty}\{\mu'(p+n) + n/\mu'\}\{\mu(p+n) + n/\mu\}\, I_n(|p+n|\mu_<)\cdot K_n(|p+n|\mu_>)
\end{aligned}
\right\} . \qquad (9.18)
$$

Substituting (9.16) in (9.15), we have

$$
\overline{P} \;=\; -\frac{h^2}{4}\;\frac{1}{8\pi^2\,\Omega h c}\int^* dS \int^* dS'\, \Pi_1\cdot(\pi_r\pi_r' + \pi_i\pi_i')\,\sin\alpha \qquad \begin{array}{c}(9.19)\\ (\text{Cont.})\end{array}
$$

$$- \frac{h^2}{4} \frac{1}{8\pi\Omega h\rho} \int^\bullet dS \int^\bullet dS' \mathbb{M}_2 \cdot (\pi_r \pi_r' + \pi_i \pi_i') \cos \beta$$

$$- \frac{h^2}{4} \frac{1}{8\pi^2\Omega h\rho} \int^\bullet dS \int^\bullet dS' \mathbb{M}_1 \cdot (\pi_r \pi_i' - \pi_i \pi_r') \cos \alpha$$

$$- \frac{h^2}{4} \frac{1}{8\pi\Omega h\rho} \int^\bullet dS \int^\bullet dS' \mathbb{M}_2 \cdot (\pi_r \pi_i' - \pi_i \pi_r') \sin \beta, \qquad (9.19)$$

where

$$\alpha = \frac{1}{2} (\lambda + n)(\tau - \tau') + \frac{2n\pi}{\ell} (m - m')$$

$$\beta = \frac{p}{2} (\tau - \tau') - \frac{2n\pi}{\ell} (m - m') .$$

If π_r and π_i have no singularity, the first and the third terms of (9.19) are equal to zero, because they are transformed into the expressions to be equal in magnitude and opposite in sign by changing the order of the integration with respect to S and S'. Consequently, we obtain

$$\bar{P} = - \frac{h}{32\pi\Omega\rho} \int^\bullet dS \int^\bullet dS' \mathbb{M}_2 \cdot (\pi_r \pi_r' + \pi_i \pi_i') \cos \beta$$

$$- \frac{h}{16\pi\Omega\rho} \int^\bullet dS \int^\bullet dS' \mathbb{M}_2 \cdot \pi_r \pi_i' \sin \beta . \qquad (9.20)$$

Equation (9.20) is a formal expression, as the integral is divergent (see appendix B). In practical evaluation, we must carry out the partial integration with respect to μ' and evaluate Cauchy's principal value.

10. ENERGY THEOREM

We now consider the kinetic energy present in the field of flow behind the propeller. The increase of this energy should be equal to the work done on the blades by external forces. This fact shall be verified in the following analysis. The energy increase in unit time is usually derived by calculating the kinetic energy in a strip between two vertical planes at the distance $2\pi v/\nu$. But in this section, we derive the average energy increase by calculating the dissipation of energy in Rayleigh's fluid field. This method was propounded by H. Lamb [10] and applied to the problem of wave-resistance. As the average dissipation of energy $\bar{E}$ in unit of time in Rayleigh's fluid field is equal to $2\mu'$ times the kinetic energy

$$\bar{E} = \mu'\rho \frac{\nu}{2\pi} \int_0^{2\pi/\nu} dt \iiint \left\{ \left(\frac{\partial\Phi}{\partial x}\right)^2 + \left(\frac{\partial\Phi}{\partial y}\right)^2 + \left(\frac{\partial\Phi}{\partial z}\right)^2 \right\} dx \, dy \, dz , \qquad (10.1)$$

100

where the volume integral extends over the whole space. This integral can be transformed into surface integral, to be extended along the helical locus of the blades, because the velocity field does not present any discontinuity except at the helical surface, namely,

$$\overline{E} = -\mu' \rho \frac{\nu}{2\pi} \int_0^{2\pi/\nu} dt \iint \Phi \frac{\partial \Phi}{\partial n} dS. \qquad (10.2)$$

The surface integral extends over both the sides of the helical surface and n is a normal directed outward from the helical surface. At the upper and lower sides of this surface, Φ is equal in magnitude in front of the propeller, and is equal in magnitude and opposite in sign behind the propeller, with each other. Therefore, the surface integral extending all over the helical surface is equal to the surface integral extending over the helical locus. In the following analysis we shall first derive the respective surface integral along the upper and lower sides of this surface separately. And then we shall get the energy $\overline{E}$ by adding up both the integrals. If $E_{(-)}$ denotes the surface integral along the lower side, it is written

$$E_{(-)} = -\mu\rho \frac{\Omega h^2}{2} \frac{\nu}{2\pi} \int_0^{2\pi/\nu} dt \sum_m \int_0^{\mu_0} \sqrt{1+\mu^2} \, d\mu \int_{-\infty}^{\infty} \left[\Re e \, \Phi \cdot \Re e \, \frac{\partial \Phi}{\partial \mathbf{n}} \right]_{(-)} d\tau. \qquad (10.3)$$

where $[\quad]_{(-)}$ denotes that the function in the bracket takes the value at the lower side.

If $\overline{\Phi}_o$ denotes a conjugate complex of Φ_o, we have

$$\frac{\nu}{2\pi} \int_0^{2\pi/\nu} \Re e \, \Phi \cdot \Re e \, \frac{\partial \Phi}{\partial \mathbf{n}} \, dt = \frac{1}{2} \left(\Phi_r \frac{\partial \Phi_r}{\partial \mathbf{n}} + \Phi_i \frac{\partial \Phi_i}{\partial \mathbf{n}} \right)$$

$$= \frac{1}{2} \Re e \left(\Phi_o \cdot \frac{\partial \overline{\Phi}_o}{\partial \mathbf{n}} \right),$$

where

$$\Phi_o = \Phi_r + i\Phi_i.$$

Therefore, $\overline{E}$ is written

$$E_{(-)} = -\frac{\mu\rho h^2 \Omega}{4} \sum_{m=0}^{\ell-1} \int_0^{\mu_0} \sqrt{1+\mu^2} \, d\mu \int_{-\infty}^{\infty} \Re e \left[\Phi_o(\tau + 2m\pi/\ell, \sigma + 2m\pi/\ell, \mu) \right.$$

$$\times \left. \partial \overline{\Phi}_o(\tau + 2m\pi/\ell, \sigma + 2m\pi/\ell, \mu)/\partial \mathbf{n} \right]_{\sigma - \sigma' = -0} d\tau. \qquad (10.4)$$

If we write λ for $\lambda + n$ in (4.1),

101

$$\Phi_o(\tau,\sigma,\mu) \;=\; \frac{1}{8\pi^2\,\Omega\rho} \sum_{m=0}^{\ell-1} \int_0^{\mu_o} d\mu' \int_{\tau_1}^{\tau_2} \pi_o' \; e^{-i\,2pm\pi/\ell}\, d\tau'$$

$$\times \sum_{n=-\infty}^{\infty} \int_{-\infty}^{\infty} \frac{\mu'(\lambda-n)-n/\mu'}{\lambda+p-i\mu} \; e^{\frac{i}{2}\lambda(\tau-\tau')-\frac{i}{2}(\lambda-2n)(\sigma-\sigma')-i\,2nm\pi/\ell}$$

$$\times \; I_n(\,|\lambda-n|\mu_<)\cdot K_n(\,|\lambda-n|\mu_>)\,d\lambda\,, \qquad (10.5)$$

we can derive $\partial\overline{\Phi}_o/\partial\mathbf{n}$, from (10.5), as

$$\frac{\partial\overline{\Phi}_o}{\partial\mathbf{n}} \;=\; \frac{-i}{8\pi^2\,\Omega h\,\rho\,\sqrt{1+\mu^2}} \sum_{m=0}^{\ell-1} \int_0^{\mu_o} d\mu' \int_{\tau_1}^{\tau_2} \overline{\pi}_o(\tau',\mu')\; e^{i\,2pm\pi/\ell}\, d\tau'$$

$$\times \sum_{n=-\infty}^{\infty} \int_{-\infty}^{\infty} \frac{\{\mu(\lambda-n)-n/\mu\}\{\mu'(\lambda-n)-n/\mu'\}}{\lambda+p+i\mu} \; I_n(\,|\lambda-n|\mu_<)$$

$$\times \; K_n(\,|\lambda-n|\mu_>)\cdot e^{-\frac{i}{2}\lambda(\tau-\tau')+\frac{i}{2}(\lambda-2n)(\sigma-\sigma')+i\,2nm\pi/\ell}\, d\lambda \qquad (10.6)$$

by virtue of (2.7).

Substituting (10.5) and (10.6) in (10.4) and carrying out the integration with respect to τ by virtue of the formula

$$\int_a^b f(\tilde\lambda)\,d\tilde\lambda \int_{-\infty}^{\infty} e^{\frac{i}{2}\tau(\tilde\lambda-\lambda)}\, d\tau \;=\; 4\pi f(\lambda), \qquad a<\lambda<b\,, \qquad (10.7)$$

we obtain

$$E_{(-)} \;=\; \lim_{\epsilon\to-0} \mathfrak{Re}\,-\,\mu\pi ch^2\,\Omega \sum_m \int_0^{\mu_o} d\mu\,\frac{1}{8^{-2}\,\Omega c} \sum_{m'} \int_0^{\mu_o} d\mu' \int_{\tau_1'}^{\tau_2'} \pi_o' \, e^{-i\,2pm'\pi/\ell}\, d\tau'$$

$$\times \sum_{n=-\infty}^{\infty} \int_{-\infty}^{\infty} \frac{\mu'(\lambda-n)-n/\mu'}{(\lambda+p)^2+\mu^2} \; e^{\frac{i}{2}\lambda(\tau-\tau')-\frac{i}{2}(\lambda-2n)\epsilon+in(m-m')2\pi/\ell}$$

$$\times \; I_n(\,|\lambda-n|\mu_<)\cdot K_n(\,|\lambda-n|\mu_>) \,\frac{-i}{8^{-2}\,\Omega h c} \sum_{m^*} \int_0^{\mu_o} d\mu^* \int_{\tau_1^*}^{\tau_2^*} \overline{\pi}_o^* \, e^{i\,2pm^*-\ell}\, d^{-*}$$

$$\times \sum_{n^*=-\infty}^{\infty} \{\mu(\lambda-n^*)-n^*/\mu\}\{\mu^*(\lambda-n^*)-n/\mu^*\}\cdot I_{n^*}(\,|\lambda-n^*|\mu_<^*)$$

(Cont.)

102

$$\Phi_o(\tau,\sigma,\mu) = \frac{1}{8\pi^2 \Omega\rho} \sum_{m=0}^{\ell-1} \int_0^{\mu_o} d\mu' \int_{\tau_1}^{\tau_2} \pi'_o \, e^{-i \, 2pm\pi/\ell} \, d\tau'$$

$$\times \sum_{n=-\infty}^{\infty} \int_{-\infty}^{\infty} \frac{\mu'(\lambda-n) - n/\mu'}{\lambda + p - i\mu} \, e^{\frac{i}{2}\lambda(\tau-\tau') - \frac{i}{2}(\lambda-2n)(\sigma-\sigma') - i \, 2nm\pi/\ell}$$

$$\times I_n(\,|\lambda-n|\mu_<) \cdot K_n(\,|\lambda-n|\mu_>) \, d\lambda \,, \tag{10.5}$$

we can derive $\partial\overline{\Phi}_o/\partial\mathbf{n}$, from (10.5), as

$$\frac{\partial\overline{\Phi}_o}{\partial\mathbf{n}} = \frac{-i}{8\pi^2 \Omega h \rho \sqrt{1+\mu^2}} \sum_{m=0}^{\ell-1} \int_0^{\mu_o} d\mu' \int_{\tau_1}^{\tau_2} \overline{\pi}_o(\tau',\mu') \, e^{i \, 2pm\pi/\ell} \, d\tau'$$

$$\times \sum_{n=-\infty}^{\infty} \int_{-\infty}^{\infty} \frac{\{\mu(\lambda-n) - n/\mu\}\{\mu'(\lambda-n) - n/\mu'\}}{\lambda + p + i\mu} \, I_n(\,|\lambda-n|\mu_<)$$

$$\times K_n(\,|\lambda-n|\mu_>) \cdot e^{-\frac{i}{2}\lambda(\tau-\tau') + \frac{i}{2}(\lambda-2n)(\sigma-\sigma') + i \, 2nm\pi/\ell} \, d\lambda \tag{10.6}$$

by virtue of (2.7).

Substituting (10.5) and (10.6) in (10.4) and carrying out the integration with respect to τ by virtue of the formula

$$\int_a^b f(\tilde{\lambda}) \, d\tilde{\lambda} \int_{-\infty}^{\infty} e^{\frac{i}{2}\tau(\tilde{\lambda}-\lambda)} \, d\tau = 4\pi f(\lambda), \qquad a < \lambda < b \,, \tag{10.7}$$

we obtain

$$E_{(-)} = \lim_{\epsilon \to -0} \Re - \mu \pi c h^2 \Omega \sum_m \int_0^{\mu_o} d\mu \, \frac{1}{8\pi^2 \Omega c} \sum_{m'} \int_0^{\mu_o} d\mu' \int_{\tau'_1}^{\tau'_2} \pi'_o e^{-i \, 2pm'\pi/\ell} \, d\tau'$$

$$\times \sum_{n=-\infty}^{\infty} \int_{-\infty}^{\infty} \frac{\mu'(\lambda-n) - n \mu'}{(\lambda+p)^2 + \mu^2} \, e^{\frac{i}{2}\lambda(\tau^*-\tau') - \frac{i}{2}(\lambda-2n)\sigma + in(m-m')2\pi/\ell}$$

$$\times I_n(\,|\lambda-n|\mu_<) \cdot K_n(\,|\lambda-n|\mu_>) \, \frac{-i}{8\pi^2 \Omega h c} \sum_{m^*} \int_0^{\mu_o} d\mu^* \int_{\tau^*_1}^{\tau^*_2} \overline{\pi}^*_o e^{i \, 2pm^*\pi/\ell} \, d^*$$

$$\times \sum_{n^*=-\infty}^{\infty} \{\mu(\lambda-n^*) - n^* \mu\}\{\mu^*(\lambda-n^*) - n\mu^*\} \cdot I_{n^*}(\,|\lambda-n^*|\mu_<)$$

(Cont.)

102

$$\times\, K_{n\bullet}(|\lambda - n^{\bullet}|\mu_{>}^{\bullet}) \cdot e^{\frac{i}{2}(\lambda - 2n^{\bullet})\epsilon + in^{\bullet}(m-m^{\bullet})2\pi/\ell}\, d\lambda\,,$$

where $\mu_{>} = \mu$, $\mu_{<} = \mu'$ when $\mu > \mu'$, and $\mu_{>}^{\bullet} = \mu$, $\mu_{<}^{\bullet} = \mu^{\bullet}$ when $\mu > \mu^{\bullet}$.

When $\mu \to 0$,

$$E_{(-)} = \lim_{\epsilon \to -0} \mathcal{R}e\, \frac{h}{8\pi} \sum_{m} \int_{0}^{\mu_{0}} d\mu \sum_{m'} \int_{0}^{\mu_{0}} d\mu' \int_{\tau_{1}'}^{\tau_{2}'} \pi_{0}'\, e^{-i\,2pm'\pi/\ell}\, d\tau'$$

$$\times \sum_{n=-\infty}^{\infty} \{\mu'(p+n) + n/\mu'\}\, e^{-\frac{i}{2}p(\tau^{\bullet}-\tau') + \frac{i}{2}(p+2n)\epsilon + in(m-m')2\pi/\ell}$$

$$\times I_{n}(|p+n|\mu_{<}) \cdot K_{n}(|p+n|\mu_{>})\, \frac{-i}{8\pi\,\Omega\rho} \sum_{m^{\bullet}} \int_{0}^{\mu_{0}} d\mu^{\bullet} \int_{\tau_{1}^{\bullet}}^{\tau_{2}^{\bullet}} \bar{\pi}_{0}^{\bullet}\, e^{i\,2pm^{\bullet}\pi/\ell}\, d\tau^{\bullet}$$

$$\times \sum_{n=-\infty}^{\infty} \{\mu(p+n^{\bullet}) + n^{\bullet}/\mu\}\, \{\mu^{\bullet}(p+n^{\bullet}) + n^{\bullet}/\mu^{\bullet}\}\, I_{n\bullet}(|p+n^{\bullet}|\mu_{<}^{\bullet})$$

$$\times K_{n\bullet}(|p+n^{\bullet}|\mu_{>}^{\bullet}) \cdot e^{-\frac{i}{2}(p+2n^{\bullet})\epsilon + in^{\bullet}(m-m^{\bullet})2\pi/\ell}\,. \tag{10.8}$$

Substituting (4.9) in (10.8), we get

$$E_{(-)} = \lim_{\epsilon \to -0} \mathcal{R}e\, \frac{h}{16\pi} \sum_{m} \int_{0}^{\mu_{0}} d\mu \sum_{m^{\bullet}} \int_{0}^{\mu_{0}} d\mu^{\bullet} \int_{\tau_{1}^{\bullet}}^{\tau_{2}^{\bullet}} \bar{\pi}_{0}^{\bullet}\, e^{i\,2pm^{\bullet}\pi/\ell}$$

$$\times \Phi_{0\,\infty}(\tau^{\bullet} + 2m\pi/\ell,\, \epsilon + 2m\pi/\ell,\, \mu)\, d\tau^{\bullet} \sum_{n=-\infty}^{\infty} \{\mu(p+n^{\bullet}) + n^{\bullet}/\mu\}$$

$$\times \{\mu^{\bullet}(p+n^{\bullet}) + n^{\bullet}/\mu^{\bullet}\}\, I_{n\bullet}(|p+n^{\bullet}|\mu_{<}^{\bullet}) \cdot K_{n\bullet}(|p+n^{\bullet}|\mu_{>}^{\bullet})$$

$$\times e^{-\frac{i}{2}(p+2n^{\bullet})\epsilon + in(m-m^{\bullet})2\pi/\ell}\,. \tag{10.9}$$

If $E_{(+)}$ denotes the surface integral along the upper side of the helical surface which corresponds to (10.3), the expression of $E_{(+)}$ can be derived along the similar course. For $E_{(+)}$, the operation $\partial/\partial n$ leads to a result which is opposite to $E_{(-)}$ in sign.

Therefore, we have

$$\overline{\mathbf{E}} = \mathbf{E}_{(+)} + \mathbf{E}_{(-)} = \mathcal{R}e \frac{h}{16\pi} \sum_m \int_0^{\mu_o} d\mu \sum_{m^*} \int_0^{\mu_o} d\mu^* \int_{\tau_1^*}^{\tau_2^*} \overline{\pi}_o^* e^{i 2pm^* \pi/\ell}$$

$$\times \left\{ \Phi_{o\,\infty}^{(\ell)}(\tau^* + 2m\pi/\ell,\ 2m\pi/\ell,\ \mu) - \Phi_{o\,\infty}^{(u)}(\tau^* + 2m\pi/\ell,\ 2m\pi/\ell,\ \mu) \right\} d\tau^*$$

$$\times \sum_{n=-\infty}^{\infty} \left\{ \mu(p+n) + n/\mu \right\} \left\{ \mu^*(p+n) + n/\mu^* \right\} I_n(|p+n|\mu_<)$$

$$\times K_n(|p+n|\mu_>^*)\ e^{i n(m-m^*) 2\pi/\ell}, \tag{10.10}$$

where

$$\left. \begin{array}{l} \lim\limits_{\epsilon \to -0} \Phi_{o\infty}(\tau + 2m\pi/\ell,\ \epsilon + 2m\pi/\ell,\ \mu) = \Phi_{o\infty}^{(\ell)}(\tau + 2m\pi/\ell,\ 2m\pi/\ell,\ \mu) \\[2em] \lim\limits_{\epsilon \to +0} \Phi_{o\infty}(\tau + 2m\pi/\ell,\ \epsilon + 2m\pi/\ell,\ \mu) = \Phi_{o\infty}^{(u)}(\tau + 2m\pi/\ell,\ 2m\pi/\ell,\ \mu) \end{array} \right\} . \tag{10.11}$$

By using (3.5) and (3.7), we get

$$\Phi_{o\infty}^{(\ell)}(\tau' + 2m\pi/\ell,\ 2m\pi/\ell,\ \mu) - \Phi_{o\infty}^{(u)}(\tau' + 2m\pi/\ell,\ 2m\pi/\ell,\ \mu)$$

$$= \frac{-e^{-\frac{ip}{2}\tau'}}{2\Omega\rho} \int_{\tau_1}^{\tau_2} \pi_o(\mathbf{T} + 2m\pi/\ell,\ 2m\pi/\ell,\ \mu)\ e^{\frac{ip}{2}\mathbf{T}}\ d\mathbf{T}$$

$$= \frac{-e^{-\frac{ip}{2}\tau'}}{2\Omega\rho} \int_{\tau_1}^{\tau_2} \pi_o(\tau,\mu)\ e^{-i 2pm\pi/\ell + \frac{ip}{2}\tau}\ d\tau . \tag{10.12}$$

Substituting (10.12) in (10.10), we obtain

$$\overline{\mathbf{E}} = \mathcal{R}e \frac{-h}{32\pi\Omega\rho} \sum_m \int_0^{\mu_o} d\mu \int_{\tau_1}^{\tau_2} \pi_o(\tau,\mu)\ e^{-i 2pm\pi/\ell + \frac{ip}{2}\tau}\ d\tau$$

$$\times \sum_{m'} \int_0^{\mu_o} d\mu' \int_{\tau_1'}^{\tau_2'} \overline{\pi}_o'\ e^{i 2pm'\pi/\ell - \frac{ip}{2}\tau'}\ d\tau' \sum_{n=-\infty}^{\infty} \left\{ \mu(p+n) + n/\mu \right\} \left\{ \mu'(p+n) + n/\mu' \right\}$$

$$\times I_n(|p+n|\mu_<) \cdot K_n(|p+n|\mu_>)\ e^{i n(m-m') 2\pi/\ell}. \tag{10.13}$$

By using the symbols as shown in (9.17) and (9.18), we have, finally,

$$\overline{E} = \frac{-h}{32\pi\Omega\rho} \int^{\bullet} dS \int^{\bullet} dS'\mathbb{M}_2 \cdot (\pi_r \pi'_r + \pi_i \pi'_i) \cos \beta$$

$$- \frac{h}{16\pi\Omega\rho} \int^{\bullet} dS \int^{\bullet} dS'\mathbb{M}_2 \pi_r \pi'_i \sin \beta. \tag{10.14}$$

This expression coincides with (9.20). By (9.12), (9.20) and (10.14), it is verified that the energy theorem

$$\overline{E} = P^* + \Omega\overline{Q} + V\overline{D} \tag{10.15}$$

is satisfied in the velocity field.

11. MEAN PROPULSION

In section 9, we assumed that π_o has no singularity. But, in general, π_o has an infinite singularity at the leading edge of the blade as shown in (8.4). In this case, the first term of (9.19) does not disappear.

The average work $\overline{P}$ is written in the form

$$\overline{P} = \frac{\ell h}{4} \int_0^{r_o} \sqrt{1 + \omega^2} \; dr \int_{\tau_1}^{\tau_2} \Re e \, (w_o \cdot \overline{\pi}_o) \, d\tau \tag{11.1}$$

as mentioned in section 9.

Using (8.4) and (B.13), we can write the singular part of the downwash in the form

$$w'_o = \frac{1}{4\pi\rho V \sqrt{1 + \omega^2}} \int_0^{\omega_o} d\omega' \int_{\tau_1}^{\tau_2} A_1 u_1(\omega') \sqrt{\frac{\frac{c}{2} - \tau'}{\frac{c}{2} + \tau'}} \; \frac{1}{\tau - \tau'} \; d\tau' \; \frac{\partial}{\partial\omega'} \operatorname{sgn}(\omega' - \omega). \tag{11.2}$$

When we calculate $\overline{P}$ by substituting (11.2) in (11.1), we may exactly carry out the calculation only in the region near the leading edge. Therefore, we may consider that τ_1 and τ_2 are independent of ω'. If we perform the partial integration, we have

$$w'_o = \frac{-A_1}{4\pi\rho V \sqrt{1 + \omega^2}} \int_0^{\omega_o} \frac{\partial u_1}{\partial\omega'} \operatorname{sgn}(\omega' - \omega) \, d\omega' \int_{\tau_1}^{\tau_2} \frac{1}{\tau - \tau'} \sqrt{\frac{\frac{c}{2} - \tau'}{\frac{c}{2} + \tau'}} \; d\tau'$$

$$= \frac{A_1 u_1(\omega)}{2\pi\rho V \sqrt{1 + \omega^2}} \int_{\tau_1}^{\tau_2} \frac{1}{\tau - \tau'} \sqrt{\frac{\frac{c}{2} - \tau'}{\frac{c}{2} - \tau'}} \; d\tau' = \frac{A_1 u_1(\omega)}{2\rho V \sqrt{1 + \omega^2}} \tag{11.3}$$

105

Substituting (11.3) in (11.1) and performing the integration

$$\bar{P}' = \frac{\ell h (A_r^2 + A_i^2)}{8 \rho V} \int_0^{r_o} u_1(\mu)^2 \, dr \int_{\tau_1}^{\tau_2} \sqrt{\frac{\frac{c}{2} - \tau}{\frac{c}{2} + \tau}} \, d\tau$$

$$= \frac{\pi \ell (A_r^2 + A_i^2)}{8 \rho} \int_0^{r_o} \frac{u_1^2 \hat{C}}{W} \, dr > 0 , \tag{11.4}$$

where $A_1 = A_r + i A_i$ and $\hat{C}$ is the chord length of the blade.

The average "suction" force $\bar{S}$ arising from the infinite vorticity at the leading edge of the blade element is equal to

$$\bar{S} = \frac{\pi (A_r^2 + A_i^2) u_1^2 \hat{C}}{8 \rho \Psi^2} \tag{11.5}$$

as shown in Ref. [9]. Therefore $\bar{P}'$ is annulled by the average negative work done by the "suction" force, and the energy theorem is also satisfied.

The average torque $\bar{Q}'$ and thrust $\bar{T}'$ caused by the "suction" force is given by

$$\left. \begin{array}{l} \bar{Q}' = -\ell \int_0^{r_o} r \bar{S} \cos \epsilon \, dr = -\ell \int_0^{r_o} S_t \, r \, dr < 0 \\[4mm] \bar{T}' = \ell \int_0^{r_o} \bar{S} \sin \epsilon \, dr = \ell \int_0^{r_o} S_a \, dr > 0 \end{array} \right\} . \tag{11.6}$$

where S_t and S_a denote the tangential and axial components of $\bar{S}$. Therefore, the "suction" force reduces the propeller torque and increases the thrust, and the rate shall be given by

$$\tau_i = \frac{\bar{P}'}{\bar{P}} = \frac{\ell \int_0^{r_o} \bar{S} W \, dr}{\bar{P}} = \frac{\ell \int_0^{r_o} (S_t \cos \epsilon + S_a \sin \epsilon) W \, dr}{\bar{P}}$$

$$= \frac{-\Omega \bar{Q}' + V \bar{T}'}{\bar{P}} . \tag{11.7}$$

When a propeller moves in non-uniform flow or in oblique flow, the fluid field around the blade is non-steady, even if the propeller does not oscillate. The average forces acting on the blade disappear except the "suction" force, because the attitude of the blade does not vary. Garrick [11] has treated the propulsion on a flapping wing and calculated its efficiency which corresponds to

η of (11.7). He presented the result that the efficiency is 50 percent for infinitely rapid oscillations and 100 percent for infinitely slow flapping. The results of this theory seem to contradict the results of the experiment, as Santis's experiment shows $\overline{Q}' > 0$ and $\overline{T}' > 0$ [12]. It seems that the quantitative agreement with experimental values can hardly be expected within the frame of linearized theory. But, theoretically, we may expect that the propulsive efficiency of a propeller in non-uniform flow is higher than in uniform flow.

Appendix

KERNEL FUNCTION

The problem of the oscillating propeller is reduced to an integral equation relating the lift and downwash distributions. It seems that the kernel of the integral equation is one of the most complicated kernel functions which appear in the boundary-value problem connected with lifting systems. The main purpose of this appendix is to provide some materials for evaluating this function.

A. EXPRESSIONS OF KERNEL FUNCTION

The integral equation appears as a divergent form of integral. This integral is reduced to a form that can be accurately evaluated by numerical procedures. And the integral equation will be handled by routine numerical methods, though laborious. In this section, the kernel function is converted into the expression appropriate for numerical calculation.

Introducing dimensionless quantities, the integral equation is written in the form

$$g(\tau, \omega) = \int_0^{\tau_0} d\omega' \int_{\tau_1}^{\tau_2} U(\tau', \omega') \cdot K(\tau, \tau'; \omega, \omega') \, d\tau'.$$

where $\qquad$ (A.1)

$$U(\tau, \omega) = \tau_o(\tau, \omega) \, (\varepsilon V^2)$$

$$g(\tau, \omega) = w_o \sqrt{1 + \omega^2} \, / \, V$$

and

$$K(\tau, \tau'; \omega, \omega') = \lim_{\mu \to 0} \frac{i}{S^{-2}} \sum_{n=-\infty}^{\infty} \int_{-\infty}^{\infty} \frac{(\omega' \lambda - n \, \omega')(\omega \lambda - n \, \omega)}{\lambda + p + n - i\mu}$$

$$\times \, I_n(\lambda \, \omega_<) \cdot K_n(\lambda \, \omega_>) \, e^{\frac{i}{2}(\lambda+n)(\tau-\tau')} \sum_{\ell=0}^{\ell-1} e^{-i2(n+p)\pi \ell}. \qquad (A.2)$$

107

Referring to the equation

$$\frac{1}{\sqrt{v^2 + \mu^2 + \mu'^2 - 2\mu\mu' \cos \varphi}} = \frac{1}{\pi} \sum_{n=-\infty}^{\infty} \int_{-\infty}^{\infty} e^{iv\lambda + in\varphi} \times I_n(|\lambda|\mu_<) \cdot K_n(|\lambda|\mu_>)\, d\lambda, \quad (A.3)$$

we can derive the following relations, by differentiating with respect to v and φ,

$$\left. \begin{array}{l} \dfrac{-v}{\sqrt{v^2 + \mu^2 + \mu'^2 - 2\mu\mu' \cos \varphi}^{\,3}} = \dfrac{i}{\pi} \sum\limits_{n=-\infty}^{\infty} \int\limits_{-\infty}^{\infty} \lambda\, e^{iv\lambda + in\varphi} \times I_n(|\lambda|\mu_<) \cdot K_n(|\lambda|\mu_>)\, d\lambda \\[4mm] \dfrac{-\mu\mu' \sin \varphi}{\sqrt{v^2 + \mu^2 + \mu'^2 - 2\mu\mu' \cos \varphi}^{\,3}} = \dfrac{i}{\pi} \sum\limits_{n=-\infty}^{\infty} n \int\limits_{-\infty}^{\infty} e^{iv\lambda + in\varphi} \times I_n(|\lambda|\mu_<) \cdot K_n(|\lambda|\mu_>)\, d\lambda \end{array} \right\} \quad (A.4)$$

If we introduce those formulas in (A.2), we have

$$K(\tau, \tau'; \mu, \mu') = -\frac{1}{8\pi} \sum_{m=0}^{\ell-1} e^{-i2pm\pi/\ell} \left\{ \frac{\mu\mu'v - (\mu^2\mu'^2 + \mu^2 + \mu'^2) \sin(v - 2m\pi/\ell)}{R(v, v - 2m\pi/\ell)^3} \right.$$

$$\left. + \frac{ip\mu\mu'}{R(v, v - 2m\pi/\ell)} \right\} + \lim_{\mu \to 0} \frac{j}{8\pi^2} \sum_{n=-\infty}^{\infty} \sum_{m=0}^{\ell-1} e^{-i2pm\pi/\ell}$$

$$\times \int_{-\infty}^{\infty} \frac{\mu\mu'(p-n) + n\mu\mu'_<(p-n) + n\mu_<}{\lambda + p - n - i\mu} I_n(\lambda\mu_<) \cdot K_n(\lambda\mu_>)$$

$$\times e^{iv(\lambda+n) - i2nm\pi/\ell}\, d\lambda \qquad (A.5)$$

where

$$\left. \begin{array}{l} v = \dfrac{\tau - \tau'}{2} \\[3mm] R(v, \varphi) = \sqrt{v^2 + \mu^2 + \mu'^2 - 2\mu\mu' \cos(v - 2m\pi/\ell)} \end{array} \right\} \qquad (A.6)$$

since

$$\frac{(\mu'\lambda - n\mu')(\mu\lambda - n\mu)}{\lambda + p + n - i\mu} = \mu\mu'\lambda - n(\mu\mu' + \mu\mu' - \mu'\mu) - (p - i\mu)\mu\mu'$$

$$- \frac{\mu\mu'(p - n - i\mu) + n\mu\mu'_<(p - n - i\mu) + n\mu_<}{\lambda - p - n - i\mu}$$

In the first and second terms of (A.5) are designated by $K^{(1)}$ and $K^{(2)}$ respectively, $K^{(2)}$ is written as

108

$$K^{(2)} = \frac{i}{8\pi^2} \sum_{n=-\infty}^{\infty} \sum_{m=0}^{\ell-1} e^{-i2pm\pi/\ell} \{\mu'(p+n) + n/\mu'\}$$

$$\times \{\mu(p+n) + n/\mu\} V_n e^{in(v-2m\pi/\ell)}, \tag{A.7}$$

where

$$V_n = \lim_{\mu \to 0} \int_0^\infty \left\{ \frac{e^{iv\lambda}}{\lambda + q - i\mu} - \frac{e^{-iv\lambda}}{\lambda - q + i\mu} \right\} I_n(\lambda\varpi) \cdot K_n(\lambda\varpi) \, d\lambda \tag{A.8}$$

and $q = p + n$.

In (A.8), we can convert the integral of λ into the integral along imaginary axis by the same manner as shown in section 4. Consequently, we obtain

$$V_n = s_+^{(n)} + i2\pi e^{-ivq} I_n(q\varpi) \cdot K_n(q\varpi), \quad v > 0$$

$$V_n = s_-^{(n)}, \quad v < 0 \tag{A.9}$$

where

$$s_+^{(n)} = -i\pi \int_0^\infty \frac{e^{-v\lambda}}{\lambda - iq} J_n(\lambda\varpi) \, J_n(\lambda\varpi') \, d\lambda$$

$$s_-^{(n)} = i\pi \int_0^\infty \frac{e^{v\lambda}}{\lambda - iq} J_n(\lambda\varpi) \, J_n(\lambda\varpi') \, d\lambda \tag{A.10}$$

Therefore, $s_-^{(n)}$ tends to zero as v tends to infinity.

It appears to be difficult to evaluate $s_\pm^{(n)}$ immediately.

Referring to the equation

$$\frac{e^{\mp v\lambda + ivq}}{\lambda \mp iq} - \frac{1}{\lambda \mp iq} = \mp \int_0^v e^{\mp s\lambda + isq} \, ds. \tag{A.11}$$

we can convert (A.10) into the form

$$s_\pm^{(n)} = i\pi e^{-ivq} \int_0^v e^{-isq} \int_0^\infty e^{\mp s\lambda} J_n(\lambda\varpi) \, J_n(\lambda\varpi') \, d\lambda - t_\pm^{(n)}. \tag{A.12}$$

where

109

$$t_{\pm}^{(n)} = \mp i - e^{-ivq} \int_0^z \frac{J_n(\cdot-) \; J_n(\cdot-')}{\cdot \mp iq} \; d\cdot . \tag{A.13}$$

If we refer to the equation

$$\int_0^z \frac{\cdot}{\cdot^2 + q^2} \; J_n(\cdot-) \; J_n(\cdot-') \; d\cdot = I_n(\cdot q -) \cdot K_n(\cdot q -) , \tag{A.14}$$

$t_{\pm}^{(n)}$ is written as

$$t_{\pm}^{(n)} = \mp i - e^{-ivq} \; I_n(|q|-) \cdot K_n(|q|-) \; + - e^{-ivq} \; X_n(\cdot-') . \tag{A.15}$$

where

$$X_n(-,-') = \int_0^z \frac{q}{\cdot^2 - q^2} \; J_n(\cdot-) \; J_n(\cdot-') \; d\cdot \tag{A.16}$$

and $X_n = 0$ for $q = 0$.

If we substitute (A.12), (A.13) and (A.16) in (A.9), we get

$$V_n = i - \int_0^v e^{-iq(s-v)} \; ds \int_0^z e^{\cdot s} \; J_n(\cdot-) \; J_n(\cdot-') \; d\cdot$$

$$- - e^{-ivq} \left\{ i I_n(\cdot q -) \cdot K_n(\cdot q -) - X_n(--) \right\} , \quad v , 0 . \tag{A.17}$$

Referring to the equation

$$\frac{1}{R(s,\cdot)} = \sum_{n=-\infty}^{\infty} e^{in\cdot} \int_0^z e^{\cdot s} \; J_n(\cdot-) \; J_n(\cdot-) \; d\cdot \tag{A.18}$$

we find that

$$K^{(2)} = - \frac{\cdot}{6-} \sum_{-=0}^{i-1} e^{\cdot i2p-i} \int_0^v e^{\cdot ip(v-s)} \; \Bigg[- \frac{1}{\cdot} \; - - \frac{1}{\cdot}$$

$$\times \left\{ \frac{\cos (s - 2-i)}{R(s,s - 2-i)^3} - \frac{3- \sin^2 (s - 2-i)}{R(s,s-2-i)^5} \right\} - ip \; 2- - \frac{-}{\cdot} - \frac{-}{\cdot}$$

$$\frac{\sin (s - 2-i)}{R(s,s - 2-i)^3} - \frac{p^2}{R(s,s - 2-i)} \Bigg] \; ds \tag{A.19}$$
(Cont.)

110

$$+ \frac{i}{8\pi} \sum_{m=0}^{\ell-1} \sum_{n=-\infty}^{\infty} \{\mu(p+n) + n/\mu; \mu'(p+n) + n/\mu'\}$$

$$\times\, e^{-i2(p+n)m\pi/\ell - ipv} \left\{ i I_n(\,q\,\mu_<)\cdot K_n(\,q\,\mu_>) + X_n(\mu,\mu') \right\} . \tag{A.19}$$

If we perform the partial differentiation, the final expression of the kernel function is written in the form

$$K(\tau,\tau';\mu,\mu') = -\frac{1}{8\pi} \sum_{m=0}^{\ell-1} e^{-i2pm\pi/\ell} \left[\frac{\mu\mu'v + \sin(v - 2m\pi/\ell)}{R(v, v - 2m\pi/\ell)^3} \right.$$

$$+ \int_0^v e^{-ip(v-s)} \left\{ \frac{3(1+\mu^2)(1+\mu'^2)\, s\, \sin(s - 2m\pi/\ell)}{R(s, s - 2m\pi/\ell)^5} \right.$$

$$\left. - \frac{ip(\mu\mu's + \sin(s - 2m\pi/\ell))}{R(s, s - 2m\pi/\ell)^3} \right\} ds \left] - \frac{1}{8\pi} \sum_{m=0}^{\ell-1} e^{-ip(v-2m\pi/\ell)} \right.$$

$$\times \left\{ \frac{(1+\mu^2)(1+\mu'^2)\sin(2m\pi/\ell)}{\left(\sqrt{\mu^2 + \mu'^2 - 2\mu\mu'\cos(2m\pi/\ell)}\right)^3} - \frac{ip\mu\mu'}{\sqrt{\mu^2 + \mu'^2 - 2\mu\mu'\cos(2m\pi/\ell)}} \right\}$$

$$+ \frac{i\ell}{8\pi} \sum_{k=-\infty}^{\infty} \{\mu\ell k + (\ell k - p)\mu\mu'\ell k + (\ell k - p)/\mu'\} e^{-ivp}$$

$$\times \left\{ i I_{\ell k - p}(\,\ell k\,\mu_<)\cdot K_{\ell k - p}(\,\ell k\,\mu_>) + X_{\ell k - p}(\mu,\mu') \right\} . \tag{A.20}$$

This expression seems to be suitable for the numerical evaluation of the kernel function.

On the other hand, we can immediately derive the kernel function form (2.5) or (3.1). It is written in the form

$$K(\tau,\tau';\mu,\mu') = -\frac{h^3}{16\pi} \sum_{m=0}^{\ell-1} e^{-i2p\pi m/\ell} \sqrt{1-\mu^2}\,\sqrt{1-\mu'^2}$$

$$\times \frac{\partial}{\partial n} \int_{-\infty}^{\infty} e^{-\frac{ip}{2}(v-T)} \frac{\partial}{\partial n} \frac{1}{R}\bigg|_{\tau=\tau'} dT . \tag{A.21}$$

After some calculations, we find that

$$K(\tau,\tau';\mu,\mu') = -\frac{1}{8\pi}\sum_{m=0}^{\ell-1} e^{-i2pm\pi/\ell}\left[\frac{\mu\mu'v + \sin(v-2m\pi/\ell)}{R(v, v-2m\pi/\ell)^3}\right.$$

$$+ \int_{-\pi}^{v} e^{-ip(v-s)}\left\{\frac{3(1+\mu^2)(1+\mu'^2) s \sin(s-2m\pi/\ell)}{R(s,s-2m\pi/\ell)^5}\right.$$

$$\left.\left.-\frac{ip\{\mu\mu's + \sin(s-2m\pi/\ell)\}}{R(s,s-2m\pi/\ell)^3}\right\} ds\right]. \tag{A.22}$$

The integral from 0 to π in (A.22) corresponds to the second and third members of (A.20). This relationship is easily verified by referring to (A.18).

It appears to be convenient to have the kernel function expressed in a separated form

$$\left.\begin{array}{l} K(\tau,\tau';\mu,\mu') = \dfrac{\bar{K}(\tau,\tau';\mu,\mu')}{(\mu-\mu')^2}. \\[3mm] K^{(1)} = \dfrac{\bar{K}^{(1)}}{(\mu-\mu')^2}, \qquad K^{(2)} = \dfrac{\bar{K}^{(2)}}{(\mu-\mu')^2} \end{array}\right\} \tag{A.23}$$

as Watkins [13] has pointed out, because K has a second order singularity which will be shown in next section.

B. SINGULARITY OF KERNEL FUNCTION

The kernel function contains singularities. The forms that the kernel function takes when it becomes singular are of particular importance to the numerical calculation of the integral equation.

If we write

$$M_n = \lim_{\mu\to 0}\sum_{m=0}^{\ell-1} e^{-i2pm\pi/\ell}\int_{-\pi}^{\pi}\frac{\mu'(p+n)+n\mu'/\mu(p+n)+n\mu'}{\mu+p+n-i\mu}$$

$$\times I_n(\cdots) \cdot K_n(\cdots) e^{iv\pm in(v-2m\pi/\ell)}ds. \tag{B.1}$$

$\bar{K}^{(2)}$ is given by

$$\bar{K}^{(2)} = \frac{i(\mu-\mu')^2}{s-2}\sum_{n=-\pi}^{\pi} M_n. \tag{B.2}$$

When n is large, we may use the asymptotic functions (4.5) for (B.1). We thus have

$$M_n = \lim_{\mu \to 0} \sum_{m=0}^{\ell-1} e^{-i2pm-\ell} \frac{1}{2\,n} \left(\frac{-\ell}{-\ell}\right)^n$$

$$\cdot \int_{-\pi}^{\pi} \frac{\ell_m'(p+n)+n_{-}'\!/\!\ell(p+n)+n_{-\ell}}{\cdot + p+n-i\mu} e^{iv\cdot+in(v+2m-\ell)} d\cdot \quad (B.3)$$

The integral of $\cdot$ can be carried out by considering the integral

$$\frac{1}{2\pi i} \int \frac{e^{iv\cdot}}{\cdot + p+n-i\mu} d\cdot$$

taken round suitable contours. When $v > 0$, the contour is chosen with a loop bound by the real axis and a large semicircle on the upper side of the real axis. When $v < 0$, the contour is chosen with a loop bound by the real axis and a large semicircle on the lower side of the real axis.

As the integral round the large semicircle tends to zero as the radius tends to infinity. Hence

$$\int_{-\pi}^{\pi} \frac{e^{iv\cdot}}{\cdot + p+n-i\mu} d\cdot = \begin{cases} 2\pi i e^{-iv(p+n)}, & v > 0 \\ 0, & v < 0 \end{cases}$$

Hence

$$M_n = i\pi \sum_{m=0}^{\ell-1} e^{-i2pm-\ell} \frac{1}{n} \left(\frac{-}{-\ell}\right)^n \ell_m'(p+n)+n_{-}$$

$$\cdot \ell_m(p+n)+n_{-} e^{-ivp+i2\pi n-n\ell} \quad v > 0 \qquad \qquad (B.4)$$

$$M_n = 0, \quad v < 0$$

In the following analysis, we consider only M_n for $v > 0$. If u denotes a large positive integer, sum of M_n for $n \geq u$ is written

$$\sum_{n=u}^{\infty} (M_n + M_{-n}) = i\pi \sum_{m=0}^{\ell-1} e^{-i p(v+2m-\ell)} \left[a_{-1} \sum_{n=u}^{\infty} \frac{1}{n} (x^n + y^n) \right.$$

$$\left. + a_0 \sum_{n=u}^{\infty} (x^n + y^n) + a_1 \sum_{n=u}^{\infty} n(x^n + y^n) \right] \qquad (B.5)$$

where

$$a_{-1} = \mu\mu'p^2, \qquad\qquad a_o = p(2\mu\mu' + \mu/\mu' + \mu'/\mu)$$

$$a_1 = (\mu + 1/\mu)(\mu' + 1/\mu')$$

$$x = \frac{\mu\mu'}{\mu} e^{-i 2m\pi/\ell}, \qquad y = \frac{\mu\mu'}{\mu} e^{i 2m\pi/\ell} \qquad\qquad (B.6)$$

When $\mu = \mu'$, (B.5) is absolutely convergent.

By applying the well known formulas

$$\sum_{n=1}^{\infty} \frac{x^n}{n} = \ell n \frac{1}{1-x}, \qquad \sum_{n=1}^{\infty} x^n = \frac{x}{1-x}, \qquad \sum_{n=1}^{\infty} n x^n = \frac{x}{(1-x)^2}, x < 1 \qquad (B.7)$$

to (B.5), we obtain

$$\bar{K}^{(2)} = -\frac{(\mu-\mu')^2}{8\pi} \sum_{r=0}^{\ell-1} e^{-ip(v+2m\pi-\ell)}\left[a_{-1}\left(\ell n \frac{1}{1-x} - \ell n \frac{1}{1-y}\right)\right.$$

$$\left. + a_o\left(\frac{x}{1-x} - \frac{y}{1-y}\right) + a_1\left(\frac{x}{(1-x)^2} + \frac{y}{(1-y)^2}\right)\right] + (\mu-\mu')^2 \cdot R. \qquad (B.8)$$

R corresponds to the sum of M_n in the range $-u < n < n$ and it is finite, even if $\mu = \mu'$. And then applying the equation

$$\frac{x}{(1-x)^2} = \frac{\mu\mu' e^{-i2m\pi-\ell}}{(\mu\mu' - \mu\mu e^{-i2m\pi-\ell})^2}, \qquad \ell n \frac{1}{1-x} = \ell n \frac{\mu\mu'}{\mu\mu' - \mu\mu e^{-i2m\pi-\ell}}$$

we see that $K^{(2)}$ has singularities at $\mu = \mu'$ for $m = 0$. In (B.8), when $m = 0$, the term multiplied by a_o is equal to zero. Hence, it is found that for vanishingly small value of $\mu - \mu'$ the limiting value of (B.8) is

$$K^{(2)} \sim -\frac{e^{-\frac{ip}{2}(\mu-\mu')}}{4\pi}\left\{-a_{-1}(\mu-\mu')^2 \ell n |\mu-\mu'| - a_1\mu\mu'\right\} - O(\epsilon^2), \quad \mu - \mu' > 0$$

$$K^{(2)} \sim 0, \qquad\qquad\qquad \mu - \mu' < 0 \qquad (B.9)$$

where $\epsilon \sim \mu - \mu'$.

If $\mu = \mu'$,

$$\lim_{\mu \to \mu'} \bar{K}^{(1)} = 0.$$

114

Therefore,

$$
\begin{aligned}
\lim_{\mu \to \mu'} \ \overline{K}(\tau,\tau';\mu,\mu') &= -\frac{(1+\mu^2)^2}{4\pi}\, e^{-\frac{i}{2}p(\tau-\tau')}, \quad &\tau-\tau' > 0 \\
\lim_{\mu \to \mu'} \ \overline{K}(\tau,\tau';\mu,\mu') &= 0, \quad &\tau-\tau' < 0
\end{aligned}
\Biggr\} \ . \qquad (B.10)
$$

We see that $\overline{K}(\tau,\tau';\mu,\mu')$ contains no infinite singularity but possesses one finite singularity at $\tau-\tau' = \mu-\mu' = 0$. This form of the singularity is in conformity with the kernel function in case of an oscillating wing [13]. This nature of the singularity leads to no special difficulty for the numerical procedure of solving the integral equation.

The integral equation (A.1) is written in a divergent form. But if we perform the integration by parts and evaluate Cauchy's principal value of the integral, we obtain a finite limit. This result coincides with the limiting value of the downwash at the boundary of a blade.

Let us consider the nature of the singularity of the kernel function of the above mentioned integral equation at $\tau-\tau' = 0$.

If we write

$$
B(v) = v^2 - \mu^2 \sin^2(v - 2\pi - i)
$$

$$
R(v) = \sqrt{v^2 + \mu^2 - \mu'^2 - 2\mu\mu' \cos(v - 2\pi - i)}
$$

$$
\zeta_v = v - 2\pi - i, \qquad \zeta_s = s - 2\pi - i
$$

we have

$$
\frac{\mu\mu' v + \sin \zeta_v}{R(v)^3} = \frac{\partial}{\partial \mu'}\left[\frac{-\mu v B(v) - (\mu^2 v \cos \zeta_v - \sin \zeta_v)(\mu' - \mu \cos \zeta_v)}{B(v)\cdot R(v)} \right]
$$

$$
\frac{3(1-\mu^2)(1-\mu'^2)\, s \sin \zeta_s}{R(s)^5} = (1-\mu^2)\, s \sin \zeta_s \frac{\partial}{\partial \mu'}\ \frac{1}{B(s)\,R(s)}\left[3(\mu' - \mu \cos \zeta_s) \right.
$$

$$
+ 2\mu \cos \zeta_s \cdot B(s) - \frac{(s^2 - \mu^2 - 2\mu^2 \cos^2 \zeta_s - 1)(\mu' - \mu \cos \zeta_s)}{R(s)^2}
$$

$$
\left. - \frac{2(s^2 - \mu^2 - 2\mu^2 \cos^2 \zeta_s - 1)(\mu' - \mu \cos \zeta_s)}{B(s)} \right] .
$$

Hence, (A.22) is written in the form

115

$$K(\tau,\tau';\mu,\mu') = -\frac{1}{8\pi}\sum_{m=0}^{\ell-1} e^{-i2pm\pi/\ell}\ \frac{\partial}{\partial\mu'}\left[\frac{-\mu v B(v) + (\mu^2 v\cos\tau_v + \sin\tau_v)\mu'}{B(v)\cdot R(v)}\right.$$

$$\left.-\frac{(\mu^2 v\cos\tau_v + \sin\tau_v)\mu\cos\tau_v}{B(v)\ R(v)}\right] - \frac{1}{8\pi}\sum_{m=0}^{\ell-1} e^{-i2pm\pi/\ell}\ \oint_{-\pi}^{v} e^{-ip(v-s)}$$

$$\times\left[(1+\mu^2)s\ \sin\tau_s\ \frac{\partial}{\partial\mu'}\ \frac{\mu'-\mu\cos\tau_s}{B(s)\cdot R(s)}\left\{3+\frac{2\mu\cos\tau_s\cdot B(s)}{\mu'-\mu\cos\tau_s}\right.\right.$$

$$\left.- (s^2+\mu^2-2\mu^2\cos^2\tau_s-1)\left(\frac{1}{R(s)^2}+\frac{2}{B(s)}\right)\right\} - ip\ \frac{\partial}{\partial\mu'}\left\{\frac{-\mu s\ B(s)}{B(s)\cdot R(s)}\right.$$

$$\left.\left.+\frac{(\mu^2 s\cos\tau_s + \sin\tau_s)(\mu'-\mu\cos\tau_s)}{B(s)\cdot R(s)}\right\}\right]\ ds\ .\qquad(B.11)$$

We see that the integrand contains the first- and second-order singularities.

Hence, if we write, for $m = 0$,

$$-\frac{1}{8\pi}\ \frac{\partial}{\partial\mu'}\ \oint_{-\pi}^{v} e^{-ip(v-s)}\left[(1+\mu^2)s\ \sin s\ \cdot\frac{\mu'-\mu\cos s}{B(s)\cdot R(s)}\right.$$

$$\times\left\{3+\frac{2\mu\cos s\cdot B(s)}{\mu'-\mu\cos s} - (s^2-\mu^2-2\mu^2\cos^2 s-1)\left(\frac{1}{R(s)^2}+\frac{2}{B(s)}\right)\right\}$$

$$-ip\left\{\frac{-\mu sB(s) + (\mu^2 s\cos s + \sin s)(\mu'-\mu\cos s)}{B(s)\cdot R(s)}\right\}$$

$$\left.-\left(\frac{2}{s^2}-\frac{ip}{s}\right)\ \mathrm{sgn}\ (\mu'-\mu)\right]\ ds$$

$$+\frac{1}{8\pi}\ \frac{\partial}{\partial\mu'}\ \mathrm{sgn}\ (\mu'-\mu)\ \oint_{-\pi}^{v} e^{-ip(v-s)}\left(-\frac{2}{s^2}-\frac{ip}{s}\right)\ ds$$

the first member is non-singular and second member is singular at $\mu-\mu' = 0$.
Performing the integration of the second member, we have

$$\frac{1}{8\pi}\ \frac{\partial}{\partial\mu'}\ \mathrm{sgn}\ (\mu'-\mu)\left\{\frac{2}{v}+ip\ \int_{-\pi}^{v}\frac{e^{-ip(v-s)}}{s}\ ds\right\}\ .\qquad(B.12)$$

Therefore, it is found that for vanishingly small value of $\mu-\mu'$, the limiting
value of (B.11) is

116

$$I_o(\mathbb{C} q) = \sum_{m=-\infty}^{\infty} (-)^m I_m(q\_) \cdot I_m(q \_') e^{im\phi}. \tag{C.5}$$

And an expression for $L_o(x)$ in the form of an ascending series of powers of x is given by

$$L_o(x) = \frac{2}{\pi} \sum_{m=0}^{\infty} \frac{x^{2m+1}}{\overline{(2m-1)!!}^2}. \tag{C.6}$$

where $(2m-1)!! = 1 \cdot 3 \cdot 5 \ldots (2m-1)$.

If we use these expressions for the integration of (C.4), we get

$$X_n(\_,\_') = \text{sgn}\, q \cdot \frac{\pi}{2} (-)^n I_n(q\_) I_n(q\_') - \frac{1}{2} \sum_{m=0}^{\infty} \frac{(\_q)^{2m+1} a_{m+n}^{(n)}}{\overline{(2m-1)!!}^2}. \tag{C.7}$$

An expression for $a_s^{(n)}$ is given by

$$\frac{1}{2} a_s^{(n)} = \frac{1}{\pi} \int_0^\pi (1 - \_^2 - 2\_ \cos \_)^s \cos n\_ \, d\_. \tag{C.8}$$

where $\_ = \_,\_.$, $s > 0$ and a method for the numerical evaluation of this function will be given in the last place of this section. The formula (C.7) is available for the numerical evaluation of X_n when $(\_,-\_) q$ is small.

An asymptotic expansion of $S_o(x)$ for large value of x is given by

$$S_o(x) \sim \frac{2}{\pi} \sum_{j=0}^{u-1} \overline{(2j-1)!!}^2 \frac{1}{x^{2j+1}} + O(x^{-2u}). \tag{C.9}$$

where $(2j-1)!! = 1 \cdot 3 \cdot 5 \cdots (2m-1)$, and $(2j-1)'' = 1$ for $j = 0$. If we use this expansion for the integration of (C.4), we get

$$X_n(\_,\_') \sim \frac{\text{sgn}\, q}{2} \sum_{j=0}^{u-1} \overline{(2j-1)!!}^2 \frac{b_{j+n}^{(n)}}{(\_,q)^{2j+1}} + O\left(\_^{-2u} q^{-2u}\right). \tag{C.10}$$

where for $s > 0$,

$$\frac{1}{2} b_s^{(n)} = \frac{1}{\pi} \int_0^\pi (1 - \_^2 - 2\_ \cos \_)^{-s} \cos n\_ \, d\_. \tag{C.11}$$

The formula (C.10) is available for the evaluation of X_n when $(\_,-\_) q$ is large.

118

When $(\mu_{,} - \mu_{,})|q|$ and $(\mu_{,} + \mu_{,})|q|$ take moderate values, the evaluation of X_n becomes time consuming. On that occasion, it seems to be easy that the integration of (C.4) is carried out by numerical procedure.

Arbitrary function of φ is approximately expressed by

$$g(\varphi) = \frac{1}{m+1} \sum_{r=0}^{m+1} \epsilon_r \, g(\varphi_r) \sum_{k=0}^{m+1} \epsilon_k \cos k\varphi_r \cos k\varphi \qquad (C.12)$$

in the range from 0 to π, where

$$\epsilon_{r,k} = \begin{cases} 1; & r,k = 0, \ m+1 \\ 2; & r,k = 0, \ m+1 \end{cases}.$$

If we put (C.12) for S_o in (C.4) and perform the integration, we get, for $n < m+1$

$$X_n(\mu, \mu') = \frac{\pi \, \text{sgn} \, q}{2(m+1)} \sum_{r=0}^{m+1} \epsilon_r \, S_o(\varphi_r) \cos n\varphi_r, \qquad (C.13)$$

where

$$S_o(\varphi_r) \equiv S_o \left(q \sqrt{\underline{\ }^2 + \underline{\ }'^2 - 2\underline{\ }\underline{\ }' \cos \varphi_r} \right).$$

We can easily evaluate the value of X_n by the use of (C.13) approximately, if we extract the values of S_o from the tables of $I_o(x)$ and $L_o(x)$ [16].

We can construct a recurrence formula for X_n. The proof of the formula is given in the following.

If we write

$$S_1(x) = I_1(x) - L_1(x). \qquad (C.14)$$

the recurrence formulas for $S_n(x)$ is given by

$$\left. \begin{array}{l} S_o'(x) = S_1(x) - \dfrac{2}{\underline{\ }} \\[2mm] x \, S_o(x) = \dfrac{d}{dx} \left(x \cdot S_1(x) \right) \end{array} \right\} . \qquad (C.15)$$

Performing the partial integration in (C.4), we get

$$X_n(\underline{\ }, \underline{\ }') = - \frac{\underline{\ }'q}{2n} \int_0^{\ } \frac{S_o'(\varphi \, q)}{\varphi} \sin \varphi \sin n\varphi \, d\varphi. \qquad (C.16)$$

119

Now we introduce a new function

$$X_n^{(1)}(\mu, \mu') = \frac{1}{q} \int_0^{\pi} S_1(\tilde{z}|q|) \tilde{z} \cos n\tilde{z} \, d\tilde{z} . \tag{C.17}$$

Performing the partial integration in (C.17) by the use of

$$\frac{d}{d\tilde{z}} \left\{ \tilde{z} \cdot S_1(\tilde{z}|q|) \right\} = \mu\mu'|q| S_0(\tilde{z}|q|) \sin \tilde{z} ,$$

we get

$$X_n^{(1)} = - \frac{\mu\mu' \, \text{sgn} \, q}{n} \int_0^{\pi} S_0(\tilde{z}|q|) \sin \tilde{z} \sin n\tilde{z} \, d\tilde{z}$$

$$= - \frac{\mu\mu'}{n} \left\{ X_{n-1} - X_{n+1} \right\} . \tag{C.18}$$

From (C.17), we have

$$X_{n-1}^{(1)} - X_{n+1}^{(1)} = \frac{2}{q} \int_0^{\pi} S_1(\tilde{z}|q|) \tilde{z} \sin \tilde{z} \sin n\tilde{z} \, d\tilde{z} . \tag{C.19}$$

Using the recurrence formulas (C.15), we get

$$X_{n-1}^{(1)} - X_{n+1}^{(1)} = \frac{2}{q} \int_0^{\pi} S_0'(\tilde{z}|q|) \tilde{z} \sin \tilde{z} \sin n\tilde{z} \, d\tilde{z} - \frac{4}{-q} \int_0^{\pi} \tilde{z} \sin \tilde{z} \sin n\tilde{z} \, d\tilde{z}$$

$$= \frac{2(\mu^2 - \mu'^2)}{q} \int_0^{\pi} \frac{S_0'(\tilde{z}|q|)}{\tilde{z}} \sin \tilde{z} \sin n\tilde{z} \, d\tilde{z}$$

$$- \frac{2\mu\mu'}{q} \int_0^{\pi} \frac{S_0'(\tilde{z}|q|)}{\tilde{z}} \sin \tilde{z} \{\sin(n-1)\tilde{z} - \sin(n-1)\tilde{z}\} \, d\tilde{z}$$

$$- \frac{\pi}{q} \left\{ a_{1\ 2}^{(n-1)} - a_{1\ 2}^{(n+1)} \right\} .$$

Substituting (C.16), we get

$$X_{n-1}^{(1)} - X_{n+1}^{(1)} = - \frac{4n(\mu^2 - \mu'^2)}{\mu\mu' q^2} X_n - \frac{4(n-1)}{q^2} X_{n+1}$$

$$+ \frac{4(n-1)}{q^2} X_{n+1} - \frac{\pi}{q} \left\{ a_{1\ 2}^{(n-1)} - a_{1\ 2}^{(n+1)} \right\} . \tag{C.20}$$

120

Eliminating $X_n^{(1)}$ from the equations (C.18) and (C.20) and using (C.28), we get the recurrence formula for X_n,

$$X_n \cdot \left\{ \frac{\mu\mu'}{n+1} + \frac{\mu\mu'}{n-1} + \frac{4n(\mu^2 + \mu'^2)}{\mu\mu'q^2} \right\} = \frac{\mu\mu'}{n-1} X_{n-2} + \frac{\mu\mu'}{n+1} X_{n+2} + \frac{4(n+1)}{q^2} X_{n+1}$$

$$+ \frac{4(n-1)}{q^2} X_{n-1} - \frac{2}{3} \frac{n\mu}{q\alpha} a_{3/2}^{(n)}. \qquad (C.21)$$

By the use of this equation, we can evaluate the value of X_n from X_{n+1}, X_{n+2}, X_{n+3} and X_{n+4}.

The function $b_s^{(n)}$ defined by (C.11) is called Laplace's coefficient [17] of which theory has been constructed for the purpose of the development of the disturbing function in dynamical astronomy.

An expression for $b_s^{(n)}$ in the form of an ascending series of powers of α is given by

$$\frac{1}{2} b_s^{(n)} = \frac{s(s+1)\dots(s+n-1)}{n!} \alpha^n F(s, s+n; n+1; \alpha^2), \qquad (C.22)$$

where $F(a,b;c;x)$ denotes the hypergeometric function. Brown and Brouwer [18] constructed a table of $G_s^{(n)}$ which is related with $b_s^{(n)}$ by

$$b_s^{(n)} = (1-\alpha^2)^{-s} \alpha^n G_s^{(n)}. \qquad (C.23)$$

In Brown's table, the values of $G_s^{(n)}$ are given for the ranges of n and s from $n=0$ to $n=11$ and from $s=1/2$ to $s=7/2$. We can evaluate $G_s^{(n)}$ for larger values of n or s by the use of Legendre's recursions formulas

$$\left. \begin{aligned} \frac{1}{2}\left\{ b_{s+1}^{(n)} + b_{s-1}^{(n+1)} \right\} &= \frac{(n+s) b_s^{(n)} - (n-s-1) b_s^{(n+1)}}{2s(1-\alpha)^2} \\[2mm] \frac{1}{2}\left\{ b_{s+1}^{(n)} - b_{s-1}^{(n+1)} \right\} &= \frac{(n+s) b_s^{(n)} - (n-s-1) b_s^{(n+1)}}{2s(1-\alpha)^2} \end{aligned} \right\} . \qquad (C.24)$$

Referring to the theory for $b_s^{(n)}$, we can derive the expansion and the recurrent relations for $a_s^{(n)}$.

From (C.8), we can derive the relation

$$(1+\alpha^2 - 2\alpha \cos \varepsilon)^s = \frac{1}{2} \sum_{n=-\infty}^{\infty} a_s^{(n)} e^{in\varepsilon}. \qquad (C.25)$$

because $a_s^{(n)} = a_s^{(-n)}$. If we write $e^{i\varepsilon} = Z$, (C.25) is written in the form

121

$$(1 - aZ)^s (1 - aZ^{-1})^s = \frac{1}{2} \sum_{n=-\infty}^{\infty} a_s^{(n)} Z^n . \tag{C.26}$$

Differentiating (C.25) with respect to Z and multiplying by Z, we get

$$- as (1 - aZ)^{s-1} (1 - aZ^{-1})^{s-1} \left(Z - \frac{1}{Z} \right) = \frac{1}{2} \sum_{n=-\infty}^{\infty} n a_s^{(n)} Z^n . \tag{C.27}$$

If we substitute the series given by (C.26) for $(1 - aZ)^{s-1} \cdot (1 - aZ^{-1})^{s-1}$ in (C.27), by equating the terms multiplied by Z^n, we get

$$a_s^{(n)} = - \frac{as}{n} \left\{ a_{s-1}^{(n-1)} - a_{s-1}^{(n+1)} \right\} . \tag{C.28}$$

If we multiply (C.27) by $(1 - aZ) \cdot (1 - aZ^{-1})$ and put the right-hand member of (C.26) in place of $(1 - aZ)^s \cdot (1 - aZ^{-1})^s$, by equating the terms multiplied by Z^{n-1}, we get

$$a_s^{(n)} = \frac{n-1}{n+s} \left(a + \frac{1}{a} \right) a_s^{(n-1)} - \frac{n-s-2}{n+s} a_s^{(n-2)} . \tag{C.29}$$

From (C.28) and (C.29), we can derive the formula

$$a_{s+1}^{(n)} = - \frac{s+1}{n-s-1} \left\{ (1 + a^2) a_s^{(n)} - 2a a_s^{(n)} \right\} . \tag{C.30}$$

Formulas (C.29) and (C.30) are the recursions formulas of $a_s^{(n)}$.

If we expand the left-hand member of (C.26) in power series of Z by means of the binomial theorem, by equating coefficients we get

$$\frac{1}{2} a_s^{(n)} = {}_sc_n (-a)^n F(-s, -s+n; n+1; a^2) . \tag{C.31}$$

where

$${}_sc_n = \frac{s(s-1) \dots (s-n+1)}{n!} . \qquad {}_sc_o = 1 .$$

When s is an integer, $a_s^{(n)}$ becomes a polynomial. And we see that $a_o^{(o)} = 2$, and $a_s^{(n)} = 0$ for $s < n$, and $F = 1$ for $s = n$, $F = 1 - a^2$ for $s = n+1$.

We know a relation, for hypergeometric function

$$F(a,b;c;x) = (1-x)^{c-a-b} F(c-b, c-a; c; x) .$$

If we apply this relation to (C.31), we get

Hydrodynamics of an Oscillating Screw Propeller

$$\frac{1}{2} a_s^{(n)} = {}_s c_n (-a)^n (1-a^2)^{2s+1} F(s+1, s+1+n; n+1; a^2) . \tag{C.32}$$

From (C.22) and (C.32), we get a prominent relation

$$a_s^{(n)} = (-)^n \frac{s(s-1)\dots(s-n+1)}{(s+1)(s+2)\dots(s+n)} (1-a^2)^{2s+1} b_{s+1}^{(n)} \tag{C.33}$$

or

$$a_s^{(n)} = (-)^n \frac{s(s-1)\dots(s-n+1)}{(s+1)(s+2)\dots(s+n)} a^n (1-a^2)^s G_{s+1}^{(n)} . \tag{C.34}$$

where, for $n = 0$,

$$\{s(s-1)\dots(s-n+1)\}/\{(s+1)(s+2)\dots(s+n)\} = 1 .$$

Therefore, we can easily evaluate $a_s^{(n)}$ by using Brown's table.

REFERENCES

1. Isay, W. H., "Der Schraubenpropeller im Nachstrom eines Schiffsrumphes," Schiffstechnik, 5, Heft 28, 1958.

2. Loewy, R. G., "A Two-Dimensional Approximation to the Unsteady Aerodynamics of Rotary Wings," J. Aero. Sci., Vol. 24, 1957.

3. Timman, R. and van de Vooren, A. I., "Flutter of a Helicopter Rotor Rotating in its Own Wake," J. Aero. Sci., Vol. 24, 1957.

4. Kondo, K., "The Potential-Theoretical Fundamentals of Aerodynamics Concerning the Screw Propeller," Memo. Faculty of Eng., Kyushu Imperial University, Vol. IX, No. 3, 1942.

5. Lamb, H., "Hydrodynamics," 1932.

6. von Kármán, Th., "Supersonic Aerodynamics—Principles and Applications, J. Aero. Sci., Vol. 14, 1947.

7. Flax, A. H., "General Reverse Flow and Variational Theorems in Lifting-Surface Theory," Vol. 19, 1952.

8. Birnbaum, W., "Die tragende Wirbelfläche als Hilfsmittel zur Behandlung des ebenen Problems der Tragflügeltheorie," Z.A.M.M. Bd. 3, 1923.

9. Durand, W. F., "Aerodynamic Theory, Vol. II," Springer, 1935.

10. Lamb, H., "On Wave Resistance," Roy. Soc. Proc., Vol. III, 1926.

11. Garrick, I. E., "Propulsion of a Flapping and Oscillating Airfoil," N.A.C.A. Tech. Rep. 567, 1936.

12. de Santis, R., "The Effect of Inclination Immersion, and Scale on Propellers in Open Water," T.I.N.A., 1934.

13. Watkins, C. E., Woolston, D. S., and Cunningham, H. J., "A Systematic Kernel Function Procedure for Determining Aerodynamic Forces on Oscillating or Steady Finite Wings at Subsonic Speeds," N.A.S.A. Rep. R-48, 1959.

14. Sibagaki, W., "0.01% Tables of Modified Bessel Functions," Baifukan, Tokyo, 1955.

15. Watson, G. N., "Bessel Functions," 1922.

16. "Tables of the Struve Functions $L_\nu(x)$ and $H_\nu(x)$," Jour. Math. and Phys., Vol. XXV, No. 3, Oct. 1946.

17. Schwarzschild, K. und Oppenheim, S., "Encyklopädie der Mathematischen Wissenschaften VI, 2, A, Astronomie," Leipzig, 1905-1923.

18. Brown, E. W. and Brouwer, D., "Tables for the Development of the Disturbing Function," Cambridge, 1933.

*   *   *

Monday, August 27

Afternoon Session

PROPULSION

Chairman: K. E. Schoenherr

David Taylor Model Basin
Washington, D. C.

DESIGN DIAGRAMS OF MODERN FOUR, FIVE, SIX AND SEVEN-BLADED PROPELLERS DEVELOPED IN JAPAN

Atsuo Yazaki
Transportation Technical Research Institute
Tokyo, Japan

INTRODUCTION

In Japan, design diagrams have been published for the three and four-bladed propellers with the Unken-type aerofoil blade section, and have been used widely for design purposes [1,2,3]. With the ever-increasing speed and power of modern ships, however, it has been desired to develop modern propellers having higher performance not only in efficiency but also in cavitation and vibration characteristics. To meet this requirement, we have successfully developed many types of propellers with AU type aerofoil blade sections (hereinafter will be called as AU type propellers) improved from the Unken-type aerofoil [4], by using the results of preliminary tank tests [5] and cavitation tests [6] employing many model propellers.

The systematic testing works with AU type propellers have so far been conducted for four, five, six and seven-bladed propellers, and many kinds of design diagrams based on these tests have been made and used for actual designs.

MODEL PROPELLERS

Particulars of model propellers used for the open water test series of AU type propellers are given in Table 1. These model propellers are made of aluminum alloy with a diameter of 25 centimeters, and were accurately finished with the model propeller shaping machine. Each of them has a constant pitch, and the boss ratio 0.180 and the blade thickness ratio 0.050. Main series of the six-bladed propellers have the wash-back at the trailing edge of the blade section, but the other groups of propellers have not such wash-back.

As an example of the general plan of model propellers, the plan of the four-bladed propeller with expanded area ratio 0.40 is shown in Fig. 1.

127

Table 1
Model Propellers

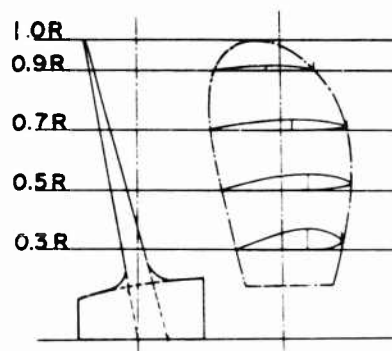| No. of blades	4		5		6			7	
Model prop No.	1305 ~1309	1310 ~1314	1128 ~1132	1133 ~1137	1189 ~1192	1193 1196	1197 ~1200	1144	1147
Pitch ratio	0.5, 0.6, 0.8, 1.0, 1.2		0.4, 0.6, 0.8, 1.0, 1.2		0.5, 0.7, 0.9, 1.1			0.6	
Blade Section	AU		AU		AU	AU*		AU	
Diameter (m)	0.250		0.250		0.250			0.250	
Exp. area ratio	0.40	0.55	0.50	0.65	0.70	0.70	0.55	0.65	0.758
Boss ratio	0.180		0.180		0.180			0.180	
Blade thickness ratio	0.050		0.050		0.050			0.050	
Rake angle	10°	0	10°	0°	10°		0	10°	0

Fig. 1 - General plan of AU4-40

Particulars and ordinates of propeller forms are given in Table 2. Ordinates of blade sections of the standard AU type with no wash-back are shown in Table 3, and those of blade sections of the type with the wash-back on the trailing edge (will be called as AUw type blade sections), which are used for six-bladed propellers, are given in Table 4.

All propeller models have been tested over a 100% slip range at the immersion to the center of propeller shaft equal to the screw diameter, and number of revolutions was kept constant, and the speed of advance was changed from zero to the speed for zero thrust.

For fixing the net thrust, the correction for the resistance of the screw hub at various speed of advance was applied. The Reynolds number in the test of each group of model propellers is shown in Table 5.

TEST RESULTS AND $\sqrt{B_p}$ - δ TYPE DESIGN DIAGRAMS

The results of the tests for each group were shown in Figures 2 - 9. The J, K_T, K_Q and η_o are defined as follows:

$$ J = \frac{V_A}{nD} \cdot \quad K_T = \frac{T}{\rho n^2 D^4} \cdot \quad K_Q = \frac{Q}{\rho n^2 D^5} \cdot \quad \eta_o = \frac{J K_T}{2\pi K_Q} $$

where V_A: The propeller speed of advance; D: the screw diameter; T: the net thrust with the idle thrust deducted; Q: the measured torque; and ρ: the density of tank water.

$\sqrt{B_p}$ - δ type design diagrams were made using these figures, and are given in Figures 10 - 17. The metric units were used, and the density of sea water is

Design Diagrams of Bladed Propellers Developed in Japan

Table 2
Dimensions of AU-4 Series Prop.

r/R	0.2	0.3	0.4	0.5	0.6	0.66	0.7	0.8	0.9	0.95	1.00	
Width of Max. Blade Width as % of Blade Width — From Generator Line to Trailing Edge	27.96	33.45	38.76	43.54	47.96	49.74	51.33	52.39	48.49	42.07	17.29	Max. Blade Width at 0.66 $r/R = 0.226\ D$ for $A_E/A = 0.40$
From Generator Line to Leading Edge	38.58	44.25	48.32	50.80	51.15	50.26	48.31	40.53	25.13	13.55		
Total Blade Width	66.54	77.70	87.08	94.34	99.11	100.00	96.64	92.92	73.62	55.62		
Blade Thickness as % of D	4.06	3.59	3.12	2.65	2.18	1.90	1.71	1.24	0.77	0.54	0.30	MaxBlade Thickness at Prop Axis = 0.050 D
Distance of the point of Max Thickness From the Leading Edge as % of Blade Width	32.0	32.0	32.0	32.5	34.9	37.9	40.2	45.4	48.9	50.0		

Table 3
Offsets of AU-Type Propeller

1) ORDINATES OF X VALUE ARE GIVEN AS % OF BLADE WIDTH   2) ORDINATES OF Y VALUE ARE GIVEN AS % OF Ymax

r/R		0	2.00	4.00	6.00	10.00	15.00	20.00	30.00	32.00	40.00	50.00	60.00	70.00	80.00	90.00	95.00	100.00
0.20	X	0	2.00	4.00	6.00	10.00	15.00	20.00	30.00	32.00	40.00	50.00	60.00	70.00	80.00	90.00	95.00	100.00
	$Y_.$	35.00	51.85	59.75	66.15	76.05	85.25	92.20	89.80	100.00	97.75	89.95	78.15	63.15	45.25	25.30	15.00	4.50
	Y_v			24.25	19.05	15.00	10.00	5.40	2.35									
0.30	X	0	2.00	4.00	6.00	10.00	15.00	20.00	30.00	32.00	40.00	50.00	60.00	70.00	80.00	90.00	95.00	100.00
	$Y_.$	35.00	51.85	59.75	66.15	76.05	85.25	92.20	99.80	100.00	97.75	89.95	78.15	63.15	45.25	25.30	15.00	4.50
	Y_v			24.25	19.05	15.00	10.00	5.40	2.35									
0.40	X	0	2.00	4.00	6.00	10.00	15.00	20.00	30.00	32.00	40.00	50.00	60.00	70.00	80.00	90.00	95.00	100.00
	$Y_.$	35.00	51.85	59.75	66.15	76.05	85.25	92.20	99.80	100.00	97.75	89.95	78.15	63.15	45.25	25.30	15.00	4.50
	Y_v			24.25	19.05	15.00	10.00	5.40	2.35									
0.50	X	0	2.03	4.06	6.09	10.16	15.23	20.31	30.47	32.50	40.44	50.37	60.29	70.22	80.15	90.07	95.04	100.00
	$Y_.$	35.00	51.85	59.75	66.15	76.05	85.25	92.20	99.80	100.00	97.75	89.95	78.15	63.15	45.25	25.30	15.00	4.50
	Y_v			24.25	19.05	15.00	10.00	5.40	2.35									
0.60	X	0	2.18	4.36	6.54	10.91	16.36	21.81	32.72	34.90	42.56	52.13	61.70	71.28	80.85	90.43	95.21	100.00
	$Y_.$	34.00	49.60	58.00	64.75	75.20	84.80	91.80	99.80	100.00	97.75	89.95	78.15	63.15	45.25	25.30	15.00	4.50
	Y_v			23.60	18.10	14.25	9.45	5.00	2.25									
0.70	X	0	2.51	5.03	7.54	12.56	18.84	25.12	37.69	40.20	47.23	56.03	64.42	73.62	82.41	91.21	95.60	100.00
	$Y_.$	30.00	42.90	52.20	59.90	71.65	82.35	90.60	99.80	100.00	97.75	89.95	78.15	63.15	45.25	25.30	15.00	4.50
	Y_v			20.50	15.45	11.95	7.70	4.10	1.75									
0.80	X	0	2.84	5.68	8.51	14.19	21.28	28.38	42.56	45.40	51.62	59.85	67.88	75.91	83.94	91.97	95.99	100.00
	$Y_.$	21.00	32.45	41.70	50.10	64.60	78.45	88.90	99.80	100.00	97.75	89.95	78.15	63.15	45.25	25.30	15.00	4.50
	Y_v			14.00	10.45	8.05	5.05	2.70	1.15									
0.90	X	0	3.06	6.11	9.17	15.28	22.92	30.56	45.65	48.90	54.91	62.42	69.94	77.46	84.97	92.49	96.24	100.00
	$Y_.$	8.30	21.10	31.50	40.90	57.45	74.70	87.45	99.70	100.00	98.65	92.75	83.00	69.35	51.85	30.80	19.40	6.85
	Y_v			4.00	2.70	2.85	1.20	0.70	0.30									
0.95	X	0	3.13	6.25	9.38	15.63	23.44	31.25	46.87	50.00	55.88	63.23	70.59	77.94	85.30	92.65	96.32	100.00
	$Y_.$	6.00	19.65	30.00	39.60	56.75	74.30	87.30	99.65	100.00	99.00	93.85	84.65	71.65	54.30	33.50	21.50	8.90
	Y_v																	

Table 4
Offsets of AUw-Type Propeller

1) ORDINATES OF X VALUE ARE GIVEN AS % OF BLADE WIDTH 2) ORDINATES OF Y VALUE ARE GIVEN AS % OF Ymax

r/R		0	2.00	4.00	6.00	10.00	15.00	20.00	30.00	32.00	40.00	50.00	60.00	70.00	80.00	90.00	95.00	100.00
0.20	X	0	2.00	4.00	6.00	10.00	15.00	20.00	30.00	32.00	40.00	50.00	60.00	70.00	80.00	90.00	95.00	100.00
	Y_o	35.00	51.85	59.75	66.15	76.05	85.25	92.20	99.80	100.00	97.80	91.10	81.25	69.35	56.60	42.00	34.20	25.55
	Y_u		24.25	19.05	15.00	10.00	5.40	2.35					2.25	5.00	10.00	15.80	19.55	
0.30	X	0	2.00	4.00	6.00	10.00	15.00	20.00	30.00	32.00	40.00	50.00	60.00	70.00	80.00	90.00	95.00	100.00
	Y_o	35.00	51.85	59.75	66.15	76.05	85.25	92.20	99.80	100.00	97.80	90.50	79.85	66.95	52.40	37.40	29.55	19.80
	Y_u		24.25	19.05	15.00	10.00	5.40	2.35					1.00	4.00	7.50	12.15	14.85	
0.40	X	0	2.00	4.00	6.00	10.00	15.00	20.00	30.00	32.00	40.00	50.00	60.00	70.00	80.00	90.00	95.00	100.00
	Y_o	35.00	51.85	59.75	66.15	76.05	85.25	92.20	99.80	100.00	97.80	90.30	78.50	63.95	47.95	31.15	22.40	12.80
	Y_u		24.25	19.05	15.00	10.00	5.40	2.35						0.25	2.30	5.75	8.05	
0.50	X	0	2.03	4.06	6.09	10.16	15.23	20.31	30.47	32.50	40.44	50.37	60.29	70.22	80.15	90.07	95.04	100.00
	Y_o	35.00	51.85	59.75	66.15	76.05	85.25	92.20	99.80	100.00	97.80	90.00	78.20	63.20	45.65	26.25	16.35	5.60
	Y_o		24.25	19.05	15.00	10.00	5.40	2.35								0.25	1.20	
0.60	X	0	2.18	4.36	6.54	10.91	16.36	21.81	32.72	34.90	42.56	52.13	61.70	71.28	80.85	90.43	95.21	100.00
	Y_o	34.00	49.69	58.00	64.75	75.20	84.80	91.80	99.80	100.00	97.75	89.95	78.15	63.15	45.00	25.30	15.00	4.50
	Y_u		23.60	18.10	14.25	9.45	5.00	2.25										
0.70	X	0	2.51	5.03	7.54	12.56	18.84	25.12	37.69	40.20	47.23	56.03	64.82	73.62	82.41	91.21	95.60	100.00
	Y_o	30.00	42.90	52.20	59.90	71.65	82.35	90.60	99.80	100.00	97.75	89.95	78.15	63.15	45.25	25.30	15.00	4.50
	Y_u		20.50	15.45	11.95	7.70	4.10	1.75										
0.80	X	0	2.84	5.68	8.51	14.19	21.28	28.38	42.56	45.40	51.82	59.85	67.88	75.91	83.94	91.97	95.99	100.00
	Y_o	21.00	32.45	41.70	50.10	64.60	78.45	88.90	99.80	100.00	97.75	89.95	78.15	63.15	45.25	25.30	15.00	4.50
	Y_c		14.00	10.45	8.05	5.05	2.70	1.15										
0.90	X	0	3.06	6.11	9.17	15.28	22.92	30.56	45.85	48.90	54.91	62.42	69.94	77.46	84.97	92.49	96.24	100.00
	Y_n	8.30	21.10	31.50	40.90	57.45	74.70	87.45	99.70	100.00	95.65	92.75	83.05	69.35	51.65	30.65	19.40	6.85
	Y_c		4.00	2.70	2.05	1.20	0.70	0.30										
0.95	X	0	3.13	6.25	9.38	15.63	23.44	31.25	46.87	50.00	55.88	63.23	70.59	77.94	85.30	92.65	96.32	100.00
	Y_s	6.00	19.65	30.00	39.60	56.75	74.30	87.30	99.65	100.00	99.00	93.85	84.65	71.65	54.30	33.50	21.50	8.09
	Y_c																	

Table 5
Reynolds Number

GROUP OF PROP	R_n 1	R_n 2	R_n 3
AU 4 – 40	5.21 · 10⁵	5.21 · 10⁺	1.00 · 10⁵
AU 4 – 55	5.21 · "	7.17 · "	1.37 ·
AU 5 – 50	4.84 · "	4.84 ·	0.93 ·
AU 5 – 65	4.84 · "	6.29 · "	1.20 ·
AU_w 6 – 50	5.60 ·	5.13 ·	0.95 · "
AU_w 6 – 75	5.60 ·	6.53 · "	1.25 ·
AU 6 – 70	5.60 ·	6.53 ·	1.25 ·
AU 7 – 65	7.02 · "	6.52 ·	1.25 ·

1    $R_n = nD^2 / \nu$ Z No. of blades

2    $R_n = nD^2 / \nu \cdot a_E Z$ a_E Expanded area ratio

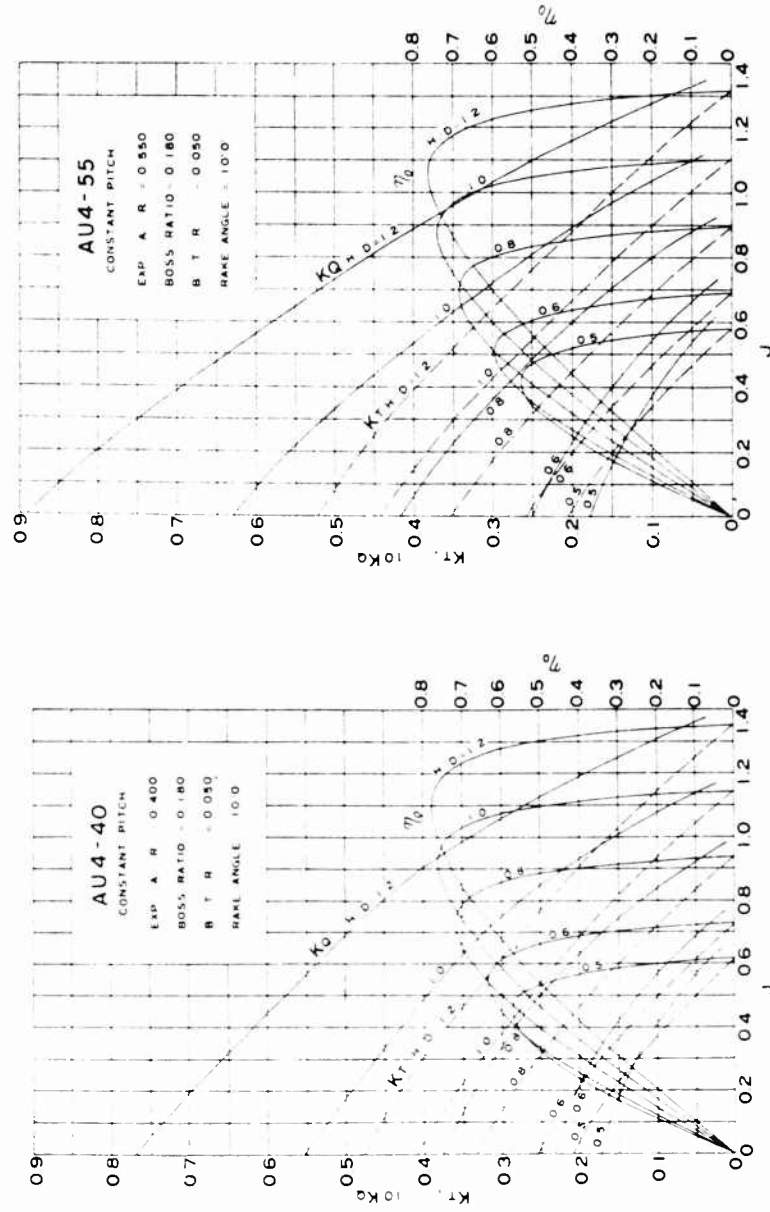3. $R_n = b_m \cdot nD^2 / L$ b_m Mean blade Width ratio

Fig. 3 – Open Test Result of AU4-55

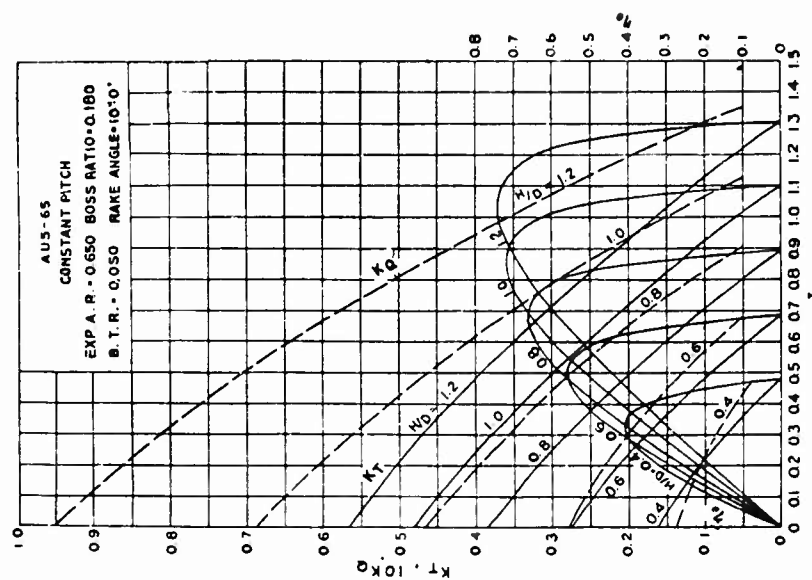Fig. 2 – Open Test Result of AU4-40
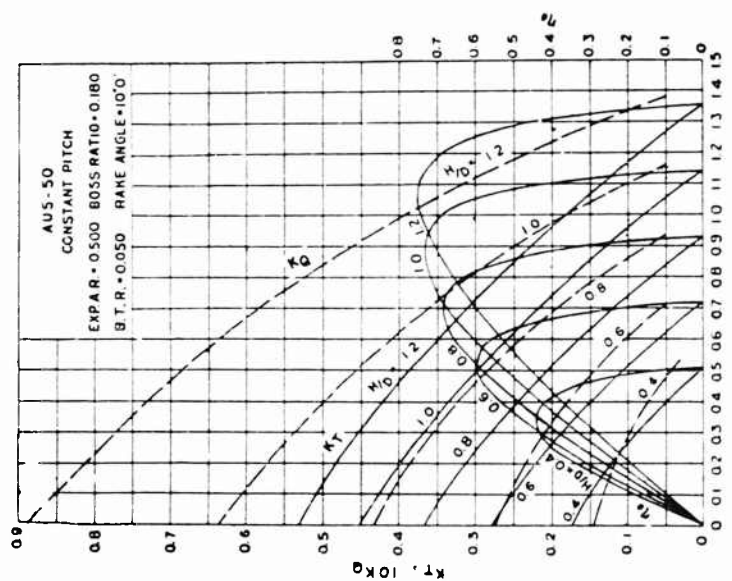
131

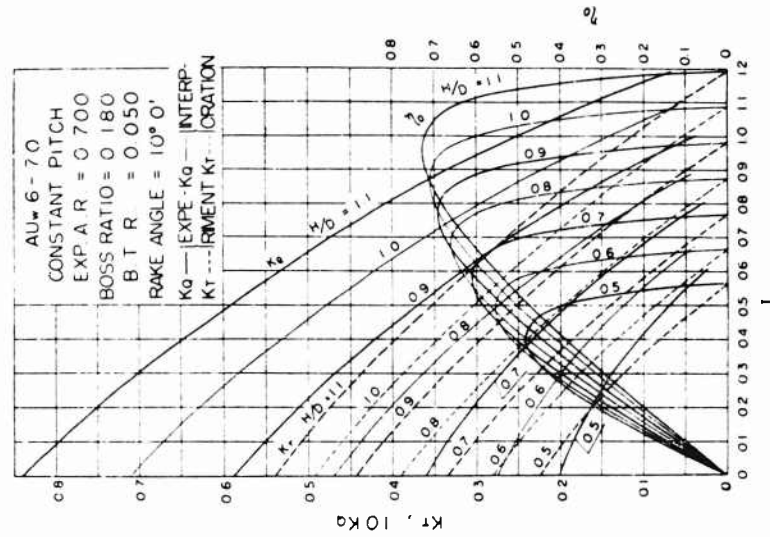Fig. 5 - Open Test Result of AU5-65

Fig. 4 - Open Test Result of AU5-50
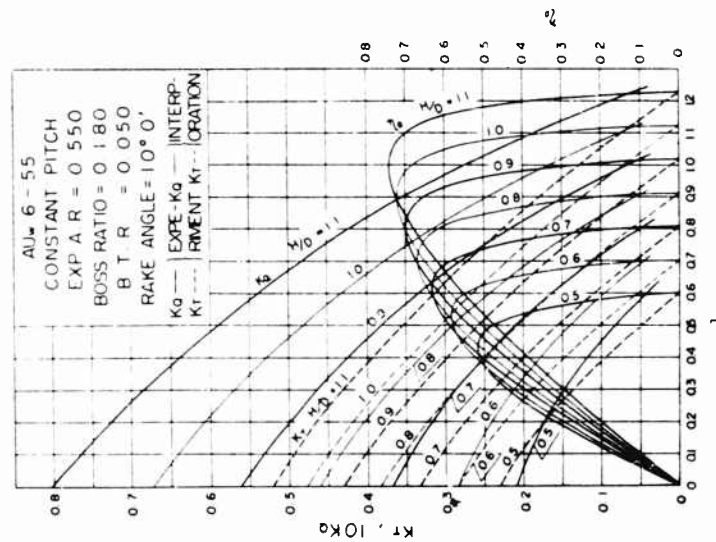
Fig. 7 – Open Test Result of AUw6-70

Fig. 6 – Open Test Result of AUw6-55

133
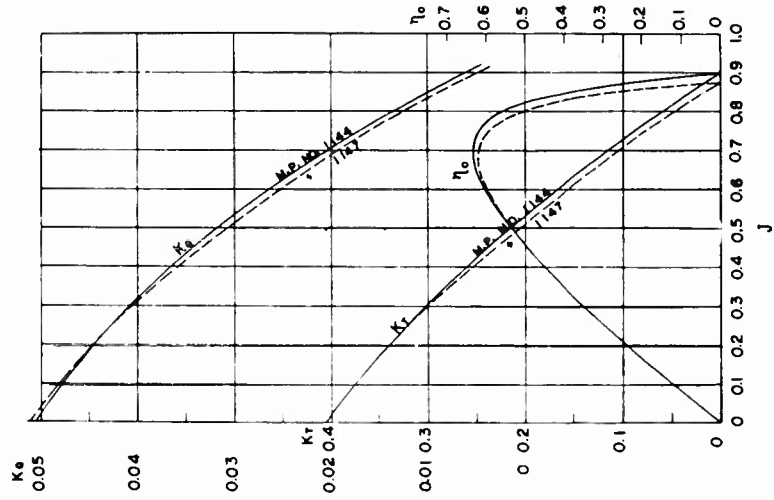
Fig. 9 - Open Test Result of
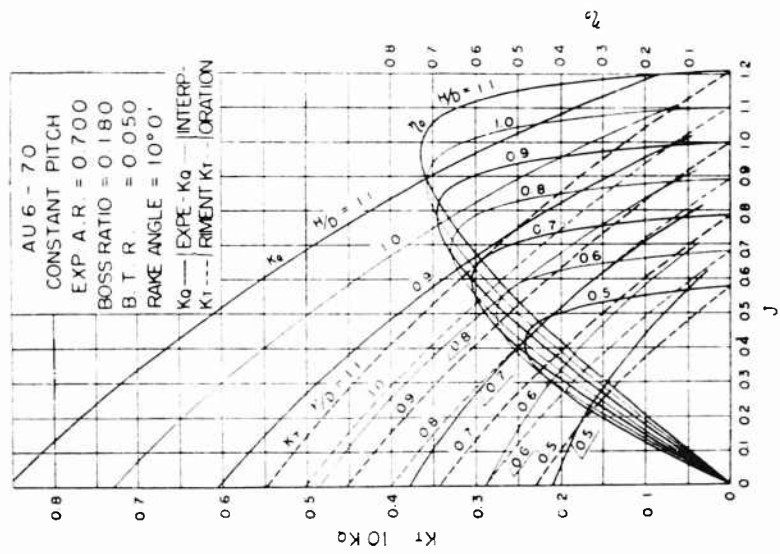Seven-bladed Propellers

Fig. 8 - Open Test Result of AU6-70

134
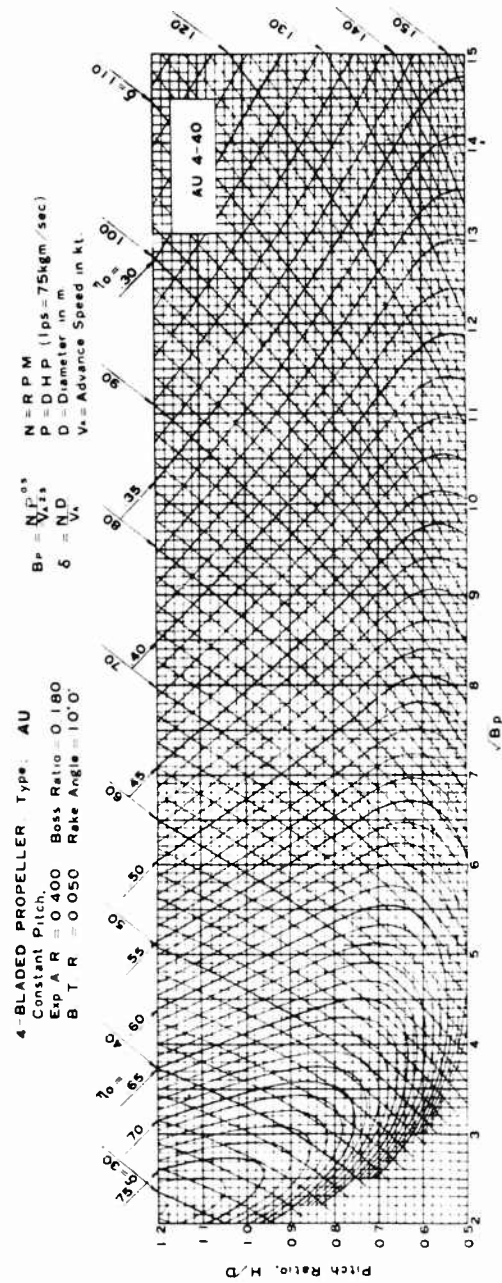
Fig. 10 - Design Diagram of AU4-40

135
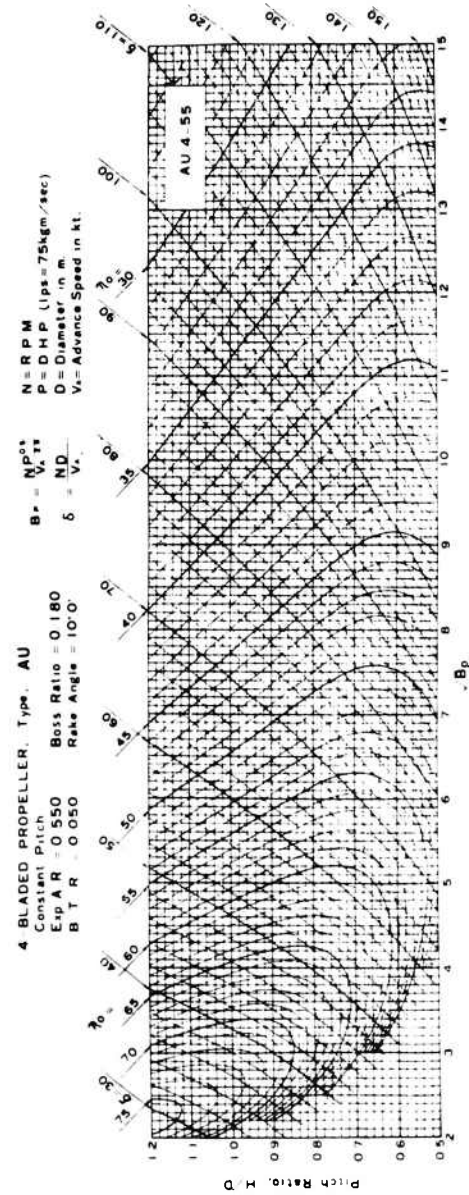
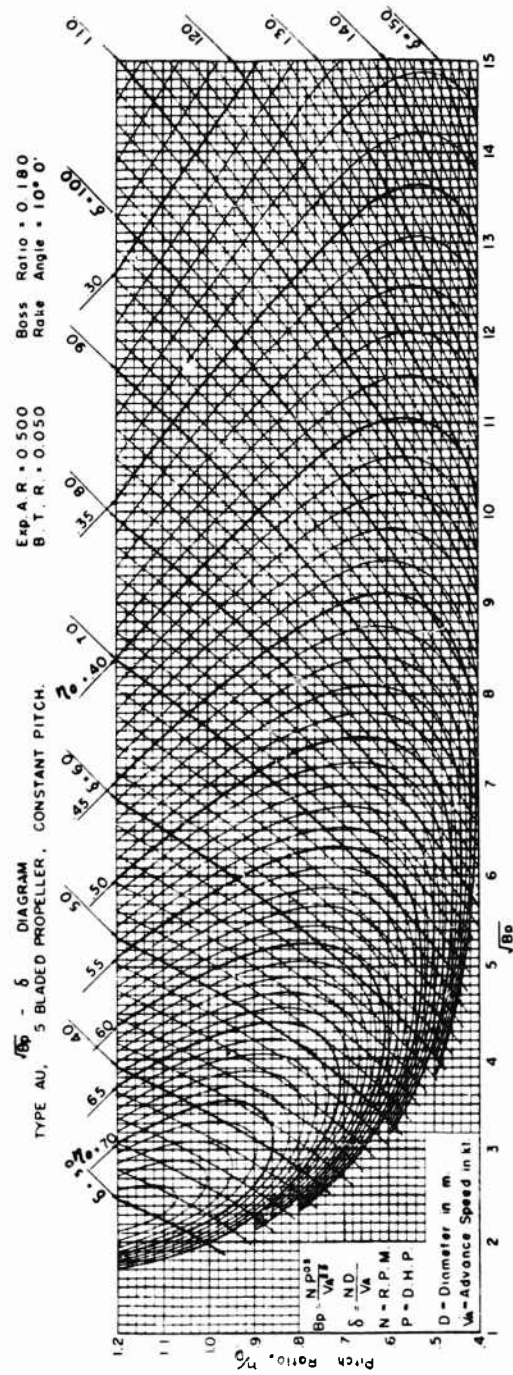Fig. 11 - Design Diagram of AU4-55

136

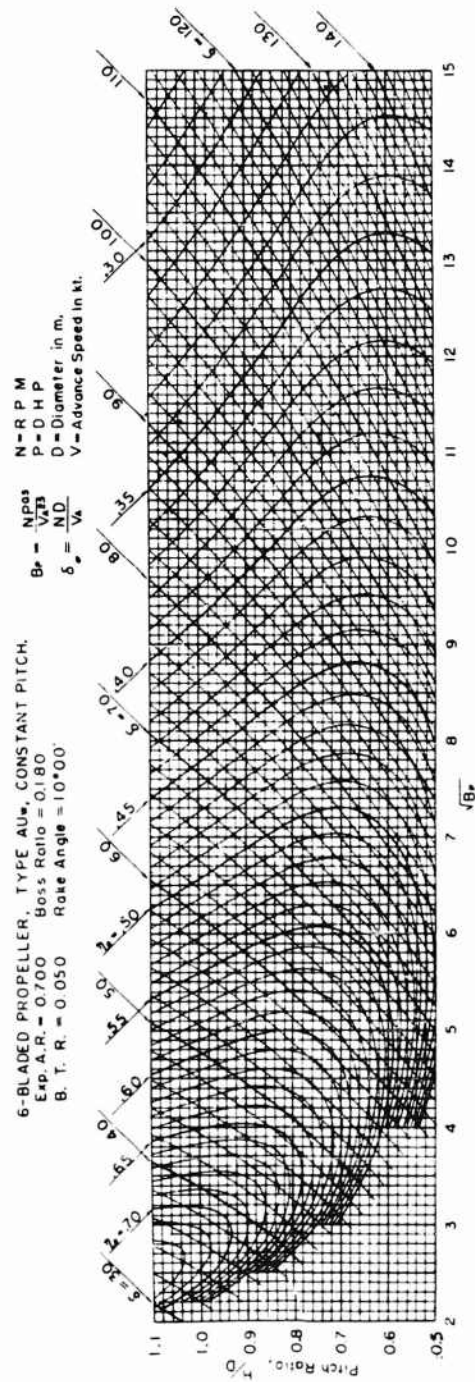Fig. 12 – Design Diagram of AU5-50
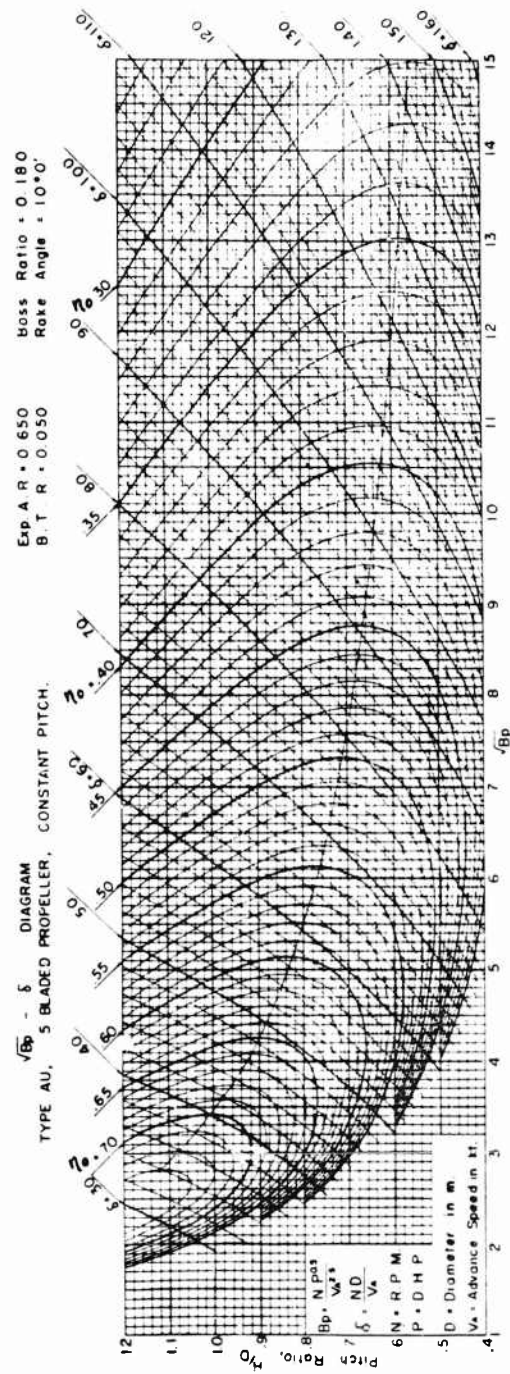
Fig. 13 - Design Diagram of AU5-65

138

Fig. 14 – Design Diagram of AUw6-55

139

6-BLADED PROPELLER, TYPE AUw, CONSTANT PITCH.
Exp. A.R. = 0.700   Boss Ratio = 0.180
B. T. R. = 0.050   Rake Angle = 10°00'

$B_P = \dfrac{N \cdot P^{0.5}}{V_A^{2.5}}$

$\delta_* = \dfrac{N \cdot D}{V_A}$

N = R P M
P = D H P
D = Diameter in m.
V = Advance Speed in kt.

Pitch Ratio, $^H/_D$

$\sqrt{B_P}$
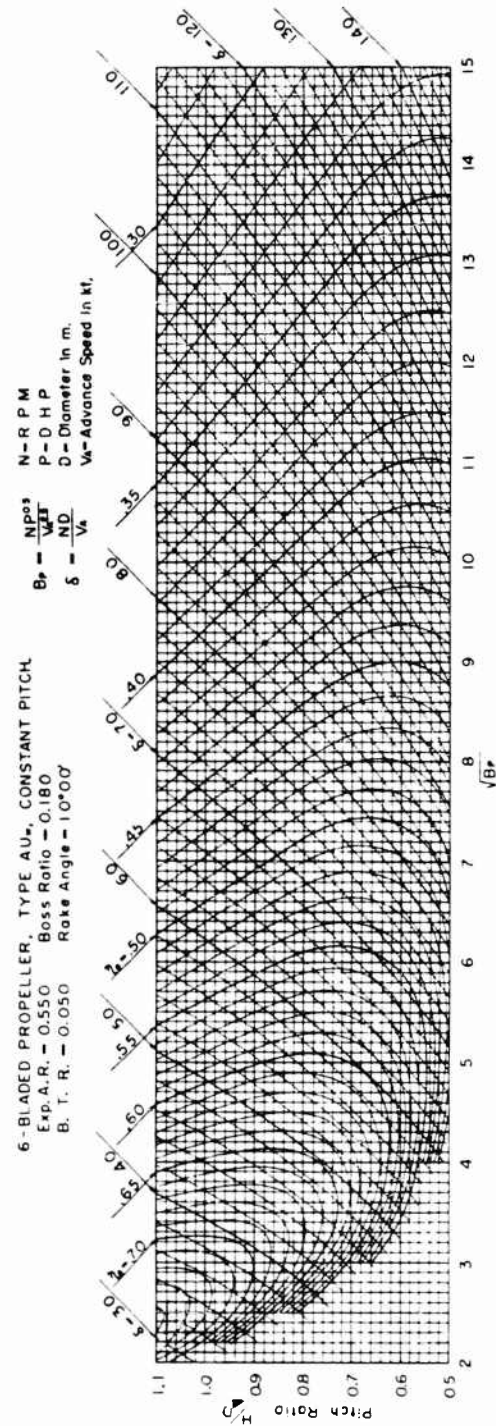
Fig. 15 – Design Diagram of AUw6-70

140
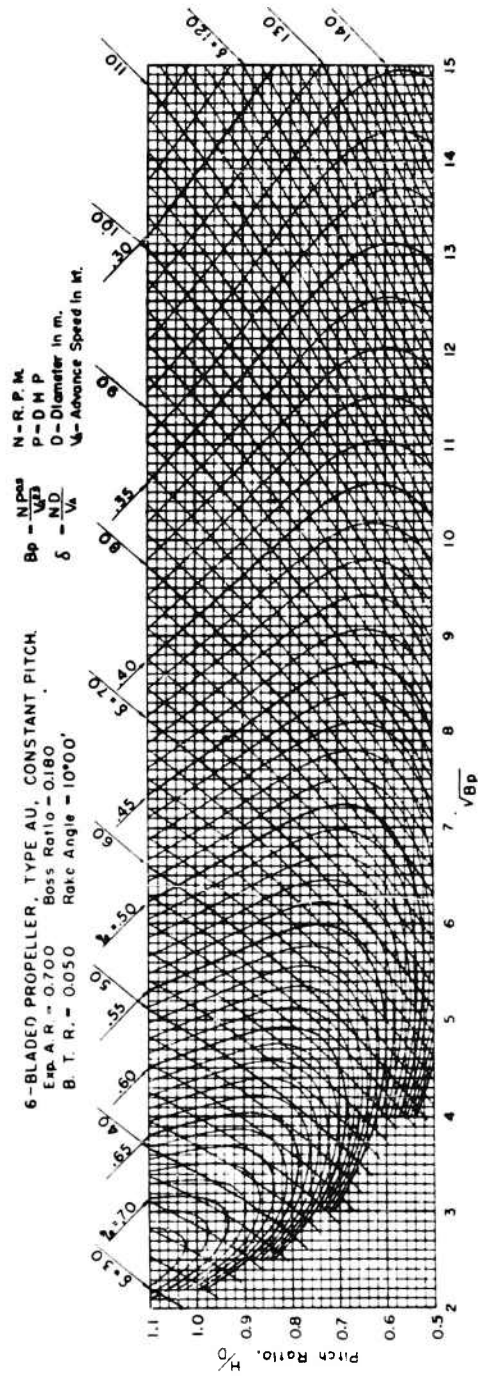
Fig. 16 – Design Diagram of AU6-70

141

7-BLADED PROPELLER, TYPE AU, CONST. PITCH

EXP. A. R. = 0.650   BOSS RATIO = 0.180

B . T. R. = 0.050   RAKE ANGLE = 10° 00'
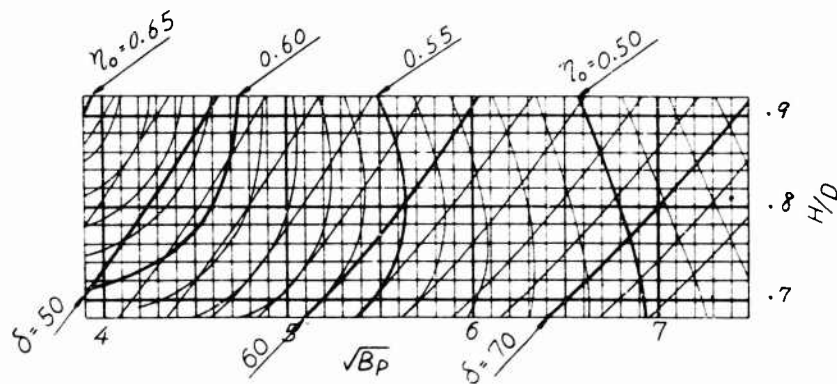
Fig. 17 - Design Diagram of 7-bladed Propeller

assumed as 104.51 kg m⁻⁴ sec². $\sqrt{Bp}$ was used instead of Bp as the abscissa in order to improve the reading accuracy.

The design diagram of seven-bladed propellers was drawn based on the results of open test of two seven-bladed model propellers shown in Table 1, and also considering the results of systematic tests of four to six-bladed propellers.

NEW TYPE DESIGN DIAGRAMS FOR EASY USE

We devised several kinds of design diagrams in which the diameter, pitch ratio, propeller efficiency, etc., can easily be read, without making complex computation, from given design conditions such as the speed, delivered horse power and propeller revolutions [7]. The typical one of those diagrams will be explained here.

This diagram consist of two sheets: one for getting the diameter of the optimum propeller and the other for the pitch ratio and propeller efficiency.

Diagrams to Obtain the Diameter of the Optimum Propeller

The relation between the power factor Bp and the diameter factor of a propeller of the best efficiency (hereinafter will be called as the optimum propeller; its diameter will briefly be called as the optimum diameter) can be shown with a practically sufficient accuracy by the following formula:

$$\zeta_o = k \left(\sqrt{Bp} \right)^2 \tag{1}$$

142

Design Diagrams of Bladed Propellers Developed in Japan

that is

$$D_o = \frac{K \dfrac{P^{a/4}}{N^{1-a/2}}}{V_A^{(5/4)a-1}} \qquad (2)$$

where P: delivered horse power; N: number of propeller revolutions per minute; V_A: the propeller speed of advance in knots.

The coefficient K and a for the formula (2) for the propeller of each group is given in Table 6. The formula (2) can be expressed in the form of a diagram with a group of straight lines by using the coefficients given in Table 6. Therefore, a

figure to get the optimum diameter can be obtained when the delivered horsepower, the number of propeller revolutions and the speed are given. This is illustrated in Figures 18 and 20 with respect to the AU type four-bladed propeller and AUw type six-bladed propeller. The order of reading is shown in Fig. 18 with dotted lines.

Table 6
Values of K and a

	k	a
A U 4 – 4 0	14. 15	0. 860
A U 4 – 5 5	14. 75	0. 864
A U 5 – 5 0	13. 97	0 872
A U 5 – 6 5	13. 80	0. 868
A U$_w$6 – 5 5	13. 85	0. 876
A U$_w$6 – 7 0	14. 32	0. 852
A U 6 – 7 0	14. 32	0. 852

Diagrams to Obtain the Pitch Ratio and Propeller Efficiency

The pitch ratio H/D_o and efficiency $_o$ of the optimum propeller can be shown by one curve (the line of $D = 0$ in Figs. 19 and 21) respectively against the $_o$; therefore they can easily be obtained if the diameter, namely, $_o$, is determined.

Actually, however, there are many cases when the optimum diameter can not be adopted because of the stern arrangement and other factors. On such cases, therefore, it is necessary to provide a figure to get the pitch ratio and propeller efficiency. When the rate of change in the diameter from the optimum one, that is D, is definite, the pitch ratio and propeller efficiency are respectively represented by fixed curves for the $_o$ as in the case of the optimum propeller; therefore such curves should be provided for the possible range of D. As example, diagrams for the four and six-bladed propellers are given in Figs. 19 and 21.

SUPPLEMENTARY TESTS AND SOME CONSIDERATIONS

Various tests were conducted to prepare the supplementary data to design the propeller effectively using these design diagrams. Some results obtained from these tests are stated as follows:

Effect of the number of blades

Generally speaking, the optimum diameter decreases with the increase in the number of blades under a certain power factor. However, propeller efficiency
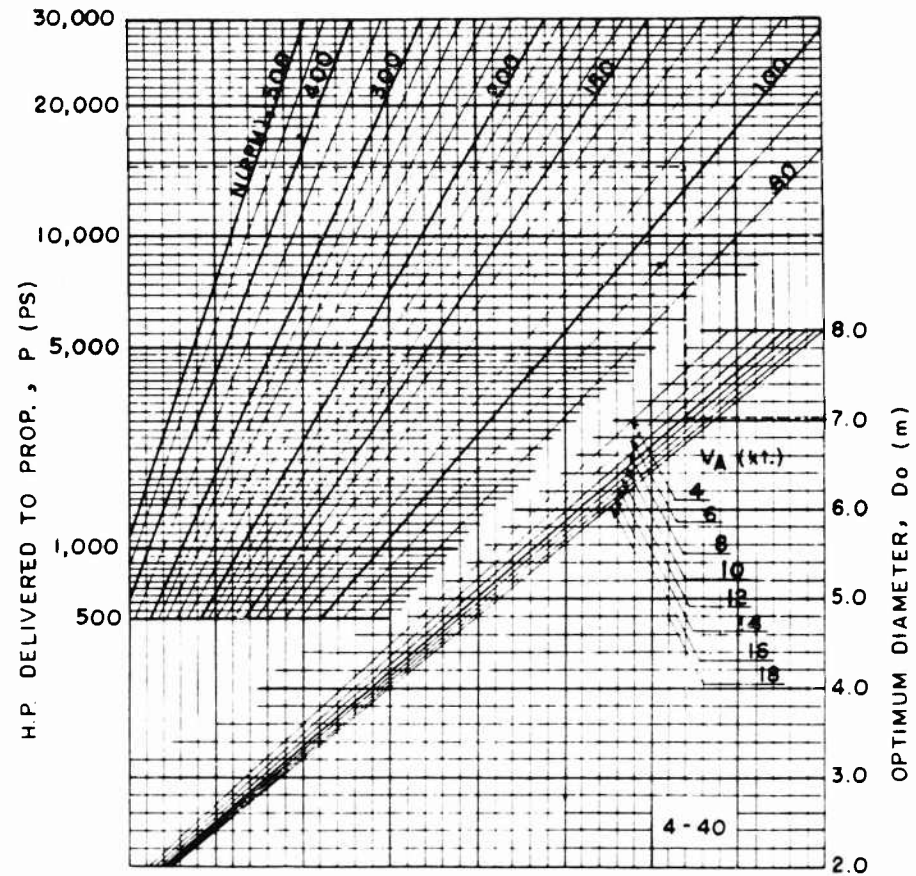
143

Fig. 18 - Diagram of AU4-40

does not necessarily decrease even if the number of blades increases. In case the number of blades has been changed, for instance, under a fixed expanded area ratio, the propeller efficiency will be the highest when the number of blades is such that the thickness-cordlength ratio of the 0.7 R blade section (R represents the radius of the propeller) represents the optimum value (about 6.5% in case of the AU type propeller and about 7% in case of the AUw type). Also, the cascade effect of blades is hardly recognized in the range of ordinary area ratio in the case of propellers up to six-bladed ones, but such effect becomes considerable in seven-bladed propellers. Therefore, depending upon the blade area needed for a propeller, the optimum diameter can be reduced and at the same time the propeller efficiency can be expected to increase by increasing the number of blades and choosing an appropriate value of thickness-cordlength ratio of the 0.7 R blade section. Therefore, also from the stand point of propeller efficiency, the six-bladed propellers can be used practically.

144

Design Diagrams of Bladed Propellers Developed in Japan

$$\delta_0 = \frac{N D_0}{V_A}$$
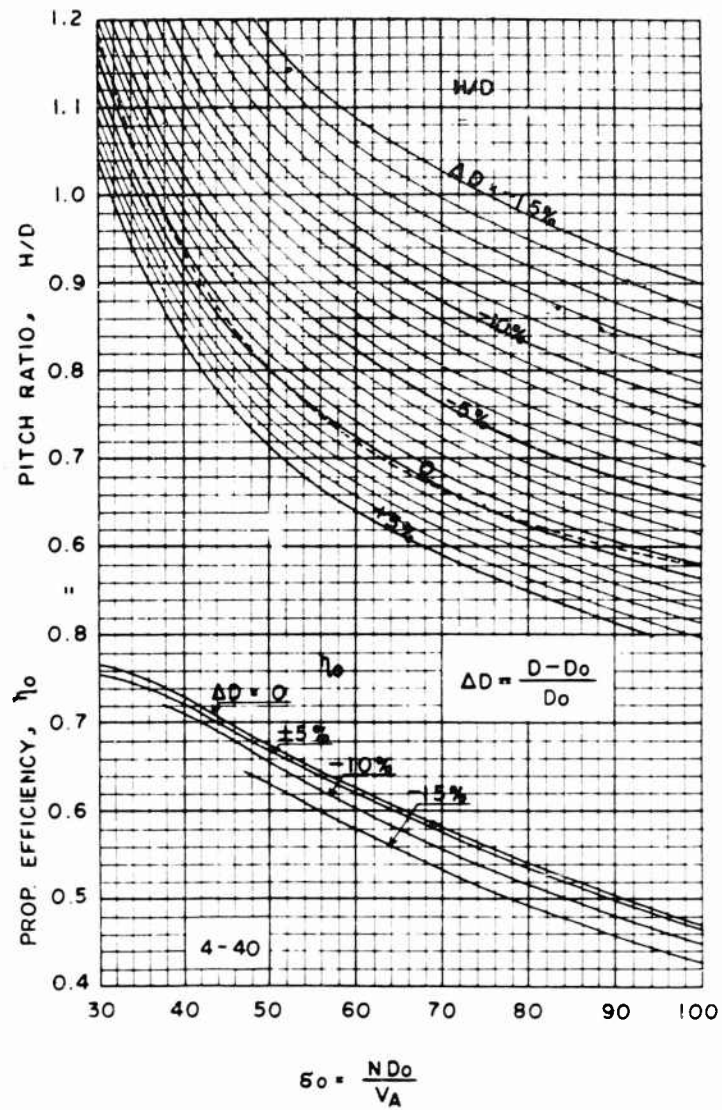
Fig. 19 - Diagram of AU4-40
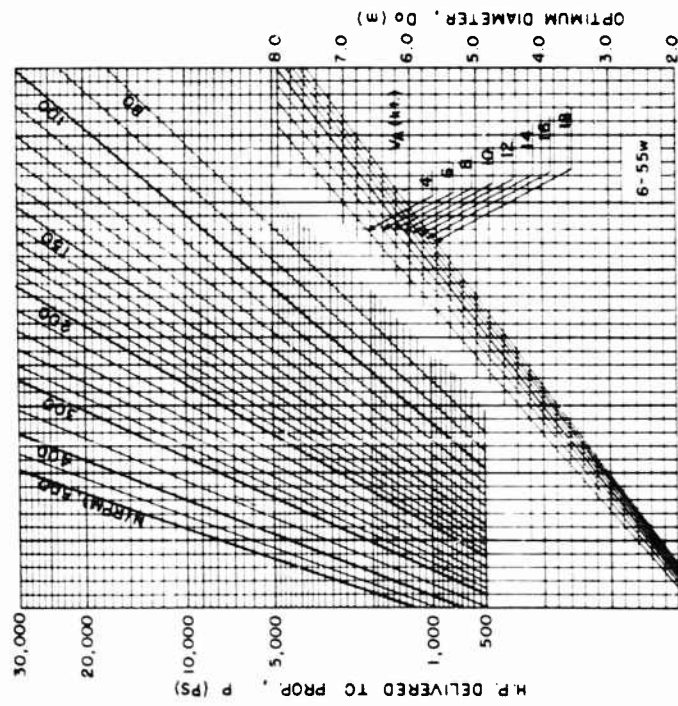
145

Yazaki

Fig. 21 - Diagram of AUw6-55

Fig. 20 - Diagram of AUw6-55

Needless to say, the choice of the number of blades must be done not only from the consideration of efficiency but also from the stand point of eliminating the vibration due to the propeller.

Effect of the Blade Area

In the case of propellers with the same number of blades, the value of the optimum diameter under a certain power factor generally beccmes smaller almost linearly with the increase in the blade area.

In designing a propeller with a given area ratio, it is often necessary to interpolate or extrapolate the value of propeller efficiency read from design diagrams for different area ratio. However, as design diagrams are drawn based on the results of the parent propeller with a fixed blade thickness ratio, linear interpolation and extrapolation by area ratio will bring rather approximate results. This is because a change of the expanded area of a propeller with a fixed blade thickness ratio will be accompanied by a change in the thickness-cordlength ratio of the blade section. Besides an excessively small expanded area ratio and also an excessively large one will reduce propeller efficiency; accordingly special attention must be paid in extrapolating the value of the efficiency against the area ratio.

Relations between the area ratio and the propeller efficiency of the propeller with a fixed blade thickness ratio are diagramed in Fig. 22 in the case of the four-bladed propellers.

Effect of the Boss Ratio

Propellers actually designed often have different boss ratios from the parent propellers given in design diagrams. When the boss ratio becomes larger, the thrust coefficient, torque coefficient and the propeller efficiency at the same slip ratio become lower. For the AU and AUw type propellers, propeller characteristics modification diagrams for the boss ratio were made.

The aforesaid diagrams are intended to estimate propeller characteristics for the case where only the boss ratio of the parent propeller is changed as shown in Fig. 23. These diagrams consist of two sheets: one giving the thrust modification coefficient Y_T and the other giving the torque modification coefficient Y_Q. The former is shown in Fig. 24 and the latter in Fig. 25. In these diagrams, s represents the slip ratio, and X_M, which is determined by the following formula, indicates an average boss ratic of two propellers:

$$X_M = \frac{1}{2}(X_0 - X_1)$$

where X_0: boss ratio of a parent propeller (equal to 0.180); X_1: value of a given boss ratio. The thrust coefficient, torque coefficient and propeller efficiency of a propeller with a boss ratio of X_1 as shown in Fig. 23 can be estimated from the characteristics of the parent propeller by the following formulas:
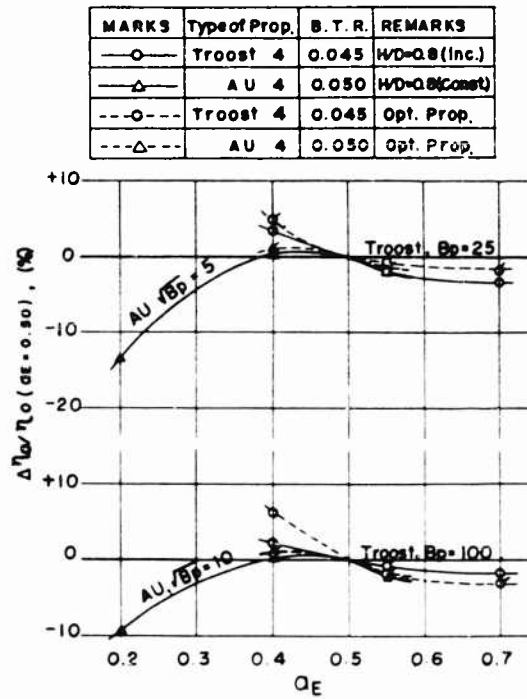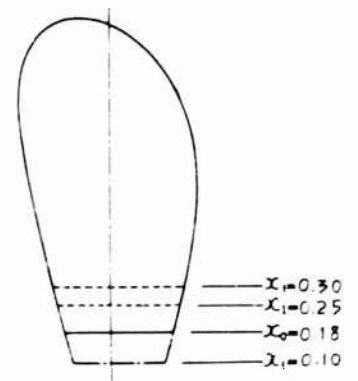
147

MARKS	Type of Prop.	B.T.R.	REMARKS
——o——	Troost 4	0.045	H/D=0.8(Inc.)
——△——	A U 4	0.050	H/D=0.8(Const)
---o---	Troost 4	0.045	Opt. Prop.
---△---	AU 4	0.050	Opt. Prop.

Fig. 22 - Effect of blade area ratio

Fig. 23 - Typical change of boss ratio

148

Design Diagrams of Bladed Propellers Developed in Japan

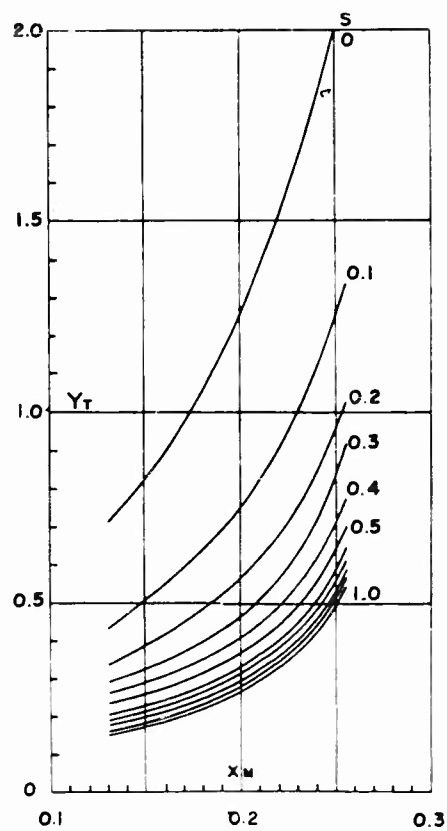

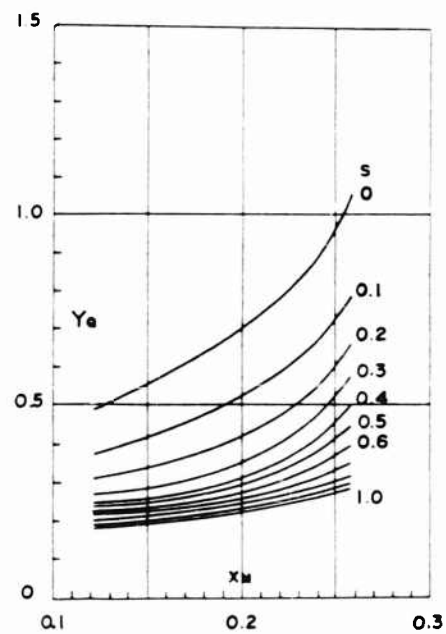Fig. 24 - Thrust Modification
Coefficient

Fig. 25 - Torque Modification
Coefficient

Yazaki

$$\frac{\triangle K_T}{K_T} = -Y_T \ (X_1 - X_0) \tag{3}$$

$$\frac{\triangle K_Q}{K_Q} = -Y_Q \ (X_1 - X_0) \tag{4}$$

$$\frac{\triangle \eta_o}{\eta_o} = \frac{\triangle K_T}{K_T} - \frac{\triangle K_Q}{K_Q} \tag{5}$$

where K_T, K_Q and η_o show the thrust coefficient, torque coefficient and propeller efficiency of the parent propeller respectively; $\triangle K_T$, $\triangle K_Q$ and $\triangle \eta_o$ being the modification of each; and Y_T and Y_Q show the values of modification coefficients read from Figs. 24 and 25 respectively.

Figures 24 and 25 were made with the value of X_0 fixed at 0.180; however, they can be considered to be applicable to the estimation of propeller characteristics of any boss ratio on the basis of a certain propeller with a different value of X_0.

In designing a propeller, it is of course necessary to try to get the propeller which gives the best propulsive efficiency behind a certain ship besides to improve its efficiency in open condition. More research works on these problems are now under study in our Institute utilizing the self-propulsion tests, behind tests, etc.

REFERENCES

1. Kan, S. and Umesawa, H., "Open Water Tests With Four-bladed Propeller Models" Journ. of Zosen-Kiokai, 1940

2. Tsuchida, K., "Open Water Tests With Wide Four-bladed Propeller Models", Report of Senpaku-Shikensho, 1944

3. Tsuchida, K., "Open Water Tests With Three-bladed Propeller Models", Journ. of Zosen-Kiokai, 1948

4. Yazaki, A., "The Design of AU-type Ship Screw Propellers", Report of T.T.R.I., Vol. 11, No. 7, 1961

5. Yazaki, A., "Open Water Tests of AU-Series Propeller Models (Varying Number of Blades From 4 to 7)", Journ. of Zosen-Kiokai, 1958

6. Takahashi, H., "A Prevention From Face Cavitation by Varying The Form of Blade Section of A Screw Propellers", English Report of T.T.R.I., No. 38, 1959

7. Kan, S. and Kuramochi, E., "Propeller Design Diagrams for Easy Use", Report of T.T.R.I. Vol. 5, No. 1, 1954

150

THEORY OF THE ANNULAR AIRFOIL
AND DUCTED PROPELLER

Wm. B. Morgan
David Taylor Model Basin
Washington 7, D. C.

ABSTRACT

A theory of the annular airfoil and ducted propeller is presented which is based on a linearized annular airfoil theory and a lifting-line propeller theory. Both the direct and inverse problem of the annular airfoil is treated, i.e., for a given airfoil shape the pressure distribution is determined and for a given pressure distribution the airfoil shape is determined. The problem of the annular airfoil of arbitrary shape is also discussed, as well as an approximation to the nonlinear theory. As with propeller theory an explicit solution cannot be obtained for the ducted propeller problem so a process of iteration is used.

I. INTRODUCTION

A recent interest has been shown both in aeronautics and in naval architecture for the application of ducted propellers. This application in aeronautics is mainly for hovering flight and vertical take-off while in naval architecture, it is for delaying cavitation and for increasing the efficiency of heavily loaded propellers. The interest in those systems has led to various experimental and theoretical investigations.

A number of experimental studies are available for ducted systems but because of the large number of variables to be investigated, these results are not very comprehensive for ducts in general. However, one systematic study worth noting for "Kort nozzle" systems is that done by van Manen at the Netherlands Ship Model Basin [1-4]. The theoretical approaches have not yet proved useful for design purposes, although some of the more recent work [5,6] undoubtedly will. A general review of the state of the art of ducted propellers, which considers both experimental and theoretical studies, has been given by Sacks and Burrill [7]. Because of this work, the historical development of ducted systems will not be discussed here nor will many of the pertinent references be cited.

151

The work presented in the present paper is essentially a recapitulation and extension of the study in Ref. 6. In this reference the duct shape was assumed known and the flow field around the duct was determined. One problem not considered previously but considered here will be the inverse problem: i.e., given a pressure distribution determine the duct shape.

The ducted system is assumed to consist of an annular airfoil of finite length with an internally operating propeller with a finite number of blades. It is assumed that the nozzle flow field can be represented by a linearized theory and the propeller by lifting line theory. The following assumptions are made about the fluid and the flow field.

1.   The fluid is inviscid and incompressible and no separation occurs on the duct.

2.   Body forces such as gravity are neglected.

3.   The free-stream flow is axisymmetric and steady with respect to a co-ordinate system attached to the propeller.

4.   The annular airfoil is, in general, axisymmetric and of finite length.

5.   The thickness and camber of the annular airfoil are small which implies that a linearized theory can be used.

6.   The linearized flow around the annular airfoil can be represented mathematically by a distribution of ring vortices and ring sources along a cylinder of constant diameter.

7.   The trailing vortex system of the duct has the constant diameter of the duct and extends from the duct to infinity.

8.   The influence of all induced velocities on the shape of the trailing vortex system of the duct is neglected.

9.   The propeller flow field can be represented by a lifting line and heli-coidal trailing vortices. Each trailing vortex line lies on a cylinder of constant diameter and is of constant pitch.

A general discussion of the annular airfoil will be given first and then the propeller and its effects will be considered. Both the direct and inverse problem of the annular airfoil will be presented and the optimum pitch distribution will be derived for the propeller in the duct under certain restricted conditions.

II.   LINEARIZED THEORY OF THE ANNULAR AIRFOIL

The method of singularities will be used here for representation of the flow field about the annular airfoil. The mathematical model used will be a distribution of ring vortices and ring sources laying on a cylinder of a diameter representative of the diameter of the duct and of length equal to the chord of the duct. This approach was first used by Dickmann [8] who considered only a distribution

152

of ring vortices; thus thickness effects were neglected. Weissinger [9,10] has extended this approach to include thickness and also considered ducts of arbitrary shape and at an angle of attack.

In the method of singularities a solution is formed from a summing of the velocities induced by individual singularities, ring vortices and sources for the annular airfoil. The resulting equation is usually a singular integral equation which must be solved for the strengths of the different singularities.

II.1 Linearized Boundary Conditions
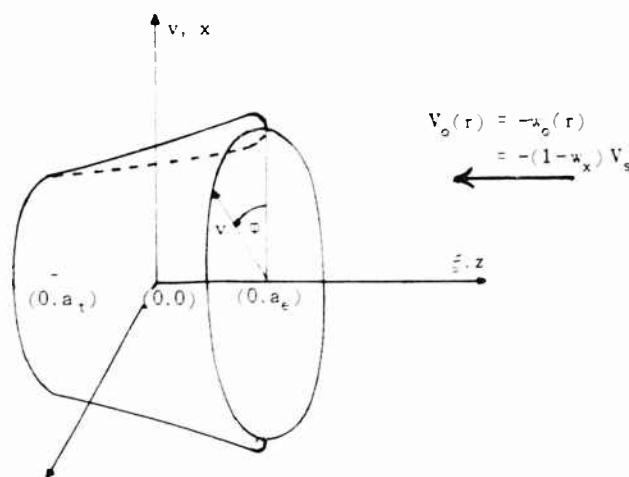
Fig. 1 - The annular airfoil coordinate system

The coordinate system used is a cylindrical system (r, z, φ) with the zero of the axial coordinate (ς) located on the propeller axis at the plane of the propeller, and the reference radius (R_d) taken as the duct radius at the propeller. In the presence of the propeller, the coordinate system is assumed to be rotating with the propeller. For convenience the axial coordinate will be assumed to be nondimensionalized by the annular airfoil chord (a) and the radial coordinate by the propeller radius (R_p), i.e.,

$$z = \frac{\text{axial coordinate}}{\text{duct chord}} = \frac{\varsigma}{a} \ .$$

$$x = \frac{\text{radial coordinate}}{\text{propeller radius}} = \frac{r}{R_p} \ . \tag{2.1-1}$$

$$x_d = \frac{\text{duct radius}}{\text{propeller radius}} = \frac{R_d}{R_p} \ .$$

The free-stream velocity is from right to left and for convenience for the naval architect the wake fraction

153

$$\left(1 - w_x = \frac{w_o(x)}{V_s}\right)$$

is introduced. The use of this term implies that the velocity may have a radial variation but in the present investigation must be axisymmetric. If a radial variation is present, the representative velocity will be taken as the ship speed, V_s, and if not, the representative velocity will be taken as the free-stream velocity, w_o. In the latter case the wake fraction is unity, i.e., $(1 - w_x) = 1$.

The annular airfoil section is assumed known and will be delineated, as shown in the following diagram, into a thickness distribution, a camber distribution and an angle of attack.
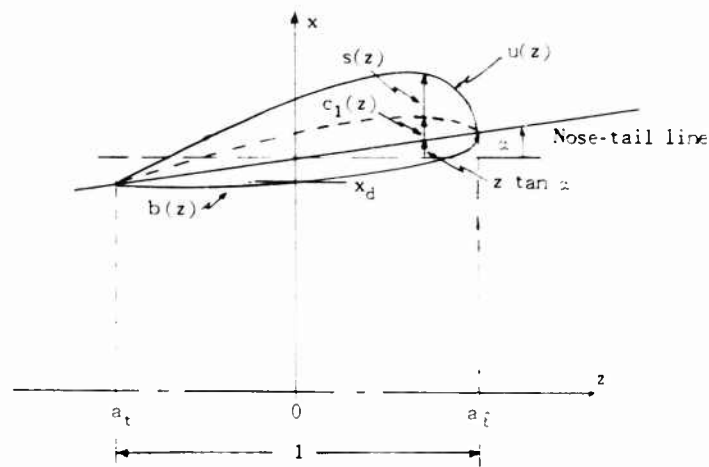
Fig. 2 - Delineation of the annular airfoil section

In terms of the upper and lower surface, $u(z)$ and $b(z)$, of the foil and as measured from the x-axis the camber line ordinate $c_1(z)$ and angle of attack (α) are

$$c_1(z) + z \tan \alpha = c_1(o) - s(o) - x_d + \frac{1}{2} [u(z) - b(z)] \qquad (2.1-2)$$

and the half-thickness ordinate $s(z)$ is

$$s(z) = \frac{1}{2} [u(z) - b(z)] . \qquad (2.1-3)$$

The boundary conditions which must be satisfied on the annular airfoil are, first, that on the surface the normal velocity must be zero and second, at the

154

trailing edge the Kutta condition is satisfied. As shown in Ref. 6, the first linearized boundary condition is

$$\frac{w_r}{V_s} (x_d \pm 0, \varphi, z) = -\left(1 - w_{x_d}\right) \left[c_1'(z) + \tan \alpha \pm s'(z)\right], \quad a_t \le z \le a_\ell \quad (2.1-4)$$

and the second

$$\frac{w_r}{V_s} (x_d \pm 0, \varphi, a_t) = 0 . \tag{2.1-5}$$

Equation (2.1-4) implies that the ratio (w_r/w_0) at the reference radius must be equal to the annular airfoil slope and Eq. (2.1-5) implies that at the trailing edge the radial velocity is zero. The boundary conditions are satisfied on the surface of a cylinder of diameter x_d and chord a $(a = 1)$ and the "plus" sign refers to the outside of the cylinder and the "negative" sign refers to the inside of the cylinder.

II.2 Derivation of the Vortex and Source Distribution to Represent the Annular Airfoil at Zero Incidence

Using the boundary conditions just derived, the strength of the ring vortex and source distributions are determined. The nondimensional elementary strength of the ring vortices will be taken as $\gamma(\varphi, z)$ and of the ring sources as $q(\varphi, z)$. If a propeller is in the duct, or the duct is at an angle of incidence, the ring vortex strength is dependent on the angular position around the duct and a trailing vortex system exists behind the duct. This system has a strength of $(1 \ x_d) (\partial \gamma/\partial z)$ and the induced velocities from this system must be added to that of the ring vortices and sources. Since the velocities are linear, all the velocities are added and the first boundary condition on the duct is expressed by the following equation:

$$\left[\frac{w_r}{V_s} (x_d, \varphi, z)\right]_\gamma + \left[\frac{w_r}{V_s} (x_d \pm 0, \varphi, z)\right]_\sigma - \left[\frac{w_s}{V_s} (x_d, \varphi, z)\right] - \frac{\partial \gamma}{\partial z}$$

$$+ \left[\frac{w_r}{V_s} (x_d, \varphi, z)\right]_p = -\left(1 - w_{x_d}\right) \left[c_1'(z) - \tan \alpha \pm s'(z)\right] \tag{2.2-1}$$

where

$\left[w_r(x_d, \varphi, z)\right]_\gamma$ is the radial velocity induced on the duct by the ring vortex system,

$\left[w_r(x_d, \varphi, z)\right]_q$ is the radial velocity induced on the duct by the ring source system,

155

$w_r(x_d, \varsigma, z)_{\frac{\partial \gamma}{\partial \varsigma}}$ is the radial velocity induced on the duct by the trailing vortex system,

$w_r(x_d, \varsigma, z)_{r}$ is the radial velocity induced on the duct by the propeller or by any other singularities in the flow.

The radial velocities induced by the ring vortex on the cylinder are given in Ref. 6 as:

$$\left[\frac{w_r}{V_s}(x_d, \varsigma, \bar{z}) \right]_\gamma = \frac{h}{2\pi} \int_0^1 \int_0^{2\pi} \frac{2h(\bar{z} - z')\cos(\varsigma - \varsigma')\gamma(\varsigma', z')\,d\varsigma'dz'}{\left[4h^2(\bar{z} - z')^2 - 4\sin^2\frac{1}{2}(\varsigma - \varsigma') \right]^{3/2}} \quad (2.2-2)$$

and for the ring source as

$$\left[\frac{w_r}{V_s}(x_d, \varsigma, \bar{z}) \right]_q = \frac{h}{2\pi} \int_0^1 \int_0^{2\pi} \frac{[1 - \cos(\varsigma - \varsigma')]\, q(\varsigma', z')\,d\varsigma'dz'}{\left[4h^2(\bar{z} - z')^2 - 4\sin^2\frac{1}{2}(\varsigma - \varsigma') \right]^{3/2}} = \frac{1}{2}\, q(\varsigma, \bar{z}). \quad (2.2-3)$$

where

$$\bar{z} = z - a_\varsigma.$$

$$h = \frac{a}{2R_d}.$$

If these radial velocities and $(w_r)_{\frac{\partial \gamma}{\partial \varsigma}}$ and w_{r_p} are substituted into the boundary condition (2.2-1), an equation is obtained for the vortex and source strength. From this substitution it can be concluded that the source-sink strength must be a function of the thickness slope only, i.e.,

$$q(\varsigma, \bar{z}) = -2\left(1 - w_{x_2} \right) s'(\bar{z}). \quad (2.2-4)$$

which implies, at least for the axisymmetric duct, that within the linearized theory the source strength is independent of angle. With this information on the source distribution and Eq. (2.8-12), the vortex distribution is given by an integro-differential equation

$$\frac{h}{2\pi} \int_0^1 \int_0^{2\pi} \frac{2h(\bar{z} - z')\cos(\varsigma - \varsigma')\gamma(\varsigma, z)\,d\varsigma\,dz}{\left[4h^2(\bar{z} - z')^2 - 4\sin^2\frac{1}{2}(\varsigma - \varsigma') \right]^{3/2}} - \left[\frac{w_2}{V_s} \right]_{x_d, \varsigma, \bar{z}}^{\frac{\partial \gamma}{\partial \varsigma}}$$

$$= -\left(1 - w_{x_2} \right)\left\{ \left[c_1'(\bar{z}) + \tan \alpha \right] - \frac{h}{\pi} \int_{-1}^1 s(z)\, k\, [K(k) - E(k)]\,dz \right\} - \left[\frac{w_2}{V_s} \right]_{x_d, \varsigma, \bar{z}}^{p}$$

$$\quad (2.2-5)$$

where
$$k^2 = \frac{1}{h^2(\bar{z} - z')^2 - 1}.$$

156

$$K(k) = \int_0^{\pi/2} \frac{d\theta}{\sqrt{1 - k^2 \sin^2 \theta}} \qquad \text{complete elliptic integral of the first kind,}$$

$$E(k) \int_0^{\pi/2} \sqrt{1 - k^2 \sin^2 \theta}\; d\theta \qquad \text{complete elliptic integral of the second kind.}$$

From Eqs. (2.2-4) and (2.2-5), it can be seen that the ring source strength is a function of thickness only and that the ring vortex strength is a function of both thickness and camber as well as the radial velocities of any other singularities in the flow field. These equations will now be examined for certain special cases.

II.3 The Integral Equation and Its Reduction for an Axisymmetric Annular Airfoil

For the axisymmetric annular airfoil by itself at zero angle of attack, the vortex strength (γ) is not a function of the polar angle (z') so the integration with respect to (z') can be carried out in Eq. (2.2-5), and also, there are no trailing vortices. For this particular case Eq. (2.2-5) reduces [6] to

$$\oint_0^1 g(\bar{z} - z') \frac{\gamma(z')}{(\bar{z} - z')}\, dz' = H(\bar{z}). \tag{2.3-1}$$

where

$$g(\bar{z} - z') = k \left\{ 4h^2(\bar{z} - z')^2 [K(k) - E(k)] - 2E(k) \right\}. \tag{2.3-2}$$

$$H(\bar{z}) = 4\left(1 - w_{x_d}\right)\left\{ -\left[c_1'(\bar{z}) - \tan z\right] - h \int_0^1 s'(z') k [K(k) - E(k)]\, dz' \right\}. \tag{2.3-3}$$

Equation (2.3-1) is a singular integral equation for the unknown vortex distribution $\gamma(z')$ in terms of the slope of the camber and thickness distribution. By a method proposed by Muskhelishvili [11] this equation can be reduced to a Fredholm equation of the second kind for the vortex distribution. The term $g(z' - z') = g(0)$ is added to and subtracted from the kernel in Eq. (2.3-1). Since $g(z' - z') = 2$, Eq. (2.3-1) becomes

$$\int_0^1 \frac{\gamma(z')}{(\bar{z} - z')}\, dz' = \frac{1}{2}\int_0^1 [2 - g(\bar{z} - z')] \frac{\gamma(z')}{(\bar{z} - z')}\, dz' - \frac{1}{2} H(\bar{z}) = f_0(z). \tag{2.3-4}$$

The integrand of the integral on the right side is not singular at the point $\bar{z} = z'$ but has an indeterminate form which can be shown to be zero. This equation is in the form of the well-known Cauchy type singular integral equation [11] and has a unique inverse given by

157

$$\gamma(\bar z) = \frac{1}{\pi \sqrt{\bar z(1-\bar z)}} \left[\frac{1}{\pi} \oint_0^1 \frac{\sqrt{z'(1-z')}}{(z'-\bar z)} f_0(z') \, dz' + 2 \int_0^1 \gamma(z') \, dz' \right]. \qquad (2.3\text{-}5)$$

The second boundary condition, the Kutta condition Eq. (2.1-5), implies that the circulation at the trailing edge, $\gamma(0)$, must be zero. The last term in the preceding equation is a constant and it is chosen so that at $\bar z = 0$, $\gamma(0) = 0$. Substituting for $f_0(z)$ in Eq. (2.3-5) and choosing the constant as just described, a Fredholm equation of the second kind is obtained for the vortex strength.

$$\gamma(\bar z) = -\frac{1}{2\pi^2} \sqrt{\frac{\bar z}{1-\bar z}} \int_0^1 \sqrt{\frac{(1-z')}{z'}} \frac{H(z')}{(z'-\bar z)} \, dz'$$

$$+ \frac{1}{2\pi^2} \sqrt{\frac{\bar z}{(1-\bar z)}} \int_0^1 \left[\oint_0^1 \sqrt{\frac{1-z''}{z''}} \frac{[2 + g(z''-z')]}{(z''-\bar z)(z''-z')} \, dz'' \right] \gamma(z') dz'). \qquad (2.3\text{-}6)$$

This equation cannot be solved in this form since $\gamma(\bar z)$ has a singularity at $\bar z = 1$, i.e., the leading edge. To remove this singularity a new dependent variable is defined as

$$\gamma^*(\bar z) = \sqrt{1-\bar z} \; \gamma(\bar z).$$

Equation (2.3-6) then becomes

$$\gamma^*(\bar z) = \sqrt{1-\bar z} \; \gamma(\bar z) = f(\bar z) - \int_0^1 K_1(\bar z, z') \frac{\gamma^*(z')}{\sqrt{1-z'}} \, dz', \qquad (2.3\text{-}7)$$

where

$$f(\bar z) = -\frac{1}{2\pi^2} \sqrt{\bar z} \oint_0^1 \frac{1}{(z'-\bar z)} \sqrt{\frac{1-z'}{z'}} \, H(z') \, dz'.$$

$$K(\bar z, z') = \frac{1}{2\pi^2} \sqrt{\bar z} \oint_0^1 \sqrt{\frac{1-z''}{z''}} \frac{[2 + g(z''-z')]}{(z''-\bar z)(z''-z')} \, dz''.$$

Both $f(\bar z)$ and $K(\bar z, z')$ are Cauchy principle value integrals. The integrals in these equations can both be reduced to nonsingular integrals and integrated numerically by a method given by Muskhelishvili [11]. Another method which is convenient for this type of problem is to expand part of the integrand in a Fourier Series. For convenience, a change of variable is made in Eq. (2.3-7) of the form

$$z = \frac{1}{2}(1 - \cos \bar z)$$

for the axial coordinates. This equation then becomes

158

$$\gamma^{*}(\bar{\theta}) = \gamma(\bar{\theta}) \sin \frac{1}{2} \bar{\theta} = f(\bar{\theta}) + \int_{0}^{\pi} K(\bar{\theta},\theta') \gamma^{*}(\theta') d\theta' , \qquad (2.3-8)$$

where

$$f(\bar{\theta}) = - \frac{1}{2\pi^2} \cos \frac{1}{2} \bar{\theta} \oint_{0}^{\pi} \frac{(1 - \cos \theta')}{(\cos \theta' - \cos \bar{\theta})} H(\theta') d\theta' , \qquad (2.3-9)$$

$$K(\bar{\theta},\theta') = \frac{1}{\pi^2} \cos \frac{1}{2} \bar{\theta} \cos \frac{1}{2} \theta' \int_{0}^{\pi} \frac{(1 - \cos \theta'')}{(\cos \theta'' - \cos \bar{\theta})} \left[\frac{2 + g(\cos \theta'' - \cos \theta')}{(\cos \theta'' - \cos \theta')} \right] d\theta'' .$$
$$(2.3-10)$$

A method is desired for evaluating Eqs. (2.3-9) and (2.3-10) which will have as general an application as possible. One approach is to expand the thickness distribution in a Fourier Sine Series in θ, i.e., let

$$s(\bar{z}) = s[\theta(\bar{z})] = \sum_{m=1}^{\infty} s_{m} \sin m\theta . \qquad (2.3-11)$$

where

$$s_{m} = \frac{2}{\pi} \int_{0}^{\pi} s(\theta) \sin m\theta \, d\theta , \qquad m = 1,2,3 \ldots .$$

The slope is given by differentiation with respect to z and is

$$s'(\bar{z}) = \frac{ds}{d\bar{z}}[\theta(z)] = - \frac{2}{\sin \theta} \sum_{m=1}^{\infty} m s_{m} \cos m\theta . \qquad (2.3-12a)$$

From the form of this equation and the properties of Fourier series, it is seen that the slope of the thickness distribution may be infinite at the leading and trailing edges of the duct. This causes no difficulty as will be seen when this equation is substituted into the equation for $H(\theta)$. The camber distribution causes somewhat more difficulty if the slopes are infinite at the leading and trailing edges. In fact, if the slope of the camber line is infinite at the trailing edge ($\bar{z} = 0$), it is not clear that $f(\bar{z})$ even exists at this point. For a solution of the Fredholm equation, $f(\bar{z})$ must exist everywhere on $0 \leq \bar{z} \leq 1$. To facilitate a solution, the camber slope will be expanded in a Fourier cosine series in θ, i.e.,

$$c_{1}'(\bar{z}) = \bar{c}(\theta) = \sum_{m=0}^{\infty} \bar{c}_{m} \cos m\theta . \qquad (2.3-12b)$$

where

159

$$\bar{c}_o(\theta) = \frac{1}{\pi} \int_0^\pi \bar{c}(\theta) \, d\theta ,$$

$$\bar{c}_m(\theta) = \frac{2}{\pi} \int_0^\pi \bar{c}(\theta) \cos m\theta \, d\theta , \quad m = 1, 2, 3 \dots .$$

This implies that the slope of the camber line is not infinite at the leading and trailing edges which is more restrictive at the leading edge than necessary for solution of the Fredholm equation.

Introducing the expressions for the slopes into Eq. (2.3-3), $H(\theta')$ is obtained as

$$H(\theta') = (1 - x_{x_d}) \left\{ 4 - \left[\tan \alpha - \sum_{m=0}^{\infty} \bar{c}_m \cos m\theta' \right] \right.$$

$$\left. - 4h \sum_{m=1}^{\infty} m s_m \int_0^\pi k \left[K(k) - E(k) \right] \cos m\theta'' d\theta'' . \right. \tag{2.3-13}$$

The elliptic integral of the first kind $K(k)$ has a logarithmic singularity at $k = 1$ which can be removed by making the change in variable $\theta' - \theta'' = t^3$, then

$$\int_0^\pi k \left[K(k) - E(k) \right] \cos m\theta'' d\theta'' = 3 \int_{-\sqrt[3]{\pi - \theta'}}^{\sqrt[3]{\theta'}} t^2 k \left[K(k) - E(k) \right] \cos m(\theta' - t^3) \, dt \tag{2.3-14}$$

$$= 3 G(\theta', m) .$$

where

$$h^2 = \frac{4}{h^2 \left[\cos m' - \cos (\theta' - t^3) \right]^2 - 4} .$$

This integral can now be evaluated numerically. To complete the solution the function $G(\theta', m)$ is expanded in a Fourier cosine series in θ', i.e.,

$$G(\theta', m) = \sum_{p=1}^{\infty} a_p(m) \cos p\theta' \tag{2.3-15}$$

where

$$a_o(m) = \frac{1}{\pi} \int_0^\pi G(\theta', m) \, d\theta'$$

$$a_p(m) = \frac{2}{\pi} \int_0^\pi G(\theta', m) \cos p\theta' d\theta' , \quad p = 1, 2, 3 \dots$$

160

Using this expression for $G(\mathfrak{s}',m)$ and substituting Eq. (2.3-13) into Eq. (2.3-9), the integral for $f(\mathfrak{s})$ can be evaluated by interchanging the order of integration and summation. The resulting integrals are of the Glauert type and their evaluation is given in Ref. 12.

$$
f(\overline{\mathfrak{s}}) = \left(1 - w_{x_d}\right) \left\{ \left[2(\tan \alpha + \overline{c}_0) + \sum_{m=1}^{\infty} s_m F_m \right] \cos \frac{1}{2} \overline{\mathfrak{s}} \right.
$$

$$
\left. + \left[-2 \sum_{m=1}^{\infty} \overline{c}_m \sin m\overline{\mathfrak{s}} + \sum_{m=1}^{\infty} s_m B_m(\mathfrak{s}) \right] \sin \frac{1}{2} \overline{\mathfrak{s}} \right\},
$$

(2.3-16)

where

$$
F_m = \frac{6h}{\pi} m\, a_0(m) \,,
$$

$$
B_m(\overline{\mathfrak{s}}) = -\frac{6h}{\pi} m \left[\sum_{p=1}^{\infty} a_p(m) \sin p\overline{\mathfrak{s}} \right] \,.
$$

The functions F_m and $B_m(\overline{\mathfrak{s}})$ are independent of the annular airfoil section shape so they can be tabulated for different chord-diameter ratios (h). The kernel $K(\overline{\mathfrak{s}}, \mathfrak{s}')$, Eq. (2.3-10) also involves evaluation of a Cauchy principle value integral. One method of evaluation is to expand the term

$$
\left[\frac{2 + g(\cos \mathfrak{s}'' - \cos \mathfrak{s}')}{\cos \mathfrak{s}'' - \cos \mathfrak{s}'} \right]
$$

in a Fourier cosine series in $\mathfrak{s}''$. This function is continuous everywhere for $0 \le \mathfrak{s}'' \le \pi$ and has the value of zero for $\mathfrak{s}'' = \mathfrak{s}'$. Expanding this term in an even series, it becomes

$$
\left[\frac{2 + g(\cos \mathfrak{s}'' - \cos \mathfrak{s}')}{(\cos \mathfrak{s}'' - \cos \mathfrak{s}')} \right] = \sum_{n=0}^{\infty} b_n(\mathfrak{s}') \cos n\mathfrak{s}'' . \tag{2.3-17}
$$

where

$$
b_0(\mathfrak{s}') = \frac{1}{\pi} \int_0^{\pi} \left[\frac{2 + g(\cos \mathfrak{s}'' - \cos \mathfrak{s}')}{\cos \mathfrak{s}'' - \cos \mathfrak{s}'} \right] d\mathfrak{s}'' \,.
$$

(2.3-18)

$$
b_n(\mathfrak{s}') = \frac{2}{\pi} \int_0^{\pi} \left[\frac{2 + g(\cos \mathfrak{s}'' - \cos \mathfrak{s}')}{\cos \mathfrak{s}'' - \cos \mathfrak{s}'} \right] \cos n\mathfrak{s}'' d\mathfrak{s}'' .
$$

Substituting Eq. (2.3-17) into the equation for the kernel, Eq. (2.3-10), and interchanging the order of integration and summation, the Cauchy principle

161

value integral [12] can be evaluated:

$$K(\bar{\vartheta}, \vartheta') = \frac{1}{\pi} \cos \frac{1}{2} \vartheta' \left[-b_o(\vartheta') \cos \frac{1}{2} \bar{\vartheta} + \left(\sin \frac{1}{2} \bar{\vartheta} \right) \sum_{n=1}^{\infty} b_n(\vartheta') \sin n\bar{\vartheta} \right]. \quad (2.3\text{-}19)$$

Since the kernel is a function of only the axial coordinates $\bar{\vartheta}$ and ϑ' and the chord-diameter ratio, it can be tabulated.

The functions $f(\bar{\vartheta})$ given by Eq. (2.3-16) and $K(\bar{\vartheta}, \vartheta')$ by Eq. (2.3-19) are continuous and are now in a form so that the Fredholm equation of the second kind for the pseudo-circulation $\gamma^*(0)$ can be evaluated. Since various methods exist and are well-known for evaluating this type of integral equation [13], the solution will not be discussed further. It should be mentioned, however, that the kernel in the form of Eq. (2.3-19) is a degenerate (or product) kernel, so the special method appropriate to this type of kernel can be used. Once the pseudo-circulation is determined, the circulation $\gamma(\bar{z})$ can easily be determined.

II.4 Ideal Angle of Attack of the Annular Airfoil Section

In the integral equation for the circulation strength, Eq. (2.3-6), a singularity exists at the annular airfoil leading edge which made it necessary to solve for a pseudo-circulation. This singularity does not exist if the airfoil section has a stagnation point at the leading edge. The angle of attack at which the section is operating when a stagnation point occurs at the leading edge is known as the ideal angle of attack (α_{id}). This angle can be calculated from Eq. (2.3-6) by setting the circulation equal to zero at the leading edge and solving for the angle α.

$$\tan \alpha_{id} = \frac{1}{2\pi^2 \left(1 - w_{x_d}\right)} \oint_0^1 \frac{f_1(z')}{\sqrt{(1 - z')z'}} \, dz'. \quad (2.4\text{-}1)$$

where

$$f_1(z') = f_o(z') - 2\left(1 - w_{x_d}\right) \tan \alpha.$$

The function $f_o(z')$ is given by Eq. (2.3-4). If this equation for the ideal angle of attack is substituted into Eq. (2.3-6), an equation for the ideal lift coefficient is obtained as

$$\gamma_{id} = f_{id}(\bar{z}) - \int_0^1 K_{id}(\bar{z}, z') \gamma_{id}(z') \, dz'. \quad (2.4\text{-}2)$$

where

$$f_{id}(\bar{z}) = -\frac{1}{2\pi^2} \sqrt{\bar{z}(1 - \bar{z})} \oint_0^1 \frac{\left[H(z') - 4 - (1 - w_{x_d}) \tan \alpha \right]}{(z' - \bar{z}) \sqrt{z'(1 - z')}} \, dz'.$$

162

$$K_{id}(\bar{z}, z') = \frac{1}{2\pi^2} \sqrt{\bar{z}(1-\bar{z})} \oint_0^1 \frac{[2 + g(z''-z')]dz''}{(z''-z') \sqrt{z''(1-z'')} (z''-\bar{z})}$$

It can be seen from the form of this equation that a singularity no longer occurs at the leading edge. Following the procedure in the last section, the coefficients $f_{id}(\bar{z})$ and $K_{id}(\bar{z}, \bar{z}')$ can be obtained as follows:

$$f_{id}(\bar{z}) = \left(1 - w_{x_d}\right)\left[-2 \sum_{m=1}^{\infty} \bar{c}_m \sin m\bar{z} + \sum_{m=1}^{\infty} s_m B_m(\bar{z})\right] \tag{2.4-3}$$

and

$$K_{id}(\bar{z}, \bar{z}') = \frac{1}{2\pi} \sin \bar{z}' \sum_{n=1}^{\infty} b_n(\bar{z}') \sin n\bar{z}. \tag{2.4-4}$$

The coefficients C_m, $B_m(\bar{z})$ and $b_n(\bar{z}')$ are the same functions as given in the previous section. Once γ_{id} is obtained, the ideal angle of attack is obtained from Eq. (2.4-1) as

$$\tan \alpha_{id} = \frac{1}{4\pi\left(1 - w_{x_d}\right)} \int_0^\pi b_0(\bar{z}') \gamma_{id}(\bar{z}') \sin \bar{z}' d\bar{z}' - \left(\bar{c}_0 - \frac{1}{2} \sum_{m=1}^{\infty} s_m F_m\right). \tag{2.4-5}$$

II.5 Linearized Theory of the Annular Airfoil at an Angle of Incidence and of Arbitrary Shape

In the previous sections the annular airfoil was considered to be axisymmetric and rotating with the propeller. This causes no difficulty since the axisymmetric airfoil by itself (stationary coordinate system) induces no tangential velocities. A solution without propeller can also be obtained quite easily for an axisymmetric duct at an angle of incidence or for an asymmetric duct. Considerable difficulty exists, however, if a propeller is located in such a duct since the duct by itself (stationary coordinate system) induces tangential velocities which become time dependent in the rotating coordinate system of the propeller.

For the duct of arbitrary shape, the linearized boundary condition is still satisfied on a cylinder of a representative radius so there cannot be too great a variation in shape. Referring to section II.1, the linearized boundary condition for a duct of arbitrary shape is similar to that given by Eq. (2.1-4) except that the section slope is a function of angular position, i.e.,

$$\frac{w_r}{V_0} (x_d = 0, \sigma, z) = -\left[\frac{\partial c_1}{\partial z} (\sigma, z) - \tan \alpha(\sigma) + \frac{\partial s}{\partial z} (\sigma, z)\right] \tag{2.5-1}$$

and

$$\frac{w_r}{V_0} (x_d = 0, \sigma, a_t) = 0. \tag{2.5-2}$$

163

In these equations, the velocity has been nondimensionalized by the free-stream velocity w_o and it is assumed that the free-stream velocity is uniform and the radial coordinate has been nondimensionalized by the duct radius, i.e., on the duct $x_d = 1$. As before it is assumed that the mathematical model of the flow can be represented by ring vortices and ring sources and since there is an angular variation in vortex strength, a trailing vortice of strength $(1/x_d)$ $(\partial \gamma/\partial z)$ is shed from each point on the duct. The paths of these vortices follow stream-lines and an approximation to this path is that the shed vortex follows a straight line from the duct to infinity.

Similarly to Eq. (2.2-1), the boundary condition can be expressed by the induced radial velocities of the different singularities in the system.

$$\left[\frac{w_r}{V_o}\,(x_d, z, z)\right]_\gamma + \left[\frac{w_r}{V_o}\,(x_d = 0, z, z)\right]_q - \left[\frac{w_r}{V_o}\,(x_d, z, z)\right]_{\frac{\partial \gamma}{\partial z}}$$

$$= -\left[\frac{\partial c_1}{\partial z}\,(z, z) + \tan z(z) \pm \frac{\partial s}{\partial z}\,(z, z)\right]. \qquad (2.5\text{-}3)$$

The induced radial velocities of the ring vortices and ring sources are given by Eqs. (2.2-2) and (2.2-3), respectively. The radial velocity induced on the duct by the trailing vortices has been derived in Appendix C of Ref. 6 and is

$$\left[\frac{w_r}{V_o}\,(x_d, z, z)\right]_{\frac{\partial \gamma}{\partial z}} = \frac{h}{2\pi}\int_0^1\int_0^{2\pi}\left[\cot\frac{1}{2}\,(z - z')\right]$$

$$\times\left[\frac{2h(\bar{z} - z')}{\sqrt{4h^2(\bar{z} - z')^2 - 4\,\sin^2\frac{1}{2}\,(z - z')}} - 1\right]\frac{\partial \gamma}{\partial z'}\,(z', z')\,dz'dz'. \qquad (2.5\text{-}3)$$

Substituting Eqs. (2.2-2), (2.2-3) and (2.5-4) into the first boundary condition, an equation is obtained for the vortex and source strengths. As in section II.2 from making this substitution, it can be concluded the source strength $q(z, z)$ must be a function of the thickness slope only, i.e.,

$$q(z, z) = -2\,\frac{\partial s}{\partial z}\,(z, z).$$

From this equation it can be seen that source strength is a function of both axial and angular position. With this value for the source strength an integro-differential equation is obtained for the vortex distribution.

$$\frac{h}{2\pi}\int_0^1\int_{-\pi}^{\pi}\frac{2h(\bar{z} - z')\cos(z - z') \cdot (z', z')\,dz'dz'}{\left[4h^2(\bar{z} - z')^2 - 4\,\sin^2\frac{1}{2}\,(z - z')\right]^{3/2}} - \frac{h}{2\pi}\int_0^1\int_{-\pi}^{\pi}\left[\cot\frac{1}{2}\,(z - z')\right]$$

$$(2.5\text{-}4)$$
$$(\text{Cont.})$$

164

$$\times \left[\frac{2h(\bar{z} - z')}{\sqrt{4h^2(\bar{z} - z')^2 + 4 \sin^2 \frac{1}{2} (\varphi - \varphi')}} + 1 \right] \frac{\partial \gamma}{\partial \varphi} (\varphi', z') \, d\varphi' dz'$$

$$= - \left[\frac{\partial c_1}{\partial z} (\varphi, \bar{z}) + \tan \alpha(\varphi) - \frac{h}{\pi} \int_0^1 \int_{-\pi}^{\pi} \frac{[1 - \cos(\varphi - \varphi')] \frac{\partial s}{\partial z'} (\varphi', z') \, d\varphi' dz'}{\left[4h^2(\bar{z} - z')^2 + 4 \sin^2 \frac{1}{2} (\varphi - \varphi') \right]^{3/2}} \right]$$

$$= \bar{U}(\varphi, \bar{z}). \tag{2.5-4}$$

The right-hand side of this equation is a known function of φ and $\bar{z}$. The integral involving the thickness slope is complicated but can be evaluated using techniques used in earlier sections. To solve for the vortex strength a technique is used proposed by Weissinger [9]. An assumption is made that the vortex distribution can be expanded in a Fourier series in φ'. If the duct is symmetrical about at least one plane, only an odd or even series needs to be used. For the completely arbitrary duct however, the following is obtained:

$$\gamma(\varphi', z') = \sum_{n=0}^{\infty} y_n(z') \cos n\varphi' + \sum_{n=1}^{\infty} h_n(z') \sin n\varphi' \tag{2.5-5}$$

and it follows that

$$\frac{\partial \gamma}{\partial \varphi'} (\varphi', z') = - \sum_{n=1}^{\infty} n \, g_n(z') \sin n\varphi' + \sum_{n=1}^{\infty} n \, h_n(z') \cos n\varphi'. \tag{2.5-6}$$

The function $\bar{U}(\varphi, \bar{z})$ is also expanded in a Fourier series in φ.

$$\bar{U}(\varphi, \bar{z}) = \sum_{n=0}^{\infty} \bar{u}_n \cos n\varphi + \sum_{n=1}^{\infty} \bar{v}_n \sin n\varphi. \tag{2.5-7}$$

where

$$\bar{u}_o = \frac{1}{2\pi} \int_{-\pi}^{\pi} \bar{U}(\varphi, \bar{z}) \, d\varphi$$

$$\bar{u}_n = \frac{1}{\pi} \int_{-\pi}^{\pi} \bar{U}(\varphi, \bar{z}) \cos n\varphi \, d\varphi, \quad n = 1, 2, 3 \ldots$$

$$\bar{v}_n = \frac{1}{\pi} \int_{-\pi}^{\pi} \bar{U}(\varphi, \bar{z}) \sin n\varphi \, d\varphi, \quad n = 1, 2, 3 \ldots.$$

These last three equations are substituted into Eq. (2.5-4) and the order of integration and summation interchanged. Since a Fourier series is unique, the

165

coefficients can be equated and a singular integral equation is obtained for each of the Euler coefficients of the vortex strengths, i.e., $g_n(z')$ and $h_n(z')$

$$\bar{u}_n = \frac{1}{2\pi} \int_0^1 \frac{g_n(z')}{(\bar{z} - z')} \; [\bar{G}(\bar{z}, z')] \; dz' \, ,$$

$$\tilde{v}_n = \frac{1}{2\pi} \int_0^\pi \frac{h_n(z')}{(\bar{z} - z')} \; [\bar{G}(\bar{z}, z')] \; dz' \, ,$$

(2.5-8)

where

$$\bar{G}(\bar{z}, z') = \frac{na_1}{2} + a_1^2 \left\{ - \left[Q'_{n+\frac{1}{2}}(\bar{k}) - nQ_{n-\frac{1}{2}}(\bar{k}) \right] + 2n \int_0^{\pi/2} \frac{\sin 2n\theta' \; \cot \theta' d\theta'}{\left[a^2 + 4 \sin^2 \theta' \right]^{1/2}} \right\}$$

$$a_1 = 2h(\bar{z} - z')$$

$$\bar{k} = 1 + \frac{a_1^2}{2} \, .$$

The function $Q_{n-\frac{1}{2}}(\bar{k})$ is the half order Legendre function of the second kind and $Q'_{n+\frac{1}{2}}(\bar{k})$ is the first derivative with respect to the argument $\bar{k}$. These functions are well-known and have been tabulated in some detail by Sluyter [14]. The Legendre functions are singular at $a_1 = 0$ but it can easily be shown that

$$\lim_{a_1 \to 0} a_1^2 \left[Q'_{n+\frac{1}{2}}(\bar{k}) - nQ_{n-\frac{1}{2}}(\bar{k}) \right] = -1 \, .$$

Both Eqs. (2.5-7) and (2.5-8) are singular integral equations similar to Eq. (2.3-1) but with considerably more complicated coefficients. Each of these equations can be reduced, however, by the same technique used in section II.3, so a Fredholm equation of the second kind is obtained for each of the Euler coefficients. It should be noted that the second boundary condition, Eq. (2.5-2), implies that $g_n(0) = h_n(0) = 0$.

For an axisymmetric annular airfoil at an angle of attack, these equations reduce to a more simplified form. Consider that the free-stream velocity is at a small angle to the duct as shown in Fig. 3. The linearized kinematic boundary condition is (see Eq. (2.5-1))

$$\frac{w_r}{V_o} (x_d \pm 0, \bar{z}) = -[c'(\bar{z}) \pm s'(\bar{z})] - \alpha_r \cos \bar{z}, \quad (0 \leq \bar{z} \leq 1) \qquad (2.5-9)$$

and

$$\frac{w_r}{V_o} (x_d \pm 0, a_t) = 0 \, .$$

166

Fig. 3 - Free-stream velocity at an angle
to the annular airfoil

Since the annular airfoil is axisymmetric, it can be seen that the source
strength is

$$q(\bar{z}) = -2 s'(\bar{z}) ,$$

which is the same as obtained in section II.3. If the right-hand side of Eq.
(2.5-9) is expanded in a Fourier series in z, as given by Eq. (2.5-7), it is found
that only two terms exist, i.e.,

$$\bar{u}_o(\bar{z}) = -\frac{\bar{U}(\bar{z})}{4-}$$

$$\bar{u}_1(\bar{z}) = -z_r$$

$$\bar{u}_n(\bar{z}) = 0. \quad (n = 2, 3, \ldots)$$

$$\bar{v}_n(\bar{z}) = 0. \quad (n = 1, 2, 3, \ldots) .$$

These results imply that the Euler coefficient $h_n(z)$ is zero, as it must be
since the flow is even about the x-$\bar{z}$ plane. All the coefficients $g_n(\bar{z})$ for $n = 2$,
$3 \ldots \infty$ are also zero and therefore only g_o and g_1 exist. If these coefficients
are substituted into Eq. (2.5-7), it is found first of all, that $g_o(\bar{z}) = \gamma(\bar{z})$, where
$\gamma(\bar{z})$ is the circulation distribution for the annular airfoil at zero incidence.
The solution for $g_o(z)$ is given, therefore, by Eq. (2.3-15).

The Euler coefficient $g_1(\bar{z})$ is found by letting $n = 1$ in Eq. (2.5-7) and
substituting for $\bar{u}_1(\bar{z})$. The resulting equation, after reducing the kernel $\bar{G}(\bar{z}, z')$
to its simplest form, is

$$\int_0^1 \frac{g_1(z')}{(\bar{z} - z')} W_1(\bar{z} - z') \, dz' - h \int_0^1 g_1(z') \, dz' = -2 z_r . \qquad (2.5\text{-}10)$$

167

where

$$W_1(\bar{z} - z') = \frac{1}{k^3} \left[(2 - k^2)^2 \, E(k) - 4(1 - k^2)^2 \, K(k) \right]$$

$$k^2 = \frac{1}{h^2(\bar{z} - z')^2 + 1} .$$

It can easily be shown that

$$\lim_{z' \to \bar{z}} \left[W_1(\bar{z} - z') \right] = 1 .$$

Equation (2.5-10) gives the contribution to the circulation due to the angle of attack and is independent of the section shape and depends only on the chord-diameter ratio (h) and the angle of attack (α_r). The reduction of this equation to a Fredholm equation of the second kind follows exactly the procedure given in section II.3. The resulting equation is

$$g_1^*(\bar{\theta}) = \left(\sin \frac{1}{2} \bar{\theta} \right) g_1(\bar{\theta}) = 2\alpha_r \cos \frac{1}{2} \bar{\theta} - \frac{2}{\pi} \int_0^{\pi} \left(\cos \frac{1}{2} \bar{\theta}' \left[-b_0(\bar{\theta}') \cos \frac{1}{2} \bar{\theta} \right. \right.$$

$$\left. \left. + \left(\sin \frac{1}{2} \bar{\theta} \right) \sum_{m=1}^{\infty} b_m(\bar{\theta}') \sin m\bar{\theta} \right] \right) g_1^*(\bar{\theta}') \, d\bar{\theta}' . \quad (2.5-11)$$

where

$$b_0(\bar{\theta}') = \frac{\pi}{2} h + \frac{1}{\pi} \int_0^{\pi} \left[\frac{W_1 (\cos \bar{\theta}'' - \cos \bar{\theta}') - 1}{(\cos \bar{\theta}'' - \cos \bar{\theta}')} \right] d\bar{\theta}''$$

$$b_m(\bar{\theta}') = \frac{2}{\pi} \int_0^{\pi} \left[\frac{W_1 (\cos \bar{\theta}'' - \cos \bar{\theta}') - 1}{(\cos \bar{\theta}'' - \cos \bar{\theta}')} \right] \cos m\bar{\theta}'' d\bar{\theta}'' .$$

The circulation distribution for the duct at an angle of incidence can readily be calculated from Eq. (2.5-5) as

$$\gamma(\bar{\theta}, \bar{z}) = g_0(\bar{z}) + g_1(\bar{z}) \cos \bar{\theta}$$

$$= \gamma(\bar{z}) + \bar{g}_1(\bar{z}) \cos \bar{\theta} . \quad (2.5-12)$$

II.6 Inverse Problem of the Annular Airfoil

The inverse problem is to determine the annular airfoil shape when the pressure distribution on the airfoil is given. For this problem the duct will be taken as axisymmetric and at zero incidence. It is, of course, not possible to determine the section shape in the presence of the propeller with a finite number of blades since the pressure distribution is essentially time-dependent. It

is possible, however, to consider the average effect of the propeller which corresponds to a propeller with an infinite number of blades.

The coordinate system taken will be the same as given in section II.1, with w_+ denoting the velocity tangent to the outer surface and w_- denoting the velocity tangent to the inner surface. The linearized Bernoulli equation is

$$\frac{p(x_d, z) - p_o}{\frac{1}{2} \rho V_o^2} = \frac{2 w_a(x_d, z)}{V_o} \quad . \tag{2.6-1}$$

where $p(x_d, z)$ is the local pressure on the duct, p_o is the pressure infinitely far ahead of the propeller, $w_a(x_d, z)$ is the perturbation axial velocity on the duct, and ρ is the mass density. Within linearized theory giving the pressure distribution is equivalent to giving the perturbation velocity. Also within linearized theory the axial velocity is assumed to be equal to the tangential velocity. The velocity w_- is given by the velocities induced by the different singularities in the flow and the total tangential velocity is given by

$$\left[\frac{w_a}{V_s}\right]_{total} = \left[\frac{w_a}{V_s}\right]_\gamma - \left[\frac{w_a}{V_s}\right]_q - \left[\frac{w_a}{V_s}\right]_{p_{aver}} - \frac{w_o(r)}{V_s} \quad . \tag{2.6-2}$$

where γ refers to the ring vortices, q to ring sources and p_{aver} to the average velocity induced by the propeller. From this equation the perturbation velocity distribution w_a is

$$\left[\frac{w_a}{V_s}\right]_{total} - \frac{w_o(r)}{V_s} = \frac{w_a}{V_s} = \left[\frac{w_r}{V_s}\right]_\gamma - \left[\frac{w_a}{V_s}\right]_q - \left[\frac{w_a}{V_s}\right]_{p_{aver}} \quad . \tag{2.6-3}$$

From Ref. 6, the velocities induced by the vortex cylinder and source cylinder are obtained as

$$\left[\frac{w_a}{V_s}\right]_\gamma = \frac{h}{2\pi} \int_0^1 \gamma(z') \, k \, [K(k) - E(k)] \, dz' = \frac{1}{2} \gamma(\bar{z}) \tag{2.6-4}$$

$$\left[\frac{w_a}{V_s}\right]_q = - \frac{1}{\pi} \oint_0^1 \frac{s'(z') \, k \, E(k)}{(\bar{z} - z')} \, dz'. \tag{2.6-5}$$

where

$$k^2 = \frac{1}{h^2(\bar{z} - z')^2 - 1} \quad .$$

Substituting Eqs. (2.6-4) and (2.6-5) into Eq. (2.6-3) gives the perturbation velocity.

169

$$\left[\frac{w_a(x_d, \bar{z})}{V_s}\right]_{\pm} = \frac{h}{2\pi} \int_0^1 \gamma(z') \, k[K(k) - E(k)] dz' \pm \frac{1}{2} \gamma(\bar{z})$$

$$- \frac{1}{\pi} \oint_0^1 \frac{s'(z') \, k \, E(k) \, dz'}{(\bar{z} - z')} + \left[\frac{w_a}{V_s}\right]_{P_{aver}} \qquad (2.6\text{-}6)$$

A mean velocity will be defined

$$\left[\frac{w_a(\bar{z})}{V_s}\right]_{mean} = \frac{1}{2}\left[\frac{w_a(\bar{z})}{V_{s+}} + \frac{w_a(\bar{z})}{V_{s-}}\right] . \qquad (2.6\text{-}7)$$

Substituting Eq. (2.6-6) into this equation gives the following equation:

$$\left[\frac{w_a(\bar{z})}{V_s}\right]_{mean} = \frac{h}{2\pi} \int_0^1 \gamma(z') \, k[K(k) - E(k)] dz'$$

$$- \frac{1}{\pi} \int_0^1 \frac{s'(z') \, kE(k) \, dz'}{(\bar{z} - z')} + \left[\frac{w_a}{V_s}\right]_{P_{aver}} . \qquad (2.6\text{-}8)$$

A velocity difference is also defined as

$$\left[\frac{w_a(\bar{z})}{V_s}\right]_{diff} = \left[\frac{w_a(\bar{z})}{V_{s+}} - \frac{w_a(\bar{z})}{V_{s-}}\right] \qquad (2.6\text{-}9)$$

and substituting in Eq. (2.6-6) gives

$$\left[\frac{w_a(\bar{z})}{V_s}\right]_{diff} = \gamma(\bar{z}) . \qquad (2.6\text{-}10)$$

Since $(w_a V_s)_{mean}$ and $(w_a V_s)_{diff}$ are both known, substituting Eq. (2.6-10) into Eq. (2.6-8) gives a singular integral equation for the slope of the thickness distribution.

$$\oint_0^1 \frac{s'(z') \, k \, E(k)}{(\bar{z} - z')} \, dz' = -\pi \left[\frac{w_a(z)}{V_s}\right]_{mean} - \frac{h}{2} \int_0^1 \left(\frac{w_a}{V_s}\right)_{diff} k[K(k) - E(k)] dz'$$

$$- \pi \left[\frac{w_a(\bar{z})}{V_s}\right]_{P_{aver}} . \qquad (2.6\text{-}11a)$$

Once the thickness slope is known, the slope of the camber line, including the section angle of attack, is given by Eq. (2.3-1) where $\gamma(\bar{z})$ is given by Eq. (2.6-10). If the propeller is in the duct, the average radial velocity induced by

170

the propeller must be included. The angle of attack is obtained by integrating Eq. (2.3-1) with respect to $\bar{z}$ from 0 to 1 and noting that

$$\int_0^1 c_1'(\bar{z})d\bar{z} = 0.$$

Following the procedure given in section II.3, the equation for the thickness slope can be reduced to a Fredholm equation of the second kind. For convenience, Eq. (2.6-11) is rewritten as follows:

$$\oint_0^1 \bar{g}(\bar{z} - z') \frac{s'(z')}{(\bar{z} - z')} dz' = \bar{H}(\bar{z}), \qquad (2.6\text{-}11b)$$

where

$$\bar{g}(\bar{z} - z') = k E(k),$$

$$\bar{H}(\bar{z}) = \frac{h}{2} \int_0^1 \left(\frac{w_a}{V_s}\right)_{diff} k[K(k) - E(k)]dz' + \pi\left(\frac{w_a}{V_s}\right)_{P_{aver}} - \pi\left(\frac{w_a}{V_s}\right)_{mean}.$$

The term $\bar{g}(0)$ is added to and subtracted from the integrand of the integral in Eq. (2.6-11b)

$$\bar{g}(0) \oint_0^1 \frac{s'(z')}{(\bar{z} - z')} dz' + \oint_0^1 \left[\bar{g}(\bar{z} - z') - \bar{g}(0)\right] \frac{s'(z')}{(\bar{z} - z')} dz' = \bar{H}(\bar{z}). \quad (2.6\text{-}12)$$

And since $g(0) = 1$, this equation simplifies to

$$\oint_0^1 \frac{s'(z')}{(\bar{z} - z')} dz' = \bar{H}(\bar{z}) - \int_0^1 \left[\bar{g}(\bar{z} - z') - 1\right] \frac{s'(z')}{(\bar{z} - z')} dz'$$

$$= \bar{f}_o(\bar{z}). \qquad (2.6\text{-}13)$$

As discussed in section II.3, this equation has a unique inverse given by

$$s'(\bar{z}) = \frac{1}{\pi\sqrt{\bar{z}(1 - \bar{z})}} \left[\frac{1}{\pi} \oint_0^1 \frac{\sqrt{z'(1 - z')}}{(z' - \bar{z})} \bar{f}_o(z') dz' + 2 \int_0^1 s'(z') dz'\right].$$

Since the section must be closed

$$\int_0^1 s'(z') dz' = 0$$

and substituting for $\bar{f}_o(z')$ a Fredholm equation of the second kind is obtained for the thickness slope.

171

$$s'(\bar{z}) = \frac{1}{\sqrt{\bar{z}(1-\bar{z})}} \left[-\bar{f}(\bar{z}) + \int_0^1 \overline{K}(\bar{z},z') \; s'(z') \, dz' \right], \qquad (2.6\text{-}14)$$

where

$$\bar{f}_1(\bar{z}) = -\frac{1}{\pi^2} \oint_0^1 \frac{\sqrt{z'(1-z')}}{(z'-\bar{z})} \; \overline{H}(z') \, dz',$$

$$\overline{K}(\bar{z},z') = \frac{1}{\pi^2} \oint_0^1 \frac{\sqrt{z''(1-z'')} \; [1 - g(z''-z')]}{(z''-\bar{z})(z''-z')} \, dz''.$$

This equation cannot be solved in this form since the thickness slope has a square-root singularity at both the leading and trailing edges of the section. To remove, the following change in variable of the type $z = 1/2(1 + \cos \bar{z})$ is made and the following relationship for the slopes in the two coordinates system is noted.

$$s'(\bar{z}) = -\frac{2}{\sin \bar{z}} \, s'(\bar{z}).$$

Equation (2.6-14) then becomes

$$s'(\bar{z}) = \bar{f}(\bar{z}) + \int_0^{\bar{z}} \overline{K}(\bar{z},z') \; s'(z') \, d\bar{z}'. \qquad (2.6\text{-}15)$$

where

$$\bar{f}(\bar{z}) = -\frac{1}{-2} \oint_0^{\bar{z}} \overline{H}(z') \; \sin^2 \bar{z}' d\bar{z}'.$$

$$\overline{K}(\bar{z},z') = \frac{1}{-2} \int_0^{\bar{z}} \frac{[1 - k \, E(k)] \; \sin^2 \bar{z}'' d\bar{z}''}{(\cos \bar{z}'' - \cos \bar{z})(\cos \bar{z}'' - \cos \bar{z}')}.$$

Both $\bar{f}(\bar{z})$ and $\overline{K}(\bar{z},z')$ can be evaluated by using Muskhelishvili's [11] method for evaluating Cauchy principle integrals or by expanding part of the integrand in a Fourier series and interchanging the order of integration and summation as was done in section II.3. The Fredholm equation of the second kind, for the thickness slope, Eq. (2.6-15), can be evaluated using one of the methods given in Ref. 13.

In this section the vortex strength of the ring vortex has been shown to be equal to the difference between the velocity inside and outside the duct. The thickness slope was shown to be given by a Fredholm equation of the second kind and the camber slope was given by evaluating integrals of the difference velocity and the thickness slope.

172

II.7 Approximate Nonlinear Theory of Annular Airfoils

Consider an annular airfoil in a uniform stream which has an angle of incidence (α_r) to the axis of the airfoil. Such an airfoil is shown in Fig. 3, where equation of the surface is given by $r = f(z,\phi)$ or $F(r,\phi,z) = 0$. If $\mathbf{r}_r$, $\mathbf{r}_o$ and $\mathbf{V}_z$ are unit vectors in polar coordinates, the velocity $\mathbf{V}$ in terms of the polar coordinate velocities is given by

$$\mathbf{V} = w_r \mathbf{r}_r + w_t \mathbf{r}_t + \bar{w}_a \mathbf{r}_z . \tag{2.7-1}$$

The radial, tangential and axial velocities, w_r, w_t, and $\bar{w}_a$, respectively, in terms of the cartesian coordinates velocities $(\bar{w}_k, \bar{w}_y, \bar{w}_a)$ are

$$\left.\begin{aligned} w_r &= \bar{w}_x \cos \phi + \bar{w}_y \sin \phi \\ w_t &= -\bar{w}_x \sin \phi + \bar{w}_y \cos \phi \end{aligned}\right\} , \tag{2.7-2}$$

$$\bar{w}_a = \bar{w}_a . \tag{2.7-3}$$

In terms of the free-stream velocity and the perturbation velocities arising from singularities representing the duct, the velocities $\bar{w}_x$, $\bar{w}_y$ and $\bar{w}_a$ are

$$\begin{aligned} \bar{w}_x &= w_o \sin \alpha_r + w_x , \\ \bar{w}_y &= w_y , \\ \bar{w}_a &= -w_o \cos \alpha_r + w_a . \end{aligned} \tag{2.7-4}$$

The velocities w_x, w_y, and w_a are the perturbation velocities arising from the singularities. The unit tangent vector to the surface of the duct is

$$\mathbf{t} = \frac{dr}{ds} \mathbf{r}_r + r \frac{d\phi}{ds} \mathbf{r}_t + \frac{dz}{ds} \mathbf{r}_z , \tag{2.7-5}$$

where

$$ds = \sqrt{dr^2 + r^2 d\phi^2 + dz^2} = dz \sqrt{1 + r^2 \left(\frac{d\phi}{dz}\right)^2 + \left(\frac{dr}{dz}\right)^2} .$$

If the annular airfoil is axisymmetric then $d\phi \, ds = 0$ and denoting the surface by $r = f(z)$, the unit tangent vector is

$$\mathbf{t} = \frac{1}{\sqrt{1 + [f'(z)]^2}} \left[f'(z) \mathbf{r}_r + \mathbf{r}_z \right] . \tag{2.7-6}$$

The tangential velocity on the surface of the airfoil is given by

$$V_t = \mathbf{V} \cdot \mathbf{t} = \frac{1}{\sqrt{1 + [f'(z)]^2}} \left[w_r f'(z) + \bar{w}_a \right] . \tag{2.7-7}$$

173

The unit normal vector on the surface of the airfoil is

$$\mathbf{n} = \frac{\text{grad } F(r, \varphi, z)}{|\text{grad } F|} = \frac{F_r \mathbf{r}_r + F_z \mathbf{r}_z + \frac{1}{r} F_\theta \mathbf{r}_t}{\sqrt{F_r^2 + F_z^2 + \frac{1}{r^2} F_\theta^2}}. \tag{2.7-8}$$

The normal velocity on the surface of the airfoil is given by $\mathbf{V} \cdot \mathbf{n}$ and it must be zero to satisfy the kinematic boundary condition for a solid body.

$$V_n = \mathbf{V} \cdot \mathbf{n} = \frac{1}{\sqrt{F_r^2 + F_z^2 + \frac{1}{r^2} F_\theta^2}} \left(w_r F_r + \frac{1}{r} F_\theta w_t + F_z \bar{w}_a \right) \tag{2.7-9}$$

$$= 0.$$

If the body is axisymmetric, then $F_\theta = 0$ and denoting the surface by $F(r, \varphi, z) = f(z) - r = 0$

$$F_r = -1,$$
$$F_z = f'(z). \tag{2.7-10}$$

Substituting this into Eq. (2.7-9), the boundary condition becomes

$$f'(z) = \frac{w_r}{\bar{w}_a}. \tag{2.7-11}$$

In the linearized form which has been discussed in previous sections, the kinematic boundary condition is not satisfied along the airfoil surface but along a circular ring representing the airfoil. Also, the velocities w_r and w_a have square-root singularities at the duct leading edge in the linearized solution. Actually along the representative cylinder the tangential velocity is taken to be the axial velocity, i.e., $V_t = \bar{w}_a$, and since the linearized w_a is singular at the leading edge a physically impossible flow is predicted. It seems reasonable to assume that the perturbation velocities w_a and w_r in Eq. (2.7-12) are approximated by their values along the ring. If the squared terms are neglected, the tangential velocity becomes

$$V_t(z) = \frac{1}{\sqrt{1 + [f'(z)]^2}} \left[-w_o \cos \alpha_r + w_a(z) \right]. \tag{2.7-13}$$

The perturbation velocity w_a is assumed to be the linearized velocity. If the duct is not axisymmetric, this equation can also be used but in this case w_a is also a function of the angular position and the slope $f'(z)$ is taken as $\partial f / \partial z (\varphi, z)$. In the form of Eq. (2.7-13) the tangential velocity is not singular at the leading edge since normal airfoil shapes will have infinite slopes at their leading edge which will cancel the singularity arising from the perturbation velocity.

174

The argument for the validity of Eq. (2.7-13) is heuristic in nature and not very satisfactory. For instance, if both linearized velocities are substituted into Eq. (2.7-12), it is found that the tangential velocity, given by this substitution, is singular at the leading edge of the duct. However, if the radial velocity is neglected, Eq. (2.7-13), this velocity is finite. Only a comparison with experimental results or the exact theory, which of course is not known, will establish the validity of this equation.

In two-dimensional flow, where the exact theory for many shapes is known, the approximation given by Eq. (2.7-13) is known as Goldstein's second approximation [12]. The comparison of this approximation to both exact theory and experimental results is quite good. In fact, for the ellipse Eq. (2.7-13), using the linearized perturbation velocity w_a, can be reduced to the equation given by the exact theory.

II.8 Velocity and Pressure Distribution and Forces on the Annular Airfoil

The velocity field of the ducted propeller is found by summing the free-stream velocity, the velocity induced by the duct including the trailing vortex system, and the velocity induced by the propeller. The linearized pressure distribution on the duct is given in section II.6 as

$$\frac{p(x_d, z) - p_o}{\frac{1}{2} \rho V_o^2} = \frac{2 w_a(x_d, z)}{V_o} , \qquad (2.6-1)$$

where $w_a(x_d, z)$ is the total perturbation velocity in the field. For the purely axisymmetric case the axial velocities induced on the duct are given by Eqs. (2.6-4) and (2.6-5). The pressure distribution on an axisymmetric duct at an angle of incidence is given by the same equation since the trailing vortex system induces no axial velocity. If the equation for the tangential velocity developed in the last section is substituted into this equation for w_a, the calculated pressure distribution will better approximate the experimental value. For the general problem where the duct is not axisymmetric or a propeller is present, the axial velocities induced by the vortex and source cylinder are considerably more complicated. These velocities, including also radial and tangential components, have been derived from the law of Biot-Savart in Ref. 6 and are given here without the derivation. For the vortex cylinder the velocities induced at any point in space except on the cylinder are

$$\frac{w_a}{V_s}(x, \phi, \bar{z})_\gamma = -\frac{h}{2\pi} \int_0^1 \int_0^{2\pi} \frac{[(x'x_d)\cos(\phi - \phi') - 1]}{R^3} \gamma(\phi', z') \, d\phi' dz', \qquad (2.8-1)$$

$$\frac{w_r}{V_s}(x, \phi, \bar{z})_\gamma = +\frac{h}{2\pi} \int_0^1 \int_0^{2\pi} \frac{2h(\bar{z} - z')\cos(\phi - \phi')}{R^3} \gamma(\phi', z') \, d\phi' dz', \qquad (2.8-2)$$

$$\frac{w_t}{V_s}(x,\phi,\bar{z})_\gamma = -\frac{h}{2\pi}\int_0^1\int_0^{2\pi}\frac{2h(\bar{z}-z')\sin(\varphi-\varphi')}{R^3}\gamma(\varphi',z')\,d\varphi'dz', \qquad (2.8\text{-}3)$$

where

$$R^2 = \left[\left(1+\frac{x}{x_d}\right)^2+4h^2(\bar{z}-z')^2-2\left(\frac{x}{x_d}\right)\cos(\varphi-\varphi')\right]. \qquad (2.8\text{-}4)$$

On the ring itself, the velocity is found by letting $x = x_d$ in these equations. For the axial velocity, however, there is a discontinuity in the axial component which follows from the properties of vortex sheets. Thus on the ring itself, the axial component is given as

$$\left[\frac{w_a}{V_s}(x_d\pm 0,\varphi,\bar{z})\right]_\gamma = -\frac{h}{2\pi}\int_0^1\int_0^{2\pi}\frac{[\cos(\varphi-\varphi')-1]\,\gamma(\varphi',z')\,d\varphi'dz'}{\left[4h^2(\bar{z}-z')^2+4\sin^2\frac{1}{2}(\varphi-\varphi')\right]^{3/2}}$$

$$\pm\frac{1}{2}\gamma(\varphi,\bar{z}),\quad 0\leq\bar{z}\leq 1. \qquad (2.8\text{-}5)$$

The plus signs refer to the outside of the duct and the minus signs to the inside. For the axisymmetric duct, i.e., γ is not a function of φ, the tangential velocity is zero and Eqs. (2.8-1) and (2.8-2) reduce to

$$\left[\frac{w_a(x,\bar{z})}{V_s}\right]_\gamma = \frac{h}{2\pi}\int_0^1\frac{\gamma(z')}{\left(\frac{x}{x_d}\right)^{1/2}}k_1\left[K(k_1)-E(k_1)-\frac{2\left(\frac{x}{x_d}-1\right)E(k_1)}{4h^2(\bar{z}-z')^2+\left(\frac{x}{x_d}-1\right)^2}\right]dz', \quad (2.8\text{-}6)$$

$$\left[\frac{w_r(x,\bar{z})}{V_s}\right]_\gamma = -\frac{h}{2\pi}\int_0^1\frac{\gamma(z')}{\left(\frac{x}{x_d}\right)^{3/2}}k_1 2h(\bar{z}-z')\left[K(k_1)-E(k_1)-\frac{2\left(\frac{x}{x_d}\right)E(k_1)}{4h^2(\bar{z}-z')^2+\left(\frac{x}{x_d}-1\right)^2}\right]dz'. \quad (2.8\text{-}7)$$

where

$$k_1 = \frac{4\left(\frac{x}{x_d}\right)}{4h^2(\bar{z}-z')^2+\left(\frac{x}{x_d}+1\right)^2}.$$

At the duct itself these equations reduce to those given by Eqs. (2.6-4) and (2.3-1).

The velocities induced by the source cylinder as obtained in Ref. 6 for a general point in space, except on the duct, are

176

$$\left[\frac{w_a}{V_s}(x,\phi,\bar{z})\right]_q = \frac{h}{2\pi}\int_0^1\int_0^{2\pi}\left(\frac{2h(\bar{z}-z')q(\phi',z')}{R^3}\right)d\phi'dz', \qquad (2.8\text{-}8)$$

$$\left[\frac{w_r}{V_s}(x,\phi,\bar{z})\right]_q = \frac{h}{2\pi}\int_0^1\int_0^{2\pi}\frac{[(x/x_d)-\cos(\phi-\phi')]q(\phi',z')}{R^3}d\phi'dz', \qquad (2.8\text{-}9)$$

$$\left[\frac{w_t}{V_s}(x,\phi,\bar{z})\right]_q = \frac{h}{2\pi}\int_0^1\int_0^{2\pi}\frac{\sin(\phi-\phi')q(\phi',z')}{R^3}d\phi'dz'. \qquad (2.8\text{-}10)$$

The velocities induced on the source cylinder itself are found by considering the properties of source surfaces. Such surfaces have a discontinuity in the normal velocity which is given by Eq. (2.2-3). The axial and tangential velocities on the cylinder are found by letting $x = x_d$ in Eqs. (2.8-8) and (2.8-9), respectively. If the source distribution is independent of angle, the tangential induced velocity is zero and Eqs. (2.8-8) and (2.8-10) reduce to

$$\left[\frac{w_a}{V_s}(x,\bar{z})\right]_q = \frac{h}{2\pi}\int_0^1\frac{q(z')k_1}{\left(\frac{x}{x_d}\right)^{1/2}}\left[\frac{2[2h(\bar{z}-z')]E(k_1)}{4h^2(\bar{z}-z')^2+\left(\frac{x}{x_d}-1\right)^2}\right]dz', \qquad (2.8\text{-}11)$$

$$\left[\frac{w_r}{V_s}(x,\bar{z})\right]_q = \frac{h}{2\pi}\int_0^1\frac{q(z')k_1}{\left(\frac{x}{x_d}\right)^{3/2}}\left[K(k_1)-\left(1-\frac{2\frac{x}{x_d}\left(\frac{x}{x_d}-1\right)}{4h^2(\bar{z}-z')^2+\left(\frac{x}{x_d}-1\right)^2}\right)E(k)\right]dz'. \qquad (2.8\text{-}12)$$

On the duct itself these equations reduce to those given by Eq. (2.6-4) and

$$\left[\frac{w_r}{V_s}(x_d\pm0,\bar{z})\right]_q = \frac{h}{2\pi}\int_0^1 q(z')\,k\,[K(k)-E(k)]dz'\pm\frac{1}{2}q(\bar{z}). \qquad (2.8\text{-}13)$$

In the equations just given for the velocities induced by the ring vortices and sources which are dependent on the angle, some simplification can be obtained by expanding the ring vortex strength $\gamma(\phi,z)$ and ring source strength $q(\phi,z)$ in a Fourier series in ϕ. The integration with respect to the angle can, in general, be performed in terms of Legendre functions [14]. This was shown in section II.5. Many of the integrals are Cauchy principal value integrals which have been discussed in previous sections.

In the general problem, trailing vortices are shed from the duct and velocities induced by these vortices must be included. In the presence of the propeller these vortices follow helices to infinity and in the case of nonaxisymmetric duct or the duct at an angle of attack, these vortices follow straight lines to infinity. The velocity induced by helical vortices will be discussed in section

177

III.3. The straight line trailing vortices do not induce any axial velocities and the other components are [6].

$$\left[\frac{w_r}{V_s}(x,\phi,\bar{z})\right]_{\frac{\partial\gamma}{\partial\phi}} = \frac{h}{\pi}\int_0^1\int_0^{2\pi}\frac{\sin(\phi-\phi')}{\left[(x/x_d)^2 + 1 - 2(x/x_d)\cos(\phi-\phi')\right]}$$

$$\times\left[\frac{2h(\bar{z}-z')}{R} + 1\right]\frac{\partial\gamma}{\partial\phi'}\,d\phi'dz' \tag{2.8-14}$$

and

$$\left[\frac{w_t}{V_s}(x,\phi,\bar{z})\right]_{\frac{\partial\gamma}{\partial\phi}} = -\frac{h}{2\pi}\int_0^1\int_0^{2\pi}\frac{\left[\frac{x}{x_d} - \cos(\phi-\phi')\right]}{\left[\left(\frac{x}{x_d}\right)^2 + 1 - 2\left(\frac{x}{x_d}\right)\cos(\phi-\phi')\right]}$$

$$\times\left[\frac{2h(\bar{z}-z')}{R} + 1\right]\frac{\partial\gamma}{\partial\phi'}\,d\phi'dz'. \tag{2.8-15}$$

On the vortex cylinder ($x/x_d = 1$) and the radial velocity reduces to Eq. (2.5-3).

The force F on any section of the duct is given by the Kutta-Joukowski law [12] which can be expressed as

$$F = \rho V\Gamma. \tag{2.8-16}$$

The velocity V is the velocity perpendicular to the direction of the force and Γ is the total circulation about each section. The velocity V does not include the self-induced velocities, i.e., does not contain the velocities induced by the vortex and source rings. To obtain the total force, the force of each section is integrated around the duct.

The induced drag coefficient of the annular airfoil then follows from Eq. (2.8-16) as

$$c_{D_i} = \frac{D_i}{\frac{\rho}{2}V_o^2 aR_d} = -2\int_0^1\int_0^{2\pi}\gamma(\phi,\bar{z})\left(\left[\frac{w_r}{V_o}\right]_{\frac{\partial\gamma}{\partial\phi}} + \left[\frac{w_r}{V_o}\right]_p\right)d\phi\,d\bar{z}. \tag{2.8-17}$$

It should be noted that for the axisymmetrical duct at zero incidence and without the propeller that the induced drag is zero. For the case of the axisymmetrical duct at an angle of incidence this equation reduces to

$$c_{D_i} = -h\int_0^1 g_1(\bar{z})\left(\int_0^1 g_1(z')\left[\pi + \frac{4h(\bar{z}-z')}{k}\left(K(k) - E(k)\right)\right]dz'\right)d\bar{z}. \tag{2.8-18}$$

178

The lift coefficient also follows from Eq. (2.8-16). For the lift coefficient, the lift of each section, $dL(\varphi)$, is determined. This lift is normal to each section and positive outwards. An arbitrary direction must be defined, the lift force of each section determined in that direction ($dL \cos \varphi$), and then integrated around the duct, or

$$c_L = \frac{L}{\frac{\rho}{2} V_o^2 aR_d} = -2 \int_0^{2\pi} \cos\phi \int_0^1 \gamma(\phi,\bar{z}) \left(\left[\frac{w_a}{V_o}\right]_{\frac{\partial\gamma}{\partial\phi}} + \left[\frac{w_a}{V_o}\right]_p - 1 \right) d\bar{z}\, d\varphi .\quad (2.8-19)$$

It is obvious that the axisymmetric duct by itself at zero incidence has no lift and it is not difficult to reason that lift on the axisymmetric duct in the presence of the propeller must be zero. For the case of the axisymmetric duct at an angle of attack, the axial velocity induced by the trailing vortex system is zero and this equation reduces to

$$c_L = 2\pi \int_0^1 g_1(z')\, dz' .\quad (2.8-20)$$

The moment on the axisymmetric duct at zero incidence in the presence of the propeller or not must also be zero. The moment about the leading edge of the axisymmetric duct at an angle incidence is

$$c_M = \frac{M}{\frac{\rho}{2} V_o^2 a^2 R_d} = \frac{\pi}{2} \int_0^1 g_1(\bar{z})(\bar{z}-1)\, d\bar{z} .\quad (2.8-21)$$

Some of these coefficients for the duct at an angle of attack have been tabulated by Weissinger [9]. It should be noted that although the duct at zero incidence produces no lift or moment each section of the duct does and these equations can be used to calculate the stress in the duct if the integration with respect to the angle is carried only around half the duct, i.e., from $-\pi/2$ to $\pi/2$.

III. THE PROPELLER AND ITS INTERACTION WITH THE DUCT

The velocities induced by the duct at the propeller depend on the propeller circulation while the velocities induced by the propeller at the duct depend on the duct circulation. Because of the complexity of the problem, however, these interaction velocities must be assumed known. To consider that they are interdependent implies that the circulation distribution representing the duct and the propeller blade circulation must be determined simultaneously. This, of course, is not possible and one must resort to a method of iteration. For instance, the duct problem could be solved first without the propeller and then using the resulting induced velocities the propeller problem solved. This process is then repeated, using each time the last derived induced velocities, until satisfactory convergence is obtained.

179

In the following sections the velocities induced at the duct by the propeller will be given. The optimum circulation distribution of the propeller while operating in the duct will be derived as well as the circulation induced on the duct by the propeller.

III.1 Velocities Induced by the Propeller at the Duct

Lerbs has developed the theory of the moderately loaded propeller and his general approach was used to derive the equations presented here [6]. In this theory Lerbs considers that the flow about each blade of the propeller can be represented mathematically by a lifting line and a helicoidal trailing vortex sheet. The influence of the induced velocities at the lifting line on the pitch of the helical vortex sheet is considered but the effects of centrifugal force and contraction of the slip-stream is neglected. In addition, the change in shape of the vortex lines are neglected in the axial direction, i.e., they are of constant pitch. The vortex sheets need not form true helical surfaces since the pitch may vary radially but each shed vortex line is of constant pitch.

The boundary condition imposed on the bound circulation is that it be zero at the hub [15]. The circulation at the tip is also zero if there is tip clearance but may have a finite value if there is no clearance. Using these assumptions the velocity required for solving the interaction problem can be derived. Specifically, the radial velocity induced by the propeller at the duct as required has been derived in Ref. 6 as

$$\left[\frac{w_r}{V_s}(x_d, \varnothing, z)\right]_p = \frac{1}{2}\int_{x_h}^{1} G_s'(x_d)\left[i_r^{(1)}\left(\frac{x_o}{x_d}, \varnothing, z\right) - i_r^{(3)}\left(\frac{x_o}{x_d}, \varnothing, z\right)\right]dx_o. \quad (3.1\text{-}1)$$

where $G_s(x_o) = \Gamma(x_o)/2\pi R_p V_s$ is the nondimensional circulation distribution of the propeller,

$$i_r^{(1)}\left(\frac{x_o}{x_d}, \varnothing, z\right) = \left(\frac{x_o}{x_d}\right)\left(\frac{1}{x_d}\right)\sum_{p=1}^{6}\int_0^{\infty}$$

$$\times \left(\frac{\left[\left(\frac{z_p}{x_d}\right) + z\left(\frac{x_o}{x_d}\right)\tan\beta_i\right]\cos(\varnothing - \varnothing_p + z) - \left(\frac{x_o}{x_d}\right)\tan\beta_i\sin(\varnothing - \varnothing_p + z)}{\left[\left(1 - \frac{x_o}{x_d}\right)^2 + \left(\frac{z_p}{x_d} + z\frac{x_o}{x_d}\tan\beta_i\right)^2 + 4\left(\frac{x_o}{x_d}\right)\sin^2\frac{1}{2}(\varnothing - \varnothing_p + z)\right]^{3/2}}\right)dz. \quad (3.1\text{-}2)$$

$$i_r^{(3)}\left(\frac{x_o}{x_d}, \varnothing, z\right) = \frac{1}{x_d}\sum_{p=1}^{b}\left(\frac{\left(\frac{z_p}{x_d}\right)\sin(\varnothing - \varnothing_o)}{\left[\left(\frac{z_p}{x_d}\right)^2 + \sin^2(\varnothing - \varnothing_p)\right]}\right) \quad \begin{matrix}(3.1\text{-}3)\\(\text{Cont.})\end{matrix}$$

$$\times \left[\frac{\left(\dfrac{x_o}{x_d}\right) - \cos(\phi - \phi_p)}{\sqrt{\left(\dfrac{z_p}{x_d}\right)^2 + \left(1 - \dfrac{x_o}{x_d}\right)^2 + 4\left(\dfrac{x_o}{x_d}\right)\sin^2 \dfrac{1}{2}(\phi - \phi_p)}} + \frac{\cos(\phi - \phi_p)}{\sqrt{\left(\dfrac{z_p}{x_d}\right)^2 + 1}} \right] \right) , \qquad (3.1\text{-}3)$$

where

    b is the propeller number of blades,

$\tan \beta_i$ is the hydrodynamic pitch angle of the propeller,

    z_p is the axial coordinate nondimensionalized by the propeller radius,

  $\Gamma(x_o)$ is the local circulation of a propeller blade, and

    ϕ_p is the angular location of propeller blade number.

The function $i_r^{(1)}$ is a nondimensional velocity component induced by the propeller trailing vortex system and $i_r^{(3)}$ is a nondimensional velocity component induced by the propeller bound vortex line. These velocity components are related to Lerbs' induction factors [6] and are dependent only on geometry. Unlike induction factors, they may be singular at certain points and such difficulties are discussed in Ref. 6. The velocity component $i_r^{(1)}$ involves the evaluation of an integral with infinite limits. Through the use of a Fourier series expansion this infinite integral can be evaluated in terms of Bessel functions which must be integrated over a finite limit. This method is discussed in Ref. 6.

III.2 The Propeller Design and the Optimum Circulation
Distribution of a Propeller in a Duct

Lerbs has derived the theory of a moderately loaded propeller [15] and the same theory can be used for the propeller in the duct [6]. The modification of this theory is quite simple if the following propeller section velocity diagram is considered.
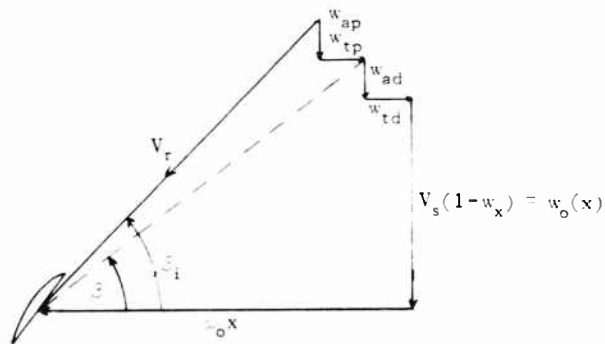
where

ω_o is the angular velocity of the propeller blade,

β is the propeller advance angle,

w_{ap}, w_{tp} are the axial and tangential velocities induced by the propeller itself, and

w_{ad}, w_{td} are the axial and tangential velocities induced by the duct.

The difference between this diagram and that of a free-running propeller is the inclusion of the velocities induced by the duct. Including these velocities in the theory of the moderately loaded propeller results in a simple modification. For instance, the propeller thrust and torque coefficients for inviscid flow become simple [6].

$$\left(c_{T_{s i}}\right)_p = \frac{T_i}{\frac{\rho}{2} R_p^2 \pi V_s^2} = 4b \int_{x_h}^1 G_s(x)\left[\frac{x}{\lambda} - \left(\frac{w_{td}}{V_s} + \frac{w_{tp}}{V_s}\right)\right] dx , \qquad (3.2\text{-}1)$$

$$\left(c_{P_{s i}}\right)_p = \frac{\omega_o Q_i}{\frac{\rho}{2} R_p^2 \pi V_s^2} = \frac{4b}{\lambda_s} \int_{x_h}^1 x\, G_s(x)\left[(1 - w_x) + \left(\frac{w_a}{V_s}\right)_d + \left(\frac{w_a}{V_s}\right)_p\right] dx . \qquad (3.2\text{-}2)$$

where

$$\lambda_s = \frac{V_s}{\omega_o R_p} ,$$

T_i is the inviscid thrust, and

Q_i is the inviscid torque.

For the free-running propeller w_{td} and w_{ad} are zero. The induced velocities w_{tp} and w_{ap} are velocities induced at the lifting line by the vortex system of the propeller. In terms of the induction factors (i_a and i_d) derived by Lerbs [15], these velocities are

$$\left(\frac{w_a}{V_s}\right)_p = \frac{1}{2} \int_{x_h}^1 \frac{dG_s}{dx_o} \frac{1}{(x - x_o)} i_a dx_o$$

and $\qquad (3.2\text{-}3)$

$$\left(\frac{w_t}{V_s}\right)_p = \frac{1}{2}\left[\frac{b}{x} G_s(1) + \int_{x_h}^1 \frac{dG_s}{dx_o} \frac{1}{(x - x_o)} i_t dx_o\right] .$$

The term $G_s(1)$ is the nondimensional circulation at the propeller blade tip which must be zero for the free-running propeller.

In the lifting line theory of the propeller an integro-differential equation is derived [6], using the velocity diagram and Eq. (3.2-3), for the circulation distribution which for the propeller in duct is

$$\frac{1}{2} \int_{x_h}^{1} \frac{dG_s}{dx_o} \frac{1}{(x - x_o)} \left[i_t \tan \beta_i + i_a \right] dx_o = \left[\frac{x}{s} - \frac{w_{td}}{V_s} - \frac{bG_s(1)}{2x} \right] \tan \beta_i$$

$$- (1 - w_x) - \left(\frac{w_a}{V_s} \right) d \qquad (3.2-4)$$

with boundary conditions.

$$G_s(x_h) = 0 \quad \text{and} \quad G_s(1) = \begin{cases} 0 & \text{if } R_p = R_d \\ A & \text{if } R_p = R_d \end{cases}.$$

For the free-running propeller $G_s(1)$, w_{ad} and w_{td} are all equal zero. Since in either the case of the ducted propeller or free-running propeller, the right-hand side of the equation is assumed known, the numerical method given by Lerbs for solution of this equation can be used without modification.

For the free-running propeller a question arises as to what is the circulation distribution so that a propeller produces a given thrust with a minimum amount of power. A similar question arises for the ducted system but the force on the duct itself enters the problem. The problem could also include determination of the shape of the duct as well as the propeller circulation distribution.

The combined problem of optimum duct shape and optimum circulation distribution along the propeller blade is a formidable one since it is not possible, within the concepts of the theory discussed here, to obtain the interference velocities in explicit form. The problem, which can reasonably be solved reduces to the determination of the circulation distribution on a propeller blade so that the propeller produces a given thrust with minimum torque. For a solution it is also necessary to assume that the circulation at the blade tip is zero and that the free-stream velocity is a constant.

A method which can be used for determination of the optimum circulation distribution is the method of the calculus of variations. This method was applied in Ref. 6 to determine the optimum circulation distribution using the assumptions given previously. The result was that circulation must be such that the following equation is satisfied:

$$\frac{\left[1 + \dfrac{w_a(x)}{w_o}\, d + \dfrac{w_a(x)}{w_o}\, p\right] x' - \dfrac{1}{2}\, \dfrac{\partial}{\partial x}\, \displaystyle\int_{x_h}^{1} \dfrac{x'G(x')}{(x'-x)}\, i_a\left(\dfrac{x}{x'}\right) dx'}{\left[\dfrac{x'}{\lambda} - \dfrac{w_t(x')}{w_o}\, d - \dfrac{w_t(x')}{w_o}\, p\right] + \dfrac{1}{2}\, \dfrac{\partial}{\partial x}\, \displaystyle\int_{x_h}^{1} \dfrac{G(x')}{(x'-x)}\, i_t\left(\dfrac{x}{x'}\right) dx'} = \text{constant}. \qquad (3.2\text{-}5)$$

If the integrals in this equation are zero, then this implies $x \tan \beta_i = $ constant. For a free-running, lightly-loaded propeller, $x \tan \beta_i = $ constant is known as Betz's theorem. Betz's theorem was derived using momentum theory so it would not be expected that the more exact theory applied here would give exactly the same results. It would be expected, however, that the integrals in Eq. (3.2-5) would be small.

III.3 The Integral Equation for the Circulation Distribution of the Annular Airfoil in the Presence of the Propeller

In this section it will be assumed that the annular airfoil is axisymmetrical and at zero incidence, however, the free-stream flow need only be axisymmetric. The integral equation for the ring vortex and ring source strength of the annular airfoil of arbitrary shape was derived in section II.5. It was found that the ring source strength was a function of the thickness slope only and since the annular airfoil is assumed axisymmetrical in this section, the ring source strength is given by Eq. (2.2-4). Also in section II.5 the ring vortex strength was found to be given by the integro-differential Eq. (2.5-4). For the annular airfoil with a propeller, the vortex strength is given by a very similar equation. The only difference being that the function $\overline{U}(z, \bar{z})$ must include the radial velocities induced by the propeller at the duct and the duct trailing vortex system applying to the present case must be used.

A trailing vortex is shed from each point on the duct when the bound vortex has an angular variation in strength. As discussed previously the trailing vortex strength is $(1\, R_d)\,(\, , \,)$ and the vortices are shed at an angle equal to the flow angle. In the presence of the propeller, these vortices follow streamlines in the rotating coordinate system. This implies, as in the case of the propeller, that the induced velocities from all the components in the flow field have an effect on the trailing vortex system. This represents a problem considerably more difficult than the propeller problem since the helical vortices are shed from all over the duct rather than along a line. To obtain an equation in a form which is amenable to solution, it will be assumed that the helical vortices are all shed at the advance angle of the duct which is

$$\tan \beta_d = \frac{(1 - w_{xd})}{w_o R_d}\, V_s. \qquad (3.3\text{-}1)$$

The radial velocity induced on the duct by the trailing vortex system was derived in Ref. 6 as

184

$$\left[\frac{w_r}{V_s}\ (x_d,\phi,\bar{z})\right]_{\frac{\partial\gamma}{\partial\phi}} = \frac{h}{2\pi}\int_0^1\int_0^{2\pi}\frac{\partial\gamma}{\partial\phi'}\ (\phi',z')$$

$$\times\left(\int_0^{\infty}\left[\frac{[2h(\bar{z}-z')+a\tan\beta_d]\cos(\phi-\phi'+a)-\tan\beta_d\sin(\phi-\phi'+a)}{\left\{2[1-\cos(\phi-\phi'+a)]+[2h(\bar{z}-z')+a\tan\beta_d]^2\right\}^{3/2}}\right]dx\right)d\phi'dz'.$$

(3.3-2)

This equation is substituted into Eq. (2.5-4) in place of the straight line shed vortices to give the integro-differential equation for the vortex strength. In the present case the function $\bar{U}(\phi,\bar{z})$ is found to be

$$\bar{U}(\phi,\bar{z}) = -\frac{H(\bar{z})}{4\pi} - \left[\frac{w_r}{V_s}\ (x_d,\phi,\bar{z})\right]_p,$$

(3.3-3)

where $H(\bar{z})$ is given by Eq. (2.3-3) and w_{rp} by Eq. (3.3-1).

To solve the resulting integro-differential equation for the vortex strength, the same approach is used as for Eq. (2.5-4) and equations similar to (2.5-7) and (2.5-8) are derived, i.e., a Fourier series expansion is used. The principle difference is that the equations for the Euler coefficients are now coupled. This coupling arises from the form of the duct helical trailing vortex system. The two linear singular integral equations for the Euler coefficients of the ring vortex strength $g_n(\bar{z})$ and $h_n(\bar{z})$, in terms of the known coefficients $u_n(\bar{z})$ and $v_n(\bar{z})$ are

$$u_n(\bar{z}) = \frac{1}{2\pi}\int_0^1\frac{1}{(\bar{z}-z')}\left[g_n(z')\ M_n(\bar{z}-z') + h_n(z')\ i_n^{(c)}(\bar{z}-z')\right]dz'.$$

(3.3-4)

$$v_n(\bar{z}) = \frac{1}{2\pi}\int_0^1\frac{1}{(\bar{z}-z')}\left[-g_n(z')\ i_n^{(c)}(\bar{z}-z') + h_n(z')\ M_n(\bar{z}-z')\right]dz'.$$

where

$$M_n(\bar{z}-z') = -8[h(\bar{z}-z')]^2\left[Q'_{n+\frac{1}{2}}(\bar{k})-nQ_{n-\frac{1}{2}}(\bar{k})\right] - i_n^{(s)}(\bar{z}-z')$$

$$\bar{k} = 1 + 2h^2(\bar{z}-z')^2.$$

(3.3-5)

$$i_n^{(c)}(\bar{z}-z') = n[2h(\bar{z}-z')]\int_{-\pi}^{\pi}\cos n\theta$$

$$\times\left(\int_0^{\infty}\left[\frac{[2h(\bar{z}-z')+a\tan\beta_d]\cos(\theta+a)-\tan\beta_d\sin(\theta+a)}{\left\{[2h(\bar{z}-z')+a\tan\beta_d]^2+4\sin^2\frac{1}{2}(\theta+a)\right\}^{3/2}}\right]da\right)d\theta$$

(3.3-6)

185

$$i_n^{(s)}(\bar{z} - z') = n[2h(\bar{z} - z')] \int_{-\pi}^{\pi} \sin n\theta$$

$$\times \left(\int_0^{\pi} \left[\frac{[2h(\bar{z} - z') + a\tan\beta_d]\cos(\theta + a) - \tan\beta_d \sin(\theta + a)}{\left\{ [2h(\bar{z} - z') + a\tan\beta_d]^2 + 4\sin^2\frac{1}{2}(\theta + a) \right\}^{3/2}} \right] da \right) d\theta$$

$$\tag{3.3-7}$$

$$u_n(\bar{z}) = \begin{cases} -\dfrac{b}{2\pi x_d} \displaystyle\int_{x_h}^1 G_s'(x_o) \left(\dfrac{x_o}{x_d}\right) \left[j_{nc}^{(1)}\left(\dfrac{x_o}{x_d}, \bar{z}\right) \right] dx_o, & \text{if} \quad n = mb \\ & \qquad m = 1, 2, 3 \ldots \\[4pt] 0, & \text{if} \quad n \neq mb \end{cases}$$

$$v_n(\bar{z}) = \begin{cases} -\dfrac{b}{2\pi x_d} \displaystyle\int_{x_h}^1 G_s'(x_o) \left(\dfrac{x_o}{x_d}\right) \left[j_{ns}^{(1)}\left(\dfrac{x_o}{x_d}, \bar{z}\right) \right] + 4h(\bar{z} - a_t)\left[i_{rn}^{(g)}\left(\dfrac{x_o}{x_d}, \bar{z}\right) \right] dx_o, \\ & \text{if} \quad n = mb \\ & \qquad m = 1, 2, 3 \ldots \\[4pt] 0, & \text{if} \quad n \neq mb \end{cases}$$

$$i_{rn}^{(3)}\left(\frac{x_o}{x_d}, \bar{z}\right) = (-1)^{n-1}\left(\frac{x_o}{x_d}\right)^{1/2} k^2 \int_0^{\pi/2} \frac{\sin 2n\psi \, \sin 2\psi \, d\psi}{[4h^2(\bar{z} - a_t)^2 + \sin^2 2\psi]\sqrt{1 - k^2\sin^2\psi}}$$

$$+ (-1)^{n-1}\left(\frac{x_o}{x_d}\right)^{-1/2}\frac{k^2}{2} \int_0^{\pi/2} \frac{\sin 2n\psi \, \sin 4\psi \, d\psi}{[4h^2(\bar{z} - a_t)^2 + \sin^2 2\psi]\sqrt{1 - k^2\sin^2\psi}}$$

$$- \frac{1}{2\sqrt{4h^2(\bar{z} - a_t)^2 + 1}} \int_0^{\pi/2} \frac{\sin 2n\psi \, \sin 4\psi \, d\psi}{[4h^2(\bar{z} - a_t)^2 + \sin^2 2\psi]}, \quad k^2 \neq 1$$

For $k^2 = 1$ $\quad i_{rn}^{(3)} = 0$.

$$k^2 = \frac{4\left(\dfrac{x_o}{x_d}\right)}{4h^2(\bar{z} - a_t)^2 + \left(1 - \dfrac{x_o}{x_d}\right)^2}$$

$$j_{nc}^{(1)}\left(\frac{x_o}{x_d}, \bar{z}\right) = \int_{-\pi}^{\pi} \cos n\bar{\alpha}$$

$$\times \left(\int_0^z \left[\frac{\left[2h(\bar{z}+a_t) + \alpha\left(\frac{x_o}{x_d}\right)\tan\beta_i \right]\cos(\bar{\alpha}+\alpha) - \left(\frac{x_o}{x_d}\right)\tan\beta_i \sin(\bar{\alpha}+\alpha)}{\left[\left(1-\frac{x_o}{x_d}\right)^2 + \left[2h(z+a_t)+\alpha\frac{x_o}{x_d}\tan\beta_i\right]^2 + 4\left(\frac{x_o}{x_d}\right)\sin^2\frac{1}{2}(\bar{\alpha}+\alpha)\right\}^{3/2}} \right] d\alpha \right) d\bar{\alpha}$$

$$\bar{j}_{ns}^{(1)}\left(\frac{x_o}{x_d}, \bar{z}\right) = \int_{-\pi}^{\pi} \sin n\bar{\alpha}$$

$$\times \left(\int_0^\alpha \left[\frac{\left[2h(\bar{z}+a_t) + \alpha\left(\frac{x_o}{x_d}\right)\tan\beta_i \right]\cos(\bar{\alpha}+\alpha) - \left(\frac{x_o}{x_d}\right)\tan\beta_i \sin(\bar{\alpha}+\alpha)}{\left[\left(1-\frac{x_o}{x_d}\right)^2 + \left[2h(\bar{z}+a_t)+\alpha\frac{x_o}{x_d}\tan\beta_i\right]^2 + 4\left(\frac{x_o}{x_d}\right)\sin^2\frac{1}{2}(\bar{\alpha}+\alpha)\right\}^{3/2}} \right] d\alpha \right) d\bar{\alpha}.$$

From the equations for $u_n(\bar{z})$ and $v_n(\bar{z})$ it can easily be concluded that no Euler coefficients $g_n(z)$ and $h_n(z)$ exist, except for $g_o(z)$, which are not harmonic with the number of blades. From a practical point of view this fact greatly reduces the number of coefficients which must be calculated. The integrals occurring in the equations for $i_n^{(c)}$, $i_n^{(s)}$, $j_{nc}^{(1)}$ and $j_{ns}^{(1)}$ have been discussed in more detail in Ref. 6 with particular reference to their evaluation and the singularities occurring. It was found possible to obtain the infinite integrals in the form of Bessel and Struve functions which considerably simplifies their evaluation.

The coupled integral equations for the function g_n and h_n, Eq. (3.3-4), can be reduced to two coupled Fredholm equations of the second kind by application of the method of section II.3. With the boundary condition that $g_n(0)$ and $h_n(0) = 0$, these coupled Fredholm equations of the second kind and their solution is discussed in Ref. 6. It should be mentioned that Ordway in Ref. 5 used a somewhat different approach for obtaining the Euler coefficients.

Of particular interest is the zero order case of Eq. (3.3-4). It can easily be shown that for $n = 0$ that this equation reverts to Eq. (2.3-1) with a term added to the right-hand side for the average radial velocity induced by the propeller which causes no difficulty. The average radial velocity induced at the duct by the propeller is found by letting $n = 0$ in Eq. (3.3-7). The equation for the average velocity induced by the propeller then can be reduced to

$$\left[\frac{w_r}{V_s}\right]_{P_{aver}} = \frac{2b}{\pi x_d} \int_{x_h}^1 \frac{G_o' x_o}{\tan\beta_i} \frac{1}{k} \left(\frac{x_d}{x_o}\right)^{3/2} \left[(2-k^2) K(k) - 2E(k)\right] dx_o. \quad (3.3-8)$$

187

where

$$k^2 = \frac{4\left(\dfrac{x_o}{x_d}\right)}{\left(1 + \dfrac{x_o}{x_d}\right)^2 + 4h^2(\bar{z} + a_t)^2}$$

It should be noted that the bound vortices do not contribute to the average radial velocity. Using this equation the singular integral equation for the vortex distribution becomes

$$\oint_0^1 g(\bar{z} - z') \frac{\gamma(z')}{(\bar{z} - z')} \, dz' = H(\bar{z}) + 2\pi\left[\frac{w_r}{V_s}\right]_{P_{aver}}$$

This is such a simple modification to Eq. (2.3-1) that it is not necessary to discuss its solution. Of interest is that Eq. (3.3-8) represents the velocity induced at the duct by a propeller with an infinite number of blades.

IV. COMMENTS ON THE USE OF THE ANNULAR AIRFOIL AND DUCTED PROPELLER THEORY

In problems of the type discussed in this paper physical reality very often becomes lost in mathematical details. As the difficulty of the problem increases these details become more involved and detract immeasurably from the physical significance of the problem. The actual numerical values of the often discussed ring vortex and ring source strength, for instance, reveal little information as to the performance of annular airfoils and ducted propellers. To somewhat offset the mass of mathematical details developed so far in this paper, this section will be devoted to a discussion of the use of these theories and the progress of numerical calculations and experimental verification. The annular airfoil will be discussed first and then, the ducted propeller, both without out regard to the validity of the assumptions made.

IV.1 Applying the Annular Airfoil Theory

Many problems concerning the annular airfoil were considered in the previous sections and each of these will be discussed considering application of the theory. The first is the "direct" problem of the axisymmetric annular airfoil for which the annular airfoil shape is given. The problem might be posed as follows: For an axisymmetric annular airfoil, determine the pressure distribution and forces on and the flow field around the foil. For this problem the following steps must be followed.

1. Describe the annular airfoil section by a thickness distribution, camber distribution and angle of attack as shown in Fig. 2.

2. With the thickness distribution calculate the ring source strength from Eq. (2.2-4) and with the camber distribution and angle of attack, calculate the ring vortex strength from Eq. (2.3-8).

3. The total velocity induced at a point in space by the annular airfoil is found by summing the velocities induced by the ring vortex and ring source. The induced axial and radial velocities from the ring vortex are calculated from Eqs. (2.8-6) and (2.8-7) and the induced axial and radial velocities from the ring source are calculated from Eqs. (2.8-11) and (2.8-12). For the axisymmetric annular airfoil, the tangential induced velocity is zero.

4. To determine the pressure distribution on the duct, the axial velocity induced by the ring vortex and source on the duct is substituted into Eq. (2.6-1). On the duct itself, the axial velocity induced by the vortex ring is given by Eq. (2.6-4) and that induced by the source ring is given by Eq. (2.6-5). For better results each of these induced velocities should be corrected by the approximate nonlinear theory as given by Eq. (2.7-13).

5. For the axisymmetric annular airfoil at zero incidence, no net forces act on the duct except for viscous drag. The viscous drag problem is considered in Ref. 10.

This problem of the axisymmetric annular airfoil has been programmed for the high-speed digital computers at the David Taylor Model Basin and preliminary results are available. All the coefficients occurring in this problem which are independent of the thickness and camber will be tabulated. For verifying the theory three annular airfoils have been designed and built and are presently being tested. It should be mentioned that Weissinger used a different approach for this problem and has tabulated a number of coefficients for his method.

The second problem considered will be to determine the pressure distribution and forces on and the flow field around an axisymmetric annular airfoil of a given shape at an angle of incidence. The linearized flow field about such a duct was shown to be a linear combination of the flow about the airfoil at zero incidence and an Euler coefficient involving the angle of incidence. Since the first part is the same as the previous problem only the angle of incidence term need be considered in detail.

1. The Euler coefficient, $g_o(z)$, is calculated from Eq. (2.5-11) and the contribution to the circulation of this term is obtained from Eq. (2.5-12).

2. The total velocity induced at a point in space is found by adding the velocities obtained in step 3 of the previous problem to velocities obtained from the added circulation term $g_1(z) \cos z$, and the trailing vortex system which arises. The axial, radial and tangential velocities induced by the added circulation term are given by substituting the added circulation into Eqs. (2.8-1), (2.8-2) and (2.8-3). The radial and tangential velocities induced by the trailing vortex system are obtained from Eqs. (2.8-14) and (2.8-15). For the trailing vortex system arising in this problem, there is no induced axial velocity.

3. To determine the pressure distribution, the axial velocity induced by the added circulation term is substituted into Eq. (2.6-1) and the resulting

189

pressure added to that obtained in step 4 of the previous problem. On the duct itself, the axial velocity induced by the added circulation is obtained from Eq. (2.8-5). This velocity should also be corrected by Eq. (2.7-13).

4. The induced drag, lift and moment on the annular airfoil at an angle of incidence are obtained by substituting the values of the Euler coefficient, $g_1(z)$, calculated in step 1 into Eqs. (2.8-18), (2.8-20) and (2.8-21). To the induced drag must be added the viscous drag as discussed in step 5 of the previous problem.

The third problem to be considered is to determine the ideal angle of attack of a section of an axisymmetric annular airfoil when the camber and thickness distributions are given. The forces and the flow around the resulting annular airfoil are also desired.

1. The ideal circulation distribution is calculated from Eq. (2.4-2) and substituted into Eq. (2.4-5) to obtain the section ideal angle of attack.

2. The ideal circulation is used in problem one to obtain the flow field and pressure distribution. The only net force is the viscous drag force.

This problem is programmed for the high-speed computers at DTMB and preliminary results are available. All coefficients occurring in this problem which are independent of the section shape, will be tabulated. Experimental verification will be undertaken at some future date.

The fourth problem is to determine the pressure distribution and forces on and the flow field around an asymmetrical annular airfoil of a given shape. The steps are as follows:

1. Describe the annular airfoil sections by a thickness distribution, camber distribution and angle of attack as shown in Fig. 2. For this problem the sections are a function of their angular position.

2. With the thickness distribution, calculate the elemental ring source strength from Eq. (2.5-3). With the camber distribution and section angle of attack, calculate the Euler coefficients for the elemental ring vortex strength from Eqs. (2.5-7) and (2.5-8). The elemental ring vortex strength is then obtained from Eq. (2.5-5). Since the annular airfoil is asymmetrical, trailing vortices are generated. The strength of these is calculated using Eq. (2.5-6).

3. The total velocity induced at a point in space is found by summing the velocities induced by the ring vortex, ring source and the trailing vortex system. The axial, radial and tangential velocities induced by the ring vortices are given by Eqs. (2.8-1), (2.8-2) and (2.8-3) and the radial and tangential velocities induced by the trailing vortices are given by Eqs. (2.8-14) and (2.8-15). For the source ring the axial, radial and tangential velocities are given by Eqs. (2.8-8), (2.8-9) and (2.8-10). As for problem 2 the trailing vortices induce no axial velocity.

4. To determine the pressure distribution on the duct, the axial velocity induced by the ring vortex and source are substituted into Eq. (2.6-1). For this

problem the pressure distribution on a section is a function of the angular position of that section. The axial velocity induced by the ring vortex on the duct is given by Eq. (2.8-5) and the axial velocity induced by the ring source is given by Eq. (2.8-8) with $x = x_d$. These velocities should also be correction by the approximate nonlinear theory as given by Eq. (2.7-13).

5. The induced drag and lift of the asymmetric annular airfoil are given by Eqs. (2.8-17) and (2.8-19). The velocities induced by the trailing vortices have been discussed in step 3.

No plans have been made to program this problem at the present time. Some of the coefficients which arise have been tabulated, however.

The fifth problem is the "inverse" problem, i.e., given a pressure distribution on an axisymmetric annular airfoil at zero incidence, determine the section thickness and camber distribution and angle of attack. The steps for this problem are as follows:

1. Using the pressure distribution, calculate the axial velocity on the inner and outer surfaces from Eq. (2.6-1).

2. With the velocity on the inner and outer surfaces, calculate a mean velocity and a velocity difference from Eqs. (2.6-7) and (2.6-9).

3. With the velocities just calculated, the slope of the thickness distribution can be obtained from Eq. (2.6-15).

4. The slope of the camber distribution and angle of attack combined is obtained from Eq. (2.3-1) using the thickness slope just calculated and the vortex strength obtained from Eq. (2.6-10). The camber and angle of attack are separated by integrating the combined slope for the trailing edge to the leading edge. Since the integral over this range of the camber slope is zero, the result will give the tangent of the angle of attack.

This particular problem will not be programmed for the computers nor will experimental results be obtained until problem one and two are satisfactorily in hand.

IV.2 Applying the Ducted Propeller Theory

Because of the more complicated nature of the problem, it is not possible to give as much detail in a step-by-step procedure for problems of the ducted propeller as for the annular airfoil. The first problem to be considered is to design a propeller for operation in an axisymmetrical duct of a given shape so that a given total thrust is obtained.

1. Using problem one of the previous section calculate the axial velocity induced at the propeller by the duct.

2. With this velocity go through a propeller design as described in section 3.2 using an assumed hydrodynamic pitch distribution. Calculate the radial velocity induced on the duct from Eq. (3.1-1).

3. With this propeller induced radial velocity, calculate the Euler coefficients of the duct circulation from Eq. (3.3-4) and then the elemental duct circulation from Eq. (2.5-5). Helicoidal trailing vortices are generated and their elemental strength is calculated from Eq. (2.5-6).

4. The axial and tangential velocities induced by the duct at the propeller must be calculated next. Velocities induced by the ring sources, ring vortices and trailing vortex system must be summed. The axial velocities induced by the ring sources were obtained in step one and remain unchanged. The axial and tangential velocities induced by the ring vortices are given by Eqs. (2.8-1) and (2.8-2). Equations for the axial and tangential velocities induced by the duct helicoidal trailing vortex system have been derived in Ref. 6.

5. With the axial and tangential velocities induced by the duct at the propeller, again go through a propeller design as discussed in step two.

6. Repeat steps 3 through 5 until the computed value of the duct circulation converges. When convergence has been obtained, calculate the induced duct drag from Eq. (2.8-17) and the viscous drag from Ref. 10. Calculate the thrust of the propeller from section 3.2 and add the duct drag to this thrust.

7. The net thrust is then compared to the design thrust and if the comparison is not satisfactory the propeller pitch must be changed and steps 3 to 6 repeated until a satisfactory comparison is obtained.

8. Once the ducted propeller produces the desired thrust, the propeller design can be completed as discussed in Ref. 6.

The second problem to be discussed is to determine the ideal angle of attack of the duct section when the propeller is within the duct. The ideal angle can only be considered for the average velocity induced on the duct by the propeller.

1. Calculate the average radial velocity induced on the duct by the propeller from Eq. (3.3-8).

2. With this radial velocity calculate the ideal circulation distribution from Eq. (2.4-2) where the function $H(z)$ is modified as shown in Eq. (3.3-9).

3. Substitute this circulation distribution into Eq. (2.4-5) and calculate the section ideal angle of attack.

The third problem to be discussed is to determine the annular airfoil shape from the pressure distribution when a propeller of a given design is within the duct. This problem can, also, only be done for the average velocity induced by the propeller.

1. Calculate the average axial velocity induced by the propeller at the duct from Ref. 6.

2. Calculate the section shape with this axial velocity included using problem five of the previous section. The equations cited in this problem all include reference to the average propeller induced velocity.

Programming of the first problem discussed in this section is being pursued and many of the functions will be tabulated. The last two problems can be solved by simple modifications to programs discussed in the previous section. Computer programs which are being developed in this section will incorporate the last two problems.

Another problem which could be considered is to determine the optimum circulation distribution for a ducted propeller. Once a propeller circulation is obtained a check can be made by using Eq. (3.2-5) to see if it is optimum. If it is not, it is not a simple matter to obtain the optimum. The integrals in Eq. (3.2-5) will be computed for a number of designs to determine their magnitude. For a first estimate of the optimum circulation distribution, it would probably be best to neglect these integrals and then, the optimum circulation can easily be obtained since the equation would imply that $x \tan \beta_i$ is a constant.

V. CONCLUSIONS

It is hoped that the theory of the annular airfoil and ducted propeller has been given in enough detail so that some appraisal can be made of the adequacy of the theory. Certain mathematical details which are important are not given to keep the paper of reasonable length. In all cases where questions may arise, however, adequate coverage can be found in the references.

The validity of many of the assumptions cannot be assessed without more complete experimental results. Two assumptions are made, i.e., of an inviscid fluid and that the propeller can be represented by a lifting line, with full realization that for adequate representation of the flow corrections must be made. Accepting the validity of the assumptions, the following comments can be made about the theory of annular airfoils and ducted propellers.

1. Linearization of the annular airfoil boundary conditions results in the radial velocities induced by the singularities in the flow being equal to the airfoil surface slope on a cylinder representing the duct.

2. The strength of the annular airfoil source is dependent only on the thickness slope.

3. The strength of the annular airfoil vortex depends on both camber and thickness and radial velocities induced by other singularities.

4. When the duct is not axisymmetric, is at an angle of incidence, or is in the presence of other singularities in the flow, trailing vortices are shed from the duct.

193

5. In the presence of the propeller, the only Euler coefficients of the circulation strength of the duct which arise are those which are harmonic with the number of blades. The zero-order term includes the average radial velocity induced at the duct by the propeller and the annular airfoil thickness and camber.

6. The induced drag of the duct is zero if the duct is by itself at zero incidence and axisymmetric.

VI. ACKNOWLEDGMENT

Some of this work has been carried out as part of the Fundamental Hydromechanics Research Program of the Bureau of Ships, which is directed and administered for the Bureau by the David Taylor Model Basin. I wish to express my appreciation to Dr. W. L. Haberman and LCDR N. O. Larson for their review of this paper. I am also grateful for the contributions of Mr. E. B. Caster and Mr. O. Stephans.

VII. NOTATION

a duct chord

a_1 axial distance between leading edge of duct and propeller

a_x axial distance between trailing edge of duct and propeller

b number of blades

$c_1(z)$ mean line ordinate of the duct section measured from the nose-tail line

$E(k)$ complete elliptic integral of the second kind

G_s nondimensionalized circulation distribution of the propeller

h $(a/2R_d)$ chord-diameter ratio of the duct

k modulus of the elliptic integrals

$K(k)$ complete elliptic integral of the first kind

Q propeller torque

q ring source strength

R_d duct radius

R_p propeller radius

(r, z, θ) cylindrical coordinates

194

Theory of the Annular Airfoil and Ducted Propeller

$s(z)$ half-thickness ordinate of the duct section

T propeller thrust

V_s ship speed

w_a axial component of induced velocity

$w_o(r)$ radial component of induced velocity

w_t tangential component of induced velocity

w_x local wake fraction

x, r, z nondimensionalized cylindrical coordinates

x radial coordinate nondimensionalized by the propeller radius

z axial coordinate nondimensionalized by the duct chord

z_p axial coordinate nondimensionalized by the propeller radius

z $z - a_x$

   angle of attack of a duct section

$i d$ ideal angle of attack of duct section

   relative angle between free-stream velocity and duct

   propeller advance angle

d duct advance angle

   propeller hydrodynamic pitch angle

   ring vortex strength

o angular velocity

Subscripts

d duct

p propeller

q ring source

   ring vortex

   trailing vortex system of the vortex cylinder

Note: Many functions are defined in the text.

195

REFERENCES

1. Manen, J.D. van, "Open-Water Test Series with Propellers in Nozzles," International Shipbuilding Progress, Vol. 1, No. 2 (1954), pp. 83-108.

2. Manen, J.D. van, "Recent Research on Propellers in Nozzles," Journal of Ship Research (1957), Vol. 2, pp. 13-46.

3. Manen, J.D. van, and Superina, A., "The Design of Screw Propellers in Nozzles," International Shipbuilding Progress, Vol. 6, No. 55 (1959), pp. 95-113.

4. Manen, J.D. van, "Effect of Radial Load Distribution on the Performance of Shrouded Propellers," Presented to the Royal Institution of Naval Architects, London, March 29, 1962.

5. Ordway, D.E., Sluyter, M.M., and Sonnerrup, V.O.V., "Three-Dimensional Theory of Ducted Propellers," Therm Advance Research Report TAR-TR602, Therm, Inc., Ithaca, New York (Aug. 1960).

6. Morgan, W.B., "A Theory of the Ducted Propeller with a Finite Number of Blades," University of California, Institute of Engineering Research, Berkeley (May 1961).

7. Sacks, A.H. and Burnell, J.A., "Ducted Propellers — A Critical Review of the State of the Art," to be published in "Progress in Aeronautical Sciences," Vol. 2, Pergamon Press, New York (1962).

8. Dickmann, H.E., "Grundlagen zur Theorie ringförmigen Tragflügel (frei umströmte Düsen)," Ingenieur-Archiv, Vol. 11 (1940, pp. 36-52). (Translation, Polytechnic Institute of Brooklyn Pibal Report 353.)

9. Weissinger, J., "Zur Aerodynamik des Ringflügels, I. Die Druckverteilung dunner, fast drehsymmetrischer Flügel in Unterschallströmung," Deutsche Versuchsanstalt Für Luftfahrt, E.V. Bericht Nr. 2, Mulheim (Sep. 1955). (Translation, David Taylor Model Basin, DTMB Aero Report 899.)

10. Weissinger, J., "Ring Airfoil Theory — Problems of Interference and Boundary Layer," ARDC Contract AF 61 (514-1207), ASTIA AD No. 211609.

11. Muskhelishvili, N.I., "Singular Integral Equations," P. Noordhoff, N.V. Groninge, Holland (1953).

12. Robinson, A. and Laurmann, J.A., "Wing Theory," Cambridge University Press, Great Britain (1956).

13. Mikhlin, S.G., "Integral Equations," Pergamon Press, New York (1957).

14. Sluyter, M.M., "A Computational Program and Extended Tabulation of Legendre Functions of Second Kind and Half-Order," TAR-TR 601, Therm Advanced Research, August 1960.

15. Lerbs, H.W., "Moderately Loaded Propellers with a Finite Number of Blades and an Arbitrary Distribution of Circulation," Transactions SNAME, Vol. 60 (1952), pp. 73-123.

*   *   *

DESIGN DIAGRAMS OF THREE-BLADED
CONTROLLABLE PITCH PROPELLERS

Kiyoshi Tsuchida
Transportation Technical Research Institute
Tokyo, Japan

1. INTRODUCTION

Controllable pitch propellers have been widely used for tug boats, fishing boats, ferries, etc. in Japan. To study the performance of the controllable pitch propellers, the open water tests of their models have been performed by the author at the Model Basin of Transportation Technical Research Institute for several types of propellers. The tests results and the design diagrams of three-bladed controllable pitch propellers are reported here.*

2. MODEL PROPELLERS

The particulars, dimensions and forms of the model propellers are shown in Table 1, Table 2 and Fig. 1 respectively. The diameter of the propellers is 0.22 meters and the boss ratio 0.34. The blade sections are nearly similar to the Wageningen B-series aerofoils. There are two series of propellers with the expanded blade area ratios of 0.35 and 0.50. As shown in Fig. 1, the two series of the propellers have the same form of bosses and have the same section shape at the roots of the blades. Four model propellers having the constant initial pitch ratios of 0.4, 0.6. 0.8 and 1.0 were manufactured for each of the series of propellers.

As shown in Fig. 2-a, the model propellers are of built-up type and each of the blades of the propellers can be fixed to the boss by four set-screws. In these experiments four bosses have been manufactured. The tapped holes on the sides of each boss are made at an interval of 20-degree and the tapped holes of each

Table 1
Model Propellers and Test Conditions

M.P. No.		979	980	981	982	983	984	985	986
Diameter (m)			0.220				0.220		
Boss ratio			0.340				0.340		
Pitch ratio		0.400	0.600	0.800	1.000	0.400	0.600	0.800	1.000
Expanded area ratio			0.350				0.500		
Max. blade width ratio			0.319				0.473		
Mean blade width ratio			0.278				0.397		
Blade thickness ratio			0.050				0.050		
Angle of rake			0				0		
Number of blades			3				3		
Test Condi-tions	Revolution per minutes (m)		11				11		
	Immersion of shaft (m)		0.220				0.220		
	Temperature of water (c°)		14.3 - 17.0				14.3 - 18.5		
	Reynolds number (nD^2/ν)		$4.6 - 4.9 \times 10^5$				$4.6 - 5.1 \times 10^5$		

Table 2
The Ordinates of the Blade Sections

r R	Distance of the Ordinates from the Max. Thickness											
	To Trailing Edge					To Leading Edge						
	100%	80%	60%	40%	20%	20%	40%	60%	80%	90%	95%	100%
	(Ordinates for the Back)											
0.40	-	48	70	86	97	98	93	84	70	60	52	-
0.50	-	44	18	86	97	98	92	82	67	56	48	-
0.70	-	40	66	85	96	98	89	75	56	43	35	-
0.90	-	45	70	87	97	97	87	70	45	30	24	-
0.95	-	45	70	89	97	97	89	70	45	32	25	-
	(Ordinates for the Face)											
0.40	18	6	2	-	-	-	-	2	7	13	18	35
0.50	10	2	-	-	-	-	-	-	4	9	13	30
0.70	-	-	-	-	-	-	-	-	-	-	2	16

Note: The ordinates are given in percent of the max. thickness of the section.
The thickness at the blade tip is 3% of the diameter.

200

Design Diagrams of Three-Bladed Controllable Pitch Propellers
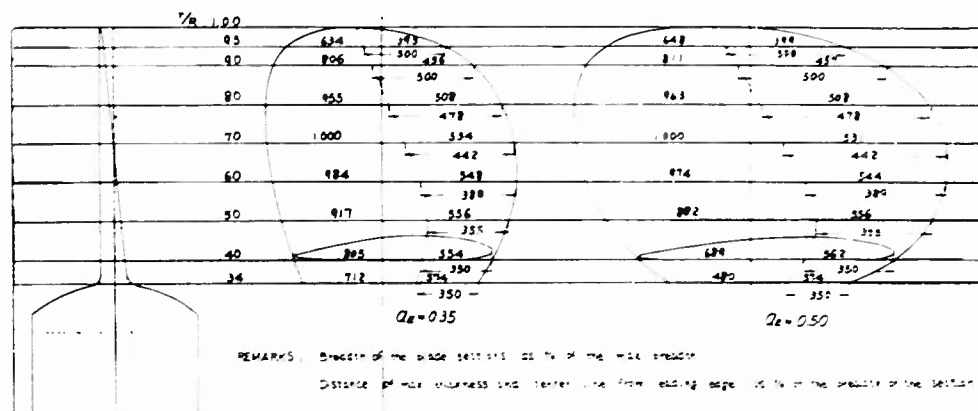
Fig. 1 - General plan of the three-bladed controllable pitch propellers

a. old type   b. new type
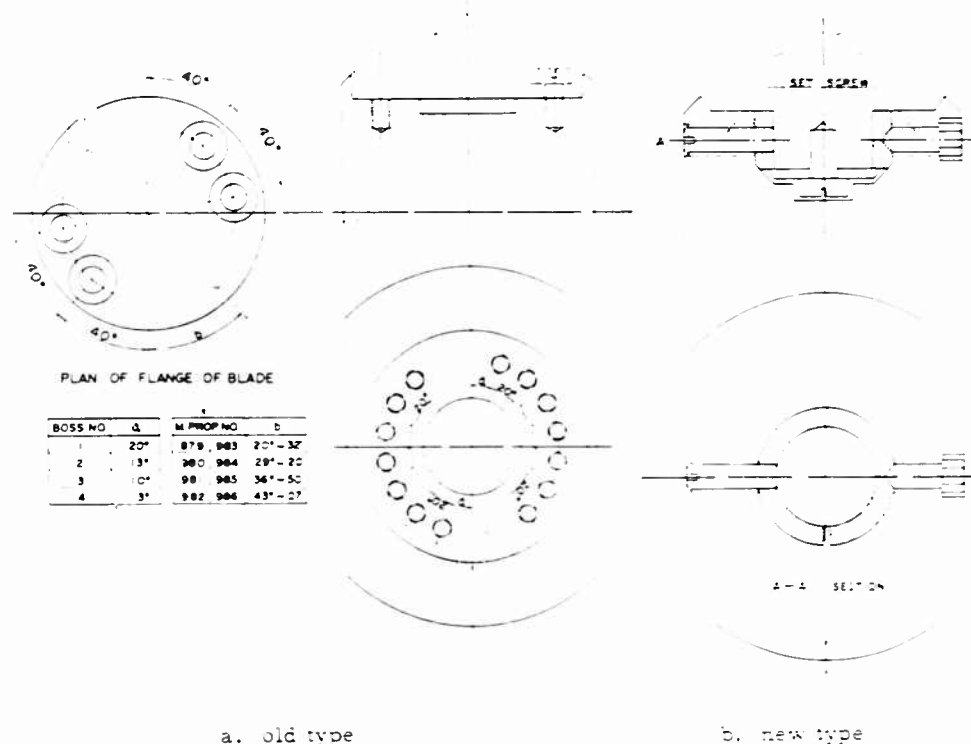
Fig. 2 - Arrangement of bosses

boss differ in position by 5-degree, so that the angle of the blade installation might be changed every 5-degree by using the four bosses in turns. Using four bosses in turns also makes the arrangements of tests easy.

In recent experiments the blades can be fixed to the boss at any given angle, using the models as shown in Fig. 2-b.

3. OPEN WATER TESTS

Model tests were conducted by changing the speed of advance of the propellers with the constant number of revolutions, 11 revolutions per second. As the water temperature at the time of the tests was 14.3°-18.5°C, Reynolds number ($nD^2 \nu$) was 4.6-5.1×10^5. The immersion of the propeller shaft was 0.22 meters.

The angle of the blade installation was changed every 5.0-degree on the basis of the initial pitch ratio ($\theta = 0^\circ$) as follows:

Initial pitch ratio	0.4	0.6	0.8	1.0
Range of blade installation angle ($\circ$)	-25° $--20^\circ$	-30° $--15^\circ$	-35° $--10^\circ$	-40° $--5^\circ$

As the blade angle is turned toward the negative side, the thrust and the torque of the propellers become gradually smaller. The thrust becomes nearly zero at the zero speed of advance of the propellers when the blade angles are about -10°, -15°, -20° and -25° for the propellers of initial pitch ratios of 0.4. 0.6, 0.8 and 1.0 respectively.

Tests of the astern conditions were conducted with the propellers of much smaller blade installation angles. In this case the propellers were installed reversely to the shaft of the propeller dynamometer which revolved reversely.

4. TESTS RESULTS AND DESIGN DIAGRAMS

The tests results are shown in Figs. 3-6 for the series of propellers of 0.35 expanded area ratio and in Figs. 7-10 for the series of 0.50 in the dimensionless form. The symbols in the figures are given as follows:

the thrust coefficient $\quad - \; K_T = T \; n^2 D^4$

the torque coefficient $\quad - \; K_Q = Q \; n^2 D^5$

the advance coefficient $\quad - \; J = v_A \, nD$

the propeller efficiency (open) $- \; \eta_o = J K_T \, 2 \pi K_Q$

where

T = the thrust of the propeller with the boss resistance deducted (kg)

202
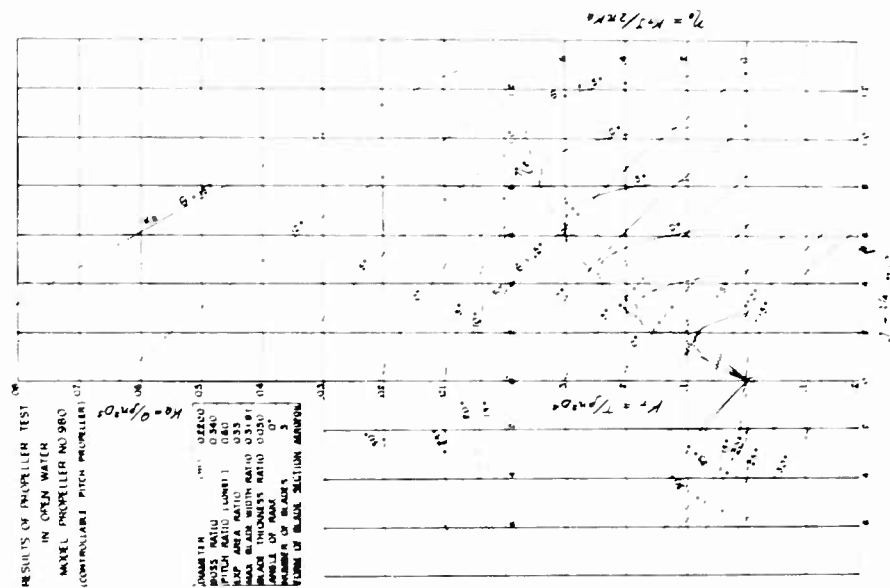
Fig. 4 — Test results (M.P. No. 980)

Fig. 3 — Test results (M.P. No. 979)

203
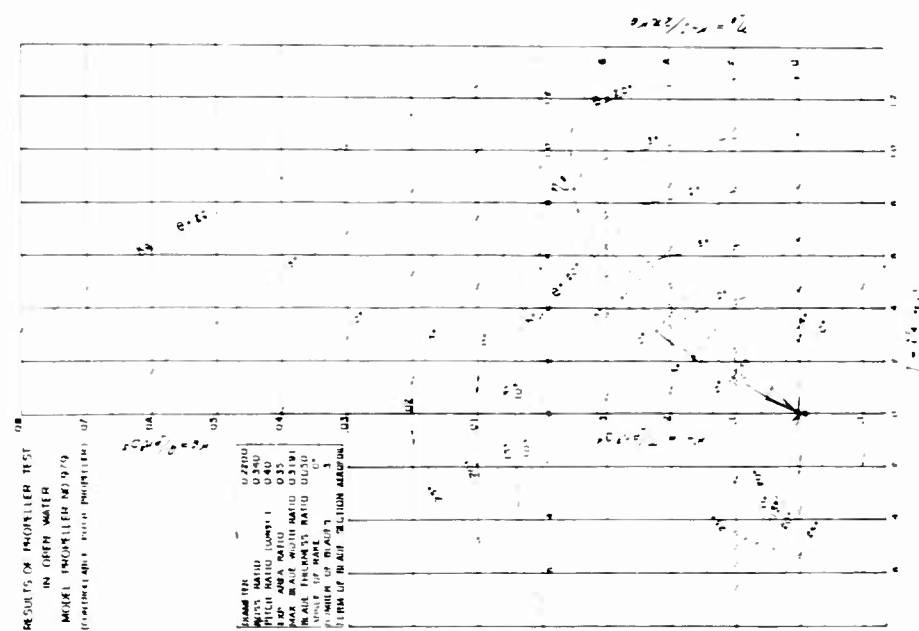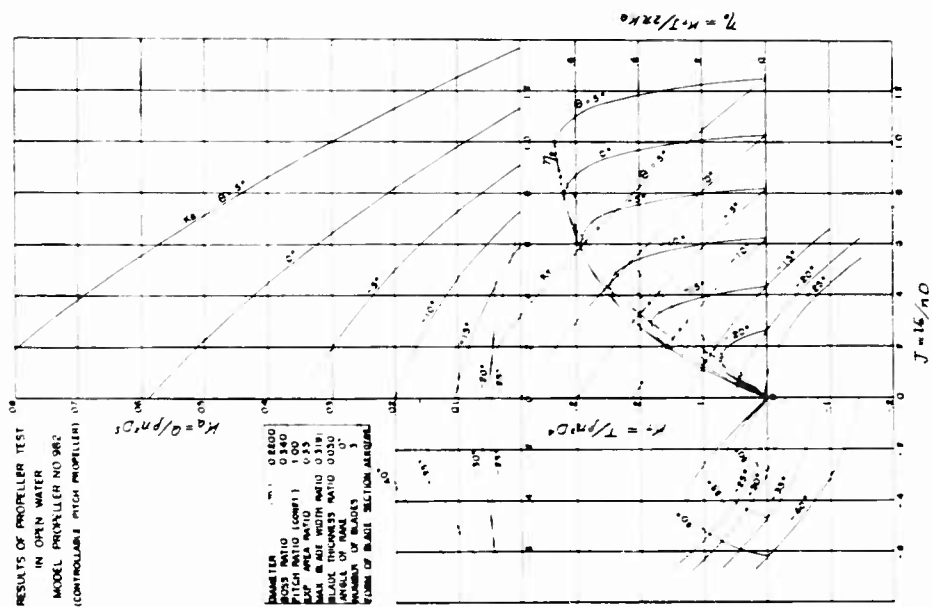
Fig. 6 - Test results (M.P. No. 982)
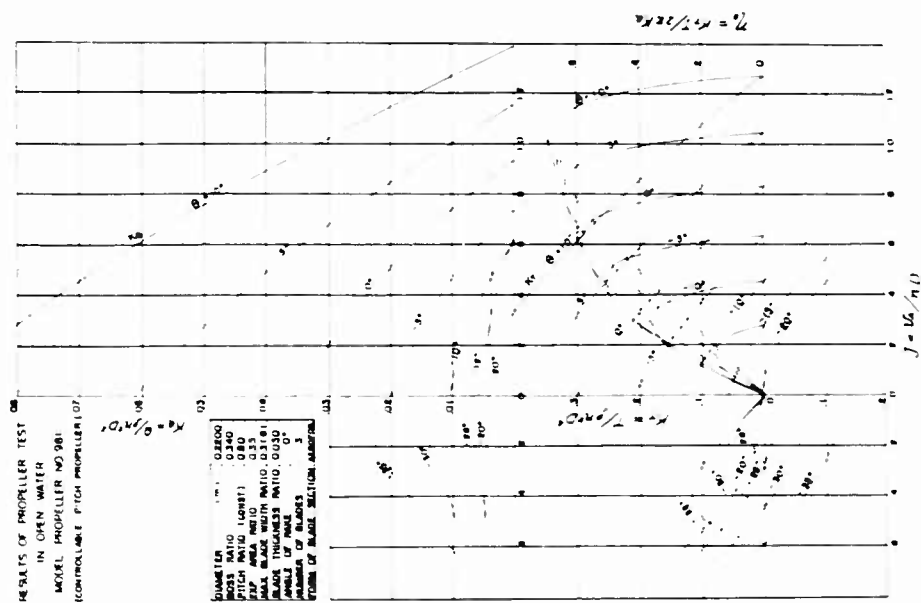
Fig. 6 - Test results (M.P. No. 981)

Design Diagrams of Three-Bladed Controllable Pitch Propellers
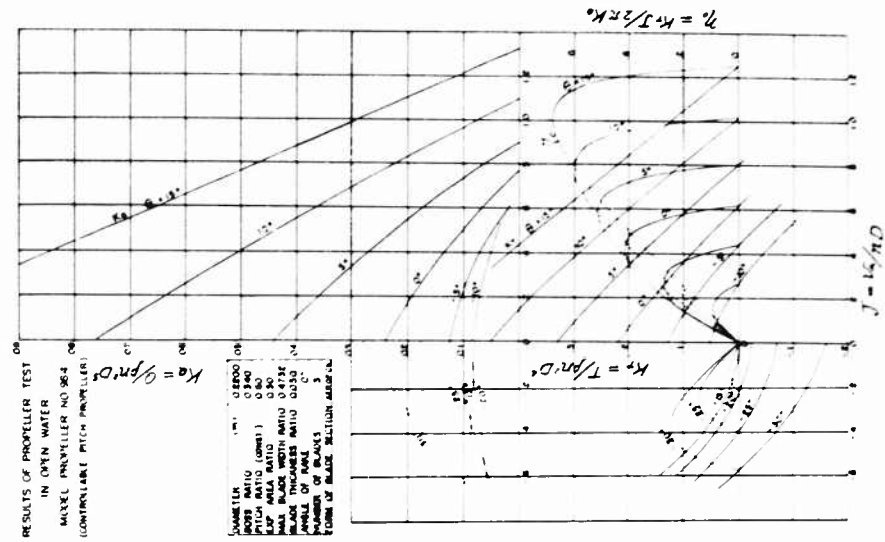
Fig. 8 – Test results (M.P. No. 984)
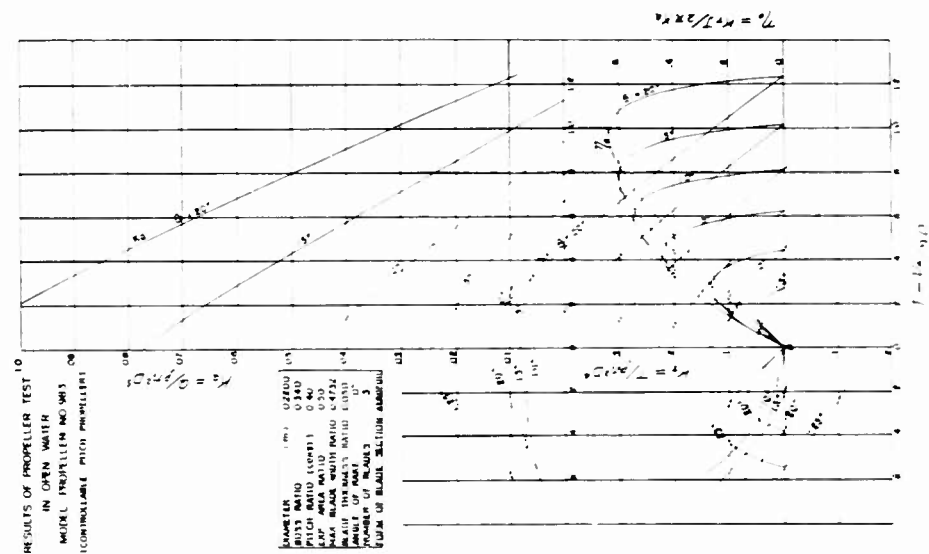
Fig. 7 – Test results (M.P. No. 983)

205
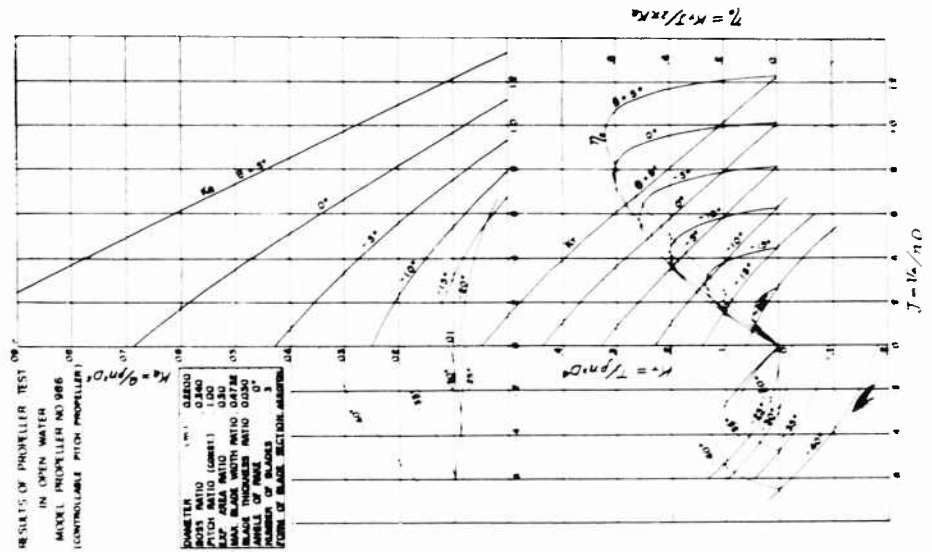
Fig. 10 – Test results (M.P. No. 986)
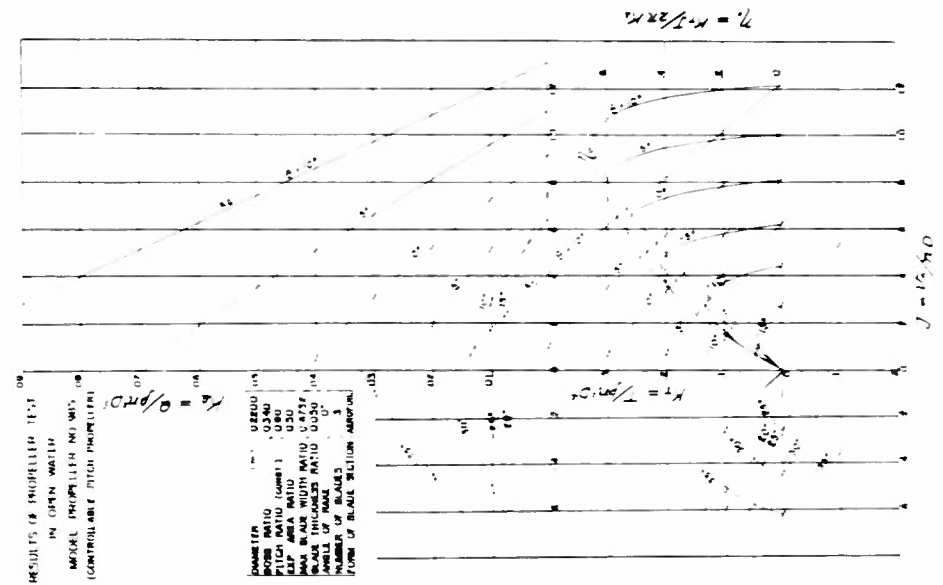
Fig. 9 – Test results (M.P. No. 989)

Q = the torque of the propeller (kg-m)

n = the number of revolutions of the propeller (rps)

D = the diameter of the propeller (m)

v_A = the speed of advance of the propeller (m/sec)

ρ = the density of water (kg-sec^2/m^4).

The positive sign of the advance coefficient means the ahead condition and the negative sign the astern condition. The positive and negative signs of the thrust coefficient also mean the ahead and astern directions respectively.

The tests results of the propellers at $\gamma = 0°$ are summarized in Figs. 11 and 12. From these figures, the design diagrams of $\sqrt{B_P}$ - δ and $\sqrt{B_U}$ - δ type for the propellers of initial pitch are obtained and shown in Figs. 13-16. The density of sea water was taken as 104.51 kg-sec^2/m^4, and the symbols in the diagrams are given as follows:

$B_P = NP^{0.5} V_A^{2.5}$

$B_U = NU^{0.5} V_A^{2.5}$

$\delta = ND V_A$

N = the number of revolutions of the propeller (rpm)

V_A = the speed of advance of the propeller (metric knot: 1852 m/hour)

P = the delivered horse power (PS: 75 kg-m/sec)

U = the thrust horse power (PS)

D = the diameter of the propeller (m)

H = the pitch of the propeller (m)

H/D = the pitch ratio of the propeller.

These diagrams can be used by the designers at the stage of the initial design of the controllable pitch propellers, to determine the diameter, the initial pitch and the efficiency. Figures 3-10 can be used to calculate their performances under the various working conditions.
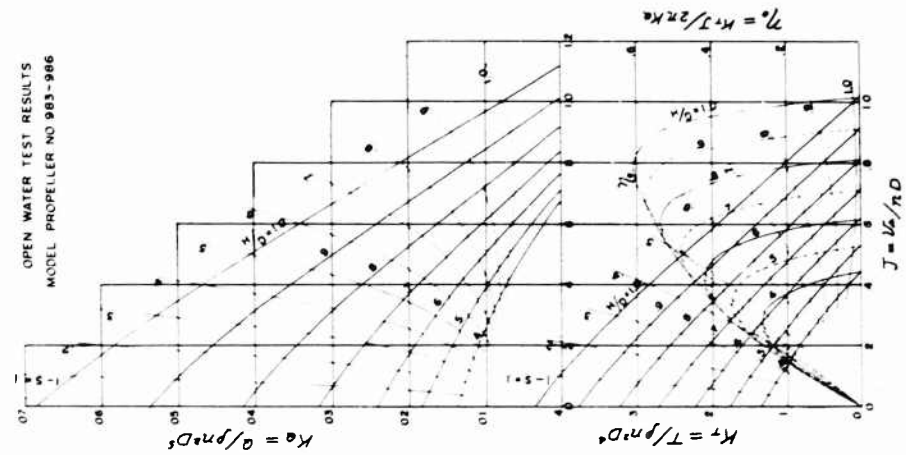
Fig. 12 – Test results -- $\beta = 0$
(M.P. Nos. 983-986)
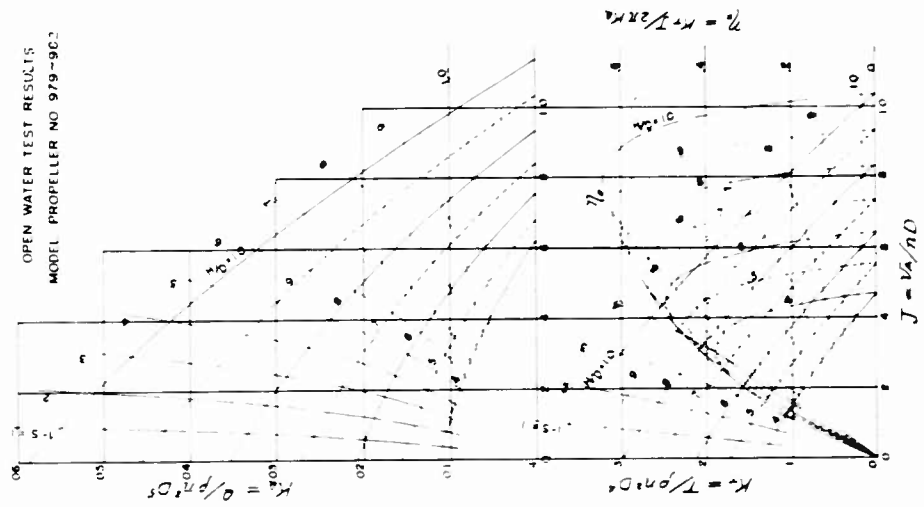
Fig. 11 – Test results -- $\beta = 0$
(M.P. Nos. 979-982)
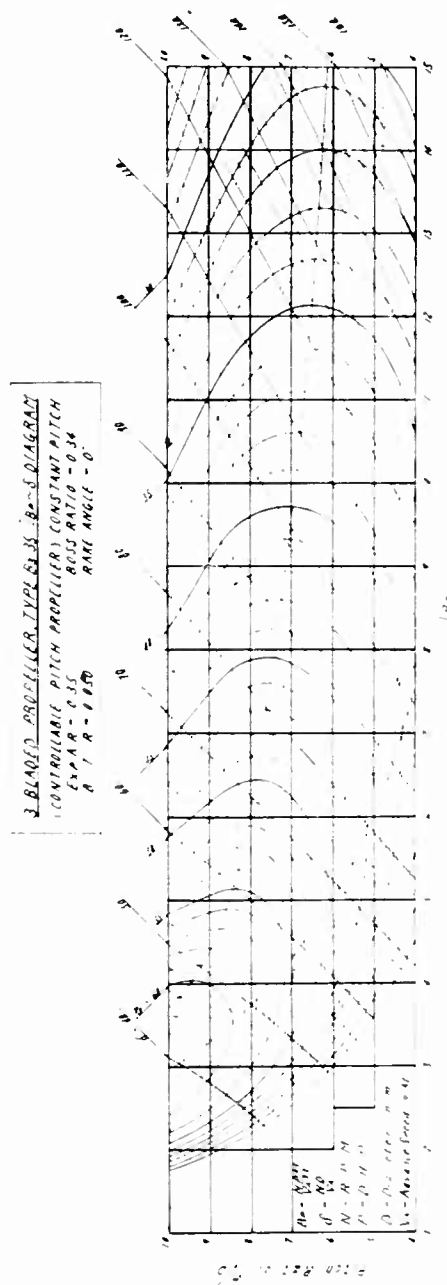
Fig. 13 - $\sqrt{B_p}$ - δ diagram (exp. area ratio = 0.35)

Fig. 14 - $\sqrt{B_p}$ - δ diagram (exp. area ratio = 0.50)

209
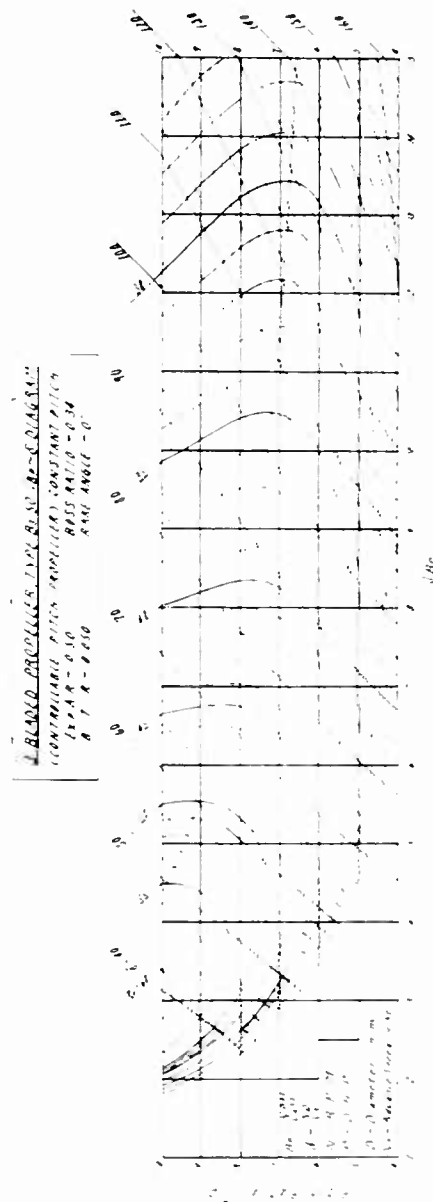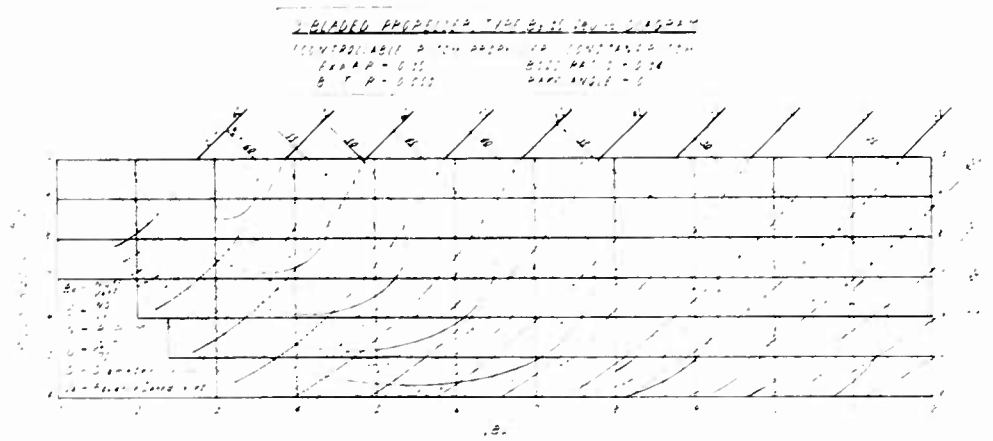
Fig. 15 - $\sqrt{B_U}$ - diagram (exp. area ratio = 0.35)
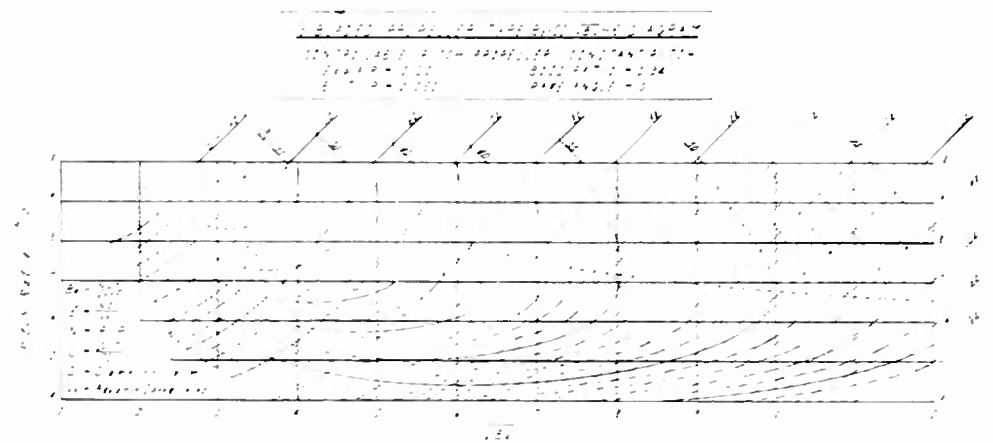
Fig. 16 - $\sqrt{B_U}$ - diagram (exp. area ratio = 0.50)

*   *   *

LARGE HUB TO DIAMETER RATIO PROPELLERS WITH PROGRAMMED BLADE CONTROL

W. P. A. Joosen, J. D. van Manen and F. van der Walle
Netherlands Ship Model Basin
Wageningen, Netherlands

with an Introduction by CDR F. R. Haselton,
Office of Naval Research, Department of the Navy, Washington, D. C.

ABSTRACT

A theory has been formulated for calculating the properties of large hub to diameter ratio propellers with cyclic pitch control.

In addition experimental results have been given for the efficiency and maneuvering characteristics of such a device.

INTRODUCTION

In October 1961 an eight months' feasibility study was started by the N.S.M.B. under an O.N.R.-research contract on propellers with a large hub to diameter ratio and cyclic pitch control.

The purpose of this research was to investigate the efficiency of such a device, the excitation of transverse forces by the propeller due to the cyclic pitch changes and finally the power required for generating a certain transverse force.

The various parameters are defined in Fig. 1. The pitch angle $\dot{}$ is controlled according to a prescribed program as a function of the rotation angle $\dot{}$ of the propeller blade. Owing to this cyclic pitch control transverse forces F_y and F_z and moments M_y and M_z are generated in addition to the propeller thrust T and the torque Q. The magnitudes of these additional forces can be varied by changing the cyclic pitch program.

211

The application possibilities of this propulsion system both for submarines (maneuverability) and surface vessels (reduction of cavitation and vibration due to the non-uniform wake) are considered as much promising.

The N.S.M.B. started simultaneously the development of a quasi-stationary theory for this special propeller type and the design and manufacture of a model for experiments.

This report gives the first results of both the theoretical and the experimental part of the program.
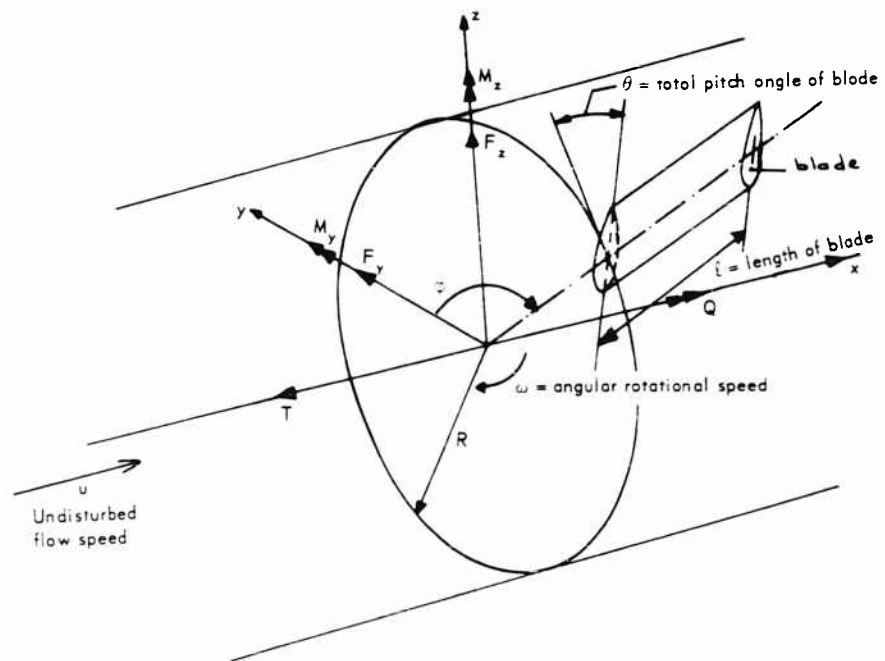
Fig. 1 - Definition of axis and symbols

THEORETICAL ANALYSIS OF SHROUDED LARGE HUB TO DIAMETER RATIO PROPELLER

The mathematical model of the geometrical configuration of the hub-propeller-shroud system can be composed by means of vortex and source distributions. As the reduced frequency is very small, the problem is considered to be quasi-stationary. The singularity distributions are therefore only functions of the dimensionless space coordinates (x, y, z) (or x, r, φ). The propeller tip radius is arbitrarily chosen as equal to 1.

It is assumed that the number of blades of the propeller is infinite, that the circulation on the blades is constant in the radial direction and that the propeller diameter is equal to the shroud diameter. Thus the propeller disk is replaced by a continuous bound vortex distribution of strength $\Gamma(\varphi)$. For $\Gamma(\varphi)$ is taken

$$\Gamma(\varphi) = d_o + c_1 \sin \varphi + d_1 \cos \varphi.$$

The shroud, radius = 1, length σ, camber $\varepsilon(x)$, thickness $d(x)$, is replaced by a bound-vortex distribution

$$\Gamma_1(x,\varphi) = \bar{f}_o(x) + g(x) \sin \varphi + f(x) \cos \varphi.$$

and a source distribution $g(x) = d'(x)$. See Ref. [1].

In the same way a bound ring vortex distribution of strength

$$\Gamma_2(x,\varphi) = \bar{h}_o(x) + p(x) \sin \varphi + h(x) \cos \varphi$$

exists on the hub with radius λ.

A distribution of free helical vortices on the cylinder $r = 1$ of strength $\Gamma(\varphi)$ starts from the tip of the blades. In the same way the bound vortices of the blades can be thought to continue at the hub as helical vortices of the same strength. The bound vortices on shroud and hub produce a system of free straight line vortices in the wake, respectively with strength

$$\frac{\partial}{\partial \varphi} \Gamma_1(x,\varphi) \text{ at } r = 1$$

and

$$\frac{\partial}{\partial \varphi} \Gamma_2(x,\varphi) \text{ at } r = \lambda.$$

The fact that these vortices are situated on straight lines becomes clear by the consideration that the loading on hub and shroud is stationary in the case of an infinite number of blades.

A mathematical explanation is given in chapter 2 of Ref. [2].

Besides the quantities

$$d_o, c_1, d_1, \sigma = \frac{\text{shroud length}}{\text{shroud radius}}.$$

and

$$\lambda = \frac{\text{hub diameter}}{\text{shroud diameter}}$$

there are two other parameters in the problem, viz., $\lambda = \omega R_1 / U$, where ω is the angular speed, U is the forward speed and R_1 is the shroud radius and finally a

213

constant a, which determines the position of the shroud in regard to the propeller plane $x = 0$.

The total mathematical model is summarized in the following sketch, where w_a, w_t and w_r are the dimensionless velocities induced by all the vortices (respectively in the axial, tangential and radial direction).
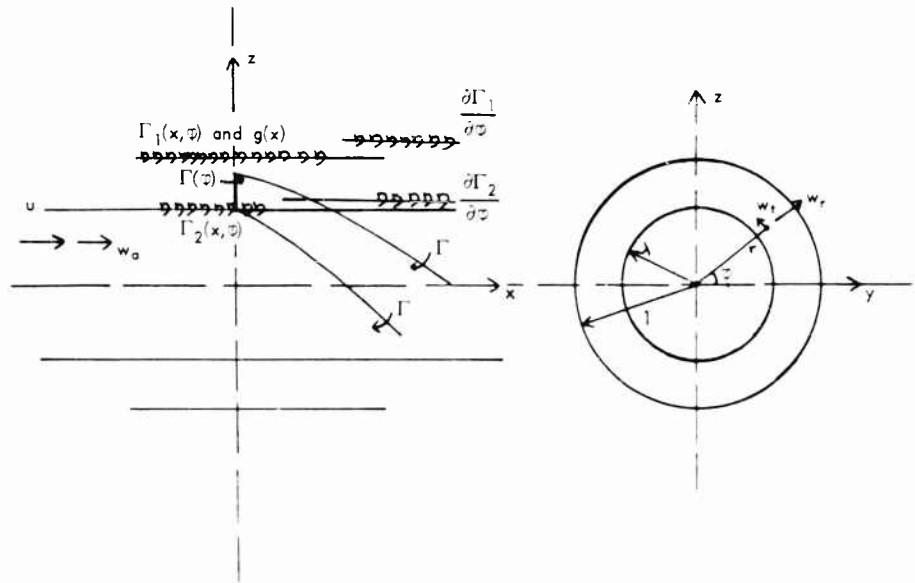
The problem is to find a solution for the functions $\Gamma_1(x,\varphi)$ and $\Gamma_2(x,\varphi)$ or $\bar{f}_o(x)$, $g(x)$, $f(x)$, $\bar{h}_o(x)$, $p(x)$ and $h(x)$.

The linearized boundary conditions on shroud and hub enable the derivation of six integral equations for the six unknown functions by separating the parts independent on φ, dependent on $\sin \varphi$ and dependent on $\cos \varphi$.

These boundary conditions are on the shroud $w_r = \epsilon(x)$ and on the hub $w_r = 0$.

The velocities induced by the vortices can be expressed in Bessel functions and complete elliptic functions (see chapter 4 through 6 of Ref. [2]). In order to see the influence of the respective parts of the given circulation at the blades $d_o - c_1 \sin \varphi - d_1 \cos \varphi$ the unknown functions are split up as follows:

$$\bar{f}_o(x) = d_o f_o(x) \qquad\qquad g(x) = c_1 g_1(x) - d_1 g_2(x)$$

$$\bar{h}_o(x) = d_o h_o(x) \qquad\qquad h(x) = c_1 h_1(x) - d_1 h_2(x)$$

$$f(x) = c_1 f_1(x) - d_1 f_2(x) \qquad\qquad p(x) = c_1 p_1(x) - d_1 p_2(x)$$

214

Then the integral equations can be split up as well and 5 sets of each two simultaneous equations are obtained. These equations show that a $\sin \varphi$ or $\cos \varphi$ distribution on the blades results in a combined $\sin \varphi$ and $\cos \varphi$ distribution on shroud and hub. This is due to the helical effect of the blade tip vortices. (Chapter 7 of Ref. [2].) As a consequence it can be expected that a $\sin \varphi$ variation in the cyclic pitch will lead to a transverse force in the y- as well as in the z-direction (see Fig. 1).

A singularity arises in the integral equations for $x = 0$. In order to remove this singularity it is necessary to assume a jump discontinuity in the vortex distributions on shroud and hub at $x = 0$. It is clear that this discontinuity is the mathematical formulation for the pressure jump across the propeller disc.

A second point, which needs attention is the asymptotic behaviour of the hub vortex distribution for $x \rightarrow \infty$. Due to the helical vortices the radial induced velocity on the hub for $x \rightarrow \infty$ behaves like $A \cos x + B \sin x$. In order to satisfy the boundary condition, the hub vortex distribution should approach to $C \cos x + D \sin x$. It is possible to derive the values C and D and after that to subtract these asymptotic functions from the integral equations, which enables a more convenient numerical computation. (See chapter 8 of Ref. [2].)

The integral equations can be transformed into systems of linear equations by substituting series with unknown coefficients for the distribution functions. Finally the induced velocities w_a and w_t in some point (o, r, φ) of the propeller disc can be written in the form:

$$w_a = T_1 d_o + (T_2 c_1 - T_3 d_1) \sin \varphi - (T_4 c_1 - T_5 d_1) \cos \varphi \ldots$$

$$w_t = T_6 d_o - (T_7 c_1 - T_8 d_1) \sin \varphi - (T_9 c_1 - T_{10} d_1) \cos \varphi \ldots$$

(1)

The T-factors are integrals over the distribution functions and follow from chapter 10 of Ref. [2].

As a first step the N.S.M.B. Computer Centre started programming of the fixed pitch condition $\varphi(\varphi) = d_o$. The main point in the program is the solution of the two simultaneous integral equations for the unknown shroud- and hub-vortex distribution functions.

For convenience sake the shroud distribution is supposed to be known. Then the hub distribution and the shroud camber line can be computed. For a special case of given camber the solution can be built up for instance with the elementary shroud distribution functions: $\sin m \varphi$.

DESCRIPTION OF MODEL AND MEASURING TECHNIQUE

It is essential for large hub to diameter ratio propellers that the propeller is tested in combination with some kind of body. For the experiments described in this paper a body of revolution was chosen as this resembles more or less the shape of a modern submarine. A photograph of the model is shown in Fig. 2.

215
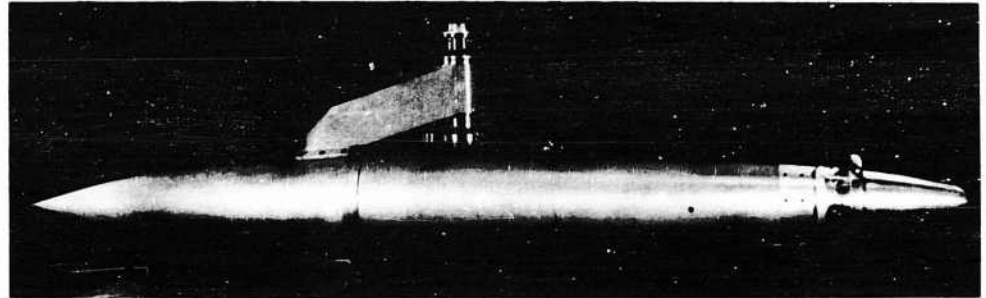
Fig. 2 - Photograph of model

A rather forward location of the propeller arrangement was chosen in order to reduce boundary layer and model support effects as much as possible. Moreover this arrangement enables a comparison to be made between the efficiencies in open water of this type of propeller and those of more conventional propeller types.

A shroud was fitted to the propeller arrangement from an efficiency point of view; it is clear, however, that the shroud can have an undesirable effect on the generated transverse forces as these forces are accompanied by a sideways deflection of the propeller jet. In order to minimize this effect the shroud was put rather forward with respect to the propeller disc. In addition shroud supports were only fitted in front of the rotor disc. Close-ups of the front part of the model are shown in Figs. 3 and 4.

The following dimensions were chosen for the propeller model:

Hub diameter	=	180 mm	=	7.1"
Propeller tip diameter	=	240 mm	=	9.5"
Shroud length	=	72 mm	=	2.85"
Shroud thickness ratio	=	7 %		
Number of blades	=	12		
Blade chord	=	12 mm	=	0.49"
Blade span	=	30 mm	=	1.2"
Blade profile	=	NASA 0016		
Percentage of shroud length in front of rotor disc	=	60 %		

No attempt was made to optimize the design of the propeller system, partly because of the exploratory, short-term character of this study and partly because design data for this kind of propulsion system are not available. The design of the shroud was based on the experience with more conventional shrouded propellers with small hubs. The shroud shape was corrected for the streamline-curvature and inclination as induced by the body.

216
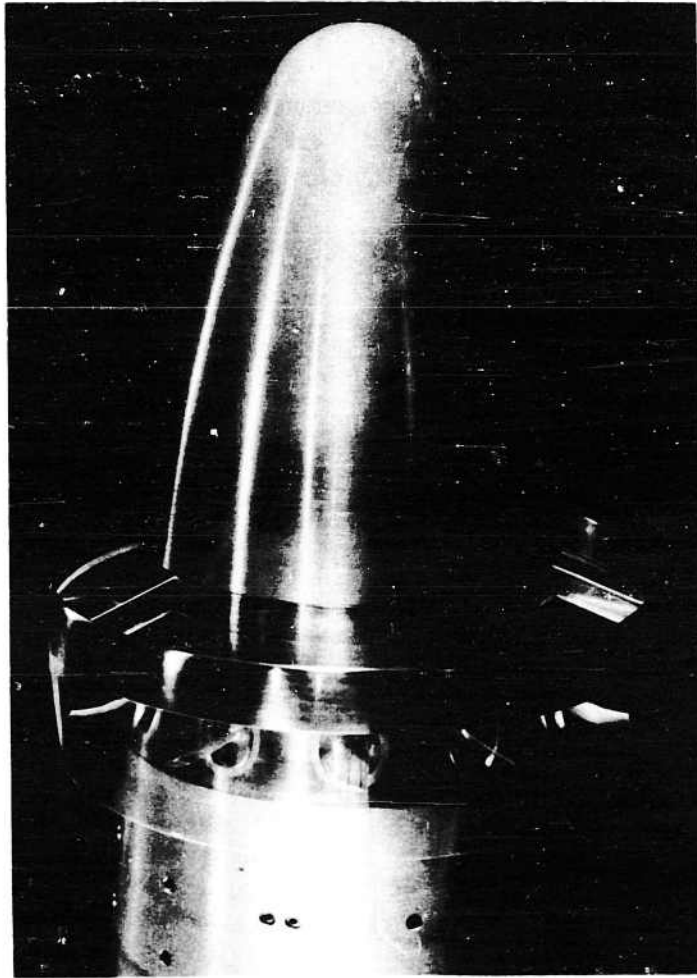
Fig. 3 - Front part of model

217
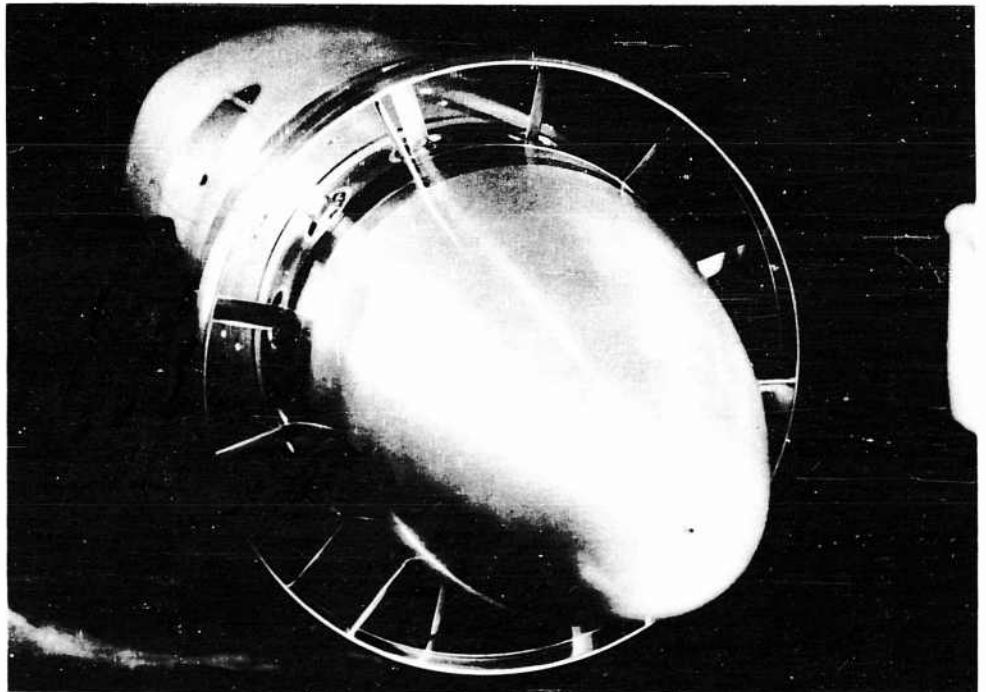
Fig. 4 - Forward view of model

① six components bolonce ⑧ guide ring for pitch control   section A-A
② stoy   ⑨ cyclic pitch control
③ forebody with propeller ⑩ meon pitch control
④ ofterbody fixed to stoy
⑤ electric motor
⑥ propeller blode
⑦ shroud
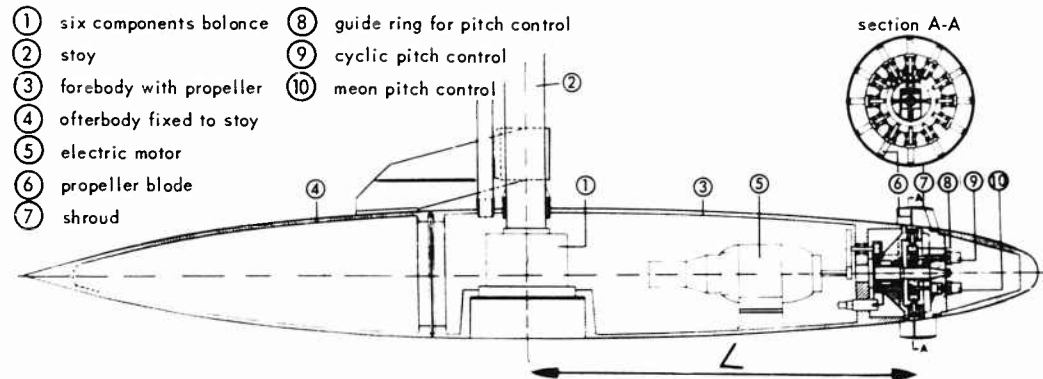
Fig. 5 - Schematic drawing of model

A sketch of the internal geometry of the model is given in Fig. 5.

The pitch control was accomplished in the following way. Each blade can pivot around an axis, the rotation of this axis being prescribed by a lever arm connected to a ball that can slide in a cylindrical race. This cylindrical race itself can be moved parallel in the axial direction of the body, leading to a change in the collective propeller pitch. In addition, this race can rotate around a horizontal axis; this results in a cyclic pitch.

In the experiments the total pitch angle θ for each blade can be varied according to the following program (see Fig. 1):

$$\theta = \theta_o + \theta_i \sin \varphi$$

The pitch angle for positive θ_i is therefore largest in the top position of the blade and smallest in the bottom position.

Some photographs of the pitch control mechanism were taken during assembly; see Figs. 6, 7 and 8. The two knobs by which the collective and cyclic pitch parameters θ_o and θ_i can be varied, are clearly visible. As already remarked in the introduction the experiments were carried out in order to yield data with respect to

1. The efficiency as a propulsion device

2. The generated transverse forces due to cyclic pitch control

3. The power required for generating the transverse forces.

The model was equipped with a six component balance (see Fig. 5). As the time available for the preparation of the experiments was rather short, an already existing balance of a rather high load capacity had to be installed. Consequently the accuracy was rather low for the following components:

219

Fig. 6 - Model before installation of blades
and pitch change mechanism
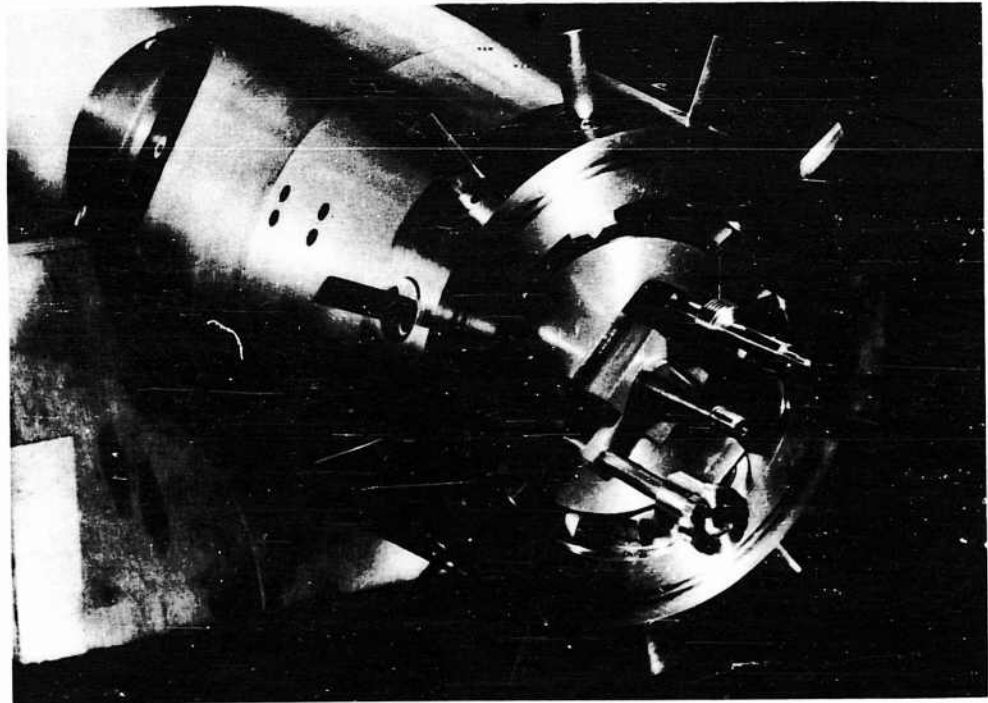
Fig. 7 - View of pitch change mechanism

221
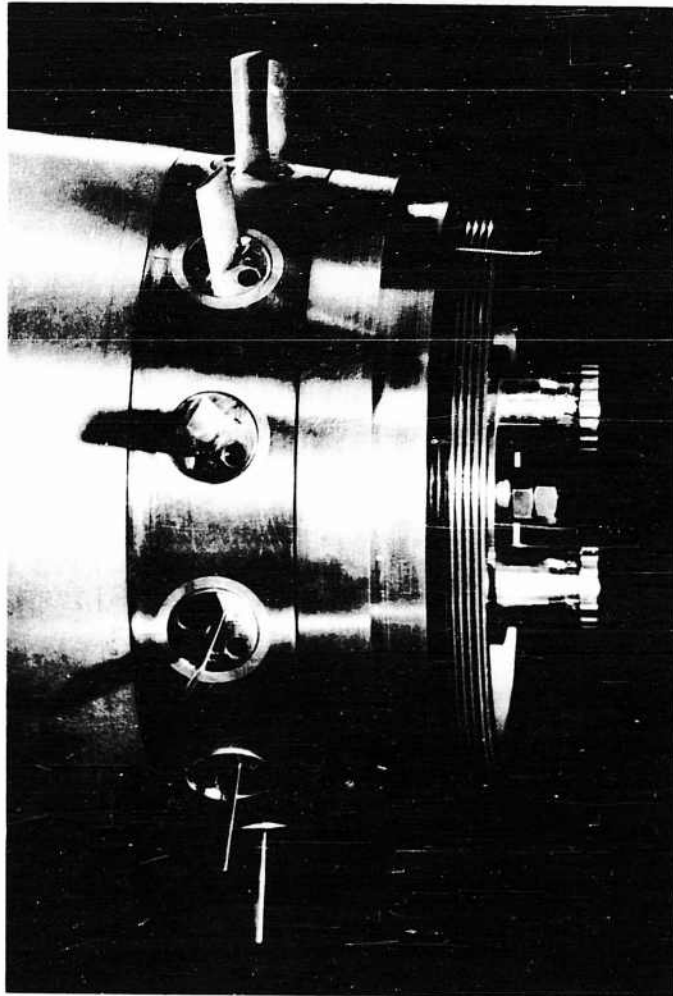
Fig. 8 - View of propeller blades and knobs
for pitch control

(a) the transverse forces

(b) the propeller torque.

The first limitation was not considered as essential as the transverse forces could also be derived from the moments around y- and z-axis of the balance. The balance sensitivity for these moments was acceptable especially since only an exploratory study was initiated. The low accuracy in measuring the propeller torque, however, was unacceptable as the obtained efficiency is an important criterion for the usefulness of this propulsion and maneuvering device. A second series of tests was therefore undertaken in which the propeller torque was measured directly on the propeller shaft.

In order to eliminate the friction losses as much as possible the pitch control-mechanism was removed, restricting these tests to zero cyclic pitch. All tests were performed in a towing tank of the N.S.M.B. at carriage velocities between zero and 4 msec at a depth of immersion of 0.9 meter. Only tests at zero angle of attack and yaw have been performed so far. The reduction of the data was obtained as follows:

1. Thrust. The measured total axial force acting on the model was corrected by the resistance of the body without propeller and shroud. The resultant net thrust T was made non-dimensional in the following way:

$$K_T = \frac{T}{\rho n^2 D^4}$$

where

ρ = specific density of water

n = number of revolutions

D = diameter of propeller tip.

2. Torque. The measured total torque was corrected by the friction losses measured on the shaft without the propeller. The resultant net torque Q was made non-dimensional by

$$K_m = \frac{Q}{\rho n^2 D^5}$$

3. Transverse forces. The moments around y- and z-axis of the balance were measured for zero cyclic pitch and for the particular angle ϵ_i considered. The difference of these moments yielded the net yawing and pitching moment M_z and M_y around the balance axis.

The following non-dimensional parameters were introduced:

$$k_y = \frac{M_z}{\rho n^2 D^4 L}$$

223

$$k_z = \frac{M_y}{\rho n^2 D^4 L}$$

where L = distance between propeller plane and center of balance (see Fig. 5).

This particular type of non-dimensional coefficients was chosen because k_y and k_z give directly the transverse forces in the propeller plane if the interacting forces on the body can be neglected. The ratios k_y/k_T and k_z/k_T are then in fact the ratios of the generated transverse force and the thrust.

RESULTS OF THE EXPERIMENTS

Results for Zero Cyclic Pitch

Thrust and torque were measured for collective pitch angles of 22°, 26°, 30° and 34°. The reduction of the data has been described already in paragraph 3. The non-dimensionless thrust and torque coefficients k_T and k_m and the efficiency η have been plotted in Fig. 9 as a function of the advance coefficient $\Lambda = V/nD$.

The maximum efficiency attained is around 70% at a value for Λ of around 1.3. This maximum efficiency is of about the same level as found for normal propellers in open water tests. In addition the thrust of the shroud alone has been plotted. The same test data have been plotted in Fig. 10 as a function of the parameter

$$B_p = \frac{n \cdot (P)^{0.5}}{V^{2.5}}$$

with

n = revolutions per minute

P = horsepower

V = undisturbed stream speed in knots.

For comparison, efficiency curves for typical normal propeller series with and without shroud have been given also. It is evident that the large hub propeller attains lower efficiencies at the same value of B_p. However, it must be emphasized that the B_p-values for two different kinds of propellers can not be compared directly with each other. The large hub propeller is due to its geometry a small r.p.m. device which will cause the efficiency curves to shift to lower B_p-values. This tendency is shown by Fig. 10. The following design data may be typical for instance for a large hub propeller for a submarine:

N =   50 r.p.m.

P = 7500 H.P.

V =   30 knots

224
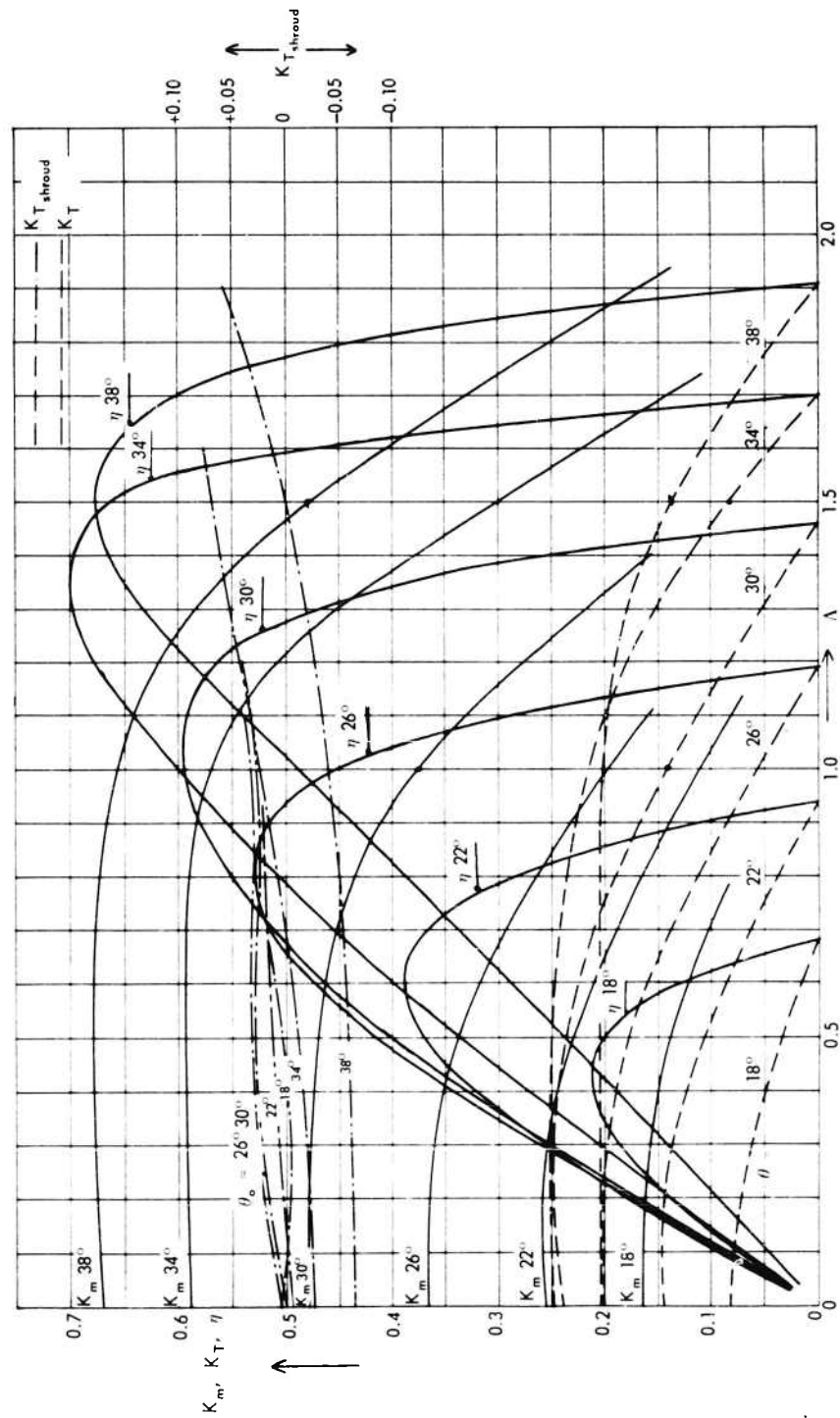
Fig. 9 - Thrust and torque coefficients and efficiency as a function of Λ with collective pitch angle θ_o as parameter
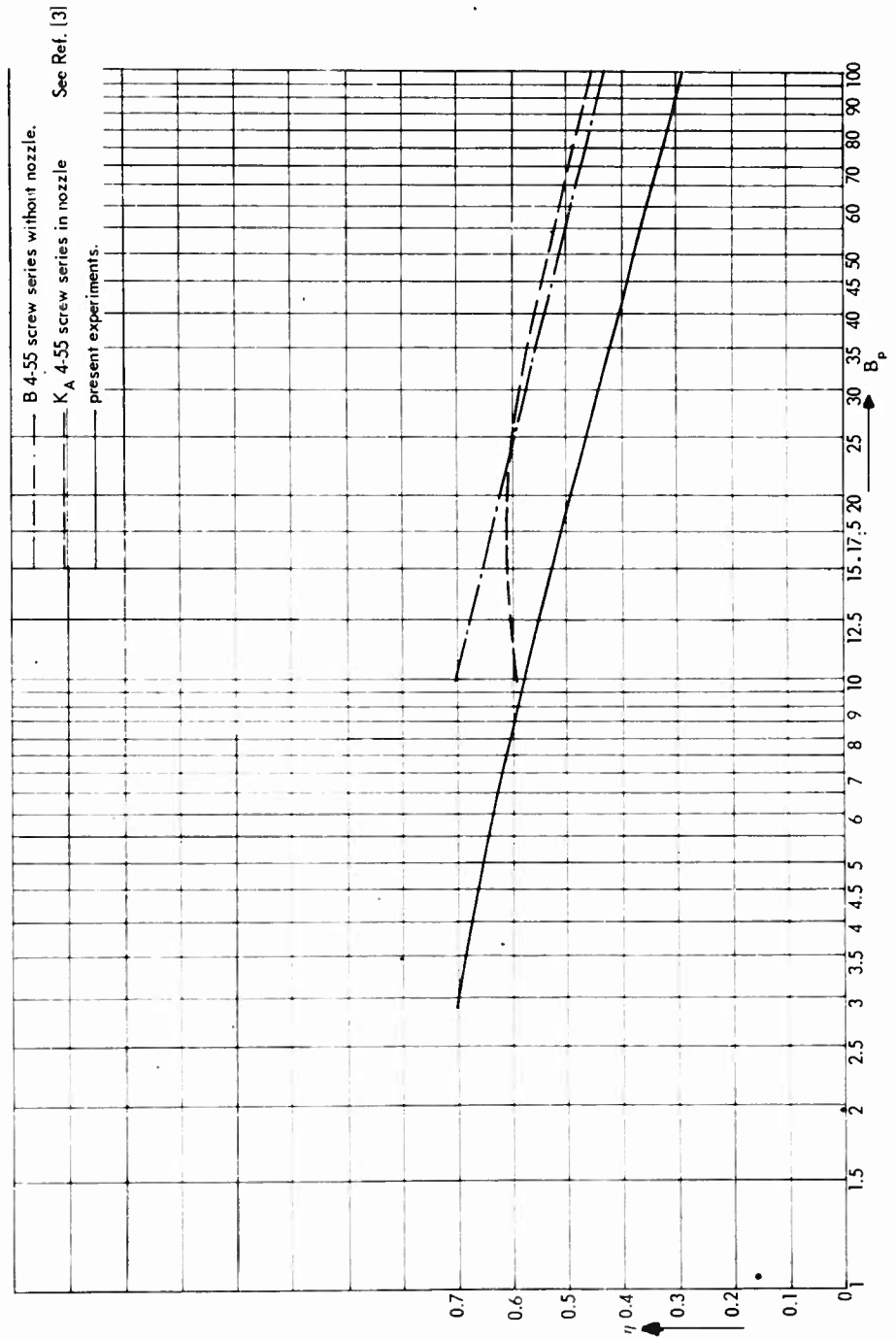
Fig. 10 - The optimum efficiencies as a function of B_p for three types of propeller systems

The resulting value of B_p becomes then: $B_p = 0.9$ which is a very low figure in comparison to the values for more normal propellers.

Results for the Transverse Forces due to Cyclic Pitch

The transverse forces have been measured for collective pitch angles of $22°$, $26°$ and $30°$ and for cyclic pitch amplitudes θ_i of $8°$ for a range of $\Lambda = V/nD$ values.

Three phenomena are of interest with respect to the generated side forces, namely:

a. The magnitude and the direction of the generated side force

b. The change in the thrust due to cyclic pitch

c. The change in the torque due to cyclic pitch.

The non-dimensional transverse force coefficients k_y and k_z have been calculated from the test data according to the procedure described in paragraph 3. The results have been plotted in Figs. 11a, b and c as a function of Λ. It is evident that an appreciable rotation of the transverse force takes place when V/nD increases.

This is more clearly visible in Figs. 12a, b and c where the data have been plotted in vectorial form. The arrows represent the resultant transverse force both in magnitude and in direction as seen by an observer upstream of the propeller. The propeller rotation is clockwise.

For the cases considered the side force increases somewhat with increasing values of Λ. The rotation of the force vector is in accordance with the qualitative theoretical results described in paragraph 2. It is not clear, however, how much of the variation in direction and magnitude of the transverse force is due to interaction of the downstream vortex field with the propeller loading and how much is due to side forces generated on the aft body.

In a further extension of these experiments it is planned to measure the forces on the propeller and the aft body separately.

The generation of side force is accompanied in general by a decrease in thrust and an increase in torque. The additional thrust coefficient Δk_T has been plotted in Fig. 13 and the additional torque coefficient Δk_m in Fig. 14.

CONCLUSIONS AND SUGGESTIONS FOR FURTHER RESEARCH

From the experimental results the following conclusions can be drawn:

a. The maximum propulsion efficiency is of the same order as obtained with more normal propeller types.
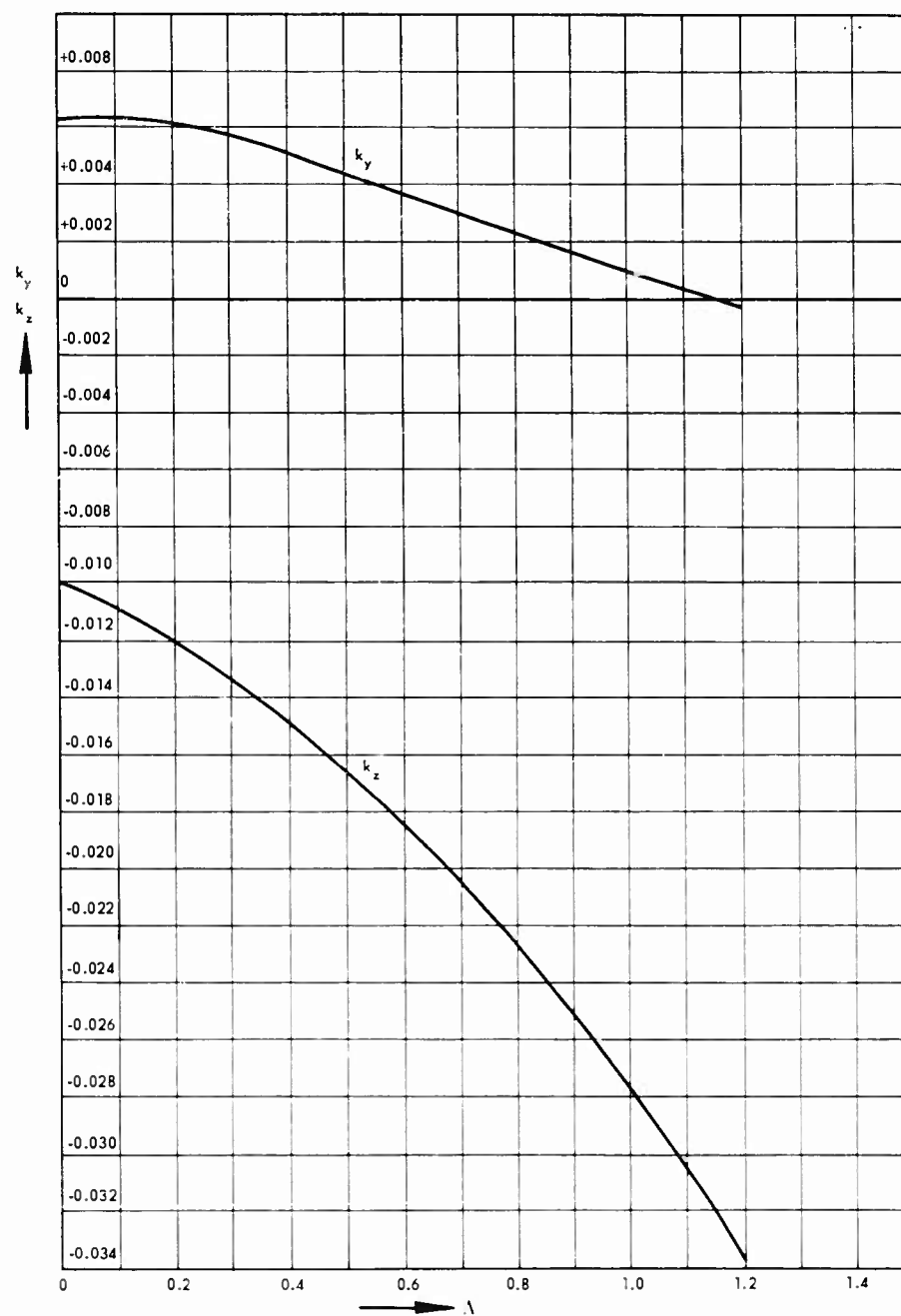
Fig. 11a - The transverse force coefficients k_y and k_z as a function of Λ for $\theta_o = 22°$ and $\theta_i = 8°$

228

Large Hub to Diameter Ratio Propellers with Programmed Blade Control
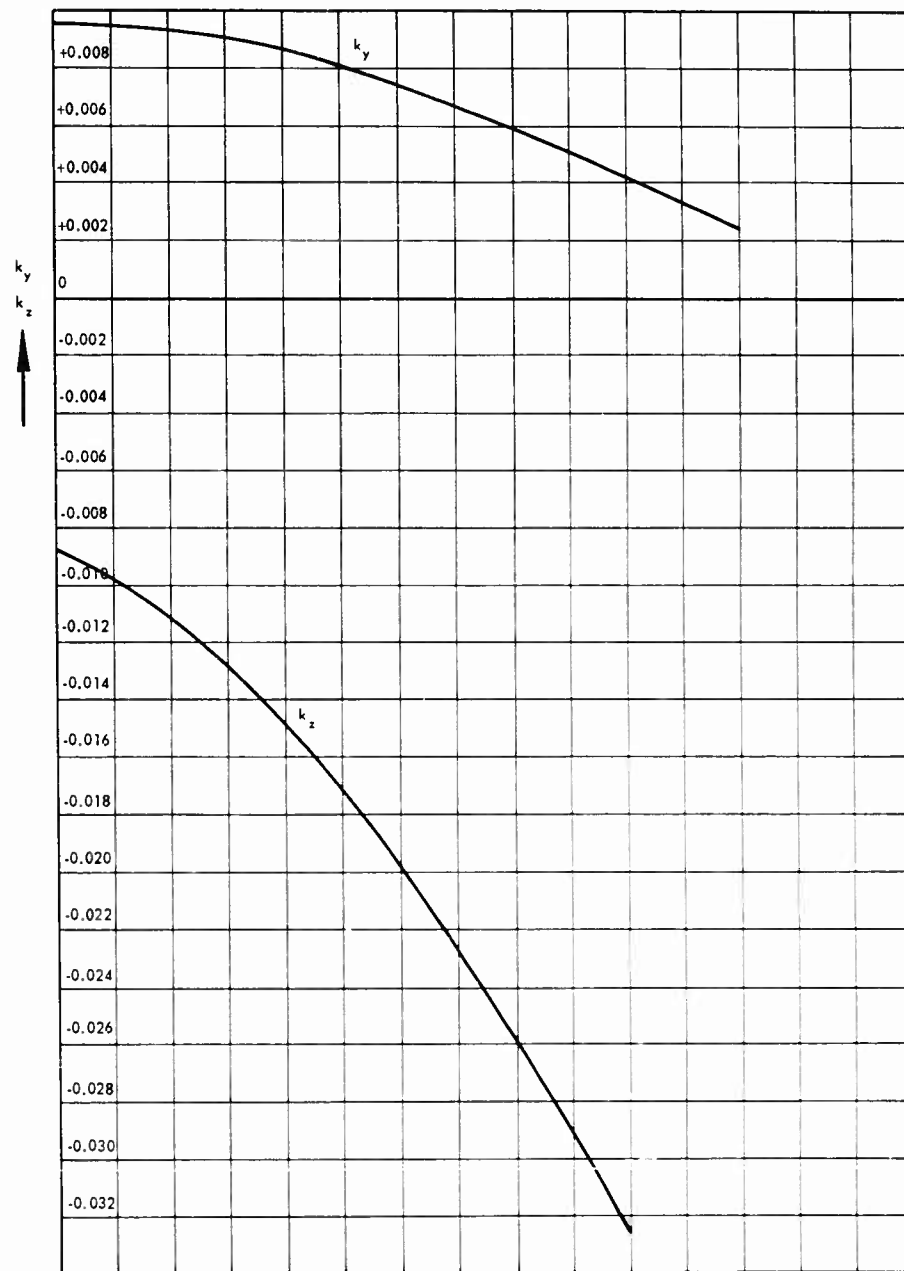
Figure 11b
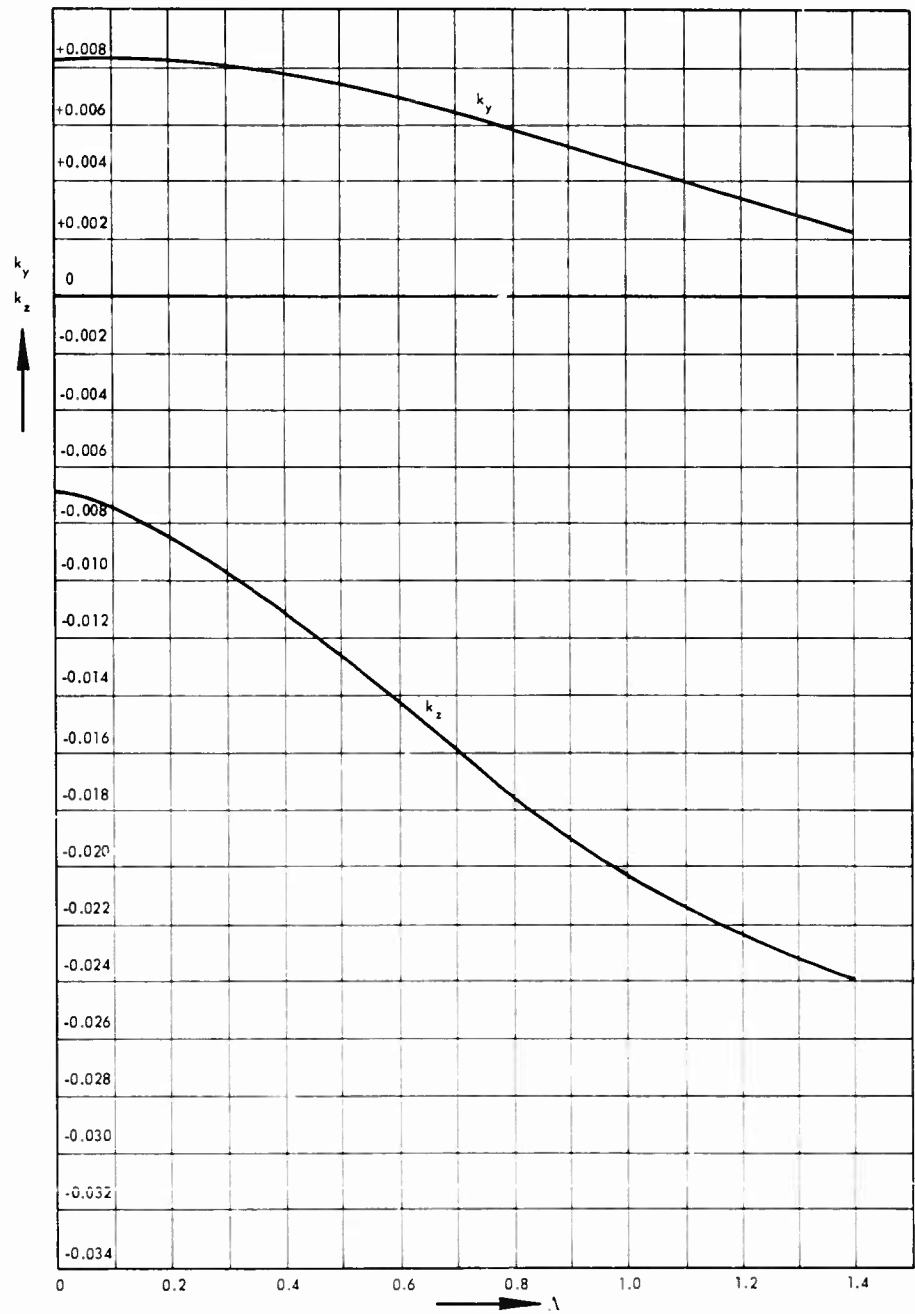
Fig. 11c - The transverse force coefficients k_y and k_z as a function of Λ for $\vartheta_o = 30°$ and $\vartheta_i = 8°$
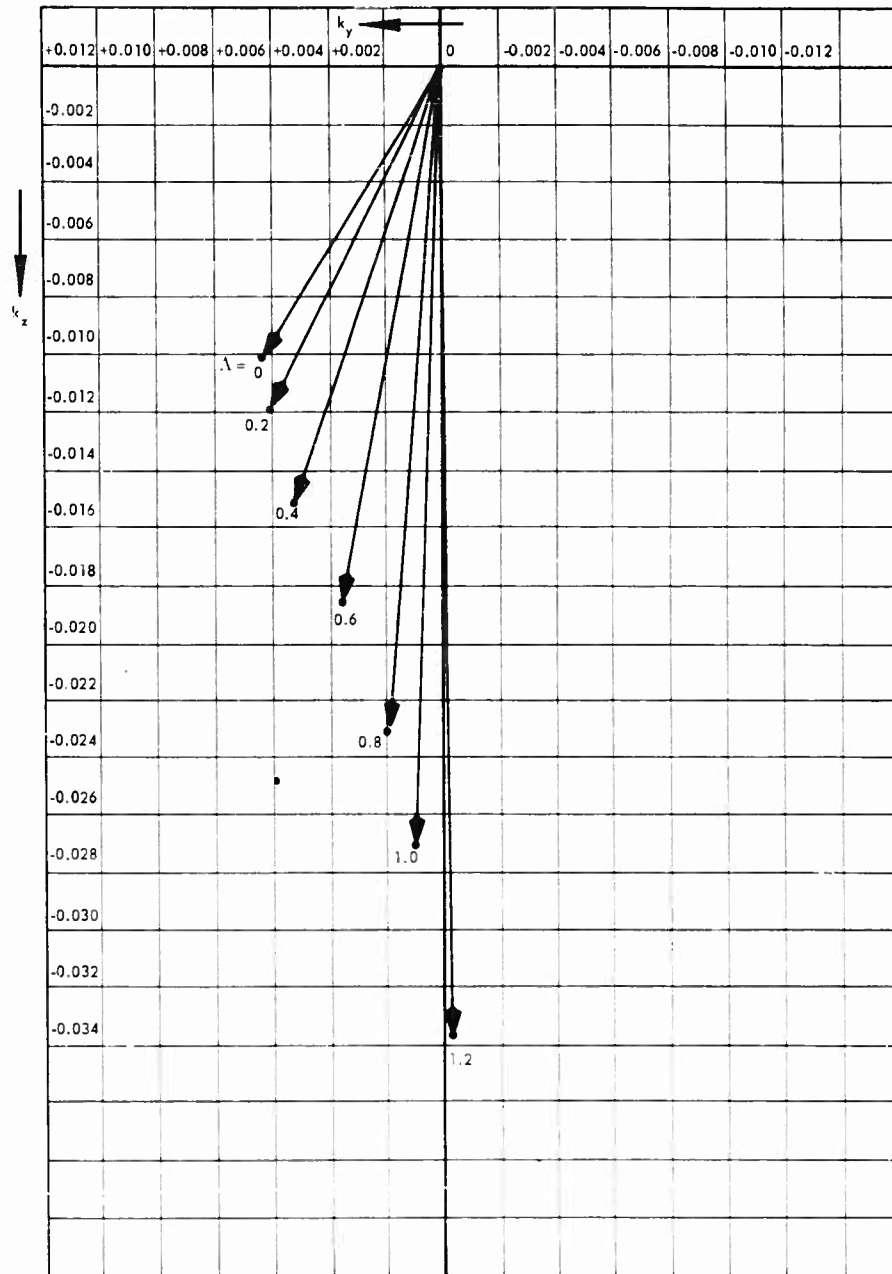
Fig. 12a - Vectorial representation of the transverse force
as a function of Λ for $\beta_o = 22°$ and $\beta_i = 8°$
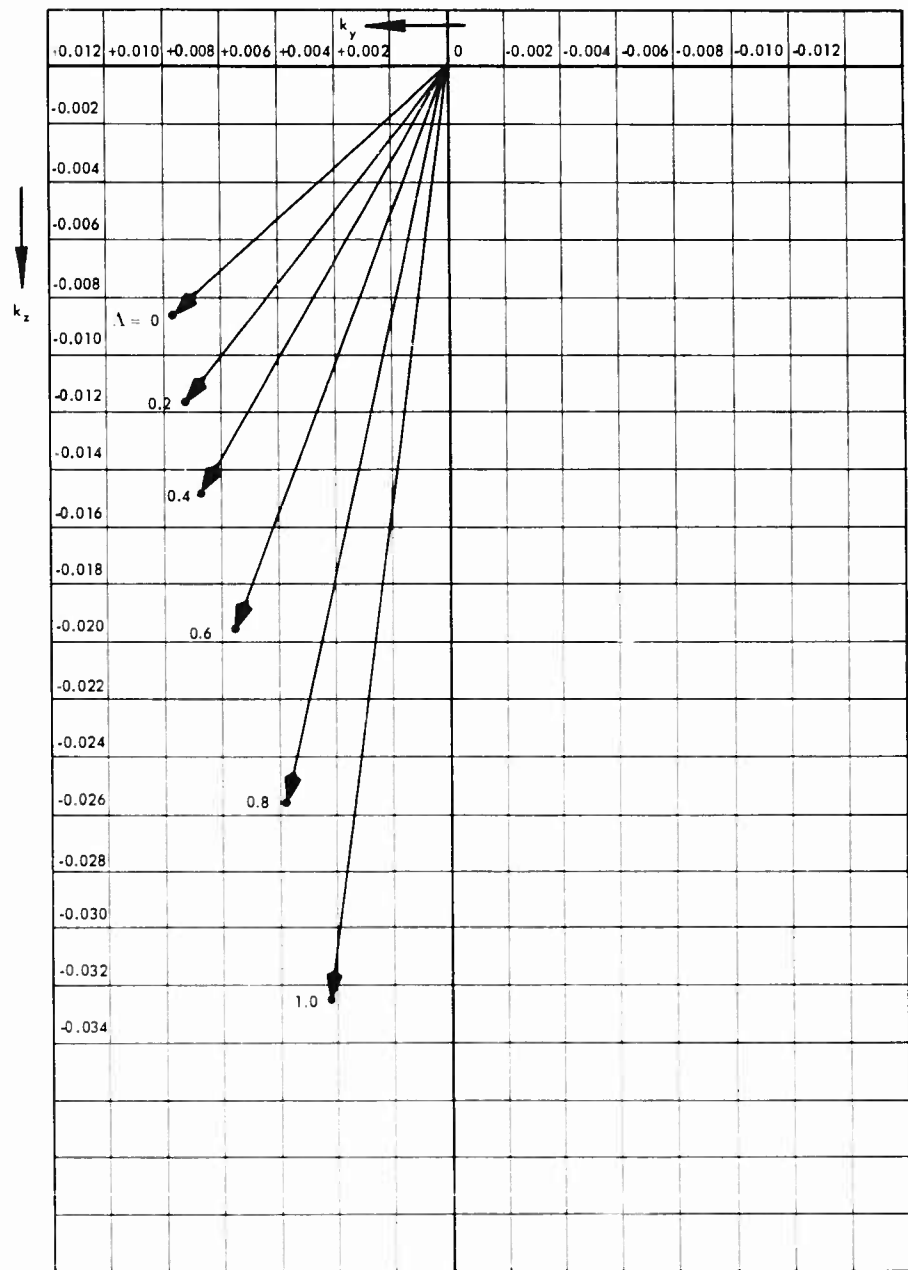
Fig. 12b - Vectorial representation of the transverse force
as a function of λ for $\varepsilon_o = 26°$ and $\varepsilon_i = 8°$
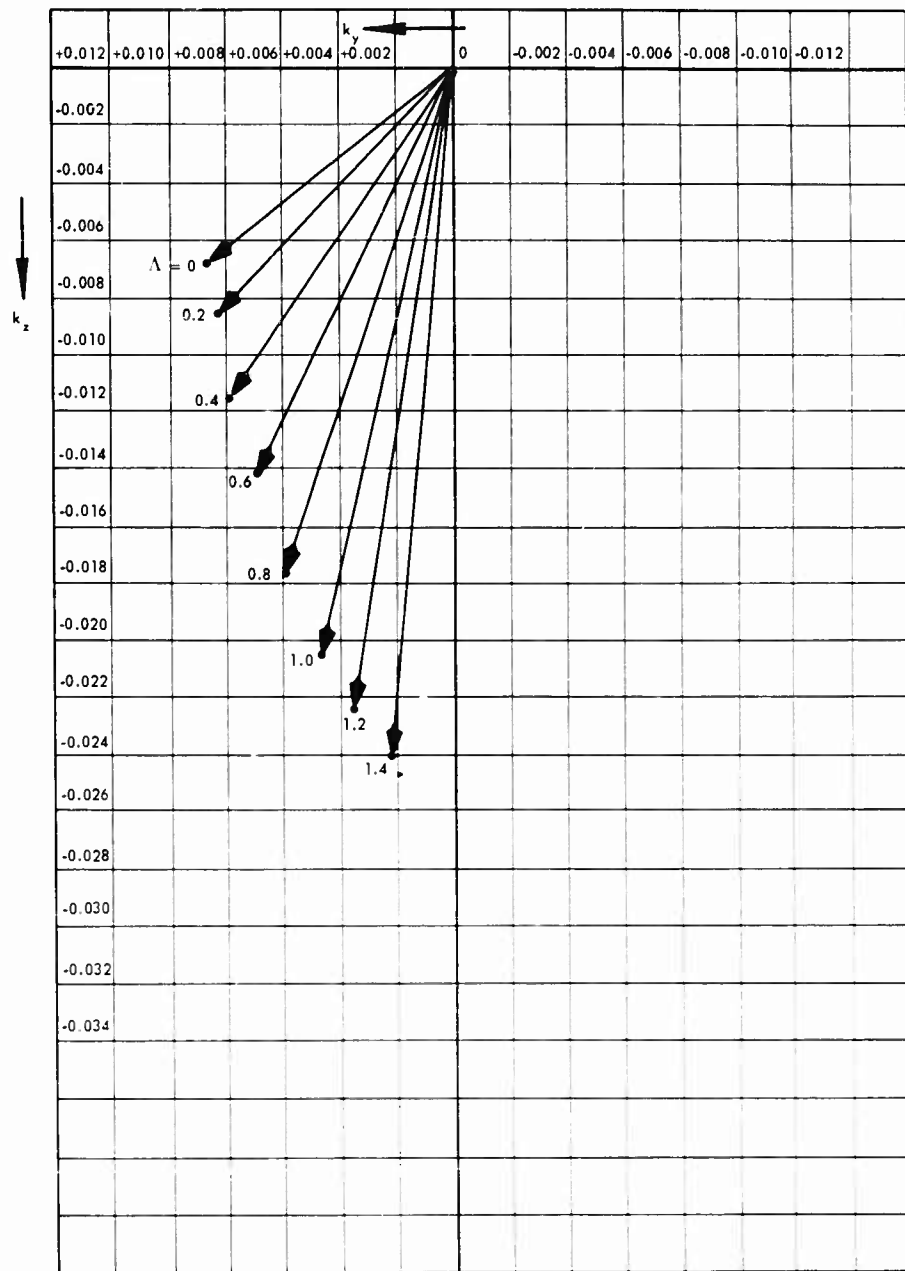
Fig. 12c - Vectorial representation of the transverse force
as a function of Λ for $\beta_o = 30°$ and $\beta_i = 8°$

Fig. 13 - The additional thrust coefficient ΔK_T due to cyclic pitch for $\theta_i = 8°$ as a function of θ_o and λ
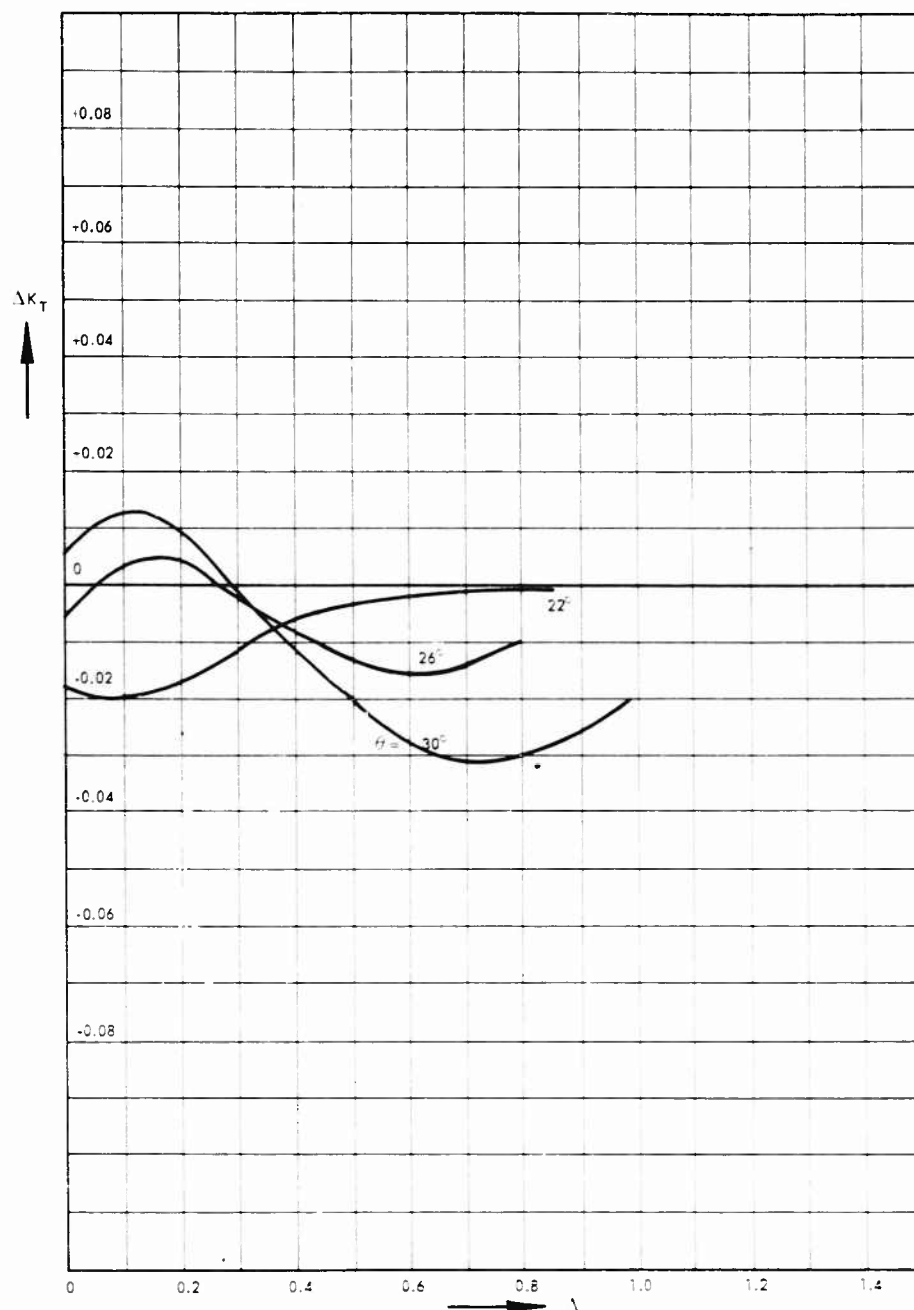
Fig. 14 - The additional torque coefficient K_T due to cyclic pitch for $\vartheta_i = 8°$ as a function of ϑ_o and λ

b. The transverse force does not decrease with increasing velocity in the range of the test variables. In some cases there is even some increase.

c. The direction of the transverse force changes by an appreciable amount when the velocity is increased.

It seems advisable to extend this research in the following directions:

1. The determination of the optimum shape of the shroud as a function of the design variables (hub to diameter ratio, propeller load, etc.).

2. The determination of the influence of thick boundary layers on the characteristics as a propulsive and maneuvering device.

3. A more detailed determination of the generated transverse forces and measurement of the interaction of the body with the deflected propeller jet.

4. Determination of the influence of an angle of yaw on the characteristics.

REFERENCES

1. Weissinger, J., "The Influence of Profile Thickness on Ring Airfoils in Steady Incompressible Flow," ARDC AF 61(514) - 904 (1957).

2. Joosen, W.P.A., "The Induced Velocities at the Blades of a Tandem Propeller with Programmed Blade Control in a Shroud," N.S.M.B. Laboratory Memorandum No. 3 (January 1962).

3. Manen, J.D.van, "Effect of Radial Load Distribution on the Performance of Shrouded Propellers," Paper No. 7, The Royal Institution of Naval Architects, March 29, 1962.

*   *   *

Tuesday, August 28

Morning Session

PROPULSION

Chairman: H. Lerbs

Hamburgische Schiffbau-
Versuchsanstalt
Hamburg, Germany

SUPERCAVITATING PROPELLERS - HISTORY, OPERATING CHARACTERISTICS, MECHANISM OF OPERATION

Marshall P. Tulin
HYDRONAUTICS, Incorporated
Laurel, Maryland

ABSTRACT

This paper contains discussions of: The historical development of supercavitating and ventilated propellers; their operating characteristics; and the mechanism of their operation. A good deal of the material referring to the latter two subjects is presented here for the first time.

The part on historical development includes a discussion, for the first time in recent Western literature on the subject, of the pioneering research of the Soviet scientist V.L. Posdunine and his colleagues.

The operating characteristics are discussed largely in terms of four regimes of propeller operation for which definitions are given. These are: subcavitating, partially cavitating, supercavitating, and fully-supercavitating. The presentation of propeller characteristics in various forms and their meaning is discussed. The arched shape of the fully-supercavitating characteristic curve (k_t vs. J) is described and explained.

New phenomena which dominate the mechanism of operation of supercavitating propellers are described. These are cavity blockage and blade-cavity interference. Some quantitative theoretical results relating to these phenomena are presented. It is explained how these phenomena account for effects on thrust and efficiency, observed experimentally, but not previously understood. Fundamental differences in the mechanism of operation of sub and supercavitating propellers are revealed.

239

INTRODUCTION

Ten years have passed since the systematic development and exploitation of supercavitating and ventilated propellers was begun in this country. Our progress has been slow but steady. Our present knowledge of the whys and wherefores of these propellers is not by any means detailed enough, but we have sufficient acquaintance with them to be encouraged to design them for installation on large high speed hydrofoil ships and planing craft. In fact, such applications seem likely to grow, since no reasonable alternative for ship propulsion in the speed range between 40 and 80 knots has yet presented itself to us. This is a very important reason why we must continue to work hard on supercavitating propeller problems.

We have had to face a number of very sobering facts since our first experimentation in this country with supercavitating propellers. We early became aware of the terrible strength problems which accompany very high speed propeller operation in sea water. These problems are much aggravated by the thin leading edges with which we would like to equip supercavitating propellers, and they are brought to a virtual crisis by the deterioration of fatigue strength properties in most high yield materials due to sea-water corrosion. We have been learning through experience how to live with these problems and to accept the penalties in performance caused by them.

We have also discovered that the thrusting action of heavily supercavitating propellers is unexpectedly poor during off-design operation. For this reason, the provision of adequate thrust to a hydrofoil boat at take-off has become an important element in supercavitating propeller selection and design.

Further, despite our initial successes, we have finally been forced to admit that our only published design methods allow us to predict the thrust or efficiency of supercavitating propellers only roughly, and finally, we have realized that hydrodynamic effects occur during the operation of supercavitating propellers which we had not in the beginning expected or predicted, and we have therefore had to reconstruct the theory of their operation. This has been done to a certain extent, although many details remain to be provided. Nor will this task be easily finished.

I suppose that these experiences are not at all untypical of those associated with new developments of this kind. Typically, too, we somewhat exaggerated the "newness" of the subject. The history of supercavitating propellers does not begin in the 1950's, nor even in the 40's at the time of intensive Soviet studies — but probably in 1894 with the trials of the British steam vessel TURBINIA. It is a very interesting history.

In the present paper I will first try to tell something about the historical development of supercavitating propellers and especially of the pioneering research of the Soviet scientist Posdunine, then to discuss in general terms the important operating features of supercavitating and ventilated propellers and some aspects of their design, and finally to describe briefly those "new" hydrodynamic phenomena which we have recently discovered to be associated with their behaviour. By the latter I refer particularly to the phenomena of blade cascade interference and cavity blockage. The reader must obviously look

240

elsewhere for a discussion of systematic experimental data or for a bold and clear cut formulation of the design process,* but it is hoped that this paper will help him in the interpretation of data or in carrying out an actual design by providing some familiarity with the fairly complicated operating characteristics and mechanism of operation of supercavitating propellers. Much of this material is being presented here for the first time.

HISTORY

Parsons and the TURBINIA

The affair of the British steam vessel TURBINIA provides a very important chapter in the history of ship development. This vessel displaced 44-1/2 tons and was 100 ft in length and 9 ft in beam. She was designed and built in 1894 under the sponsorship of a syndicate formed to test the application of the compound steam turbine to marine propulsion. The sponsors hoped that an "unprecedented" speed would be obtained, i.e., a speed somewhat in excess of 30 knots. A single turbine and propeller were initially installed without gear reduction. The turbine was designed to develop upwards of 1500 horsepower at a speed of 2500 RPM. The first trials were terrible failures, speeds of only about 20 knots being obtained. In Sir Charles Parsons own words [2], "Trials were made with screws of various patterns, but the results were unsatisfactory, and it was apparent that a great loss of power was taking place in the screw."

Almost nothing was known about the effects of cavitation on screws prior to the design of the TURBINIA, although at just about that time the trials of the British warship DARING drew attention to the subject, and caused research to be done by S.W. Barnaby and J.I. Thornycroft [3]. This research, together with that conducted subsequently by Parsons, revealed that heavy cavitation was undoubtedly occurring on the TURBINIA's screws and it was thus concluded that this heavy cavitation was the cause of the "great loss of power."

Parsons' account of the TURBINIA affair [2], is decidedly unemotional in style, but it is not difficult to imagine the effect of the first TURBINIA trials on both designer and sponsors, for the failure, which was due to completely unanticipated effects, clearly threatened to jeopardize their entire venture and investment. In fact, the severity of the difficulties drove the designers finally to a rather extreme but successful solution involving the replacement of the single turbine by three smaller turbines of equivalent total horsepower; these drove, without reduction, nine screws arranged three in tandem on each of three parallel shafts. In 1897 several sets of screws of different pitch were tried and the refitted TURBINIA finally achieved a speed of 32.61 knots, bringing success to the venture and what must have been immeasurable relief to the designers and sponsors. Parsons and his colleagues subsequently crowned this achievement with further technical and business success in the development, adaptation, and manufacture of steam turbines for marine use. Of course, the eventual success of the steam turbine depended very much on the introduction by Parsons of reduction gears — thus really saving the "cavitation crisis."

---

*In Ref. [1] the reader will find the most complete available attempt along these lines.

Parsons' experimental studies in the two years following the initial trial failures were made on 2 inch screw models operating in a circular tank of almost boiling water and observed with a stroboscope (of his own design!). In this way he was able to observe not only the onset of cavitation but even supercavitating operation. He described some of his observations as follows: "It appeared that a cavity or blister first formed a little behind the leading edge and near the tip of a blade; then, as the speed of revolution was increased, it enlarged in all directions, until, at a speed corresponding to that in TURBINIA's propeller, it had grown so as to cover a sector of the screw-disc of 90 degrees. When the speed was still further increased, the screw as a whole revolved in a cylindrical cavity, from one end of which the blades scraped off layers of solid water, delivering them on to the other. In this extreme case nearly the whole energy of the screw was expended in maintaining this vacuous space. It also appeared, when the cavity had grown to be a little larger than the width of the blade, that the leading edge acted like a wedge, the forward side of the edge giving negative thrust."

The exact connection between such observations and the operation of the TURBINIA's screw remains unclear, both because the experiments were carried out in water whose speed was undetermined, and because the scaling procedure utilized is rather vague. Nevertheless, the first failures of the TURBINIA and these experiments together made evident in dramatic fashion the horrors that can attend the operation of heavily cavitating propellers. The experience of others in Britain at about the same time taught of the ills to be visited in the form of blade erosion by permitting even relatively small amounts of cavitation to exist on a screw. These lessons were perhaps too well learned; the horrors thus revealed seem in fact to have been sufficiently blinding so that for the following forty years man felt hardly compelled, even out of scientific curiosity, to study in a rational and systematic way the operation of heavily cavitating screw propellers. Thus our scientific understanding remains relatively underdeveloped even at the present time.

The practical possibilities for high speed propulsion utilizing supercavitating operation were of course not completely neglected during this period, and without the aid of any theory or rational design methods, heavily cavitating screw propellers were and still are successfully used to propel small racing boats at speeds well in excess of 100 knots. A great deal of trial and error in propeller choice must be involved in such applications since the attainment of proper rotative speed is crucial for the optimum performance of racing engines.

Early Soviet Work — V.L. Posdunine

In about 1940, V.L. Posdunine, a Soviet scientist and member of the Academy of Sciences of the USSR, seems to have commenced his systematic studies of heavily cavitating screw propellers [4-11]; he also inspired other Soviet work [12-15]. Posdunine's studies are remarkable in a number of respects. In the first place, they comprise, as far as I know, the first really rational and systematic studies of the subject, although other individuals had certainly tested and observed in isolated instances, propellers operating under heavily cavitating conditions. Posdunine's work was especially strong on the experimental and intuitive side (the theory being weaker) and he observed and discussed phenomena

242

which have only recently received notice and attention in our own work. For instance, he was well aware that the inflow to a supercavitating propeller is quite different than that to be expected from the theory of subcavitating propellers or from actuator disc theory; in fact, he wrote of observing during water tunnel tests that the inflow speed at a heavily supercavitating screw was actually <u>less</u> than the approach speed far ahead of the screw; for this reason he undoubtedly inspired a series of Soviet theoretical studies [12-14], attempting (unsuccessfully) to derive an appropriate momentum theory for supercavitating propellers. He also seemed to understand the importance of blade interference for the operation of supercavitating propellers; he had conducted (others actually performed the tests) experiments on a systematic series of screws with blade numbers from 2 to 16 and blade area ratios from .09 to 1.12; he also stimulated theoretical work on non-linear cascades of flapped supercavitating profiles [15]. Posdunine was in fact so impressed by the new effects introduced into propeller operation in the supercavitating regime that he wrote "The operational differences between supercavitating and ordinary noncavitating propellers are so great in point of physical phenomena that no common theory of operation or single type of construction will suit the two kinds of screw." He clearly recognized the importance of blade profile shape and by 1945 had carried out experiments on at least 28 hydrofoils in a wide variety of shapes; the most advanced of these look like good shapes to us except that they are much thicker than we would ordinarily use, see Fig. 1. He failed, probably for this reason, to produce lift-drag ratios greater than 8.5. Posdunine did, however, determine from his experiments at least two very fundamental facts about supercavitating profiles: (i) that their quality decreases with increasing thickness, and (ii) that for best results they should be operated at an incidence close to that for "shock-free entry." Much of his systematic experimentation, particularly on screws themselves, has not yet been paralleled by us and, unfortunately, he described his results in only general terms.

In his published work (1941-47) on supercavitating propellers, Posdunine made a plea for a better theoretical understanding of the various important aspects of supercavitating propeller flow, including: supercavitating flow about profiles and the inflow to a supercavitating propeller. The published Soviet work in emphasizing fundamentals, seems to fail in presenting useful formulae or methods which allow for the design of a cavitating screw or for the prediction of its performance, and we are left only to wonder whether supercavitating propellers of rational design have found application in the USSR. Posdunine's insight into the problems of supercavitating propellers seem most impressive, despite the fact that his insights found, at best, weak expression in analytical terms. While foreseeing most of the problems he did, however, seem to neglect in his published work the structural problems that must be dealt with in supercavitating propeller development — or can this perhaps be the reason that he experimented, finally, with such thick hydrofoil sections?

The existence of Posdunine's work was vaguely known in the West, but except for an early article in English, published in the Transactions of the Institution of Naval Architects [5], it was not read. Posdunine's views and his simple theory as expressed in his short British paper of 1943 are difficult to understand — the theory is in fact incorrect in its assumptions — and this is probably the reason why he did not inspire us. He did of course succeed in introducing

243

Tulin

POSDUNINE   (1945)

TMB-TULIN   (1954)

NEWTON-RADER (1960)

HYDRONAUTICS (1961)
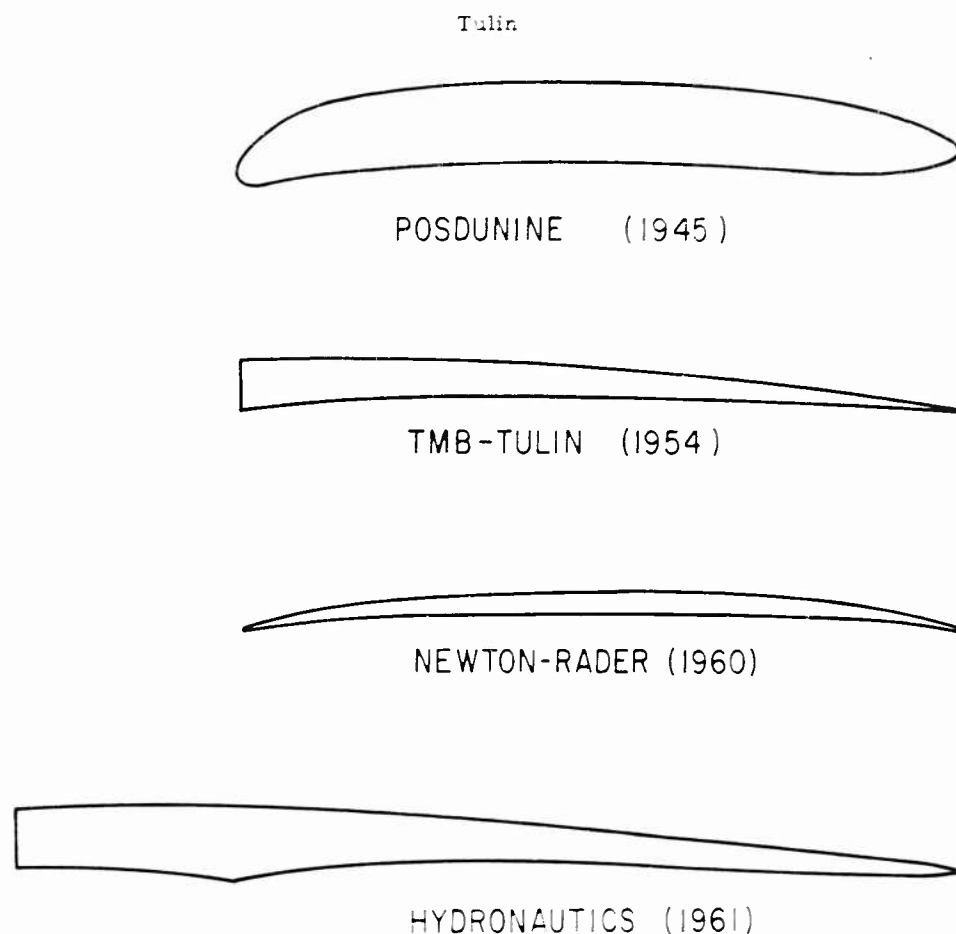
Fig. 1 - Supercavitating propeller profiles

the word "supercavitating" into the English language, through the publication of Ref. [5]. From Great Britain this word seems to have been imported directly into the David Taylor Model Basin.*

Developments at the David Taylor Model Basin

Without any knowledge of the history so far recited, I began theoretical studies of supercavitating two-dimensional flows at the David Taylor Model Basin in about 1952. These were at first definitely not inspired by a specific interest in propellers or hydrofoil craft, but by a simple curiosity about the

---

*In view of this fact it does seem a little ironical that a great literature having been built up here on the subject of supercavitation and supercavitating propellers, a movement has been inaugurated recently in Great Britain to introduce instead the use of the term "heavily-cavitating."

244

form of theory for thin bodies in cavity flow. For my beginning knowledge and interest in cavity flows, I was entirely indebted to Refs. [16-17] and to conversations with Phillip Eisenberg. The first application of linearized theory to supercavitating flow was for the case of thin strut shapes [18], and then with a growing interest in practical applications (as anticipated in the Introduction to Ref. [20]) for the case of lifting hydrofoil sections [19-21]. Thus the principal of design for low drag was discovered and applied, as an example, to the design of a particular hydrofoil section.

These theoretical results suggested, somewhat optimistically, "that supercavitating hydrofoil sections could be designed with efficiencies comparable to those of fully wetted sections." Thereupon the utilization of a theoretical low drag section in a supercavitating propeller was undertaken in early 1954, at first by H. Lerbs and later by A. Tachmindji.* As part of this effort, the calculation of upper cavity streamlines was undertaken in 1954 by the author and Miss Phyllis Burkardt, but was unfortunately not included in any unclassified work. It was first attempted to design a three-bladed propeller, but this was too highly stressed because of the thin blade sections being utilized, and a two-bladed design was finally accomplished, TMB Propeller 3460. It was lightly loaded (C_T = 0.145); of low blade area ratio (BAR = .196), and of moderate pitch (Pitch Ratio = 1.107). It is further described together with its performance and the design method utilized in Ref. [23]. This initial supercavitating propeller, designed according to theory and without the use of any experimental hydrofoil data whatsoever, was exceedingly successful in that the design performance with regard to thrust and efficiency were very closely verified during tests. The design method utilized may be described as imbedding two-dimensional supercavitating theory (linearized) for the profile performance into conventional (Ref. [22]) modern blade element theory. Thus no account at all is taken of possible interference (blade cascade) effects on the blade elements, of possible blockage effects that the thick cavity body might have on the approaching flow, or of the possible effect of the cavities on curvature or pitch corrections. Indeed, the experimental results in verifying the design performance suggested that such effects could be safely ignored, and such was the interpretation universally given them. This interpretation was strengthened by the similar success of a second supercavitating propeller of somewhat different characteristics (TMB Propeller No. 3509, Ref. [23]; C_T = 0.28; 3 blades; BAR = .332; Pitch Ratio = 1.533), which was in addition to laboratory tests installed on a small hydrofoil craft. Problems of propeller strength were to a certain extent recognized and dealt with during these early developments and a practical design method incorporating hydrodynamic (as previously indicated) and structural considerations resulted, Refs. [23-24]. However, the structural design remained based on the criteria of spanwise bending stresses (Taylor's method), ignoring chordwise bending. The latter turn out to be important for high speed propellers with thin leading edges. This design method thus ignores both important hydrodynamic and structural effects. It nevertheless has served valiantly, succeeding very well in its early applications and it remains the only design method for

---

*A number of other people at the Taylor Model Basin played an important role in this early development, including: Mr. William Morgan and CDR (now CAPT) Patrick Leehey, USN.

supercavitating propellers yet set forth in print; designers are therefore much indebted to the Taylor Model Basin and the authors of this method.

These initial developments at the Taylor Model Basin have been steadily expanded there, mainly through further propeller testing in both tunnels, towing tanks, and on small boats [25-34]; these are well reviewed in [1]. These tests have resulted in a better understanding of what may be expected in the way of operational characteristics of supercavitating propellers, if not in an increased understanding of their mechanism of operation. Outstanding, in our opinion, among the revelations of these tests were the discoveries: (a) that the thrust coefficient for a fully supercavitating propeller possesses a maximum, (b) that strength problems including leading edge vibration or "flutter" are of great importance in actual applications of supercavitating propellers and (c) finally, that the conventional method of analysis of supercavitating propellers often does not lead to accurate predictions of thrust or efficiency. The Taylor Model Basin also introduced the ventilated propeller, which operates with artificial cavities created by the introduction of air to the suction side of the blades [25,28]. This work was then followed here very closely by intensive studies of ventilated propellers at the Naval Ordnance Test Station (NOTS) in Pasadena, California.

Ventilation

It had been known at least since the wartime work of Reichardt in his water tunnel at Göttingen [35], that air may be used to create cavities behind blunt bodies and thereby produce flows which may be quite precisely correlated with natural cavitating flows on the basis of equal cavitation number, defined as the ratio of the difference between ambient and cavity pressure to the dynamic head. Some of Reichardt's experiments were repeated at the Taylor Model Basin just after the war by Phillip Eisenberg and Hartley Pond. Attention was drawn not only in this way to so-called ventilated flows, but during the same period a good deal of experimental and theoretical interest in cavity flows had been stimulated by problems involving the air-filled cavities formed during the water entry of air launched torpedoes. We were therefore quite consciously aware of the possibility of ventilated flows from the beginning of our research.

In 1955 just after the publication of Ref. [20] and apparently in response to the predictions of the theory contained therein, personnel of the Hydrodynamics Division of the Langley Laboratory of the then National Advisory Committee for Aeronautics (NACA) began both experimental and theoretical studies of supercavitating flows. The greatest part of this work was done by Virgil E. Johnson, Jr. The aim of Johnson and his co-workers was to provide information which might lead to improved take-off and alighting gear for water-based aircraft. They saw in supercavitating operation a possible way to avoid the dangerous transition from fully wetted to cavitating flows which had up to that time prevented the use of hydrofoils at high speeds. In the beginning of this work it was realized that ventilated rather than naturally cavitating operation offered the better prospect for smooth operation from relatively low speeds to take-off. The NACA work did indeed confirm the advantages and reveal the feasibility of ventilated wing systems [36]. In fact, at the very early initiative of Eugene Handler of the Bureau of Naval Weapons a ventilated hydrofoil was designed and has been successfully applied to a small water-based aircraft [37]. Further,

246

in good part as a derivative of the early NACA work, very intensive studies of ventilated wing systems for high speed hydrofoil craft are being carried out today in various laboratories, including our own.

Thus was the stage well set for the introduction of the ventilated propeller in 1959. Taylor Model Basin tests, including air requirement measurements, on a simple propeller operating both ventilated and with natural cavitation showed, as was to be expected, that performance was the same in the two modes of operation, the cavitation number being fixed [25]. More recent Soviet tests have shown the same thing [38]. The Soviets have gone on to utilize ventilation in order to operate supercavitating propellers on self-propelled models at Froude scaled speeds. In this way and by pressure measurements on the model stern they have shown that supercavitating propellers may be expected to reduce thrust deduction. Theory leads to the same conclusion, as we shall see in a later section of this paper.

The Naval Ordnance Test Station (NOTS) in Pasadena, California, together with the Ordnance Research Laboratory at Penn. State University, has during the last four or five years conducted intensive studies of ventilated propellers of both the supercavitating and base ventilated type. They have published very interesting accounts of their research [39-42], which included tests both in a water tunnel and on a 10 ft torpedo-like body run on a cableway. The effect of air flow rate to the propellers on the thrust, efficiency and radiated noise were determined. This research was of a pioneering nature in many regards. Almost in their own words, "a number of important advances... (were) made for the first time: (a) a ventilated propeller was used to propel a marine vehicle, (b) a gas other than air was used for propeller ventilation, and (c) a supercavitating propeller was used to propel a torpedo-like vehicle." Although the final consequences of the NOTS test are unclear, they certainly demonstrated the general feasibility of ventilated propellers for real applications. In connection with the NOTS experimental studies of ventilated propellers, particularly of the base-vented type, it should be mentioned that these were unquestionably very much stimulated by certain theoretical and experimental work on base-vented hydrofoil sections conducted in the same laboratory [43-44]; this work closely parallels that of Johnson [45], and has been followed by more recent studies [46].

Ventilation clearly offers the possibility of operating supercavitating propellers at lower forward speeds than would otherwise be possible — even, as the Soviets showed, at the very low speeds associated with towing tests. This is certainly an enticing possibility, but no full scale applications to ships of any size have, to the best of my knowledge, been made. The development of ventilated propellers is continuing, though, as for instance through studies of air requirements, ventilation inception, and cavity pulsations [47-50].

It is worth noting, incidentally, that almost all steady cavity flow theory is equally applicable to ventilated and natural supercavitating flows since no account is taken of the exact nature of the light gas within the cavity. This is not, however, true of unsteady cavity flow theory where the compressibility of the cavity gas is crucial and must be taken into account.

Developments Abroad

Following the publication of the early Taylor Model Basin work and the 2nd ONR symposium on Naval Hydrodynamics, active interest in supercavitating propellers spread abroad, particularly in Sweden, Great Britain, the Netherlands and Japan. Activity has involved actual application to high speed planing boats (about which no detailed reports on performance or operating experience are yet available) and tunnel testing. These foreign tests contribute well over half of the more than 30 separate supercavitating propeller test results available today [51-54]. In addition, some foreign tests have not been reported, as in the case of a series of 12 propellers which have been tested by KaMeWa of Sweden. Incidentally, all of the test results available refer to propellers tested according to the DTME design method [24], with the exception of the so-called Newton-Rader series [51]. These latter propellers utilize blade sections developed empirically and quite unlike our own sections, Fig. 1.

Variable pitch supercavitating propellers were quite early suggested and tested by KaMeWa of Sweden, and the latter has made available some test results which show what might be gained during off-design operation by a variable pitch installation [54].

These are confirmed by some tests conducted in our own water tunnel for the Hamilton Standard Division of the United Aircraft Corporation [55], which I shall touch upon again later.

Among the more interesting tests conducted abroad were those at the NSMB in Wageningen [52], in which supercavitating screws of different sizes were tested in a solid wall tunnel in order to obtain information on wall effects. These revealed the existence of no such effects, and this may be explained theoretically, as we mention again later in discussing the momentum theory of supercavitating propellers. Also in connection with wall effects, certain propeller tests carried out for HYDRONAUTICS in a solid wall tunnel at the Swedish State Experimental Towing Tank in Goteborg are interesting. In these tests we specified that the length of the cavity behind the propeller be measured. In fact, over part of the measurement range, which included very low advance coefficients, the cavity extended completely down the tunnel — thus causing choking. This phenomena may also be explained and predicted theoretically with the aid of momentum theory.

Other Developments Here

We have already referred herein to the work at the Taylor Model Basin and to ventilated propeller tests at the Naval Ordnance Test Station in Pasadena. Besides these, other very important work related to the theory and application of supercavitating propellers has been conducted elsewhere in the United States during the last nine or ten years.

Motivated by the promise held forth by the predictions of the earliest theory [19-20], and by the possibility of supercavitating applications to hydrofoil boats and propellers, the Mechanics Branch of the Office of Naval Research deliberately undertook to support, encourage, and co-ordinate a research program in

the area of supercavitating flows starting in late 1955. A number of groups in Universities were supported under this program, including those in the Hydrodynamics Laboratory at the California Institute of Technology, the St. Anthony Falls Laboratory of the University of Minnesota, the Mathematics Departments at the Renssalaer Polytechnic Institute and at the Delft Technical University (the Netherlands), and the Ordnance Research Laboratory at the Pennsylvania State University. In addition the ONR undertook to provide the means for technical co-ordination of the Navy's in-house interests in this field, particularly between certain interested groups in the Bureau of Ships, the Bureau of Naval Weapons and their laboratories. The ONR further sought to encourage scientific interest in supercavitating flows through the 2nd ONR Symposium on Naval Hydrodynamics in 1958, one-half of which was devoted to that subject. In fact the collected papers of that Symposium already reflect the success of the ONR, even at that early date, in stimulating activity in this field of research. Much of this work, which was both theoretical and experimental, served to elucidate our understanding of supercavitating flow past foils and wings, of wall interference, of cascade flows, and of unsteady effects. It has provided an invaluable foundation for the research and applications which followed, both in reference to propellers and hydrofoil wings.

During the past five years the groups most active in theoretical research on supercavitating flows have been located at the California Institute of Technology, NOTS, Pasadena, Stanford University, and at HYDRONAUTICS, Incorporated. A thorough review of the literature is not available, but reasonably lengthy bibliographies are available (in the form of references) in Refs. [56-57]; these are supplemented by certain references in the present paper.

The intensive HYDRONAUTICS effort in the field of supercavitating flows has been very closely associated with propeller development. This work has been supported primarily by the Bureau of Ships of the U.S. Navy. It has involved theoretical and experimental research and full scale design. Some of the results of our theoretical research on the mechanism of operation of supercavitating propellers are indicated in another section of this paper; these results largely explain the off-design operation of supercavitating propellers and have led to improvements in design. In addition to this work, detailed studies of the performance of a wide variety of hydrofoil sections, including strength as a parameter have been carried out [58-59]. Without results such as these it is not possible properly to design supercavitating propellers taking strength into account. We have also introduced two new features in section design, which improve very much the strength qualities of useful sections. These are: (a) the section annex, which is appended to the base of the usual section within the cavity envelope, thus increasing its bending strength without interfering with its hydrodynamic operation while supercavitating and (b) the use of almost parabolic thickness in addition to camber and incidence, thus increasing in an optimum way both the strength of the nose in chordwise bending and the spanwise bending strength of supercavitating sections. A section utilizing both of these features is shown at the bottom of Fig. 1.

In early 1960, HYDRONAUTICS undertook studies of propellers, pod and tail strut for the H. S. DENNISON, a 100 ton, 60 knot hydrofoil ship built by the Grumman Aircraft Corporation for the U. S. Maritime Administration. It was recognized from the beginning that the propellers would have to be supercavitating.

249

After a study of alternatives, including dual propellers mounted fore and aft on a nacelle, it was decided to utilize a single propeller mounted at the aft end of a fully wetted pod and attached to the hull by a vertical strut of very special design. It was during the first tests (at the DTMB) of a three bladed propeller of our design for the DENNISON that it was first discovered that a supercavitating propeller suffers adverse loss of thrust at low advance coefficients; previous available supercavitating propeller tests had not been conducted at sufficient low advance coefficients to reveal the arched shape of the fully supercavitating thrust characteristic curve. It was this discovery that sparked our studies of cavity blockage and blade interference effects, which are discussed later in this paper. This first propeller proved unsuitable for a number of reasons and we subsequently designed and had manufactured in stainless steel a two-bladed 42 inch propeller of pitch ratio 0.98 employing low-drag annexed sections and a blade area ratio of 0.25. Many of the design features incorporated were a result of concern about the provision of adequate thrust at take-off, as this became of great importance to us following the revelations of the earlier tests. This two-bladed propeller was tested, final revisions in design incorporated, manufactured, and finally utilized to power the DENNISON during her very first trials in July 1962. Quite adequate hydrodynamic performance both off-design and at the cruise speed were attained, the propeller being very well matched to the turbine [60], as is essential for fuel economy and best turbine utilization. After a few hours of operation this propeller failed in an outboard region near the leading edge probably due to corrosion fatigue. This failure had been preceded about a week earlier by the very similar failure of a quite different three-bladed supercavitating propeller of Taylor Model Basin design during high speed model tests. These failures together led to the realization that chordwise bending could not be neglected in the design of supercavitating propellers and that available methods of propeller stress analysis are therefore quite inadequate. An alternate three-bladed propeller of Taylor Model Basin design was already under construction prior to and during the first trials of the DENNISON and following the failure of our two-bladed propeller, this alternate screw was modified to thicken the leading edges and was subsequently utilized [60].

The DENNISON was a successful and very useful pioneer in many respects. Speaking only of the propeller, she demonstrated that a supercavitating screw could successfully take-off and propel a large hydrofoil boat at speeds even in excess of 60 knots with propeller efficiencies in the neighborhood of 60 percent and while absorbing powers approaching 15,000 h.p. Furthermore it was demonstrated that this would be done while obtaining a good matching between the propeller and turbine. This achievement involved a solution to the problem of mating the propeller, pod and supporting strut, and of the recognition and partial solution of the off-design problem for supercavitating propellers. Finally, of course, the experience with the DENNISON taught us the invaluable lesson that stress problems for high speed propellers operating in seawater are more severe even than we had thought.

The design and construction of the DENNISON was overall a bold project. In connection with propulsion it must be particularly pointed out that the successful development of shafting, gears, and turbine by the General Electric Company, to deliver over 15,000 h.p. from the hull to the submerged screw through a long right-angle drive system was a noteworthy engineering achievement.

The use of naturally supercavitating propellers is limited to sufficiently high forward speeds and loadings; therefore difficulties arise in many potentially fruitful applications involving speeds where the operation of subcavitating propellers is inevitably accompanied by serious harmful cavitation, but which are yet not high enough for naturally supercavitating propellers [61]. The ventilated propeller offers the possibility of supercavitating operation at quite low forward speeds, as we have commented here already. So, too, does the naturally supercavitating propeller in a Kort nozzle which we have proposed and studied analytically [62]. This system seems to offer particular advantages for the propulsion of hydrofoil craft in the speed range between about 20-40 knots and would therefore seem to deserve some experimental study.

In order to bring this history right up to date, a recent interesting development might be mentioned. It involves the proposal for a variable camber supercavitating propeller by George Rosen of the Hamilton Standard Division of the United Aircraft Corporation. The propeller would employ a hinged forward portion. We have recently designed and tested such a supercavitating propeller for the United Aircraft Corporation [55]; these tests indicate that a marked improvement in off-design thrust capability is attainable with a variable camber propeller in comparison both with fixed pitch and variable pitch propellers. These results are not only of potential practical importance, but they seem to us to confirm our theoretical conclusions (as discussed later in this paper) regarding the nature of the off-design problem and the importance of camber in dealing with it.

GENERAL CHARACTERISTICS OF CAVITATING PROPELLERS

Definition of Supercavitating Operation

The onset of cavitation on a marine propeller has been described many times. Cavitation may occur first in the hub vortex, the tip vortices, or on the blades. At first appearance it has little effect on the propeller performance, although it may be accompanied by blade erosion and radiated noise. The appearance and extent of cavitation depends both upon the cavitation number based on rotative speed, σ_n, and the propeller loading. In general the spread of cavitation over a blade is accelerated by reducing σ_n and increasing the propeller loading. Cavitation generally spreads from the tip downward to the hub. This is illustrated in Fig. 2, showing the cavitation patterns and thrust associated with propeller operation over a range of rotative speeds, the forward speed and ambient pressure being fixed. The spread of cavitation is seen to be accompanied by a diminishing of the rate at which thrust increases with rotative speed, until when cavitation occurs over nearly the whole blade, an increase of RPM may (as in the case illustrated) result in no additional thrust, or even a slight decrease of the latter. In these cases the losses due to cavitation completely absorb the additional power supplied to the screw. If, however, the rotative speed is even further increased, then the thrust generally rises again. This is illustrated in Fig. 3 which is schematic based on actual test data. At the same time the cavities become longer and more fully developed. It is at this stage that the propeller may be said to be supercavitating. To be precise, we may define supercavitating operation as beginning at the rotative speed where the rate of thrust increase with rotative speed is first a minimum, the forward

251

Tulin
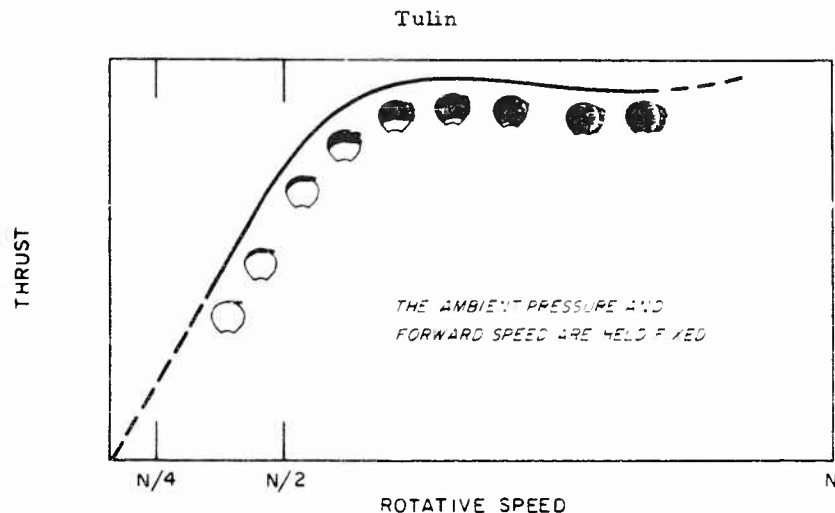
Fig. 2 - Cavitation development and its effect on thrust
(after Smith, 1937)

speed and ambient pressure being held fixed. This definition is in part arbitrary, but it is based on the experimental observation that the thrust increases more rapidly with rotative speed once the spread of cavitation over the blade from tip to hub is completed.

In Fig. 4a are presented the thrust characteristics of a supercavitating propeller obtained in towing tank tests with simulated cavitation (ventilation) [38]. They represent the most complete set of thrust characteristics for a single
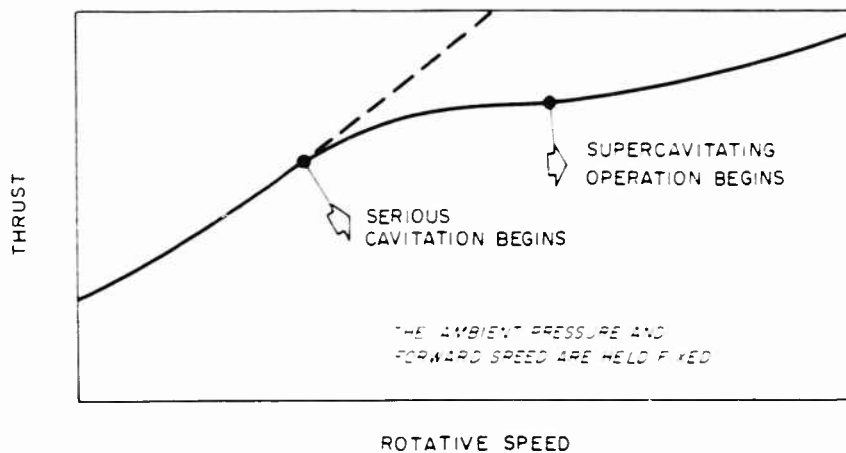
Fig. 3 - Schematic of thrust variation with rotative speed - carried into the supercavitating regime

252

propeller known to the author and they are at the same time typical of other available data. The propeller was 3 bladed, had a pitch-diameter ratio of 1.4, an area ratio of 0.51, and utilized "wedge sections which are usual for super-cavitating propellers" although "due to the necessity of setting the tubes for air supply and cavity pressure measuring, the blade thickness including the thick-ness of the leading edge was increased in comparison with the predicted values." The operating characteristics for the same propeller are shown in somewhat different form, Fig. 4b, where contours are given for constant values of σ_n rather than σ_o (note that the cavitation number based on true tip circumferen-tial speed would be about $\sigma_n/10$). These curves are very instructive. They do not, however, permit the rapid determination of conditions which correspond to supercavitating operation. For this purpose, these same thrust characteristics are presented in a different form in Fig. 5; here the slope of a given contour is proportional to the rate of change of thrust with rotative speed (forward speed and ambient pressure fixed). Utilizing the definition of supercavitating opera-tion just given, the region so defined is drawn in and is later used in construct-ing Fig. 6. The narrow extent of this region is quite evident, and particularly striking is the shrinking of this region down to the so-called fully supercavitat-ing line for low advance coefficients. This diagram also reveals that for low J's there exists a rotative speed for which the thrust is a maximum, the forward speed and ambient pressure being fixed.

The chart shown as Fig. 5 (C_T vs. $1/J$; σ_o fixed) seems very useful to us and we recommend it for propulsion system analysis. For instance, the thrust required vs. forward speed for a given craft may be plotted on the same diagram, the propeller diameter having been tentatively selected, and the required rotative
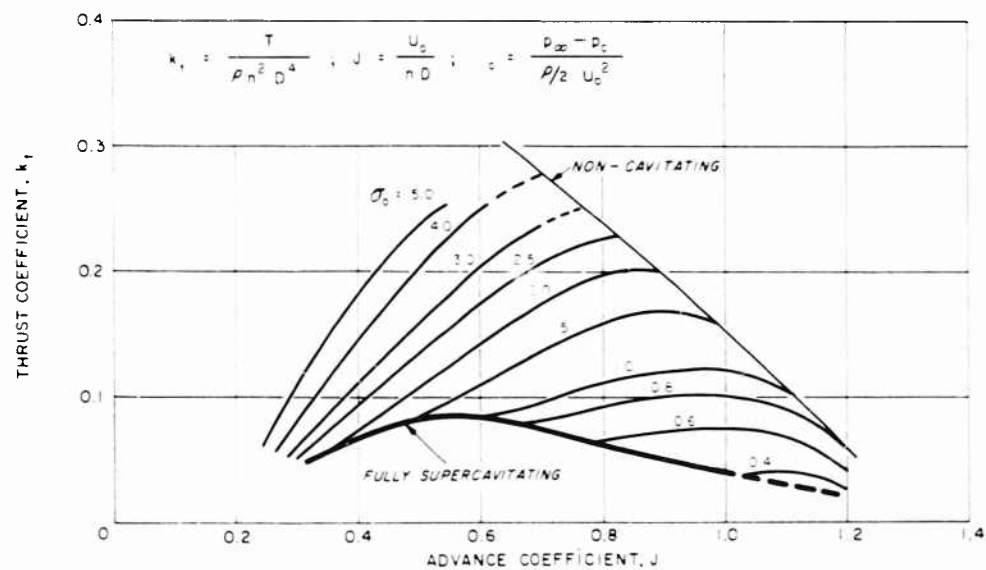
Fig. 4a - Thrust characteristic curves for a super-
cavitating propeller (σ_o fixed) (from Ref. [40])

253
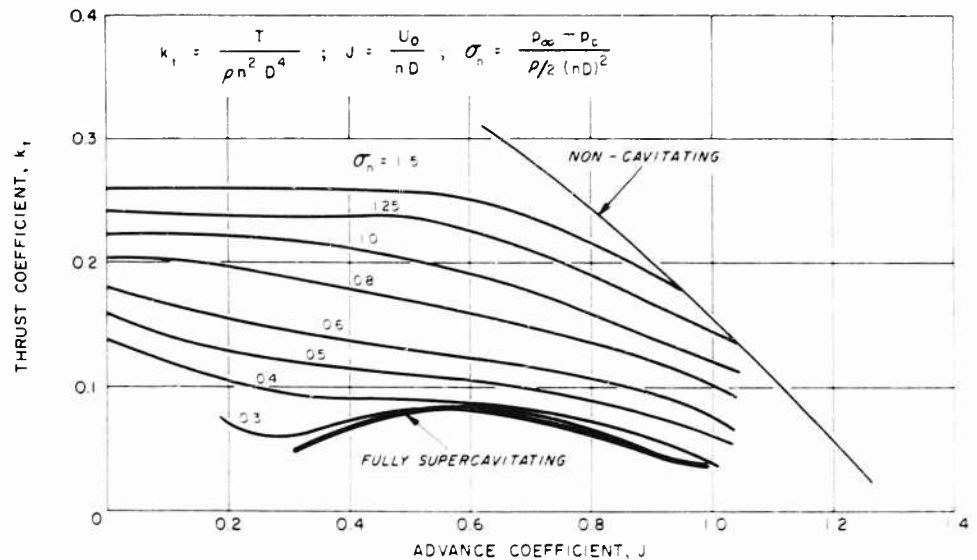
Fig. 4b - Thrust characteristic curves for a super-
cavitating propeller (σ_n fixed) (from Ref. [40])

speeds and regimes of operation of the supercavitating propeller are then ex-
hibited in a particularly clear way for the whole speed range of the craft.

Fully Supercavitating Operation

Imagine that the rotative speed of a propeller has been increased until su-
percavitating operation begins, and is now fixed along with the forward speed,
but that the ambient pressure is decreased or, equivalently, that the cavity pres-
sure is increased. The thrust acting on the propeller will now at first decrease,
because the lifting effectiveness of the blade elements is reduced by the effec-
tive increase in pressure on the suction side (reduction in blade cavitation num-
ber). As the blade cavitation numbers based on true rotative speed approach
zero (say — become less than .03 or so) further loss of effectiveness with re-
duction of ambient pressure is virtually halted. The thrust thus approaches a
certain limiting value which depends on the advance coefficient and is hardly
affected by further decrease of the cavitation number. We might then say that
the propeller is fully supercavitating. The typical characteristic curve for fully
supercavitating operation may be roughly described as a circular or parabolic
arc with a maximum near the middle of the propellers' J range. This curve is
quite apparent in Figs. 4a and 4b.

Fully supercavitating operation of propellers is of great importance for
high speed hydrofoil boats (say 50 knots and up), both at cruise and take-off con-
ditions. For example, take a boat with a cruise speed of about 50 knots (σ_o =
0.4), a take-off speed of about 23 knots (σ_o = 1.9), using the supercavitating
propeller whose characteristics we have been discussing. Suppose this propeller

254

has been designed for k_t = 0.065 and J = 0.76 at the cruise point. Further suppose that the take-off at 23 knots requires the same thrust as at cruise. Then take-off (σ_o = 1.9) will occur close to the point on the fully-supercavitating curve at J = 0.4 and k_t = 0.065. The figures used are typical for a hydrofoil craft, and they demonstrate that high speed hydrofoil boat propellers are likely to be fully supercavitating or nearly so, at both the cruise and take-off points.

Note that the cruise condition is to the right and the take-off condition to the left of the maximum in the fully-supercavitating characteristic curve. In testing a propeller for application to a high speed hydrofoil boat it is therefore important to obtain data adequate to define this curve over a reasonable range about its maximum. In fact, the first evidence that this curve possessed a maximum at all was obtained in tests at the Taylor Model Basin of a 3 bladed supercavitating propeller designed for the H. S. DENNISON. The shape of this curve
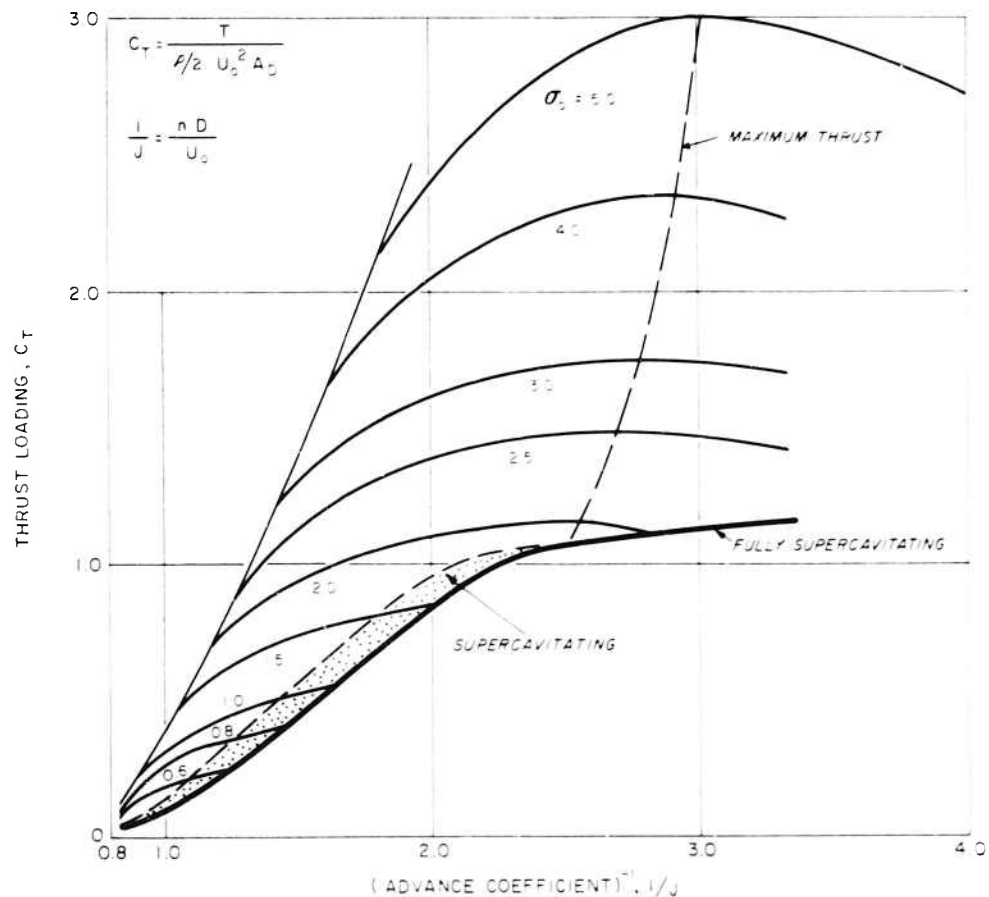
Fig. 5 - Thrust variation with rotative speed for a supercavitating propeller
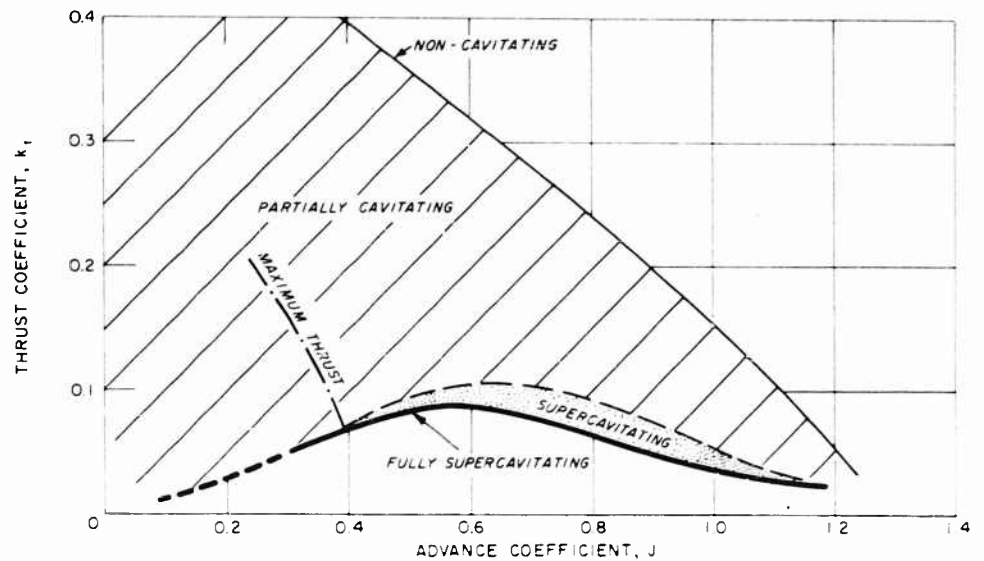
Fig. 6 - Regimes of operation for a supercavitating propeller

is, of course, unfortunate in that for the lower advance coefficients it implies reduced thrusting ability of the propeller with reduced forward speed. The propeller efficiency is at the same time dropping with decreasing advance coefficient. The attainment of adequate thrust at take-off, where more is generally needed than at cruise, is thus made difficult both because of the danger of running out of turbine RPM and of turbine torque (or power). Fortunately, properly designed supercavitating propellers generally manage at take-off if the thrust required there is not too much more than the thrust required at cruise.

The shape of the fully supercavitating characteristic curve is at first glance startling and unexpected, for the reason that it implies for operation to the right of the maximum in the curve a loss of lifting ability on the blades (reduced k_t) accompanying an increase in the relative flow angle to the blades (reduced J). In fact, we are now quite convinced that this actually occurs, and that the explanation lies in the interference between a blade and the cavity shed from the preceding blade. This interference tends to reduce the blade lift by an amount which increases as the spacing between blade and preceding cavity narrows — as occurs when the advance coefficient is reduced. Over all of the fully-supercavitating operating range this blade-cavity (or cascade, as we sometimes call it) interference is important and it dominates the flow behavior at the lower advance coefficients. Later on in this paper we shall give some theoretical justification for these statements and we shall describe in a little more detail the nature of the flow through and about fully-supercavitating propellers. Let us only state here that quite different phenomena than we are used to for non-cavitating propellers accompany the operation of fully-supercavitating propellers; that not only is the interference between blades and cavities important, but also the overall blockage to the flow which is due to the great volume of

256

cavities around the blades; and that as a result we must be prepared to construct a new and appropriate theory of the operation of fully-supercavitating propellers.

Partially Cavitating Operation

The particular supercavitating propeller under consideration seems to operate over almost all of its thrust characteristic diagram in a partially cavitating state. By the latter we mean that a cavitation sheet does not completely cover the blade back. Generally speaking, operation in the partially cavitating regime is to be avoided as it may be accompanied by harmful cavitation.

The partially cavitating regime may be divided into two parts, separated by a line of "maximum thrust." To the high J side of this line an increase in rotative speed, the forward speed and ambient pressure being fixed, results in an increase in propeller thrust, while to the low J side of this line the same increase in rotative speed causes a loss in thrust. This latter behaviour is similar to that experienced by a fully supercavitating propeller at suitably low advance coefficients, and is probably due both to the spread of the cavitation pattern down to the inboard portion of the propeller and to the onset of blade-cavity interference. The existence of these regions and the line of maximum thrust are of considerable practical importance, for they reveal that only limited amounts of thrust can be produced by a given propeller for a given σ_o, and that this maximum thrust is not necessarily produced at the highest attainable rotative speed.

The Four Regimes of Propeller Operation

A great deal more might be said about supercavitating propeller operation such as can be deduced from the various thrust characteristic curves of the type presented here, but we must be satisfied for the present to have defined and briefly commented on the various regimes of operation and briefly to discuss the static thrust situation.

The four (or five) regimes of propeller operation discussed so far are depicted in Fig. 6. A map such as this is useful in the interpretation of data presented in the usual $k_t - J$ diagram. The definitions of these regimes have been given earlier in this paper and we have also given some idea about how the flow about the propeller is different in these various regions. This information is summarized below:

1. Non-Cavitating - No significant cavitation. Thrusting ability increases sharply with decreasing advance coefficient. Thrust increases at least as rapidly as rotative speed squared. A single thrust characteristic curve.

2. Partially Cavitating - Significant cavitation present, but cavitation patterns are not completely developed. Part of the blades may not be cavitating. A family of thrust characteristic curves which depend upon a cavitation number. Thrusting ability generally decreases sharply with decreasing advance coefficient (for σ_o fixed) or cavitation number (for J fixed). Regime divided into two parts by a line of maximum thrust (for fixed σ_o):

(a) INCREASING THRUST REGIME: On the low J side of the maximum thrust line an increase in rotative speed results in an increase in thrust. Cavitation effect thus relatively weak.

(b) DECLINING THRUST REGIME: On the high J side of the maximum thrust line an increase in rotative speed causes a loss in thrust. Effect of spreading cavitation and blade-cavity interference thus predominate.

3. Supercavitating - Cavitation patterns fully developed. All blade elements operating in supercavitating flow. However, local section cavitation numbers are high enough so that effectiveness of blade elements decreases with decreasing σ_n, causing thrust loss. A compact family of thrust characteristic curves. Interference effects between blade and the cavity from the preceding blade are important. Cavity volume large and causes important blockage effects on the inflow to the propeller.

4. Fully-Supercavitating - Section cavitation numbers very low (σ_n approximately less than 0.25 - 0.30 for most of the J range), so that effectiveness of blade elements ceases to change significantly with decreasing σ_n. A single thrust characteristic curve of arched shape. Pronounced blade interference and blockage effects. Inflow and blade element performance quite different than for non-cavitating propellers. This regime is of considerable importance for high speed hydrofoil craft and for ship propulsion at speeds in excess of 40 - 45 knots.

Static Thrust

A propeller can suffer severe deterioration of its thrusting ability due to cavitation even at zero forward speed if it is operating at high rotative speeds. In fact, based on the evidence presented in Fig. 6 it seems likely that static thrust operation often occurs in the "declining thrust" portion of the partially cavitating regime, and this means that the propeller operation is dominated by the effects of cavitation, including blade-cavity interference. There exists no adequate theory to deal with operation in this regime. It is therefore especially useful to have such thrust data as is presented in Fig. 4a for low and zero advance ratio. These data are not presented in that figure in their most useful form for the rapid estimation of static thrust, and in Fig. 7 are shown the results of a replotting in the form of $8 k_t - \sigma_n$ vs. $1 \sigma_n$. The advantage of this curve is that it immediately allows an estimation of the variation of thrust with rotative speed.

Efficiency

A subcavitating marine propeller suffers power losses on account of the friction acting on its blades and on account of the kinetic energy which it transfers to the fluid passing through its disc (induced losses). The former depends on the blade area and to a certain extent on the blade loading, while the latter depends largely on the net thrust loading, C_T; therefore the relative losses due to these two distinct causes depends very much on the net thrust loading. For moderately or lightly loaded subcavitating propellers, the frictional losses will usually predominate.

258
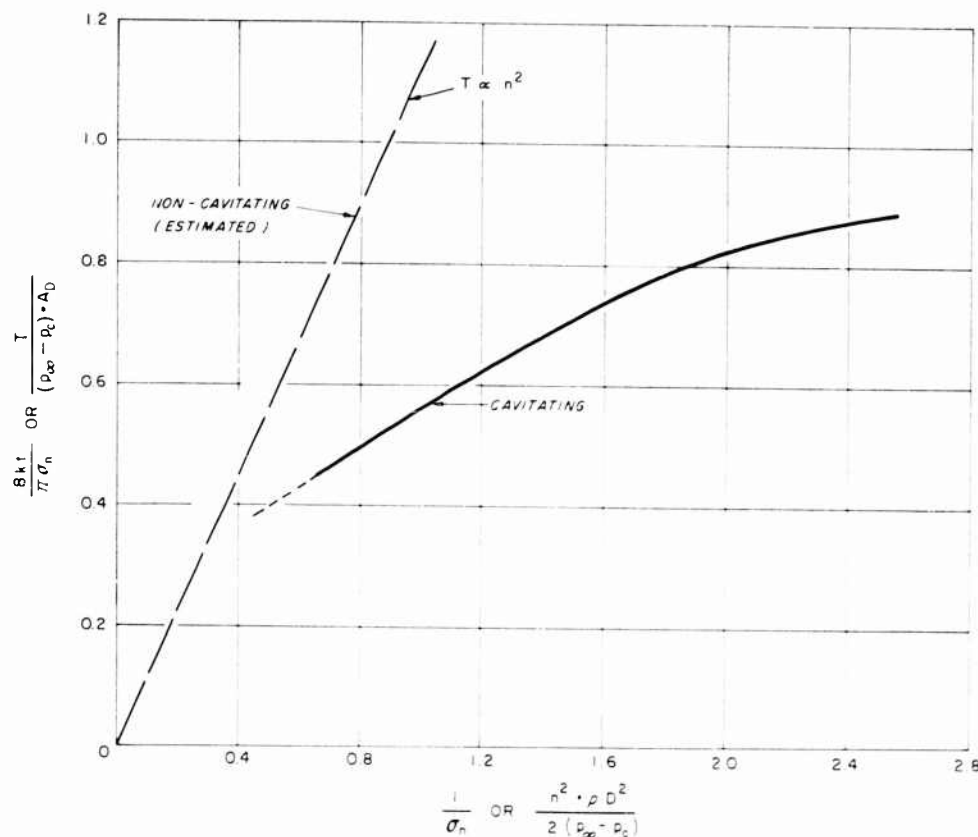
Fig. 7 - Effect of cavitation on static thrust

A supercavitating body generally (although not always) experiences a pressure drag which accompanies the separation of the flow streamlines and which has no counterpart in the smooth flow about a streamlined body such as a subcavitating blade element at normal loadings. The shape of modern supercavitating foils is constructed to minimize this pressure or cavity drag. Nevertheless, the losses suffered by a heavily supercavitating propeller are largely due to cavity drag. Other losses, usually smaller, are also incurred due to the friction drag on the pressure face and in many cases where the cavity thickness is inadequate, by friction on the upper blade surface. The induced losses are, we believe, much less for a supercavitating propeller than for its subcavitating counterpart operating at the same net thrust loading. In fact, ideal efficiencies greater than unity may in fact be experienced by supercavitating propellers. This situation is discussed later on in this paper.

Despite the possible alleviation of frictional and induced losses, the efficiencies of supercavitating propellers are in general not as high as those enjoyed by properly designed subcavitating propellers operating at the same thrust and advance coefficients. Of course it is often not at all possible to avoid cavitation, because the speed or loading is too high, and in such cases a properly

259

designed supercavitating propeller is called for, not always because of efficiency but often in order to avoid blade erosion. But all of this is well known [1,24,61].

The cavity drag of supercavitating blade elements depends very much on the foil shape [19-21], and the use of appropriate camber is crucial for the production of optimum blade efficiency. Detailed theoretical studies of two-dimensional supercavitating foil design including strength as a parameter have been carried out [58-59]. It has not generally been appreciated, however, that the two-dimensional efficiency of supercavitating blade elements is degraded in application to a propeller or wing due to the reduction in blade lift effectiveness caused by finite span effects; this is discussed again later in this paper.

Achievable supercavitating efficiencies depend upon a variety of parameters. Foremost among these are: loading (C_T), advance coefficient (J), and strength requirements. The influence of loading is seen from the experimental points in Fig. 8, which all refer to propellers designed according to the TMB method [24]. Therefore, they all have similar strength characteristics. However, they do represent different, although typical, values of advance coefficient. Despite this the influence of loading is clearly to be seen. Also shown are estimations of efficiency for a family of typical propellers calculated according to the TMB method [24], which is known generally to overestimate efficiency [1], and as estimated by our own method, which takes into account the effect of wide-bladedness and back-wetting on sectional efficiency. These calculations have been carried out by Mr. R. Barr of HYDRONAUTICS.

In our opinion the strength of propellers designed according to Ref. [24] may often not be adequate, so that generally thicker blades must often be utilized. Neither are such propellers designed to operate in strongly non-uniform flows, which require increases in the mean incidence of the elements in order to avoid face cavitation. For both of these reasons the efficiencies indicated in Fig. 8 are not necessarily to be achieved in practice.

In the early stages of design a cruise advance coefficient must be selected. The achievable efficiency depends very much on this selection, which is usually based on a compromise between the interests of the gear and shaft designers and the propeller designer. Therefore the improvement of supercavitating propeller efficiencies in high speed applications depends not only on the solution of hydrodynamic problems, but also upon mechanical developments.

The variation of propeller efficiency during heavily supercavitating operation at off-design conditions is of considerable importance for hydrofoil applications, as the possibility of running out of turbine power at take-off is by no means unsignificant. The detailed calculation of off-design efficiency is not in general possible, but good estimations may be made. In fact, the behaviour of the efficiency is rather simple; at sufficiently low advance coefficients the supercavitating efficiency becomes essentially independent of the cavitation number and linearly dependent on J! This is illustrated in Fig. 9 which is a schematic. This result, which has been found for many supercavitating propellers, is at first glance surprising, since at a given J, the thrust produced by the cavitating propeller depends a great deal on the cavitation number. There is, however, a simple explanation for this result.

Supercavitating Propellers
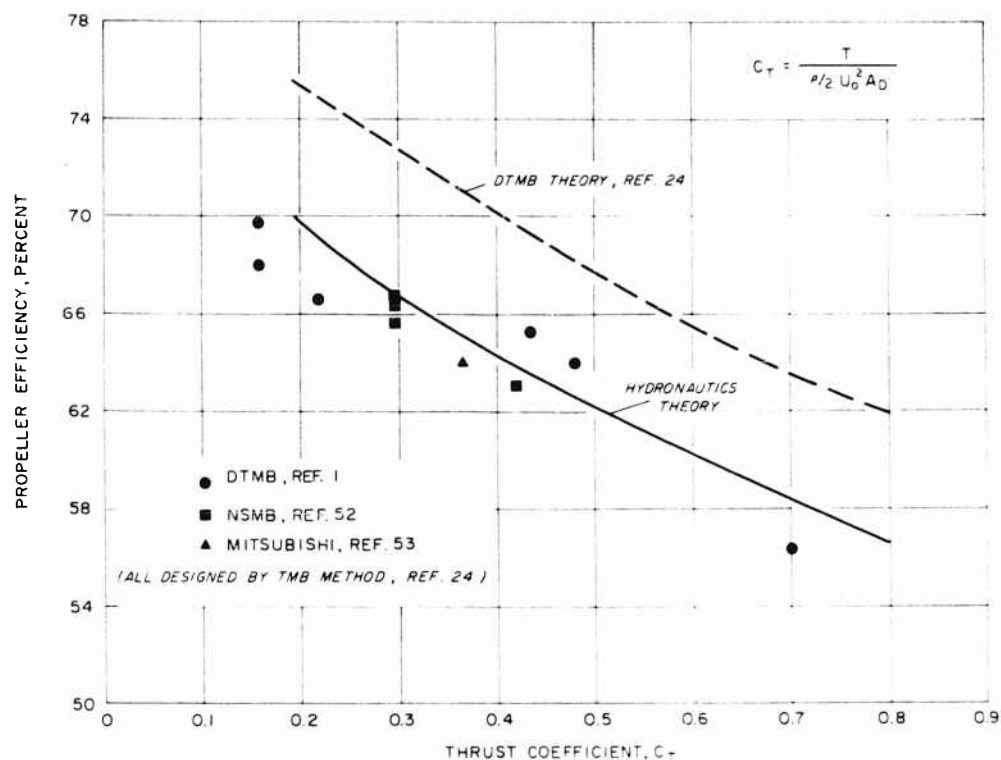
Fig. 8 - Supercavitating propeller efficiencies at design conditions

At sufficiently low advance coefficients the production of thrust due to blade incidence will dominate the camber produced thrust. The force acting on each blade element will thus very closely be normal to the line between the blade leading and trailing edges. This force decomposes into contributions to the thrust and torque whose ratio depends only on the blade pitch but not on the magnitude of the blade normal force; this ratio is thus independent of the inflow conditions. Under these conditions the blade efficiency becomes independent of cavitation number, and linearly dependent on advance coefficient. This result is indicated in the sketch inset in Fig. 9, which shows, for simplicity, a flat-faced blade element.

THE MECHANISM OF OPERATION OF SUPERCAVITATING PROPELLERS

Subcavitating Propellers - Review

The observation in water tunnels of operating supercavitating propellers reveals, the existence of substantial cavity formations, such as are shown in Figs. 10a - 10d. Indeed, the existence of these large cavities was noted by

261
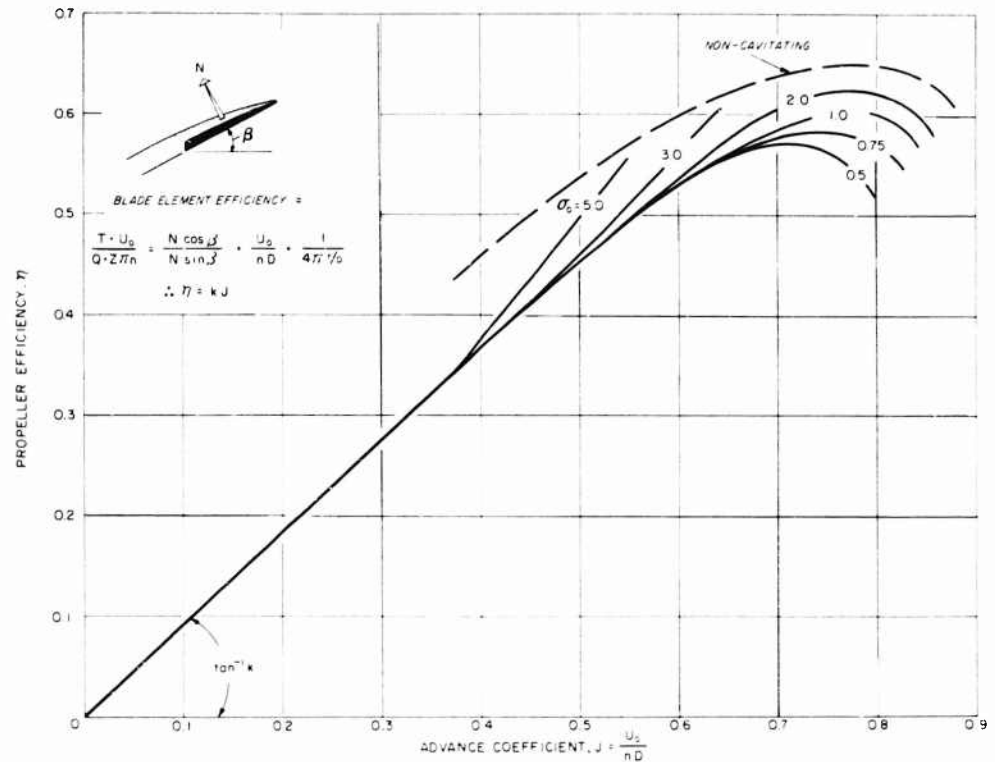
Fig. 9 - Schematic of propeller efficiency under cavitating conditions

Parsons some 70 years ago. These cavities are so large and their proximity to the blades so close that it would be really surprising should they not seriously affect the operation of the propeller. In fact, they cause the flow through a supercavitating propeller to be altogether different than for a subcavitating propeller. Let us review some of the things we know about the latter.

Usual subcavitating propeller blades are sufficiently thin so that the effect of their thickness on the flow is not in any way essential. The action of the blades is thus primarily due to their camber. They may thus be thought of as vortex surfaces composed of continuous distributions of vortex lines. These lines must of course be continuous in the fluid, so that they are shed from the blades into the propeller wake to form there one continuous trailing helical sheet per blade. The space behind the propeller is thus to a certain extent filled by shed vorticity. The latter may at each point where it exists be vectorially decomposed into a longitudinal and circumferential component, which induce, respectively, rotational and axial velocities in the flow.

If the number of blades becomes very large and the chord of each very short, it becomes possible to represent the axial flow field due to the propeller by consideration only of the effect of the circumferential component of the shed

262

Fig. 10a - σ_o = 1.0, J = 0.75

Fig. 10b - σ_o = 1.0, J = 0.60

Fig. 10c - σ_o = 0.5, J = 0.60
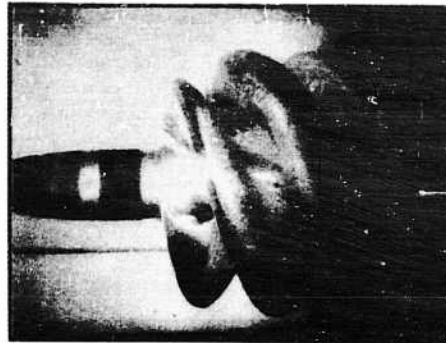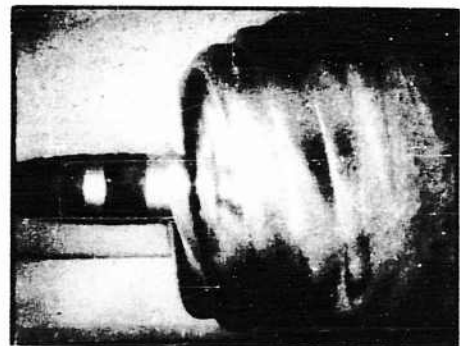
Fig. 10d - σ_o = 0.5, J = 0.40

Fig. 10 - Supercavitating propeller flows (taken at HYDRONAUTICS)

vorticity. This vorticity, may, in turn be thought of as comprising a continuous distribution of concentric vortex sheaths. These are of a radius which contracts behind the propeller, but for light loadings this contraction may be neglected. The propeller blades themselves degenerate into a disc composed of essentially radial vortex lines. These induce equal but opposite circumferential velocities across the disc. The longitudinal shed vorticity induces angular velocities which exactly cancels out the influence of the disc at any point in front of or outside the propeller slipstream, where the flow, in view of its irrotationality, cannot possess angular momentum. The angular velocities just behind the disc are thus half due to the longitudinal component of shed vorticity and half due to the bound vorticity in the disc. The increase in angular momentum at any point across the disc is in reaction to and linearly related to the local torque on the blade system.

Simple momentum theories incorporate the axial flow system as described above plus an assumed discontinuity in flow stagnation pressure across the disc,

263

but neglects the rotational flow in the slipstream — this may be shown to be a consistent procedure. Furthermore, in the case of light loadings it is possible to represent the flow field due to the trailing vortex sheath by a disc of sink singularities whose radial strength depends on the loading distribution, and the actuator disc rather than the vortex sheath picture is usually taken as the starting point of the momentum theory. Despite the usual neglect of rotation, the idealization of the propeller action introduced in the simple actuator disc model is fair enough in portraying the propeller as a device functioning continuously to accelerate fluid aft and to do useful work as a result of the reaction on the blades and shaft. The axial flow field is asymmetric when viewed from the propeller plane by an observer moving with the speed that prevails there. This asymmetry has as a consequence that the total increase in flow momentum as observed in the wake far downstream where the pressure has returned to ambient is just twice the increase in flow momentum as observed at the propeller disc. The pressure just behind the disc is, of course, greater than ambient and therein is stored half of the momentum eventually to be delivered to the slipstream. In view of continuity the flow velocity immediately in front of the disc is identical to the velocity just aft of it, but no work having been done on those fluid elements which have yet to pass through the disc, the increased momentum of the incoming flow has been realized at the expense of the pressure, which is suitably reduced.

In the absence of blade friction or form drag, the work done on an element of the flow on passing through the disc is simply the pressure increase across the disc times the velocity of the flow at the disc, say U_1, while the useful work done by the corresponding element of the propeller is simply the net thrust loading times the absolute forward velocity of the propeller, say U_o. The net thrust loading is also just equal to the head rise across the disc. The ideal efficiency is thus U_o/U_1. The pressure increase across the actuator disc, which equals the local net thrust loading, is also just equal to the gain in kinetic energy represented by the acceleration of the flow from far upstream to far downstream. As noted earlier, this pressure rise is also equal to the loss in rotational kinetic energy across the disc. These last facts allow the derivation of the result that the induced velocity at any point in the propeller disc is normal to the resultant relative velocity of a blade section.

A prediction of the actual thrust produced by a given propeller depends of course upon the hydrodynamic performance of the blades themselves, and this is usually predicted from two-dimensional theory or tests, suitably corrected for "wide-blade" or aspect ratio effects through the application of so-called "curvature corrections," see [63-65]. These are generally designed to compensate for the reduction in blade lift effectiveness due to spanwise changes in the blade and due to the flow spillage about the tip. A most noteworthy aspect of the situation for subcavitating blades is that the performance of the separate blade elements is hardly at all affected by the presence of the other blades [64]. In other words, blade interference or cascade effects are of negligible importance. This is in sharp contrast to the case of supercavitating blades, as we shall see.

Cavity Blockage

The shed vortex field which we have described above also exists in the case of a thrusting supercavitating propeller, but superimposed upon this is an equally

important field due to the cavities themselves. The latter flow may be thought of as due to cavity drag, while the former is due to thrust. The shape of cavities shed from a supercavitating propeller are highly variable; they depend upon the propeller thrust and efficiency, and upon the cavitation number. They may also depend upon tunnel wall effects — especially in the case of a completely closed water tunnel test section. These cavities originate in the plane of the propeller blades and extend downstream of the latter. Their length increases with decreasing cavitation number and becomes infinite for $\sigma_o = 0$. Generally, however, cavity lengths lie between 1/2 and 2 propeller diameters. By reducing the available flow area behind the propeller disc they cause the flow speed there to accelerate rapidly. In fact, they cause the flow speed behind the disc to take on a value which just corresponds to a flow pressure there equal to the cavity pressure.

The rotating cavities act in the manner of an obstacle to the flow approaching them and thus tend to retard this flow. The smaller the blade cavitational efficiency the stronger is this action. Due to this effect the accelerating action of thrust upon the approach flow may often be largely eliminated for a fully supercavitating propeller and it may not be uncommon for such propellers to operate with a net retardation of the inflow at the disc. It is clear that the usual subcavitating predictions of axial inflow are inapplicable; these facts are demonstrated by Eq. (1), given later. On the other hand, the angular induced velocity at the disc is entirely torque dependent and may be calculated in much the same way for subcavitating and supercavitating propellers. Note that the net induced velocity at the disc of a supercavitating propeller is not normal to the relative blade velocity as it is in the subcavitating case.

For a subcavitating propeller, the ideal efficiency always takes on values less than unity. In the present case, however, the inflow may be retarded, and the ideal efficiency may thus assume values in excess of unity. This is, at first, startling to contemplate. However, it is well known that even subcavitating propellers operating in strong wakes (regions of retarded flow) may enjoy efficiencies greater than unity. In blocking the oncoming flow, the cavities on a supercavitating propeller create, in a sense, a wake ahead of the propeller and in this way an increase in ideal efficiency is caused at the expense of cavity drag or blade efficiency.

Thrust Deduction

Subcavitating propellers placed behind a hull normally cause an increase in the drag of the latter because of the falling pressure gradient (suction field) which accompanies the acceleration of the flow in front of the disc. This drag or so-called "thrust deduction" is often significant. In the case of a supercavitating propeller placed behind a hull the thrust deduction may be largely eliminated; this has been noticed experimentally [38,66]. The thrust deduction may conceivably take on negative values, especially in the case of very close proximity of the hull and supercavitating propeller. This effect arises because of the flow retardation due to cavity blockage, as this retardation may result in net rising pressure gradients around the ships stern. In considering the combined effects of the thrust field and the drag (or cavity) field on the thrust deduction, it should be kept in mind that the spatial decay of these two fields directly ahead

265

of the screw are different, the induced velocities due to thrust decaying in the far field like (distance)$^{-1}$, while those induced due to drag decay like (distance)$^{-2}$. It is thus conceivable that the flow might be retarded directly before the screw, but slightly accelerated at larger distances forward. For this reason there probably exist no very simple relation between the ideal efficiency and thrust deduction accompanying fully supercavitating operation.

Typical flow patterns accompanying sub and supercavitating operation are shown in Fig. 11. It is worthwhile to examine those carefully. The altogether different character of the supercavitating and the subcavitating cases is easily seen.

New Momentum Theory for Supercavitating Flows

The designer will be interested to know just how serious are the cavity blockage effects on the inflow, for he must accurately predict the latter if his design is to meet the specifications. I have recently derived a momentum theory suitable for fully supercavitating propellers which allows a prediction of the
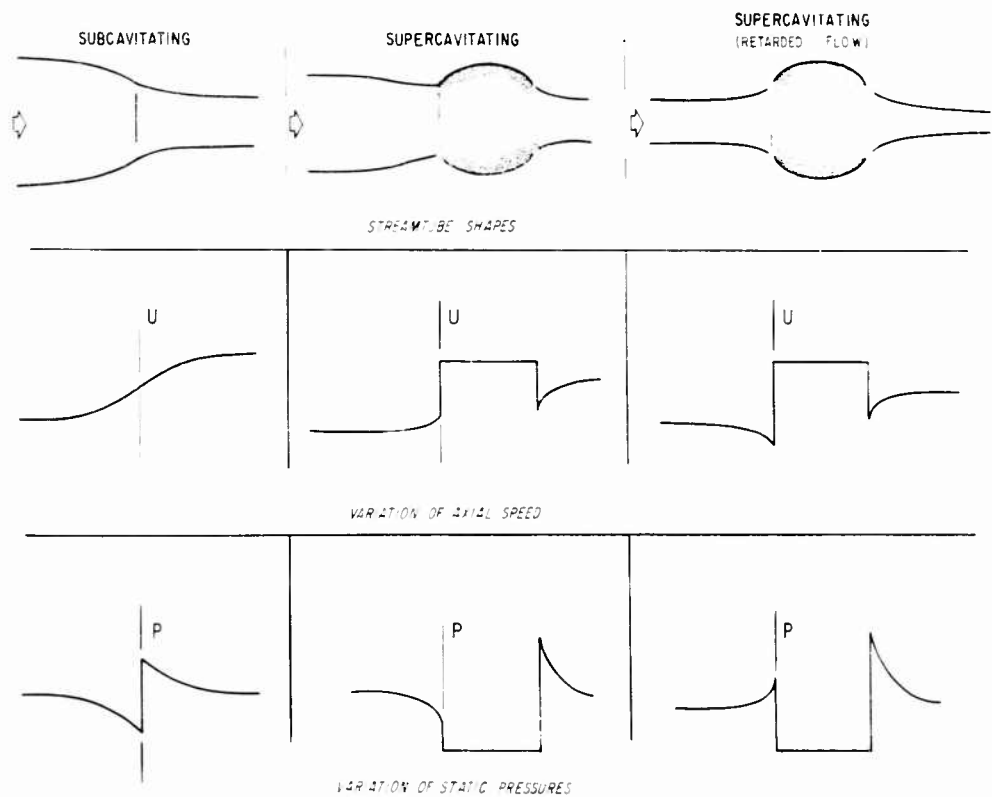
Fig. 11 - Schematic flows past thrusting propellers

266

axial induced velocity at the propeller disc in terms of the non-dimensional thrust loading (C_T), the blade cavitation efficiency (η_c), and the free stream cavitation number (σ_o). An important result of this theory is:

$$\frac{U_1}{U_o} = \sqrt{1 + \sigma_o + C_T/\eta_c} - \sqrt{C_T(1 - \eta_c)/\eta_c} \qquad \underline{\text{supercavitating}} \quad (1)$$

where

U_o is the free stream speed

U_1 is the axial speed at the propeller disc

σ_o is the free stream cavitation number, $p_\infty - p_c \big/ \frac{1}{2} \rho U_o^2$

C_T is the thrust coefficient, $T \big/ \frac{1}{2} \rho U_o^2 A_d$

η_c is the blade cavitation efficiency, η/η_i

η_i is the ideal efficiency, U_o/U_1

η is the net propeller efficiency.

This result may be compared with that from the usual (subcavitating) momentum theory:

$$\frac{U_1}{U_o} = \frac{1 + \sqrt{1 + C_T}}{2} \qquad \underline{\text{subcavitating}} \quad (2)$$

Numerical calculations from Eq. (1) for typical values of C_T, σ_o and η_c show quite clearly that the distribution of flow velocities and pressures which attend the operation of a heavily supercavitating propeller will not at all correspond to the predictions of theory for subcavitating propellers, as we have stated earlier. The use of the latter thus seem to us to be unjustified. Even for a relatively weakly supercavitating propeller it seems problematical that predictions of inflow speed based on subcavitating propeller theory are useful.

A number of other very useful facts may be deduced from this new momentum theory. It can, for instance, be shown that in an unbounded stream the cavity length is finite for $\sigma_o > 0$ and is infinite for $\sigma_o = 0$. The cavity maximum diameter is shown in the latter case to be finite only when the inflow and free stream speeds are identical. In the case of cavities of finite length, a loss of head occurs across the region of cavity collapse. The resulting head in the wake is still higher than the free stream head for a thrusting propeller and lower for a drag disc. The outflow speed just behind the region of cavity collapse is shown to be greater than the inflow speed for all cases of retarded inflow and for moderate degrees of accelerated inflow; for sufficiently large thrusts the reverse may be true. It can also be shown that no corrections to inflow speed are required for a supercavitating propeller operating either in an open jet or between solid walls; this is somewhat in contrast to the case of the subcavitating

267

propeller for which inflow speeds must be corrected for the presence of solid walls. Finally it may be shown that conditions occur under which a supercavitating propeller will choke a solid wall water tunnel; that is, the cavity length will become infinite at non-zero cavitation number ($\sigma_o > 0$). All of these results should serve to convince us that in dealing with the design, testing, and operation of supercavitating (or ventilated) propellers we are faced with certain phenomena which have no counterpart in our previous propeller experience.

Blade Interference Effects

Supercavitating blades of the same propeller, unlike their subcavitating counterparts, interact with each other in a most serious way. In fact, as we have already discussed earlier, it is essential to take into account the interference between a blade and the cavity shed from the preceding blade in order to understand and explain the arched shape of the fully supercavitating characteristic curve (k_t vs. J). Furthermore, these effects generally occur not only during off-design operation, but at the design point too.

In order to understand the nature of blade interference it is conceptually useful first of all to depict the blade section as an element in a two-dimensional cascade, Fig. 12, although we should not forget that the real connection between cascade and propeller flows is somewhat vague. For the high stagger angles (low pitch angles) usually utilized in supercavitating propellers, the largest part of the cascade effect would seem to be taken into account simply by allowing for the presence of a free surface beneath the blade element, Fig. 13. This is much simpler to do than to deal with the cascade flow itself and as long as the cascade turning angle is small, leads to reasonably good agreement (for the hydrofoil force coefficients) with results from the cascade theory itself, as we show later (Figs. 14 and 15). This simple theory is, furthermore, probably just as valid as cascade theory in application to propeller flows.

In a fully supercavitating propeller, the gap between the pressure face of each blade and the cavity shed from the preceding blade is not large relative to the blade chord. If the cavity is thin, then this gap — in ratio to the blade chord and measured normal to the chord — depends upon the ratio of the local advance ratio of the blade, and the local blade area ratio; as the cavity thickens, this ratio decreases. Thus,

$$\frac{\text{Gap}}{\text{Chord}} < \frac{U_o \times \cos \beta}{n \, B \, c} = \frac{\cos \beta}{\pi} \left(\frac{U_o}{nD_\ell}\right) \times \left(\frac{\pi D_\ell}{Bc}\right), \tag{3}$$

where

- U_o is the free stream speed
- n is the rotative speed in rev./unit time
- D_ℓ is the local disc diameter at the section
- B is the number of blades
- c is the local chord
- β is the local pitch angle.

268

Supercavitating Propellers
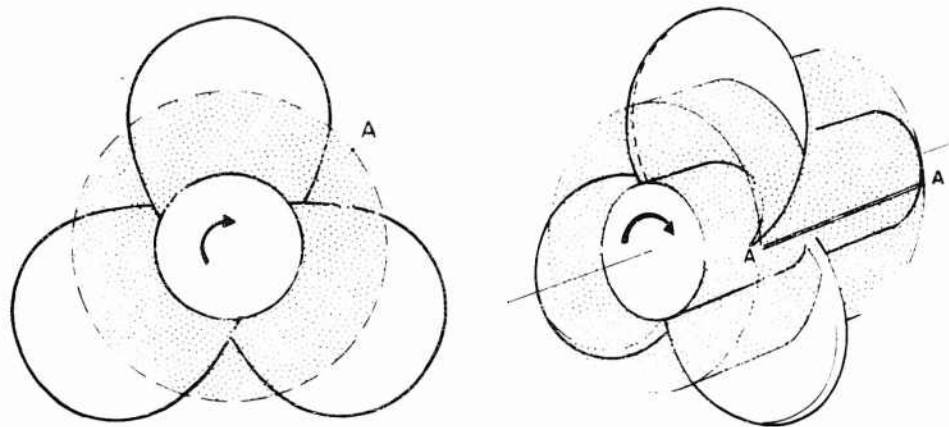
Front view - marine propeller
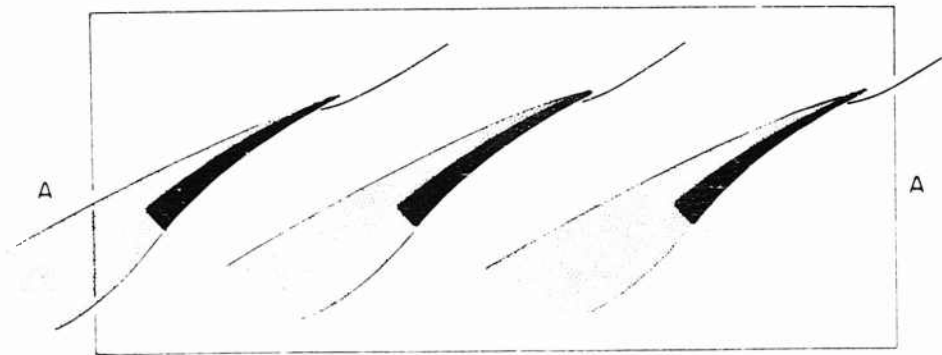
Typical cascade section

Fig. 12 - Conventional development of a cascade section

As an approximation for the entire propeller, this may be written,

$$\frac{\text{Gap}}{\text{Chord}} < \frac{J}{\pi \times \text{BAR}}$$ (4)

where J is the usual advance ratio and BAR is the expanded blade area ratio. It is thus clear that for usual supercavitating propellers (J < 1.0; BAR > 0.3) the gap-chord ratios for the blades are always less than 1.0. In fact, they are often less than 0.5.

When a supercavitating hydrofoil operates under a free surface at depth-chord ratios less than 1.0, it is well known that the performance characteristics of the hydrofoil are very much influenced by the proximity of the free surface [58]. The same proves to be true when a hydrofoil operates above a free surface.

269
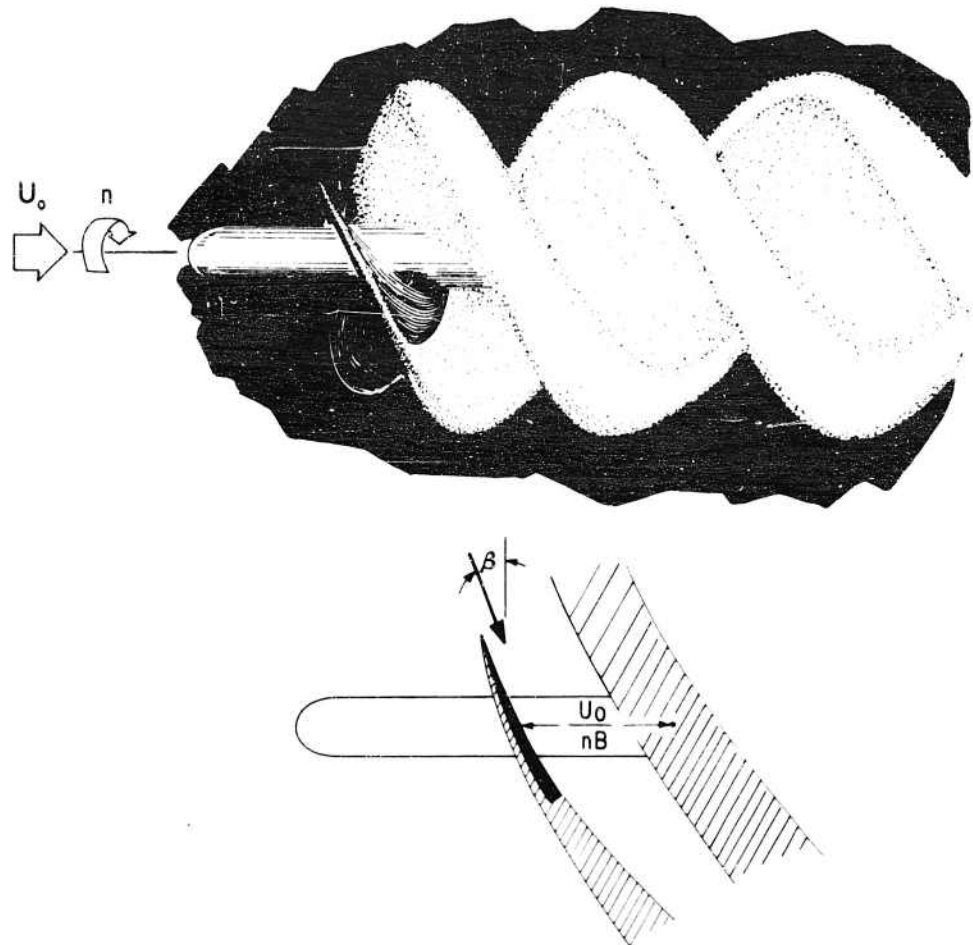
Fig. 13 - Interference between supercavitating blade and neighboring cavity

The solution of the appropriate boundary value problem is given in Ref. [56] for a flat plate hydrofoil at $\sigma = 0$, and the result is presented in Fig. 14. The lift is increasingly reduced as the plate approaches the free surface, as is to be expected. For a cambered foil, the effect of the surface is not as pronounced, as is shown in Fig. 15, which is based on unpublished theory and calculations. This fact can be taken advantage of in designing to mitigate the adverse effects of blade-cavity interference during off-design operation.

Also shown in Figs. 14 and 15, for comparison, are results taken from more elaborate computations based on cascade theory and presented in Refs. [67-68] (for the flat plate) and [69] (for the cambered plate). The former of these utilizes exact theory and the latter (two) linearized theory. Two of these theories (Refs. [67,69]) are based on a choked flow model, i.e., the cavitation
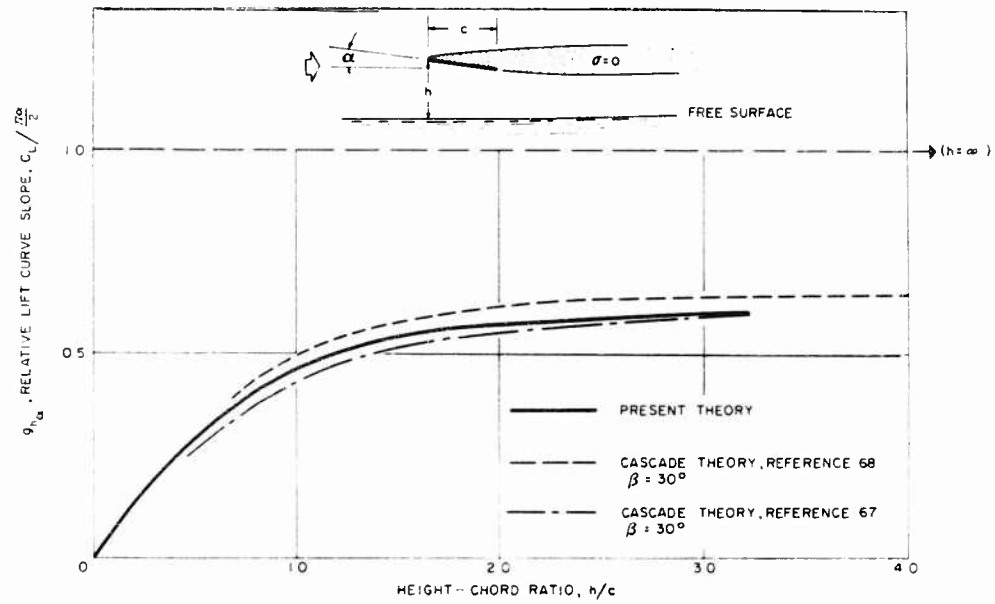
Fig. 14 - Lift curve for a supercavitating flat plate over a free surface
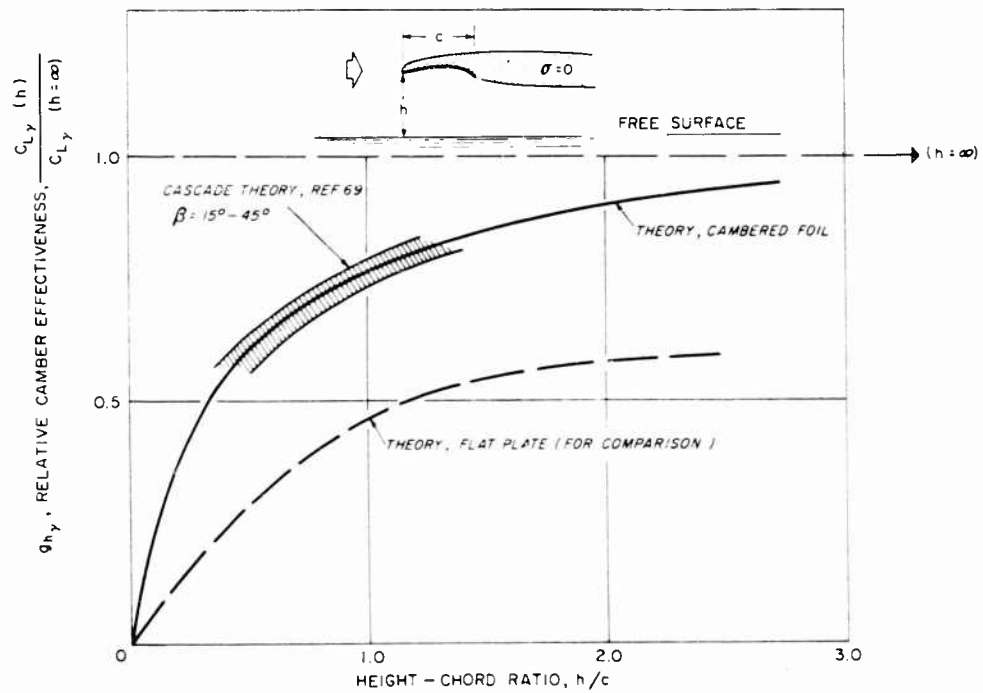
Fig. 15 - Camber effectiveness for a supercavitating foil over a free surface

271

number is not fixed in advance, but varies with the geometrical parameters (stagger angle, incidence, camber, and solidity) so as to produce an infinite length cavity. Other theory relating to choked cascade flows is presented in Refs. [15,70-71]. The only detailed study of cascade flows with finite cavities has been carried out by Cohen and Sutherland [68], using linearized theory, and it relates to flat plate cascades.

The phenomena of cascade choking has implications for fully supercavitating propeller flows and is therefore important to discuss, although it is not likely to occur in propellers because of the relieving effects of the radial flow. Two-dimensional choking is most easily understood through reference to a non-lifting, or simple cascade such as a series of vertical plates arrayed at equal intervals — one above another. The flow around one of these plates is exactly like the flow around the same plate between solid walls which are separated by the same distance as separates the plates in cascade, Fig. 16. The drag on the plate must result in a net axial momentum difference between the flow far upstream and far downstream. If the cavity pressure, p_c, is identical with the upstream pressure, p_o, then the velocities far upstream and far downstream are identical and no plate drag can be accounted for — nor, incidentally can the mass flow be balanced unless the cavity thickness vanishes. If the plate drag is not zero it is thus quite clear that the cavitation number corresponding to infinite cavity length must of necessity be greater than zero. Indeed, a simple relationship between choking cavitation number, σ^*, and the product of plate drag coefficient and plate spacing ratio may be derived:

$$C_D \times \left(\frac{c}{h} \right) = \sigma^* + 2 - 2\sqrt{1 + \sigma^*} . \tag{5}$$

This is shown as Fig. 16.

An increase in lift on the cascade element lowers the choking cavitation number as the net consequence of flow turning between far upstream and far downstream. The relations governing a choked cascade flow may be derived from momentum considerations and are:

$$C_D \times \left(\frac{c}{h_o} \right) = \sigma^* + 2 - 2 \cos \delta \sqrt{1 + \sigma^*} \tag{6}$$

$$C_L \times \left(\frac{c}{h_o} \right) = 2 \sin \delta \sqrt{1 + \sigma^*} - \sigma^* \ctn \beta . \tag{7}$$

where

- C_L is the lift coefficient

- δ is the turning angle (see Fig. 17)

- β is the pitch angle (see Fig. 17), and

- σ^* is the choking cavitation number based on the relative speed to the section.

272
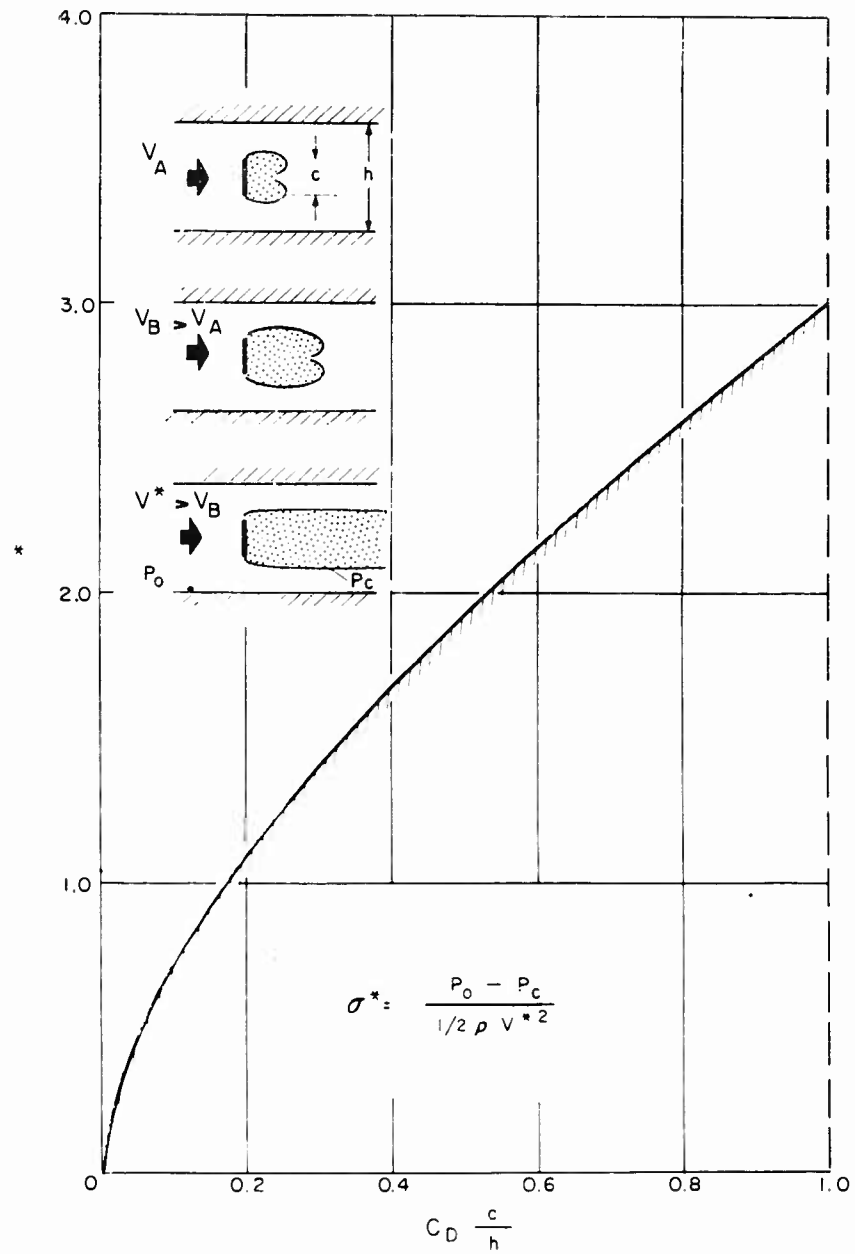
Fig. 16 - Choking in a simple cascade
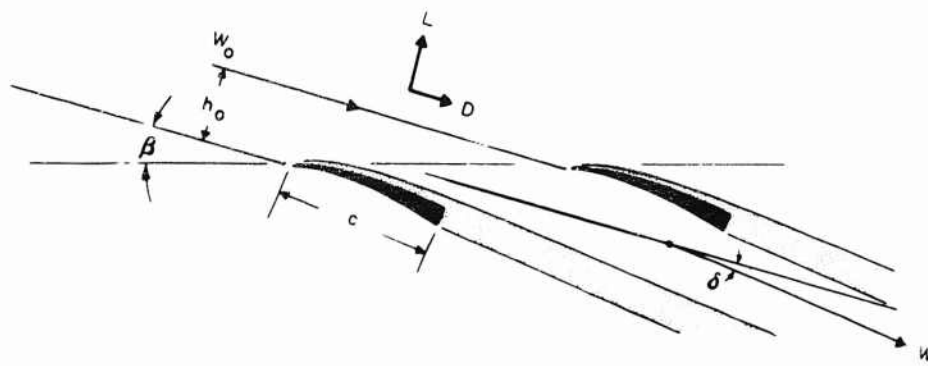
$$C_D \cdot \frac{c}{h_o} \;=\; \sigma^* + 2 - 2\sqrt{1 + \sigma^*}\,\cos\delta$$
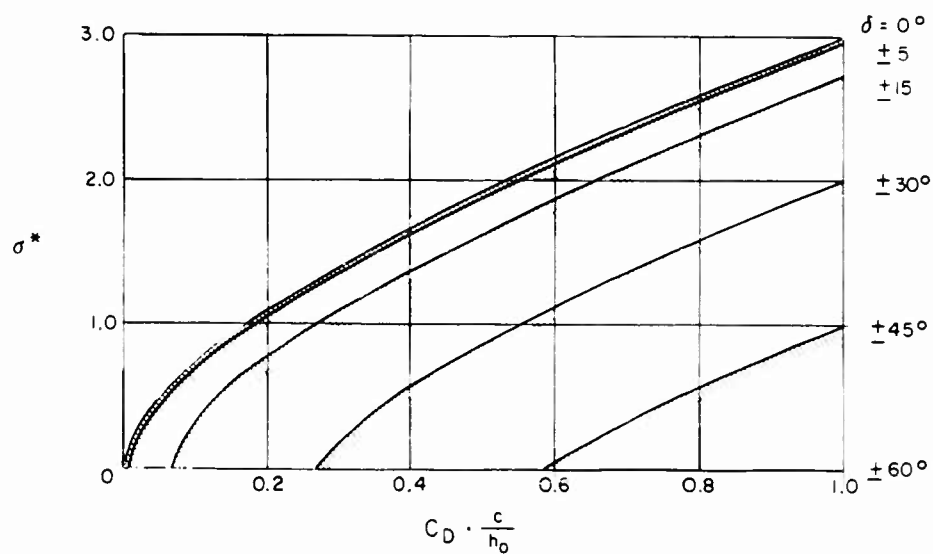
for operation at $\sigma^* = 0$: $\dfrac{L}{D} > 4\,\dfrac{h_o}{c}\,\dfrac{1}{C_L}$

Fig. 17 - Choking in a lifting cascade

274

The relieving effect of flow turning due to lift on the choking cavitation number
is indicated in Fig. 17. It is even seen to be possible to operate a turning cas-
cade at zero cavitation number provided that the blade efficiencies (L/D) are
suitably high. If $(D/L)^2 \ll 1$, then for $\sigma^* = 0$:

$$\frac{L}{D} = \frac{h_o}{c} \times \frac{4}{C_L} . \tag{8}$$

For smaller L/D's than given by (8), σ^* is greater than zero. With the aid of
(8) it may be shown that a flat plate cascade typical of a supercavitating propel-
ler is much too inefficient to operate unchoked at low but typical section cavita-
tion numbers (several hundredths); even a cambered cascade is unlikely to op-
erate unchoked down to zero cavitation number.

We have already commented that the radial flow that occurs in the flow
through a propeller probably relieves the tendency toward cascade choking. It
is nevertheless useful to understand the two-dimensional results, for they serve
to convince us that we cannot likely make estimates of the length or shape of the
cavities shed from the blades on the basis of isolated flow results pertaining to
the length and shape of cavities shed by the individual sections. On the contrary,
the overall length and shape of the collective cavity or "bubble" behind the pro-
peller disc is almost surely determined by the flow around the outside of that
bubble together with gross characteristics such as thrust coefficient (C_T), for-
ward cavitation number (σ_o), and blade cavitational efficiency (η_c).

The existence of cascade choking and a lower bound to possible cavitation
numbers in the two-dimensional theory hampers us in its application to propel-
lers, since theoretical predictions at suitably low section cavitation numbers
may not therefore be attainable. Furthermore, the validity of a cascade model
for a typical propeller flow is somewhat dubious. For these reasons and be-
cause of its much greater simplicity we very much favor the interference model
based on a hydrofoil operating over a free surface. This model has in our ex-
perience proven to be very useful for the estimation of propeller section force
coefficients.

Based on this model, the lift on a cascade element may be written:

$$L = \rho/2 \ U^2 \times c \times \frac{\pi}{2} \alpha \times g(h/c) , \tag{9}$$

where

   U   is the relative speed to the element

   α is the entering incidence, and

   $g(h/c)$ is a function which takes into account the effect of the gap in re-
            ducing lift (for $h/c \to \infty$, $g \to 1.0$).

It might be suggested, taking heed of Acosta's comments in [69], that the
correlation between this model and the real cascade flow might be improved by
taking into account the turning of the flow in the latter, which tends to reduce

the effective incidence of the flat plate elements. Thus, the effective angle of attack, α_{eff}, might be taken as the average of the incidence of the flow entering and leaving the cascade, or $\alpha_{eff} = \alpha - \delta/2$, where δ is the turning angle. The latter may be estimated from the following result, which may be obtained by equating the transverse force on the blade row to the rate of change of transverse momentum:

$$\delta \approx \frac{C_L \times \beta_o}{2} . \tag{10}$$

However, for low-pitch cascades such as are involved here, this angle is always small compared to the entering incidence, so that $\alpha_{eff} \approx \alpha$.

The validity of our approximations (at least relative to cascade flows) for low pitch angles may be judged by the correlation, presented earlier in Figs. 14 and 15, between the lift effectiveness as calculated thereby with calculations according to both linearized and exact theories; the correlation is seen to be quite good enough for our present purposes.

Appropriate values of $g(h/c)$ in (9) may be obtained from Fig. 14. For the flat plate:

$$g_\alpha(h/c) \approx .50 \ h/c \qquad \text{for} \quad (h/c) < 1.0 . \tag{11}$$

This useful result allows a prediction of the highly nonlinear lift curves of foils in cascade, as shown below.

The Fully Supercavitating Characteristic Curve

The parabolic or arched shape of the supercavitating characteristic curve (k_t vs. j) may now be explained. To do this we consider the performance of a flat plate cascade at a pitch angle typical for the outboard sections of a supercavitating propeller, as shown in Fig. 18.
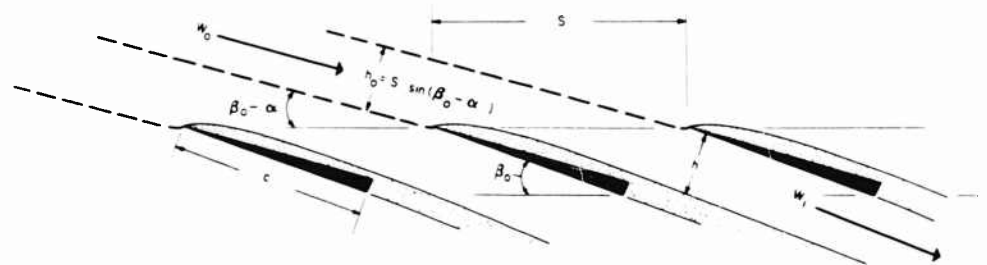
Fig. 18 - Cascade schematic

The flow entering between any two blades is conserved, so that

$$w_o \times s \times \sin (\beta_o - \alpha) = w_1 \times h ,\tag{12}$$

where it has been assumed that the flow between the plate and cavity beneath it is essentially parallel. For small σ_n, then $w_o \approx w_1$ and

$$\frac{h}{s} \approx (\beta_o - \alpha)$$

or

$$\frac{h}{c} \approx \frac{(\beta_o - \alpha)}{(BAR)} ,\tag{13}$$

where it has been assumed that $\beta_o \approx \sin \beta_o$, i.e., that $\beta_o <$ about 30°, as is usual over the most important part of the blade. Again, BAR is the propeller expanded blade area ratio.

In order to simplify the result further we may assume that $h/c <$ about 1.0, as is very often the case. Then, (9) becomes, using (11) and (13)

$$\frac{L}{qs} \approx \frac{\pi}{4} \alpha(\beta_o - \alpha) .\tag{14}$$

The lift produced by the cascade thus reaches a maximum at an incidence equal to one-half of the section pitch angle, i.e., when $\alpha = \beta_o/2$. The maximum lift reached is

$$\frac{L}{qs} (max.) \approx \frac{\pi \beta_o^2}{16} .\tag{15}$$

The maximum lift is seen, in this approximation at least, to be independent of the blade area ratio or cascade solidity.

The meaning of the result (14), is that the decrease in blade-cavity gap which accompanies an increase in entering incidence (α) causes a loss in lift effectiveness which for sufficiently small gaps (corresponding to $\alpha > \beta_o/2$) more than offsets the increase in lift due to increasing incidence along. This is the way in which the arched shape of the fully supercavitating thrust characteristic curve may be explained. We may, in fact, write

$$k_t \approx \left(\frac{\pi^3}{8}\right) \times \frac{L}{qs} \approx \frac{\pi^4}{32} \left[\lambda(\beta_o - \lambda)\right]$$

or

$$k_t \approx 4 k_t(max.) \times \left[\frac{\lambda}{\beta_o} \left(1 - \frac{\lambda}{\beta_o}\right)\right].\tag{16}$$

where we have neglected terms of the order β_o^3, where λ is J/π, and where

$$k_t(\text{max.}) \approx \frac{\pi^4}{128} \times \beta_o^2 . \tag{17}$$

It would be surprising if this analysis, in addition to explaining qualitatively the observed behaviour of fully supercavitating propellers could be used as well for prediction, for many approximations have been made. For example, the change in propeller inflow which accompanies changes in the thrust and cavitational efficiency has been neglected. Nevertheless we have made a comparison between the experimentally determined fully supercavitating characteristic curve earlier presented in Fig. 4, with the prediction according to (16). The result is shown as Fig. 19.
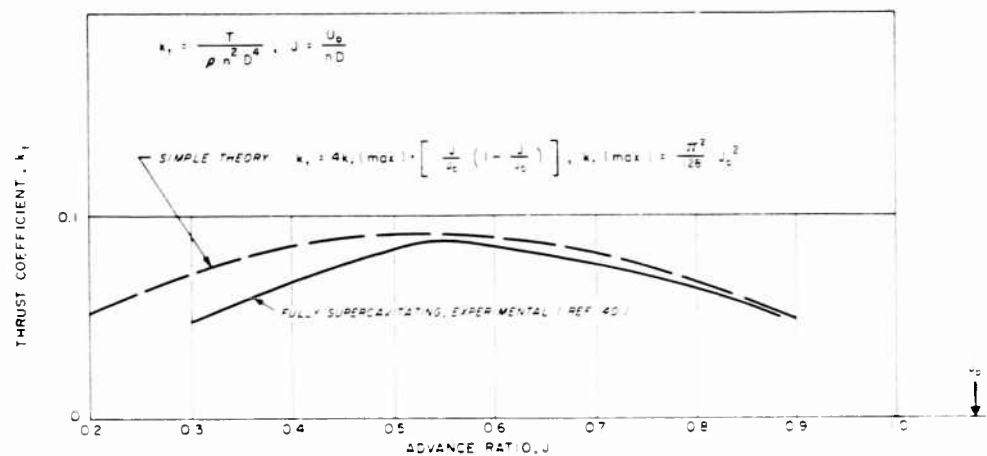
Fig. 19 - Comparison of predicted fully supercavitating thrust with experiment for flat-faced blades

The Advantages of Camber

It is well known that the use of camber in supercavitating hydrofoils is essential for the optimization of the lift-drag ratio [20], and intensive quantitative studies of optimum foil design have been carried out taking into account the foil strength. (The latter is, incidentally, absolutely crucial to consider in any realistic comparison of foils, and conclusions reached in the absence of structural considerations are not likely to be meaningful.)

Further, our preceding analysis of blade-cavity interference reveals the additional advantage of camber in improving the thrusting performance of fully supercavitating propellers during off-design operation. This advantage lies in the relatively milder effect of the cavity proximity in reducing lift due to camber in comparison to its effect on lift due to incidence, as is shown by comparison

278

of Figs. 14 and 15. Experience bears out theory in this respect, to the extent that larger maximum values of k_t are attainable with cambered blades than without.

The Effects of Blade-Cavity Interference at the Design Point

It seems crucial to consider interference effects in estimating performance not only during off-design operation but at the design point itself. In fact, we have found that lack of agreement, Refs. [1,52], between experimental and predicted design thrust coefficients and efficiencies for supercavitating propellers designed according to the method of Ref. [24], is very much reduced by the application of interference and blockage corrections to both thrust and efficiency. The interference corrections to the thrust take into account the reduced lift effectiveness caused by the proximity to the pressure faces of the cavity from the preceding blade, while the blockage correction takes into account the increased incidence due to reduced inflow speeds. These two effects act in opposite directions and often tend to cancel each other. This is, in our opinion, the reason why in the case of the first few supercavitating propellers designed and tested at the Taylor Model Basin such good results were obtained. However, these effects do not always negate each other, as in the case of the three supercavitating propellers tested at the NSMB [52]. The agreement with design k_t was not good. When account is taken of interference effects in the prediction of k_t, however, good agreement is obtained as is shown in Fig. 20. The latter is based on calculations carried out by Mr. R. Barr of HYDRONAUTICS. In these calculations curvature corrections derived from subcavitating theory were used and pitch corrections based on curvature corrections were utilized, as we believe is appropriate. The generally good agreement that we have obtained leads us to believe that supercavitating curvature corrections are unlikely to differ very significantly from the subcavitating case. The experience of Johnson [36], in his very successful application of the subcavitating Jones finite-span correction to low aspect ratio supercavitating wings further reinforces our belief. At any rate we cannot agree with Ref. [1] in blaming the disagreement between conventional predictions and experimental values of thrust on incorrect curvature corrections. Rather we believe that most of the disagreement lies in the neglect of blockage and blade interference effects.

It is also now agreed [1], that experimental efficiencies at the design point consistently fail to attain the values predicted by the conventional design method [24]. The explanation for this is not, in our opinion, to be found in any single weakness of the theory, but rather is due to a number of faults. First of all, and very important, a reduction of lift effectiveness whether in incidence or camber inevitably results in a proportionate reduction in lift-drag ratio. The reason for this lies simply in the fact that following a reduction of lift effectiveness an increase in incidence or camber must be employed to maintain approximately the same pressure distribution or lift; and since the drag is proportional to the product of the bottom slopes of the hydrofoil and the bottom pressures, the drag itself is consequently increased in proportion to the incidence or camber. The lift effectiveness of two-dimensional sections in isolated flow is reduced when these sections are employed in a propeller both on account of blade-cavity interference and finite span effects (the curvature correction). In fact, over the outboard regions of supercavitating propellers the lift effectiveness and

279
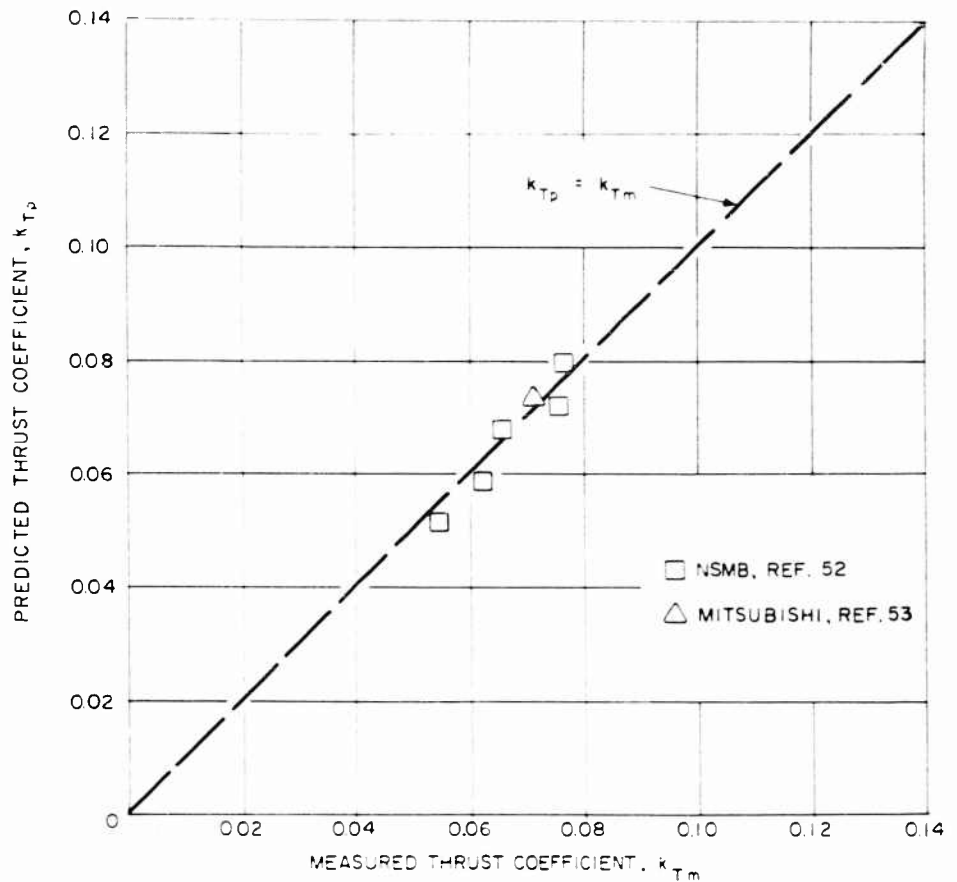
Fig. 20 - Comparison of predicted and measured thrust coefficients

resultant section efficiencies (L·D) may be reduced to 1/4 of the theoretical values for isolated flow. The conventional method of efficiency prediction does not take this reduction into account. A second important reason for disagreement between predictions and results lies in the usual assumption that the backs of the blades are not wetted and therefore do not suffer frictional resistance. It is a fact [1], that many supercavitating propellers do not in fact operate with cavities well clear of the blade backs. This is probably partly due to the incorrectness of the basic design procedure and partly to the employment of sections whose backs have been designed empirically. Mr. Barr of HYDRONAUTICS has estimated the design point efficiencies of supercavitating propellers taking into account by theory the loss of section L D due to reduced lift effectiveness and assuming that the frictional resistance of the backs is 50 percent of that of the faces. The results are compared with experimental measurement from various sources and are seen to be in good general agreement.

280

We have been using a design method taking into account all of the factors discussed in the foregoing and have experienced good results. We are thus convinced that we have at least approached a good understanding of the mechanism of operation of fully supercavitating propellers.

SUMMARY AND CONCLUSIONS

The present paper is designed to serve a number of purposes. It contains a review of the historical background and development of supercavitating propellers. This review includes a discussion of the pioneering research of the Soviet scientist Posdunine and of the early work at the Taylor Model Basin, as well as a brief survey of other U. S. and foreign work carried out up to the present time. This paper also discusses in general terms the important operating features of supercavitating and ventilated propellers and some aspects of their design. Four regimes of propeller operation are defined: subcavitating, partially cavitating, supercavitating, and fully-supercavitating. Further, the partially cavitating regime is shown generally to be divided into two regions wherein the thrust either increases or decreases with increasing rotative speed. A non-ambiguous definition of supercavitating operation is given, as beginning where the rate of change of thrust with rotative speed is a minimum. It is shown how to present propeller data so as to allow rapid determination of the supercavitating regime of operation, and it is shown with a specific example that the supercavitating regime occupies a relatively small region of the complete propeller operating map. The characteristic arched shape of the fully-supercavitating curve (k_t vs. J) is described and explained in terms of blade-cavity interference. The relatively simple shape of the supercavitating efficiency curve at moderate and low advance coefficients is also described and rationalized.

An important purpose of this paper is to briefly describe the mechanism of operation of supercavitating propellers and especially to introduce some "new" hydrodynamic phenomena which are associated with their behaviour. By the latter I refer particularly to blade-cavity interference and cavity blockage. Taken together, these effects cause the flow about supercavitating propellers to be fundamentally quite different than the flow about subcavitating propellers. Cavity blockage even causes the inflow to a supercavitating propeller to be retarded, and may thus result in negative thrust deductions and ideal efficiencies exceeding unity. Blade-cavity interference drastically effects the lift effectiveness and profile efficiency of supercavitating blade elements. It is directly responsible for the arched shape of the fully-supercavitating characteristic curve (k_t vs. J) and thus for the poor thrusting ability of supercavitating propellers at very high rotative speed. Supercavitating cascades and choking are also discussed herein in connection with blade-cavity interference. Quantitative results pertaining to both cavity blockage and blade-cavity interference are given. The latter lend further importance to the use of camber, not only to optimize design efficiencies but also to improve off-design performance. Finally it is stated that performance predictions which take into account the "new" phenomena discussed herein are in good general agreement with experimental results, and some specific results of calculations are given. We conclude, therefore, that we have at least approached a good understanding of the mechanism of operation of fully-supercavitating propellers. At the same time it must be admitted that present theory is entirely inadequate to calculate many details of the flow about

supercavitating propellers, and that a great deal of work therefore remains to be done.

REFERENCES

1. Venning, E., and Haberman, W.L., "Supercavitating Propeller Performance," Transactions of the SNAME, Vol. 70, 1962.

2. Parsons, C., "The Application of the Compound Steam Turbine to the Purpose of Marine Propulsion," Transactions of the Institute of Naval Architects, Vol. 38, 1897.

3. Barnaby, S.W., "On the Formation of Cavities in Water by Screw Propellers at High Speeds," Transactions of the Institute of Naval Architects, Vol. XXXIX, 1898.

4. Posdunine, V.L., "Problems of Ship Propellers," Soviet Science, No. 2, 1941.

5. Posdunine, V.L., "On the Working of Supercavitating Screw Propellers," (in English!), Doklady AN SSSR, Vol. XXXIX, No. 8, 1943; also, Transactions of the Institute of Naval Architects, Vol. 86, 1944.

6. Posdunine, V.L., "Supercavitating Propellers," Izvestia OTN AN SSSR, Nos. 1-2, 1944.

7. Posdunine, V.L., "The Construction and Performance of Supercavitating Propellers," Izv. OTN AN SSSR, Nos. 1-2, 1945.

8. Posdunine, V.L., "Basic Theory of the Construction and Performance of Supercavitating Propellers," Izv. OTN AN SSSR, Nos. 10-11, 1945.

9. Posdunine, V.L., "On Some Problems of the Hydromechanics of Flow Over Bodies with Separation," Izv. OTN, No. 2, 1946.

10. Posdunine, V.L., "The Quality of Supercavitating Propellers," Doklady AN SSSR, Vol. 57, No. 2, 1947.

11. Posdunine, V.L., "The Effectiveness of Supercavitating Propellers," Izv. OTN AN SSSR, No. 10, 1947.

12. Basin, A.M., "On the Theory of the Ideal Cavitating Propeller," Doklady AN SSSR, Vol. 49, 1945.

13. Lavrent'yev, V.M., "Theory of the Ideal Cavitating Propeller," Doklady AN SSSR, Vol. 50, 1945.

14. Epshteyn, L.A., "On the Action of the Ideal Supercavitating Propeller," Inzhenerniy Sbornik, Vol. 9, 1951.

15. Lambin, N.V., "The Separated Flow from Broken Profiles in Cascade," (PMM) Applied Mathematics and Mechanics, SSSR, Vol. 8, No. 3, 1944.

16. Eisenberg, P., "On the Mechanism and Prevention of Cavitation," TMB Rpt. 712, July 1950, and an Addendum, TMB Rpt. 842, October 1952.

17. Birkhoff, G., "Hydrodynamics," Princeton University Press for the University of Cincinnati, 1950.

18. Tulin, M.P., "Steady Two-Dimensional Cavity Flows About Slender Bodies," TMB Rpt. 834, May 1953.

19. Tulin, M.P., In Proceedings of an ONR-Admiralty Symposium on Hydro-ballistics, Office of Naval Research, September 1954 (Classified).

20. Tulin, M.P., and Burkart, M.P., "Linearized Theory for Flows about Lifting Foils at Zero Cavitation Number," DTMB Rpt. C-638, February 1955.

21. Tulin, M.P., "Supercavitating Flow Past Foils and Struts," NPL Symposium on Cavitation in Hydrodynamics (1955), Her Majesty's Stationery Office, London, England, 1956.

22. Eckhardt, M., and Morgan, W.B., "A Propeller Design Method," Transactions of the SNAME, Vol. 63, 1955.

23. Tachmidji, A.J., Morgan, W.B., Miller, M.L., and Hecker, R., "The Design and Performance of Supercavitating Propellers," DTMB Rpt. C-807, February 1957.

24. Tachmindji, A.J., and Morgan, W.B., "The Design and Estimated Performance of a Series of Supercavitating Propellers," Proceedings of the 2nd ONR Symposium on Naval Hydrodynamics (Government Printing Office), Washington, D.C., 1958.

25. Morgan, W.B., "Performance of a Ventilated Propeller," DTMB Contributed Paper to the American Towing Tank Conference, Berkeley, California, June 1959.

26. Caster, E.B., "TMB 3-Bladed Supercavitating Propeller Series," DTMB Rpt. 1245, August 1959.

27. Venning, E., "Applicability of a Supercavitating Propeller to a Small Speedboat," DTMB Rpt. 1459, November 1960.

28. Hecker, R., "Powering Performance of a Ventilated Propeller," DTMB Rpt. 1487, June 1961.

29. Hecker, R., and Peck, J.G., "Experimental Performance of TMB Supercavitating Propellers 3767, 3768, 3769, 3770, 3785, and 3820, DTMB Rpt. 1553, August 1961.

30. Hecker, R., and McDonald, N.A., "Backing Characteristics of Supercavitating Propellers," DTMB Rpt. 1604, January 1962.

31. Hecker, R., "Windmilling and Locked Shaft Performance of Supercavitating Propellers," DTMB Rpt. 1625, July 1962.

32. McDonald, N.A., and Hecker, R., "Steady-State Tests of Supercavitating Propellers for the Prediction of Crashback and Crashahead Performance," DTMB Rpt. 1629, August 1962.

33. Caster, E.B., "TMB 2-, 3-, 4-Bladed Supercavitating Propeller Series," DTMB Rpt. 1637, January 1963.

34. Hecker, R., Peck, J.G., and McDonald, N.A., "Experimental Performance of TMB Supercavitating Propellers," DTMB Rpt. 1432, January 1964.

35. Reichardt, H., "The Laws of Cavitation Bubbles at Axially Symmetric Bodies in a Flow," Reports and Translations Number 766, Ministry of Aircraft Production, 15 August 1946 (Distributed in the U.S. by the Office of Naval Research).

36. Johnson, V.E., "The Influence of Submersion, Aspect Ratio and Thickness on Supercavitating Hydrofoils Operating at Zero Cavitation Number," Proceedings of the Second ONR Symposium on Naval Hydrodynamics (Government Printing Office), Washington, D.C., 1958.

37. Handler, E., "The Bureau of Naval Weapons Hydrofoil Seaplane," Naval Engineers Journal, Vol. 75, No. 2, May 1963.

38. Bavin, V.F., and Miniovich, I.J., "Experimental Investigations of Interaction Between Hull and Cavitating Propeller," Contribution of the Leningrad Ship Model Basin, USSR, to the 10th International Towing Tank Conference, London, September 1963.

39. Hoyt, J.W., "Ventilated Propellers," Proceedings of the Fourth ONR Symposium on Naval Hydrodynamics, ACR-73, Vol. 1, Washington, D.C., August 1962.

40. Roberts, P.C., "Studies of a Ventilated Supercavitating Propeller on a Torpedo Test Vehicle, Part 1, Performance Results," NAVWEPS Report 7628(1), Naval Ordnance Test Station, China Lake, California, February 1961.

41. Mosteller, G.G., "Base-Vented Propeller," NAVWEPS Report 8058, Naval Ordnance Test Station, China Lake, California, May 1963.

42. Hoyt, J.W., "Studies of a Ventilated Supercavitating Propeller on a Torpedo Test Vehicle. Part 3. Water-Tunnel and Final Cableway Tests, and Over-All Summary of the Project," NAVWEPS Report 7628(3), Naval Ordnance Test Station, China Lake, California, June 1963.

43. Lang, T.G., "Base-Vented Hydrofoils," NAVORD Report 6606, Naval Ordnance Test Station, China Lake, California, October 1959.

44. Lang, T.G., and Daybell, D.A., "Water-Tunnel Tests of a Base-Vented Hydrofoil Having a Cambered Parabolic Cross Section," NAVWEPS Report 7584, Naval Ordnance Test Station, China Lake, California, October 1960.

45. Johnson, V.E., and Rasnick, T.A., "Investigation of a High Speed Hydrofoil with Parabolic Thickness Distribution," NASA TN D-119, November 1959.

46. Johnson, V.E., and Starley, S., "The Design of Two-Dimensional, Low Drag, Base-Vented Hydrofoil Sections for Operation at Arbitrary Depth," HYDRONAUTICS, Incorporated Technical Report 001-15, January 1964.

47. Barr, R.A., "Ventilation Inception," HYDRONAUTICS, Incorporated Technical Report 127-4, March 1963.

48. Barr, R.A., "Air Requirements for Ventilated Propellers," HYDRONAUTICS, Incorporated Technical Report 127-5, March 1963.

49. Song, C.S., "Pulsation of Ventilated Cavities," Journal of Ship Research, Vol. 5, No. 4, March 1962.

50. Hsu, C.C., and Chen, C.F., "On the Pulsation of Finite Cavities," HYDRONAUTICS, Incorporated Technical Report 115-4, November 1962.

51. Newton, R.N., and Rader, H.P., "Performance Data of Propellers for High-Speed Craft," Transactions of the Royal Institution of Naval Architects, Vol. 103, 1960.

52. van de Voorde, C.B., and Esveldt, J., "Tunnel Tests on Supercavitating Propellers," Proceedings of the Fourth ONR Symposium on Naval Hydrodynamics, ACR-73, Vol. 1, Washington, D.C., August 1962.

53. Taniguchi, K., and Tanibayashi, H., "Cavitation Tests on a Series of Supercavitating Propellers," Proceedings of the IAHR Symposium on Cavitation and Hydraulic Machinery, Institute of High Speed Mechanics, Tohoku University, Sendai, Japan, 1962.

54. Lövstad, C.D., "A Written Contribution to the Discussion of the Tulin Paper," Proceedings of the Fourth ONR Symposium on Naval Hydrodynamics, Washington, D.C., August 1962.

55. Barr, R.A., and Cox, G.C., "An Experimental Investigation of a Variable Camber Supercavitating Propeller," HYDRONAUTICS, Incorporated Technical Report 482-1, April 1964.

56. Tulin, M.P., "Supercavitating Flows - Small Perturbation Theory," Journal of Ship Research, Vol. 7, No. 3, January 1964.

57. Tulin, M.P., "Supercavitating Flows, Section 12, Part II, Handbook of Fluid Dynamics" (V. Streeter, editor), McGraw-Hill Book Company, Inc., New York, 1961.

58. Auslaender, J., "The Linearized Theory for Supercavitating Hydrofoils Operating at High Speeds Near a Free Surface," Journal of Ship Research, Vol. 6, No. 2, 1962.

59. Mercier, J., "Low Drag Supercavitating Sections for Propellers," HYDRO-NAUTICS, Incorporated Technical Report 127-3, January 1963.

60. Sullivan, E.K., and Higgins, J.A., "Tests and Trials of the H. S. DENNISON," Hovering Craft and Hydrofoil Magazine, London, Vol. 3, Nos. 3 and 4, December 1963 and January 1964.

61. Tulin, M.P., and Barr, R.A., "On the Range of Applicability of Supercavitating and Ventilated Propellers," HYDRONAUTICS, Incorporated Technical Report 134-1, September 1961.

62. Chen, C.F., "Shrouded Supercavitating Propellers," Proceedings of the Fourth ONR Symposium on Naval Hydrodynamics, ACR-73, Vol. 1, Washington, D.C., August 1962.

63. Nakajima, Y., "Theory of Wide-Bladed Propellers and its Application," Proceedings of the Soc. of Naval Architects of Japan, Vol. 109, 1961.

64. Cox, G.G., "Corrections to the Camber of Constant Pitch Propellers," Transactions of the Royal Institution of Naval Architects, Vol. 103, 1961.

65. van Manen, J.D., and Bakker, A.R., "Numerical Results of Sparenberg's Lifting Surface Theory for Ship Screws," Proceedings of the Fourth Symposium on Naval Hydrodynamics, ACR-73, Vol. 1, Washington, D.C., August 1962.

66. Beveridge, J.L., "Induced Velocity Field of a Fully Cavitating Propeller on Interaction Experiments with Fully Cavitating Propeller Behind a Hydrofoil," DTMB Report 1832, April 1964.

67. Betz, A., and Peterschn, E., "Application of the Theory of Free Jets," NACA TM 667, April 1932 (Translated from Ingenieur-Archiv, May 1931).

68. Cohen, H., and Sutherland, C.D., "Finite Cavity Cascade Flow," Rensselaer Polytech. Inst. Math. Rpt. 14, April 1958.

69. Acosta, A.J., "Cavitating Flow Past a Cascade of Circular Arc Hydrofoils," Calif. Inst. of Tech. Rpt. E-79-2, March 1960.

70. Cornell, W.G., "The Stall Performance of Cascades," Proceedings 2nd U.S. National Congress of Applied Mathematics, June 1954.

71. Jakobsen, J.K., "Supercavitating Cascade Flow Analysis," ASME Paper 64-FE-11, May 1964.

*　　*　　*

TUNNEL TESTS ON SUPERCAVITATING PROPELLERS

C. B. van de Voorde and J. Esveldt
Netherlands Ship Model Basin
Wageningen, Netherlands

SUMMARY

This paper presents the results of tests on several supercavitating propeller models (c = 42 cm) with different profiles. The tests were carried out in the NSMB 90 x 90 cm cavitation tunnel with homogeneous flow. The propellers were designed mainly according to the method as outlined by Tachmindji. The results show a considerable shortage in effective pitch and efficiency. The effect of the tunnel walls on the measured propeller characteristics was examined by testing three geometrically similar models with diameters of 30, 36 and 42 cm respectively.

Based on the very small differences in results it can be concluded that no significant tunnel wall interference occurs.

1. INTRODUCTION

In recent years there has been increased interest in supercavitating propellers for use on high-speed ships. "Supercavitating" indicates such a flow configuration, that the suction side of the blade sections is completely enclosed within a cavity, which originates at the sharp leading edge of the blade and extends beyond the trailing edge.

Both Tulin [1] and Johnson [2] have theoretically analysed the characteristics of low drag supercavitating sections. Morgan [3] has shown that the optimum lift coefficient (for minimum drag-lift ratio) for the Tulin S.C. section with the prescribed limits for angle of attack is 0.16. Moreover he shows that the Johnson five-term section has theoretically the least drag for a given lift. Tachmindji and Morgan [4] have developed the procedure for the design of S.C. propellers.

The purpose of the research carried out by the N.S.M.B. was to establish experimentally the properties of the various sections, i.e., Tulin's two-term and Johnson's three- and five-terms sections, by investigating propeller models, which were designed for each type of section according to Ref. [4]. The results of these tests showed, that none of the propeller models meets the design requirements, but that each has a considerable shortage in effective pitch and efficiency.

The design of the propellers and the results of the tests carried out in the N.S.M.B. cavitation tunnel with homogeneous flow, will be discussed in this paper. Appendix A deals with the investigation into the effect of the tunnel walls on the test results. Due to the large cavities behind a S.C. propeller model the wall effect might be considerably larger than for a conventional propeller model. In order to examine whether this is true, three geometrically similar propeller models, having diameters of 30,00 cm, 36,00 cm and 42,14 cm respectively were tested. Appendix B deals with a mathematical analysis of some tunnel test results.

2. PROPELLER MODELS

The following models were tested:

No. 2873 - with Tulin sections. In order to investigate the effect of the Ludwieg-Ginzel camber correction factor, this correction was omitted here for comparison purposes with propeller model No. 3010 (with camber correction factor). The design angle of attack $\alpha = 2^\circ$ for $0.0548 < C_1 < 0.2$, i.e., for the sections outward of $0.4\,R$ and $\alpha = 10\,C_1$ for $C_1 > 0.2$, i.e., for the inner sections, as recommended in Ref. [4].

No. 2900 - with Johnson three-term sections. $\alpha = 2^\circ$ constant for each radius.

No. 2901 - with Johnson three-term sections. $\alpha = 3.5^\circ$ constant for each radius.

No. 2948 - with Johnson five-term sections. $\alpha = 3.5^\circ$ constant for each radius.

No. 3010 - with Tulin sections. For the sections outward of $0.7\,R$ $\alpha = 2^\circ$ and for the inner sections α gradually increases from $\alpha = 2^\circ$ at $x = 0.7$ to $\alpha = 4^\circ$ at the hub ($x = 0.25$).

The mentioned models were manufactured in propeller bronze and have a diameter of 42.14 cm (scale 1 : 1.922). The principal full scale dimensions are given in Table 1; further details on the propeller drawings, Figs. 1 through 4.

3. DESIGN DATA

The propellers were designed for a triple screw high speed motor boat, complete test results of which were available.

Tunnel Tests on Supercavitating Propellers

Table 1

Propeller No.	2873	2900	2901	2948	3010
Diameter	810 mm	810 mm	810 mm	810 mm	810 mm
Number of blades	3	3	3	3	3
Pitch at root	774 mm	734 mm	780 mm	757 mm	799 mm
Pitch at tip	818 mm	779 mm	863 mm	851 mm	828 mm
Pitch at 0.7 R	794 mm	759 mm	822 mm	807 mm	809 mm
P/D at 0.7 R	0.980	0.937	1.014	0.996	0.999
Blade area ratio	0.388	0.388	0.388	0.388	0.414
Hub-diameter ratio	0.25	0.25	0.25	0.25	0.25

PROPELLER 2873, 2900, 2901 and 2948
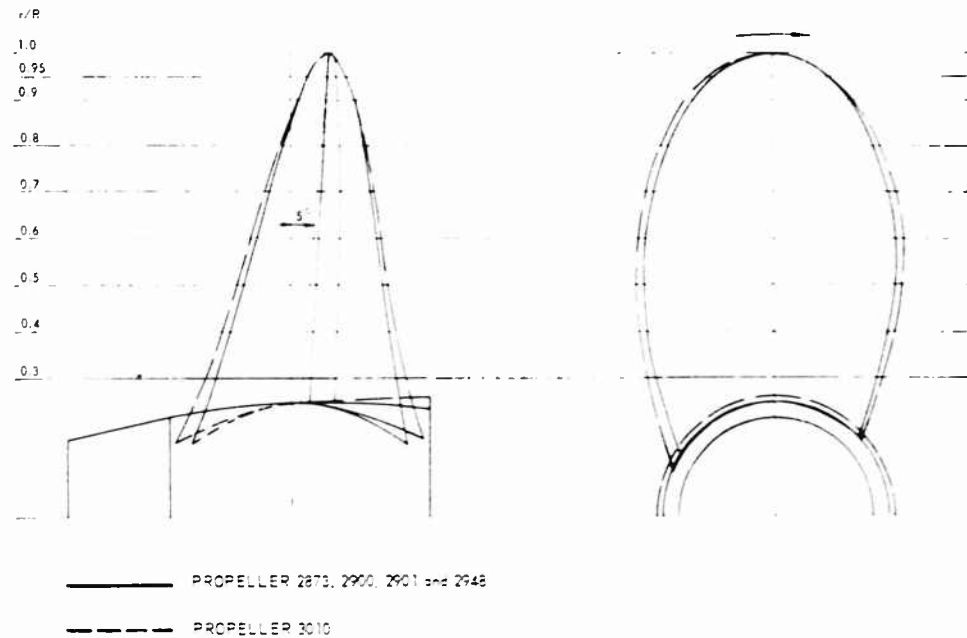
PROPELLER 3010

Fig. 1 - General arrangement of propellers

The design data are:

2800 DHP (metric) per shaft
Speed of advance, 41 knots (assuming zero wake)
$C_p = 0.828$ $n_{opt.} = 2360$ rpm giving $J = 0.66$
$C_T = 0.534$ $\sigma_0 = 0.5$
$K_T = 0.0914$ $\sigma_{0.7} = 0.040$
$K_Q = 0.0149$
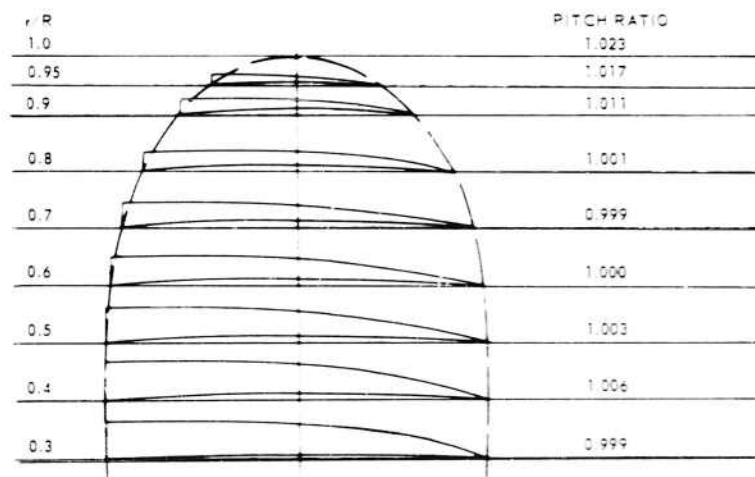
289

PROPELLER 2873

PROPELLER 3010

Fig. 2 - Blade sections of the propellers
with Tulin profiles

PROPELLER 2900

r/R		PITCH RATIO
1.0		0.962
0.95		0.959
0.9		0.955
0.8		0.946
0.7		0.936
0.6		0.927
0.5		0.919
0.4		0.913
0.3		0.908

PROPELLER 2901

r/R		PITCH RATIO
1.0		1.065
0.95		1.057
0.9		1.050
0.8		1.033
0.7		1.014
0.6		0.996
0.5		0.981
0.4		0.970
0.3		0.964
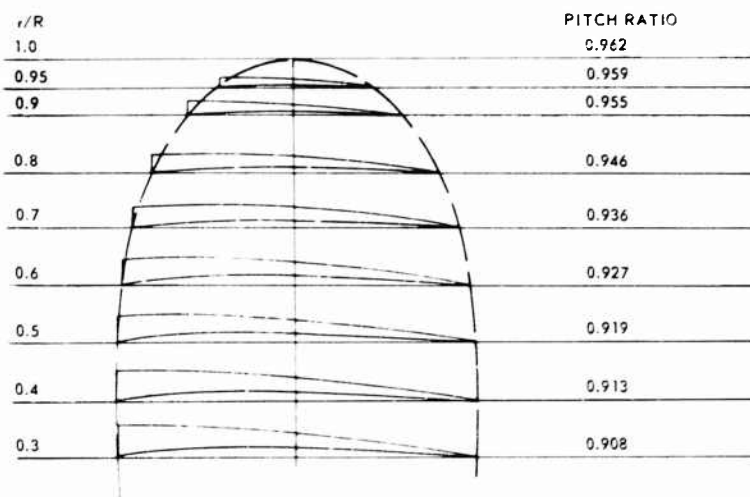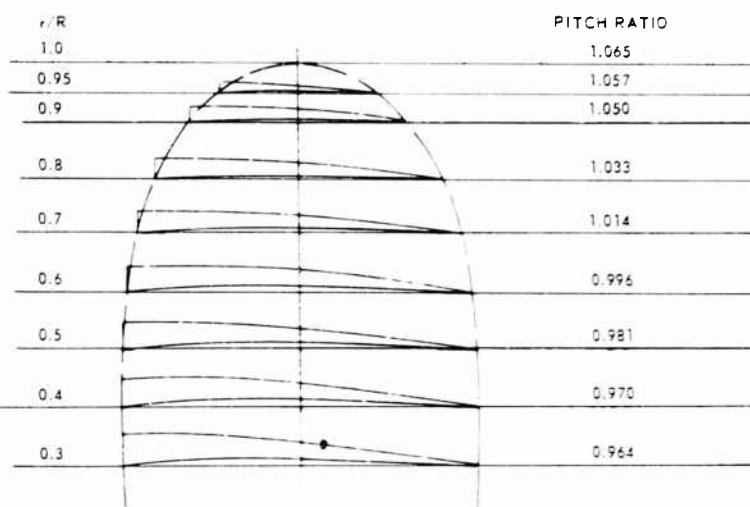
Fig. 3 - Blade sections of the propellers with
Johnson 3-term profiles

PROPELLER 2948
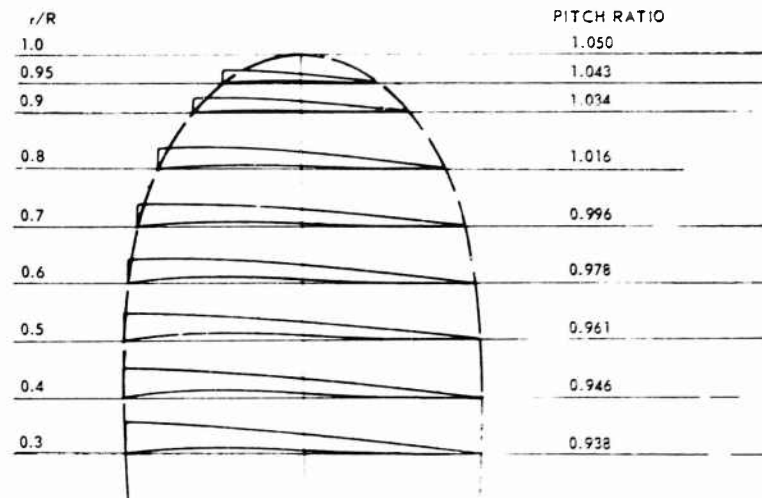
Fig. 4 - Blade sections of the propellers with
Johnson 5-term profiles

The efficiency for operation at zero cavitation number $\tau_{p_{opt}}$ = 0.665 is
based on Fig. 6 of Ref. [4]. From Fig. 14 of the same reference a drop in effi-
ciency of 3% was estimated for the difference between the actual cavitation num-
ber σ_o = 0.5 and σ_o = 0, resulting in τ_p = 0.646.

Plotting the design point J = 0.66 and 100 $H V_x^2$ = 2.26 (notation according
to Ref. [4]) in Fig. 1 of Ref. [4] shows that this point lies in the marginal region
for practical application of supercavitating propellers.

4. PROPELLER DESIGN

4.1 Calculation of the Lift Distribution

For all propellers, except No. 3010, the non-viscous thrust coefficient has
been calculated to be C_{T_i} = 0.559 (C_T = 0.534). With τ_{p_i} = 0.838 according to
Kramer's diagram the lift distribution has been established, making use of the
Goldstein reduction factors. With c_l = 0.16 at 0.7 R and the recommended
radial distribution of $c \, c_{0.7}$ [4], the lift coefficient c_l at each radius was
known.

Owing to the poor results of the propellers, it was decided at the time of
designing propeller No. 3010, to abandon the original purpose of comparing only
the influence of the camber correction, but to make a completely new design in
order to meet the design requirements as close as possible. For this purpose

the following alterations were introduced in the design of propeller 3010, as compared with that of propeller 2873 (both propellers with Tulin profiles):

a. a camber correction,

b. an artificially increased non-viscous thrust coefficient $C_{T_i} = 0.574$ (with $\eta_{P_i} = 0.823$),

c. the Tachmindji reduction factors,

d. a radial distribution of the design angle of attack α, as mentioned in item 3, in order to obtain a supercavitating sheet emanating from the leading edge all over the blade.

4.2 Calculation of the Blade Sections

4.2.1 Face ordinates

For the Tulin-profiles (propellers 2873 and 3010):

$$\frac{y_{face \cdot r}}{c} = \frac{A_1}{2} \left[\frac{x'}{c} + \frac{8}{3} \left(\frac{x'}{c} \right)^{3/2} - 4 \left(\frac{x'}{c} \right)^2 \right]$$

with respect to the reference line

$$\frac{y_{face \cdot c}}{c} = \frac{A_1}{2} \left[\frac{x'}{c} + \frac{8}{3} \left(\frac{x'}{c} \right)^{3/2} - 4 \left(\frac{x'}{c} \right)^2 \right] - \frac{x'}{c} \alpha_i$$

with respect to the chord (α_i is small)

$$A_1 = \frac{8}{5} c \ell_o$$

$$\alpha_i = \frac{-y_{face \cdot r} \text{ for } x' = c}{c} = \frac{A_1}{6}$$

Fig. 5 - Sketch for defining the face ordinates

$y_{face \cdot c}/c$ has its maximum for $x'/c = 0.5317$. From this can be calculated

$$\left(\frac{y_{face \cdot c}}{c} \right)_{max.} = 0.3060 \, A_1$$

293

or

$$\left(\frac{y_{face} \cdot c}{c}\right)_{max.} = 0.3060 \, \frac{8}{5\pi} \left(c_\ell - \frac{\pi}{114.6} \, z\right)$$

or

$$\left(\frac{y_{face} \cdot c}{c}\right)_{max.} = 0.1553 \, c_\ell - 0.00426 \, z. \tag{A}$$

Now

$$\frac{y_{face} \cdot c}{c} = \frac{A_1}{2}\left[\frac{4}{3}, \frac{x'}{c} - \frac{8}{3}\left(\frac{x'}{c}\right)^{3/2} - 4\left(\frac{x'}{c}\right)^{2}\right].$$

Hence

$$\frac{\dfrac{y_{face} \cdot c}{c}}{\left(\dfrac{y_{face} \cdot c}{c}\right)_{max.}} = \frac{1}{0.612}\left[\frac{4}{3}, \frac{x'}{c} - \frac{8}{3}\left(\frac{x'}{c}\right)^{3/2} - 4\left(\frac{x'}{c}\right)^{2}\right]. \tag{B}$$

The values of this ratio for various x' are given in Table 1 of Ref. [4].

With the aid of Eqs. (A) and (B) and with the known values of c_ℓ, z and c the distribution of $y_{face} \cdot c$ at each radius has been calculated.

For the three-term Johnson profiles (propellers 2900 and 2901):

$$\frac{y_{face} \cdot r}{c} = \frac{A_1}{10}\left[5\left(\frac{x'}{c}\right) - 20\left(\frac{x'}{c}\right)^{3/2} - 80\left(\frac{x'}{c}\right)^{2} - 64\left(\frac{x'}{c}\right)^{5/2}\right]$$

$$A_1 = \frac{4}{3z} \times c_{\ell_o} = \frac{4}{3z}\left(c_\ell - \frac{-}{114.6} \, z\right)$$

$$z_i = \frac{-y_{face} \cdot r \text{ for } x' = c}{c} = -\frac{A_1}{10}$$

$$\frac{y_{face} \cdot c}{c} = \frac{A_1}{10}\left[4\left(\frac{x'}{c}\right) - 20\left(\frac{x'}{c}\right)^{3/2} - 80\left(\frac{x'}{c}\right)^{2} - 64\left(\frac{x'}{c}\right)^{5/2}\right].$$

For the five-term Johnson profiles (propeller 2948):

$$\frac{y_{face} \cdot r}{c} = \frac{A_1}{315}\left[210\left(\frac{x'}{c}\right) - 2240\left(\frac{x'}{c}\right)^{3/2} - 12600\left(\frac{x'}{c}\right)^{2} - 30912\left(\frac{x'}{c}\right)^{5/2}\right.$$

$$\left. - 35840\left(\frac{x'}{c}\right)^{3} - 15360\left(\frac{x'}{c}\right)^{7/2}\right]$$

$$A_1 = \frac{6}{5z} \times c_{\ell_o} = \frac{6}{5z}\left(c_\ell - \frac{-}{114.6} \, z\right)$$

294

$$a_i = \frac{-y_{face'} \cdot r \ \text{for} \ x' = c}{c} = -\frac{138}{315} A_1$$

$$\frac{y_{face'} \cdot c}{c} = \frac{A_1}{315} \left[72 \left(\frac{x'}{c}\right) - 2240 \left(\frac{x'}{c}\right)^{3/2} + 12600 \left(\frac{x'}{c}\right)^2 - 30912 \left(\frac{x'}{c}\right)^{5/2} \right.$$
$$\left. + 35840 \left(\frac{x'}{c}\right)^3 - 15360 \left(\frac{x'}{c}\right)^{7/2} \right].$$

The distribution of $y_{face'} c$ has been determined at each radius with the aid of the calculated value of A_1 for the known values of c_ℓ, z and c. The face ordinates were corrected for the effect of flow curvature (except those of propeller 2873) with the known Ludwieg-Ginzel correction factors

$$\left(\frac{y_{face'} \cdot c}{c}\right)_{corrected} = k_1 k_2 \left(\frac{y_{face'} \cdot c}{c}\right).$$

4.2.2 Thickness distribution

For the Tulin-profiles (propellers 2873 and 3010). The chordwise distribution of the thickness (t) at each section was calculated by $t \ c = F' c_\ell - N' z$. F' and N' are given in Table 1 of Ref. [4].

For the Johnson-profiles (propellers 2900, 2901 and 2948) the blade thicknesses were found by calculating the cavity boundary for $\sigma_{local} = 0$. The cavity boundary is given by

$$\frac{y_{cav'} \cdot r}{c} = \frac{\left(\frac{y_{cav'} \cdot r}{c}\right)_z}{z} \cdot z - \frac{\left(\frac{y_{cav'} \cdot r}{c}\right)_{camber}}{c_{\ell_o}} \cdot c_{\ell_o}$$

(with respect to the reference line), where

$$\frac{\left(\frac{y_{cav'} \cdot r}{c}\right)_z}{z} = \frac{1}{2}\left(1 - \sqrt{\frac{x'}{c}}\right)\sqrt{\frac{x'}{c} - \sqrt{\frac{x'}{c}}} - \frac{1}{4} \ln\left(1 - 2\sqrt{\frac{x'}{c}} - 2\sqrt{\frac{x'}{c} - \sqrt{\frac{x'}{c}}}\right)$$

and

$$\frac{\left(\frac{y_{cav'} \cdot r}{c}\right)_{camber}}{c_{\ell_o}} = k\left[\sqrt{\frac{x'}{c}} - a \ \ln \frac{a - \sqrt{\frac{x'}{c}}}{a}\right].$$

For Johnson three-term sections

$$k = \frac{2}{3z}: \quad a = \frac{3}{4}.$$

295

For Johnson five-term sections

$$k = \frac{3}{5\pi} ; \quad a = \frac{5}{6} .$$

For Tulin sections

$$k = \frac{4}{5\pi} ; \quad a = \frac{5}{8} .$$

The thickness according to

$$\frac{t}{c} = \frac{y_{cav} \cdot r}{c} - \frac{y_{face} \cdot r}{c}$$

leads to extreme thin sections near the nose for propeller 2900 with $\alpha = 2°$. Therefore the thicknesses near the nose of this propeller were taken the same as those of propeller 2901 with $\alpha = 3.5°$. (These thicknesses are about equal to those of propeller 2873.)

The trailing edge thickness of all three propellers has been taken equal to that of propeller 2873.

4.3 Calculation of the Pitch

The effect of finite cavitation number is combined with both the ideal and the design angle of attack into one additional angle of attack α_1, which is given by

For the Tulin sections (propellers 2873 and 3010):

$$\alpha_1 = K_\sigma (\alpha - \alpha_i) = 57.3 \, K_\sigma \left\{ \frac{\alpha}{57.3} - \frac{1}{6} \cdot \frac{8}{5\pi} \left(c_\ell - \frac{\pi}{114.6} \alpha \right) \right\}$$

$$= 57.3 \, K_\sigma \left\{ 0.0849 \, c_\ell - 0.01512 \, \alpha \right\} .$$

For the Johnson three-term sections (propellers 2900 and 2901):

$$\alpha_1 = 57.3 \, K_\sigma \left\{ \frac{\alpha}{57.3} - \frac{1}{10} \cdot \frac{4}{3\pi} \left(c_\ell - \frac{\pi}{114.6} \alpha \right) \right\}$$

$$= 57.3 \, K_\sigma \left\{ - 0.0424 \, c_\ell - 0.01862 \, \alpha \right\} .$$

For the Johnson five-term sections (propeller 2948):

$$\alpha_1 = 57.3 \, K_\sigma \left\{ \frac{\alpha}{57.3} - \frac{138}{315} \cdot \frac{6}{5\pi} \left(c_\ell - \frac{\pi}{114.6} \alpha \right) \right\}$$

$$= 57.3 \, K_\sigma \left\{ - 0.1673 \, c_\ell - 0.02204 \, \alpha \right\} .$$

K_σ has been taken from **Fig. 4** of Ref. [4] for $\sigma_{0.7} = 0.0414$. The correction in pitch angle α_2 for lifting surface effects, calculated according to the formulas given in Ref. [4], amounts to $\alpha_2 = 2.035°$. The pitch correction is then defined by

$$1 + \frac{\Delta P/D}{P/D} = \frac{tg(\beta_i + \alpha_1 + \alpha_2)_{0.7}}{tg(\beta_i + \alpha_1)_{0.7}} .$$

The same percentage is applied to the other radii, hence the final pitch is given as

$$P/D = \pi x \left(1 + \frac{\Delta P/D}{P/D}\right) tg(\beta_i + \alpha_1) .$$

5. TESTS CARRIED OUT AND THEIR RESULTS

The propeller models were tested and observed over a certain range of J and at various σ_0 viz. 4.0; 1.5; 0.9; 0.6 and 0.5. The speed of the water and the pressure in the tunnel were kept constant for each σ_0.

The curves of K_T, K_Q and τ_p as a function of J for the various σ_0 are presented in Figs. 6 through 20. The cavitation phenomena for the various σ_0 and the design J-value of 0.66 are given in the sketches (Figs. 21 through 25). The sketches on Fig. 26 show the cavitation phenomena on the propellers at full power absorption (2800 DHP).

6. DISCUSSION ON THE RESULTS

The curves show that none of the propellers meets the design requirements $K_T = 0.0914$; $K_Q = 0.0149$ and $\tau_p = 0.646$ at J = 0.66 and $\sigma_0 = 0.5$.

A performance prediction has been made for each propeller behind the triple screw motor boat concerned.

Starting from the known thrust-speed relationship of the motor boat and the measured K_T, K_Q - J relations, the required shaft horse power and the corresponding number of revolutions were determined for various ship speeds, which correspond to the cavitation numbers as tested viz. $\sigma_0 = 4.0$; 1.5; 0.9; 0.6 and 0.5. In Fig. 27 these values of DHP and r.p.m. are plotted on basis of ship speed.

The performances at the design power of 2800 DHP and the shortages in effective pitch and efficiency, expressed as percentages of design r.p.m. and design τ_p are listed in Table 2.

The shortage in effective pitch of the propellers 2900 and 3010 is considerably smaller than that of the other propellers.

The cavitation sketches show that at J = 0.66:

297
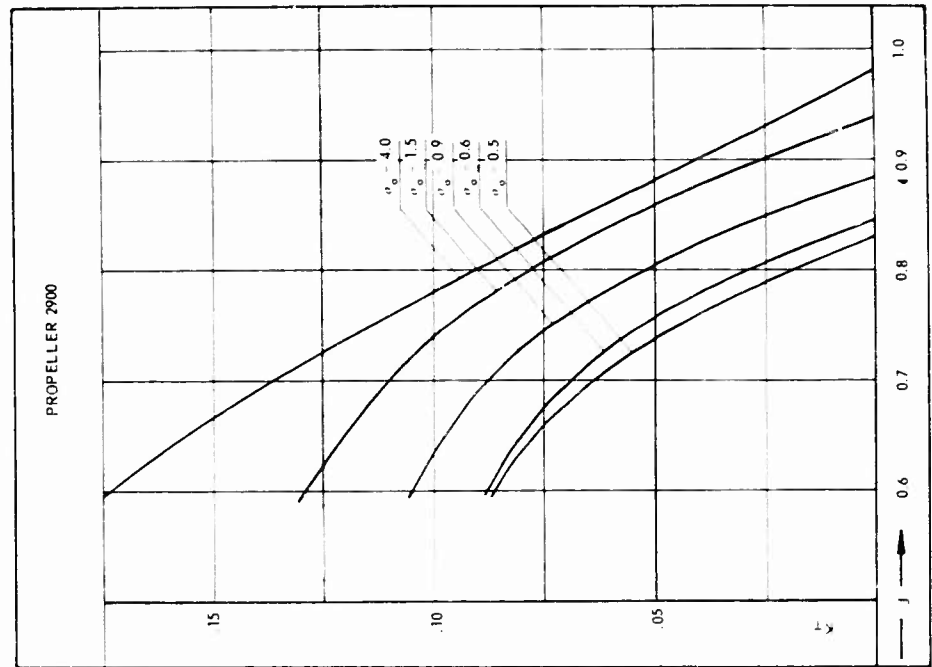
Fig. 7 - K_T to base of J

Fig. 6 - K_T to base of J

298
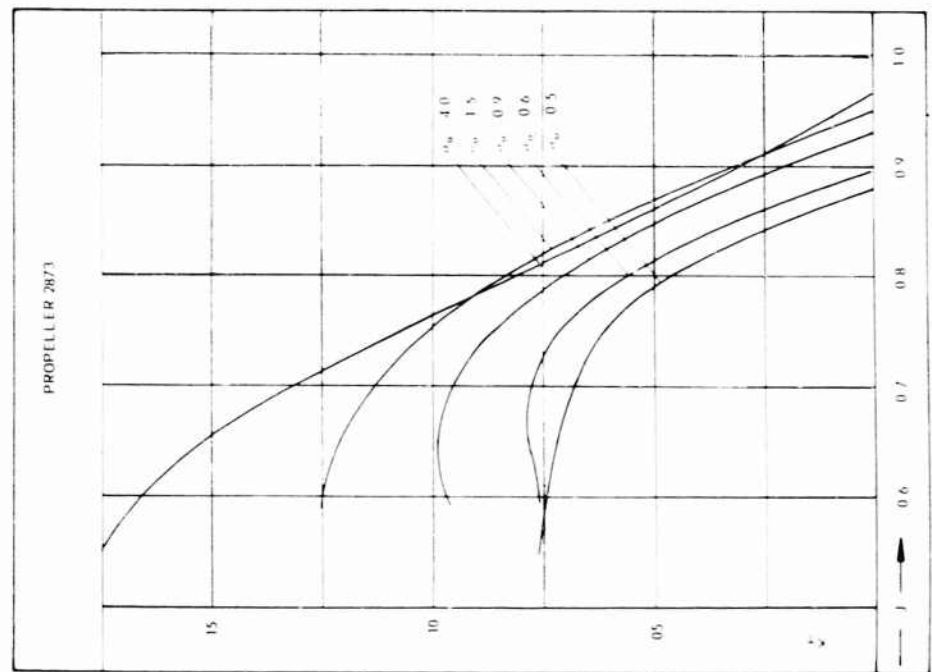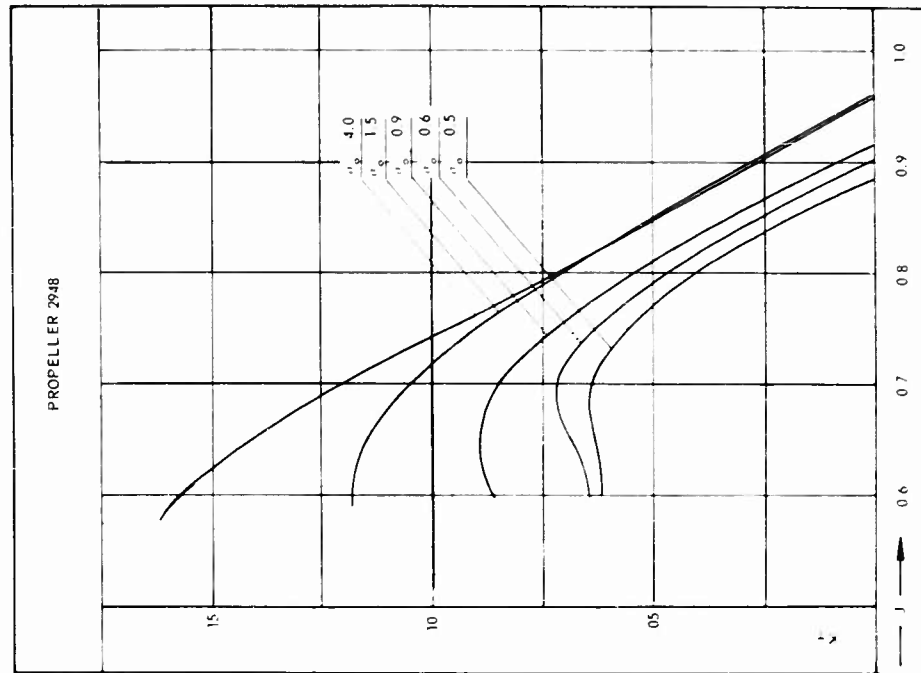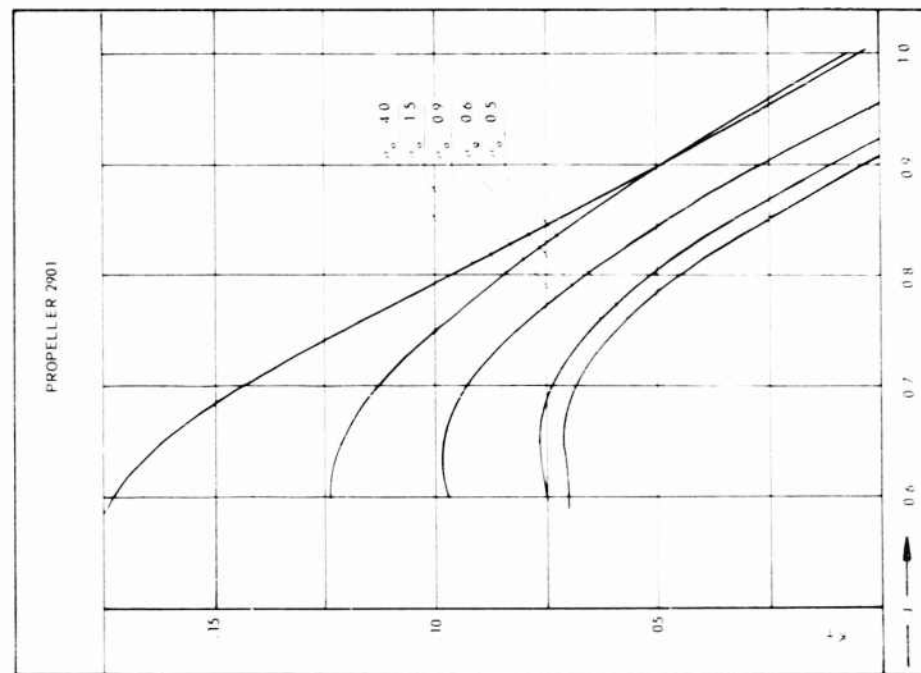
Fig. 9 - K_T to base of J

Fig. 8 - K_T to base of J
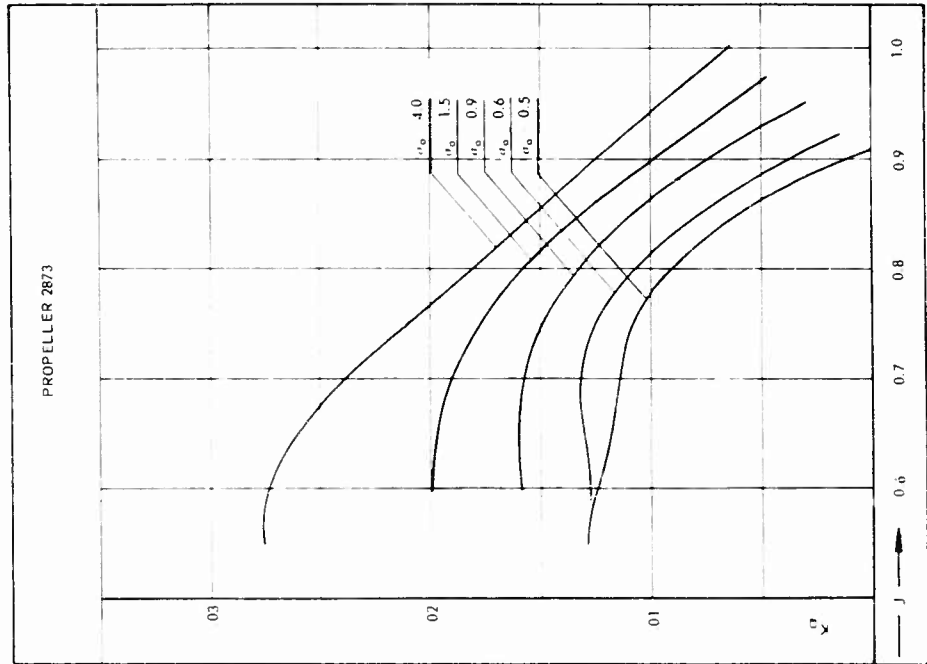
Fig. 11 - K_Q to base of J
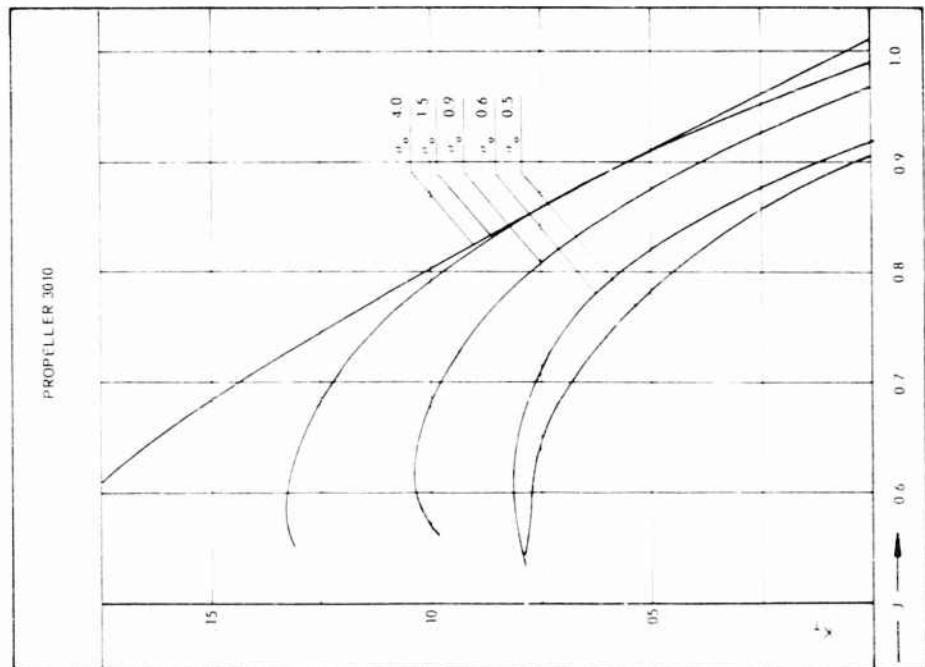
Fig. 10 - K_T to base of J
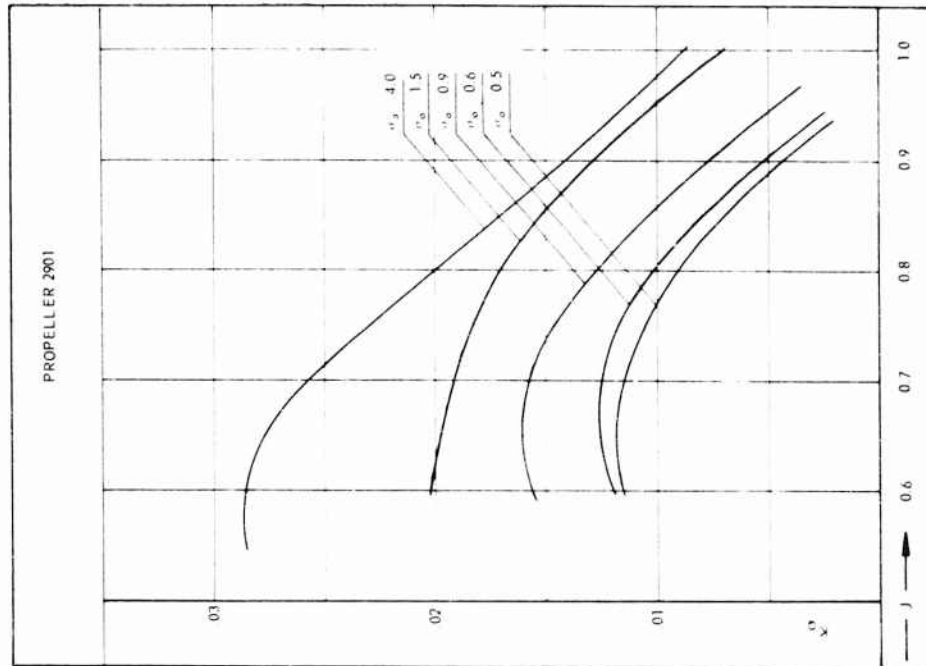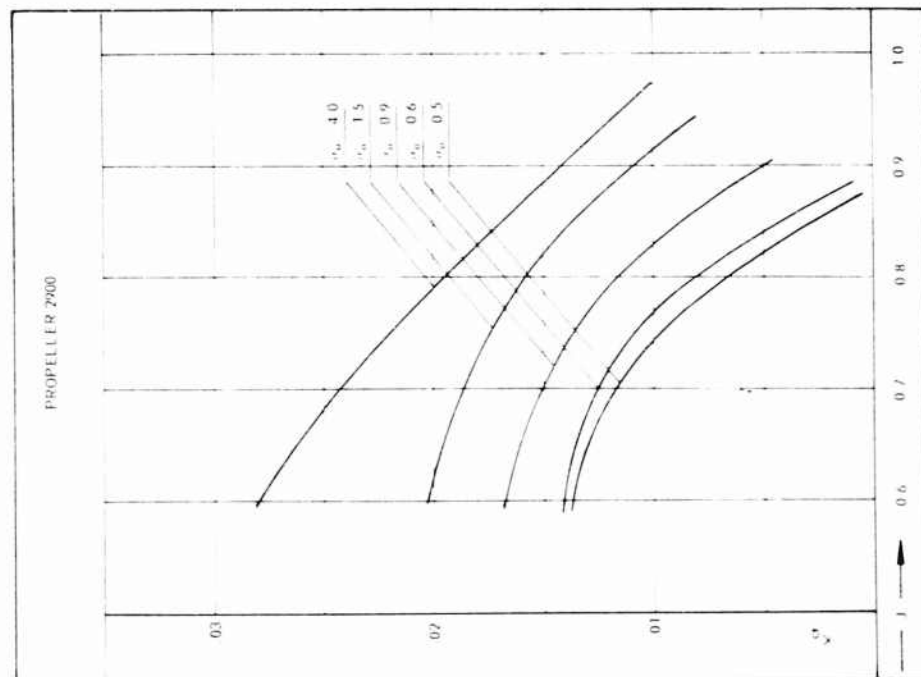
Fig. 13 - K_Q to base of J

Fig. 12 - K_Q to base of J

301
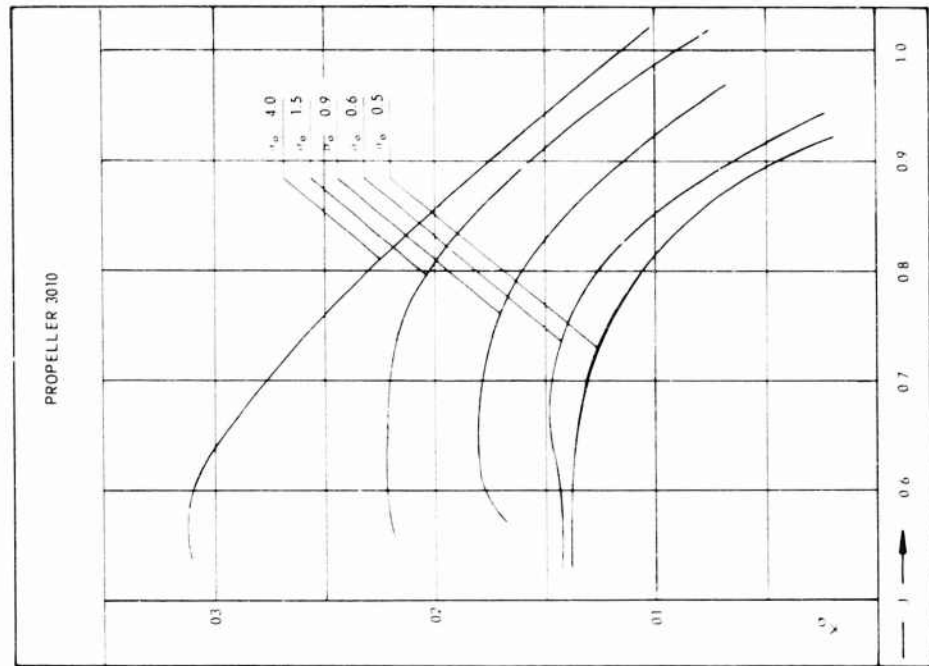
Fig. 15 - K_Q to base of J
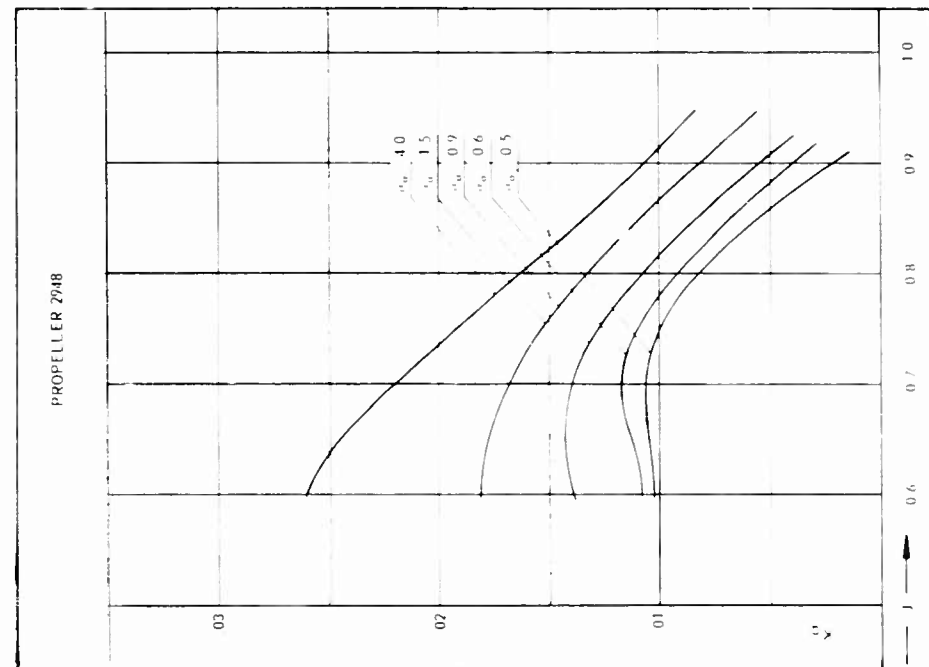
Fig. 14 - K_Q to base of J
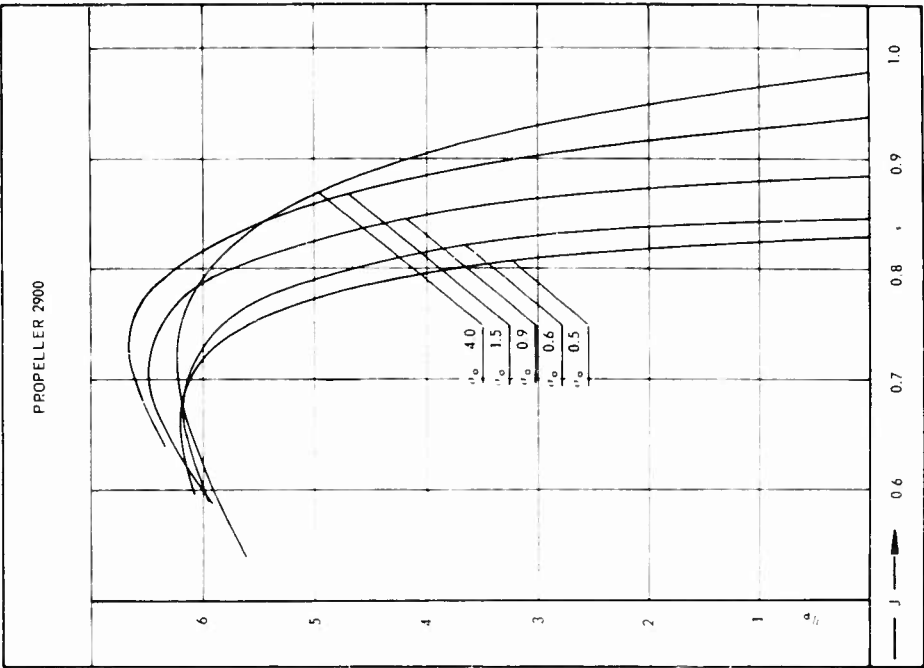
Fig. 17 - η_p to base of J
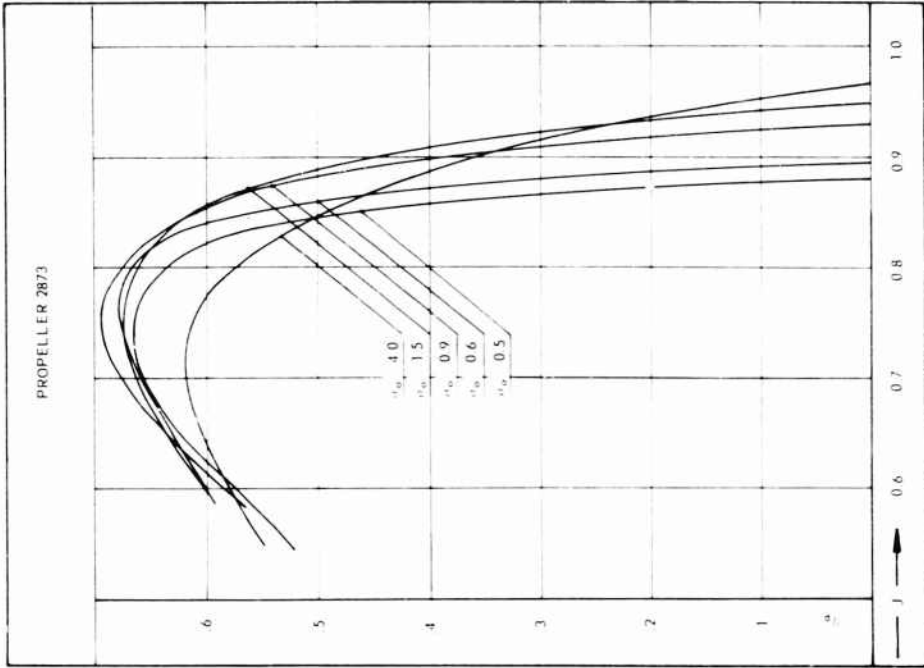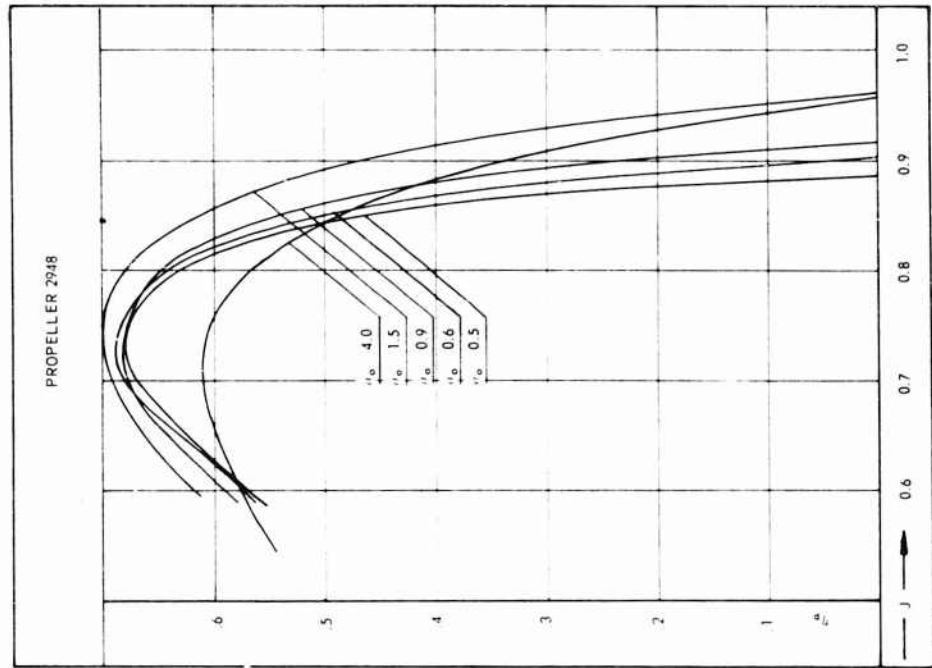
Fig. 16 - η_p to base of J

303

Fig. 19 - η_p to base of J

Fig. 18 - η_p to base of J

304
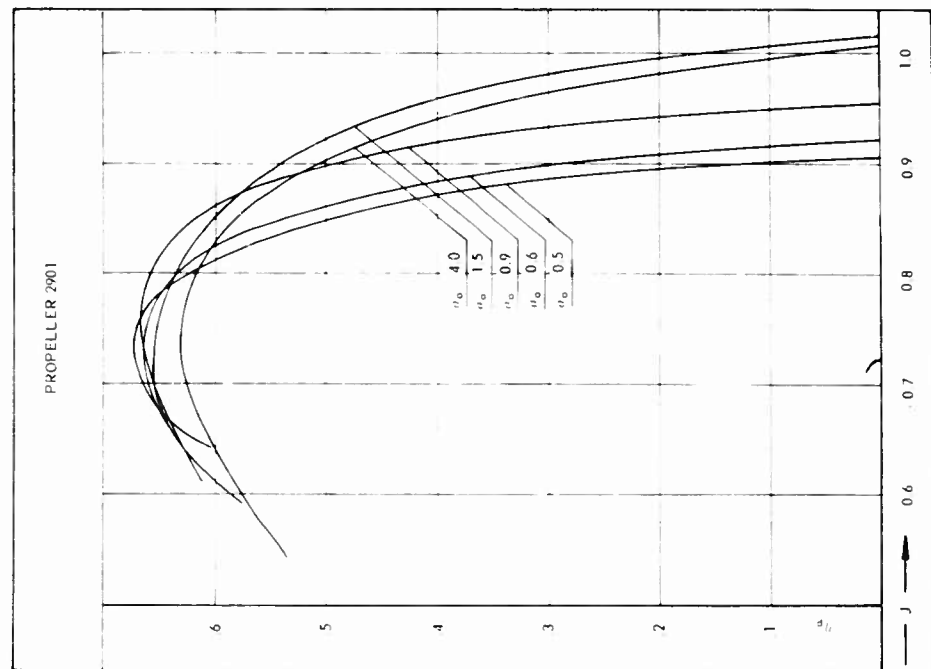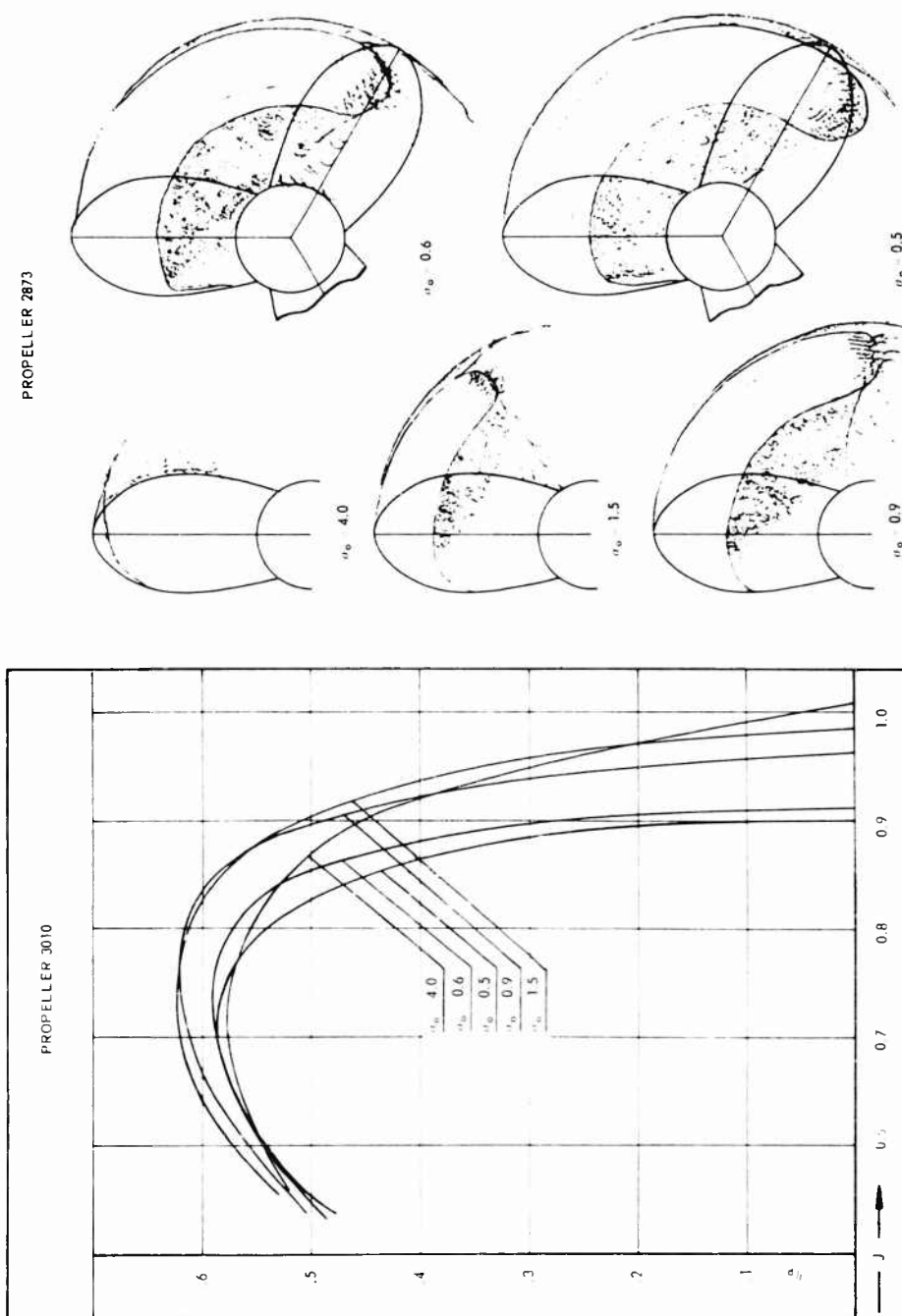
Fig. 21 - Cavitation phenomena at J = 0.66

Fig. 20 - η_p to base of J

PROPELLER 2901

σ_o 0.6

σ_o 0.5

σ_o 4.0

σ_o 1.5

σ_o 0.9
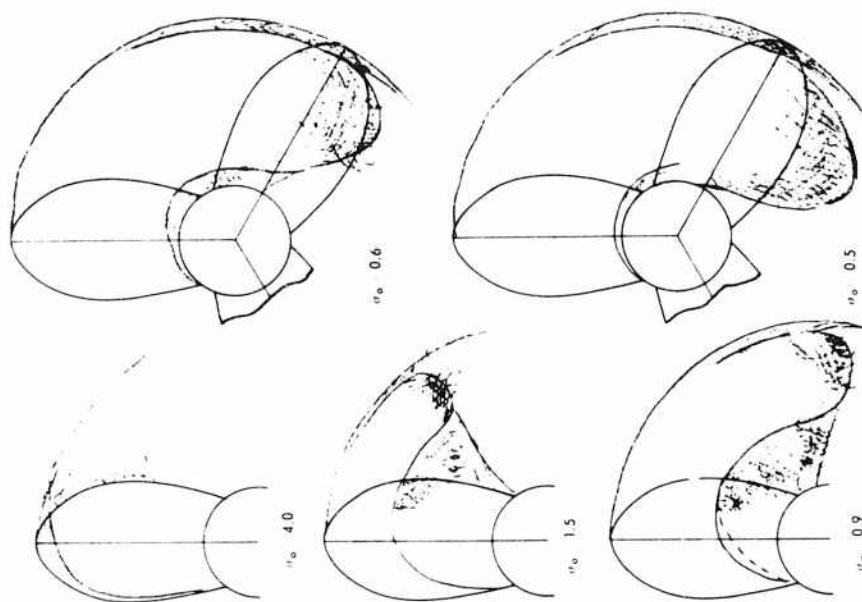
Fig. 23 - Cavitation phenomena at J = 0.66

PROPELLER 2900

σ_o 0.6

σ_o 0.5

σ_o 4.0

σ_o 1.5

σ_o 0.9
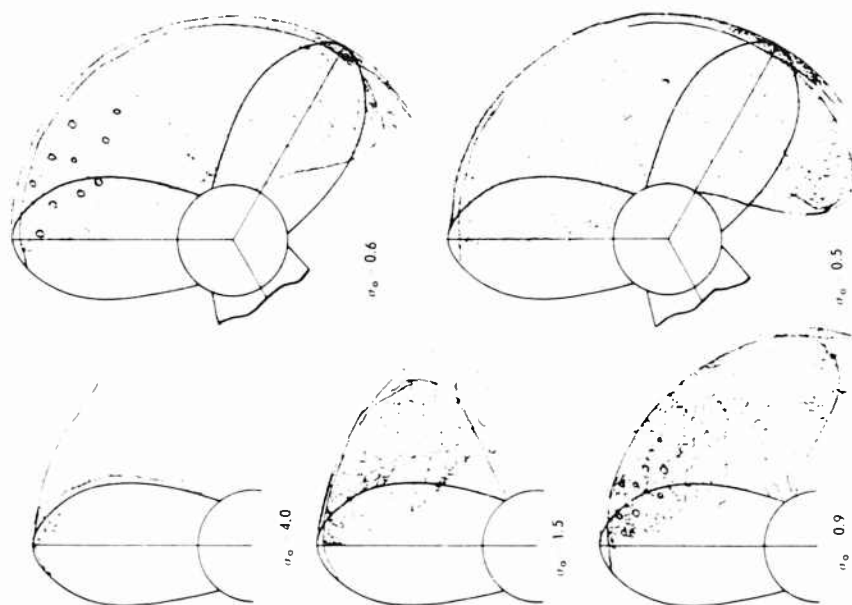
Fig. 22 - Cavitation phenomena at J = 0.66

PROPELLER 3010

σ_o 0.6

σ_o 0.5

σ_o 4.0

σ_o 1.5

σ_o 0.9
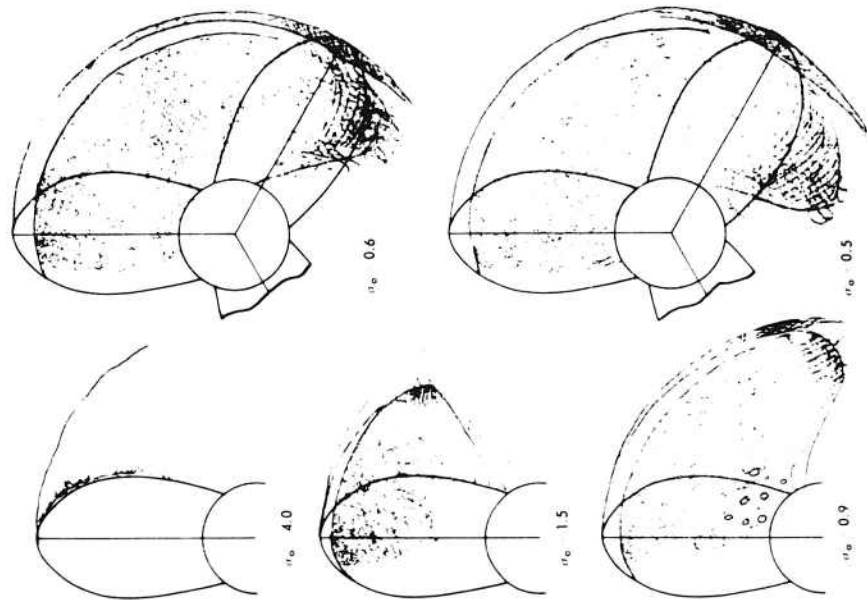
Fig. 25 - Cavitation phenomena at J = 0.66

PROPELLER 2948

σ_o 0.6

σ_o 0.5

σ_o 4.0

σ_o 1.5

σ_o 0.9
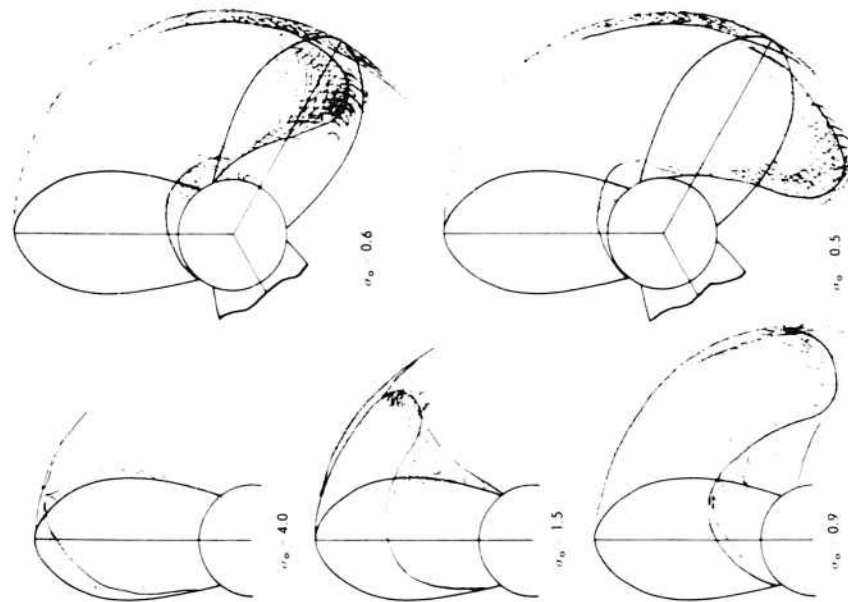
Fig. 24 - Cavitation phenomena at J = 0.66

307
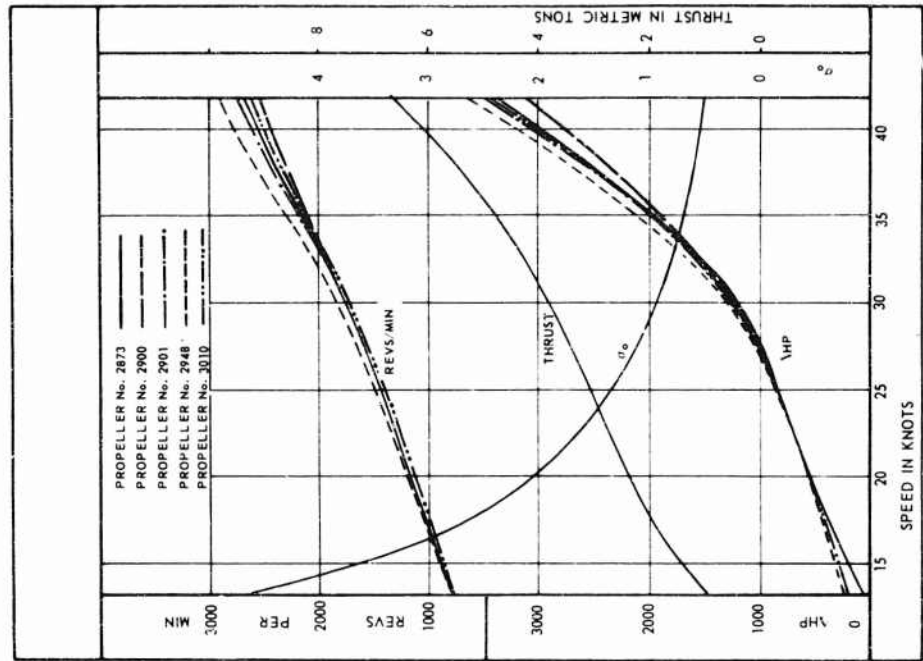
Fig. 27 - Predicted performances of the propellers
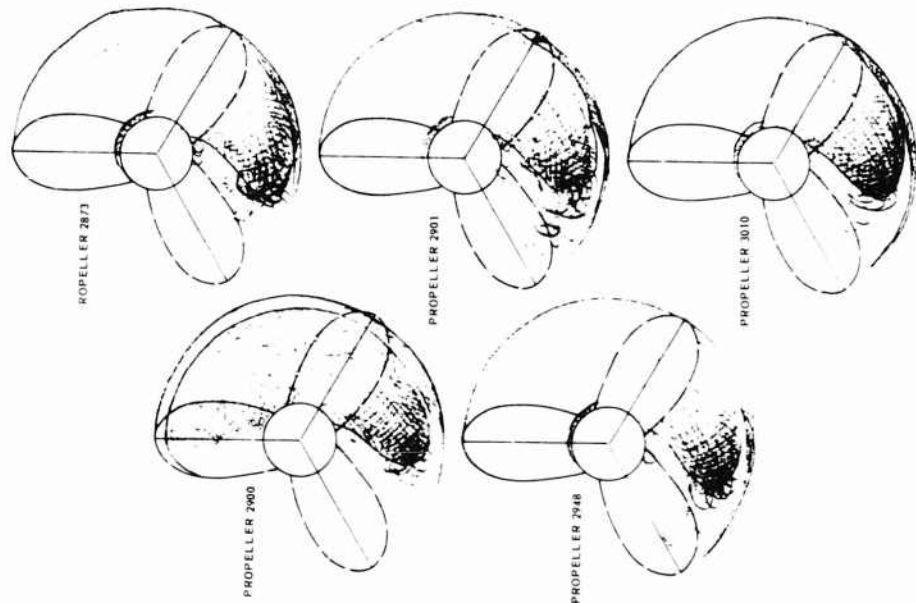
Fig. 26 - Cavitation phenomena at full power absorption

Table 2

Propeller No.	Speed in Knots at 2800 DHP	R.P.M.	σ_o	J	η_p	R.P.M. Percent-age too High	η_p Percent-age too Low
2873	39.2	2515	0.545	0.595	0.560	6.5	13.3
2900	40.3	2455	0.535	0.624	0.607	4.0	6.0
2901	39.0	2540	0.552	0.588	0.558	7.6	13.6
2948	38.2	2640	0.575	0.551	0.530	11.9	17.0
3010	39.0	2430	0.552	0.611	0.558	3.0	13.6
Design	41.0	2360	0.500	0.660	0.646	-	-

a. Propeller 2900 with Johnson profiles $\alpha = 2°$ produces no supercavitating sheet emanating from the leading edge of the blades.

b. Propellers 2901 and 2948 with Johnson profiles $\alpha = 3.5°$ are fully super-cavitating at $\sigma_o < 0.7$.

c. Propeller 2873 with Tulin profiles produces no supercavitating sheet emanating from the leading edge of the blades at the inner radii with $\alpha = 10\,c_\ell$. (For this reason α was increased at the inner radii in the design of propeller 3010.)

d. Propeller 3010 produces no supercavitating sheet. (It has been observed that at a lower J-value $J = 0.60$ and $\sigma_o = 0.5$, a sheet is generated at all radii.

7. CONCLUSIONS

The poor supercavitation properties of propeller 2900 are apparently due to a too small design angle of attack α.

That the propellers 2873 and 3010 are not supercavitating, is likely to be caused by too thick sections near the nose. These propellers have Tulin pro-files, with thicknesses based on the formula $t/c = F'c_\ell + N'\alpha$, making use of the values for F' and N' as given in Ref. [4]. These values result in sections, which are considerably thicker than the theoretical cavity shape for $\sigma_{local} = 0$.

With another propeller model with Tulin profiles, designed for a high speed craft exactly according to Ref. [4], the same discrepancies were found as for the propellers 2873 and 3010 viz. a too small effective pitch, a too low efficiency and no supercavitating sheet emanating from the leading edge.

This propeller model was modified by removing material from the back, so that this was just within the calculated cavity boundary for $\sigma_x = 0$. The modified model showed good supercavitation properties and a considerable increase in efficiency as well as in effective pitch.

A similar modification will be applied to propeller model 3010.

Propellers 2901 and 2948 show good supercavitation properties. Nevertheless these two propellers have the largest shortage in effective pitch and efficiency; propeller 2948 still more than 2901.

These discrepancies might be due to imperfections in the design method.

It appeared that for the lowest σ_o-value of 0.5 the difference in head of water at 0.7 R in the vertical upper and lower position amounts to about 23-1/2% of the pressure in the tunnel at the shaft centre line (for a 42 cm ϕ propeller and V_a = 7 m/sec. So the variation in the cavitation number along the circumference of the circle with a radius of 0.7 R amounts to about -12% for the upper to +12% for the lower position. The higher the speed of advance at which the propellers are tested in the tunnel, the lower this variation will be. (If this speed could be increased so that the law of Froude is fulfilled, the variations in the tunnel will be equal to those in full scale conditions.)

In how far the described variations are responsible for the discrepancies between the design requirements and the tunnel test results, cannot yet be overlooked. As for example, that

a. the actual contributions of the camber and of the design angle of attack to the lift may be lower than the theoretical values;

b. the application of the normal Ludwieg-Ginzel correction factors may be incorrect in the case of supercavitating propellers, for which the cavity has probably to be considered as a part of the profile sections;

c. the application of the correction for finite cavitation number may be erratic, as the same correction factor K_σ is used for each section, whereas the sectional cavitation number varies.

REMARK

During the tests on the propellers a considerable difference in cavity length behind the trailing edge of a blade in the vertical upper and lower position was observed, especially at low values of σ_o (low pressure-levels in the tunnel; σ_o based on the pressure in the tunnel at shaft centre). See Fig. 28.

Appendix A

INVESTIGATION INTO THE EFFECT OF TUNNEL WALLS ON THE MEASURED PROPELLER CHARACTERISTICS

During the tests previously discussed it was observed that immediately behind the propeller model the cavitation area expanded radially, whereas behind a normal propeller a contraction of the flow occurs (see Figs. 28 and 29).

310

Fig. 28 - Silhouette of
a S.C. propeller model
in the cavitation tunnel
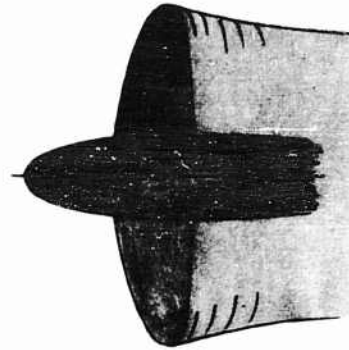
Fig. 29 - Silhouette of a
conventional propeller
model in the cavitation
tunnel

This phenomenon raised the idea, that supercavitating propeller models might suffer more from tunnel wall interference than normal propeller models.

In order to investigate whether this idea is true, tests were carried out on two new propeller models, geometrically similar to propeller model 2901. The diameters of these new models are 30 and 36 cm, whereas the original model 2901 has a diameter of about 42 cm. The results of the tests are given in Fig. 30. This figure shows the relative unimportant role of tunnel wall interference at $J = 0.66$, if there is any.

It seems at least reasonable to state that the discrepancies between the design requirements and the actual test results can not be attributed to tunnel wall influence.

Appendix B

ANALYSIS OF SOME TUNNEL TEST RESULTS

The theoretical values for the contributions of the camber and the design angle of attack to the lift have been used for the design of the propellers. It has been tried to calculate these values, based on the results of the tunnel measurements, and the assumption that all other quantities are introduced correctly.

The following equations are valid:

$$C_{T_i} = 8 \int_{x=0.25}^{x=1.0} \kappa \cdot x \; \frac{1}{tg^2\beta} \times \frac{(tg\,\beta_i - tg\,\beta)\,(1 + tg\,\beta\,tg\,\beta_i)\,tg\,\beta_i}{(1 + tg^2\,\beta_i)^2}\,dx \qquad (1)$$

311
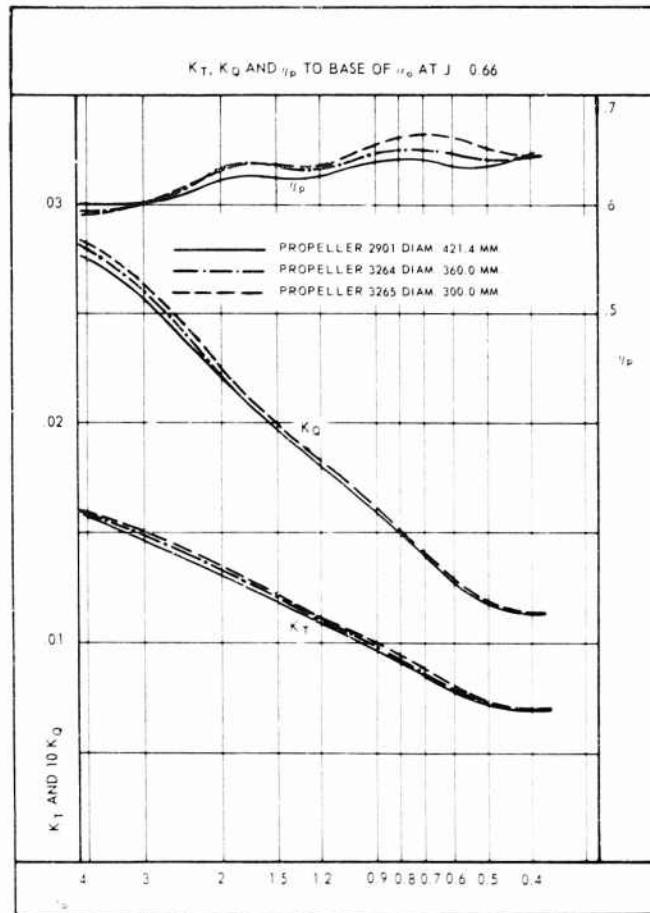
Fig. 30 - Results of investigation
into tunnel wall effect

$$c_{\ell(x)} = \frac{4\pi D}{2} \times \frac{1}{c(x)} \times \kappa \times x \times \sin \beta_i \, \text{tg} (\beta_i - \beta) \tag{2}$$

$$c_{\ell(x)} = \left[pA_1 + q\alpha \right] \times \left[1 + \frac{\sigma_o}{\left(1 + \frac{\pi^2 x^2}{J^2} \right) \cos^2 (\beta_i - \beta)} \right] \tag{3}$$

$$\alpha = (\beta_i + \alpha_1) - \alpha_i - \beta_i \tag{4}$$

$$\beta_i + \alpha_1 = \text{arc. tg} \frac{P/D}{\pi x \left(1 + \frac{\Delta P/D}{P/D} \right)} \ . \tag{5}$$

312

The contributions of the camber and of the angle of attack to the lift have been introduced as unknowns by respectively the factors p and q.

Contrary to the method of correction for finite cavitation number as described in Ref. [4], and as used for the design, this correction is taken into account as follows:

$$c_{\ell_\sigma} = c_{\ell_{\sigma=0}} (1 + \sigma_x) ,$$

where $c_{\ell_{\sigma=0}} = pA_1 + q\alpha$.

The following quantities in the Eqs. (1) through (5) are known:

C_{T_i}, J, σ_o the equations refer to the measured value of K_T at a certain J and σ_o; hence $C_T = K_T (8/\pi J^2)$ is known and C_{T_i} can be estimated,

κ the Tachmindji reduction factor for an estimated value of $\lambda_{i_{0.7}}$,

β from $\operatorname{tg} \beta = J/\pi x$,

$D, z, c_{(x)}, A_{1(x)}$ and $(P/D)_x$ from the propeller geometry,

$1 + \dfrac{\Delta P/D}{P/D}$ the correction for lifting surface effect; for this correction the value used in the design has been taken,

$\alpha_i = +\dfrac{A_1}{6}$ for the Tulin profiles,

$\alpha_i = -\dfrac{A_1}{10}$ for the three-term Johnson's profiles.

Substitution of α = (known quantity) - β_i from Eqs. (4) and (5) into Eq. (3) yields with Eqs. (1) and (2) three equations with four unknowns, viz, p, q, β_i and c_ℓ.

By taking into consideration another measuring point six equations are obtained with six unknowns, viz, p, q, β_{i_1}, β_{i_2}, c_{ℓ_1} and c_{ℓ_2} (indices 1 and 2 refer to the two measuring points).

In this way p and q have been solved for the three-term Johnson profile by considering the following two measuring points for propeller 2901:

From this follows	$\sigma_o = 0.5$ and $J = 0.64$ $K_T = 0.0690$ $C_{T_i} = 0.452$	From this follows	$\sigma_o = 0.5$ and $J = 0.70$ $K_T = 0.0660$ $C_{T_i} = 0.358$

The results are:
$$p = 3.253$$
$$q = 0.008.$$

The theoretical values are

$$p = \frac{3\pi}{4} = 2.355$$

and

$$q = \frac{\pi}{2} \times \frac{1}{57.3} = 0.028 .$$

The same procedure has been followed for the Tulin profiles of propeller 3010. The measuring points were:

$$\left.\begin{array}{l} \sigma_o = 0.5 \text{ and} \\ J = 0.61 \\ K_T = 0.078 \\ C_{T_i} = 0.559 \end{array}\right] \quad \text{and} \quad \left[\begin{array}{l} \sigma_o = 0.5 \text{ and} \\ J = 0.56 \\ K_T = 0.084 \\ C_{T_i} = 0.714 \end{array}\right.$$

The results are: $p = 1.740$
                   $q = 0.0148,$

whereas the theoretical values are

$$p = \frac{5\pi}{8} = 1.962$$

and

$$q = \frac{\pi}{2} \times \frac{1}{57.3} = 0.028 .$$

Finally the calculations were carried out for the Tulin profiles by considering one test point of propeller model 2873 and a second one of propeller model 3010.

Propeller 2873	Propeller 3010

$$\left.\begin{array}{l} \sigma_o = 0.5 \text{ and} \\ J = 0.60 \\ K_T = 0.074 \\ C_{T_i} = 0.546 \end{array}\right] \qquad \left.\begin{array}{l} \sigma_o = 0.5 \text{ and} \\ J = 0.56 \\ K_T = 0.084 \\ C_{T_i} = 0.714 \end{array}\right]$$

The results are: $p = -0.954$
                   $q = 0.050.$

It is concluded that the results are far away from being consistent, notwithstanding the fact that only test points have been considered at which the propeller model was completely supercavitating.

Calculations were also carried out for two test points (of propeller model 2901) with the same J but different σ_o. This results into a negative value for q.

The general conclusion is that there must be other factors than a possible deviation of p and q from the theoretical values, which have played an important role in the causes that the propellers did not meet their design requirements.

NOTATION

Propeller Characteristics

D   propeller diameter

R   max. propeller radius $= D/2$

r   radius of any propeller blade section

x   non-dimensional radius (r/R)

P   pitch

ρ density of fluid

n   number of revolutions per unit time

V_a speed of advance

J   speed coefficient (V_a/nD)

DHP   delivered horse power

T   propeller thrust

Q   propeller torque

K_T thrust coefficient $(T/\rho n^2 D^4)$

K_Q torque coefficient $(Q/\rho n^2 D^5)$

C_T thrust coefficient $(T / \frac{1}{2} \rho V_a^2 \frac{\pi}{4} D^2)$

C_p power coefficient $(2\pi Q n / \frac{1}{2} \rho V_a^3 \frac{\pi}{4} D^2)$

C_{T_i} non-viscous thrust coefficient

η_p propeller efficiency

η_{P_i} ideal propeller efficiency

σ_o cavitation number relative to shaft center line

z   number of blades

ection Characteristics

c	blade section chord (nose-tail line of section face)
x'	fractional distance along chord measured from leading edge
$y_{face,r}$	face ordinate with respect to reference line
$y_{face,c}$	face ordinate with respect to chord
$y_{cav,r}$	cavity ordinate with respect to reference line
t	section thickness
F'	coefficient for determining section thickness
N'	coefficient for determining section thickness
c_ℓ	section lift coefficient
c_{ℓ_o}	section lift coefficient due to camber (c_ℓ at $\alpha = 0$)
A_1	coefficient for determining the face ordinates
α	design angle of attack with respect to the reference line
α_i	ideal angle of attack = the angle of the flow in the direction of the reference line with respect to the chord
α_1	geometrical angle of attack corrected for finite cavitation number
α_2	additional angle of attack due to lifting surface effect
k_1, k_2	camber correction factors
K_σ	correction factor for finite cavitation number
σ_x	cavitation number based on inflow velocity at the section x
κ	Tachmindji reduction factor
β	advance angle
β_i	advance angle taking into account the induced velocities
$\lambda_{i_{0.7}}$	advance coefficient taking into account the induced velocities, at $x = 0.7$, $\lambda_{i_{0.7}} = 0.7\ \text{tg}\ \beta_i$
p	factor determining the contribution of the camber to the lift $p = \partial c_\ell / \partial A_1$

q   factor determining the contribution of the design angle of attack
     to the lift $q = \partial c_\ell / \partial \alpha$ per degree

REFERENCES

1. Tulin, M.P. and Burkart, M.P., "Linearized Theory for Flows About Lifting
    Foils at Zero Cavitation Numbers," David Taylor Model Basin Report
    C-638

2. Johnson, V.E., "Theoretical Determination of Low-Drag Supercavitating
    Hydrofoils and their Two-Dimensional Characteristics at Zero Cavitation
    Number," NACA RM L 57 G 11a

3. Morgan, W.B., "Optimum Supercavitating Sections," David Taylor Model
    Basin Report C-856

4. Tachmindji, A.J. and Morgan, W.B., "The Design and Estimated Perform-
    ance of a Series of Supercavitating Propellers," Proceedings of the Second
    Symposium on Naval Hydrodynamics, Aug. 1958

*   *   *

VENTILATED PROPELLERS

J. W. Hoyt
U. S. Naval Ordnance Test Station
Pasadena, California

Midway between the best operating points of conventional propellers for low speed ship propulsion and supercavitating propellers for very high speed there exists a region where the application of mixed gas-water flows to propeller design seems to be most appropriate.

Two major design techniques have been suggested. If a gas is admitted into the vapor cavity of a supercavitating propeller, the propeller is said to be ventilated, and early experiments [1,2] have indicated the feasibility of doing this in practice. The effective cavitation number of the propeller is reduced, thus allowing the "supercavitating" type of operation to extend over a somewhat lower speed range. It seems possible that radiated noise may be reduced, together with cavitation erosion caused by portions of the cavity collapsing on the blade surface.

Another approach is to design the propeller specifically for operation with gas flow, using recently developed base-vented blade sections which have good cavitation resistance and low drag when ventilated. These sections offer the possibility of achieving high propeller efficiency in the intermediate range between conventional and supercavitating propellers.

This paper will present some results from experiments with both a ventilated supercavitating propeller, and a base-vented propeller designed for high efficiency. Both propellers were designed to operate in the wake of a body of revolution 15 inches in diameter and about 120 inches long. The experiments were conducted on the underwater cableway of the Naval Ordnance Test Station, and in the Garfield Thomas Water Tunnel of the Ordnance Research Laboratory.

VENTILATED SUPERCAVITATING PROPELLER

This propeller was designed by the David Taylor Model Basin to operate in the wake of an existing cableway test dynamometer. The design conditions of the propeller were 65 knots forward speed, 7500 rpm, and a thrust of 1341

pounds at a propeller efficiency of 70%. The propeller diameter is 11 inches, thus giving a design advance ratio, $J = V/nD$, of 0.96, where

V = forward velocity, ft/sec

n = rotative speed, rev/sec

D = propeller diameter, ft.

Two views of the propeller are given in Fig. 1. The blade sections are of the Tulin type, modified by the addition of two drilled holes for ventilation gas on the upper surface of each blade. One hole can be seen near the blade root; the other terminates in a slot extending over the outer region of the blade. All ventilation holes communicate to the hub of the propeller.
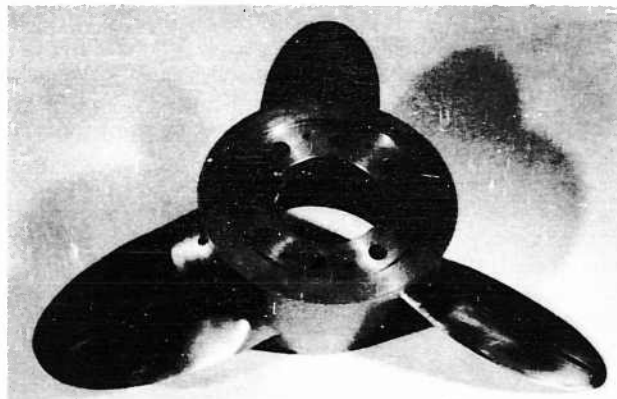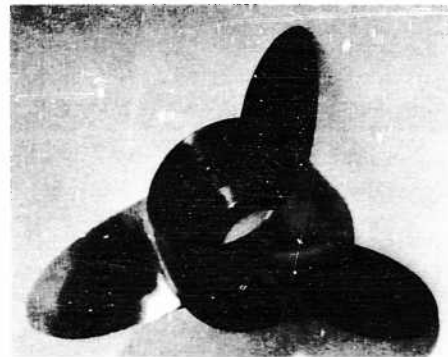
Fig. 1 - Two views of the ventilated, supercavitating propeller

A sketch of the cableway dynamometer is shown in Fig. 2. A turbine operating on decomposed hydrogen peroxide drives the propeller; the gaseous exhaust products from the turbine then pass down the propeller shaft and into the propeller. A metering arrangement in the hub allows various flow rates to be admitted into the propeller; the remainder is discharged axially from the propeller hub.
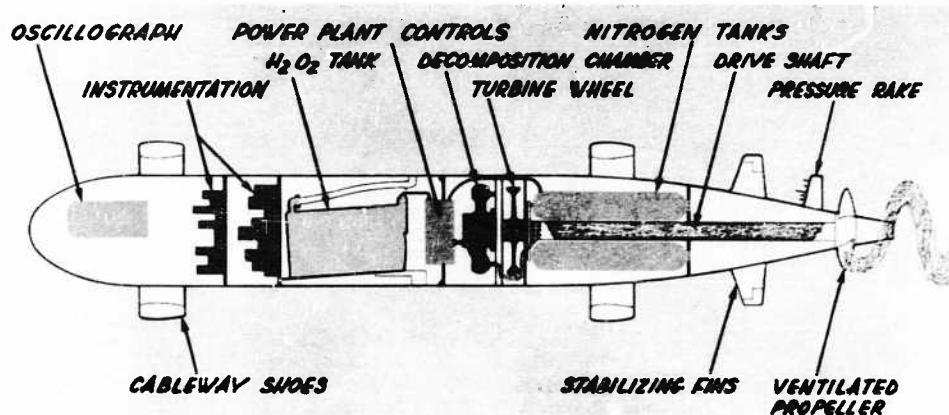
Fig. 2 - Sketch of the cableway dynamometer

The Underwater Cableway facility is located at Morris Dam, near Azusa, California. It consists of a pair of steel cables stretched under the surface of a lake to form a path about 1000 yards long, and about 60 feet deep at the maximum point. The artist's sketch (Fig. 3) gives the general idea. Internal instrumentation in the dynamometer gives temperature, pressure, and forward speed information; hydrophones are arranged to study the radiated noise of the vehicle. Figure 4 shows the vehicle attached to the cables before submerging for a test run.

A summary of the principal test data taken on the cableway is given in Table 1. Most of the experiments were run at about 43 knots; two were made in the 55-60 knot range. Ventilation flow rates ranged from 0 to 50 cubic feet per minute (CFM) at standard temperature and pressure, and in calculating this flow the steam in the exhaust products passing into the propeller was disregarded. The propeller was thus considered to be ventilated with oxygen gas only.

Figure 5 is a plot of the velocity and rotative speed for Run 12. The pressure in the hydrogen peroxide decomposition chamber is also given. The figure illustrates the rapid acceleration of the test dynamometer; the peak forward velocity of 100 ft/sec was achieved 6 seconds after the run began.

In general, good propulsion performance was indicated. Based upon the estimated drag of the dynamometer plus an allowance for thrust deduction, and the measured torque and rotative speed, propeller efficiencies of about 75%
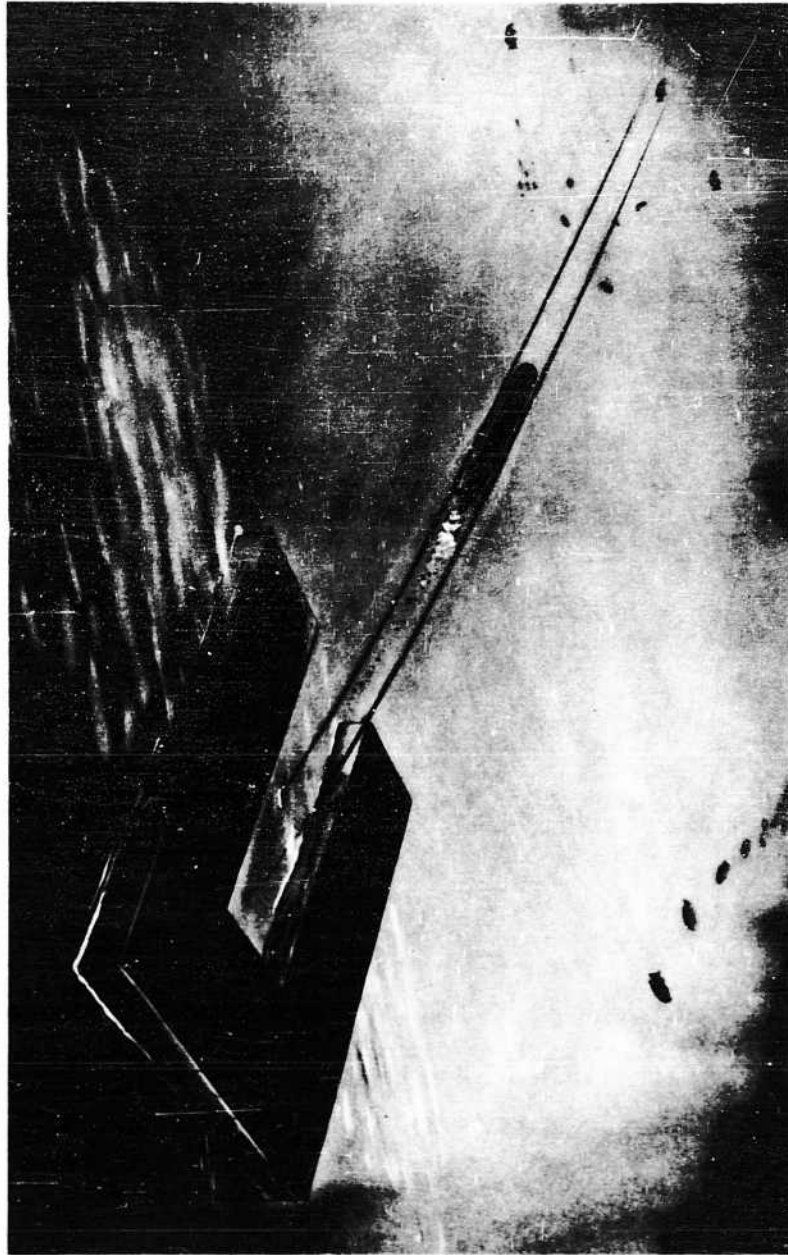
Fig. 3 – Artist's sketch of dynamometer operating on the underwater cableway.
Launching barge in foreground.

Fig. 4 - View of dynamometer before
test run
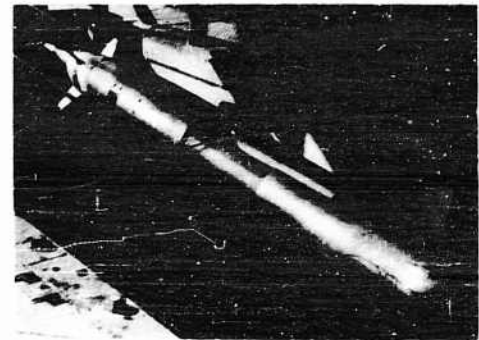
Table 1
Cableway Test Data Ventilated Supercavitating Propeller

	Run Number						
	1	2	3	5	6	12	13
Speed, knots	42.8	42.9	42.9	45.8	41.5	59.3	56.3
RPM	4410	4430	4500	5000	4800	6600	6300
Advance ratio, J	1.08	1.07	1.05	1.02	0.96	1.00	0.99
Ventilation flow, CFM	0	0.7	3	20	50	40	50

All data taken at 50 ft depth.
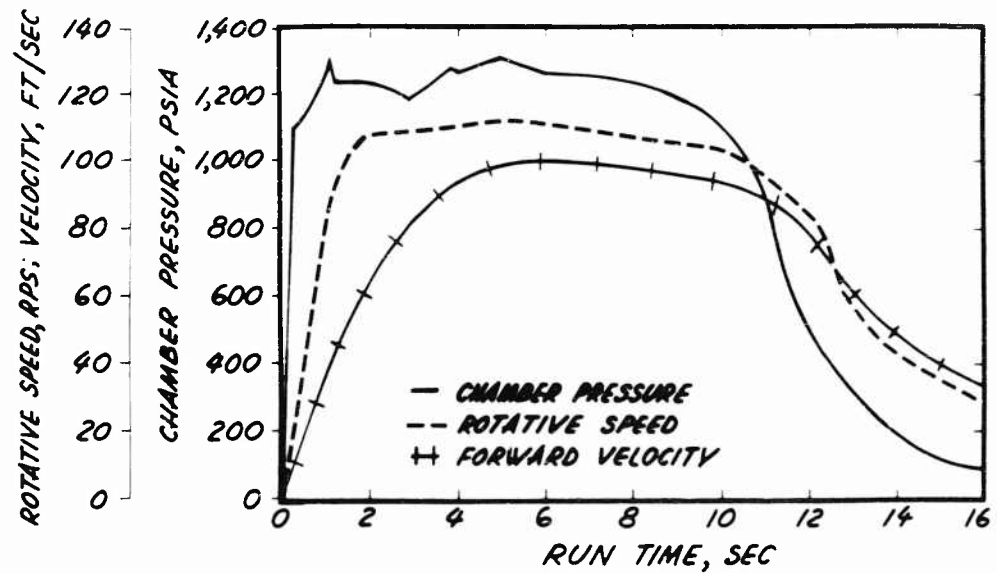
Fig. 5 - Typical test record from run on the underwater cableway

323

were achieved. However, in examining the test data it was noticed (Fig. 6) that the self-propulsion advance ratio, J, varied over a wide range depending upon both depth and ventilation rate. (Additional data from Run 7, a repeat of Run 3, are included in this figure.) The variation of self-propulsion advance ratio with operating depth may impose a severe problem in considering this type of device for underwater vehicle operation, however, it is expected that J will approach some constant value as depth is further increased. If a constant operating depth is assumed, the self-propulsion advance ratio is seen to decrease with increasing ventilation flow rate.
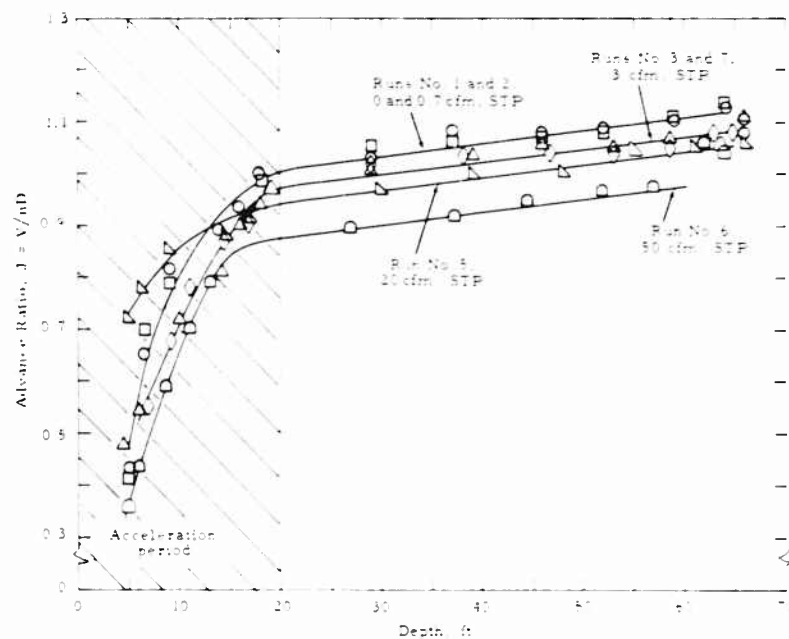
Fig. 6 - Plot of advance ratio as a function of operating depth and ventilation flow rate

In order to obtain further information on the performance of this propeller, the full-scale vehicle was placed in the Garfield Thomas Water Tunnel of the Ordnance Research Laboratory, State College, Pennsylvania. This is a 48 inch diameter working section tunnel with provision for gas removal by a vacuum-pump system. The working section of the tunnel was fitted with a contoured liner to better approximate open-flow streamlines at the tunnel wall. The turbine drive of the cableway vehicle was replaced by a calibrated electric motor, and air was introduced into the propeller by piping through the support strut of the vehicle. The external size and contour of the test body was identical to the cableway configuration with the exception that the cableway attachment struts were removed. Before test data were taken, the velocity profile just ahead of

the propeller was adjusted, by empirical roughness additions, to that measured at the same location during the cableway tests.

Data were taken over a range of advance ratios from 0.85 to 1.20 at cavitation numbers σ_v, based upon the vapor pressure of water, ranging from about 0.45 to 1.35. The tunnel was operated at a working section velocity of 35 ft/sec, and air was discharged through the propeller at rates from 0 to about 7 cfm STP.
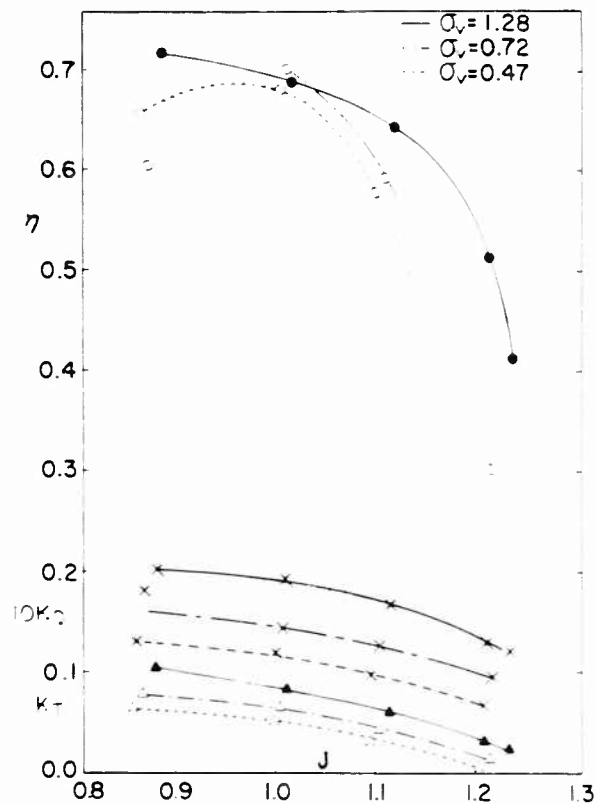
Fig. 7 - Variation of efficiency, torque coefficient, and thrust coefficient for propeller, without ventilation, as a function of advance ratio

Figure 7 is a plot of efficiency, η, torque coefficient, K_Q, and thrust coefficient, K_T, as a function of advance ratio, J, for the propeller without air flow, i.e., as a supercavitating propeller. The coefficients are defined as follows:

$$K_Q = \frac{Q}{\rho g \, n^2 \, D^5}$$

325

$$K_T = \frac{T}{\varrho \, g \, n^2 \, D^4}$$

$$\eta = \frac{K_T \, J}{K_Q \, 2\pi}$$

where

Q = torque

ϱ = density of fluid

n = propeller rotative speed

D = propeller diameter

T = thrust of propeller.

At the design J of 0.96, efficiency appears to maximize near the design value of 70% for three values of σ_v tested. However, the character of the flow changes as J is increased from 0.85 to 1.0 as shown by the photographs. Figure 8 shows the cavity from the leading edge of the propeller typical of super-cavitating operation, with J = 0.85. The situation when J is increased to 1.0 is shown in Fig. 9, and it is seen that the point of cavity formation has moved back to the ventilation slot. At this J, the propeller could not be made to cavitate from the leading edge of the blade, even at the lowest σ_v tested.
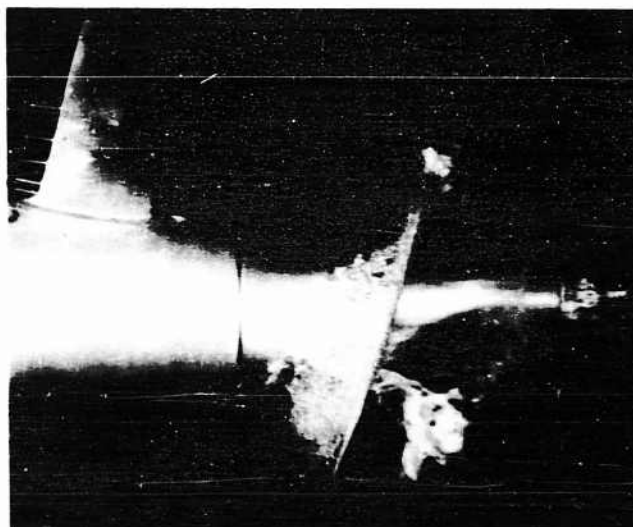
Fig. 8 - Water tunnel photo of propeller with J = 0.85, σ_v = 0.450, and no airflow

326
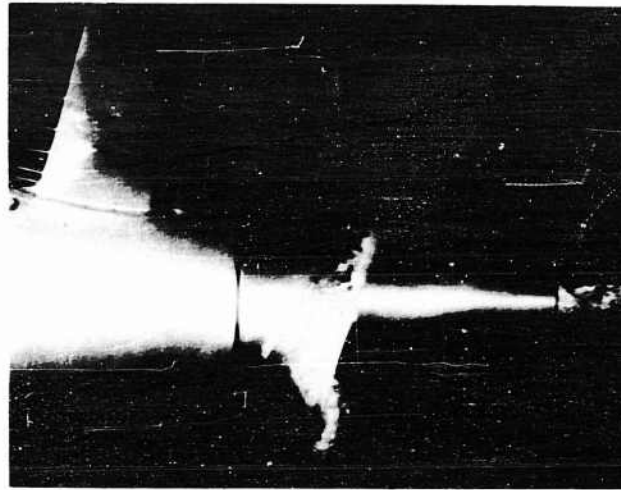
Fig. 9 - Water tunnel photo of propeller
with $J = 1.0$, $\sigma_v = 0.73$ and no airflow.

This change in the flow pattern has important effects as air is introduced into the propeller. Figure 10 shows that the performance at $J = 0.85$ falls off somewhat as the air flow parameter, Q', is increased. Torque and thrust coefficients appear to approach a constant value as Q' is further increased thus indicating the efficiency curves will tend to merge at a constant value also.

The drop-off in efficiency is probably due to the influence of blade friction. In potential-flow theory, ventilation should lower both lift and drag coefficients of the blade section, but their ratio should remain constant. The influence of friction is unchanged by ventilation and thus the $L/D = C_L/(C_D - C_f)$ of the blade section decreases, and hence the propeller efficiency also.

The airflow parameter is defined

$$ Q' = \frac{14.7}{P_{local}} \times \frac{Q_{STP}}{ZA_B \sqrt{V^2 - (2\pi r_c n^2)}} $$

where

Q_{STP} = airflow rate, STP

Z = number of blades

A_B = base area of each blade

r_c = radius of centroid of A_B.

327
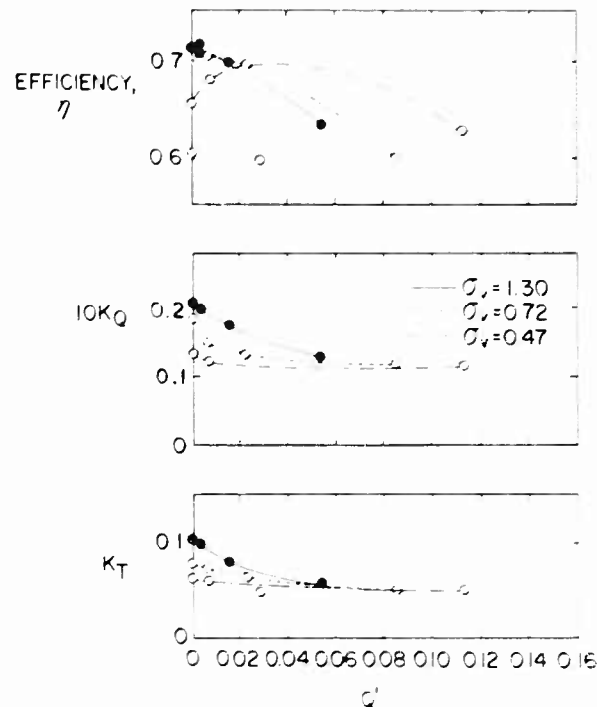
Fig. 10 - Effect of airflow on performance
of ventilated, supercavitating propeller
with J = 0.65

and may be thought of as the ratio of the local gas flow to the volume swept out
by the blunt base or trailing edge of the propeller blades as they move through
the water. As a comparison, values of Q' ranging from 0 to about 0.075 were
measured at the 50 foot depth during the runs on the underwater cableway.

At $J = 1.0$, air addition causes immediate lowering of the efficiency, as
shown in Fig. 11. The difference between behavior at $J = 0.65$ and $J = 1.0$ is
believed to be because of the difference in cavity attachment point location and
the occurrence of some pressure-face ventilation. Figures 12 and 13 compare
the ventilated cavity appearance for the two J conditions. Maximum ventilation
($Q' = 0.10$) would not force the cavity forward to the leading edge when $J = 1.0$.
Some pressure-face ventilation is barely detectable in Fig. 13. Pressure-face
cavitation was noticed at all higher J values, and it is probable that separation
occurs near $J = 1.0$. Strong ventilation would tend to flow into that region,
around the blade tip.

A.G. Fabula [3] has shown in a theoretical study that flat plates ventilated
at mid-chord, for example, lose lift much more rapidly when the cavitation
number based upon cavity pressure, σ_k, is decreased than a corresponding flat

328

plate ventilated at its leading edge. This may explain the foregoing curves, as well as the data replotted as a function of σ_k, where

$$\sigma_k = \frac{P_{local} - P_{cavity}}{\frac{1}{2} \rho g V^2}$$

The cavity pressures were measured by a static pressure tap on one propeller blade at the 0.7 radius point, located between the ventilation slot and the trailing edge as shown in Fig. 14.

Plots of efficiency and thrust and torque coefficients as functions of σ_k for $J = 0.85$ and 1.0 are given in Fig. 15. A shortcoming of these data is that even for no ventilation airflow, σ_k is always much less than σ_v, suggesting either
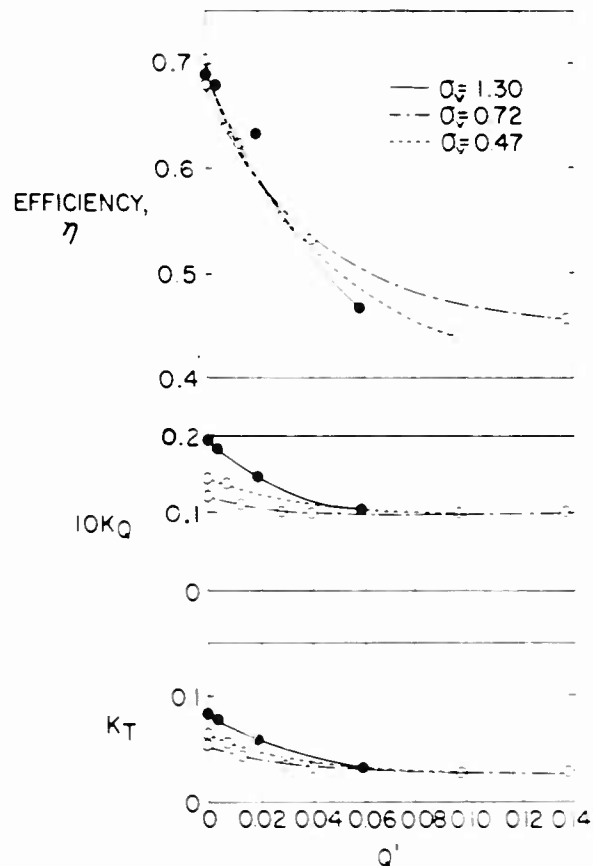
Fig. 11 - Effect of airflow on performance of ventilated, supercavitating propeller with J = 1.0

329
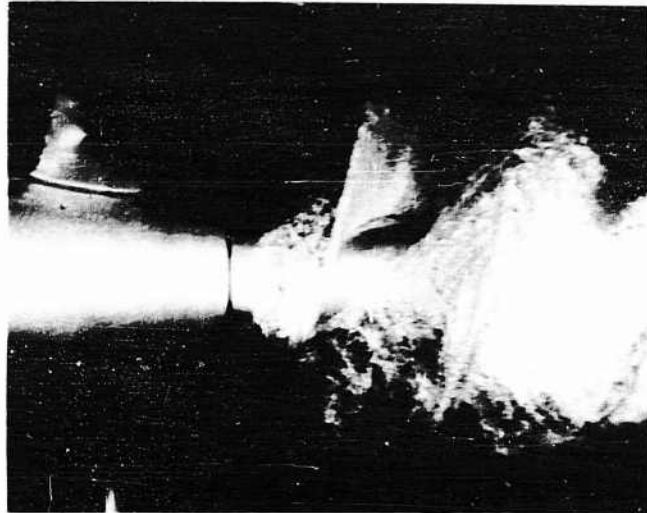
Fig. 12 - Water tunnel photo of propeller
in operation with J = 0.65, σ_v = 0.467, and
Q' = 0.112
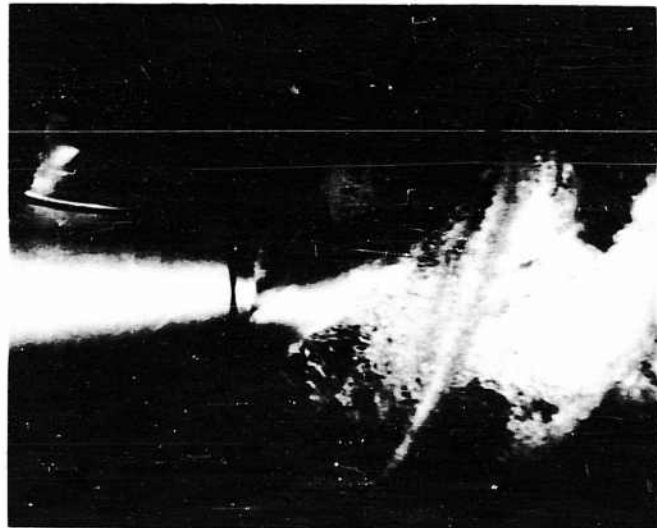
Fig. 13 - Water tunnel photo of propeller
in operation with J = 1.0, σ_v = 0.73 and
Q' = 0.745

cavity pressurization from dissolved or free air in the recirculating water flow of the tunnel, or inadequacies in the measuring method. (The range of σ_v in these data is from 0.47 to 1.30.) Since the cavity pressure method involves a rotating seal and complex passages, the latter is far from impossible. The blade pressures and the performance data were taken during different runs under presumably identical conditions. The data serve to illustrate the considerable difference in the effect of σ_k on the efficiency at the two J values.

The water-tunnel tests also shed some light on another problem observed during the cableway tests. Song and Silberman [4] have shown experimentally that ventilation reduces the radiated noise of cavities shed from simple bodies over a wide range of frequencies. However, as shown in Table 2, ventilation of this supercavitating propeller reduced the radiated noise of the cableway

Fig. 14 - View of cavity-pressure measuring tap on propeller blade

test dynamometer in the higher frequencies only. At frequencies below 1 kc, the radiated noise actually increased for increased ventilation. The water tunnel photographs offer a partial explanation of this result. Figure 16 shows the propeller in operation at $J = 1.07$ and $Q' = 0.22$, i.e., very heavy ventilation. The hole at the root of the propeller blade is seen to vent directly into solid water, and pulsations appear on the surface of the air cavity. Song [5] has studied pulsations in ventilated cavities and concluded that the frequency of vibration is a function of cavity length and number of modes of pulsation. Song writes

$$\frac{f\lambda}{U} = n'(1 - \sigma_k)^{1/2}.$$

where

   f = frequency of vibration

   λ = cavity length

   n' = number of modes

   U = local velocity.

Estimates of cavity pulsation frequency based upon the above formula and observed cavity lengths and number of vibration modes indicate that the low frequency noise peaks measured on the cableway may be due to this source.

Song's theory requires a free surface near the resonating cavity for steady pulsation; evidently an adjacent cavity can serve in this regard also.

It is planned to operate this propeller on the underwater cableway again, with the root ventilation hole closed, to determine experimentally whether this was the source of low frequency noise observed in the cableway runs.

331

Fig. 15 - Propeller performance as a function of σ_k. Airflow rate, Q', varies from 0 to 0.14 and σ_v varies from 0.47 to 1.30

BASE VENTED PROPELLERS

T.G. Lang [6,7] has pioneered in the experimental study of a family of base-vented profiles which offer good cavitation resistance, structural strength, and low drag. A base-vented cambered parabola is shown operating in Fig. 17. When applied to a propeller, these profiles should allow a design having high efficiency and fairly rugged blade sections. They should find a place midway between the operating regimes of conventional propellers and supercavitating propellers. A five-bladed base-vented propeller has recently been designed for the test dynamometer described above. The design conditions are 4500 rpm at 45 knots ($J = 1.11$) and $\sigma_v = 0.9$. The propeller (Fig. 18) has the same hub size and tip diameter (11 inches) as the supercavitating propeller previously discussed. Four small holes in the blunt base of each blade provide ventilation. The basic blade section is an ellipse with a parallel after-section. All lift is accomplished through camber, using the NACA $a = 0.8$ camber line.

332

Table 2
Change in Radiated Noise Level with Propeller Ventilation

Frequency, cycles/sec	Ventilation Flow Rate, CFM			
	0.7	3	20	50
300	+5.0	+7.0	-1.0	+8.5
500	3.0	1.5	5.5	11.0
1,000	1.5	3.7	5.5	4.3
1,500	-0.3	7.0	-3.3	0
2,000	3.5	5.0	-0.7	0
3,000	4.3	-2.0	-6.3	-7.1
5,000	1.2	-6.8	-1.3	-12.5
10,000	0.3	-4.2	-6.2	-10.7
20,000	-8.3	-11.3	-13.8	-13.3

Values shown in the table are the changes in radiated noise (in decibels) from that recorded from during non-ventilated operation. All data taken at 43 knots and 50 foot depth.
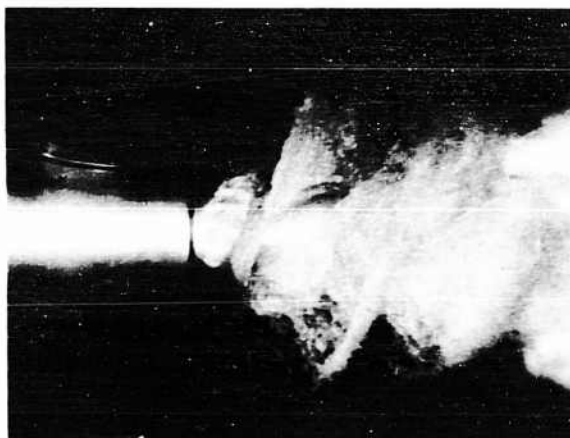
Fig. 16 - Water tunnel photo showing propeller in operation at $J = 1.07$. $\sigma_v = 0.78$, and $Q' = 0.22$

This propeller was also tested in the Garfield Thomas Water Tunnel. The primary object of these tests was to obtain the efficiency of the propeller operating in the wake for which it was designed, to study the effect of airflow on propeller performance, and to determine the cavitation resistance of the propeller.

Figure 19 shows the propeller efficiency as a function of advance ratio, for a Q' of 0.037. At a σ_v of 1.29, good efficiency was attained, reaching over 80%

333
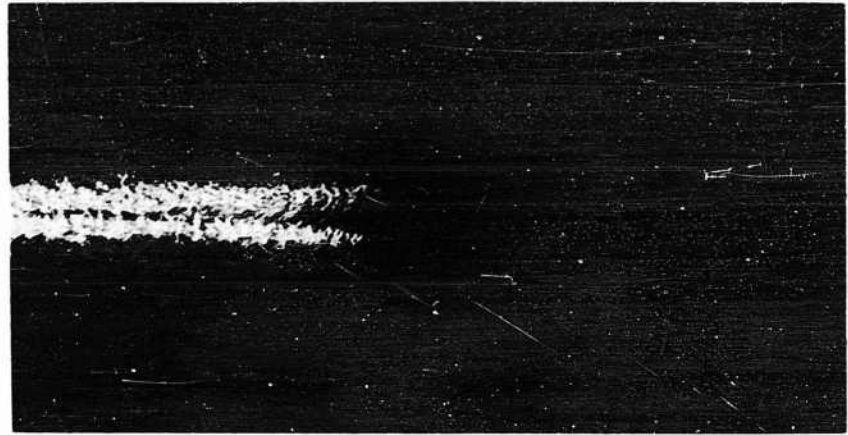
Fig. 17 - View of a base-vented cambered parabola blade
section operating in a water tunnel

Fig. 18 - View of a base-vented propeller

at $J = 1.16$. For cavitation numbers below the design value of $\sigma_v = 0.9$ the efficiency is much lower, indicating that performance is being affected by severe cavitation.

The effect of airflow rate upon performance (Fig. 20) is also indicative of cavitation effects. The curve at $\sigma_v = 1.3$ as in the theory rises to the peak efficiency and remains at that level with increased airflow. The data point at $Q' = 0.037$, $\sigma_v = 1.3$, did not match with independent measurements of electrical power to the motor, and this point was disregarded in fairing the data. Instead, an estimate based upon the electrical measurements was used. For a

334
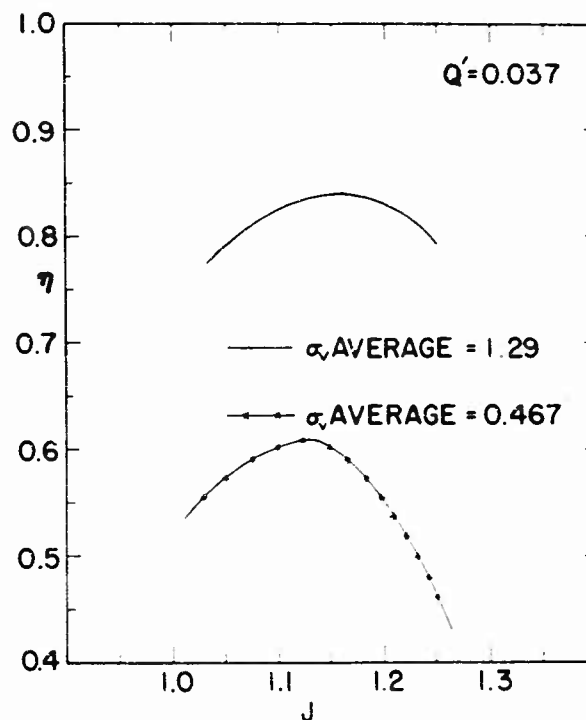
Fig. 19 - Base-vented propeller efficiency
as a function of advance ratio with Q' = 0.037

lower σ_v, air addition causes lowering of performance, as with the ventilated supercavitating propeller.

After the performance tests were completed, a cavitation diagram was prepared for the propeller as shown in Fig. 21. Due to slight differences in manufacturing and some hand-finishing on the leading edges, each of the five blades has a different point of incipient cavitation. The cavitation-free zone drawn in the diagram is based upon the poorest blade in the propeller from the standpoint of cavitation resistance. The diagram shows that the design σ_v of 0.9 could not be reached without cavitation at the leading edge of the suction face, and "burbling" over the suction side of most of the blades. One or more blades may have reached the cavitation-resistance design goal. The performance tests at σ_v = 1.30 and J = 1.16 are inside the cavitation-free zone, as determined without airflow. Tests at other J and σ_v values are clearly in the cavitation region, with adverse effects from cavitation aggravated by air addition.

Figure 22 is a water-tunnel photograph showing the propeller operating near the peak performance conditions. Further plans for this propeller include operation on the underwater cableway to obtain self-propulsion advance ratio and radiated noise information.
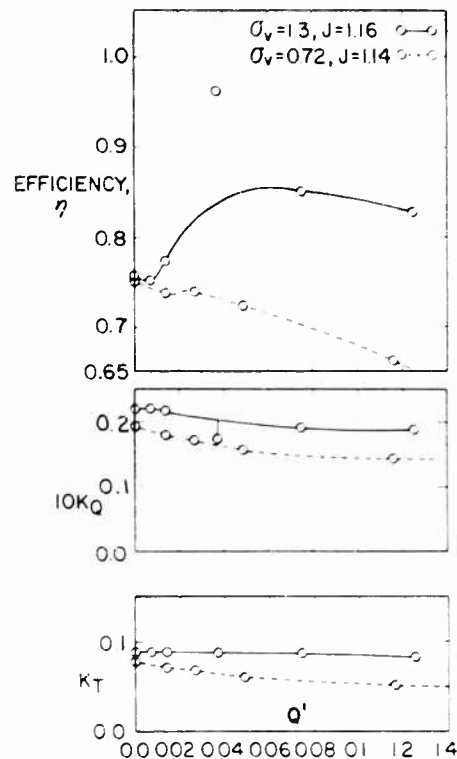
Fig. 20 - Effect of airflow on performance of base-vented propeller
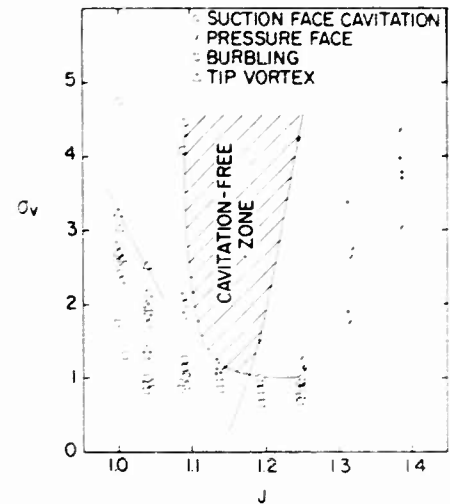
Fig. 21 - Cavitation diagram for base-vented propeller without airflow. (Base cavitation neglected.)

SUMMARY

The experimental evaluation of both the ventilated supercavitating propeller and the base-vented propeller has indicated a number of problems as well as considerable promise in each type of design.

The water-tunnel tests as well as the cableway evaluation [8] of the ventilated supercavitating propeller have shown large changes in performance with changes in ventilation flow and advance ratio. The method of ventilation needs further attention, since it appears that under some conditions, ventilation is ineffective in reducing radiated noise.

The base-vented propeller suffered from excessive cavitation near the design point, thus rendering the analysis of its performance difficult. This was probably due to the general propeller design method and manufacturing techniques, rather than deficiencies in blade section theory. Further work is needed to clarify the areas of good performance achievable in practice with this type of propeller. First results indicate considerable gains in efficiency over the supercavitating propeller can be realized through the base-venting technique.

Ventilated Propellers

Fig. 22 - Base-vented propeller operating
near peak performance conditions

ACKNOWLEDGMENTS

REFERENCES

1. Morgan, W.B., "Performance of a Ventilated Propeller," Prepared for the
    American Towing Tank Conference, Berkeley, California, 31 August 1959,
    David Taylor Model Basin, June 1959.

2. Hecker, Richard, "Powering Performance of a Ventilated Propeller," David
    Taylor Model Basin Report 1487, June 1961.

3. Fabula, A.G., "Thin-Airfoil Theory Applied to Hydrofoils with a Single
    Finite Cavity and Arbitrary Free-Streamline Detachment," Journal of Fluid
    Mechanics, Volume 12, Part 2, p. 227, 1962.

4. Song, C.S. and Silberman, E., "Experimental Studies of Cavitation Noise in
    a Free-Jet Tunnel," St. Anthony Falls Hydraulic Laboratory, Technical
    Paper No. 33, Series B, July 1961.

5. Song, C.S., "Pulsation of Ventilated Cavities," Journal of Ship Research,
    Volume 5, Number 4, p. 8, March 1962.

6. Lang, T.G., "Base-Vented Hydrofoils," NAVORD Report 6606, Naval Ordnance Test Station, China Lake, California, 19 October 1959.

7. Lang, Thomas G. and Daybell, Dorothy A., "Water-Tunnel Tests of a Base-Vented Hydrofoil having a Cambered Parabolic Cross Section," NAVWEPS Report 7584, Naval Ordnance Test Station, China Lake, California, 10 October 1960.

8. Roberts, Paul C., "Studies of a Ventilated Supercavitating Propeller on a Torpedo Test Vehicle, Part I, Performance Results," NAVWEPS Report 7628, Naval Ordnance Test Station, China Lake, California, 21 February 1961.

*   *   *

SHROUDED SUPERCAVITATING PROPELLERS

C. F. Chen
HYDRONAUTICS, Incorporated
Rockville, Maryland

I. INTRODUCTION

The supercavitating propeller offers the possibility for efficient marine propulsion at speeds sufficiently high to guarantee supercavitating operation of the blade sections. The minimum speed for the effective utilization of a super-cavitating propeller depends on the shaft depth and propeller advance ratio, but ranges from about 35 knots for small craft to over 40 knots for very large vessels [1]. In order to extend the useful range of supercavitating operation to lower ship speeds, Tulin has proposed the use of supercavitating propellers in accelerating (Kort) nozzles; a shrouded propeller system with pre-turning vanes is shown in Fig. 1. In the period from April 1960 to August 1961, personnel of HYDRONAUTICS, Incorporated have conducted a detailed feasibility study of
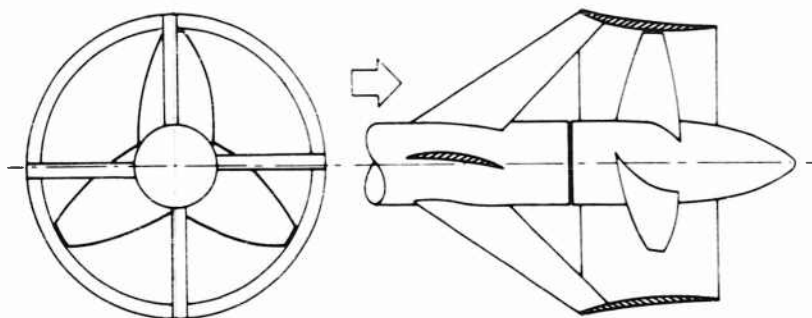
Fig. 1 - Shrouded propeller system with pre-turning vanes

339

shrouded supercavitating propellers under contract NObs-78451 with the Bureau of Ships, whose Code 436 has technical cognizance. This paper summarizes some of the results obtained in the course of research.

The problem of shrouded subcavitating propellers has been treated by many authors since its conception by Kort; the number of papers on this subject is increasing rapidly because of the application of ducted propellers for vertical take-off aircraft. An excellent bibliography is provided by Morgan in his paper on shrouded subcavitating propellers appearing in the same volume.

In this paper, by using the one-dimensional momentum consideration, simple, approximate relationships have been found for the determination of thrust developed on the nozzle, and the mean through flow velocity induced by the nozzle for given loading and geometry of the nozzle and the disk loading on the propeller. These simple relations give results which compare favorably with the results of more accurate calculations by Dickmann and Weissinger [2] and Kobylinsky [3]. Based on these relationships, the pressure reduction obtainable at the plane of the propeller can then be calculated. A method of performance characteristics of the shrouded subcavitating or supercavitating propeller system can be calculated when the geometry of the system and the performance of the isolated propeller is known. Calculated results for shrouded subcavitating propellers compare favorably with the test results of van Manen [4]. Pressure distribution on the shroud is estimated so that the approximate range of forward speeds within which operation of such a system is feasible can be established. In conclusion, a discussion on the method of design is given.

II. ESTIMATE OF THE THRUST DEVELOPED ON AND THE PRESSURE REDUCTION IN THE NOZZLE

It is customary to idealize a lightly loaded, many bladed subcavitating propeller to be an actuator disk in the momentum considerations of the problem. This idealization greatly simplifies the analysis. For supercavitating propellers, the actuator disk model must be modified because of the blockage effects of the trailing cavities as discussed by Tulin elsewhere in the same volume. Since the present investigation was concluded before the initiation of Tulin's research, blockage effects have not been included. In this respect, the present analysis is yet to be extended.

For the one-dimensional momentum consideration, we consider a cylindrical coordinate system x, r, θ with the origin at the center of the propeller, and the x-axis in the direction of the uniform stream velocity U_o (see Fig. 2). Let the propeller be in the center of the nozzle and have a radius R; the nozzle extends from $x = -C/2$ and $x = C/2$. Let the nozzle radius be R at the propeller plane, $x = 0$. Applying the one-dimensional momentum consideration, the total thrust T acting on the fluid due to the action of the propeller and the nozzle is [5]

$$T = \rho A \left[U_o + u \right] u_o. \tag{1}$$

where A is the area of the disk, u is the mean additional velocity induced by the nozzle-propeller system at $x = 0$, and u_o is the additional velocity in the slipstream at $x = \infty$. The thrust developed by the propeller, T_p, can be obtained by

340

Shrouded Supercavitating Propellers
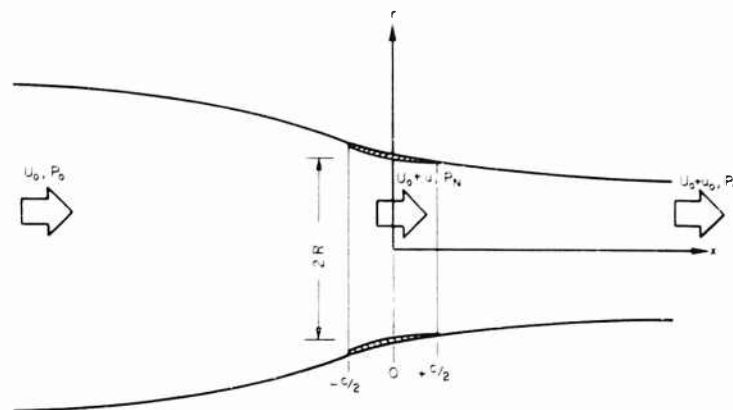
Fig. 2 - Schematic diagram showing the coordinate system

calculating the pressure difference across the actuator disk through the use of Bernoulli's equation as

$$T_p = \rho A \left(U_o + \frac{1}{2} u_o \right) u_o . \tag{2}$$

This is exactly the same expression as in the case of a propeller operating in a free stream. The areas of the slipstream in these two cases are, however, necessarily different. The thrust developed by the nozzle, T_N, due to the action of the cross flow on the ring vortices is

$$T_N = T - T_p = \rho A \left(u - \frac{1}{2} u_o \right) u_o . \tag{3}$$

It is thus clear that the mean velocity induced by the nozzle is

$$u_N = u - \frac{1}{2} u_o . \tag{4}$$

If the reasonable assumption is made that the effect of the nozzle may be considered as due to ring vortices of constant radius R with vorticity distribution $\gamma(x)$, for $-C/2 \le x \le C/2$, then

$$T_N = 2 \pi R \rho U_o \int_{-C/2}^{C/2} \gamma(x,R) \frac{v_r(x,R)}{U_o} dx . \tag{5}$$

where $v_r(x,R)$ is the radial velocity induced by the propeller. (The vortex strength is considered positive when the lift generated is toward the interior of the nozzle.) For a linearized analysis, the vorticity distribution $\gamma(x)$ may be considered as the sum of 1) the vorticity generated by the radial angle of attack

341

due to the induced radial velocity of the propeller, $\gamma_a(x)$, 2) the vorticity due to camber, $\gamma_\delta(x)$, and 3) the vorticity due to the thickness of the profile, $\gamma_t(x)$. For given nozzle geometry, $\gamma_\delta(x)$ and $\gamma_t(x)$ may be determined by the methods of Dickmann [6] and of Weissinger [7] respectively. $\gamma_a(x)$, however, is inter-related to the flow field of the propeller.

The radial velocity induced by the propeller is a function of the total disk loading as well as of its distribution on the propeller. It has been shown by Yim and Chen [8] that a loading distribution proportional, $r^5 \times (R - r)$, induces an effective radial velocity at $r = R$ not significantly different from that induced by a uniformly loaded propeller of the same total loading. We therefore assume that the loading on the propeller is radially uniform. The radial velocity induced by a uniformly loaded propeller is expressible in terms of complete elliptic integrals (see for example Ref. [5]). Therefore, the evaluation of the integral in Eq. (5) requires numerical methods. For an approximate evaluation of Eq. (5), however, we make the simplifying assumption that $\gamma(x)$ in Eq. (5) may be re-placed by its mean $\bar{\gamma}$ defined as

$$\bar{\gamma} = (1/C) \int_{-C/2}^{C/2} \gamma(x) \, dx \; . \tag{6}$$

Then Eq. (5) becomes

$$T_N = 2\pi R \rho U_o \bar{\gamma} C \; \frac{\bar{v}_r}{U_c} \; . \tag{7}$$

where $\bar{v}_r$ is the mean value of $v_r(x,R)$. Normalizing T_N with respect to the free stream dynamic pressure, $1/2 \rho U_o^2$ and the area of the propeller disk, A, and by using the definition of sectional lift coefficient

$$C_L \equiv \frac{\rho U_o \bar{\gamma} C}{1/2 \rho U_o^2 C} \; , \tag{8}$$

Eq. (7) can be written as

$$C_{TN} = 2 \; \frac{C_L C}{R} \; \frac{\bar{v}_r}{U_o} \; . \tag{9}$$

The propeller may be regarded as operating in open water in an equivalent stream of velocity $U_o + u_n$. Then $\bar{v}_r/U_o$ may be written as [9]

$$\frac{\bar{v}_r}{U_o} = \frac{C_{Tp}}{1 + u_n/U_o} \; v_r^* \; . \tag{10}$$

where v_r^* is evaluated as a function of C/R from the known results of the radial flow field of a uniformly loaded actuator disk. The value of $(C/R) v_r^*$ is plotted as a function of C/R in Fig. 3. When Eq. (10) is substituted into Eq. (9), we obtain
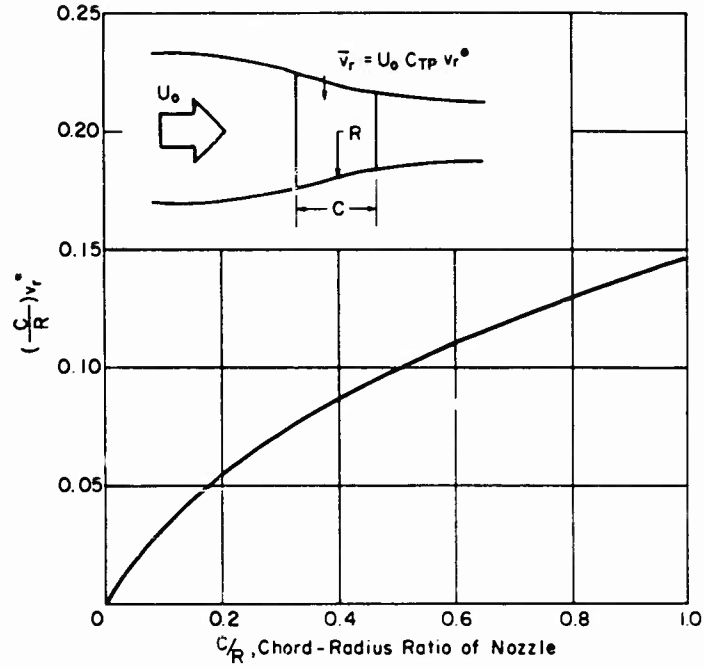
Fig. 3 - Non-dimensional mean radial velocity
induced by the propeller at the nozzle surface

$$C_{TN} = \frac{2 C_{Tp} C_L}{1 + u_n/U_o} \frac{C v_r^{\bullet}}{R} . \tag{11}$$

Solving Eqs. (11) and (3) simultaneously yields

$$\frac{u_n}{U_o} = \frac{1}{2} \left[\left(1 + \frac{4 C_{Tp} C_L}{u_o/U_o} \frac{C v_r^{\bullet}}{R} \right)^{1/2} - 1 \right] , \tag{12}$$

where

$$\frac{u_o}{U_o} = \left[1 + C_{Tp} \right]^{1/2} - 1 , \tag{13}$$

as is easily obtained from Eq. (2). Equations (11) and (12) are the desired rela-
tionships from which the thrust developed on the nozzle, C_{TN}, and the mean
through flow velocity induced by the nozzle, u_N, are readily computed once the

343

nozzle chord-radius ratio, C/R, nozzle sectional lift coefficient, C_L, and the propeller thrust coefficient, C_{Tp}, are given.

Since Eqs. (11) and (12) will serve as the basis for all subsequent calculations, we now compare our results with those obtained by Dickman and Weissinger [2]. In their paper, the propeller is represented by a uniformly loaded actuator disk located at the entrance of the nozzle and the vortex distribution for the nozzle is elliptic. The ratio T_N/T_p have been calculated by the use of Eqs. (3), (11), and (12) for the case $C_{Tp} = 1$, and $C/R = 0.5$ and 1. Our results compare favorably with those obtained by Dickmann and Weissinger [2] as shown below:

C/R	T_N/T_p Dickmann and Weissinger	T_N/T_p Present Results*
0.5	0.162	0.164
1.0	0.202	0.186

Now we extend the results to include the effect of a finite hub. Applying the momentum theorem, the expressions for the total thrust, Eq. (1), and the thrust developed by the propeller, Eq. (2), remain the same as in the case of no hub. However, the area to be used in these expressions must be that of the annular region between the hub and the nozzle. By the same procedure, one easily obtains for a hub of radius R_h

$$\frac{u_n}{U_o} = \frac{1}{2}\left\{\left[\left(1 + \frac{u_h}{U_o}\right)^2 + \frac{4\,C_{Tp}\,C_L}{\left(1 - R_h^2/R^2\right)^2 u_o/U_o}\,\frac{Cv_r^{\bullet}}{R}\right]^{1/2} - \left(1 + \frac{u_h}{U_o}\right)\right\}. \quad (14)$$

and

$$\frac{u_o}{U_o} = \left[1 - \frac{C_{Tp}}{1 - \frac{R_h^2}{R^2}}\right]^{-1/2} - 1. \quad (15)$$

The average increment in velocity due to the hub, u_h, is estimated as follows: at $x = -(1/2)R$, we locate a source whose strength is such that when combined with the uniform flow, it generates a half body of radius R_h at $x = 0$: the average through flow in the annular region $R_h \leq r \leq R$ at $x = 0$ is then computed and the mean velocity is evaluated. The value of u_h thus calculated is shown in Fig. 4.

We are now in a position to estimate the pressure reduction achieved by the use of a nozzle. We define the mean cavitation number at the propeller plane, σ, as the difference between the mean static pressure and the vapor pressure there normalized with respect to the local dynamic pressure

---

*In the present calculation, $v_r^{\bullet}$ is different from that presented in Fig. 3 because the position of the propeller is not at the center of the nozzle.
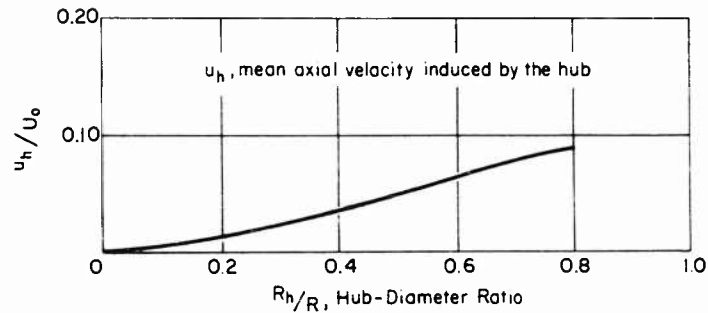
Fig. 4 - Mean increment of axial velocity
due to the hub as a function of hub size

$$\sigma = \frac{p - p_v}{1/2\rho \left[U_o + u_n + u_h \right]^2} . \tag{16}$$

By defining the pressure coefficient C_p

$$C_p = \frac{p - p_o}{1/2\rho U_o^2} \approx 2 \frac{u_n + u_h}{U_o} .$$

and the cavitation number of the free stream

$$\sigma_o = \frac{p_o - p_v}{1/2\rho U_o^2} .$$

(16) can be written as

$$\sigma = \frac{C_p + \sigma_o}{1 - C_p} . \tag{17}$$

Calculations of σ corresponding to different forward speeds at a depth of submergence of 20 feet have been made for nozzles with the same lift coefficient, $C_L = 1$, but different values of $C R$, and a hub of radius $R_h = 0.4 R$. The results are shown in Fig. 5. Supposing that the rotational speed and the pitch of propeller is such that supercavitating operation is possible when the mean cavitation number is below 0.5, the range of speeds between $\sigma = 0$ and $\sigma = 0.5$ for each size nozzle may be considered as approximating the maximum range of possible operation. It is remarked here that the blockage effects of the trailing cavities further reduces the pressure in front of the propeller. Supercavitating operation would then be possible for even higher mean cavitation numbers, or equivalently, lower forward speeds.

345
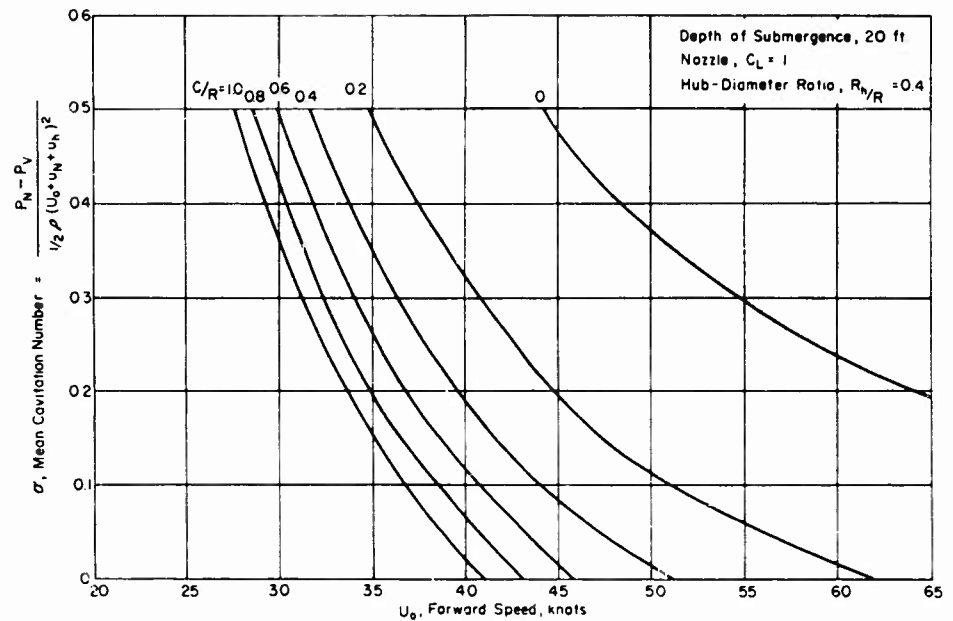
Fig. 5 - Mean cavitation number as function of
nozzle size and forward speed

III. PERFORMANCE CALCULATIONS

In this section, a method is developed to allow calculation of the performance of a propeller (whether supercavitating or subcavitating), enclosed by a nozzle from knowledge of the performance of such a propeller in open water and of the nozzle geometry. We assume that the sectional lift due to camber, thickness, and angle of attack of the nozzle may be linearly superposed. The lift due to the thickness distribution can be calculated by the method given by Weissinger [7]. The lift due to camber and angle of attack can be calculated by the method given by Dickmann [6]. It is noted here that the effective angle of attack of the nozzle will be altered by the induced radial velocity of the propeller. Let now the maximum thickness ratio of the nozzle profile be t, the maximum camber ratio δ (which is defined as the maximum distance of the camber line from the nose-tail line divided by the chord length), and the angle of attack of nose-tail α_o, then the lift coefficient developed on the nozzle section is

$$C_L = C_{Lt} \times t + C_{L\delta} \times \delta + C_{L\alpha} \left[\frac{C_{Tp} v_r^*}{\left(1 + \frac{u_n + u_h}{U_o}\right)\left(1 - \frac{R^2}{R_h^2}\right)} - \alpha_o \right] \tag{18}$$

346

in which the first term in the bracket is the radial angle of attack α_{i_p} induced by the propeller flow field. The lift due to thickness, C_{L_t}, is a function of C/R and the thickness distribution. Since its magnitude is very small, we shall use the value calculated by Weissinger [7] for a Joukowsky profile as shown in Fig. 6. The lift due to camber can be calculated by the method of Dickmann [6]; for an elliptic vorticity distribution, with a resulting camber which is nearly parabolic,*

$$C_{L_\delta} = 4\pi \left[1 + \frac{9 - 6 \, \ell n \left(32 \, \frac{R}{c} \right)}{128 \, \frac{R^2}{c^2}} \right] \qquad (19)$$

The value of $C_{L_\delta}/4\pi$ is shown as a function of C/R in Fig. 7. The lift due to radial angle of attack for ring-airfoils has been calculated by Dickmann [6]. The lift generated on the ring-airfoil is larger than that generated on a flat plate set at the same angle. This ratio of lift coefficients, or equivalently the ratio of total circulation generated, is shown in Fig. 8.

For given total thrust coefficient C_T to be developed by the nozzle-propeller system, the geometry of the nozzle, and the hub radius, Eqs. (3), (11), (14) and (18) give the four unknowns C_{TN}, C_{Tp}, C_L, and u_n/U_o. Now we assume that the propeller is operating in an equivalent free stream of velocity $U_o + u_N + u_h$, therefore, with respect to this stream, the thrust coefficient of the propeller is

$$C'_{Tp} = \frac{C_{Tp}}{\left(1 - \frac{R_h^2}{R^2} \right) \left(1 + \frac{u_n + u_h}{U} \right)^2} , \qquad (20)$$
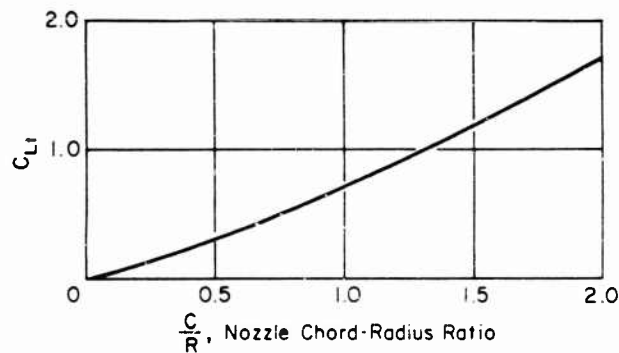
Fig. 6 - Lift due to thickness effect (Weissinger)

*Although the theory of Dickmann is for small values of C/R (≈ 1), the values of the induced velocities due to camber on the nozzle surface, Eq. (28), are within 5% of those given by Küchemann and Weber [5] up to $C/R = 2$. It is assumed, then, Eq. (9) is valid for C/R up to 2.
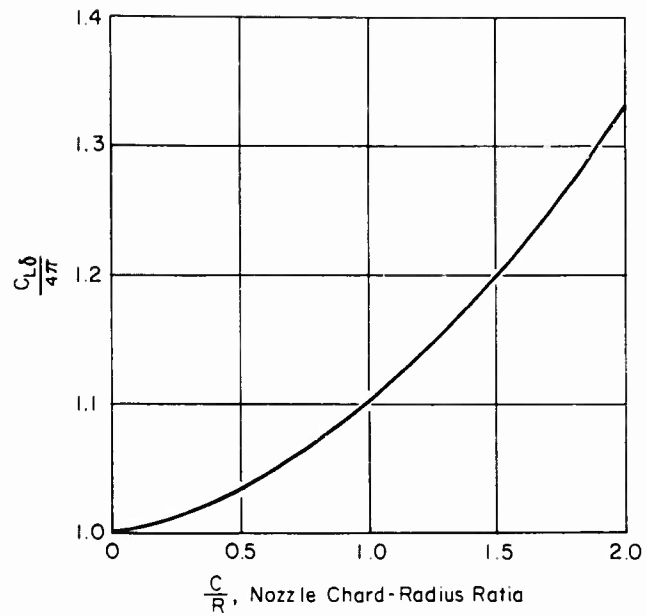
Fig. 7 - Lift due to camber effect (Dickmann)
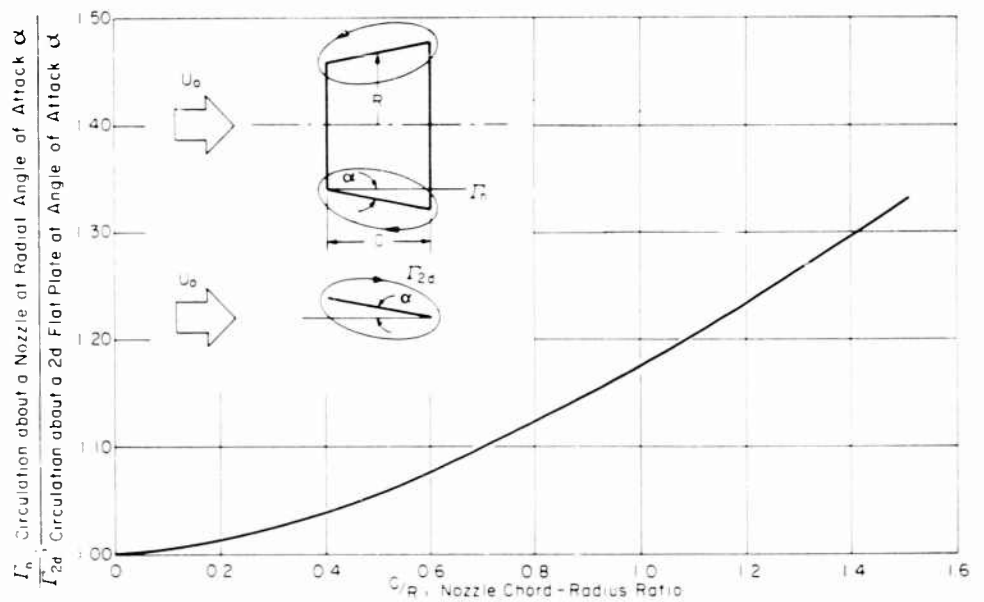
Fig. 8 - Increment in circulation about a nozzle
as a function of nozzle size (Dickmann)

348

where the prime denotes quantities referred to the equivalent free stream. With this value of C'_{T_p}, and given pitch ratio of the propeller, one can find from the performance characteristics of the propeller in open water the efficiency, η', and the advance ratio, J'. Since the efficiency of the propeller, η', is defined as

$$\eta' = \frac{T_p(U_o + u_N + u_h)}{Q\omega} , \qquad (21)$$

where Q is the torque input and ω is the angular velocity in radians per second, the overall efficiency, η, of the nozzle-propeller system is

$$\eta = \frac{(T_n + T_p - D_{pn})\, U_o}{Q\omega}$$

$$= \eta' \frac{U_o}{U_o + u_n + u_h} \times \frac{T - D_{pn}}{T_p} , \qquad (22)$$

in which D_{pn} denotes the profile drag of the nozzle section. The advance ratio J of this system is

$$J = J' \frac{U_o}{U_o + u_n + u_h} . \qquad (23)$$

With these results, one is able to construct a performance curve of the nozzle-propeller system, under the assumption that the losses on the propeller are exactly the same as those of a free propeller operating in this equivalent stream.

There exist no data for shrouded supercavitating propeller systems. However, van Manen [4] has tested certain shrouded subcavitating propeller systems using Wageningen Series propellers whose open-water performance is known [10], and these results afford the possibility of comparison with predicted performance. The geometry of the nozzle chosen for comparison is as follows:

Chord-Radius Ratio, C/R	1
Section Profile	NACA 5415
Angle of Attack	12.7°

The nozzle encloses a Wageningen Series B3-50 propeller. Calculations of the efficiency, η, the total thrust coefficient, K_T, and the thrust coefficient of the nozzle, K_{TN} at different values of advance coefficient J, have been made and compared with test results for propellers of pitch-diameter ratio, P/D, of 0.6 and 1.4 in Fig. 9. The profile drag is estimated from the data presented in Ref. [11] for NACA 4-digit series airfoil sections. It is seen that for P/D = 0.6, up to J = 0.4, the calculated values of η, K_T, and K_{TN} agree very well with the test results. In the high pitch-diameter ratio case, P/D = 1.4, up to J = 0.8, agreement between the calculated values of η and those obtained by tests are good. However, predictions on the thrust coefficients are not as good as in the P/D = 0.6 case.

349
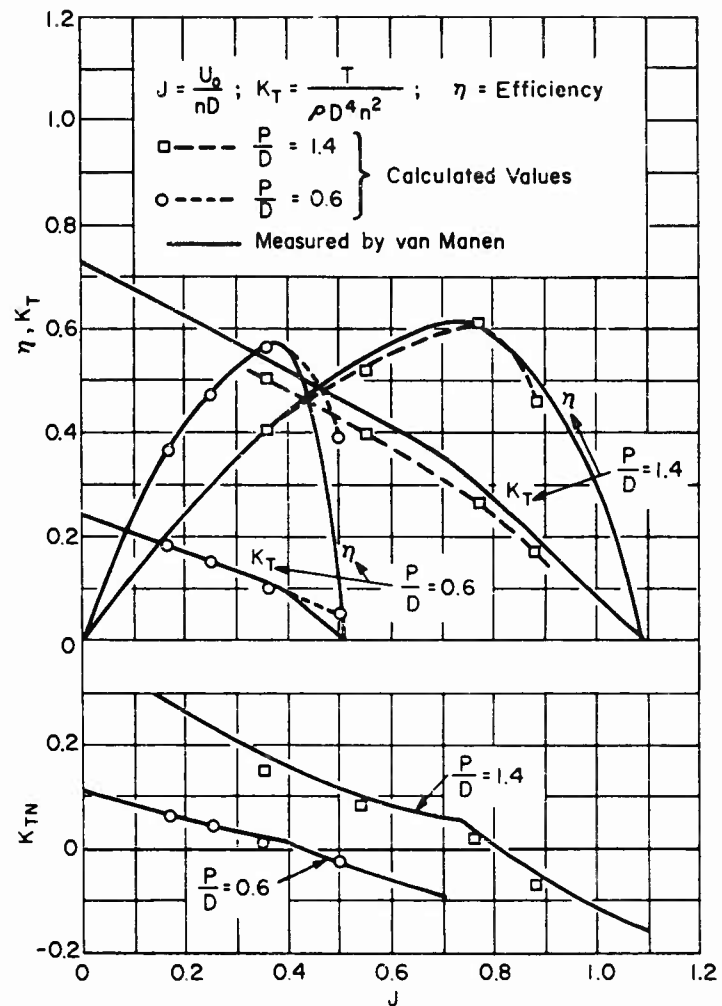
Fig. 9 - Comparison of calculated performance charac-
teristics with test results for a nozzle-subcavitating
propeller system

In a recent paper, Kobylinsky [3] has modified the method of Dickmann and
Weissinger [2] to include the effect of load variation on the propeller disk. A
nozzle-propeller system which gives a $C_{T_p} = 3.07$ has been designed and tested.
From the geometry of the system, we have computed the ratio of the thrust de-
veloped on the nozzle and that developed on the propeller, T_n/T_p, according to
the method stated above. Our result compares favorably with the theoretically
calculated value by Kobylinsky:

	Kobylinsky [2]		Present
	Theoretical	Experimental	Calculation
T_N/T_p	0.407	0.380	0.410

It seems that the method developed here is quite adequate for shrouded sub-cavitating propeller systems. The validity for shrouded supercavitating propeller systems, however, is yet to be verified by systematic experimentation.

IV. PRESSURE DISTRIBUTION ON THE NOZZLE SURFACE

Should cavitation occur on the interior surface of the nozzle, where the pressure is low, the propeller would no longer be operating in a homogeneous fluid. Should cavitation occur on the exterior surface of the nozzle, the drag of the nozzle would become excessive. In either case, the efficiency of the system would begin to decrease, and cavitation erosion difficulties would ensue. There-fore, cavitation on the nozzle must be prevented. This is especially difficult in view of the fact that as the thrust requirement is changed, so does the induced radial velocity of the propeller, thus resulting an effective angle of attack for the nozzle sections different from that at design. In order to evaluate the cavitation characteristics of the nozzle, the pressure distribution must thus be found for a range of operating conditions.

The additional velocity due to the thickness, u_t, on the surface of the nozzle can be found by the method of Weissinger [7], and Bagley, Kirby, and Marcer [12]. However, the results are obtained by series solutions of integral equations, and they are difficult to apply. We have developed a simple correction formula based on a continuity argument, which gives results in good agreement with those of Bagley et al. [12]. Consider 1) a nozzle of radius R with profile of maximum thickness ratio t, and 2) a two-dimensional configuration consisting of airfoils of the same profile placed symmetrically opposite each other with a gap of 2R. The area change $\Delta A/A$ for the nozzle is

$$\left(\frac{\Delta A}{A}\right)_N = t \frac{C}{R} + 0(t^2) , \tag{24}$$

and for the two-dimensional configuration is

$$\left(\frac{\Delta A}{A}\right)_{2d} = t \frac{C}{2R} . \tag{25}$$

By simple continuity argument, the relative increase in velocity from the two-dimensional case to the nozzle case is

$$\frac{(U_o + u_t)_N}{(U_o + u_t)_{2d}} = \frac{(\Delta A/A)_N}{(\Delta A/A)_{2d}}$$

$$= 1 + \frac{tC}{2R} + 0(t^2) . \tag{26}$$

351

It is known that the velocity increase on one of the profiles due to the presence of the other profile in two-dimensional flow is of the order $(tC/R)^2$. If we limit our considerations to nozzles of C/R not very much larger than 1, this slight increment may be neglected. Therefore, we arrive at the result on the interior surface of the nozzle

$$\frac{U_o + u_t}{U_o} = \left(\frac{U_o + u_t}{U_o}\right)_{sect} \left(1 + \frac{tC}{2R}\right), \tag{27}$$

in which the subscript "sect" denotes sectional value. Comparison of the results obtained by this method and those by the more exact method of Bagley et al. [12] is shown in Fig. 10 for a R.A.E. 101 - 10% section with C/R = 1 and 2. It is seen that the simple approximate method is adequate, and the error is on the conservative side. For the exterior surface, we will assume the velocity increment is the same as the sectional value.
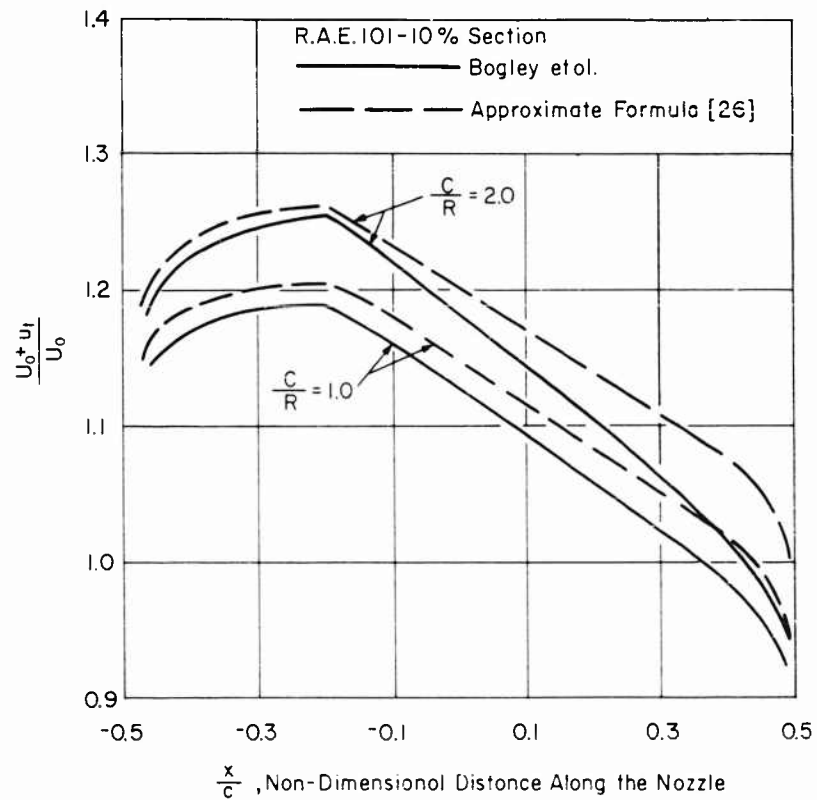
Fig. 10 - Increment in axial velocity on nozzle surface due to thickness

If we assume the chordwise vorticity distribution is elliptic on the nozzle surface

$$\gamma_\delta(x) = \frac{2}{\pi} U_o C_{L\delta} \delta \left[1 - (2x/C)^2\right]^{1/2},$$
(28)

the additional velocity due to camber calculated according to the method of Dickmann [6] is*

$$\frac{u_\delta}{U_o} = \frac{C_{L\delta}\delta}{\pi} \left\{ \pm \left[1 - (2x/C)^2\right]^{1/2} + \frac{\ln(32\,R/C) - 1}{8\,R/C} - \frac{8\,x^2/C^2 - 1}{16\,R/C} \right\}, \quad -C/2 < x < C/2.$$
(29)

The plus and minus signs refer to the interior and exterior surfaces of the nozzle respectively. The camber line is nearly parabolic.

The effect of the propeller slipstreams is to produce an effective radial angle of attack on the nozzle. According linear theory, when the effective radial angle of attack is finite, the velocity at the leading edge becomes infinite. In the actual case, the leading edge of the foil is rounded; the velocity there is finite, though very large. Since near the leading edge, the flow is approximately two-dimensional, the values given by Abbott et al. [11] can be used here. The additional velocity due to angle of attack, then, is

$$\frac{u_\alpha}{U_o} = 2\pi(\alpha_{ip} - \alpha_o)\left(\frac{u_\alpha}{U_o}\right)_{sect}.$$
(30)

To obtain the pressure on the nozzle surface, we use the following formula:

$$\frac{p - p_o}{1/2\rho\,U_o^2} = 1 - \frac{1}{U_o^2}\left[u_t \pm u_\delta \pm u_\alpha\right]^2,$$
(31)

with appropriate signs for u_δ and u_α. Although this formula is not consistent with the linear theory, it proves to be more successful for airfoil sections than its linear counterpart [11]. The minimum pressure determines the cavitation inception speed.

For the purpose of illustration, the inception speeds of the nozzle on a shrouded supercavitating propeller system designed for a hydrofoil craft have been calculated and shown in Fig. 11. The sectional characteristics are given by Patterson and Braslow [13]. At the design speed of 35 knots, there is little or no effective radial angle of attack. As the speed is increased, the required C_T decreased, thus moving the stagnation point to the interior surface of the nozzle. Eventually the pressure on the exterior surface near the leading edge becomes so low that cavitation results. If the speed is decreased from that of design, the C_T required increases, with the stagnation point moving to the

---

*See footnote for Eq. (19).
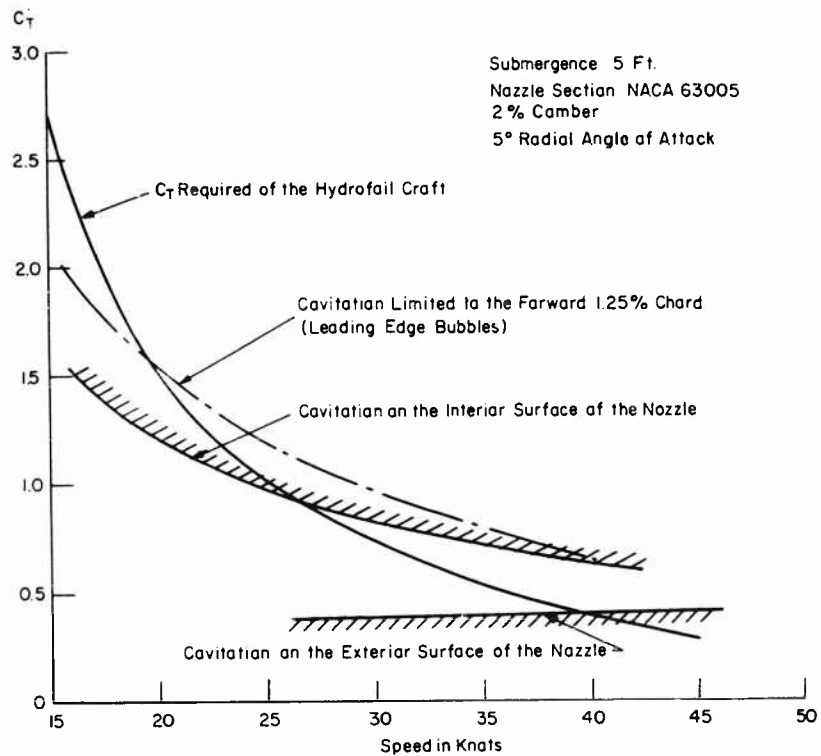
Fig. 11 - Nozzle cavitation characteristics of a shrouded supercavitating propeller system designed for a hydrofoil craft

exterior surface of the nozzle. Cavitation on the interior surface results. It is of interest to note that if one is willing to accept leading edge bubbles, which would hardly affect the operation of the propeller, the range of applicability of the shrouded supercavitating propeller is considerably increased.

V. DISCUSSION ON THE METHOD OF DESIGN

In the design of a shrouded supercavitating propeller system, the following factors must be considered:

1. Supercavitating operation of the propeller at design speed.

2. Avoidance of cavitation on the nozzle surface at design speed.

3. Propeller blade strength requirements.

4. Propulsive efficiency.

354

5. Off design considerations: nozzle cavitation and supercavitating opera-
tion of the propeller; thrust requirement.

6. Mating of the shrouded supercavitating propeller system with the propul-
sion pod or the hull.

The general procedure is to determine first the nozzle size and shape (there-
fore the propeller size) and the rotational speed of the propeller taking into ac-
count the factors listed above. Then, a thrust distribution which minimizes the
losses must be calculated. Finally, the blade section must be designed to give
adequate strength and low drag-lift ratios.

Since the tip effect of the propeller is minimized by the presence of the
nozzle, it may be profitable to design the blades to produce the optimum thrust
distribution calculated according to the assumption of light loading and very
large number of blades. Glaurt [14, p. 258] has given the optimum thrust dis-
tribution for such a case taking into account the profile drag (in the present
case, this consists of the cavity as well as the frictional drag) of the blades. In
his derivation, which was mainly for aircraft application, the inflow speed is
neglected when compared with the tangential speed of the propeller. This situa-
tion is easily remedied as shown by Chen [15]; the result indicates that even at
$J = 1$, the difference between these two "optimum" thrust distribution is very
small.

Once the thrust distribution is determined, the radial variation of the prod-
uct of sectional lift coefficient and the chord can be calculated by the blade ele-
ment theory. The choice of the chord distribution or equivalently the lift dis-
tribution, rests on strength and efficiency considerations. The blade section
can then be designed according to the method given by Auslaender [16]. To
obtain the pitch distribution, the velocity induced by the nozzle, the hub, as well
as the propeller itself (without tip effects) must be taken into account. When the
shrouded supercavitating propeller system has to be mounted on a propulsion
pod; as is the case for hydrofoil craft applications, the supporting vane should
be designed to pre-turn the flow such as to reduce rotational losses.

The three-dimensional (camber correction) as well as the cascade or block-
age effects (association with heavy cavitation) on the blade section designs have
been purposely left out of this discussion. Needless to say, there remains much
to be done both in theoretical and in systematic experimental investigations.

REFERENCES

1. Tachmindji, A.J., Morgan, W.B., Miller, M.L., and Hecker, R., "The De-
sign and Performance of Supercavitating Propellers," DTMB Report C-807,
February 1957

2. Dickmann, H.E. and Weissinger, J., Beitrag zur Theorie optimaler Düsen-
schrauben (Kortdüsen), Jahrbuch der Schiffbautechnischen Gesellshaft,
Band 49, 1955

3. Kobylinsky, L., "The Calculation of Nozzle Propeller Systems Based on the Theory of Thin Annular Airfoils with Arbitrary Circulation Distribution," International Shipbuilding Progress, Vol. 8, No. 88, December 1961

4. van Manen, J.D., "Recent Research on Propellers in Nozzles," Journal of Ship Research, Vol. 1, No. 2, July 1957

5. Küchemann, D. and Weber, J., "Aerodynamics of Propulsion," McGraw-Hill Book Co., New York, 1953

6. Dickmann, H.E., Grundlagen zur Theorie Ringförmiger Tragflügel (Frei Umstromte Düsen), Ingenier-Archiv, Vol. 11, 1940 (English translation: Polytechnic Institute of Brooklyn), PIBAL Report No. 353

7. Weissinger, J., "The Influence of Profile Thickness on Ring Airfoils in Steady Incompressible Flow," ARDC AF 61(514)-904, October 1957

8. Yim, B. and Chen, C.F., "The Flow Field of an Infinitely Bladed Propeller with Radially Non-uniform Loading," HYDRONAUTICS, Incorporated Technical Report 005-2, February 1961

9. Chen, C.F., "Feasibility Study of Supercavitating Propellers in Kort Nozzles, Phase I.," HYDRONAUTICS, Incorporated Technical Report 005-1, December 1960

10. van Manen, J.D., "Fundamentals of Ship Resistance and Propulsion - Part B," Netherlands Ship Model Basin Publication No. 132a

11. Abbot, I.H., v. Doenhoff, A.E., and Stivers, L.S., Jr., "Summary of Airfoil Data," NACA Report No. 824, 1945

12. Bagley, J.A., Kirby, N.B., and Marcer, P.J., "A Method of Calculating the Velocity Distribution on Annular Aerofoils in Incompressible Flow," ARC R and M No. 3146, June 1958

13. Patterson, E.W., and Braslow, A.L., "Ordinates and Theoretical Pressure-Distribution Data for NACA 6- and 6A-Series Airfoil Sections with Thickness from 2 to 21 and from 2 to 15 Percent Chords Respectively," NACA TN 4322, September 1958

14. Glauert, H., "Airplane Propellers, Division L of 'Aerodynamics Theory,'" edited by W.F. Durand, p. 258, Durand Reprint Committee, C.I.T., Pasadena, California, 1943

15. Chen, C.F., Final Report on the Feasibility Study of Supercavitating Propellers in Kort Nozzles, HYDRONAUTICS, Incorporated Technical Report 005-5, September 1961

16. Auslaender, J., "The Linearized Theory for Supercavitating Hydrofoils Operating at High Speeds Near a Free Surface," HYDRONAUTICS, Incorporated Technical Report 001-5, June 1961

*   *   *

ON THE GROWTH OF NUCLEI AND THE RELATED
SCALING FACTORS IN CAVITATION INCEPTION

F. van der Walle*
Netherlands Ship Model Basin
Wageningen, Holland

ABSTRACT

A mathematical model has been formul .ted for the growth of nuclei that
are transported in the flow around profiles. In addition the formation of
nuclei from crevices in the surface has been treated. The various scaling
laws have been derived for the different types of cavitation mechanisms.
Results of numerical calculations have been given for the inception values
of the cavitation number for hemispherical bodies. The results are dis-
cussed and compared with already published experimental data.

1. INTRODUCTION

It is generally accepted now that cavitation inception and some of the full-
grown cavitation patterns are influenced to a large extent by the presence of
nuclei in the waterstream. Such a nucleus grows first by gas diffusion until a
certain critical size has been reached after which it bursts into vaporous cavi-
tation [1]. The source of these nuclei is two fold. In the first place nuclei may
be present in the oncoming stream itself; in many cases however these nuclei
will not be the most important ones, as the available time is often too short for
growth by gas diffusion to a sufficiently large size. These nuclei will be denoted
by stream-nuclei. The other source of nuclei is found in crevices in the wall of
the body that is immersed in the flow. Every crevice can generate a continuous
stream of nuclei just as can often be seen in a glass of sodawater where such
continuous streams of small bubbles emerge from slight imperfections in the
wall of the glass. These nuclei will be denoted by wall-nuclei.

In many cases these wall-nuclei play a more important role than stream-
nuclei as the available growth times are essentially larger due to the fact that
these nuclei are attached to the wall during at least part of their life. This is

---

*Head of the Department for Fluid Mechanics of the Netherlands Ship Model
Basin, Wageningen, Holland.

demonstrated for instance by the experimental results of Kermeen, McGraw and Parkin [2].

The function of the wall as a generator of nuclei can be characterized as a "seeding action" by which nuclei are introduced into the stream at certain positions on the body. After these nuclei have been generated at the wall, they will be transported within the boundary layer at a velocity that can be appreciably less than the velocity of the main stream. Kermeen, McGraw and Parkin found that the transport velocity averaged around 50% of the main stream velocity [2].

Although the influence of nuclei and their growth process have been known more or less for some time, no corresponding scaling laws have been derived in the literature.

The work of Oshima [3] is a first approach in this direction. It is evident that a mathematical model has to be formulated for the nuclei and the growth and generation processes.

As the exact characteristics of nuclei are rather complicated and probably of a statistical nature this mathematical model has to be of an approximate nature.

As indicated already by Silverleaf [4], it can be expected that cavitation inception will appear to be a rather complicated phenomenon in which no single effect plays a dominating role; i.e., the contributions of the various effects are more or less of equal magnitude and therefore all have to be taken into account. As a consequence the equations that govern the generation, the growth and the inception of nuclei tend to be rather complicated which necessitates the use of electronic computing methods.

In this report an attempt is made to present an at least qualitatively correct picture of the phenomena that lead to cavitation inception and of the scaling laws that govern these phenomena. In chapter 2 the various physical processes and allowable approximations have been discussed qualitatively whereas in chapter 3 a summary has been given of the scaling laws and of the expressions that determine the inception value of the cavitation number σ.

In chapter 4 the results are compared with experimental data.

2. BASIC CONSIDERATIONS

2.1 General

In analysing cavitation inception it will be acceptable in general to neglect the dimensions of the bubbles in comparison with the other involved distances as f.i., the distance between the bubbles and the length of the cavitating body.

As a consequence no direct interaction effects between the various bubbles will have to be considered and it will suffice therefore for this qualitative discussion to consider one single bubble.

358

In addition it will be possible to consider the pressure inside the bubble as uniform.

When a bubble is transported in a flow field, the static pressure in the fluid surrounding the bubble will change.

As a consequence the bubble radius and the temperature, pressure and density inside the bubble will vary, leading therefore to a heat flow across the bubble liquid interface and to a gas-diffusion in the liquid.

In addition evaporation and condensation can take place at this interface and inside the bubble. Therefore the relationship between the static pressure p_ℓ and the bubble radius R is governed by the following equations resp. phenomena:

(1) The dynamic equation, including the effects of surface tension $\bar{\sigma}$ and dynamic viscosity μ, etc. This equation reads (see f.i. [5]):

$$P_a + P_v - P_\ell - \frac{2\bar{\sigma}}{R} = \rho_\ell \left\{ R \frac{d^2R}{dt^2} + \frac{3}{2} \left(\frac{dR}{dt}\right)^2 \right\} + 4 \frac{\mu}{R} \frac{dR}{dt} \tag{2.1}$$

where

P_a = gas pressure inside bubble,

P_v = vapour pressure inside bubble,

P_ℓ = liquid pressure at large distances from bubble,

ρ_ℓ = liquid density,

μ = dynamic viscosity of liquid,

t = time.

(2) The heat conduction equation. This equation is in spherical coordinates of the following type when convection terms are neglected:

$$\frac{\delta T}{\delta t} = \frac{D_t}{\eta^2} \frac{\delta \left(\eta^2 \frac{\delta T}{\delta t} \right)}{\delta \eta} \tag{2.2}$$

where

T = temperature,

D_t = thermal diffusivity = $\lambda/c\rho$,

λ = coefficient of heat conduction,

c = specific heat at constant pressure,

ρ = density.

359

The heat-flux that is flowing through the interface is given by:

$$Q = 4\pi R^2 \lambda \left(\frac{\delta T}{\delta \eta}\right)_{r=R} \tag{2.3}$$

(3) The gas diffusion equation in case other gases than the liquid vapour come into play. This equation reads:

$$\frac{\delta P_{ae}}{\delta t} = \frac{D_a}{\eta^2} \frac{\delta\left(\eta^2 \frac{\delta P_{ae}}{\delta \eta}\right)}{\delta \eta} \tag{2.4}$$

where

P_{ae} = equilibrium pressure of dissolved gas in the liquid,

D_a = diffusion coefficient.

The mass flow of gas crossing the interface is given by:

$$\frac{dM_a}{dt} = a \, D_a \frac{\rho_a}{P_a} 4\pi R^2 \left(\frac{\delta P_{ae}}{\delta \eta}\right)_{r=R} \tag{2.5}$$

where

a = solubility = volume of gas that dissolves in liquid/volume of liquid in which gas dissolves,

ρ_a = gas density.

(4) The equation of state of the gas-vapour mixture inside the bubble in combination with the equation that governs evaporation and condensation.

(5) The equation that governs the transport of the bubble through the fluid.

The complete set of equations is a rather complicated one; a solution can only be attained with reasonable effort when certain simplifications are introduced.

The influence of viscosity can be neglected safely in normal hydraulic applications. The viscosity term of Eq. (2.1) is only important in ultrasonic applications of very high frequency ($> 10^5$ c.p.s.) and during the forming of foam materials from solidifying highly viscous fluids. Even with this simplification, the set of equation is still rather complicated. It is possible however to isolate certain important phenomena that may become dominant at certain values of the controlling parameters. As such can be mentioned:

a. The static stability of small bubbles.

b. The influence of gas diffusion on the growth speed of small bubbles.

c. The opposing influence of dynamic and heat conduction effects on the ultimate growth speed of larger bubbles.

d. The forces acting on a bubble in a fluid stream with streamwise pressure gradient.

These phenomena will be discussed now in the next paragraphs.

2.2 The Static Stability of Small Bubbles [1]

Neglecting frictional effects equation (2.1) can be written as

$$\rho_\ell \left\{ R \frac{d^2R}{dt^2} + \frac{3}{2} \left(\frac{dR}{dt}\right)^2 \right\} = P_a + P_v - P_\ell - \frac{2\bar{\sigma}}{R} \tag{2.6}$$

When gas diffusion can be neglected and the bubble temperature is assumed constant, P_a and P_v can be written as:

$$P_a = P_{a_o} \left(\frac{R_o}{R}\right)^3$$

$$P_v = P_{v_o} \tag{2.7}$$

The index o applies to the equilibrium condition with

$$\frac{dR}{dt} = \frac{d^2R}{dt^2} = 0$$

Assume further that the bubble is in equilibrium at $t = 0$. This equilibrium will only be stable against disturbances in the radius R when:

$$\frac{d\left[\rho_\ell\left\{ R \frac{d^2R}{dt^2} + \frac{3}{2} \left(\frac{dR}{dt}\right)^2 \right\}\right]}{dR} = \frac{d\left\{ P_{a_o} \left(\frac{R_o}{R}\right)^3 + P_{v_o} - P_\ell - \frac{2\bar{\sigma}}{R} \right\}<0}{dR} < 0 \tag{2.8}$$

Only under this condition the bubble will return to its original equilibrium condition after a small change in the radius R_o.

Static instability is attained therefore as soon as:

$$\frac{d\left\{ P_{a_o} \left(\frac{R_o}{R}\right)^3 \right\}}{dR} = \frac{d\left(\frac{2\bar{\sigma}}{R}\right)}{dR} \tag{2.9}$$

or

$$P_a = \frac{2}{3} \frac{\bar{\sigma}}{R} = P_\ell - P_v - \frac{2\bar{\sigma}}{R} \tag{2.10a}$$

or in dimensionless form:

$$\eta = -\frac{4}{3(c_p + \sigma)} \tag{2.10b}$$

where

$$\eta = \frac{\rho u_\infty^2 R}{2\bar{\sigma}}$$

$$C_p = \frac{P_\ell - P_\infty}{\frac{1}{2}\rho u_\infty^2}$$

$$\sigma = \frac{P_\infty - P_v}{\frac{1}{2}\rho u_\infty^2}$$

ρ_∞ = pressure in undisturbed stream.

As soon as the pressure coefficient C_p and the bubble radius parameter η satisfy relation (2.10b) the bubble becomes essentially unstable against disturbances.

As a consequence the bubble will grow continuously in size even without gas diffusion; the growth speed being determined by either dynamic limitations or heat conduction effects (see par. 2.5). Dependent on which of these two limitations is the important one the growth process will be termed cavitation or boiling.

If the critical condition as given by Eq. (2.10a) is attained by a reduction of the liquid pressure p_ℓ to a value p_c (cavitation pressure) it can easily be derived that [1]

$$P_c = P_{v_o} - \frac{2}{g}\sqrt{3}\frac{\frac{2\bar{\sigma}}{R_o}}{1 + (P_\ell - P_{v_o})\frac{R_o}{2\bar{\sigma}}} \tag{2.11}$$

This equation expresses the well known fact that the onset of vaporous cavitation in the absence of gas diffusion is only possible when the liquid pressure falls below the vapour pressure.

This is also evident from Eq. (2.10b) as the critical radius parameter η attains only a positive value for $C_p < -\sigma$.

When the bubble is in stable equilibrium, growth of the bubble at a constant liquid pressure is only possible by gas diffusion (see par. 2.3) or by boiling.

2.3 The Influence of Gas Diffusion on the Growth of Small Bubbles

From Eq. (2.4) it follows that a diffusion length L_a can be defined as follows:

$$L_a = \sqrt{D_a \cdot t_c} \tag{2.12}$$

where t_c is a characteristic time, i.e., either a period in case of an acoustical disturbance or a passage time in case of the flow along a body.

The diffusion length L_a is a measure of the radial extent by which the dissolved gas equilibrium pressure has been disturbed in the liquid surrounding the bubble.

Equation (2.12) is valid for not too large values of t_c; the diffusion length is maximum of the order of the bubble radius R, i.e.:

$$L_a \leq R \quad (\text{see } \S\ 2.7). \tag{2.13}$$

From Eq. (2.5) it follows that the change in gas volume is proportional to:

$$V = a\ D_a\ 4\pi R^2\ \frac{t_c}{L_a} = a\ 4\pi R^2\ L_a$$

The relative change in the gas volume is given by:

$$\Sigma_a = \frac{a4\pi R^2 L_a}{\frac{4}{3}\pi R^3} = 3a\ \frac{L_a}{R} \tag{2.14}$$

The influence of the gas diffusion will be small for small values of Σ_a. Now is for air in water at atmospheric temperature:

$D_a = 2.10^{-9}\ m^2/sec,$

$a = 0.017.$

An impression of the importance of the gas diffusion can be obtained by calculating the value of the characteristic time t_c for which Σ_a is equal to one.

These values have been given in Table 2.1. In Fig. 1 the quantity Σ_a has been plotted as a function of t_c and R_0.

Table 2.1
Required Times for Appreciable Growth of Air Bubbles in Water

$R_o = 1$ mm	0.1 mm	0.01 mm	0.001 mm
$t_c = 10^4$ sec	10^2 sec	1 sec	10^{-2} sec

van der Walle
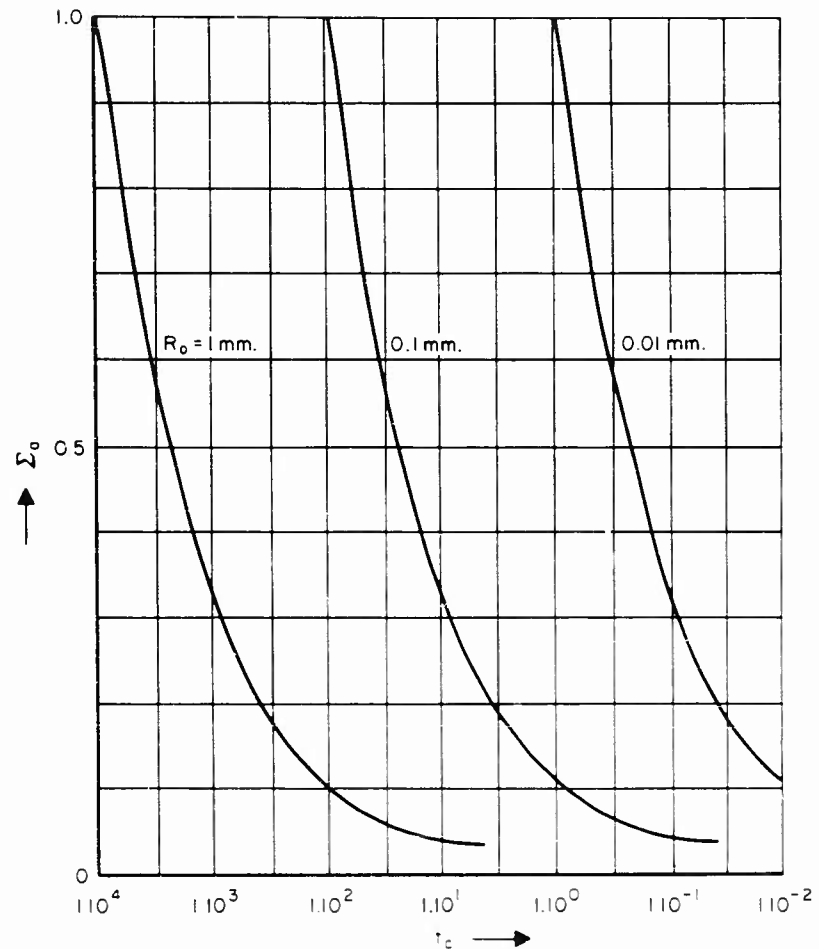
Fig. 1 - The gas diffusion parameter Σ_a as a function
of bubble radius R_o and characteristic time t_c

It follows from this table that in normal flow problems gas diffusion is only important for very small bubbles where the characteristic times are mostly of the order of 10^{-2} seconds or less and are therefore of the same order of magnitude as the passage times. For larger bubbles the characteristic times are normally appreciably larger than the passage time and gas diffusion is therefore rather unimportant.

When acoustical disturbances are considered of frequencies above 1000 Hz the gas diffusion appears to have no effect for bubbles larger than 0.001 mm. However, there can be a slow change due to rectified diffusion when the acoustic excitation extends over long times. Rectified diffusion is a non-linear effect that is caused by the fact that in the low pressure part of the acoustic cycle the inflow of dissolved gas occurs over a slightly larger area than in the high pressure part.

364

2.4 The Opposing Influence of Dynamic and Heat Conduction
Effects on the Ultimate Growth Speed of Larger Bubbles

At the radial velocities that are of interest in cavitation and boiling it can be assumed that the vapour conditions inside the bubble are always in equilibrium with the liquid temperature at the bubble wall [6].

When the pressure-temperature condition around a bubble is altered suddenly by a certain amount from the vapour equilibrium conditions the bubble starts to grow. It will be assumed that the bubble sizes are such that surface tension effects can be neglected. The ultimate growth-speed of the bubble is limited then to that of either one of the following two limiting cases:

a. The temperature conditions are such that the bubble wall is essentially isothermal, i.e., heat conduction is assumed to occur infinitely fast. In that case the vapour pressure is constant and equal to the equilibrium vapour pressure corresponding to T_ℓ. It follows from Eq. (2.1) that the growth-speed due to a sudden drop in temperature is limited to

$$\frac{dR}{dt} = C_1 = \sqrt{\frac{2 \cdot p}{3 \alpha}} \left(\frac{d^2R}{dt^2} = 0 \right) \tag{2.23}$$

i.e., the growth speed is determined by dynamic effects.

b. The heat diffusion is the limiting parameter. At any time the vapour pressure is equal to the liquid pressure, i.e., it is assumed that dynamic effects due to the bubble expansion are unimportant. In the case of a sudden drop in pressure, the temperature of the bubble is then given by:

$$T_b = T_\ell - \frac{\cdot p}{B} \tag{2.24}$$

with $B = d_{p_v}$ dT = gradient of vapour pressure curve as a function of temperature, and

$\cdot p$ = sudden drop in pressure.

The growth-speed is essentially determined by the rate of evaporation; the heat flux available for evaporation being given by Eq. (2.3).

Introducing again the concept of diffusion length (see par. 2.3) the order of magnitude of this heat flux becomes:

$$Q = 4 - R^2 \, \sqrt{\frac{T_\ell - T_b}{L_{t\ell}}}$$

The diffusion length $L_{t\ell}$ is again a measure for the radial extent by which the temperature distribution in the liquid is disturbed. A dimensionless measure for this diffusion length is the quantity
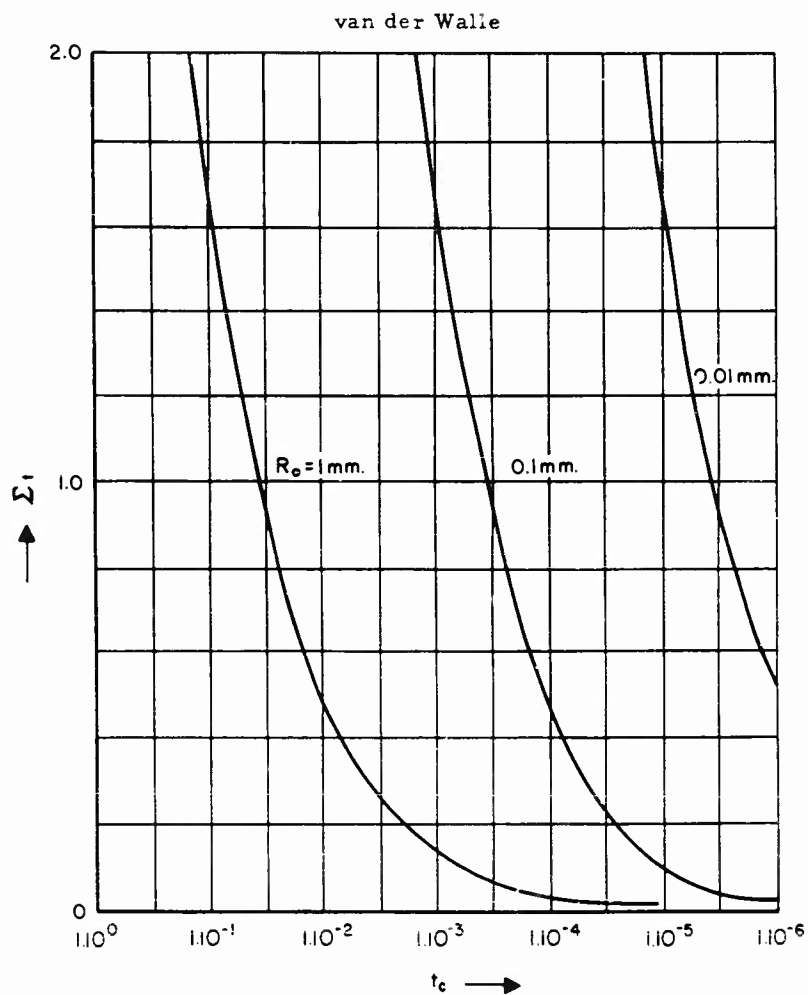
Fig. 2 - The heat diffusion parameter Σ_t as a function of the bubble radius R_o and the characteristic time t_c

$$\Sigma_t = \frac{L_{t_j}}{R}$$

Σ_t has been plotted in Fig. 2 as a function of the characteristic time t_c and the bubble radius R_o.

Comparison of Figs. 1 and 2 reveals that heat diffusion is an essentially quicker process than gas diffusion.

The heat flux Q is available for evaporation of a mass of water m for which the relation holds:

366

$$\frac{dm}{dt} = \frac{Q}{A}$$

with A = latent heat of evaporation.

The volume growth of the bubble is given by:

$$\frac{d\frac{4}{3}\pi R^3}{dt} = \frac{1}{\rho_v}\frac{dm}{dt}$$

The limiting growth-speed becomes then:

$$\frac{dR}{dt} = C_2 = \frac{\lambda_\ell}{\rho_v L_{t\ell}}\frac{AP}{B.A} \tag{2.25}$$

Which one of these limiting cases determines the growth-speed, is dependent upon the ratio of C_1 and C_2:

$$\Sigma_e = \frac{C_1}{C_2} \approx \frac{p_v}{\sqrt{\rho_1}}\frac{L_{t\ell} B.A}{\sqrt{\Delta p}\lambda_\ell} \tag{2.26}$$

For $\Sigma_e \ll 1$ dynamic effects are the important ones and heat diffusion occurs such fast that the bubble wall is essentially isothermal, and for $\Sigma_e \gg 1$ dynamic effects are unimportant; heat diffusion being the limiting factor.

Use will be made of the following data for water [6].

Table 2.3

Temperature	15°C	100°C	210°C	
V	0.129×10^{-1}	5.98×10^{-1}	95.9×10^{-1}	kg/m³
P_v	0.017×10^5	1.01×10^5	19.1×10^5	N/m³
$B = dp_v/dT$	1.10×10^2	36.2×10^2	382×10^2	N/m²°C
A	2.46×10^6	2.26×10^6	1.90×10^6	N$_{m/kg}$
$\rho\ell$	0.999×10^3	0.958×10^3	0.853×10^3	kg/m³
λ_ℓ	0.587	0.68	$0.659 \times$	N/sec°K
$D_{t\ell}$	1.41×10^{-7}	1.89×10^{-7}	2.35×10^{-7}	m²/sec

Equation (2.26) can be written as:

$$Z_e = \frac{P_v \sqrt{D_{t,j} \, B.A}}{\sqrt{\rho_j \, \wedge_j} \, \sqrt{\frac{dp}{dt}}}$$

(2.27)

where $L_{t,j}$ has been taken to be:

$$L_{t,j} = \sqrt{D_t . A_t}$$

and where dp/dt = derivative of pressure with respect to time.

The quantity $Z_e \sqrt{dp/dt}$ has been given in Table 2.4 as a function of the temperature T.

Table 2.4
The Quantity $Z_e \sqrt{dp \ dt}$ as a Function of T

$T =$	$15°C$	$100°C$	$210°C$
$Z_e \sqrt{dp \ dt} =$	$57.8 \ \dfrac{N^{1\ 2}}{m/sec^{1\ 2}}$	$8.22 \times 10^4 \dfrac{N^{1\ 2}}{m/sec^{1\ 2}}$	$14.3 \times 10^6 \dfrac{N^{1\ 2}}{m/sec^{1\ 2}}$

It is evident from Table 2.4 that Z_e is much larger at the higher temperatures. As a consequence it is found that the growth-speed of vapour bubbles at these temperatures is essentially limited by the heat diffusion process [6].

Practical applications for this type of problems are for instance in instationary boiling in atomic reactors. In that case the bubble growth is caused by a temperature gradient instead of a pressure gradient and the analogous expression for Eq. (2.27) becomes:

$$Z_e = \frac{{}_v \sqrt{D_{t,j}} \ \sqrt{B.A}}{\sqrt{}} \ \sqrt{\frac{dT}{dt}}$$

(2.28)

The quantity $Z_e \sqrt{dT \ dt}$ has been given in Table 2.5 as a function of the temperature T.

Table 2.5
The Quantity $Z_e \sqrt{dT \ dt}$ as a Function of T

$T =$	$15°C$	$100°C$	$210°C$
$Z_e \sqrt{dT \ dt} =$	$5.52 \ \dfrac{°C^{1\ 2}}{sec^{1\ 2}}$	$1.37 \times 10^3 \dfrac{°C^{1\ 2}}{sec^{1\ 2}}$	$7.31 \cdot 10^4 \dfrac{°C^{1\ 2}}{sec^{1\ 2}}$

In normal boiling-applications the temperature increase rates are of the order of $0.01°C/sec$, whereas in nuclear reactors values of up to $2000°C/sec$ can be encountered [6]. Comparison with the data of Table 2.4 shows that even for the very high heating rates the bubble growth is essentially determined by the heat diffusion process in boiling applications ($z_e \gg 1$). In normal cavitation on ship propellers temperatures of around $15°C$ will prevail.

An estimate of the order of magnitude of dp/dt has been obtained in Table 2.6 for some typical cases:

Table 2.6

	Full Scale Application	Model Scale
Propeller circum-ferential speed V =	20 m/sec	10 m/sec
Characteristic length of cavitating zone l =	0.3 m	0.015 m
Order of magnitude of $dp/dt = (\frac{1}{2})\rho V^3 / l$	$= 1.34 \times 10^7$ N/m² sec	3.34×10^7 N/m² sec
z_e at T = 15°C	0.016	0.010

In both cases the values for z_e are small compared to one. Therefore in normal cavitation the cavity can safely be assumed to be isothermal and the growth-speed of the bubbles is essentially determined by the dynamic effects.

2.5 The Forces Acting on a Bubble in a Fluid Stream With Streamwise Pressure Gradient

The forces that act on a bubble either in the free stream or originating from a wall crevice are:

1. The drag D of the bubble.

2. The streamwise component T of the surface tension forces between bubble and wall in case the bubble is attached to the wall.

3. The buoyancy force F on the bubble due to a streamwise pressure gradient.

All forces will be taken positive when directed in the streamwise direction.

Neglecting inertia forces, the equilibrium condition becomes for a bubble that is attached to the wall:

369

$$D + T + F = 0 \tag{2.29}$$

Due to these forces, the shape of the bubble will deviate from a spherical one. A qualitative estimate of the various forces can be given as follows:

$$D = C_{D}.\frac{1}{2} \rho_\ell \bar{V}^2 \pi R^2 \tag{2.30}$$

$$-\bar{\sigma}.2R < T < + \bar{\sigma}.2R \tag{2.31}$$

$$F = -\frac{4}{3}\pi R^3.\frac{dp}{ds} = -\frac{2}{3}\pi R^3 \rho_\ell U_\infty^2 \frac{dC_p}{ds} \tag{2.32}$$

where

$\bar{V}$ = mean velocity in boundary layer along height of the bubble,

R = characteristic length of the bubble, analogous to the radius of a spherical bubble,

$\bar{\sigma}$ = surface tension,

C_D = drag coefficient,

ρ_ℓ = density of the fluid,

C_p = pressure coefficient,

U_∞ = undisturbed stream speed.

The surface tension force is similar to a friction force, in that its direction can be reversed and its magnitude can adjust itself within two limiting values.

The important point to note, is that both surface tension force T and buoyancy force F can compensate in principle the drag D; therefore making it possible for the bubble to remain stationary with respect to the wall. The buoyancy F is only stabilizing for positive values of the pressure gradient.

The surface tension force is proportional to R and the buoyancy force to R^3. It is evident therefore that for small bubbles surface tension is the dominating stabilizing effect whereas with larger bubbles this role is fulfilled by the buoyancy force.

The drag coefficient C_D is dependent upon the Reynolds number R_e based on the bubble "diameter" $2R$. Now is:

$$R_e = \frac{\rho \bar{V} 2R}{\mu} \tag{2.33}$$

where μ = dynamic viscosity of the fluid.

The dependency of C_D upon the bubble radius R is relatively small; it follows therefore from Eqs. (2.30), (2.31) and (2.32) that the surface tension force T is proportional to R, the drag D more or less to R^2 and the buoyance force F to R^3.

As a consequence, the force equilibrium for small bubbles is mainly determined by D and T whereas for larger bubbles D and F are dominant.

Introducing Eqs. (2.30) and (2.31) in (2.29) it can be shown therefore that a maximum value for R exists in a first approximation above which no stable position on a body is possible due to surface tension effects alone in case the buoyancy force F can be neglected. This maximum value is given by:

$$R_{max} = \frac{4}{\pi C_D} \cdot \frac{\bar{\sigma}}{\rho \bar{v}^2} \tag{2.34}$$

In the same way it is found for larger bubbles from Eqs. (2.29), (2.31) and (2.32) that a minimum value for R exists below which no stable position is possible due to a positive pressure gradient alone in case T can be neglected.

The minimum value is given by:

$$R_{min} = \frac{3}{4} \cdot \frac{C_D}{\frac{dcp}{ds}} \cdot \left(\frac{\bar{v}}{U}\right)^2 = \frac{3}{4} \frac{C \cdot C_D}{\frac{dcp}{d\xi}} \left(\frac{\bar{v}}{u}\right)^2 \tag{2.35}$$

where C = characteristic length of body, and $\xi = s/c$.

This minimum value decreases with increasing values of the gradient of the pressure coefficient. This means that once a bubble has grown to such a size that it floats in equilibrium in the pressure gradient, it will stay in equilibrium when it increases in size. During its increase in size the bubble shifts upstream towards a position with a smaller pressure gradient.

Qualitatively it can be stated that in general such a condition can only be attained with the characteristic slow growth speeds due to gas diffusion when the value for R_{min} as given by Eq. (2.35) is equal to or smaller than the value for R_{max} given by Eq. (2.34). Only in such a case will it be possible for a bubble to remain in stable equilibrium during the whole period of growth from its origination from the wall crevice to the ultimate bursting in vaporous cavitation. This procedure seems a logical explanation for the typical occurrence of sheet cavitation on blade leading edges with their associated large pressure gradients as distinct from blade cavitation that is more characterized by bubbles that sweep along the cavitating body. In this last case, in general no pressure gradient will be available of sufficient magnitude to stabilize the position of the bubbles with respect to the blade.

It must be said, however, that once R_{min} and R_{max} have approximately the same value, the basic assumptions underlying Eq. (2.34) and (2.35) are not fulfilled anymore as all three forces, D, T and F are of the same order of magnitude then. In that case the full equation (2.29) has to be considered.

371

In the flow around not too slender shapes, as ogives for instance somewhat mixed conditions may exist if compared with sheet cavitation on one hand and blade cavitation on the other hand.

The pressure gradients will not be large enough to keep the bubble attached during its whole growth period. As a consequence the bubble will detach once it has reached a certain size. During its transportation in the boundary layer it will continue to grow until it may either burst into vaporous cavitation, become attached again as a fixed cavity of either the gaseous or the vaporous type, or it may collapse again at a more downstream position. That an increase in size due to gaseous or vaporous cavitation can cause the bubble to remain stationary due to buoyancy effects has been demonstrated by the experiments of Kermeen, McGraw and Parkin [2].

Under these conditions the function of the wall as a generator of nuclei can be characterized therefore as a "seeding action" by which nuclei are introduced into the stream at certain positions on the body. The important point to note is that the stabilizing influence of the buoyancy force F is limited to regions with positive pressure gradient. This gives an explanation of the experimentally found fact that inception occurs in many cases preferably in the region aft of suction peaks.

For those cases that the three forces D, T and F are more or less of the same order of magnitude the full Eq. (2.29) has to be used. The following relations hold:

$-2\,T\,R \leq D - F \leq 2\,T\,R$ the bubble remains fixed to the wall,

$D - F > 2\,T\,R$ the bubble will detach and move in the downstream direction,

$D - F < -2\,T\,R$ the bubble will detach and move in the upstream direction.

Introducing the dimensionless variables: $\xi = s/c$ with c = characteristic length (chord f.i.) and $\tau = \rho u^2 R/2T$, the relations become with

$$A = \frac{D - F}{T} = \frac{\tau}{2} - \left\{ C_D \left(\frac{v}{u}\right)^2 - \frac{4r}{3} = \frac{r}{\rho u^2 c} \frac{dcp}{d\xi} \right\}$$

a. For a stable bubble: $(A) \leq 1$.   (2.36)

b. For a bubble that will detach and move downstream $A > 1$.   (2.37)

c. For a bubble that will detach and move upstream $A < -1$.   (2.38)

d. A bubble that has been detached already will become attached again as soon as A becomes negative.

A qualitative picture of the pressure distribution at the suction side of a hydrofoil is given in Fig. 3.
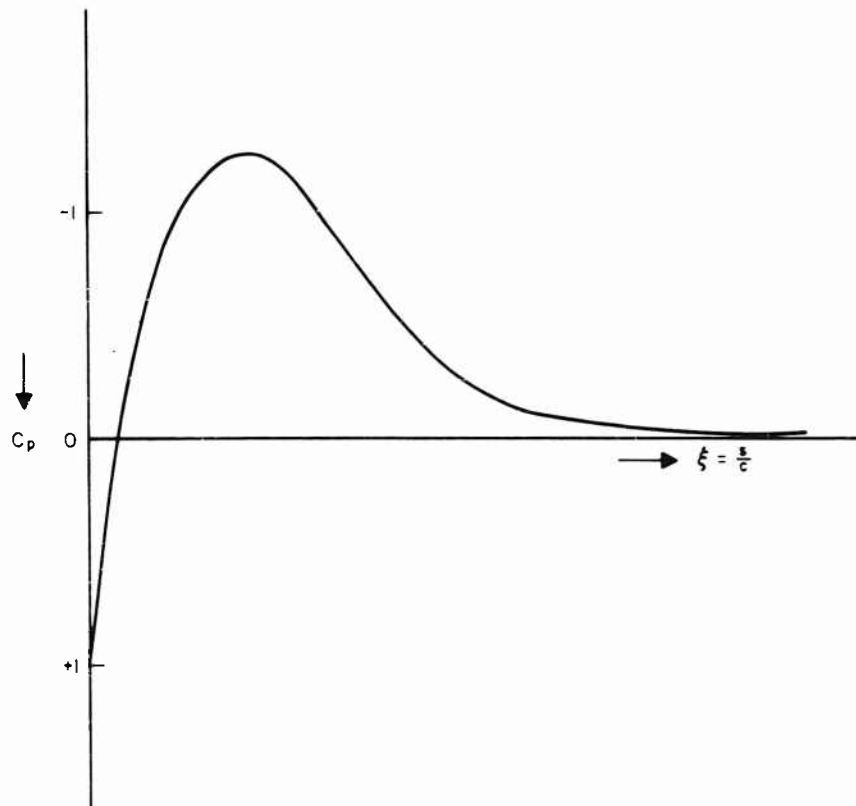
Fig. 3 - Qualitative picture of the pressure distribution on the
suction side of a hydrofoil

As has been remarked already the most favourable region for the genera-
tion of wall-nuclei is around point C where the pressure gradient attains a
maximum positive value and where the stabilizing influence of the buoyancy
force F is the largest therefore.

As soon as the absolute value of A will surpass 1 the bubble will detach;
for positive values of A the bubble will move downstream at an ever increasing
speed when no additional growth takes place.

On the other hand, for negative values of A, the bubble will move upstream
until equilibrium is attained somewhere between points B and C at such a value
of the pressure gradient that the net force on the bubble is zero again.

In case the bubble keeps on growing this stable position will approach more
and more the pressure minimum in B. This kind of cavitation with fixed cavi-
ties is possible therefore even when the static pressure is everywhere larger
than the vapor pressure. It can be termed gaseous cavitation with stabilization
of the cavity by pressure gradient effects.

373

It can easily be shown that the quantity A is solely dependent upon the following dimensionless parameters.

1. $R_e = \rho U_\infty C/\mu$ = Reynolds number based on the chord C.

2. $\bar{\sigma}/\mu u_\infty = R_e \cdot \bar{\sigma}/\rho u^2_\infty c$ a dimensionless measure for the surface tension.

3. $\eta = \rho \mu^2_\infty R/2\bar{\sigma}$ a dimensionless measure for the bubble radius.

4. $dcp/d\xi$

5. $\xi = s/c$ i.e., the place where the bubble is originated.

6. The relationship between C_D and $\rho \bar{v} R/\mu$ (Reynolds number based on the flow condition around the bubble).

Some calculations have been made of the quantity A as a function of these parameters. It has been assumed that the shape of the bubble is an ellipsoid with an axis-ratio of 2. The relationship between C_D and $\rho \bar{v} R/\mu$ is then a given function and A is then solely dependent upon R_e, $\bar{\sigma}/\mu u_\infty$ and η for given values of $dcp/d\xi$ and ξ.

Two typical cases have been considered namely:

a. $dcp/d\xi = 100$ and $\xi = 0.04$.

   This is thought to be typical of the condition in leading edge cavitation inception.

b. $dcp/d\xi = 2$ and $\xi = 0.75$.

   This is considered to be typical of blade cavitation.

In both cases laminar as well as turbulent boundary layers have been considered. For sake of simplicity the flat plate boundary layer thicknesses have been used in the calculations.

Results of calculations have been plotted in Figs. 4a through 4h. Instead of the two parameters $R_e = \rho u_\infty c/\mu$ and $\bar{\sigma}/\mu u$ the data have been plotted with the velocity U and the chord C as parameters; the quantities $\bar{\sigma}$, μ and ρ will normally be constants in most hydraulic applications. Although the curves can only be expected to give qualitatively correct results, it is evident that complete stabilization of bubbles is only possible under leading edge cavitation conditions.

Once the bubble is detached from the wall, it will be transported downstream within the boundary layer. During its travel the bubble will tend to grow by gas diffusion (see section 2.7) whereas the static pressure surrounding the bubble will increase (see Fig. 3). Vaporous cavitation will occur as soon as condition (2.10b) is attained, i.e., when

374
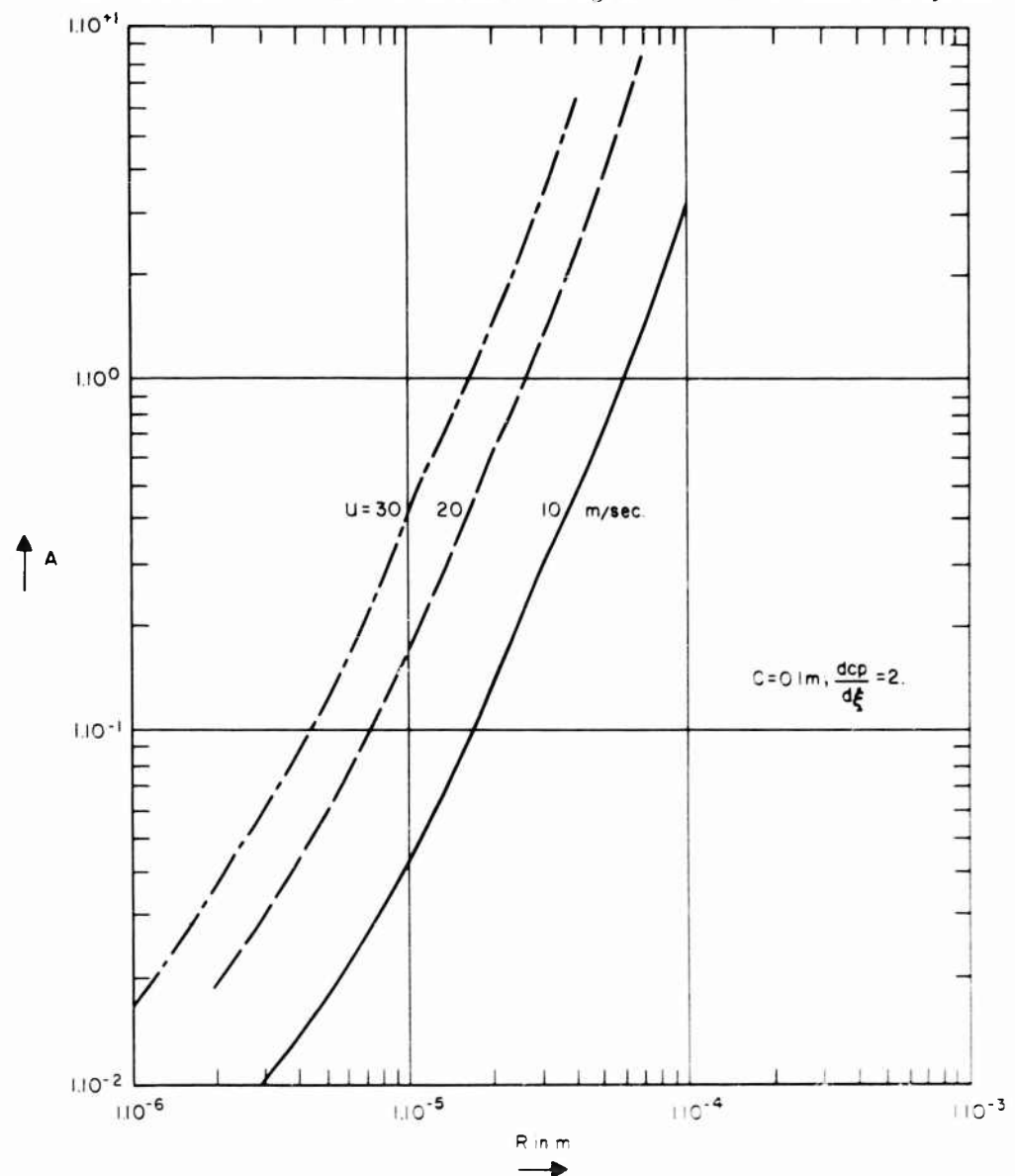
Fig. 4a - The quantity A as a function of R.
Blade cavitation - laminar flow.

$$\sigma = \sigma_{cn} = \frac{-4}{3(\sigma - C_p)} \tag{2.39}$$

where σ = cavitation number.

375
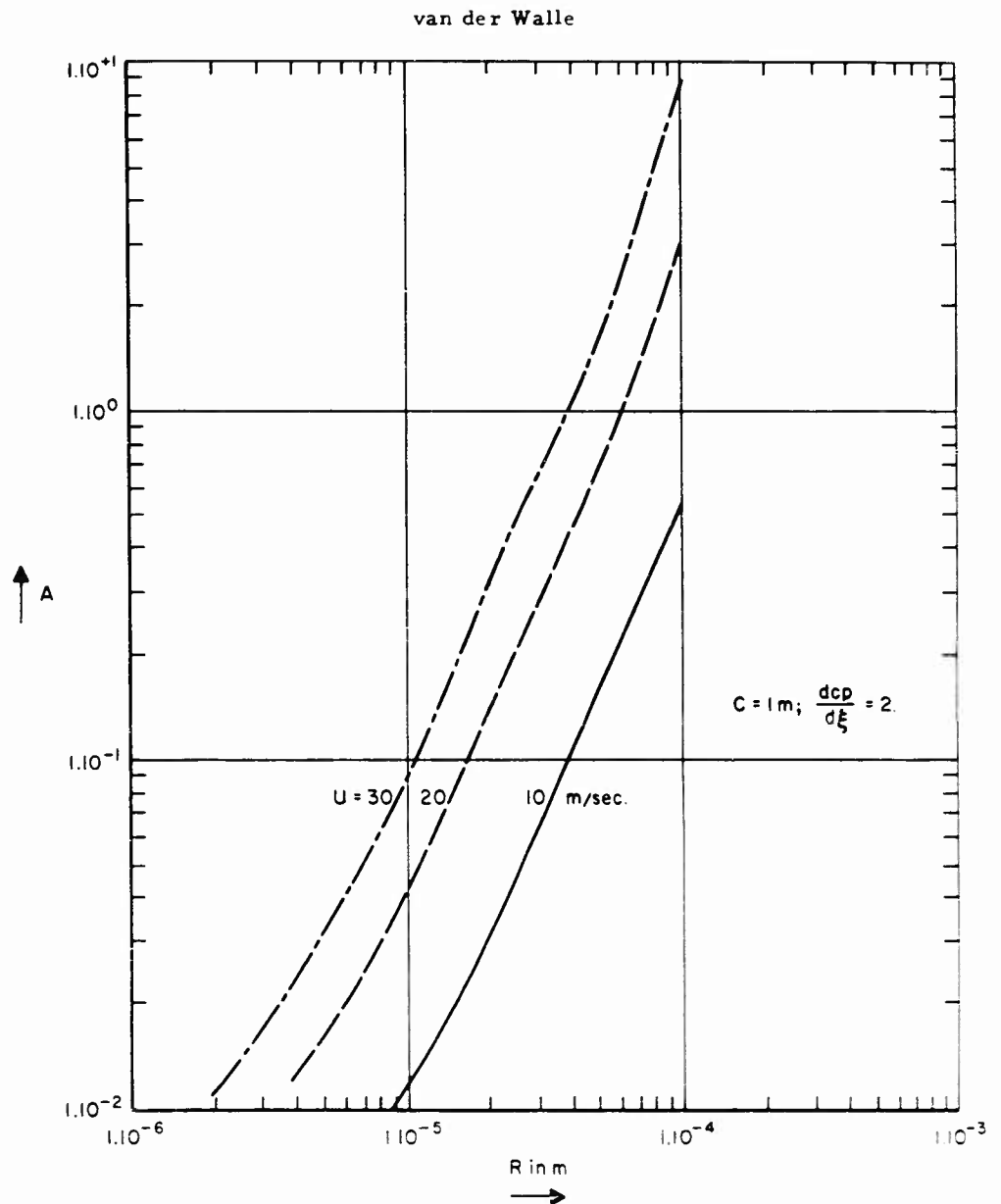
Fig. 4b - The quantity A as a function of R.
Blade cavitation - laminar flow.

This critical value of τ will increase continuously with increasing values of C_p. In addition it is evident that vaporous cavitation is only possible when $C_p \leq -\tau$ (static pressure below vapor pressure).

Once vaporous cavitation has started, the bubble will expand to macroscopic dimensions. It is dependent then upon the pressure gradient parameter and the speed of growth whether or not the cavity will become fixed to the surface as a

376
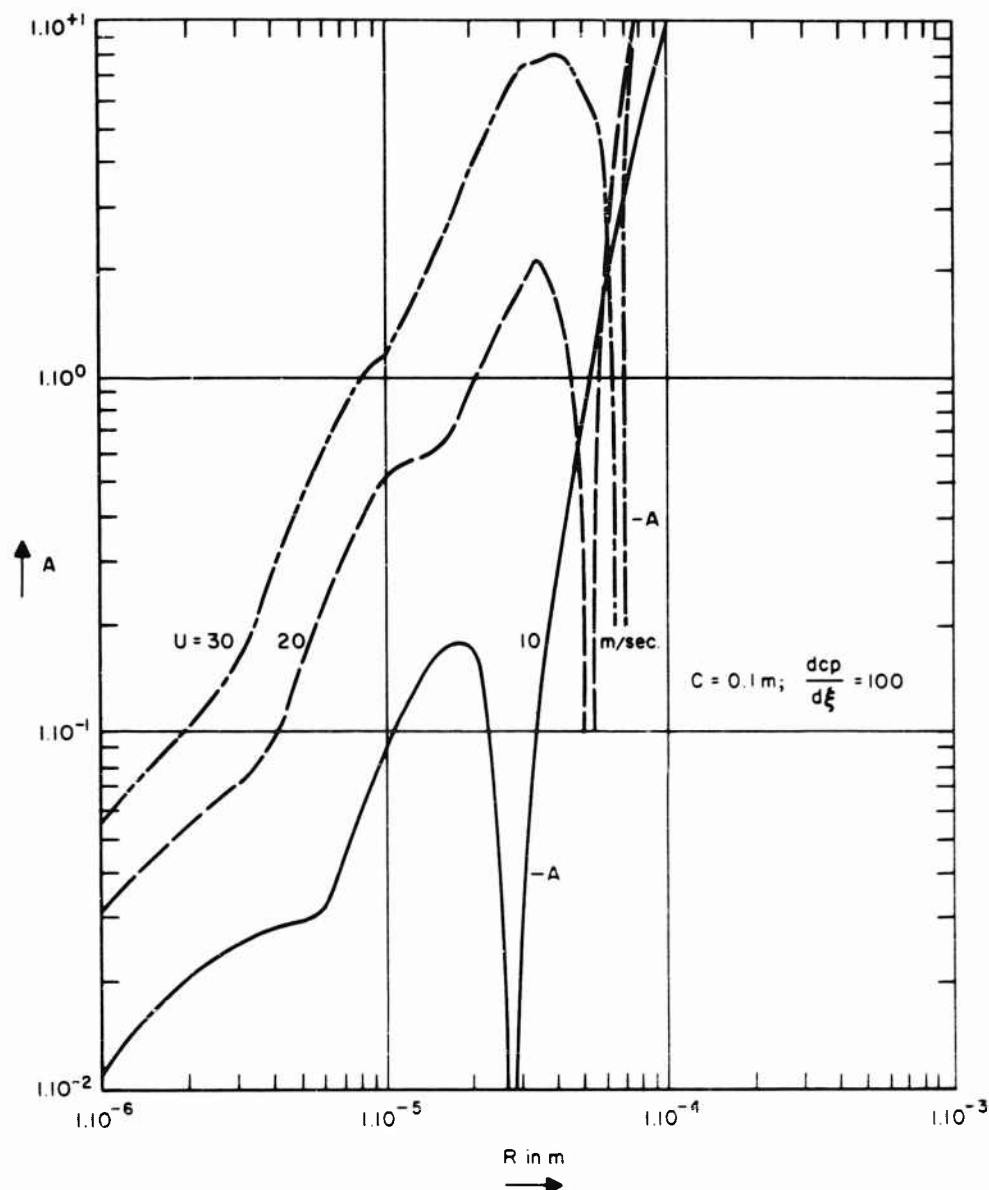
Fig. 4c - The quantity A as a function of R.
Leading edge cavitation - laminar flow.

cavitating sheet. It has often been found in experiments that a visible cavity may develop in regions where the static pressure is higher than the vapour pressure. From Eq. (2.39) it follows that vaporous cavitation can not be a possible explanation of this phenomenon.

377
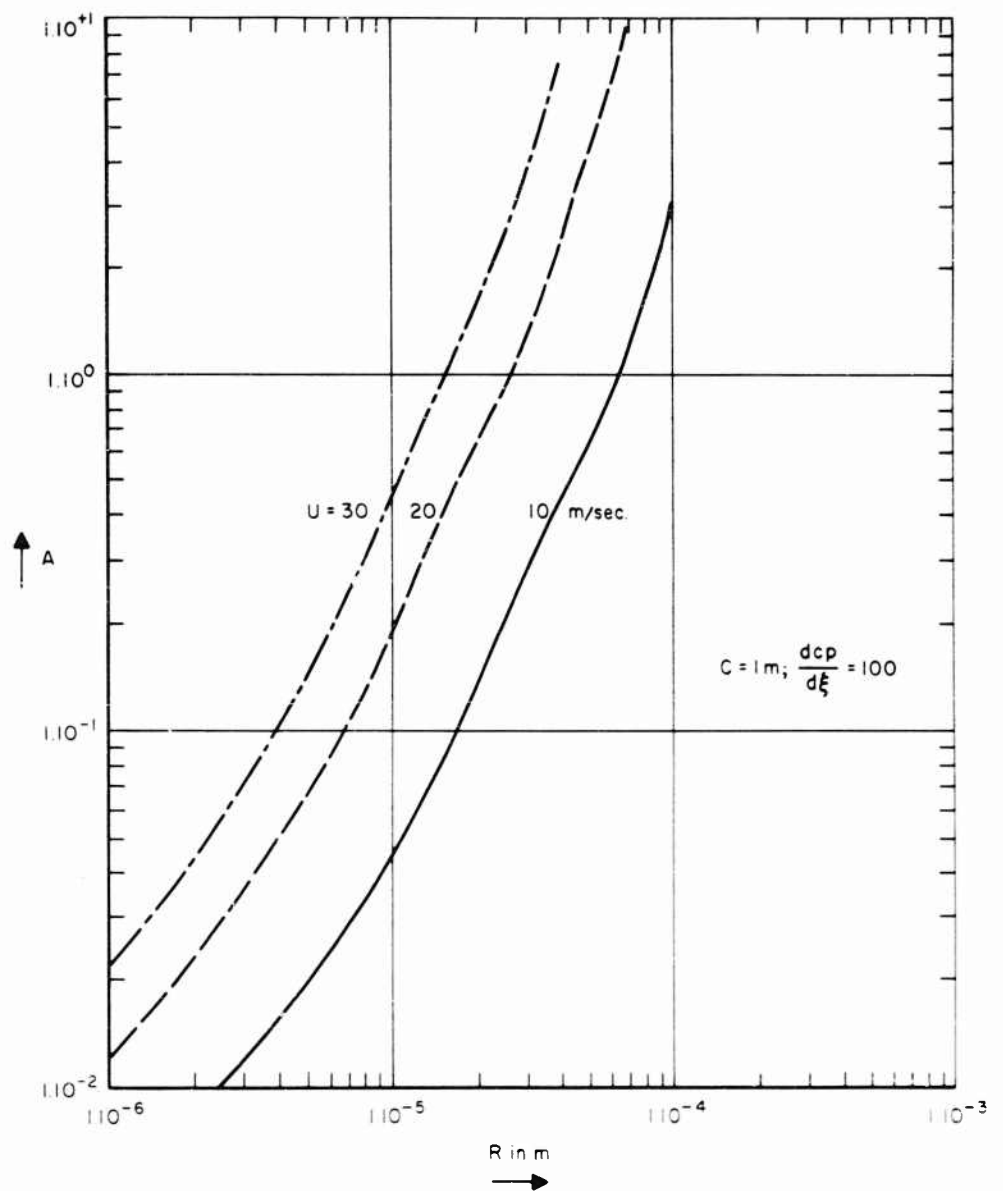
Fig. 4d - The quantity A as a function of R.
Leading edge cavitation - laminar flow.

The only possibility seems to be that this kind of fixed bubble cavitation is caused by gaseous cavitation in a bubble that is fixed to the wall in a region of sufficiently large positive pressure gradients.

One may speculate whether these conditions might occur in the cases shown in Fig. 4c for U = 20 and 30 m/sec.

378
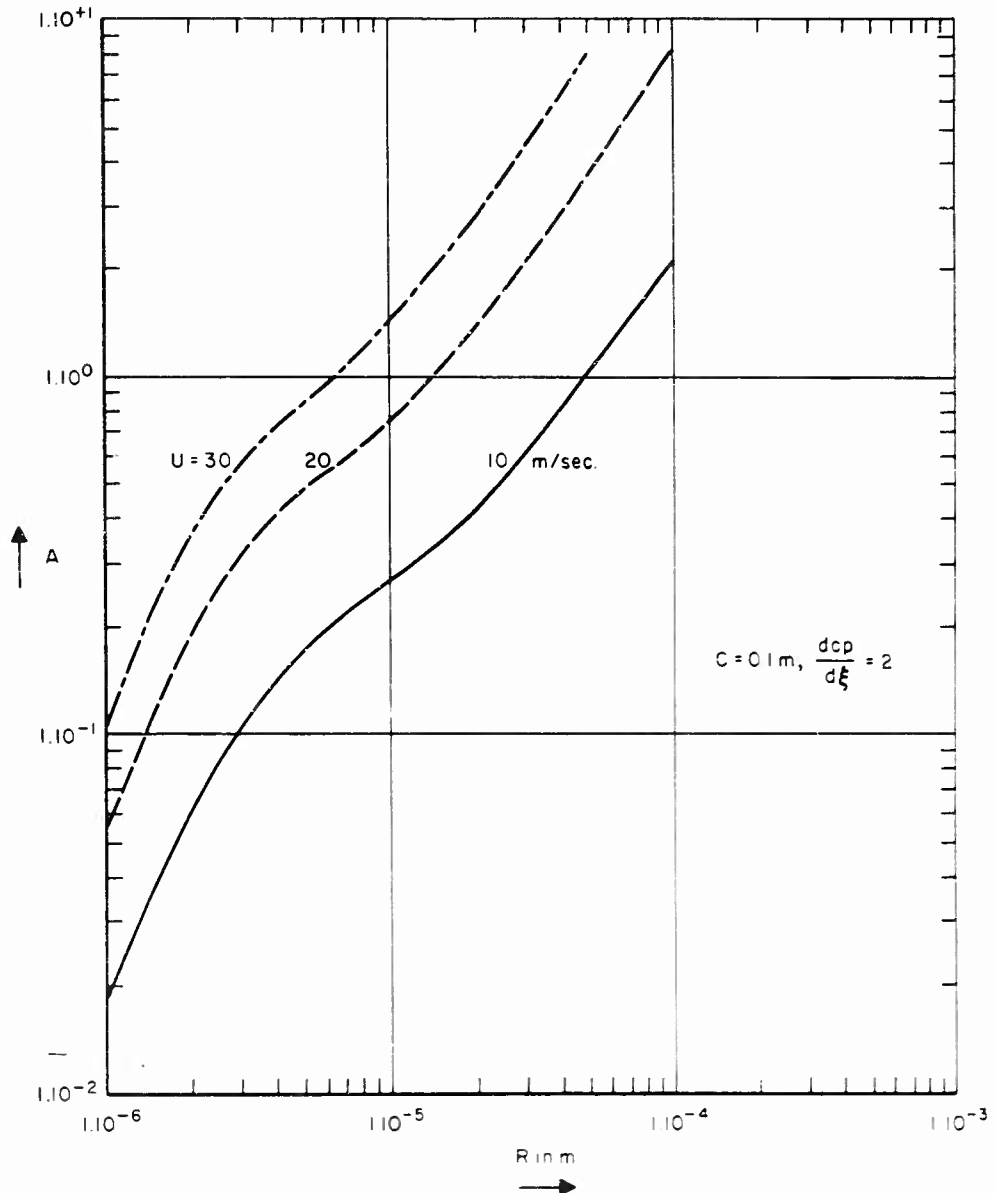
Fig. 4e - The quantity A as a function of R.
Blade cavitation - turbulent flow.

In these cases the pressure gradients near the leading edge have been somewhat too small to cause a complete stabilization of the bubble over the whole range of bubble radii. As a consequence the bubble detaches once a critical size R_1 has been attained. Figure 4c shows however that at a slightly larger value, R_2 of R, complete stabilization will be possible again in case the bubble grows sufficiently quick in the region where the pressure gradient is of the same order of magnitude.

379
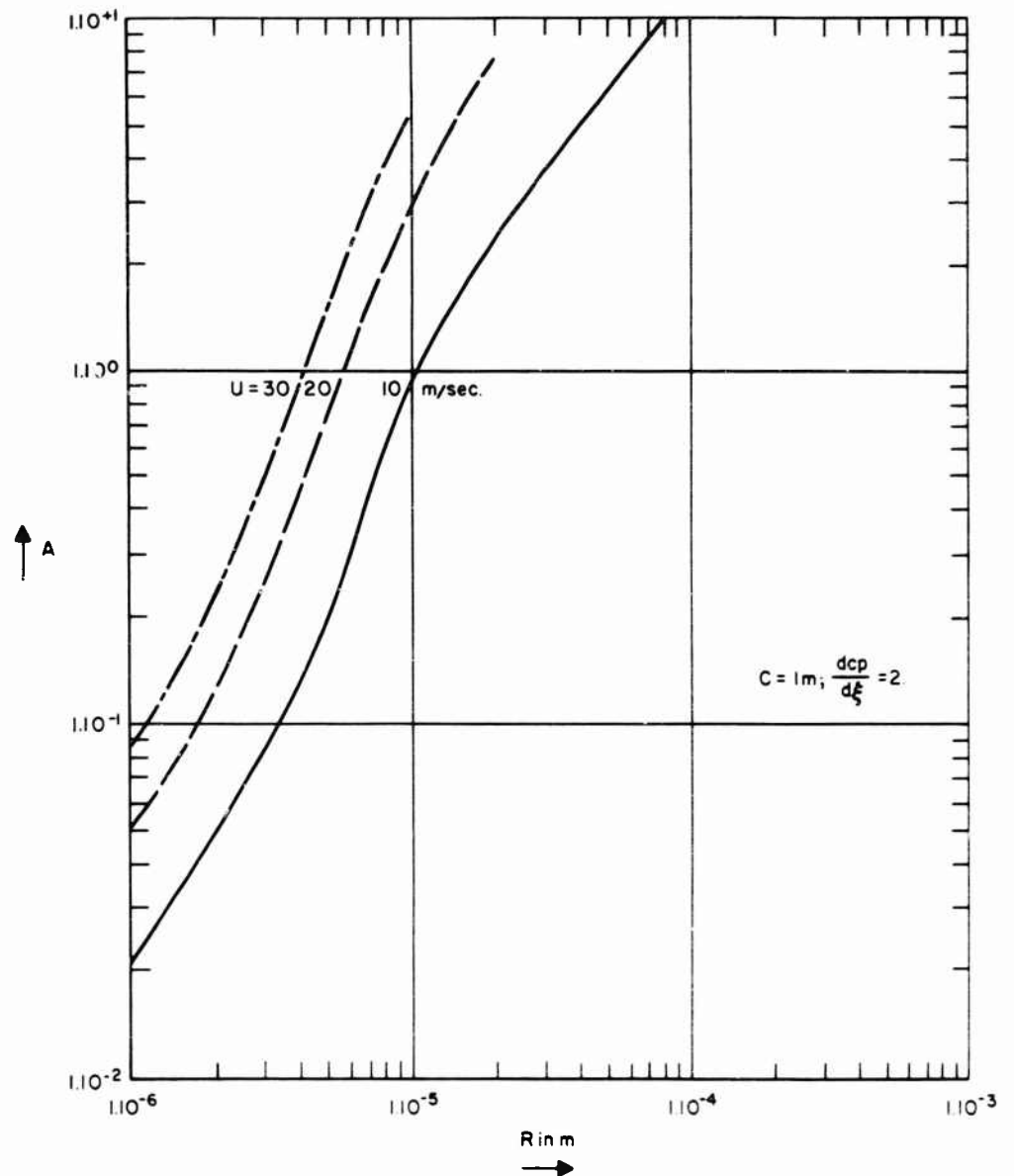
Fig. 4f - The quantity A as a function of R.
Blade cavitation - turbulent flow.

It is shown by Fig. 4c that the value of R for which A becomes smaller than 1 again is about the same as the value of R for which A passes through zero.

The attachment limit for traveling bubbles and attached bubbles is therefore about the same. The growth in size from R_1 to R_2 may be possible now by gas diffusion during the travel of the detached bubble. There are indications that the position of the transition point plays a dominating role in this growth process

380
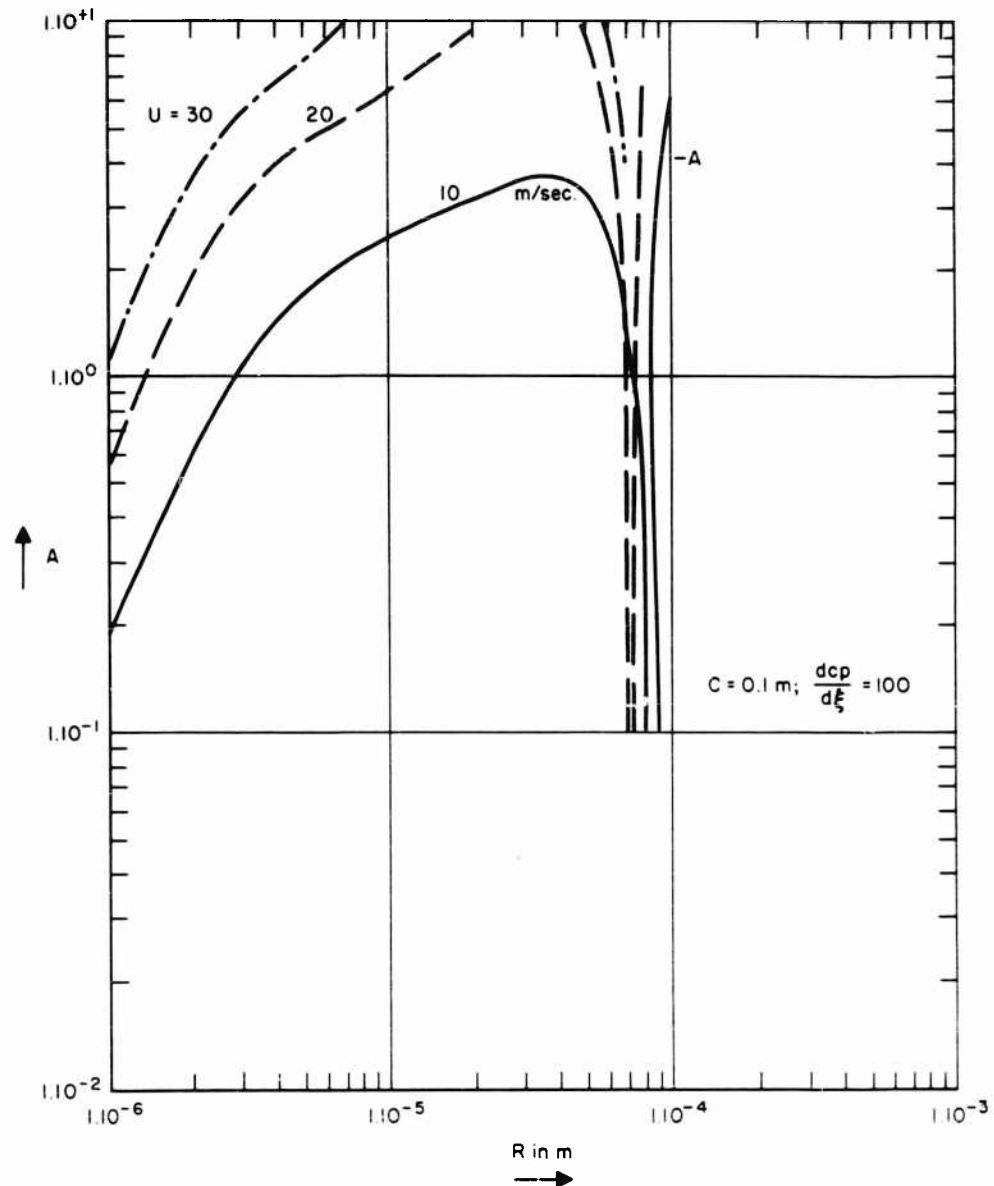
Fig. 4g - The quantity A as a function of R.
Leading edge cavitation - turbulent flow.

(see section 4). Once the new equilibrium condition has been established, the cavity will remain attached to the wall and may continue to grow by gas diffusion even if the static pressure is above vapor pressure.

The ultimate size of the cavity is determined in this case by the equilibrium between gas transportation to the bubble by gas diffusion and transportation from

381
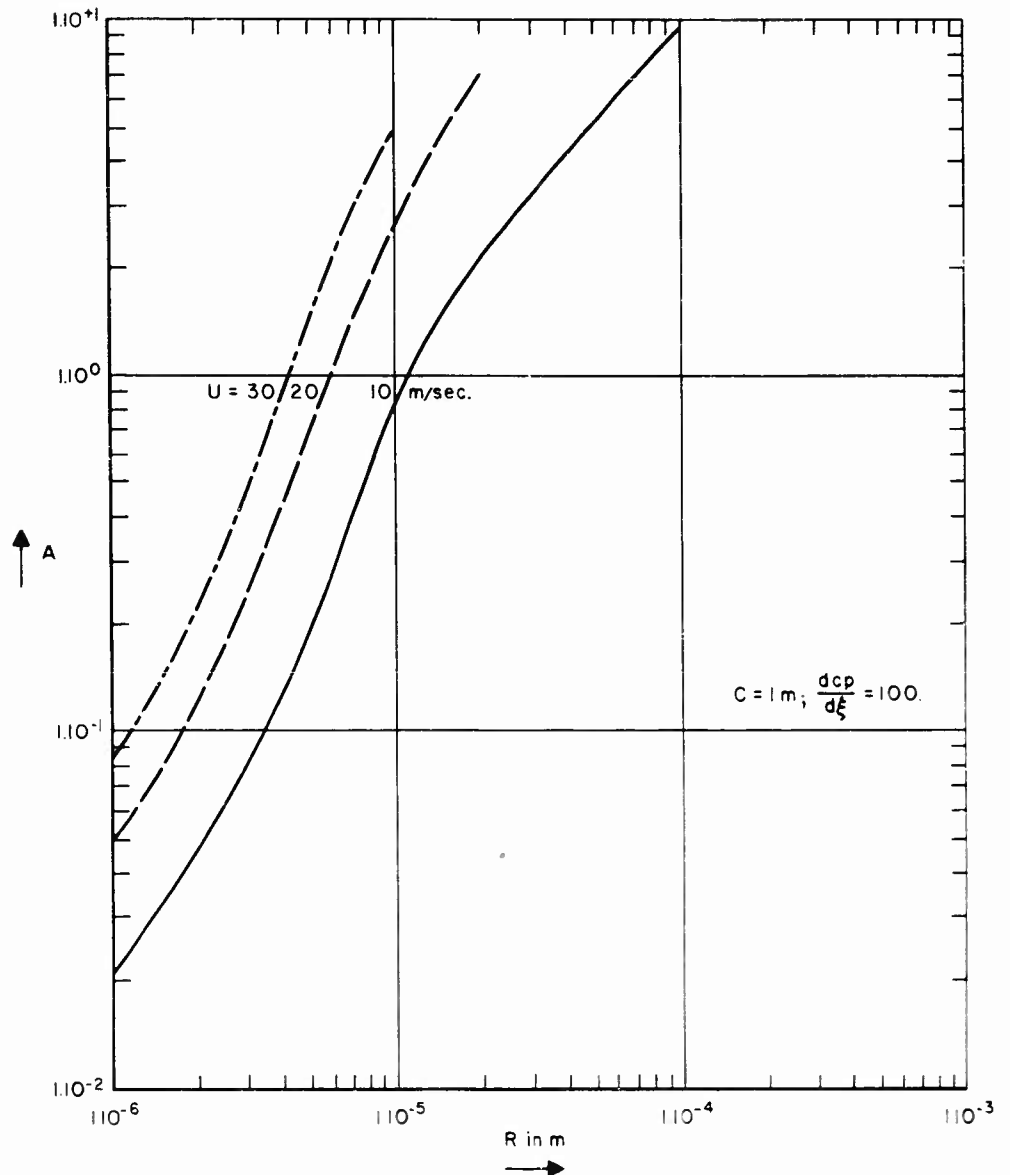
Fig. 4h – The quantity A as a function of R.
Leading edge cavitation - turbulent flow.

the bubble by entrainment. Summarizing, it can be stated that basically three types of the curve of A versus - have to be considered, namely:

a. Those cases where always $A < 1$. (The case of complete stabilization.)

b. Those cases where only in a rather small region of values of -, A is larger than 1. (The partly not stabilized cases.)

382

    c. Those cases where A is only smaller than 1 in a limited region of η values between zero and some positive value. (The only partly stabilized case.)

2.6 The Generation of Nuclei from Crevices in the Wall

    The process of generation of nuclei by a crevice is shown pictorially in Fig. 5a through 5d. If the pressure in the mainstream is sufficiently low, the

(a)

(b)

(c)

(d)
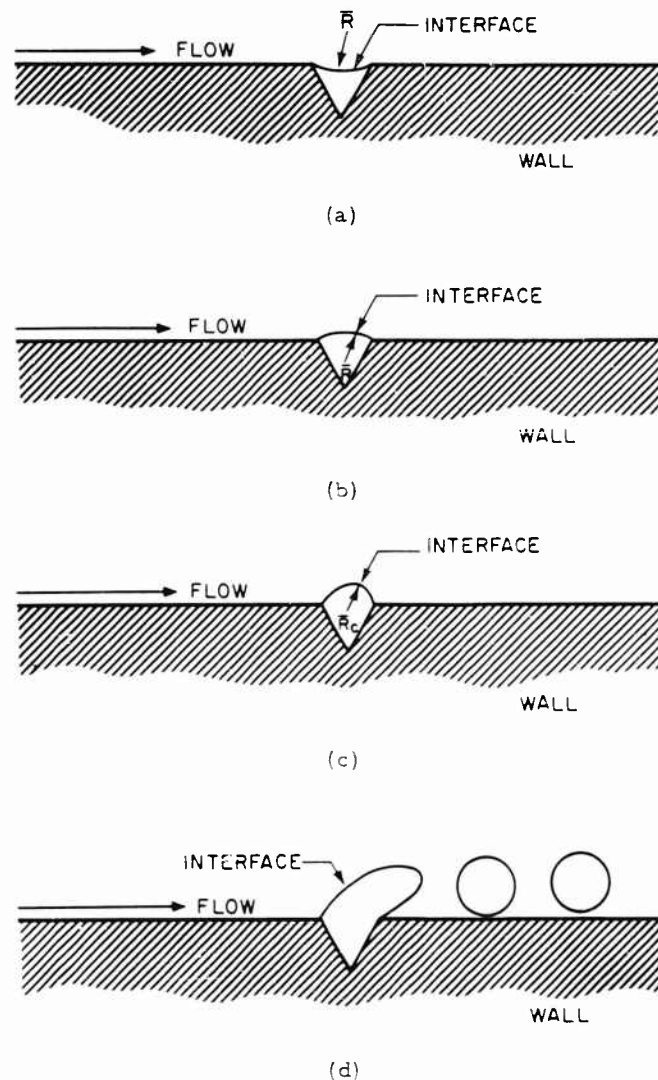
Fig. 5 - The process of generation of wall-nuclei

383

small gas pocket in a crevice will start to grow. The radius of curvature of the bubble liquid interface will change from convex to concave during this process. The radius of curvature attains a minimum and the internal bubble pressure therefore a maximum when the gas pocket has grown to a certain critical size (see Fig. 5c). This is approximately the case when the bubble forms more or less a hemisphere above the surface of the wetted body. This minimum radius of curvature R_c is an important characteristic property of the crevice. For a stationary bubble, Eq. (2.1) becomes:

$$P_a + P_v - P_\ell - \frac{2\bar{\sigma}}{\bar{R}} = 0 \tag{2.40}$$

where $\bar{R}$ = radius of curvature of interface (see Fig. 5a - d) or, written in dimensionless form:

$$C_{p_a} - C_p - \sigma - \frac{2}{\bar{\eta}} = 0 \tag{2.41}$$

where

$$
\left.
\begin{aligned}
C_{p_a} &= \frac{P_a}{\frac{1}{2}\rho u_\infty^2} \\[2ex]
C_p &= \frac{P_\ell - P_\infty}{\frac{1}{2}\rho u_\infty^2} \\[2ex]
\sigma &= \frac{P_\infty - P_v}{\frac{1}{2}\rho u_\infty^2} \\[2ex]
\bar{\eta} &= \frac{\rho u_\infty^2 \, \bar{R}}{2\bar{\sigma}}
\end{aligned}
\right\}
\tag{2.42}
$$

Growth of a bubble by gaseous diffusion is only possible when the equilibrium pressure of the dissolved gas p_{ae} is larger than the internal gas pressure p_a. Or if:

$$C_{p_{ae}} > C_{p_a} \tag{2.43}$$

with

$$C_{p_{ae}} = \frac{P_{ae}}{\frac{1}{2}\rho u_\infty^2} \tag{2.44}$$

Growth of a bubble is only possible therefore if:

$$C_{p_{ae}} > C_p - \sigma - \frac{2}{\bar{\eta}} \tag{2.45}$$

384

The right hand side of this inequality attains for given values of C_p and σ a maximum at the minimum value η_c for the radius parameter $\bar{\eta}$ (i.e., if $R = R_c$).

Growth above the critical condition $R = R_c$ is therefore only possible if:

$$C_{p_{a,e}} \geq C_p + \sigma + \frac{2}{\eta_c} \tag{2.46}$$

where

$$\eta_c = \frac{\rho u_x^2 R_c}{\frac{1}{2} \rho u_x^2}$$

It will be assumed that after detachment of a gas pocket with $R = R_c$ a bubble will be formed with radius R_c.

The characteristic crevice parameter $\eta_c = \rho u_x^2 R_c / 2 \bar{\sigma}$ determines therefore the maximum value of σ above which no growth of a bubble to larger values of R is possible.

The same reasoning applies to stream nuclei if it is assumed that these nuclei are formed in crevices of solid particles in the main stream. In order to distinguish between wall- and stream-nuclei the critical radius parameter of curvature will be denoted by

$$\tau_x = \frac{\rho u_x^2 R_x}{2 \bar{\sigma}} \tag{2.47}$$

in that case.

A second limitation exists for bubbles with less air content than corresponding to the critical bubble with radius R_c. These bubbles can be formed on the wall even if the relation (2.45) is not satisfied. In case these bubbles are sheared off from the wall, they will quickly dissolve again unless the dissolved gas content is sufficiently high. This is due to the fact that the internal bubble pressure becomes essentially larger for these bubbles once they are detached from the wall.

These bubbles will not be dissolved after detachment only if Eq. (2.45) is satisfied with R_c replaced by R (i.e., the bubble radius after detachment) or if:

$$\tau \geq \frac{2}{C_{p_{a,e}} - C_p - \sigma} \tag{2.48}$$

In deriving (2.48) it has been assumed that the air pressure p_a in the bubble equals the equilibrium saturation pressure of the dissolved gas at the instant of detachment. Normally the air pressure p_a will lag behind the equilibrium saturation pressure of the dissolved gas. This lag will be negligible in case the inception condition is approached sufficiently slow. In the remainder an infinitely

385

slow approach of the inception conditions will be assumed, making p_a equal to p_{ae} at the instant of detachment.

Equation (2.48) yields therefore a lower size-limit for the wall-nuclei that can effectively contribute to inception.

Once a wall-nucleus becomes detached, the bubble will be compressed in general due to the normally increasing pressure in the downstream direction. If gas diffusion can be neglected, the total air content of the bubble is constant and it can easily be shown that the following relation holds for the radius parameter τ:

$$\frac{\tau_2}{\tau_1} = \sqrt{\frac{C_{p_1} - \frac{2}{\tau_1} - \sigma}{C_{p_2} - \frac{2}{\tau_c} - \sigma}} \tag{2.49}$$

where the index 1 applies to the condition at detachment and 2 applies to the downstream position considered. Now is

$$C_{p_1} - \sigma - \frac{2}{\tau_1} = C_{p_{ae}} = \frac{p_{ae}}{\frac{1}{2}\rho u_\infty^2} \tag{2.50}$$

where p_{ae} = equilibrium pressure of the dissolved gas.

The decrease in the bubble radius will be more pronounced at lower values of the dissolved gas content parameter $C_{p_{ae}}$.

2.7 The Growth of Nuclei by Gas Diffusion

The growth of wall-nuclei by gaseous diffusion need not be considered as in principle an infinitely large time is available for growth in that case.

With stream nuclei however the situation is quite different as the available time is of the order of the passage time for fluid particles that flow along the wetted body. The growth of the bubbles is determined by the Eqs. (2.4) and (2.5).

If some approximations are made the following relation can be derived for the variation of the bubble radius parameter τ as a function of the streamwise coordinates.

$$\left(C_p - \sigma - \frac{2}{\tau}\right)\left(\frac{\tau}{\tau_x}\right)^3 = \sigma - \frac{2}{\tau_x} - \frac{3aX^2}{\tau_x^3}\int_{\xi_0}^{\xi} -(C_{p_{ae}} - C_p)d\bar{\xi} - \frac{3aX}{\tau_x^3}\int_{\xi_0}^{\xi} \frac{-2\left(C_{p_{ae}} - C_p\right)}{\sqrt{4 - (\xi - \bar{\xi})}} d\bar{\xi}$$

$$\tag{2.51}$$

386

On the Growth of Nuclei and the Related Scaling Factors in Cavitation Inception

where

$$\tau_\infty = \text{value of } \tau \text{ at } \xi = \xi_0,$$

$$\xi = s/c,$$

$$c = \text{characteristic length,}$$

$$a = \text{solubility} = \text{volume of gas that is dissolved in liquid/} \\ \text{volume of liquid in which gas dissolves,}$$

$$X = \sqrt{U_\infty^3 \, C D_a / 2} = \text{dimensionless diffusion coefficient,} \qquad (2.52)$$

$$C_{p_{ae}} = P_{ae} / \tfrac{1}{2} \, \rho \, U_\infty^2 = \text{dimensionless gas concentration parameter.} \qquad (2.53)$$

The first two terms of Eqs. (2.51) form in fact the law of Boyle for a gas bubble of constant gas content (pressure × volume = constant). The two integrals represent the inflow of gas due to diffusion. For a more detailed derivation of Eq. (2.51) the reader is referred to Ref. 9. Equation (2.51) contains an inconsistency in that the surface tension influence has not been neglected in the first three terms whereas it is neglected in the two integrals giving the gas diffusion flow towards the bubble. This inconsistency is due to the somewhat "mystic" character of the nuclei which necessitates the neglect of surface tension effects for explaining the growth of these nuclei whereas the retainment of the surface tension influence is necessary in the later phases of the growth period in order to find the correct instability limit as given by Eq. (2.10b). In these later phases the nucleus has increased its size so much that it can be regarded as a normal bubble where surface tension effects have to be considered in the normal way.

The derivation of Eq. (2.51) is justifiable therefore from this point of view.

Some results of calculations have been given in Fig. 6.

A sinusoidal pressure distribution has been considered of the type

$$C_p = -C_{p_{min}} \sin \pi \, \xi$$

The point where the travelling bubble bursts into vaporous cavitation is determined by relation (2.10b). The location of this point is a function of the initial bubble size as characterized by τ_∞ and of the cavitation number σ.

For every value of σ there is a minimum value for τ_∞ for which vaporous cavitation takes place. This minimum value has been calculated for the following cases:

1. $C_{p_{min}} = -1.5$; $\pi = 20$ (typical of leading edge cavitation conditions),

2. $C_{p_{min}} = -0.6$; $\pi = 1$ (typical of blade cavitation conditions).

In both cases two values of X and $C_{p_{ae}}$ have been considered, one corresponding to full scale conditions and one to model size.

387
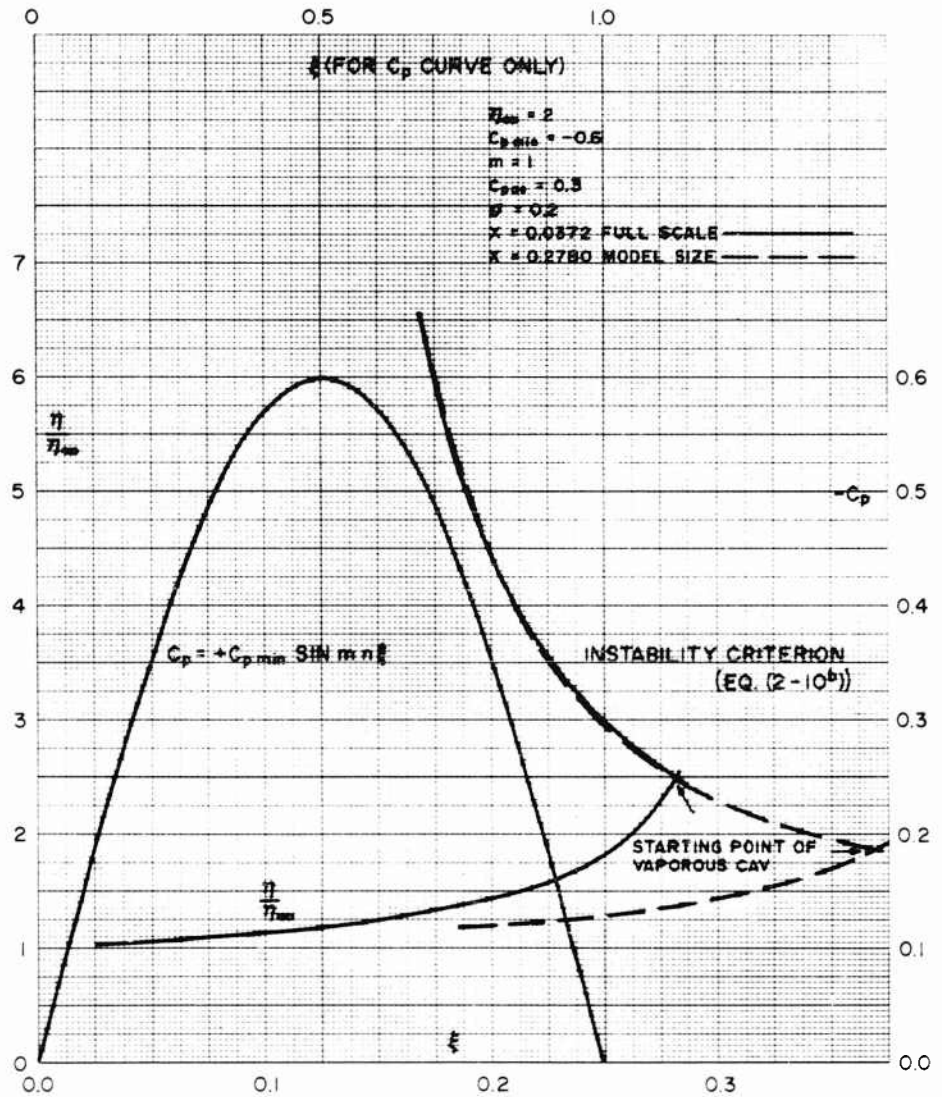
Fig. 6a - The growth of a travelling bubble by gas diffusion
around a hydrofoil at blade cavitation condition
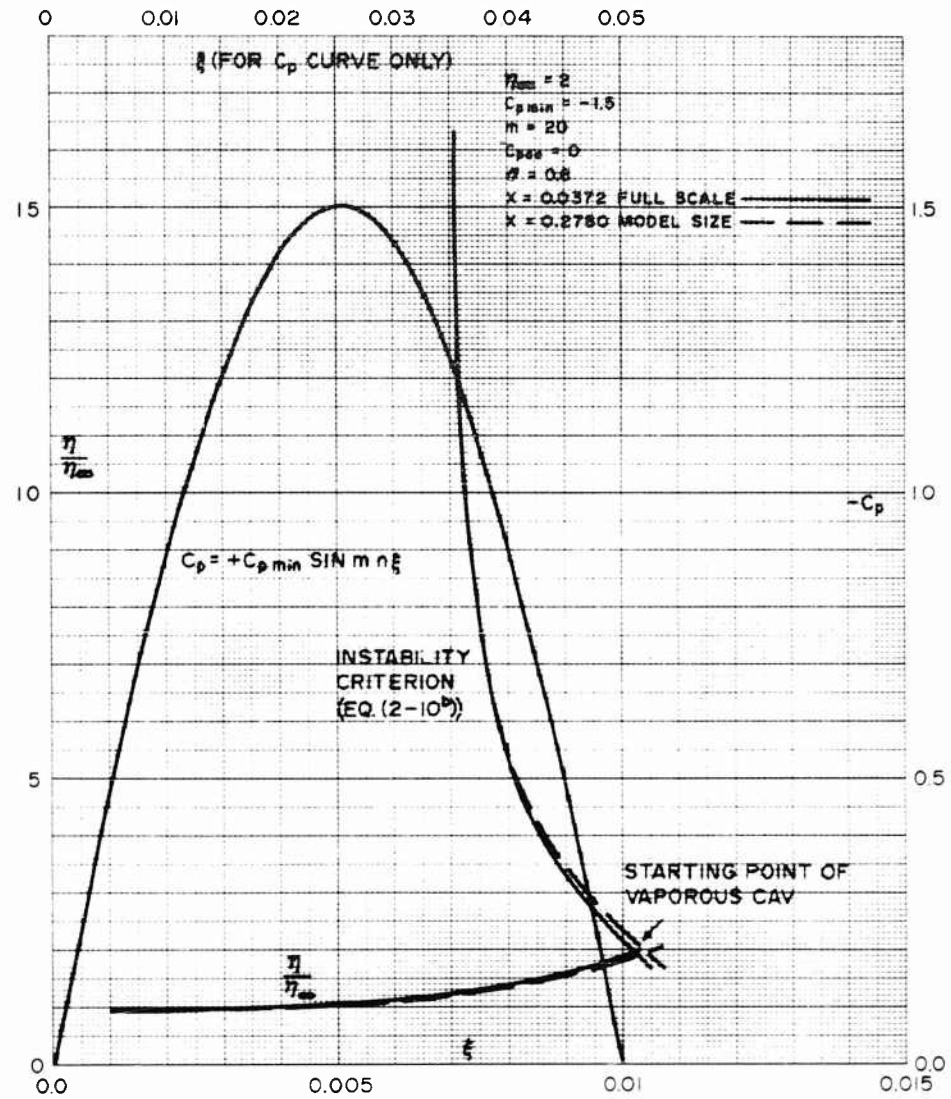
Fig. 6b - The growth of a travelling bubble by gas diffusion
around a hydrofoil at leading edge cavitation conditions

389

The values for η_{min} have been plotted in Figs. 7a and 7b.

Scale effects are present in two respects:

1. The values for η_{min} may be different for full scale and model size.

2. The values for X and $C_{P_{a_r}}$ will differ appreciably between full scale and model size.

The curves show the correct tendencies in that $\sigma_i \rightarrow -C_{P_{min}}$ for $\eta_{min} \rightarrow \infty$ and that $\sigma_i \rightarrow -\infty$ for $\eta_{min} \rightarrow 0$.

The results show that vaporous cavitation due to stream nuclei will only occur at rather low values of σ if the radius parameter η_z of the nuclei in the undisturbed stream is of the order of unity. This corresponds to nuclei of a couple of microns in diameter.

It is not expected that appreciably larger nuclei will be present normally in the mainstream.

Based upon these results one could expect that the contribution of stream nuclei to the inception process will be rather small compared to that of wall nuclei.

It must be remarked however that the derivation of Eq. (2.51) is based on the assumption that the bubbles move with the same speed as the main stream.

From paragraph 2.5 it can be concluded however that appreciable amounts of slip may be present between bubble and main stream due to streamwise pressure gradients.

This will increase the gas diffusion appreciably as additional convection terms have to be considered in Eq. (2.4).

Further research in this direction is necessary therefore in order to be able to compare quantitatively the influence of stream nuclei with those of wall-nuclei.

3. SUMMARY OF THE SCALING FACTORS AND THE
   RELATIONS FOR THE INCEPTION VALUE OF σ

From the discussions of paragraph 2 the relations for the inception value σ_i of σ can be derived. The scaling factors follow directly from these relations. It is evident from paragraph 2 that several possibilities for the inception process exist (gaseous versus vaporous cavitation and due to stream nuclei versus wall-nuclei, etc.).

Each of these possibilities has to be considered and the one with the highest value of σ_i is the critical one. It is also possible that the cavity patterns are different for different cavitation processes. In such a case more than one
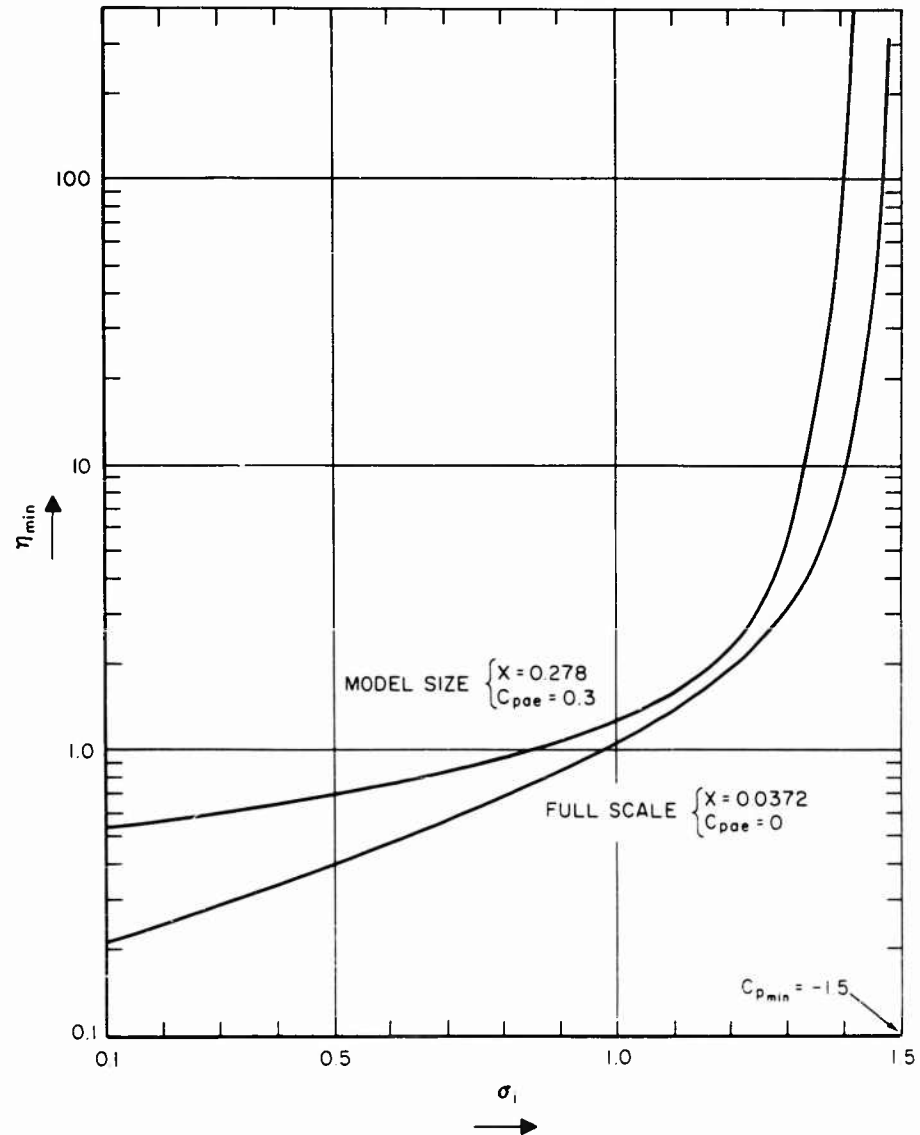
Fig. 7a - The minimum value of the nuclei radius parameter η_{min} that will lead to vaporous cavitation as a function of σ for m = 20; $C_{p_{min}}$ = -1.5 (leading edge cavitation)
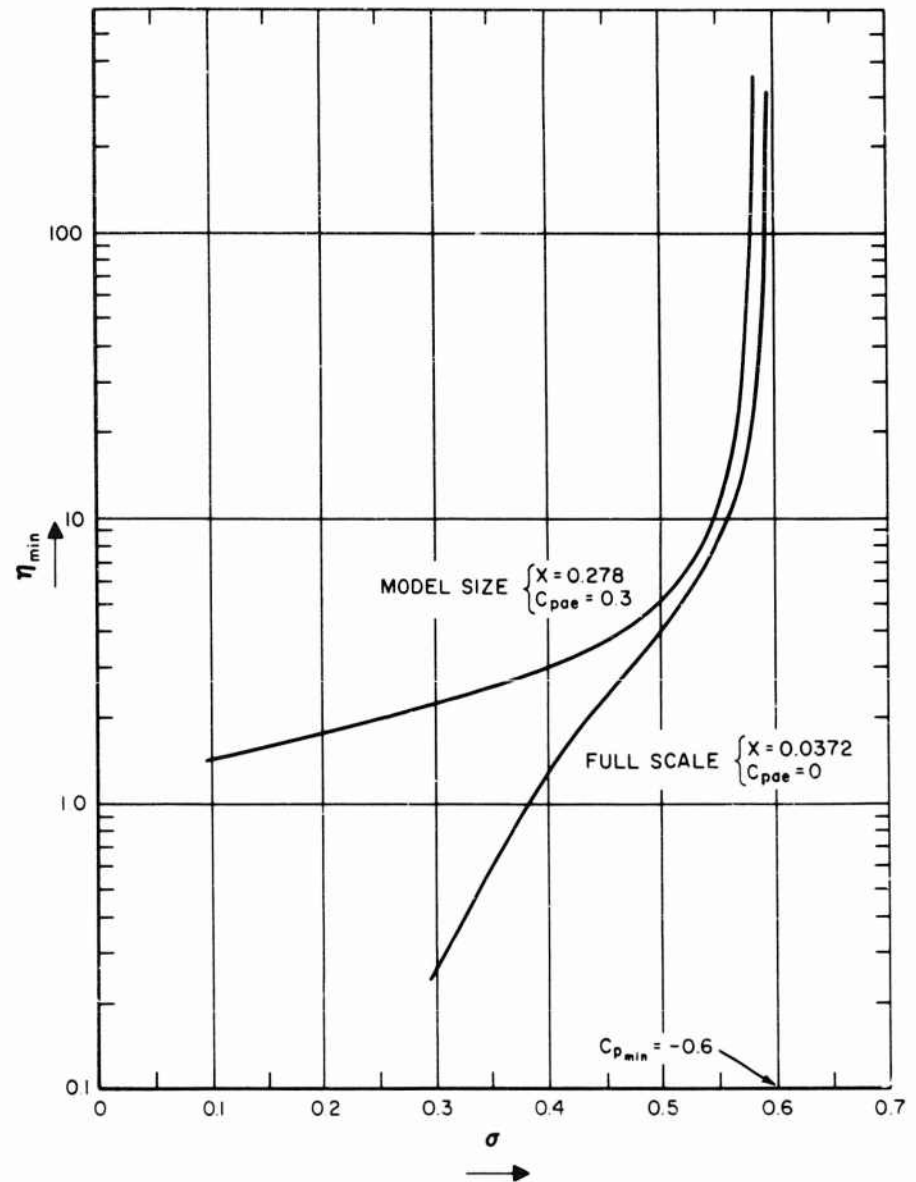
Fig. 7b – The minimum value of the nuclei radius parameter η_{min} that will lead to vaporous cavitation as a function of σ for $m = 1$; $C_{p_{min}} = -0.6$ (blade cavitation)

inception value for σ can be defined each of which will be related to one cavity pattern (see f.i., Ref. 7 and 8).

The various possibilities for the cavitation mechanism can be characterized according to the following criteria:

1. The type of nuclei, i.e., either wall- or stream-nuclei.

2. The type of cavitation, i.e., gaseous or vaporous.

3. The type of the curve of A versus η.

The results of paragraph 2 can be summarized as follows:

1. Heat conduction effects can be neglected as soon as

$$\Sigma_e = \frac{\rho_v \sqrt{D_{t\ell}} \ B.A}{\sqrt{\rho_\ell} \ \lambda_\ell \sqrt{\frac{dp}{dt}}} = \frac{\rho_v \sqrt{D_{t\ell}} \ \sqrt{BA}}{\sqrt{\rho_\ell} \ \lambda_\ell \sqrt{\frac{dT}{dt}}} << \underline{1}$$

2. Vaporous cavitation takes place as soon as:

$$\eta = \frac{-4}{3(C_p + \sigma)}$$

or if

$$C_p = -\sigma - \frac{4}{3\eta}$$

For very large values of η this reduces to:

$$C_p = -\sigma$$

3. Gaseous cavitation takes place as soon as:

$$C_{p_{ae}} \geq C_p + \sigma + \frac{2}{\eta}$$

4. Stream nuclei have to be characterized by the dimensionless parameter:

$$\eta_\infty = \frac{\rho u_x^2 \ R_\infty}{2\sigma}$$

5. Growth of nuclei by gaseous diffusion during transportation in the main stream is determined by the similarity parameters:

$$X = \frac{\rho \sqrt{u_\infty^3 C D_a}}{2\bar{\sigma}}$$

393

a = solubility,

and

$C_{P_{ae}}$ = dissolved gas content parameter.

6. The generation of wall-nuclei is influenced by the shape of the curve of A versus η. The type of the curve is to a large extent determined by the pressure gradient in the following way:

a. Large positive pressure gradient; $A < 1$. (Fully stabilized case.) Bubbles of every size are stabilized.
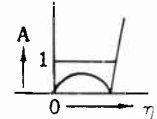
b. Medium positive pressure gradient; $A > 1$ for $\eta_1 < \eta < \eta_2$. (Partly not stabilized case.) The bubbles detach for η values between η_1 and η_2.
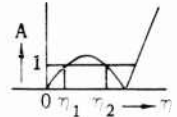
c. Small positive pressure gradient (partly stabilized case). $A > 1$ for $\eta > \eta_1$. The bubbles detach for η values larger than η_1.
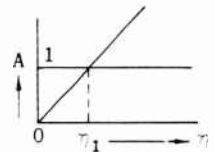
The quantitative values for η_1 and η_2 are determined by the following similarity parameters:

1. $R_e = \rho u_\infty c / \mu$ (Reynolds number).

2. $\sigma / U_\infty \mu$ (dimensionless measure for the surface tension).
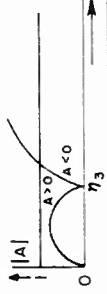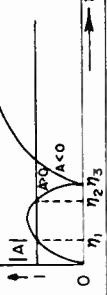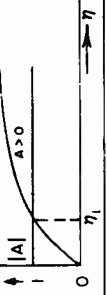
The inception criteria have been summarized in Table 3.1, according to the above described classification.

The scaling factors appear to differ appreciably for the various cavitation process.

The following general remarks can be made:

1. For all cases considered σ_i approaches the limiting value $-(C_p)_{min}$ if U_∞ increases monotonically and all other variables are kept constant.

2. The influence of the shape manifests itself in two ways:

a. By means of the curve of A versus η which is influenced appreciably by the pressure distribution.

b. The gaseous growth of travelling bubbles is influenced by the pressure distribution.

394

TABLE 3.1 $a = \text{solubility} = \dfrac{\text{volume of dissolved}}{\text{vol. of gas in which it dissolves}}$ $\eta = \dfrac{\rho U_\infty^2 R}{\sigma}$ $\rho\sqrt{U_\infty^2 CD_a}{\sigma}$

Type of cavitation	Type of curve A versus η	Type of nuclei			

Gaseous

Wall-nuclei

Fully stabilized nuclei (fixed cavity)

Eq: $\sigma_1 - {}^c p_{ae} = -{}^c p - \dfrac{2}{\eta_c}$

Scaling factors: $\sigma_1 - {}^c p_{ae} = F(\text{shape}; \eta_c)$

Fixed cavity at that point where eq. (1) is satisfied first (in general at ${}^c p_{min}$)

Remark: σ_1 is independent of length L, but dependent on U_∞ because of ${}^c p_{ae}$ and η_c

Partly not stabilized nuclei (fixed cavity preceded by travelling bubbles)

Eq: $\eta_1 = F(Re, \dfrac{\bar\sigma}{u\mu}; \text{type of boundary layer})$

$\sigma_1 - {}^c p_{ae} < -{}^c p - \dfrac{2}{\eta_1}$

Scaling factors: a: $\sigma_1 - {}^c p_{ae} = F(Re, \dfrac{\bar\sigma}{u\mu} \text{type, b, L, shape})$ (if growth is very quick)

b: $\sigma_1 - {}^c p_{ae} = F(Re, \dfrac{\bar\sigma}{u\mu} \text{type, b, L, shape, } {}^c p_{ae}, a, X)$ (if growth is slow)

Fixed cavity aft of pressure minimum

Only partly stabilized nuclei (travelling bubbles)

Eq: $\sigma_1 - {}^c p_{ae} = -{}^c p - \dfrac{2}{\eta_1}$

$= F(Re, \dfrac{\bar\sigma}{u\mu}, \text{type, b, L})$

Scaling factors: $\sigma_1 - {}^c p_{ae} = F(Re, \dfrac{\bar\sigma}{u\mu}, \text{shape, type, b, L})$

Increase in size of travelling bubbles is further determined by X and a.

Remark: Normally not visible (travelling small bubbles)

Stream-nuclei

Eq: $\sigma_1 - {}^c p_{ae} = -{}^c p - \dfrac{2}{\eta_3}$ $\eta_3 = F(Re, \dfrac{\bar\sigma}{u\mu}, \text{type, b, L})$

$\eta_3 - \eta_\infty = F(X, a, \text{shape})$

Scaling factors: $\sigma_1 - {}^c p_{ae} = F(Re, \dfrac{\bar\sigma}{u\mu}, X, a, \text{shape, type, b, L})$

Remark: This case will not be very important as normally wall-nuclei will lead to larger σ_1.

Same case

Eq: $\sigma_1 - {}^c p_{ae} = -{}^c p - \dfrac{2}{\eta}$

$\eta - \eta_\infty = F(X, a, {}^c p_{ae}, \text{shape})$

Scaling factors: $\sigma_1 - {}^c p_{ae} = F(\eta_\infty, X, a, {}^c p_{ae}, \text{shape})$

Remark: Normally not visible (travelling small bubbles)

Vaporous

Wall-nuclei

Eq: $\sigma_1 = (-{}^c p)$ at position of gaseous cavity.

Scaling factors: σ_1 is directly determined by the position of the gaseous cavity.

Remark: Normally σ_1 will be only weakly dependent on U_∞ and L.

$\sigma_1 - {}^c p_{ae} < -{}^c p - \dfrac{2}{\eta_1}$

Eq: $\sigma_1 = (-{}^c p)$ at position of gaseous cavity.

Scaling factors: σ_1 is directly determined by the position of the gaseous cavity.

Remark: Normally σ_1 will be only weakly dependent on U_∞ and L especially if gaseous growth of the travelling nuclei is quick.

Eq: $\sigma_1 - {}^c p_{ae} < -{}^c p - \dfrac{2}{\eta_1}$

$\eta = \dfrac{1}{3({}^c p + \sigma_1)}$ or $\sigma_1 = -{}^c p - \dfrac{1}{3\eta}$

$\eta - \eta_1 = F(X, a, \text{shape})$

Scaling factors: $F(Re, \dfrac{\bar\sigma}{u\mu}, \text{type, b, L, shape})$ in case gaseous growth is quick

b: $\sigma_1 = F(Re, \dfrac{\bar\sigma}{u\mu}, X, a, {}^c p_{ae}, \text{type, b, L, shape})$ in case gaseous growth is slow

Stream-nuclei

Eq: $\sigma_1 = (-{}^c p)$ at position of gaseous cavity.

Scaling factor: σ_1 is directly determined by the position of the gaseous cavity.

Remark: Influence of U_∞ and L can be large due to Re, $\dfrac{\bar\sigma}{u\mu}$ and X.

Same case

Eq: $\eta = \dfrac{1}{3({}^c p + \sigma_1)}$ or $\sigma_1 = -{}^c p - \dfrac{1}{3\eta}$

$= F(X, a, {}^c p, \text{shape})$

Scaling factors: $\sigma_1 = F(\eta_\infty, X, a, {}^c p_{ae}, \text{shape})$

3. In the case of gaseous cavitation it appears advisable to plot $\sigma_i - C_{p_{ae}}$ against the various parameters involved.

4. The influence of the Reynolds number is twofold:

   a. An increase in the Reynolds number at equal $\bar{\sigma}/U_\infty\mu$ tends to increase the boundary layer thicknesses. As a consequence, the curve of A versus η will shift more or less to the fully stabilized case. This will be a rather smooth influence.

   b. An increase in Reynolds number can shift the transition point to more forward positions. If the transition shifts into or upstream of the region where the nuclei are generated or are growing by gaseous diffusion a sharp influence on σ_i may be expected. σ_i can be decreased as well as increased by such a forward shift. In the above mentioned case 6b it can be expected that a shift of the transition point upstream of the generation point of the wall nuclei will lead to a drastic decrease in η_1 and therefore to a decrease in σ_i for the cavitation pattern due to wall-nuclei.

If, however, the transition moved upstream to a position between the generation point of wall-nuclei and the place where the cavity becomes attached to the body, it could well be that the increased turbulence intensity around the growing bubble would increase the diffusion process in such a way that an increase in σ_i resulted from it.

5. The influence of the velocity is rather complicated as many parameters are influenced by it.

6. It is advisable to describe the dissolved gas content in terms of $C_{p_{ae}} = p_{ae}/\frac{1}{2}\rho U_\infty^2$ instead of in the more usual form of gas concentration in parts per million (P.P.M.) [7].

4. COMPARISON WITH AVAILABLE EXPERIMENTAL DATA

Much experimental data has been obtained on hemispheres of various sizes and at different flow velocities [2,8]. The quantity A has been determined therefore as a function of η for this body shape for a number of values of R_e and $\bar{\sigma}/U_\infty\mu$

For the sake of simplicity the flat plate boundary layer equations have been used for the determination of boundary layer thickness and velocity profile.

The value η_1 of η for which A becomes greater than 1 has been plotted in Figs. 8a and 8b. Laminar as well as turbulent flow has been considered.

The value of η_1 determines directly the size of the bubbles that detach from the wall. As can be seen from Fig. 8a for laminar flow, η_1 values of around 20-100 are attained, corresponding to bubble diameters of the order of some hundredth's of a millimeter. This corresponds roughly with the bubble sizes measured by Kermeen a.o. [2].

396
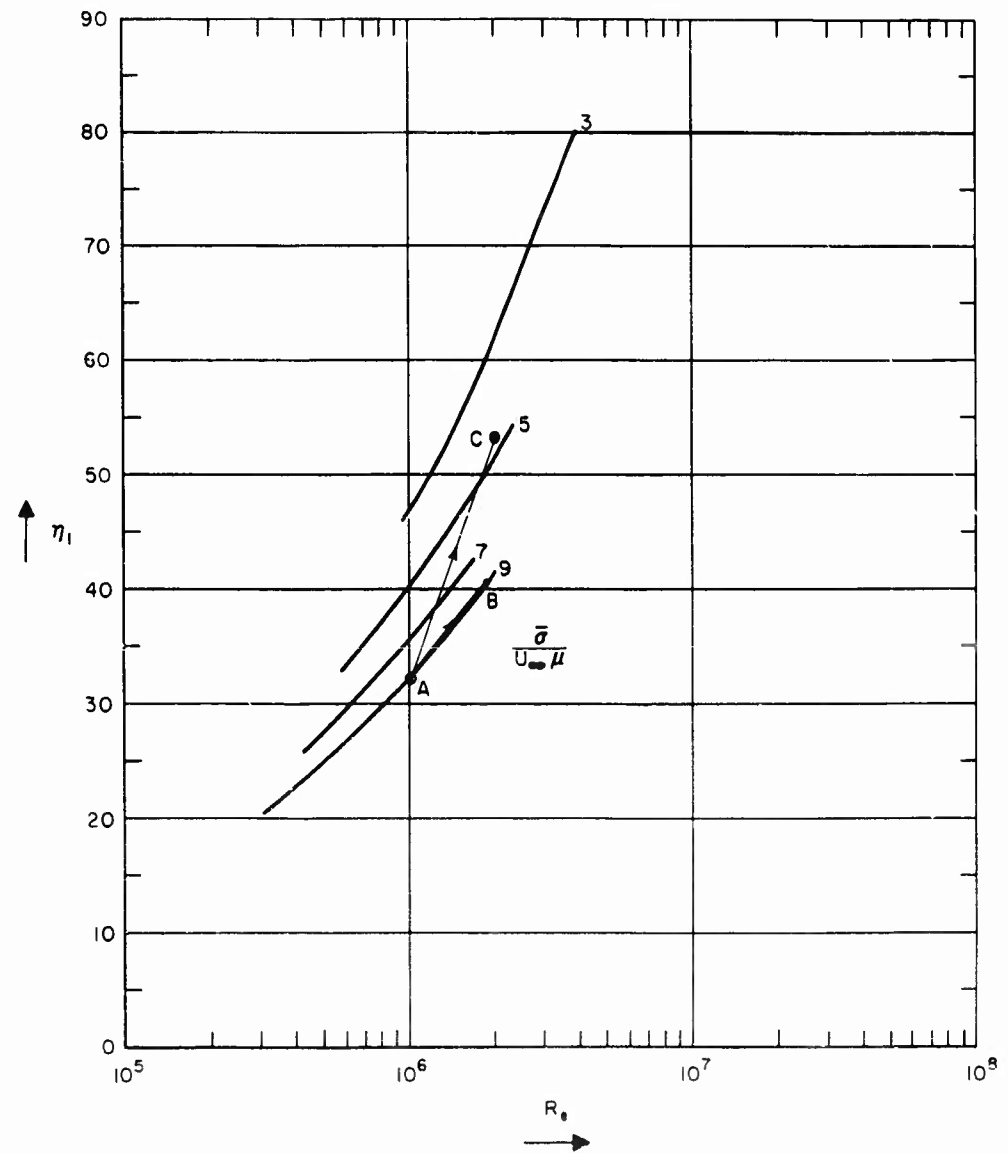
Fig. 8a - The radius parameter η_1 at detachment for wall nuclei as a function of the Reynolds number Re and of $\bar{\sigma}/U_\infty\mu$ for laminar flow around hemispheres
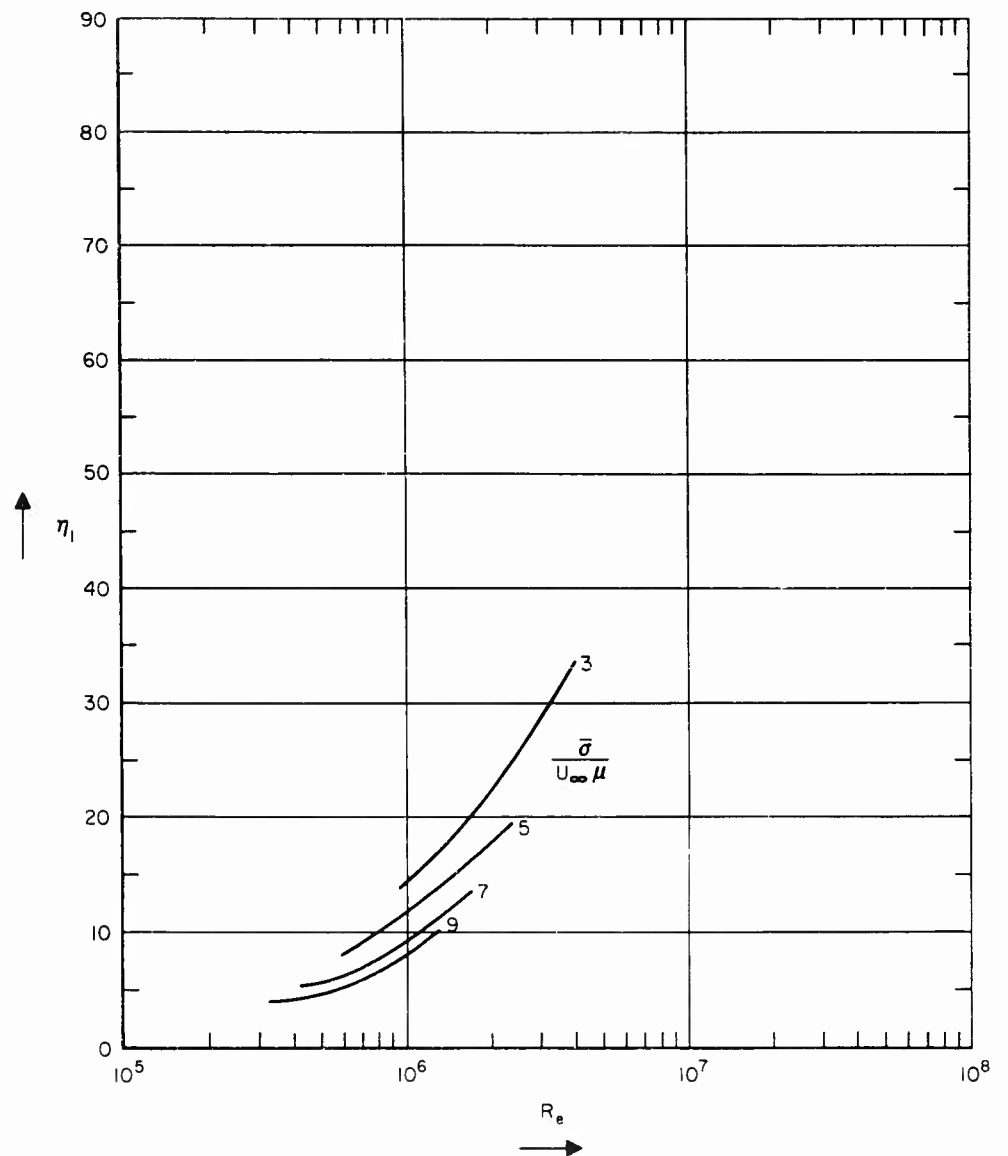
Fig. 8b - The radius parameter η_1 at detachment for wall nuclei as a function of the Reynolds number Re and of $\bar{\sigma}/U_\infty\mu$ for turbulent flow around hemispheres

In addition it can be mentioned that these values for η_1 are appreciably larger than the expected corresponding values for stream nuclei (see par. 2.7).

Increasing values of η_1 will lead to increasing values of σ_i.

It follows from Fig. 8a that the influence of the velocity is appreciably larger than the influence of the size. This is shown by the three cases; A, B and C. Doubling the scale (A → B) gives an increase in η_1 of around 32% whereas doubling the velocity results in an increase of η of around 68%. Probably this gives an explanation for the experimentally found fact that the inception value of σ seems to correlate in some cases with the parameter $U_\infty \sqrt{C}$ [8]. The correct correlation parameter is then:

$$\sqrt{\frac{U_\infty \mu}{\sigma}} \qquad \sqrt{\frac{\rho U_\infty C}{\mu}} = U_\infty \sqrt{\frac{C\rho}{\sigma}}$$

(see also the discussion of Ref. 2).

It is evident however that the dependency is more complicated than this simple parameter suggests.

Figure 8b shows that an appreciable reduction in η_1 will result from a forward shift of the transition upstream of the generation point of the nuclei. This will cause a drastic decrease in the inception value of σ.

The experimental results of Kermeen a.o. on inception on hemispheres have been plotted in Fig. 9 as a function of Re and $\sigma/U_\infty \mu$.

As the cavitation pattern is evidently due to gaseous cavitation $\sigma_i - C_{p_{ae}}$ has been plotted instead of σ itself.

For the same geometry the values of η_1 have been calculated.

In the tests of Kermeen it has been found that the transition point lies between the point of generation of the nuclei and the attachment point of the fixed cavity.

All along the wall upstream of the transition point wall nuclei will be generated. The largest ones will be created just in front of the transition point as the boundary layer will be thickest there.

Aft of the transition point the wall nuclei will be appreciably smaller due to the higher shearing stresses in the wall region of the turbulent boundary layer.

This is demonstrated also by Figs. 8a and 8b, which give the values for η_1 for laminar and turbulent flow.

The radius parameter η_1 is appreciably smaller in the case of turbulent flow.

Some typical curves of the quantity A as a function of the bubble radius R have been plotted in Figs. 10a and 10b.
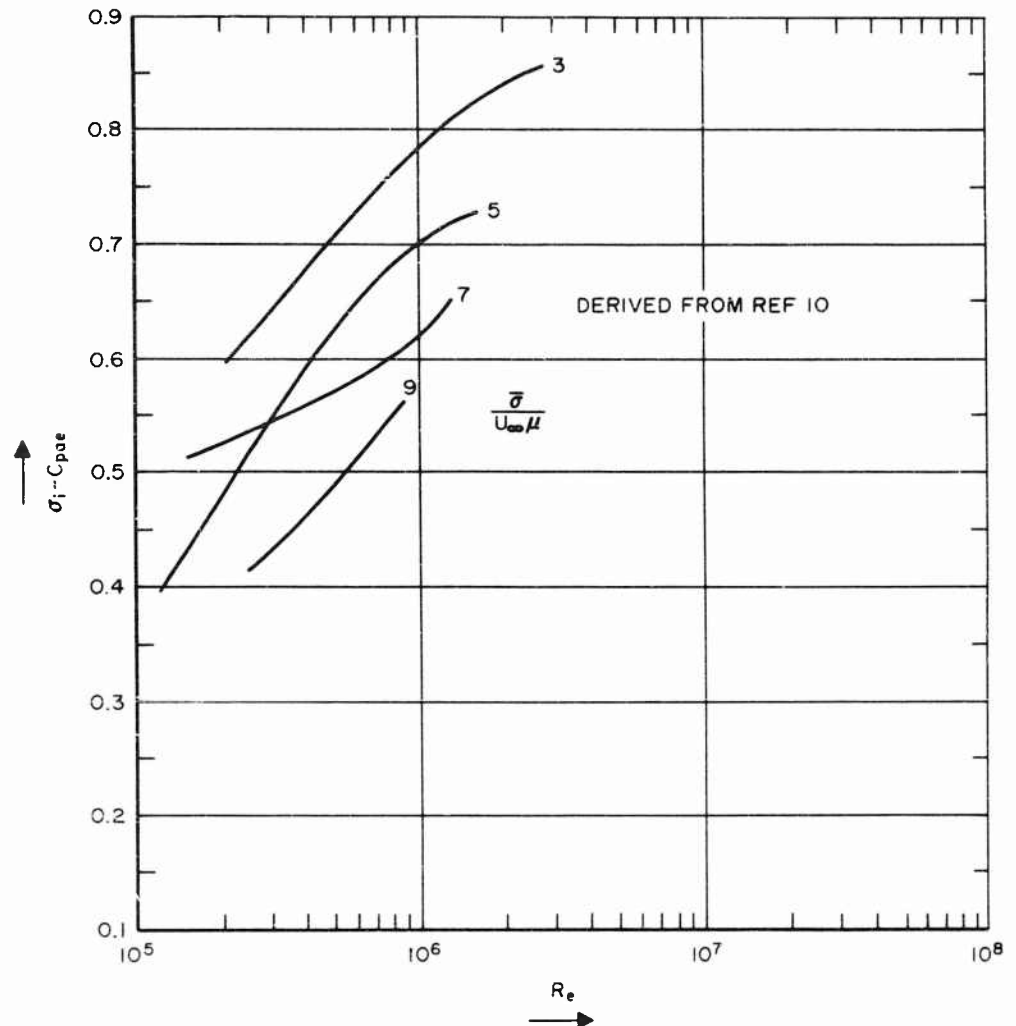
Fig. 9 - The cavitation number for inception σ_i as
measured for hemispheres

It is evident that the flow along a hemisphere belongs to the partly not sta-
bilized case of Table 3.1. It is found from theoretical calculations that the bub-
ble radii at the moment of detachment are of the order of 0.01 - 0.1 mm in the
laminar case, whereas attachment occurs again for radii of around 3 mm in the
laminar as well as in the turbulent case. This has to be compared with the ex-
perimentally found figures of around 0.01 mm and 0.5 mm. In view of the rather
rough approximation that was used in the calculation of the boundary layer the
agreement can be considered quite reasonably. The following inception process
suggests itself on the basis of these considerations.

The wall nuclei that will determine the inception conditions are those that
are generated just in front of the transition point as these will be the largest

400
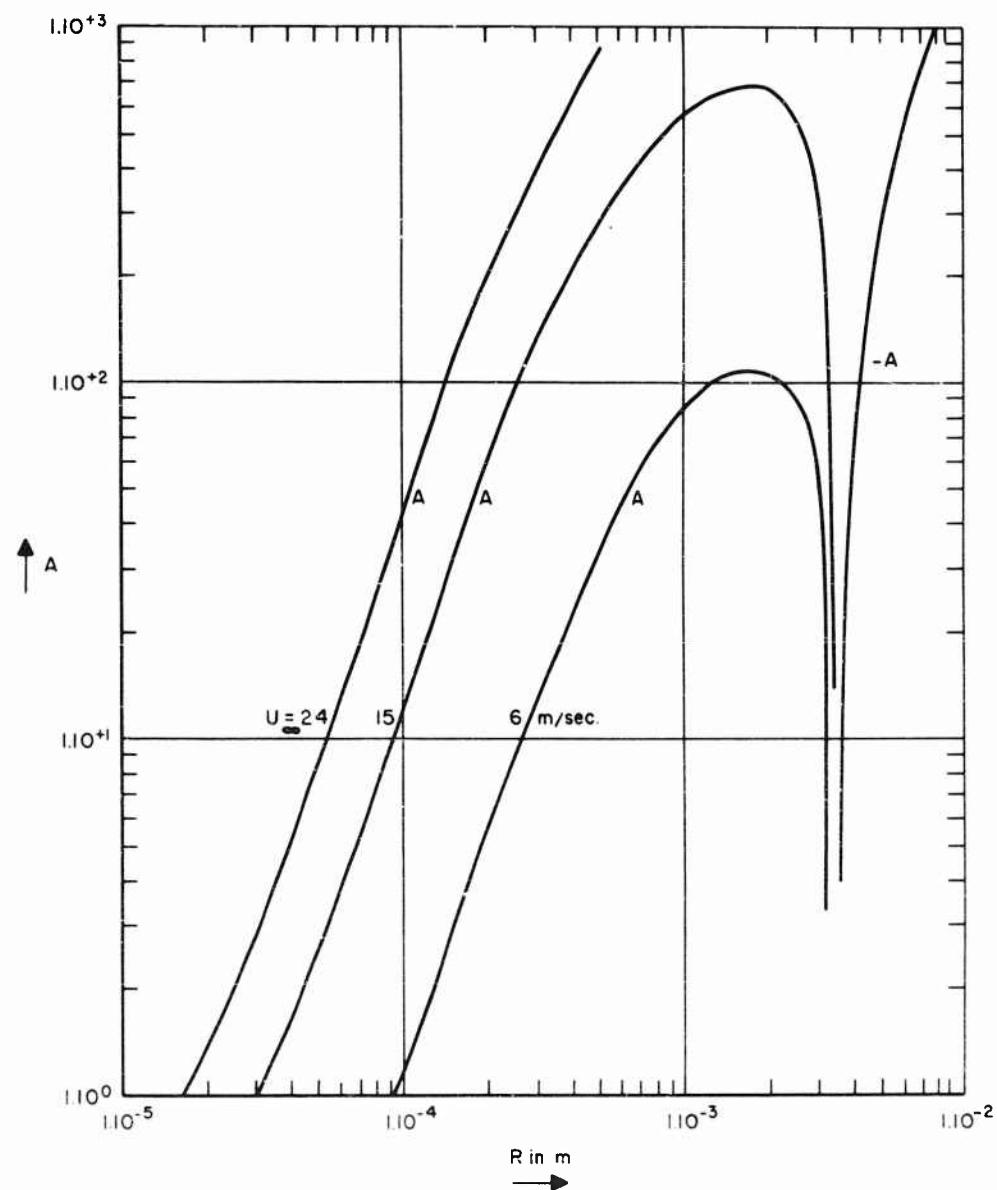
Fig. 10a - The quantity A as a function of the bubble radius R for laminar flow around a 4" hemisphere
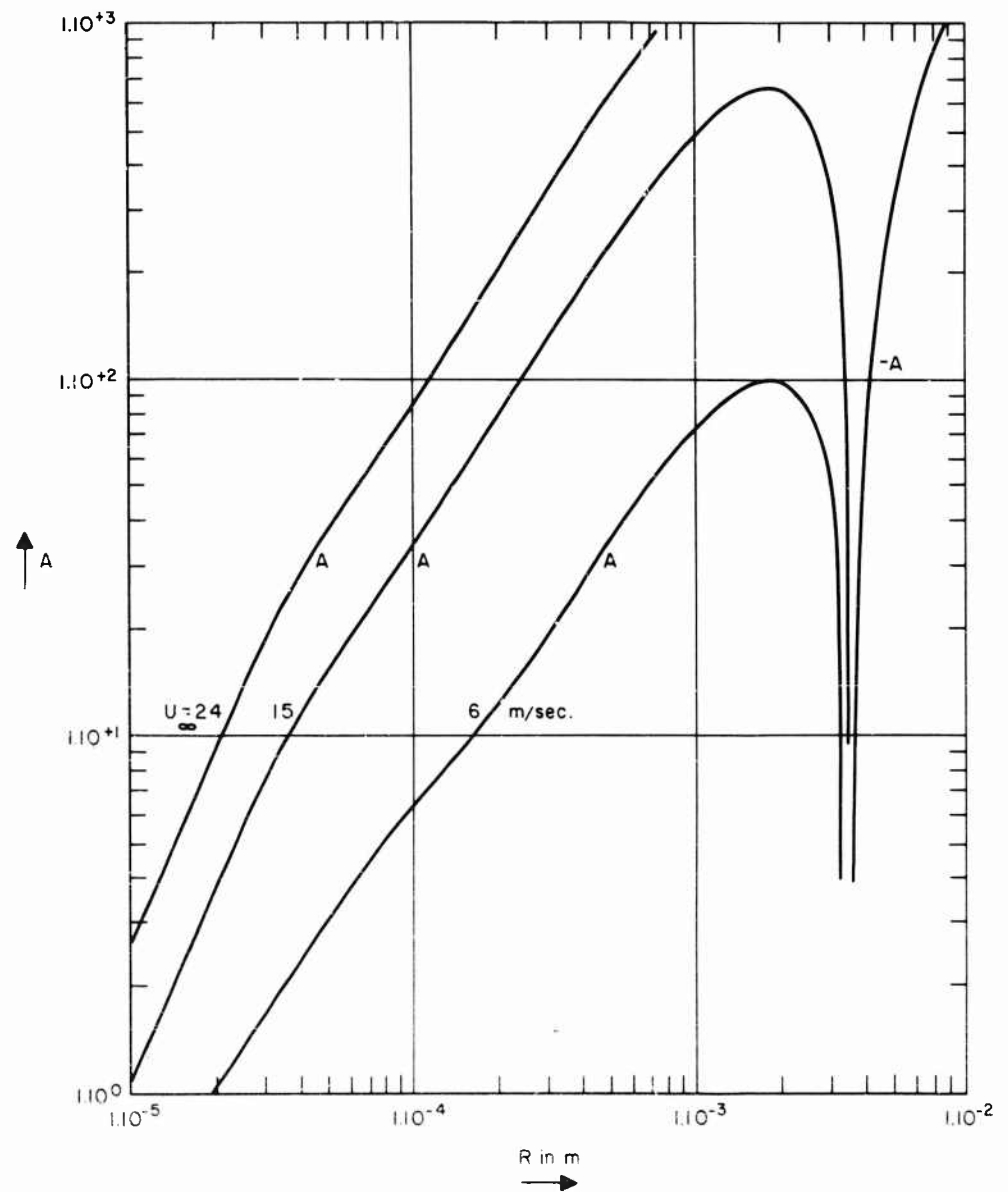
Fig. 10b - The quantity A as a function of the bubble
radius R for turbulent flow around a 4" hemisphere
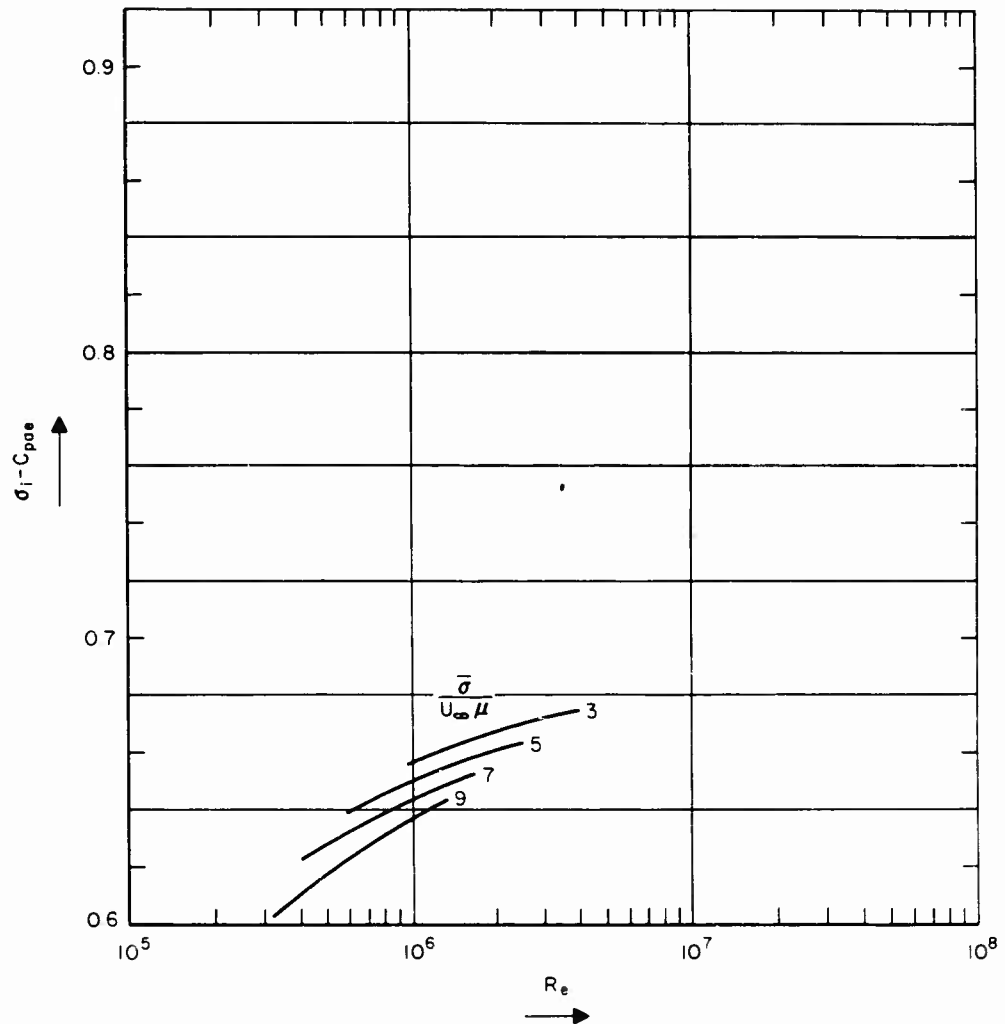
Fig. 11 - The cavitation number for inception σ_i
as calculated by theory for hemispheres

ones available. In the transition region very high gas diffusion rates will be realized due to the highly turbulent nature of the flow. The nucleus will grow enormously therefore if this nucleus satisfies the gaseous cavitation criterion at the moment of detachment; it will implode by gas diffusion when this criterion is not satisfied.

It will be assumed now that the growth in the transition region is such rapid that the inception conditions are reached as soon as the gaseous cavitation criterion is satisfied at the point of detachment.

403

The inception values of σ_i have been calculated accordingly and the results have been plotted in Fig. 11. These purely theoretical values should be compared with experimentally determined data of Fig. 9.

The close resemblance of the curves can be called quite good especially if the rough approximation in the calculation of the boundary layer is taken into account.

REFERENCES

1. Strasberg, M., "The Influence of Air-Filled Nuclei on Cavitation Inception," D.T.M.B. Report 1078, May 1957.

2. Kermeen, R.W., McGraw, J.T., and Parkin, B.R., "Mechanism of Cavitation Inception and the Related Scale Effects Problem," Trans. ASME, May 1955, pp. 533-541.

3. Oshima, R., "Theory of Scale Effects on Cavitation Inception on Axially Symmetric Bodies," Trans. ASME, Journal of Basic Eng., Sept. 1961, pp. 379-384.

4. Silverleaf, A., "Note on Basic Studies on the Phenomenon of Cavitation," I.T.T.C. Cavitation Committee, 1961.

5. Devin, C., "Survey of Thermal, Radiation and Viscous Damping of Pulsating Air Bubbles in Water," D.T.M.B. Report 1329, August 1959.

6. Plesset, M.S., "Physical Effects in Cavitation and Boiling," Naval Hydrodynamics, Publ. 515, Nat. Acad. Sciences, Nat. Res. Council, 1957.

7. Holl, J.W., "An Effect of Air Content on the Occurrence of Cavitation," ASME paper 60, Hyd. 8.

8. Robertson, J.M., McGinley, J.H., and Holl, J.W., "Similitude et Cavitation," La Houille Blanche No. 4, September 1957, pp. 540-549.

9. van der Walle, F., "A Survey of the Hydrodynamic Properties of Liquid Gas Bubble Mixtures," Dec. 1961, N.S.M.B. Lab. Memorandum No. 2.

10. "Incipient-Cavitation Scaling Experiments for Hemispherical and 1.5-Caliber Ogive-Nosed Bodies." A joint study by the Hydrod. Lab., Cal. Inst. Techn. and Ordn. Res. Lab. of Penn. State Coll., May 15, 1953.

*   *   *

Tuesday, August 28

Afternoon Session

PROPULSION

Chairman: C. W. Prohaska

Hydro-og Aerodynamisk
Laboratorium
Lyngby, Denmark

EXPERIMENTAL AND ANALYTICAL RESULTS OF THRUST MEASUREMENTS ON ACTUAL MERCHANT SHIPS

Masao Kinoshita, Dr. Eng., Shōjirō Okada, Dr. Eng., and Shōichi Sudō
The Technical Research Laboratory of
Hitachi Shipbuilding & Engineering Co., Ltd.
Osaka, Japan

ABSTRACT

At the Technical Research Laboratory of Hitachi Shipbuilding & Engineering Co., Ltd., the authors have conducted the measurement of the torque and thrust of newly-built merchant ships in recent years at their speed trials, and have successfully obtained the results of simultaneous measurements which are believed quite reliable, concerning the relations among the speeds of ships, propeller revolutions, torque and thrust.

In this paper, an attempt is made to briefly explain the method of the thrust measurement used, followed by the analysis of the results of these speed trials as compared with those of model experiments. Finally, the scale effect on the self-propulsion factors are examined.

As a conclusion, it may be said that as far as the relative rotative efficiency is concerned, there exists very little scale effect between full-scale ships and similar models. Accordingly, it is believed that ΔC_F values calculated directly from the measured thrust will not be very different from those which are calculated indirectly by using the values of measured torque, the open propeller characteristics and self-propulsion factors derived from the model experiments.

INTRODUCTION

In order to analyze the propulsive performance of a ship, it is strongly desired to know the exact value of thrust as well as that of torque acting on an intermediate shaft of an actual vessel at her speed trial on the mile-post course.

At the technical research laboratory of Hitachi Shipbuilding & Engineering Co., Ltd., the authors have been engaged in the measurement of torque and thrust, at the speed trials, of the merchant ships newly-built at their shipyards

407

in recent years, and have obtained the results of measurements which are be-
lieved quite reliable.

This paper deals with the method of measuring the thrust of any merchant
ship at any time desired without much trouble, and further explains the analyti-
cal results obtained at the speed trials, by comparing them with those of model
experiments. Finally, the scale effect on the self-propulsion factors are ex-
amined.

THE METHOD OF MEASURING THRUST

Up to this time, a thrust meter of the Michell type has been widely used for
the purpose of thrust measurement at sea, but it is not possible for this meter
to be applied to any ship and at any time desired. In order to investigate the
problem of ship propulsion, therefore, the authors have made an effort in obtain-
ing a kind of thrust meter which may be easily attached to and removed from a
ship without remodeling any part of it.

Accordingly, the method adopted by the authors for the thrust measurement
at sea trials of actual ships, is to pick up the compressive strain caused on the
intermediate shaft by the thrust, using the wire strain gauges attached on it. At
first, 16 sheets of strain gauges were arranged as in the case of "A" ship shown
in Fig. 1. Soon after that, however, the arrangement of the gauges was altered
as in the case of "B" ship which is shown in the same figure, in order to make
the work simpler and more accurate.
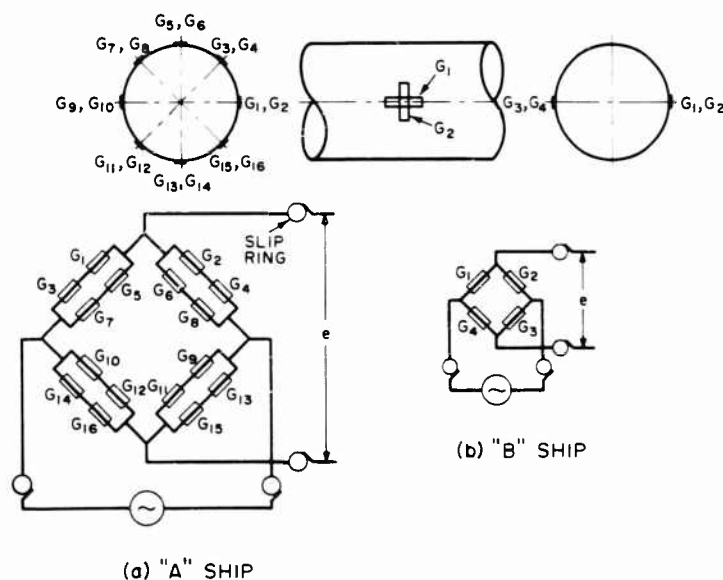
Fig. 1 - Arrangement of strain gauges

A slip ring and a brush were used to supply or take out the current to or from the strain gauges attached on the rotating shaft, but it was found that this circuit contained some substantially unstable factors. In view of the above, the authors gave up this method and adopted FM strain telemeter to eliminate these unstable factors from the circuit. Thus, eliminated from the circuit were the slip ring, the brush and the long wire cords connecting the strain gauges with the strain meter in the measuring room.

In the FM telemeter method, battery box (source), subcarrier oscillator, bridge balancer and FM transmitter are firmly bound on the shaft, as shown in Fig. 2, and the strain signal is transmitted on FM carrier. The strain signal can be easily caught by the antenna arranged around the shaft, and led to the receiving set in the measuring room. This is the simplest and most reliable of any measuring method which the authors have ever tried by means of wire strain gauges.

"E" SHIP
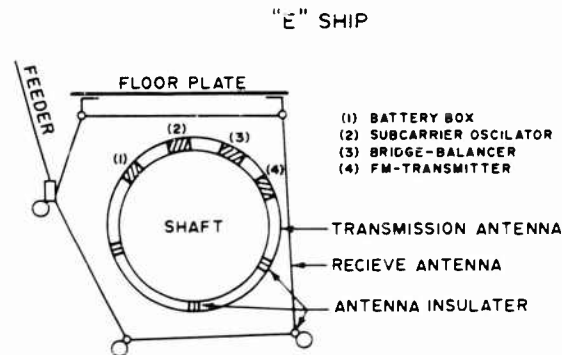
Fig. 2 - Arrangement of
parts of telemeter

An example of the arrangement of slip ring and brush, and that of the arrangement of FM strain telemeter on the shaft, are shown in Fig. 3 and Fig. 4 respectively. An example of oscillogram recording the value of thrust by FM strain telemeter is shown in Fig. 5.

THE RESULTS OF THRUST MEASUREMENTS

At the first stage, it was found difficult to keep the zero point constant throughout the entire measurement. Accordingly, the authors aimed at the measurement of the amplitude of thrust fluctuations rather than the absolute values of thrust, concerning the analysis of the longitudinal vibration of the crank shaft of diesel engine. Figure 6 shows the results of the measurements at this stage. The thrust was measured only when the engine was powered up step by step, and at each step, the engine was kept steady for a few minutes with a constant number of revolutions, for the purpose of torsional vibration test of the shaft.
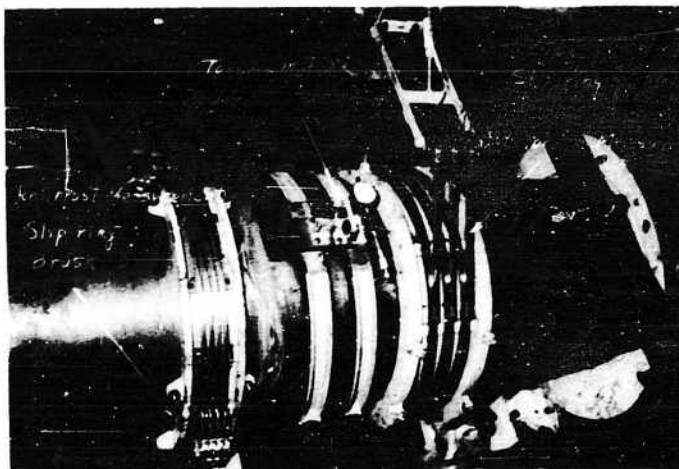
Fig. 3 - A photograph of brush and
slip-ring (B ship)
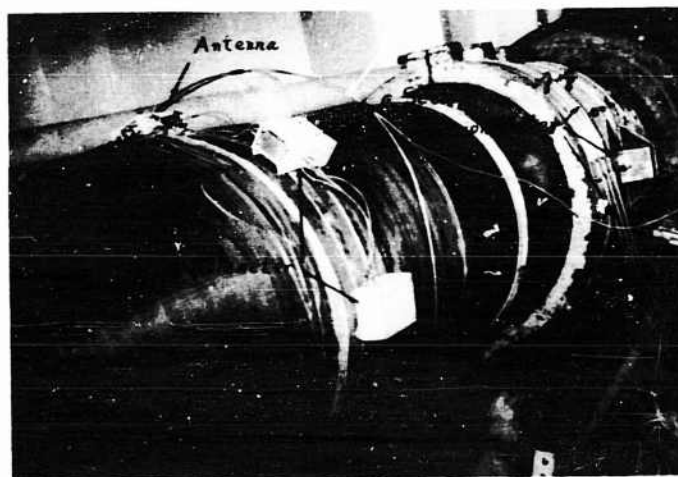
Fig. 4 - A photograph of telemeter (F ship)
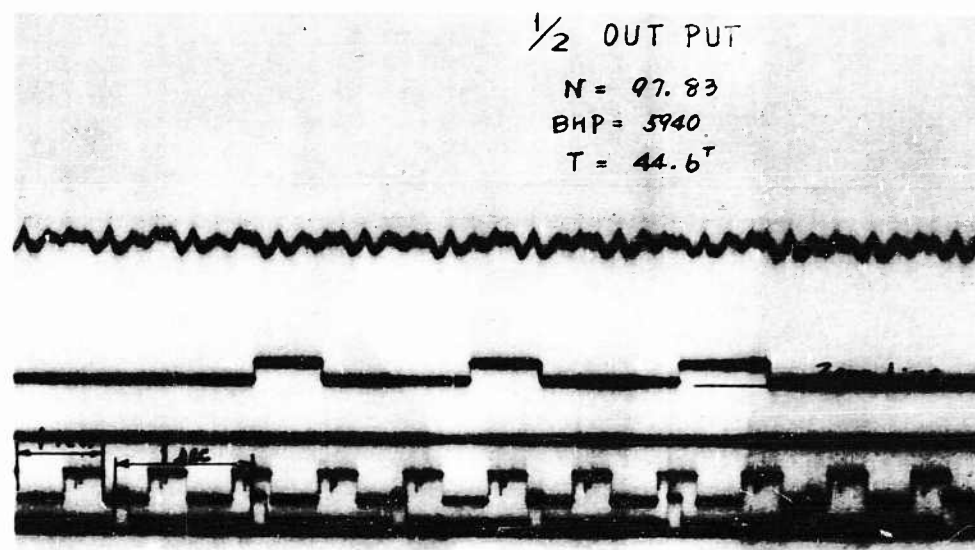
Fig. 5 - An oscillogram recording the value of thrust

"A" SHIP, CARGO LINER

145^m x 19.6^m x 12.4^m
ENG 12,500 BHP x 115 RPM

Δ = 8,225 t

"B" SHIP, SUPER TANKER

197^m x 26.4^m x 15.1^m
ENG 15,000 BHP x 115 RPM

Δ = 43,520 t

THRUST IN TONS

NO OF PROPELLER REVOLUTIONS PER MINUTE
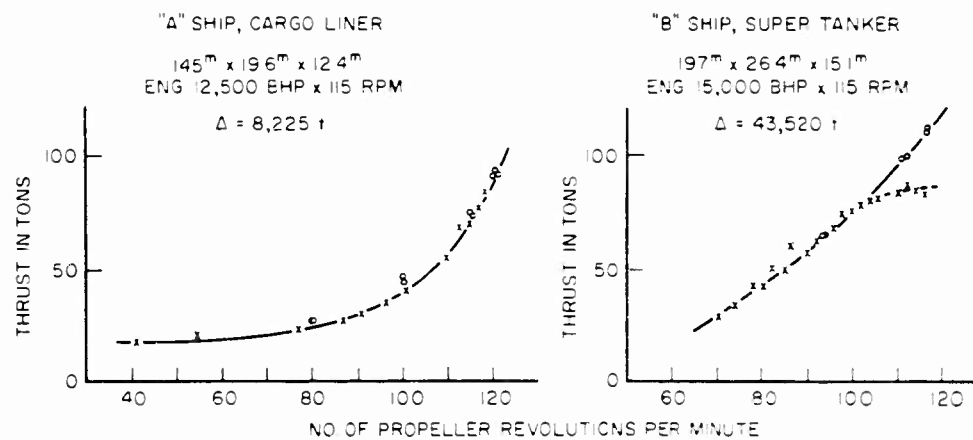
○ CALCULATED VALUES ACCORDING TO TORQUE MEASURED,
PROPELLER CHARACTERISTICS AND SELF-PROPULSION
FACTORS DERIVED FROM MODEL TEST

x MEASURED VALUES

Fig. 6 - Results of thrust measurements at the first stage

411

Referring to the figure, the cross-marks show the values of the measured thrust, but the circular-marks indicate the calculated values of thrust from the torque measured at the speed trial on the mile-post course, the open propeller characteristics, and the self-propulsion factors derived from the model experiment. Although these two kinds of values are not values of simultaneous measurement, they coincide pretty well in the case of "A" ship. In the case of "B" ship it may be supposed from Fig. 6 that the zero began to move from the point which had been set before the engine was started.

After making some further experiments, the authors were successful in obtaining satisfactory results of simultaneous measurement of torque and thrust at the standardization trial of "C" ship conducted by the 41st Research Committee of Shipbuilding Research Association of Japan in 1960.

The measurement was carried out mainly at the speed trial on the mile-post course, and also when the engine was powered up in the manner as mentioned above, soon after the engine was started, and during the torsional vibration test. All the test results are plotted in Fig. 7, and the fact that the plots lie on the $45°$-line in the figure means that the relation between torque and thrust measured at the model can be applied as it is to that of the full-scale ship.

"C" SHIP. SUPER TANKER
$211.8^m \times 31.7^m \times 15.1^m$
ENG. 17500 SHP $\times$ 105 RPM
$\Delta_F = 61,440$ t (FULL)
$\Delta_L = 38,040$ t (LIGHT)

FULL LOAD, AT SPEED TRIAL
D.º SOON AFTER ENG. STARTED.
D.º AT TORSIONAL VIB. TEST.
LIGHT LOAD, AT SPEED TRIAL
D.º AT TORSIONAL VIB. TEST.

THRUST MEASURED (TONS)

THRUST IN TONS, CALCULATED ACCORDING TO TORQUE MEASURED, PROP. CHARACTERISTICS AND SELF-PROPULSION FACTORS
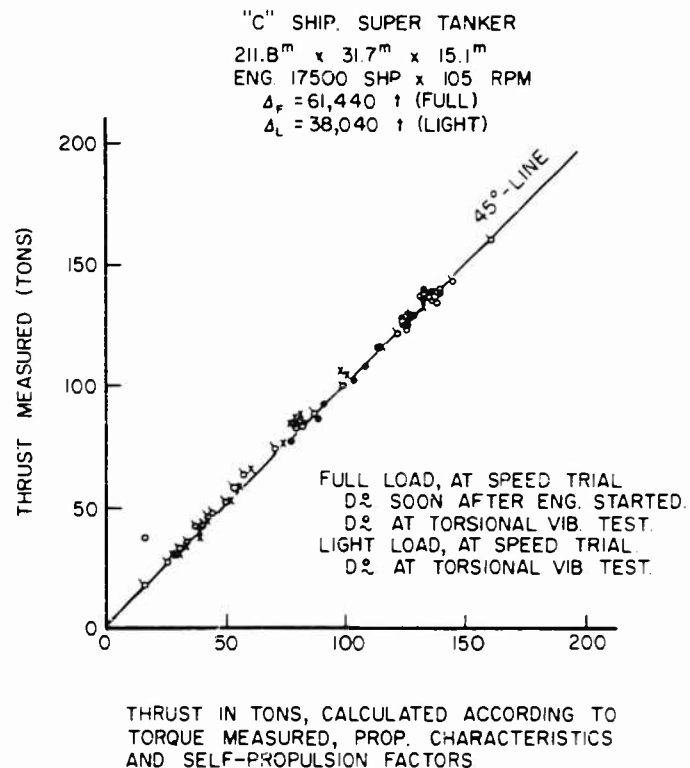
Fig. 7 - Comparison between values of thrust, measured and calculated

412
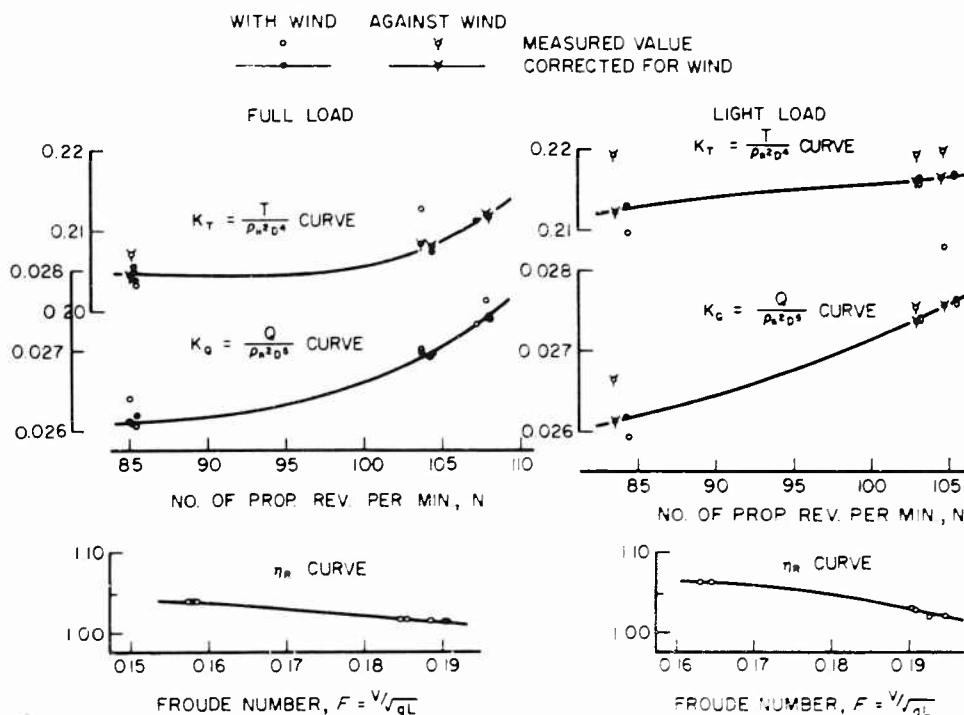
Fig. 8 - K_T, K_Q and η_R curves of "C" ship

Based on the results of the speed trial, the curves of torque and thrust co-efficients, obtained in the course of analysis by the standardized method adopted by the J.T.T.C., and the relative rotative efficiency of the ship calculated from these values of torque and thrust, are shown in Fig. 8.

Ever since, the authors have been conducting simultaneous measurement of the torque and thrust at the speed trials of various types of merchant ships. Following are the results of these measurements in the same form as shown in Fig.8.

Among them, "D" ship, for which the results of measurement are shown in Fig. 9, was still measured by the slip ring-brush method. FM telemeter method was applied to "E" ship for the first time, the results of which are shown in Fig. 10 both for the full load and light load conditions.

This method has always been used since then, and was applied to "F" and "G" ships, the results of which are shown in Fig. 11 and Fig. 12 respectively. "F" ship is a sister ship of "A" ship. Their hulls, engines and propellers are just the same, and so in Fig. 11, the same curve as in Fig. 6 was added.

Fig. 5, inserted before as an example, is one of the measuring records on "G" ship. It is the most recent measurement.

413

"D" SHIP, REFRIGERATED BOAT

$75^m \times 12.6^m \times 6.3^m$
ENG. 2,400 BHP x 200 RPM

$\Delta = 1,644$ t

WITH WIND   AGAINST WIND
   o   ∀   MEASURED VALUE

CORRECTED FOR WIND
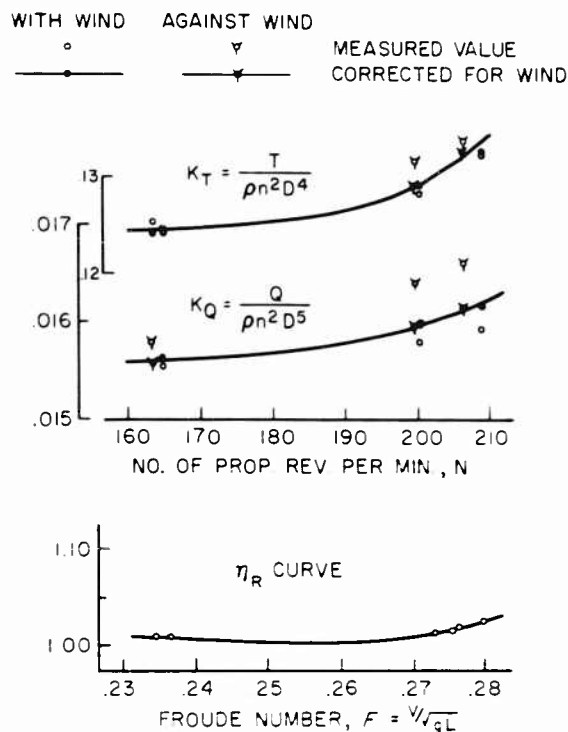
Fig. 9 - K_T, K_Q and η_R curves
of "D" ship

ANALYTICAL RESULTS OF THE TRIAL DATA

These trial data were analyzed and corrected for wind and tidal current by the method of standardized analysis of speed trial results adopted by the J.T.T.C. as mentioned before. Accordingly, reliable values of ship's speed, number of propeller revolutions per minute, torque and thrust in the condition of no wind and still water could be obtained at the speed trials, corresponding to those obtained at the self-propulsion test of the similar models.

The final results of the speed trials were further analyzed, and the wake fraction and relative rotative efficiency of actual ships could be calculated. The open propeller characteristics used in the calculation, except in the case of "C" ship, were deduced from the Troost B-series, and corrected for boss ratio, blade area ratio and so on, because the propellers of those ships belong to the modified Troost type. In the special case of "C" ship, the open test of the model

414

Fig. 10 - K_T, K_Q and η_R curves of "E" ship

propeller quite similar to the actual one was carried out, and its result was used in the calculation.

The model experiments, except in the case of "D" ship, were carried out at Mejiro Model Basin of Transportation Technical Research Institute, but "D" ship only was experimented at the experimental tank of Osaka Pref. University with a small model, and the values of torque at the self-propulsion test could not be measured. Moreover, the sectional size of the tank seemed to be small in relation to that of the model. Accordingly, the wake fraction depending on K_Q and relative rotative efficiency of the model ship are left in blank, and the wake fraction depending on K_T seems to be less reliable than others.

The wake fraction and relative rotative efficiency are calculated as follows:

1. to calculate the thrust coefficient K_T and torque coefficient K_Q, where $K_T = T / \rho n^2 D^4$; $K_Q = Q / \rho n^2 D^5$.

2. to find the advance coefficient J_T and the open propeller efficiency η_P in the chart of open propeller characteristics corresponding to K_T.

415
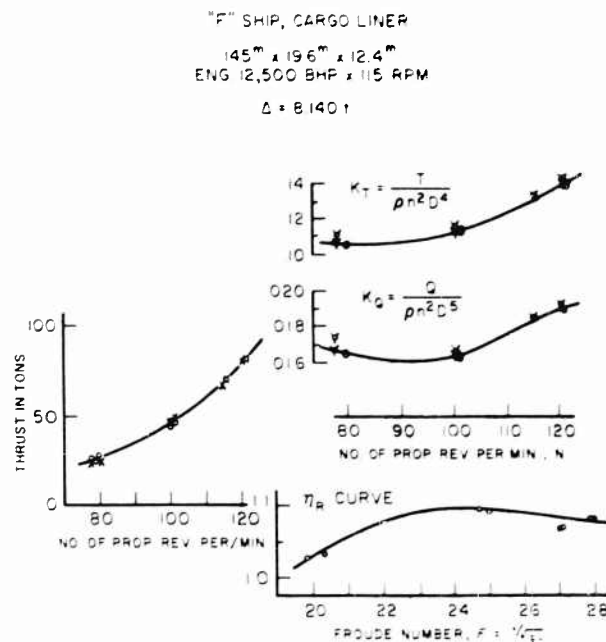
Fig. 11 - K_T, K_Q and η_R curves
of "F" ship
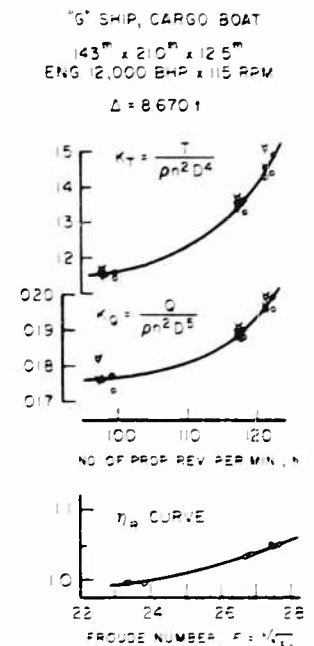
Fig. 12 - K_T, K_Q and η_R
curves of "G" ship

3. to find the advance coefficient J_Q corresponding to K_Q as mentioned above.

4. to calculate the advance speed of propeller V_{1T} and V_{1Q}, depending on K_T and K_Q respectively; where $V_1 = nDJ$.

5. to calculate the wake fractions, as $1 - w = V_1/V_S$. Thus, two kinds of wake fractions w_T and w_Q are obtained depending on K_T and K_Q respectively.

6. to calculate the propeller efficiency behind the ship η_p', where $\eta_p' = K_T J_T / 2\pi K_Q$. Then the relative rotative efficiency $\eta_R = \eta_p'/\eta_p$.

Thus, the scale effect on the two of the self-propulsion factors is clarified in comparison with the values of similar models. It is regretted, however, that the thrust deduction coefficients cannot be examined because the resistance of the hulls is unmeasurable.

The wake fractions and relative rotative efficiencies thus obtained are tabulated both on the actual ships and the similar models in Tables 1-C to 1-G, and the ratios of wake fractions of an actual ship to that of a model ship, expressed $1 - w_S / 1 - w_M$, are plotted in Fig. 13-1 and Fig. 13-2 based on K_T and K_Q respectively. The same ratios of relative rotative efficiency, η_{RS}/η_{RM} are shown in Fig. 14.

416

"C" Ship, Super Tanker

L x B x D	211.8 m x 31.7 m x 15.14 m
Load Condition	Full Load
Draught (mean)	11.378 m
Displacement	61,470 t
Coefficients $\begin{cases} C_B \\ C_P \\ C \end{cases}$	0.766 0.791 0.994
Machinery	17,500 SHP x 105 RPM
Propeller	
Dia. x Pitch Ratio	6.605 m x 0.765
Model Length	6.500 m
Scale of Model	1/32.58

Table 1-C
Analytical Results

V_S in K_t		14.298	14.205	14.293	16.651	16.760	16.720	17.034	17.159	17.234
		0.1563	0.1573	0.1562	0.1847	0.1855	0.1851	0.1866	0.1903	0.1906
R_e x 10^{-4} (Hull)		1.229	1.221	1.229	1.434	1.441	1.437	1.464	1.475	1.482
R_e x 10^7 (Prop.)		2.370	2.363	2.368	2.879	2.894	2.895	2.975	2.993	2.998
Wake Fraction	w_{TS}	0.418	0.417	0.420	0.403	0.404	0.402	0.405	0.409	0.411
	w_{TM}	0.465	0.466	0.465	0.450	0.450	0.450	0.445	0.445	0.445
	$1-w_{TS}\ 1-w_{TM}$	1.088	1.092	1.084	1.085	1.084	1.087	1.075	1.071	1.067
	w_{QS}	0.389	0.388	0.390	0.388	0.390	0.390	0.394	0.398	0.400
	w_{QM}	0.428	0.430	0.428	0.404	0.404	0.404	0.406	0.406	0.407
	$1-w_{QS}\ 1-w_{QM}$	1.057	1.074	1.067	1.027	1.024	1.024	1.017	1.014	1.012
Rel. Rot. E.	$\bar{}_{RS}$	1.038	1.038	1.038	1.015	1.016	1.015	1.015	1.014	1.014
	$\bar{}_{RM}$	1.028	1.027	1.028	1.030	1.029	1.029	1.026	1.025	1.024
	$\bar{}_{RS}/\bar{}_{RM}$	1.010	1.011	1.010	0.985	0.989	0.989	0.989	0.989	0.990
$1-t_M$		0.795	0.795	0.795	0.802	0.802	0.802	0.803	0.803	0.804

Table 2-C
ΔC_F Values x 10^3

Based on K_T	I.T.T.C. 1957	-0.027	-0.015	-0.037	0.001	0.001	0.005	0.055	0.035	0.025
	Schoenherr	-0.116	-0.102	-0.126	-0.081	-0.079	-0.076	-0.022	-0.041	-0.053
	Hughes	0.297	0.310	0.287	0.313	0.316	0.319	0.370	0.348	0.337
Based on K_Q	I.T.T.C. 1957	-0.056	-0.047	-0.066	0.046	0.047	0.050	0.102	0.084	0.068
	Schoenherr	-0.145	-0.134	-0.155	-0.036	-0.033	-0.031	0.022	0.005	-0.010
	Hughes	0.268	0.278	0.258	0.378	0.382	0.384	0.414	0.394	0.380

Note: Hughes' Form Factor K = 0.307

417

"C" Ship, Super Tanker

L x B x D	211.8 m x 31.7 m x 15.14 m
Load Condition	Half Load
Draught (mean)	7.315 m
Displacement	35,040 t
Coefficients $\begin{cases} C_B \\ C_p \\ C \end{cases}$	0.760 0.767 0.990
Machinery	17,500 SHP x 105 RPM
Propeller	
Dia. x Pitch Ratio	6.605 m x 0.735
Model Length	6.500 m
Scale of Model	1/32.58

Table 1-C'

Analytical Results

	V_S in K_t	14.666	14.713	17.149	17.091	17.553	17.447
	F	0.1646	0.1629	0.1898	0.1892	0.1946	0.1931
	$R_e \times 10^{-9}$ (Hull)	1.211	1.195	1.397	1.392	1.432	1.421
	$R_e \times 10^{-7}$ (Prop.)	2.259	2.235	2.757	2.753	2.822	2.800
Wake Fraction	w_{TS}	0.470	0.465	0.450	0.449	0.452	0.451
	w_{TM}	0.522	0.522	0.515	0.515	0.512	0.513
	$1-w_{TS} \quad 1-w_{TM}$	1.109	1.113	1.134	1.136	1.123	1.127
	w_{QS}	0.422	0.421	0.426	0.425	0.433	0.431
	w_{QM}	0.510	0.511	0.500	0.500	0.493	0.490
	$1-w_{QS} \quad 1-w_{QM}$	1.150	1.154	1.145	1.150	1.105	1.116
Rel. E. Rot. E.	$_{RS}$	1.065	1.065	1.030	1.031	1.023	1.025
	$_{RM}$	1.006	1.005	1.015	1.015	1.017	1.016
	$_{RS} \quad _{RM}$	1.059	1.060	1.015	1.016	1.006	1.009
	$1-t_M$	0.795	0.795	0.803	0.803	0.802	0.803

Table 2-C'
$\Delta C_F \times 10^3$

Based on K_T	I.T.T.C. 1957	0.171	0.182	0.281	0.297	0.202	0.222
	Schoenherr	0.087	0.093	0.208	0.221	0.127	0.147
	Hughes	0.472	0.482	0.577	0.591	0.493	0.515
Based on K_Q	I.T.T.C. 1957	-0.035	-0.021	0.225	0.235	0.175	0.183
	Schoenherr	-0.122	-0.110	0.152	0.162	0.103	0.105
	Hughes	0.263	0.279	0.521	0.532	0.469	0.476

Note: (1) Hughes' Form Factor $K = 0.315$.

(2) Water on the mile-post course is 35 m in depth, so the shallow water seems
to have an effect on the values. But ΔC_F values are corrected for the shal-
low water effect by Sudō's method (J.S.. N.A. of Japan No. 105, 1960).

"D" Ship, Refrigerated Boat

L x B x D	75.0 m x 12.6 m x 6.3 m
Load Condition	about 1/5 Load
Draught (mean)	2.77 m
Displacement	1,664 t
Coefficients $\begin{cases} C_B \\ C_P \\ C \end{cases}$	0.619 0.671 0.992
Machinery	2,400 BHP x 200 RPM
Propeller	
Dia. x Pitch Ratio	3.300 m x 0.661
Model Length	2.273 m
Scale of Model	1/33.0

Table 1-D
Analytical Results

	V_s in K.		12.753	12.595	14.663	14.759	14.872	15.063
	τ		0.2394	0.2415	0.2746	0.2770	0.2785	0.2821
	$R_e \times 10^{-9}$ (Hull)		0.4153	0.4190	0.4764	0.4804	0.4832	0.4894
	$R_e \times 10^{-7}$ (Prop.)		1.235	1.249	1.511	1.523	1.561	1.580
Wake Fraction	w_{TS}		0.369	0.369	0.344	0.346	0.342	0.345
	w_{TM}		0.560	0.555	0.515	0.513	0.512	0.510
	$1-w_{TS}\ 1-w_{TM}$		1.434	1.427	1.352	1.348	1.345	1.330
	w_{QS}		0.362	0.362	0.334	0.336	0.329	0.332
	w_{QM}							
	$1-w_{QS}\ 1-w_{QM}$							
Rel. Rot. E.	η_{RS}		1.011	1.012	1.015	1.015	1.019	1.025
	η_{RM}							
	η_{RS}/η_{RM}							
	$1-t_M$		0.765	0.765	0.765	0.765	0.765	0.765

Table 2-D
$\Delta C_F \times 10^3$

Based on K_T		I.T.T.C. 1957	0.653	0.635	0.115	-0.004	0.179	-0.032
		Schoenherr	0.505	0.455	-0.044	-0.166	0.015	-0.189
		Hughes	1.067	1.016	0.475	0.359	0.537	0.331
Based on K_Q		I.T.T.C. 1957						
		Schoenherr						
		Hughes						

Note: (1) Hughes' Form Factor $K = 0.292$.

(2) Size of the exp. tank used is small in relation to that of the model.
($A/A_T = 0.033$). Results of exp. were corrected for the restricted effect by
Nagasaki Method (Tech. Rep. of Mitsubishi Zōsen). But values of w_{TM} still
seem to have some effect.

"E" Ship, Small Tanker

L x B x D	112.0 m x 16.8 m x 8.80 m
Load Condition	Full Load
Draught (mean)	7.310 m
Displacement	10,024 t
Coefficients $\begin{cases} C_B \\ C_P \\ C \end{cases}$	0.713 0.722 0.988
Machinery	3,800 BHP x 200 RPM
Propeller Dia. x Pitch Ratio	3.600 m x 0.642
Model Length	5.500 m
Scale of Model	1/20.36

Table 1-E
Analytical Results

	V_S in K_t		11.709	11.723	13.576	13.615	14.200	14.166
	$\overline{v}$		0.1794	0.1796	0.2080	0.2086	0.2176	0.2171
	$R_e \times 10^{-9}$ (Hull)		0.6280	0.6287	0.7281	0.7302	0.7616	0.7597
	$R_e \times 10^{-7}$ (Prop.)		1.611	1.606	1.918	1.923	2.022	2.017
Wake Fraction	$\overline{w}_{TS}$		0.437	0.436	0.450	0.450	0.444	0.444
	$\overline{w}_{TM}$		0.350	0.350	0.350	0.350	0.350	0.350
	$1-\overline{w}_{TS}$ $1-\overline{w}_{TM}$		0.905	0.907	0.887	0.887	0.897	0.897
	$\overline{w}_{QS}$		0.419	0.421	0.396	0.396	0.388	0.388
	$\overline{w}_{QM}$		0.364	0.364	0.371	0.372	0.374	0.374
	$1-\overline{w}_{QS}$ $1-\overline{w}_{QM}$		0.914	0.911	0.960	0.962	0.975	0.975
Rel. Rot. E.	$\overline{\eta}_{RS}$		1.021	1.020	1.055	1.055	1.056	1.056
	$\overline{\eta}_{RM}$		1.020	1.020	1.015	1.015	1.013	1.013
	$\overline{\eta}_{RS}/\overline{\eta}_{RM}$		1.001	1.000	1.039	1.039	1.042	1.042
	$1-t_M$		0.794	0.794	0.791	0.791	0.789	0.789

Table 2-E
ΔC_F Values x 10^3

Based on K_T	I.T.T.C. 1957	0.661	0.632	0.704	0.684	0.605	0.614
	Schoenherr	0.576	0.548	0.629	0.608	0.532	0.540
	Hughes	0.892	0.862	0.925	0.905	0.821	0.829
Based on K_Q	I.T.T.C. 1957	0.656	0.632	0.524	0.505	0.406	0.414
	Schoenherr	0.571	0.548	0.449	0.429	0.333	0.340
	Hughes	0.888	0.862	0.745	0.726	0.622	0.629

Note: Hughes' Form Factor K = 0.275.

"E" Ship, Small Tanker

L x B x D	112.0 m x 16.8 m x 8.80 m
Load Condition	Half Load
Draught (mean)	4.855 m
Displacement	6,221 t
Coefficients $\begin{cases} C_B \\ C_p \\ C \end{cases}$	0.671 0.684 0.980
Machinery	3,800 BHP x 200 RPM
Propeller Dia. x Pitch Ratio	3.600 m x 0.642
Model Length	5.500 m
Scale of Model	1/20.36

Table 1-E'
Analytical Results

	12.514	12.602	14.376	14.311	14.869	14.828
V_S in K_t						
$\tilde{c}$	0.1917	0.1931	0.2202	0.2193	0.2278	0.2272
$R_e \times 10^{-9}$ (Hull)	0.6532	0.6578	0.7504	0.7470	0.7762	0.7740
$R_e \times 10^{-7}$ (Prop.)	1.618	1.624	1.909	1.922	2.039	2.035

		12.514	12.602	14.376	14.311	14.869	14.828
Wake Fraction	W_{TS}	0.420	0.422	0.422	0.421	0.424	0.422
	W_{TM}	0.429	0.429	0.420	0.420	0.418	0.419
	$1-W_{TS}/1-W_{TM}$	1.016	1.012	0.997	0.998	0.990	0.995
	W_{QS}	0.426	0.430	0.405	0.407	0.395	0.395
	W_{QM}	0.424	0.424	0.415	0.415	0.410	0.410
	$1-W_{QS}/1-W_{QM}$	0.997	0.990	1.012	1.014	1.025	1.025
Rel. Rot. E.	$\tilde{\eta}_{RS}$	0.991	0.992	1.017	1.016	1.032	1.031
	$\tilde{\eta}_{RM}$	1.010	1.010	1.010	1.010	1.010	1.010
	$\tilde{\eta}_{RS}/\tilde{\eta}_{RM}$	0.981	0.982	1.007	1.006	1.022	1.021
$1-t_M$		0.794	0.793	0.751	0.751	0.750	0.750

Table 2-E'
$\triangle C_F$ Values x 10^3

Based on K_T		I.T.T.C. 1957	0.493	0.460	0.557	0.579	0.674	0.685
		Schoenherr	0.404	0.371	0.478	0.500	0.599	0.612
		Hughes	0.711	0.677	0.764	0.788	0.881	0.895
Based on K_Q		I.T.T.C. 1957	0.580	0.545	0.522	0.545	0.569	0.584
		Schoenherr	0.491	0.456	0.443	0.466	0.494	0.511
		Hughes	0.798	0.762	0.729	0.754	0.776	0.794

Note: Hughes' Form Factor $K = 0.276$.

"F" Ship, Cargo Liner

L x B x D	145.0 m x 19.6 m x 12.4 m
Load Condition	about 1/5 Load
Draught (mean)	4.59 m
Displacement	8,141 t
Coefficients $\begin{cases} C_B \\ C_P \\ C \end{cases}$	0.606 0.625 0.965
Machinery	12,500 BHP x 115 RPM
Propeller Dia. x Pitch Ratio	6.100 m x 0.820
Model Length	6.000 m
Scale of Model	1/24.167

Table 1-F
Analytical Results

V_S in K_t			15.18	14.77	18.61	18.39	20.21	20.15	20.76	20.78
		ε	0.2039	0.1984	0.2500	0.2470	0.2715	0.2707	0.2789	0.2791
R_e x 10^{-9} (Hull)			1.075	1.046	1.317	1.302	1.431	1.427	1.470	1.471
R_e x 10^{-7} (Prop.)			1.969	1.921	2.498	2.473	2.834	2.823	2.963	2.958
Wake Fraction		W_{TS}	0.267	0.267	0.259	0.256	0.271	0.270	0.280	0.282
		W_{TM}	0.298	0.300	0.289	0.289	0.289	0.289	0.289	0.289
		$1-W_{TS}$ $1-W_{TM}$	1.043	1.047	1.042	1.046	1.025	1.027	1.013	1.010
		W_{QS}	0.255	0.255	0.222	0.218	0.236	0.235	0.235	0.237
		W_{QM}	0.274	0.276	0.261	0.262	0.250	0.251	0.244	0.244
		$1-W_{QS}$ $1-W_{QM}$	1.026	1.029	1.053	1.059	1.019	1.021	1.012	1.009
Rel. Rot. E.		η_{RS}	1.034	1.029	1.096	1.098	1.073	1.072	1.085	1.085
		η_{RM}	1.072	1.072	1.074	1.073	1.088	1.087	1.090	1.091
		η_{RS}/η_{RM}	0.965	0.960	1.020	1.023	0.986	0.986	0.995	0.995
$1-t_M$			0.777	0.780	0.754	0.755	0.748	0.748	0.748	0.748

Table 2-F
ΔC_F x 10^3

Based on K_T	I.T.T.C. 1957	0.014	0.043	0.069	0.104	0.213	0.220	0.223	0.176
	Schoenherr	-0.052	-0.020	0.006	0.043	0.173	0.183	0.177	0.139
	Hughes	0.158	0.187	0.202	0.237	0.345	0.351	0.362	0.323
Based on K_Q	I.T.T.C. 1957	0.141	0.190	-0.010	0.016	0.299	0.279	0.241	0.198
	Schoenherr	0.075	0.127	-0.073	-0.045	0.259	0.242	0.195	0.161
	Hughes	0.285	0.331	0.123	0.149	0.434	0.410	0.350	0.345

Note: Hughes' Form Factor $K = 0.232$.

"G" Ship, Cargo Ship

L x B x D	143.0 m x 21.0 m x 12.5 m
Load Condition	about 1/5 Load
Draught (mean)	4.370 m
Displacement	8,673 t
Coefficients $\begin{cases} C_B \\ C_P \\ C \end{cases}$	0.636 0.652 0.975
Machinery	12,000 BHP x 115 RPM
Propeller	
Dia. x Pitch Ratio	6.100 m x 0.790
Model Length	5.500 m
Scale of Model	1/26.0

Table 1-G
Analytical Results

V_S in K_t		17.012	17.333	17.047	19.521	19.386	19.434	19.594	20.092	19.913
		0.2322	0.2366	0.2327	0.2665	0.2646	0.2653	0.2715	0.2742	0.2718
$R_e \times 10^{-9}$ (Hull)		0.8755	0.8920	0.8772	1.005	0.9976	1.000	1.024	1.034	1.025
$R_e \times 10^{-7}$ (Prop.)		2.171	2.213	2.175	2.607	2.595	2.599	2.670	2.690	2.664
Wake Fraction	w_{TS}	0.285	0.287	0.287	0.307	0.302	0.304	0.330	0.342	0.330
	w_{TM}	0.340	0.340	0.340	0.331	0.331	0.331	0.325	0.326	0.325
	$1-w_{TS}/1-w_{TM}$	1.083	1.080	1.080	1.036	1.043	1.040	0.997	0.977	0.997
	w_{QS}	0.286	0.288	0.287	0.295	0.293	0.294	0.302	0.307	0.307
	w_{QM}	0.320	0.320	0.320	0.301	0.303	0.302	0.295	0.292	0.295
	$1-w_{QS}/1-w_{QM}$	1.050	1.047	1.048	1.009	1.014	1.012	0.990	0.985	0.988
Rel. Rot. E.	$\tilde{}_{RS}$	0.999	0.996	1.000	1.024	1.020	1.020	1.049	1.059	1.047
	$\tilde{}_{RM}$	1.045	1.045	1.045	1.048	1.047	1.047	1.050	1.051	1.050
	$\tilde{}_{RS}/\tilde{}_{RM}$	0.956	0.953	0.957	0.977	0.975	0.975	0.999	1.007	0.997
$1-t_M$		0.730	0.729	0.730	0.723	0.723	0.723	0.722	0.722	0.722

Table 2-G
ΔC_F Values x 10^3

Based on K_T	I.T.T.C. 1957	-0.039	-0.066	-0.044	0.114	0.145	0.165	0.175	0.133	0.147
	Schoenherr	-0.101	-0.128	-0.106	0.052	0.083	0.106	0.115	0.072	0.086
	Hughes	0.130	0.100	0.125	0.280	0.314	0.335	0.343	0.305	0.312
Based on K_Q	I.T.T.C. 1957	0.152	0.141	0.147	0.230	0.276	0.305	0.180	0.086	0.152
	Schoenherr	0.090	0.079	0.085	0.168	0.214	0.241	0.117	0.025	0.091
	Hughes	0.321	0.307	0.316	0.396	0.445	0.470	0.345	0.256	0.317

Note: Hughes' Form Factor K = 0.262.

MARKS	NAME OF SHIP
o	C SHIP, FULL
●	C SHIP, HALT
□	D SHIP
△	E SHIP, FULL
▲	E SHIP, HALT
x	F SHIP
+	G SHIP
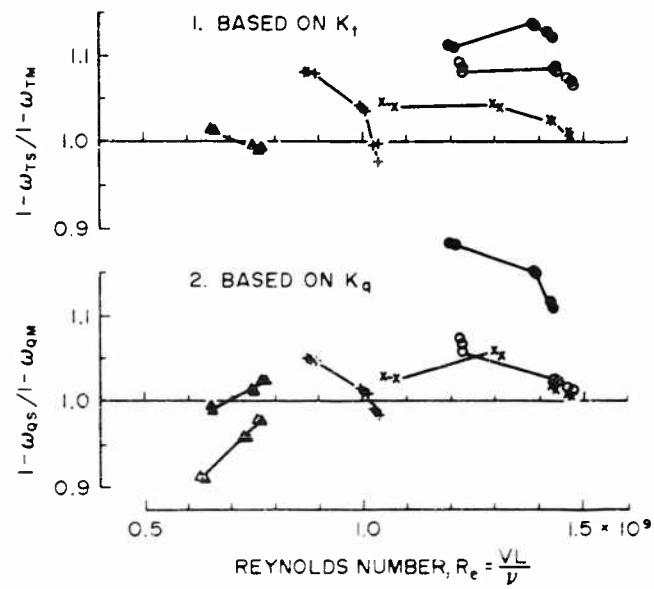
Fig. 13 - The ratio of $1 - w_S$ $1 - w_M$
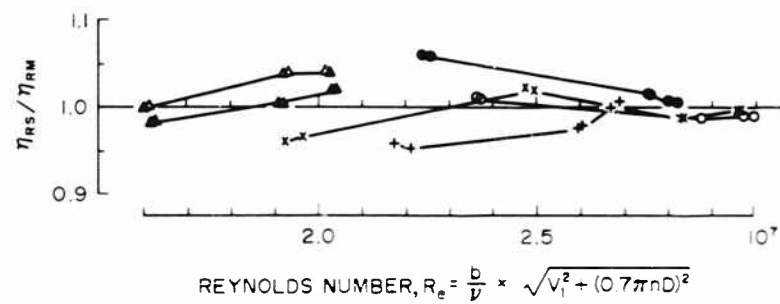
Fig. 14 - The ratio of η_{RS} η_{RM}

424

The so-called ΔC_F values, calculated directly from the values of measured thrust assuming that the thrust deduction coefficients are the same in the actual ship and the model, are compared with those which calculated indirectly from the measured torque, by using the open propeller characteristics and self-propulsion factors derived from the model experiments. These results are summarized in Tables 2-C to 2-G, and also plotted in Figs. 12-1 to 12-3 which are based on the I.T.T.C. 1957 Model-Ship Correlation Line, Dr. Schoenherr's Friction Line and Dr. Hughes' Method respectively.

BASED ON K_T	BASED ON K_Q	NAME OF SHIP
	------o------	C SHIP, FULL
	------•------	C SHIP, HALF
	-----o------	D SHIP
	------▲------	E SHIP, FULL
	------▲------	E SHIP, HALF
	------•------	F SHIP
	------•------	G SHIP

I. BASED ON ITTC 1957 LINE
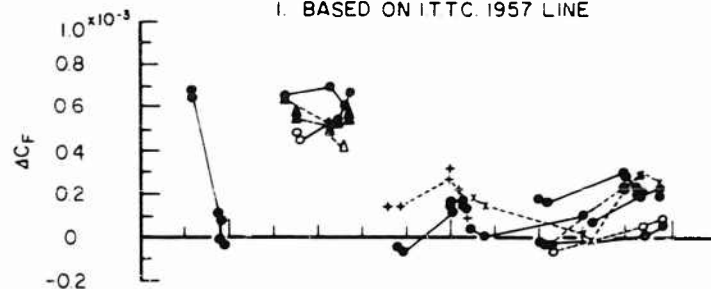
2. BASED ON SCHOENHERR'S LINE
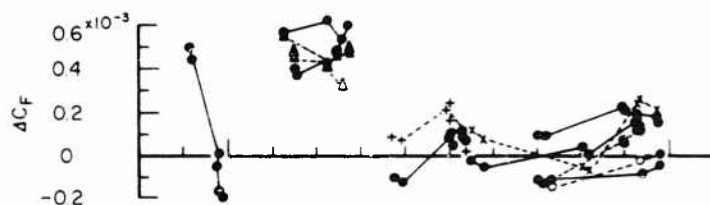
3. BASED ON HUGHES' METHOD

REYNOLDS NUMBER $R_e = \dfrac{VL}{\nu}$
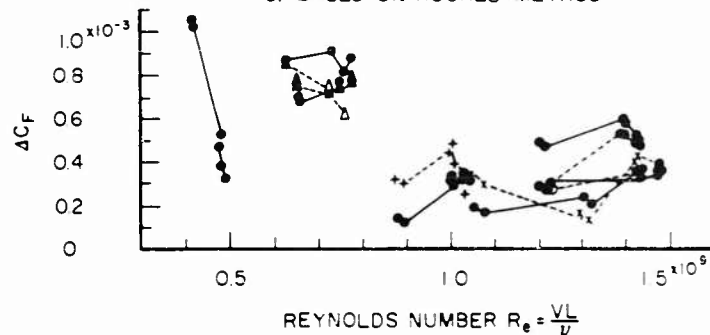
Fig. 15 - ΔC_F values

No definite conclusion can be deduced from these tables and figures, concerning the scale effect on the self-propulsion factors. In order to investigate this subject, it may require more results of the speed trials of actual ships compared with those of self-propulsion tests of similar models.

But it may be said that, as far as the relative rotative efficiency is concerned, there seems to exist very little scale effect between full-scale ships and similar models. Accordingly, it is believed that $\angle c_F$ values calculated directly from the measured thrust would not show much difference from those which are calculated indirectly using the values of measured torque, the open propeller characteristics and self-propulsion factors derived from the model experiments.

CONCLUSION

The authors were successful in measuring the thrust of an actual merchant ship on the mile-post course, and obtained reliable results of the speed trials at sea which are quite similar to the results of self-propulsion tests at the experimental tank. Ever since, they have been making an effort in measuring the thrust of various types of merchant ships and analyzing them in order to investigate the scale effect on the self-propulsion factors.

Though the number of these trial results which have been obtained so far is too small to investigate the subject sufficiently, the outline of the scale effect on the self-propulsion factors may be roughly supposed by referring to the tables and figures in this paper. In conclusion, it may be said that, as far as the relative rotative efficiency is concerned, there seems to exist very little scale effect between the full-scale ship and the similar model.

The authors intend to continue the work of the thrust measurement, and wish to contribute to the investigation of the scale effect on the self-propulsion factors.

SYMBOLS

The symbols used in the paper are as follows:

V_S Speed of ship in knot

Q   Torque in Kg-m

T   Thrust in Kg

n   Number of propeller revolutions per sec

N   Number of propeller revolutions per min

    Density of water in Kg-sec^2/m^4

g   Acceleration due to gravity in m/sec^2

D   Diameter of propeller in m

b   Mean breadth of propeller blade in m

V   Speed of ship or model in m/sec

V_1 Advance speed of propeller in m/sec or knot

$\mathcal{F}$ Froude Number defined $\mathcal{F} = V/\sqrt{gL}$

R_e Reynolds Number defined

$$R_e = \frac{VL}{\nu} \qquad\qquad \text{for hull}$$

$$R_e = \frac{b}{\nu}\sqrt{V_1^2 - (0.7\,\pi\,n\,D)^2} \qquad \text{for propeller}$$

J   Advance coefficient defined $J = V_1 / nD$

K_T Thrust coefficient defined $K_T = T / \rho n^2 D^4$

K_Q Torque coefficient defined $K_Q = Q / \rho n^2 D^5$

w   Wake fraction

t   Thrust deduction coefficient

η_P Open propeller efficiency read in the chart

η_P' Propeller efficiency behind the ship

η_R Relative rotative efficiency defined $\eta_R = \eta_P' / \eta_P$

The first suffix attached to the symbol T or Q means that the value is based on thrust or torque respectively, and the second suffix S or M means that the value corresponds to the actual ship or the model ship. For example, w_{TS} indicates the wake fraction of an actual ship calculated from the measured thrust.

<center>*   *   *</center>

SEA TRIAL ANALYSIS OF THE VERTICAL AXIS PROPELLERS

K. Taniguchi
Mitsubishi Experimental Tank
Nagasaki, Japan

ABSTRACT

Sea trial results of the seven ships equipped with the vertical axis propellers which were designed by the author are analyzed and compared with the calculation.

The fairly good agreement is obtained between the results of the bollard trials and the calculations. The wake fractions obtained from the analysis of speed trials are 0.25-0.35, which are a little bit larger than the expected ones from the model tests. The similarly analyzed resistance-thrust ratios are very smaller than expected and there remains a room for further study.

THE PERFORMANCE CHARACTERISTICS OF VERTICAL AXIS PROPELLER

The author obtained the theoretical formulas [1] of vertical axis propellers which enable to calculate the thrust, torque and efficiency under the adequate assumptions.

In his second paper [2] he got the correction factor of the formulas by carrying out the model experiments. Further he has developed the designing method of this propeller [3,4]. Several types of vertical axis propellers up to 1.000 ps have been designed by the author and manufactured.

In the present paper the author reports the trial analysis results of the seven ships which are installed with these vertical axis propellers.

The method proposed by the author for calculating the performance characteristics of vertical axis propellers is based on the following assumptions:

---

[1]References are listed on page 446.

1. The motion is quasi-steady.

2. Only the longitudinal component of induced velocities contributes to the thrust and torque of the propeller.

3. The longitudinal component of induced velocities is thought to have uniform value over the transverse section of propeller stream. (The correction factor K is introduced for the non-uniformity correction.)

Then choosing the blade motion of the orthodox type which satisfies the relation

$$\tan z = \frac{e \cos \gamma}{1 - e \sin \gamma} \tag{1}$$

between the blade angle z, the eccentricity e and the orbit angle γ, and also choosing the semi-elliptic blade outline in order to obtain the constant induced velocity over the spanwise length of blade, the following formulas are derived.

$$C_T = \frac{\pi^4}{8} a \pi (e - _1) I_1 \tag{2}$$

$$C_T = 2^{-2} \frac{1}{K} (\cdot_1 - \cdot) \tag{3}$$

$$C_Q = \frac{1}{2} C_T \cdot \frac{\pi^4}{8} \cdot \left\{ \frac{C_{x_0}}{2} I_2 - \frac{k}{2} (e - _1)^2 I_3 \right\} \tag{4}$$

$$e_P = \frac{1}{2} \cdot \frac{C_T}{C_Q} \tag{5}$$

where,

$$I_1 = \frac{1}{\pi} \int_{-\pi/2}^{\pi/2} \frac{\sqrt{1 - \cdot_1^2 - 2\cdot_1 \sin \gamma}}{1 - e\cdot_1 - (e - \cdot_1) \sin \gamma} \cos^2 \gamma \, d\gamma$$

$$I_2 = \frac{1}{\pi} \int_{-\pi/2}^{\pi/2} (1 - _1 \sin \gamma) \sqrt{1 - \cdot_1^2 - 2 \sin \gamma} \, d\gamma$$

$$I_3 = \frac{1}{\pi} \int_{-\pi/2}^{\pi/2} \frac{(1 - _1 \sin \gamma) \sqrt{1 - \cdot_1^2 - 2\cdot_1 \sin \gamma}}{\cdot 1 - e\cdot_1 - (e - \cdot_1) \sin \gamma \cdot^2} \cos^2 \gamma \, d\gamma$$

C_T is obtained by solving Eqs. (2) and (3) simultaneously. K in Eq. (3) is the correction factor (project area reduction factor) for the assumption of the uniform distribution of the longitudinal component $\times$ of the induced velocities. Its value can be estimated, provided the distribution of $\times$ is assumed adequately. For instance, K becomes 1.33, if the distribution of $\times$ is assumed as a parabola of third power. C_{x_0} and k in Eq. (4) are the parameters to express the two dimensional drag coefficient C_x of the blade section as follows.

430

$$C_x = C_{x_o} \cdot k\lambda^2 \tag{6}$$

The values of C_{x_o} and k can be derived from the experimental data on aerofoil sections. In the present case the author obtained the values of K, C_x and k from the analysis of the model experiments of the vertical axis propeller, the diameter of which is 200 mm, numbers of blades are 6, $\sigma = 0.4$ and $s/D = 0.6$. In Figs. 1 and 2 the analyzed results are shown
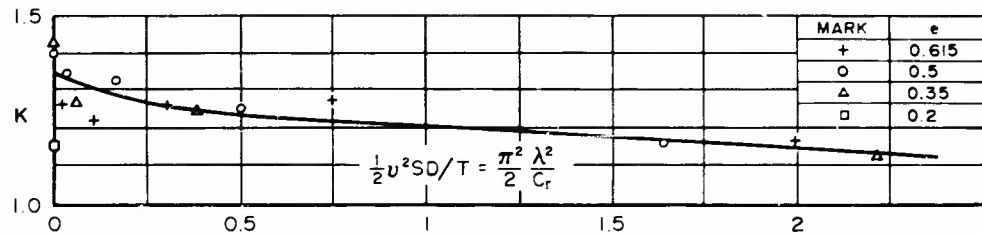
Fig. 1 - Plot for evaluating K
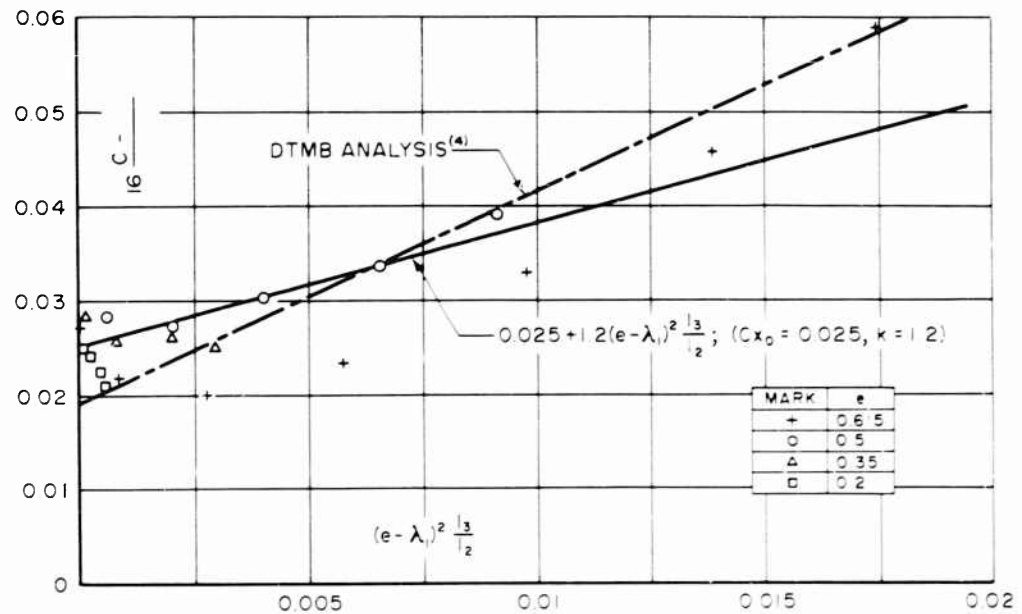
Fig. 2 - Plot for evaluating the section drag coefficient

Generally the minimum drag coefficient C_{x_o} of aerofoil sections can be derived from the frictional resistance coefficient C_f of the flat plate of equivalent size by correcting the thickness effect adequately. By author's experiments C_{x_o} may be expressed approximately by the following equation:

431

$$C_{x_o} = 2C_f\{1 + 38(t/c)^2\}$$ (7)

Since the Reynolds Number based on the mean chord length of blades, i.e., defined as $\overline{C}(\pi n D)/\nu$, is nearly 1.7×10^5 in the case of the author's model tests, the frictional resistance coefficient of the corresponding flat plate may be taken to $C_f = 0.0066$. Also the effective mean chord-thickness ratio is 0.15. Therefore

$$C_{x_o} = 2 \times 0.0066 \{1 + 38 \times 0.15^2\} = 0.0245$$

and this is in good agreement with the analyzed result $C_{x_o} = 0.025$, as being shown in Fig. 2. From this analysis it seems reasonable to correct C_{x_o} for the actual propeller according to its Reynolds Number. Since the Reynolds Number of the blades of the actual vertical propellers of $100 \sim 1,000$ ps is $(3 \sim 5) \times 10^6$, C_f of the blades of actual propellers may be taken to be a half of that of the model in the mean value, i.e., $C_f = 0.0033$. Therefore $C_{x_o} = 0.0125$ is estimated for the actual propeller.

The performance characteristics of actual propellers are calculated by Eqs. (2), (3), and (4) with K and k values given in Figs. 1 and 2 and also C_{x_o} value (0.0125) which is given above.

Figure 3 shows as an example the calculated characteristics for the actual propeller of $z = 6$, $\sigma = 0.4$ and $s/D = 0.6$.

SEA TRIAL

The principal dimensions of the vertical axis propellers designed by the author and those of typical seven ships on which these propellers are installed, are shown in Table 1. These ships have twin vertical axis propellers at the stern and are harbour tugs except Ship B which is a car ferry boat.

The blades of these propellers are all made of Ni-Al-Bz alloy. The outline of the blade is of trapezoid, of which the tip root chord ratio is nearly 0.6 and the tip corners are rounded.

The blade axis is chosen on 40% of the chord length from the leading edge. The thickness form of blade section is symmetrical and its camber line is curved into a circle whose radius is $1.4R$, in order to get an effectively symmetrical section for the mean trochoidal path of blade.

The relation between the blade angle α and the orbit angle θ is not the same as that of the orthodox motion given in Eq. (1), but slightly deformed in the actual case by the limitation from its mechanism. The values of θ at which the maximum and minimum values of α occur are shifted slightly toward $0°$ and $180°$ respectively from the orthodox $\alpha - \theta$ distribution.

In all ships the propeller in the port side rotates counterclockwise and that in the starboard side rotates clockwise, when looking downward.

432
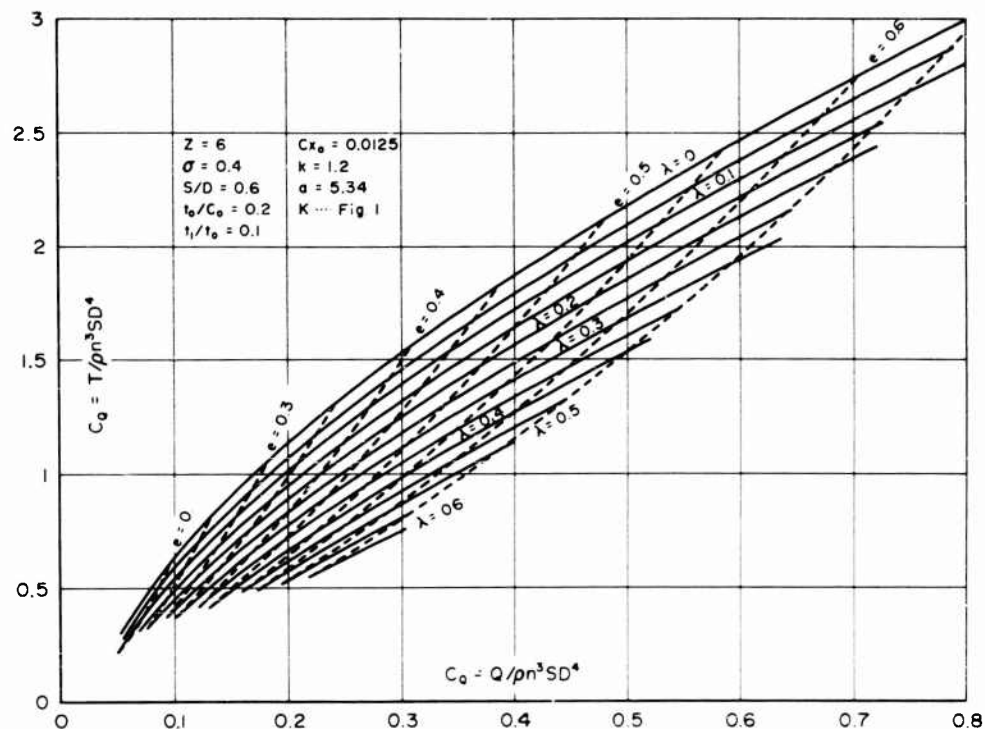
Fig. 3 - Characteristic curves of a vertical axis propeller
(calculated for actual ship)

The bollard trials (except Ship B) and the speed trials were conducted with these seven ships and their powers absorbed by each vertical axis propeller, pull force, ship speed, etc., were measured.

Ship models were made for most ships and the resistance tests were carried out at the same conditions as those of the corresponding ships in the sea trials. The wake measurements at the propeller position were also made using Pitot-tubes on the typical models.

The conditions of actual ships in sea trials and of models in tests are given in Table 2.

The pull force in bollard trials was measured by the tension meter, mainly of strain gauge type. The length of the towing rope used in tests is nearly three times as much as the ship length.

The power absorbed by vertical axis propellers was measured by the torsion meter of the inductance type on the pinion shaft near the propeller. The measured power, named SHP in the present paper, includes not only the power absorbed by propeller blades, named DHP in this paper, the calculations of which

433

Table 1
Principal Particulars of Ships and Vertical Axis Propellers

	Ships	A	B	C	D	E	F	G
Ship Particulars	Type	Tug	Car Ferry	Tug	Tug	Tug	Tug	Tug
	G.T.	20 Ton	260	150	Same as C	220	183	240
	L_{WL}	13.0^m	41.0	28.5		31.0	27.5	32.1
	B_{mld}	4.2^m	8.8	7.6		8.4	8.2	8.5
	$d_{R.L.}$	1.0^m	2.1	2.3		2.6	2.8	2.8
	∇	29.8^t	468.4	281.6		372	315	399
	$C_{b.wl}$	0.533	0.635	0.548		0.535	0.485	0.513
Propeller Particulars	Main Engine	2×130^{PS}	2×320	2×550		2×750	2×900	2×990
	No. of Prop.	2	2	2		2	2	2
	Z	4	5	6		6	6	6
	D	1.000^m	1.600	2.000		2.200	2.400	2.500
	S/D	0.6000	0.6250	0.6000		0.5909	0.6042	0.6000
		0.3820	0.4029	0.4011		0.3993	0.4178	0.4202
	Designed PS/prop.	120^{PS}	320	550		750	850	990
	Designed RPM	192	130.95	105		95.5	87.5	84

Table 2-1.
Particulars of Sea Trials and Model Tests

Ships	A		B	C		D	
			SEA TRIALS				
Trial	Bollard	Speed	Speed	Bollard	Speed	Bollard	Speed
Date	15 Dec. '59	1 Jan. '60	28 Oct. '61	1 Sept. '60	2 Sept. '60	19 Sept. '60	20 Sept. '60
Weather	Rainy	Cloudy	Cloudy	Fine	Fine	Rain	Fine
Wind	-	NNW 1-2 $^{m/s}$	WNW 5 $^{m/s}$	W 2 $^{m/s}$	NNW 2 $^{m/s}$	E 1 $^{m/s}$	NW 6 $^{m/s}$
Sea Cond.	Smooth	Smooth	Smooth	Smooth	Smooth	Smooth	Smooth
Water Temp.	18°C	13.5	23	27	27	29	29
Draft (mean)	1.02 ^{m}	1.030	1.78	2.250	2.262	2.275	2.24
Trim	0.145A^m	0.180A	0.62A	0.105F	0.110F	0.11F	0.04A
Dispt.	32.0^t	33.29	322.7	269.1	271.2	272.0	268.6
			MODEL TESTS				
Scale	1/6.5		1/10	1/10			
L_{wl}	13.02^m		40.41	28.486		Same as C	
$B_{incl. skin}$	4.212^m		4.816	7.616			
Draft (mean)	1.0585^m		1.770	2.241			
Trim	0		0.410A^m	0			
Dispt.	31.238^t		355.0	270.0			
Skin Area	60.28^{m2}		384.0	247.9			
Cb_{wl}	0.5165		0.5463	0.5398			
Cp_{wl}	0.6145		0.5965	0.6004			
Note	Ship lines were modified after model tests.						

435

Table 2-2.
Particulars of Sea Trials and Model Tests

Ships	E		F		G	
	Bollard	Speed	Bollard	Speed	Bollard	Speed
SEA TRIALS						
Trial	Bollard	Speed	Bollard	Speed	Bollard	Speed
Date	10 Nov. '61	11 Nov. '61	8 Feb. '62	6 Feb. '62	21 Dec. '61	20 Dec. '61
Weather	Fine	Fine	Cloudy	Fine	Fine	Fine
Wind	-	NW 2-3 $^{m/s}$	-	W 2-3 $^{m/s}$	SW 8 $^{m/s}$	W 8 $^{m/s}$
Sea Cond.	Smooth	Smooth	Smooth	Smooth	Slight	Slight
Water Temp.	22°C	22	8	8	12	12
Draft (mean)	2.47^m	2.485	(Not measured about same as speed trial)	2.814	2.85	2.87
Trim	0.10A^m	0.03A		0.511A	0.27	0.27A
Dispt.	349^t	352	323.1	323.1	403	408
MODEL TESTS						
Scale				1/10		1/10
L_{wl}				27.409 ^{m}		32.072
$B_{incl. skin}$				8.216 ^{m}		8.516
Draft (mean)				2.849 ^{m}		2.849
Trim				0.511A^m		0.299A
Dispt.				323.1^t		410.0
Skin Area				263.1 $^{m^2}$		314.8
Cb_{wl}				0.4900		0.5126
Cp_{wl}				0.5641		0.5876
Note						

were treated in chapter 1, but also the windage loss of the propeller disk and the mechanical loss of the propeller disk and the mechanical loss of the inner mechanisms of propeller. The difference between SHP and DHP is named idle power.

The measuring methods of speed, revolutions of propeller, etc., are quite same as in the case of the speed trials of ordinary ships.

The eccentricity of actual vertical propeller was obtained from the following procedure. At first the eccentric movement of its needle pointer on the top of the propeller is measured in each run.

Then the maximum and minimum values of z are obtained from this measured movement by the use of the drawings of the vertical axis propeller.

The eccentricity e is taken to be equal to the e value of the orthodox movement corresponding to those maximum and minimum values of z.

ANALYSIS OF BOLLARD TRIALS

Figures 5 and 6 show the results of the measurements of pull force (P) and SHP at the bollard trials in non-dimensional forms, i.e., $P/\rho n^2 s D^3$ and

$$C_{QS} = \frac{75}{2\pi} \frac{SHP}{\rho n^3 s D^4}$$

respectively, and they are plotted on the base of e which is obtained as described above.

In Fig. 4 there are shown not only the values of $P/\rho n^2 s D^3$ derived from the trial results but also the curves of C_T obtained from the author's model tests and obtained from the calculation as described in chapter 1 (Fig. 3). From this figure it can be seen that C_T-curve obtained from the model tests is in fairly good coincidence with those obtained from the calculation and that these curves are in reasonable relations with the values of $P/\rho n^2 s D^3$ derived from trials, since a small thrust deduction may exist among them.

The measured results of Ship G (plotted by + mark) show consistently lower values. This may partly depend on the fact that a strong wind (8 m/s) which was accompanied with waves blew from the bow during the bollard trials.

Although the measured points of $P/\rho n^2 s D^3$ are considerably scattered, their tendency against e seems to agree better with C_T-curve obtained from the model tests than those obtained from the calculation, if Fig. 4 is examined carefully. However, the amount of this difference is so small that C_T-value derived from calculation may be used in order to calculate the thrust deduction factor. Thus calculating the thrust deduction factors on all measured 33 points, we get the mean value of 0.056. This is a reasonable value when compared with the bollard trial results of ordinary tug boats equipped with screw propellers.

In Fig. 5 there are shown not only the values of C_{QS} derived from the measurements at sea trials, but also the curves of C_Q obtained from the calculation
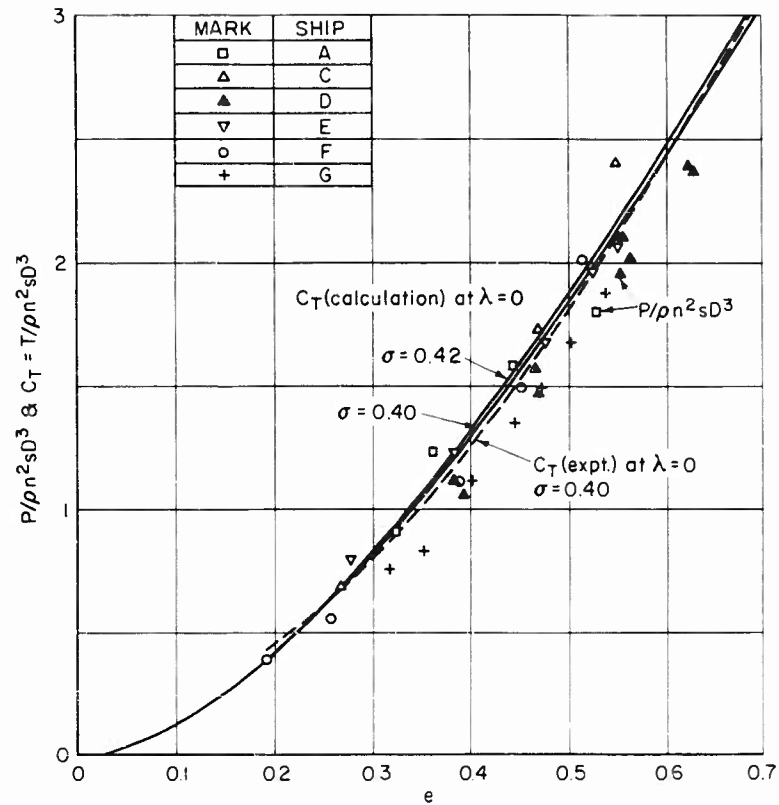
Fig. 4 - Plot of $P/\rho n^2 sD^3$ and C_T (bollard trial)

for actual propellers as described in chapter 1 and obtained from the author's model tests. In this case C_Q of the model tests have been also corrected to the actual propeller, using the difference of the calculated C_Q-values for model and for ship.

The measured values of C_{QS} at $e = 0$ are also shown in this figure. The curves of C_Q obtained from the calculation and from the model tests coincide nearly with each other. Since the calculated values of C_T have been shown to be reasonable as described above, the calculated values of C_Q may be thought to be also correct.

Therefore the difference of C_{QS} and C_Q may be considered to give the idle torque constant C_{Qi} of the propeller. Figure 6 shows C thus obtained on the base of C_{QS}. Though C_{Qi}-values scatter considerably, they increase proportionally to C_{QS} and the relation

$$C_{Qi} = \frac{1}{3} \cdot C_{QS}$$

may be chosen as mean value.

438
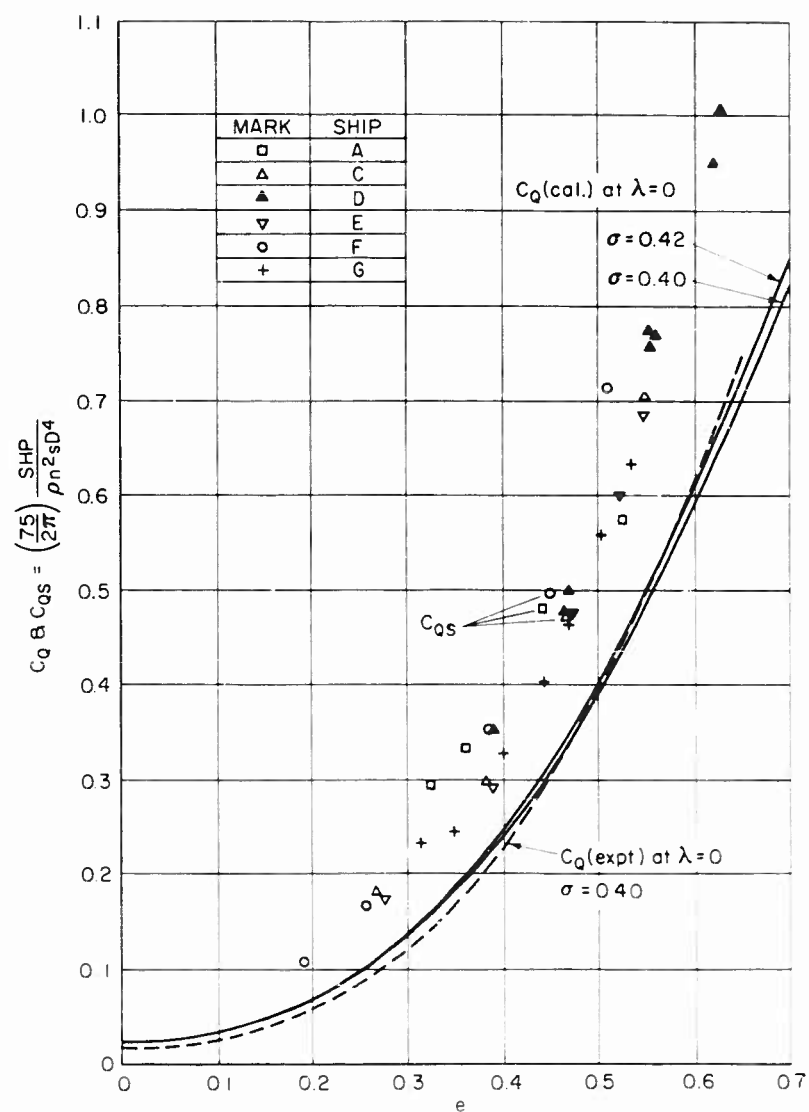
Fig. 5 - Plot of C_{QS} and C_Q (bollard trial)
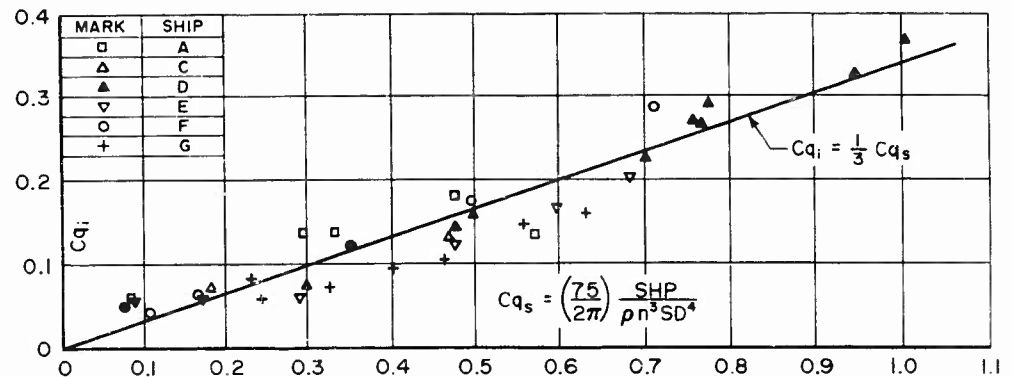
Fig. 6 - Plot of idle torque coefficient

It means that on the vertical axis propellers about $1/3$ of the input power is consumed inside the propeller mechanism as a loss and only about $2/3$ is delivered to the propeller blades. At no load condition, i.e., $e = 0$, the mean value of C_{Qi} is equal to 0.06 and this is approximately 9% of C_{QS} at the designed condition, but with the increase of propeller load C_{Qi} increases remarkably.

The C_{Qi}-values of Ship G are comparatively lower than others.

This may be chiefly due to the fact that the oil pump of this propeller by which the blades are drived is driven by the separate motor outside the propeller, while in all other cases blades are drived by the gear pump which is installed inside the propeller.

The idle power loss is so large that it is very essential to endeavour to reduce it for the further improvement of vertical axis propeller.

Figure 7 shows the direct comparison between the pull force (P) and the input power of the propeller (SHP) at the bollard trials. From this figure it may be seen that the pull force per 100 ps is in the order of 1-1.3 tons. This pull force ratio is somewhat smaller compared with the case of tug boats equipped with controllable pitch propellers and it depends on the larger idle power loss inside the vertical axis propellers.

ANALYSIS OF SPEED TRIALS

Though the idle torque constant C_{Qi} shown in Fig. 6 is obtained from the analysis of bollard trials, it may be applicable also to the case of speed trials. C_Q can be obtained by subtracting C_{Qi} from the measured value of C_{QS}. From this C_Q -value and the e -value measured, the effective wake fraction w_S of the actual ship and the thrust (T) of the propeller are calculated by the torque identity method using the propeller characteristic curves. Thus the resistance-thrust ratio τ is obtained from the propeller thrust (T) and the resistance (R_S), which is deduced from the model tests.
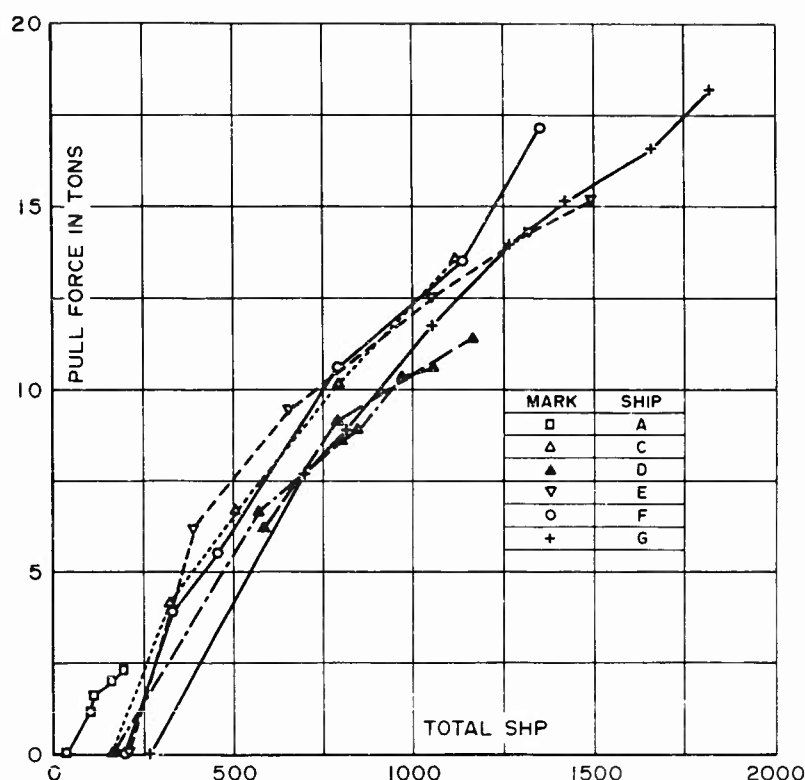
Fig. 7 - Plot of pull force versus total SHP

The speed trial results of seven ships listed in Table 2 have been analyzed by this method. Where the mean value of C_{Qi} as shown in Fig. 6, i.e., $C_{Qi} = 1/3\ C_{QS}$, was used for the correction of idle power, instead of taking individual C_{Qi} of each ship. The propeller characteristics are calculated for σ-value of each propeller by the method described in chapter 1. In the resistance calculation of the actual ship from the model test, the I.T.T.C.-1957 model ship correlation line is used with the roughness allowance of $\triangle C_f = 0.3 \times 10^{-3}$. Figure 8 shows the values of w_S, τ, and the propeller efficiency e_p obtained from these analyses on the bases of Froude's Number. It can be seen that the plot of w_S shows the same trend and is distributed in the range of 0.25 - 0.35. The values of e_p are nearly 0.6 except the lower speed zone irrespective of ships.

The values of w_S are somewhat larger than expected. The wake measurements at the propeller position have been made on the ship model and their volume means were 0.15 - 0.20. Therefore it was expected that the wake of the actual ships might still be less than these values.

The values of τ are considerably different among the ships as shown in Fig. 8 and all ships have the similar trend to increase their values as the speed increases. τ may be expressed as

441
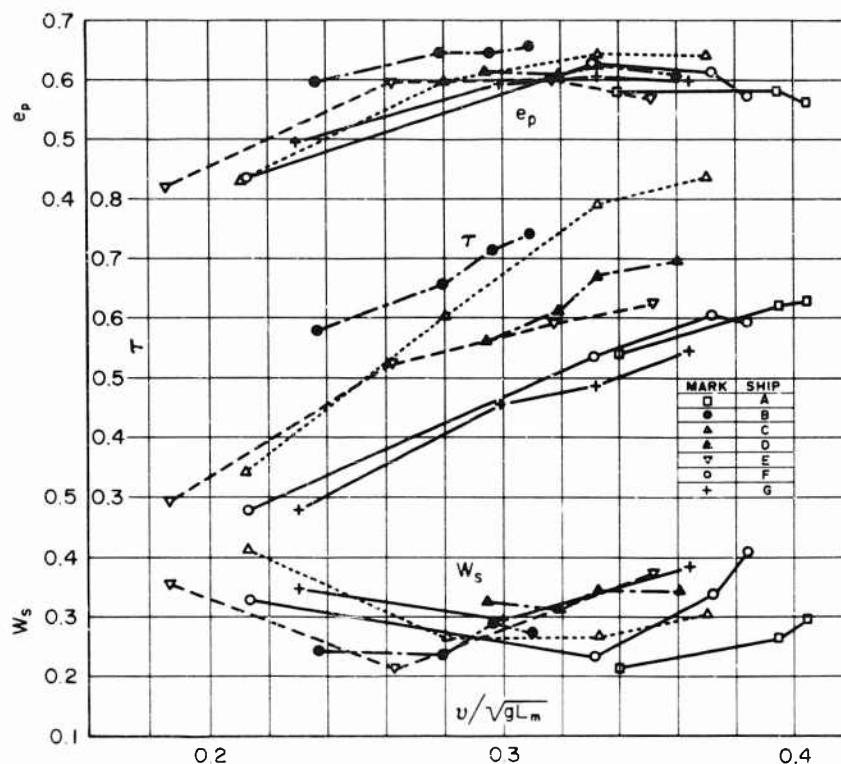
Fig. 8 - Plot of w_S, τ and e_p (speed trial)

$$\tau = e_r \cdot (1 - t)$$

according to its definition, where e_r means the relative rotative efficiency de-
fined on the torque base and t means the thrust deduction factor.

In the case of ordinary tug boats equipped with screw propellers, t is almost
in the same order as w_S and e_r is nearly 1. In the present case, if these rela-
tions hold, τ must be nearly in the same order as $(1 - w_S)$. But τ reaches
nearly the same order as $(1 - w_S)$ only in its maximum value. In the lower
speed zone τ remains considerably smaller than $(1 - w_S)$.

The reason why τ remains in these smaller values must depend on whether
the prediction of the resistance of hulls is too small or the prediction of the
propeller thrust is too large or both. As for the resistance of hulls, it might be
considered that the predicted value is in the tendency to make the under-
estimation, since the roughness allowance of $\triangle C_f = 0.3 \times 10^{-3}$ used in the cal-
culation might be a little bit smaller for the small ship of this kind and incre-
ment of resistance caused by wind and waves should be also considered. Since
the thrust is predicted from the measured torque, the over-estimation of the
thrust means the over-estimation of C_Q and the fact that the values of w_S are
larger than expected as described above seems to support the opinion that the

442

over-estimation of C_Q exists. Though the over-estimation of thrust and w_s can occur also from the incorrectness of the propeller characteristic curves, it might be hard to consider that the over-estimation comes solely from it. Because the prediction of thrust is fairly good coincidence with the measured pull forces in bollard trials, i.e., in the case of $\lambda = 0$, as shown already in Fig. 4.

The author thinks that it comes from the following causes. Firstly, these ships could not be free from the zig-zag runs during the speed trials, because the captain has not been experienced sufficiently to maneuver his ship equipped with the vertical axis propellers. Secondly, the propellers were used partly as a rudder during the runs in order to keep the course from the yawing caused by wind and waves. These actions may consume the considerably large power comparing with the power needed in absolute straight course, especially in low speed. Thus the larger C_Q values might be measured in the trials and the thrust corresponding to these C_Q might become too large when compared directly with the resistance in the straight running.

Besides these, it may be also considered that the thrust deduction of vertical axis propeller becomes considerably larger comparing with the case of screw propeller, as the propeller stream flows in close contact with the bottom of hull.

But it may be hard to discuss these problems further unless the self-propulsion tests are carried out. It is highly desirable to carry out such further researches in order to make clear of these points.

CONCLUSION

The author has made the theoretical and experimental studies on the vertical axis propellers and developed a design method in his previous papers. The several vertical axis propellers ranging 100-1,000 ps have been designed by this method and manufactured. In this paper, the results of sea trials of typical seven ships equipped with these propellers are analyzed and compared with the results of calculations and of model experiments.

The following results are obtained.

1. The pull force measured in bollard trials are in good coincidence with the values estimated from the propeller characteristics which are obtained from the calculations and the model tests (Fig. 4).

2. The pull force per 100 shaft horse power is 1-1.3 tons (Fig. 7).

3. The value of the mechanical loss of propellers, i.e., the idle torque is estimated from the analysis of bollard trials (Figs. 5 and 6). The mean value of it is about $1/3$ of SHP and it is mostly necessary to reduce the idle torque in order to improve the performance of the vertical propellers.

4. The effective wake fraction is obtained from the analysis of the speed trials. It may be taken as 0.25 - 0.35 for the kinds of ships treated in this

analysis (Fig. 8). These values are a little bit larger than the values predicted from the wake measurements on models.

5. The resistance-thrust ratio obtained from the analysis of the speed trials remain in considerably smaller values than expected from the predictions of the relative rotative efficiency and thrust deduction factor. The tendency that the resistance-thrust ratio remains in lower value becomes more remarkable in the lower speed zone.

The reason why it remains in such lower value is not so completely clear at present. It needs further study for this point and also for the larger value of wake fraction by carrying out the self-propulsion tests. But it may be thought that the main reason of it lies in the zig-zag runs during the speed trials.

6. Applying the analyzed results shown in this paper, it is possible to predict the performance in running and bollard pull conditions of ships which are equipped with the vertical axis propellers, with the sufficient accuracy in practical use.

NOMENCLATURE

- D Diameter of propeller (2R)

- s Length of blade (span of blade)

- c Chord length of blade ($\bar{c}$ effective mean of c)

- t Thickness of blade section and thrust deduction factor

- e Eccentricity

- z Number of blades

- V_s Ship speed in knot

- v Speed of advance of propeller

- w Longitudinal component of induced velocities

- v_1 $v + w$

- n R.P.S. of propeller

- T Propeller thrust

- Q Propeller torque delivered to blades

- SHP Power measured at pinion shaft

- DHP Power delivered to propeller blades

444

σ Solidity

ϕ Blade angle

θ Orbit angle

α Angle of incidence

a   Derivative of the lift curve of blade section

K   Project area reduction factor

c_z Lift coefficient of blade section

c_x Drag coefficient of blade section $(c + k)$

c_f Frictional resistance coefficient of flat plate

C_T $T/\rho n^2 s D^3$ thrust constant

C_Q $Q/\rho n^2 s D^4$ torque constant

C_{QS} $(75/2\pi) \cdot SHP/\rho n^3 s D^4$

C_{Qi} $C_{QS} - C_Q$, idle torque constant

e_p Propeller efficiency

e_r Relative rotative efficiency

τ Resistance-thrust ratio

λ Advance ratio, $v/\pi nD$

λ_1 $V_1/\pi nD$

w_S Wake fraction (Taylor's)

ACKNOWLEDGMENT

445

REFERENCES

1. Taniguchi, K., "An Approximate Solution of the Voith-Schneider Propeller," JL of Zosen Kiokai (Trans. Soc. of Naval Arch. of Japan) Vol. 74 (1944), pp. 153-161.

2. Taniguchi, K., "Hydrodynamical Investigations of the Blade Wheel Propeller," JL of Zosen Kiokai, Vol. 88 (1950), pp. 63-74.

3. Taniguchi, K., "Studies on a Trochoidal Propeller," Doctor of Engineering Thesis, Tokyo University (1960).

4. Haberman, W.L. and Harley, E.E., "Performance of Vertical Axis (Cycloidal) Propellers calculated by Taniguchi's Method," DTMB Report 1564 (1961, Nov.).

5. Taniguchi, K. and Watanabe, K., "A New Electric Torsion Meter for High Speed Naval Craft," JI of Zosen Kiokai, Vol. 108 (1960), pp. 105-113.

*   *   *

WATER-JET PROPULSION
FOR SURFACE CRAFT

C. A. Gongwer
Aerojet-General Corporation
Azusa, California

The recent introduction of water-jet propulsion to the commercial market has renewed general interest in the subject. Previous experiments and efforts dating as far back as the 19th century and beyond are known. However, these efforts failed because efficient pumps were not then in existence and also because the systems were usually misapplied. One of the application errors made was to use the wrong ratio of jet velocity to desired forward speed. This meant that efficient propulsion with reasonable sized pumps and ducting could not be obtained and the energy was wasted in high jet velocity.

Also, the design of water intakes for low drag, high ram energy conversion, and resistance to fouling has been a stumbling block.

Furthermore, for high-speed planing hull boats where the running trim angle has a major effect on the drag, the thrust line position and angle is of major importance in that adverse nose-down effects at high speed can result. The outboards and out-drives are examples of excellent competitive solutions to this problem in that the low, nearly horizontal, thrust line holds the nose up well at speeds.

From the above it can be seen that water-jet propulsion is a "system" problem and any particular application must be optimized with all factors taken into account.

GENERAL DISCUSSION - OPTIMUM JET VELOCITY RATIO

Considerations of the energy remaining in the jet wake have caused emphasis on "soft jet" systems where the term "soft jet" means a low value of the ratio, $\Delta v/v$, where Δv is the relative spouting velocity less the forward speed, v. Reference 1 gives an analysis for optimum $\Delta v/v$ in terms of a loss factor, K, which represents total losses in feet of head divided by the velocity head due to forward speed, $v^2/2g$.

Figure 1 gives the results from Reference 1 and shows that for any given loss factor an optimum value of $\Delta V/V$ is obtained. In general, for ducted systems, the optimum values of $\Delta V/V$ lie between 0.7 and 1.2. Below these values the duct and pump sizes increase for a given thrust to handle the larger mass flow and the losses mount correspondingly which results in a large, heavy, ineffective, inefficient system. Above these values in the hard jet region machinery size and weight go down, but the losses in the jet wake become prohibitive.

From the analysis shown in Fig. 1 it also follows that efficiencies of optimized systems will lie in the low and middle sixties. To obtain higher values some convenient means of boundary-layer rather than free-stream induction or some other method must be used.

PUMP SPECIFIC SPEEDS

Pumps are necessarily the actuators for jet-propulsion systems and therefore it is desirable to discuss them briefly. The types considered here are of the turbo-machine type ranging from propeller or axial-flow pumps through the mixed-flow, to the centrifugal or radial-flow types. Positive displacement pumps
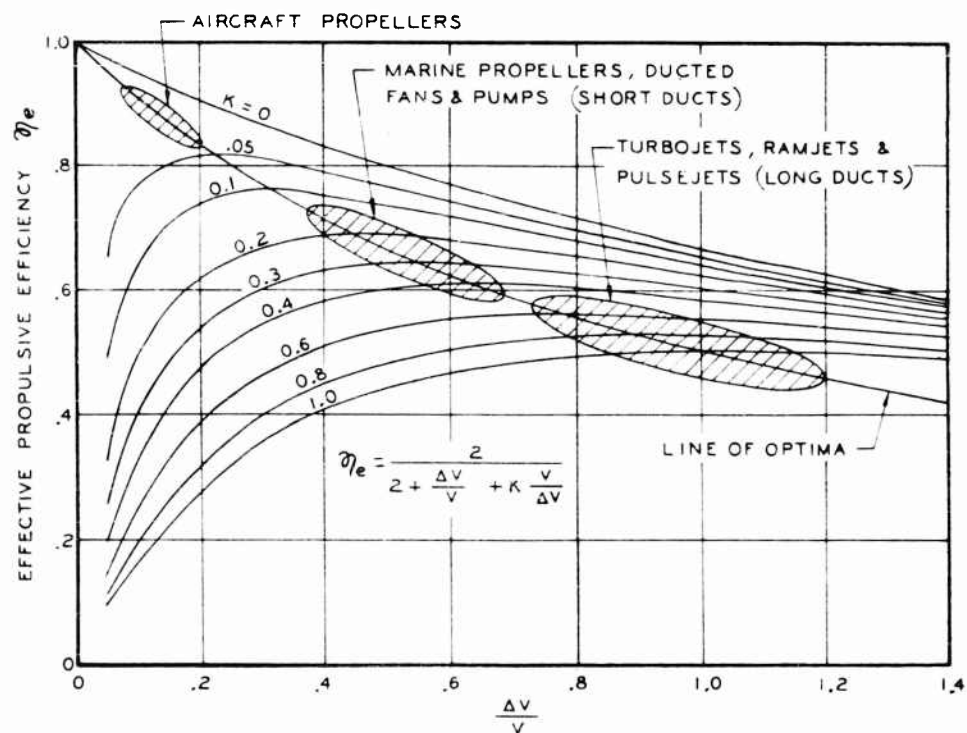
Fig. 1 - Effect of losses on optimum value of $\Delta V/V$

are not suitable at present for jet propulsion because of lower efficiencies and higher weights at the desired operating points.

The operating regime of a pump is described by the term, specific speed,

$$N_s = \frac{N\,Q}{H^{3/4}} \tag{1}$$

where

N is the rotative speed

Q is the volume flow rate

H is the head across the pump or energy added per unit mass of fluid handled.

At their best operating points, single-stage propeller pumps have high specific speeds, mixed-flow pumps have lower and radial-flow or centrifugal pumps have the lowest. Until recently, the best efficiencies were obtainable with centrifugal pumps but advances have removed this difference and, to a first approximation, all the turbo-pump types can have about the same peak efficiencies. One exception is that for radial impellers designed for extremely low specific speeds, the impeller becomes so big in diameter compared to the eye diameter that disc friction causes a fall-off. In this case, multistaging is usually employed.

VARIATION OF PUMP SPECIFIC SPEED WITH FORWARD SPEED

Since the desirable velocity ratios for a wide range of installations fall within the limits of 0.7 to 1.2 it can be shown that the specific speed and hence the best pump type varies with the desired forward speed. For any particular installation which is required to run over a wide range of speed-length ratios the best pump is a propeller type at low speeds, a mixed-flow at speed-length ratios of one or so and a centrifugal type at high speed-length ratios where planing occurs. As a result, compromises must be used and a wide variety of selections can and have been made. These considerations can be altered by multistaging, however, where a three- or four-stage axial flow is equivalent to a single-stage mixed-flow and so on.

PUMP CAVITATION REQUIREMENTS

A pump used for jet propulsion must maintain thrust while accelerating at low forward speed. Under these conditions there is little or no pressure and the diffusing action of the intake scoop may be absent because it is operating off its design point. In fact, the scoop which is designed for a higher speed may act as a restricting orifice. This puts the pump under severe cavitation conditions, particularly for a powerful installation. In this regard, the use of screw inducers ahead of the main pump can have advantageous effects. Recent developments in inducers to increase cavitation resistance, particularly for rocket-propellant

449

pumps, can be borrowed, modified and applied. Since this adverse cavitation condition is normally only a transient there is not a cavitation damage problem.

SCOOP DESIGN

In general, the design of water-jet scoops is similar to that for aircraft scoops. Cavitation and free-surface effects provide a crude analogy with compressibility effects in air. However, fouling and trash intake complicate the water problem.

Scoops may be of the straight ram, flush, and vane lattice types as shown in Fig. 2.

The regimes over which a scoop must operate are shown in Fig. 3. The captive area, A_1, to inlet area, A_2, ratio is an important parameter. The captive area is that enclosed at infinity between the stagnation streamlines which impinge on the scoop lips. At the design point where there are no internal (or external) burbles, Bernoullis' theorem gives the following relationship:

$$H_1 + \left(\frac{Q}{A_1}\right)^2 \frac{1}{2g} = H_2 + \left(\frac{Q}{A_2}\right)^2 \frac{1}{2g} \tag{2}$$

or

$$\frac{H_2 - H_1}{\left(\frac{Q}{A_1}\right)^2 \frac{1}{2g}} = 1 - \frac{A_1^2}{A_2^2} = R \tag{3}$$

when R is the percentage of external diffusion or ram recovery at the scoop entrance as a fraction of the free-stream velocity head. It is usually desirable to have 50 to 75% external diffusion since this type of diffusion is loss-free, provided the external burble is not produced. It can be seen that the angle of attack of the diffuser lips can vary widely as the speed ratio changes and therefore the intake should be carefully rounded to suppress stall and/or cavitation over as wide a range as possible.

It is interesting to note that on acceleration, with a jet unit using a leading edge or vane lattice scoop, the point of diffuser flow attachment and disappearance of the internal burble, Fig. 3 (c) to (d), is definitely noticeable by an increase in thrust and a switch from a vacuum to an overpressure in the ducting.

The vane lattice scoop has the desirable property of providing an easily clearable trash rack.

A JET-PROPULSION HYDROFOIL

A small boat with surface-piercing hydrofoils and water-jet propulsion (Aerojet's "Jet-Foil" boat) has been in operation for a period of 18 months. The general arrangement of this system can be seen in Fig. 4.

Rom or
Leoding-edge
Scoop
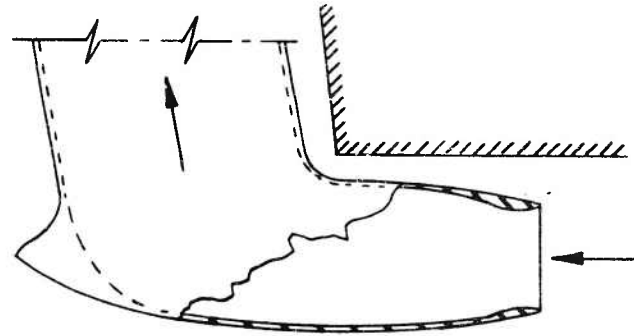
Flush
Scoop
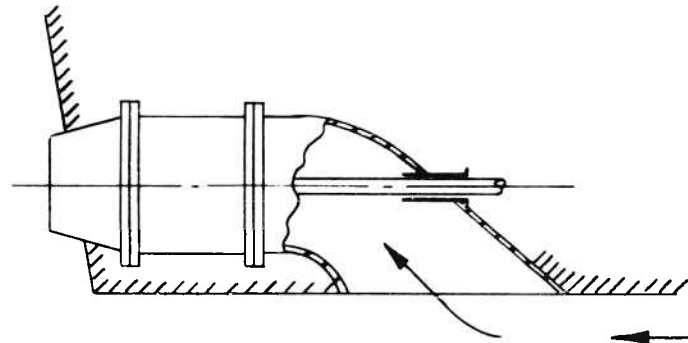
Vone
Lottice
Scoop
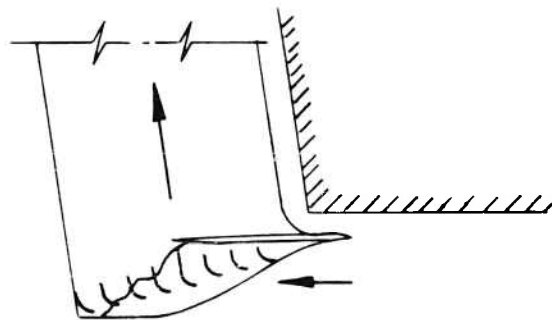
Fig. 2 - Some types of scoops

451

(a) Inlet Flow
at Starting

Internal
burble

(b) Low Forward
Speed

Internal
burble

Capture
Area

(c) Below
Design Speed

Internal
burble

Capture
Area

(d) Design
Speed

Capture
Area

(e) Above
Design Speed

External
burble

Capture
Area
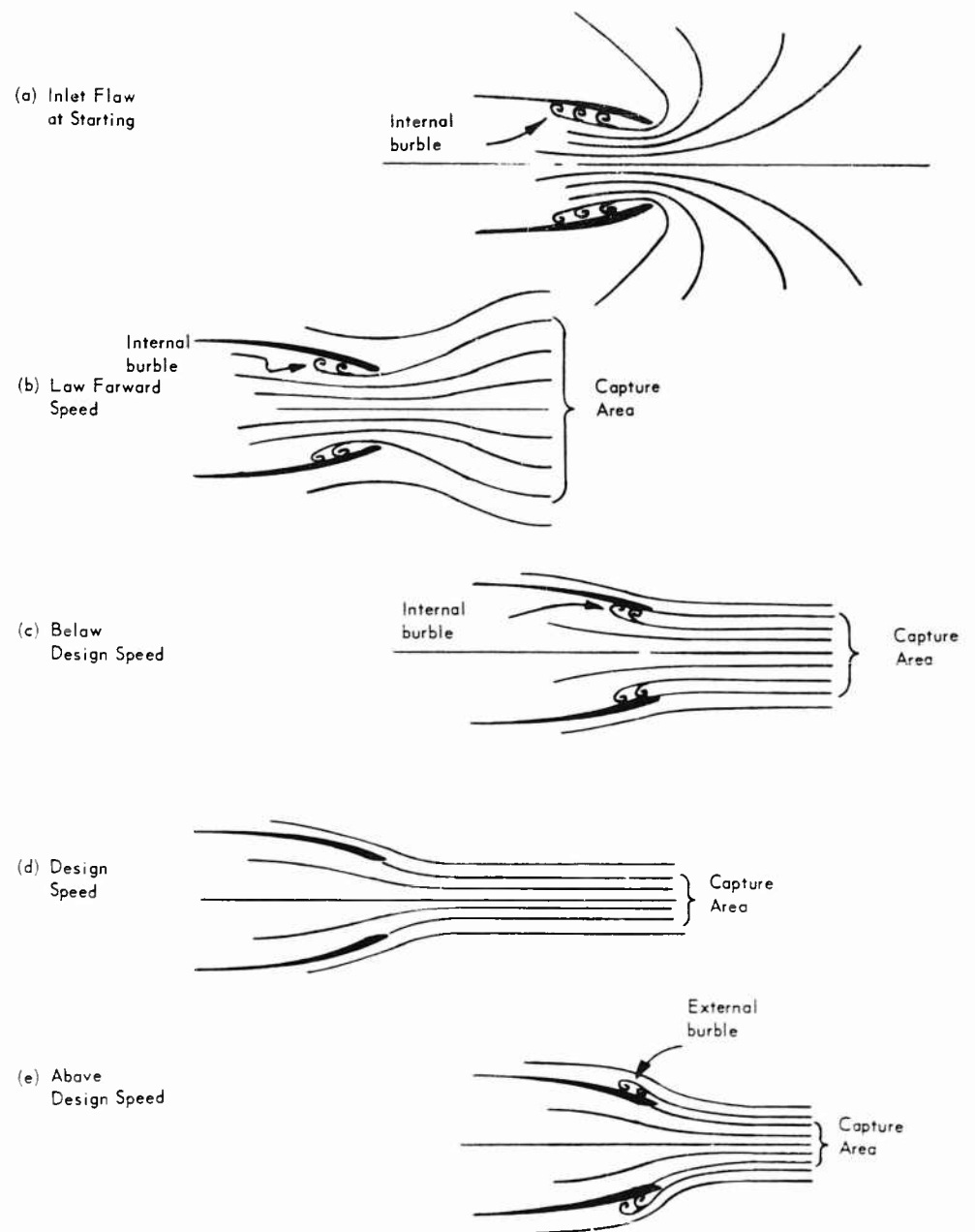
Fig. 3 - Effect of Advance Speed Ratio on Inlet Flow
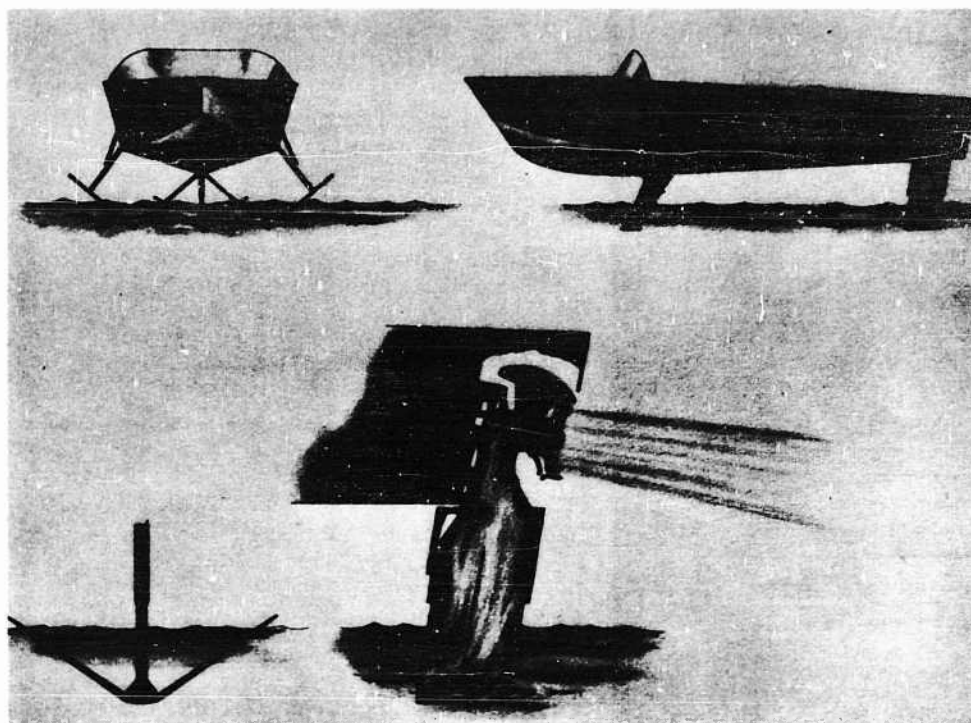
Fig. 4 - Arrangement of water-jet propelled hydrofoil ("Jet-Foil" boat)

Water is inducted up the hollow rear strut and through an axial inducer stage, a stator, and into a special radial-flow impeller with nozzles on its periphery. This particular jet system is the "Hydrocket" of Aerojet-General. It combines the pumping characteristics of a radial-flow pump with certain advantages which include elimination of the pump casing and spiral volute with its diffusion requirement. This eliminates weight, disc friction, pump reverse leakage, diffusion losses in the volute, and ducting on the discharge side of the pump.

The bow aspect of the "Jet-Foil" boat showing the hydrofoil configuration and the stern aspect displaying the hydrocket unit are presented in Figs. 5 and 6. The "Jet-Foil" in operation is shown in Fig. 7.

The system is the first of its kind and is for illustrative purposes. The machinery is extremely simple and light in weight. Also, the underwater noise is of low magnitude.

It is expected that this application of water-jet propulsion may have great significance for the future.
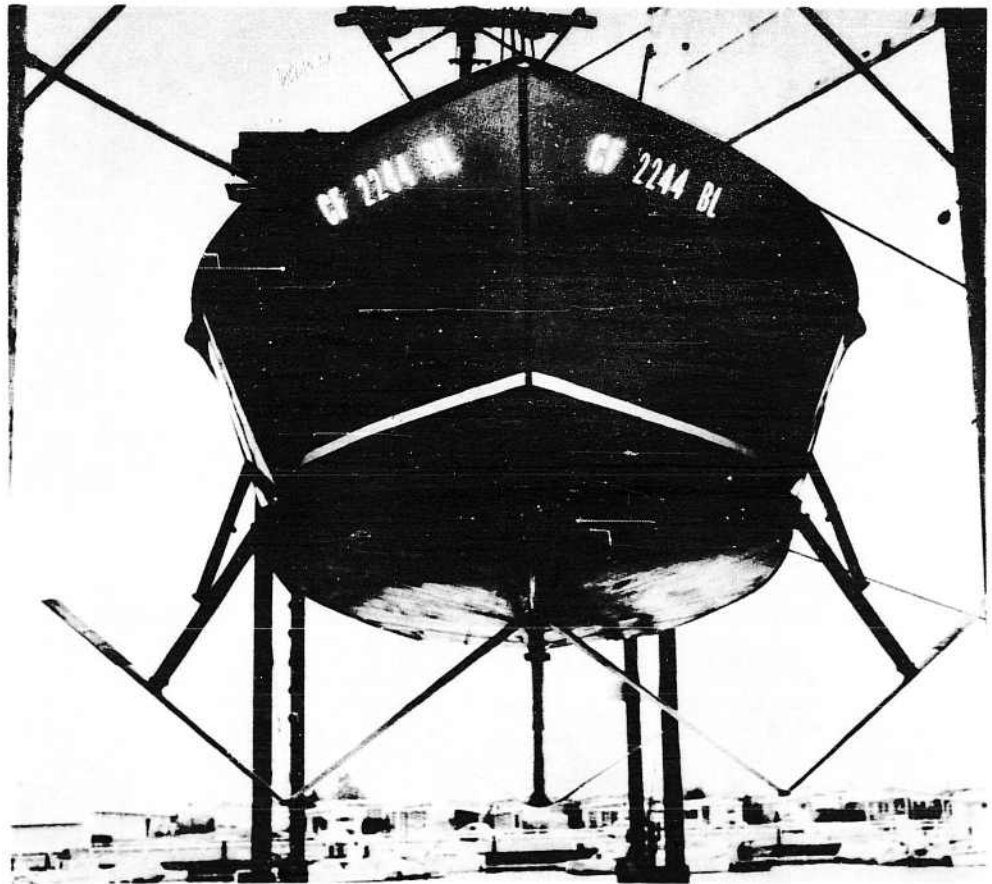
Fig. 5 - Bow aspect of "Jet-Foil" boat showing the hydrofoil configuration
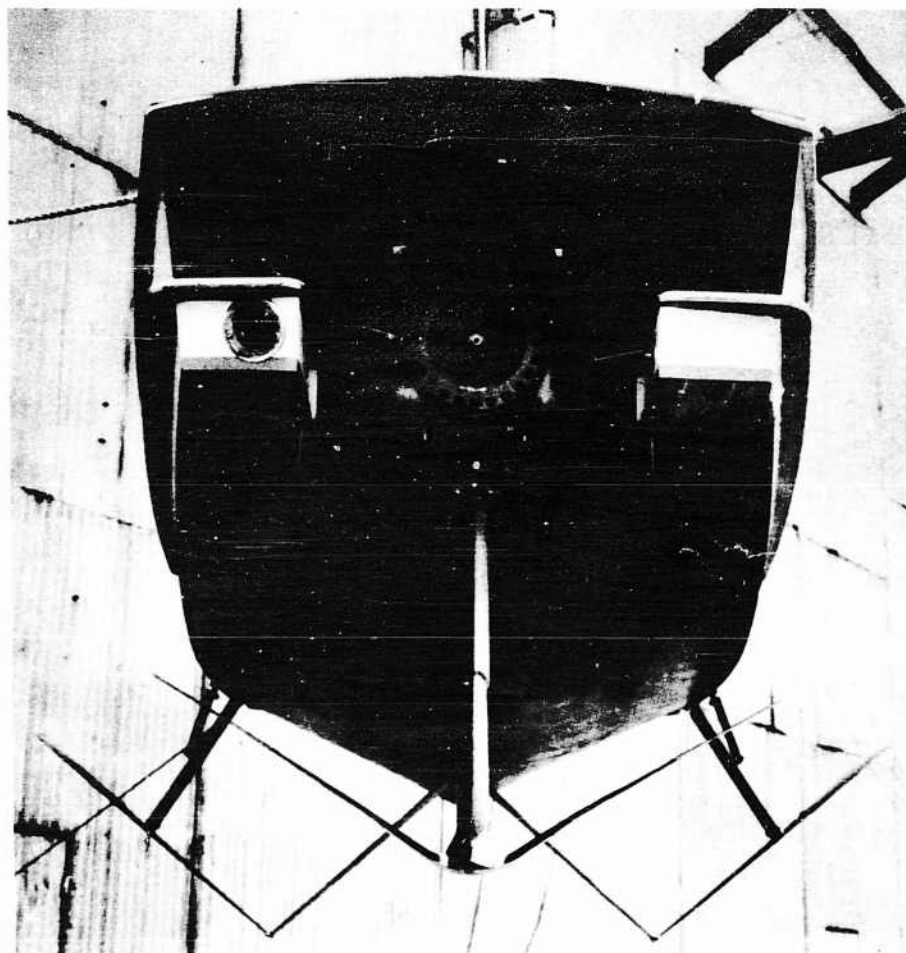
Fig. 6 - Stern aspect of "Jet-Foil" boat showing the hydrojet installation
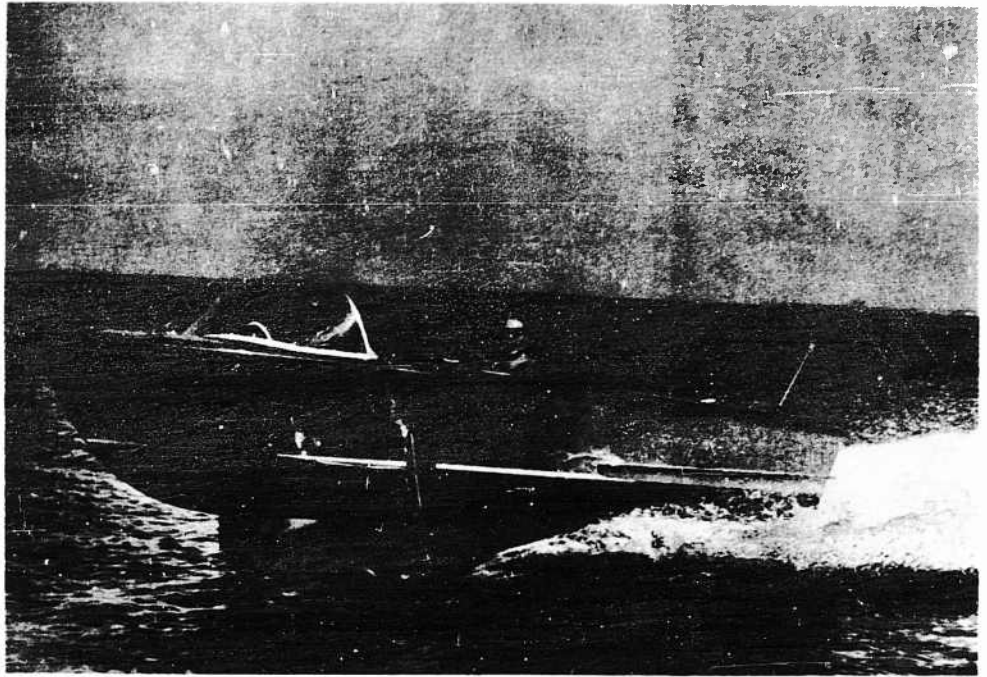
Fig. 7 - "Jet-Foil" boat in operation

REFERENCES

1. Gongwer, C.A., "The Influence of Duct Losses on Jet Propulsion Devices," Jet Propulsion, November-December 1954, Vol. 24, No. 6.

2. Engel, W.N. and Cochran, R.L., "The Use of Axial Flow Pumps for Marine Propulsion," Automotive Engineering Congress, Detroit, Michigan - January 8-12, 1962.

3. Wislicenus, G.F., "Fluid Mechanics of Turbo-Machinery," McGraw-Hill Book Company, Inc., New York, N.Y., 1947.

*   *   *

ACCELERATED SWIMMING
OF A WAVING PLATE

T. Yao-tsu Wu
California Institute of Technology
Pasadena, California

ABSTRACT

This paper deals with the two-dimensional potential flow around a flexible, waving plate which executes a rectilinear swimming motion, the forward velocity of the plate being assumed an arbitrary function of the time. The thrust, power required, and the energy imparted to the wake are determined for this general swimming motion; from these quantities the propulsive efficiency can be evaluated. As a special case of interest, the small time behavior of the solution is examined when the plate starts to swim from the initial state at rest.

INTRODUCTION

From various investigations of the hydrodynamical and bio-chemical performance of fish (such as migratory salmon, see, e.g., Osborne [1] and the references cited therein) and aquatic mammals (such as porpoises and whales, see, e.g., Gray [2,3], Johannessen and Harder [4], Lang [5]), it has frequently been noted that swimming speeds attained by these swimmers are remarkably high in regard to the estimated muscle power available. Attempts to examine in detail their energy requirements have usually led to suggest one or more of the following possible explanations: (1) the ability of fish and cetacea to maintain a laminar boundary layer which would partly become turbulent, or even with separation, at the same Reynolds number if the body should become rigid; (2) their ability to attain a high swimming efficiency so that only a small fraction of the energy input is wasted as a result of the vortex wake they create; (3) an ingenuous navigation in seeking of a low-velocity water route; and (4) an indication of their ability to extract energy from the eddies in the river (the so-called Betz-Knoller effect, which is similar to "tacking" by a sailboat). Their ability of maintaining such top performance under such varied conditions has been long regarded as an astounding engineering achievement.

The analysis of the potential flow outside the boundary layer around the swimming body and its vortex wake is important since, for one reason, it

457

determines the thrust and the ideal power required (for producing the thrust and supplying the energy lost in the vortex wake). The resulting flow field also provides the boundary conditions which are needed in the treatment of the unsteady boundary layer in order to determine how the boundary layer flow develops and how much is the frictional drag.

This external flow has been evaluated in several cases. The swimming of slender fish has been treated by Lighthill [6,7]. There it has been found that in order to give a high propulsive efficiency, the recommended procedure is for the fish to pass a wave down its body at a speed of around $5/4$ of the desired swimming speed, the amplitude increasing from zero over the front portion to a maximum at the tail. Furthermore, the span of the tail should exceed a certain critical value, and the waveform should include both a positive and a negative phase so that angular recoil is minimized.

In a previous paper [8], this author treated the two-dimensional potential flow around a flexible, waving plate of finite chord, the forward swimming speed of the plate being assumed constant. As a numerical example of the general solution, the waving motion with linearly varying amplitude was carried out in detail. The results indicate again that in order to attain a high propulsive efficiency (of the order 95%), the wave velocity of the body motion should be slightly greater than the desired swimming speed, and the wave amplitude should increase gradually towards the tail. This qualitative feature at high propulsive efficiency is thus similar to the case of slender fish. This two-dimensional problem has also been treated by Smith and Stone [9] with some different approximations (the effect of the wake being neglected). A series of experiments on the two-dimensional swimming motion has been conducted by Kelly [10]. Aside from the frictional drag which has not been precisely determined, the measured thrust over a range of wave frequency and wavelength of the body motion provides a substantial support to the theoretical result of Wu.

In this work the previous two-dimensional theory is generalized to the accelerated swimming of a waving plate along an approximately straight course, the forward velocity of the plate being assumed an arbitrary function of the time. Similar to the previous theory, the present problem is formulated by using the acceleration potential and the analysis is carried out by the method of series expansion. (An alternative method is to formulate this problem as a Hilbert problem.) As a special case of interest, the small time behavior of the solution is examined when the plate starts to swim from the initial state at rest. This point of interest arises partly from the observation that the acceleration of some species of fish and cetacea from zero to a maximum speed has been noted to be remarkably high (see, e.g., Gray [11]).

GENERAL FORMULATION

We consider the two-dimensional incompressible flow of an inviscid fluid generated by a deformable thin plate which moves along a straight line in the fluid with an arbitrary time-dependent velocity $U(t)$ and at the same time executes an arbitrary waving motion of small amplitude in the transverse direction. The solid plate is taken to be flexible so that it can simulate a swimming motion.

To fix idea, we choose a Cartesian co-ordinate system (x',y') which is fixed relative to the fluid at infinity such that in this inertial frame the forward velocity(positive in the negative x'-direction)of the plate is $U(t)$. In this paper $U(t)$ is limited to be positive definite so that $0 < U(t) < \infty$ for $t > 0$, but otherwise arbitrary and continuous. (The continuity of $U(t)$ may often be relaxed to some extent.) This implies that the plate may speed up or slow down in the inertial frame, but may never halt to stop or reverse its direction (see **Fig. 1**). Under this assumption the leading edge and trailing edge of the plate will maintain their individual role for $t > 0$.
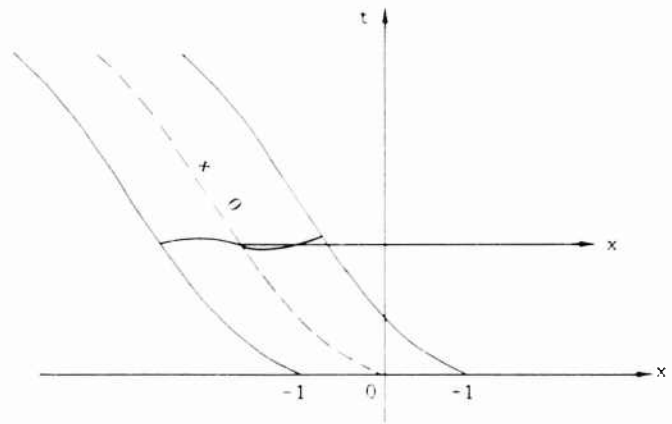
Fig. 1 - The co-ordinate systems

By the Galelian transformation

$$x = x' - \int_0^t U(t)\,dt \quad , \quad y = y' \quad .$$

the motion is referred to a co-ordinate system (x,y) fixed at the plate such that the plate spans (approximately) from $x = -1$ to $x = 1$ and the free stream has the velocity $U(t)$ in the positive x-direction. The motion of the flexible plate may be expressed as: $y = 0$ for $t < 0$ and

$$y = h(x,t) \quad \text{for} \quad -1 < x < 1 \quad , \quad t > 0 \quad . \tag{1}$$

where $h(x,t)$ is an arbitrary continuous function of x for every time t, the amplitude of h and $\partial h/\partial x$ being assumed small compared with unity. The x- and y-component of the perturbed flow velocity will be denoted by $\bar{q} = (u,v)$. By assuming the perturbation velocity (u,v) to be small so that the nonlinear terms may be neglected, the momentum equation can be linearized to give

459

$$\left(\frac{\partial}{\partial t} + U(t) \frac{\partial}{\partial x}\right) \vec{q} = -\frac{1}{\rho} \operatorname{grad} p = \operatorname{grad} \phi \tag{2}$$

where

$$\phi(x, y, t) = (p_\infty - p)/\rho \tag{3}$$

in which ρ is the density, p the pressure of the fluid and p_∞ the pressure at infinity. The function ϕ is Prandtl's acceleration potential, as $\operatorname{grad} \phi$ gives the acceleration of the flow. It follows from (2) and the continuity equation, $\operatorname{div} \vec{q} = 0$, that ϕ is a harmonic function of (x, y) for every t. Consequently a conjugate harmonic function $\psi(x, y, t)$ may be defined by

$$\partial\phi/\partial x = \partial\psi/\partial y \quad , \quad \partial\phi/\partial y = -\partial\psi/\partial x \tag{4}$$

so that in terms of the complex variables $z = x + iy$, the complex acceleration potential

$$f(z, t) = \phi(x, y, t) + i\psi(x, y, t) \tag{5}$$

is an analytic function of z for all t. In terms of $f(z, t)$ and the complex velocity

$$w(z, t) = u(x, y, t) - iv(x, y, t) . \tag{6}$$

(2) may also be written

$$\frac{\partial f}{\partial z} = \frac{\partial w}{\partial t} + U(t) \frac{\partial w}{\partial z} . \tag{7}$$

The boundary condition that the normal component of the velocity relative to the moving solid boundary must vanish may be linearized to give

$$v = \frac{\partial h}{\partial t} + U \frac{\partial h}{\partial x} \quad \text{on} \quad y = 0\pm , \quad (-1 < x < 1) . \tag{8}$$

The corresponding condition on $f(z, t)$ is derived from (7) and (8) as

$$-\frac{\partial \psi}{\partial x} = \frac{\partial v}{\partial t} + U \frac{\partial v}{\partial x} = \left(\frac{\partial}{\partial t} + U \frac{\partial}{\partial x}\right)^2 h \quad \text{on} \quad y = 0\pm , \quad (-1 < x < 1) . \tag{9}$$

The above two conditions indicate that v and ψ are even in y, hence from the Cauchy-Riemann equations, u and ϕ are odd in y. Since ϕ (or the pressure) is regular everywhere inside the flow, it follows that

$$\phi(x, o, t) = 0 \quad \text{for} \quad x > 1 \quad \text{and for all } t . \tag{10}$$

At the trailing edge of the plate, $z = 1$, we impose the Kutta condition that

$$|f(1, t)| < \infty \quad \text{for all } t . \tag{11}$$

460

Furthermore, we require that

$$f(z,t) \to 0 \quad \text{as} \quad |z| \to \infty \quad ; \quad w(z,t) \to 0 \quad \text{as} \quad z \to -\infty . \tag{12}$$

This completes the statement of the problem. It may be pointed out that the complex velocity w, unlike the acceleration potential f, may admit discontinuities across the vortex wake. In the present case when the starting motion is of concern, with the trailing vortex sheet lengthening with increasing time, it is particularly convenient to work with the acceleration potential rather than the velocity potential.

The solution of this problem can be obtained by a Fourier series method which is similar to that used previously by Wu [8] for the case of simple harmonic swimming motion. By the conformal transformation

$$z = \frac{1}{2}(\zeta + \zeta^{-1}) \tag{13a}$$

the original z-plane, cut along the x-axis between -1 and 1, is mapped onto the region outside the unit circle $|\zeta| = 1$. On the unit circle, $\zeta = \exp(i\theta)$, and hence

$$x = \cos\theta , \quad -\pi < \theta < \pi . \tag{13b}$$

Since the plate has zero thickness, h and $\partial h/\partial x$ are even functions of θ. We assume that h can be expanded in a Fourier cosine series

$$h(x,t) = \frac{1}{2}\beta_0 + \sum_{n=1}^{\infty} \beta_n \cos n\theta \tag{14a}$$

where

$$\beta_n(t) = \frac{2}{\pi}\int_0^\pi h(x,t)\cos n\theta\, d\theta \quad (n = 0,1,2,\dots) . \tag{14b}$$

It follows that

$$\frac{\partial h}{\partial x} = -\frac{1}{\sin\theta}\frac{\partial h}{\partial\theta} = \sum_{n=1}^{\infty} n\beta_n\frac{\sin n\theta}{\sin\theta} = \frac{1}{2}\gamma_0 + \sum_{n=1}^{\infty}\gamma_n\cos n\theta \tag{15a}$$

from which it is readily found that

$$\gamma_{n-1} - \gamma_{n+1} = 2n\beta_n \quad (n = 1,2,\dots) . \tag{15b}$$

The coefficients γ_n can be solved from this recursion formula to give

$$\gamma_n(t) = 2\sum_{m=0}^{\infty}(2m+n+1)\beta_{2m+n+1} \quad (n = 0,1,2,\dots) . \tag{15c}$$

461

Substituting (14) and (15) in (8), we obtain

$$v(x, \pm 0, t) = -\left[\frac{1}{2}\Lambda_o + \sum_{n=1}^{\infty} \Lambda_n \cos n\theta\right] \quad \text{on} \quad x = \cos\theta \tag{16a}$$

where

$$\Lambda_n(t) = -\left[\beta_n'(t) - U(t)\gamma_n(t)\right] \quad (n = 0, 1, 2, \ldots), \tag{16b}$$

and the prime denotes the differentiation with respect to t, $\beta'(t) = d\beta/dt$.

The acceleration potential $f(z, t)$ is noted to be regular at all interior points of the flow field for all t; it can admit a square root singularity at the leading edge $z = -1$ and possibly further singularities at the points on the plate where $\partial h/\partial x$ is discontinuous. If f is kept invariant under the mapping (13), i.e., $f(z,t) = f(z(\zeta),t)$, then the leading edge singularity of f is a simple pole in the ζ-plane at $\zeta = -1$. Therefore the solution must assume the form

$$f(z, t) = \varphi + i\psi = iU(t)\left[\frac{a_o(t)}{\zeta - 1} - \sum_{n=1}^{\infty} \frac{a_n(t)}{\zeta^n}\right] \quad \text{for} \quad \zeta > 1. \tag{17a}$$

where the coefficients a_n are real functions of t so that condition (10) is fulfilled. In particular, on the plate $\zeta = e^{i\theta}$,

$$\varphi = U\left[\frac{1}{2} a_o \tan\frac{\theta}{2} - \sum_{n=1}^{\infty} a_n \sin n\theta\right]. \tag{17b}$$

$$\psi = U\left[\frac{1}{2} a_o - \sum_{n=1}^{\infty} a_n \cos n\theta\right]. \tag{17c}$$

Substituting (16) and (17c) in (9), we readily obtain

$$a_n(t) = \Lambda_n(t) - \frac{1}{2nU(t)}\left[\Lambda_{n-1}'(t) - \Lambda_{n-1}(t)\right] \quad (n = 1, 2, 3, \ldots). \tag{18}$$

where Λ_n are given by (16b). Thus all the coefficients a_n except a_o are determined and their values are seen to depend on the instantaneous values of U, U', h, $\partial h/\partial t$, and $\partial^2 h/\partial t^2$. The coefficient a_o, however, will be seen to depend on the entire history of the motion.

To determine a_o it is convenient to introduce the variable

$$\tau = \int_0^t U(t) dt = \tau(t) \tag{19}$$

462

so that τ measures the rectilinear displacement (in time t) of the plate along the negative x'-axis. From the previous assumption that $0 < U < \infty$ for $t > 0$ it follows that τ is a monotonically increasing function of t and vice versa, hence there exists a unique inverse transformation

$$t = \int_0^\tau g(\tau)d\tau \equiv t(\tau) \tag{20a}$$

where

$$g(\tau) = dt/d\tau = 1/U(t) . \tag{20b}$$

It is also clear that τ can be used in place of the time t. By regarding f and w as functions of z and τ, Eq. (7) may be written

$$\frac{\partial f_*}{\partial z} = \frac{\partial w}{\partial \tau} - \frac{\partial w}{\partial z} \tag{21a}$$

where

$$f_* = \frac{f(z,\tau)}{U(t)} = g(\tau)f(z,\tau) = u_*(x,y,\tau) - i v_*(x,y,\tau) . \tag{21b}$$

We further introduce the Laplace transform of $f(z,\tau)$ with respect to τ by

$$\tilde{f}(z,s) = \int_0^\infty e^{-s\tau} f(z,\tau)d\tau \qquad (Re\ s > 0) . \tag{22}$$

Under the initial condition $w(z,0) = 0$ the Laplace transform of (21a) is

$$\frac{\partial \tilde{f}_*}{\partial z} = \left(s - \frac{\partial}{\partial z}\right)\tilde{w} .$$

Upon integration from $z = -\infty$ to a point z and using conditions (12), we obtain

$$\tilde{w}(z,s) = \int_{-\infty}^z e^{s(z_1 - z)} \frac{\partial \tilde{f}_*(z_1,s)}{\partial z_1} dz_1$$

$$= \tilde{f}_*(z,s) - s \int_{-\infty}^z e^{s(z_1 - z)} \tilde{f}_*(z_1,s)dz_1 . \tag{23a}$$

In particular, on the plate, $y = 0-$, $-1 < x < 1$, the above equation gives

$$\tilde{u}(x,0-,s) = \tilde{u}_*(x,0-,s) - s \int_{-1}^x e^{s(x_1 - x)} \tilde{u}_*(x,0-,s)dx_1 . \tag{23b}$$

$$\tilde{v}(x,0,s) = -\tilde{v}_*(x,0,s) - s \int_{-\infty}^x e^{s(x_1 - x)} \tilde{v}_*(x_1,0,s)dx_1 . \tag{23c}$$

463

In (23b) use has been made of $\tilde{\varphi}_*(x, 0, s) = 0$ for $|x| > 1$. To determine a_0, we may apply the condition (23c) at any point on the plate, say $x = -1 - 0$, or in the ζ-plane as $\vartheta \to \pi$. Then from (16) and (17c) we deduce

$$\tilde{v}(-1, 0, s) = -\left[\frac{1}{2} \tilde{\lambda}_o - \sum_{n=1}^{\infty} (-)^n \tilde{\lambda}_n\right],$$

$$\tilde{\psi}_*(-1, 0, s) = \frac{1}{2} \tilde{a}_o - \sum_{n=1}^{\infty} (-)^n \tilde{a}_n,$$

where $\tilde{\lambda}_n$ and $\tilde{a}_n$ are the Laplace transform of $\lambda_n(\tau)$ and $a_n(\tau)$ with respect to τ. For the $\tilde{\psi}_*(x_1, 0, s)$ in the integrand of (23c), we find from (17a) the expression

$$\tilde{\psi}_*(x_1, 0, s) = \frac{\tilde{a}_o}{\zeta_1 - 1} + \sum_{n=1}^{\infty} \frac{\tilde{a}_n}{\zeta_1^n} \quad \text{for} \quad \zeta_1 < -1$$

where

$$x_1 = \frac{1}{2}(\zeta_1 - \zeta_1^{-1}).$$

Substituting these expressions in (23c), and by appropriate integration by parts together with making use of

$$\tilde{a}_n = \tilde{\lambda}_n - \frac{s}{2n}\left[\tilde{\lambda}_{n-1} - \tilde{\lambda}_{n+1}\right] \quad (n = 1, 2, 3, \dots) \tag{24}$$

which is the Laplace transform of (18), we find that the infinite series cancel, leaving the final result as

$$(\tilde{a}_o - \tilde{\lambda}_1) \int_1^{\infty} e^{-\frac{s}{2}(\zeta + \frac{1}{\zeta})} \frac{d\zeta}{\zeta} = (\tilde{\lambda}_o - \tilde{a}_o)\left\{\frac{1}{s} e^{-s} - \int_1^{\infty} e^{-\frac{s}{2}(\zeta + \frac{1}{\zeta})} \frac{d\zeta}{\zeta^2}\right\}.$$

But

$$\int_1^{\infty} e^{-\frac{s}{2}(\zeta + \zeta^{-1})} \frac{d\zeta}{\zeta} = K_o(s).$$

$$\int_1^{\infty} e^{-\frac{s}{2}(\zeta + \zeta^{-1})} \frac{d\zeta}{\zeta^2} = K_1(s) - \frac{1}{s} e^{-s}.$$

where K_o and K_1 are the modified Bessel functions of the second kind. Therefore

$$\tilde{a}_o(s) = \left[\tilde{\lambda}_o(s) + \tilde{\lambda}_1(s) \right] \tilde{C}(s) - \tilde{\lambda}_1(s) \ , \tag{25a}$$

$$\tilde{C}(s) = \frac{K_1(s)}{K_o(s) + K_1(s)} \tag{25b}$$

Finally, the value of $a_o(\tau)$ can be written as the convolution integral

$$a_o(\tau) = \int_o^{\tau} \left[\lambda_o(\tau_1) + \lambda_1(\tau_1) \right] C(\tau - \tau_1) d\tau_1 - \lambda_1(\tau) \tag{25c}$$

in which $C(\tau)$ denotes the inverse transform of $\tilde{C}(s)$. The value of $a_o(t)$ at time t is readily obtained by making use of (19). This result shows that $a_o(t)$ depends on the motion of the plate at all instants in the past.

HYDRODYNAMIC FORCES

The pressure difference across the plate, by (3) and (17b), is

$$\triangle p \equiv p(x,0-,t) - p(x,0+,t) = \rho U(t) \left[a_o(t) \ \tan \frac{\phi}{2} + 2 \sum_1^{\infty} a_n(t) \ \sin n \phi \right] , \tag{26}$$

the positive sense of $\triangle p$ being in the positive y-direction.

(i) Lift. The instantaneous lift acting on the plate is

$$L = \int_{-1}^1 (\triangle p) dx = \int_o^{\pi} (\triangle p) \ \sin \phi \ d\phi = \pi \rho U(t) \left[a_o(t) - a_1(t) \right]. \tag{27}$$

(ii) Moment. The instantaneous moment of force about the midchord, positive in the nose-up sense, is

$$M = -\int_{-1}^1 (\triangle p) x \ dx = \frac{1}{2} \pi \rho U(t) \left[a_o(t) - a_2(t) \right] . \tag{28}$$

For the case of self-propelled bodies, L and M may admit small oscillations in such a way that the body will move approximately along a straight course (so that the present analysis can remain applicable). The trajectory of the body, however, will have to be evaluated together with the equations of motion of the solid body. This can be carried out in each specific case when the distribution of body mass and the moment of inertia are prescribed.

(iii) Thrust. The thrust, taken to be positive in the negative x-direction, acting on the plate is given by

465

$$T = \int_{-1}^{1} (\angle p) \frac{\partial h}{\partial x} dx + Ts = Tp + Ts \tag{29}$$

where Ts represents the thrust due to the leading edge suction. Substituting (15a) and (26) into the above integral for Tp, we obtain after integration

$$Tp = \frac{1}{2} \pi \rho U(t) \left\{ a_o(\gamma_o - \gamma_1) + \sum_{n=1}^{\infty} a_n(\gamma_{n-1} - \gamma_{n+1}) \right\} .$$

The leading edge suction arises from the singular pressure at the leading edge,* and its determination requires the non-linear terms in the expression for the pressure in the neighborhood of the leading edge to be taken into account. It has been noted (e.g., see Wu [8]) that the unsteady suction force presents the same problem as the steady motion since the time-dependent quantities in the pressure equation which make contribution to the suction force appear with t only as a parameter. More specifically, it is readily seen from (23a) that near the leading edge, we have $\ddot{w}(z,s) \sim \bar{f}_*(z,s) \sim i\bar{a}_o/(\zeta - 1)$ asymptotically. Hence by inverse transformation,

$$w(z,t) \sim ia_o(t)(\zeta - 1)^{-1} - O(1) \quad \text{as} \quad \zeta - 1 \to 0 .$$

Then by applying Blasius' formula to a small circle of radius ϵ around the leading edge, we obtain

$$Ts = -\frac{1}{2} i \rho \oint_\epsilon w^2 dz = \frac{1}{2} \pi \rho a_o^2 .$$

Combining Tp and Ts to give the total thrust, we find

$$T = \frac{1}{2} \pi \rho \left\{ a_o^2 + U(t) \left[a_o(\gamma_o - \gamma_1) - \sum_{n=1}^{\infty} a_n(\gamma_{n-1} - \gamma_{n+1}) \right] \right\} \tag{30a}$$

or, by (15b),

$$T = \frac{1}{2} \pi \rho \left\{ a_o^2 + U(t) \left[a_o(\gamma_o - \gamma_1) - 2 \sum_{n=1}^{\infty} n a_n \beta_n \right] \right\} . \tag{30b}$$

Upon elimination of a_n by using (18) and (16b), T can still be expressed in another form,

$$T = \frac{1}{2} \pi \rho \left\{ (a_o - U\gamma_o)(a_o - U\gamma_1) - \beta_o' \beta_1' - \frac{d}{dt} \sum_{n=1}^{\infty} \beta_n(\gamma_{n-1} - \gamma_{n+1}) \right\} \tag{30c}$$

*The leading edge suction can physically be realized only when the leading edge is sufficiently round.

466

POWER REQUIRED; ENERGY CONSERVATION

The power required to maintain the prescribed motion (14) is equal to the time rate of work done by the external force which acts equal and opposite to (Δp), or

$$P = - \int_{-1}^{1} (\Delta p) \frac{\partial h}{\partial t} \, dx \, . \tag{31}$$

Substituting (14) and (26) in (31), we obtain after integration the result

$$P = - \frac{1}{2} \pi \rho U(t) \left\{ a_o(\beta_o' - \beta_1') + \sum_{n=1}^{\infty} a_n(\beta_{n-1}' - \beta_{n+1}') \right\} . \tag{32a}$$

Upon elimination of a_n from the above series, by using (18), (15b) and (16b), we find

$$P = \frac{\pi}{2} \rho \left\{ -Ua_o(\beta_o' - \beta_1') - U\beta_o'\beta_1' - U^2(\gamma_1\beta_o' + \gamma_o\beta_1' - \sum_{n=1}^{\infty} 2n\beta_n\beta_n') \right.$$

$$\left. - \sum_{n=1}^{\infty} \frac{1}{2n} (\lambda_{n-1}' - \lambda_{n+1}')(\beta_{n-1}' - \beta_{n+1}') \right\} . \tag{32b}$$

From the principle of conservation of energy, the power input P must be equal to the time rate of work done by the thrust, TU, plus the kinetic energy E_x imparted to the fluid in unit time,

$$P = TU + E_x \, . \tag{33}$$

From (30a), (32a) and (18), we obtain

$$E_x = \frac{1}{2} \pi \rho \left\{ U(\lambda_o - a_o)(\lambda_1 - a_o) - \frac{d}{dt} \sum_{n=1}^{\infty} \frac{1}{4n} (\lambda_{n-1} - \lambda_{n+1})^2 \right\} . \tag{34}$$

When the thrust T and power P are positive, we may define the propulsive efficiency by

$$\eta = TU/P \, . \tag{35}$$

VORTEX SHEET STRENGTH; CIRCULATION AROUND
THE PLATE

The strength of the vortex sheet at a point (x, o) of the wake $(x > 1)$ is given by

467

$$\gamma(x,t) = 2u(x, +0, t) \tag{36}$$

which satisfies the equation

$$\frac{\partial \gamma}{\partial t} + U \frac{\partial \gamma}{\partial x} = 0$$

by virtue of (2) and (10). It therefore follows that γ is a function of the single variable $(x - \tau)$ only,

$$\gamma(x,t) = H(\tau - x + 1) \quad \text{for} \quad x > 1 \tag{37a}$$

where

$$H(\tau) = \gamma(1,t) = 2u(1, +0, t) . \tag{37b}$$

By Kelvin's circulation theorem, the circulation around the plate, $\Gamma(t)$, varies at the rate

$$d\Gamma/dt = - U\gamma(1,t) = - U(t) H(\tau) , \tag{38a}$$

which gives upon integration

$$\Gamma(\tau) = - \int_0^\tau H(\tau)d\tau = -2 \int_0^t U(t)u(1, +0, t)dt . \tag{38b}$$

We next calculate $u(1, +0, t)$. If we set $x = 1$ in (23b), noting that $\tilde{\varphi}_*(1, 0, s) = 0$ and substituting $\tilde{z}_*$, which can be readily deduced from (17b), into (23b), we obtain

$$\tilde{u}(1, +0, s) = -s e^{-s} \int_0^\tau e^{s \cos \theta} \left[\frac{1}{2} \tilde{a}_o (1 - \cos \theta) - \sum_{n=1}^{\infty} \tilde{a}_n \sin n\theta \sin \theta \right] d\theta .$$

By using (24) and integrating by parts, the infinite series in the above integrand terminates and the final result may be written

$$\tilde{u}(1, +0, s) = - \frac{1}{2} \pi s e^{-s} \left[(\tilde{\alpha}_1 - \tilde{a}_o)I_o(s) - (\tilde{\alpha}_o - \tilde{a}_o)I_1(s) \right]$$

where I_n are the modified Bessel functions of the first kind. By (25) and the relation

$$I_o(s)K_1(s) + I_1(s)K_o(s) = 1 s .$$

we obtain

$$\tilde{u}(1, +0, s) = - \frac{1}{2} + \tilde{D}(s) \left[\tilde{\alpha}_o(s) + \tilde{\alpha}_1(s) \right] , \tag{39a}$$

where

$$\tilde{D}(s) = e^{-s} / \left[K_o(s) + K_1(s) \right] . \tag{39b}$$

468

Taking the inverse transform, we find

$$\gamma(1,t) = 2u(1, +0, \tau) = H(\tau) \tag{40a}$$

where

$$H(\tau) = -\pi \int_0^\tau \left[\lambda_0(\tau_1) + \lambda_1(\tau_1)\right] D(\tau - \tau_1) d\tau_1 , \tag{40b}$$

and $H(\tau) = 0$ for $\tau < 0$.

From the above general result one can determine the flow field, vorticity distribution and the performance of the motion once the motion of the plate ($U(t)$ and $h(x,t)$) is known.

SMALL TIME BEHAVIOR OF A SPECIAL CASE; AN OPTIMUM PROFILE

As a typical motion let us consider the special case in which the plate moves forward with a uniform acceleration from at rest,

$$U(t) = at , \quad a > 0 . \tag{41}$$

and at the same time its lateral motion can be represented by a cubic form in x,

$$h(x,t) = \frac{1}{2} \beta_0(t) - \sum_{n=1}^{3} \beta_n(t) \cos n\theta \tag{42}$$

so that for appropriately chosen $\beta_0, \cdots \beta_3$, the profile h may include both a positive and a negative phase. This provides enough degrees of freedom so that the lateral force and angular recoil may be minimized. We further assume that in a certain time interval the coefficients β_n may be expanded for small t as

$$\beta_n(t) = \beta_{n_2} t^2 - \beta_{n_3} t^3 - \cdots \quad n = 0,1,2,3 . \tag{43}$$

The expansion starts from t^2 so that the zero initial velocity is ensured.

From this expansion it is readily derived that for t small,

$$\gamma_0 = 2(\beta_{12} - 3\beta_{32})t^2 - 2(\beta_{13} - 3\beta_{33})t^3 - O(t^4) .$$

$$\gamma_1 = 4\left[\beta_{22}t^2 - \beta_{23}t^3 - O(t^4)\right], \tag{44}$$

$$\gamma_2 = 6\left[\beta_{32}t^2 - \beta_{33}t^3 - O(t^4)\right],$$

and $\gamma_3 = \gamma_4 = \cdots = 0$;

$$\lambda_n = -2\beta_{n_2}t - 3\beta_{n_3}t^2 - O(t^3) , \quad n = 0,1,2,3 \tag{45}$$

and $\lambda_4 = \lambda_5 = \cdots = 0$;

469

$$Ua_1 = (\beta_{22} - \beta_{o_2}) + 3(\beta_{23} - \beta_{o_3})t + O(t^2) ,$$

$$2Ua_2 = (\beta_{32} - \beta_{12}) + 3(\beta_{33} - \beta_{13})t + O(t^2) ,$$

$$3Ua_3 = -\beta_{22} - 3\beta_{23}t + O(t^2) ,$$

$$4Ua_4 = -\beta_{32} - 3\beta_{33}t + O(t^2) ,$$

(46)

and $a_5 = a_6 = \cdots = 0$.

To obtain the expansion of $a_o(t)$ for t small, we first expand $\tilde{C}(s)$ in (25) by using the known asymptotic expansion of $K_n(s)$ for large values of s (see, e.g., Watson [12]), giving

$$\tilde{C}(s) = \frac{1}{2}\left[1 - \frac{1}{4s} - \frac{1}{128s^2} - O(s^{-3})\right] .$$

Substituting this in (25b) and carrying out the inverse transformation, we obtain

$$2a_o(\tau) = \lambda_o(\tau) - \lambda_1(\tau) - \frac{1}{4}\int_o^\tau \left[\lambda_o(\tau) - \lambda_1(\tau)\right]d\tau + \cdots ,$$

where τ is, by (19) and (41),

$$\tau = \alpha\int_o^t t \, dt = \frac{1}{2}\alpha t^2 .$$

(47)

Transforming the above expression for $a_o(\tau)$ in terms of t, we find

$$2a_o(t) = \lambda_o(t) - \lambda_1(t) - \frac{1}{4}\alpha\int_o^t \left[\lambda_o(t) - \lambda_1(t)\right]t \, dt + \cdots$$

$$= 2(\beta_{12} - \beta_{o_2})t + 3(\beta_{13} - \beta_{o_3})t^2 + O(t^3) .$$

(48)

This shows that the leading edge singularity grows at the rate proportional to t for t small.

Similarly, if we expand $\tilde{D}(s)$ in (39) for large values of s we find

$$\tilde{D}(s) = \sqrt{\frac{s}{2}}\left[1 - \frac{1}{8s} - \frac{5}{64s^2} - O(s^{-3})\right] .$$

(49a)

Expressing λ_o and λ_1 in (45) in terms of τ by using (47), we obtain the Laplace transform of $\lambda_o(\tau)$ and $\lambda_1(\tau)$ as

$$\tilde{\lambda}_o(s) - \tilde{\lambda}_1(s) = -\sqrt{\frac{2}{\alpha s^3}}\left[(\beta_{o_2} - \beta_{12}) - 3\sqrt{\frac{2}{\alpha}}(\beta_{o_3} - \beta_{13})\frac{1}{\sqrt{s}} - O(s^{-1})\right] \quad (49b)$$

470

Substituting (49a,b) in (39a), carrying out the inverse transformation, and finally expressing the result in terms of t, we obtain for $t > 0$,

$$\gamma(1,t) = \frac{1}{2}\frac{\pi}{\sqrt{\alpha}}\left[(\beta_{o_2} - \beta_{12}) + \frac{6}{\pi}(\beta_{o_3} + \beta_{13})t - O(t^2)\right] . \tag{50}$$

This result shows that immediately after the motion started, there is a vortex of strength $\gamma(1,t)$ generated at the trailing edge.

Finally, we substitute (42) to (48) into (27) and (28), giving

$$L/\pi\rho = (\beta_{22} - \beta_{o_2}) + 3(\beta_{23} - \beta_{o_3})\,t + O(t^2) , \tag{51}$$

$$4M/\pi\rho = (\beta_{12} - \beta_{32}) + 3(\beta_{13} - \beta_{33})\,t + O(t^2) , \tag{52}$$

If the resulting lift and moment are required to be small, we may set

$$\beta_{22} = \beta_{o_2} , \qquad \beta_{23} = \beta_{o_3} ,$$
$$\beta_{32} = \beta_{12} , \qquad \beta_{33} = \beta_{13} . \tag{53}$$

That is, $\beta_2 = \beta_o$ and $\beta_3 = \beta_1$ up to the order t^2. Under this assumption we deduce the following thrust and power required

$$2T/\pi\rho = \left[(\beta_{12} - \beta_{o_2})^2 - 2\beta_{o_2}\beta_{12}\right]t^2$$
$$- \left[3(\beta_{o_2} - 3\beta_{12})\beta_{o_3} - (3\beta_{12} - 5\beta_{o_2})\beta_{13}\right]t^3 - O(t^4) . \tag{54}$$

$$2P/\pi\rho = \left(\frac{2}{3}\beta_{o_2}^2 - \frac{1}{2}\beta_{12}^2\right)t - \left[3\beta_{o_2}\beta_{o_3} - \frac{9}{4}\beta_{12}\beta_{13} - 2(\beta_{12} - \beta_{o_2})^2\right]t^2 - O(t^3) . \tag{55}$$

It is of interest to note that the thrust is generated at the time of order t^2, whilst the power is already required at the time of order t, the initial power being positive definite for any arbitrary lateral motion. Another point of interest is that the rectilinear acceleration a does not appear in the first order terms of the above physical quantities.

A qualitative argument about the optimum profile at the initial stage can be made as follows. Up to the first order terms, the thrust is maximum for fixed power P if

$$\xi = \beta_{12}/\beta_{o_2} = -(1 - \sqrt{193})/12 = -1.24 . \tag{56}$$

this being readily verified by the method of undetermined multipliers. The determination of the higher terms is not as simple. An indication of the trend of motion, however, can still be given. If we require the second order term of P to vanish, then the second order term of T can be positive, under condition (56), if β_{13}/β_{o_2} and β_{o_3}/β_{o_2} are sufficiently large and positive.

471

Under the assumption (53), the maximum and minimum of h are given by

$$\partial h / \partial x = 12\beta_1 x^2 + 4\beta_0 x - 2\beta_1 = 0$$

or up to the first order terms,

$$x_{1,2} = \left(-1 \pm \sqrt{1 + 6\epsilon^2} \right) / 6\epsilon = -0.564, \ +0.295 \ . \tag{57}$$

When the higher terms are included, these points are seen to move back towards the trailing edge with increasing time.

REFERENCES

1. Osborne, M.F.M., "The Hydrodynamical Performance of Migratory Salmon," J. Exp. Biol. 38, 365-90, 1960.

2. Gray, J., "Propulsive Powers of the Dolphin," J. Exp. Biol. 13, 192-208, 1936.

3. Gray, J., "Aspects of the Locomotion of Whales," Nature, Lond., 161, 199-200, 1948.

4. Johannessen, C.L. and Harder, J.A., "Sustained Swimming Speeds of Dolphins," Science 132, 1550-51, 1960.

5. Lang, T.G., "Analysis of the Predicted and Observed Speeds of Porpoise, Whales and Fish," Tech. Note P5015-21, U.S. Naval Ordnance Test Station, Pasadena Annex, California, 1962.

6. Lighthill, M.J., "Mathematics and Aeronautics," J. Roy. Aero. Soc. 64, 373-94, 1960a.

7. Lighthill, M.J., "Note on the Swimming of Slender Fish," J. Fluid Mech. 9, 305-17, 1960b.

8. Wu, T. Yao-tsu, "Swimming of a Waving Plate," J. Fluid Mech. 10, 321-344, 1961.

9. Smith, E.H. and Stone, D.E., "Perfect Fluid Forces in Fish Propulsion: The Solution of the Problem in an Elliptic Cylinder Co-ordinate System," Proc. Roy. Soc. A, 261, 316-328, 1961.

10. Kelly, H.R., "Fish Propulsion Hydrodynamics," Proc. 7th Midwestern Mech. Conf. I, p. 442, 1961.

11. Gray, J., "Aquatic Locomotion," Nature, Lond., 164, 1073-75, 1949.

12. Watson, G.N., Theory of Bessel Functions, 2nd ed., Cambridge University Press, 1944.

Thursday, August 30

Morning Session

HYDROELASTICITY

Chairman: M. Eames

National Research Establishment
Halifax, Nova Scotia, Canada

FORCES AND MOMENTS ON AN
OSCILLATING HYDROFOIL

Peter Crimi and Irving C. Statler
Cornell Aeronautical Laboratory, Inc.
Buffalo 21, New York

ABSTRACT

The lift and moment acting on an oscillating hydrofoil in two-dimensional flow are computed by applying analytical and numerical techniques to the integral equation satisfied by the singularity distribution on the hydrofoil. The flow is assumed to be noncavitating, but no limitations are placed on the values of Froude number or depth-to-chord ratio.

Solutions are obtained by assuming that the vortex strength distribution on the hydrofoil is given by a Glauert series, and then solving the infinite set of linear algebraic equations resulting from the substitution of this series into the governing integral equation.

Computations were performed on a high-speed digital computer. Results are presented in graphical form, with lift and moment given as functions of reduced frequency with Froude number and depth-to-semichord ratio as parameters. Results are discussed and compared with previous related studies.

1. INTRODUCTION

Interest in high-performance hydrofoil craft has necessitated concern with problems of dynamic stability and control as well as hydroelastic instability. Theoretical investigations of these problems in turn require knowledge of the hydrodynamic forces and moments acting on an oscillating hydrofoil. If the hydrofoil is deeply submerged, the lifts and moments are well predicted by conventional incompressible unsteady thin-airfoil theory, as given by Theodorsen[1]. However, in the more practical case of submergence depths on the order of a chord length or less, important effects arise not only because of the proximity of the free surface as represented by an image, but also because surface waves are generated by the motion of the hydrofoil.

Various studies have been carried out which relate to the general unsteady hydrofoil problem. The applicability of the solutions obtained to date is limited,

however, by the simplifying assumptions which have been made. For example, Chu and Abramson [2] considered the problem assuming infinite Froude number (i.e., no surface waves) and obtained a solution by expanding in the chord-to-depth ratio. The validity of their solution is thus limited to relatively large depth and speed. Kaplan [3] formulated the problem to include the primary effects of finite Froude number. His solution lacks the desired degree of exactitude, however, because he simulates the oscillating hydrofoil with a single vortex and a doublet and, further, assumes that their strengths are the same as in an infinite medium. Tan [4] has obtained the exact linearized potential solution for a point singularity (source or vortex) of oscillating strength moving below a free surface. While this model does not of itself correspond to a physical flow, it forms the basis for the general problem in which a distribution of such singularities is used to represent the hydrofoil.

The study discussed here is directed to obtaining the exact linearized potential solution for the two-dimensional flow about a fully wetted oscillating flatplate hydrofoil near the free surface. The mathematical model assumed is analogous to that used in conventional unsteady thin-airfoil theory.

2. PROBLEM FORMULATION

Consider an oscillating hydrofoil of infinite span immersed below the free surface of an incompressible, inviscid infinitely deep fluid having a uniform velocity of magnitude U. The perturbations in fluid velocity resulting from the presence of the hydrofoil may then be obtained as the gradient of a scalar potential function. Further, assume that the hydrofoil is fully wetted, and may be represented by a plane distribution of vortex singularities of oscillating strength. Finally, assume that the vortices which are necessarily shed from the hydrofoil and convected downstream lie in the plane of the hydrofoil. The assumed model, consisting of the hydrofoil and its wake, as well as the free surface and an image system, is shown schematically in Fig. 1. The singularity distribution over the image system is identical to that of the hydrofoil and its wake. The combined effects of the image and hydrofoil systems are then such as to make the pressure at $y = D$ the same as it would be if the flow were undisturbed.

The perturbation velocity potential $\Phi(x, y, t)$ must satisfy Laplace's equation; i.e.,

$$\frac{\partial^2 \Phi}{\partial x^2} - \frac{\partial^2 \Phi}{\partial y^2} = 0 .$$

In addition, the potential must satisfy the following three boundary conditions. These boundary conditions are obtained after assuming that quantities of second order or higher in Φ, $\cdot$, $\cdot$ and their derivatives are negligible in comparison with first order quantities. It should be noted that, consistent with this linearizing assumption, Eqs. (2.1) and (2.2) apply at $y = D$ rather than at $y = D \cdot \cdot$

478

Forces and Moments on an Oscillating Hydrofoil
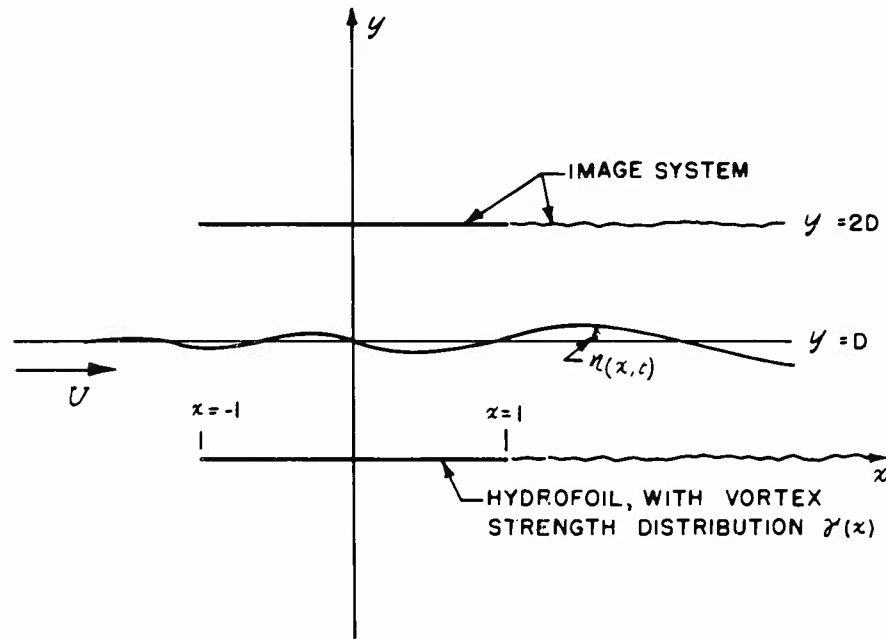
Fig. 1 - Schematic representation of the assumed model

and Eq. (2.3) applies at $y = 0$ rather than at $y = Y$. First, if the free surface is to be a streamline,

$$\frac{\partial \eta}{\partial t} + \frac{U}{b} \frac{\partial \eta}{\partial x} = \frac{1}{b} \frac{\partial \Phi}{\partial y} \qquad \text{for} \quad y = D . \tag{2.1}$$

where $\eta(x,t)$ is the displacement in the y direction of the free surface from its position when undisturbed. Second, by requiring that the pressure on the free surface is constant and equal to its value when the flow is undisturbed, it is found that

$$\frac{\partial \Phi}{\partial t} + \frac{U}{b} \frac{\partial \Phi}{\partial x} = - g \eta \qquad \text{for} \quad y = D , \tag{2.2}$$

where g is the acceleration due to gravity. Finally, if there is to be no flow normal to the hydrofoil surface,

$$\frac{\partial Y}{\partial t} + \frac{U}{b} \frac{\partial Y}{\partial x} = \frac{1}{b} \frac{\partial \Phi}{\partial y} \qquad \text{for} \quad y = 0 : \quad -1 \leq x \leq 1 , \tag{2.3}$$

where $Y(x,t)$ represents the displacement in the y direction of the hydrofoil from its mean position. The factor $1/b$ applied to derivatives with respect to x or y in Eqs. (2.1), (2.2), and (2.3) is necessary because those coordinates have been nondimensionalized with respect to the semichord b.

479

In addition to the conditions specified by Eqs. (2.1), (2.2), and (2.3), it must be required that the Kutta-Joukowski condition of finite velocity at the trailing edge of the hydrofoil be satisfied. Also, because the presence of surface waves makes the problem to some extent indeterminate, further restrictions are necessary in obtaining the potential due to the free surface. These restrictions are discussed in detail in Part 3.

3. DERIVATION OF THE INTEGRAL EQUATION

Assume that the hydrofoil oscillates harmonically so that the potential may be expressed by

$$\Phi(x,y,t) = \Re\left\{(\phi_1 + \phi_2 + \phi_3)e^{i\omega t}\right\} \tag{3.1}$$

where ω is the frequency of oscillation, and ϕ_1, ϕ_2, and ϕ_3 are functions of x and y only. Identify ϕ_1 and ϕ_2 as the contributions to the potential from the hydrofoil and image systems, respectively, and ϕ_3 as the contribution from the surface waves. The expressions for ϕ_1 and ϕ_2 follow directly from thin-airfoil theory (see, for example, Ref. 5) and are given by:

$$\phi_1(x,y) = \frac{-b}{2\pi}\int_{-1}^{1} \gamma(\xi)\ \tan^{-1}\left(\frac{y}{x-\xi}\right)\ d\xi + \frac{ik\overline{\Gamma}b}{2\pi}\int_{1}^{\infty} e^{-ik(\xi-1)}\ \tan^{-1}\left(\frac{y}{x-\xi}\right)\ d\xi \tag{3.2}$$

$$\phi_2(x,y) = \frac{-b}{2\pi}\int_{-1}^{1} \gamma(\xi)\ \tan^{-1}\left(\frac{y-2D}{x-\xi}\right)\ d\xi + \frac{ik\overline{\Gamma}b}{2\pi}\int_{1}^{\infty} e^{-ik(\xi-1)}\ \tan^{-1}\left(\frac{y-2D}{x-\xi}\right)\ d\xi \tag{3.3}$$

where

$$\overline{\Gamma} = \int_{-1}^{1} \gamma(x)dx$$

and $\gamma(x)$ is the unknown vortex strength distribution on the hydrofoil. It remains to obtain the function $\phi_3(x,y)$ in terms of $\gamma(x)$ by satisfying the free-surface boundary conditions.

Equations (2.1) and (2.2) may be combined to eliminate η, giving

$$\frac{\partial^2\Phi}{\partial t^2} + 2\frac{U}{b}\frac{\partial^2\Phi}{\partial t\partial x} + \frac{U^2}{b^2}\frac{\partial^2\Phi}{\partial x^2} = \frac{-g}{b}\frac{\partial\Phi}{\partial y}\ ; \qquad y = D\ . \tag{3.4}$$

If Eqs. (3.2) and (3.3) are substituted into Eq. (3.1), and the resulting expression for Φ is substituted into Eq. (3.4), the following differential equation for ϕ_3 is obtained:

$$-k^2 \phi_3 + 2ik \frac{\partial \phi_3}{\partial x} + \frac{\partial^2 \phi_3}{\partial x^2} + \frac{1}{F^2} \frac{\partial \phi_3}{\partial y} = \frac{b}{\pi F^2} \int_{-1}^{1} \frac{(x - \xi) \gamma(\xi) d\xi}{(x - \xi)^2 + D^2}$$

$$-ik \frac{\bar{\Gamma} b}{\pi F^2} \int_{1}^{\infty} \frac{e^{-ik(\xi - 1)} (x - \xi) d\xi}{(x - \xi)^2 + D^2} \; ; \quad y = D \; ; \quad (3.5)$$

where F and k are, respectively, the Froude number and the reduced frequency, defined by

$$F \equiv \frac{U}{\sqrt{bg}} \; ,$$

$$k \equiv \frac{\omega b}{U}$$

It may be shown that the following relationship satisfies Eq. (3.5).

$$\phi_3(x, y) = \frac{ib}{2\pi F^2} \int_{-1}^{1} \gamma(\xi) G(\xi; x, y) d\xi + \frac{k \bar{\Gamma} b}{2\pi F^2} \int_{1}^{\infty} e^{-ik(\xi - 1)} G(\xi; x, y) d\xi \qquad (3.6)$$

where

$$G(\xi; x, y) = \int_{0}^{\infty} e^{s(y - 2D)} \left[\frac{e^{is(x - \xi)}}{(S - S_1)(S - S_2)} - \frac{e^{is(x - \xi)}}{(S - S_3)(S - S_4)} \right] ds$$

$$+ D_1 e^{s_1 \left[y - 2D + i(x - \xi) \right]} - D_2 e^{s_2 \left[y - 2D + i(x - \xi) \right]}$$

$$+ D_3 e^{s_3 \left[y - 2D - i(x - \xi) \right]} - D_4 e^{s_4 \left[y - 2D - i(x - \xi) \right]}$$

and

$$(S - S_1)(S - S_2) = S^2 - \left(\frac{1}{F^2} - 2k \right) S - k^2$$

$$(S - S_3)(S - S_4) = S^2 - \left(\frac{1}{F^2} - 2k \right) S - k^2 \; .$$

The solution is indeterminate, since the values of D_1, D_2, D_3 and D_4 are as yet unspecified. A device may be employed, however, which leads to physically realistic boundary conditions at infinity and provides just sufficient information to compute the values of these constants. A small fictitious dissipative force is introduced, which is proportional to the perturbation velocity (see [6], pp. 398-406). The condition of the flow on the free surface at upstream and downstream infinity is then examined in the limit as the dissipative force goes to zero. In this manner, it is determined whether the free harmonic surface wave corresponding to each of the roots S_1 through S_4 should be allowed to exist as x tends to either positive or negative infinity.

481

Examination of the results of this analysis reveals the following physical picture. The solution admits the possibility of four wave trains. The waves associated with S_1 and S_2 travel upstream, while those associated with S_3 and S_4 propagate downstream. The direction and extent of the surface waves is found to depend on whether the roots S_1, S_2, etc., are real or complex. This, in turn, depends on the value of the product $kF^2 = \omega U/g$.

For all values of $kF^2 > 0$, S_3 and S_4 are real and positive and, therefore, at least these two harmonic waves always exist. Since these two waves propagate downstream, however, their existence upstream of the hydrofoil is physically unrealistic. Hence, there will be two harmonic waves behind the hydrofoil which propagate downstream for all $kF2 > 0$.

The roots S_1 and S_2 are real and positive for $0 < kF^2 < 1/4$. The consequent harmonic wave associated with S_1 has a group velocity (the speed at which energy is propagated by the wave) which is less than the forward speed U; hence, it must trail the hydrofoil. The group velocity of the harmonic wave associated with S_2 is greater than U; therefore, the wave must lead the hydrofoil. Hence, for $0 < kF^2 < 1/4$, there will be two harmonic waves propagating upstream, one leading and one trailing the hydrofoil.

For $kF^2 > 1/4$, S_1 and S_2 are a complex conjugate pair. The waves are, therefore, damped and contribute only local disturbances.

Two special cases should also be discussed. First, when the flow is steady ($kF^2 = 0$), the S_2 and S_4 solutions disappear and the S_1 and S_3 solutions combine to give a single standing wave extending downstream of the hydrofoil to infinity.

Second, when $kF^2 = 1/4$, $S_1 = S_2$ and the group velocities of these upstream propagating waves are equal to each other and to the hydrofoil speed, U. No solution can then be obtained because the particular integral in $G(\xi : x, y)$ associated with S_1 and S_2 does not exist. This condition might be interpreted physically as the building up of waves having the same rate of propagation as that of the disturbance, thus causing the surface waves to reinforce each other in a singular manner. It is reasonable to expect that in the immediate neighborhood of this resonance certain nonlinearities and other effects which ordinarily are of higher order, such as surface tension and viscosity, might become significant.

With this knowledge in hand, the behavior of the particular integral in $G(\xi : x, y)$ may be examined in the limit for very large x, and the values of D_1 through D_4 assigned to provide the correct free-surface boundary conditions. The values of these constants as so determined are presented in Table 1 as a function of kF^2, together with a summary of the physical interpretation of the flow at the free surface which was given above. It should be noted here that these free surface radiation conditions agree with those found for a similar problem by Kaplan [7] using a different approach.

All that remains now is to satisfy the boundary condition at the hydrofoil. This condition, given by Eq. (2.3), may be expressed in the following form:

Table 1
Free Surface Radiation Conditions

$\ell F^2 = \frac{\omega U}{g}$	S_1, S_2	S_3, S_4	FLOW CONDITIONS		D_1	D_2	D_3	D_4
			$x \to +\infty$ (DOWNSTREAM)	$x \to -\infty$ (UPSTREAM)				
0	$\frac{1}{F^2}, 0$	$\frac{1}{F^2}, 0$	SINGLE HARMONIC WAVE WAVE LENGTH $\frac{2\pi U^2}{g}$	UNDISTUPBED	$\frac{\pi i}{S_1}$	0	$\frac{\pi i}{S_3}$	0
$0 < \ell F^2 < \frac{1}{4}$	REAL AND POSITIVE	REAL AND POSITIVE	THREE HARMONIC WAVES WAVE LENGTHS $\frac{2\pi}{S_1}, \frac{2\pi}{S_3}, \frac{2\pi}{S_4}$	SINGLE HARMONIC WAVE WAVE LENGTH $\frac{2\pi}{S_2}$	$\frac{\pi i}{S_1 - S_2}$	$\frac{\pi i}{S_1 - S_2}$	$\frac{\pi i}{S_3 - S_4}$	$\frac{-\pi i}{S_3 - S_4}$
$\frac{1}{4} < \ell F^2$	COMPLEX	REAL AND POSITIVE	TWO HARMONIC WAVES WAVE LENGTHS $\frac{2\pi}{S_3}, \frac{2\pi}{S_4}$	UNDISTURBED	0	0	$\frac{\pi i}{S_3 - S_4}$	$\frac{-\pi i}{S_3 - S_4}$

$$\frac{1}{b} \frac{\partial \Phi}{\partial y} = - U \left[(1 + ikx)\alpha_0 + ikh_0\right] e^{i\omega t} \quad ; \quad y = 0, \; -1 \leq x \leq 1 ; \tag{3.8}$$

where α_0 is the complex amplitude of an oscillatory pitching motion about mid-chord (positive nose up) and h_0 is the complex amplitude (nondimensionalized with respect to semichord) of an oscillatory plunging motion, defined to be positive in the sense of decreasing y. Note that specifying the pitching motion to be about midchord does not limit the generality of the boundary condition, since any abritrary oscillatory motion may be resolved into motions of the type specified here.

If Eqs. (3.2), (3.3), and (3.6) are substituted into Eq. (3.1) and the resulting expression for Φ is substituted into Eq. (3.8), the following integral equation in $\gamma(x)$ is obtained:

$$\frac{1}{2\pi} \int_{-1}^{1} \frac{\gamma(\xi)d\xi}{x - \xi} = - \frac{1}{2\pi} \int_{-1}^{1} \gamma(\xi) \left\{ \frac{x - \xi}{(x - \xi)^2 + 4D^2} - \frac{1}{F^2} \left. \frac{\partial G(\xi:x,y)}{\partial y} \right|_{y=0} \right\} d\xi$$

$$+ \frac{ik}{2\pi} \int_{1}^{x} e^{-ik(\xi-1)} \left\{ \frac{1}{x - \xi} - \frac{x - \xi}{(x - \xi)^2 + 4D^2} - \frac{1}{F^2} \left. \frac{\partial G(\xi:x,y)}{\partial y} \right|_{y=0} \right\} d\xi$$

$$- U \left[(1 + ikx)\alpha_0 + ikh_0\right] \quad : \quad -1 \leq x \leq 1 . \tag{3.9}$$

where

$$\left. \frac{\partial G(\xi:x,y)}{\partial y} \right|_{y=0} = \int_{0}^{\infty} s e^{-2DS} \left[\frac{e^{is(x-\xi)}}{(S - S_1)(S - S_2)} - \frac{e^{-is(x-\xi)}}{(S - S_3)(S - S_4)} \right]$$

$$- S_1 D_1 e^{S_1 \left[-2D + i(x - \xi)\right]} - S_2 D_2 e^{S_2 \left[-2D + i(x - \xi)\right]}$$

$$+ S_3 D_3 e^{S_3 \left[-2D - i(x - \xi)\right]} - S_4 D_4 e^{S_4 \left[-2D - i(x - \xi)\right]}$$

483

and the Cauchy principal value is to be taken for the integral on the left-hand side. The solution to the problem is thus determined when a function $\gamma(x)$ has been found which satisfies Eq. (3.9), with the additional restriction that the velocity be finite at the trailing edge.

4. SOLUTION OF THE INTEGRAL EQUATION

The solution to Eq. (3.9) is obtained by first assuming that the vortex strength distribution may be expressed in the form of a Glauert trigonometric series. That is, let

$$\gamma(\theta) = 2U \left[A_o \cot \frac{\theta}{2} + \sum_{n=1}^{\infty} A_n \sin n\theta \right] \tag{4.1}$$

where $\cos \theta = -x$. The A_n's are, in general, complex. It may be shown that the Kutta-Joukowski condition is satisfied by a solution of this form. Also, it is easily shown that

$$\bar{\Gamma} = 2\pi U \left(A_o + \frac{A_1}{2} \right) \tag{4.2}$$

Further, from relationships derived in unsteady thin-airfoil theory [5], the lift per unit span is given by

$$L = 2\pi\rho U^2 \, b e^{i\omega t} \left[A_o + \frac{A_1}{2} - \frac{ik}{2} \left(3A_o + A_1 - \frac{A_2}{2} \right) \right] \tag{4.3}$$

and the moment per unit span about midchord, positive nose-up, is expressed in the form

$$M = \pi\rho U^2 b^2 \, e^{i\omega t} \left[A_o - \frac{A_2}{2} - \frac{ik}{2} \left(A_o + \frac{3A_1}{4} - \frac{A_3}{4} \right) \right] \tag{4.4}$$

Now, if Eq. (4.1) is substituted into the integral on the left-hand side of Eq. (3.9), it is found that

$$\frac{1}{2\pi} \oint_{-1}^{1} \frac{\gamma(\xi)d\xi}{x - \xi} = U \left[A_o - \sum_{n=1}^{\infty} A_n \cos n\theta \right]$$

Hence, if the right-hand side of Eq. (3.9) can be similarly expanded in a Fourier cosine series, a set of linear algebraic relationships in the A_n's may be obtained by equating like coefficients of $\cos n\theta$. This procedure leads to the following infinite set of linear inhomogeneous algebraic equations:

$$A_m = \sum_{n=0}^{\infty} C_{mn} A_n + r_m \quad ; \quad m = 0, 1, 2, \cdots \tag{4.5}$$

484

Considerable algebraic manipulation is required to obtain the expressions for the C_{mn}'s in terms of system parameters, but the computations are straightforward. The resulting expressions generally involve definite integrals which cannot be evaluated analytically, but which present no serious obstacles to their determination by digital computation. For example, the real part of the leading diagonal element is found to be given by:

$$\Re\{C_{00}\} = -\int_0^\infty e^{-2DS}J_0(S)\left\{\left[1 + \frac{S}{F^2}\left(\frac{1}{(S-S_1)(S-S_2)} + \frac{1}{(S-S_3)(S-S_4)}\right)\right]J_1(S)\right.$$

$$+ k\sin S\left[\frac{k}{k^2-S^2} + \frac{S}{F^2}\left(\frac{1}{(k+S)(S-S_1)(S-S_2)} + \frac{1}{(k-S)(S-S_3)(S-S_4)}\right)\right]\right\}dS$$

$$- k\int_1^\infty \frac{\sin[k(\xi-1)]\,d\xi}{\sqrt{\xi^2-1}} - \frac{\pi}{F^2(S_1-S_2)}\left\{S_1\,e^{-2DS_1}J_0(S_1)\left[J_0(S_1) - \frac{k\cos S_1}{k+S_1}\right]\right.$$

$$\left. + S_2\,e^{-2DS_2}J_0(S_2)\left[J_0(S_2) - \frac{k\cos S_2}{k+S_2}\right]\right\}$$

$$- \frac{\pi}{F^2(S_3-S_4)}\left\{S_3\,e^{-2DS_3}J_0(S_3)\left[J_0(S_3) - \frac{k\cos S_3}{k-S_3}\right]\right.$$

$$\left. - S_4\,e^{-2DS_4}J_0(S_4)\left[J_0(S_4) - \frac{k\cos S_4}{k-S_4}\right]\right\}$$

where J_0 and J_1 are Bessel functions of the first kind of order zero and one, respectively. The terms involving e^{-2DS_1} and e^{-2DS_2} are, of course, omitted when S_1 and S_2 are complex, which corresponds to setting D_1 and D_2 equal to zero (see Table 1). Similar expressions are obtained for the imaginary part of C_{00} and for the remaining C_{nn}'s. The inhomogeneous terms arise from the hydrofoil boundary condition, and are found to be given by

$$r_0 = \alpha_0 - ikh_0 ,$$

$$r_1 = ik\alpha_0 ,$$

$$r_m = 0 ; \quad m \geq 2 .$$

It is not possible, except in certain special cases, to show that a solution to a set of equations of the form of Eqs. (4.5) exists (see [8]). However, examination of the behavior of the C_{mn}'s with increasing m and/or n indicates that a solution can be obtained. If a solution does exist, it may be shown [8] that this solution can be obtained in the following manner. First, the solution to a truncated set of, say, N equations is obtained. Subsequently, the solutions to $N - 1$, $N + 2$, etc., are obtained, until the limiting values of the unknowns become apparent. Of course, the larger the number of equations solved, the more unknowns determined in this manner. Since, for this problem, only the first four unknowns

are needed to evaluate lift and moment (Eqs. (4.3) and (4.4)), the procedure need only be carried out until these four values are obtained. It was found, in fact, that even for depths as shallow as half a chord length, with a relatively small Froude number ($F = 1.0$), only seven complex (or 14 real) equations were needed to determine A_0 through A_3 to within 0.1%.

The evaluation of the C_{mn}'s, the solution of Eqs. (4.5), and the computation of lift and moment according to Eqs. (4.3) and (4.4) were carried out on a high-speed digital computer for a wide range of values of F, D and k. Certain of the results are presented graphically in Figs. 2 through 7, and are discussed in Section 5.
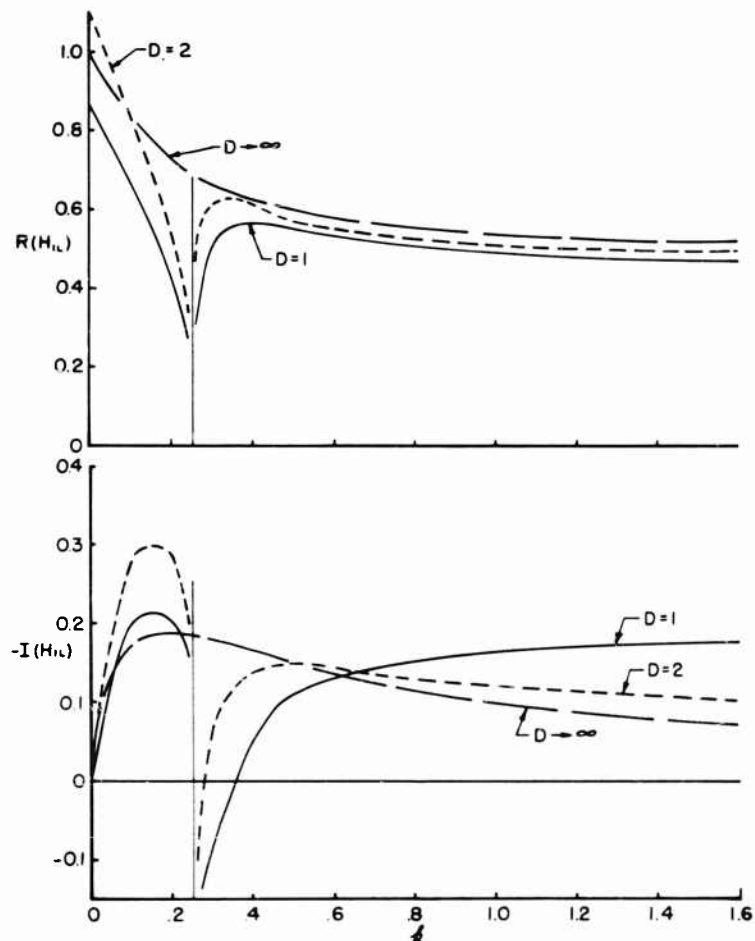
Fig. 2 - Lift due to plunging versus reduced frequency with depth in semichords as parameter; Froude number $F = 1.0$ and singularity at $k = 0.25$
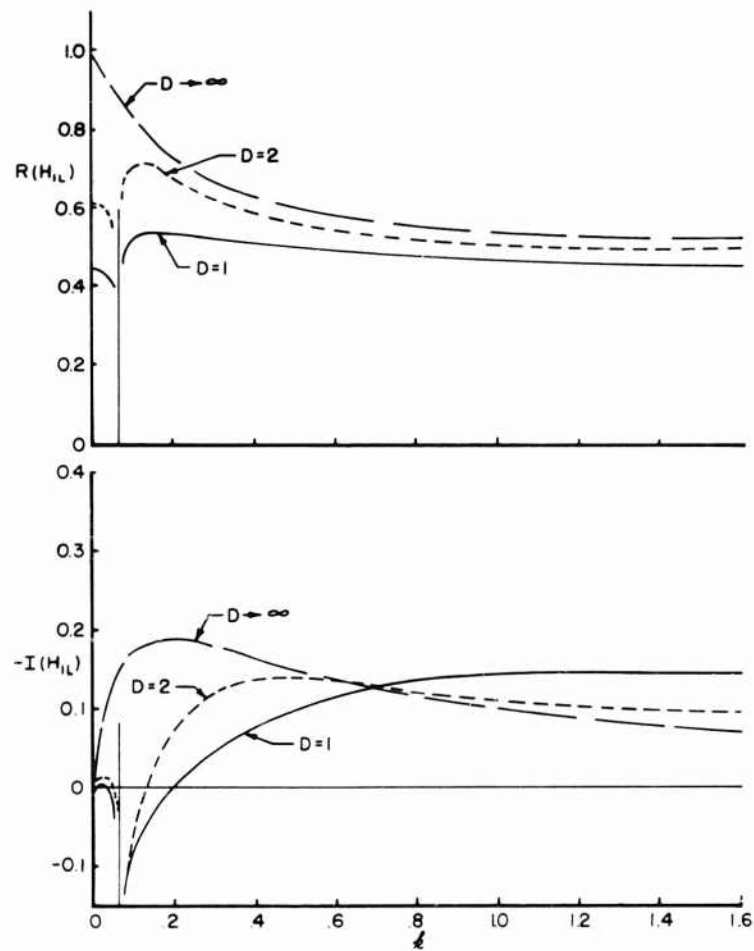
Fig. 3 – Lift due to plunging versus reduced frequency
with depth in semichords as parameter; Froude number
$F = 2.0$ and singularity at $k = 0.0625$

487
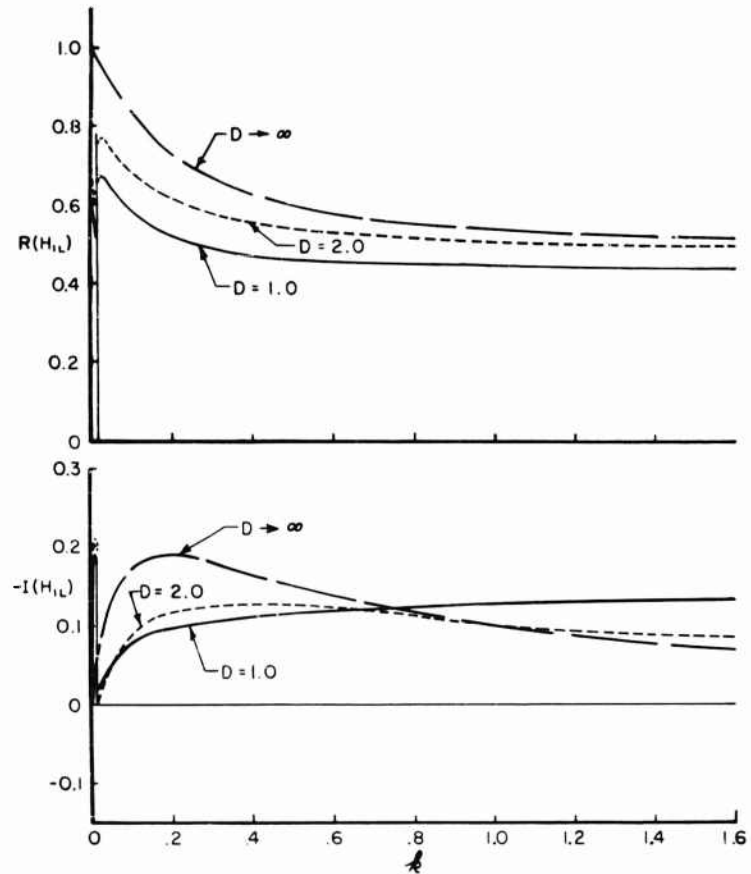
Fig. 4 - Lift due to plunging versus reduced frequency
with depth in semichords as parameter; Froude number
F = 4.0 and singularity at k = 0.015625
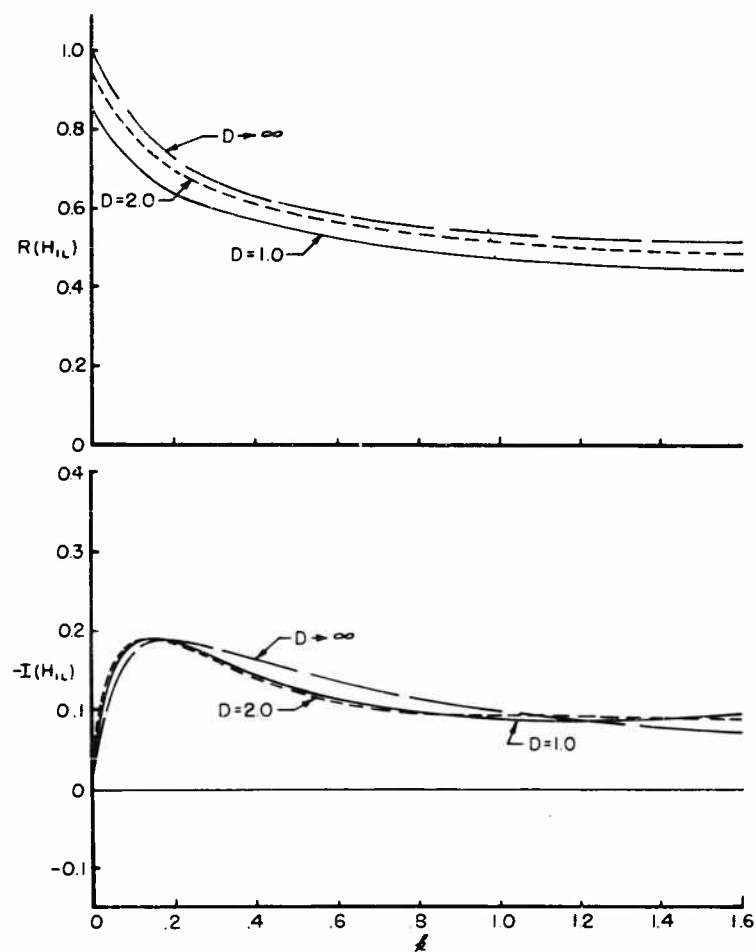
Fig. 5 - Lift due to plunging versus reduced
frequency with depth in semichords as param-
eter; Froude number $F \to \infty$
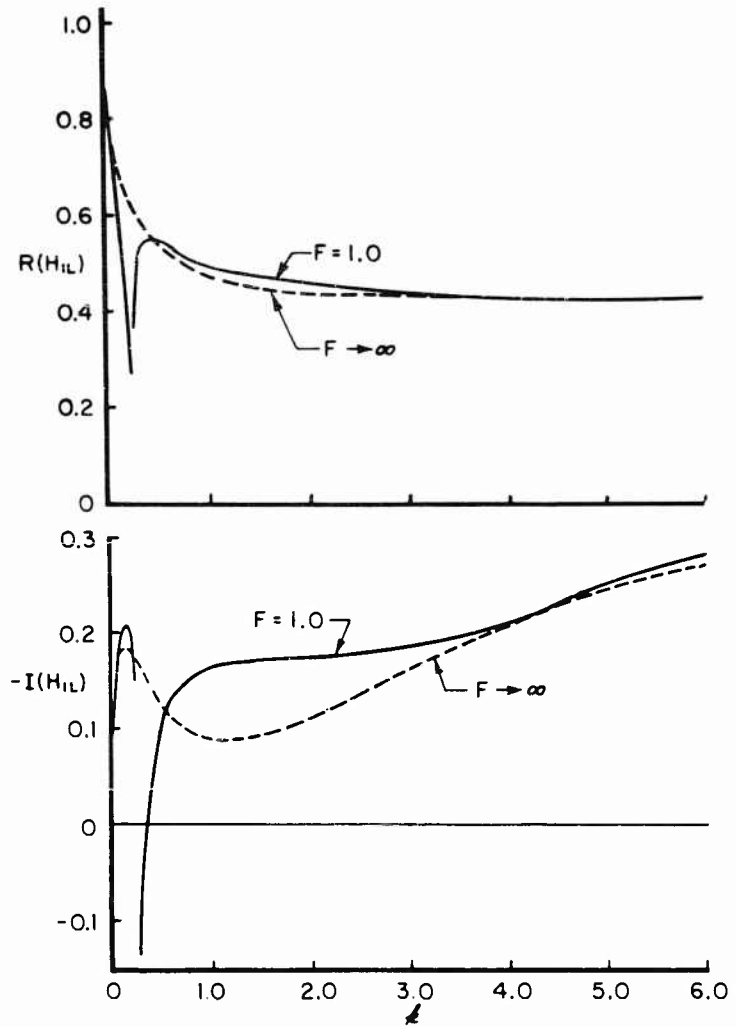
Fig. 6 - Lift due to plunging versus reduced frequency
with Froude number as parameter depth in semichords
D = 1.0
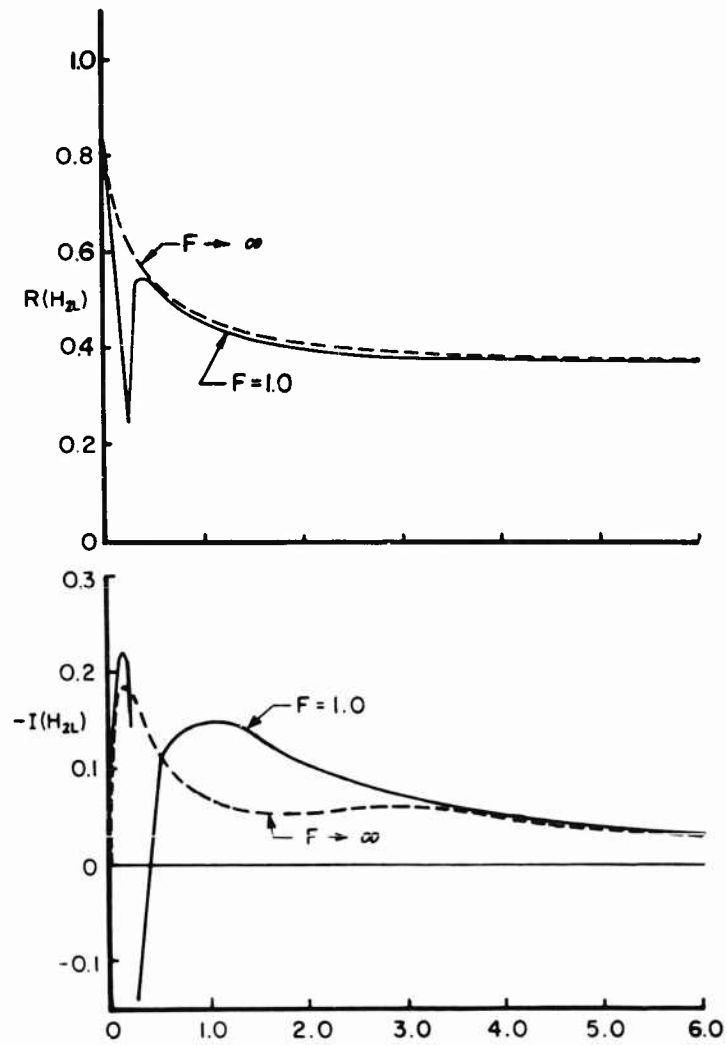
Fig. 7 - Lift due to plunging versus reduced frequency
with Froude number as parameter depth in semichords
$D = 1.0$

491

5. DISCUSSION OF RESULTS

In order to provide meaningful comparisons, the plotted results do not contain noncirculatory terms. The lift and moment about midchord are given, in terms of the plotted functions H_{1L}, H_{2L}, H_{1M}, and H_{2M}, by

$$\frac{Le^{-i\omega t}}{2\pi\rho U^2 b} = -\frac{k^2}{2}(h_0 - a\alpha_0) + \frac{ik}{2}\alpha_0$$

$$+ ikH_{1L}(h_0 - a\alpha_0) + H_{2L}\left(1 + \frac{ik}{2}\right)\alpha_0$$

$$\frac{Me^{-i\omega t}}{\pi\rho U^2 b^2} = \left(-\frac{ik}{2} + \frac{k^2}{8}\right)\alpha_0 + ikH_{1M}(h_0 - a\alpha_0) + H_{2M}\left(1 + \frac{ik}{2}\right)\alpha_0 \tag{5.1}$$

where $a \cdot b$ is the distance aft of midchord of the center of rotation of the pitching motion. H_{1L}, H_{2L}, H_{1M}, and H_{2M} are, in general, functions of Froude number, F, depth-to-semichord ratio, D, and reduced frequency, k. In the limit of infinite submergence depth, all these functions reduce to the well-known Theodorsen function $C(k)$.

In Figs. 2 through 5, the real and imaginary parts of H_{1L}, which relate to the unsteady lift due to plunging, are plotted as functions of reduced frequency for Froude numbers of 1, 2, 4, and infinity, respectively. On each figure, the function is plotted for depths of one and two semichords, as well as for infinite depth. The variations of the functions H_{2L}, H_{1M} and H_{2M} are very similar to that of H_{1L} over the reduced frequency range shown in these figures, and so these functions are not shown. It is observed from these results that, at least in the range of k shown, the behavior of H_{1L} is dominated by the presence of the resonance condition at $k = 1/4F^2$. While the real part of H_{1L}, which is in phase with the plunging motion, is not drastically affected except in the immediate vicinity of the singularity, the imaginary part shows marked departures from the variation at infinite depth. It should be particularly noted that for finite values of Froude number, the imaginary part of H_{1L} is positive near the singularity; hence, the circulatory lift leads the motion. This indicates the possibility of unusual hydroelastic characteristics, such as one-degree-of-freedom flutter, in hydrofoil systems.

The decrease in importance of the surface waves is evident as the Froude number changes from 1.0 (Fig. 2), where the singularity at $k = .25$ dominates, to infinity (Fig. 5), where there is no singularity and the curves for all depths do not deviate appreciably from those for the infinite depth case. The results for infinite Froude number agree with computations made by Chu and Abramson [2]. It should also be noted here that the results for $k = 0$ agree very well with treatments of the steady case. In fact, there is remarkable agreement with a lifting line analysis performed by Strandhagen and Seikel [9], even for $D = 1$ and $F = 1$.

In Fig. 6, H_{1L} is plotted out to a reduced frequency of 6.0 for a depth of one semichord and Froude numbers of 1.0 and infinity. As seen from this figure, the effects of surface waves become unimportant for reduced frequencies above

about 3.0. The effect of the image system is to cause the real and imaginary parts of H_{1L} to approach an asymptote for large k, the value of which depends, of course, on the depth. As the depth becomes infinite, the asymptote of $\Re(H_{1L})$ approaches 0.5, and that of $\Im(H_{1L})$ approaches zero.

It was found that the image system influences each of the functions H_{1L}, H_{2L}, etc., in a different manner at high reduced frequency. The function H_{2L}, associated with the lift due to pitching, is plotted in Fig. 7 for the same depth and Froude numbers as Fig. 6. While the general character of the curves is the same, it may be seen that the real and imaginary parts of H_{2L} approach different asymptotic values than do those of H_{1L}. This is contrasted with the behavior at low reduced frequency, where the surface wave effects predominate and the differences among the functions H_{1L}, H_{2L}, etc., are small for given values of the system parameters.

In summary, then, it was found that at reduced frequencies below about 3.0 and at practical values of Froude number and submergence depth, the behavior of the unsteady lift and moment is dictated by the considerable influence of the surface waves. In particular, the large effect of the free surface waves on the phases of the forces and moments makes the inclusion of these waves mandatory for hydrofoil stability considerations in the low reduced frequency range. At sufficiently high reduced frequencies ($k \geq 3.0$ for $F \geq 1.0$), the effects of the surface waves become less important, but the image system causes the functions relating to lift and moment to approach asymptotes with increasing reduced frequency. The values of these asymptotes depend on the depth of the hydrofoil. It appears then, in view of the diminished effect of surface waves at high reduced frequencies, that, in this regime, the assumption of infinite Froude number can result in satisfactory approximations for the unsteady lift and moment.

Complete tabulations and plots of all computations made will be included in a report to be published in the near future [10].

REFERENCES

1. Theodorsen, T., "General Theory of Aerodynamic Instability and the Mechanism of Flutter," NACA Report 496, 1935.

2. Chu, W.H. and Abramson, H.N., "Effect of the Free Surface on the Flutter of Submerged Hydrofoils," Journal of Ship Research, Vol. 3, No. 1, June 1959.

3. Kaplan, P., "A Hydrodynamic Theory for the Forces on Hydrofoils in Unsteady Motion," Doctorate Dissertation, Stevens Institute of Technology, 1955.

4. Tan, H.S., "On Source and Vortex of Fluctuating Strength Travelling Beneath a Free Surface," Quarterly of Applied Mathematics, Vol. 13, No. 3, October 1955.

5. von Karman, T. and Sears, W.R., "Airfoil Theory for Nonuniform Motion," Journal of the Aeronautical Sciences, Vol. 5, 1938.

6. Lamb, H., "Hydrodynamics," Sixth Edition, Dover Publications, New York, 1932.

7. Kaplan, P., "The Waves Generated by the Forward Motion of Oscillatory Pressure Distributions," Proceedings of the 5th Midwestern Conference on Fluid Mechanics, Ann Arbor, Michigan, 1957.

8. Kantorovich, L.V. and Krylov, V.I., "Approximate Methods of Higher Analysis," Interscience Publishers, Inc., New York, 1958.

9. Strandhagen, A.G. and Seikel, G.R., "Lift and Wave Drag of Hydrofoils," Proceedings of the 5th Midwestern Conference on Fluid Mechanics, Ann Arbor, Michigan, 1957.

10. Crimi, P. and Statler, I.C., "Forces and Moments on an Oscillating Hydrofoil," Cornell Aeronautical Laboratory Report (to be published).

*   *   *

UNSTEADY CHARACTERISTICS OF THE SUBMERGED HYDROFOIL PERFORMING HEAVE OR PITCH AT CONSTANT FORWARD SPEED UNDER SINUSOIDAL WAVES

Tetsuo Nishiyama
Tohoku University
Sendai, Japan

INTRODUCTION

Applying the Kárman and Sears' unsteady aerofoil theory [1,8] for the sinusoidally varying gust to the submerged hydrofoil performing heave or pitch while moving at constant forward speed, Kaplan [2] firstly studied the unsteady characteristics of hydrofoil from the theoretical stands. However, in the Kár-. mán and Sears' unsteady aerofoil theory, any account does not be taken only for the existence of free water surface, but also for the horizontal velocity component by the orbital motion of waves.

Ogilivie [3], Schwanecke [4], Leehey [5] and Abramson [6] also discussed the same problem under including the same weak points as before or other defects. Recently, these theoretical defects have been improved excellently by Isay [7]. But, on the other hand, calculating procedures proposed for obtaining the unsteady characteristics are extremely so complicated and consequently, introduction of rough approximation does not admit to enter into details and essentials of unsteady characteristics.

Thus, it is not too much to say that the unsteady characteristics of hydrofoil advancing at constant speed under waves have not been discussed and understood thoroughly and exactly in the stage of existing unsteady hydrofoil theory.

When examining the dynamical stability of hydrofoil craft among waves and hydroelastic properties such as flutter, it is, first of all, of primary importance to grasp the unsteady characteristics itself exactly.

From these circumstances, it seems that the following points should be improved out timely and thoroughly;

1. Neglecting unduly the existence of the free water surface, the results obtained are not effectively applicable.

2. Paying no attention to the actual condition of operation, numerical procedures for obtaining the unsteady characteristics are meaninglessly and extremely complicated.

3. Discussing in a lump the unsteady characteristics which result from some different causes, no considerations entering into details can be made.

Taking the above stated reasons into account and adopting suitably the the Kármán's [8] and Jones' [9] analytical methods, this present paper is aimed to renew and improve the existing unsteady hydrofoil theories as minutely as possible. In particular, it should be noted that the main object of considerations lies in clarifying the mutual relation between the unsteady effect and the free water surface effect.

In the first and second part, the unsteady characteristics are obtained analytically and discussed in details respectively for the hydrofoil moving at constant forward speed under sinusoidal waves and for the hydrofoil performing heave or pitch while moving at constant forward speed in still water.

In the third part, applying and combining the results in the first and second part, the unsteady characteristics are obtained for the hydrofoil performing heave or pitch at constant forward speed under sinusoidal waves.

1. UNSTEADY CHARACTERISTICS OF HYDROFOIL MOVING AT CONSTANT SPEED UNDER SINUSOIDAL WAVES

1.1 Orbital Velocity by Wave Motion

Take the origin o on the free water surface, with ox horizontal and oy vertically upwards and suppose the propagation of wave to be of velocity v in the direction of ox.

The velocity potential of wave motion of amplitude h is, referred to fixed coordinate (X, Y)

$$\phi_w = vhe^{i\nu t - ikx + ky} \quad ; \quad k = g/v^2 \quad , \quad \nu = kv \tag{1}$$

Rewriting down (1), referred to moving coordinate (x, y) of velocity c to the negative direction of ox, we have

$$\phi_w = vhe^{i\omega t - ikx + ky} \tag{2}$$

where

$$\omega = k(c \pm v) \tag{3}$$

Upper sign denotes the value in "against waves." Lower sign denotes the value in "with waves."

In the normal condition of operation, c is usually larger than v and so we can safely regard a sign of ω as positive. Then, the orbital velocity is given by

$$u_w = \mp ikvhe^{i\omega t - ikx + ky} \quad ; \quad v_w = \pm kvhe^{i\omega t - ikx + ky} \tag{4}$$

1.2 Induced Velocity by Bound Vortex Distribution

The pressure and kinematical condition on the free water surface is given by, respectively

$$- g\eta = \partial\phi/\partial t + c\partial\phi/\partial x \tag{5}$$

$$\partial\eta/\partial t + c\partial\eta/\partial x = \partial\phi/\partial y \tag{6}$$

Eliminating η from (5) and (6), the linearized boundary condition on the free water surface can be expressed

$$\frac{\partial^2\phi}{\partial t^2} + 2c\frac{\partial^2\phi}{\partial t\partial x} + c^2\frac{\partial^2\phi}{\partial x^2} + g\frac{\partial\phi}{\partial y} = 0 \quad ; \quad y = 0 \tag{7}$$

Now, a hydrofoil is supposed to be situated at depth of submersion f, a middle point of which being just under the origin 0 on the free water surface, as shown in Fig. 1.
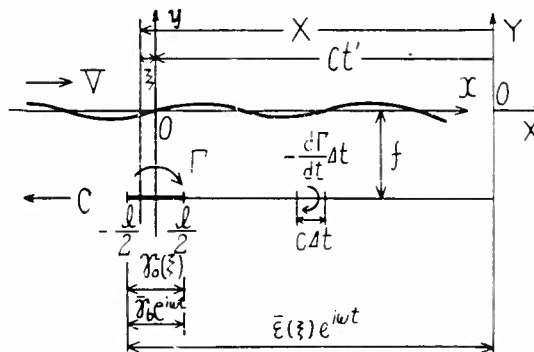
Fig. 1 - coordinate

Then, a hydrofoil may be substituted by vortex distribution over the range $\ell/2 \geq x \geq -\ell/2$, because the present theory stands on small perturbation linearized. Taking an actual condition of advancing at constant speed under sinusoidal waves into account, the bound vortex may be put in a form

$$\gamma_0(\xi) + \overline{\gamma}_b(\xi) \cdot e^{i\omega t} \tag{8}$$

The velocity potential which corresponds to $\gamma_0(\xi)$ and $\overline{\gamma}_b(\xi)$ can be determined from (7).

Now, we put ϕ_b in an appropriate form

$$\phi_b = \frac{1}{2\pi} \int_{-\ell/2}^{\ell/2} \overline{\gamma}_b(\xi) \cdot e^{i\omega t} \, d\xi \int_0^\infty e^{-k(f+y)} \sin k \, (x-\xi) \, \frac{dk}{k}$$

$$+ \frac{1}{2\pi} \int_{-\ell/2}^{\ell/2} \overline{\gamma}_b(\xi) \cdot e^{i\omega t} \, d\xi \int_0^\infty e^{-k(f-y)} \left\{ A \sin k \, (x-\xi) + B \cos k \, (x-\xi) \right\} \frac{dk}{k} \tag{9}$$

Substituting (9) into (7), we can decide the unknown functions

$$A = - \frac{(\tau^2 k^2 - \nu k - \nu^2)(\tau^2 \nu^2 + \nu k - \nu^2)}{\left\{ \tau^2 k^2 + k(2\tau\nu - \nu) + \nu^2 \right\} \left\{ \tau^2 k^2 - k(2\tau\nu + \nu) + \nu^2 \right\}} \tag{10}$$

$$B = - \frac{4 i \tau \nu^2 k}{\left\{ \tau^2 k^2 + k(2\tau\nu - \nu) + \nu^2 \right\} \left\{ \tau^2 k^2 - k(2\tau\nu - \nu) + \nu^2 \right\}}$$

where

$$\tau = \omega c/g \quad , \quad \nu = \omega^2/g \tag{11}$$

Transforming to more convenient form, (9) can be reduced to

$$\phi_b = \frac{1}{2\pi} \int_{-\ell/2}^{\ell/2} \overline{\gamma}_b(\xi) \cdot e^{i\omega t} \, d\xi \int_0^\infty e^{-k(f+y)} \sin k \, (x-\xi) \, \frac{dk}{k} - \frac{1}{2\pi} \int_{-\ell/2}^{\ell/2} \overline{\gamma}_b(\xi)$$

$$\times \, e^{i\omega t} \, d\xi \int_0^\infty e^{-k(f-y)} \sin k \, (x-\xi) \, \frac{dk}{k} + \frac{i\nu}{2\pi} \int_{-\ell/2}^{\ell/2} \overline{\gamma}_b(\xi)$$

$$\times \, e^{i\omega t} \, d\xi \int_0^\infty e^{-k(f-y)} \left\{ \frac{e^{ik(x-\xi)}}{\tau^2 k^2 - k(2\tau\nu - \nu) + \nu^2} - \frac{e^{-ik(x-\xi)}}{\tau^2 k^2 - k(2\tau\nu - \nu) + \nu^2} \right\} dk \tag{9.1}$$

The second term in (9.1) means the image potential to the free water surface and the third term, which shows the wave disturbance caused, is not final one, because it does not satisfy the radiation condition in an infinite forward.

In order to satisfy the radiation condition, we must examine minutely the properties of the regular waves caused by bound vortex; as known from the third term in (9.1), four kinds of regular waves exist and its propagating velocity is

$$w/k_1 \quad , \quad w/k_2 \quad , \quad w/k_3 \quad , \quad w/k_4 \tag{12}$$

where

$$\begin{pmatrix} k_1 \\ k_2 \end{pmatrix} = \frac{\nu}{2\tau^2} \left(1 - 2\tau \pm \sqrt{1 - 4\tau} \right) \tag{13}$$

$$\begin{pmatrix} k_3 \\ k_4 \end{pmatrix} = \frac{\nu}{2\tau^2} \left(1 + 2\tau \pm \sqrt{1 - 4\tau} \right) \tag{14}$$

After examining the propagating direction and, at the same time, the magnitude of propagating velocity compared with that of hydrofoil, we can conclude that the regular wave in an infinite forward is suffice to exist only for k_2. Thus, rewriting down so as to satisfy the radiation condition, (9.1) can be reduced to

$$
\begin{aligned}
\phi_b = {} & \frac{1}{2\pi} \int_{-\ell/2}^{\ell/2} \overline{\gamma}_b(\xi) e^{i\omega t} \, d\xi \int_0^\infty e^{-k(f+y)} \sin k \, (x-\xi) \frac{dk}{k} - \frac{1}{2\pi} \int_{-\ell/2}^{\ell/2} \overline{\gamma}_b(\xi) \\
& \times e^{i\omega t} \, d\xi \int_0^\infty e^{-k(f-y)} \sin k \, (x-\xi) \frac{dk}{k} - \frac{i\nu}{2\pi} \int_{-\ell/2}^{\ell/2} \overline{\gamma}_b(\xi) e^{i\omega t} \, d\xi \\
& \times \left[\int_0^\infty e^{-k(f-y)} \left\{ \frac{e^{ik(x-\xi)}}{\tau^2 k^2 + k(2\tau\nu - \nu) - \nu^2} - \frac{e^{-ik(x-\xi)}}{\tau^2 k^2 - k(2\tau\nu - \nu) - \nu^2} \right\} dk \right. \\
& + \frac{i\pi}{k_1 - k_2} \left\{ e^{-k_1(f-y) + ik_1(x-\xi)} - e^{-k_2(f-y) + ik_2(x-\xi)} \right\} \\
& \left. - \frac{i\pi}{k_3 - k_4} \left\{ e^{-k_3(f-y) - ik_3(x-\xi)} - e^{-k_4(f-y) - ik_4(x-\xi)} \right\} \right]
\end{aligned}
\tag{9.2}
$$

Then the induced velocity by bound vortex distribution can be given by

$$u_0 = \partial\phi_0/\partial x \qquad v_0 = \partial\phi_0/\partial y \tag{15}$$

$$u_b = \partial\phi_b/\partial x \qquad v_b = \partial\phi_b/\partial y \tag{16}$$

1.3 Induced Velocity by Free Vortex Distribution

The time variation of bound vortex produces, according to Helmholtz' law, a free vortex of equal but opposite circulation in wake region. The free vortex stands still at the position produced at every instant, and will constitute a continuously distributed vortex layer called by wake vortex.

499

From the assumptions in the present linearized theory, the displacement of wake vortex by the orbital motion of wave may be considered as negligible small; then the wake vortex distributes on the line $y = -f$, over which the hydrofoil passed, as shown in Fig. 1.

Now setting the fixed coordinate (X, Y) in the past before an infinite time, the relation between the moving and fixed coordinates is

$$-ct' + \xi = x \tag{17}$$

So, we rewrite (9.1) in the fixed coordinate

$$\phi_b = \frac{1}{2\pi} \int_{-\ell/2}^{\ell/2} \overline{\gamma}_b(\xi) \cdot e^{i\omega(t+t')} \, d\xi \int_0^\infty e^{-k(f+y)} \sin k \ (x-X) \ \frac{dk}{k} + \frac{1}{2\pi} \int_{-\ell/2}^{\ell/2} \overline{\gamma}_b(\xi)$$

$$\times \ e^{i\omega(t+t')} \, d\xi \int_0^\infty e^{-k(f-y)} \sin k \ (x-X) \ \frac{dk}{k} + \frac{i\nu}{2\pi} \int_{-\ell/2}^{\ell/2} \overline{\gamma}_b(\xi)$$

$$\times \ e^{i\omega(t+t')} \, d\xi \int_0^\infty e^{-k(f-y)} \left\{ \frac{e^{ik(x-X)}}{\tau^2 k^2 + k(2\tau\nu - \nu) + \nu^2} - \frac{e^{-ik(x-X)}}{\tau^2 k^2 - k(2\tau\nu + \nu) + \nu^2} \right\} dk \tag{18}$$

According to Helmholtz' law, the velocity potential of free vortex can be expressed by

$$\phi_f = \int_0^\infty \frac{\partial \phi_b}{\partial t'} \, dt' \tag{19}$$

Then, substituting (18) into (19), we have

$$\phi_f = -\frac{i\omega}{c} \frac{1}{2\pi} \int_\xi^x e^{\frac{i\omega}{c}(\xi-X)} \, dX \left[\int_{-\ell/2}^{\ell/2} \overline{\gamma}_b(\xi) \cdot e^{i\omega t} \, d\xi \int_0^\infty e^{-k(f+y)} \sin k \ (x-X) \ \frac{dk}{k} \right.$$

$$- \int_{-\ell/2}^{\ell/2} \overline{\gamma}_b(\xi) \cdot e^{i\omega t} \, d\xi \int_0^\infty e^{-k(f-y)} \sin k \ (x-X) \ \frac{dk}{k}$$

$$- \int_{-\ell/2}^{\ell/2} \overline{\gamma}_b(\xi) \cdot e^{i\omega t} \, d\xi \int_0^\infty e^{-k(f+y)} \sin k \ (x-\xi) \ \frac{dk}{k} + i\nu \int_{-\ell/2}^{\ell/2} \overline{\gamma}_b(\xi) \cdot e^{i\omega t} \, d\xi$$

$$\times \int_0^\infty e^{-k(f-y)} \left\{ \frac{e^{ik(x-X)}}{\tau^2 k^2 + k(2\tau\nu - \nu) + \nu^2} - \frac{e^{-ik(x-X)}}{\tau^2 k^2 - k(2\tau\nu + \nu) + \nu^2} \right\} dk \right] \tag{19.1}$$

(19.1) is simply a formal expression, because it does not at all satisfy the radiation condition.

Taking the radiation condition and also the wave disturbance by wake vortex into account, we can complete in final form

$$
\begin{aligned}
\phi_f = \ &- \frac{i\omega}{c} \frac{1}{2\pi} \int_\xi^\infty e^{\frac{i\omega}{c}(\xi - X)} \, dX \left[\int_{-\ell/2}^{\ell/2} \overline{\gamma}_b(\xi) \cdot e^{i\omega t} \, d\xi \int_0^\infty e^{-k(f+y)} \sin k \, (x - X) \, \frac{dk}{k} \right. \\
&- \int_{-\ell/2}^{\ell/2} \overline{\gamma}_b(\xi) \cdot e^{i\omega t} \, d\xi \int_0^\infty e^{-k(f-y)} \sin k \, (x - X) \, \frac{dk}{k} + i\nu \int_{-\ell/2}^{\ell/2} \overline{\gamma}_b(\xi) \\
&\times \ e^{i\omega t} \, d\xi \int_0^\infty e^{-k(f-y)} \left\{ \frac{e^{ik(x-X)}}{\tau^2 k^2 + k(2\tau\nu - \nu) + \nu^2} - \frac{e^{-ik(x-X)}}{\tau^2 k^2 - k(2\tau\nu + \nu) + \nu^2} \right\} dk \right] \\
&+ \frac{\nu}{2\pi} \frac{\frac{\pi\omega}{c}}{k_3 - k_4} \int_{-\ell/2}^{\ell/2} \overline{\gamma}_b(\xi) \cdot e^{i\omega t} \left\{ \frac{e^{-k_3(f-y)}}{k_3 - \frac{\omega}{c}} \left(e^{\frac{i\omega}{c}(\xi - x)} - e^{ik_3(\xi - X)} \right) \right. \\
&- \left. \frac{e^{-k_4(f-y)}}{k_4 - \frac{\omega}{c}} \left(e^{\frac{i\omega}{c}(\xi - x)} - e^{ik_4(\xi - X)} \right) \right\} d\xi
\end{aligned}
\tag{19.2}
$$

where the last integral exists only for $x > \xi$. It can be easily known that (19.2) is in exact coincidence with Isay's results obtained by somewhat different method.

Then the induced velocity by free vortex distribution can be given by

$$
u_f = \partial \phi_f / \partial x \quad , \quad v_f = \partial \phi_f / \partial y
\tag{20}
$$

1.4 Boundary Condition and Integral Equation

When putting the camber line of hydrofoil by

$$
y = g(x)
\tag{21}
$$

the boundary condition is given by, at every instant

$$
dg/dx = (v_w + v_b + v_f + v_0) / (c - u_w + u_b + u_f - u_0)
\tag{22}
$$

Then, the coefficients depending or independing on $e^{i\omega t}$ should be always zero respectively

$$
dg/dx = v_0 / (c - u_0)
\tag{23}
$$

$$
dg/dx = (\overline{v}_w + \overline{v}_b + \overline{v}_f) / (\overline{u}_w + \overline{u}_b + \overline{u}_f)
\tag{24}
$$

From (23) we can obtain an integral equation which determines the steady vortex distribution γ_o and, on the other hand, from (24) the unsteady vortex distribution $\overline{\gamma}_b$.

501

Now we write down the latter integral equation

$$vkhe^{-kf}\left(\cos kx + \frac{dg}{dx}\sin kx\right) = \frac{1}{2\pi}\int_{-\ell/2}^{\ell/2}\overline{\gamma}_b(\xi)\left\{\frac{1}{x-\xi} - \frac{i\omega}{c}\int_{\xi}^{\infty}\frac{e^{\frac{i\omega}{c}(\xi-X)}}{x-X}\,dX\right.$$
$$\left. + K_1(x,\xi;X)\right\}d\xi \tag{25}$$

where

$$K_1(x,\xi;X) = \frac{(x-\xi) - 2f\dfrac{dg}{dx}}{(x-\xi)^2 + 4f^2} - \frac{i\omega}{c}\int_{\xi}^{\infty}e^{\frac{i\omega}{c}(\xi-X)}\frac{(x-X) - 2f\dfrac{dg}{dx}}{(x-X)^2 + 4f^2}\,dX + i\nu\int_0^{\infty}e^{-2kf}\,k$$

$$\times\left\{\frac{\left(1 + i\dfrac{dg}{dx}\right)e^{ik(x-\xi)}}{\tau^2 k^2 + k(2\tau\nu-\nu) + \nu^2} - \frac{\left(1 - i\dfrac{dg}{dx}\right)e^{-ik(x-\xi)}}{\tau^2 k^2 - \tau(2\tau\nu+\nu) + \nu^2}\right\}dk$$

$$- \frac{\pi\nu}{k_3-k_4}\left(1 - i\dfrac{dg}{dx}\right)\left\{k_3 e^{-2k_3 f + ik_3(x-\xi)} - k_4 e^{-2k_4 f - ik_4(x-\xi)}\right\}$$

$$+ \nu\frac{\omega}{c}\int_{\xi}^{\infty}e^{\frac{i\omega}{c}(\xi-X)}\,dx\int_0^{\infty}e^{-2kf}\,k\left\{\frac{\left(1 + i\dfrac{dg}{dx}\right)e^{ik(x-X)}}{\tau^2 k^2 + k(2\tau\nu-\nu) + \nu^2}\right.$$

$$\left. - \frac{\left(1 - i\dfrac{dg}{dx}\right)e^{-ik(x-X)}}{\tau^2 k^2 - k(2\tau\nu+\nu) + \nu^2}\right\}dk - \frac{\pi\nu\dfrac{\omega}{c}}{k_3-k_4}\left[\frac{e^{-2k_3 f}}{k_3 - \dfrac{\omega}{c}}\left\{\left(k_3 - i\frac{\omega}{c}\frac{dg}{dx}\right)e^{\frac{i\omega}{c}(\xi-x)}\right.\right.$$

$$\left. - \left(1 - i\frac{dg}{dx}\right)k_3 e^{ik_3(\xi-x)}\right\} - \frac{e^{-2k_4 f}}{k_4 - \dfrac{\omega}{c}}\left\{\left(k_4 - i\frac{\omega}{c}\frac{dg}{dx}\right)e^{\frac{i\omega}{c}(\xi-x)}\right.$$

$$\left.\left. - \left(1 - i\frac{dg}{dx}\right)k_4 e^{ik_4(\xi-x)}\right\}\right] \tag{26}$$

The first and second term in (25) means the induced velocity in an infinite fluid by the bound and free vortex respectively, and the third term the additive one due to the existence of free water surface.

1.4.1 Unsteady Bound Vortex Distribution

We put the bound vortex distribution by introducing the unknown coefficients as follows:

$$\overline{\gamma}_b = w_0\overline{\gamma}_0(\tau) + w_1\overline{\gamma}_1(\tau) + w_2\overline{\gamma}_2(\tau) + w_3\overline{\gamma}_3(\tau) + w_4\overline{\gamma}_4(\tau) \tag{27}$$

where

$$\overline{\gamma}_0(\tau) = 2\, S\, \cot \frac{\tau}{2} + 2i\, \frac{\omega \ell}{2c} \sin \tau$$

$$\overline{\gamma}_1(\tau) = -2 \sin \tau + \cot \frac{\tau}{2} + i\, \frac{\omega \ell}{2c} \left(\sin \tau + \frac{\sin 2\tau}{2} \right)$$

$$\overline{\gamma}_n(\tau) = -2 \sin n\tau + i\, \frac{\omega \ell}{2c} \left\{ \frac{\sin (n+1)\,\tau}{n+1} - \frac{\sin (n-1)\,\tau}{n-1} \right\} ; \quad n = 2,3,4 \quad (28)$$

and S occurring in the definition of $\overline{\gamma}_0$ is given in term of the Hankel function $H_0^{(2)}$, $H_1^{(2)}$ by

$$S = \frac{H_1^{(2)}\left(\frac{\omega \ell}{2c}\right)}{H_1^{(2)}\left(\frac{\omega \ell}{2c}\right) + H_2^{(2)}\left(\frac{\omega \ell}{2c}\right)} \tag{29}$$

$$x = -\frac{\ell}{2} \cos t \quad, \quad \xi = -\frac{\ell}{2} \cos \tau \quad; \quad 0 \le \frac{t}{\tau} \le \tau \tag{30}$$

and, furthermore

$$vkhe^{-kf} \left(\cos kx - \frac{dg}{dx} \sin kx \right) = \frac{1}{\sin \tau} \sum_1^5 G_n \sin n t \tag{31}$$

$$\frac{\ell}{2} \sin t \cdot K_1(\tau, t) = \sum_{\mu=1}^5 \sum_{\nu=0}^6 b_{\mu\nu} \sin \mu t \cdot \cos \nu t \tag{32}$$

then, the coefficients in (32) is given by

$$b_{\mu\nu} = \frac{\ell}{18} \sum_{j=1}^5 \sin \mu t_j \left[\sum_{k=1}^5 \sin t_j \cdot K_1(t_j, \tau_k) \cos \nu \tau_k \right.$$

$$\left. - \frac{\sin t_j}{2} \left\{ K_1(t_j, 0) + (-1)^\nu K_1(t_j, \pi) \right\} \right] \tag{33}$$

where one half of (33) should be taken for the case $\nu = 0.6$.

Substituting (27), (31) and (32) into (25) and comparing the coefficients of $\cos n t$, we have

$$G_1 + G_3 + G_5 = w_0 - \frac{1}{2} w_1 - \frac{1}{2} \left\{ C_0(b_{10} + b_{30} + b_{50}) - \frac{1}{2} \sum_1^5 C_s(b_{1s} + b_{3s} + b_{5s}) \right\}$$

$$2G_2 - 2G_4 = w_1 \qquad - \frac{1}{2} \left\{ 2C_0(b_{20} + b_{40}) - \sum_1^5 C_s(b_{2s} + b_{4s}) \right\} \tag{34}$$
$$\text{(Cont.)}$$

503

$$2G_3 + 2G_5 = w_2 + \frac{1}{2}\left\{2C_0(b_{30} + b_{50}) + \sum_1^5 C_\beta(b_{3\beta} + b_{5\beta})\right\}$$

$$2G_4 = w_3 + \frac{1}{2}\left(2C_0 b_{40} + \sum_1^5 C_\beta b_{4\beta}\right)$$

$$2G_5 = w_4 + \frac{1}{2}\left(2C_0 b_{50} + \sum_1^5 C_\beta b_{5\beta}\right) \tag{34}$$

where

$$C_0 = 2 w_0 S + \frac{1}{2} i \frac{\omega \ell}{2c} (2w_0 + w_1 - w_2)$$

$$C_1 = 2 w_0 S + w_1 - w_2 + \frac{1}{2} i \frac{\omega \ell}{2c}\left(\frac{1}{2} w_1 - w_3\right)$$

$$C_2 = w_1 - w_3 - \frac{1}{2} i \frac{\omega \ell}{2c}\left(2w_0 + w_1 - \frac{4}{3} w_2 + \frac{1}{3} w_3\right)$$

$$C_3 = w_2 - w_4 - \frac{1}{2} i \frac{\omega \ell}{2c}\left(\frac{1}{2} w_1 - \frac{3}{4} w_3\right) \tag{35}$$

$$C_4 = w_3 - \frac{1}{2} i \frac{\omega \ell}{2c}\left(\frac{1}{3} w_2 - \frac{8}{15} w_4\right)$$

$$C_5 = w_4 - \frac{1}{2} i \frac{\omega \ell}{2c} \times \frac{1}{4} w_3$$

Then, the unknown complex coefficients w_n can be easily determined from ten simultaneous equations obtained from the real and imaginary part of (34). Further, when numerical calculations are made, it is convenient to use the Kussner's function [10] T made in the numerical table by the relation

$$2S - 1 = T \tag{36}$$

1.4.2 Free Vortex Distribution

Correspondingly to $\bar{\gamma}_b$ determined, the wake vortex can be obtained from (19.1); i.e.,

$$\bar{\epsilon} = - i \frac{\omega \ell}{2c} e^{-i \frac{\omega \ell}{2c} \xi} \int_{-1}^{\xi} \bar{\gamma}_b(\xi) e^{i \frac{\omega \ell}{2c}} d\xi \quad : \quad -1 \leqq \xi \leqq 1 \tag{37}$$

$$\bar{\epsilon} = - i \frac{\omega \ell}{2c} e^{-i \frac{\omega \ell}{2c} \xi} \int_{-1}^{1} \bar{\gamma}_b(\xi) e^{i \frac{\omega \ell}{2c}} d\xi \quad ; \quad \xi \geqq 1 \tag{38}$$

504

Putting (27) into (37) and (38) and transforming, we obtain

$$\bar{\varepsilon} = -2i \frac{\omega\ell}{2c} w_0 \left[\sin\tau + e^{-i\frac{\omega\ell}{2c}\xi} \left\{ \left(SJ_0 \left(\frac{\omega\ell}{2c} \right) \right. \right. \right.$$

$$\left. + i(1-S)J_1 \left(\frac{\omega\ell}{2c} \right) \right) \tau + 2 \sum_1^\infty (-1)^n \frac{\sin n\tau}{n} \left(SJ_n \left(\frac{\omega\ell}{2c} \right) - i(1-S)J_n'\left(\frac{\omega\ell}{2c} \right) \right) \right\} \right]$$

$$- i \frac{\omega\ell}{2c} w_1 \left(\sin\tau + \frac{\sin 2\tau}{2} \right) - i \frac{\omega\ell}{2c} w_n \left\{ \frac{\sin(n+1)\tau}{n+1} - \frac{\sin(n-1)\tau}{n-1} \right\} \qquad (37.1)$$

$$\bar{\varepsilon} = -2\pi i \, w_0 \frac{\omega\ell}{2c} e^{-i\frac{\omega\ell}{2c}\xi} \left\{ SJ_0 \left(\frac{\omega\ell}{2c} \right) + i(1-S)J_1 \left(\frac{\omega\ell}{2c} \right) \right\} \qquad (38.1)$$

where J_0 and J_1 is the Bessel function of the first kind and J_n is a derivative with its argument. Thus, we can calculate the strength of the wake vortex at arbitrary point from (37.1) and (38.1).

1.4.3 Quasi-Steady Bound Vortex Distribution

When neglecting the induced velocity by wake vortex, (24) is reduced to

$$dg/dx = (\bar{v}_w - \bar{v}_b)/(\bar{u}_w - \bar{u}_b) \qquad (39)$$

This can be regarded as the boundary condition in case when considering the instantaneous induced velocity is hold steadily and so gives an integral equation determining the quasi-steady vortex distribution.

The integral equation is

$$vkhe^{-kf} \left(\cos kx + \frac{dg}{dx} \sin kx \right) = \frac{1}{2\pi} \int_{-\ell/2}^{\ell/2} \bar{\gamma}_q(\xi) \left\{ \frac{1}{x-\xi} - K_2(x,\xi) \right\} d\xi \qquad (40)$$

where

$$K_2(x,\xi) = \frac{(x-\xi) - 2f \frac{dg}{dx}}{(x-\xi)^2 - 4f^2} + i \int_0^\infty e^{-2kf} k$$

$$\times \left\{ \frac{\left(1 - i \frac{dg}{dx} \right) e^{ik(x-\xi)}}{-^2k^2 + k(2-) - ^2} - \frac{\left(1 - i \frac{dg}{dx} \right) e^{-ik(x-\xi)}}{-^2k^2 - k(2-) + ^2} \right\} dk$$

$$- \frac{}{k_3 - k_4} \left(1 - i \frac{dg}{dx} \right) \left\{ k_3 e^{-2k_3 f + ik_3(x-\xi)} - k_4 e^{-2k_4 f - ik_4(x-\xi)} \right\} \qquad (41)$$

Putting the quasi-vortex distribution in a form

$$\overline{\gamma}_q(\tau) = \frac{1}{\sin \tau}\left(\frac{q_0}{\sqrt{\pi}} + \sqrt{\frac{2}{\pi}}\sum_1^5 q_\beta \cos \beta\tau\right) \tag{42}$$

and substituting (31), (32) and (42) into (40), we have the relation

$$G_n = \frac{1}{\sqrt{2\pi}}\left(q_n + \frac{q_0}{\sqrt{2}}b_{n0} + \frac{1}{2}\sum_1^5 q_\beta b_{n\beta}\right) \quad ; \quad n = 1,2,3,4,5 \tag{43}$$

Then, the unknown coefficients can be determined from five simultaneous equations and the remained constant q_0 from the Kutta's condition at trailing edge, i.e.,

$$\overline{\gamma}_q(\pi) = 0 \tag{44}$$

1.5 Unsteady Characteristics

It is easy to calculate the steady characteristics from γ_0 obtained by solving an integral equation (23). However, as the thin hydrofoil is considered to be only a special case of hydrofoil of arbitrary section, the previous method [11] is also applicable.

1.5.1 Unsteady Lift

$$L = \rho c \int_{-\ell/2}^{\ell/2} \overline{\gamma}_q(\xi)\cdot e^{i\omega t}\, d\xi - \rho\frac{\partial}{\partial t}\int_{-\ell/2}^{\ell/2}\overline{\gamma}_q(\xi)e^{i\omega t}\,\xi d\xi - \rho c \int_{\ell/2}^{\infty}\frac{\overline{\epsilon}(\xi)e^{i\omega t}}{\sqrt{\xi^2 - \frac{\ell^2}{4}}}d\xi \tag{45}$$

$$L = \rho c \int_{-\ell/2}^{\ell/2}\overline{\gamma}_b(\xi)\cdot e^{i\omega t}\, d\xi \tag{46}$$

As already known, the first term is a quasi-steady lift which corresponds to the steady lift by the Kutta-Joukowsky's law. The second term is a lift due to virtual mass, and the third term is a lift produced by wake vortex distribution.

Substituting (38.1) and (42) into (45) and expressing in nondimensional form, we have

$$\overline{C}_a = \overline{C}_{a0} - \overline{C}_{a1} - \overline{C}_{a2} \tag{47}$$

where

$$\overline{C}_{a0} = \frac{\sqrt{\pi}}{c}q_0 \tag{47.1}$$

506

$$\overline{C}_{a1} = \frac{i}{4} \frac{\omega \ell}{c} \frac{\sqrt{2\pi}}{c} q_1 \tag{47.2}$$

$$\overline{C}_{a2} = -2\pi i \frac{w_0}{c} \frac{\omega \ell}{c} K_0 \left(i \frac{\omega \ell}{2c}\right) \left\{S J_0\left(\frac{\omega \ell}{2c}\right) + i(1-S) J_1\left(\frac{\omega \ell}{2c}\right)\right\} \tag{47.3}$$

with the modified Bessel function of second kind K_0

$$\overline{C}_a = \frac{\pi}{c} \left\{2 w_0 \left(S + \frac{i}{2} \frac{\omega \ell}{2c}\right) - \frac{1}{2} i \frac{\omega \ell}{2c} (w_1 - w_2)\right\} \tag{48}$$

1.5.2 Unsteady Moment

The unsteady moment about origin is

$$M = \rho c \int_{-\ell/2}^{\ell/2} \overline{\gamma}_q(\xi) \cdot e^{i\omega t} \xi d\xi - \frac{1}{2} \rho \frac{d}{dt} \int_{-\ell/2}^{\ell/2} \overline{\gamma}_q(\xi) \cdot e^{i\omega t} \left(\xi^2 - \frac{\ell^2}{8}\right) d\xi$$

$$- \frac{1}{8} \rho c \ell^2 \int_{-\ell/2}^{\pi} \frac{\overline{\varepsilon}(\xi) \cdot e^{i\omega t}}{\sqrt{\xi^2 - \frac{\ell^2}{4}}} \tag{49}$$

$$M = \rho c \int_{-\ell/2}^{\ell/2} \overline{\gamma}_b(\xi) \cdot e^{i\omega t} \xi d\xi \tag{50}$$

The physical meaning of each term is wholly similar to (47). In the nondimensional form, we have

$$\overline{C}_m = \overline{C}_{m0} - \overline{C}_{m1} - \overline{C}_{m2} \tag{51}$$

where

$$\overline{C}_{m0} = -\sqrt{\frac{\pi}{8}} \frac{q_1}{c} \tag{51.1}$$

$$\overline{C}_{m1} = -\frac{1}{8} \sqrt{\frac{\pi}{c}} \frac{\omega \ell}{c} \frac{q_1}{c} \tag{51.2}$$

$$\overline{C}_{m2} = \frac{1}{2} \pi i \frac{w_0}{c} \frac{\omega \ell}{2c} K_0 \left(i \frac{\omega \ell}{2c}\right) \left\{S J_0\left(\frac{\omega \ell}{2c}\right) - i(1-S) J_1\left(\frac{\omega \ell}{2c}\right)\right\} \tag{51.3}$$

$$\overline{C}_m = -\frac{1}{4} \frac{\pi}{c} (2S w_0 - w_1) \tag{52}$$

Therefore, the position of the point of action of the respective lift is given by

$$\overline{C}_{m0}/\overline{C}_{a0} \quad \cdot \quad \overline{C}_{m1}/\overline{C}_{a1} \quad \cdot \quad \overline{C}_{m2}/\overline{C}_{a2} \tag{53}$$

and further, from (47.3) and (51.3) we have

$$\bar{C}_{m2}/\bar{C}_{a2} = -\ell/4 \tag{54}$$

This shows that the lift due to wake vortex always passes through the quarter chord point.

1.5.3 Wake Energy

The strength of free vortex in wake region by

$$\epsilon = 2\pi \frac{\omega\ell}{2c} \left[\left\{ w_{01}(A \sin \omega t + B \cos \omega t) - w_{02}(A \cos \omega t - B \sin \omega t) \right\} \cos \frac{\omega\ell}{2c} \xi \right.$$

$$\left. - \left\{ w_{01}(A \cos \omega t - B \sin \omega t) - w_{02}(A \sin \omega t + B \cos \omega t) \right\} \sin \frac{\omega\ell}{2c} \xi \right] \tag{55}$$

where

$$A + iB = SJ_0\left(\frac{\omega\ell}{2c}\right) - i(1-S)J_1\left(\frac{\omega\ell}{2c}\right)$$

$$w_0 = w_{01} - iw_{02} \tag{56}$$

In general, the kinetic energy of wake vortex per unit length is

$$E_1 = \frac{1}{2} \rho \oint \sigma \frac{\partial \sigma}{\partial n} dx \tag{57}$$

Then, using the relation on the vortex sheet

$$\sigma = \frac{i}{2} \int \epsilon \, dx \quad , \quad \frac{\partial \sigma}{\partial n} = \frac{1}{2\pi} \int \frac{\epsilon}{x - \xi} d\xi \tag{58}$$

and putting (55) into (57), we have

$$F_1 = \frac{-2}{2} \rho \ell \frac{\omega\ell}{2c} \left[w_{01} \left\{ -A \sin \left(\omega t - \frac{\omega\ell}{2c} \xi \right) - B \cos \left(\omega t - \frac{\omega\ell}{2c} \xi \right) \right\} \right.$$

$$\left. + w_{02} \left\{ A \cos \left(\omega t - \frac{\omega\ell}{2c} \xi \right) - B \sin \left(\omega t - \frac{\omega\ell}{2c} \xi \right) \right\} \right]^2 \tag{59}$$

Now, taking the time average, we obtain

$$\bar{E}_1 = \frac{\omega}{2\pi} \int_0^{2\pi-\omega} \bar{E}_1(t) \, dt = \frac{-2}{4} \rho \ell \frac{\omega\ell}{2c} \left(w_{01}^2 + w_{02}^2 \right) (A^2 + B^2) \tag{60}$$

508

This shows that the average increase in kinetic energy in unit time is constant independently on the position produced. Therefore it can be safely said that the hydrofoil experiences the constant resistance which should be called as the vortex making resistance depending on the reduced frequency and form of camber line of hydrofoil.

1.6 Actual Condition of Operation

1.6.1 High Speed

It is of primary importance to determine the vortex distribution $\bar{\gamma}_b$ and $\bar{\gamma}_q$ to obtain the unsteady characteristics. However, the computational procedures for solving the integral equation at arbitrary Froude number is extremely complicated and troublesome. This is exclusively due to K_1 in (26) and K_2 in (41).

The advancing speed of hydrofoil is very high in the normal condition of operation. This fact means that the inertia force is of large magnitude compared with the gravity and then the effect of Froude number on the characteristics of hydrofoil is negligible small.

The hydrodynamic behavior of free water surface can be known by examining the boundary condition (7) in the extremely high speed; i.e.,

$$\lim_{c \to \infty} \left| \frac{\partial^2 \varphi}{\partial t^2} + 2c \frac{\partial^2 \varphi}{\partial t \partial x} + c^2 \frac{\partial^2 \varphi}{\partial x^2} + g \frac{\partial \varphi}{\partial y} \right| = \frac{\partial^2 \varphi}{\partial x^2} = 0 \tag{7.1}$$

This shows that the free water surface in high speed behaves as the free boundary. Taking this into account, numerical procedures will be moderately simplified.

$$\lim_{c \to \infty} K_1(x, \xi; X) = \frac{(x - \xi) - 2f \frac{dg}{dx}}{(x - \xi)^2 - 4f^2} - \frac{i\omega}{c} \int_{\xi}^{x} e^{\frac{i\omega}{c}(\xi - X)} \frac{(x - X) - 2f \frac{dg}{dx}}{(x - X)^2 - 4f^2} dX \tag{26.1}$$

$$\lim_{c \to \infty} K_2(x, \xi) = \frac{(x - \xi) - 2f \frac{dg}{dx}}{(x - \xi)^2 + 4f^2} \tag{41.1}$$

This also means that the image vortex distribution is taken to satisfy the boundary condition (7.1) and the effect of Froude number is completely neglected.

In practical numerical work, the second term in (26.1) can be transformed to the closed form by using the exponential function E_i and $\bar{E}_i$.

1.6.2 Reduced Frequency

As already known, the magnitude of reduced frequency influences decidedly on the unsteady characteristics. The reduced frequency in the normal condition of operation is given as shown in Fig. 2.
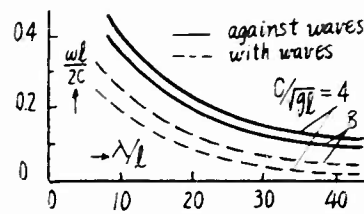
Fig. 2 - Reduced frequency

$\omega \ell/2c = 0.4 \sim 0.1$ for "against waves"
$\omega \ell/2c = 0.2 \sim 0.05$ for "with waves"

Then, we can easily see that the unsteadiness is larger in against waves than in with waves.

1.7 Numerical Examples and its Considerations

We adopt the following case as a concrete example: flat plate hydrofoil,

attack angle	$\alpha = 5°$
submergence depth	$f = 1.251$
Froude number	$c/\sqrt{gf} = 4.0$

The wave length of progressive wave is as follows:

Table 1
Amplitude of Progressive Wave ($h = 0.5f$)

$\omega \ell/2c$	0.418	0.183	0.103
Against waves	-2	2.5^{-2}	5^{-2}
With waves	5.89	11.85	18.65

1.7.1 Unsteady Vortex Distribution

Curves are shown in Figs. 3 and 4 for quasi-steady and unsteady vortex distribution respectively.
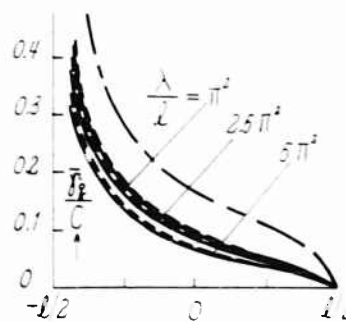
Fig. 3 - Quasi-steady
bound vortex distribution
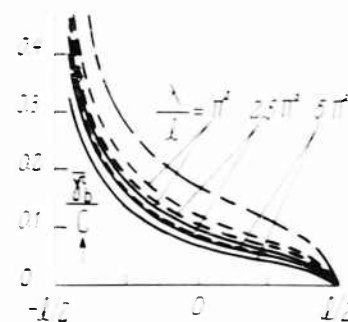
Fig. 4 - Unsteady bound
vortex distribution

510

The strength of vortex distribution increases with the decrement of wave length. This can be introduced as being caused by the large variation of attack angle due to the orbital motion of waves. As the dotted line shows the corresponding one in an infinite fluid, the difference between the full and dotted line is due to the existence of free water surface; from this we can see that in the quasi-steady vortex distribution its amount is almost independent on the wave length and in the unsteady vortex distribution increases with the decrement of wave length. This shows that the amount of effect of free water surface increases with the decrement of wave length when taking the effect of wake vortex into account.

Illustrating more minutely, the strength of the quasi-vortex distribution decreases by the effect of free water surface as shown in Fig. 3 and, correspondingly to this, the strength of wake vortex also decreases. Further, when the induced velocity of wake vortex influences on the flow around the hydrofoil, the existence of free water surface gives again some effect. These processes make the effect of free water surface more predominant.

Curves are shown in Fig. 5 for the unsteady vortex distribution induced on the chord by the wake vortex only to make the above considerations more distinct; the amount of effect of unsteadiness and free water surface either increases with the decrement of wave length. This tendency is in the same direction as that of unsteady bound vortex shown in Fig. 4.

Moreover, for the convenience of comparison, the steady vortex distribution is shown by the chain line.

1.7.2 Unsteady Lift

The absolute value of lift coefficients is shown in Fig. 6 for the against waves and with waves. The steady lift coefficient for this case is 0.528.

The lift due to wake vortex and virtual mass either increases with the decrement of wave length, and besides the former is comparatively larger than the latter. At the same wave length, both lift is larger in against waves than in with waves.

The difference between full and dotted line, which is exclusively due to the existence of free water surface, shows that the effect of free water surface increases with the decrement of wave length for the lift due to wake vortex and,
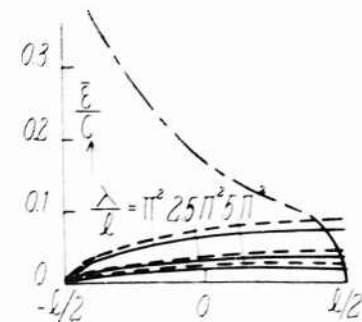
Fig. 5 - Unsteady free vortex distribution over the chord
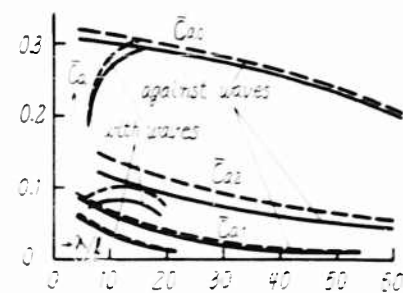
Fig. 6 - Absolute value of unsteady lift

511

on the other, is almost constant independently on the wave length for the quasi-steady lift. This corresponds to the general tendency of vortex distribution in Figs. 3 and 5.

Now we define to enter into the details

$$k = \bar{C}a/(\bar{C}a)_\infty$$

This dimensionless coefficient may be considered as showing qualitatively the degree of effect of free water surface and therefore we call hereafter k "the coefficient for the effect of free water surface," which is shown in Table 2. We can see that k is independent on the wave length and k for the lift due to wake vortex is small compared with that for the other. This is due to the before mentioned reasons.

Table 2

k	
Steady lift	0.981
Quasi-steady lift	0.957
Unsteady lift due to virtual mass	0.957
Unsteady lift due to wake vortex	0.815

Besides, as clearly shown in Table 2, k is larger for the steady lift than for the unsteady lift; from this we can say that the degree of effect of free water surface is larger for unsteady flow field than for the steady flow field.

Summarizing up, the degree of the effect of free water surface is larger for the lift due to wake vortex which is peculiar to the unsteady flow field than for the steady lift, and the amount of the effect of free water surface increases with the decrement of wave length.

Curves in a vector diagram are shown in Fig. 7 for the unsteady lift; the lift due to virtual mass is ahead 90° in phase and the lift due to wake vortex is lag about 180° in phase, compared with the quasi-steady lift which is in same phase as the waves. However, as the latter is relatively larger in absolute value, the resultant lift is lag in phase compared with the quasi-steady lift.

$$\frac{\lambda}{\ell} = \pi^2$$

$$2.5\pi^2$$

$$5.0\pi^2$$

$$0.1$$
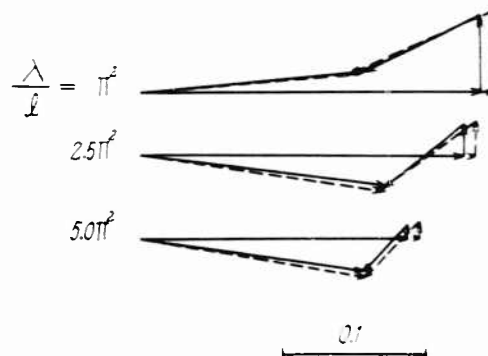
Fig. 7 - Vector diagram of unsteady lift in against waves

512
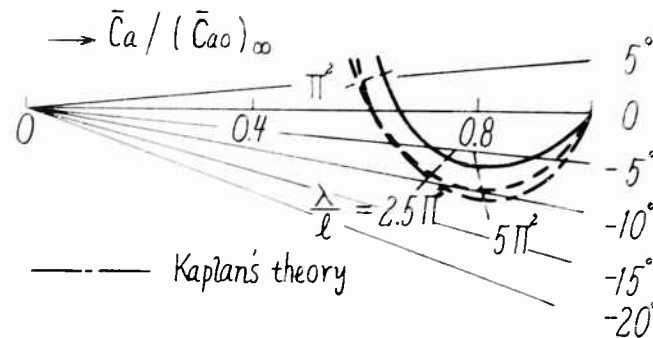
Fig. 8 - Effect of unsteadiness and effect
of free water surface on the lift

Curves are shown in Fig. 8 for the unsteady lift to make the unsteadiness more distinctly; the lift decreases in absolute value and lags in phase by steadiness compared with the quasi-steady lift. Thus we can acknowledge clearly the weak points in the quasi-steady theory [12]. The differences between the full and dotted line show that by the effect of free water surface the absolute value of the unsteady lift decreases in the small wave length and increases in the large wave length, and the phase lag decreases independently on the wave length. Kaplan's results shown by chain line, though not suitable for the reason of standing on the neglection of the horizontal component of orbital velocity, may be compared with the dotted line.

From the above considerations, we can say that the both effect of unsteadiness and free water surface, though the former is clearly larger than the latter, acts in the same direction in the range of large wave length and in the adverse direction in the range of small wave length for the absolute value of lift, and also acts in the adverse direction for the phase lag.

In the last place, as a practical application, it seems to be sufficient to take the following value for the most probable condition of operation.

Table 3

	Absolute Value	Phase
Against waves ($\lambda i/2c = 0.2$)	30% Decrement	7° lag
With waves ($\lambda i/2c = 0.05$)	10% Decrement	5° lag

1.7.3 Unsteady Moment

Curves are shown in Fig. 9 for the absolute value of unsteady moment. The steady moment coefficient is 0.134 for this case. Also, curves are shown in Fig. 10 for illustrating the unsteadiness. From both curves we can see that the unsteady moment has the almost same tendency as that of unsteady lift.

513
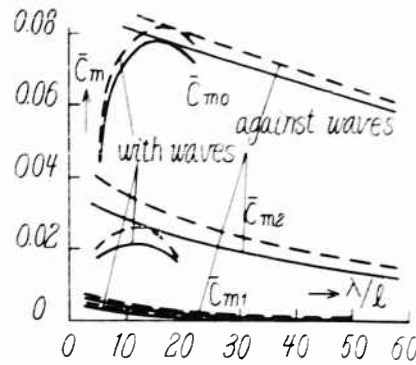
Fig. 9 - Absolute value
of the unsteady moment
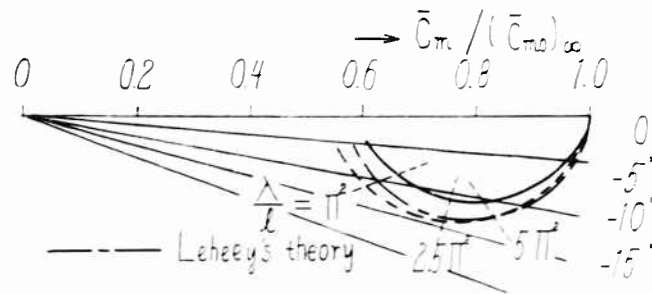
Fig. 10 - Effect of unsteadiness and effect
of free water surface on the moment

For the convenience of comparison, the Leehey's results shown by chain
line, though not suitable for the reasons of standing on the neglection of the hori-
zontal component of orbital velocity, may be compared with the dotted line.

1.7.4 Wake Vortex and its Energy

Calculating from (38.1) the free vortex in the wake region, comparisons are
made with Kaplan's results as follows.

Table 4

	τ C		
κ ℓ	5^{-2}	2.5^{-2}	$^{-2}$
Present theory	0.01728	0.03637	0.07310
Kaplan's theory	0.01824	0.03891	0.07887

The discrepancy is due to the neglection of the effect of free water surface and horizontal component velocity of orbital motion of waves.

The wake energy in against waves is shown in Fig. 11; the differences between full and dotted line show that the effect of free water surface decreases the wake energy which decreases with wave length. This comes from the decrement of strength of unsteady bound vortex distribution by the effect of free water surface as shown in Fig. 4.

Fig. 11 - Wake energy
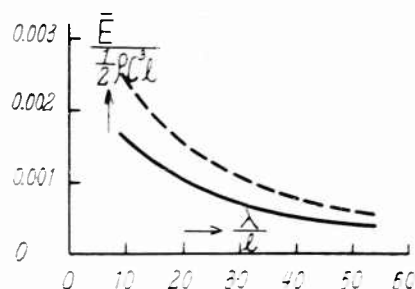
2. UNSTEADY CHARACTERISTICS OF THE SUBMERGED HYDROFOIL PERFORMING HEAVE OR PITCH AT CONSTANT FORWARD SPEED IN STILL WATER

2.1 Boundary Condition and Integral Equation

When the heaving and pitching of hydrofoil is given by

$$y = iy_o e^{i\sigma t} \tag{61}$$

$$\alpha = \alpha_o e^{i\sigma t} \tag{62}$$

then the vertical displacement at an arbitrary point over the chord length is

$$\zeta = iy_o e^{i\sigma t} - (x - x_o) \alpha_o e^{i\sigma t} \tag{63}$$

As the vertical velocity can be given

$$w = \frac{\partial \zeta}{\partial t} - c \frac{\partial \zeta}{\partial x} \tag{64}$$

Then, we have

$$w = c e^{i\sigma t} \left\{ i \frac{\sigma}{c} y_o - i \frac{\sigma}{2c} (\cos \theta - \cos \theta_o) \alpha_o - \alpha_o \right\} \tag{65}$$

515

As known from the assumptions in the linearized theory, it is sufficient to satisfy the boundary condition on the mean position of harmonic oscillation;

$$w = v_f + v_b \tag{66}$$

This leads to

$$c \left\{ i \frac{\omega \ell}{c} y_o - i \frac{\omega \ell}{2c} (\cos \tau - \cos \tau_o) \alpha_o + \alpha_o \right\}$$

$$= - \frac{1}{2\pi} \int_{-\ell/2}^{\ell/2} \overline{\gamma}_b(\xi) \left\{ \frac{1}{x - \xi} - \frac{i\omega}{c} \int_{\xi}^{x} \frac{e^{\frac{i\omega}{c}(\xi - X)}}{x - X} dX + K_3(x, \xi; X) \right\} d\xi \tag{67}$$

where

$$K_3(x, \xi; X) = \frac{x - \xi}{(x - \xi)^2 + 4f^2} - \frac{i\omega}{c} \int_{\xi}^{x} e^{\frac{i\omega}{c}(\xi - X)} \frac{x - X}{(x - X)^2 + 4f^2} dX$$

$$+ i\nu \int_{0}^{x} e^{-2k f} k \left\{ \frac{e^{ik(x-\xi)}}{\tau^2 k^2 + k(2\nu - \nu) + \nu^2} - \frac{e^{-ik(x-\xi)}}{\tau^2 k^2 - k(2\nu - \nu) + \nu^2} \right\} dk$$

$$- \frac{\pi\nu}{k_3 - k_4} \left\{ k_3 e^{-2k_3 f + ik_3(x-\xi)} - k_4 e^{-2k_4 f + ik_4(x-\xi)} \right\}$$

$$+ \nu \frac{\omega}{c} \int_{\xi}^{x} e^{\frac{i\omega}{c}(\xi - X)} dX \int_{0}^{x} e^{-2k f} k$$

$$\times \left\{ \frac{e^{ik(x-X)}}{\tau^2 k^2 + k(2\nu - \nu) + \nu^2} - \frac{e^{-ik(x-X)}}{\tau^2 k^2 - k(2\nu - \nu) + \nu^2} \right\} dk - \frac{-\nu \frac{\omega}{c}}{k_3 - k_4}$$

$$\times \left[\frac{k_3 \cdot e^{-2k_3 f}}{k_3 - \frac{\omega}{c}} \left(e^{\frac{i\omega}{c}(\xi - x)} - e^{ik_3(\xi - x)} \right) - \frac{k_4 \cdot e^{-2k_4 f}}{k_4 - \frac{\omega}{c}} \left(e^{\frac{i\omega}{c}(\xi - x)} - e^{ik_4(\xi - x)} \right) \right] \tag{68}$$

This can be regarded as an integral equation determining the unsteady bound vortex distribution, the solution of which being wholly similar to that in Part 1. Thus, the unsteady characteristics can be obtained from (47) and (51).

2.2 Propulsive Force and Propulsive Efficiency

The work must be done to maintain the heaving and pitching because the hydrofoil experiences the unsteady lift and moment while oscillation.

516

The mean work done in unit time is

$$\bar{W}_h = -\frac{\omega}{2\pi} \int_0^{2\pi/\omega} L \times \frac{dy}{dt} dt \quad \text{for heaving} \tag{69}$$

$$\bar{W}_p = -\frac{\omega}{2\pi} \int_0^{2\pi/\omega} M \times \frac{d\alpha}{dt} dt \quad \text{for pitching} \tag{70}$$

Substituting (47) and (51) into (69) and (70), we have, after some reduction

$$\bar{W}_h \bigg/ \frac{1}{2} \rho c^3 \ell = \frac{\omega \ell}{2c} y_0 \left[\frac{\sqrt{\pi}}{c} q_0 i + \pi^2 \frac{\omega \ell}{2c} \left\{ A \left(\frac{w_{02}}{c} J_0 - \frac{w_{01}}{c} N_0 \right) + B \left(\frac{w_{01}}{c} J_0 + \frac{w_{02}}{c} N_0 \right) \right\} \right] \tag{71}$$

$$\bar{W}_p \bigg/ \frac{1}{2} \rho c^3 \ell = \frac{\omega \ell}{2c} \alpha_0 \left[\sqrt{\frac{\pi}{8}} q_1 + \frac{\sqrt{\pi}}{8} \frac{\omega \ell}{c} q_2 - \frac{\pi^2 \omega \ell}{8c} \left\{ A \left(\frac{w_{02}}{c} J_0 - \frac{w_{01}}{c} N_0 \right) - B \left(\frac{w_{01}}{c} J_0 + \frac{w_{02}}{c} N_0 \right) \right\} \right] \tag{72}$$

where N_0 is the Neumann function.

On the other hand, the average increase of wake energy in unit time is

$$\bar{E} = c \bar{E}_1 \tag{73}$$

then, from (60) we have

$$\bar{E} \bigg/ \frac{1}{2} \rho c^3 \ell = \frac{\omega \ell}{4c} \pi^2 (A^2 + B^2) \left(w_{01}^2 + w_{02}^2 \right) \tag{74}$$

As the mean work done in unit time by propulsive force is $\bar{T} \cdot c$, we have the following relation for the consideration of energy balance.

$$\bar{W} = \bar{E} - \bar{T} \cdot c \tag{75}$$

where

$\bar{T}$ = propulsive force for $\bar{W} > \bar{E}$,

$\bar{T}$ = resistance for $\bar{W} < \bar{E}$.

Therefore the propulsive efficiency is

$$\eta = (\bar{W} - \bar{E}) \bar{W} \tag{76}$$

517

2.3 Numerical Examples

Numerical calculations are made for the same example as in Part 1, and we are confined to the heaving only.

Figure 12 shows the absolute value of the unsteady lift; the lift due to virtual mass is small compared with the lift due to wake vortex. As the dotted line shows the corresponding value in an infinite fluid, the differences between the full and dotted lines may be considered to be exclusively due to the effect of free water surface. Therefore, we can say that the amount of the effect of free water surface increases with the reduced frequency.

Figure 13 shows the coefficient for the effect of free water surface; the coefficient for the lift due to wake vortex is smaller than that due to virtual mass, which being due to the wholly same reasons as in the sinusoidal waves already discussed. Further, the chain line shows the corresponding value for the steady lift; from this we can see that the degree of the effect of free water surface is larger in the unsteady flow field than in the steady flow field.

Fig. 12 - Absolute value of unsteady lift

Figure 14 shows the vector diagram for the unsteady lift; the lift due to virtual mass is ahead $90°$ in phase and the lift due to wake vortex is lag about $180°$ in phase, compared with the quasi-steady lift.

Figure 15 shows the difference between the unsteadiness including the effect of free water surface and quasi-steadiness for the lift and moment; the absolute value decreases and the phase
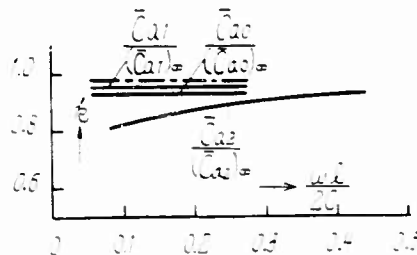
Fig. 13 - Coefficient for the effect of free water surface
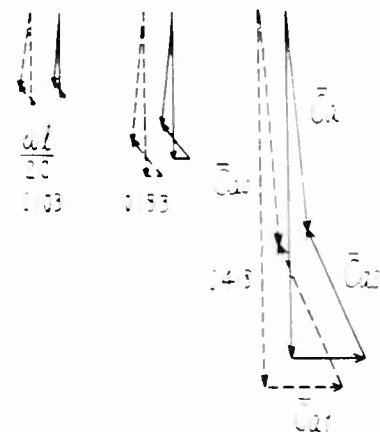
Fig. 14 - Vector diagram of unsteady lift

518
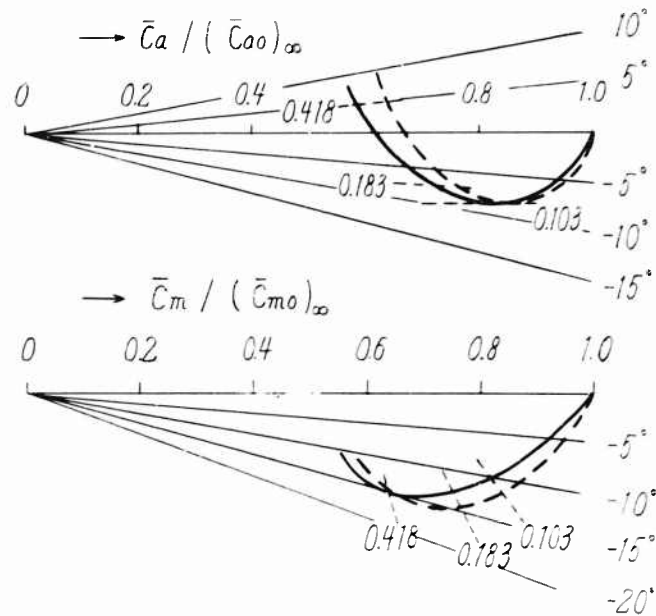
Fig. 15 - Effect of unsteadiness and effect of
free water surface on the lift and moment

lags by the unsteadiness, and then by addition of the effect of free water surface, the absolute value decreases further but the phase lag is almost constant.

Figure 16 shows the work done and wake energy. Though the former is larger than the latter, the differences between the full and dotted lines, on the contrary, are larger in the latter than in the former. This can be illustrated from the relation

$$\overline{W} = k(\overline{W})_\infty$$

$$\overline{E} = k^2(\overline{E})_\infty$$

In other words, we can say that the decrement by the effect of free water surface is larger in wake energy than in work done.

Correspondingly to this, the propulsive force or thrust and the propulsive efficiency increases by the existence of free water surface and its increment increases with the reduced frequency, as shown in Fig. 17. Thus we can say that the existence of free water surface acts favorably to the propulsion of hydrofoil performing heaving.

519
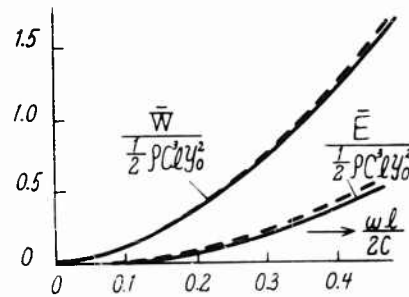
Fig. 16 - Work done and
wake energy
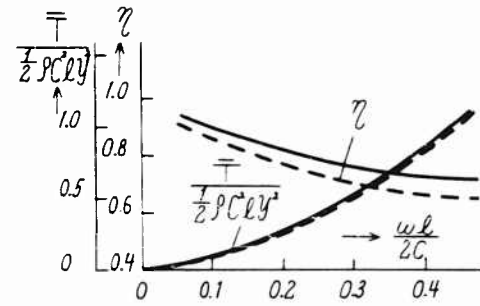
Fig. 17 - Propulsive force
and propulsive efficiency

2.4 Comparison with the Former Theories

Now, taking the limiting value ($f \to \infty$) in the already introduced equations, we obtain the unsteady characteristics in an infinite fluid. For the purpose of checking the present analytical method and its accuracy, comparisons are made with the former unsteady aerofoil theory.

Table 5 shows the unsteady lift in heaving calculated from present method, Kármán's method and Theodorsen's method [13].

Table 5

	$\bar{C}_{ao}/y_o$			$\bar{C}_{a1}/y_o$			$\bar{C}_{a2}/y_o$		
	0.103	0.183	0.418	0.103	0.183	0.418	0.103	0.183	0.418
Theodorsen, Karman	1.3012	2.3089	5.2566	0.0673	0.2121	1.0994	0.2241 -0.2186i	0.4356 -0.5904i	0.8515 -2.0037i
Present method	1.3013	2.3089	5.2566	0.0674	0.2121	1.0994	0.2302 -0.2258i	0.4424 -0.5996i	0.8473 -2.0001i

Table 6 shows the work done, wake energy and propulsive efficiency from present method and Garrick's method [14]. We may be considered as confirming the appropriateness and accuracy of present method from both comparisons.

Table 6

	$\bar{w}/\frac{1}{2}\rho c^3 \ell y_o^2$			$\bar{E}/\frac{1}{2}\rho c^3 \ell y_o^2$			η		
$\omega \ell/2c$	0.103	0.183	0.418	0.103	0.183	0.418	0.103	0.183	0.418
Garrick	0.1114	0.3144	1.3617	0.0151	0.0662	0.4605	0.863	0.789	0.661
Present method	0.1116	0.3143	1.3615	0.0152	0.0663	0.4605	0.863	0.788	0.661

520

3. UNSTEADY CHARACTERISTICS OF THE SUBMERGED HYDROFOIL PERFORMING HEAVE OR PITCH AT CONSTANT FORWARD SPEED UNDER SINUSOIDAL WAVES

3.1 Unsteady Characteristics

Now we put the wave motion, the heaving or pitching of hydrofoil in a form

$$z_w = V h e^{i \omega_1 t - i k x + k y} \tag{77}$$

$$y = \ell y_o e^{i \omega_2 t + i \beta} \tag{78}$$

$$z = z_o e^{i \omega_2 t + i \beta} \tag{79}$$

where

ω_1 = frequency of encounter

ω_2 = frequency of heaving or pitching

β = phase lag.

Reminding the present theory stands on the linearized assumption of small perturbation, we can apply the law of superposition; the unsteady characteristics of hydrofoil performing heave or pitch at constant forward speed under sinusoidal waves consists of two parts, that resulting from the orbital motion of waves and that resulting from the oscillatory motion of hydrofoil. In other words, the former can be calculated from the results of Part 1 neglecting the oscillation of hydrofoil, and the latter due to the oscillation can be calculated from Part 2, just as though the oscillation was doing in still water.

Then, the unsteady characteristics can be given by:

Bound Vortex

$$\gamma_o = \overline{\gamma}_w \times e^{i \omega_1 t} + \overline{\gamma}_h \times p \times e^{i \omega_2 t + i \beta} \tag{80}$$

Lift

$$L = \frac{1}{2} \rho c^2 t \left(C_{ao} + \overline{C}_{aw} \times e^{i \omega_1 t} + \overline{C}_{ak} \times p \times e^{i \omega_2 t + i \beta} \right) \tag{81}$$

Moment

$$M = \frac{1}{2} \rho c^2 \ell^2 \left(C_{mo} + \overline{C}_{mw} \times e^{i \omega_1 t} + \overline{C}_{mh} \times p \times e^{i \omega_2 t + i \beta} \right) \tag{82}$$

The coefficients $\overline{C}_{aw}$, $\overline{C}_{mw}$ and $\overline{C}_{akp}$, $\overline{C}_{mhp}$ can be known respectively from Part 1 and 2.

521

3.2 Propulsive Force

Substituting (81) and (82) into (69) and (70), the mean work done in unit time is, after some reduction

$$\bar{W}_h \Big/ \frac{1}{2}\rho c^3 \ell \times \frac{\omega_2 \ell y_o}{4\pi^2}$$

$$= \left[\frac{\sqrt{\pi}}{c} q_0' - \frac{1}{4} \frac{\omega_1 \ell}{c} \frac{\sqrt{2\pi}}{c} q_1'' - \omega^2 \frac{\omega_1 \ell}{2c} \left\{ \left(\frac{\varkappa_{01}}{c} J_o + \frac{\varkappa_{02}}{c} N_o \right) A - \left(\frac{\varkappa_{01}}{c} N_o - \frac{\varkappa_{02}}{c} J_o \right) B \right\} \right]_\varkappa$$

$$\times \left[-\frac{\omega_2}{\omega_1 + \omega_2} \left\{ \cos\left(\frac{\omega_1 + \omega_2}{\omega_2} 2\pi \right) - 1 \right\} \cos \beta + \frac{\omega_2}{\omega_1 - \omega_2} \left\{ \cos\left(\frac{\omega_1 - \omega_2}{\omega_2} 2\pi \right) - 1 \right\} \cos \beta \right.$$

$$\left. + \frac{\omega_2}{\omega_1 + \omega_2} \sin\left(\frac{\omega_1 + \omega_2}{\omega_2} 2\pi \right) \sin \beta + \frac{\omega_2}{\omega_1 - \omega_2} \sin\left(\frac{\omega_1 - \omega_2}{\omega_2} 2\pi \right) \sin \beta \right]$$

$$+ \left[\frac{\sqrt{\pi}}{c} q_0 + \frac{\omega_1 \ell}{4c} \frac{\sqrt{2\pi}}{c} q_1'' - \omega^2 \frac{\omega_1 \ell}{2\pi} \left\{ \left(\frac{\varkappa_{02}}{c} J_o - \frac{\varkappa_{01}}{c} N_o \right) A + \left(\frac{\varkappa_{01}}{c} J_o - \frac{\varkappa_{02}}{c} N_o \right) B \right\} \right]_\varkappa$$

$$\times \left[\frac{\omega_2}{\omega_1 + \omega_2} \sin\left(\frac{\omega_1 + \omega_2}{\omega_2} 2\pi \right) \cos \beta - \frac{\omega_2}{\omega_1 - \omega_2} \sin\left(\frac{\omega_1 - \omega_2}{\omega_2} 2\pi \right) \cos \beta \right.$$

$$\left. + \frac{\omega_2}{\omega_1 + \omega_2} \left\{ \cos\left(\frac{\omega_1 + \omega_2}{\omega_2} 2\pi \right) - 1 \right\} \sin \beta - \frac{\omega_2}{\omega_1 - \omega_2} \left\{ \cos\left(\frac{\omega_1 - \omega_2}{\omega_2} 2\pi \right) - 1 \right\} \sin \beta \right]$$

$$+ 2\pi \left[\frac{\sqrt{\pi}}{c} q_0 i + \omega^2 \frac{\omega_2 \ell}{2c} \left\{ A \left(\frac{\varkappa_{02}}{c} J_o - \frac{\varkappa_{01}}{c} N_o \right) - B \left(\frac{\varkappa_{01}}{c} J_o - \frac{\varkappa_{02}}{c} N_o \right) \right\} \right]_h \tag{83}$$

$$\bar{W}_p \Big/ \frac{1}{2} \rho c^3 \ell \times \frac{\omega_2 \ell z_o}{4\pi^2}$$

$$= \left[\sqrt{\frac{\pi}{8}} q_1' - \frac{\sqrt{\pi}}{8} \frac{\omega_1 \ell}{c} q_2 - \frac{\omega^2}{4} \frac{\omega_1 \ell}{2c} \left\{ (\varkappa_{01} J_o - \varkappa_{02} N_o) A - (\varkappa_{01} N_o - \varkappa_{02} J_o) B \right\} \right]_\varkappa$$

$$\times \left[-\frac{\omega_2}{\omega_1 - \omega_2} \left\{ \cos\left(\frac{\omega_1 - \omega_2}{\omega_2} 2\pi \right) - 1 \right\} \cos \beta - \frac{\omega_2}{\omega_1 - \omega_2} \left\{ \cos\left(\frac{\omega_1 - \omega_2}{\omega_2} 2\pi - 1 \right) \right\} \cos \beta \right.$$

$$\left. - \frac{\omega_2}{\omega_1 - \omega_2} \sin\left(\frac{\omega_1 - \omega_2}{\omega_2} 2\pi \right) \sin \beta - \frac{\omega_2}{\omega_1 - \omega_2} \sin\left(\frac{\omega_1 - \omega_2}{\omega_2} 2\pi \right) \sin \beta \right]$$

$$+ \left[\sqrt{\frac{\pi}{8}} q_1'' - \frac{\sqrt{\pi}}{8} \frac{\omega_1 \ell}{c} q_2' - \frac{\omega^2}{4} \frac{\omega_1 \ell}{2c} \left\{ (\varkappa_{02} J_o - \varkappa_{01} N_o) A - (\varkappa_{01} J_o - \varkappa_{02} N_o) B \right\} \right]_\varkappa \tag{84}$$

$$\times \left[\frac{\omega_2}{\omega_1 + \omega_2} \sin\left(\frac{\omega_1 + \omega_2}{\omega_2} 2\pi \right) \cos \beta - \frac{\omega_2}{\omega_1 - \omega_2} \sin\left(\frac{\omega_1 - \omega_2}{\omega_2} 2\pi \right) \cos \beta \right.$$

$$\left. + \frac{\omega_2}{\omega_1 + \omega_2} \left\{ \cos\left(\frac{\omega_1 + \omega_2}{\omega_2} 2\pi \right) - 1 \right\} \sin \beta + \frac{\omega_2}{\omega_1 - \omega_2} \left\{ \cos\left(\frac{\omega_1 - \omega_2}{\omega_2} 2\pi \right) - 1 \right\} \sin \beta \right]$$

$$+ 2\pi \left[\sqrt{\frac{\pi}{8}} \, q_1 + \frac{\sqrt{\pi}}{8} \frac{\omega_2 \ell}{c} q_2 - \frac{\pi^2}{4} \frac{\omega_2 \ell}{2c} \left\{ A(w_{02} J_o - w_{01} N_o) + B(w_{01} J_o + w_{02} N_o) \right\} \right]_p \quad (84)$$

where

$$q_0 = q_0' + iq_0'', \qquad q_1 = q_1' + iq_1'', \qquad q_2 = q_2' + iq_2''.$$

The first and second term in (83) and (84) is the additive one depending on the frequency of encounter and the phase lag. The third term is the corresponding one in still water which is in agreement with (71) and (72).

On the other hand, the average increase of wake energy in unit time is:

Heaving

$$\bar{E}_k \bigg/ \frac{1}{2} \rho c^3 \ell = \frac{\pi^2}{4} \frac{\omega_1 \ell}{c} \left\{ \left(\frac{w_{01}}{c} \right)^2 + \left(\frac{w_{02}}{c} \right)^2 \right\}_w (A^2 + B^2)_w$$

$$+ \frac{\pi^2}{4} \frac{\omega_2 \ell}{c} \left\{ \left(\frac{w_{01}}{c} \right)^2 - \left(\frac{w_{02}}{c} \right)^2 \right\}_k (A^2 + B^2)_h \quad (85)$$

Pitching

$$\bar{E}_p \bigg/ \frac{1}{2} \rho c^3 \ell = \frac{\pi^2}{4} \frac{\omega_1 \ell}{c} \left\{ \left(\frac{w_{01}}{c} \right)^2 + \left(\frac{w_{02}}{c} \right)^2 \right\}_w (A^2 + B^2)_w$$

$$- \frac{\pi^2}{4} \frac{\omega_2 \ell}{c} \left\{ w_{01}^2 - w_{02}^2 \right\}_p (A^2 - B^2)_p \quad (86)$$

The first term results from the wave motion and the second term from the oscillation of hydrofoil. Then, the propulsive force can be obtained from (76)

3.3 Numerical Examples

Numerical calculations are made for the same example as in Part 1 and 2, and also the amplitude of heaving is $y_o = 0.05$. Further, present considerations are confined to the propulsive force only.

3.3.1 Effect of Phase Lag

In order to examine the effect of phase lag between the heaving and wave motion encountered, the propulsive force is shown in Fig. 18 for the case of resonance $\omega_1 = \omega_2$; as the chain line shows the corresponding one in still water,

we can say that the propulsive force increases for $\beta = \pi/2$ but decreases for $\beta = 0$, π and $3\pi/2$. This results from strengthening or annulling between the lift $\bar{C}_{aw}$ and $\bar{C}_{ah}$ which is in different phase.
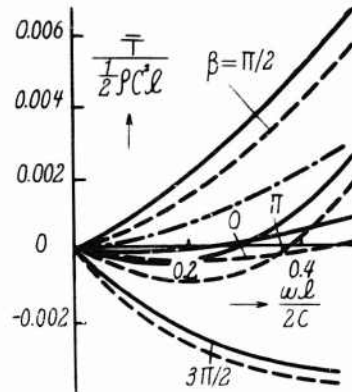
Fig. 18 - Effect of
phase lag
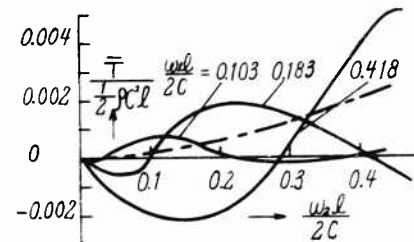
Fig. 19 - Effect of frequency
of heaving on the propulsive
force under waves

3.3.2 Effect of Frequency of Oscillation

In order to examine the effect of frequency of oscillation, the propulsive force is shown in Fig. 19 for $\beta = \pi/2$; as the chain line shows the corresponding one in still water, we can see that the propulsive force increases with approach of the frequency of heaving to the frequency of encounter, and its amount of increment become maximum when resonance.

CONCLUSIONS

In this paper, after reviewing the existing two dimensional unsteady hydrofoil theories, a minutely improved theory is developed for obtaining the unsteady characteristics of hydrofoil performing heave or pitch at constant forward speed under the sinusoidal waves.

Numerical calculations are made in details.

Considerations are mainly directed to the mutual interference between the effect of unsteadiness and effect of free water surface.

/

REFERENCES

1. Sears, W.R., "Some Aspects of Non-Stationary Airfoil Theory and its Practical Application," Jour. of Aero. Sci., Vol. 8, 1941.

2. Kaplan, P., "A Hydrodynamic Theory for the Forces on Hydrofoils in Un-Steady Motion," Dr. Thesis, Stevens Inst. of Tech., 1955; "The Forces Acting on Hydrofoils in Unsteady Motion," Proc. 9th Intern. Cong. of Appl. Mech., 1956; "The Drag of Hydrofoils in Unsteady Motion," Exp. T. T., Stevens Inst. of Tech. Report 617.

3. Ogilvie, F., "The Theoretical Prediction of the Longitudinal Motions of Hydrofoil Craft," Jour. of Ship Research, Vol. 4, 1959.

4. Schwanecke, H., "Beitrag zur Theorie der Instationären Tragflügelstromung," Schiffstechnik. Bd. 5, 1958.

5. Leehey, P., "The Hilbert Problem for an Airfoil in Unsteady Motions," Jour. of Math. and Mech., Vol. 6, 1957.

6. Abramson, H.N., "Effect of the Free Surface on the Flutter of Submerged Hydrofoils," Jour. of Ship Research, 1959.

7. Isay, W.H., "Zur Theorie der Unterwassertragflügel bei Wellenförmiger Anströmung," Ing. Arch. Bd. 29, 1960; "Zur Berechnung der Unterwasser-tragflügel bei Wellenförmiger Anströmung," Ing. Arch. Bd. 30, 1961.

8. Karman, T.V., "Airfoil Theory for Non-Uniform Motions," Jour. of Aero. Sci., Vol. 5, 1938.

9. Jones, W.P., "Aerodynamic Forces on Wings in Simple Harmonic Motions," Rep. and Mem. 2026, 1945.

10. Küssner, H.G., "Allgemeine Tragflächentheorie," Luftfahforschung. Bd. 17, 1940.

11. Nishiyama, T., "Hydrodynamic Investigations of the Submerged Hydrofoil - Part 1," Jour. of Amer. Soc. of Nav. Eng., Vol. 69, 1958.

12. Kaplan, P., "The Forces and Moment Acting on a Tandem Hydrofoil System in Waves," Stevens Inst. of Tech. Report 506, 1955.

13. Theodorsen, T., "General Theory of Aerodynamic Instability and the Mechanism of Flutter," NACA TR 496, 1935.

14. Garrick, J.E., "Propulsion of a Flapping and Oscillating Airfoil," NACA Report 567, 1936.

*　　*　　*

SOME FREE SURFACE EFFECTS ON UNSTEADY HYDRODYNAMIC LOADS AND HYDROELASTICITY

Marten T. Landahl, Holt Ashley and Sheila M. Widnall
Massachusetts Institute of Technology
Cambridge, Massachusetts

ABSTRACT

The emergence of hydroelastic stability as a practical design consideration has generated, among other requirements, an urgent need for new analytical tools of the highest possible precision. Prominent among these is a theory of unsteady hydrodynamic loading on two- and three-dimensional foils operating in a variety of orientations near the free surface. The paper describes a systematic approach to the construction and numerical solution of the integral equations which result when this problem is linearized for small-amplitude simple harmonic motion. Basic to the method is the oscillating acceleration potential doublet, from which kernel functions can be deduced that apply in particular physical circumstances. The example of the three-dimensional, subcavitated foil at very high Froude number is first worked out. A procedure for solving the integral equation to find pressure distribution, lift and moment is described. Although no quantitative results are furnished, no numerical difficulty has been encountered and these will be available shortly. Turning to the more difficult case of finite Froude number, a closed mathematical form is derived for the kernel function appropriate to arbitrary small oscillation of a two-dimensional foil.

INTRODUCTION

It may fairly be asserted that events of the past four years have brought dynamic hydroelastic stability from a theoretical curiosity to a design consideration of frequent practical importance. To an aeronautical engineer, the history of this problem displays a clear parallel with that of aircraft wing flutter. When flutter was an unlikely nuisance, whose possible occurrence on a given design could be checked almost as an afterthought, the simplest analytical and experimental tools sufficed to estimate the large margins of safety that were usually inherent after strength requirements had been met. As major structural modifications began to be called for to assure safety, however, much more stringent

demands were put on both the model builder and the theoretician. They responded with techniques having a degree of accuracy, sophistication and complexity that are matched only at a very few other stages in the design process of any type of vehicle.

Not many would dispute that the manufacturer of hydrofoil craft will be faced very shortly with similar needs. The present paper is prepared with the aim of describing what the authors believe will be the most fruitful direction for research and methods development to meet one of these, namely, a comprehensive theory predicting water loads due to unsteady motion of three-dimensional foils of arbitrary shape and orientation. The examples given below embody certain restrictions, such as to small, simple harmonic oscillation in the subcavitated condition with or without a free surface. It is felt, however, that these proposals hold promise of extension to cover several more complicated unsteady phenomena, short of nonlinearity. An essential element of the authors' philosophy, motivated by the widespread availability and ease of application of high-speed computers, is partially to abandon the search for complete, closed-form expressions in favor of the broader utility and systematization that result from numerical solutions. This is not to say that "rules of thumb" or simple physical understanding are disparaged or dismissed. Rather, the objective here is final-design tools of the highest possible accuracy within the comprehensive limits of linearized theory.

By way of introduction, some remarks are in order about the emergence of hydrofoil flutter as a practical problem. Early speculation regarding its unlikelihood (Ref. 1 contains an example) stemmed from a tendency to overconcentrate on the structure-to-fluid mass ratio parameter μ as the primary quantity distinguishing hydrofoils from aircraft wings. Simple calculations, made with approximate representations of lifting surfaces having flexibility in bending and torsion, go at least as far back as Theodorsen and Garrick [2] in predicting that instability does not occur in the μ-range characteristic of hydrofoils. There now exists ample negative experimental evidence (cf. Henry [3], and work cited in [1]) to confirm the existence of this "window," but only on models without any structural sweepback which were tested in a condition of cantilever or simple support. The conclusion that conventional hydrodynamic theory does not estimate flutter speeds accurately in the vicinity of the so-called critical μ (Ref. 3 and others) emphasizes the sensitivity of stability to small alterations in system properties. But it is not regarded as an indication that these simplified models will become unstable in water, where μ is normally five to ten times lower than the critical value.

A more recent and wholly unanticipated development concerns the overwhelming influence of small changes in sweep angle on hydrofoil flutter. The first clue to this behavior appears in some tests by Hilborne [4]. It was systematically studied in the experiments of Baird, Squires and Caporali [5], and Herr [6] has made important contributions to its theoretical understanding. The present authors, in collaboration with G. Zartarian, have carried out an analytic study of this phenomenon, using as their example the model designated as No. 2 in [6]. The more significant results are summarized in Figs. 1 and 2, where the predicted critical speeds U of bending-torsion divergence and flutter are plotted versus the angle of sweepback Λ in the range between 0 and $20°$. This wing is a uniform cantilever of span-to-chord ratio 6, its other properties not
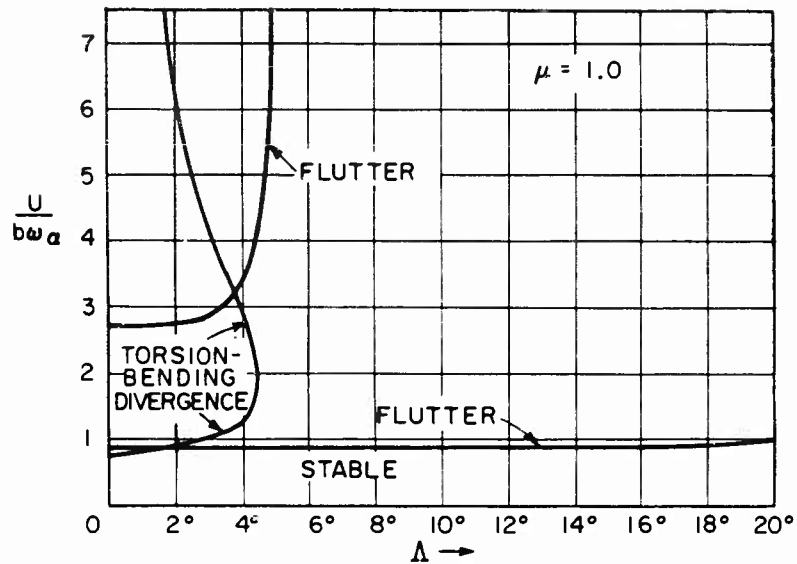
Fig. 1 - Dimensionless flutter and divergence speeds plotted vs sweep angle Λ for the cantilever lifting-surface model No. 2 of Ref. 6, operating as a mass ratio typical of moderate-to-low density fluids
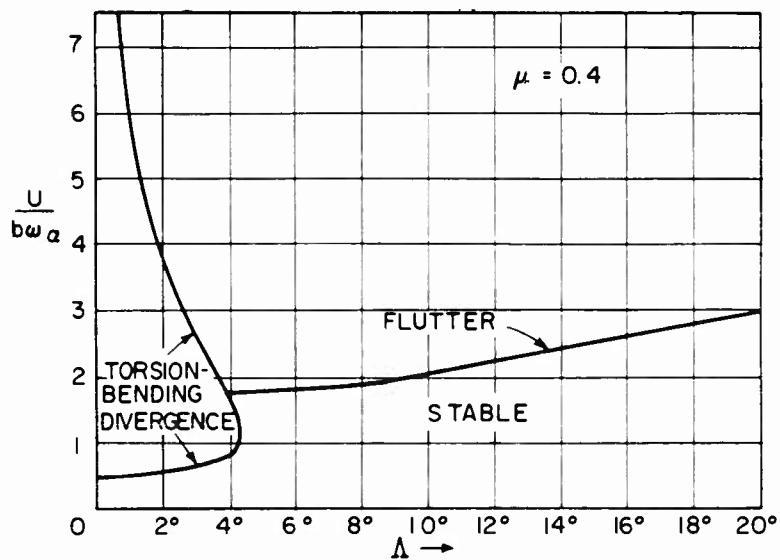
Fig. 2 - Dimensionless flutter and divergence speeds for the lifting surface of Fig. 1, operating at a mass ratio typical of water

529

being listed here since they are representative of a large class of such foils and are not germane to the discussion.

The speeds on Figs. 1 and 2 were computed by a two-degree-of-freedom Rayleigh type of approximation, assuming the uncoupled normal mode shapes of bending and torsion of a uniform cantilever and introducing two-dimensional steady or unsteady linearized hydrodynamic theory on a strip basis (cf. Chap. 9 of Ref. 7). Other symbols appearing in the figures are wing semichord b, uncoupled frequency of torsional oscillation ω_α, and $\mu = m/\pi\rho b^2$ with m the structural mass per unit spanwise distance and ρ the density of water.

Figure 1 displays stability boundaries that may be called typical of relatively low-density fluid like air. Flight at a speed above the lower branch of any one of the curves would result in destruction due to the type of instability indicated thereon. Although the μ of 1.0 is quite small for aircraft operation, qualitative changes in the forms of these curves are not anticipated even up to high mass ratios. The lower (hence practically significant) flutter speed is seen to vary only quite slowly as the surface is swept back. The divergence boundary rises rapidly with increasing Λ, and this instability wholly disappears beyond about $\Lambda = 4\text{-}1/4°$ owing to the relieving action of the angle-of-attack reduction from the combined effects of sweepback and bending slope.

The flutter behavior alters radically below a transitional value of mass ratio that can be pinpointed just as closely as the "critical μ" for an unswept wing (for Herr's model 2 the metamorphosis sets in at $\mu = 0.665$). Figure 2 shows the stability boundaries at a condition ($\mu = 0.4$) typical of the high-density fluid regime. The form of the divergence curve remains similar to Fig. 1, as might be expected since divergence is governed by the dynamic pressure $1/2\,\rho U^2$ independently of the μ-range. Flutter instability is now observed, however, only at the higher Λ's. As Λ approaches $3.97°$, the critical frequency drops gradually to zero, and the flutter and divergence boundaries merge. Only the static type of instability is predicted to occur below this angle of sweep.

At present writing there is no reason to believe that actual hydrofoils do not exhibit the sweep-angle sensitivity revealed by these calculations. Further research may well uncover other system parameters, such as the manner of root attachment or the presence of dynamically-coupled degrees of freedom of the supporting body, whose effects are similarly critical for stability. One safe conclusion concerns the urgent requirement, mentioned in the opening paragraphs, for analytical tools of the greatest possible precision, which will permit the hydrofoil designer to foresee and correct both static and dynamic instabilities long before a vehicle is fabricated or committed to the water. One class of such tools, presently in an unsatisfactory state, involves three-dimensional, unsteady hydrodynamic load theory. The influences of aspect ratio and planform shape on both the circulatory and virtual-mass portions of the flow field must be elucidated. Nearly all hydrofoils pierce or approach the free surface, whose influence on loading and stability has already undergone preliminary examination [5,9]. Loads on nonplanar and otherwise mutually-interfering foil configurations need to be estimated on a fully-rational basis. Finally, the more intractable effects of cavitation combined with unsteady motion loom on the immediate horizon.

At the time of writing of Ref. 6, the test speeds of around 50 kts achieved by Herr could reasonably be considered quite high for hydrofoil operation. Today, with speeds in excess of 100 kts under common discussion, one feels inclined to modify his conclusion that "the practical significance of flutter at low mass ratios cannot be said to have been established."

A parallel line of investigation, whose results must be deferred to a future paper but hold interesting promise, consists of the attempt to achieve simplified physical understanding of the roles of sweep and mass ratio by adapting the procedures of Pines [10] and Zimmerman [11]. One model which seems to embody most of the principal influences is a flat, rigid lifting surface suspended at one end by a leaf spring (bending) and a watch spring (torsion). By varying the sweep angle, the contribution of the "bending slope" to stability can be introduced. When approximating the loads, however, more is needed than merely the lift due to angle of attack employed in Refs. 10 and 11. As first observed in Ref. 6, the fluid damping forces also play an essential part in determining dynamic hydroelastic stability.

USE OF THE PRESSURE DOUBLET IN THE UNSTEADY
LOADING PROBLEM

The general unsteady liquid flow past a thin lifting foil, which may adjoin a plane free surface $z = 0$ but need not itself be planar, is formulated by reference to Fig. 3. A uniform stream of speed U parallels the x-direction, and all disturbance velocities due to chordwise slopes and normal motions of the foil are taken small compared with U. As set forth, for instance, in Chapter 2 of Stoker [8], the flow external to boundary layers and wakes will be irrotational. Hence there is a velocity potential

$$\Phi = U\ell \left[x + \varphi(x, y, z, t) \right] . \tag{1}$$

Here ℓ is some characteristic streamwise dimension, such as the midspan chord. φ is a nondimensional disturbance potential. The Cartesian coordinates x, y, z and other lengths in the problem have been made dimensionless by division with ℓ, while t is physical time multiplied by U/ℓ.

By virtue of continuity, both Φ and φ satisfy Laplace's equation

$$\nabla^2 \varphi = 0 . \tag{2}$$

The condition of uniform pressure at the free surface may be linearized to (Ref. 8)

$$\left(\frac{\partial}{\partial t} + \frac{\partial}{\partial x} \right)^2 \varphi + F^{-2} \varphi_z = 0 , \quad \text{at} \quad z = 0 , \tag{3}$$

$F = U/\sqrt{g\ell}$ being Froude number and g the gravitational constant.

A second well-known scalar field variable, whose utility approaches that of φ, is the acceleration potential ψ. This may be introduced either by relating its
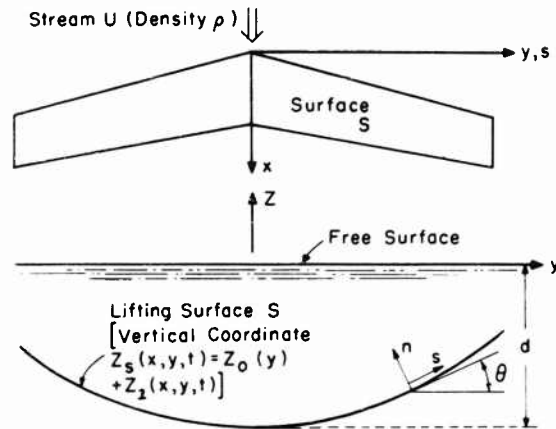
Fig. 3 - Top and rear elevations of a
nonplanar lifting foil performing small
unsteady motions normal to an X-wise
uniform stream of velocity U

gradient to the particle acceleration vector or, within the linearized framework,
by its proportionality to the pressure perturbation:

$$\psi = \frac{p_\infty - p}{\rho U^2} \, . \tag{4}$$

Equation (4) defines a dimensionless form of ψ and is a direct consequence of
the Euler equations of fluid motion. p is static pressure at an arbitrary field
location, exclusive of any time independent hydrostatic increments, while p_∞ is
the value of p in the uniform stream at distant points. It follows from the un-
steady Bernoulli equation that ψ is related to ϕ by

$$\psi = \phi_x + \phi_t \tag{5}$$

and that ψ therefore also satisfies Eqs. (2) and (3).

Additional boundary conditions on ϕ or ψ are furnished by the shape and
motion of surface S. For simplicity, it is assumed that S has zero thickness.
Actually, when S is almost plane and remote from the free surface, these thick-
ness effects may be treated separately and independently from those of angle of
attack, camber and oscillation. This separation is otherwise not possible in
steady flow, and non-zero thickness must be represented by distributing sources
over S, which interact with the doublets describing the lifting part of the field.
The procedure is straightforward but adds nothing of essence to the present dis-
cussion, so it is deferred to a future paper. In Fig. 3 the undeformed and un-
cambered mean position of the foil is the developable surface $z_0(y)$. Its unsteady
displacement is the small quantity $z_1(x, y, t)$, which may be presumed known.
This displacement is prescribed to be a simple harmonic oscillation by means
of the standard complex notation

532

$$z_1(x, y, t) = \bar{z}_1(x, y) e^{ikt} , \tag{6}$$

where k, the reduced frequency, is related to the dimensional frequency ω rad/sec by

$$k = \frac{\omega l}{U} . \tag{7}$$

Given the values of $\bar{z}_1$ over S, it is an easy matter to find the normal displacement

$$\bar{n}(x, y) e^{ikt} = \bar{z}_1(x, y) e^{ikt} \sec \theta(y) . \tag{8}$$

Here θ is the angle $\tan^{-1}(dz_o/dy)$ illustrated in Fig. 3. The normal velocity of fluid particles in contact with the surface is then

$$\frac{v_n}{U} (x, y, t) = \left[\frac{\partial \bar{n}}{\partial x} + ik\bar{n} \right] e^{ikt} . \tag{9}$$

Equation (9) supplies the required condition on the disturbance potential

$$\phi_n(x, s) = \frac{\partial \bar{n}}{\partial x} + ik\bar{n} , \quad \text{for } (x, y, z) \tag{10}$$

or (x, s) on S, where we have adopted the curvilinear coordinates x and s to identify points on the foil surface and dropped the explicit dependence of ϕ on time since it is known to be proportional to e^{ikt}.

A boundary condition for ψ is constructed by integrating the simple harmonic version of Eq. (5), taking account of the simultaneous vanishing of ϕ and ψ upstream as $x \to -\infty$,

$$\phi = e^{-ikx} \int_{-\infty}^{x} \psi(\lambda, y, z) e^{ik\lambda} d\lambda . \tag{11}$$

From Eqs. (10) and (11) there follows

$$e^{-ikx} \int_{-\infty}^{x} \frac{\partial \psi}{\partial n} (\lambda, y, z) e^{ik\lambda} d\lambda = \frac{\partial \bar{n}}{\partial x} + ik\bar{n} . \tag{12}$$

for (x, y, z) on S.

The loading problem is solved by distributing over S a layer of acceleration-potential (pressure) doublets with axes parallel to the local normal. By classical methods the strength of such a layer can be proved locally proportional to the discontinuity of ψ between the upper and lower surfaces of S, so that one is led to

$\psi(x, y, z)$

$$= \frac{1}{4\pi} \iint_S [\psi_u - \psi_L] \frac{\partial}{\partial n^1} \left[\frac{1}{\sqrt{(x-x_1)^2 + (y-y_1)^2 + (z-z_o(y_1))^2}} \right] dx_1 ds_1$$

$$= \frac{1}{4\pi\rho U^2} \iint_S \Delta p(x_1, s_1) \frac{\partial}{\partial n^1} \left[\frac{1}{\sqrt{(x-x_1)^2 + (y-y_1)^2 + (z-z_o(y_1))^2}} \right] dx_1 ds_1 \cdot \quad (13)$$

Here Δp is the complex amplitude of pressure difference between the lower and upper sides of the foil and n^1 is the normal direction at point $(x_1, y_1, z_o(y_1))$ or (x_1, s_1) in the sense indicated by the figure. Henceforth, the simple harmonic time factor e^{ikt} is systematically omitted. Combining Eqs. (12) and (13) yields the final integral equation

$$\frac{\partial \bar{n}}{\partial x} + ik\bar{n} = \frac{1}{4\pi\rho U^2} \iint_S \Delta p(x_1, s_1) \, Kdx_1 ds_1 \qquad (14)$$

with the singular kernel function

$$K = \lim_{z \to z_o(y)} \left\{ e^{-ik(x-x_1)} \frac{\partial^2}{\partial n \, \partial n^1} \int_{-\infty}^{(x-x_1)} \frac{e^{ik\lambda} \, d\lambda}{\sqrt{\lambda^2 + (y-y_1)^2 + (z-z_o(y_1))^2}} \right\}. \qquad (15)$$

The double integral here is to be evaluated in the sense of Mangler [12], the singularity being identifiable as associated with a factor $(y-y_1)^{-2}$. Solution procedures are discussed in the succeeding section. After extensive manipulation, paralleling the work of Watkins et al. [13] for planar lifting surfaces, one can derive the following explicit formula for K:

$$K = \sin \left[\mathcal{C}(y) + \mathcal{C}(y_1) \right] \frac{y_o z_{oo}}{r_1^4} \left\{ \frac{x_o[3r_1^2 + 2x_o^2]}{r_o^3} - i \frac{kx_o^2}{r_o} \right.$$

$$- ie^{-ikx_o} \int_o^{kx_o} \frac{\lambda e^{i\lambda} d\lambda}{\sqrt{\lambda^2 - k_1^2}} - e^{-ikx_o} \int_o^{kx_o} \frac{\lambda^2 e^{i\lambda} d\lambda}{\sqrt{\lambda^2 + k_1^2}}$$

$$\left. - k_1^2 e^{-ikx_o} \left[K_2(k_1) - \frac{-i}{2} \left(I_2(k_1) - L_2(k_1) \right) \right] + ie^{-ikx_o} \left[\frac{k_1^3}{3} - k_1 \right] \right\}$$

$$\frac{- \cos \mathcal{C}(y) \cos \mathcal{C}(y_1)}{r_1^2} \left\{ \frac{y_o^2}{r_1^2} \left[- \frac{x_o}{r_o} + ie^{-ikx_o} \int_o^{kx_o} \frac{\lambda e^{i\lambda} d\lambda}{\sqrt{\lambda^2 + k_1^2}} \right] \right.$$

$$\left. + \frac{z_{oo}^2}{r_1^2} \left[\frac{x_o[x_o^2 + 2r_1^2]}{r_o^3} - i \frac{kx_o^2}{r_o} - e^{-ikx_o} \int_o^{kx_o} \frac{\lambda^2 e^{i\lambda} d\lambda}{\sqrt{\lambda^2 + k_1^2}} \right] \right. \qquad \begin{array}{l} (16) \\ (\text{Cont.}) \end{array}$$

Some Free Surface Effects

$$z_1(x,y,t) = \bar{z}_1(x,y) e^{ikt} , \tag{6}$$

where k, the reduced frequency, is related to the dimensional frequency ω rad/sec by

$$k = \frac{\omega l}{U} . \tag{7}$$

Given the values of $\bar{z}_1$ over S, it is an easy matter to find the normal displacement

$$\bar{n}(x,y) e^{ikt} = \bar{z}_1(x,y) e^{ikt} \sec \theta(y) . \tag{8}$$

Here θ is the angle $\tan^{-1}(dz_0/dy)$ illustrated in Fig. 3. The normal velocity of fluid particles in contact with the surface is then

$$\frac{v_n}{U}(x,y,t) = \left[\frac{\partial \bar{n}}{\partial x} + ik\bar{n} \right] e^{ikt} . \tag{9}$$

Equation (9) supplies the required condition on the disturbance potential

$$\phi_n(x,s) = \frac{\partial \bar{n}}{\partial x} + ik\bar{n} , \quad \text{for } (x,y,z) \tag{10}$$

or (x,s) on S, where we have adopted the curvilinear coordinates x and s to identify points on the foil surface and dropped the explicit dependence of ϕ on time since it is known to be proportional to e^{ikt}.

A boundary condition for ψ is constructed by integrating the simple harmonic version of Eq. (5), taking account of the simultaneous vanishing of ϕ and ψ upstream as $x \to -\infty$,

$$\phi = e^{-ikx} \int_{-\infty}^{x} \psi(\lambda,y,z) e^{ik\lambda} d\lambda . \tag{11}$$

From Eqs. (10) and (11) there follows

$$e^{-ikx} \int_{-\infty}^{x} \frac{\partial \psi}{\partial n}(\lambda,y,z) e^{ik\lambda} d\lambda = \frac{\partial \bar{n}}{\partial x} + ik\bar{n} . \tag{12}$$

for (x, y, z) on S.

The loading problem is solved by distributing over S a layer of acceleration-potential (pressure) doublets with axes parallel to the local normal. By classical methods the strength of such a layer can be proved locally proportional to the discontinuity of ψ between the upper and lower surfaces of S, so that one is led to

$$
\begin{aligned}
&+ \frac{(k_1 z_{oo})^2}{r_1^2} \, e^{-ikx_o} \left[K_2(k_1) - \frac{\pi i}{2} \left(I_2(k_1) - L_2(k_1) \right) + i \, \frac{k_1}{3} - \frac{i}{k_1} \right] \\
&- k_1 e^{-ikx_o} \left[K_1(k_1) + \frac{\pi i}{2} \left(I_1(k_1) - L_1(k_1) \right) - i \right] \Bigg\} \\
&- \frac{\sin \theta(y) \, \sin \theta(y_1)}{r_1^2} \left\{ \frac{z_{oo}^2}{r_1^2} \left[- \frac{x_o}{r_o} + ie^{-ikx_o} \int_o^{kx_o} \frac{\lambda e^{i\lambda} \, d\lambda}{\sqrt{\lambda^2 + k_1^2}} \right] \right. \\
&+ \frac{y_o^2}{r_1^2} \left[\frac{x_o[x_o^2 + 2r_1^2]}{r_o^3} - i \, \frac{kx_o^2}{r_o} - e^{ikx_o} \int_o^{kx_o} \frac{\lambda^2 e^{i\lambda} \, d\lambda}{\sqrt{\lambda^2 + k_1^2}} \right] \\
&+ \frac{(k_1 y_o)^2}{r_1^2} \, e^{-ikx_o} \left[K_2(k_1) - \frac{\pi i}{2} \left(I_2(k_1) - L_2(k_1) \right) + i \, \frac{k_1}{3} - \frac{i}{k_1} \right] \\
&\left. - k_1 e^{-ikx_o} \left[K_1(k_1) + \frac{\pi i}{2} \left(I_1(k_1) - L_1(k_1) \right) - i \right] \right\} \, .
\end{aligned}
\tag{16}
$$

Here I_j, K_j, and L_j are modified Bessel and Lommel functions of order j, in standard notation. The auxiliary symbolism in Eq. (16) is as follows:

$$
\left.
\begin{aligned}
&x_o = x - x_1 \, , \quad y_o = y - y_1 \, , \quad z_{oo} = z_o(y) - z_o(y_1) \, , \\
&r_1 = \sqrt{y_o^2 + z_{oo}^2} \, , \qquad\qquad r_o = \sqrt{x_o^2 + y_o^2 + z_{oo}^2} \, , \\
&\qquad\qquad\qquad k_1 = kr_1 \, .
\end{aligned}
\right\}
\tag{17}
$$

In the absence of a free surface, the problem statement provided by Eqs. (14) and (16) is complete. Evidently its solution would be unthinkable without the aid of high-speed computing equipment. It is worth pointing out, however, that Watkins and collaborators have successfully programmed the planar case for compressible as well as incompressible fluid. Although it involves the reduction $\theta(y) = \theta(y_1) = 0$, the Watkins kernel function is actually more complicated than Eq. (16) because of the presence of flight Mach number as an additional parameter. Details of these authors' work appear in [14], and copies of their program suitable for IBM 704, 709, etc., may be obtained from Langley Research Center of NASA. The approach of Hsu [15] to the same problem deserves citing, and several other groups in the American and foreign aircraft industries have developed alternative procedures.

An important feature of the numerical solution of Eqs. (14) - (16) is that the kernel function appears only as an isolated subroutine of a much longer program, which also includes setting up and inverting a large system of simultaneous, complex algebraic equations. In a variety of related problems, among them hydrofoils adjacent to or piercing a free surface, foils with large dihedral, intersecting foils and biplanes, the principal difference occurs in the form of K.

535

Even the y_o^{-2} singularity remains unchanged from one of these cases to the next. In certain other instances, it becomes necessary to solve a pair of coupled integral equations rather than a single one, but clear guidelines will result from success with Eq. (14).

Space limitations prevent writing explicit forms of K for several examples. One illustration will be given which underlies the numerical results of the next section. This concerns the single planar foil running a (dimensionless) distance d below and parallel to the free surface at $F \gg 1$. Such high Froude number has often been suggested to be consistent with the large dynamic pressures at which hydroelastic instabilities will occur. The $z = 0$ boundary condition, Eq. (3), is known to simplify to $\phi = 0$, and this can be satisfied by placing an identical "image" foil at $z = +d$ while causing it to be loaded in the same magnitude and sense as S. The kernel function for Eq. (14) is constructed as follows. One sets $\theta(y) = \theta(y_1) = 0$, $s = y$, $s_1 = y_1$ and $z_o = -d$ in Eq. (16) to get the contribution of the foils' own loading to its "upwash" on S. One then adds, for the image, an identical quantity except with $z_o(y) = -d$, $z_o(y_1) = d$, $z_{oo} = -2d$. Thus is obtained

$$
\begin{aligned}
K(x_o, y_o; d) &= \frac{1}{y_o^2} \left\{ \frac{x_o}{\sqrt{x_o^2 + y_o^2}} - ie^{-ikx_o} \int_0^{kx_o} \frac{\lambda e^{i\lambda} d\lambda}{\sqrt{\lambda^2 + (ky_o)^2}} \right. \\
&\quad + k|y_o| e^{-ikx_o} \left[K_1(k|y_o|) + \frac{\pi i}{2} \left(I_1(k|y_o|) - L_1(k|y_o|) \right) - i \right] \bigg\} \\
&\quad - \left[\frac{1}{\sqrt{y_o^2 - (2d)^2}} \right]^2 \left\{ \frac{y_o^2}{y_o^2 - (2d)^2} \left[-\frac{x_o}{\sqrt{x_o^2 + y_o^2 + (2d)^2}} + ie^{-ikx_o} \right. \right. \\
&\quad \times \left. \int_0^{kx_o} \frac{\lambda e^{i\lambda} d\lambda}{\sqrt{\lambda^2 + k_d^2}} \right] - \left[\frac{2d}{\sqrt{y_o^2 + (2d)^2}} \right]^2 \frac{x_o\left[x_o^2 + 2y_o^2 + 8d^2\right]}{\left[x_o^2 + y_o^2 + (2d)^2\right]^{3/2}} \\
&\quad - \frac{ikx_o^2}{\sqrt{x_o^2 + y_o^2 + (2d)^2}} - e^{-ikx_o} \left. \int_0^{kx_o} \frac{\lambda^2 e^{i\lambda} d\lambda}{\sqrt{\lambda^2 + k_d^2}} \right] \\
&\quad - k_d e^{-ikx_o} \left[K_1(k_d) + \frac{\pi i}{2} \left(I_1(k_d) - L_1(k_d) \right) - i \right] \\
&\quad + \frac{(2dk_d)^2 e^{-ikx_o}}{y_o^2 + (2d)^2} \left[K_2(k_d) - \frac{\pi i}{2} \left(I_2(k_d) - L_2(k_d) \right) + i\frac{k_d}{3} - \frac{i}{k_d} \right] \bigg\}
\end{aligned}
$$
(18)

with

$$ k_d = k\sqrt{y_o^2 + (2d)^2} . $$
(19)

In connection with the approach taken below to the development of a kernel function for a two-dimensional foil at finite F, an alternative statement of the problem leading to Eqs. (14) and (18) is set down. It can be shown without difficulty that the K in Eq. (18) is given by

$$K(x - x_1, \ y - y_1) = e^{-ikx} \int_{-\infty}^{x} e^{ik\lambda} \ \psi_z(\lambda - x_1, \ y - y_1, -d) \ d\lambda$$

$$= \int_{-\infty}^{x - x_1} e^{-ik(x - x_1 - \lambda_1)} \ \psi_z(\lambda_1, \ y - y_1, -d) \ d\lambda_1, \tag{20}$$

where, in turn, ψ is a solution of Laplace's equation which vanishes at large distances and satisfies the boundary conditions

$$\psi(x, \ y, \ -d + o) - \psi(x, \ y, \ -d - o)$$
$$\equiv \Delta\psi(x, \ y, \ -d) = \delta(x - x_1, \ y - y_1) \tag{21}$$

and

$$\psi = 0, \quad \text{at} \quad z = 0. \tag{22}$$

$\delta(x - x_1, \ y - y_1)$ is a Dirac delta function which equals zero at all points except $x = x_1, \ y = y_1$ and yields unity if integrated over any area containing that point. When proceeding from infinite to finite Froude number, the only change that must be made in this latter statement is to replace Eq. (22) by Eq. (3), expressed in terms of ψ.

In closing this section, one can make the obvious remark that loadings due to small time-dependent motions which are not sinusoidal can be computed from the simple harmonic results by Fourier series or integral superposition. Of practical significance is that this task has actually been carried out on the IBM 7090 for aircraft responses to atmospheric gusts, with frequency harmonics included up to roughly the fiftieth order.

EFFECTS OF THE FREE SURFACE AT VERY LARGE FROUDE NUMBER

A computing program has been written and demonstrated on the Massachusetts Institute of Technology IBM 7090 computer which calculates the pressure distribution over the oscillating nonplanar hydrofoil in the vicinity of a free surface at $F \gg 1$. The foil shape function $z_o(y)$ is assumed symmetrical about the x-z-plane, thus permitting any possible small motion to be decomposed into symmetrical and antisymmetrical parts. The integral equation (14) can then be solved by collocation at a suitably large number of control points distributed over the right-hand half span of S, the effect of the image being added by a modification to K.

537

Since the solution procedure constitutes a fairly direct generalization of that given by Watkins and collaborators [14], only the broad outlines will be sketched here. Emphasis is placed on the planar foil with $z_o(y) = -d$, since the numerical examples refer to this case. The key idea of Ref. 14 is to approximate $\Delta p(x, y)$ with a series of functions which represent very naturally the expected chordwise and spanwise variations of loading, while satisfying the Kutta condition of $\Delta p = 0$ along the trailing edge and also vanishing with the correct infinite slope at the tips. Specifically, a so-called Glauert series is used for the x-variation; the spanwise series is one that played an important part in the theory of the lifting line. Let the tips be located at $y = \pm B/2$ and the leading and trailing edges along the curves $x_L(y)$ and $x_T(y)$, such that the local chord is

$$c(y) = x_T - x_L .$$

Let the following auxiliary independent variables be defined so as to transform the planform S onto a rectangle between $\eta = -1, +1$ and $\theta = 0, \pi$:

$$\left. \begin{aligned} y &= \frac{B}{2} \eta \\[2mm] x &= \frac{x_T(y) + x_L(y)}{2} - \frac{c(y)}{2} \cos \theta \end{aligned} \right\} . \tag{23}$$

Watkins' representation for Δp then reads

$$\Delta p(\theta, \eta) = 4 \pi \rho U^2 \; \frac{B}{c(y)} \sqrt{1 - \eta^2} \left\{ \sum_{m=0} a_{om} \eta^m \cot \frac{\theta}{2} \right. $$
$$\left. + \sum_{n=1} \sum_{m=0} \frac{4}{2^{2n}} a_{nm} \eta^m \sin n\theta \right\} . \tag{24}$$

(It should be mentioned here that $\cot \theta/2$ describes the chordwise $\Delta p(\theta)$ on a two-dimensional, slightly-inclined flat plate running at infinite depth. $\sqrt{1 - \eta^2}$ corresponds to elliptic spanwise loading.) If conditions are symmetrical with respect to the x-z-plane, only even m's appear in Eq. (24), whereas odd m's describe antisymmetrical loading.

When Eq. (24) is inserted into Eq. (14), along with appropriate integration limits and the area element

$$dx_1 ds_1 = dx_1 dy_1 = \frac{B}{4} c(\eta_1) \sin \theta_1 d\theta_1 d\eta_1 \tag{25}$$

the integrals may be evaluated numerically for a set of stations (x, y) (or (θ, η)) on the half-span equal to the number of coefficients a_{nm} required for satisfactory convergence. The integrations must be performed with care on account of the η_1-singularity, a matter to which Ref. 14 devotes considerable attention. The results may be case in the matric form

$$[K] \{a_{nm}\} = \left\{ \frac{\bar{w}}{U} \right\} , \tag{26}$$

where $\{a_{nm}\}$ is a column of unknown coefficients from the series (24), $\{\bar{w}/U\}$ is an equal-order column of known vertical velocities, and $[K]$ is a square matrix whose elements consist of weighted integrals of the kernel function (Eq. (18)) times individual terms in the series (24). In the M.I.T. program $[K]$ is internally inverted for each value of reduced frequency k, yielding a solution of Eq. (26) in the form

$$\{a_{nm}\} = [K]^{-1} \left\{ \frac{\bar{w}}{U} \right\} . \tag{27}$$

This last step was made possible by the availability of a standard subroutine for inverting large matrices of complex numbers.

For any mode and frequency of oscillatory motion, the coefficients in the pressure series are finally computed by a single matric multiplication. Very rapid convergence is found in practice.

In an effort to study simultaneously the influence of submergence depth and aspect ratio, the M.I.T. program has been used to compute the oscillatory lifts and moments on a set of three hydrofoils. All had rectangular planforms.

Span-to-chord ratios of 1, 2 and 20 were chosen, the largest value being expected to give a reasonable estimate of depth effects in two-dimensional flow for comparison with results of Chu and Abramson [9]. The lower-aspect-ratio foils were caused to move in (1) vertical translation (heave), the displacement being

$$h = \bar{h} e^{ikt} \tag{28}$$

positive downward, and (2) pitch about the quarter-chord axis, the rotation being

$$\alpha = \bar{\alpha} e^{ikt} \tag{29}$$

positive in a sense to displace the leading edge upward. These motions simulate the bending and twisting components of flutter, and the lifts and pitching moments they produce can be employed for simplified analyses of hydroelastic phenomena (cf. Refs. 1 and 3, for example). The particular selection of pitching axis was made because in two-dimensional, steady flow at infinite depth the moment should vanish; hence, its deviations from zero provide a direct measure of the importance of three-dimensionality, etc.

With pressure distribution available in the form of the series (24), a convenient dimensionless measure of total normal force or lift is the "lift coefficient" C_L. This is related to lift L and to the individual coefficients by

$$C_L = \frac{L}{\frac{\rho}{2} U^2 S}$$

$$= \pi^3 \frac{B}{c} \left\{ \left[a_{oo} + \frac{1}{2} a_{10} \right] + \frac{1}{4} \left[a_{02} + \frac{1}{2} a_{12} \right] \right.$$
$$\left. + \frac{1}{8} \left[a_{04} + \frac{1}{2} a_{14} \right] + \frac{5}{64} \left[a_{06} + \frac{1}{2} a_{16} \right] + \cdots \right\} \quad . \tag{30}$$

Similarly, a moment coefficient may be defined for the leading-edge-up pitching moment $M_{c}/4$ about the quarter chordline:

$$C_M = \frac{\frac{M_c}{4}}{\frac{\rho}{2} U^2 S} = -\frac{1}{4} C_L$$

$$+ \frac{\pi^3}{4} \frac{B}{c} \left\{ \left[a_{oo} + \frac{1}{8} a_{20} \right] + \frac{1}{4} \left[a_{02} + \frac{1}{8} a_{22} \right] \right.$$
$$\left. + \frac{1}{8} \left[a_{04} + \frac{1}{8} a_{24} \right] + \frac{5}{64} \left[a_{06} + \frac{1}{8} a_{26} \right] + \cdots \right\} \quad . \tag{31}$$

C_L and C_M are, of course, complex amplitudes of simple harmonic quantities. In Eqs. (30) and (31), $S = Bc$ is used to denote the plan area, c $(= 1)$ being the chordlength.

Unfortunately, time limitations associated with preparing the paper for publication render it impossible to present detailed numerical results herewith. For the two lower aspect ratios, it is planned to give these in terms of the magnitude of the load coefficient per unit amplitude of the generating motion (e.g., $|C_L/\bar{z}|$) and the phase angle by which the load leads this motion. These will be so defined that the phase angle approaches zero as $k \to 0$, so that amplitude changes and phase shifts can be directly associated with flow unsteadiness.

For the large-aspect-ratio, "two-dimensional" foil, only heaving is being analyzed. The computed quantities correspond to certain loads determined in Ref. 9, i.e., the lift and moment magnitudes for a depth of one chordlength as ratioed to their values for $d = \infty$. On the basis of preliminary work, there is reason to believe that both the two- and three-dimensional results will confirm the conclusion of Chu and Abramson that the free-surface influence on a sub-cavitated foil is relatively minor until depths less than one chordlength are reached.

In all cases a 5×5 network of control stations over the semispan is being employed for the solution of Eq. (14). Indications of satisfactory convergence and numerical accuracy are obtained.

THE KERNEL FUNCTION FOR TWO-DIMENSIONAL FLOW AND FINITE FROUDE NUMBER

The problem of finding the kernel function for the general three-dimensional case with finite Froude number and arbitrary orientation of the pressure doublet is quite complicated. However, much can be learned about free-surface effects by studying the case of two-dimensional flow for which a closed-form solution for the kernal can be found. In addition, the two-dimensional ("strip theory") solution provides a practically useful approximation for flutter analysis of high aspect ratio straight or swept hydrofoils.

In two-dimensional flow the boundary value problem (cf. Eqs. (20) - (22)) for the kernel function becomes

$$K(x) = \int_{-\infty}^{x} e^{-ik(x-x_1)} \psi_z(x_1, -d) \, dx_1 \tag{32}$$

$$\nabla^2 \psi = 0 \tag{33}$$

$$\psi(x, -d+0) - \psi(x, -d-0) = \Delta \psi(x, -d) = \delta(x) \tag{34}$$

$$\left(ik + \frac{\partial}{\partial x}\right)^2 \psi + F^{-2}\psi_z = 0, \quad \text{at } z = 0. \tag{35}$$

The pressure doublet (lifting element) is assumed to be located at $z = -d$, δ denotes the Dirac delta function. To obtain the solution of the set (32) - (35) we apply the Fourier transformation with respect to x. Setting

$$\hat{\psi}_{(x;s)} = \frac{1}{\sqrt{2\pi}} \int_{-\infty}^{\infty} \psi(x, z) e^{-isx} dx, \text{ etc.} \tag{36}$$

we obtain

$$\hat{K} = -\frac{i}{s+k} \hat{\psi}_z(-d) \tag{37}$$

$$\hat{\psi}_{zz} - s^2 \hat{\psi} = 0 \tag{38}$$

$$\Delta \hat{\psi}(x, -d) = \frac{1}{\sqrt{2\pi}} \tag{39}$$

$$(k+s)^2 \hat{\psi} - F^{-2}\hat{\psi}_z = 0, \quad \text{at } z = 0. \tag{40}$$

The solution of (38) may be written as follows:

$$\hat{\psi} = A_+ e^{|s|z} + B_+ e^{-|s|z} \quad \text{for} \quad z > -d \Bigg\}$$
$$\hat{\psi} = A_- e^{|s|z} + B_- e^{-|s|z} \quad \text{for} \quad z < -d \Bigg\}.$$

(41)

In order for the disturbance to vanish as $z \to -\infty$, B_- must be zero. The other constants are obtained by introducing (41) into (39) and (40), and requiring $\hat{\psi}_z$ to be continuous at $z = -d$. Hence it is found that

$$A_+ = -\frac{(k+s)^2 + F^{-2}|s|}{(k+s)^2 - F^{-2}|s|} \frac{e^{-|s|d}}{\sqrt{2\pi}}$$

(42)

$$B_+ = \frac{e^{-|s|d}}{\sqrt{8\pi}}$$

(43)

$$A_- = A_+ - \frac{e^{|s|d}}{\sqrt{8\pi}}.$$

(44)

Substituting these results into (37) gives the Fourier transform of the kernel function:

$$\hat{K} = \frac{i|s|}{\sqrt{8\pi}\,(s+k)} \left[1 + \frac{(k+s)^2 + F^{-2}|s|}{(k+s)^2 - F^{-2}|s|} e^{-2|s|d}\right].$$

(45)

Before proceeding to evaluate the inverse transform of (45) it is convenient to rewrite it as follows:

$$\hat{K} = \hat{K}^{(\infty)} + \hat{K}^{(s)},$$

(46)

where

$$\hat{K}^{(\infty)} = \frac{i|s|}{\sqrt{8\pi}\,(s+k)}$$

(47)

and

$$\hat{K}^{(s)} = \frac{i|s|}{\sqrt{8\pi}\,(s+k)} \left[\frac{(k+s)^2 + F^{-2}|s|}{(k+s)^2 - F^{-2}|s|}\right] e^{-2|s|d}.$$

(48)

The first term corresponds to the kernel function for infinite depth. This term has a x^{-1} singularity at the origin and the inversion integral

$$K^{(\infty)} = \frac{1}{\sqrt{2\pi}} \int_{-\infty}^{\infty} \hat{K}^{(\infty)}(s)\, e^{isx}\, ds$$

(49)

is therefore divergent. The singular portion can be obtained by first calculating the upwash at $z = -d - \epsilon$ (which amounts to multiplying the transform by $e^{-|s|\epsilon}$) and then, after the inversion has been carried out, letting $\epsilon \to 0$. The result may be written

542

$$K^{(\infty)} = -\frac{1}{2\pi x} + \frac{ik}{2\pi} e^{-ikx} \left[Ei(ikx) + \pi i \right] , \qquad (50)$$

where $Ei(q)$ is the exponential integral defined by

$$Ei(q) = \int_{-\infty}^{q} \frac{e^t}{t} \, dt . \qquad (51)$$

This function has a branch point at the origin, and in order to make it single-valued a cut is introduced in the complex q-plane along the positive real axis, defining $arg(q) = 0$ for points on the upper side of the positive real axis. Some properties of the exponential integral are discussed in Appendix I. For purely imaginary arguments

$$Ei(is) = Ci(s) + i \left[Si(s) - \frac{\pi}{2} \right], \qquad (52)$$

where Ci and Si are the cosine and sine integrals, respectively, tables of which can be found in, for example, Ref. 16. Eq. (50) is exactly equivalent to the result first given by Fettis [17]. The second part of the kernel representing the effect of the free surface is nonsingular. Application of the inversion integral gives

$$K^{(s)} = \frac{i}{4\pi} \left\{ - \int_{-\infty}^{0} \frac{s \, ds}{s+k} \left[\frac{(k+s)^2 - F^{-2}s}{(k+s)^2 + F^{-2}s} \right] e^{2sd+isx} \right.$$

$$\left. + \int_{0}^{\infty} \frac{s \, ds}{s+k} \left[\frac{(k+s)^2 + F^{-2}s}{(k+s)^2 - F^{-2}s} \right] e^{-2sd+isx} \right\} . \qquad (53)$$

The first integral has poles at

$$s_0 = -k \qquad (54)$$

$$s_1 = -k \left[1 + (1/2) f^{-1} + (1/2) f^{-1} \sqrt{4f+1} \right] \qquad (55)$$

$$s_2 = -k \left[1 + (1/2) f^{-1} - (1/2) f^{-1} \sqrt{4f+1} \right] . \qquad (56)$$

where $f = kF^2 = \omega U/g$. These are all located on the real axis along the path of integration. Also, the second integral has poles located at

$$s_3 = -k \left[1 - (1/2) f^{-1} + (i/2) f^{-1} \sqrt{4f-1} \right] \qquad (57)$$

$$s_4 = -k \left[1 - (1/2) f^{-1} - (i/2) f^{-1} \sqrt{4f-1} \right] \qquad (58)$$

i.e., along the positive real axis for $f \leq 1/4$. For $f > 1/4$ they constitute a complex conjugate pair which for $1/4 < f < 1/2$ is located in the first and fourth quadrants. For $f > 1/2$, s_3 and s_4 are located in the second and third quadrants.

Since the poles give rise to terms representing wave trains, it is important to know on which side of the poles the path of integration should be taken. The simplest and most straightforward way to decide this is to assume that k has an infinitesimal negative imaginary part, i.e., that the oscillation started out at $t = -\infty$ with zero amplitude. Thereby, the poles will become separated from the real axis. Hence, the pole at s_0 will be located above the real axis, and by use of Cauchy's integral theorem with the integration path completed as shown in figure
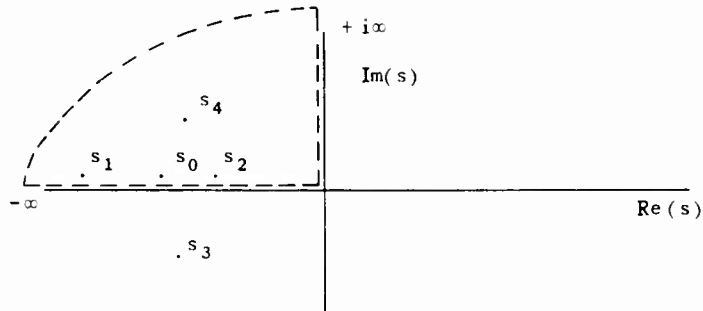
Integration path for $x > 0$

we find that for large positive x, the pole will give rise to a term of the form $\exp(-ikx)$. Hence the wave train corresponding to s_o is stationary with the fluid and simply represents the effect of the vortices shed behind this pressure doublet. The other poles give rise to genuine gravity waves. These have been discussed at length by Kaplan [18] for the three different ranges of f. In practical hydrofoil flutter problems, f is of the order of 10, hence only the case $f > 1/2$ will be considered in the present paper. Then there will be no waves due to s_3 and s_4. The poles s_1 and s_2 will be located in the second quadrant, and will thus give rise to two downstream wave trains with positive phase velocities. The one corresponding to s_1 will advance into the fluid whereas the other will recede.

To evaluate the integrals in (53) we separate the integrands into partial fractions upon which we obtain:

$$K^{(s)} = \frac{i}{4\pi} \left\{ \int_{-\tau}^{\pi} \frac{|s|}{s} e^{-2|s|d+isx} ds + \int_{-\pi}^{0} \left(-\frac{k}{s+k} + \frac{a_1}{s-s_1} + \frac{a_2}{s-s_2} \right) \right.$$

$$\times\ e^{2sd+isx} ds$$

$$\left. + \int_0^{\pi} \left(\frac{k}{s+k} - \frac{a_3}{s-s_3} - \frac{a_4}{s-s_4} \right) e^{-2sd+isx} ds \right\} . \tag{59}$$

where

$$a_1 = k \left[1 + f^{-1} + (3 + f^{-1})(4f + 1)^{-1/2} \right] \tag{60}$$

$$a_2 = k \left[1 + f^{-1} - (3 + f^{-1})(4f + 1)^{-1/2} \right] \tag{61}$$

$$a_3 = k \left[1 - f^{-1} + i(3 - f^{-1})(4f - 1)^{-1/2} \right] \tag{62}$$

$$a_4 = k \left[1 - f^{-1} - i(3 - f^{-1})(4f - 1)^{-1/2} \right] . \tag{63}$$

The first integral is easily evaluated whereas the others may be expressed as a sum of exponential integrals of complex arguments. Thus the following final result is obtained:

$$
\begin{aligned}
K^{(s)} = & -\frac{x}{2\pi(x^2 + 4d^2)} - \frac{ik}{4\pi} e^{-q_o} \left[Ei(q_o) + \pi i \left(1 + \frac{|x|}{x} \right) \right] \\
& - \frac{ik}{4\pi} e^{q_o^*} Ei(-q_o^*) + \frac{ia_1}{4\pi} e^{-q_1} \left[Ei(q_1) + \pi i \left(1 + \frac{|x|}{x} \right) \right] \\
& + \frac{ia_2}{4\pi} e^{-q_2} \left[Ei(q_2) + \pi i \left(1 + \frac{|x|}{x} \right) \right] + \frac{ia_3}{4\pi} e^{q_3} Ei(-q_3) \\
& + \frac{ia_4}{4\pi} e^{q_4} Ei(-q_4) .
\end{aligned}
\tag{64}
$$

where a star denotes complex conjugate and

$$
\begin{aligned}
q_o &= k(2d + ix) \\
q_1 &= -s_1(2d + ix) \\
q_2 &= -s_2(2d + ix) \\
q_3 &= -s_3(2d - ix) \\
q_4 &= -s_4(2d - ix) .
\end{aligned}
\tag{65}
$$

The extra terms proportional to $-i$ inside the brackets appear because of the cut defining the exponential integral. Thus for $x < 0$

$$\arg(2d + ix) = 2- - \tan^{-1} \frac{x}{2d} . \tag{66}$$

From (64) a number of interesting limiting cases can be obtained. For infinite Froude number, i.e., infinite f, it reduces to

$$K^{(s)} \sum_{f=\infty} = - \frac{x}{2\pi (x^2 + 4d^2)} + \frac{ik}{4\pi} e^{-q_o} \left[Ei(q_o) + \pi i \left(1 + \frac{|x|}{x} \right) \right]$$

$$+ \frac{ik}{4\pi} e^{q_o^*} Ei(-q_o^*) ,\tag{67}$$

which can be shown to be identical to the upwash at $z = -d$ created by an oscillatory pressure doublet at $z = d$. For most practical applications k will be small (of the order $1/10$). A useful approximation is therefore obtained by expanding (64) in a power series in k. Using the series expansion for Ei given in the Appendix and retaining only first-order terms we obtain

$$K^{(s)} = - \frac{x}{2\pi (x^2 + 4d^2)} + \frac{ik}{2\pi} \left[\ln k \sqrt{x^2 + 4d^2} + \frac{\pi i}{2} + 2i f^{-1} \tan^{-1} \frac{x}{2d} \right.$$

$$+ (3 + f^{-1}) (4f + 1)^{-1/2} \ln \left[1 + (1/2) f^{-1} + (1/2) f^{-1} \sqrt{4f + 1} \right]$$

$$\left. - (3 - f^{-1}) (4f - 1)^{-1/2} \tan^{-1} \frac{\sqrt{4f - 1}}{2f - 1} \right] + O (k^2 \ln k) .\tag{68}$$

In addition, f is often very large so we may simplify this further by expanding in f^{-1}, which leads to

$$K^{(s)} = - \frac{x}{2\pi (x^2 + 4d^2)} + \frac{ik}{2\pi} \left[\ln k \sqrt{x^2 + 4d^2} + \frac{\pi i}{2} \right.$$

$$\left. + 2i f^{-1} \tan^{-1} \frac{x}{2d} + O (f^{-3/2}) \right] + O (k^2 \ln k) .\tag{69}$$

The effect of finite Froude number is given by the last term alone which in many practical cases is small and can be neglected. For $x = d = 1$, $k = 0.1$ and $f = 10$ it is only 5 percent of the first term.

APPENDIX I

The exponential integral, defined by

$$Ei(w) = \int_{-\infty}^{w} \frac{e^{w_1}}{w_1} dw_1 \tag{A.1}$$

is a function that is analytic in the q-plane cut along the real axis. We will assume that $\arg(w) = 0$ for points on the upper side of the real axis.

Some Free Surface Effects
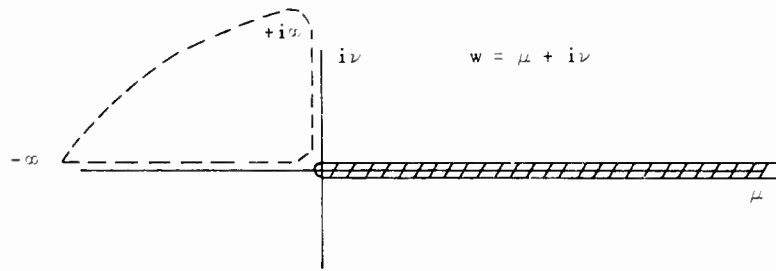
Figure A.1

For purely imaginary q we may deform the path of integration as shown in the Figure. Then

$$\text{Ei}(i\nu) = \int_{i\infty}^{i\nu} \frac{e^{w_1}}{w_1}\, dw_1 = \int_{\infty}^{\nu} \frac{e^{i\nu_1}}{\nu_1}\, d\nu_1 = \text{Ci}(\nu) + i\left[\text{Si}(\nu) - \frac{\pi}{2}\right], \qquad (A.2)$$

where Ci and Si are the integral cosine and sine functions. For small $\nu = \epsilon$ (see, e.g., Jahnke and Emde [16]).

$$\text{Ci}(\epsilon) = \gamma + \ell n\,\epsilon + O(\epsilon^2) \tag{A.3}$$

$$\text{Si}(\epsilon) = O(\epsilon).$$

Thus

$$\text{Ei}(i\epsilon) = \gamma + \ell n\,\epsilon - \frac{\pi i}{2} + O(\epsilon). \tag{A.4}$$

To obtain a series expansion for general w we first integrate along the path shown to $w = i\epsilon$ and then from $i\epsilon$ to w. By expanding e^{w_1} into a power series and integrating term by term we obtain

$$\text{Ei}(w) = \gamma + \ell n\,w + \sum_{1}^{\infty} \frac{w^n}{nn!} - \pi i. \tag{A.5}$$

This series is convergent for all $w < \infty$. For large w the following asymptotic formula may be used

$$\text{Ei}(w) \sim \frac{e^w}{w}. \tag{A.6}$$

547

REFERENCES

1. Henry, Charles J., Dugundji, John, and Ashley, Holt, "Aeroelastic Stability of Lifting Surfaces in High-Density Fluids," AFOSR Technical Note No. 58-626, June 1958 (also published in Journal of Ship Research, Vol. 2, No. 4, March 1959, pp. 10-21).

2. Theodorsen, Theodore and Garrick, I.E., "Mechanism of Flutter - A Theoretical and Experimental Investigation of the Flutter Problem," NACA Report 685, 1940.

3. Henry, C.J., "Hydrofoil Flutter Phenomenon and Airfoil Flutter Theory," paper presented at 30th Annual Meeting, Institute of the Aerospace Sciences, New York, January 1962.

4. Hilborne, D.V., "The Hydroelastic Stability of Struts," Admiralty Research Laboratory Report ARL/R1/G/HY/5/3, Teddington, Middlesex, England, November 1958.

5. Baird, E.F., Squires, C.E., Jr., and Caporali, R.L., "Investigation of Hydrofoil Flutter," Report No. DA 10-480.3, Grumman Aircraft Engineering Corporation, February 1962. (See also the paper presented by the same authors at 30th Annual Meeting, Institute of the Aerospace Sciences, New York, January 1962.)

6. Herr, Robert W., "A Study of Flutter at Low Mass Ratios with Possible Application to Hydrofoils," NASA Technical Note D-831, May 1961.

7. Bisplinghoff, R.L., Ashley, H., and Halfman, R.L., "Aeroelasticity," Addison-Wesley Publishing Company, Reading, Massachusetts, 1955.

8. Stoker, J.J., "Water Waves," Interscience Publishers, New York, 1957.

9. Chu, W.H. and Abramson, H.N., "Effect of the Free Surface on the Flutter of Submerged Hydrofoils," Southwest Research Institute Technical Report No. 3, Contract No. Nonr 2470(00), September 1958.

10. Pines, S., "An Elementary Explanation of the Flutter Mechanism," Proceedings of the National Specialists Meeting on Dynamics and Aeroelasticity, Ft. Worth, Texas, November 1958.

11. Zimmerman, N.H., "Elementary Static Aerodynamics Adds Significance and Scope in Flutter Analyses," Proceedings of the Symposium on Structural Dynamics of High Speed Flight, Los Angeles, California, April 1961.

12. Mangler, K.W., "Improper Integrals in Theoretical Aerodynamics," British Royal Aircraft Establishment, Report No. Aero 2424.

13. Watkins, C.E., Runyan, H.L., and Woolston, D.S., "On the Kernel Function of the Integral Equation Relating the Lift and Downwash Distributions of Oscillating Finite Wings at Subsonic Speeds," NACA Report 1234, 1955.

548

14. Watkins, C.E., Woolston, D.S., and Cunningham, H.J., "A Systematic Kernel Function Procedure for Determining Aerodynamic Forces on Oscillating or Steady Finite Wings at Subsonic Speeds," NASA Technical Report R-48, 1959.

15. Hsu, P T., "Some Recent Developments in Flutter Analysis of Low-Aspect-Ratio Wings," Proceedings of the National Specialists Meeting on Dynamics and Aeroelasticity, Ft. Worth, Texas, November 1958.

16. Jahnke, E. and Emde, F., "Tables of Functions with Formulae and Curves," Fourth Edition, Dover Publications, New York, 1945.

17. Fettis, H., "An Approximate Method for the Calculation of Nonstationary Air Forces at Subsonic Speeds," USAF Wright Air Development Center Technical Report No. 52-56, 1952.

18. Kaplan, P., "The Waves Generated by the Forward Motion of Oscillatory Pressure Distributions," Proceedings of the Fifth Midwestern Conference on Fluid Mechanics, University of Michigan, Ann Arbor, April 1957, pp. 316-329.

*   *   *

UNSTEADY FLOW PAST PARTIALLY CAVITATED HYDROFOILS

H. Steinberg
Technical Research Group, Inc.
Syosset, New York

and

S. Karp
New York University
New York, New York

NOMENCLATURE

ϱ normalized pressure (or acceleration potential) $= (p_z - p)\,d$, where p is the actual pressure and d is the density

ϱ normalized cavity pressure (cavitation number $= \varrho/(1/2)U^2$)

G Green's function for regular term for pressure

ℓ one-half the length of the hydrofoil

c position of the rear end of the cavity (assuming hydrofoil between $-\ell$ and ℓ)

a $\sqrt{\ell-c}/\sqrt{\ell+c}$

Φ velocity potential

U free stream velocity

ν oscillation frequency

Ω $\nu\ell/U$ (reduced frequency)

$M(t)$ slope of hydrofoil

$B(t)$ y intercept of hydrofoil

f   force perpendicular to hydrofoil

m   moment on hydrofoil

ω $\ell + c/2\ell$ (fractional length of cavity)

We are presenting here the results of a study of the unsteady flow past an oscillating partially cavitated hydrofoil. For simplicity we have considered only a flat plate of infinite span in an infinite fluid. Moreover, we are concerned only with angles of attack sufficiently small to allow the use of linearized theory and assume further that the unsteady motion consists of small simple harmonic oscillations around the steady motion, either pitching or heaving, allowing us to make a "second linearization," as a result of which the higher harmonics of the flow may be neglected.

Various approaches have been made to this problem but as will be seen in what follows it has not been possible to make a completely unambiguous mathematical formulation of the problem, since the physics of the situation is not sufficiently well enough understood.

Timman [1] formulated the problem using a model which seems physically unacceptable, i.e., the vertical component of the velocity in the wake was discontinuous. Guerst [2] has formulated the problem to force continuity by dropping the condition that the cavity be closed. Although physically both conditions apparently should hold, we felt that the linearization procedure was more likely to effect closure in the unsteady case, so that in this solution we used Guerst's formulation. In our solution we found that by using the acceleration potential as used by Timman, we are able to obtain a relatively clear development. Therefore we have followed Timman's approach in setting up the problem.

Let Φ be the velocity potential, then

$$\zeta = U \frac{\partial \Phi}{\partial x} - \frac{\partial \Phi}{\partial t}$$

is the acceleration potential. In his development, Timman first obtained an expression for ζ to satisfy the conditions

  $\zeta = \sigma$ (normalized cavity pressure) along the cavity surface,

  $\zeta_y = Uw_x + w_t$, where w = the vertical component of the velocity along the
  wetted surface.

Using the mapping in Fig. 1, Timman obtained the solutions

$$\zeta = \sigma - \frac{1}{2\pi} \int_{\substack{\text{wetted} \\ \text{surface}}} f(x',t) \, G(x',o:x,y) \, dx' - c_1 \zeta_1 - c_1 \zeta_2 . \tag{1}$$

where

$$f = Uw_x + w_t .$$

552
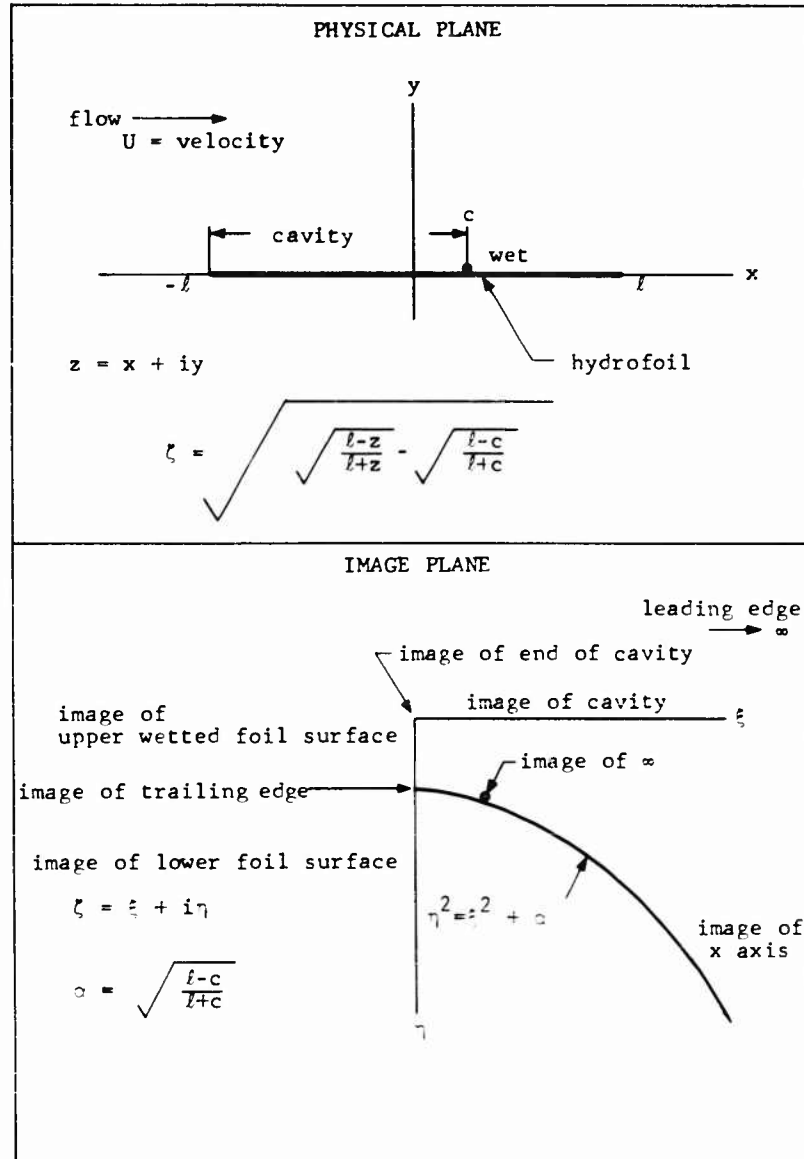
Figure 1

G is the Green's function defined so that

$$\varphi - \frac{1}{2\pi} \int f G \, dx'$$

satisfies the above boundary conditions. In this formulation, there are two possible points of singularity, at the leading edge and at the rear end of the cavity (the Kutta condition removes any possible trailing edge singularity). φ_1 and φ_2 are defined to be singular at the leading edge and the rear of the cavity respectively, satisfying Laplace's equation with the boundary conditions

$$\varphi_k = 0 \quad \text{on the cavity surface,}$$

$$\varphi_{ky} = 0 \quad \text{on the wetted surface.}$$

Further, the singularities must be integrable (i.e., the velocity finite) at the points of singularity.

Timman obtained G, φ_1, and φ_2 to be:

$$G = \ell n \left(\frac{u + i\zeta}{u - i\zeta} \right) - \ell n \left(\frac{u - i\zeta}{u - i\zeta} \right) .$$

where

$$u = \sqrt{z \pm \sqrt{\frac{\zeta - x}{\zeta - x}}}$$

(where ($-$) is used on the upper surface and ($+$) on the lower surface),

$$\zeta = \sqrt{\sqrt{\frac{\zeta - z}{\zeta - z}} - z}$$

and

$$z = \sqrt{\frac{\zeta - c}{\zeta - c}} .$$

Let

$$\zeta = \xi - i\eta$$

$$\varphi_1 = \frac{-\eta}{\eta^2 + \xi^2} = \text{Im} \left(\frac{1}{\zeta} \right)$$

$$\varphi_2 = -\eta = \text{Im}(\zeta) .$$

For a flat plate the integration may be carried out explicitly (all analytical details are from Steinberg [3]). Let

$$h = M(t)x - B(t)$$

be the profile of the hydrofoil, then

$$w = M'x + B' + MU \qquad (w = Uh_x + h_t)$$

$$f = M''x + B'' + 2M'U$$

and

$$\phi = \sigma + \sum_{1}^{4} c_k \phi_k ,$$

where

$$\phi_3 = \operatorname{Im}\left[i \left(\frac{1}{\beta(\beta + i\zeta)} + \frac{1}{\overline{\beta}(i\zeta - \overline{\beta})} \right) \right]$$

$$\phi_4 = \operatorname{Im}\left[-\frac{1}{4}\left(\frac{1}{\beta^2(\beta + i\zeta)^2} + \frac{1}{\overline{\beta}^2(\overline{\beta} - i\zeta)^2} \right) \right.$$

$$\left. -\frac{1}{4}\left(\frac{1}{\beta^3(\beta + i\zeta)} + \frac{1}{\overline{\beta}^3(\overline{\beta} - i\zeta)} \right) - \frac{i}{2}\left(\frac{1}{\beta(\beta + i\zeta)} - \frac{1}{\overline{\beta}(\overline{\beta} - i\zeta)} \right) \right].$$

where

$$\beta = \sqrt{a + i}$$

and

$$c_3 = \lambda (B'' + 2M'U)$$

$$c_4 = \lambda^2 M'' .$$

At this point the problem has been reduced to determining three unknown functions of time, c_1 and c_2, the strength of the singularities, and c, the length of the cavity (for computational purposes it was found more convenient to use $a = \sqrt{\lambda - c/\lambda + c}$, rather than c, for the third unknown).

To determine these functions it is necessary to prescribe three more conditions. Possible conditions are as follows:

(1) The pressure at x should be finite and continuous:

$$c(x) = 0.$$

(2) The velocity should satisfy the boundary condition (along the wetted surface)·

$$\Phi_y = w(x, y), \quad \begin{cases} -\lambda \le x \le \lambda, & y = 0^- \\ c \le x \le \lambda, & y = 0^- \end{cases}$$

(3) The cavity should be closed:

$$h(c,t) - h(-\ell,t) = \frac{1}{U} \int_{-\ell}^{c} \Phi_y \left(x', o^+, t - \frac{c - x'}{U} \right) dx'.$$

(4) The vertical component of velocity should be continuous in the wake

$$\Phi_y(x, o^+, t) = \Phi_y(x, o^-, t), \quad x > \ell.$$

Conditions (1) and (2) seem quite satisfactory on physical and mathematical grounds, so that the choice lies between (3) and (4). For the steady state problem (4) is automatically satisfied so that (3) is the only condition left. However in the unsteady problem, the physics of the problem seem to us more reasonable if (4) is used rather than (3). This is the view of Guerst, Wu [4] and others, and this approach is used here.

To solve this problem we will use condition (1) to obtain Φ in terms of z

$$\Phi(x, y, t) = \frac{1}{U} \int_{-z}^{x} z \left(x', y, t - \frac{x - x'}{U} \right) dx' \tag{2}$$

$$= \frac{1}{U} \int_{-z}^{x} \left[z + \sum_{1}^{4} c_k \left(t - \frac{x - x'}{U} \right) z_k \right] dx'. \tag{3}$$

Therefore Φ_y, the vertical component of the velocity is given by:

$$\Phi_y = \frac{1}{U} \int \sum c_k \left(t - \frac{x - x'}{U} \right) z_{ky} dx'. \tag{4}$$

Let ψ_k be the conjugate harmonic function of z_k, defined so that $\psi_k(z) = 0$ (in the x, y plane). Using the Cauchy-Riemann equations:

$$\Phi_y = \frac{1}{U} \int_{-z}^{z} \sum c_k \left(t - \frac{x - x'}{U} \right) \psi_{kx'} dx'. \tag{5}$$

Note that

$$\psi_{kx'} = \frac{\partial \psi_k}{\partial x'}.$$

where

$$\psi_k = \psi_k \left[x', y, z \left(t - \frac{x - x'}{U} \right) \right].$$

We wish to eliminate the $\partial \psi_k / \partial x'$ terms; therefore

$$\frac{\partial \psi_k}{\partial x'} = \frac{d \psi_k}{dx'} - \frac{1}{U} \frac{\partial \psi_k}{\partial z} \frac{\partial z}{\partial t}.$$

556

where

$$\frac{1}{U} \frac{\partial a}{\partial t} = \frac{\partial a}{\partial x'} .$$

Further

$$c_k' = \frac{\partial c_k}{\partial x'} = \frac{1}{U} \frac{\partial c_k}{\partial t} \left(t - \frac{x - x'}{U} \right) .$$

Therefore

$$\Phi_y = \frac{1}{U} \left\{ \sum_{k=1}^{4} \left[c_k(t) \, \psi_k \big(k, y, a(t)\big) \right. \right.$$

$$\left. \left. - \frac{1}{U} \frac{d}{dt} \int_{-\pi}^{x} c_k(\tau) \, \psi_k \big(x', y, a(\tau)\big) \, dx' \right] \right\} . \tag{6}$$

where

$$\tau = t - \frac{x - x'}{U} .$$

We will solve the problem in two stages, first obtain the steady state solution, and then carry out the "second linearization" to obtain an unsteady term as a small perturbation on the steady state solution.

For the steady state case, $c_3 = c_4 = 0$. Let

$$A = \sqrt{\frac{\sqrt{a^2 - 1} - a}{2}}$$

$$B = \sqrt{\frac{\sqrt{a^2 - 1} - a}{2}} .$$

Then conditions (1), (2), and (3) become

$$(1) \qquad \frac{c_1 A}{\sqrt{a^2 + 1}} - c_2 A + \tau = 0$$

$$(2) \qquad MU^2 - \frac{c_1 B}{\sqrt{a^2 - 1}} - c_2 B = 0$$

$$(3) \quad U^2 M(c - a) = c_1 \int_{-a}^{c} \left(\frac{\xi}{a^2 - \xi^2} - \frac{B}{\sqrt{a^2 - 1}} \right) dx - c_2 \int_{-a}^{a} \big(\xi - B \big) \, dx$$

Using (2) and carrying out the integrations (3) reduces to

$$(3^*) \qquad \left(\sqrt{\alpha^2+1} + 2\alpha\right) \frac{c_1}{\sqrt{\alpha^2+1}} + \sqrt{\alpha^2+1}\ c_2 = 0.$$

Solving the equations

$$c_1 = -\alpha B \left(1+\alpha^2\right)\left(\sqrt{\alpha^2+1} - \alpha\right)$$

$$c_2 = \alpha B \left(\alpha\sqrt{\alpha^2+1} + 1 - \alpha^2\right)$$

$$\sigma = -\frac{U^2 M}{\alpha}\left(\sqrt{\alpha^2+1} - \alpha\right)^2$$

or

$$c_1 = \frac{U^2 MB}{\alpha}\left(\alpha^2+1\right)\left(\alpha + \sqrt{\alpha^2+1}\right)$$

$$c_2 = -\frac{U^2 MB}{\alpha}\left(3\alpha^2+1-3\alpha\sqrt{\alpha^2+1}\right).$$

where as stated $\alpha = \sqrt{4 + c} \sqrt{4 + c}$.

Let us now proceed to the unsteady case and carry out the "second linearization," i.e., we will assume that the unsteady effect is due to small simple harmonic oscillation around the steady state, where higher order terms are neglected.

Because of the form of the steady state solution, it was found convenient to use α rather than $U^2 M$ as the parameter characterizing the steady state about which the perturbation is to be carried out.

Then

$$\alpha = \alpha_0 + \alpha_1 \cos\left(\omega t - \phi_\alpha\right)$$

$$c_k = c_{k0} + c_{k1} \cos\left(\omega t - \phi_k\right) \qquad (k = 1,2,3,4.$$

where α_0, c_{10}, c_{20} are the steady state values.

Let $h(x,t) = M(t)x + B(t)$. As before we will assume the perturbation is given by oscillations of $M(t)$ or $B(t)$ at the same frequency but arbitrary amplitude and relative phase.

$$M(t) = M_0 + M_1 \cos \omega t$$

$$B(t) = B_1 \cos\left(\omega t - \phi_B\right). \qquad (7)$$

($B_o = 0$ since the problem was formulated to put the foil on the x axis.) From this we have

$$c_{30} = 0$$

$$c_{31} = -\nu\lambda\sqrt{(\nu B_1)^2 + 4(M_1 U)^2 + 4\nu B_1 M_1 U \sin \zeta_B}$$

$$\zeta_3 = \tan^{-1}\left(\tan \zeta_B + \frac{2M_1 U}{\nu B_1 \cos \zeta_B}\right)$$

$$c_{40} = 0$$

$$c_{41} = -\nu^2 \lambda^2 M_1$$

$$\zeta_4 = 0.$$

Applying the second linearization

$$c_k(t)\, \phi_k(x, y, z) = c_{ko}\, \phi_k(x, y, z_o) - c_{k1} \cos(\nu t - \zeta_k)\, \phi_k(x, y, z_o)$$

$$- c_{ko}\, \frac{\partial \phi_k}{\partial z_o}(x, y, z_o)\, z_1 \cos(\nu t - \zeta_z).$$

Similarly for $c_k z_k$.

Let $\hat{\Phi}$ and $\hat{z}$ be the unsteady parts of Φ and z. Then

$$\hat{\Phi}_y = \frac{1}{U}\sum_{k=1}^{4}\left[c_{k1} \cos(\nu t - \zeta_k)\, \phi_k - c_{ko}\, \frac{\partial \phi_k}{\partial z_o}\, z_1 \cos \nu t \right.$$

$$- \frac{\nu}{U}\int_{-\infty}^{x} c_{k1} \sin\left[\nu\left(t - \frac{x - x'}{U}\right) - \zeta_k\right]\phi_k(x', y, z_o)$$

$$\left. - c_{ko}\, \frac{\partial \phi_k}{\partial z_o}\, z_1 \sin\left[\nu\left(t - \frac{x - x'}{U}\right) - \zeta_z\right] dx' \right]. \tag{8}$$

Also

$$\hat{z} = \sum\left[c_{k1} \cos(\nu t - \zeta_k)\, z_k - c_{ko}\, \frac{\partial z_k}{\partial z_o}\, z_1 \cos(\nu t - \zeta_z) \right]. \tag{9}$$

We now impose conditions (1), (2) and (4)

Condition (1)

$$\sum_{k=1}^{4} \left[c_{k1} \cos (\nu s - \bar{\delta}_k) \, \tau_k(x) + c_{ko} \frac{\partial \tau_k(x)}{\partial z_o} \, z_1 \cos (\nu s - \bar{\delta}_2) \right] = 0 .$$

Let $\Omega = \nu \ell / U$ be the reduced frequency. Let

$$J_{k,c} = \Omega \int_{-\infty}^{-\ell} \psi_k(x', 0, z_o) \cos \left[\Omega \left(\frac{x' + \ell}{\ell} \right) \right] \frac{dx'}{\ell}$$

$J_{k,s}$ defined as above using sine instead of cosine

$J_{k,c}^{\bullet}$ and $J_{k,s}^{\bullet}$ defined using $\partial \psi_k / \partial z_o$ instead of ψ_k.

Then condition (2) may be written as

$$\sum_{k=1}^{4} \left\{ c_{k1} \left[\left(J_{k,s} + \psi_k(-\ell, 0^-, z_o) \right) \cos (\nu s - \bar{\delta}_k) + J_{k,c} \sin (\nu s - \bar{\delta}_k) \right] \right.$$

$$+ z_1 c_{ko} \left[\left(J_{k,s}^{\bullet} + \frac{\partial \psi_k}{\partial z_o} (-\ell, 0^-, z_o) \right) \cos (\nu s - \bar{\delta}_2) + J_{k,c}^{\bullet} \sin (\nu s - \bar{\delta}_2) \right]$$

$$\left. - \frac{c_{31}}{\Omega} \sin (\nu s - \bar{\delta}_3) + c_{41} \left(\frac{\sin (\nu s - \bar{\delta}_4)}{\Omega} - \frac{\cos (\nu s - \bar{\delta}_4)}{\Omega^2} \right) \right\} = 0 .$$

where

$$s = t - \frac{x - \ell}{U} .$$

Let

$$I_{k,c} = \frac{1}{8} \int_{-\ell}^{\ell} \left[\psi_k(x', 0^+, z_o) - \psi_k(x', 0^-, z_o) \right] \cos \left[\Omega \left(\frac{x' - \ell}{\ell} \right) \right] \frac{dx'}{\ell} .$$

Similarly $I_{k,s}$, $I_{k,c}^{\bullet}$, and $I_{k,s}^{\bullet}$ are defined. Then condition (4) becomes

$$\sum_{1}^{4} \left\{ c_{k1} \left[I_{k,c} \sin (\nu s - \bar{\delta}_k) + I_{k,s} \cos (\nu s - \bar{\delta}_k) \right] \right.$$

$$\left. + z_1 c_{ko} \left[I_{k,c}^{\bullet} \sin (\nu s - \bar{\delta}_2) + I_{k,s}^{\bullet} \cos (\nu s - \bar{\delta}_2) \right] \right\} = 0 .$$

Since the conditions must hold for arbitrary time, we can reduce these equations to six linear equations in six unknowns.

Let

$$d_{k,c} = c_{k1} \cos \theta_k \qquad k = 1, \dots, 4$$

$$d_{k,s} = c_{k1} \sin \theta_k$$

$$\alpha_c = \alpha_1 \cos \theta_2 \tag{10}$$

$$\alpha_s = \alpha_1 \sin \theta_2.$$

The unknowns are $d_{1,c}$, $d_{1,s}$, $d_{2,c}$, $d_{2,s}$, α_c, α_s while the six equations are obtained from the vanishing of the coefficients of $\cos \nu s$ and $\sin \nu s$ in the three conditions.

Once these are obtained, they may be then inserted into Eqs. (9) and (8) to obtain the unsteady parts of z and Φ_y.

The lift and moment of the hydrofoil may be expressed in terms of these coefficients as follows:

$$f = f_o + f_c \cos \nu t - f_s \sin \nu t \tag{11}$$

$$m = m_o - m_c \cos \nu t - m_s \sin \nu t.$$

where

$$f_o = -\frac{d}{2} \sum_{k=1}^{2} c_{ko} R_k$$

$$f_c = -\frac{d}{2} \left(\alpha_c R_2 + \sum_{k=1}^{4} d_{k,c} R_k \right)$$

$$f_s = -\frac{d}{2} \left(\alpha_s R_2 - \sum_{k=1}^{4} d_{k,s} R_k \right)$$

$$m_o = -\frac{d}{2} \sum_{k=1}^{2} c_{ko} S_k \tag{12}$$

$$m_c = -\frac{d}{2} \left(\alpha_c S_2 - \sum_{k=1}^{4} d_{k,c} S_k \right)$$

$$m_s = -\frac{d}{2} \left(\alpha_s S_2 - \sum_{k=1}^{4} d_{k,s} S_k \right).$$

561

where R_a, R_k, S_a, S_k may be obtained explicitly by:

$$R_a = 2 \sum_{k=1}^{2} c_{ko} \int_{-\ell}^{\ell} \frac{\partial}{\partial z} \left[z_k(x,0^-,z) - z_k(x,0^+,z) \right] dx$$

$$R_k = 2 \int_{-\ell}^{\ell} \left[z_k(x,0^-,z) - z_k(x,0^+,z) \right] dx$$

$$S_a = 2 \sum_{k=1}^{2} c_{ko} \int_{-\ell}^{\ell} (x-\ell) \frac{\partial}{\partial z} \left[z_k(x,0^-,z) - z_k(x,0^+,z) \right] dx$$

$$S_k = 2 \int_{-\ell}^{\ell} (x+\ell) \left[z_k(x,0^-,z) - z_k(x,0^+,z) \right] dx .$$

The results of these calculations are given in Table I.

It is of interest to see what happens as the length of the cavity approaches zero, equivalent to $z \to \infty$. We find that the number of unknowns reduces from 6 to 2. z_c and z_s are not needed at all, while only a particular combination of $d_{1,c}$ and $d_{2,c}$ and also $d_{1,s}$ and $d_{2,s}$ are required. The only condition needed is (2). Not too surprisingly the limiting solution agrees with unsteady airfoil theory. However, this does not give us any indication about whether or not condition (4) is preferred to condition (3), since the limiting solution, being dependent only on condition (2) would be the same in either case.

Since the integrals given as "J" and "I" must be evaluated numerically, we are able to give results only in numerical form. In Table II we tabulate the following quantities:

$$f_c^* = \frac{f_c}{d \ell U^2 M_o}$$

$$f_s^* = \frac{f_s}{d \ell U^2 M_o}$$

$$m_c^* = \frac{m_c}{d \ell^2 U^2 M_o}$$

$$m_s^* = \frac{m_s}{d \ell^2 U^2 M_o} .$$

(13)

where f_c, f_s, m_c, m_s are the amplitudes introduced in Eqs. (11) and (12). Let $\alpha = (\ell + c) 2\ell$ be the normalized cavity length. Then

$$\alpha = \alpha_o - \alpha_c \cos \omega t - \alpha_s \sin \omega t .$$

(14)

562

Unsteady Flow Past Partially Cavitated Hydrofoils

Table I

R (Force Terms)

Index

1) $\dfrac{2\pi\ell A\left(\sqrt{\alpha^2+1}-2\alpha\right)}{\left(\alpha^2+1\right)^{3/2}}$ where $A = \sqrt{\dfrac{\sqrt{\alpha^2+1}+\alpha}{2}}$

2) $\dfrac{-2\pi\ell A}{\left(\alpha^2+1\right)^{1/2}}$

3) $\dfrac{\pi\ell}{2\left(\alpha^2+1\right)^2}\left[2\alpha^4+3\alpha^2+3+2\alpha(\alpha^2+1)^{3/2}\right]$

4) $\dfrac{-\ell}{4\left(\alpha^2+1\right)^3}\left[\alpha(\alpha^2+1)\left(\sqrt{\alpha^2+1}+\alpha\right)-4\alpha^2\right]$

2) $\dfrac{-U^2 M\ell\pi}{\alpha\left(\alpha^2+1\right)^{3/2}}\left(4\alpha+\sqrt{\alpha^2+1}\right)$

$f_o = dU^2 M\ell\pi\left(\dfrac{\alpha+\sqrt{\alpha^2+1}}{\alpha}\right)$

S (Moment Terms)

1) $\dfrac{-\ell^2 A\left[\alpha(\alpha^2+13)+\sqrt{\alpha^2+1}\,(\alpha^2-5)\right]}{2\left(\alpha^2+1\right)^{5/2}}$ •

2) $\dfrac{-\ell^2 A\left(3+\alpha^2+\alpha\sqrt{\alpha^2+1}\right)}{2(\alpha^2+1)^{3/2}}$

3) $\dfrac{-\ell^2}{4\left(\alpha^2+1\right)^3}\left[4\alpha^6+11\alpha^4+9\alpha^2+6+\alpha\sqrt{\alpha^2+1}\,(4\alpha^4+9\alpha^2+5)\right]$

4) $\dfrac{-\ell^2}{64\left(\alpha^2+1\right)^4}\left(8\alpha^8+40\alpha^6+65\alpha^4+30\alpha^2+9+4\alpha\sqrt{\alpha^2+1}\,\left[2\alpha^6+9\alpha^4+12\alpha^2+5\right]\right)$

2) $\dfrac{-U^2 M\ell^2}{2\alpha\left(\alpha^2+1\right)^{5/2}}\left[\alpha(-5\alpha^2+19)+\sqrt{\alpha^2+1}\,(-5\alpha^2+4)\right]$

$m_o = dU^2 M\ell^2\left(\dfrac{4+\alpha\sqrt{\alpha^2+1}\left(\sqrt{\alpha^2+1}+\alpha\right)^2}{4\alpha\left(\alpha^2+1\right)^{3/2}}\right)$

563

Table II

Unsteady Lift Force Perpendicular to Foil due to Unit Heave

f_c^*

ω_0 (Cavity Length)	0	.125	.25	.375	.5	.625	.75
σ (Reduced Frequency)							
0.0	0.0	0.0	0.0	0.0	0.0	0.0	0.0
.05	-.0332	-.0394	-.0519	-.0769	-.135	-.324	-1.52
.1	-.0768	-.0889	-.116	-.171	-.288	-.599	-1.74
.3	-.0553	-.0465	-.0876	-.199	-.429	-.901	-2.00
.5	.312	.394	.382	.251	-.0470	-.628	-1.83
1.0	2.51	2.95	3.11	2.97	2.48	1.55	-.0890
1.5	6.38	7.41	7.85	7.70	6.98	5.66	3.51
2.0	11.8	13.7	14.5	14.4	13.4	11.7	9.05
2.5	18.9	21.8	23.0	22.9	21.7	19.6	16.3
3.0	27.5	31.7	33.4	33.3	31.8	29.2	25.0
3.5	37.7	43.3	45.6	45.5	43.8	40.5	34.7
4.0	49.5	56.8	59.6	59.5	57.4	53.2	45.2

f_s^*

σ	0	.125	.25	.375	.5	.625	.75
0.0	0.0	0.0	0.0	0.0	0.0	0.0	0.0
.05	.286	.314	.353	.414	.517	.727	.706
.1	.523	.570	.633	.722	.859	+1.08	1.01
.3	1.25	1.35	1.47	1.61	1.79	1.99	2.01
.5	1.88	2.03	2.20	2.39	2.59	2.81	2.90
1.0	3.39	3.70	4.03	4.34	4.61	4.81	4.87
1.5	4.91	5.41	5.94	6.39	6.67	6.76	6.64
2.0	6.45	7.17	7.96	8.55	8.81	8.75	8.53
2.5	7.99	9.00	10.1	10.8	11.0	10.9	10.9
3.0	9.54	10.9	12.4	13.2	13.4	13.4	13.8
3.5	11.1	12.9	14.8	15.8	16.0	16.2	17.2
4.0	12.7	14.9	17.3	18.4	18.8	19.4	20.5

564

Table II (Continued)

Unsteady Lift Force Perpendicular to Foil due to Unit Pitch

f_c

σ_0 (Cavity Length) ω (Reduced Frequency)	0	.125	.25	.375	.5	.625	.75
0.0	-6.28	-6.98	-8.01	-9.68	-12.9	-22.5	-
.05	-5.73	-6.30	-7.10	-8.30	-10.4	-14.6	-14.3
.1	-5.28	-5.76	-6.39	-7.30	-8.68	-10.9	-10.4
.3	-4.35	-4.70	-5.10	-5.59	-6.18	-6.87	-6.95
.5	-3.99	-4.35	-4.72	-5.10	-5.51	-5.91	-6.03
1.0	-3.70	-4.23	-4.66	-4.98	-5.17	-5.22	-5.06
1.5	-3.62	-4.45	-5.04	-5.34	-5.36	-5.14	-4.73
2.0	-3.59	-4.84	-5.64	-5.93	-5.80	-5.40	-4.94
2.5	-3.57	-5.37	-6.41	-6.70	-6.45	-5.99	-5.64
3.0	-3.56	-6.02	-7.33	-7.61	-7.29	-6.82	-6.58
3.5	-3.55	-6.77	-8.38	-8.65	-8.28	-7.81	-7.45
4.0	-3.55	-7.63	-9.52	-9.79	-9.39	-8.81	-8.03

f_s

σ_0 (Cavity Length) ω (Reduced Frequency)	0	.125	.25	.375	.5	.625	.75
0.0	0.0	0.0	0.0	0.0	0.0	0.0	-
.05	-.521	-.647	-.897	-1.40	-2.55	-6.32	-30.4
.1	-.507	-.632	-.909	-1.46	-2.64	-5.76	-17.2
.3	.443	.455	.295	-.110	-.923	-2.57	-6.34
.5	1.56	1.70	1.64	1.32	.650	-.617	-3.16
1.0	4.21	4.61	4.68	4.43	3.82	2.76	.971
1.5	6.71	7.32	7.48	7.22	6.59	5.61	4.14
2.0	9.14	9.95	10.1	9.84	9.23	8.34	7.07
2.5	11.6	12.5	12.7	12.3	11.8	10.9	9.66
3.0	13.9	15.0	15.1	14.8	14.2	13.3	11.8
3.5	16.3	17.5	17.5	17.1	16.5	15.5	13.4
4.0	18.7	19.9	19.7	19.3	18.7	17.4	14.8

Table II (Continued)
Unsteady Moment due to Unit Heave

$\dot{m}_c$

ω_2 (Cavity Length) Ω (Reduced Frequency)	0	.125	.25	.375	.5	.625	.75
0.0	0.0	0.0	0.0	0.0	0.0	0.0	0.0
.05	-.0127	-.0101	-.0123	-.0257	-.0719	-.261	-1.71
.1	-.0227	-.0134	-.0149	-.0431	-.141	-.473	-1.95
.3	.114	.175	.212	.177	-.0197	-.592	-2.22
.5	.549	.689	.806	.815	.587	-.126	-1.97
1.0	2.83	3.28	3.75	4.00	3.77	2.74	.231
1.5	6.72	7.67	8.68	9.30	9.14	7.82	4.70
2.0	12.2	13.8	15.5	16.6	16.6	15.0	11.5
2.5	19.3	21.7	24.3	25.9	26.0	24.4	20.5
3.0	27.9	31.4	34.9	37.0	37.4	35.7	31.1
3.5	38.1	42.8	47.3	50.0	50.7	49.0	43.1
4.0	49.9	55.9	61.5	64.8	65.9	64.1	56.2

$\dot{m}_s$

Ω (Reduced Frequency)	0	.125	.25	.375	.5	.625	.75
0.0	0.0	0.0	0.0	0.0	0.0	0.0	0.0
.05	.143	.126	.137	.189	.314	.605	.795
.1	.261	.230	.248	.334	.526	.901	1.14
.3	.627	.551	.596	.781	1.14	1.70	2.26
.5	.939	.835	.915	1.20	1.70	2.44	3.26
1.0	1.69	1.54	1.76	2.33	3.20	4.30	5.48
1.5	2.46	2.28	2.71	3.64	4.88	6.22	7.48
2.0	3.22	3.06	3.80	5.17	6.75	8.24	9.60
2.5	4.00	3.89	5.04	6.89	8.79	10.4	12.2
3.0	4.77	4.78	6.45	8.80	11.0	12.9	15.5
3.5	5.55	5.73	8.01	10.8	13.2	15.6	19.3
4.0	6.33	6.76	9.72	13.0	15.6	18.5	23.1

Unsteady Flow Past Partially Cavitated Hydrofoils

Table II (Continued)
Unsteady Moment due to Unit Pitch

$\dot{m}_c^*$

ω_0 (Cavity Length) / Ω (Reduced Frequency)	0	.125	.25	.375	.5	.625	.75
0.0	-3.14	-2.80	-3.10	-4.41	-7.81	-18.7	-
.05	-2.87	-2.53	-2.76	-3.80	-6.30	-12.2	-16.1
.1	-2.64	-2.32	-2.50	-3.37	-5.32	-9.12	-11.6
.3	-2.14	-1.88	-2.04	-2.69	-3.92	-5.85	-7.80
.5	-1.90	-1.71	-1.91	-2.53	-3.58	-5.09	-6.72
1.0	-1.46	-1.45	-1.85	-2.58	-3.51	-4.54	-5.46
1.5	-.927	-1.18	-1.89	-2.82	-3.72	-4.41	-4.80
2.0	-.222	-.830	-1.94	-3.11	-3.98	-4.44	-4.65
2.5	.670	-.386	-1.97	-3.38	-4.24	-4.59	-4.92
3.0	1.76	.163	-1.94	-3.57	-4.43	-4.81	-5.35
3.5	3.03	.822	-1.82	-3.66	-4.55	-5.01	-5.59
4.0	4.51	1.60	-1.59	-3.61	-4.59	-5.12	-5.38

$\dot{m}_s^*$

ω_0 (Cavity Length) / Ω (Reduced Frequency)	0	.125	.25	.375	.5	.625	.75
0.0	0.0	0.0	0.0	0.0	0.0	0.0	-
.05	-.103	-.0526	-.0946	-.362	-1.28	-5.05	-34.1
.1	.0606	.157	.141	-.143	-1.12	-4.45	-i9.3
.3	1.16	1.39	1.52	1.38	.669	-1.33	-6.94
.5	2.35	2.68	2.93	2.90	2.34	.738	-3.23
1.0	5.24	5.83	6.30	6.43	5.98	4.63	1.76
1.5	8.07	8.90	9.54	9.72	9.27	8.01	5.65
2.0	10.9	11.9	12.7	12.8	12.3	11.2	9.28
2.5	13.6	14.9	15.7	15.7	15.3	14.3	12.5
3.0	16.4	17.8	18.5	18.5	18.0	17.1	15.2
3.5	19.2	20.7	21.3	21.2	20.7	19.8	17.4
4.0	21.9	23.6	24.0	23.8	23.4	22.3	19.3

Table II (Continued)

Unsteady Fractional Cavity Change due to Unit Heave

$\dot{q}_c$

$\dot{q}_s$

ω_0 (Reduced Frequency)	x_0 (Cavity Length) 0	.125	.25	.375	.5	.625	.75
0.0	0.0	0.0	0.0	0.0	0.0	0.0	0.0
.05	.0131	.0147	.0171	.0210	.0289	.0514	.164
.1	.0345	.0384	.0440	.0523	.0669	.0997	.190
.3	.108	.120	.135	.151	.173	.204	.252
.5	.151	.174	.197	.220	.242	.267	.297
1.0	.201	.269	.324	.363	.386	.393	.387
1.5	.221	.359	.458	.509	.514	.484	.429
2.0	.231	.462	.607	.648	.606	.512	.404
2.5	.236	.584	.763	.761	.637	.472	.329
3.0	.240	.722	.914	.829	.605	.384	.253
3.5	.242	.874	1.05	.843	.522	.292	.233
4.0	.244	1.04	1.15	.805	.418	.243	.294
0.0	0.0	0.0	0.0	0.0	0.0	0.0	0.0
.05	-.0909	-.0902	-.0901	-.0914	-.0956	-.106	-.0719
.1	-.166	-.163	-.160	-.158	-.156	-.155	-.101
.3	-.399	-.380	-.359	-.334	-.305	-.265	-.186
.5	-.598	-.562	-.521	-.474	-.420	-.353	-.254
1.0	-1.08	-.996	-.897	-.784	-.661	-.528	-.379
1.5	-1.56	-1.43	-1.25	-1.05	-.841	-.644	-.455
2.0	-2.05	-1.84	-1.56	-1.25	-.967	-.726	-.526
2.5	-2.54	-2.25	-1.83	-1.41	-1.06	-.818	-.644
3.0	-3.04	-2.64	-2.06	-1.53	-1.17	-.961	-.834
3.5	-3.53	-3.01	-2.25	-1.64	-1.31	-1.18	-1.08
4.0	-4.03	-3.35	-2.40	-1.76	-1.51	-1.45	-1.32

Table II (Continued)
Unsteady Fractional Cavity Change due to Unit Pitch

$\dot{C}_c$

ℓ_0 (Cavity Length) $\rightarrow$ Ω (Reduced Frequency)	0	.125	.25	.375	.5	.625	.75
0.0	2.00	2.01	2.05	2.15	2.41	3.34	-
.05	1.82	1.81	1.81	1.83	1.92	2.14	1.46
.1	1.68	1.65	1.63	1.60	1.58	1.56	1.03
.3	1.38	1.32	1.24	1.16	1.05	.914	.642
.5	1.27	1.19	1.10	.997	.876	.731	.523
1.0	1.18	1.06	.936	.800	.659	.514	.358
1.5	1.15	.992	.819	.652	.300	.369	.254
2.0	1.14	.921	.699	.511	.371	.278	.216
2.5	1.14	.843	.573	.385	.286	.251	.242
3.0	1.13	.755	.448	.289	.255	.281	.302
3.5	1.13	.658	.332	.230	.272	.340	.351
4.0	1.13	.555	.231	.211	.323	.396	.355

$\dot{C}_s$

ℓ_0 (Cavity Length) $\rightarrow$ Ω (Reduced Frequency)	0	.125	.25	.375	.5	.625	.75
0.0	0.0	0.0	0.0	0.0	0.0	0.0	-
.05	.266	.295	.341	.417	.573	1.02	3.27
.1	.361	.396	.446	.525	.668	.994	1.91
.3	.459	.484	.515	.556	.615	.710	.867
.5	.502	.518	.534	.550	.570	.599	.640
1.0	.661	.659	.644	.614	.571	.518	.457
1.5	.866	.846	.790	.701	.589	.468	.350
2.0	1.09	1.05	.930	.762	.574	.394	.245
2.5	1.32	1.24	1.05	.788	.528	.314	.169
3.0	1.56	1.44	1.14	.783	.473	.260	.150
3.5	1.80	1.62	1.20	.760	.433	.255	.190
4.0	2.05	1.79	1.24	.735	.427	.302	.261

where

$$\omega_o = 1/(\alpha_o^2 + 1)$$

$$\omega_o = -2\alpha_o \omega_o^2 \alpha_c \tag{15}$$

$$\omega_s = -2\alpha_o \omega_o^2 \alpha_s .$$

In Table II we also tabulate

$$\alpha_c^* = \omega_c/\omega_o$$

$$\alpha_s^* = \omega_s/\omega_o . \tag{16}$$

Unit heave motion is defined by $B_1 = \ell M_o$, while unit pitch motion is defined by $M_1 = M_o$; see Eq. (7). Heave is positive upward, pitch is positive counterclockwise, and M_o is negative. The lift force (which is also the total force) is normal to the foil and positive when its y-component is positive. The moment is around the leading edge, positive counterclockwise (see Fig. 2).

Also included in Table II are the zero-frequency values of f_c^*, f_s^*, m_c^*, m_s^*, α_c^*, α_s^*, obtained by quasi-steady analysis, and zero-cavity-length values of the same quantities, obtained by asymptotic expansion of the analytic solution (see Steinberg [5] for details). The upper limit of α_o in Table II is $3/4$, the upper limit for physically meaningful solutions in the steady problem.

We now call attention to some overall features of the data. As the reduced frequency approaches zero, and for $\alpha < 3/4$, for heaving motion all quantities are $\pm\pi/2$ out of phase with the motion, while for pitching motion all quantities are in phase (modulo π) with the motion. For the unstable $3/4$ cavity length case the phase effect cannot be precisely inferred. Another feature of interest is the fact that the magnitude of the leading edge moment as a function of cavity length has a minimum in the neighborhood of $\alpha_o = 1/8$ for low reduced frequency.

In Figs. 3, 4, and 5 we present examples of polar plots obtained by plotting the sine component against the cosine component and indicating the constant α and α_o contours. Since in many cases, particularly for pitching motion, the low and high frequency behavior are quite different, separate plots for these cases, such as Figs. 4 and 5, are helpful in showing the functional behavior.

ACKNOWLEDGMENT

Figure 2

571
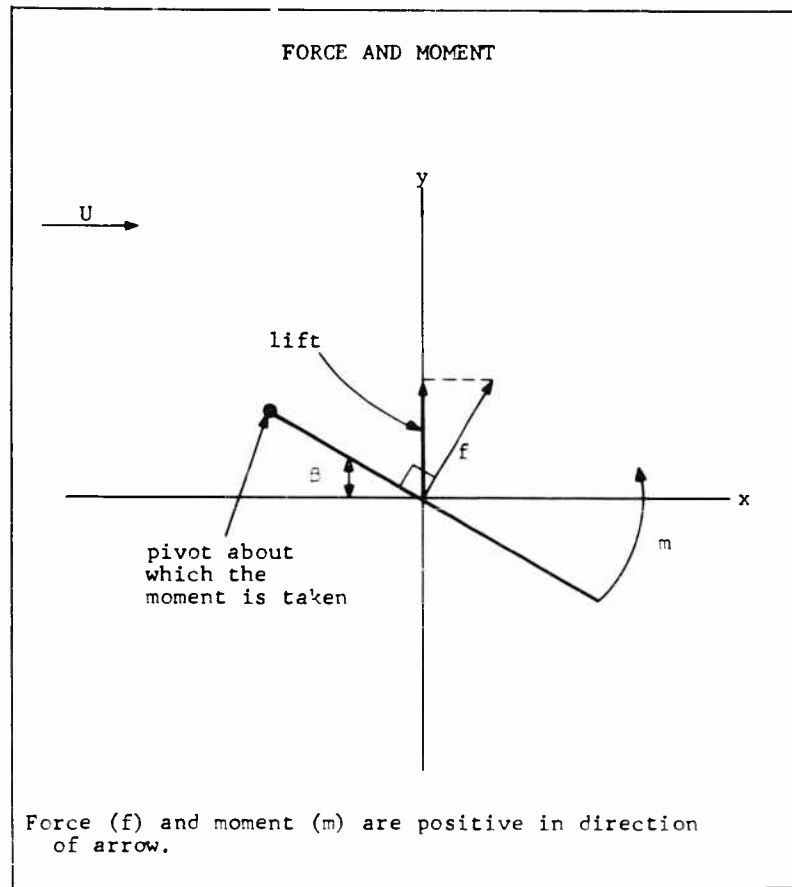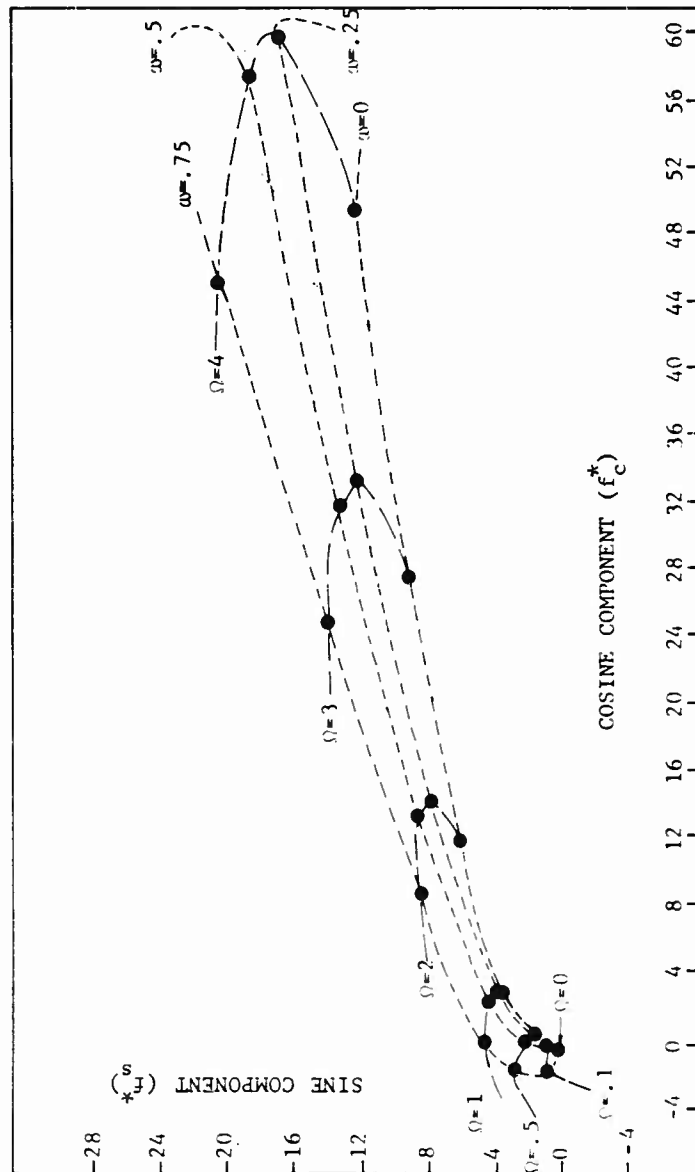
Fig. 3 - Force due to unit heave
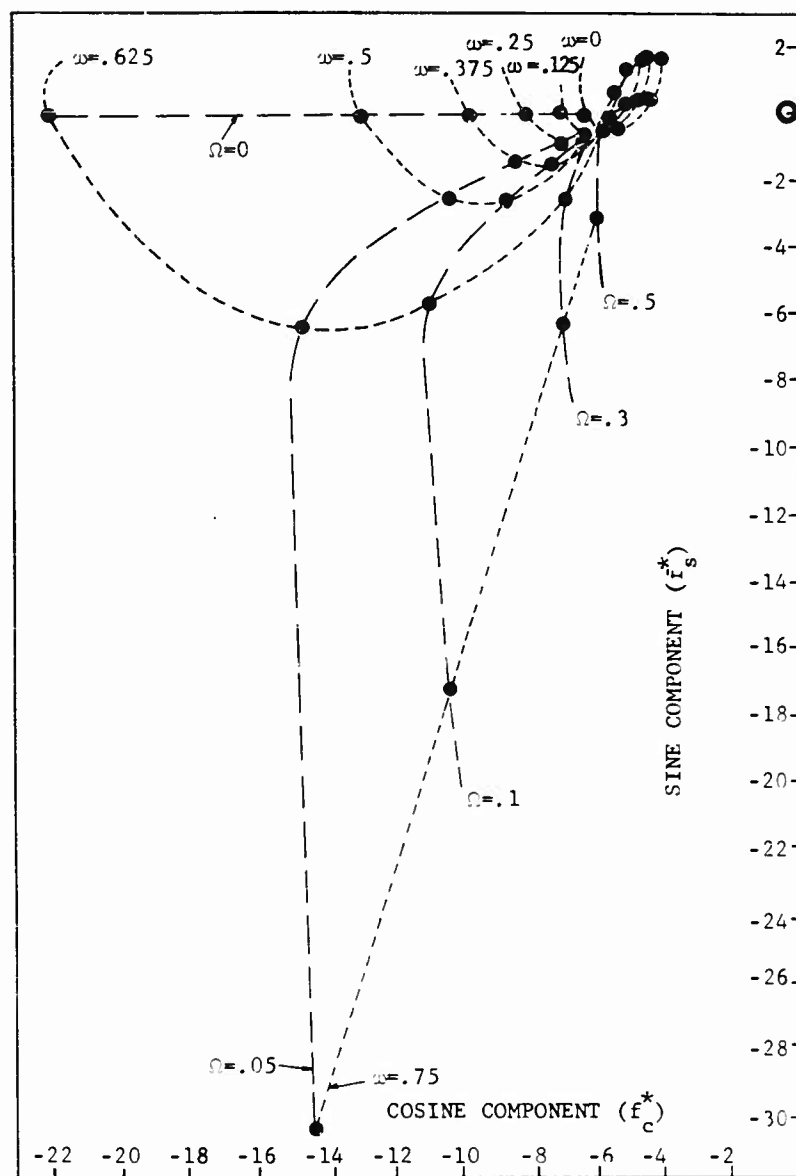
Fig. 4 - Force due to unit pitch (low frequencies)
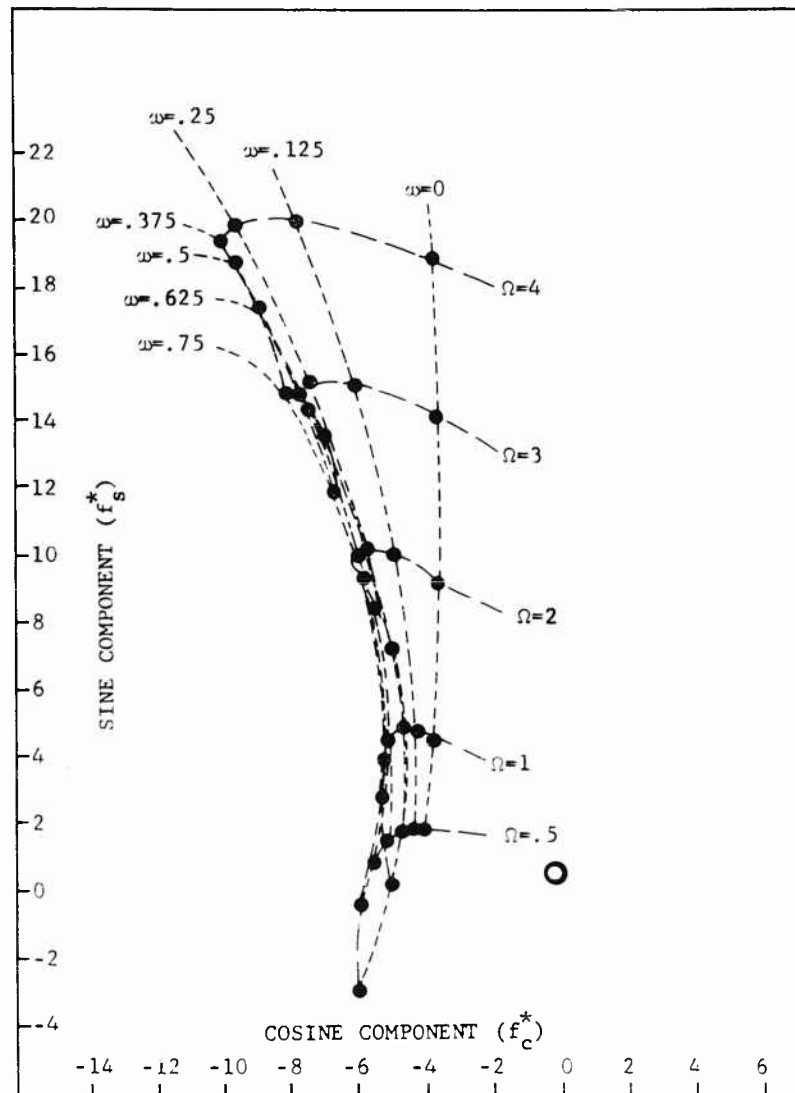
Fig. 5 - Force due to unit pitch (high frequencies)

REFERENCES

1. Timman, R., "A General Linearized Theory for Cavitating Hydrofoils in Nonsteady Flow," Second Symposium on Naval Hydrodynamics, Washington, D.C., 1958.

2. Guerst, J.A., "Some Investigations of a Linearized Theory for Unsteady Cavity Flows," Arch. Rational Mech. Anal., Vol. 5, No. 4, 1960.

3. Steinberg, H., "Linearized Theory of the Unsteady Motion of a Partially Cavitated Hydrofoil," TRG Report No. 153-SR-1, March 1962.

4. Wu, T.Y., "Unsteady Supercavitating Flows," Second Symposium on Naval Hydrodynamics, Washington, D.C., 1958.

5. Steinberg, H., "Unsteady Lift, Moment, and Cavity Length Calculations for an Oscillating Partially Cavitated Hydrofoil," TRG Report No. 153-FR, to be published, 1962.

*   *   *

BOUNDARY CONDITIONS FOR UNSTEADY SUPERCAVITATING FLOWS

CAPT Patrick Leehey, USN
Ship Silencing Branch
Bureau of Ships
Washington 25, D. C.

ABSTRACT

Two-dimensional unsteady flows about supercavitating foils and wedges are formulated as linearized compressible flow problems. Boundary conditions sufficient to determine unique closed cavity steady flows are specified and asymptotic values of cavity length, cavity area, and lift coefficient at small cavitation numbers for the foil and the inclined wedge are given. The condition of constant cavity area is shown to be invalid for non-separable unsteady closed cavity flows as a result of the examination of the near and far field characteristics of the compressible flow about a symmetrical body of oscillating thickness. The velocity field for an incompressible flow about a symmetrically oscillating wedge with a closed cavity of variable area is uniquely determined under the assumption that the wedge and the cavity termination point can be replaced by singularities of fixed location but of sinusoidally time variable strength.

1. INTRODUCTION

The purpose of this paper is to examine the various boundary conditions proposed for steady and unsteady two-dimensional supercavitating flows in order to determine those which are physically acceptable and yet are sufficient to determine unique mathematical solutions for the velocity fields.

Today the steady state theory of closed cavity flows is well in hand, at least for small cavitation numbers. Questions raised as to the validity of Tulin's linearization in 1953 [1] for thin bodies in cavity flow have been set to rest by the subsequent theoretical work of Wu [2,3], Guerst and Timman [4], and Guerst [5,6,7], and the experiments of Parkin[2] and Meyer[8]. It is now clear that for closed cavity flows, the linearized theory is the correct linearization of both the Riabouchinsky and the re-entrant jet models. Wu's square root singularity at

577

the cavity termination point is confirmed as the proper condition for closed cavity flows and hence valid at least for vapor cavities.

The unsteady flow theory is not so well off and meaningful experimental results for unsteady vapor cavity flows are practically non-existent. It is obviously desirable to solve a two-dimensional unsteady flow problem before attempting the corresponding three-dimensional problem. It also appears preferable to solve an incompressible flow problem before attempting the corresponding compressible flow problem, particularly since most practical applications occur at low subsonic speeds. But the unsteady incompressible closed cavity two-dimensional flow contains a paradox pointed out by Wu [9, p. 2]. If the cavity area does not remain constant, the pressure increases beyond bound in all directions away from the cavity and the kinetic energy of the flow becomes infinite. On the other hand, except for a limited class of flows which we shall call separable, the cavity area and cavity length may be seen from inspection of the steady state solutions to vary with change in attitude or dimension of the cavitating body.

In his discussion of a paper by Timman [10, p. 580], Tulin pointed out that the above difficulty could probably be resolved by accounting for the effect of compressibility in the flow field. We take this approach in the present paper and determine from compressibility considerations sufficient boundary conditions to permit a return to the more tractable assumption of incompressibility.

2. FORMULATION OF THE BOUNDARY VALUE PROBLEM

We direct our attention to the two problems represented schematically in Fig. 1: those of the foil and of the wedge. The flow is assumed to be two-dimensional, inviscid and barotropic. The cavity pressure p_c and the pressure at infinity p_∞ are assumed known and constant. The velocity of the body U and the chord c are constant, but the half-wedge angle γ and the angle of attack α may be time dependent. (In the foil problem γ is assumed equal to zero.) In consequence, S, the total body plus cavity area, and ℓ, the cavity length, may be time dependent.
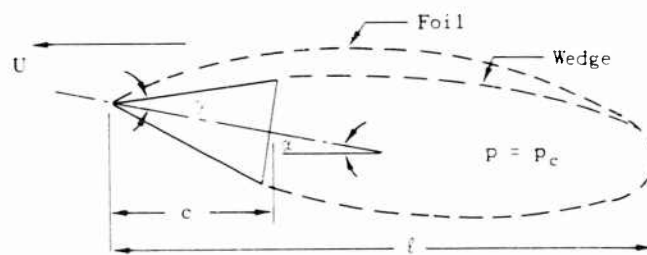
Figure 1

We define the cavitation number as

$$\sigma = (p_\infty - p_c) \; \frac{1}{2} \rho_\infty U^2 \tag{1}$$

where ρ_∞ is the density of the fluid at infinity. Neglecting gravity, we may write the Eulerian equations of motion and the continuity equation with respect to an inertial frame with the fluid at rest at infinity as

$$\frac{D\vec{u}}{Dt} = -\frac{1}{\rho} \nabla p, \tag{2}$$

and

$$\frac{D\rho}{Dt} = -\rho \nabla \cdot \vec{u}, \tag{3}$$

respectively, where $\vec{u} = (u,v)$ denotes the vector velocity field.

We assume the flow is irrotational away from the body plus cavity plus wake. This implies the existence of a velocity potential ϕ such that

$$\vec{u} = \nabla \phi. \tag{4}$$

Assuming angles α and γ, and their time derivatives sufficiently small, we may linearize Eqs. (2) and (3) in accordance with the small perturbation theory for compressible flow (see, for example, Sears [11, p. 63ff]). Upon integration we obtain the Bernoulli equation

$$\frac{\partial \phi}{\partial t} = (p_\infty - p)\big/ \rho_\infty = \psi \tag{5}$$

where ψ is the acceleration potential. We have assumed $\psi_t = 0$ at infinity. This may be done without loss of generality in any problem where the ultimate objective is the determination of the resultant force and moment on the body. The theory also requires that the wave equation:

$$\left\{ \nabla^2 - \frac{1}{a_\infty^2} \frac{\partial^2}{\partial t^2} \right\} (\phi, \; \psi, \; \rho', \; \vec{u}) = 0 \tag{6}$$

be satisfied in the flow field by all quantities indicated. Here a_∞ is the mean velocity of sound in the fluid phase, $\rho' = \rho - \rho_\infty$, and the equation is understood to apply to each component of the velocity $\vec{u}$.

We now change our reference to axes fixed in the moving body and render all quantities dimensionless with respect to the parameters c and U. The Bernoulli equation becomes

$$\phi_x + \phi_t = \psi. \tag{5a}$$

and the wave equation becomes

579

$$\left\{ \beta^2 \frac{\partial^2}{\partial x^2} + \frac{\partial^2}{\partial y^2} - 2M^2 \frac{\partial^2}{\partial x \partial t} - M^2 \frac{\partial^2}{\partial t^2} \right\} (\phi, \; \varphi, \rho', \; \vec{u}) = 0 \qquad (6a)$$

where $\beta^2 = 1 - M^2$ and $M = U/a_\infty$ is the Mach number of the flow. Figure 2 represents schematically the body plus cavity in this system for the upper half plane $y \geq 0$. We shall consider only subsonic flow, i.e. $\beta > 0$. Although the body plus cavity is denoted by the single relation $y = h(x,t)$ for $0 < x < \ell$, this relation is known only for the wetted portions of the body. We shall consider only those cases where the cavity detachment point is known and fixed, e.g. at $x = 0$ or $x = 1$. Partially cavitated flows, those for which $\ell < 1$, will not be considered explicitly in this paper, however our conclusions regarding boundary conditions apply to these flows as well.
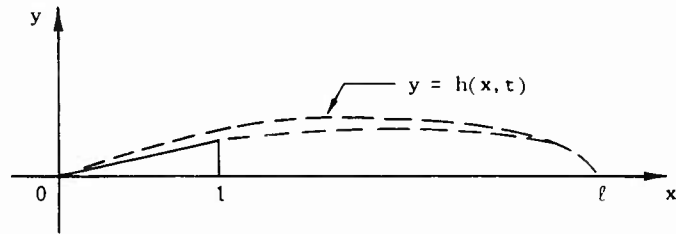
Figure 2

The following boundary conditions are fundamental to both the foil and wedge problems for steady or for unsteady flow:

(a) The cavity pressure is constant; that is, the equation

$$\phi_x + \phi_t = \varphi = \frac{\sigma}{2} \qquad (7)$$

must be satisfied from above and from below on the part of the x-axis representing the cavity walls.

(b) The kinematic condition

$$v = \phi_y = h_x + h_t \qquad (8)$$

must be satisfied from above and from below on the part of the x-axis representing the wetted body.

(c) The cavity closure condition

$$h^\pm (\ell, t) = 0 \qquad (9)$$

must be satisfied.

(d) The quantities ϕ, φ, ρ', $\vec{u}$ must be bounded at the trailing edge of the foil or wedge (Kutta condition).

(e) The circulation

$$\Gamma = \oint \vec{u} \cdot d\vec{x} \tag{10}$$

about the body plus cavity plus wake must remain constant (Kelvin circulation condition).

(f) The quantities ϕ, φ, ρ', $\vec{u}$ must vanish at infinity.

It is implicit in the linearization leading to Eqs. (5) and (7) that the assumption $\sigma \ll 1$ has been made. We remark that for unsteady flow this assumption is consistent with the linearization of the problem to the first order in the velocity perturbation.

3. SUPERCAVITATING WEDGE AND FOIL IN STEADY FLOW

Assuming incompressible flow, Tulin [1] and Wu [12] solved the problem for the flow past a symmetrical wedge at zero inclination but for finite cavitation number. Tulin [1] and Guerst [6] solved the problem for a lifting foil at finite cavitation number. These problems, together with that for an inclined wedge, are simply treated as Hilbert problems for functions of a complex variable by the methods of Muskhelishvili [13]. We sketch the development of this incompressible flow theory.

If we let the Mach number $M \to 0$, Eq. (6a) reduces to

$$\nabla^2(\phi, \varphi, u, v) = 0 \tag{11}$$

We may deal with either the complex acceleration potential

$$F(z, t) = \varphi + i\psi \tag{12}$$

or with the complex velocity

$$w(z, t) = u - iv = \phi_x + i\phi_y \tag{13}$$

as functions analytic in the exterior flow region. They are related by the expression

$$\frac{\partial F}{\partial z} = \frac{\partial w}{\partial t} + \frac{\partial w}{\partial z} \tag{14}$$

as may be verified by considering Eqs. (5a) and (11).

581

For the contour C in Fig. 3, the following relations hold

$$\oint_C w(z,t)dz = \Gamma + i\frac{dS}{dt},\tag{15}$$

and

$$S = -\text{Im}\oint_C zw(z,t)\,dz,\tag{16}$$

where it is understood that C shall envelop any downstream free wake vortex distribution when unsteady lift is generated.
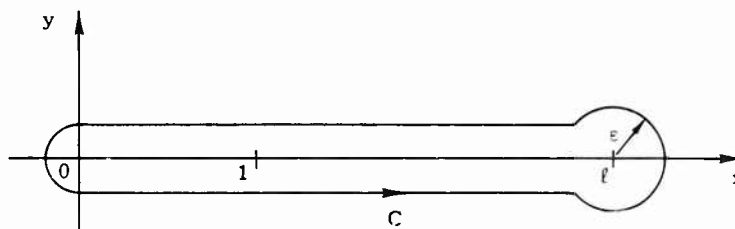
Figure 3

We have further that the lift coefficient C_L may be determined from

$$C_L = -2(1 + \sigma)\,\text{Re}\int F(z,t)\,dz\tag{17}$$

provided the circular path of radius ε about the point $z = \ell$ is subtracted from C, and the limiting value as $\varepsilon \to 0$ is taken in this integration. In Eq. (17) the contour C does not need to envelop the wake because $F(z,t)$ is analytic in z on the wake portion of the x-axis.

For steady flow, assuming $\sigma \ll 1$, Eq. (14) reduces to

$$F_o(z) = w_o(z)\tag{18}$$

We may express the closure condition (9) as

$$\oint_C w_o(z)\,dz = \Gamma_o,\tag{19}$$

an obvious consequence of (15). It is worth noting, however, that (19) may be derived directly from (9), for

582

$$\oint_C h_x dx = h^+(\ell) - h^-(\ell) = 0 = \oint_C v_o dx = -\text{Im} \oint_C w_o dz .$$

The complex velocity for the steady flow about an inclined wedge of half-wedge angle γ_o, and attack angle α_o for finite cavitation number can be considered as the sum of the complex velocities of two flows: one about a symmetrical wedge with finite cavity and half-wedge angle γ_o, the other about a non-cavitating flat plate of attack angle α_o. The Hilbert problem solutions, under boundary conditions set forth in Section 2 above, are

$$w_{\gamma_o}(z) = -\frac{\gamma_o}{\pi}\sqrt{\frac{z-1}{z-\ell_o}} \int_0^1 \sqrt{\frac{\ell_o-\xi}{1-\xi}} \frac{d\xi}{\xi-z} - \frac{\sigma}{2}\left\{\sqrt{\frac{z-1}{z-\ell_o}} - 1\right\} \qquad (20)$$

and

$$w_{\gamma_o}(z) = \frac{\alpha_o}{\pi i}\sqrt{\frac{z-1}{z}} \int_0^1 \sqrt{\frac{\xi}{1-\xi}} \frac{d\xi}{\xi-z} \qquad (21)$$

where

$$\sqrt{\frac{z-1}{z-\ell_o}}$$

and

$$\sqrt{\frac{z-1}{z}} = \to +1$$

as $|z| \to \infty$.

When $w_o = w_{\gamma_o} + w_{\alpha_o}$ is substituted from Eqs. (20) and (21) into Eq. (19), one obtains $\ell_o = \ell_o(\gamma_o, \sigma)$ and $\Gamma_o = \Gamma_o(\alpha_o)$. Similarly the cavity area $S_o = S_o(\alpha_o, \ell_o)$ is obtained from Eq. (16) and the lift coefficient $C_{L_o} = C_{L_o}(\alpha_o, \sigma)$ is obtained from Eq. (17). The integrations may be readily performed using theorems on the inversion of contour and arc integrations [14, pp. 438-440]. For $\sigma \ll 1$, or equivalently $\ell_o \gg 1$, one obtains for the inclined wedge the asymptotic results:

$$\left.\begin{aligned} \sigma &= \frac{8}{\pi}\gamma_o \ell_o^{-\frac{1}{2}} \\ S_o &= \gamma_o \ell_o^{\frac{3}{2}} \\ C_{L_o} &= 2\pi(1+\sigma)\alpha_o \end{aligned}\right\} \qquad (22)$$

The above problem is separable in the sense that for given cavitation number σ, the cavity length and cavity area depend only upon the half-wedge angle γ_o while the circulation and lift depend only upon the angle of attack α_o.

One may demonstrate [13, pp. 73-75] from Eqs. (20) and (21) that the complex velocity w_o is logarithmically singular near $z = 0$, bounded at $z = 1$, and

583

singular of the order $1/2$ near $z = \ell_o$. The latter singularity was postulated by Wu [19, p. 18]. He argued that the map from the z plane to the w_o plane was non-conformal at $z = \ell_o$ and

$$w_o(z) \sim K_o(z - \ell_o)^{-\frac{1}{2}}, \ K_o < 0, \tag{23}$$

near $z = \ell_o$. This followed from consideration of velocity symmetry and the fact that extrema of harmonic functions must occur on boundaries. Wu's condition is a consequence of, rather than a condition for, our solution.

Under the conditions $w_{\gamma_o}(z) \to 0$, $w_{a_o}(z) \to 0$ as $|z| \to \infty$ solutions (20) and (21) are readily demonstrated to be unique. For suppose we have another solution $w_{\gamma_o}^*(z)$ to the former problem, with singularities of less than integer order at $z = 0$ and $z = \ell_o$ and bounded at $z = 1$. Subtract the constant $\sigma/2$ from each solution. Let us consider the function

$$\Omega(z) = \left[w_{\gamma_o}(z) - w_{\gamma_o}^*(z) \right] \bigg/ \sqrt{\frac{z-1}{z-\ell_o}} \ .$$

It follows [13, p. 37] that $\Omega(z)$ is analytic throughout the plane except for isolated singularities of less than integer order at $z = 0$, $z = 1$ and $z = \ell_o$. Since $\Omega(z) \to 0$ as $|z| \to \infty$, we have by Liouville's theorem that $\Omega(z) \equiv 0$. It is worthy of note that $w_{\gamma_o}^*$ could be singular to the order $3/2 - \varepsilon$ for $\varepsilon > 0$ at $z = \ell_o$ without affecting the uniqueness conclusion. The same circumstance evolves in the unsteady cavity flows where compressibility must be considered (see Section 6). A similar argument shows w_{a_o} to be unique; the only singularity in this case appears at $z = 0$.

Guerst [7, pp. 21-30] has shown that the above solution of the linearized wedge problem is a proper linearization of both the Riabouchinsky and the re-entrant jet non-linear flows in the sense that both reduce to the $1/2$ order singularity, Eq. (23), at the cavity end upon linearization. Other models have been studied: namely, the "singularity free" ($K_o = 0$) model by Song [15], and the linearization of the transition flow, or Roshko, model by Cohen, Sutherland and Tu [16]. Song's model yields the asymptotic result for $\sigma \ll 1$:

$$\sigma = \frac{4}{\pi} \gamma_o \ell_o^{-\frac{1}{2}}$$

That of Cohen, Sutherland and Tu yields twice this result provided one assumes that the transition point in the cavity flow is at half the cavity length. Cavity closure cannot be obtained with Song's model.

A general study of cavity termination models for linearized supercavitating flows has been made by Fabula [17] for a range of wake thicknesses. His results cannot be compared directly with those above for his analysis specifically excludes the wedge problem.

Guerst's theory for the partially cavitated hydrofoil uses the $1/2$ order singularity at the cavity termination [5]. His results are well confirmed by the experiments of Meyer both with respect to the cavitation number - cavity length

relationship and by the appearance of a stagnation point at the end of the cavity [8], a stagnation point being a point of singularity for perturbation velocity in linearized theory. Meyer worked with vapor cavities. Experimental results for super-cavitating flows have not yet been reported for cavitation numbers low enough to verify the relationship expressed by Eq. (23).

In this paper we shall restrict our attention to closed cavity flows wherein the wake, if it exists, is assumed to have zero thickness; that is, it can be modeled in the linearized theory by a free vortex sheet extending downstream along the x-axis. Across this sheet only discontinuities in the u component of the perturbation velocity are permitted.

The supercavitating hydrofoil with finite closed cavity in steady incompressible flow can also be treated in linearized theory as Hilbert problem for the complex velocity field. However, a mapping of the form

$$\zeta = i\sqrt{\frac{z(\ell_o - 1)}{z - \ell_o}}, \quad \left(\rightarrow i\sqrt{\ell_o - 1} \quad \text{as} \quad |z| \rightarrow \infty \right),$$ (24)

is first required. This mapping transforms the cavity termination point $z = \ell_o$ to the point $\zeta = \infty$. Wu's termination condition, Eq. (23), must be invoked as a boundary condition upon the problem in order that uniqueness of the solution can be demonstrated by the above method.

The following asymptotic results for $\sigma \ll 1$ are obtained for the super-cavitating flat plate hydrofoil at angle of attack α_o:

$$\left. \begin{array}{l} \sigma = 2\alpha_o \ell_o^{-\frac{1}{2}}, \\[2mm] S_o = \frac{\pi}{2} \alpha_o \ell_o^{\frac{3}{2}}, \\[2mm] C_{L_o} = \frac{\pi}{2} (1 + \sigma) \alpha_o. \end{array} \right\}$$ (25)

4. SUPERCAVITATING WEDGE AND FOIL IN UNSTEADY FLOW - ASSUMPTION OF INCOMPRESSIBILITY

The asymptotic results for the wedge, Eqs. (22), and for the foil, Eqs. (25), give indications as to what must be expected when unsteady flow conditions are introduced. Consider the wedge undergoing oscillations as follows:

$$\gamma = \gamma_o,$$

$$\alpha = \alpha_o + \alpha_1 e^{-ikt},$$

where $k = \omega c/U$ is the reduced frequency. Here the steady problem $\{\gamma_o, \alpha_o\}$ and the unsteady problem $\{\alpha_1 e^{-ikt}\}$ are separable. For as indicated by Eqs. (22), $\ell = \ell(\gamma_o, \sigma)$ and $S = S(\gamma_o, \sigma)$ only. Wu [9] solved the problem of the wedge

585

undergoing heaving oscillations under the assumption of incompressible flow. His case is also separable in the same sense.

On the other hand, quasi-steady considerations implicit in Eqs. (25) tell us that when a supercavitating hydrofoil undergoes oscillations in angle of attack α both cavity length and cavity area must vary in a non-linear fashion. The non-linear variation in cavity length is a severe mathematical complexity. However, within linearized theory, the variation in cavity length for fixed cavitation number $\sigma \ll 1$ is evidently of second order with respect to variation in angle of attack. Guerst [7, p. 151] introduced a second linearization in the unsteady flow problem based upon this consideration. The variation in cavity area leads to a physical difficulty. For in incompressible flow,

$$\frac{dS}{dt} \neq 0$$

implies that $p_\infty = \infty$ and that the kinetic energy of the fluid is also infinite. If $\sigma = 0$ neither the length nor the area difficulties arise; Woods [18,19] and Parkin [20] give incompressible flow solutions for this case.

A number of attempts have been made to solve non-separable closed cavity problems within the framework of incompressible flow theory: Guerst [7] dealt with the oscillating supercavitating foil, Steinberg [21] dealt with the oscillating partially cavitated foil, and Cumberbatch [22] dealt with the supercavitating wedge in surging acceleration. In each case an assumption equivalent to

$$\frac{dS}{dt} = 0 \tag{26}$$

was introduced as a boundary condition. We shall demonstrate in the next section that this assumption is unwarranted because the compressibility of the fluid has not been accounted for.
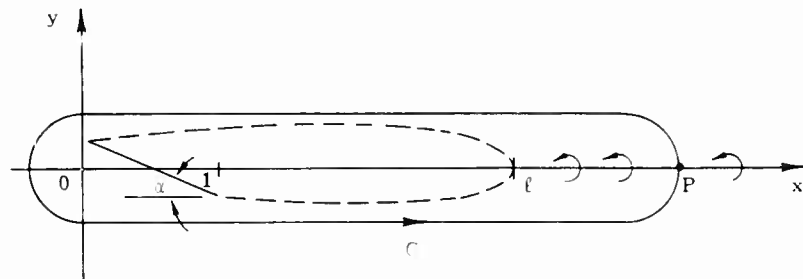
Figure 4

A remark is required to show that Guerst's condition [7, p. 48] is, in fact, equivalent to Eq. (26), since his treatment of unsteady flow problems using the complex acceleration potential $F(z,t)$ is not readily interpretable in terms of the complex velocity field $w(z, t)$. With reference to Fig. 4, Guerst's condition may be stated that the jump in the vertical component of the perturbation velocity across any point P in the wake shall be zero; that is,

$$[v]_P = v(x_P, o+, t) - v(x_P, o-, t) = 0 .$$

Taking the integral of Eq. (14) about the contour C as shown, we get from Eq. (15) that

$$\frac{d}{dt} \left(\Gamma + i \frac{dS}{dt} \right) + [w]_P = [F]_P = 0$$

since $F(z, t)$ is analytic in z in the wake. Hence

and

$$\left.\begin{array}{lll}
[u]_P = 0 & \longleftarrow - & \frac{d\Gamma}{dt} = 0 , \\
\\
\\
[v]_P = 0 & \longleftrightarrow & \frac{d^2S}{dt^2} = 0 .
\end{array}\right\} \tag{27}$$

Thus for sinusoidal oscillations, the second result of (27), together with the second linearization, imply Eq. (26).

5. OSCILLATING THICKNESS PROBLEM IN COMPRESSIBLE FLOW

In order to investigate the validity of the assumption $dS/dt = 0$ we turn our attention away from unsteady cavity flows to a more tractable problem - yet one which preserves the characteristic of variable area S. Referring to Fig. 5, we consider the problem of determining the linearized compressible flow about a thin two-dimensional body moving at forward velocity U while undergoing a symmetrical oscillation of infinite duration. For dimensionless coordinates fixed in the moving body, the equation of the body profile is given as

$$y = h(x, t) = h_o(x) + h_1(x)e^{-ikt}, \quad 0 \le x \le 1 , \tag{28}$$

where $k = \omega c/U$ is the reduced frequency. Equation (6a) must be satisfied in the flow field for all quantities $\phi, \sigma, \sigma', \vec{u}$. These quantities must vanish at infinity. The steady flow and the unsteady flow problems are separable.

y = h_o + h_1 e^{-ikt}
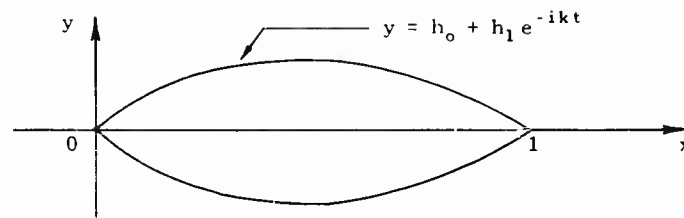
Figure 5

Steady Flow Problem

Using the Prandtl-Glauert transformation, the steady flow problem is readily disposed of. We consider the complex velocity $w_o(z) = u_o - iv_o$ as a function of the complex variable $z = x + i\beta y$ analytic exterior to the portion $0 \leq x \leq 1$ of the x-axis and vanishing at infinity. By symmetry, $w_o(z) = w_o(\bar{z})$ hence on the x-axis it satisfies the Hilbert problem conditions:

$$
\begin{aligned}
w_o^+ - w_o^- &= 0, \quad x < 0, \\
&= -i\frac{2}{\beta} h_{ox}, \quad 0 < x < 1, \\
&= 0, \quad 1 < x .
\end{aligned}
\tag{29}
$$

The solution

$$
w_o(z) = -\frac{1}{\pi\beta} \int_o^1 \frac{h_{ox}(\xi)}{\xi - z} d\xi
\tag{30}
$$

is immediate, as may be verified by the Plemelj formulas [13, p. 42].

Writing the velocity potential as

$$
\varphi(x,y,t) = \varphi_o(x,y) + \varphi_1(x,y) e^{-ikt}
\tag{31}
$$

we see that the corresponding velocity potential for the steady flow problem is

$$
\varphi_o(x,y) = \frac{1}{\pi\beta} \int_o^1 h_{ox} \ell n r d\xi
\tag{32}
$$

where $r^2 = (x - \xi)^2 + \beta^2 y^2$. Equation (32) represents a source distribution on $0 < x < 1, y = 0$.

Unsteady Flow Problem

From Eqs. (6a), (28) and (31) we find that the unsteady velocity potential ϕ_1, must satisfy the problem:

$$\left.\begin{array}{c} \beta^2\phi_{1xx} + \phi_{1yy} + 2ikM^2\phi_{1x} + k^2M^2\phi_1 = 0 , \\[2mm] \phi_{1y} = \pm(h_{1x} - ikh_1), \quad 0 < x < 1, \quad y = \pm C , \\[2mm] \phi_{1x}, \ \varphi_{1y}, \ \phi_1 \rightarrow 0 \text{ at } \infty . \end{array}\right\} \tag{33}$$

If we set $\phi_1 = \phi_2 e^{-iKx}$ where $K = kM^2/\beta^2$ the differential equation of (33) reduces to

$$\beta^2\phi_{2xx} + \phi_{2yy} + \frac{k^2M^2}{\beta^2}\phi_2 = 0 . \tag{34}$$

We take the Fourier transform

$$\Phi(\alpha,y) = \frac{1}{\sqrt{2\pi}}\int_{-\infty}^{\infty} \phi_2(x,y)\, e^{i\alpha x}\, dx$$

of Eq. (34). Whence, noting the conditions at infinity in (33), Eq. (34) becomes

$$\Phi_{yy} - \gamma^2\Phi = 0 \tag{35}$$

where we define

$$\gamma = \beta(\alpha^2 - \alpha_o^2)^{\frac{1}{2}}, \quad (\gamma \rightarrow \beta\,|\sigma| \text{ as } |\sigma| \rightarrow \infty) , \tag{36}$$

with cuts in the $\alpha = \sigma + i\tau$ plane taken as shown in Fig. 6. Here $\alpha_o = \sigma_o + i\tau_o$ where $\sigma_o = kM/\beta^2$ and the Rayleigh damping factor $\tau_o > 0$ is introduced to exclude waves radiating from infinity.

The complete solution of Eq. (35) is

$$\Phi(\alpha,y) = A(\alpha)\, e^{-\gamma y} + B(\alpha)\, e^{\gamma y}. \tag{37}$$

By symmetry, we may restrict $y \geq 0$. It is therefore sufficient for the inverse transform

$$\phi_2(x,y) = \frac{1}{\sqrt{2\pi}}\int_{-\infty+i\tau}^{\infty+i\tau} \Phi(\alpha,y)\, e^{-i\alpha y}\, d\alpha, \quad -\tau_o < \tau < \tau_o , \tag{38}$$

to exist uniquely that we take $B(\alpha) = 0$. We remark that Φ is analytic in α in the strip $-\tau_o < \tau < \tau_o$. For a detailed discussion of this argument, see Noble [23, pp. 29-30].
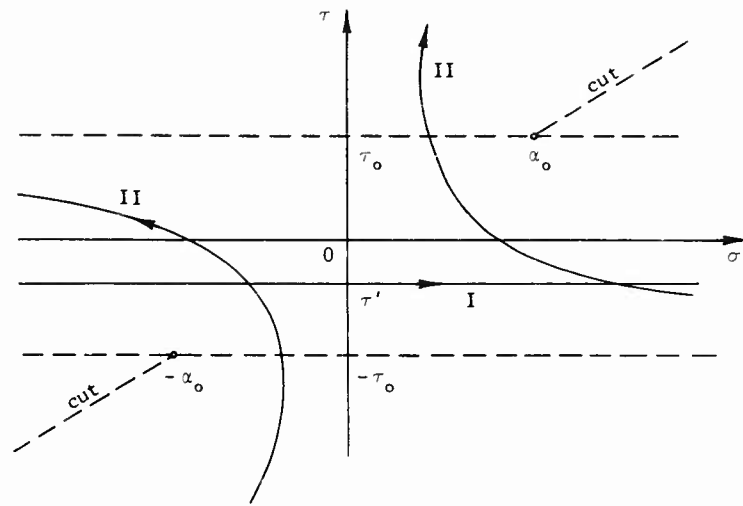
Figure 6

Noting that ϕ_{2y} is odd in y, we define

$$g(x) = \phi_{2y}(x,0+) = 0, \quad x < 0,$$
$$= e^{iKx}(h_{1x} - ikh_1), \quad 0 < x < 1,$$
$$= 0, \quad 1 < x. \tag{39}$$

The Fourier transform of $g(x)$ is

$$G(\alpha) = \frac{1}{\sqrt{2\pi}} \int_0^1 g(x)\, e^{i\alpha x}\, dx. \tag{40}$$

From Eq. (37), letting $y \to 0-$, we obtain $G(\alpha) = -\,\gamma A(\alpha)$. Taking the inverse transform (38), we have

$$\phi_2(x,y) = \frac{1}{\sqrt{2\pi}} \int_{-\infty+i\tau'}^{\infty+i\tau'} \left[-\frac{1}{\gamma} G(\alpha) \right] e^{-i\alpha x - \gamma y} d\alpha \tag{41}$$

where $-\tau_0 < \tau' < \tau_0$.

We introduce Eq. (40) into Eq. (41), invert the order of integration, and deform the path of integration in the α plane from path I to the hyperbolic paths II with focal points $\pm \alpha_0$ as in Fig. 6. Using the integral transformation given in Noble [23, p. 32], we obtain

590

$$\phi_2(x,y) \; = \; \frac{i}{2\beta} \int_0^1 h_1(\xi) \, e^{i\xi K} \left\{ \frac{ik}{\beta^2} \, H_o^{(1)}(\alpha_o r) \, + \, \alpha_o \, \cos \, \theta \, H_1^{(1)}(\alpha_o r) \right\} d\xi \qquad (42)$$

where $r^2 = (x - \xi)^2 + \beta^2 y^2$, $\cos \theta = x - \xi/r$ and $H_o^{(1)}$, $H_1^{(1)}$ are Hankel functions of the first kind of orders zero and one, respectively.

Letting $\tau_o \to 0$, we may readily verify that Eq. (42) satisfies the problem (33) and the Sommerfeld radiation condition:

$$\lim_{r \to \infty} \; r^{\frac{1}{2}}(\phi_{2r} - i\alpha_o \phi_2) \; = \; 0 \, .$$

For, using the Prandtl-Glauert transformation, Eq. (34) becomes

$$\nabla^2 \phi_2 + \alpha_o^2 \phi_2 \; = \; 0 \, .$$

Considering the polar form of the Laplacian operator, we see that $H_o^{(1)}(\alpha_o r)$ is a solution. Considering the rectangular form of the Laplacian operator, we see immediately that

$$\frac{\partial}{\partial X} \, H_o^{(1)}(\alpha_o r) \; = \; -\alpha_o \, \cos \, \theta \, H_1^{(1)}(\alpha_o r)$$

is also a solution. It follows that the integral (42) likewise satisfies Eq. (34). The radiation condition is satisfied by both $H_o^{(1)}(\alpha_o r)$ and $H_1^{(1)}(\alpha_o r)$ and hence by Eq. (42) as $\cos \theta$ is independent of r for large $\alpha_o r$. Integrating Eq. (42) by parts, taking the derivative with respect to y and evaluating the singular behavior of the integrand as $y \to 0\pm$ at $x = \xi$ leads us to the satisfaction of the boundary condition (33) on the body surface.

Asymptotic Considerations

As the Mach number $M \to 0$, we see that $K \to 0$, $\alpha_o \to \tilde{K} = \omega c/a_\infty$ and

$$\phi_1 \to \phi_2 \to \frac{i}{2} \int_0^1 h_1(\xi) \left\{ ikH_o^{(1)}(\tilde{K}r) + \tilde{K} \, \cos \, \theta H_1^{(1)}(\tilde{K}r) \right\} d\xi \qquad (43)$$

where $r^2 \to (x - \xi)^2 + y^2$. The differential equation of (33) becomes the ordinary wave equation of acoustics:

$$\nabla^2 \phi_1 + \tilde{K}^2 \phi_1 \; = \; 0 \, . \qquad (44)$$

Using asymptotic results for the Hankel functions $H_o^{(1)}$ and $H_1^{(1)}$, [24, pp. 128, 132 and 134], we obtain for the

591

(a) Far field, $\tilde{K}r \gg 1$,

$$\phi_1 \sim \frac{e^{i(5\pi/4)}}{\sqrt{2\pi \tilde{K}r}} \; \frac{S_1}{2} \; e^{i\tilde{K}(r - at/U)} \; (k - \tilde{K} \cos \theta) \tag{45}$$

where

$$S_1 = 2 \int_0^1 h_1(\xi) \, d\xi$$

is the amplitude of variable component of the body area. Equation (45) represents cylindrical waves radiating from the body and decaying $\mathcal{O}(r^{-1/2})$ in amplitude as $r \to \infty$. It is evident that the variable component of pressure decays to zero by cylindrical spreading loss as $r \to \infty$. For the

(b) Near field, $\tilde{K}r \ll 1$,

$$\phi_1 \sim -\frac{1}{\pi} \int_0^1 h_1(\xi) \left\{ ik\ell nr - \frac{\cos \theta}{r} \right\} d\xi . \tag{46}$$

The oscillating thickness problem in incompressible flow for the complex velocity $w(z,t) = w_o(z) + w_1(z)e^{-ikt}$ can be solved in precisely the same fashion as that used for the steady component $w_o(z)$ alone. The solution for $w_1(z)$ has a velocity potential ϕ_1 identical with that of Eq. (46). It is important to note that $S_1 \neq 0$ in this solution.

We see that for $M \to 0$ and $r \ll 1/\tilde{K}$ (a wavelength) the incompressible flow solution is the limiting case of the compressible flow solution. No requirement of constant body area is needed, for the pressure is bounded at infinity as a result of cylindrical spreading loss. In a manner of speaking, the flow is locally hydrodynamic within an acoustic wavelength of the body provided the speed of advance U is sufficiently small.

This result has a general implication: since the boundary conditions on the fluid flow at large distances from a source-like disturbance must be independent of the precise nature of the disturbance, it follows that the condition

$$\frac{dS}{dt} = 0$$

cannot be imposed in any unsteady incompressible flow problem as a physical boundary condition. In particular, this includes unsteady closed cavity flows.

6. SUPERCAVITATING WEDGE IN SYMMETRICAL OSCILLATION

We consider the unsteady cavity flow problem for a supercavitating wedge in symmetrical oscillation where

$$\left.\begin{array}{l} \gamma(t) = \gamma_o + \gamma_1 e^{-jkt}, \\ \\ \alpha(t) = 0. \end{array}\right\} \tag{47}$$

The notation $j = \sqrt{-1}$ is introduced in this section in order to reserve the symbol $i = \sqrt{-1}$ for use with the complex number $z = x + iy$. We note that $j^2 = -1$, $i^2 = -1$, but $ji \neq -1$.

The linearization $u, v \ll U$ and consequently $\sigma \ll 1$ is assumed. This problem is non-separable. We therefore make a second linearization in the form

$$\ell = \ell_o(\gamma_o, \sigma). \tag{48}$$

The cavity termination point is thus fixed by the steady state solution although the nature of the singularity at this point remains to be determined. We may consider the flow to be incompressible provided we keep in mind the results of Section 5 that $S_1 \neq 0$ and that our solution will represent only the locally hydrodynamic flow within an acoustic wavelength of the wedge.

The second linearization implies that the complex perturbation velocity can be written as

$$w(z, t) = w_o(z) + w_1(z)e^{-jkt} \tag{49}$$

where $|w_1| \ll |w_o|$. Thus only the sinusoidal component of the unsteady velocity with time factor e^{-jkt} is determined. The problem has now been made separable.

The steady state solution is given by Eq. (20) and the explicit statement of Eq. (48) is contained in Eq. (22). We shall, however, make a further simplification of the problem. Since $\ell_o \gg 1$, we assume that the wedge can be represented as a time dependent singularity at the origin of the moving coordinate system. Referring to Fig. 7, we see from Eqs. (7) and (8) that

$$u + \phi_t = \sigma/2 \quad \text{for} \quad 0 < x < \ell_o, \quad y = 0\pm. \tag{50}$$

From Section 2(d) we have

$$|w(z, t)| \to 0 \quad \text{as} \quad |z| \to \infty. \tag{51}$$

By symmetry,

$$w(z, t) = \overline{w(\overline{z}, t)}. \tag{52}$$

The cavity boundary

$$y = h(x, t) = h_o(x) + h_1(x) e^{-jkt} \tag{53}$$

is unknown, but must satisfy the closure condition (9). For the steady flow component w_o this condition reduces to Eq. (19) with $\Gamma_o = 0$.

593
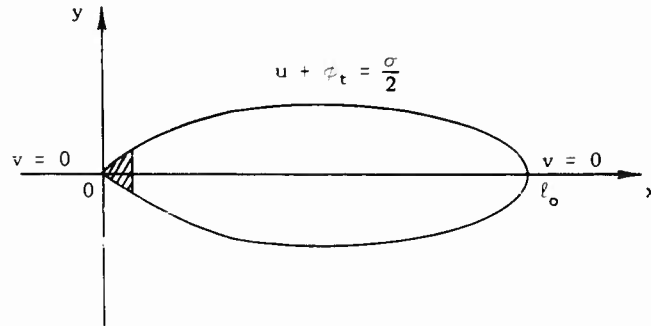
Figure 7

In order to obtain an expression for cavity closure for the unsteady flow, we return momentarily to the wedge of unit chord. The kinematic condition, Eq. (8), can be solved as a first order partial differential equation in h. Restricting our attention to the upper wedge plus cavity boundary, we obtain

$$h(x,t) = -\int_x^\ell v(\xi,\ 0+,\ \xi - x + t)\, d\xi , \tag{54}$$

where $h(\ell,t) = 0$ by closure and $h(1,t) = \gamma(t)$ by Eq. (47). We have from Eqs. (47), (48), (49), and (54) that

$$\gamma_1 = -\int_1^{\ell_0} v_1(\xi,\ 0-)\, e^{-jk(\xi - 1)}\, d\xi . \tag{55}$$

When the wedge is considered as a singularity at the origin, Eq. (55) reduces to

$$\gamma_1 = -\int_0^{\ell_0} v_1(\xi,\ 0-)\, e^{-jk\xi}\, d\xi . \tag{55a}$$

Guerst [7, pp. 120-121] obtained the elementary solution

$$w_0(z) = \frac{\sigma}{2} - \frac{\sigma}{4}\left[\sqrt{\frac{z - \ell_0}{z}} - \sqrt{\frac{z}{z - \ell_0}}\right] \tag{56}$$

to the steady state problem where

$$\sqrt{\frac{z - \ell_0}{z}},\quad \sqrt{\frac{z}{z - \ell_0}} \to -1 \quad \text{as} \quad |z| \to \infty .$$

594

Using our result from Eq. (22) that for $\sigma \ll 1$,

$$\sigma \sim \frac{8}{\pi} \gamma_o \ell_o^{-\frac{1}{2}}$$

we find from Eq. (56) that

$$w_o(z) \sim \frac{-2\gamma_o}{\pi\sqrt{-z}} \quad \text{as} \quad z \to 0 , \tag{57}$$

where $\sqrt{-x} = |x|^{1/2}$ for $x < 0$. We assume that

$$w_1(z) \sim \frac{-2\gamma_1}{\pi\sqrt{-z}} \quad \text{as} \quad z \to 0 . \tag{58}$$

It is readily verified that Eqs. (57) and (58) satisfy the kinematic boundary condition (8) in the limit as $z \to 0$ for $x > 0$ and $y = 0\pm$.

On the cavity boundary, Eq. (50) reduces to the condition

$$u_1(x, 0\pm) = Ce^{jkx} \tag{59}$$

for $0 < x < \ell_o$ where the constant C is as yet unknown. We are thus led to the following Hilbert problem for $w_1(z)$:

$$\left.\begin{array}{ll} w_1^+ - w_1^- = 0, & -\infty < x < 0 , \\[2ex] w_1^+ + w_1^- = 2Ce^{jkx}, & 0 < x < \ell_o , \\[2ex] w_1^+ - w_1^- = 0, & \ell_o < x < \infty \end{array}\right\} \tag{60}$$

where

$$|w_1| \to 0 \quad \text{as} \quad |z| \to \infty .$$

The solution of this problem with singularities of less than integer order permitted at $z = 0$ and at $z = \ell_o$ is

$$w_1(z) = \frac{1}{2\pi i} X(z) \int_o^{\ell_o} \frac{g(\xi)\, d\xi}{X^+(\xi)\, (\xi - z)} + A X(z) \tag{61}$$

where

$$X(z) = \frac{1}{\sqrt{z(z - \ell_o)}} \cdot \left(\to \frac{1}{z} \quad \text{as} \quad |z| \to \infty\right), \tag{62}$$

$$g(\xi) = 2Ce^{jk\xi} , \tag{63}$$

and A is an unknown constant.

The solution (61) may be verified by application of the Plemelj formulas. In particular, for $0 < \xi_o < \ell_o$,

$$w_1(\xi_o, 0+) = \frac{X^+(\xi_o)}{2\pi i} \int_o^{\ell_o} \frac{g(\xi)\,d\xi}{X^+(\xi)(\xi - \xi_o)} + \frac{g(\xi_o)}{2} + AX^+(\xi_o) \tag{64}$$

where

$$X^+(\xi_o) = -i\Big/ \sqrt{\xi_o(\ell_o - \xi_o)} .$$

Taking real and imaginary parts of Eq. (64), we obtain

$$\left. \begin{aligned} u_1(\xi_o, 0+) &= Ce^{jk\xi_o} , \\[2mm] v_1(\xi_o, 0+) &= \frac{C}{\pi\sqrt{\xi_o(\ell_o - \xi_o)}} \int_o^{\ell_o} \frac{e^{jk\xi}\sqrt{\xi(\ell_o - \xi)}\,d\xi}{\xi - \xi_c} + \frac{A}{\sqrt{\xi_o(\ell_o - \xi_o)}} . \end{aligned} \right\} \tag{65}$$

Applying the closure condition (55a) to the second equation of (65) and performing the integrations, we obtain after some calculation

$$C - A \left[\frac{2}{\ell_o} e^{-j\frac{k\ell_o}{2}} J_o\left(\frac{k\ell_o}{2}\right) \right] = \frac{2\gamma_1}{\pi\ell_o} . \tag{66}$$

Applying results concerning the evaluation of a Cauchy integral near the ends of the line of integration [13, p. 74], noting that

$$X(z) \sim \frac{\ell_o^{-\frac{1}{2}}}{\sqrt{-z}} \quad \text{as} \quad z \to 0 ,$$

and using Eq. (58), we obtain from solution (61) after integration that

$$C\left[\frac{\ell_o}{2} e^{j\frac{k\ell_o}{2}} \left\{ J_o\left(\frac{k\ell_o}{2}\right) - jJ_1\left(\frac{k\ell_o}{2}\right) \right\} \right] + A = \frac{-2\gamma_1}{\pi} \ell_o^{\frac{1}{2}} . \tag{67}$$

The functions J_o and J_1 are Bessel functions of the first kind of orders zero and one respectively.

The system of Eqs. (66) and (67) can be solved algebraically for C and A as functions of γ_1, k, and σ. C and A are evidently real in i but complex in j. For the limiting case of very slow oscillation, $k\ell_o \to 0$, we have

$$C = \frac{\gamma_1}{\pi \ell_o} \left(1 - 2\ell_o^{\frac{1}{2}} \right) \cdot \left. \right\}$$

$$A = \frac{-\gamma_1}{2\pi} \left(1 + 2\ell_o^{\frac{1}{2}} \right) \cdot \left. \right\} \tag{68}$$

The solution (61) is now completely determined. It is singular to the order $1/2$ at $z = 0$ and $z = \ell_o$, hence Wu's cavity termination condition (23) applies to both the steady and the unsteady supercavitating wedge problems as a <u>derived</u> condition. The constant K_o of Eq. (23) is complex in j in the unsteady case and approaches the value $-\gamma_1/\pi\ell_o^{1/2}$ as $k\ell_o \to 0$.

Applying Eq. (15) with $\Gamma = 0$ to solution (61), one may readily demonstrate [14, p. 438] that

$$S_1 = j \frac{2\pi A}{k} \tag{69}$$

where

$$S = S_o + S_1 e^{-jkt}$$

and the asymptotic value of S_o for $\sigma \ll 1$ is given by Eq. (22).

By an argument similar to that used in Section 3, we can show any solution w_1^* of (60), with singularity at $z = 0$ given by (58), satisfying the closure condition and singular to the order $3/2 - \epsilon$ with $\epsilon > 0$ at $z = \ell_o$ must be identical with the w_1 we have obtained. Guerst [7, pp. 122-124] assumed a second linearization of the cavity length in the form

$$\ell(t) = \ell_o(\gamma_o, \sigma) + \ell_1 e^{-jkt}$$

and obtained a solution $w_1(z)$ singular to the order $3/2$ at $z = \ell_o$. Apart from other considerations (he assumed $dS/dt = 0$, for example) his solution cannot be demonstrated to be unique by the method we have used.

The effect of compressibility can be introduced by using the approach of Section 5. We are led to a problem of Weiner-Hopf type for the Fourier transform $\Phi(\alpha, y)$ of the function $\phi_2(x, y)$ under assumptions corresponding to those of Eqs. (48) and (58). This problem may be solved by the approximate method of D. S. Jones [23, p. 178ff] through use of asymptotic expansions in negative powers of the cavity length ℓ_o. Although such considerations are beyond the intent of the present paper, it is of interest to note that the uniqueness of $\Phi(\alpha, y)$ can be demonstrated by the application of Liouville's theorem in the complex α plane, provided the singularities of ϕ_2 and $2\partial\phi_2/\partial y$ are at most of order $3/2 - \epsilon$ with $\epsilon > 0$ at the cavity termination point – the same circumstance as obtains for incompressible flow. The classical Abelian theorem [25, p. 31] relating the behavior of ϕ_2 and $2\partial\phi_2/\partial y$ at the cavity termination point to the behavior of Φ at $\alpha = \infty$ must be extended in the finite part sense of Riesz [26] in order that we may arrive at this conclusion.

REFERENCES

1. Tulin, M.P., "Supercavitating Flow Past Foils and Struts," Cavitation in Hydrodynamics, Proceedings of Symposium at the National Physical Laboratory, Teddington, Sept. 1955.

2. Wu, T.Y., "A Free Streamline Theory for Two-Dimensional Fully Cavitated Hydrofoils," California Institute of Technology, Hydrodynamics Laboratory, Report No. 21-17, July 1955.

3. Wu, T.Y., "A Note on the Linear and Nonlinear Theories for Fully Cavitated Hydrofoils," California Institute of Technology, Hydrodynamics Laboratory, Report No. 21-22, Aug. 1956.

4. Guerst, J.A., and Timman, R., "Linearized Theory of Two-Dimensional Cavitational Flow Around a Wing Section," Ninth International Congress of Applied Mechanics, Brussels, 1956.

5. Guerst, J.A., "Linearized Theory for Partially Cavitated Hydrofoils," International Shipbuilding Progress, 6, No. 60, Aug. 1959.

6. Guerst, J.A., "A Linearized Theory for the Unsteady Motion of a Supercavitating Hydrofoil," Technische Hogeschool, Delft, Report No. 22, April 1960.

7. Guerst, J.A., "Linearized Theory of Two-Dimensional Cavity Flows," Dissertation, Technische Hogeschool, Delft, 1961.

8. Meyer, M.C., "Some Experiments on Partially Cavitating Hydrofoils," International Shipbuilding Progress, 6, No. 60, Aug. 1959.

9. Wu, T.Y., "A Linearized Theory for Nonsteady Cavity Flows," California Institute of Technology, Engineering Division, Report No. 85-6, Sept. 1957.

10. Timman, R., "A General Linearized Theory for Cavitating Hydrofoils in Nonsteady Flow," Proceedings Second Symposium on Naval Hydrodynamics, Office of Naval Research, ACR-38, Aug. 1958.

11. Sears, W.R., "General Theory of High Speed Aerodynamics - Small Perturbation Theory," Vol. 6, Section C, "High Speed Aerodynamics and Jet Propulsion," Princeton, 1954.

12. Wu, T.Y., "A Simple Method for Calculating the Drag in the Linear Theory of Cavity Flows," California Institute of Technology, Engineering Division, Report No. 85-5, Aug. 1957.

13. Muskhelishvili, N.I., "Singular Integral Equations," P. Noordhoff, Groningen, 1953.

14. Leehey, P., "The Hilbert Problem for an Airfoil in Unsteady Flow," Journal of Mathematics and Mechanics, 6, No. 4, July 1957.

15. Song, C.S., "Unsteady, Symmetrical, Supercavitating Flows Past a Thin Wedge in a Jet," University of Minnesota, St. Anthony Falls Hydraulic Laboratory, Technical Paper No. 34-B, Jan. 1962.

16. Cohen, H., Sutherland, C.D., and Tu, Y-O, "Wall Effects in Cavitating Hydrofoil Flow," Journal of Ship Research, $\underline{1}$, No. 3, Nov. 1957.

17. Fabula, A. G., "Thin-Airfoil Theory Applied to Hydrofoils with a Single Finite Cavity and Arbitrary Free-Streamline Detachment," Journal of Fluid Mechanics, $\underline{12}$, Part 2, 1962.

18. Woods, L.C., "Unsteady Plane Flow Past Curved Obstacles with Infinite Wakes," Proceedings of the Royal Society, London, A, $\underline{229}$, 1955.

19. Woods, L.C., "Aerodynamic Forces on an Oscillating Aerofoil Fitted with a Spoiler," Proceedings of the Royal Society, London, A, $\underline{239}$, 1957.

20. Parkin, B.R., "Fully Cavitating Hydrofoils in Nonsteady Motion," California Institute of Technology, Engineering Division, Report No. 85-2, July 1957.

21. Steinberg, H., "Linearized Theory of the Unsteady Motion of a Partially Cavitated Hydrofoil," Technical Research Group, Report No. TRG-153-SR-1, March 1962.

22. Cumberbatch, E., "Accelerating, Supercavitating Flow Past a Thin Two-Dimensional Wedge," Journal of Ship Research, $\underline{5}$, No. 1, June 1961.

23. Noble, B., "Methods Based on the Wiener-Hopf Technique," Pergamon Press, 1958.

24. Jahnke, E., and Emde, F., "Tables of Functions," 4th Edition, Dover Publications, 1945.

25. Erdélyi, A., "Asymptotic Expansions," Dover Publications, 1956.

26. Riesz, M., "L' Integral de Riemann-Liouville et le Problème de Cauchy," Acta Mathematica, $\underline{81}$, 1949.

*   *   *

Thursday, August 30

Afternoon Session

HYDROELASTICITY

Chairman: J. P. Craven

Special Projects Office
Washington, D. C.

Page

REVIEW AND EXTENSION OF THEORY FOR NEAR-FIELD PROPELLER-INDUCED VIBRATORY EFFECTS

J. P. Breslin
Davidson Laboratory
Stevens Institute of Technology
Hoboken, New Jersey

A review of the theoretical studies of ship propeller-induced pressures and forces on nearby boundaries in the last decade is given with emphasis only on principal results. In the course of this, new and very simple formulas for the near-field pressures are given for the first time. Extension of the theory for determining the blade frequency vibratory force and couple generated on bodies with transverse curvature is accomplished by finding the pressures on a cylinder generated by an m-bladed propeller and its image in the cylindrical surface. Surprisingly simple formulas are found and their evaluations show the strong dependence of the excitation on blade number and tip clearance. A method for calculating vibratory forces on actual ship forms is recommended for future work and conclusions based on present knowledge are drawn.

NOMENCLATURE

A.B. coefficients
a.b

B plate width in multiples of propeller radius

b propeller radius

D propeller diameter

$D(x. \bar{})$ differential operators

F force

603

f distance from propeller axis to plate in multiples of propeller radius

$\hat{i},\hat{j},\hat{k}$ direction vectors

$J = U/nD$ advance ratio

J_n Bessel function of first kind, order n

k dummy variable

ℓ subscript denoting loading

M source strength

m number of blades in propeller

n revolutions per second

n order of harmonic

$\bar{n}$ unit normal to helicoid

p pressure

q subscript denoting torque

Q_ν Legendre function of second kind, non-integral order ν

R distance between a field point and an element of the propeller blade

s radial distance to point on blade span

s_e effective radius

T thrust

$T' = T - b^2$ thrust-disk area ratio

$T_c = T' \frac{1}{2} \cdot U^2$ thrust coefficient

t subscript denoting thrust

t c maximum thickness to chord length ratio at effective radius

U forward speed

V resultant velocity

x, y, z Cartesian coordinates of a point

604

x, r, γ cylindrical coordinates of a point

$$Z = \frac{x^2 + r^2 + s^2}{2rs}$$

Z_e value of Z at $s = s_e$

β plate-chord ratio

Γ circulation strength

ϵ_n factor of nth term of harmonic series

ϵ phase lag angle

θ instantaneous blade angle

$\lambda = x + U\tau$

ν order of Legendre function

ξ, η, ζ coordinates defined in Eq. (4)

ρ mass density of the fluid

σ angle on sector projection of the blade in the y-z plane

σ_o half-sector angle of blade projection in y-z plane

τ dummy variable (elapsed time)

τ blade thickness

$\phi = \tan^{-1} f/B$ in Eq. (27)

ϕ potential

ϕ_p propeller potential

ω angular velocity of blade

Additional Symbols

A   diameter of cylinder in multiples of propeller diameter

a   radius of cylinder

C   tip clearance in fraction of propeller diameter

d   inter-axial distance (see Figs. 10 and 11)

605

$f(x,k)$ function defined in Eq. (53)

$H_n(x,r,s)$ integral defined in Eq. (53)

i   subscript denoting image

K_n modified Bessel function of second kind, order n

M_{zz} moment about vertical axis

n   normal to the surface of sources

r' distance defined in Figs. 10 and 11

S   surface of sources

v_n normal velocity of flow

x', y', z' propeller Cartesian coordinates

$\beta = m\omega/U$

γ' angle defined in Figs. 10 and 11

$\delta(\cdot)$ Dirac delta function of $\cdot$

φ' angle defined in Fig. 10

INTRODUCTION

Naval and merchant ships are all too frequently subject to objectionable vibration in spite of the very able efforts of their designers and builders to avoid such difficulties. Vibrations may arise from unbalanced machinery, shafting and propellers. More often than not this type of vibration is associated with shaft frequency or once-per-revolution and, moreover, it can be eliminated with appropriate care by dynamic balancing of rotating parts. In many instances the source of most objectionable vibration is the propeller which can generate vibratory forces and moments at integer multiples of blade frequency, i.e., integer multiples of the number of blades times the shaft revolutions per second. Of these blade-frequency effects, generally the fundamental is the strongest and responsible for the most serious vibration. This paper is concerned only with the near-field pressures and associated induced forces at blade frequency, the second and higher harmonics being neglected for sake of simplicity. The vibratory effects generated by the varying thrust and torque developed on the blades moving through the hull wake are important mechanisms for vibration, but these are not considered herein.

One may reasonably ask—why bother to investigate the near field pressures since we know intuitively that increasing the number of blades and increasing the clearances between the propeller and the surrounding structural members will invariably reduce the effectiveness of the propeller field in causing

606

appreciable vibratory forces? The answer to this is simply that a ship (like all structures) must meet many requirements and hence its design must be a series of compromises. But compromises cannot be rationally assessed without knowing the relative gain which is achieved by changing one or more parameters. Until one can assess numerically the advantage (in regard to reduction of excitation) of, say, increasing the number of blades from 3 to 5 against the degrading of propeller efficiency, it is not possible to make the choice intelligently. This, then, is the reason for the research reported upon in this paper—to give methods by which the reduction of propeller-generated excitation, with increase of blade number, tip clearance and size of boundary (relative to the propeller), can be described numerically. When this can be done for practical ship-propeller configurations, then and only then will the naval architect have a foundation for judging how far he may prejudice a ship design toward abatement of propeller near-field excitation.

This work has been largely supported by the Bureau of Ships' Fundamental Hydromechanics Research Program, technically administered by the David W. Taylor Model Basin.

REVIEW OF EXISTING THEORETICAL STUDIES

Fields Generated by Propellers in Uniform Inflow

Mathematical analysis of the flow at the blades of a ship propeller date back many years. However, the application of vortex line theory to predict the near field effects about marine propellers* was first made (to the writer's knowledge) by Russian investigators during the early 1950's. This work has been summarized in a recent book by Babaev and Lentjakov [2] which deals in part with hydrodynamic studies and in part with the vibratory response of ship hulls. Since this text has come to hand during the writing of this paper, it is not possible to give an authoritative assessment of this Russian research. It does seem that their chief three-dimensional hydrodynamic pressure field analysis is limited to the vortex line representation of a propeller having an inclination to the direction of motion. These formulas have been checked for the case of zero inclination with results obtained independently by Pohl [3] and Breslin [4]. Babaev's expressions for zero shaft inclination in the absence of boundaries is, for a single blade, given by (our notation)

$$P = P_1 - P_2 - P_3 .$$

where P_1, P_2, P_3 are the contributions of the helical, bound and hub vortex respectively. These are given by

$$P_1 = \frac{\dot{\omega}\bar{\Gamma}_0}{4\pi} \left\{ \frac{x}{\sqrt{x^2 - r^2 - b^2 - 2br \cos(\theta - \omega)}} - 1 \right\} . \tag{1a}$$

*Gutin [1] gave formulas for the far field sound of an airscrew at zero forward speed (which embraced the incompressible case) in 1948.

$$P_2 = \frac{\rho \omega \Gamma_o}{2\pi^2} \quad \frac{r \left[J \sin(\theta - \gamma) + \pi x \cos(\theta - \gamma) \right]}{x^2 + r^2 \sin^2(\theta - \gamma)}$$

$$\cdot \left\{ \frac{r \cos(\theta - \gamma) - b}{\sqrt{x^2 + r^2 + b^2 - 2br \cos(\theta - \gamma)}} - \frac{r \cos(\theta - \gamma)}{\sqrt{x^2 + r^2}} \right\} \qquad (1b)$$

$$P_3 = \frac{\rho \omega \Gamma_o}{4\pi} \left(1 - \frac{x}{\sqrt{x^2 + r^2}} \right), \qquad (1c)$$

where

ρ is the mass density of the fluid

ω is the angular velocity of the blade

Γ_o is the circulation strength (taken to be constant)

x, r, γ are cylindrical coordinates with origin at the propeller center

θ is the instantaneous blade angle measured counterclockwise from the horizontal positive y axis.

The hub vortex contributes no blade frequency effects since it is independent of θ as is to be expected on physical grounds. For an m-bladed propeller the Russian analysis adds the corresponding terms from each blade by indexing the angle θ appropriately and then presumably performs a harmonic analysis on this sum to pick out the blade-frequency pressure and its integer harmonics. This is a "frontal assault" on the determination of the blade frequency content of the pressure which gives no insight into the dependence on blade number and upon location of the field point of interest. It is fair to say that the analysis given in this present paper goes far beyond this by avoiding the necessity for the considerable numerical work entailed in calculating the harmonic coefficients. Moreover, Babaev does not develop formulas to account for the pressure field associated with blade thickness which, as will be shown later, appears to us to be essential in order to interpret existing data. It would be most interesting to learn from Babaev how they can get the agreement with pressure measurements which are exhibited in his book.

Electrical analog work by the pioneer in the field of ship vibration, Professor Frank M. Lewis, was carried out in the mid 1930's [5]. This work produced interesting contours of pressure by measuring the magnetic field set up by the electric current through a set of wires shaped in a helicoid to represent the vortex pattern similar to that shown schematically in Fig. 1. However, this procedure proved so laborious that Professor Lewis did not vary parameters such as clearance, loading and number of blades. Furthermore, as we shall see later, the vortex representation of a propeller is not sufficient to describe the hydrodynamic field.

Concurrent work in Germany by Pohl and in the United States by Breslin yielded expressions for the total pressure arising from the thrust and torque

608

load distribution on the blades. Neither investigator at that time (1956) showed how to find the harmonic content of the total pressure except by performing a harmonic analysis on the signature from a single blade using numerical procedures.

Initial numerical results from this simple lifting line representation by Breslin appeared to give good agreement with pressure measurements made by Tachmindji and Dickerson [6]. However, checks conducted by Tsakonas revealed numerical errors (but no errors in principle!) and when these were corrected, the predictions of the pressure field from vortex theory were far below those obtained from measurement. Furthermore, these data showed a large fore-and-aft asymmetry in the magnitude of the pressure distribution, whereas the theory shows a symmetrical distribution of the modulus of the pressure.

It was then conjectured by the writer that the blade thickness might be responsible for a pressure signature which would be as important as that arising from blade loading. This thought follows from the exceedingly simple formula [7] for the minimum pressure on two-dimensional foil sections having thickness ratio t/c and lift coefficient C_L from camber alone:
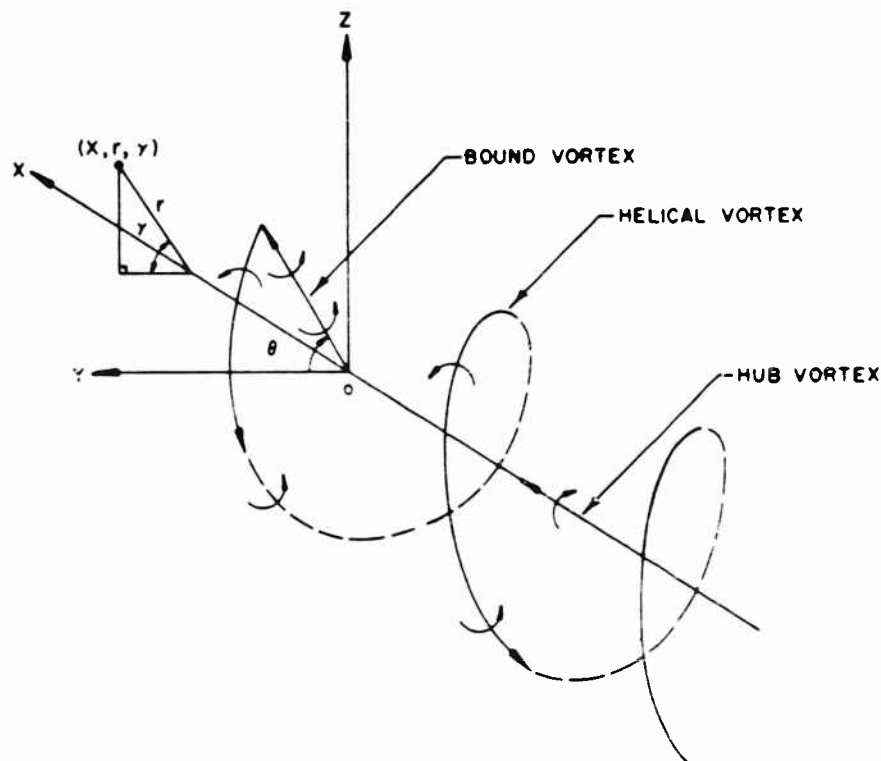
Fig. 1 - Arrangement of axes and vortex representation of propeller

609

$$\frac{\Delta p}{\frac{1}{2} \rho U^2} = -\left[a \left(\frac{t}{c}\right) + b\, C_L \right], \tag{2}$$

where the coefficients a and b depend upon the shape of the thickness distribution and the shape of the camber line respectively. Practical values of a range from 2 to 3 and values of b from 0.5 to 0.7; sections designed to avoid cavitation will have values of $a \sim 2.3$ and $b \sim 0.6$. Insertion of practical values of t/c and C_L in the equation

$$\frac{\Delta p}{\frac{1}{2} \rho U^2} = -\left(2.3\, \frac{t}{c} + 0.6\, C_L \right) \tag{3}$$

will show that the contribution from thickness will be nearly equal to that from designed lift. Since this is true on the foil, it may be expected to be true in the near field. Some regions of the field will be more affected by thickness than loading and the reverse will be true for other regions because the flows (in two dimensions) due to sources and sinks (thickness) are orthogonal to those due to vortices (thrust and torque loading).

Calculations were then made to include the effect of blade thickness. In the course of this work, Tsakonas [8] developed formulas for the blade frequency constituents of the pressure, expressing them in closed form in terms of tabulated elliptic integrals. Comparison with experiments then showed striking agreement. A sketch of the theory and the pertinent formulas expressed in a new form may serve to clarify these remarks.

The velocity potential of a propeller can be written in terms of a distribution of doublets whose axes are perpendicular to the helicoidal surface swept out by the advancing blade (or bound vortex). It is convenient to superpose a uniform flow $-U$ to bring the translational motion of the propeller to rest. The velocity potential is then

$$\phi = \frac{1}{4\pi} \int_0^b \int_0^\pi \Gamma(s)\, (\vec{n} \cdot \vec{\nabla})\, R^{-1}\, ds'\, ds - Ux . \tag{4}$$

where

  b is the propeller radius

  Γ is the circulation distribution

  $R = \left[(x - \xi)^2 + (y - \eta)^2 + (z - \zeta)^2 \right]^{1/2}$

  $\xi = -Ut; \ \eta = s \cos (\theta - \omega \tau); \ \zeta = s \sin (\theta - \omega \tau)$

  $\vec{n}$ is the unit normal to the helicoid given by

$$\vec{n} = \vec{s} \times \vec{V} = \frac{1}{s\sqrt{U^2 + (\omega s)^2}} \begin{vmatrix} \hat{i} & \hat{j} & \hat{k} \\ 0 & s\cos(\theta - \omega\tau) & s\sin(\theta - \omega\tau) \\ -U & \omega s\sin(\theta - \omega\tau) & -\omega s\cos(\theta - \omega\tau) \end{vmatrix}$$

and

$$\vec{\nabla} = \hat{i}\,\frac{\partial}{\partial\xi} + \hat{j}\,\frac{\partial}{\partial\eta} + \hat{k}\,\frac{\partial}{\partial\zeta}$$

s is the radial distance to any point on the blade span or point in the wake

ds' is an element of the arc-length in the helix
$= (U^2 + (\omega s)^2)^{1/2}\,d\tau$.

From the above formula we can see that the helicoid is entirely covered by doublets which may be thought of as merely drifting downstream at the orientation they had when they were formed at the "trailing edge" or bound vortex. The dummy variable τ may be thought of as elapsed time, $-U\tau$ being the x-wise drift of any doublet element during the time τ. Introduction of cylindrical coordinates x, r, γ and reduction of the vector product yields for the propeller potential

$$\varphi_p = \frac{1}{4\pi}\int_0^b \int_0^\pi \Gamma(s)\,D(x,\theta)\,R^{-1}\,d\tau\,ds. \tag{5}$$

where R now is in the form

$$R = \left[(x - U\tau)^2 + r^2 + s^2 - 2rs\cos(\theta - \gamma - \omega\tau)\right]^{1/2}$$

and $D(x,\theta)$ is a differential operator given by

$$D(x,\theta) = \left(\omega s\,\frac{\partial}{\partial x} - \frac{U}{s}\,\frac{\partial}{\partial\theta}\right). \tag{6}$$

It will now be demonstrated that the pressure field due to the circulation or loading distribution depends only on the loading over the blade and not upon the wake. To do this, it is necessary to prepare Eq. (5) by letting $\lambda = x - U\tau$; then $d\tau = 1/U\,d\lambda$. This puts the potential of the propeller in (5) in the form

$$\varphi_p = \frac{1}{4\pi U}\int_0^b \int_x^\infty \Gamma(s)\,D(x,\theta)\left\{\frac{d\lambda\,ds}{\left[\lambda^2 + r^2 + s^2 - 2rs\cos\left(\theta - \frac{\omega x}{U} - \gamma - \frac{\omega\lambda}{U}\right)\right]^{1/2}}\right\}. \tag{7}$$

The linearized pressure difference p calculated with respect to axes fixed at the point about which the propeller rotates is specified by

$$P_p = \rho \left(\frac{\omega \partial}{\partial \theta} - \frac{U \partial}{\partial x} \right) \varphi_p .$$ (8)

Application of (8) to (7) results in

$$P_p = + \frac{\rho}{4\pi} \int_0^b \Gamma(s) \left[\frac{D(x,\theta)}{\left[x^2 + r^2 + s^2 - 2rs \cos \left(\theta - \frac{\omega}{U}(x-\cdot) - \gamma \right) \right]^{1/2}} \right]_{\cdot = x} ds$$

$$+ \frac{\rho}{4\pi U} \int_0^b \Gamma(s) \int_x^z D(x,\theta) \left(\frac{\omega \partial}{\partial \theta} - \frac{U \partial}{\partial x} \right) \frac{d\cdot\, ds}{\left[x^2 + r^2 + s^2 - 2rs \cos \left(\theta - \frac{\omega x}{U} - \frac{\omega\cdot}{U} - \gamma \right) \right]^{1/2}}$$ (9)

The last integral which represents the effect of the wake is seen to be zero because the θ- and x-differentiations of $\cos (\theta + \omega x/U - \omega\cdot/U - \gamma)$ produce opposite and equal terms. The first integral in (9) is evaluated very readily giving

$$P_p = \frac{\partial \theta}{4\pi} \frac{\partial}{\partial x} \int_0^b \frac{s\,\Gamma(s)\, ds}{\left[x^2 + r^2 + s^2 - 2rs \cos (\theta - \cdot) \right]^{1/2}}$$

$$- \frac{\omega U}{4\pi} \frac{\partial}{\partial \theta} \int_0^b \frac{s^{-1}\,\Gamma(s)\, ds}{\left[x^2 + r^2 + s^2 - 2rs \cos (\theta - \cdot) \right]^{1/2}} .$$ (10)

From the structure of these terms which can be seen to be potentials of x-directed and θ- or tangentially-directed doublets, we may infer that they are the pressures associated with thrust and torque-producing loadings respectively.

The blade frequency content of this single-bladed pressure field can be adroitly secured by making use of the expansion

$$\frac{1}{\left[x^2 + r^2 + s^2 - 2rs \cos (\theta - \cdot) \right]^{1/2}} = \sum_{n=0}^{\infty} \epsilon_n \int_0^{\infty} J_n(kr)\, J_n(ks)\, e^{-x\,k}\, dk \cos n(\theta - \cdot)$$ (11)

where

$\epsilon_n = 1$ for $n = 0$,
$\quad = 2$ for $n > 0$, and
J_n is the Bessel function of the first kind, order n.

Since each blade produces an exactly similar term with $\cdot$ increased by the angle between the blades, the pressure at blade frequency for an m-bladed propeller is simply m-times that of the mth harmonic of the pressure from a single blade. Hence

612

$$p_p^{(m)} = p_t^{(m)} + p_q^{(m)} \tag{12}$$

$$p_t^{(m)} = \frac{\rho m \omega}{2\pi} \frac{\partial}{\partial x} \int_0^b s\Gamma(s) \int_0^\infty J_m(kr) J_m(ks) e^{-|x|k} dk\, ds\, \cos m(\theta - \gamma)$$

$$p_q^{(m)} = \frac{\rho m U}{2\pi} \frac{\partial}{\partial \theta} \int_0^b s^{-1} \Gamma(s) \int_0^\infty J_m(kr) J_m(ks) e^{-|x|k} dk\, ds\, \cos m(\theta - \gamma) . \tag{13}$$

Inspection of the last expressions shows that $p_t^{(m)}$ is an odd function of x whereas $p_q^{(m)}$ is an even function of x and is out of phase with $p_t^{(m)}$ since $p_q^{(m)} \sim \sin m(\theta - \gamma)$.

The integrals in (10) can be carried out in terms of elliptic integrals for constant Γ as shown by Tsakonas [8]. However, these expressions are cumbersome and now a more adroit reduction is afforded by the fact that the k-integral can be expressed in terms of a tabulated function, i.e.,

$$\int_0^\infty J_m(kr) J_m(ks) e^{-|x|k} dk = \frac{1}{\pi \sqrt{rs}} Q_\nu(Z) . \tag{14}$$

where

$$Z = \frac{x^2 + r^2 + s^2}{2rs} . \qquad \nu = m - \frac{1}{2}$$

and Q_ν is the Legendre function of the second kind of non-integer order ν.

Then the pressure constituents can be written

$$p_t^{(m)} = \frac{\rho m \omega x}{2\pi^2 r^{3/2}} \int_0^b \frac{\Gamma(s)}{s^{1/2}} Q_\nu'(Z)\, ds\, \cos m(\theta - \gamma)$$

$$\tag{15}$$

$$p_q^{(m)} = \frac{-\rho m^2 U}{2\pi^2 r^{1/2}} \int_0^b \frac{\Gamma(s)}{s^{3/2}} Q_\nu(Z)\, ds\, \sin m(\theta - \gamma) .$$

A useful and sufficiently good approximation may now be made by setting $s = s_e$ an "effective radius." Experience with exact and "effective radius" calculations shows $s_e \sim 0.6b$.

The circulation may be written in terms of the thrust per blade by taking $\Gamma(s) = \Gamma_0 \cdot s(b-s)$ ($\Gamma = 0$ at root and blade tip) and by making use of the Kutta-Joukowsky relation

$$\frac{T}{m} = \rho \omega \int_0^b s\Gamma(s)\, ds .$$

613

one may find $\Gamma_o = 12T/\rho m_\sigma b^4$. Using these relations (15) can be put into the form

$$\frac{P_t^{(m)}}{T'} = \frac{-6}{\pi} \frac{\left(m + \frac{1}{2}\right)}{\left(Z_e^2 - 1\right)} \left(\frac{x}{r}\right) \left(\frac{b - s_e}{b}\right) \left(\frac{s_e}{r}\right)^{1/2} \left\{Z_e Q_\nu(Z_e) - Q_{\nu+1}(Z_e) \cos m(\theta - \gamma)\right\}$$

(16)

$$\frac{P_q^{(m)}}{T'} = \frac{-6Jm}{\pi^2} \frac{(b - s_e)}{(rs_e)^{1/2}} Q_\nu(Z_e) \sin m(\theta - \gamma) .$$

where

$$Z_e = \frac{x^2 + r^2 + s_e^2}{2rs_e} , \qquad \nu = m - \frac{1}{2} .$$

$$T' = \frac{T}{\pi b^2} .$$

the total thrust-disk area ratio and J is the advance ratio U/nD, n being revolutions per second and D propeller diameter.

This solution* for the blade-frequency pressure is particularly useful now that Sluyter [9] and his colleagues have published more extensive tables of the Legendre function $Q_\nu(Z)$ than have previously existed.

The effect of blade thickness may be estimated from a source-sink distribution in the form of a circular sector in the y, z plane whose centerline is at the blade position θ which is specified by the angular interval $\theta - \sigma_o$ to $\theta - \sigma_o$. The source strength M at any location is taken as in thin body theory to be

$$M(s, \sigma) = -\frac{2V}{s} \frac{d\tau}{d\sigma} , \qquad V = \left[U^2 + (s\omega)^2\right]^{1/2} .$$

(17)

where τ is the local blade thickness.

The velocity potential is

$$\phi_\tau = -\frac{1}{2\pi} \int_0^b \int_{-\sigma_o}^{\sigma_o} V(s) \frac{\tau' d\sigma\, ds}{\left[x^2 + r^2 + s^2 - 2rs \cos (\theta - \gamma - \sigma)\right]^{1/2}} .$$

(18)

The blade frequency contribution from the thickness distribution of all n blades is

$$P_\tau^{(m)} = + \frac{m\sigma U}{\pi} \frac{\tau}{\partial x} \int_0^b \int_{-\sigma_o}^{\sigma_o} \int_0^\infty J_m(kr) J_m(ks) e^{-xk} dk\, V(s)\, \tau' \cos m(\theta - \gamma - \sigma) d\sigma\, ds$$

(Cont.)

---

*This form of the blade frequency pressure has not been previously published.

$$-\frac{m\rho\omega}{\pi}\,\frac{\partial}{\partial\phi}\int_0^b\int_{-\sigma_0}^{-\sigma_0}\int_0^\pi J_m(kr)\,J_m(ks)\,e^{-|x|k}\,dk\,\,V(s)\,\tau'(\sigma)\cos m(\phi-\gamma-\sigma)\,d\sigma\,ds.$$

As before, the k-integrals may be replaced by Legendre functions of the second kind. The σ-integrals can be carried out with ease for the simple case of a bi-convex blade section which has a finite slope at the leading and trailing edges and a constant radius of curvature. These operations reduce the above expressions to

$$p_\tau^{(m)} = \frac{2\rho U}{\pi^2}\,\frac{x}{r^{3/2}}\int_0^b\frac{V(s)}{s^{3/2}}\,\sqrt{[\tau'(\sigma_0)]^2 + \left(\frac{\nu}{m}\right)^2}\,\,Q_\nu'(Z)\,ds\,\cos(m\sigma_0-\epsilon)\,\sin m(\phi-\gamma)$$

$$-\frac{2m\rho\omega}{\pi^2}\,\frac{1}{r^{1/2}}\int_0^b\frac{V(s)}{s^{1/2}}\,\sqrt{[\tau'(\sigma_0)]^2 + \left(\frac{\nu}{m}\right)^2}\,\,Q_\nu(Z)\,ds\,\cos(m\sigma_0-\epsilon)\,\cos m(\phi-\gamma).$$

where

$$\epsilon = \tan^{-1}\left(\frac{\nu}{m\tau'(\sigma_0)}\right);$$

ν and Z are as defined above. The term $(\nu/m)^2 \ll \tau'(\sigma_0)$ for thin sections; in addition the product $V(s)\,\tau'(\sigma_0)$ is nearly constant over the blade span. The effective radius concept can again be used (the singularity at $s = 0$ due to $s^{-3/2}$ is only apparent, being absorbed by Q_ν').

This pressure may be reduced to the same basis as the thrust and torque contributions by introducing the thrust loading coefficient defined by $T' = 1/2\,\rho U^2 T_c$. The result is

$$\frac{p_\tau^{(m)}}{T'} = -\frac{8(t/c)}{\pi^2}\,\frac{m-\frac{1}{2}\sqrt{1-\left(\frac{s_e\nu}{bJ}\right)^2}}{T_c\left(Z_e^2-1\right)}\,\left[Z_e\,Q_\nu(Z_e) - Q_{\nu-1}(Z_e)\right]\,\frac{bs_e x}{(rs_e)^{3/2}}$$

$$\times\cos(m\sigma_0-\epsilon)\,\sin m(\phi-\gamma)$$

$$-\frac{8m(t/c)}{\pi J T_c}\,\sqrt{1-\left(\frac{s_e\nu}{bJ}\right)^2}\,\,Q_\nu(Z_e)\,\sqrt{\frac{s_e}{r}}\,\cos(m\sigma_0-\epsilon)\,\cos m(\phi-\gamma). \tag{19}$$

where a factor

$$\sqrt{1-\left(\frac{1}{m\sigma_0}\right)^2}$$

has been taken to be unity since $1/m\sigma_0 \ll 1.0$.

615

Use has been made of the geometric relationships

$$\tau'(\sigma_o) = -2s_e(t/c)$$

and

$$\tau'' = \frac{-2s_e(t/c)}{\sigma_o} \quad \text{and} \quad \epsilon = \tan^{-1}\left(\frac{1}{m\sigma_o}\right).$$

The ratio t/c is the blade thickness at the effective radius s_e.

Inspection of (16) and (19) shows that both thickness and loading effects are made up of two terms, one odd in x, the other even in x. They may be written in the following form to reveal their constructive and destructive interference for points forward and aft of the propeller respectively:

$$\frac{P_t^m}{T'} = -\left(\frac{x}{r}\right) A_t^m(x,r) \cos m(\theta - \gamma) - B_q^m(x,r) \sin m(\theta - \gamma) \tag{20}$$

$$\frac{P_-^m}{T'} = -A_-^m(x,r) \cos m(\theta - \gamma) - \frac{b s_e x}{(r s_e)^{3/2}} B_-^m(x,r) \sin m(\theta - \gamma).$$

where

$$A_t^m(x,r) = \frac{6}{\pi} \frac{\left(m - \frac{1}{2}\right)}{\left(Z_e^2 - 1\right)} \left(\frac{b - s_e}{b}\right) \left(\frac{s_e}{r}\right)^{1/2} \left\{ Z_e Q_\nu(Z_e) - Q_{\nu-1}(Z_e) \right\} \tag{21}$$

$$B_q^m(x,r) = \frac{6Jm}{\pi^2} \frac{(b - s_e)}{(r s_e)^{1/2}} Q_\nu(Z_e) \tag{22}$$

$$A_-^m(x,r) = \frac{8m(t/c)}{\pi J T_c} \sqrt{1 - \left(\frac{s_e \pi}{bJ}\right)^2} \left(\frac{s_e}{r}\right)^{1/2} Q_\nu(Z_e) \cos(m\pi_o - \epsilon) \tag{23}$$

$$B_-^m(x,r) = \frac{8\left(m - \frac{1}{2}\right)\left(\frac{t}{c}\right)}{\pi^2 T_c \left(Z_e^2 - 1\right)} \sqrt{1 - \left(\frac{s_e \pi}{bJ}\right)^2} \left\{ Z_e Q_\nu(Z_e) - Q_{\nu-1}(Z_e) \right\} \cos(m\pi_o - \epsilon). \tag{24}$$

(A factor $\sqrt{1 - (m\pi_o)^{-2}}$ has been taken as unity since $(m\pi_o)^{-2} \ll 1.0$).

Here all the A's and B's are even functions of x. Thus it is clear that both in-phase components add together for points forward of the propeller, but are opposed in sign aft of the propeller. Thus the modulus or amplitude

$$\left[\left(P_t^m\right)^2 - \left(P_-^m\right)^2 \right]^{-1/2}$$

616

will show a marked variation with x, being much larger forward of the propeller than aft and this is a basic feature revealed by pressure measurements [6].

Asymptotic formulas which reveal the rate at which these pressure fields decay beyond about one radius may be easily deduced from the series expansion of the Legendre function:

$$Q_{\nu}(Z) = \frac{\Gamma(\nu+1)\Gamma\left(\frac{1}{2}\right)}{2^{\nu+1}\Gamma\left(\nu+\frac{3}{2}\right)} Z^{-(\nu+1)} \, _2F_1\left(\frac{\nu+2}{2};\ \frac{\nu+1}{2};\ \nu+\frac{3}{2};\ \frac{1}{Z^2}\right). \qquad (25)$$

where $\Gamma(\mu)$ is the Gamma function.

$$_2F_1(a,b;c;x) = 1 + \frac{abx}{1!c} + \frac{a(a+1)b(b+1)x^2}{2!c(c+1)} + \cdots.$$

the hypergeometric series.

It is sufficient to retain only the first term of the hypergeometric series. Table 1 shows the coefficients for the various terms for 3, 4 and 5-bladed propellers. It is clear that the fields decay extremely rapidly with increase of blade number.

Application of (16) and (19) to conditions obtained in model tests by Tachmindji and Dickerson [6] and unpublished data obtained at the National Physical Laboratory in England are shown on Figs. 2 and 3. The variation with x at a tip clearance of about 0.10D is seen to be fairly good in spite of the fact that the theory is not expected to be good for such low tip clearances.

Table 1
Asymptotic Formulas for the Free Space Pressure Field

Blade Number m	$\dfrac{P_T}{T' \cos m(\theta-\psi)}$	$\dfrac{P_Q}{T' \sin m(\theta-\psi)}$
3	$\dfrac{\frac{-105}{8}\left(1-\frac{s_e}{b}\right) s_e^5 x r^3}{\left[x^2-r^2-s_e^2\right]^{9/2} - 4r^2 s_e^2\left[x^2-r^2-s_e^2\right]^{5/2}}$	$\dfrac{\frac{-J}{2}\left(\frac{45}{4}\right)\left(1-\frac{s_e}{b}\right) b\, s_e^3 r^3}{\left[x^2+r^2-s_e^2\right]^{-2}}$
4	$\dfrac{\frac{-945}{64}\left(1-\frac{s_e}{b}\right) s_e^6 x r^4}{\left[x^2+r^2-s_e^2\right]^{11/2} - 4r^2 s_e^2\left[x^2+r^2-s_e^2\right]^{7/2}}$	$\dfrac{\frac{-J}{2}\left(\frac{105}{8}\right)\left(1-\frac{s_e}{b}\right) b\, s_e^4 r^4}{\left[x^2-r^2-s_e^2\right]^{9/2}}$
5	$\dfrac{\frac{-2079}{128}\left(1-\frac{s_e}{b}\right) s_e^7 x r^5}{\left[x^2-r^2-s_e^2\right]^{13/2} - 4r^2 s_e^2\left[x^2+r^2-s_e^2\right]^{9/2}}$	$\dfrac{\frac{-J}{2}\left(\frac{945}{64}\right)\left(1-\frac{s_e}{b}\right) b\, s_e^5 r^5}{\left[x^2-r^2-s_e^2\right]^{11/2}}$

Note: A practical value for s_e is 0.6b.

617
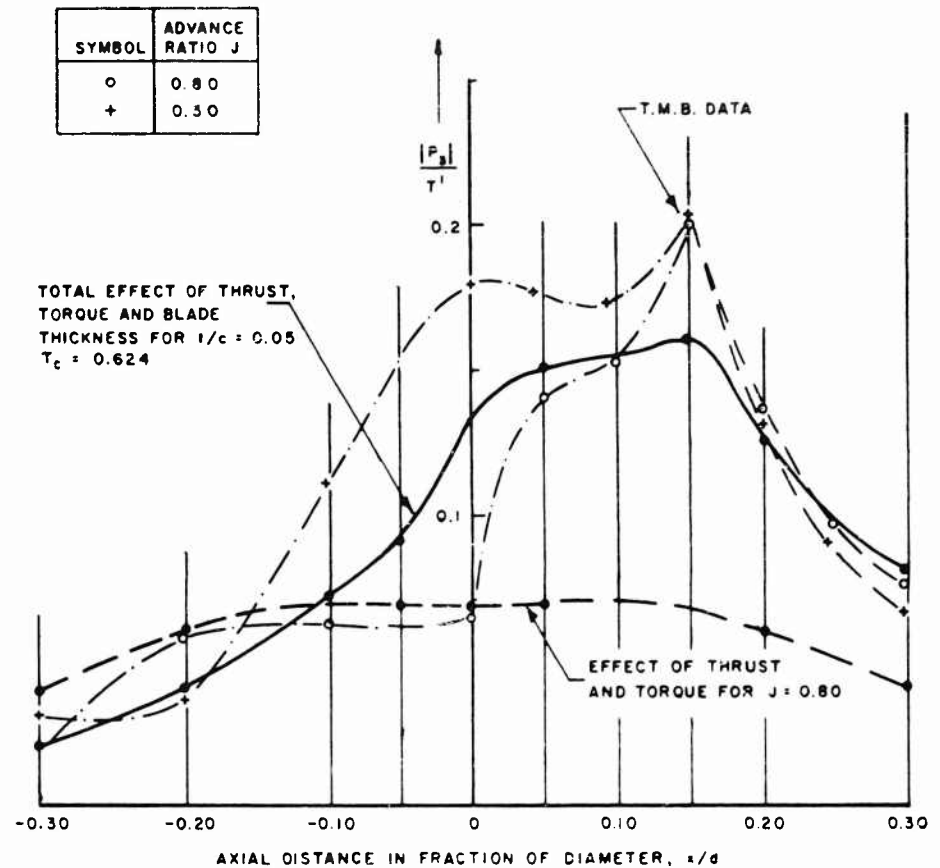
Fig. 2a - Variation of blade-frequency pressure with axial
distance along a line of constant r/b = 1.196

Figure 3a shows that the theory underestimates the NPL data. This is not sur-
prising since the development is applicable only to lightly loaded propellers. A
more complete treatment would be required to encompass this condition for low
values of the advance ratio (J = 0.30). This would involve accounting for the
shape and magnitude of the chordwise loading and possibly contributions from
non-linear relations between section lift and angle of attack. It is not believed
important for the more important applications of the theory to go into these
complications. It is rewarding to note that the general asymmetrical character
of the pressure field is correctly indicated even in this case and that at least
the order of magnitude is given by this relatively simple theory. Very good
agreement is indicated for practical tip clearances > 0.15 D.

618
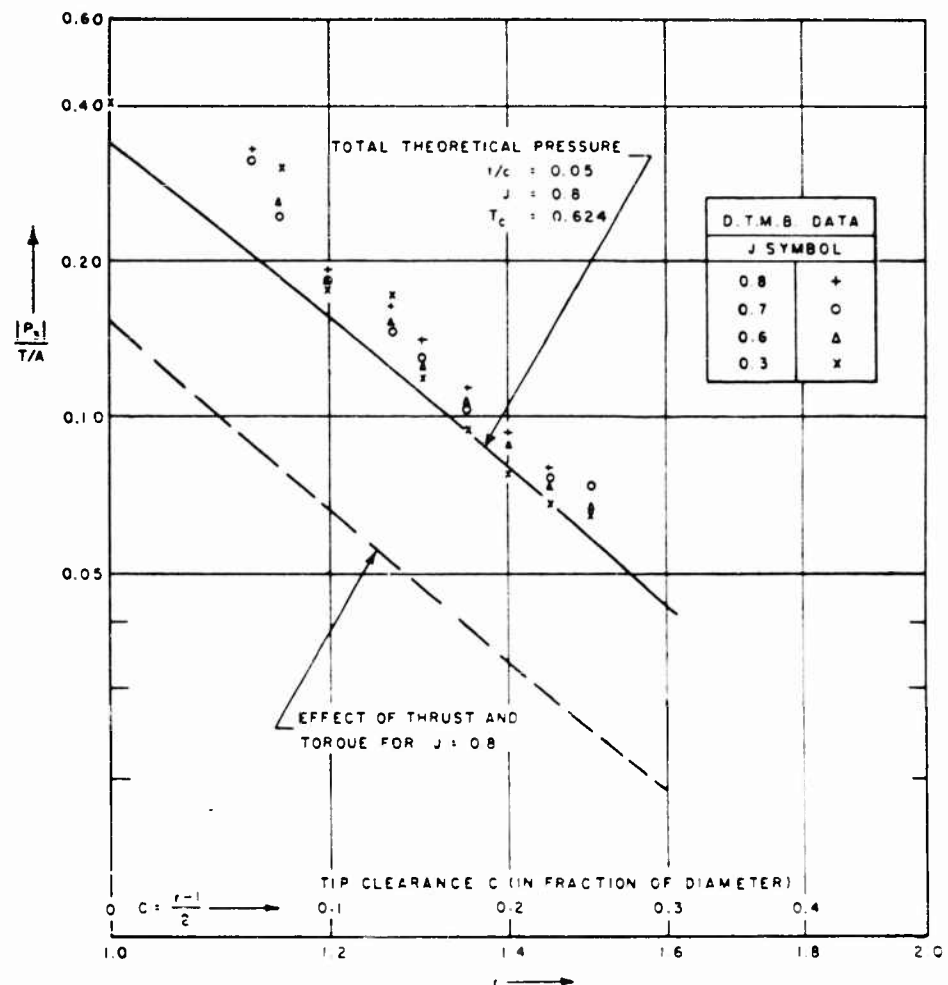
Fig. 2b - Variation of blade-frequency pressure
with tip clearance at x D = 0.153

Fields Generated in Non-Uniform Inflow

When the flow to a propeller is spatially non-uniform, the pressure distribution over the blades is non-stationary and hence the near field pressures may be expected to be considerably different than in the case of uniform inflow. The circulation distribution may now be thought of as being replaced by a directed pressure loading which contains all blade harmonics, in principle. These harmonics combine with the harmonics of the space function 1 R to give an entire range of cross products of differing harmonics. Again one retains only those combinations of loading and space-function harmonics which are at blade frequency as all others (except integer multiples of these) sum to zero. Thus the

619
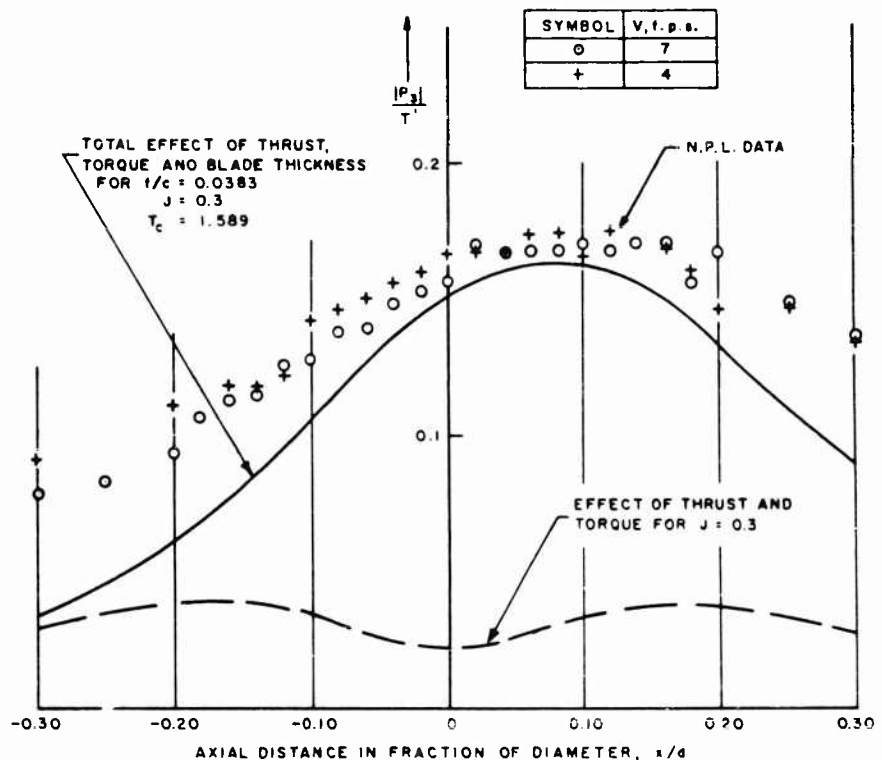
Fig. 3a - Variation of blade-frequency pressure with axial
distance along a line of constant r b = 1.25

blade frequency content of the blade loading combines with the zero harmonic of
1 R and all other possible combinations up to the zero harmonic of the loading
with the blade harmonic of 1 R. Only certain of these terms are dominant, but
in the near field it is not possible to make a simple rule applicable to all points.
It is certainly obvious that the not-too-near field, say beyond a propeller radius,
will be dominated by the term involving the blade frequency part of the loading
with the zero harmonic of the space-function since this has the slowest spatial
decay. The calculations which are quite involved are detailed by Tsakonas [10]
and will not be given here for brevity. Figure 4 shows results of such calcula-
tions. Here it can be seen that very close to the propeller the increase due to
non-uniformity is at most 20 percent but beyond x D = 0.4 the percentage change
in the pressure over the uniform case is much greater. At such distances all
the pressures are small, but the slow rate of decay of the constituents arising
from non-uniformity may have an important effect on vibratory forces and mo-
ments associated with these pressures. It must be noted, however, that the
pressure due to thickness is not included in Fig. 4 so that the relative effect
close to the propeller arising from non-uniform inflow is of the order of 10
percent for the particular wake used in these calculations.
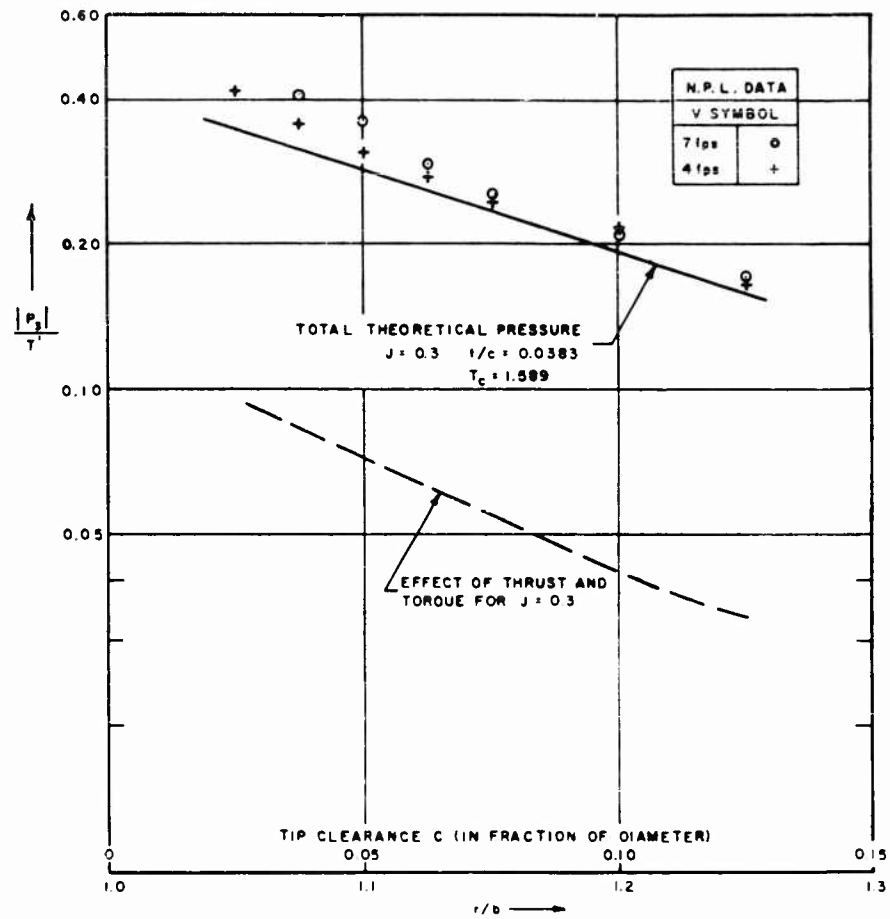
Fig. 3b - Variation of blade-frequency pressure
with tip clearance at $x \cdot D = 0.10$

Forces Generated on Boundaries

A two-dimensional analysis yielding the cross force generated by a single blade represented as a single vortex traversing a stream in the neighborhood of a plate has been given by the writer [11]. The lateral force on the plate was found to be

$$F(y) = \frac{1}{2} F_0 + F_1 . \tag{26}$$

where

F_0 is the quasi-steady force associated with the distributed instantaneous angle of attack induced on the plate, and

621
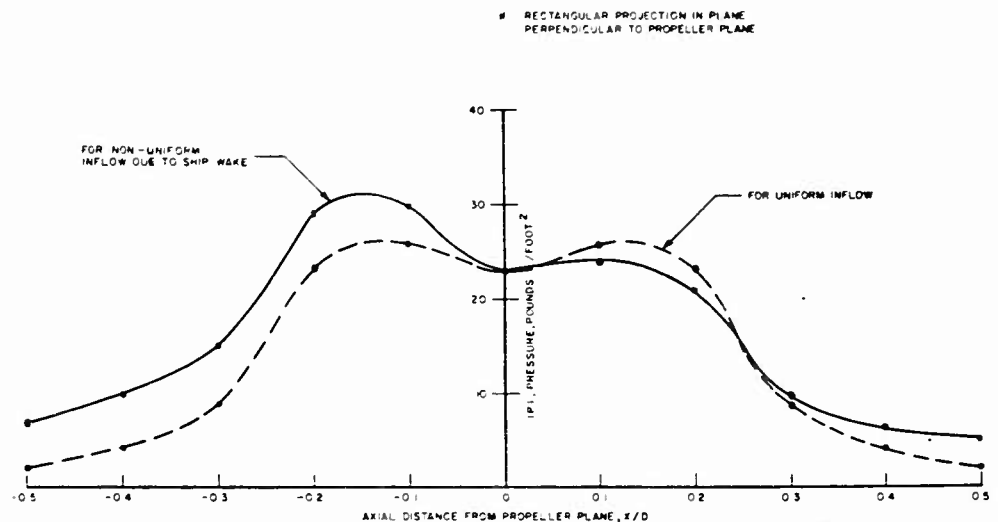
Fig. 4 - Near-field pressure distribution for the first blade harmonic
of 4-blade propeller analog I* (radial distance r = 0.6D)

F_1 is the added-mass effect due to the acceleration induced by the vor-
tex flow.

The factor of $1/2$ is the limit of the unsteady correction to the circulation-
associated force for a practical value of the ratio of vortex traversing speed to
the free stream speed. Results of the calculations are shown on Figs. 5, 6, and
7. Comparison of Figs. 5 and 6 shows a much larger force associated with the
case of a plate upstream of the vortex (skeg or strut-propeller configuration) as
compared with the plate downstream (rudder-propeller arrangement). Figure 7
shows the variation of the maxima of these forces with clearance to plate-chord
ratio $\beta = a L$. The forces decay relatively slowly with β. It is of interest that
the cross forces can be of the order of the thrust on the vortex. This theory is
most assuredly rudimentary, further work to extend the analysis to include
effects of finite blade chord and blade-plate interaction having been recently
done by Lurye [12] and colleagues. Effects of blade thickness will also be im-
portant and these have not been determined.

Forces have been calculated [13] on a plate of finite width and infinite length
due to the pressure distribution generated by an m-bladed propeller on an axis
parallel to the longitudinal centerline of the plate. The pressures on the plate
are taken as twice the free space pressures generated by loading and blade
thickness. Thus the answers are approximate for plate widths small compared
to the propeller radius. Only one term from the loading (torque) and one from
the blade thickness (that due to rotation) contribute to the force. The blade-
frequency vertical force from loading is given by

Fig. 5 - Sum of forces $(1/2\ F_o + F_1)$ developed on a flat plate directly downstream of a traversing vortex as a function of vortex position and clearance ratio (for a speed ratio $r = V U = 2.0$)

$$
\frac{F_z^{(m)}}{T} = -\frac{4J}{\pi^2 m (m-1)}\ \frac{\sin(m-1)\phi}{(B^2+f^2)^{\frac{m-1}{2}}}\ \cos m\phi, \qquad m = 1 \text{ and odd}
$$

$$
= \frac{4J}{\pi^2 m (m-1)}\ \frac{\cos(m-1)\phi}{(B^2+f^2)^{\frac{m-1}{2}}}\ \sin m\phi, \qquad m \text{ even}
$$

(27)

where

$\phi = \tan^{-1} f B$

B   is the plate width in multiples of propeller radius

f   is the distance from the propeller axis to the plate in multiples of propeller radius.

623

Fig. 6 - Sum of forces $(1/2\, F_o + F_1)$ developed on a flat plate directly upstream of a traversing vortex as a function of vortex position and clearance ratio (for a speed ratio $r = V/U = 2.0$)

The blade-thickness contribution results in the force:

$$\frac{F_-}{T} = \frac{16\left[(0.7\pi)^2 + J^2\right]^{1/2}}{\pi J^2 T_c m(m+1)(m-1)} \frac{\sin(m-1)\phi}{(B^2+f^2)^{\frac{m-1}{2}}} \left[\tau' \cos m\sigma_o - \frac{\pi}{m} \sin m\sigma_o\right] \sin m\theta; \quad \begin{array}{l} m\ \text{odd} \\ m \neq 1 \end{array}$$

$$= \frac{16\left[(0.7\pi)^2 + J^2\right]^{1/2}}{\pi J^2 T_c} \frac{\cos(m-1)\phi}{m(m+1)(m-1)} \frac{\left[\tau' \cos m\sigma_o \frac{\pi}{m} \sin m\sigma_o\right]}{(B^2+f^2)^{\frac{m-1}{2}}} \cos m\theta; \quad m\ \text{even}$$

$$\tag{28}$$

624

Fig. 5 - Sum of forces $(1/2\ F_o + F_1)$ developed on a flat plate directly downstream of a traversing vortex as a function of vortex position and clearance ratio (for a speed ratio $r = V/U = 2.0$)

$$
\left.
\begin{aligned}
\frac{F_z^{(m)}}{T} &= - \frac{4J}{\pi^2 m(m-1)} \ \frac{\sin(m-1)\phi}{(B^2+f^2)^{\frac{m-1}{2}}} \ \cos m\theta, \quad m \neq 1 \text{ and odd} \\[2em]
&= \frac{4J}{\pi^2 m(m-1)} \ \frac{\cos(m-1)\phi}{(B^2+f^2)^{\frac{m-1}{2}}} \ \sin m\theta, \quad m \text{ even}
\end{aligned}
\right\} \tag{27}
$$

where

$\phi = \tan^{-1} f/B$

B   is the plate width in multiples of propeller radius

f   is the distance from the propeller axis to the plate in multiples of propeller radius.

623

Fig. 6 - Sum of forces $(1/2\, F_o + F_1)$ developed on a flat plate directly upstream of a traversing vortex as a function of vortex position and clearance ratio (for a speed ratio $r = V/U = 2.0$)

The blade-thickness contribution results in the force:

$$\frac{F_\tau}{T} = \frac{16\left[(0.7\,\pi)^2 + J^2\right]^{1/2}}{\pi J^2 T_c\, m(m+1)(m-1)}\; \frac{\sin(m-1)\phi}{(B^2+f^2)^{\frac{m-1}{2}}}\left[\tau'\cos m\sigma_o - \frac{\tau''}{m}\sin m\sigma_o\right]\sin m\theta; \quad \begin{array}{l} m\ \text{odd} \\ m \neq 1 \end{array}$$

$$= \frac{16\left[(0.7\,\pi)^2 + J^2\right]^{1/2}}{\pi J^2 T_c}\; \frac{\cos(m-1)\phi}{m(m+1)(m-1)}\; \frac{\left[\tau'\cos m\sigma_o - \frac{\tau''}{m}\sin m\sigma_o\right]}{(B^2+f^2)^{\frac{m-1}{2}}}\cos m\theta; \quad m\ \text{even} \tag{28}$$

624

Fig. 7 - Maximum force on a plate
forward and aft of traversing vortex

and similar expressions for the moments about a transverse axis arising from the companion pressure terms. Figures 8 and 9 give results for the total force amplitude for three- and four-bladed propellers as a function of plate width. It will be noted that as the plate width is made infinite, the force decays quickly to zero, a result which had been previously obtained by Pohl [3] and Breslin [11]. Application to a cruiser or a destroyer where the half-beam in way of the propellers is the order of 2 diameters could result in a force of the order of 2 percent of the total thrust considering twin screws operating in phase. At high speed the thrust required by a destroyer is of the order of 4 percent of the displacement (say 4000 long tons) or a thrust of 160 long tons. Thus the vibratory force may be of the order of 3.2 long tons. Such a force acting at the resonant frequencies of one or more of the hull (or sub-structural) modes can produce very objectionable vibration of the main hull girder or local sub-structure.

Forces on portions of infinite plates, wedges and other shapes have been calculated by Pohl [14], but these do not take into account the influence of the shape of the boundary in modifying the pressure field. Pressures on wedges due to a moving concentrated force have been computed by Reed [15] et al, but unfortunately the resulting formula is unwieldy. Their calculations show some conditions in which the pressure on the boundary is greater than twice the free-space pressure caused by the moving force, but generally this pressure ratio is between 1.0 and 2.0.
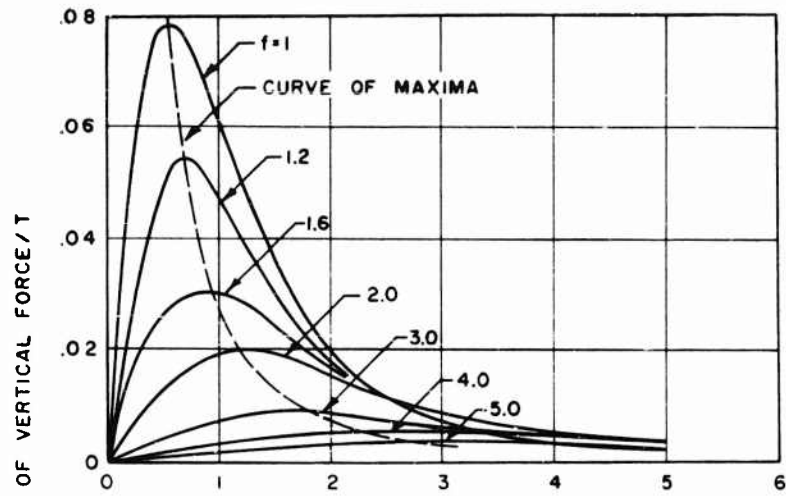
Fig. 8 - Three-bladed propeller (3192), m = 3, at varying
depths f in propeller radii b, J = 0.8
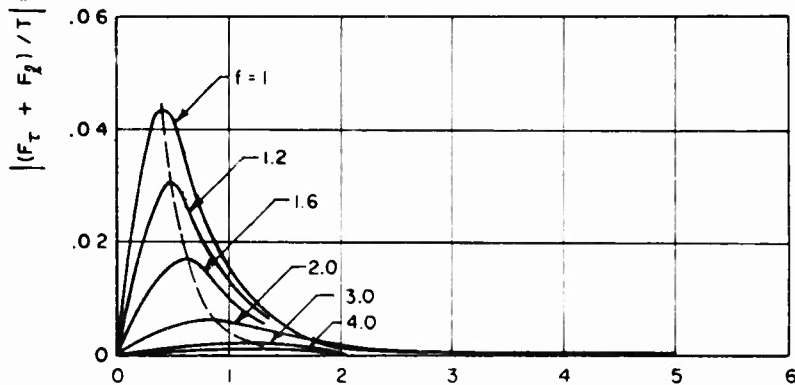
Fig. 9 - Four-bladed propeller (3192), m = 4, J = 0.8,
B = y/b, amplitude of total vertical force due to pro-
peller on infinitely long flat plates of different widths 2B

EXTENSION TO CYLINDRICAL BOUNDARIES

Force and Moment Arising from Blade Thickness

A basic requirement in calculating the force on a body due to the nearby
motion of a disturbing form is the determination of the "image" of that form in
the primary body. Since the source is the basic building block, this amounts to
finding the image of a source in the boundary. Then the complete image can be

constructed by subsequent integrations or differentiations or by both processes to build the entire disturbing form and its image.

The effect of blade thickness on the pressure developed on a cylindrical boundary clearly requires one to find the image of any source element on a blade in the cylinder. This solution can also be used for the effect of blade loading since the vortex representation of a blade and its wake is equivalent to a distribution of doublets over a helicoidal surface, and such doublets are derivable from a source by differentiation. The image of a source in a cylinder whose axis is parallel to a uniform flow will now be outlined and applied to find the vibratory force on the cylinder arising from the flow produced by the finite thickness or displacing effect of the blades.

Consider a circular sector of sources rotating about the x' axis as shown in Fig. 10, where it should be noted that the primed systems are the propeller coordinates and the unprimed systems are the body cylindrical coordinates. The blade-frequency potential of m such distributions of sources of strength density M is:

$$\phi_\tau'^m = \frac{m}{2\pi} \int_{s'=0}^b \int_{-\sigma_0}^{\sigma_0} s'M(\sigma',s') \int_0^\infty J_m(kr') J_m(ks')$$

$$\times e^{-|x'|k} dk \cos m(\theta' + \sigma' - \gamma') d\sigma'ds'. \tag{29}$$

In order to find the image of $\phi_\tau'^m$ in the cylinder, it is necessary to express this as a function of the coordinates in the cylinder to provide a means of expressing the normal derivative on the cylinder. This is accomplished through the use of the addition theorem for Bessel functions [16]:

$$e^{-im\gamma'} J_m(kr') = \sum_{n=-\infty}^{\infty} J_{m+n}(kd) J_n(kr) e^{in(\gamma-\tau)}. \tag{30}$$

where d is the inter-axial distance shown in Fig. 10.

The use of (30) in (29) will now permit the easy expression of the r-derivative of this potential which is needed because of the boundary condition imposed on the image potential $\phi_{\tau i}^m$, viz.,

$$\frac{\partial \phi_{\tau i}^m}{\partial r} = -\frac{\partial \phi_\tau^m}{\partial r} \quad \text{on} \quad r = a. \tag{31}$$

In addition, the image potential must also satisfy Laplace's equation and vanish with its derivatives at large x and r. Solution of Laplace's equation in cylindrical coordinates leads to products of sinusoids in x and γ and modified Bessel functions of the first and second kind, the latter of which are retained because they satisfy conditions at infinity. In view of the fact that the cylinder is of infinite extent, the expression for the image potential comes out in terms of integrals over the continuum of eigen values and takes the form

627
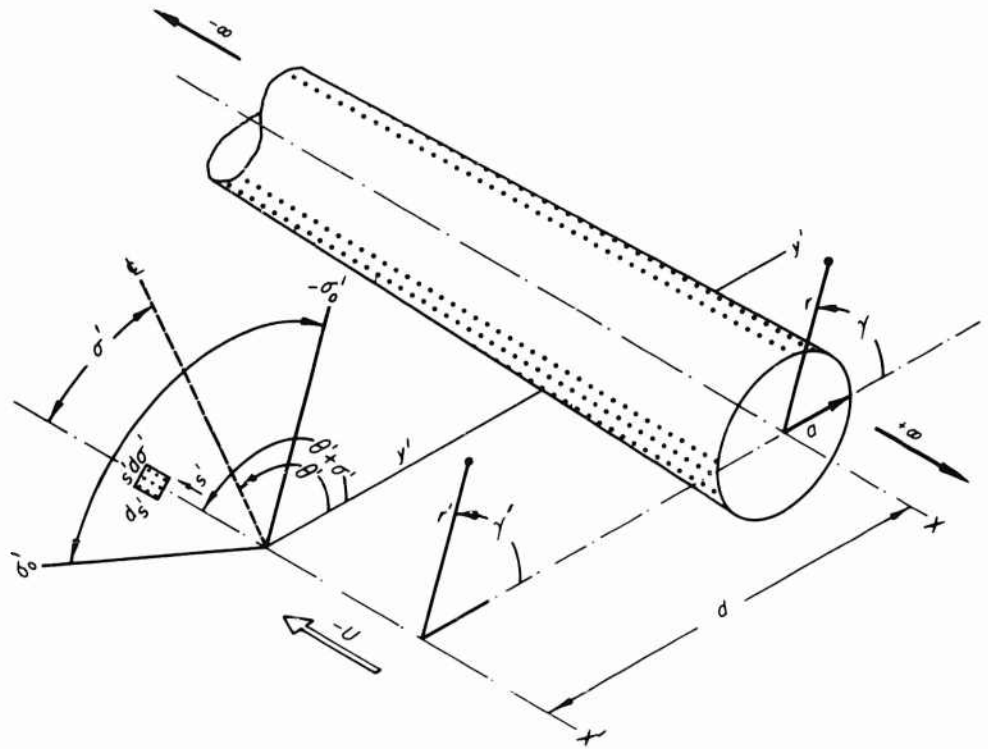
Figure 10

$$\phi_{\tau i}^{m} = -\frac{m}{2\pi^2} \int_0^b \int_{-\sigma_o}^{\sigma_o} sM(s,\sigma) \sum_{n=-\infty}^{\infty} \int_{-\infty}^{\infty} \int_0^{\infty} \int_0^{\infty} k J_m(ks) \ J_n'(ka) \ J_{mn}(kd) \ e^{-|\xi|k}$$

$$\frac{K_n(\lambda r) \ \cos \lambda(x-\xi)}{\lambda K_n'(\lambda a)} \ dk \ d\lambda \ d\xi \ e^{i[m(\theta+\sigma)+n(\gamma-\pi)]} d\sigma' ds' , \tag{32}$$

where K_n is the modified Bessel function of the second kind, order n and it is to be understood that only the real part of (32) is retained. (Primes on all the geometric quantities are now dropped for ease of writing.) It can be seen by inspection that the r-partial derivative of (32) evaluated on $r = a$ is merely the double Fourier integral representation of the negative of

$$\left.\frac{\partial \phi_{\tau}^{m}}{\partial r}\right|_a$$

as is required to fit the boundary condition.

One may now calculate the lateral vibratory force on the cylinder by integrating the pressures from the blades and their images as required by:

$$F_\tau^{\,m} = -a \int_{-\infty}^{\infty} \int_0^{2\pi} p_\tau^{\,m}(x, a, \gamma) \cos \gamma \, d\gamma \, dx \,, \tag{33}$$

where

$$p_\tau^{\,m} = \rho \left(\frac{\omega \partial}{\partial \theta} - \frac{U \partial}{\partial x} \right) \left(\phi_\tau^{\,m} + \phi_{\tau i}^{\,m} \right) \,. \tag{34}$$

Inspection of (33) and (34) reveals the immediate simplifications:

(1) The x-integrations and x-differentiations result in values of the potentials at $x = \pm \infty$ and these are zero. Hence only the θ-derivatives contribute.

(2) Since the potentials are harmonic functions of γ only the terms $n = 1$ and $n = -1$ can contribute to the force because of the presence of $\cos \gamma$ in (33).

The only complicated integral which arises in the contribution of $\partial \phi_\tau^{\,m} / \partial \theta$ is the k-integration which fortunately has been evaluated [17]. It is

$$\int_0^\infty k^{-1} J_{m+n}(kd) \, J_n(ka) \, J_m(ks') \, dk \; = \; \left.\begin{array}{ll} \dfrac{as'^m}{2d^{m+1}} & n = 1 \\[2mm] = 0 & n = -1 \end{array}\right\} \; m > 1 \,. \tag{35}$$

The force arising from the field of the blade thickness alone (the direct effect due only to $\phi_\tau^{\,m}$) reduces to

$$F_{\tau d}^{\,m} = \frac{-\rho \, \omega_a^2 m^2}{2d^{m+1}} \int_0^b \int_{-\sigma_0}^{\sigma_0} M(s, \sigma)(s)^{m+1} \sin m(\mathcal{S} + \sigma) \, d\sigma \, ds \,, \tag{36}$$

which is a simple integration over the distribution once the source strength M is specified in terms of the slope of the blade thickness.

The force arising from the image system whose potential is given by (32) involves the simple x-integration

$$\int_{-\infty}^{\infty} \cos \lambda(x - \xi) \, dx \; = \; 2\pi \cos \lambda \xi \, \delta(\lambda) \,. \tag{37}$$

where $\delta(\lambda)$ is the Dirac-delta function. This enables us to handle the λ-integration, viz.,

$$2\pi \int_0^\infty \frac{\cos \lambda \xi \, K_n(\lambda a) \, \delta(\lambda) \, d\lambda}{\lambda K_n'(a)} \tag{38}$$

through the use of the formula

$$\int_0^\infty f(\lambda) \; \delta(\lambda) \; d\lambda \;=\; \frac{1}{2} \, f(0) \;,$$ (39)

which then yields

$$\pi \; \lim_{\lambda \to 0} \; \frac{K_n(\lambda a)}{\lambda K_n'(\lambda a)} \quad .$$ (40)

Recalling that, as before, the only possible values of n are ± 1, this limit can be found to be simply

$$\pi \; \lim_{\lambda \to 0} \; \frac{K_n(\lambda a)}{\lambda K_n'(\lambda a)} \;=\; -\pi a \quad (n = \pm 1) \;.$$ (41)

The force due to the image system is thereby reduced to finding the real part of

$$F_{\tau i}^m \;=\; \frac{\rho \omega m a^2}{2} \int_0^b \int_{-\sigma_o}^{\sigma_o} s M(s,\sigma) \; \frac{\partial}{\partial \theta} \int_{-\infty}^\infty \int_0^\infty k J_m(ks) \; J_n'(ka) \; J_{m+n}(kd)$$

$$\times \; e^{-|\xi|k} \; dk \, d\xi \; e^{im(\theta + \sigma)} \; d\sigma \, ds \;,$$

where one must take the sum for $n = 1$ and -1. The ξ integral simply provides $2/k$. Then for $n = 1$ one has the k-integrals whose values are found from [17] to be

$$-\frac{1}{a} \int_0^\infty k^{-1} J_m(ks) \; J_{m+1}(kd) \; J_1(ka) \; dk \;=\; -\frac{s^m}{2 d^{m+1}}$$

and

$$\int_0^\infty J_m(ks) \; J_{m+1}(kd) \; J_o(ka) \; dk \;=\; \frac{s^m}{d^{m+1}}$$ (42)

so that their sum is simply

$$\frac{1}{2} \frac{s^m}{d^{m+1}} \quad .$$

For $n = -1$, the k-integrals are

$$\frac{1}{a} \int_0^\infty k^{-1} J_m(ks) \; J_{m-1}(kd) \; J_{-1}(ka) \; dk \;=\; 0 \;, \qquad \int_0^\infty J_m(ks) \; J_{m-1}(kd) \; J_2(ka) \; dk \;=\; 0$$ (43)

and consequently only terms involving $n = 1$ contribute. (In these calculations use has been made of the identity $J_n'(ka) = -n/ka \, J_n(ka) + J_{n-1}(ka)$).

Use of these results gives the result

$$F_{\tau i}^m = -\frac{\rho \omega \, a^2 \, m^2}{2d^{m+1}} \int_0^b \int_{-\sigma_0}^{\sigma_0} M(s,\sigma)(s)^{m+1} \sin m(\theta + \sigma) \, d\sigma \, ds , \tag{44}$$

which when compared with the result for the direct effect given by (36) shows that the force from the image generated pressure distribution is exactly equal to that produced by the blades alone, or

$$F_{\tau i}^m = F_{\tau d}^m \tag{45}$$

or the total blade thickness force is

$$F_\tau^m = 2F_{\tau d}^m . \tag{46}$$

Using slender section theory, the source strength M is related to the thickness distribution τ by

$$M = -\frac{V}{s} \frac{\partial \tau}{\partial \sigma} , \tag{47}$$

where V is the resultant velocity $\sqrt{U^2 + (\omega s)^2}$. The remaining integrations in (44) are elementary; they are expedited by using the practical relation

$$V \left(\frac{d\tau}{d\sigma} \right)_{\sigma_0} = \text{a constant}.$$

The final result for blades having sharp leading and trailing edges and whose sections are symmetrical may be written in the form:

$$\frac{F_\tau^m}{T} = \frac{-0.7m(t/c) \sqrt{(0.7\pi)^2 + J^2}}{2^{m-3}(m+1) T_c J^2} \frac{A^2}{\left[\frac{A+1}{2} + C \right]^{m+1}} \cos(m\sigma_0 + \epsilon) \cos m\theta , \tag{48}$$

where

t/c   is the blade thickness ratio at the 0.7 radius

J   is the advance ratio

T_c is the thrust loading coefficient $\dfrac{T}{1/2 \, \rho \pi b^2 U}$

A   is the cylinder diameter in multiples of the propeller diameter

C is the tip clearance in fraction of propeller diameter

$\epsilon = \tan^{-1} (1/m\sigma_o)$, $2\sigma_o$ is the sector angle formed by the projection of the blade outline in the y-z plane.

(A factor $\sqrt{1 + (1/m\sigma_o)^2}$ has been taken equal to unity.)

Numerical evaluation of (48) will be taken up after derivation of a similar expression arising from loading.

Couple About Vertical Axis

The blade frequency moment due to the direct effect of blade thickness is given by

$$M_{zz}^m = -a\rho \int_{-\infty}^{\infty} \int_0^{2\pi} x \left(\frac{\omega\partial}{\partial\theta} - \frac{U\partial}{\partial x} \right) \phi_\tau^m (x, a, \gamma) \cos \gamma \, d\gamma \, dx . \tag{49}$$

Inspection shows that ϕ_τ^m is an even function of x; hence its x-derivative will be odd in x and hence will contribute, whereas the term

$$x \frac{\partial}{\partial\theta} \phi_\tau^m$$

will integrate to zero. Since the distribution of pressure which produces a moment is an odd function about the axis, the moment is referred to as a couple.

Integration by parts will reduce (49) to the form

$$M_{zz}^m = -a\rho U \int_{-\infty}^{\infty} \int_0^{2\pi} \phi_\tau^m (x, a, \gamma) \cos \gamma \, d\gamma \, dx. \tag{50}$$

But this integration is essentially the same as was done to find the force associated with the same potential as may be seen by inspecting (33) and (34). We may write down the result immediately by merely replacing ω by U and replacing $\cos m\theta$ by $-1/m \sin m\theta$ to correct for the θ-differentiation required in (34). We then multiply the final result by 2 since the image system will produce an equal contribution. The result is

$$\frac{\left(M_{zz}^m \right)_\tau}{Tb} = \frac{0.7 \ (t/c) \sqrt{(0.7\pi)^2 + J^2}}{\pi 2^{m-3}(m+1) T_c J} \frac{A^2}{\left[\frac{A+1}{2} + C \right]^{m+1}} \cos (m\sigma_o + \epsilon) \sin m\theta . \tag{51}$$

The outstanding feature of the expressions for the vibratory force and couple as given by (48) and (51) is their very rapid attenuation with increase of blade number. Numerical evaluation will be taken up after development of similar formulas for the force and couple arising from torque and thrust loading.

632

and consequently only terms involving $n = 1$ contribute. (In these calculations use has been made of the identity $J'_n(ka) = -n/ka \, J_n(ka) + J_{n-1}(ka)$).

Use of these results gives the result

$$F^m_{\tau i} = -\frac{\rho \omega \, a^2 \, m^2}{2d^{m+1}} \int_0^b \int_{-\sigma_0}^{\sigma_0} M(s,\sigma)(s)^{m+1} \sin m(\theta + \sigma) \, d\sigma \, ds , \tag{44}$$

which when compared with the result for the direct effect given by (36) shows that the force from the image generated pressure distribution is exactly equal to that produced by the blades alone, or

$$F^m_{\tau i} = F^m_{\tau d} \tag{45}$$

or the total blade thickness force is

$$F^m_{\tau} = 2F^m_{\tau d} . \tag{46}$$

Using slender section theory, the source strength M is related to the thickness distribution τ by

$$M = -\frac{V}{s} \frac{\partial \tau}{\partial \sigma} , \tag{47}$$

where V is the resultant velocity $\sqrt{U^2 + (\omega s)^2}$. The remaining integrations in (44) are elementary; they are expedited by using the practical relation

$$V \left(\frac{d\tau}{d\sigma} \right)_{\sigma_0} = \text{a constant.}$$

The final result for blades having sharp leading and trailing edges and whose sections are symmetrical may be written in the form:

$$\frac{F^m_{\tau}}{T} = \frac{-0.7 m(t/c) \sqrt{(0.7\pi)^2 + J^2}}{2^{m-3}(m+1) T_c J^2} \frac{A^2}{\left[\frac{A-1}{2} + C \right]^{m-1}} \cos(m\sigma_0 + \epsilon) \cos m\tau . \tag{48}$$

where

    t/c is the blade thickness ratio at the 0.7 radius

    J is the advance ratio

    T_c is the thrust loading coefficient $\dfrac{T}{1/2 \, \rho \pi b^2 U}$

    A is the cylinder diameter in multiples of the propeller diameter

Force and Couple Arising from Blade Loading

The calculation of the vibratory effects on the cylinder due to blade loading follows a pattern essentially the same as developed above. Since the development of these forces has been given recently [18], only the main results will be cited here.

The total load-associated potential given by a distribution of doublets over the helicoid swept out by any one blade as given by Eq. (5) is expanded in a Fourier series in θ and only m times the mth harmonic term of this single-bladed representation is retained. This is written as

$$\phi_\ell^m = \frac{m}{2\pi} \int_0^b \int_0^\infty \Gamma(s') \, D(x',\theta') \int_0^\infty J_m(kr') \, J_m(ks')$$

$$\times \ e^{-k|x'+U\tau|} \ dk \ d\tau \ ds \ \cos m(\theta' - \gamma' - \omega\tau) \,, \tag{52}$$

where

$$D(x',\theta') = \omega s \frac{\partial}{\partial x'} + \frac{U}{s} \frac{\partial}{\partial \theta'} \ .$$

Figure 11 serves to define the coordinate system.
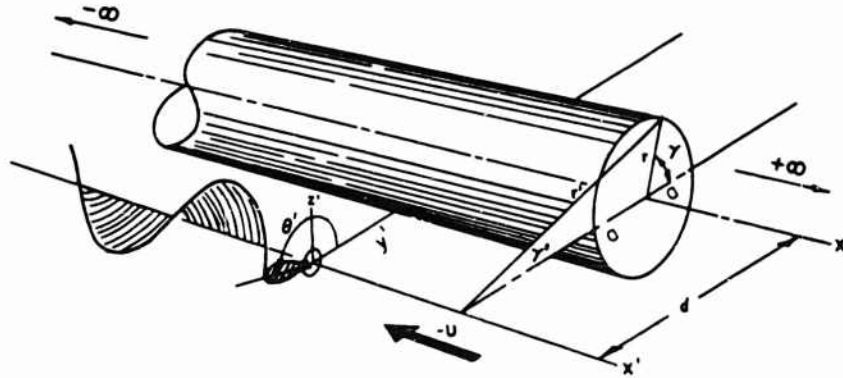
Figure 11

The τ-integration can be carried out, taking proper account of the sign of $x' + U\tau$ and this results in different expressions for positive and negative x'. This result is then expressed in terms of the coordinates fixed in the cylinder through the use of the addition theorem, Eq. (30), to provide

$$\phi_\ell^m = \frac{m}{2\pi U} \int_0^b \Gamma(s) \ D(x, \theta) \sum_{n=-\infty}^{\infty} H_n(x, r, s) \ e^{i[m\theta + n(\gamma - \pi)]} \ ds , \qquad (53)^*$$

where

$$H_n = \int_0^\infty \frac{J_n(kr) \ J_{m+n}(kd) \ J_m(ks) \ f(x,k) \ dk}{k^2 + \beta^2}$$

$$f(x,k) = (k - i\beta) \ e^{-kx} \qquad \text{for} \quad x > 0$$

$$= 2ke^{i\beta x} - (k + i\beta) \ e^{kx} \qquad \text{for} \quad x < 0$$

and

$$\beta = \frac{m\omega}{U} .$$

All primes have now been dropped for ease of writing, the quantities x, r and γ referred to the cylinder having been introduced; ξ and s remain from the old coordinate system.

The image of this potential in the cylinder is given by

$$\phi_{\ell i}^m = -\frac{m}{2\pi^2 U} \int_0^\infty \left\{ \int_{-\infty}^0 F(\xi, \lambda, r, \theta, \gamma) \ d\xi + \int_0^\infty F(\xi, \lambda, r, \theta, \gamma) \ d\xi \right\} \cos \lambda (x - \xi) \ d\lambda . \qquad (54)$$

where

$$F = \int_0^b \Gamma(s) \ D(\xi, \theta) \sum_{n=-\infty}^{\infty} \int_0^\infty \frac{k J_n'(ka) \ J_{m+n}(kd) \ J_m(ks) \ K_n(\lambda r) \ f(\xi, k)}{\lambda (k^2 + \beta^2) \ K_n'(\lambda a)}$$

$$\times \ e^{i[m\theta + n(\gamma - \pi)]} \ dk \ ds$$

$$f(\xi, k) = (k - i\beta) \ e^{-k\xi} \qquad \xi > 0$$

$$= 2ke^{i\beta\xi} - (k + i\beta) \ e^{k\xi} \qquad \xi < 0 .$$

It can be observed that differentiating (54) with respect to r, and setting $r = a$ yields the double Fourier integral representation of

$$- \left. \frac{\partial \phi_\ell^m}{\partial r} \right|_a$$

and hence the boundary condition required of the image potential is satisfied.

---

*It is to be understood that only the real part is retained.

It is again found that the force arising from the pressures due to the propeller torque loading and that from the image system are equal. As the integrations are very similar to those met in considering blade-thickness effects, we may simply state the very simple result:

$$F_q^m = \frac{-\rho m^2 a^2 U}{2d^{m+1}} \int_0^b s^{m-1} \Gamma(s)\,ds \times \sin m\theta. \tag{55}$$

Here the subscript q is used to indicate that the force is obtained from the pressure p_q^m associated with the torque-producing loading on the blades. Inspection of Eq. (13) shows that the thrust-connected pressure p_t^m is an odd function of x and will consequently integrate to zero.

This amazingly simple result for any distribution of circulation may be easily evaluated for the very practical distribution $\Gamma = \Gamma_o(b-s)s$ previously discussed. (Actually Γ should be made zero at the blade root or hub radius s_h and this could be readily accommodated.) As previously, the value of the constant Γ_o can be found and the resulting indicated expression for Γ inserted in (55).

The total lateral force due to blade loading (after multiplying by 2.0 to account for the image contribution) is then obtained in the form:

$$\frac{F_\ell^m}{T} = \frac{-3mJ}{-2^{m-1}(m+1)(m+2)} \times \frac{A^2}{\left[\frac{A+1}{2} + C\right]^{m+1}} \sin m\theta. \tag{56}$$

Comparison of this with the lateral force from blade thickness (48) shows that it is out of phase with that force but it possesses the same dependence on cylinder size A and tip clearance C.

The vibratory couple arising from blade loading is contributed only by the thrust-associated pressure since this is an odd function of x whereas the torque-connected pressures are an even function of x, which can produce no moment. Again the image distribution produces an equal contribution so that the total loading-induced couple is

$$\frac{\left(M_{zz}^m\right)_\ell}{Tb} = \frac{3}{2^{m-1}(m+3)(m+4)} \frac{A^2}{\left[\frac{A+1}{2} + C\right]^{m+1}} \cos m\theta. \tag{57}$$

This couple is, as expected, out of phase with the couple produced by blade thickness. In summary then, there are a pair of out-of-phase forces which act on the cylinder in the plane of the propeller—one associated with blade thickness, the other associated with blade loading. In addition, there are a pair of out-of-phase vibratory couples arising from the asymmetrical distributions of these pressures. Thus the excitation in the case of this symmetrical boundary is a single resultant force and a couple, each of which are out-of-phase with the blade and whose center of action is in the plane of the propeller.

Numerical Evaluation and Discussion of Results

The foregoing expressions for vibratory force have been evaluated for the cases of a 3, 4 and 5-bladed propeller operating at an advance ratio $J = 0.8$ and thrust loading coefficients $T_c = 0.529$, 0.556 and 0.636, respectively. The circular sector representing the blade outline was taken to have semi-angles $\sigma_o = 22°$, $17°$ and $16°$ for $m = 3$, 4 and 5 respectively, and the blade thickness ratio at $s = 0.7b$ is taken as $t/c = 0.05$. The tip clearance C in fraction of propeller diameter was held at 0.2 and the force-thrust ratio found for various cylinder diameters. Results for loading and thickness contributions and their resultant modulus are shown on Fig. 12.
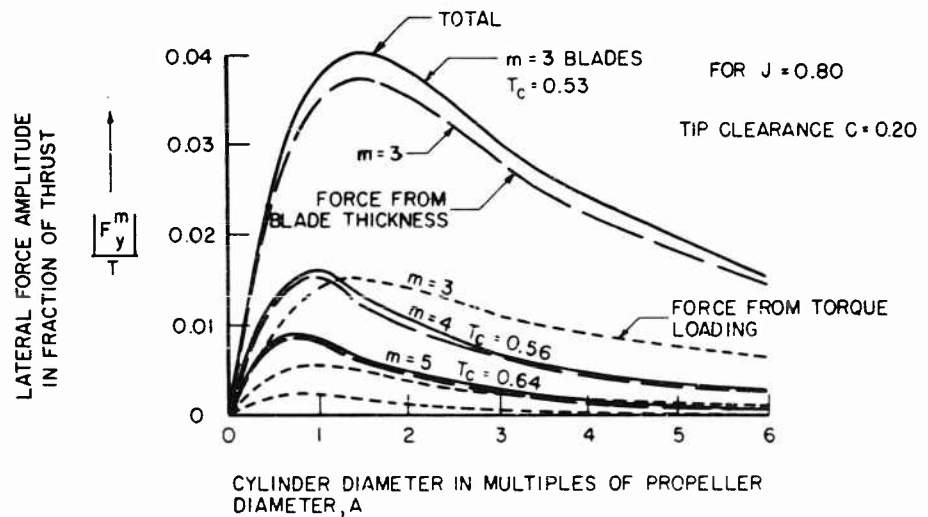
Fig. 12 - Amplitudes of blade frequency lateral force on a cylinder

It is perhaps surprising to see that the blade thickness effect predominates over the loading effect. This is due in part to taking values of T_c close to 0.5. For naval vessels, this coefficient may be as high as 0.75 which could reduce the magnitudes of F_y^m/T by 2/3. It is to be noted that the maximum force of 0.04T is achieved for a 3-bladed propeller on a cylinder relatively small with respect to the propeller.

A plot of the vibratory couples is given in Fig. 13. Here the loading effect predominates over the blade thickness effect. The variation of the couple with tip clearance for a 3, 4 and 5-bladed propeller in the case of a cylinder having a diameter equal to twice the propeller diameter is exhibited on Fig. 14. The trend of the lateral force with tip clearance would be the same. It may be seen that increasing the tip clearance from 20 to 30 percent of the propeller diameter will reduce the force by 21, 25 and 29 percent for $m = 3$, 4 and 5 blades respectively.
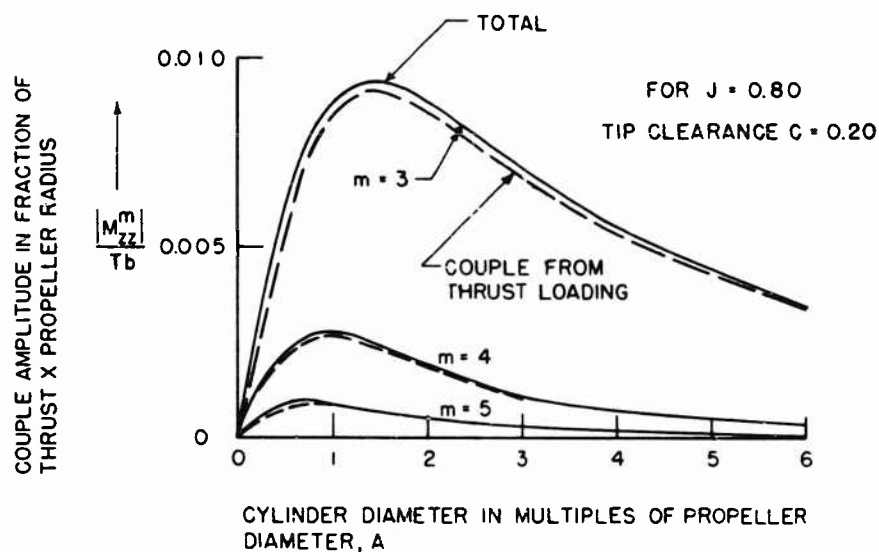
Fig. 13 - Amplitudes of blade frequency couple on a cylinder
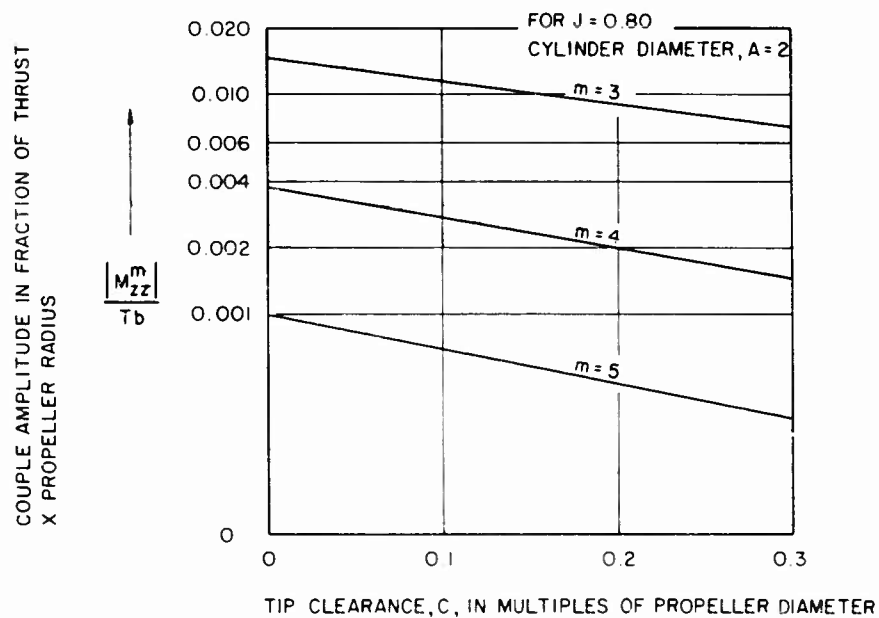
Fig. 14 - Amplitudes of blade frequency couple on a cylinder

637

RECOMMENDATIONS FOR FUTURE WORK

While the foregoing theory and resulting formulae are useful in revealing trends (and they are certainly simple in structure!) they do not apply directly to ships whose geometries are different from that of a cylinder. The case of an actual ship-propeller configuration may be attacked now because computer techniques have been devised by A. M. O. Smith [19] and his colleagues for solving three-dimensional potential flow problems.

The ship may be represented by a continuous distribution of sources over the surface which can be extended to the reflected form above the locus of the free surface for very low Froude numbers. The relation between the flow normal to this surface of sources and the source density σ is

$$v_n = \frac{\sigma}{2} - \iint_S \sigma \frac{\partial}{\partial n} \left(\frac{1}{R}\right) dS . \tag{58}$$

For the ship alone moving through calm water v_n is specified by the speed of advance and the normal to the surface at each point. Therefore (58) is a Fredholm integral equation of the second kind. Smith [21] has successfully programmed the 7090 computer to solve this integral equation for fairly arbitrary bodies. To insert a propeller into the flow, one need only find the additional source distribution σ_p which would just annul the normal incident flow imposed by the loading and thickness elements of the propeller. This presumably could also be done by the same program by limiting the mesh to the ship surface in proximity to the propeller. Once the source strengths σ and σ_p are known, the forces acting on the ship can be computed by a straightforward application of the extended Lagally theorem. The calculation may then be refined by putting in the appropriate image of the propeller in the free surface and finally the inclusion of wake effects might be attempted by calculating the pressure loading on the blades operating in a given wake distribution provided from a model test.

Thus the availability of the computer program to invert (58) and the existence of the very powerful and concise extended Lagally theorem for non-stationary flows involving sources (and doublets) places the computing of vibratory forces on actual ship hulls within our immediate grasp.

CONCLUSIONS

It is believed that the theory developed by the writer and his associates at the Davidson Laboratory shows that in certain cases the forces induced by the near field effects of a propeller can be of serious magnitude. Furthermore, the simple formulas given herein allow quantitative estimates of these forces to be made which are applicable to multiple screw ships whose hull areas in way of the propeller are relatively flat. These estimates provide a numerical scale by which one may judge the advantage to be gained by changing tip clearance, number of blades and thrust. In all cases, a manifold reduction of these excitations can be achieved by changing the number of blades from 3 to 5. The reductions of pressures and forces with increase of blade number are much larger than previous intuitive estimates.

Finally, a way is now open for computing vibratory forces on actual hulls which would overcome the limitations encountered through the use of simple mathematical surfaces such as plates and cylinders.

ACKNOWLEDGMENTS

REFERENCES

1. Gutin, L., "On the Sound Field of a Rotating Propeller," NACA TM 1195, 1958 (translation from Phys. Zeitchr., band 9, 1946, pp. 57-71).

2. Babaev, N.N., and Lentjakov, V.G., Some Aspects Concerning General Ship Vibration (book in Russian) State Publishing House, Shipbuilding Branch, 1961.

3. Pohl, K.H., "Das Instationäre Druckfeld in der Umgebung eines Schiffspropelleres und die von ihm auf Benachbarten Platten erzengten Periodischen Krafte," Schiffstechnik, Vol. 32, June 1959.

4. Breslin, J.P., "The Pressure Field Near a Ship Propeller," Jour. of Ship Research, Vol. 1, No. 4, March 1958.

5. Lewis, F.M., "Propeller Vibration," Trans. Soc. Nav. Arch. Mar. Engrs., Vol. 43, pp. 252-287, 1935.

6. Tachmindji, A.J., and Dickerson, M.C., "The Measurement of Oscillating Pressures in the Vicinity of Propellers," DTMB Report No. 1130, April 1957.

7. Breslin, J.P., and Landweber, L., "A Manual for Calculation of Inception of Cavitation on Two and Three-Dimensional Forms," T and R Bulletin No. 1-21, Soc. Nav. Arch. Mar. Engrs., N.Y., 1961.

8. Breslin, J.P., and Tsakonas, S., "Marine Propeller Pressure Field Due to Loading and Thickness Effects," Trans. Soc. Nav. Arch. Mar. Engrs., Vol. 67, 1959, pp. 386-422.

9. Sluyter, M.M., "A Computational Program and Extended Tabulation of Legendre Functions of Second Kind and Half Order," Therm Advanced Research Report TAR-TR 601, August 1960.

10. Tsakonas, S., Breslin, J.P. and Jen, J., "Pressure Field Around a Marine Propeller Operating in a Wake," Davidson Lab. Report 857, May 1962.

11. Breslin, J.P., "A Theory for the Vibratory Effects Produced by a Propeller on a Large Plate," Jour. Ship Research, Vol. 3, No. 3, December 1959.

12. Lurye, J.J., Penkus, O., and Feit, D., "The Unsteady Forces Due to Propeller-Appendage Interaction," Technical Research Group TRG-146-FR, March 1962.

13. Tsakonas, S., Breslin, J.P. and Jacobs, W.R., "The Vibratory Force and Moment Produced by a Marine Propeller on a Long Rigid Strip," Jour. Ship Research, Vol. 5, No. 4, March 1962, pp. 21-42.

14. Pohl, K.H., "Die durch eine Schiffsschraube auf benachbarten Platten erzengten periodischen hydrodynamischen Drücke," Schiffstechnik Heft 35, Band 7, Feb. 1960, pp. 5-18.

15. Reed, F.E., and Bradshaw, R.T., "Ship Hull Vibrations - 2," Conesco Report No. F-101-2, U.S. Navy Contract NObs 77150, June 1960.

16. Watson, G.N., A Treatise on the Theory of Bessel Functions, Cambridge at the University Press, 1952 (second edition).

17. Bateman Project, Tables of Integral Transforms, Volume 11, McGraw-Hill Book Company, Inc., 1954.

18. Breslin, J.P., "Propeller-Induced Vibratory Forces on a Cylindrical Ship (Arising from Blade Loading)," Presented at Symposium on Ship Theory, Institut für Schiffbau Hamburg, January 1962 (to appear Schiffstechnik 1962).

19. Smith, A.M.O., and Hess, J.L., "Calculation of Non-Lifting Potential Flow about Arbitrary Three-Dimensional Bodies," Douglas Aircraft Co. Report ES 40622, 15 March 1962.

* * *

CORRELATION OF MODEL AND FULL-SCALE PROPELLER ALTERNATING THRUST FORCES ON SUBMERGED BODIES

J. B. Hadler, P. Ruscus and W. Kopko
David Taylor Model Basin
Washington 7, D.C.

ABSTRACT

The results of full-scale trials and model tests which measured the propeller excited alternating thrust forces of two submerged submarines are presented and compared. These results are also compared to the alternating thrust as predicted by using four calculation methods which were based on propeller design theory and the wake survey as measured on the models. A description of the models and full-scale instrumentation is presented, and several methods of data processing and analysis are treated. In general, a rather limited success at correlation was attained.

INTRODUCTION

In recent years increased attention has been devoted to the fluctuations of the thrust and torque which are generated by a ship propeller operating in a circumferentially non-uniform wake field. Much experimental and theoretical work is being done by many investigators throughout the world. Most of the effort reported has been concentrated upon the measurement of these unsteady forces on ship models and the development of methods of predicting these forces from wake measurements. Although little exists in the literature on full-scale measurements, it is understood that a number of attempts have been made by various organizations with varying degrees of success. This is probably due to the complex problem of measuring these forces upon full-scale ships with elastic shafting and hull systems. A number of investigators have attempted to correlate the results of calculations with those predicted from model tests. In most of these attempts so many assumptions must be made that we do not have a clear indication of the validity of the methods of calculation.

As a consequence, the David Taylor Model Basin, as part of its Fundamental Hydromechanics Research Program, has embarked upon a program of investigations to improve our capabilities for both measuring these forces on model and

full scale, as well as predicting them by computational methods from wake measurements. In an attempt to simplify an exceedingly complex problem, the Model Basin has chosen for its initial work the single-screw submarine with the hope that a number of experimental problems will be minimized. The advantages expected in the use of the deeply submerged submarine over the surface ship are:

1. Surface waves are not generated, thus the propeller alternating force factors are essentially independent of speed, not considering Reynolds effect,

2. The model wake measurements may presently be made in a wind tunnel with greater rapidity and greater accuracy,

3. The full-scale tests are not influenced

    a. by the state of the sea,
    b. by problems of propeller cavitation,

4. The ship shafting system is usually shorter and stiffer, thus there are better chances of avoiding resonances, and

5. The hull structure is substantially stiffer, therefore, more probability of obtaining data at frequencies below hull resonance.

The initial investigations, including those contained in this report, have been further limited to the investigation of unsteady thrust only. This limitation was made for the following reasons:

1. The propeller thrust determined by computational means can usually be more accurately made because the viscous effects are usually of smaller significance to thrust than to torque.

2. The shafting systems on most of the single-screw submarines have torsional criticals somewhere in the operating range, whereas longitudinal criticals are usually above the operating range.

3. On some of the submarines, there is inadequate room for the installation of torsionmeter husks, whereas thrust bearings which can accommodate thrust-measuring equipment are installed on all vessels.

During the course of this work, it was necessary to develop techniques for measuring the model wakes in the wind tunnel and computer techniques for reducing the data into a useful form for the computation of the alternating-thrust forces. On the model, it was necessary to develop instrumentation for measuring the alternating thrust forces upon a submerged body. On the full-scale submarine, it was necessary to modify measuring equipment initially designed to obtain mean forces to measure the unsteady forces. Finally, it was necessary to develop a system for analyzing the unsteady forces measured on the model and full scale so they could be compared with each other as well as with the calculations. The descriptions of these developments are contained in this report.

Concurrently with the development of the above experimental techniques, further refinements were being made in the quasi-steady methods of calculating the alternating thrust and torque forces. Work was also started on developing an unsteady theory which might permit more precise determination of these forces.

To date, full-scale and model experiments have been carried out on two submarines with rather different wake patterns. Although these hulls are largely axi-symmetrical forms, the presence of superstructure and control surfaces provide strong enough wake variations to develop forces of measurable magnitude. The results of these experiments are presented in this report.

It was the hope of the authors that we could at this time report on the successful correlation of full-scale ship with model test results and verify the validity of some of the computational methods available. The uncertainties of the experiments, both full scale and model as well as the questionable validity of some of the computational techniques, indicate that much additional work needs to be done. Thus, this must be considered an interim report giving the current status of the work at the Model Basin with an outline of some of the problems which must yet be solved before successful correlation can be achieved.

INSTRUMENTATION

Early DTMB attempts to measure the alternating thrust forces on submerged models were hampered by a limited frequency response and a low signal to noise ratio in the test set up and instrumentation. As a consequence, a new instrumentation system has been developed for these tests. The specifications for the design of the alternating thrust dynamometer and recording system were based on the requirement that the propeller blade frequencies and its harmonics be measured up to 250 cycles per second. The instrument was designed as shown schematically in Fig. 1 with as high a natural frequency as possible above those to be measured. To accomplish this, the propeller shaft was made extremely stiff and the mass of the various components small. The stainless steel shafting was relatively short and thick, 15 1/4 inches long by 1 inch in diameter. The propellers were made of aluminum. The propeller shafting was supported by a very rigid aluminum frame, which in turn was enclosed by a fiberglass shell to form the hull-tail surface.

The natural frequency of the mechanical system was computed by using the simplified method of spring constants:

$$f = \frac{1}{2\pi} \sqrt{\frac{K}{M}}$$

where $K = \dfrac{1}{1/K_1 + 1/K_2 + 1/K_3} = 1.530 \times 10^5$ lb/in

where $M = M_1 + M_2 + M_3 = 2.67 \times 10^{-2}$

where f = natural frequency in cycles per second

M_1 = mass of propeller and fairwater = 2.2 lb/386.4"/sec^2

643

M_2 = mass of entrained water = 40% of bronze propeller = 4.0 lb/38/4''/sec^2

M_3 = mass of shaft = 4.1 lb/386.4''/sec^2

K_1 = spring constant of shaft = 7.0 × 10^5 lb/in

K_2 = spring constant of gage = 2.0 × 10^5 lb/in

K_3 = spring constant of foundation = 100 × 10^5 lb/in

$$f = \frac{1}{2\pi} \sqrt{\frac{1.530 \times 10^5}{2.67 \times 10^{-2}}} = 382 \text{ cps}$$

The natural frequency actually measured for the model and system was 325 to 450 cycles per second depending on the model, even though the thrust gage alone has a natural frequency above 5 kc.

The new instrumentation system, which was developed for these tests, employs a capacitance type force gage with a stiffness of about 200,000 lb/in. This capacitance gage is incorporated as a frequency determining element in a 1.5 mc oscillator circuit. As the diaphragm of the gage moves toward the fixed plate under the propeller thrust load, a proportional frequency shift occurs in the 1.5 mc oscillator. For typical gage configurations, this frequency shift approximates 5 kc. The fifth harmonic of the gage oscillator is processed in a super-heterodyne FM receiver with a 4.5 mc i.f. strip. The receiver yields a voltage output which is a linear function of the carrier frequency deviation which is itself a linear function of propeller thrust bearing load. Figure 2 is a block diagram of the system electronics.

The steady state component of the output of the FM receiver is removed in a potentiometer circuit. The voltage required to balance out the steady state component is, of course, the analog of the mean thrust bearing load. The alternating thrust component of output voltage, being in the order of 1 to 10 per cent of the mean thrust voltage, and being derived from a high-resistance source, is ordinarily insufficient to record directly. A DC amplifier providing a voltage gain of about 6 and a power gain of 3×10^5 is interposed between the receiver and the recording equipment. In cases where it is desired to record only selected frequency components, a continuously variable electronic filter is inserted between the amplifier and the recorder.

Two methods of data recording are used for model tests. For purposes of monitoring the progress of tests, the more useful one is a string oscillograph equipped with galvanometers having a flat frequency response up to about 300 cps. The tape recordings made during the tests are used as primary record. They can be readily analyzed in automatic data processing equipment.

Transducer, receiver, amplifier, and recorder overall sensitivity is easily determined in a static calibration procedure which consists merely of loading the transducer diaphragm with a series of known weights.

644
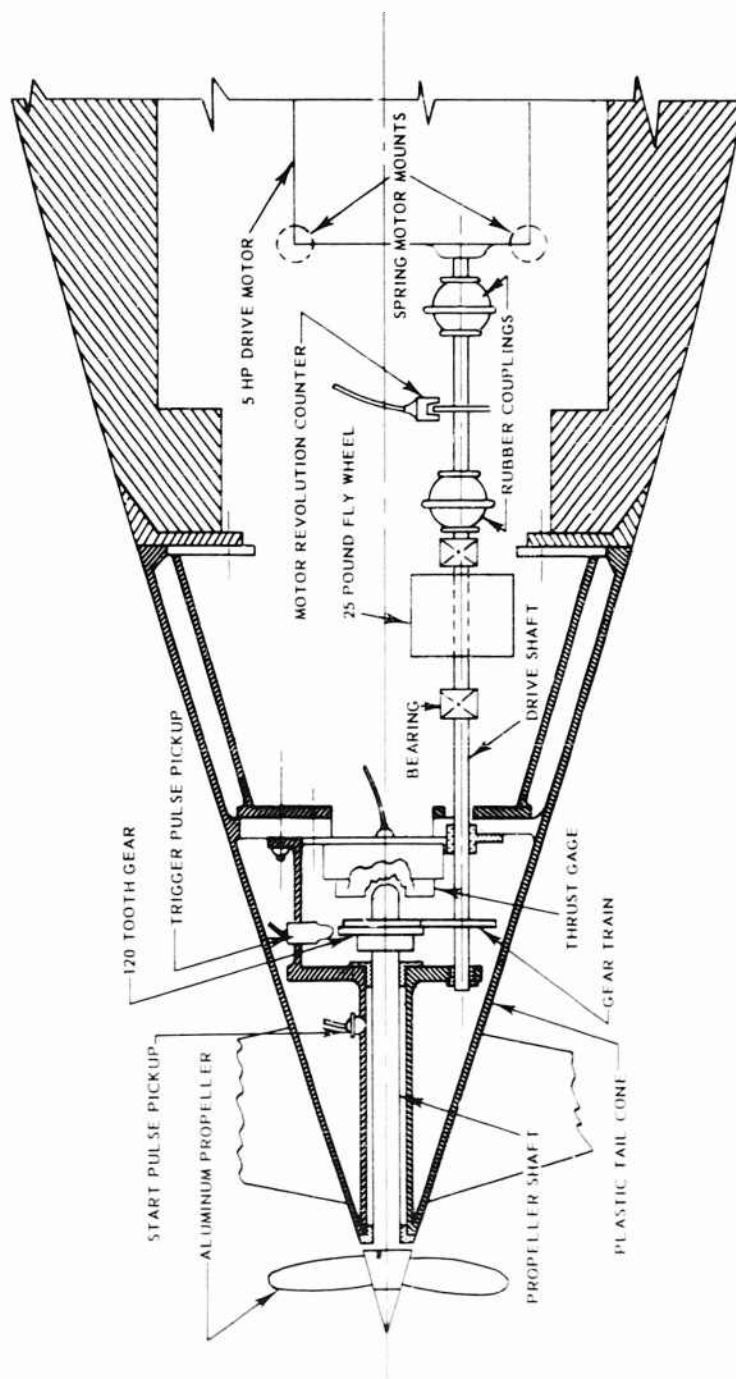
Fig. 1 - Arrangement of Alternating Thrust System in Model
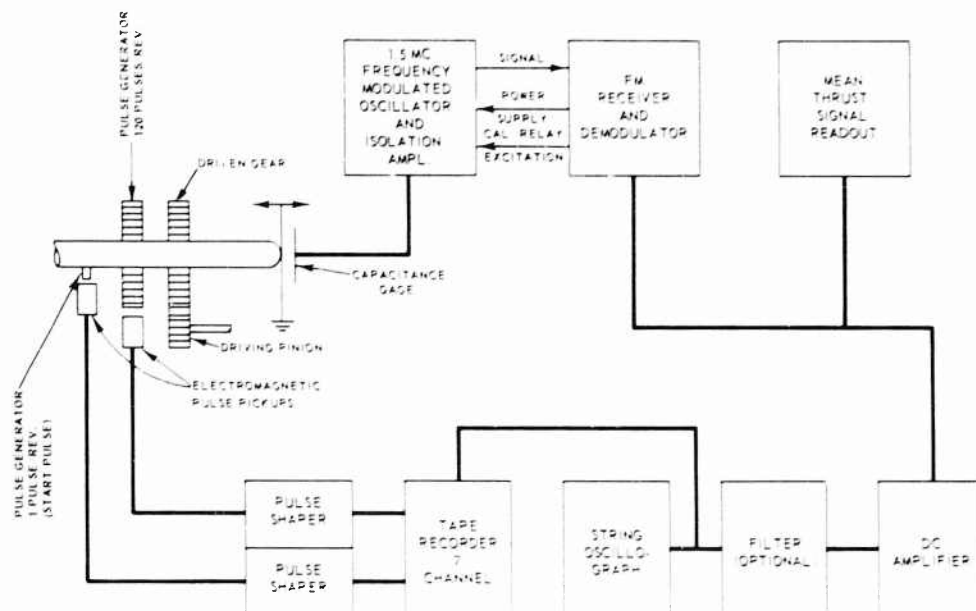
Fig. 2 - Schematic Drawing of Alternating Thrust Instrumentation
for Model

A satisfactory dynamic calibration is not so easy to achieve. With the
transducer installed in a model rigged for testing, an electromagnetic type
variable frequency vibration generator is directly coupled to the propeller shaft.
While a constant amplitude exciting current in the vibration generator armature
is varied in frequency, the overall output of the instrumentation from transducer
to recorder is observed. This type of calibration has been accomplished both
with the model in air and in water with no discernible difference in results.
Several resonance peaks are observable as the frequency of the generator is
varied from about 7 cps to 600 cps. The source of some of these peaks, at the
natural frequency of the vibration generator for instance, are easily recognized;
others, representing hull and component resonances in various modes, are not.
In the several models so far calibrated in this fashion, a high-amplitude reso-
nance has appeared in the frequency range of 325 cps to 450 cps depending upon
the model being tested. This apparent resonance is taken to be the resonant
frequency of the transducer with propeller and shafting. Consequently, during
actual carriage tests, signals higher than 250 cps are disregarded.

The magnitude of motor noise, gear noises, bearing noises, etc. coupled to
the transducer depends on the details of construction and mounting of these
various elements. To evaluate the various component arrangements which were
devised, the tail end of the shaft was enclosed in a reasonably air-tight container
and subjected to a 15-psi load. This provided a low noise source of mean thrust
on the transducer while the noise developed at various motor speeds was being
measured. It is recognized that the noise levels measured by this technique are
not necessarily the same as would be observed if the propeller shaft were sub-
jected simultaneously to a torsional load, but the arrangement at least allows a

fairly well-controlled set of conditions in which to observe mechanical noises of the system.

ANALYSIS METHODS

The unfiltered magnetic tape records are processed by two distinctly different methods, each of which yields useful although not necessarily identical results. The differences in finished data are a consequence of the characteristics of the methods of analysis employed.

In one instance, the tape is analyzed in the DTMB Seadac facility [1]*. For these tests the information output of this facility for any run is presented as a plot of the average of square root of the power available vs. frequency. Any point plotted represents the data passed through a filter having a band width of 5 cps. To the extent that shaft rpm and wake velocity are not constant, the alternating thrust forces generated are shifted in frequency. Provided that this shift in frequency does not exceed the 5 cps pass band of the Seadac filter, the data plot of the analyzer is not appreciably affected.

Typical records of the frequency spectrum produced by Seadac are shown in Figs. 3 and 4 for the models and Figs. 5 and 6 for the full-scale trials. The
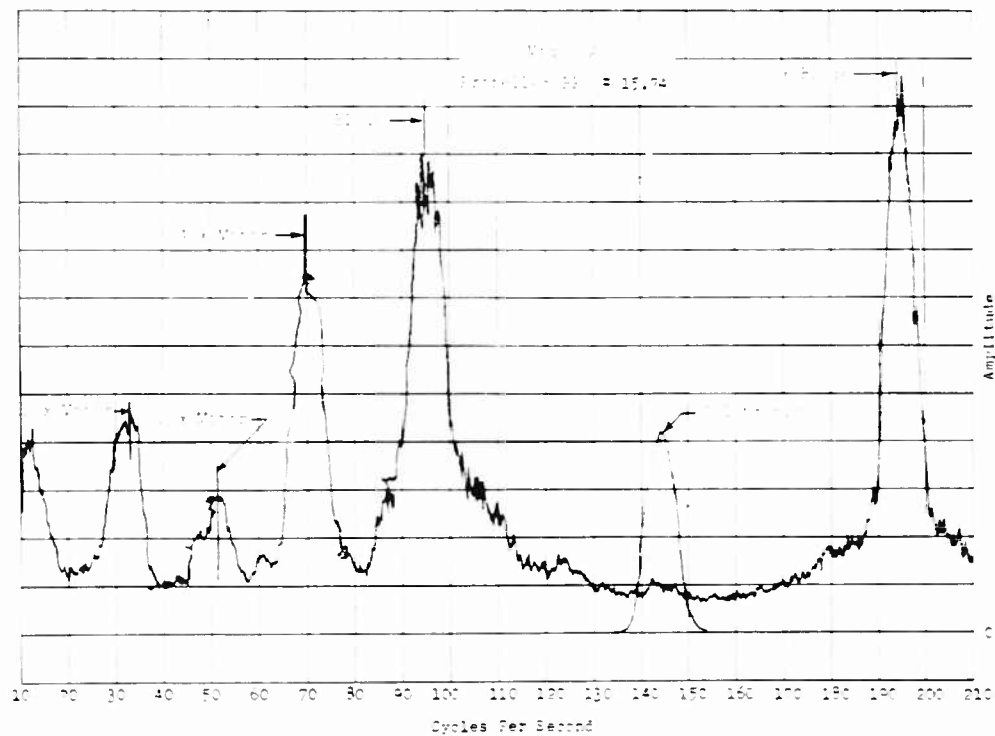
Fig. 3 - Typical Seadac Record for Model A

*References are listed at the end of this paper.
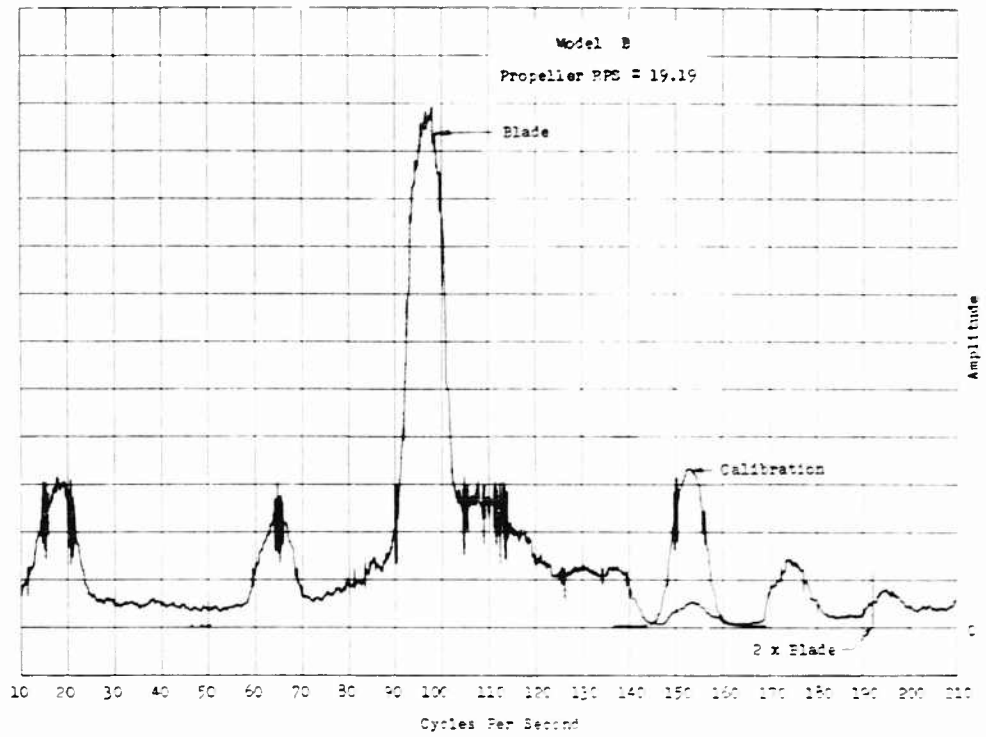
Fig. 4 - Typical Seadac Record for Model B

principal noise in the model measuring system is caused by motor frequency. its harmonics and the 60-cycle power source. It is evident from the model records that there is a general background signal level which persists over the total frequency range. The measured signal amplitude was found to vary from about zero to $1/4$ per cent of the mean thrust. These corrections were not applied to the results because the corrections were considered to be within the testing accuracy. If they were applied, however. the alternating thrust results would be lowered by approximately zero to $1/4$ per cent. In contrast. the full-scale Seadac records showed a very low noise level.

The second method of analysis consists of digitizing the signal waveform at uniform angular intervals of shaft rotation. say every 3 degrees. These intervals are marked on adjacent tape channels as the data are being recorded and are generated by two electromagnetic pickups. One pickup generated one pulse per shaft revolution. This pulse is called the start pulse. The second pickup. placed in close proximity to a steel gear. generates one pulse each time a tooth passes under it. Except where space limitation requires a smaller device. a 120-tooth gear is used. The pulse emanating from this second pickup is called the trigger pulse.

648
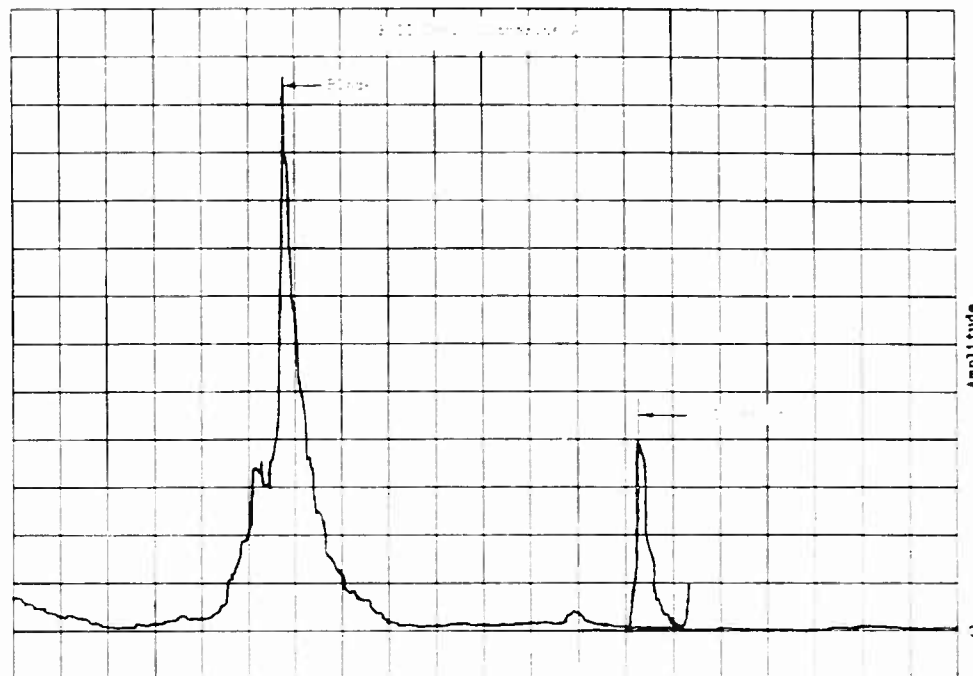
Fig. 5 - Typical Seadac Record for Full-Scale Tests of Submarine A

Operation of this data reduction system is briefly as follows: The tape signal is reproduced into the digitizing electronics. The digitizing equipment remains inoperative until arrival of a start pulse and a coincident trigger pulse. At this time the amplitude of the signal is measured and recorded in digital form. At the next trigger pulse (3 degrees later in shaft rotation), another reading of the signal amplitude is recorded until 120 pulses have been counted. The process is then repeated for a specific number of successive shaft cycles. This resulting digitized record is then entered into a digital computer which first computes the average amplitude of the signal wave for each of the 120 selected positions of the shaft. This average wave form is then analyzed for its Fourier coefficients. The plot of this average shaft rotation represents only the variation of propeller shaft thrust vs. shaft position: that is, time is not represented in this plot unless one assumes a uniform shaft rpm. If one does assume a uniform shaft rotational speed, the plot then represents the shaft frequency and its harmonics as measured after passing through the equivalent of an extremely narrow band filter (about .02 cps as compared to 5 cps for Seadac). It is this difference in band width which accounts for the diversity between outputs of the SEADAC DATA REDUCTION and the GATED DIGITAL REDUCTION SYSTEMS.

649
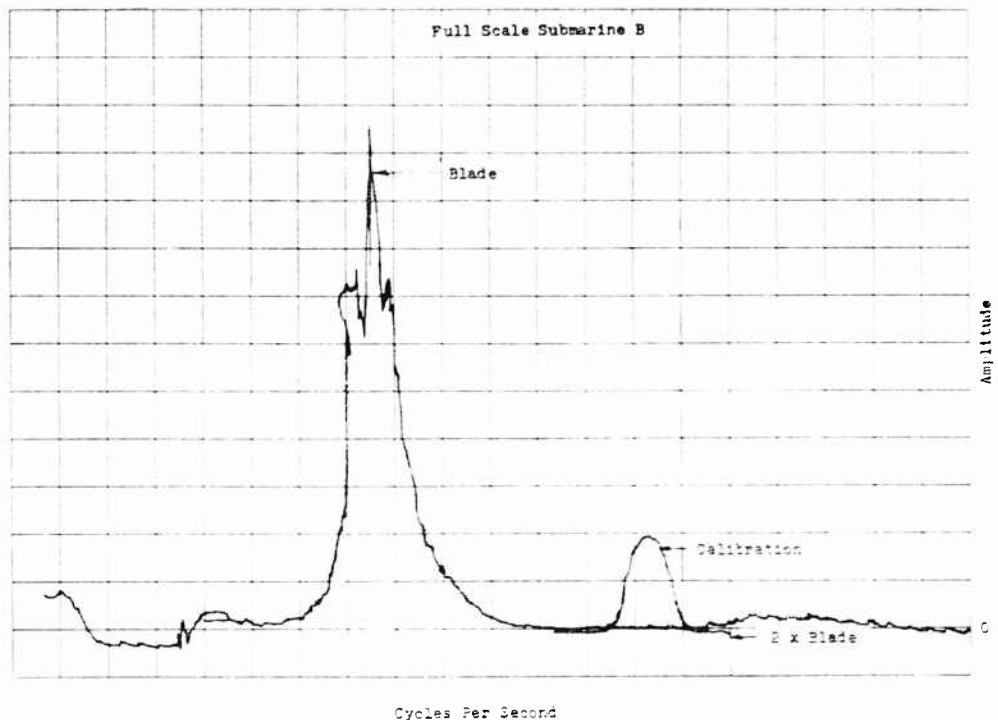
Fig. 6 - Typical Seadac Record for Full-Scale Tests of Submarine B

MODEL ALTERNATING THRUST TESTS

The alternating thrust tests were conducted with two existing models which simulate the full-scale submarines. Model A was 22.9 feet long with a plastic bow section, an aluminum mid-section and a combined wooden and plastic tail section. It was propelled by a 6-bladed aluminum propeller. Model B was a 15.0-foot mahogany model with a plastic tail section. It was driven by a 5-bladed aluminum propeller.

A photograph and schematic diagram of the alternating thrust gage and propulsion system are shown in Figs. 7 and 1 for Model B. The 5-HP motor drives the propeller through 1.11 to 1 reduction gears. This gear ratio was selected to insure that the harmonics of the driving motor frequencies would not coincide with the blade and twice-blade frequencies of 5- and 6-bladed propellers. The propeller shaft is not connected directly to the thrust gage but floats free on bearings until ahead thrust is applied. The thrust gage is mounted to a base plate which in turn is fastened to the hull bulkhead. The drive shaft was fitted in Model B with a 25-pound fly wheel. two soft couplings and soft motor mounts in an effort to reduce motor noise and torque variation. Model A. which was tested first, did not have the fly wheel. soft coupling arrangement: instead. it had a short drive shaft connected directly to the motor (not soft mounted).
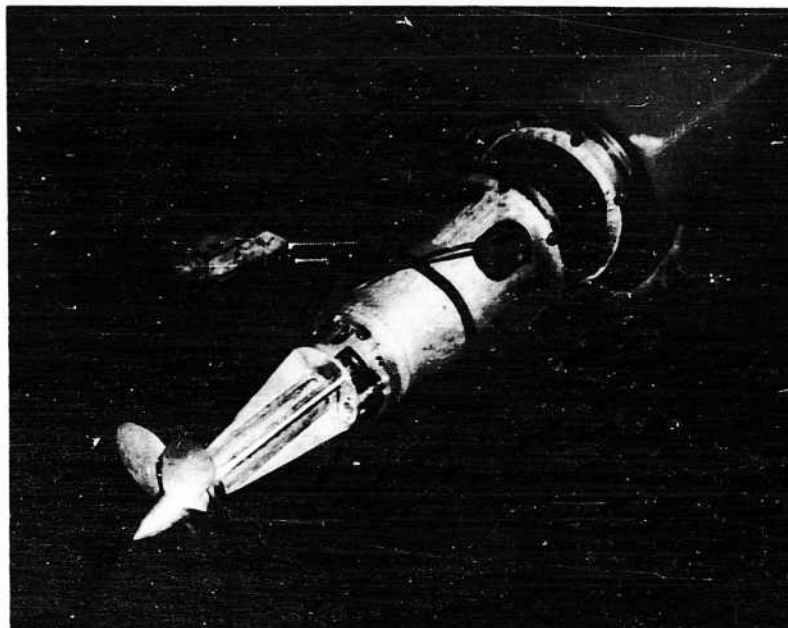
Fig. 7 - Photograph of Model with Alternating Thrust
Gage System

The model was ballasted for the test in the free-flooded condition to neutral buoyancy. During the tests, the model was towed at a deeply submerged depth by means of a towing strut which passed through the bridge fairwater. At this depth of submergence, the surface waves generated by the model are negligible so that Froude scaling could be ignored. Since the towing strut was enclosed by the sail, the distortion of the wake due to the proximity of the strut to the hull is kept to a minimum.

During the test runs, the model was propelled at the same propeller advance coefficient, J_a, as the ship. This was based on the concept that at the same J_a, the alternating thrust is a constant percentage of the steady state thrust.

$$J_a = \frac{V}{nd}$$

where J_a = propeller advance coefficient

V = speed of advance, ft/sec

n = propeller rps

d = propeller diameter, ft.

651

The J_a in the upper speed range is practically a constant, thus a single J_a was used for each model.

The fact that the tests need not be conducted according to Froude Law opened the range of propeller rotations and model speeds which can be used to obtain the ship J_a. The test results, which are based on runs at 4 or 5 different propeller frequencies, will probably give a better statistical average than a single test frequency repeated a number of times. When the results are plotted for a variety of frequencies, the evaluation and analysis are also made less difficult. Noise in the system which may distort the data, such as propeller shaft frequencies, 60-cycle line interference, motor shaft noise and its harmonics may be more easily identified and accounted for.

A satisfactory instrument operating procedure has been worked out for model testing. Before the start of a run, the propeller is run astern to achieve unloading of the thrust transducer; zero readings are then established, and the overall sensitivity is checked by means of a relay switched capacitance which shifts the gage oscillator frequency by an amount equivalent to some specific thrust load on the transducer.

After towing carriage speed and model propeller rpm have been stabilized at their desired levels, the mean thrust voltage is read and recorded. The mean thrust voltage is then removed from the receiver output, and the alternating thrust component is fed through the DC amplifier. All of the alternating thrust data are recorded on tape, that is, they are not modified by filtering. The tape record is always of sufficient length to include at least 500 shaft revolutions. The signal may also be filtered for blade rate and harmonics and applied to the recording galvanometer. Without such filtering, noise and extraneous signals would make it all but impossible to arrive at a reasonable estimate of the magnitude of the phenomena under observation.

A relatively simple and inexpensive method for obtaining a preliminary, on-site, determination of the mean amplitude of oscillation of a filtered record has been used at the Model Basin with some success. The only instrument required is a planimeter for measuring the area. The method is presented here in some detail because the results are usually consistent with those obtained from the Seadac and sampling system and are available shortly after completion of a test run. It is recommended that this method be used when the more sophisticated electronic analysers of computers are not available or when a reasonably good rapid analysis is required.

Typical records, filtered and unfiltered records, are shown in Figs. 9 and 8. It will be noted that the amplitude is not constant but shows a beat. To evaluate the record shown in Fig. 9, a convenient length of sample was chosen, in this case 10 inches. In the sample shown, the paper speed was 5 inches per second and the propeller rotation was 15.75 rps, so for a 10-inch record there were 189 cycles of propeller blade frequencies for a 6-bladed propeller. The area contained in the envelope of the frequencies of oscillation (top and bottom) is measured by means of a planimeter. The mean double amplitude of oscillation is obtained by dividing the area by the length planimetered. If the oscillations are very erratic, it may be necessary to planimeter more portions of the record to get a better statistical average.
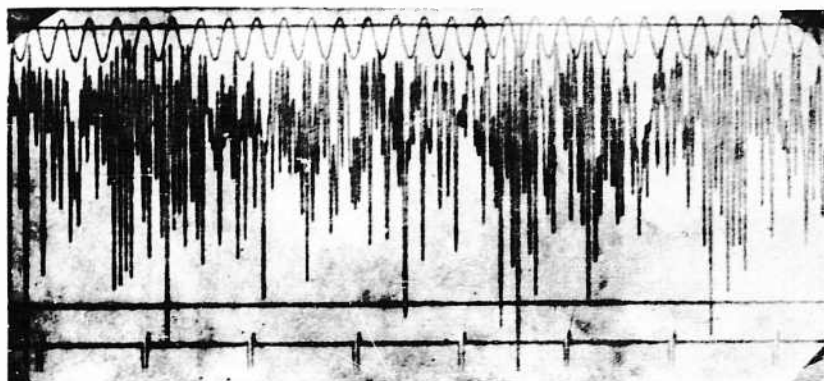
a. Not Filtered
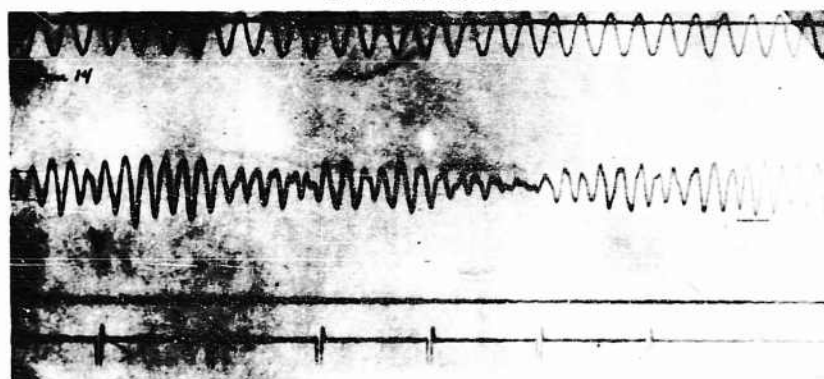
b. Filtered for Blade Rate
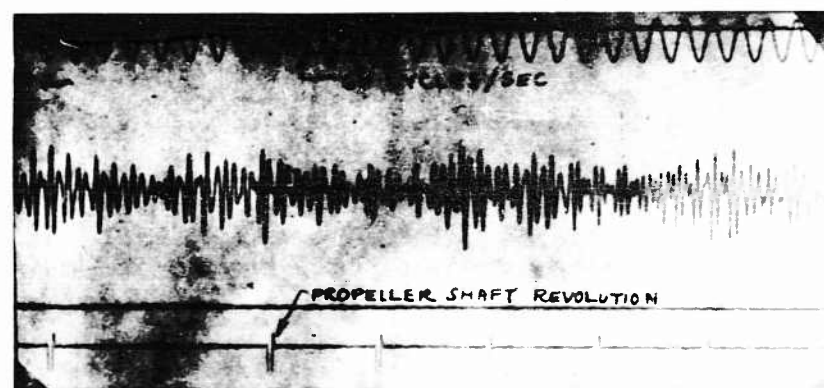
c. Filtered for 2 x Blade Rate

Fig. 8 - Typical Alternating Thrust Viscorder Record,
Record Speed 25 inch/sec.
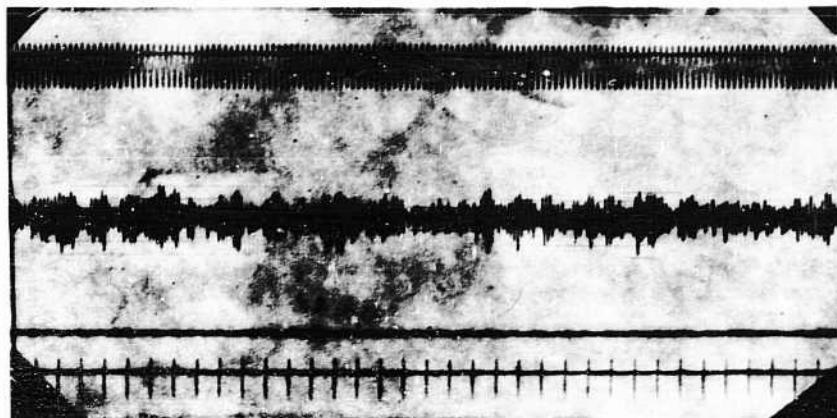
a. Filtered for Blade Rate
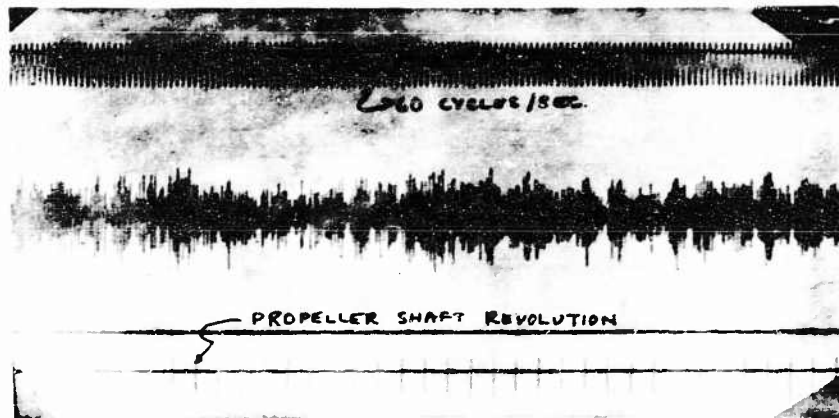
b. Filtered for 2 x Blade Rate

Fig. 9 - Typical Alternating Thrust Viscorder Record,
Record Speed 5 inch/sec.

FULL-SCALE TRIALS

The alternating thrust measurements on the full-scale ships were accomplished using a Kingsbury thrustmeter and a commercial pressure transducer. The recording instrumentation was the same as that employed in the model tests. Figure 10 is a schematic diagram of the trial instrumentation. Data analysis was accomplished by the same methods that were utilized for the model tests.

The test runs were made with the ship carefully trimmed to minimize the necessity for movement of control surfaces during the recording period. No records were made until after the ship had reached reasonably steady conditions as to speed, rpm, torque and thrust.

654
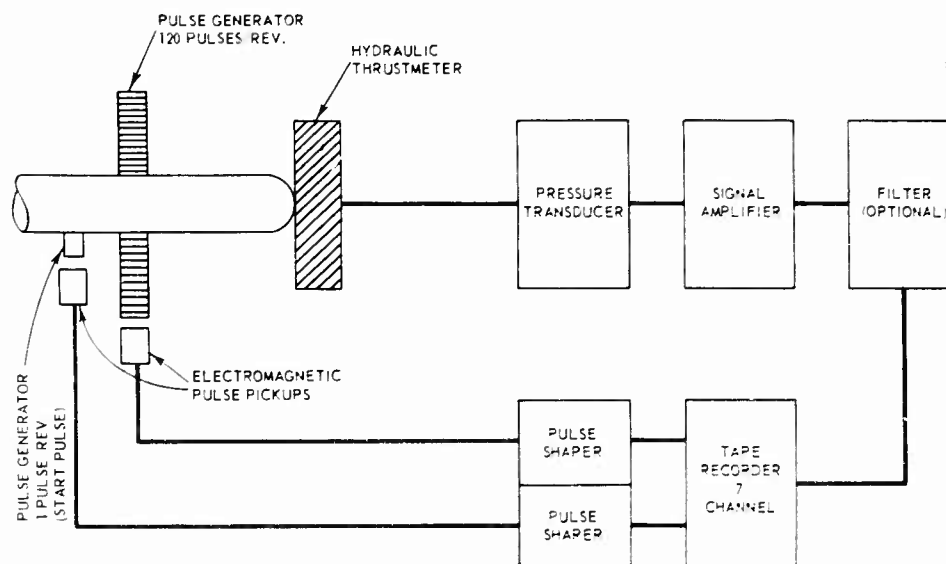
Fig. 10 - Schematic Drawing of Alternating Thrust Instrumentation
for the Full-Scale Submarine

MODEL WAKE MEASUREMENTS

The wake surveys were conducted in a wind tunnel at the Model Basin.[*]
Figure 11 shows a typical model and pitot tube rake installed in this facility.
The side of the models were mounted to the supporting strut in the tunnel. The
survey was conducted only in the upper half of the tunnel, strut interference
effects being avoided in this manner. Where the symmetry of the model was
destroyed because of angular settings on the stern control surfaces, the survey
was conducted in the upper half of the tunnel twice, first with the proper angular
control surface setting and again with the settings as they appear as a mirror
image of the other side of the ship. When the data were reduced, the two groups
of control settings were applied to the appropriate sides of the ship. The survey
was conducted at a minimum of 5 radii with approximately 48 circumferential
positions at each radius. The circumferential spacing is variable from 2.5
degrees behind control surfaces to 15 or 20 degrees in open areas.

The wake in way of the propeller was measured by a rake of 5-holed hemi-
spherical pitot tubes. The rake was previously calibrated in the wind tunnel to
derive curves for angle and head coefficients in the vertical and horizontal
planes.

For purposes of comparison, it was desirable to run the wind tunnel tests on
these models at the same Reynolds number as the tests conducted on the standard

---

[*]The use of a wind tunnel permitted the acquisition of much more data in less
time than was possible in water.
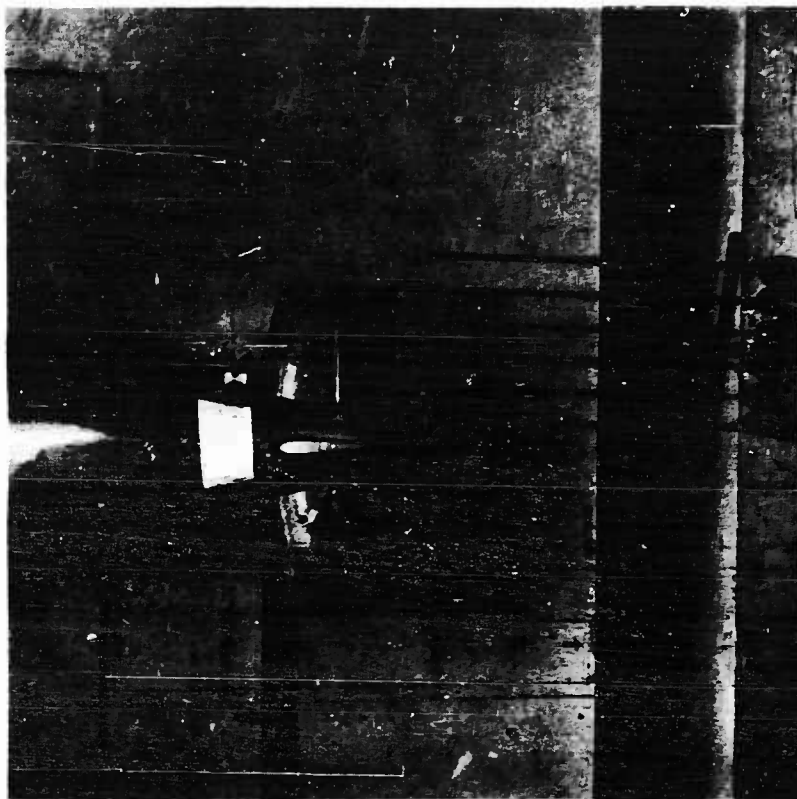
Fig. 11 - Photograph of Model in Wind Tunnel

models in water (Rn = 2.0 x 10^7). Since this would require a speed beyond the tunnel capability, it was necessary to conduct variable speed tests to determine the dependency on Reynolds number. These tests indicated that Reynolds number of 1.53 x 10^7 and larger, the velocity ratios were independent of Reynolds number. This value was then selected as the test speed.

One of the models was fitted with turbulence stimulators of the type recommended by Hama [2] around both the nose of the hull (0.05L) and the forward end of the bridge fairwater. These stimulators had no effect on the test results. It was concluded that the high-turbulence level of the tunnel made it unnecessary to stimulate turbulence.

The initial test data are reduced to longitudinal, tangential, and radial components of velocity by an ALWAC computer facility at the Model Basin.

Since the calculation of the forces can most easily be made at certain specified radii, an interpolation routine was developed for use on the IBM 7090 computer. This program is essentially a double interpolation routine whereby the measured values of velocity ratio are interpolated in both the radial and

656

circumferential directions. The interpolation formulas used assume that the desired value of y can be obtained from the following polynomial

$$y = a_0 + a_1 x + a_2 x^2 + \ldots + a_m x^m$$

in which the a_i have been determined so that this equation is satisfied by $m + 1$ pairs of the observed values $(x_i y_i)$. A value of m equal to 3 was used for this group of calculations. Output data for this program are presented at any designated radii usually 10 per cent increments of the radius, whereas the increment of circumferential position is constant at 2 1/2 degrees. Interpolated velocity ratios are shown in Figs. 12 and 13 as plots of circumferential distribution. The repeatability of the test spots from which these curves are derived is in the order of 2 per cent of free-stream velocity.

ALTERNATING THRUST CALCULATIONS

There are available to the propeller designer a number of methods for computing the alternating thrust and torque forces generated by a propeller in a non-homogeneous wake field. Most of these methods are based upon extensions of the lifting line or circulation theory evolved from the basic work of Lancaster [3], Prandtl, Betz [4] and Goldstein [5].

Much of the initial work was concerned with calculating the quasi-steady propeller forces. The propeller is assumed as it rotates through a variable wake to experience lift and drag at each blade element as if the blades were in steady flow at each instant. In these methods unsteady effects are not considered.

One of the earliest and more widely used quasi-steady methods was based on work published by Burrill [6] in 1944. His method uses the Goldstein correction factors for calculating the induced velocities; thus, the condition of normality is assumed. Corrections are made for slip-stream contraction based upon momentum considerations as well as for the theoretical blade section lift-slope curve and the theoretical no-lift angle of attack. The latter corrections are based upon experimental 2-dimensional section data for typical air foils and camber lines used in propeller design. Finally, corrections are made for cascade effects.

This method, as outlined in [6], has been programmed into an IBM 704 digital computer by the Electric Boat Division of the General Dynamics Corporation. The calculations in this report by the Burrill method were made with this program. The detailed computational steps are the same as those in DTMB report 1364 [7].

Subsequently, Lerbs [8] and Morgan [9] at DTMB developed the induction factor method of propeller design which removed the limitation of normality. This method of propeller design was programmed into an IBM 709 computer at the Model Basin. The program has now been inverted by Pien and Haskins [10]. It is used to calculate the quasi-steady forces of the moderately loaded propeller. Although the basic quasi-steady assumption is again made, it does provide a means for greater accuracies. In this program, experimental corrections to

657

Velocity Survey in Propeller Plane for
Submarine A

1. Tests conducted in Wind Tunnel with Model in Normal Condition.
2. V_x/V_m is Longitudinal Component and is Positive in the Astern Direction.
3. V_t/V_m is Tangential Component and is Positive in the Counterclockwise Direction.
4. Angle is given 0 to 360 degrees Counterclockwise from the Vertical.

DAVID TAYLOR MODEL BASIN   WASHINGTON 7, D. C.

April 1961
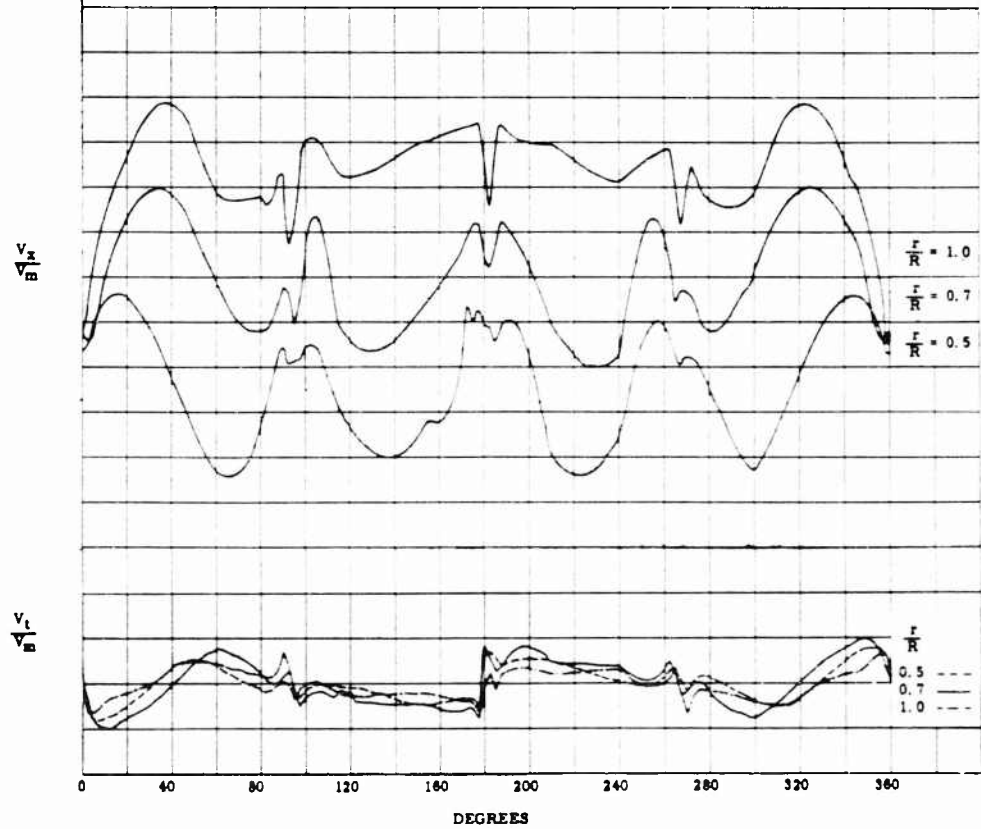
Fig. 12 - Wake Survey in Way of Propeller of Model A

VELOCITY SURVEY IN PROPELLER PLANE

FOR SUBMARINE B

1. Tests conducted in Wind Tunnel with Model in Normal Condition.

2. V_x/V_m is Longitudinal Component and is Positive in the Astern Direction.

3. V_t/V_m is Tangential Component and is Positive in the Counterclockwise Direction.

4. Angle is given 0 to 360 degrees Counterclockwise from the vertical.

DAVID TAYLOR MODEL BASIN   WASHINGTON 7, D. C.

MAY 1962
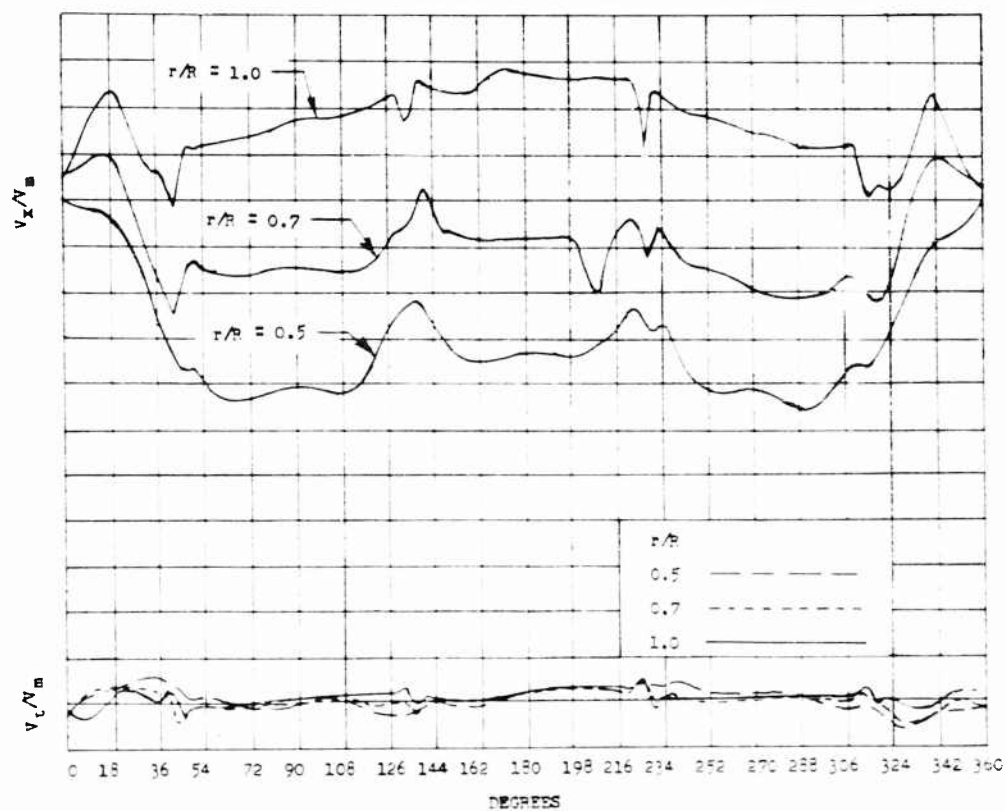
Fig. 13 - Wake Survey in Way of Propeller of Model B

the theoretical no-lift angle may be made for the type of camber line used and to the lift-slope curve for the type of section employed. Also, the removal of the condition of normality permits greater accuracy in the calculation of the induced velocities for the moderately loaded propeller. Thus, it should be expected that this method should provide greater accuracy if the basic assumption of a linearized quasi-steady theory is not overshadowing.

In recent years as the interest in the problem of unsteady propeller forces has grown, attempts have been made to add unsteady corrections derived from 2-dimensional theory of air foil sections moving rectilinearly through sinusoidal gusts. The basic hydrodynamic work upon which the unsteady corrections are derived is that published by Sears [11] in 1941. The first such work published using Sears unsteady correction was that of Ritger and Breslin [12] in 1958. This method employs Burrill's approach to calculate the quasi-steady forces and Sears' approach to calculate the unsteady forces. The detailed equations are developed in [12].

Since this method is based upon Burrill's method for calculating the quasi-steady forces, a modification has been made to the program at the Electric Boat Company by the Davidson Laboratories to calculate the unsteady forces. It was this program which was used to make the calculations by the Ritger-Breslin method.

Recently a number of investigators have been attempting to develop an unsteady propeller theory. This of necessity is an exceedingly complex problem. One of the theories has been programmed into a computer, but pilot calculations have not been satisfactory. Thus, none of the unsteady computational methods will be used in this report.

Concurrently with the above developments which are based upon progressively more complex mathematical models, a number of investigators have been attempting to provide numerically simpler means for permitting the naval architect and marine engineer to estimate relatively quickly without the use of digital computers the forces that might be expected. Such a method has been developed at DTMB by McCarthy [13] which utilizes the model open-water characteristics of the design propeller. This type of approach does not lend itself as readily to parametric studies during the early design stage unless the results of a systematic propeller series, such as the Troost Series, are available. It can be quite useful to the propeller designer for making estimates after a design has been established and a model propeller built and tested. For purposes of comparison with other more exact methods and with experimental results, predictions have been made of the unsteady forces for the ship configurations contained in this report.

The lifting line representation of the propeller blade assumes that the blades are chordless. The usual practice is to assume that the lifting line is represented at the chord mid-length. Thus, in obtaining the radial wake distribution for the quasi-steady calculations, it is usual to use the wake values that pertain at the chord mid-length. The unsteady 2-dimensional theory developed by Sears [11] uses as part of the boundary condition the unsteady flow condition which exists at the leading edge of the foil; thus, the location of the wake in relation to the chord length becomes important. In order to obtain some idea

of the magnitude of the effect, the quasi-steady calculations in this report have been made with the lifting line representation at two points, the chord mid-length and at the leading edge.

DISCUSSION OF RESULTS

Effect of Sample Size

In order to gain some insight into the consistency of experimental data, various sizes of samples were analyzed by the sampling system. For the full-scale ship trials, samples varying in size from 100 to 800 shaft revolutions were analyzed for 3 or 4 conditions on each ship. For the model, samples ranging from 25 to 400 were analyzed.

The data on Ship A and its model were very consistent both as to amplitude and to phase. For sample sizes larger than 200 on the ship, the maximum variation in the mean thrust was less than $1/2$ per cent. For blade frequency, the thrust variation was less than 0.1 per cent and for twice-blade frequency 0.13 per cent of mean thrust. The phase angle was stable, less than 0.8 degrees for blade frequency and any of the higher harmonics. All full-scale sampling system data on Ship A contained in this report are for samples larger than 300 shaft revolutions.

A similar degree of stability was noted in the results of Model A. The variation of the mean thrust was less than $1/4$ per cent for samples ranging in size from 25 to 300. The blade and twice-blade frequency forces varied less than 0.1 and 0.13 per cent, respectively, for 100 samples and greater. The phase variation was less than 0.3 degrees for the sample sizes mentioned above. The consistency of both the forces and phase measurements on model and full scale on this configuration is quite gratifying and would indicate that samples as low as 300 revolutions, full scale, and 100 revolutions, model, would be adequate for accurate results. All data on Model A is for 300 or more samples.

The data on Ship B and its model did not show the same degree of consistency. On the full-scale trials, five runs in the lower speed range have been analyzed for samples varying from 100 to 400 revolutions. Neither the amplitude nor the phase showed the consistency of hull A. Amplitude variations as great as 0.35 per cent of mean thrust were noted between 300 and 400 samples. Between 200 and 400 samples, variations as great as 1.0 per cent of mean thrust were noted. In most instances, phase angle variations between samples of 300 and 400 in size were usually less than 1 degree except in one case where the phase shifted 5 degrees. Between 200 and 400 samples, the variation was usually less than 1 degree although one case showed a 10-degree variation. This variation in phase is important in interpreting the value of the amplitude measurements. Since the sampling system acts as a "narrow" band filter, any significant variation in phase results in a tendency to produce a lower amplitude of the mean wave. In this case, the 1-degree shaft angle variation in phase (5 degrees in blade frequency) is quite small if the sample size is adequate. Thus, it may be concluded for the sampling system that the test runs which have large phase shift will tend to give lower amplitudes.

661

On the tests of Model B, the trigger pulse wave in the sampling system was not clear; therefore, it was not possible to make as complete a sample size study as that conducted on Model A. An analysis was made of two runs with samples varying from 25 to approximately 200. Within the limitations of the restricted sample size, these results tended to show consistency of data approaching that of individual runs of Model A. Comparing 75 and 200 samples showed variations in amplitude of less than 0.15 per cent for blade frequency and 0.3 per cent for twice-blade frequency of mean thrust. The phase angle variation was about 1 degree for blade frequency and less than 1/4 degree for twice-blade frequency. Between different runs, the results of Model B did not show the same consistency as Model A. The fact that less consistency in data was shown on both the ship and the model of configuration B would indicate that the cause could be other than instrumentation in origin.

Model Tests

The test results for Models A and B are shown in Figs. 14 and 15, respectively for both blade and twice-blade frequency. The amplitude values shown are single amplitude and plotted against model-propeller revolutions in cps. These values are derived by the three systems of analysis previously discussed: the sampling system, Seadac, and planimetered results of Viscorder records. The results for Model A in Fig. 14 show small variation over the model test range. The variation of the amplitude of the sampling system results is less than 0.4 per cent of the mean thrust. Table I provides a comparison of the average values for the various analyses systems. It may be noted that the planimeter method followed by the Seadac and the sampling system give progressively smaller values. This is to be expected as each system is progressively a finer filter. The agreement as a whole is quite good, particularly between Seadac and the sampling system.

The results for Model A show that the amplitude of blade frequency is less than that of twice-blade frequency. This is unexpected as other results do not support this conclusion. Although the frequency of the second harmonics is closer to the resonant frequency of the instrumentation, the fact that the amplitude and phase show virtually no change over a frequency range of 144 to 190 cps would indicate that the results are valid for the conditions which prevailed during the test.

The results of analysis by the sampling system for phase angle are also shown in Fig. 14 for Model A. The agreement in phase angle for the various runs are ±2 1/2 degrees for blade rate and ±1 degree for twice-blade rate. The agreement for the six runs appear to be too good to be a coincidence. It should be recognized, however, these results cannot be compared directly to the calculated results because certain filters in both the analysis system and the start pulse on the magnetic tape introduce a lag in the phase angle. It was hoped that the calibration for phase angle could be supplied by the manufacturer. This did not prove to be the case, and time precluded making these rather involved calibrations.

The results from Model B, shown in Fig. 15, exhibit less consistency than those from Model A, particularly the measurements of phase angle. The amplitude measurements are somewhat more consistent, but the range of variation

TABLE 1

Results of Alternating Thrust Model Tests and Calculation Methods

	Per Cent Alternating Thrust, Single Amplitude			Phase Angle, Degrees Clockwise from Top Dead Center		
MODEL A	Blade	2xBlade	3xBlade	Blade	2xBlade	3xBlade
Model Test Results						
Planimeter	2.1	3.1	—	—	—	—
Seadac	1.7	2.6	—	—	—	—
Sampling	1.6	2.3	—	9.4*	26.3*	—
Calculations						
Centerline						
Induction Factor	3.29	1.69	.39	- 3.5	25.3	16.7
Burrill	2.96	1.49	0.51	- 0.4	25.6	16.5
McCarthy	3.64	1.99	0.73	- 2.1	24.5	16.3
Ritger & Breslin	0.66	0.26	0.02	10.0	17.1	15.1
Leading Edge						
Induction Factor	3.41	1.74	0.31	-19.3	10.0	0.7
Burrill	3.85	1.85	0.41	-15.7	11.5	1.2
MODEL B						
Model Test Results						
Planimeter	3.6	2.0	—	—	—	—
Seadac	4.5	**	—	—	—	—
Sampling	3.0	0.5	—	28.0*	**	—
Calculations						
Centerline						
Induction Factor	2.52	1.84	0.54	31.7	- 1.4	10.7
Burrill	2.54	1.65	0.62	36.0	1.0	12.4
McCarthy	2.32	1.56	0.50	35.8	1.8	12.2
Ritger & Breslin	0.58	0.29	0.03	49.4	12.9	1.6
Leading Edge						
Induction Factor	2.01	0.90	0.02	9.2	-19.8	11.7
Burrill	2.01	0.92	0.29	12.8	-17.7	15.6

*Average value used and phase angle not corrected for lag introduced by filters.
**Amplitude negligible, phase angle not significant.

is somewhat greater (1 per cent of the mean thrust) than Model A. The different methods of analysis also produce greater variation. For blade frequency, an average value of 4.5 per cent of mean thrust was attained from Seadac, 3.6 from the planimetered, and 3.0 for the sampling system. The results of twice-blade frequency are very consistent within a system of analysis, but the results of different systems are widely variant ranging from a 1/4 of a per cent for the sampling system to 2 per cent for the planimetered results. As discussed previously, it is to be expected that the sampling system would give results of lower magnitude.
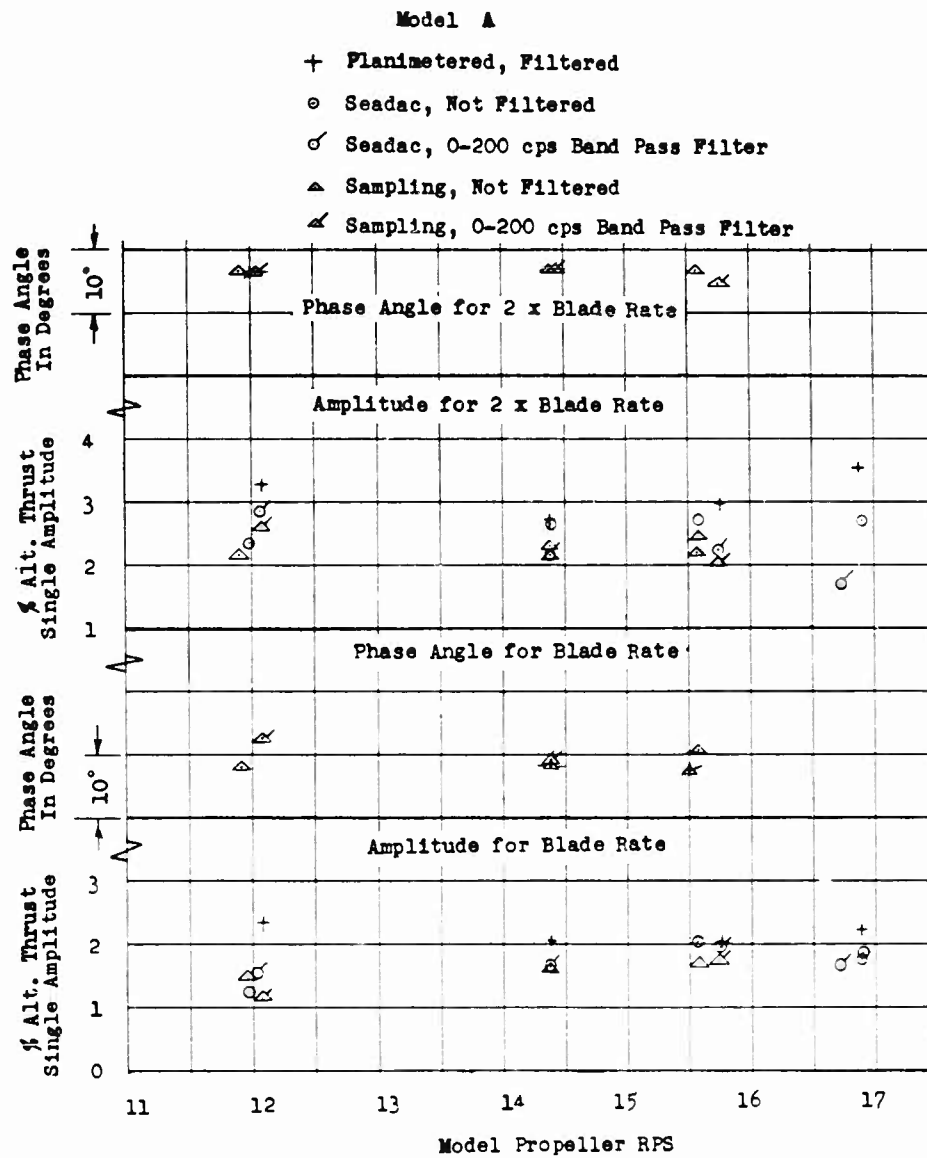
Fig. 14 - Alternating Thrust and Phase Angle as Determined
from Tests with Model A

664

Alternating Thrust Forces on Submerged Bodies
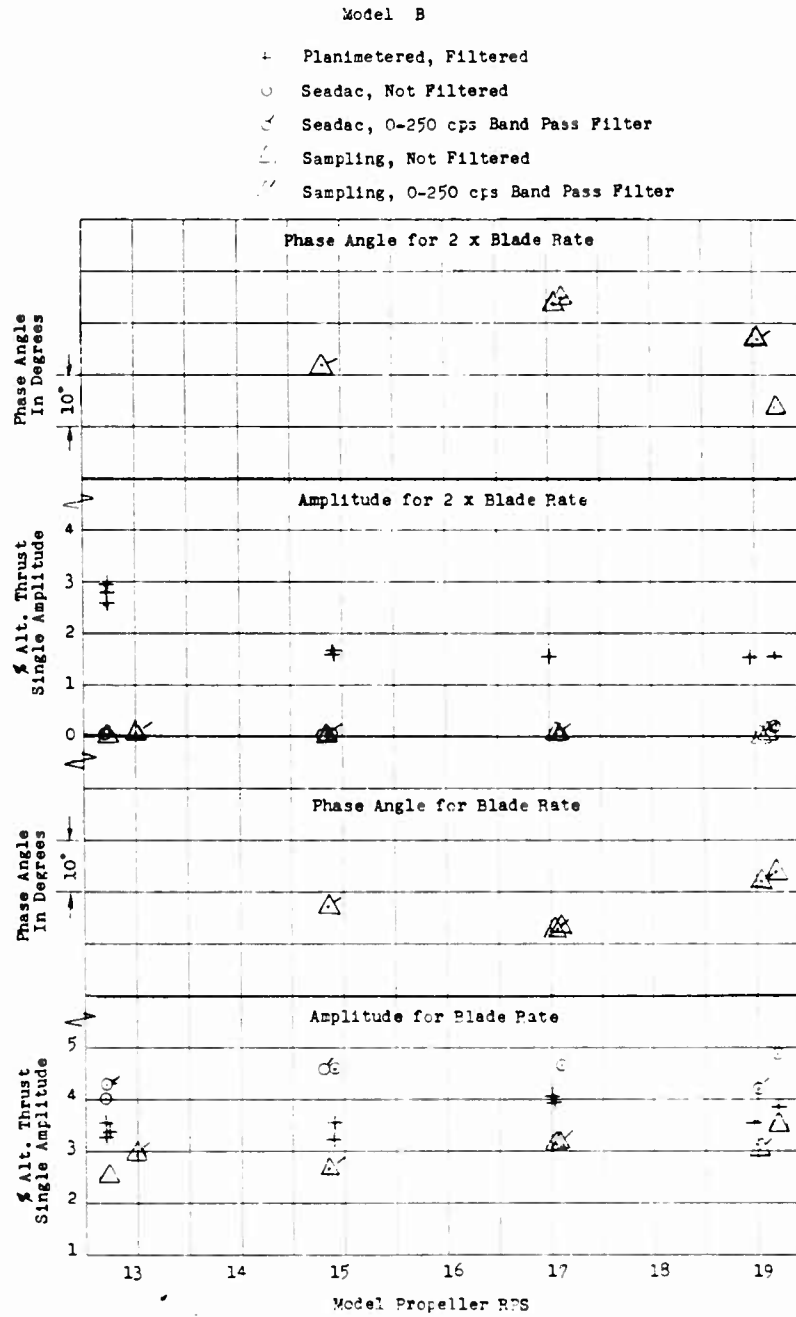
Fig. 15 - Alternating Thrust and Phase Angle as
Determined from Tests with Model B

665

CALCULATIONS

Table I and Figs. 16 and 17 compare the alternating thrust forces determined by the various calculation methods discussed previously. In the figures, the alternating thrust forces are plotted about their respective mean values. The results are plotted for one blade cycle using the top dead center as the zero reference. The reference on the propeller blade is a generating line located at the mid-length of the chord of the root sections. Table I showed the results of the harmonic analyses made of the various calculations. Both amplitude and phase are shown for blade frequency and the first two harmonics of blade frequency. The amplitudes are expressed as a percentage of the mean thrust value derived by calculations.

These results show quite clearly that the forces predicted by the various quasi-steady methods using the wake distribution at the propeller blade centerline are in reasonably good agreement. The induction factor method on Model B
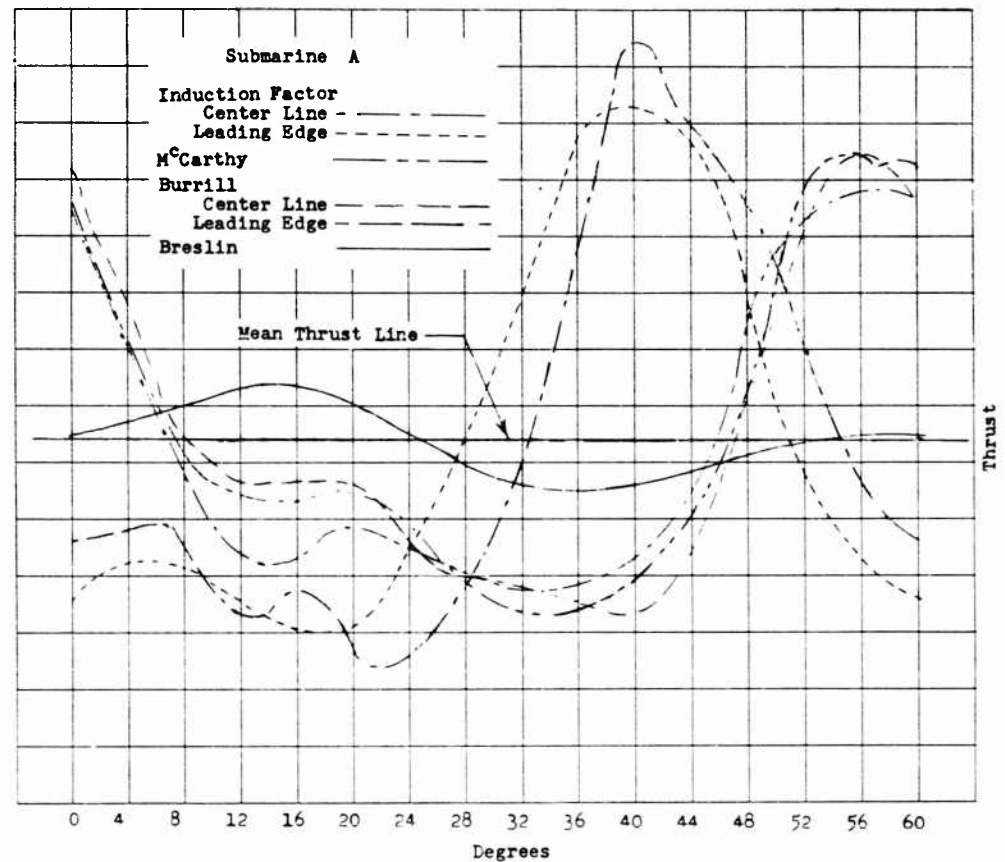
Fig. 16 - Thrust as Computed for Submarine A by Induction Factor, Burrill, McCarthy, and Breslin Methods
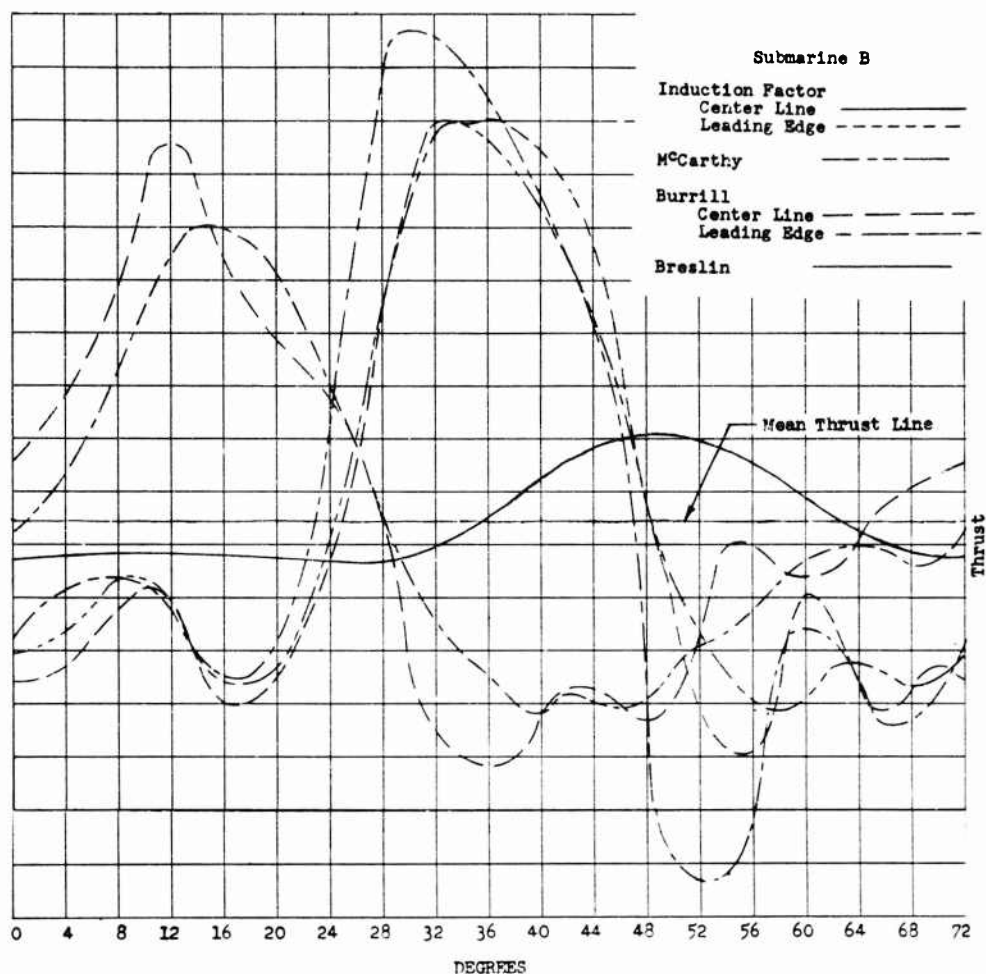
Fig. 17 - Thrust as Computed for Submarine B by Induction Factor,
Burrill, McCarthy, and Breslin Methods

shows a larger variation in magnitude; however, this does not affect the ampli-
tude of the blade frequency harmonics of interest in this report. The variation
in phase between the different quasi-steady methods is small, within 4 degrees.

The amplitude values of the calculations based upon the wake distribution
prevailing at the leading edge of the propeller are in one case greater and the
other lower than that based upon the propeller blade centerline. As would be
expected, the phase is leading that predicted by the centerline calculations.

The calculations by the method developed by Breslin show a significant
change in magnitude and phase. The magnitude of the blade and twice-blade
frequencies is reduced to 1/4 to 1/5 that predicted by the quasi-steady method.

667

The amplitudes are also substantially less than those measured on the models except for the twice-blade frequency amplitude determined by the sampling system on Model B. The blade frequency lags in phase by 10 to 17 degrees that predicted by the various quasi-steady methods which use the wake at the blade centerline.

Although we cannot at this time compare numerically the phase angle results of the model tests with the calculations, it is still possible to draw tentative conclusions. Since the correlation for the filters in the sampling system will introduce lag corrections, the results of the model tests will be brought into closer agreement with those predicted by the quasi-steady methods.

This correction will increase the disagreement between model results and the prediction by Ritger and Breslin with the model results leading the calculations. Thus, it would appear that the introduction of an unsteady correction as developed by Ritger and Breslin is in the right direction but tends to over correct.

In Table I, the results of model predictions can be compared to the predictions made by the various calculations methods. It is disconcerting to note that the model measurements did predict significantly stronger blade frequency forces for Model B, whereas the calculations did indicate significantly stronger forces for Model A. For the second harmonic the inverse is true.

In the course of making the analysis of the unsteady forces, variations were noted in the mean thrust values derived from the various calculations. They are compared in Table II with the measured mean thrust.

TABLE II

Comparison of Calculated Mean Thrust/Measure Mean Thrust

Calculation Method	Burrill	Induction Factor	Breslin
Ship A	1.28	1.24	1.36
Ship B	1.08	1.25	1.12

The calculated values deviate from the measured rather substantially. The propeller on Ship A was of very unusual design with a large pitch reduction at the root of the propeller blade. It is thought that blade interferences were more severe than normal. The methods of calculation do not take thickness interference into account although Burrill's method does provide a nominal correction for cascade effects. Model tests of this propeller indicated substantially lower efficiency than was expected from the design calculation, thus the poor agreement is not surprising. The propeller on Ship B was of conventional design. The calculations based on Burrill's method were slightly high. The calculations by Lerb's induction factors showed an unexpectedly large disagreement. At this time, the authors are unable to offer a rational explanation for this large difference. The predictions made by the Ritger-Breslin method are slightly higher than those predicted by Burrill.

In view of the rather large deviations shown in the calculated values of the mean thrust, a pilot study was performed on Ship B to determine the effect of assumed errors on the calculation of the magnitude of the alternating thrust forces. This study was made using the induction factor method. Calculations were made with the propeller pitch increased one and two degrees, and reduced one degree. A final calculation was made with a linear variation of the design pitch angle starting with a reduction of one degree at the root section, increasing to two degrees at the tip. These relatively large changes in the angle of attack showed significant changes in the mean thrust (about 12 per cent for a 1-degree change in pitch angle), but the effect on the amplitude of blade frequency and twice-blade frequency was less than 2 per cent when compared with the amplitude of the corresponding frequencies for the design propeller. Thus, it may be concluded that the effect of small errors in determining the values of the section angle of attack and lift-slope curve are very small when studying the unsteady forces but are quite significant to the mean thrust values. Although this conclusion is comforting as far as calculating alternating forces are concerned, the determination of the mean forces must be established as accurately as possible for determination of the percentage of alternating force to mean force. This is particularly important in the design stage before model test results are available to check the validity of the calculated values.

FULL-SCALE TRIALS

The results of the full-scale trials on Ships A and B are shown in Figs. 18 and 19 where they are also compared with the results of their corresponding model tests. The analysis is made by two methods: the Seadac and the sampling system. The sampling system is expected to give lower values, particularly in the speed range around resonances. Outside of the resonant range the agreement between the two systems of measurement is quite good.

The results of the trial runs on Ship A are shown in Fig. 18 and are inconclusive. The amplitudes in the speed range where the tests were conducted were markedly influenced by the hull-shaft system resonances. They show amplitudes many fold greater than those measured on the model. Only twice-blade frequency well above resonance gives values in nominal agreement with model.

In the future, it will probably be necessary to design the instrumentation to accurately measure the forces at much lower speeds, speeds which are well below any hull-shaft system resonance.

The results on Ship B are shown in Fig. 19. These trials were also analyzed by Seadac and the sampling system. Again the results of the sampling system gave lower amplitude values, particularly in the range of speeds near hull resonance. On this ship, 7 runs were made which showed little influence from the hull-shaft system resonance which occurred near the top of the test range. As discussed previously, the sampling system results are not as consistent for this ship as for Ship A. The scatter of the individual runs are greater, about 0.4 per cent of mean thrust. The average of the 7 runs below resonance show a value for the fundamental of about 1 per cent of mean thrust with variations as great as $\pm 1/2$ per cent of the mean thrust. The scatter in phase angle is also relatively large, 18.4 degrees, showing significant phase shift thus casting

FULL SCALE TEST RESULTS

SUBMARINE A

⊙ Seadac

△ Sampling
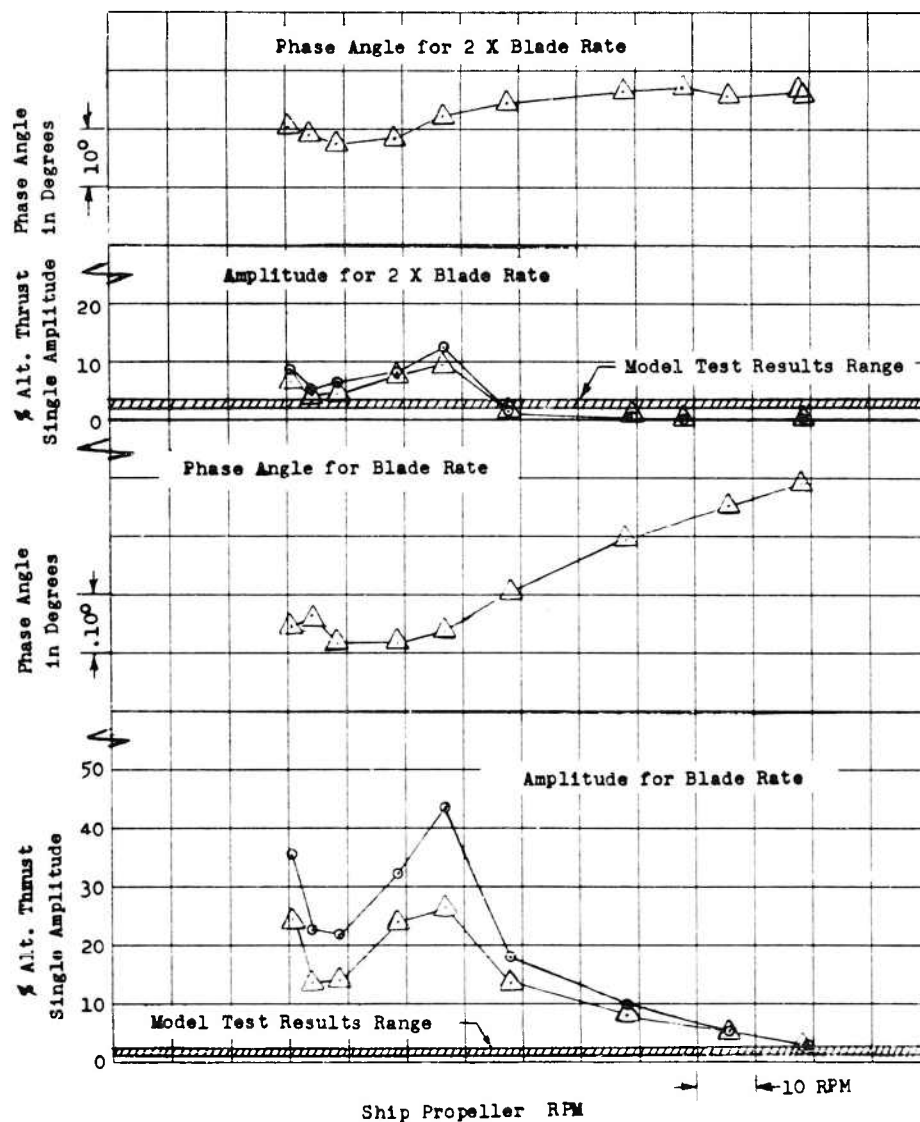
Fig. 18 - Alternating Thrust and Phase Angle as Determined
from Full-Scale Trials of Submarine A

Alternating Thrust Forces on Submerged Bodies
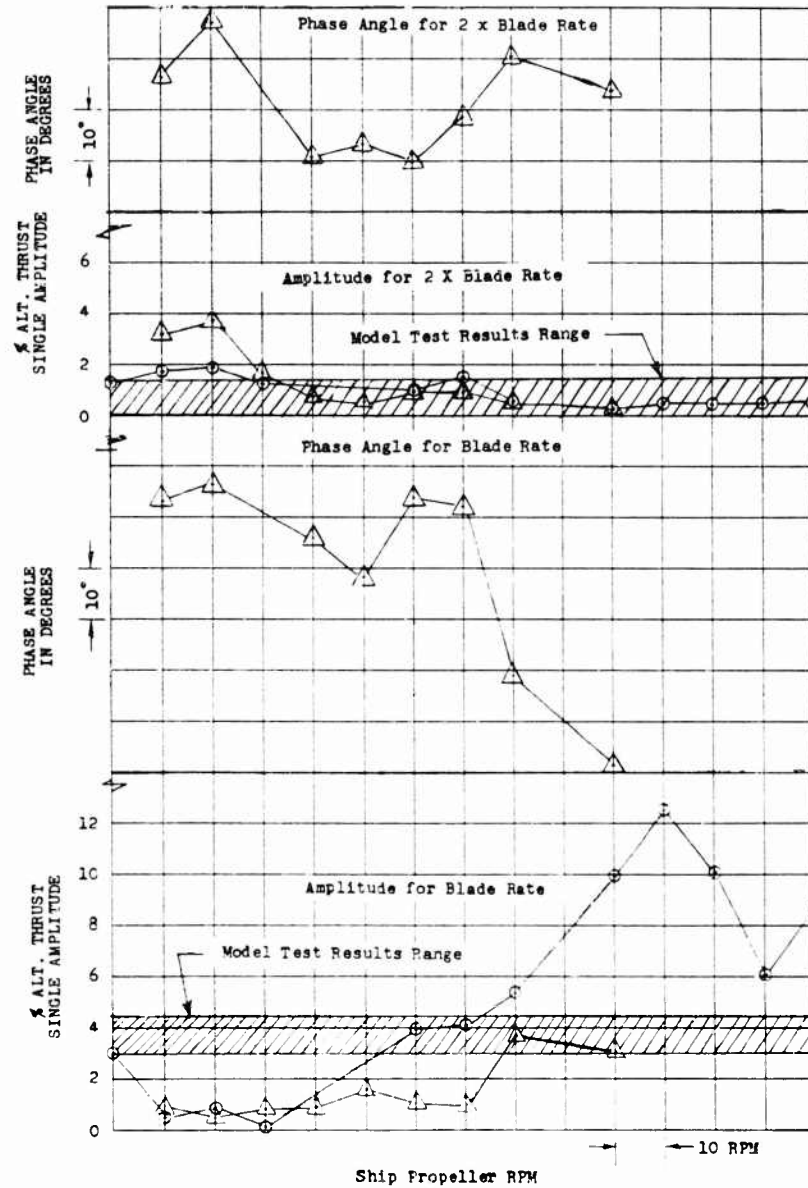
Fig. 19 - Alternating Thrust and Phase Angle as
Determined from Full-Scale Trials of Submarine B

671

further doubt upon the accuracy of the measurements. If the three runs are chosen which show good consistency in phase angle, it will be noted that the amplitudes for blade rate are also quite consistent. The value in these cases is about 1.0 per cent of mean thrust.

The second harmonic of blade frequency is influenced in the lower speed range by a hull-shaft system resonance. At the higher speeds, the amplitude measurements tend to level off to a value of about 0.6 per cent of mean thrust, but the phase angle is still erratic. The cause of the phase shift between runs must be determined before any further experimenting on this ship is warranted.

CONCLUSIONS

It had been the hope at the commencement of this work that some knowledge would be gained on the degree of correlation between existing calculation methods, model test predictions and full-scale trial results. This has not been achieved. Many problems which were not foreseen have been brought forth. Some of these are readily solved and others will need further investigation. It must be concluded that there is no clear cut indication of the validity of either calculation or model test to predict the full-scale forces. It is probable that the measurement, full scale, of the force at the thrust bearing is reasonably accurate; but it is difficult to separate this force into its various components, particularly those generated by the propeller. The problem of predicting and measuring the alternating forces generated by a ship's propeller is certainly much more difficult than first visualized. This work does point out that the choice of test vehicle, for the reasons given in the introduction, is quite valid and even more important than first visualized. In future full-scale work on submarines, the following must be considered:

1. A propeller of as low a number of blades as possible should be chosen in order to reduce the blade frequency, thus providing a better opportunity to avoid hull-shaft system resonances.

2. The ship measurements should be made at lower speeds to avoid hull resonances. It may be necessary to design instrumentation to take accurate measurements at these lower speeds. The effect of the filters in the sampling and measuring systems must be determined so that phase angle can be measured accurately and correlated with that from model tests.

3. Analysis systems such as sampling and Seadac should be used to show the various resonances and to give information on phase and stability of force measurements.

4. The torque should be measured as well as the thrust when possible to provide a check on the thrust data.

5. If hull resonances cannot be avoided, complete instrumentation must be made of the hull-propeller-shaft system so that a complete analysis can be made to determine the magnitude of the forces at the propeller.

The model forces measurements are somewhat of an enigma. The consistency of the results of measurements, both phase and amplitude, on Model A inspire confidence. The measurement of a twice-blade frequency stronger than blade frequency is inconsistent with other data. The instability of the results on Model B point out the need for a more basic knowledge of the time-dependent flow in the plane of the propeller. The following conclusions may be drawn for use in further experimentation:

1. A dynamic calibration system must be developed for accurate calibration of the model measuring system before it is possible to establish complete confidence in the results.

2. Analysis systems such as the sampling system and the Seadac should be used to show the various resonances and to give information on phase and stability of force measurements. The measurement of phase is essential in correlation with calculations and full-scale results.

3. Torque should be measured to provide a further check on the consistency of the thrust data.

4. Adequate data should be taken on each run to provide at least 300 or more cycles to check the stability of the results. If stability is demonstrated, 100 revolutions is an adequate sample.

As a result of the uncertainties of the model measurements in the complex flow field of a ship, it is considered that a more fundamental approach should be used in correlating theory with experiment. An analytically simpler flow field (for example a blade frequency sinusoidal circumferential velocity pattern) which does not experience blade and near blade frequency time-dependent variations should be used. The results of the various calculation methods showed consistency within themselves although the correlation with model measurements are inconclusive. All the calculation methods predicted stronger blade frequency forces than twice-blade frequency. But, measurements on Model A indicate higher twice-blade frequency forces than blade frequency. The calculations also predicted higher blade frequency forces for Model A than for Model B, but the test results indicate the inverse. The following tentative conclusions may be drawn for use in future calculations:

1. For conditions comparable to these ships, there is no strong indication that one quasi-steady method is better than another.

2. The unsteady method of Ritger and Breslin tends to over correct both amplitude and phase. The amplitude values are significantly lower than those predicted by quasi-steady calculations or those measured on the model except for the twice-blade frequency forces on Model B.

ACKNOWLEDGEMENT

673

REFERENCES

1. Marks, Wilbur and Strausser, P.E., "SEADAC - The Taylor Model Basin Seakeeping Data Analysis Center," TMB Report 1353 (Jul 1960).

2. Hama, Francis R., "An Efficient Tripping Device," Journal of Aeronautical Sciences, Vol. 24, No. 3 (Mar 1957).

3. Lanchaster, F.W., "Aerodynamics," Vol. 1, D. Van Nostrand Company, New York (1908).

4. Prandtl and Betz, "Helical Propellers with Minimum Energy Losses," TMB Translation 15 (1919).

5. Goldstein, "On the Vortex Theory of Screw Propellers," Proc. Royal Society, London, Vol. 123 (1929).

6. Burrill, L.C., "Calculation of Marine Propeller Performance Characteristics," Trans. NECI, Vol. 60 (1943-44).

7. Yeh, H.Y., "Thrust and Torque Fluctuations for APA 249, TMB Model 4414," TMB Report 1364 (Jan 1960).

8. Lerbs, H.W., "Moderately Loaded Propellers with a Finite Number of Blades and an Arbitrary Distribution of Circulation," Transactions of the Society of Naval Architects and Marine Engineers, Vol. 60 (1952).

9. Eckhardt, LCDR M.K. and Morgan, W.B., "A Propeller Design Method," Transactions of the Society of Naval Architects and Marine Engineers, Vol. 63 (1955).

10. "Quasi-Steady State of Alternating Propeller Thrust," Applied Mathematics Laboratory Report 143 (Nov 1961).

11. Sears, William R., "Some Aspects of Non-Stationary Airfoil Theory and Its Practical Application," Journal of the Aeronautical Sciences, Vol. 8, No. 3 (Jan 1941).

12. Ritger, Paul D. and Breslin, John P., "A Theory for the Quasi-Steady and Unsteady Thrust and Torque of a Propeller in a Ship Wake," Experimental Towing Tank, SIT, Report No. 686 (Jul 1958).

13. McCarthy, Justin H., "On the Calculation of Thrust and Torque Fluctuations of Propellers in Nonuniform Wake Flow," TMB Report 1533 (Oct 1961).

INTERACTION FORCES BETWEEN
AN APPENDAGE AND A PROPELLER

O. Pinkus, J.R. Lurye
TRG, Incorporated, Syosset, New York
and
S. Karp
New York University, New York, New York

INTRODUCTION AND STATEMENT OF PROBLEM

The problem we are concerned with is shown in Fig. 1. A propeller represented here by its blade cross section moves with a velocity v at right angles to and at a horizontal distance x_o from the center of the strut. Both the strut and propeller are subject to a free stream velocity u. Due to the rotation of the propeller, i.e. variation in y_o, the forces generated in the field will be time-dependent functions and as such will pose fatigue problems and induce vibrations either by hydrodynamical excitations of the strut or by transmission of forces via propeller shaft. The knowledge of the relation between these forces and such design parameters as tip clearance, relative size of strut and blade chord and the location and number of blades may provide means for new and improved design procedures.

Of the early work dealing with forces induced by rotating propellers are the papers by Lewis [1,2] who by use of models and electrical analogy charted the pressure field induced on a wall parallel to the propeller axis. However, the results while setting down the nature of the vibratory forces do not correlate these with the various design parameters inherent in propeller-appendage assemblies. More recent work on the subject is that of Breslin [3], who solved the problem analytically by representing the propeller blade by a single concentrated vortex sweeping by a moving plate. The present work extends Breslin's solution in several important respects. Instead of a concentrated single vortex the blade is here represented by a chord-wise vorticity distribution which in addition to yielding a more correct value for the forces on the appendage, enables us also to calculate the forces on the propeller, which was impossible to do in Breslin's case. The second important difference is that we have here included the mutual interference effects of propeller blade and appendage; for as the propeller moves through the velocity field of the appendage these velocities modify and are in turn themselves modified by the velocity potential of the travelling propeller.

677
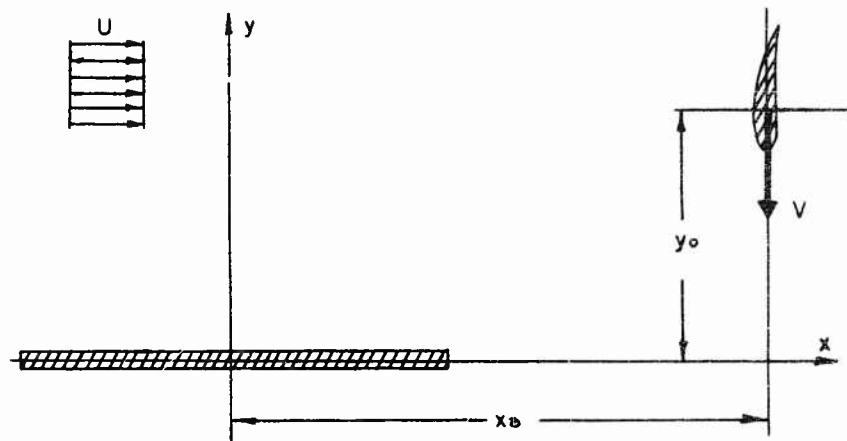
Fig. 1 - Propeller-Appendage System

The analysis is based on the usual assumptions of potential theory, namely that the flow is incompressible, irrotational, inviscid; we also assume that the velocity $V >> U$ so that the flow is nearly parallel for both the appendage and the propeller. The propeller is treated as one of a very high aspect ratio so that its three-dimensional configuration can be replaced by a representative blade cross-section of finite chord. The appendage too though infinitely long has a finite width in the plane of the propeller cross-section. The problem thus is essentially reduced to an analysis of the two dimensional unsteady flow field round two flat plates, as shown schematically in Fig. 2.
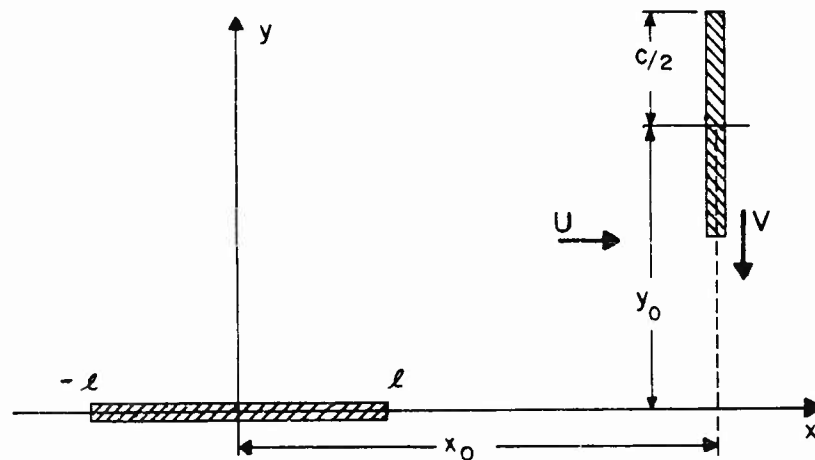
Fig. 2 - Schematic Arrangement of Propeller-Strut System

NOMENCLATURE

a = half-chord of a flat plate air foil

$a_1 = y_o - \dfrac{c}{2}$

$a_2 = y_o + \dfrac{c}{2}$

c = chord of propeller blade

$\overline{c} = c/2\,\ell$

ℓ = half-chord of appendage

q_a = coefficient in formula for Γ_{oa}

$r = V/U$

t = time

u, v = velocity components

w_o = complex potential

x, y = rectangular coordinates

x' = variable along appendage

x_a = x location of appendage substitution vortex

x_o = x distance of propeller from center of appendage

x_p = x location of propeller substitution vortex

y' = variable along propeller blade

y_a = y location of appendage substitution vortex

y_o = y distance of appendage from center of propeller

y_p = y location of propeller substitution vortex

z = complex coordinate $(= x + iy)$

$$A = \sqrt{\frac{(\overline{x}_o + 1) + i\overline{y}_p}{(\overline{x}_o - 1) + i\overline{y}_p}} \quad (x_p = x_o)$$

$$B = \sqrt{\frac{(\overline{y}_o - \overline{c}) + i(\overline{x}_o - \overline{x}_a)}{(\overline{y}_o + \overline{c}) + i(\overline{x}_o - \overline{x}_a)}} \quad (y_a = 0)$$

679

C = correction term for Appendage Wake Force

D = correction term for Propeller Wake Force

F = force per unit span

$R = \frac{Ut}{\ell}$

T = unperturbed propeller thrust, $\rho \pi c UV$

U = free stream velocity

V = velocity of propeller blade

γ = vorticity on a foil

γ_2 = vorticity on a foil due to its wake

γ_w = vorticity in wake of a foil

γ_{oa} = quasi-steady vorticity on appendage

γ_{op} = quasi-steady vorticity on propeller

γ_{pi} = quasi-steady vorticity on propeller due to γ_{oa}

$\gamma_{p\infty}$ = vorticity on propeller at infinity

ρ = density

Γ = circulation

Γ_{oa} = quasi-steady circulation on appendage

Γ_{op} = quasi-steady circulation on propeller

Γ_{pi} = quasi-steady circulation on propeller due to Γ_{oa}

$\Gamma_{p\infty}$ = circulation on propeller at infinity

Subscripts

a = appendage

i = induced

o = quasi-steady

p = propeller

m = maximum

680

Interaction Forces Between an Appendage and a Propeller

w = wake

1 = apparent-mass effect

2 = due to wake

Superscripts

‾ pertains to normalization by

(a) ℓ for all lengths (except $\bar{c} = \frac{c}{2\ell}$)

(b) $\pi U c$ for all circulations

(c) T for all forces

METHOD OF SOLUTION

The basic relations for the lift on a single airfoil subject to an unsteady flow have been derived by von Karman and Sears [4]. This unsteady lift is shown to be made up of three component forces.

1. F_o - Quasi-steady Force. This is the force that would have resulted from a steady state case in which all parameters are equal to the instantaneous values of the unsteady motion. The expression for this force is

$$F_o = \rho U \Gamma_o \tag{1}$$

where Γ_o is the quasi-steady circulation around the foil.

2. F_1 - Apparent-mass Force. This is the inertia force on the foil due to the acceleration of the mass of fluid in its vicinity. It is given by

$$F_1 = -\rho \frac{\partial}{\partial t} \int_{-a}^{a} x \gamma_o(x.t) dx \tag{2}$$

where γ_o is the quasi-steady vorticity distribution on the foil and x is the coordinate measured along the foil, the latter extending from $x = -a$ to $x = a$.

3. F_2 - Wake Force. Due to the time variation of Γ_o the foil will shed vortices behind it, giving rise to a vorticity distribution $\gamma_w(\zeta.t)$ in the wake, where ζ is distance along the wake, measured from the trailing edge of the foil. This wake vorticity will induce a wake force on the foil given by

$$F_2 = \rho U a \int_{a}^{a+Ut} \gamma_w(\zeta.t) \frac{d\zeta}{\sqrt{\zeta^2 - a}} \tag{3}$$

where the vorticity $\gamma_w(\zeta.t)$ is to be obtained from the integral equation (4)

681

$$\int_{a}^{a+Ut} \gamma_w(\zeta,t) \sqrt{\frac{\zeta-a}{\zeta+a}} \, d\zeta = -\Gamma_o(t) \tag{4}$$

The total force on the foil is then given by

$$F = F_o + F_1 + F_2$$

Since

$$\Gamma_o(t) = \int_{-a}^{a} \gamma_o(x,t)dx$$

it is seen from Eqs. 1-4, that although we are dealing with an unsteady problem, the time dependent forces can be obtained once the quasi-steady vorticity $\gamma_o(x,t)$ is known. Thus the original problem has been reduced to the determination of a certain steady flow.

The quasi-steady vorticity, it should be remembered, is in itself a function of time, the time entering as a parameter that specifies the moment at which the flow is treated as steady. Our main task is therefore to derive expressions for the quasi-steady vorticities on the appendage $\gamma_{oa}(x,t)$ and on the propeller $\gamma_{op}(y,t)$.

For our particular problem, represented schematically in Fig. 2, we have the following situation; when the propeller is far away from the appendage, (y_o is very large) there is a force on the blade due to the cross flow U given by $F_{p\infty} = \pi \rho \, c \, U V$. This result is simply the lift on a flat plate of chord c subject to a free stream velocity V at an angle of attack given by

$$\alpha = \tan^{-1}\frac{U}{V}$$

At that time the appendage being subject to a flow U parallel to itself experiences no force, or $F_a = 0$. When the propeller comes within the proximity of the appendage it begins to feel the effect of the appendage and this effect will vary with the distance y_o. Thus at any given position y_o the quasi-steady force on the propeller will be modified due to appendage interference by an additional quantity F_{pi}, such that the quasi-steady force is now

$$F_{op} = F_{p\infty} - F_{pi} \,.$$

In addition, as already mentioned, there will be an apparent mass force F_{1p} and wake force F_{2p} acting on the propeller. The appendage likewise will now experience a quasi-steady, apparent-mass and wake forces. Thus,

$F_{p\infty}$ - force on propeller at infinity

F_{pi} - quasi-steady force induced on propeller by presence of appendage

682

F_{op} - quasi-steady force on propeller $(= F_{p\infty} + F_{pi})$

F_{2p} - force on propeller induced by its wake

F_{1p} - apparent-mass force on propeller

F_{oa} - quasi-steady force on appendage

F_{2a} - force on appendage due to its wake

F_{1a} - apparent-mass force on appendage

Our main task is now to find γ_{oa} and γ_{op} since all forces can be obtained once these two quantities are known.

Since the complex potential for a simple concentrated vortex of strength C_o located at $z = z_o$ is

$$w = \frac{i}{2\pi} C_o \ln(z - z_o)$$

and for a uniform stream

$$w = - Uz$$

we have, by representing the appendage by a distributed vorticity $\gamma_{oa}(x)$ and the propeller by $\gamma_{op}(y)$, the following expression for the complex quasi-steady potential at any point, z, in the fluid:

$$w_o = - Uz - \frac{i}{2\pi} \int_{-\ell}^{\ell} \gamma_{oa}(x') \ln(z - x') dx'$$

$$+ \frac{i}{2\pi} \int_{a_1}^{a_2} \gamma_{op}(y') \ln(z - x_o - iy') dy' \tag{5}$$

where $a_1 = y_o - (c/2)$, and $a_2 = y_o + (c/2)$, and where the time dependence of γ_{oa} and γ_{op} is not explicitly indicated.

By imposing the condition of zero normal velocity on the two foils, we could use Eq. (5) to derive a pair of coupled integral equations for the unknown functions, γ_{oa} and γ_{op}. The solutions to the integral equations are not unique but become so when the Kutta condition is imposed at the trailing edge of each of the foils. However, the problem of determining γ_{oa} and γ_{op} in this way is sufficiently difficult to necessitate our using an approximate procedure instead. The method employed here is that of the substitution vortex. In this method both the appendage and the propeller are treated as finite length plates with distributed vorticities, while the effect that each of these plates has on the other is assumed to be that of a concentrated vortex whose strength equals the total distributed strength of the respective plate. The method of determining the

683

unknown strengths and locations of the propeller and appendage vortices will become clear in the course of the following analysis.

As explained previously the propeller experiences at infinity, due to the cross flow U, a vorticity $\gamma_{p\infty}(y)$. As the propeller approaches the appendage, it produces and is affected by $\gamma_{oa}(x)$, thus giving rise to an additional vorticity $\gamma_{pi}(y)$. As shown in Fig. 3 we shall now concentrate the distributed vorticity $\gamma_{oa}(x)$ at some location z_a (to be determined) and call its strength Γ_{oa}. Since $\gamma_{p\infty}$ cancels the normal velocity of the uniform stream U at the propeller, we have for the complex potential due to a concentrated vortex Γ_{oa} and a distributed vorticity γ_{pi} the following:

$$w = \frac{i\Gamma_{oa}}{2\pi} \ln (z - z_a) + \frac{i}{2\pi} \int_{a_1}^{a_2} \gamma_{pi}(y') \ln (z - x_o - iy')dy'$$
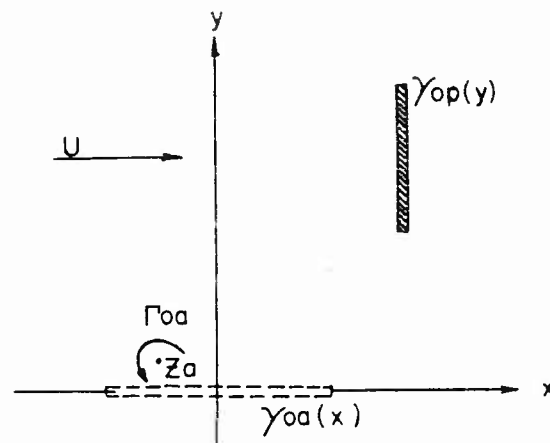
Fig. 3 - Appendage Substitution Vortex

Application of the boundary condition that the normal velocity vanish at the propeller blade leads to the integral equation for $\gamma_{pi}(y)$:

$$\fint_{a_1}^{a_2} \frac{\gamma_{pi}(y')}{y' - y} dy' = \Gamma_{oa} \frac{y - y_a}{(x_o - x_a)^2 + (y - y_a)^2} \tag{6}$$

where the bar on the integral indicates a Cauchy principal value. Similarly, we treat $\gamma_{op}(y)$ as a concentrated vortex located at some appropriate coordinate z_p (again to be determined) and write the complex potential as due to Γ_{op} and a distributed vorticity $\gamma_{oa}(x)$ along the appendage. We thus have

684

Interaction Forces Between an Appendage and a Propeller

$$w = \frac{i\Gamma_{op}}{2\pi} \ln (z - x_p - iy_p) + \frac{i}{2\pi} \int_{-\ell}^{\ell} \gamma_{oa}(x') \ln (z - x')dx'$$

The condition of vanishing normal velocity on the appendage then yields the integral equation for $\gamma_{oa}(x)$

$$\oint_{-\ell}^{\ell} \frac{\gamma_{oa}(x')}{x' - x} dx' = \Gamma_{op} \frac{x - x_p}{(x - x_p)^2 + y_p^2} \tag{7}$$

where again the integral is a Cauchy principal value.

The approximate integral equations (6) and (7) are of a form that can be solved exactly, giving approximate expressions for γ_{oa} and γ_{pi} (or equivalently, γ_{op}). The details of this process are discussed in [5].

If we now insert the solutions of Eqs. (6) and (7) into the relationships

$$\Gamma_{op} = \int_{a_1}^{a_2} \gamma_{op}(y')dy' = \int_{a_1}^{a_2} \gamma_{px}(y')dy' + \int_{a_1}^{a_2} \gamma_{pi}(y')dy'$$

$$\Gamma_{oa} = \int_{-\ell}^{\ell} \gamma_{oa}(x')dx'$$

we obtain the following expressions for Γ_{oa} and Γ_{op} in terms of z_a and z_p:

$$\Gamma_{oa} = -Uc \frac{Re(A-1)}{1 - Re(A-1)Re(B-1)} \tag{8}$$

$$\Gamma_{op} = -Uc \frac{1}{1 - Re(A-1)Re(B-1)} \tag{9}$$

where

$$A = \sqrt{\frac{(x_p + \ell) + iy_p}{(x_p - \ell) - iy_p}} \qquad B = \sqrt{\frac{\left(y_o - y_a - \frac{c}{2}\right) - i\left(x_o - x_a\right)}{\left(y_o - y_a - \frac{c}{2}\right) - i\left(x_o - x_a\right)}}$$

It remains to derive two other relationships among the four unknowns, Γ_{oa}, Γ_{op}, z_a, and z_p.

As shown in Fig. 4, (a) and (b), we consider the propeller to be replaced by a concentrated vortex at z_p with circulation Γ_{op}. We seek the location, z_a, of that vortex by which the appendage may be replaced, such that the flow at sufficiently large z due to the two vortices approximates the original flow. More precisely, z_a is to be so determined that the flow due to the two vortices agrees with the original flow to terms of order $1/z$.

685
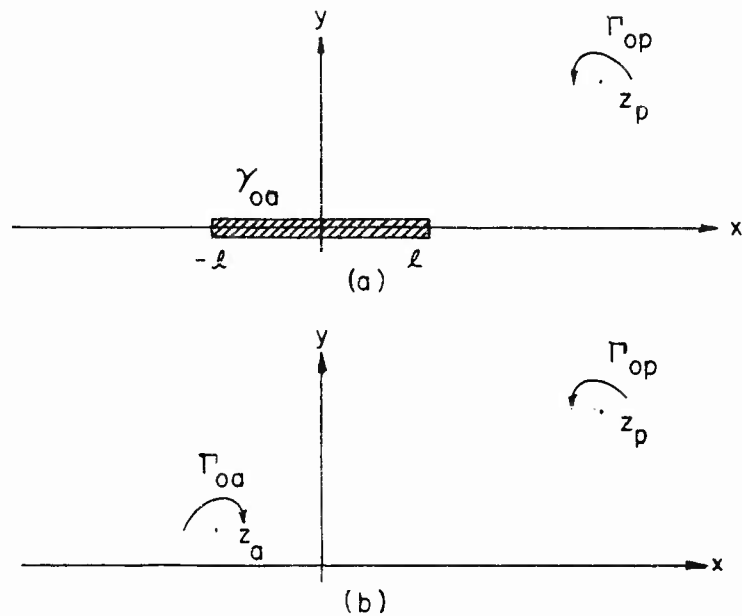
Fig. 4 - Determination of Location of Substitution Vortex

Let w_1 be the complex potential of the flow associated with the two vortices. Then

$$w_1 = \frac{i}{2\pi} \Gamma_{op} \log (z - z_p) - \frac{i}{2\pi} \Gamma_{oa} \log (z - z_a) \tag{10}$$

Expanding the second term in inverse powers of z. we have

$$w_1 = \frac{i}{2\pi} \Gamma_{op} \log (z - z_p) - \frac{i}{2\pi} \Gamma_{oa} \log z - \frac{i}{2\pi} \Gamma_{oa} \frac{z_a}{z} - o\left(\frac{1}{z}\right) \tag{11}$$

where the remainder is a power series in $1/z$ convergent for $z > z_a$.

Now denote by w_2 the potential of the actual flow induced by the vortex located at z_p in the presence of the appendage. We first express w_2 as a function of ζ, where ζ is defined by the transformation

$$z = \zeta - \frac{\ell^2}{4\zeta} .$$

In the ζ plane the appendage is mapped into a circle of radius $\ell/2$ with center at $\zeta = 0$. The vortex at z_p maps into a vortex at ζ_p with circulation Γ_{op}. Likewise the circulation Γ_{oa} around the appendage is preserved.

Using Milne-Thompson's [6] circle theorem in the ζ plane, we get

$$w_2 = \frac{i\Gamma_{op}}{2\pi} \log (\zeta - \zeta_p) - \frac{i\Gamma_{op}}{2\pi} \log \left(\frac{\lambda^2}{4\zeta} - \bar{\zeta}_p\right) + \frac{i\Gamma_{oa}}{2\pi} \log \zeta \qquad (12)$$

where ζ_p is the image of z_p and the bar over the ζ stands for the complex conjugate.

Expressing w_2 as a function of z and expanding it in inverse powers of z as far as the $1/z$ terms, we can rewrite Eq. (12) as [5]

$$w_2 = \frac{i\Gamma_{op}}{2\pi} \log (z - z_p) + \frac{i\Gamma_{oa}}{2\pi} \log z$$

$$+ \frac{i\Gamma_{op}}{2\pi} \frac{\lambda^2}{4} \left(\frac{1}{\zeta_p} - \frac{1}{\bar{\zeta}_p}\right) \frac{1}{z} + o\left(\frac{1}{z}\right) \qquad (13)$$

where the remainder is a power series convergent for $|z| > \lambda$.

Comparison of (13) with (11) to terms of order $1/z$ gives

$$z_a = -\frac{\Gamma_{op}}{\Gamma_{oa}} \frac{\lambda^2}{4} \left(\frac{1}{\zeta_p} - \frac{1}{\bar{\zeta}_p}\right) \qquad (14)$$

where $\quad \zeta_p = \frac{z_p}{2} + \frac{1}{2} \sqrt{z_p^2 - \lambda^2}$ (14a)

To determine the position of the substitution vortex for the propeller, we proceed in a manner exactly analogous to the above, except that we must remember that the incident flow on the propeller comes not only from a vortex at z_a but also from a uniform stream traveling with velocity U in the positive x direction. With this minor modification we get the following expression for z_p, the location of the substitution vortex that replaces the propeller:

$$z_p = z_0 - i \frac{U}{4 \Gamma_{op}} c^2 - i \frac{1}{16} \frac{\Gamma_{oa}}{\Gamma_{op}} c^2 \left(\frac{1}{\zeta_a'} + \frac{1}{\bar{\zeta}_a'}\right) \qquad (15)$$

where $z_0 = x_0 + iy_0$, the position of the center of the propeller, and ζ_a' is defined by

$$\zeta_a' = \frac{1}{2} i \left[z_a - z_0 + \sqrt{(z_a - z_0)^2 - \frac{c^2}{4}}\right]. \qquad (15a)$$

Equations (14) and (15) together with Eqs. (8) and (9) constitute the four desired relations for the determination of Γ_{oa}, Γ_{op}, z_a, and z_p. Once these are solved (we have done this numerically for a large number of cases) the results are put into the right hand sides of the integral equations, (6) and (7), which are then inverted to yield explicit approximate formulas for $\gamma_{oa}(x)$ and $\gamma_{op}(y)$. Note that Eqs. (14) and (15) imply that $x_p = x_0$ and $y_a = 0$, i.e., that the substitution vortices lie on the plates, the only variation occurring along and not normal to the appendage or propeller. We can thus rewrite A and B in Eqs. (8) and (9) as

687

$$A = \sqrt{\frac{(x_o + \ell) - iy_p}{(x_o - \ell) + iy_p}} \qquad\qquad B = \sqrt{\frac{\left(y_o - \frac{c}{2}\right) - i\left(x_o - x_a\right)}{\left(y_o - \frac{c}{2}\right) - i\left(x_o - x_a\right)}} \qquad (16)$$

One additional remark should be made concerning a limitation on the use of the substitution vortex method. To terms of order $1/z$, the potential due to the presence of the appendage is equal to that due to the appendage vortex, but this equality holds only for observation points z for which $|z| > \ell$, i.e., observation points exterior to a circle centered on the appendage and having a radius equal to the half-chord. Similarly, the potential due to the propeller is approximated by that of the propeller vortex for points outside a corresponding circle centered on the propeller. It follows that in treating the flow with both foils present by the substitution vortex method, neither foil should penetrate the circle associated with the other. This requirement imposes a restriction on the variables, ℓ, c, and x_o, viz.,

$$x_o > \ell - \frac{c}{2} \qquad \text{or} \qquad \bar{c}^2 \leq \sqrt{\bar{y}_o^2 - (\bar{x}_o - 1)^2} \,. \qquad (17)$$

Thus the method breaks down if the propeller passes too close to the end of the appendage. On the other hand, it seems likely that a slight penetration of the circles by the foils will not seriously spoil the accuracy of the method so that practically speaking, the inequality (17) is a little too restrictive.

EXPRESSIONS FOR THE UNSTEADY FORCES

The Quasi-Steady Forces

According to Eq. (1) the quasi-steady forces are

$$F_{oa} = \rho U \Gamma_{oa}$$

$$F_{op} = \rho V \Gamma_{op}$$

or, from Eqs. (8) and (9)

$$\frac{r F_{oa}}{T} = \frac{Re(A-1)}{1 - Re(A-1)Re(B-1)} \qquad (18)$$

$$\frac{F_{op}}{T} = \frac{1}{1 - Re(A-1)Re(B-1)} \qquad (19)$$

where $T = \rho c U V$ is the unperturbed propeller thrust and $r = \frac{V}{U}$. It will be noticed from the above that

$$F_{oa} = \frac{Re(A-1)}{r} F_{op} \,. \qquad (20)$$

Also

$$\frac{F_{pi}}{T} = \frac{Re(A-1)Re(B-1)}{1 - Re(A-1)Re(B-1)} \tag{21}$$

The Apparent-Mass Forces

As shown in Eq. (2), the determination of the apparent-mass force involves the evaluation of

$$M_a = \int_{\ell}^{\ell} x_{\ell_{oa}}(x)dx$$

for the appendage, and

$$M_p = \int_{-\frac{c}{2}}^{\frac{c}{2}} y'_{\cdot_{op}}(y')dy'$$

for the propeller.

The functions $_{\circ a}(x)$ and $_{\circ p}(y)$ having been determined approximately by the substitution vortex technique just described, the evaluation of these integrals as performed in [5] yields

$$M_a = \bar{\ }_{op}Re\left[\sqrt{(x_o - iy_p)^2 - \ell^2} - x_o\right] \tag{22}$$

$$M_p = -U\left(\frac{c}{2}\right)^2 - \bar{\ }_{oa}Re\left\{(y_o - y_a) - \sqrt{\left[(y_o - y_a) + i(x_o - x_a)\right]^2 - \left(\frac{c}{2}\right)^2}\right\} \tag{23}$$

The apparent mass forces are given by

$$F_{1a} = - \cdot \frac{\cdot}{\cdot t} M_a$$

$$F_{1p} = - \cdot \frac{\cdot}{\cdot t} M_p .$$

Since

$$\frac{\cdot}{\cdot t} = \frac{\cdot}{\cdot y_o} \frac{\cdot y_o}{\cdot t} = - V \frac{\cdot}{y_o}$$

we have

$$\frac{F_{1a}}{T} = \frac{\cdot}{\cdot y_o} \bar{\ }_{op} Re\left[\sqrt{\bar{x}_o - i\bar{y}_p}^2 - 1 - \bar{x}_o\right] \tag{24}$$

$$\frac{F_{1p}}{T} = \frac{\partial}{\partial \bar{y}_o} \bar{\Gamma}_{oa} Re \left\{ \bar{y}_o - \sqrt{\left[\bar{y}_o + i(\bar{x}_o - \bar{x}_a)\right]^2 - \bar{c}^2} \right\} \tag{25}$$

where it must be remembered that $\bar{x}_a$ and $\bar{y}_p$ are functions of $\bar{y}_o$.

The Wake Forces

As mentioned previously the unsteady circulation on both the appendage and propeller will cause the shedding of wake vortices and these in turn will induce an additional circulation round the two plates. Thus according to Eqs. (3) and (4), the integral equation for the wake vorticity $\gamma_{wa}(\xi)$ and the expression for the force induced by it on the appendage are respectively

$$\int_1^{1+R} \gamma_{wa}(\xi, t) \sqrt{\frac{\xi - 1}{\xi - 1}} \, d\xi = - \frac{\bar{\Gamma}_{oa}(t)}{\xi} \tag{26}$$

$$F_{2a} = \rho U \int_1^{1+R} \frac{\gamma_{wa}(\xi) d\xi}{\sqrt{\xi^2 - 1}} \tag{27}$$

Similarly, for the wake force on the propeller, we have

$$F_{2p} = \rho U \frac{c}{2} \int_1^{1+S} \frac{\gamma_{wp}(\tau) d\tau}{\sqrt{\tau^2 - 1}} \tag{28}$$

where $S = \frac{vt}{c\,2}$ and τ measures distance along the propeller wake from the trailing edge of the propeller.

In [5] the expression for F_{2a} was derived via the following steps. Instead of Γ_{oa} in Eq. (26) a unit impulse was used, i.e. $\Gamma_{oa} = 1$. The force $F_{2a}^{(1)}$ corresponding to $\Gamma_{oa} = 1$ could then be obtained. By means of the Duhamel integral the force due to an arbitrary input Γ_{oa} was then derived yielding

$$\frac{rF_{2a}}{T} = - \frac{1}{2}\left(\frac{rF_{oa}}{T}\right) - 2 \int_{-R}^{\tau - \tau} \frac{\bar{\Gamma}_{oa}(\bar{\tau}) d\bar{\tau}}{(4 - R - \bar{\tau})^2} \tag{29}$$

Equation (29) tells us that the wake force is always equal to minus one half the quasi-steady force plus a correction involving the expression

$$C = - 2 \int_{-R}^{\tau - \tau} \frac{\bar{\Gamma}_{oa}(\bar{\tau}) d\bar{\tau}}{(4 - R - \bar{\tau})^2} \tag{30}$$

Direct integration in Eq. (30) is difficult since $\bar{\Gamma}_{oa}$ is a complicated function. We shall represent $\bar{\Gamma}_{oa}$ by a simpler function which by a suitable choice of constants can be made to give a fair approximation to the original expression.

Γ_{oa} has in general the shape of Fig. 5 and we can write

$$\bar{\Gamma}_{oa}(y'_o) = \frac{a_a \bar{\Gamma}_{am}}{(\bar{y}'_o - \bar{y}_{om})^2 - q_a} \tag{31}$$
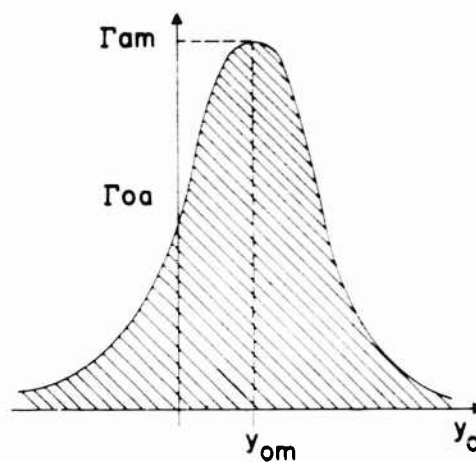
Fig. 5 - Shape of Γ_{oa}

The constant q_a is now so chosen that for large $\bar{y}_o$ the formula in Eq. (31) has the same asymptotic behaviour as the exact $\bar{\Gamma}_{oa}$. Since for large $\bar{y}_o$ Eq. (8) shows that

$$\bar{\Gamma}_{oa} \sim \frac{\bar{x}_o - \frac{1}{2}}{\bar{y}_o^2}$$

it follows that

$$a_a \bar{\Gamma}_{am} = \bar{x}_o - \frac{1}{2}$$

and thus

$$q_a = \frac{\bar{x}_o - \frac{1}{2}}{\bar{\Gamma}_{am}}$$

The integration in Eq. (30) is now easily performed yielding

691

$$C = -\frac{2q_a r \, \overline{\Gamma}_{am}}{\left[(4r-P)^2 + q_a\right]^2} \left\{ (4r-P) \, \ell n \, \frac{(4r-P)^2 + q_a}{16r^2} \right.$$

$$\left. + \frac{(4r-P)^2 - q_a}{\sqrt{q_a}} \left(\frac{\pi}{2} - \tan^{-1} \frac{P}{\sqrt{q_a}}\right) - \frac{(4r-P)^2 + q_a}{4r} \right\}. \tag{32}$$

where $P = \overline{y}_o - \overline{y}_{om}$.

Thus the force on the appendage due to the wake is

$$\frac{rF_{2a}}{T} = -\frac{1}{2}\left(\frac{rF_{oa}}{T}\right) + C . \tag{33}$$

A similar procedure for the propeller yields

$$\frac{F_{2p}}{T} = -\frac{1}{2} \frac{F_{pi}}{T} - 2 \int_o^z \frac{\overline{\Gamma}_{pi}(z)}{(4 - y_o' + z)^2} \, dz . \tag{34}$$

Thus, the wake force is equal to minus one half of the induced force plus a correction D given by

$$D = 2 \int_o^z \frac{\overline{\Gamma}_{pi}(z)}{(4 - y_o' + z)^2} \, dz \tag{35}$$

NUMERICAL EVALUATION OF FORCES

From the preceding section by summing $F = F_o + F_1 + F_2$ we obtain for the total lift on the strut and propeller

$$\frac{F_s}{T} = \frac{1}{2} \frac{F_{oa}}{T} - \frac{F_{1a}}{rT} - C ; \tag{36}$$

$$\frac{F_p}{T} = 1 - \frac{1}{2} \frac{F_{pi}}{T} - \frac{F_{1p}}{T} - D \tag{37}$$

The individual terms in the above equations are given by the following expressions

$(F_{oa} \, T)$ - by eqs. (18) and (16)

$(F_{1a} \, T)$ - by eqs. (24) and (22)

C - by eq. (32)

$(F_{pi} \, T)$ - by eqs. (21) and (16)

(F_{1p}/T) -- by eqs. (25) and (23)

D - by eq. (35)

All the above equations contain the coordinates of the substitution vortices x_a and y_p and thus we have to resort to eqs. (14), (14a), (15) and (15a) for their values.

It will be noticed that all the expressions necessary for calculating F_a and F_p are given in explicit form. The only unevaluated expression is the integral for D, eq. (35). This integral has been evaluated numerically using Simpson's rule. The entire project has been programmed on a 7090 IBM digital computer. and component as well as total forces were obtained for the following sets of parameters.

$\overline{x}_o$ - -1.6, -1.4, -1.2, -1.05, 1.05, 1.2, 1.4, 1.6

$\overline{c}$ - 0.1, 0.2, 0.3, 0.5,

r - 2, 3, 4

$\overline{y}_o$ - from -5.0 to 5.0 in intervals of $\Delta\overline{y}_o = 0.05$

The results of these computations are available in tabular form.

DISCUSSION

The various expressions for the component and total forces given in the preceding sections contain the propeller-appendage length ratio $\overline{c} = c/2\ell$ as a parameter. When in these expressions we set $c = 0$. the forces on both propeller and appendage disappear. However, in spite of this disappearance, the dimensionless ratios F/T approach definite non-zero limits as $\overline{c} \to 0$. The curves for the case $\overline{c} = 0$ are therefore to be interpreted as plots of these limiting values. These $\overline{c} = 0$ curves are, as expected, identical with the curves of Breslin who obtained the forces on the appendage by making the simplifying assumption that the propeller has both a constant non-zero circulation and zero chord.

In the discussion to follow we shall first describe the effect of varying $\overline{x}_o$. r and $\overline{c}$ on the nature and magnitude of the hydrodynamic forces and then draw some conclusions with regard to optimum design features of propeller-appendage assemblies.

Rudder Position (- x_o)

Effects on Appendage - Figures 6 through 9 show sample plots of the component forces indicating that while the apparent-mass forces go up more than proportionately with $\overline{c}$, the quasi-steady and wake forces change less than proportionately with $\overline{c}$. The complex way in which these component forces make up the total force is shown in a sample plot of Fig. 10. Figures 12 through 19 show the variations of the total forces and these can be summarized as follows:

a. The forces are predominantly positive, i.e., they act in a direction opposite to propeller motion. For reasonable spacings, $\bar{x}_o > 1.1$, a minimum in the value of F_a/T occurs around $\bar{c} = .15$ for $r - 2$ and around $\bar{c} = .1$ for $r = 4$.

b. The maximum force occurs before the propeller center passes the appendage, $0 < y_{om} < \ell$, with y_{om} moving closer to the appendage with a decrease in $\bar{c}$.

c. After the propeller has passed the appendage the forces are usually negative and negligible.

d. The maximum normalized forces decrease with an increase in propeller velocity. $\bar{F}_{am}$ is reduced by about 25% in going from $r = 2$ to $r = 4$.

e. As shown in Figs. 18 and 19 the forces go up drastically with a decrease in $\bar{x}_o$. F_{am} increases 2-1/2 times in going from $\bar{x}_o = 1.6$ to $\bar{x}_o = 1.2$.

Effects on Propeller - The apparent mass forces and also usually the wake force go up, according to Figs. 20 through 22. more than proportionately with $\bar{c}$ while the quasi steady forces go up less than proportionately with $\bar{c}$. Figure 23 shows how the three component forces make up the total force. It should be noticed that the line $Fa/T = 1$ represents the force on the propeller at infinity or the unperturbed thrust. Thus the plots in Figs. 25 to 28 represent the ratio of the actual force on the propeller to that without interference. The variation of the total force can be viewed as a small or moderate perturbation round $F_{p\approx}/T = 1$ and thus the propeller force always acts in the same direction. It can be shown that $\bar{F}_p$ is independent of r, and its dependence on $\bar{x}_o$ and $\bar{c}$ can be summarized as follows:

a. The effect of appendage interference is in general to yield forces less than the unperturbed propeller thrust. This reduction increases with propeller size.

b. The propeller force reaches a minimum before it passes the appendage in the region of $0 < \bar{y}_o < .6$.

c. A measurable maximum as shown in Fig. 30. is reached by $\bar{F}_p$ only at $\bar{x}_o < 1.2$.

d. After the propeller has passed the appendage the forces on it are slightly higher than the unperturbed thrust,

From an analytical point of view it is interesting to note in Figs. 31 to 33 the rather wide excursion of the coordinates of the substitution vortices. As explained in [5] the value of $\bar{x}_a$ does not approach the expected quarter-chord position as $y_o \to \infty$ because the line along which $z_p \to \infty$ is perpendicular to the appendage.

694

Skeg Position $(- x_o)$

Effects on Appendage - For the case where the propeller is upstream of the appendage both the quasi-steady forces and the wake forces increase more than proportionately with an increase in $\bar{c}$. However as seen in Fig. 8, the apparent mass forces exhibit a fairly complex behaviour. The depressions occurring at $\bar{y}_o > 0$ were unexpected and their influence can be noticed in the shape of the total force as exemplified in Fig. 11. From the succeeding plots of the total appendage force for a skeg position the following general comments can be made.

a. Except for $\bar{x}_o > -1.2$ the forces are predominantly negative, acting in the direction of propeller motion. The ratio F_a/T seems to increase with an increase in $\bar{c}$. Thus with an increase in propeller chord the value of F_a will increase both by virtue of an increase of T with $\bar{c}$ and an increase in the coefficient F_a/T.

b. The maximum (negative) force occurs before the propeller center passes the appendage and this occurs in the fairly narrow range, $.1 < \bar{y}_o < .5$.

c. After the propeller has passed the appendage the forces are usually positive and negligible.

d. The maximum (negative) normalized forces decrease with an increase in propeller velocity.

e. The forces go up drastically with a decrease in $\bar{x}_o$.

f. The peak forces for a skeg arrangement are quantitatively about the same and of opposite sign as the peak forces for a rudder arrangement.

Effects on Propeller - The normalized apparent mass forces go up less than proportionately with an increase in $\bar{c}$ while the quasi-steady and wake forces go up more than linearly with $\bar{c}$. From Figs. 25 to 28 the following emerges:

a. The effect of appendage interference is to increase the propeller force above that of the unperturbed thrust. For $\bar{c} = 0.5$ this increase can be as high as 25%, imposing large additional forces on the propeller blade.

b. F_p reaches a maximum in the region $.3 < \bar{y}_o < 1.0$.

c. As shown in Fig. 30 the value of the maximum force increases with a decrease in $\bar{x}_o$ and an increase in $\bar{c}$.

d. After the propeller has passed the appendage the forces on it are slightly below the value of the unperturbed thrust.

As shown in Fig. 33 the excursion of the substitution vortices is here smaller than for the propeller-rudder arrangement.

CONCLUSIONS

1. Spacings closer than $\bar{x}_o = 1.2$ between propeller and appendage should be avoided for at least two reasons; at $\bar{x}_o < 1.2$ there are two cycles of stress reversals; and the peak forces become excessive.

2. For a given propeller chord size c there exists an optimum ratio $\bar{c}$ which will produce the smallest peak force on the appendage. These values are $c \approx 2\ell/7$ for low propeller speeds ($r = 2$); and $c \approx 2\ell/10$ for high propeller speeds ($r = 4$). The above, of course, applies to the practical range of $\bar{c}$ values, $.1 < \bar{c} < .5$ and excludes the case of $\ell = 0$ when the force on the appendage would be zero.

3. Peak forces on both appendage and propeller always occur before the propeller center passes the appendage; the forces are negligible after the propeller has passed the appendage.

4. The peak forces on the appendage do not differ appreciably for either skeg or rudder arrangement.

5. The peak forces on the propeller for a rudder arrangement are essentially equal to the unperturbed thrust; for a skeg arrangement they are measurably higher.

6. On the appendage the peak forces increase less than proportionately with an increase in V; on the propeller they are proportional to its velocity.
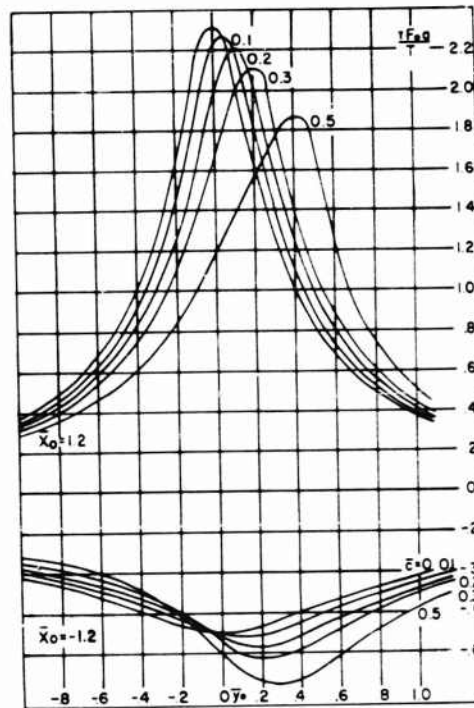
Fig. 6 - Quasi-Steady Forces on Appendage for $\bar{x}_o = \pm 1.2$
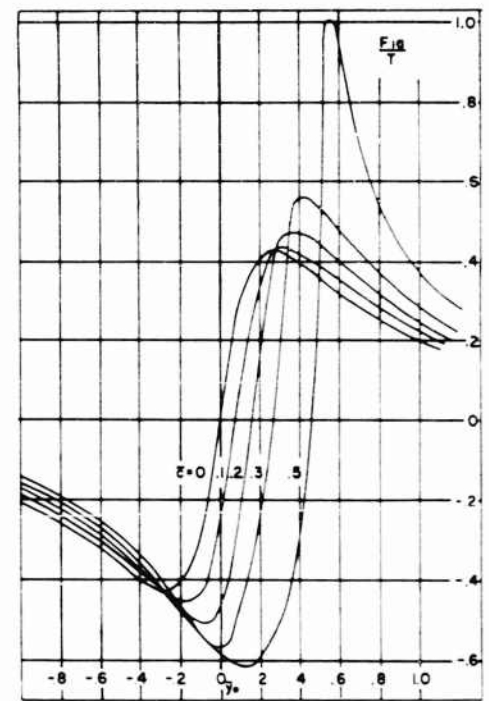
Fig. 7 - Apparent Mass Forces on Appendage for $\bar{x}_o = 1.2$

Fig. 8 - Apparent Mass Forces on
Appendage for $\bar{x}_o = -1.2$
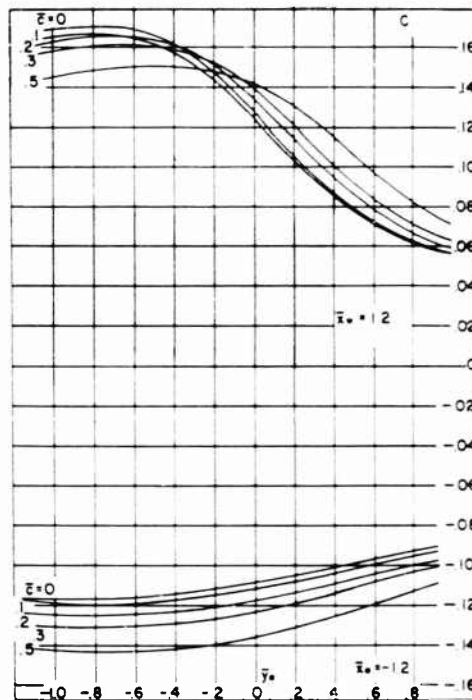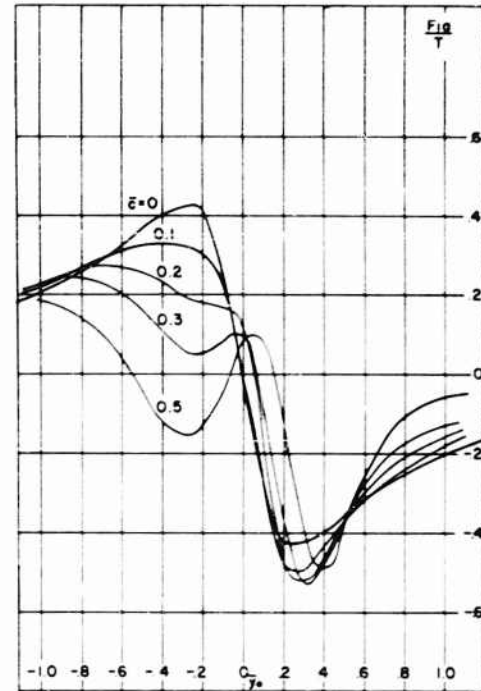
Fig. 9 - Component c of Wake Force
on Appendage vs. Propeller Position
$$\left(\frac{rF_{2a}}{T}\right) = -\frac{1}{2}\left(\frac{rF_{oa}}{T}\right) - C$$
$$r = 2$$

697
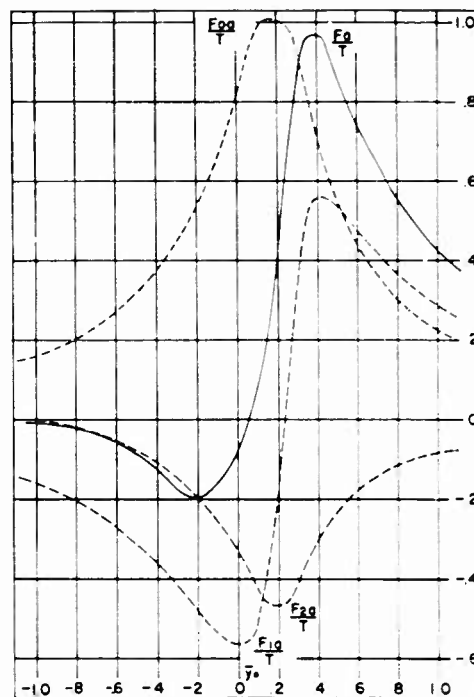
Fig. 10 - Forces on Appendage vs.
Propeller Position
$\overline{x}_o = 1.2$ $\overline{c} = 0.3$ $r = 2$

Fig. 11 - Forces on Appendage vs.
Propeller Position
$\overline{c} = 0.3$, $\overline{x}_o = -1.2$, $r = 2$

698
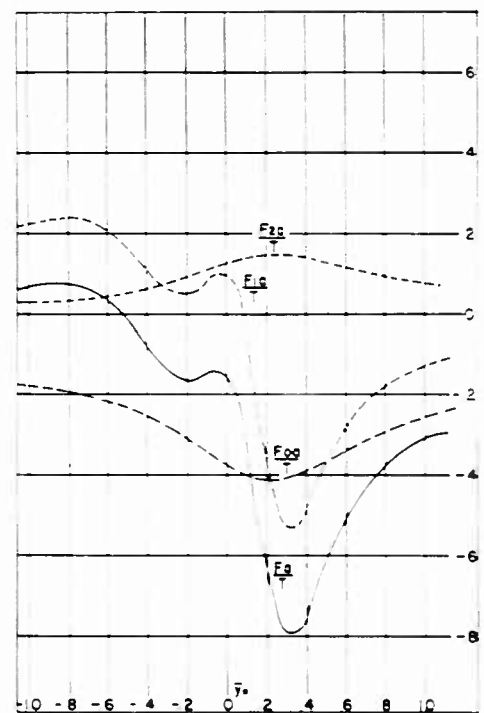
Fig. 12 - Force on Appendage vs.
Propeller Position
r = 2
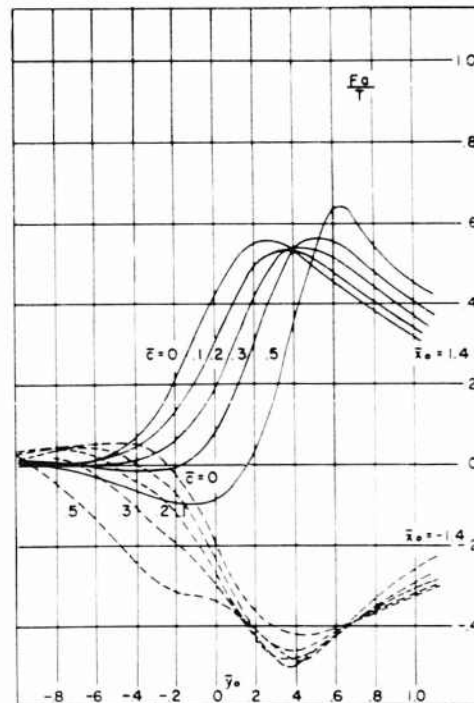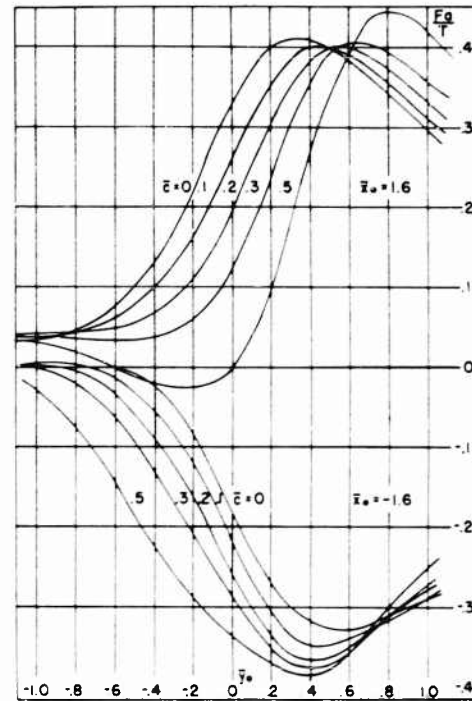
Fig. 13 - Total Force on Appendage vs.
Propeller Position
r = 2

699
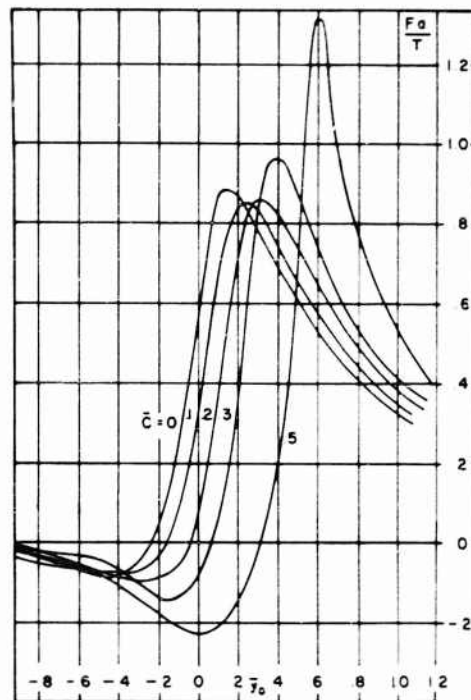
Fig. 14 - Total Force on Appendage for
$\bar{x}_o = 1.2$ $r = 2$

Fig. 15 - Total Force on Appendage for
$\bar{x}_o = -1.2$ $r = 2$
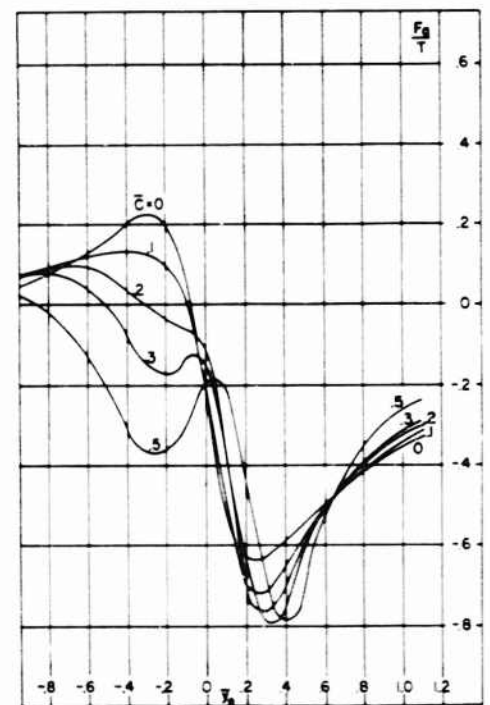
Fig. 16 - Total Force on Appendage vs.
Propeller Position
$\bar{x}_o = 1.2 \qquad r = 4$
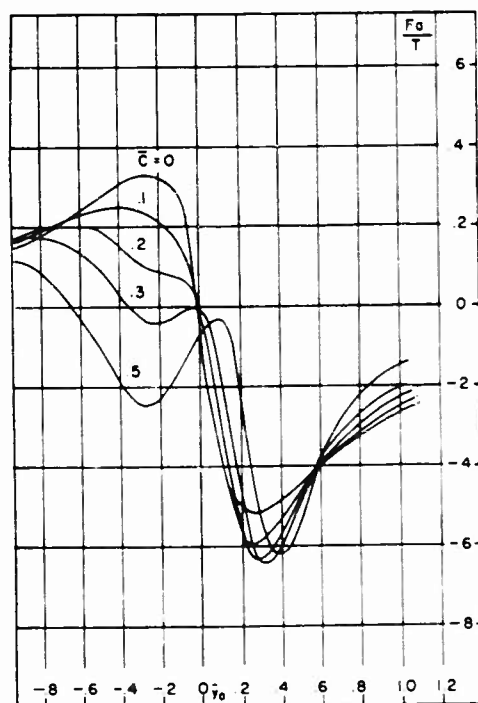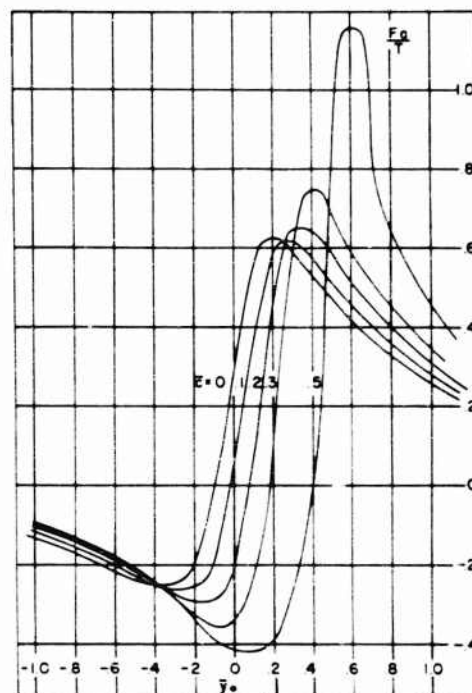
Fig. 17 - Total Force on Appendage vs.
Propeller Position
$\bar{x}_o = -1.2 \qquad r = 4$

701
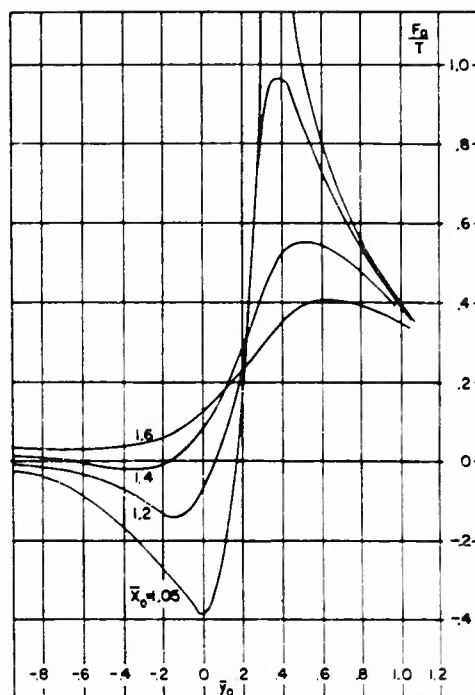
Fig. 18 - Total Force on Appendage for
$\bar{c} = 0.3$ $r = 2$

Fig. 19 - Total Force on Appendage vs.
Propeller Position
$\bar{c} = 0.3$ $r = 2$

702
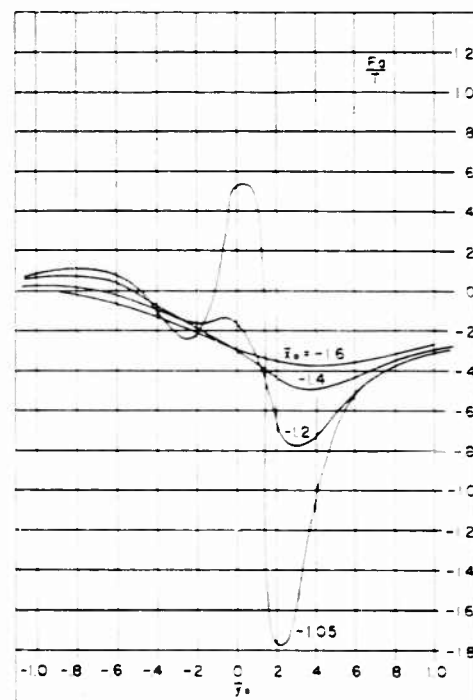
Fig. 20 - Quasi-Steady Forces on
Propeller
$\cdots\bar{x}_o = 1.2 \text{ ——— } \bar{x}_o = -1.2$
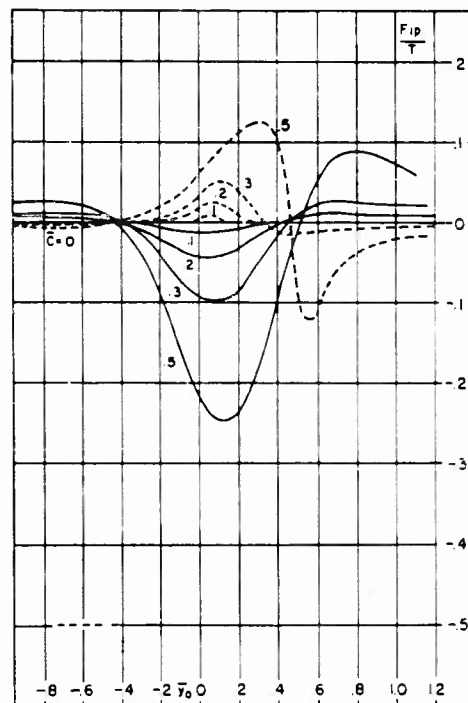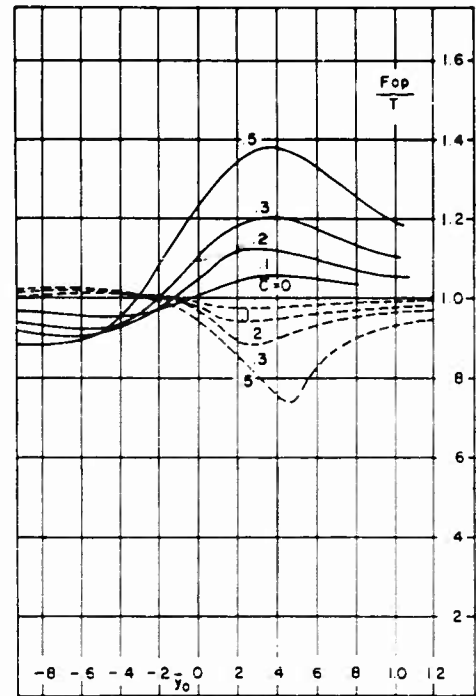
Fig. 21 - Apparent Mass Forces on
Propeller
$\cdots\bar{x}_o = 1.2 \text{ ——— } \bar{x}_o = -.12$

703
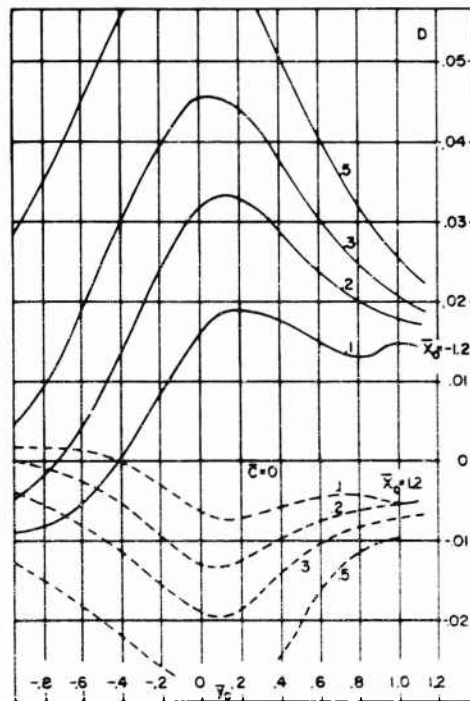
Fig. 22 - Component D of Wake Force
on Propeller

$$\frac{F_{2p}}{T} = -\frac{1}{2}\left(\frac{F_{pi}}{T}\right) + D$$

$$\overline{c} = 0$$

Fig. 23 - Forces on Propeller vs.
Propeller Position
$$\overline{x}_o = -1.2 \qquad \overline{c} = 0.3$$

704
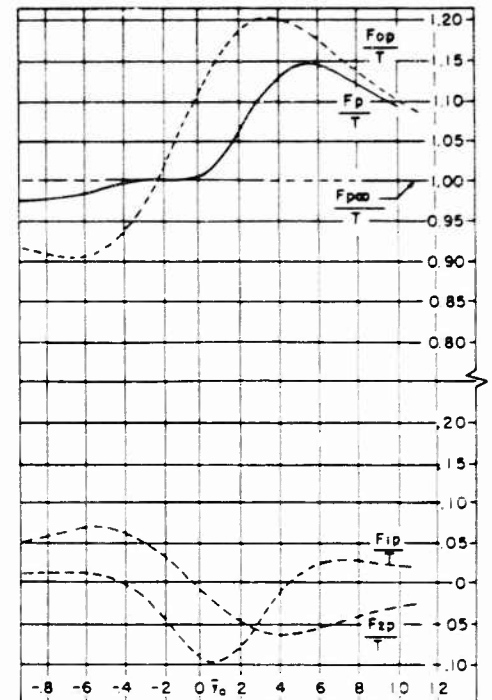
Fig. 24 - Forces on Propeller vs.
Propeller Position
$\bar{x}_o = 1.2$ $\bar{c} = 0.3$
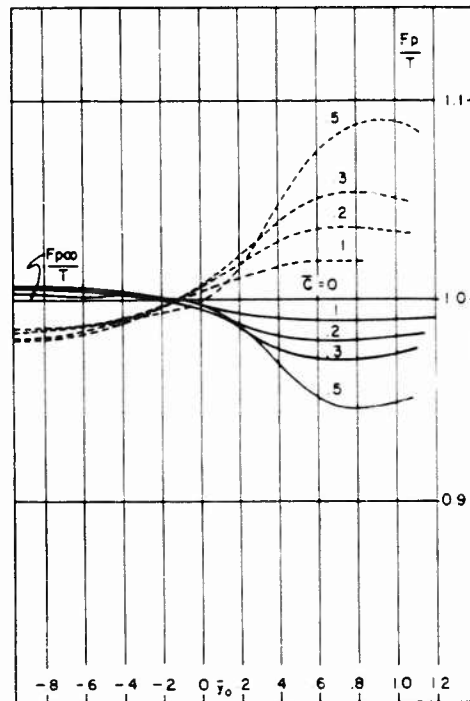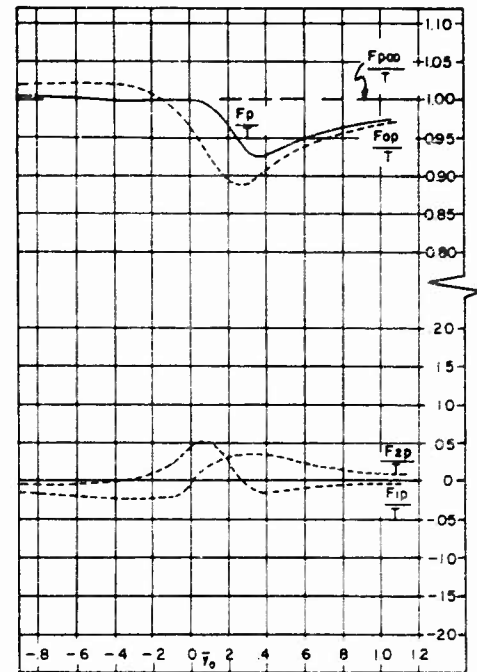
Fig. 25 - Total Force on Propeller vs.
Propeller Position
$\bar{x}_o = 1.6$ $\bar{x}_o = -1.6$

705
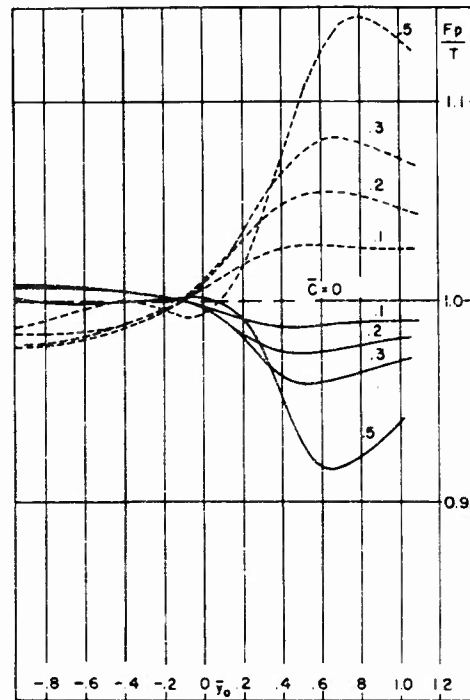
Fig. 26 - Total Force on Propeller vs.
Propeller Position
$\overline{x}_o = 1.4$ $---\overline{x}_o = -1.4$

Fig. 27 - Total Force on Propeller vs.
Propeller Position
$\overline{x}_o = 1.2$ $---\overline{x}_o = -1.2$
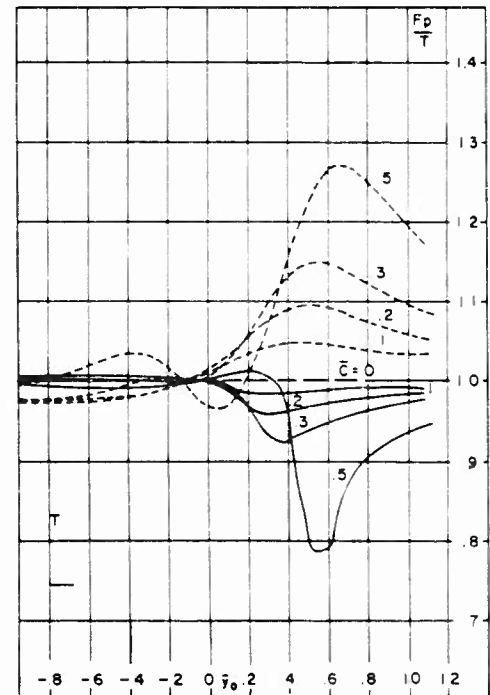
Fig. 28 - Total Force on Propeller vs.
Propeller Position
$\bar{c} = 0.3$
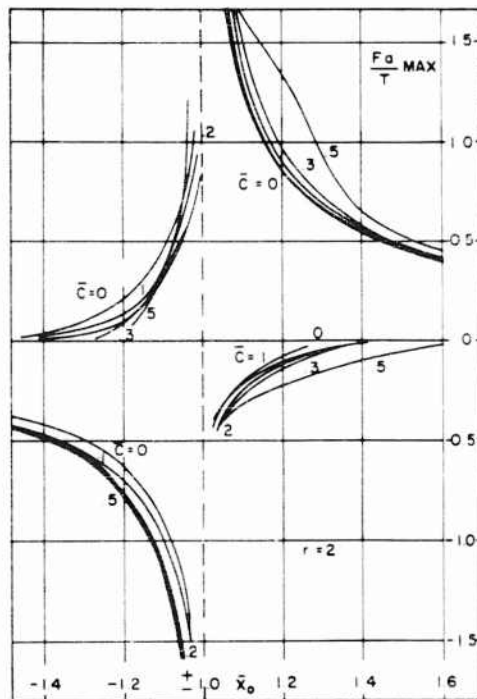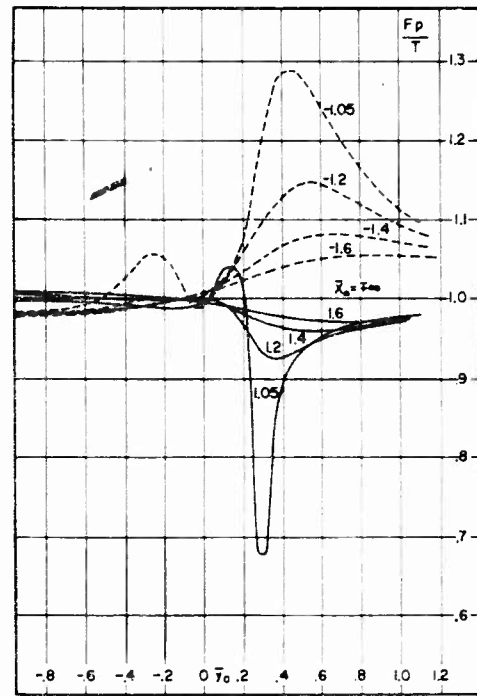
Fig. 29 - Maximum Positive and
Negative Forces on Appendage vs.
Appendage-Propeller Spacing. $r = 2$
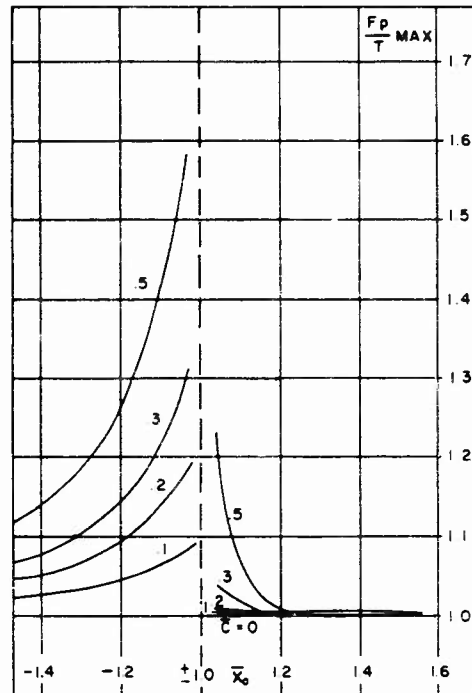
Fig. 30 - Maximum Force on Propeller vs. Appendage-Propeller Spacing

Fig. 31 - Position of Substitution Vortex on Appendage vs. Propeller Position $\bar{x}_c = 1.2$
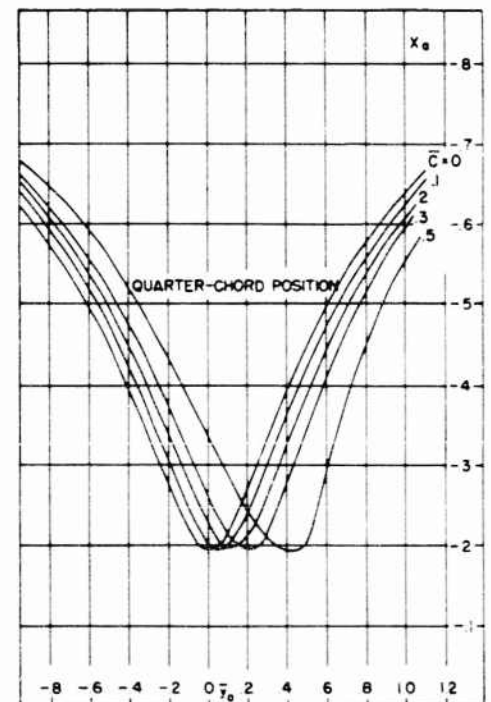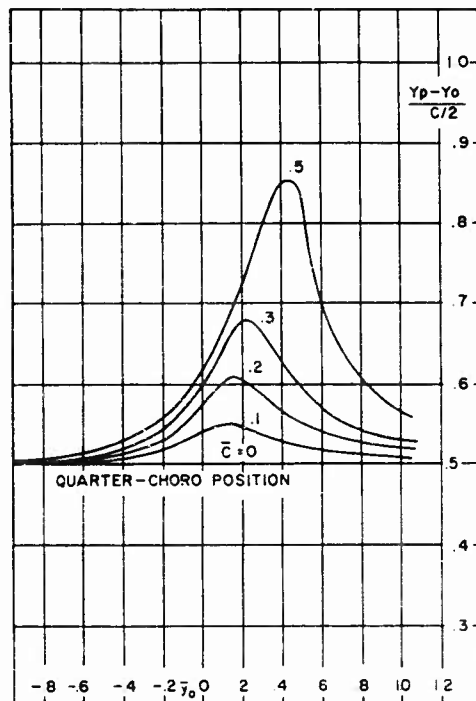
Fig. 32 - Position of Substitution Vortex on Propeller vs. Propeller Position $\overline{x}_o = 1.2$
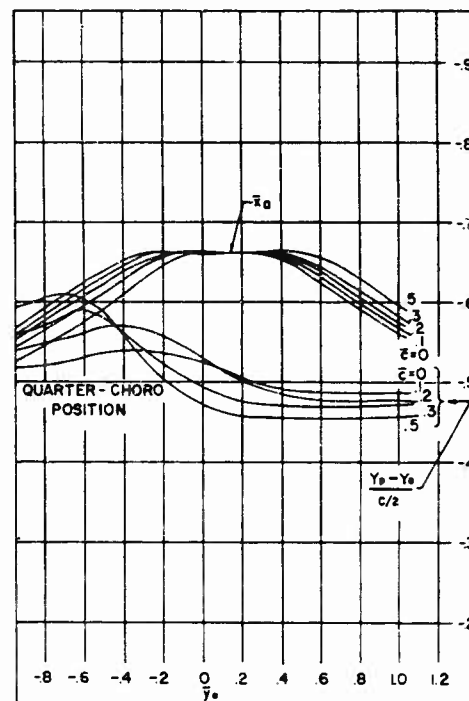
Fig. 33 - Location of Substitution Vortex vs. Propeller Position $\overline{x}_o = -1.2$

ACKNOWLEDGMENT

REFERENCES

1. Lewis, F.M. "Propeller Vibration", Trans. of Soc. of Naval Arch. and Mar. Eng., Vol. 43, pp. 252-285, 1935.

2. Lewis, F.M. "Propeller Vibration", Trans. of Soc. of Naval Arch. and Mar. Eng., Vol. 44, pp. 501-519, 1936.

3. Breslin, J.P. "The Unsteady Pressure Field Near A Ship Propeller and the Nature of the Vibratory Forces Produced on an Adjacent Surface", Stevens Inst. of Tech. Exp. Towing Tank, Report No. 609, June 1956.

4. Karman von Th. and Sears, W.R. "Airfoil Theory for Non-Uniform Motion", Jour. of Aeronautical Sciences, Vol. 5. No. 10, August 1938.

5. Pinkus, O., Lurye, J.R. and Feit, D. "The Unsteady Forces due to Propeller-Appendage Interaction", TRG Report Contract Nonr-3281(00), March 1962.

6. L.M. Milne-Thompson, Theoretical Aerodynamics, Macmillan and Co., Ltd., 3rd Edition, 1958, p. 153ff.

NUMERICAL AND EXPERIMENTAL INVESTIGATIONS OF THE DEPENDENCE OF TRANSVERSE FORCE AND BENDING MOMENT FLUCTUATIONS ON THE BLADE AREA RATIO OF FIVE-BLADED SHIP PROPELLERS*

J.K. Krohn
Hamburg Model Basin
Hamburg, Germany

I. INTRODUCTION

As the wake of a ship is not axis-symmetrical, the propeller working in this wake will experience a non-steady resulting force and a non-steady resulting moment. In recent years the components in direction of the propeller axis—namely the thrust and torque fluctuations—have been investigated fairly thoroughly. But little is known about investigations of the vertical and horizontal components of the resulting force and moment. Some experimental results were published in two papers by J.D. van Manen and R. Wereldsma [1,2]. The present paper is a further clarifying contribution to this problem. It deals in particular with the experimental and numerical determination of the influence of propeller-blade area ratio on transverse force and bending moment fluctuations. In addition to answering the specific questions, the theoretical part allows some general conclusions about the influence of wake, number of propeller-blades, etc. As example, numerical calculations were carried out for three five-bladed propellers with different blade area ratios which work in the same velocity field. The wake distribution used in these calculations is that measured behind the model used for the experimental investigation.

II. METHOD FOR CALCULATING TRANSVERSE FORCE AND BENDING MOMENT FLUCTUATIONS

The basis for the calculation of transverse force and bending moment fluctuations is the formula for the lift of an infinitely long hydrofoil. Introducing the camber corrections k_1 and k_2 for propellers [3], the lift for a blade element between r and dr is given by

$$dL = \frac{c_a}{k_1 \cdot k_2} \cdot \frac{\rho}{2} \cdot V^2 \cdot \ell \cdot R \cdot dx \quad \left(x = \frac{r}{R} \right).$$

Substituting the known formula $c_a = 2\pi(\alpha + \alpha_o)$ for the lift coefficient it follows

$$dL = \frac{\pi \cdot \rho \cdot R \cdot \ell}{k_1 \cdot k_2} \cdot V^2 \cdot (\alpha + \alpha_o) \cdot dx.$$

As a rule this equation is used for the calculation of the lift under the assumption that the field of flow in the vicinity of the propeller may be considered axis-symmetrical. That is, only the mean inflow velocity $\bar{V}_e$ over the circumference is taken. For the following considerations the assumption of rotational symmetry is omitted. The inflow velocity V_e can then be split up into the mean value over the circumference and the fluctuation ΔV_e so that $V_e = \bar{V}_e - \Delta V_e$. To simplify the calculation it is assumed that $|\Delta V_e| << \bar{V}_e$, hence that terms of second and higher power of ΔV_e can be neglected. The introduction of the term ΔV_e means that the relative velocity V as well as the angle of attack α can be split up into a mean value and a fluctuating term. This in turn means that the lift, too, can be represented by the sum of a mean value and a fluctuating term. To simplify the calculation it is assumed that the propeller is only lightly or moderately loaded. Then, the resultant of the axial and tangential component of the induced velocity is normal to the resultant relative velocity. Thus the relative velocity can be expressed in terms of the velocity U which is the resultant of the rotational speed $r.\Omega$ and the inflow velocity V_e. It follows from Fig. 1 that

$$V = U.\cos (\beta_i - \beta) = r.\Omega.\frac{\cos (\beta_i - \beta)}{\cos \beta}$$

where the angular velocity Ω is constant. Further it can be deduced from the Fig. 1 that, owing to $V_e = \bar{V}_e - \Delta V_e$, it is $\beta = \bar{\beta} - \varepsilon$ and on the other hand, owing to the constant geometrical pitch angle $\varphi = \beta_i + \alpha$, it is $\alpha = \bar{\alpha} + \Delta \alpha$ and $\beta_i = \bar{\beta}_i - \Delta \alpha$. The quantities with a bar are mean values over the circumference. Substituting the expressions for the angles in the expression for the relative velocity and developing in terms of the fluctuating quantities, one obtains

$$V = \bar{V} - \Delta V = \bar{U} \cdot \cos (\bar{\beta}_i - \bar{\beta}) - \bar{U} \cdot \cos (\bar{\beta}_i - \bar{\beta}) \cdot \left[(1 - \tau) \cdot tg(\bar{\beta}_i - \bar{\beta}) + tg\bar{\beta} \right] \cdot \varepsilon$$

where $\bar{U} = r.\Omega/\cos \bar{\beta}$ and $\tau = \Delta \alpha/\varepsilon$. The development was stopped after the linear term in ε or $\Delta \alpha$, respectively, since, owing to $|\Delta V_e| << \bar{V}_e$, it is also $|\varepsilon| << \bar{\beta}$ and $|\Delta \alpha| << \bar{\beta}_i$. After some simple calculations it is now possible to express the lift as follows

712
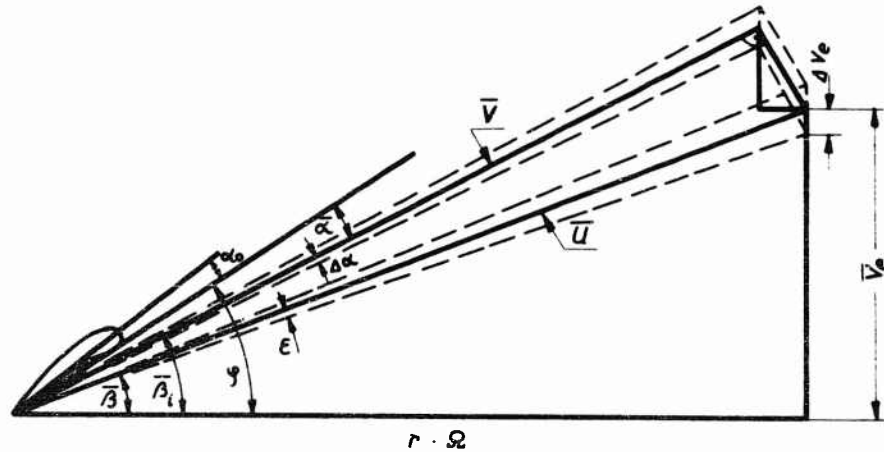
Fig. 1 - Vector-Diagram of the Velocities at a Propeller Blade Element

$$dL = d\overline{L} + d\triangle L = \frac{\pi \cdot \rho \cdot R \cdot \ell}{k_1 \cdot k_2} \cdot \overline{U}^2 \cdot \cos^2 (\overline{\beta}_i - \overline{\beta}) \cdot (\alpha_o + \varphi - \overline{\beta}_i) \cdot dx$$

$$+ \frac{\pi \cdot \rho \cdot R \cdot \ell}{k_1 \cdot k_2} \cdot \overline{U}^2 \cdot \cos^2 (\overline{\beta}_i - \overline{\beta}) \cdot \left\{ 1 - \frac{2}{\tau} \cdot (\alpha_o + \varphi - \overline{\beta}_i) \right.$$

$$\left. \cdot \left[(1 - \tau) \cdot tg \ (\overline{\beta}_i - \overline{\beta}) + tg \ \overline{\beta} \right] \right\} \cdot \triangle d \cdot dx \ .$$

Thence the tangential component dL_t is obtained by multiplying dL in $\sin \beta_i$. Developing the expression thus found, the tangential component of the lift on a blade element becomes

$$dL_t = d\overline{L}_t + d\triangle L_t = d\overline{L} \cdot \sin \overline{\beta}_i - (d\overline{L} \cdot cotg \ \overline{\beta}_i \cdot \triangle \alpha - d\triangle L) \cdot \sin \overline{\beta}_i .$$

If the blade element under consideration belongs to the j-th blade of a z-bladed propeller ($z > 1$), then the multiplication of the tangential component in $\cos \psi_j$ or $\sin \psi_j$, respectively, gives the horizontal or vertical component of the transverse force on an element for the j-th blade (see Fig. 2)

$$dT_{hor.}^{(j)} = dL_t \cdot \cos \psi_j \quad ; \quad dT_{vert.}^{(j)} = dL_t \cdot \sin \psi_j .$$

Substituting the corresponding quantities and integrating over the radius one obtains finally the horizontal and vertical component of the transverse force for the j-th blade.

$$\left. \begin{array}{l} T_{hor.}^{(j)} \\ T_{vert.}^{(j)} \end{array} \right\} = \pi \cdot \rho \cdot R \cdot \int_{x_0}^1 \frac{\ell}{k_1 \cdot k_2} \cdot \overline{U}^2 \cdot (\alpha_o + \varphi - \overline{\beta}_i) \cdot \cos^2 (\overline{\beta}_i - \overline{\beta}) \cdot \sin \overline{\beta}_i \cdot dx \cdot \left\{ \begin{array}{l} \cos \psi_j \\ \sin \psi_j \end{array} \right. \quad \begin{array}{l} \textbf{(1)} \\ \textbf{(Cont.)} \end{array}$$

713

$$\frac{\ell}{2} \cdot \cos \varphi = r \cdot \gamma$$
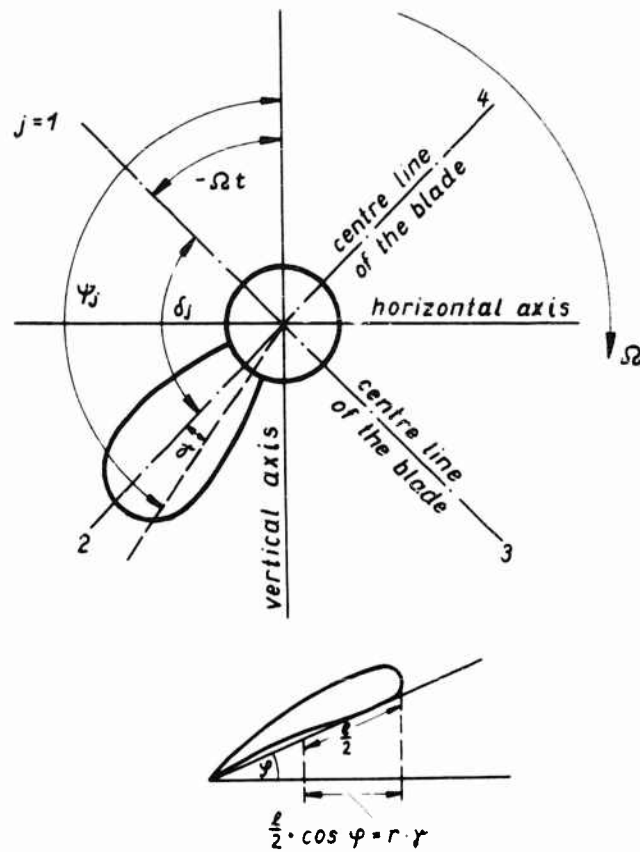
Fig. 2 - Angles and Coordinates at the Propeller

$$\left.\begin{matrix} T_{hor.}^{(j)} \\ \\ T_{vert.}^{(j)} \end{matrix}\right\} = + \pi \cdot \rho \cdot R \cdot \int_{x_0}^{1} \frac{\ell}{k_1 \cdot k_2} \cdot \bar{U}^2 \cdot \left\{ 1 - \frac{\alpha_0 - \varphi - \bar{\beta}_i}{\tau} \cdot \left[2 \cdot (1-\tau) \cdot tg \ (\bar{\beta}_i - \bar{\beta}) + tg \ \bar{\beta} \right. \right. \tag{1}$$

$$\left. \left. + \ \tau \cdot cotg \ \bar{\beta}_i \right] \right\} \cdot \cos^2 \ (\bar{\beta}_i - \bar{\beta}) \cdot \sin \bar{\beta}_i \cdot \triangle \alpha \cdot dx \cdot \left\{ \begin{matrix} \cos \psi_j \\ \sin \psi_j \end{matrix} \right. .$$

Likewise one obtains by multiplication of dL by $\cos \beta_i$ the axial component dL_a of the lift

$$dL_a = d\bar{L}_a - d\triangle L_a = d\bar{L} \cdot \cos \bar{\beta}_i + (d\bar{L} \cdot tg \ \bar{\beta}_i \cdot \triangle \alpha - d\triangle L) \cdot \cos \bar{\beta}_i .$$

Thence one arrives at the components of that part of the bending moment about the horizontal and vertical axis which is due to an element of the j-th blade by multiplying dL_a into the distance from the two axes, hence

714

$$dM^{(j)}_{hor.} = dL_a \cdot R \cdot x \cdot \cos \psi_j \quad ; \quad dM^{(j)}_{vert.} = dL_a \cdot R \cdot x \cdot \sin \psi_j.$$

Then the integration over the radius gives the horizontal and vertical components of the bending moment for the j-th blade.

$$\left.\begin{matrix} M^{(j)}_{hor.} \\ \\ M^{(j)}_{vert.} \end{matrix}\right\} = \pi \cdot \rho \cdot R^2 \cdot \int_{x_0}^1 \frac{\ell}{k_1 \cdot k_2} \cdot \bar{U}^2 \cdot (\alpha_o + \varphi - \bar{\beta}_i) \cdot \cos^2 (\bar{\beta}_i - \bar{\beta}) \cdot \cos \bar{\beta}_i \cdot x \cdot dx \cdot \begin{cases} \cos \psi_j \\ \\ \sin \psi_j \end{cases}$$

$$+ \pi \cdot \rho \cdot R^2 \cdot \int_{x_0}^1 \frac{\ell}{k_1 \cdot k_2} \cdot \bar{U}^2 \cdot \left\{ 1 - \frac{\alpha_o + \varphi - \bar{\beta}_i}{\tau} \cdot \left[2 \cdot (1 - \tau) \cdot tg (\bar{\beta}_i - \bar{\beta}) + tg \bar{\beta} \right. \right.$$

$$\left. \left. - \tau \cdot tg \bar{\beta}_i \right] \right\} \cdot \cos^2(\bar{\beta}_i - \bar{\beta}) \cdot \cos \bar{\beta}_i \cdot \Delta\alpha \cdot x \cdot dx \cdot \begin{cases} \cos \psi_j \\ \\ \sin \psi_j \end{cases}.$$

In order to obtain the transverse force and bending moment components for the propeller, eqs. (1) and (2) have to be summed over the number of blades. For the first term on the right side of the two equations this summation is easily carried out because apart from the angle δ_j contained in the angle ψ_j no other quantity depends on the index of summation. The angle δ_j is measured from the first blade to the j-th blade in the mathematically positive sense, i.e.,

$$\delta_j = 2\pi \cdot \frac{j-1}{z}$$

As known

$$\sum_{j=1}^z \cos 2\pi \cdot \frac{j-1}{z}$$

as well as

$$\sum_{j=1}^z \sin 2\pi \cdot \frac{j-1}{2}$$

vanish for all $z > 1$, so that the first terms on the right side of the eqs. (1) and (2) do not contribute to the transverse force and bending moment components. This is also understandable for physical reasons, if one notes that these terms contain only the axis-symmetrical part of the wake distribution. For, in an axis-symmetrical wake a single blade can be excited hydrodynamically to transverse force and bending moment fluctuations with a frequency which is equal to the number of revolutions, but not a multi-bladed propeller. In carrying out the summation over the second term it is to be observed that ε as well as $\Delta\alpha$ are functions of the index j. Therefore, this relation shall be determined first. For this purpose the representation of the inflow velocity V_e by a Fourier-series is used. The term which is independent of the circumferential coordinate ψ_j then corresponds to the mean inflow, whilst the value of the series is equal to the velocity fluctuation ΔV_e. Now only those parts of the inflow field are of interest

715

en

in which the propeller blades are at the moment. The circumferential coordinate of a point within a blade element of the j-th blade is given by (Fig. 2)

$$\psi_j = -\Omega \cdot t + \gamma + \delta_j \quad ; \quad \delta_j = 2\pi \cdot \frac{j-1}{z} \quad ; \quad j = 1, 2, \ldots \ldots z \ .$$

Then the fluctuation of the inflow velocity in this point relative to the velocity $\bar{U}$ is expressed by

$$\left(\frac{\Delta V_e}{\bar{U}}\right)_j = \sum_{n=1}^{\infty} \left(\text{Re } \alpha_n \cdot e^{in\psi_j} + \text{Im } b_n \cdot e^{in\psi_j}\right) \ .$$

On the other hand one can deduce the relation

$$\epsilon_j = \left(\frac{\Delta V_e}{\bar{U}}\right)_j \cdot \cos \bar{\beta}$$

from Fig. 1, so that the relationship between ϵ_j and the circumferential coordinate ψ_j is known. It remains now to determine how ϵ_j and $\Delta \alpha_j$ are related with one another; that is, a statement on τ must be made. On the basis of the afore made assumptions and calculations nothing can be said about τ since as an essential quantity the fluctuation of the velocity induced at the propeller enters into τ. In order to determine this fluctuation, fundamental research in the behaviour of a hydrofoil in three-dimensional non-steady flow is necessary. These investigations, however, exceed the limits of the method of calculation used here, where the theory of an infinitely long hydrofoil in two-dimensional flow has been applied to the propeller. For this reason it will be assumed in the following calculations that ϵ_j and $\Delta \alpha_j$ coincide in both amplitude and phase, that is, $\tau = 1$. Then the relation between ψ_j and ϵ_j holds also for $\Delta \alpha_j$ which is expressed by

$$\epsilon_j = \Delta \alpha_j = \sum_{n=1}^{\infty} \left(\text{Re } \alpha_n \cdot e^{in\psi_j} - \text{Im } b_n \cdot e^{in\psi_j}\right) \cdot \cos \bar{\beta} \ .$$

If this equation is multiplied by $\cos \psi_j$ or $\sin \psi_j$, respectively, it follows after some transformation, under consideration of the addition theorems for the trigonometric functions,

$$\Delta \alpha_j \cdot \cos \psi_j = \frac{1}{2} \cdot \sum_{n=1}^{\infty} \left\{ \text{Re } \alpha_n \cdot \left(e^{i(n+1)\psi_j} + e^{i(n-1)\psi_j} \right) + \text{Im } b_n \cdot \left(e^{i(n+1)\psi_j} - e^{i(n-1)\psi_j} \right) \right\}$$

$$= \frac{1}{2} \cdot \alpha_1 + \frac{1}{2} \cdot \left(\text{Re } \alpha_2 \cdot e^{i\psi_j} - \text{Im } b_2 \cdot e^{i\psi_j} \right) - \sum_{n=2}^{\infty} \left\{ \text{Re } \frac{\alpha_{n-1} - \alpha_{n+1}}{2} \cdot e^{in\psi_j} \right.$$

$$\left. + \text{Im } \frac{b_{n-1} + b_{n+1}}{2} \cdot e^{in\psi_j} \right\}$$

(Cont.)

716

$$\Delta \alpha_j \cdot \sin \psi_j = \frac{1}{2} \cdot \sum_{n=1}^{\infty} \left\{ \mathrm{Im}\ \alpha_n \cdot \left(e^{i(n+1)\psi_j} - e^{i(n-1)\psi_j} \right) - \mathrm{Re}\ b_n \cdot \left(e^{i(n+1)\psi_j} - e^{i(n-1)\psi_j} \right) \right\}$$

$$= \frac{1}{2} \cdot b_1 - \frac{1}{2} \cdot \left(\mathrm{Im}\ \alpha_2 \cdot e^{i\psi_j} - \mathrm{Re}\ b_2 \cdot e^{i\psi_j} \right) + \sum_{n=2}^{\infty} \left\{ \mathrm{Im}\ \frac{\alpha_{n-1} - \alpha_{n+1}}{2} \cdot e^{in\psi_j} \right.$$

$$\left. - \mathrm{Re}\ \frac{b_{n-1} - b_{n+1}}{2} \cdot e^{in\psi_j} \right\} .$$

From these equations we obtain by summation over the number of blades the formulae

$$\sum_{j=1}^{z} \Delta \alpha_j \cdot \cos \psi_j = \frac{z}{2} \cdot \alpha_1 + z \cdot \sum_{m=1}^{\infty} \left\{ \mathrm{Re}\ \frac{\alpha_{mz-1} + \alpha_{mz+1}}{2} \cdot e^{imz \cdot (-\Omega \cdot t + \gamma)} \right.$$

$$\left. + \mathrm{Im}\ \frac{b_{mz-1} + b_{mz+1}}{2} \cdot e^{imz \cdot (-\Omega \cdot t + \gamma)} \right\} \tag{3a}$$

$$\sum_{j=1}^{z} \Delta \alpha_j \cdot \sin \psi_j = \frac{z}{2} \cdot b_1 + z \cdot \sum_{m=1}^{\infty} \left\{ \mathrm{Im}\ \frac{\alpha_{mz-1} - \alpha_{mz+1}}{2} \cdot e^{imz \cdot (-\Omega t + \gamma)} \right.$$

$$\left. - \mathrm{Re}\ \frac{b_{mz-1} - b_{mz+1}}{2} \cdot e^{imz \cdot (-\Omega t + \gamma)} \right\} \tag{3b}$$

Returning now to eqs. (1) and (2) and summing them over the number of blades, the relations obtained in this way consist of terms

$$\sum_{j=1}^{z} \alpha_j \cdot \cos \psi_j$$

and

$$\sum_{j=1}^{z} \alpha_j \cdot \sin \psi_j$$

which are provided with factors and are integrated over the radius. The relations obtained from the summation do not yet represent the complete transverse force and bending moment fluctuations, but, only that part of the fluctuations which is effective on a straight line which includes the angle γ with the mean line of the blade. Then obviously the equations (3a) and (3b) are expressing the fluctuation of the angle of attack on the just mentioned straight line on all z blades. Further, however, the fluctuations must be summed over the breadth of the blade. This summation has already been carried out in a general manner by Sears [4] and is here supposed as known. Using the results obtained by Sears

717

and considering eqs. (3a) and (3b) the following expressions are obtained for the transverse force and bending moment components

$$T_{hor.} = \frac{\pi \cdot z \cdot \rho \cdot R}{2} \cdot \int_{x_0}^{1} \frac{\ell}{k_1 \cdot k_2} \cdot \overline{U}^2 \cdot \left\{ 1 - (\alpha_0 + \psi - \overline{\beta}_i) \cdot (2 \cdot tg\, \overline{\beta} + cotg\, \overline{\beta}_i) \right\}$$

$$\cdot cos^2 (\overline{\beta}_i - \overline{\beta}) \cdot sin\, \overline{\beta}_i \cdot a_1 \cdot dx + \frac{\pi \cdot z \cdot \rho \cdot R}{2} \cdot \int_{x_0}^{1} \frac{\ell}{k_1 \cdot k_2} \cdot \overline{U}^2 \cdot \left\{ 1 - (\alpha_0 + \psi - \overline{\beta}_i) \right.$$

$$\cdot (2 \cdot tg\, \overline{\beta} + cotg\, \overline{\beta}_i) \Big\} \cdot cos^2 (\overline{\beta}_i - \overline{\beta}) \cdot sin\, \overline{\beta}_i \cdot \sum_{m=1}^{\infty} \left\{ Re(\alpha_{mz-1} + \alpha_{mz+1}) \cdot F(\omega_{mz}) \right.$$

$$\cdot e^{-imz\Omega t} + Im(b_{mz-1} + b_{mz+1}) \cdot F(\omega_{mz}) \cdot e^{-imz\Omega t} \Big\} \cdot dx \tag{4a}$$

$$T_{vert.} = \frac{\pi \cdot z \cdot \rho \cdot R}{2} \cdot \int_{x_0}^{1} \frac{\ell}{k_1 \cdot k_2} \cdot \overline{U}^2 \cdot \left\{ 1 - (\alpha_0 + \psi - \overline{\beta}_i) \cdot (2 \cdot tg\, \overline{\beta} + cotg\, \overline{\beta}_i) \right\}$$

$$\cdot cos^2 (\overline{\beta}_i - \overline{\beta}) \cdot sin\, \overline{\beta}_i \cdot b_1 \cdot dx + \frac{\pi \cdot z \cdot \rho \cdot R}{2} \cdot \int_{x_0}^{1} \frac{\ell}{k_1 \cdot k_2} \cdot \overline{U}^2 \cdot \left\{ 1 - (\alpha_0 + \psi - \overline{\beta}_i) \right.$$

$$\cdot (2 \cdot tg\, \overline{\beta} + cotg\, \overline{\beta}_i) \Big\} \cdot cos^2 (\overline{\beta}_i - \overline{\beta}) \cdot sin\, \overline{\beta}_i \cdot \sum_{m=1}^{\infty} \left\{ Im(\alpha_{mz-1} - \alpha_{mz+1}) \cdot F(\omega_{mz}) \right.$$

$$\cdot e^{-imz\Omega t} - Re(b_{mz-1} - b_{mz+1}) \cdot F(w_{mz}) \cdot e^{-imz\Omega t} \Big\} \cdot dx \tag{4b}$$

$$M_{hor.} = \frac{\pi \cdot z \cdot \rho \cdot R^2}{2} \cdot \int_{x_0}^{1} \frac{\ell}{k_1 \cdot k_2} \cdot \overline{U}^2 \cdot \left\{ 1 - (\alpha_0 + \psi - \overline{\beta}_i) \cdot (2 \cdot tg\, \overline{\beta} - tg\, \overline{\beta}_i) \right\}$$

$$\cdot cos^2 (\overline{\beta}_i - \overline{\beta}) \cdot cos\, \overline{\beta}_i \cdot a_1 \cdot x \cdot dx + \frac{\pi \cdot z \cdot \rho \cdot R^2}{2} \cdot \int_{x_0}^{1} \frac{\ell}{k_1 \cdot k_2} \cdot \overline{U}^2 \cdot \left\{ 1 - (\alpha_0 + \psi - \overline{\beta}_i) \right.$$

$$\cdot (2 \cdot tg\, \overline{\beta} - tg\, \overline{\beta}_i) \Big\} \cdot cos^2 (\overline{\beta}_i - \overline{\beta}) \cdot cos\, \overline{\beta}_i \cdot \sum_{m=1}^{\infty} \left\{ Re(\alpha_{mz-1} + \alpha_{mz+1}) \cdot F(w_{mz}) \right.$$

$$\cdot e^{-imz\Omega t} + Im(b_{mz-1} - b_{mz+1}) \cdot F(w_{mz}) \cdot e^{-imz\Omega t} \Big\} \cdot x \cdot dx \tag{5a}$$

718

$$M_{vert.} = \frac{\pi \cdot z \cdot \rho \cdot R^2}{2} \cdot \int_{x_0}^{1} \frac{\ell}{k_1 \cdot k_2} \cdot \overline{U}^2 \cdot \left\{ 1 - (\alpha_0 + \psi - \overline{\beta}_i) \cdot (2 \cdot tg \, \overline{\beta} - tg \, \overline{\beta}_i) \right\}$$

$$\cdot \cos^2(\overline{\beta}_i - \overline{\beta}) \cdot \cos \overline{\beta}_i \cdot b_1 \cdot x \cdot dx + \frac{\pi \cdot z \cdot \rho \cdot R^2}{2} \cdot \int_{x_0}^{1} \frac{\ell}{k_1 \cdot k_2} \cdot \overline{U}^2 \cdot \left\{ 1 - (\alpha_0 + \psi - \overline{\beta}_i) \right.$$

$$\left. \cdot (2 \cdot tg \, \overline{\beta} - tg \, \overline{\beta}_i) \right\} \cdot \cos^2 (\overline{\beta}_i - \overline{\beta}) \cdot \cos \overline{\beta}_i \cdot \sum_{m=1}^{\infty} \left\{ Im(\alpha_{mz-1} - \alpha_{mz+1}) \cdot F(w_{mz}) \right.$$

$$\left. \cdot e^{-imz\Omega t} - Re(b_{mz-1} - b_{mz+1}) \cdot F(w_{mz}) \cdot e^{-imz\Omega t} \right\} \cdot x \cdot dx \,. \tag{5b}$$

Where

$$F(w_{mz}) = \frac{1}{i \cdot w_{mz} \cdot [K_0(i w_{mz}) + K_1(i w_{mz})]}$$

is the reduction formula of Sears, and

$$w_{mz} = \frac{m \cdot z \cdot \ell \cdot \Omega}{2 \cdot \overline{U}} \cdot \frac{\cos \psi}{\cos \overline{\beta}}$$

is the reduced frequency which is obtained by means of the relation $\ell/2 \cdot \cos \varphi = r \cdot \gamma_0$ (Fig. 2). The eqs. (4) and (5) require a short discussion, because, here a term independent of the circumferential coordinate appears besides the expected fluctuation dependent on the circumferential coordinate. This is surprising, because, when deriving the equations it appeared that only the fluctuation of the inflow velocity v_e delivers a contribution, the axis-symmetrical part, however, drops out. Physically this means that for a given number of revolutions the fluctuation of the inflow velocity to the propeller produces a constant transverse force and a constant bending moment besides the transverse force and bending moment fluctuations. This result can be explained by the example of a single screw ship. The distribution of the nominal inflow velocity in the propeller plane behind a single screw ship is symmetrical relative to the vertical axis (Fig. 2); that is, in a given interval of time the same quantity of water is flowing across the semi-plane on both the right and the left side of the vertical axis. On the other hand the distribution of the inflow velocity is asymmetrical relative to the horizontal axis. Thus, in a given interval of time a different quantity of water is flowing across the semi-planes above and below the horizontal axis. Indeed, the velocity in the lower semi-plane is higher. The transverse force components, too, show a different behaviour in relation to the axes. Inside the upper or lower semi-plane, respectively, the horizontal transverse force component has the same direction, whereas the direction between the two semi-planes is opposed. The same behaviour is found for the vertical component relative to the right and left semi-plane. Thus, it is to be expected that the whole vertical component of the transverse force disappears on account of the symmetry of the inflow velocity relative to the vertical axis; the whole horizontal component, however, differs from zero owing to the higher velocity in the

719

lower semi-plane. This consideration is only valid for that part of the transverse force which depends on the first harmonic of the inflow distribution. This is due to the difference of the behaviour in the respective two semi-planes. To summarize, it can be said that the steady state term of the transverse force resulting from the calculation and its dependence on the first harmonic of the inflow velocity is easy to explain physically. In the same way an explanation for the bending moment can be given.

Carrying out the numerical calculation of the expressions (4) and (5) all quantities which are not given as propeller data or as wake analysis can be ascertained from simple geometrical relations which are to be taken from Fig. 1. Only the determination of the angle $\overline{\beta}_i$ is an exception, since the mean induced velocity enters into it. On account of the assumption of the lightly to moderately loaded propeller one can obtain $\overline{\beta}_i$ by equating the lift coefficient derived from the simple airfoil theory

$$c_a = \frac{2\pi}{k_1 \cdot k_2} \cdot (\alpha_0 + \psi - \overline{\beta}_i)$$

to the lift coefficient following from Goldstein's calculations [5]

$$c_a = \frac{4 \cdot \pi \cdot \mathcal{H}}{z} \cdot \frac{D}{\lambda} \cdot \sin \overline{\beta}_i \cdot \text{tg} (\overline{\beta}_i - \overline{\beta}) .$$

III. TESTS AND GENERAL RESULTS OF TESTS

To carry out the tests, the model of a bulk carrier, scale 1:25, was used. The sections of this model are represented in Fig. 3. Furthermore, three propellers have been designed and manufactured for this model. The essential difference of these propellers consists in the blade area ratio. Otherwise, all propellers have the same diameter and are designed as optimum propellers for a given speed (speed of model 1.543 m/sec corresponding to a ship's speed of 15 kn). The shape of the blades and of the sections are shown in Fig.s 4 to 6. The characteristic data of both the ship model and the propeller models are as follows:

a. ship model

length between PP	L = 6120	[mm]
beam	B = 840	[mm]
draft	T = 360	[mm]
displacement	D = 1369.5	[kg]
block coefficient	δ = 0.74	

b. propeller model

diameter	230.00	230.00	230.00	[mm]
pitch	193.66	193.66	193.66	[mm]
pitch diameter ratio	0.842	0.842	0.842	
blade area ratio	0.35	0.55	0.75	
number of blades	5	5	5	

720
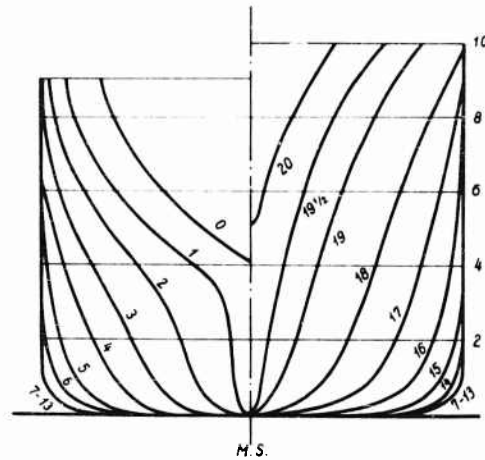
Fig. 3 - Frame Plan
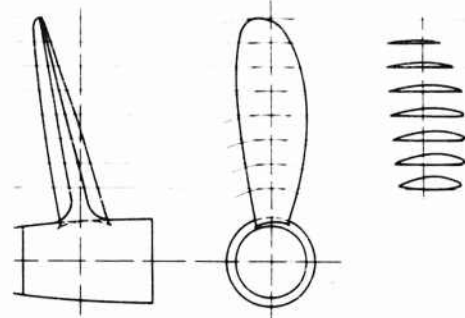
Fig. 4 - Propeller Plan
Blade Area Ratio 0.35
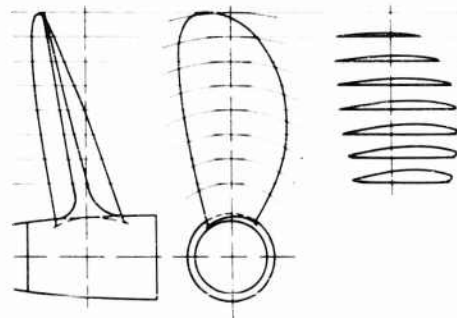
Fig. 5 - Propeller Plan
Blade Area Ratio 0.55
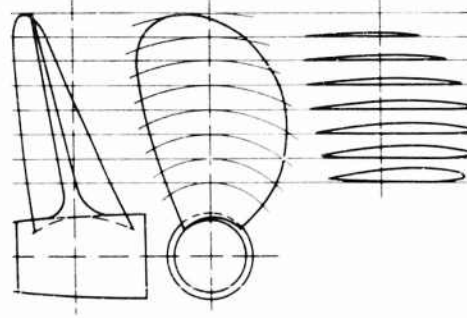
Fig. 6 - Propeller Plan
Blade Area Ratio 0.75

In order to measure the transverse force and bending moment fluctuations a special dynamometer is installed in the ship model. This instrument transforms transverse force and bending moment fluctuations into electric quantities which are recorded after amplification. The essential element of this instrument is the bearing of the propeller shaft which is supported by tubular beams as shown in Fig. 14. This suspension is axis-symmetrical, so that the forces transmitted to the beams can be registered in two directions, (horizontal and vertical) by means of strain gauges. With regard to its vibration characteristics, the instrument is so designed that the frequencies of the quantities to be measured are sufficiently below the natural frequency of the instrument. The model prepared for the test is arranged underneath the towing carriage as for a propulsion test, so that it is free to move in all directions. It is only guided fore and aft in order to keep it on a straight course. Tests with the self-propelled model are carried out at different speeds. Hence, each test point corresponds to one run. Thus, the influence of speed on the transverse force and bending moment

721

fluctuations can be determined. Hence, one series of tests had to be carried out for each of the three propellers. The results of these tests are given in the following tables. They are also shown graphically in Figs. 7 to 12. It should be noted that the fluctuations $|2 \cdot \Delta T|$ and $|2 \cdot \Delta M|$, respectively, are the differences between the recorded maximum and minimum values of the fluctuations (vide adjacent sketch) and *not* amplitudes. The relative fluctuations which are also included in the tables and graphs, are related to the mean thrust or the mean torque, respectively.

As mentioned in Section II, the mean inflow velocity V_e must be known for the computation of the transverse force and bending moment fluctuations. For this reason the nominal inflow velocity V_e (without propeller) was measured at various radii r and angles ψ for a model speed of 1.543 m/sec corresponding to a full scale speed of 15 knots. The result is shown in Fig. 13.

IV. COMPARISON OF THE EXPERIMENTAL AND THEORETICAL RESULTS

Having reported the results of the experiments and deduced a method for calculating the transverse force- and bending-moment fluctuations, the results obtained experimentally shall be compared with the results found by computation. Hence the experimental curves from Figs. 7 to 12 have to be compared with the
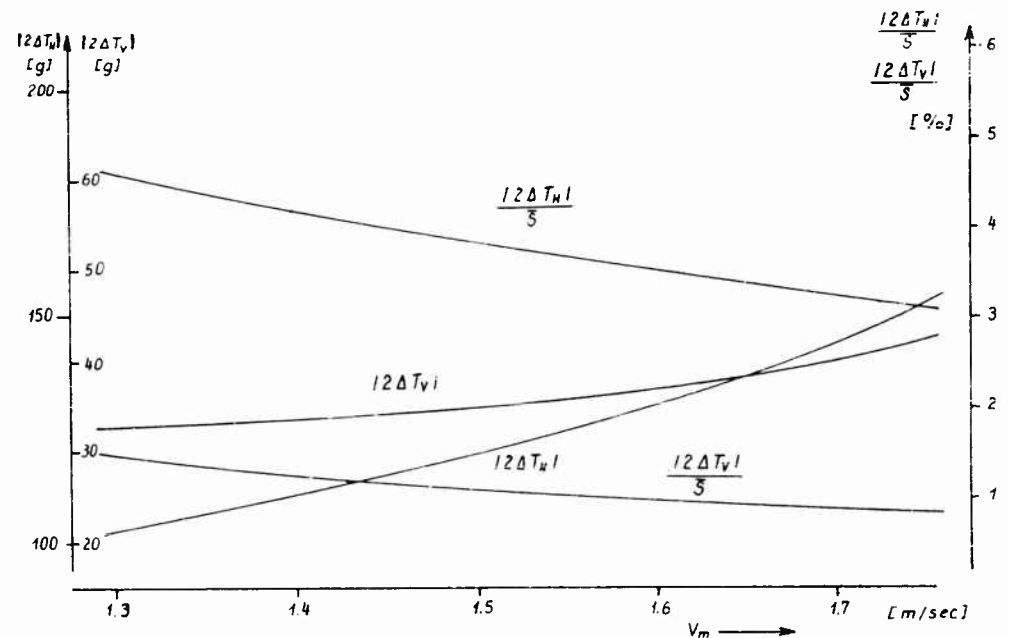
Fig. 7 - Results of Transverse Force Test $A_e/A = 0.35$

Table 1
Results of the Measured Fluctuations
of the Transverse Force and Bending Moment

V_m [m/sec]	n_m [sec^{-1}]	$\lvert 2\Delta T_{hor.}\rvert$ [g]	$\lvert 2\Delta T_{vert.}\rvert$ [g]	$\bar{S}$ [g]	$\lvert 2\Delta M_{hor.}\rvert$ [gcm]	$\lvert 2\Delta M_{vert.}\rvert$ [gcm]	$\bar{M}$ [gcm]
$A_e/A = 0.35$							
1.3	6.70	103	32.8	2250	4300	1472	7450
1.4	7.32	111	33.8	2650	4900	1500	8750
1.5	7.95	120	35.0	3130	5650	1535	10200
1.6	8.55	131	37.3	3700	6550	1585	12000
1.7	9.20	145	40.5	4450	7800	1677	14400
1.75	9.55	154	42.6	4960	8600	1750	15900

Table 2
Results of the Measured Fluctuations
of the Transverse Force and Bending Moment

V_m [m/sec]	n_m [sec^{-1}]	$\lvert 2\Delta T_{hor.}\rvert$ [g]	$\lvert 2\Delta T_{vert.}\rvert$ [g]	$\bar{S}$ [g]	$\lvert 2\Delta M_{hor.}\rvert$ [gcm]	$\lvert 2\Delta M_{vert.}\rvert$ [gcm]	$\bar{M}$ [gcm]
$A_e/A = 0.55$							
1.3	6.70	125	40	2250	5000	1593	7450
1.4	7.32	140	44	2650	5650	1630	8750
1.5	7.95	156	48.5	3130	6400	1677	10200
1.6	8.55	175	54.5	3700	7400	1735	12000
1.7	9.20	201	62.5	4450	8800	1840	14400
1.75	9.55	223	68.5	4960	9700	1915	15900

Table 3
Results of the Measured Fluctuations
of the Transverse Force and Bending Moment

V_m [m/sec]	n_m [sec^{-1}]	$\lvert 2\Delta T_{hor.}\rvert$ [g]	$\lvert 2\Delta T_{vert.}\rvert$ [g]	$\bar{S}$ [g]	$\lvert 2\Delta M_{hor.}\rvert$ [gcm]	$\lvert 2\Delta M_{vert.}\rvert$ [gcm]	$\bar{M}$ [gcm]
$A_e/A = 0.75$							
1.3	6.70	133	45.0	2290	5300	1647	7700
1.4	7.32	150	49.5	2700	6000	1685	9000
1.5	7.95	168	55.5	3180	6780	1735	10500
1.6	8.55	190	63.7	3750	7775	1800	12400
1.7	9.20	222	69.5	4525	9150	1895	14900
1.75	9.55	246	83.0	5075	10100	1995	16600

723
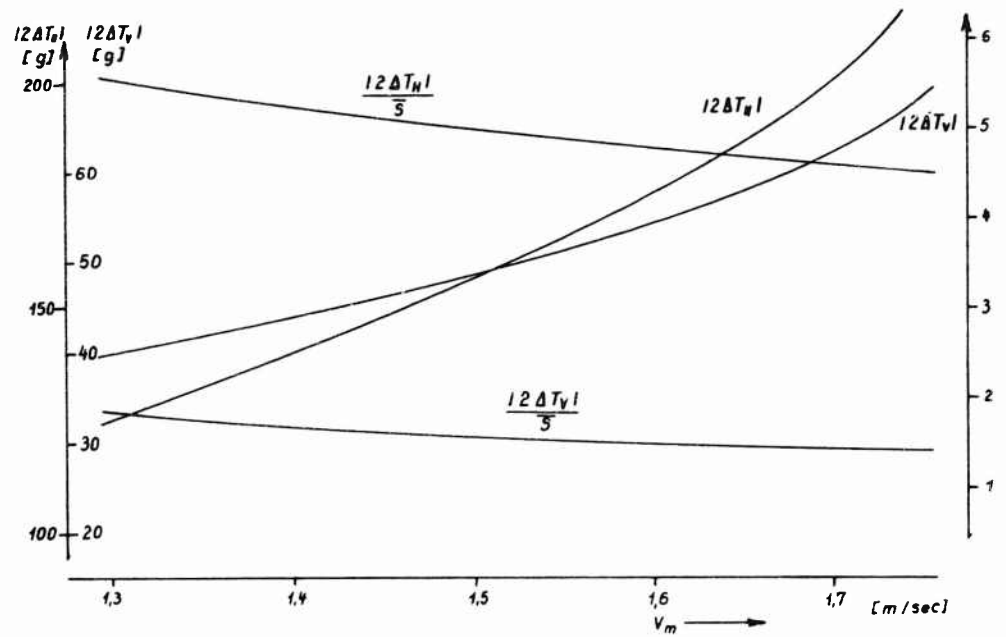
Fig. 8 - Results of Transverse Force Test $A_e/A = 0.55$
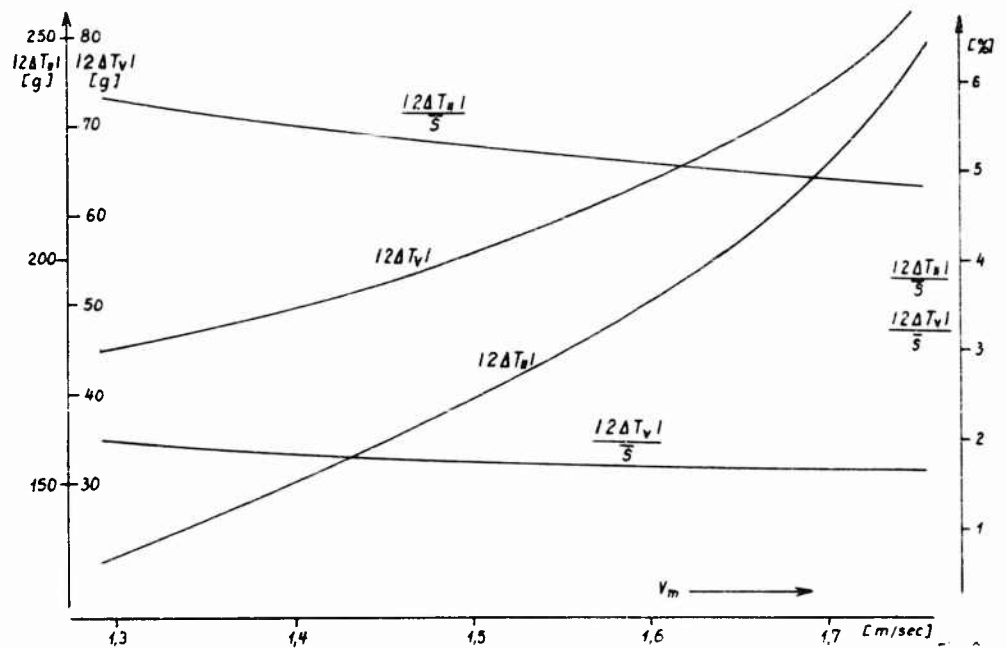
Fig. 9 - Results of Transverse Force Test $A_e/A = 0.75$

724
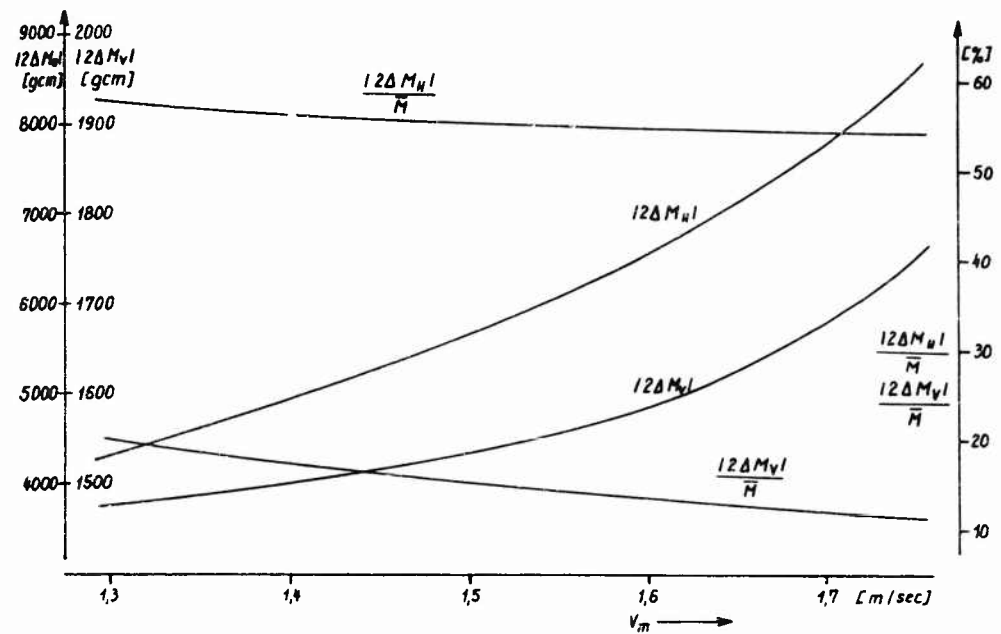
Fig. 10 - Results of Bending Moment Test $A_e/A = 0.35$
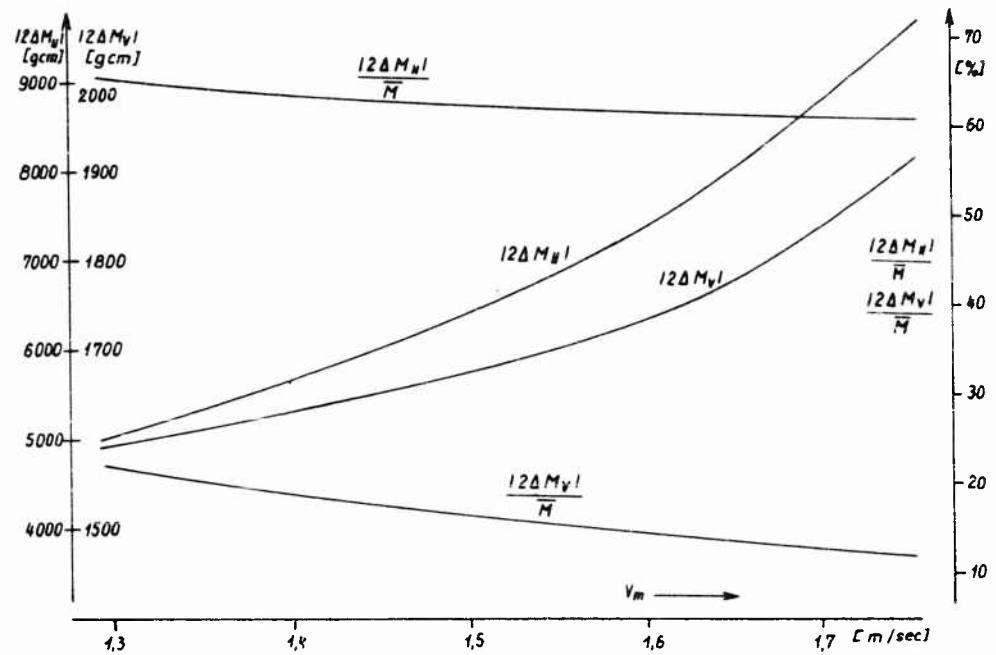
Fig. 11 - Results of Bending Moment Test $A_e/A = 0.55$

725
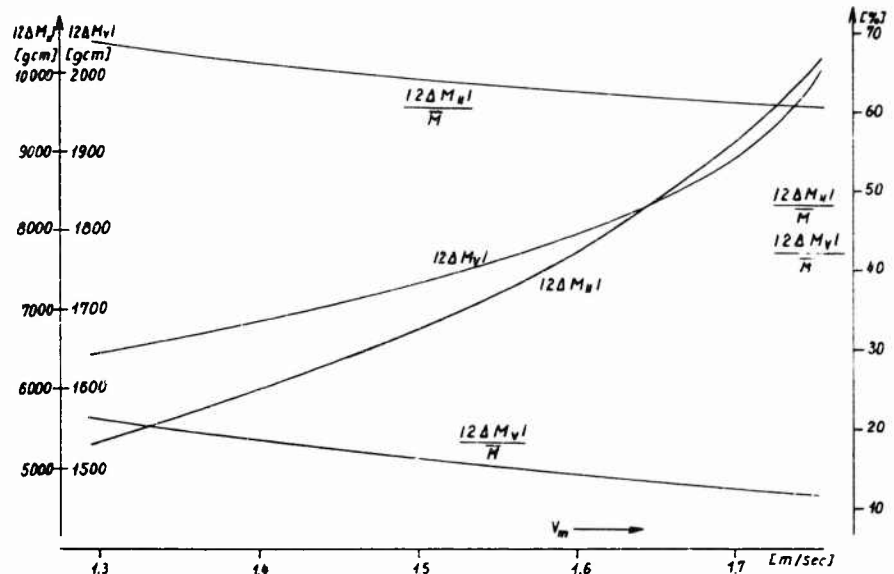
Fig. 12 - Results of Bending Moment Test $A_e/A = 0.75$
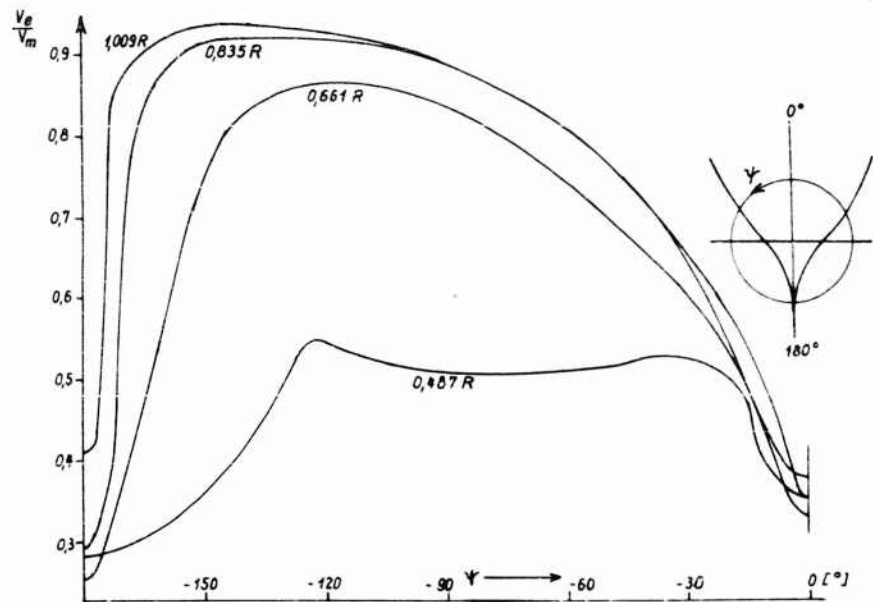
Fig. 13 - Wake Distribution
Model Speed $V_m = 1.543$ [m/sec]
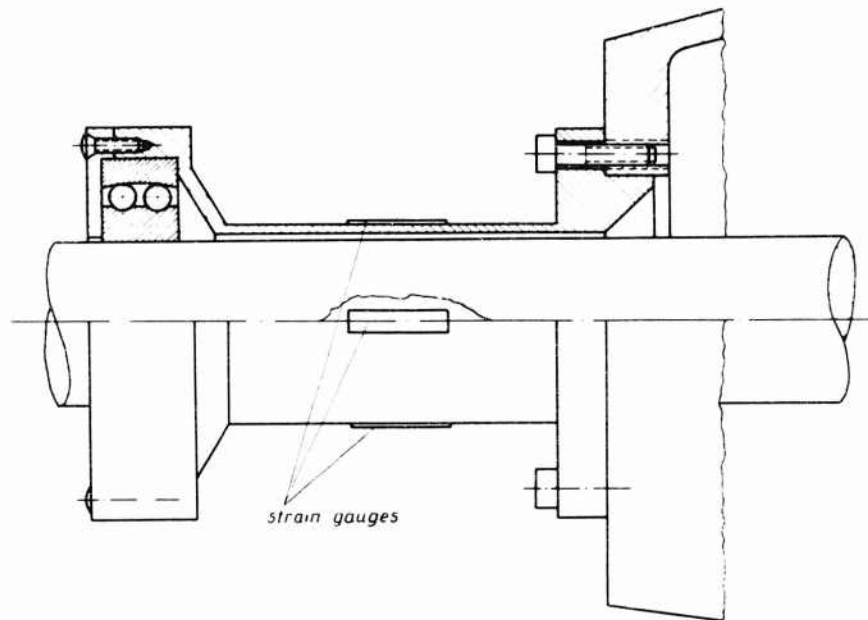
Fig. 14 - Detail of the Second Tubular Beam
The Distance between the Two Identical Beams is 644 mm.

corresponding calculated curves. However, this would mean a great deal of computational work. Therefore, the comparison shall be carried out only for the service speed. This is 1.543 m/sec for the model and corresponds to 15 knots for the full scale ship. The restriction of the comparison to one speed does not necessarily limit the validity of the conclusions. Because, it can be seen from eqs. (4) and (5) of Section II that the calculated and experimental curves as function of the model speed agree in tendency. Apart from the restriction just made, only the first term of each sum in the relations (4) and (5) is used in the calculations for the comparison of the fluctuations. The reason for this is, that the Fourier analysis of the nominal inflow velocity V_e shows that the higher terms of the series are small compared to the first term. Under these assumptions the measured and calculated values of the transverse force and bending moment fluctuations for the model speed of 1.543 m/sec are compiled in Table 4.

Table 4
Comparison between Tests and Calculations

A_e/A	$T_{hor.}$ Exp.	[g] Num.	$T_{vert.}$ Exp.	[g] Num.	$M_{hor.}$ Exp.	[gcm] Num.	$M_{vert.}$ Exp.	[gcm] Num.
0.35	62.0	68.8	18.0	17.0	3000	3137	760	804
0.55	82.0	89.6	25.5	23.6	3400	3567	850	903
0.75	88.5	95.0	29.5	26.7	3575	3675	880	922

The comparison of the calculated and measured values shows that deviations up to 10% occur. This is due mainly to the assumptions made in the calculations. Thus, for instance, the two-dimensional hydrofoil theory was applied to a propeller which works in a three-dimensional field of flow; identity of ϵ and $\Delta\alpha$ was assumed and only the velocity component in direction of the propeller axis was taken into consideration. However, the measurements, too, have a scattering range which is of the same order of magnitude as the deviations.

In spite of these differences between experiment and calculation, the question about the dependence of transverse force and bending moment fluctuations on the blade area ratio of the propeller—which was posed in this problem—can be answered definitely. As can be seen from Table 4, both experiment and calculation indicate an increase of the transverse force and bending moment fluctuations with increasing blade area ratio.

V. SUMMARY

In the foregoing work the question should be answered how the fluctuations of transverse force and bending moment depend on the blade area ratio of the propeller. To answer this question tests have been carried out with three five-bladed propellers which differ in blade area ratio. The results of the tests show that the fluctuations increase with increasing blade area ratio. In addition to these tests computations of the fluctuations have been made according to a method deduced in the paper. Calculated and experimental results agree in tendency. The absolute values differ up to 10% from each other. The calculations also give an explanation for the course deviation of a single screw ship with rudder amidships. The reason is a steady state term for the transverse force and bending moment.

VI. NOMENCLATURE

A = propeller disc area

A_e = expanded propeller blade area

a_n = coefficient

α = angle of attack

α_0 = angle of zero lift

$\bar{\alpha}$ = mean value of the angle of attack relative to $\llcorner$

$\Delta\alpha$ = fluctuation of the angle of attack

b_n = coefficient

$\beta = \beta = \tan^{-1} V_c / r$ (see Fig. 1)

$\bar{\beta}$ = mean value of β relative to $\llcorner$

728

Transverse Force and Bending Moment Fluctuations

β_i = hydromechanical pitch angle

$\overline{\beta}_i$ = mean value of β_i relative to ψ

c_a = lift coefficient

D = propeller diameter

δ_j = angle of position of the j-th blade

ϵ = fluctuation of β

$F(\omega_{m \cdot z})$ = generalized Theodorsen function

γ = angle measured to the center line of blade (see Fig. 2)

γ_o = maximum of γ

k_1, k_2 = coefficients of camber correction

K_0, K_1 = modified Bessel-functions of second kind

$\varkappa$ = Goldstein factor

L = lift

$\overline{L}_a$, $\overline{L}_t$ = mean value of the axial and the tangential component of the lift relative to ψ

ΔL_a, ΔL_t = fluctuation of the axial and the tangential component of the lift

ℓ = chord length

$\overline{M}$ = mean value of torque relative to ψ

M_{hor}, M_{vert} = horizontal and vertical component of the bending moment

ΔM_{hor}, ΔM_{vert} = fluctuation of the horizontal and the vertical component of the bending moment

$|2 \cdot \Delta M_{hor}|$, $|2 \cdot \Delta M_{vert}|$ = difference between the maximum and the minimum value of the recorded fluctuation of the components of the bending moment

Ω = angular speed of the propeller

$\omega_{m \cdot z}$ = reduced frequency

φ = geometrical pitch angle

ψ = coordinate of circumference

R = propeller radius

729

r = radial coordinate

ρ = mass density

$\bar{S}$ = mean value of thrust relative to ψ

$\Delta T_{hor}, \Delta T_{vert}$ = fluctuation of the horizontal and the vertical component of the transverse force

T_{hor}, T_{vert} = horizontal and vertical component of the transverse force

$|2 \cdot \Delta T_{hor}|$, $|2 \cdot \Delta T_{vert}|$ = difference between the maximum and the minimum value of the recorded fluctuation of the components of the transverse force

$\tau = \Delta \alpha / \varepsilon$

$U = \sqrt{r^2 \cdot \Omega^2 + V_e^2}$

$\bar{U}$ = mean value of U relative to ψ

V_e = inflow velocity (= nominal inflow velocity)

$\bar{V}_e$ = mean value of the inflow velocity relative to ψ

ΔV_e = fluctuation of inflow velocity

V = relative velocity at the propeller

$\bar{V}$ = mean value of the relative velocity relative to ψ

ΔV = fluctuation of the relative velocity

x = non-dimensional radial coordinate

z = number of blades

REFERENCES

1. v. Manen, J.D.; Wereldsma, R., Dynamic Measurements on Propeller Models, Internat. Shipb. Progr. 1959, Vol. 6

2. v. Manen, J.D.; Wereldsma, R., Vom Propeller erregte Wechselkräfte in der Welle eines Einschrauben-Tankers, Schiff und Hafen 1960, Jhrg. 12, H. 9

3. Eckhard, M.K.; Morgan, W.B., A Propeller Design Method, T.S.N.A.M.E. 1955

4. Sears, W.R., Some Aspects of Non-Stationary Airfoil Theory and its Practical Applications, Journ. of the Aeron. Sciences 1941, Vol. 8, No. 3

5. Lerbs, H., Ergebnisse der angewandten Theorie des Schiffspropellers, Jahrbuch der S.T.G. 1955, Bd. 49

Friday, August 31

Morning Session

HYDROELASTICITY

Chairman: R. L. Bisplinghoff

Massachusetts Institute of Technology
Cambridge, Massachusetts

731

DESIGN PROBLEMS IN HYDROELASTICITY

A. J. Giddings
Bureau of Ships
Washington, D. C.

Before beginning a discussion of hydroelasticity from the point of view of a "victim," rather than a "villain," it would be well to define what is meant by hydroelasticity in this paper.

Hydroelastic phenomena are considered to be those in which the nature or magnitude of a hydrodynamic load are significantly affected by the structural deformation of the body involved. Even though elastic deformation is implied, plastic deformations are not excluded.

The generality of this definition will become evident in the paragraphs to follow.

The problems in hydroelasticity facing the naval architect may conveniently be divided in two categories. There are those which have been problems for a long time, and which are either evaded in design, allowed for by "beefing up" the structure empirically or are not serious enough for attention. The other group contains those which are largely anticipated and may not actually materialize, at least in the expected form.

The first group consisting of the old familiar problems includes the hydroelastic phenomena associated with slamming, underwater explosions, hull vibration, and propeller singing. A little explanation of these terms is warranted. Slamming is the word applied by naval architects to hull impacts which can be felt aboard ship as a distinct shock. The water entry of a "V" bow is not necessarily a "slam," the entry of a "U" shaped bow is usually felt as a "slam," while the rapid water entry of a flat bottomed bow of a "shoe box hull" such as that of an LST is always a "slam." The hydroelastic nature of the phenomenon is most evident in the last case. The pressure history of flat bottomed impacts computed by rigid body theory produces infinite loads. In the real case, the pressure rise is limited by the compressibility of the sea, but more especially by the change in shape and entering velocity of the flat bottom due to elastic (and sometimes plastic) deformations.

733

Reference [1]. Underwater explosion phenomena [2] involving ship structure and pressure waves are unavoidably hydroelastic phenomena. The interaction of the structure moving and deforming in response to the pressure wave greatly changes the pressure time history at the surface of the structure. Much of the literature in this field is classified, but [3] is a good source for background.

Hull vibration problems in general have been analyzed without including the hydroelastic interaction effects. The added mass and damping due to the presence of a dense fluid with a free surface have been quite thoroughly examined for the rigid body case, and strip theory applied to the solution of real problems. It is probable that the fruits of research along these lines will be applied to the hydroelastic problem of hydrofoils near a free surface, since a new three-dimensional solution within hydrofoil theory is unlikely.

An interesting hydroelastic problem exists in which the fluid loading is hydrostatic rather than hydrodynamic. This is the problem of analyzing the depth potentialities of compressible submarines. It is possible, in theory, to design pressure hulls either more or less compressible than the fluid so that neutral buoyancy can be maintained at all depths. This depends, of course, on an assumed depth-density variation. The dynamics of the problem in a uniform density gradient are analogous to those of foil divergence.

Another problem related to hydroelasticity is that of the strength of submarine whip antennas. These are slender and flexible rods mounted so as to be vertical when out of the water. When the submarine submerges under way, or when waves pass over, the antennas are designed to deform elastically and stream aft. A careful balance of steady and unsteady hydrodynamic loading and of steady state and vibratory stress and deformation is necessary.

Propeller singing is a real and somewhat mysterious problem. The variety of "solutions" used by practitioners of the art of propeller design indicates the lack of real understanding of the phenomenon. It is apparently a local trailing edge effect, perhaps akin to trailing edge "buzz" sometimes mentioned in the aeronautical literature. Singing is detected as a high frequency tone emanating from a marine propeller at certain speeds. At low speeds, no tone is heard, then upon reaching a critical RPM, a characteristic sound occurs. As RPM is further increased essentially the same tone (frequency) remains, and then fades away, often replaced abruptly by a higher frequency tone. The frequency does not vary smoothly with RPM, but appears to "lock in" to a few characteristic tones over particular RPM ranges. Since singing involves hydrofoil lifting sections, the subject provides a convenient bridge to the other group of hydroelastic problems, those which are anticipated more than experienced.

Before going on to these problems, however, it is interesting to consider a phenomenon often met with on slow speed sail boats. It is not uncommon to experience centerboard or rudder "buzz" at speeds below four knots, when sailing downwind or slightly off the wind. Whether this is a vibration excited by vortex shedding or a flutter type phenomenon is not clear. Centerboards and rudders on small sailboats are often loosely mounted, so either possibility exists. When the noise is especially bothersome, it can usually be eliminated by changing the trip of the sails, thereby altering the flow to the control surfaces.

The anticipated problems are largely of the same nature as the aeroelastic problems already encountered in aerodynamics. They are associated with high-speed ships, especially hydrofoils. Other more usual high speed ships, however, are not ignored. The same names as those which are used in aeroelasticity are used to describe these problems; divergence, flutter, control reversal, etc.

DIVERGENCE

The high steady load concentrations on hydrofoils and ship control surfaces demand such heavy structure that divergence of a practical structure is highly unlikely. Ordinary ship rudders and submarine diving planes are designed with relatively high safety factors compared with aircraft practice. Grounding or ice contact is usually required to induce failure. Typically, the operating load on one rudder of an aircraft carrier is on the order of one and a half million pounds, and the "hinge" moment provided is 20 million inch pounds. The rudder stock to support this load, with a safety factor of 2 based on yield, is a high strength steel machined forging four feet in diameter. The particular rudder under discussion weighs 80 tons. The position of the elastic axis on ship control surfaces is always forward on the platform thereby providing even more margin against divergence. There is not yet enough design experience with hydrofoil structures to be as positive about divergence, but with the possible exception of the thin supercavitating case, divergence of practical hydrofoils and struts is unlikely.

FLUTTER

The subject of flutter is the one which has excited the most interest in hydro-elasticity, both technical and fiscal. The catastrophic potential of flutter failure in aircraft lends a sense of apprehension to the consideration of flutter in hydro-foil craft and other ships, and the size of the rudder mentioned above would make flutter quite spectacular. However, it is likely that a flutter failure on currently conceived military hydrofoils would be more embarrassing than catastrophic. A hydrofoil has only a few feet to fall, and it is anticipated that a military crew would be securely seated. The embarrassment, however, would extend beyond the immediate incident, and could be catastrophic to the realization of future hydrofoils. In a more pragmatic sense, damage consequent to a hydrofoil flutter failure would be very expensive to repair, especially if it involved the propulsion system. Concern with these possibilities has generated the Bureau of Ships program in hydroelasticity.

There are other, non-hydrofoil control surface vibration problems which appear to be linked to flutter [4, 5, 6]. These flutter cases are particularly difficult for a designer to cope with in the design stages.

Flutter of the type discussed by McGoldrick on a destroyer is very difficult to predict. The interaction of hull vibration modes and control surface modes is highly complex to analyze, and once analyzed, changes are hard to make. The structure of a ship is such that in order to change the bending or torsional stiffness significantly, such gross changes in structure are required that the overall design may be defeated. A further complication arises from the fact that ships

735

are built one at a time, or a few at a time, so that when sufficiently detailed structural plans are available to conduct a precise analysis, it is too late to affect the design. The order of precision required is sufficient to prevent confident predictions during early design phases.

As a result of the aforementioned difficulties, the designer tries to leave a way out of potential difficulty. Variations in mass balance, control system dynamics, etc., have been the "backup tools" of the aero designer. Practical changes in effective mass balance of ship control surfaces or hydrofoils are inconsequential, due to the high density fluids involved. Control system dynamics in ships can be affected slightly, but since the horsepower used in moving ship control surfaces is in the order of 40 to 200 horsepower changes after construction are not easily made. Hydrofoil control system dynamics are more susceptible to change, but similar problems of magnitude exist. The structure of a hydrofoil surface is "hollow" in name only, and there is very little free volume for application of "cures."

The ultimate designer's need in this regard is for a method of synthesis of hydrofoils and high-speed control surfaces which will avoid flutter problems. Methods of analysis are all that is expected in the near future, but in the compressed time scale and with the limited design manpower typical of shipbuilding programs, results of analysis are usually too late, and if unfavorable, costly and time consuming delays result. A useful substitute for a closed-form synthesis would be design tables and charts sufficiently general to allow the rapid and reasonably accurate prediction of flutter for a variety of hydrofoil and control surface configurations. From these the most suitable arrangement could be selected. The state of the art of the "elastic" part of the problem is well developed and automated. Reference [5] and many of the reports listed in [5] attest to the sophistication of approach in the structural side of the problem. These references also demonstrate that the immediate research aim should be a similar level of knowledge in the "hydro" part of the phenomenon. The more recent literature in the field has shown such an emphasis.

CONTROL SURFACE REVERSAL

It appears that steady load considerations will limit hydrofoil aspect ratios to low values. Subcavitating foils are not likely to have aspect ratios exceeding 6, and based on unsupported length, even smaller structural aspect ratio will occur. Supercavitating hydrofoils will rarely exceed aspect ratio 4, with values below 3 being more likely. The effective torsional stiffness associated with low aspect ratios make it appear that control reversal is an unlikely problem. Despite this, the possibility should not be ignored, especially for thin supercavitating foils with flaps or spoilers. Newer high strength low modulus materials will further complicate the matter.

It should be noted, however, that reversal may just as well occur as a result of cavity deformation due to spoilers as it might be due to elastic deformation, so that the possible occurrence of reversal on some operating boats would be difficult to interpret.

SUMMARY

Hydroelastic problems which face the naval architect include both old and new problems. Old problems are those such as slamming, explosive loading and ship vibration. Newer problems include divergence and flutter.

A body of experience exists for dealing with the older problems, but the transferral of the equivalent body of aeroelastic design experience into hydro-elastic design practice has not yet been demonstrated to be feasible. Results of current research, and ultimately, performance of high-speed hydrofoil craft, will help to determine if the extensive aeroelastic design literature can be used in naval architecture. The brevity of this discussion of naval architectural features of hydroelastic problems is testimony of the newness of the field, and to the anticipatory nature of the problems.

REFERENCES

1. Peyton, "Initial Bending Stresses in Elastic Shells Impacting into Compressible Fluids," AVCO report No. RAD-TR-7-6-35 (ASTIA No. AD-267-196).

2. Kennard, "The Effect of a Pressure Wave on a Plate or Diaphragm," DTMB report 527, March 1944.

3. "Underwater Explosion Research," ONR, 1950.

4. McGoldrick, "Rudder Excited Hull Vibration on USS FORREST SHERMAN (DD931), DTMB report 1431, June 1960.

5. McGoldrick and Jewell, "A Control Surface Flutter Study in The Field of Naval Architecture," DTMB report 1222, September 1959.

6. Jewell and McCormick, "Hydroelastic Instability of a Control Surface," DTMB report 1442, December 1962.

* * *

THE FLUTTER CHARACTERISTICS OF A HYDROFOIL STRUT*

Charles E. Squires, Jr. and Eugene F. Baird
Grumman Aircraft Engineering Corporation
Bethpage, New York

ABSTRACT

Previously reported experimental data on the effects of sweep, percent immersion, and mass-density-ratio for a particular surface-piercing hydrofoil strut configuration are briefly summarized and the results of modal analysis flutter predictions for this configuration are considered in detail.

Particular attention is paid to the convergence of the modal theory predictions, and it is seen that the number of modes required for convergence increases abruptly at low mass-density-ratios.

Certain analytical features evidently peculiar to or at least greatly exaggerated at low values of mass-density-ratio are noted, and a local maximum in the predicted flutter speed is seen to occur in the general vicinity of the so-called "critical mass-density-ratio."

INTRODUCTION

In the course of a Bureau of Ships sponsored research program recently completed by the authors, flutter of submerged lifting surfaces was experimentally demonstrated down to mass-density ratios of approximately 0.1 and limited experimental and theoretical parameter studies were conducted utilizing a series of simple, surface-piercing hydrofoil-strut models.

By far the most significant result of this program, which is summarized in part in [1] and reported in detail in [2], was simply the demonstration that hydrofoil flutter can occur.

Perhaps the second most significant finding was that a modal type of flutter analysis using ordinary aerodynamic flutter theory could, if properly applied, yield generally reasonable predictions of the experimental behavior. It was further noted, but not investigated in any detail, that the theoretical flutter speed predictions were extremely sensitive to the inclusion of higher modes in the analysis. More specifically, it was found that the inclusion of modes whose natural frequencies were many times the flutter frequency was necessary in order to obtain a converged solution, i.e., a flutter speed prediction not affected by the inclusion of additional degrees of freedom. Such a stringent requirement for simple uniform surfaces such as the Reference [2] models is contrary to most aircraft experience where a good dynamic representation is usually achieved using relatively few (two or three) of the fundamental modes.

Our purposes in the present paper are three-fold. The first is to shed further light on the subject of convergence of the modal theory at low mass ratios. To this end we have chosen a particular Reference [2] model configuration and made detailed analyses over a wide range of mass-density ratios in an attempt to provide a gradual transition from the regime typical of aircraft and familiar to most flutter analysts to the less familiar regime typical of hydrofoil operation. In so doing, our second purpose, namely to observe the behavior of a typical configuration over a wide range of mass-density ratios, particularly in the vicinity of the so-called "critical value" (see [3] and [4]), is automatically achieved. Our third purpose, inspired by the sparseness of available low-mass-density ratio flutter data, is simply to bring together in one place a comprehensive body of data, both experimental and analytical, on the flutter characteristics of a particular configuration in the hope that it may prove to be of some service to other investigators.

SYMBOLS

Λ	sweepback angle, degree
V	speed, knots or ft/sec
f	frequency, cps
V_F	flutter speed, knots
f_F	flutter frequency, cps
ω	circular frequency, radians/sec
b	semi-chord, measured perpendicular to leading edge, ft
$V/b\omega$	reduced velocity
m	mass of foil per unit span along leading edge, lb-sec^2/ft^2
ρ	mass density of fluid, lb-sec^2/ft^4
μ	mass-density ratio, (ratio of structural mass to mass of surrounding cylinder of fluid), $m/\pi\rho b^2$

μ_a critical mass-density ratio, (the value of mass-density ratio below which two-degree-of-freedom representative-section analysis yields no real flutter speed).

g structural damping coefficient required for neutral stability

DISCUSSION

I. The Model

The model to be discussed here is a four foot, constant-chord, solid, root-cantilevered strut (Fig. 1). The section is symmetrical and is composed of a circular arc from leading edge to mid-chord and constant thickness from

MODEL NO. 2: STEEL
MODEL NO. 3: ALUMINUM
ALL DIMENSIONS IN INCHES

Fig. 1 - The Model

741
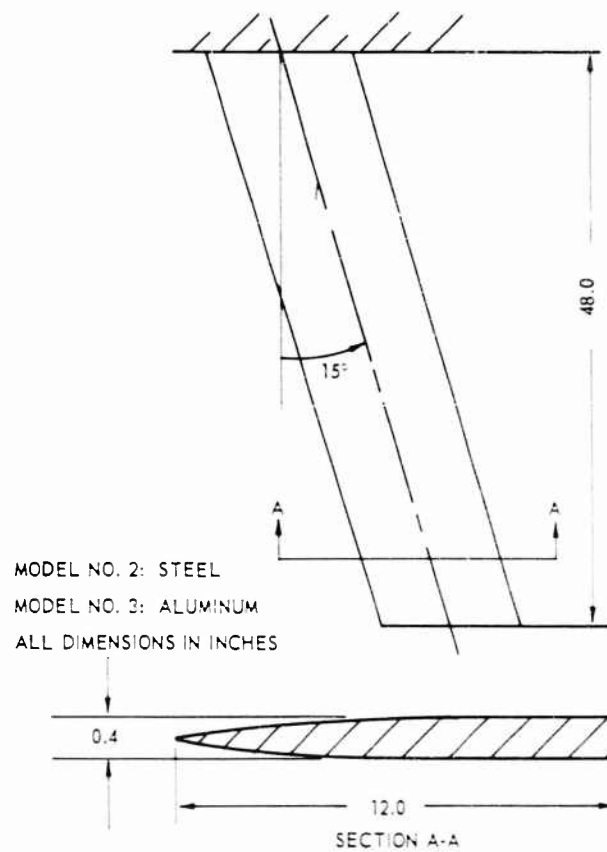
mid-chord aft. For the experimental program it was fabricated in both steel (Model No. 2) and aluminum (Model No. 3) yielding mass-density ratios in water of approximately 0.3 and 0.1 respectively. The experimental set-up was such that the model could be rotated about a pivot at its root in order to obtain a wide range of sweep angles. However, it was specifically designed for a sweep angle of 15 degrees, and the root restraint and tip are exactly streamwise only at that sweep setting.

II. Experimental Conditions vs. Analytical Assumptions

In order to provide a proper basis for the comparison of experimental and theoretical data, the analytical representation of the physical model will be clarified at the outset. It is convenient for purposes of discussion to consider the structural representation and the hydrodynamic representation separately.

The natural modes and frequencies of the model (Fig. 2) were calculated using a lumped parameter technique and an experimental check on the steel

NODE LINES

FREQUENCIES CPS

1	4.85
2	30.1
3	46.4
4	83.5
5	138.0
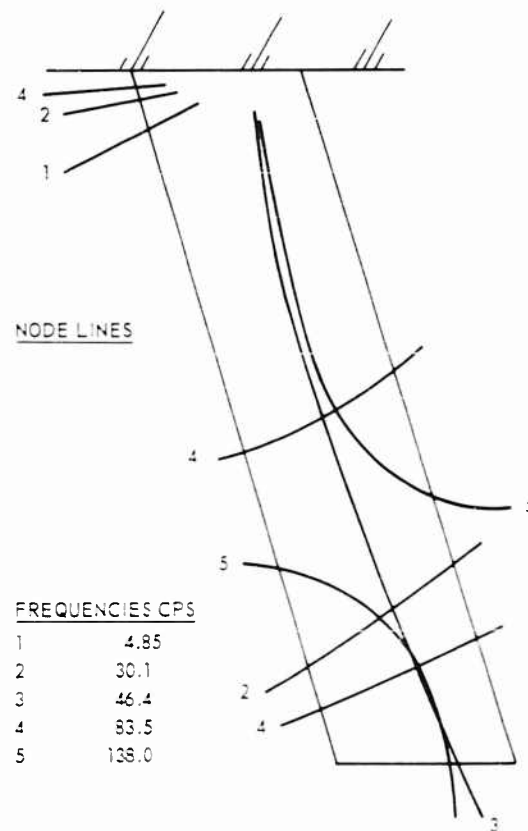
Fig. 2 - Calculated Modes, 15° Sweep

model (at the design sweep setting) showed excellent agreement with respect to both frequency and mode shape. Further, frequency checks made with the model mounted on the towing carriage indicated that the mounting system employed in the experiments provided a good cantilever root restraint. In short, the authors are of the opinion that the analytical representation of the structure is excellent for the design condition of 15 degrees (which will be the condition of primary interest here). For sweep angles other than 15 degrees, the actual root condition is somewhat complex, and the analytical representation used is inexact.

The hydrodynamic representation was idealized to a somewhat greater degree than the structural representation in that two-dimensional incompressible (Theodorsen) coefficients were used without modification.* Implicit in this are the assumptions that free-surface and finite-span effects are negligible and that the foil is fully wetted (i.e., cavitation free). With regard to the experimental conditions, it can be stated with considerable certainty that no cavitation existed on the surfaces of the models below the flutter speed with the possible exception of the highest flutter speed recorded (96 knots). However, because of the blunt trailing edge, some degree of base ventilation was noted at nearly all speeds. While the exact significance of this base vented condition (if any) is as yet unclear; we remark that the Kutta condition does not seem to be violated and tentatively assert that the base ventilation is at most of secondary importance.

III. Sweep and Immersion Depth

Experimental studies of the effect on flutter speed of strut sweep angle and percent immersion were made for a limited range of the parameters. Experimental technique, instrumentation, etc., are treated in detail in [2], and only a brief summary of the results will be given here.

The immersion depth study, which was unfortunately limited to a range of immersion depth variation of approximately 25 percent span, was performed using the steel strut. The results, given in Fig. 3 along with the corresponding analytical results, showed the flutter speed to vary inversely with immersion depth.

The sweep study, using the aluminum strut, is summarized in Fig. 4. Here it is seen that for the range investigated (10° - 30°) increasing sweep angle has a markedly beneficial effect on the flutter speed.

Further inspection of Figs. 3 and 4 shows that quintic analyses yielded conservative predictions in all cases. They were, in fact, somewhat more conservative than one might ordinarily expect. This can perhaps be rationalized, at least in part, by considering the discussion of the previous section. More striking in the opinion of the authors is the large discrepancy between the cubic and quintic results, or, more specifically, the inadequacy of the cubic analysis. This will be discussed at length in the following section. The experimental data are summarized in Table 1.

*Except as noted in Section V.

743
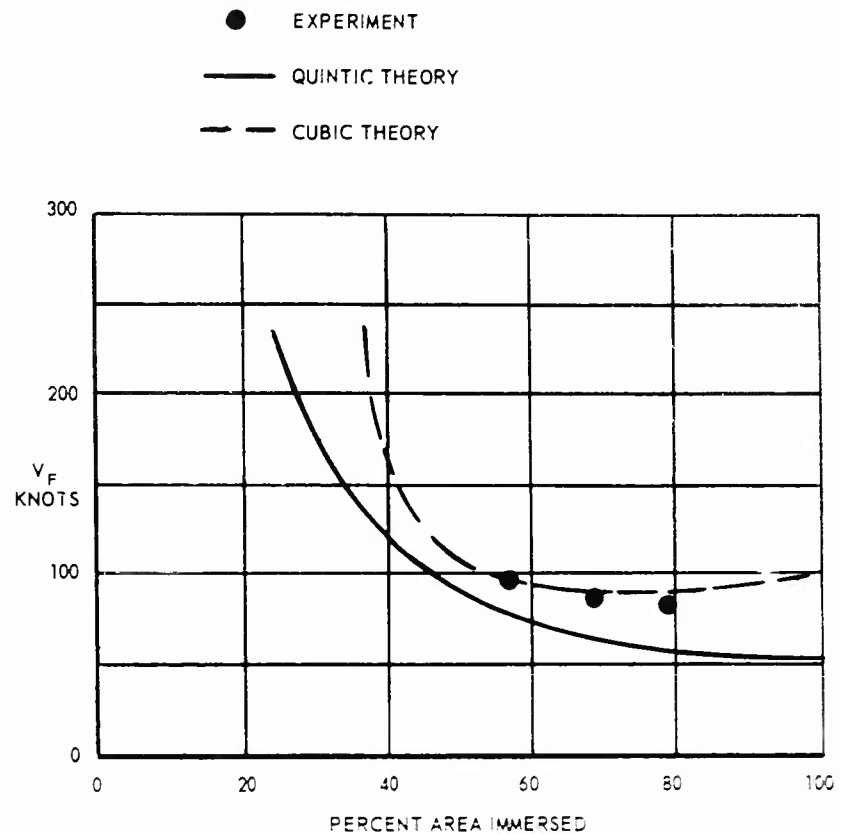
Fig. 3 - The Effect of Immersion Depth Strut No. 2, 15° Sweep

IV. The Problem of Convergence

In treating any problem in dynamics, the most basic requirement for a successful analysis is, of course, that the phenomenon under investigation must be describable by the degrees of freedom being considered. While this statement seems almost too trivial to write down, earnest consideration of the modal flutter analysis procedure from the degree-of-freedom viewpoint, as opposed to a consideration of only the modal frequencies involved, would seem to give at least partial insight into the reason for the significance of higher order modes in the hydrofoil flutter analysis problem. When the magnitude of the dynamic pressures typical of hydrofoil operation (up to 25,000 psf for the data of Table 1) is considered, there would seem to be at least some intuitive basis for expecting the flutter mode shape to be less susceptible to accurate description by two or three fundamental shapes than might be the case for the much lower dynamic pressures typical of aircraft.

744

Flutter Characteristics of A Hydrofoil Strut
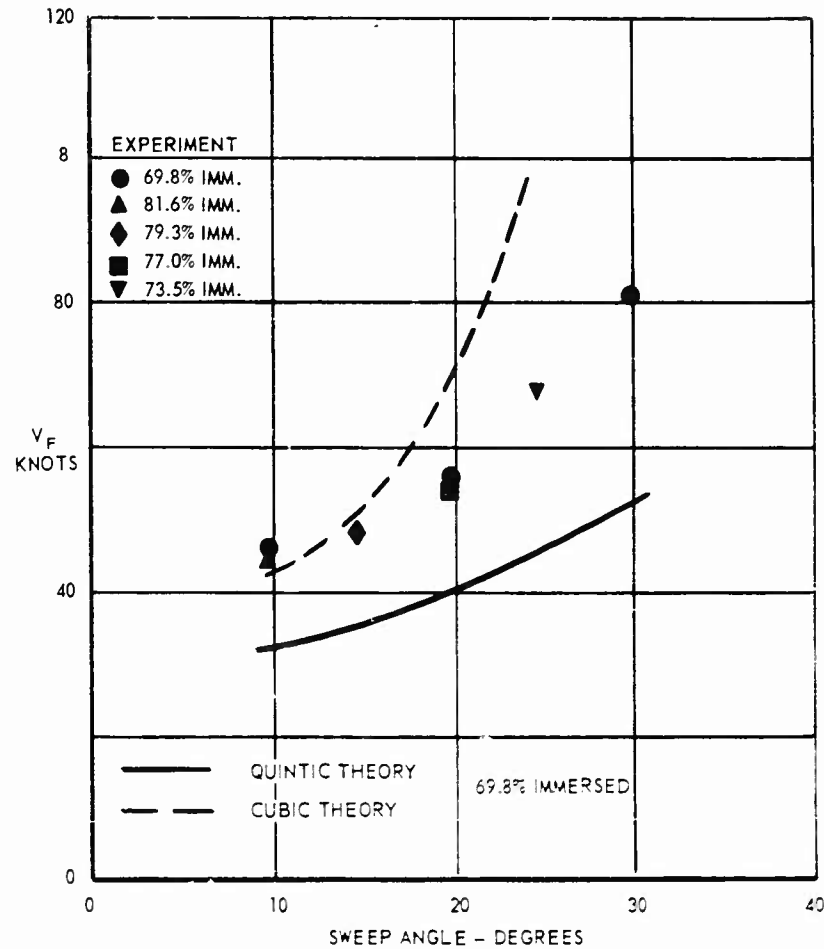
Fig. 4 - The Effect of Sweep Strut No. 3

In order to better understand the apparent "many-mode" flutter analysis requirement at low mass-density ratios noted in [2], it is helpful to isolate what we might call the "configuration-imposed" modal requirements from the "⌐-imposed" requirements. Accordingly, we have performed and compared the predictions of quadratic, cubic, quartic and quintic analyses for mass-density ratios ranging from 0.1 to 100. (Some discussion of the results of "picking and choosing" mode combinations will be given later. but. for the present study. problem size was increased simply by adding the next higher mode.) The

Table 1
Summary of Experimental Results

Strut No.	Sweepback (deg.)	Percent Area Immersed	V_F (knots)	f_F (cps)
2	15	79.3	81	4.1
	15	68.8	85	4.2
	15	56.3	96	4.2
3	10	81.6	44	1.6
	10	69.8	46	1.5
	15	79.3	48	2.3
	20	77.0	54	3.0
	20	69.8	56	3.0
	25	73.5	67	4.3
	30	69.8	82	8.0

results of these analyses are summarized in Fig. 5* and several typical solutions are shown in Figs. 6 through 9. For purposes of discussion we shall refer to the various modes according to their primary content (e.g., first bending, first torsion, etc.) even though they are actually the coupled modes of the strut. Further, we define a "converged solution" to be a flutter speed prediction unaffected by the inclusion of higher modes in the analysis. Since the solution of a ten-mode system for the lowest _ considered yielded a prediction essentially identical to that of the quintic analysis, it can be stated with reasonable certainty that the quintic results do, in all cases, represent converged solutions.

Considering the various features of Fig. 5 in detail, it is seen first of all that the quadratic predictions are of rather poor quality from the viewpoint of modal convergence, throughout the mass-density-ratio range, failing to show any instability at all at the hydrofoil end. That this system is inadequate is to be expected, since we have as yet allowed no appreciable amount of torsion to enter the picture. Thus, the need for more than the first two modes is a "configuration imposed" requirement, i.e., for this configuration the first two modes are both primarily bending modes, and hence are insufficient to describe the flutter phenomenon. It is next noted that systems of cubic degree and higher result in converged solutions for the higher _ range (_ > 1); a result in keeping with aircraft experience. However, an abrupt change in the requirement for convergence is seen to occur as one enters the hydrofoil range. Specifically, inclusion of the second torsion mode (quintic system) becomes necessary for low _ whereas only those modes up through first torsion (cubic system) are required for high _.

---

*It should be noted that the flutter speeds shown in Fig. 5 are the lowest speeds to which unstable solutions could be obtained rather than the zero-damping points. The difference is negligible (see for example Fig. 6), except in the mass-density-ratio range $0.4 < \_ < 0.8$. Here the shape of the plot is altered somewhat, but the basic characteristics of the plot (which are discussed in the following paragraphs) remain the same.
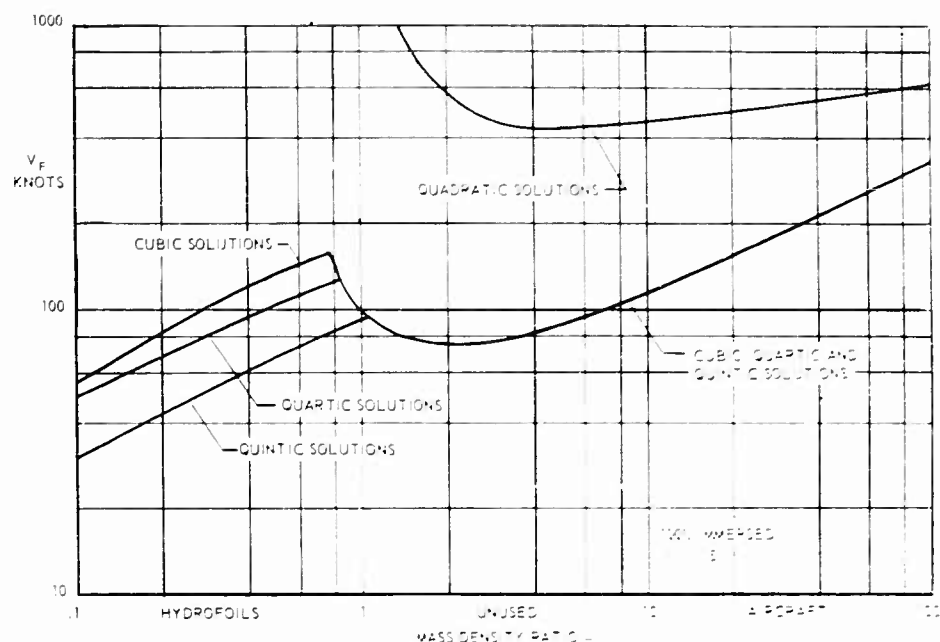
Fig. 5 - Flutter Speed as a Function of Mass Ratio

It is concluded then that the need for additional degrees of freedom above the third mode is a "_-imposed" requirement and is not due to any basic characteristic of the configuration.

It is interesting that this abrupt change in convergence requirement is accompanied by a well defined local maximum in the predicted flutter speed, and that this maximum occurs near the critical mass-density ratio, $_a$, defined from representative-section theory as the density ratio at which the flutter speed increases asymptotically to infinity. It is noted that this local maximum near $_a$ was observed previously on another configuration investigated by Herr [4], so at least partial evidence exists that this phenomenon is not a "configuration-imposed" peculiarity of any single foil, but rather is a "_-imposed" condition which might be characteristic of hydrofoils in general. It is interesting also that consideration of additional degrees of freedom tends to both lessen the severity of the local maximum and alter its location in the direction of progressively higher mass ratios.

V. Flutter Analysis Based on In-Fluid Modes

It occured to the authors that an alternate approach to the problem of obtaining a good dynamic representation of the strut at low mass ratios might be to base the analysis on a more realistic set of vibration modes, namely the natural modes of the model immersed in the fluid. In order to evaluate this

747
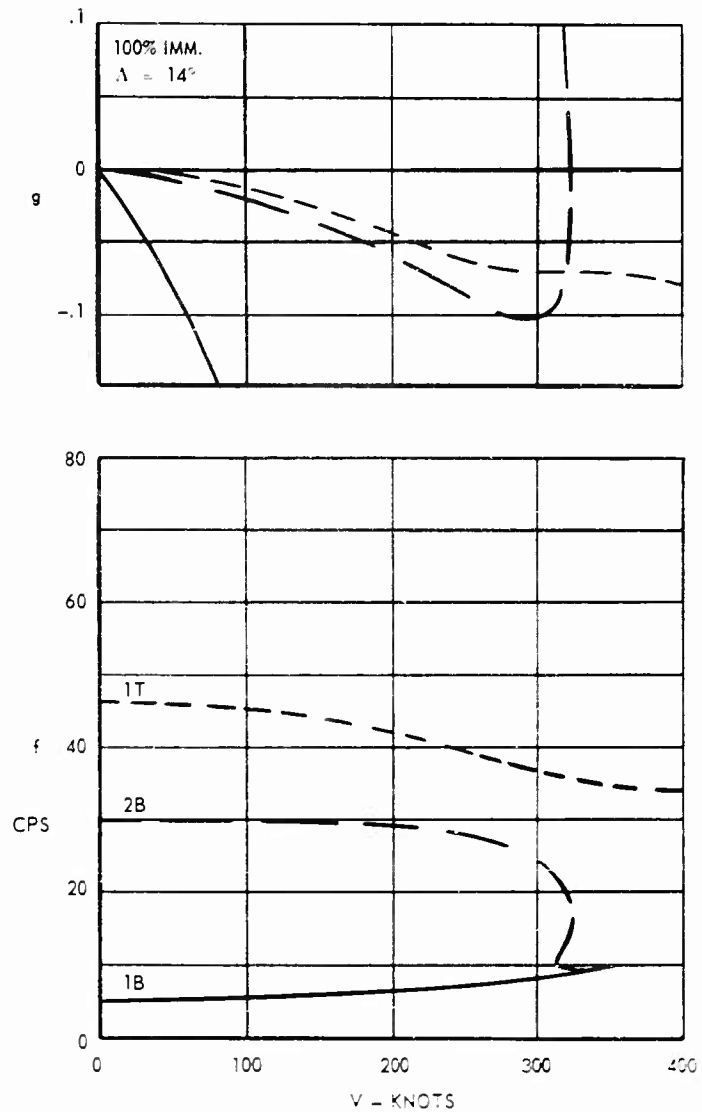
Fig. 6 - ω = 100, Cubic Analysis

possibility, parallel analyses were made for the aluminum strut, one set based on the usual modes "in vacuo" and the other on the "in-fluid" set. Beginning with a quadratic solution of the first two modes, the problem size was increased a step at a time as described in the previous section until all modes up through second torsion were included. Table 2 summarizes the mode types and frequencies used and Table 3 lists the resulting flutter speed predictions.

Flutter Characteristics of A Hydrofoil Strut
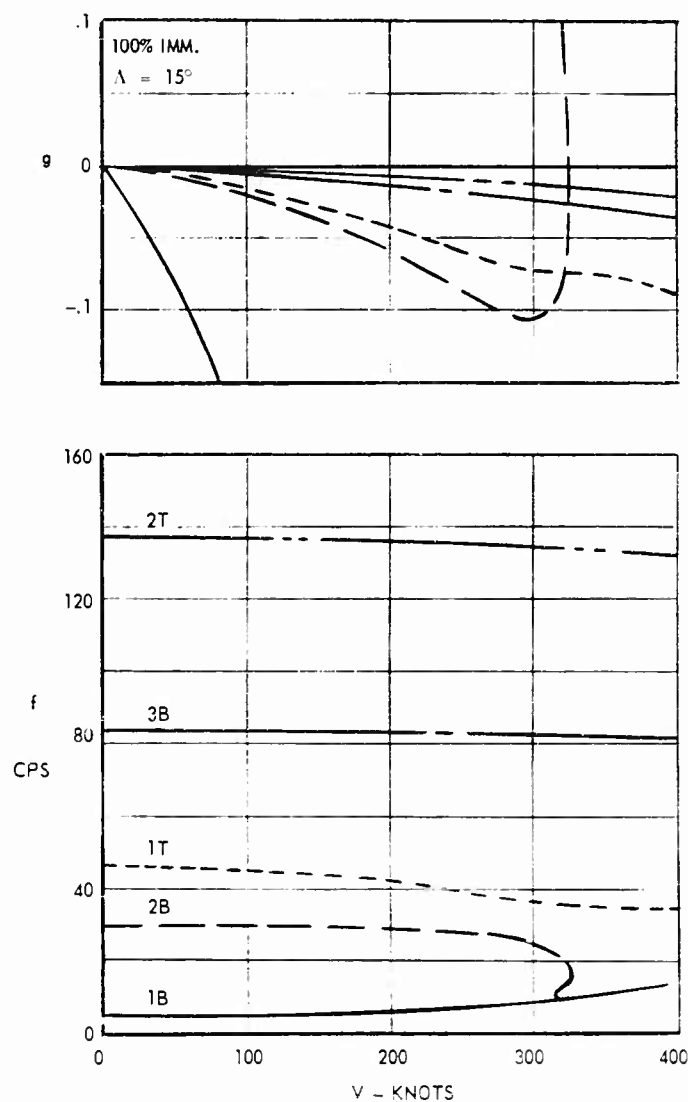
Fig. 7 - ⌣ = 100, Quintic Analysis

As might be expected, inclusion of all modes up through second torsion results in essentially identical solutions. However, the superiority of the "in-fluid" results for the smaller problem sizes is quite pronounced.

Specifically, the "in-fluid" quadratic system does predict an instability, while the "in vacuo" quadratic did not. Since the difference in mode shapes between these two sets is very minor, this result seems especially noteworthy and

749
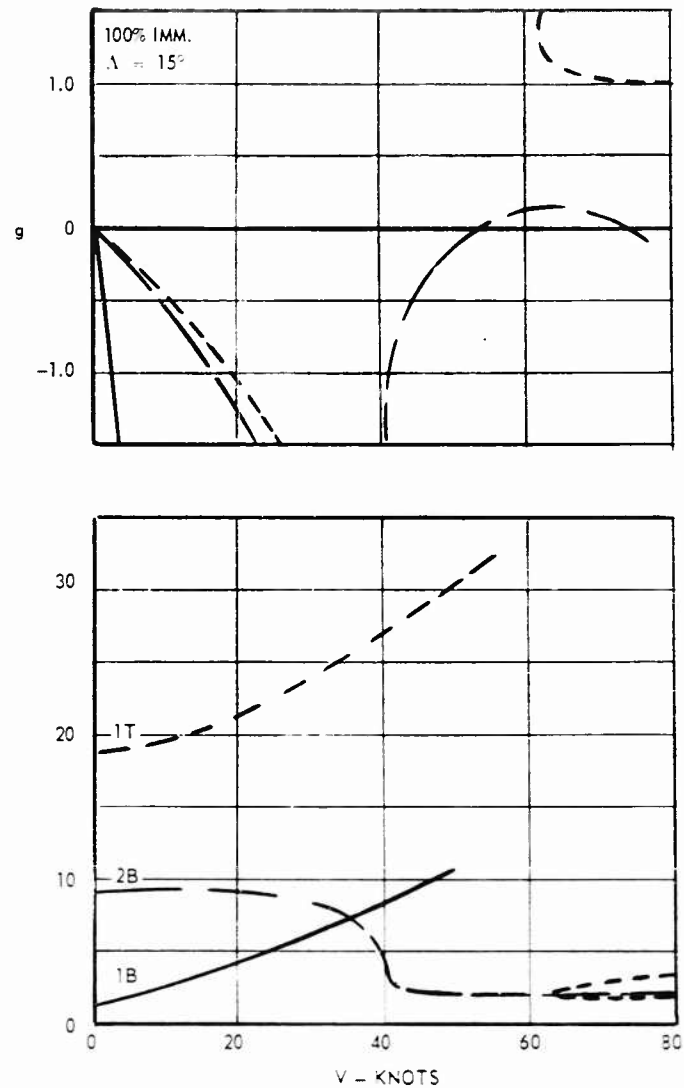
Fig. 8 - μ = 0.1, Cubic Analysis

appears to be indicative of the extreme sensitivity of flutter theory at low mass ratios. It should be mentioned by way of clarification that the "in vacuo" quadratic <u>does</u> indicate strong coupling between the modes resulting in a marked reduction in damping; however, neutral stability is never attained.

In an attempt to improve the quality of the "in-fluid" modes, the effect of correcting the virtual mass terms for finite span effects was evaluated (based on empirical data). No appreciable change in flutter speed resulted, however.

750
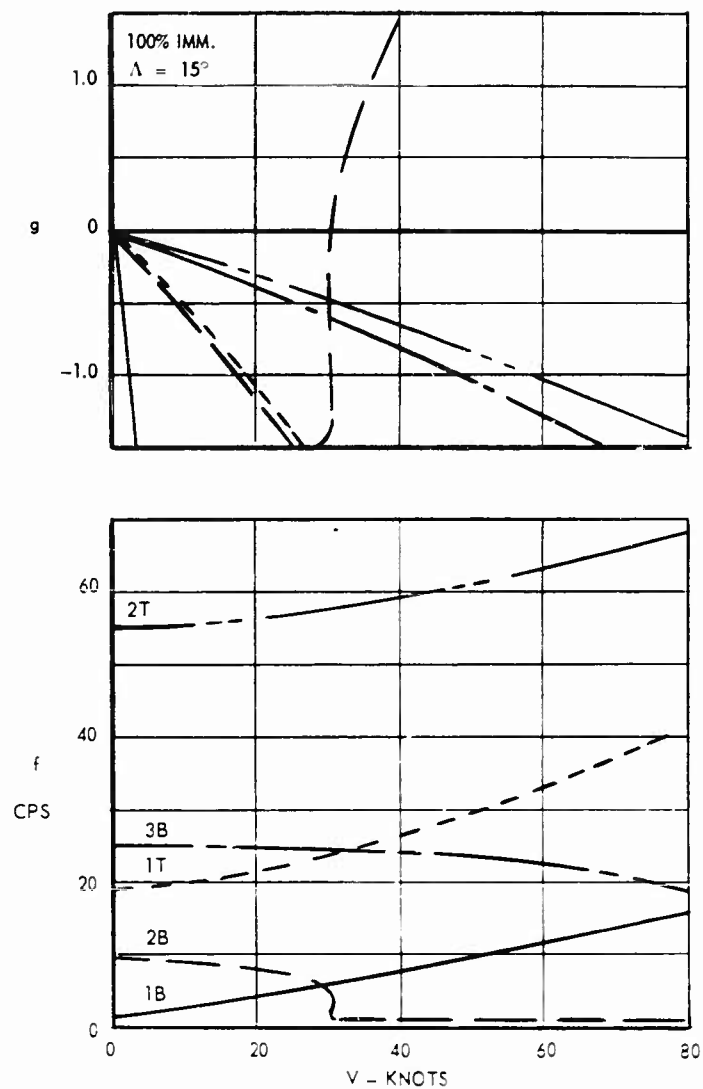
Fig. 9 - ω = 0.1, Quintic Analysis

VI. Flutter Speed vs. Density Ratio

An analytical study of the effect on flutter speed of mass-density-ratio variations over the very low mass-density-ratio range ($0 < \omega < 0.4$) was reported by the authors in [1] and [2] and is summarized here in Fig. 10. These results, together with Fig. 5, give a reasonably complete picture of the flutter characteristics of the strut as a function of ω.

751

Table 2
Summary of Modes
Strut No. 3; $\Lambda = 15°$; 100% Immersed

Mode Type	Frequency (cps)	
	In Vacuum	In Fluid
First bending	4.85	1.44
Second bending	30.10	8.87
First torsion	46.40	18.30
Third bending	83.50	24.25
Second torsion	138.00	54.00
Fourth bending	—	45.00

NOTE: The order of occurrence of second torsion and fourth
bending is reversed in going from in-vacuum to in-
fluid modes.

Table 3
Summary of Modal Analysis Results
Strut No. 3; $\Lambda = 15°$; 100% Immersed

Problem Size	Flutter Speed (knots)	
	Vacuum Modes	In-Fluid Modes
Quadratic	stable	80.0
Cubic	52.0	44.5
Quartic	49.5	43.0
Quintic	30.5	42.0
Sextic	—	30.5

Interestingly enough, the relationship $V_F \sim \sqrt{\mu}$, suggested in [5] on a semi-empirical basis for $\mu > 10$, is a good approximation to the flutter speed variation to the left of the previously mentioned "μ-peak," i.e., for $\mu < 1$. The experimental data points for the steel and aluminum struts for $\Lambda = 15°$ and an immersion depth of 79.3% span (the only common test condition) reflect this variation.

For the higher density ratios, say $\mu > 10$, the relationship $V_F \sim \sqrt{\mu}$ is again seen to give an approximation to the flutter speed variation. However, a variation of the form $V_F = C_1 \sqrt{\mu} + C_2$ seems to be somewhat better in this range.

For the intermediate range of mass-density ratios, which is of little practical interest, no simple variation seems to exist.

Due largely to the present inability to give a satisfactory physical explanation of the flutter speed maximum in the vicinity of μ_a, there is an intuitive

752

Flutter Characteristics of A Hydrofoil Strut

QUINTIC THEORY (100% IMM.)
$\Lambda = 15°$
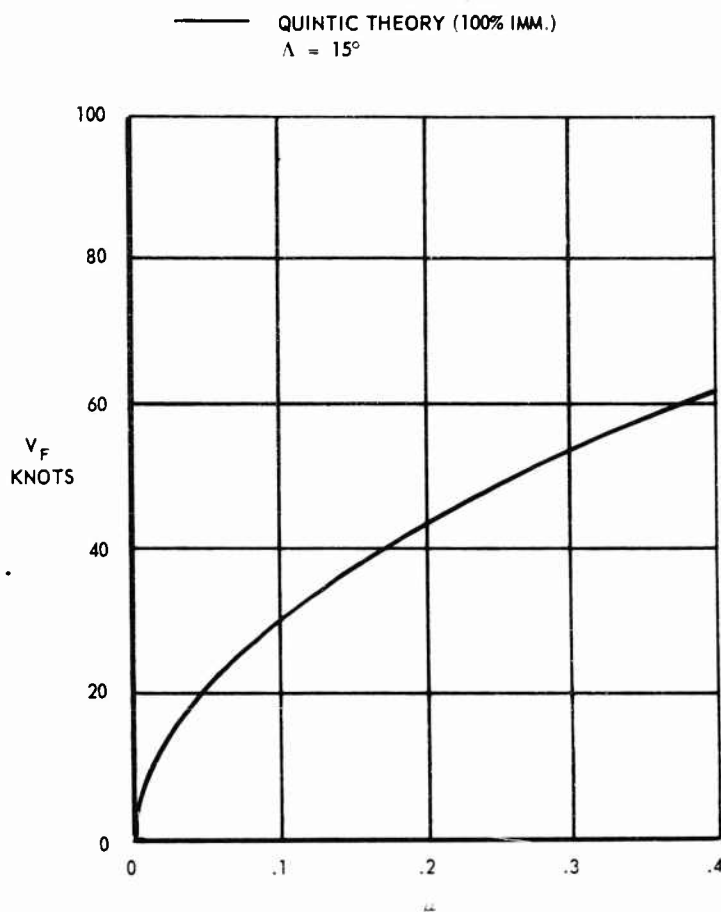
Fig. 10 - The Effect of Mass Density Ratio

tendency to doubt its validity. However, every investigation that has come to the authors' attention has indicated the existence of either a local maximum or an asymptotic rise (as μ_a is approached from above) in flutter speed in this area. In short, it appears that a maximum flutter speed, either local or absolute, does indeed occur in the vicinity of μ_a.

VII. The Basic Flutter Mechanism

Until the advent of large electronic computers, flutter analyses were performed in a manner that gave somewhat more insight into the so-called "flutter mechanism" than is the case with present-day methods. A very few years ago, solution of a quintic system was considered to be an almost monumental undertaking. As a matter of practicality the modes of a surface were analyzed two

753

and three at a time in carefully chosen combinations, and as a result the analyst usually developed a good "feel" for the flutter characteristics of the surface he was analyzing.

We have resorted to this earlier technique here in order to better define our basic flutter mechanism.

The previously discussed results indicate that the basic unstable mechanism is contained in the cubic system (first bending-second bending-first torsion) and that the addition of higher modes constitutes a refining process. It has been the authors' experience that the basic cause of instability in almost any system can be isolated by consideration of only two judiciously chosen modes of vibration. In the present case we have replaced judicious choosing by analysis of all three of the possible quadratic systems for $\mu = 0.1$ and $\mu = 100$. It was concluded earlier that the first bending-second bending quadratic formulation is unsatisfactory, particularly at the lower mass ratios. Similarly, solution of the second bending-first torsion quadratic gave no sensible result. However, the first bending-first torsion quadratic systems (Figs. 11 and 12) yield essentially the same flutter speed and frequency predictions as the cubic systems for both the high and low values of mass ratio. We conclude then that the basic flutter mechanism for the model of interest is defined by unstable coupling of the primary bending and primary torsional degrees of freedom—the most classical case. High speed motion pictures taken during the experimental program tend to bear out this finding.

VIII. Some Unusual Analytical Behavior

The fact that root-locus plots of the type shown in Figs. 6-9, 11, 12 often trace out physically "meaningless"* patterns does not come as news to any experienced analyst. Frequency curves which are triple valued with respect to velocity, such as the second bending branch in Fig. 6, are, in fact, commonplace in bending-torsion flutter analysis and it is not unusual for the corresponding damping roots to describe a closed loop.

It has been the authors' experience that this behavior of the root-locus plot is greatly magnified at low mass density ratios. The cubic analysis for $\_ = 0.55$ (Fig. 13) is a good illustration of the type of behavior to which we refer. (The arrowheads in Fig. 13 indicate the direction of increasing $V/b\omega$). It is seen here that the frequency of the torsion branch initially rises quite rapidly with increasing $V/b\omega$ and then at some very high valued combination of speed and frequency doubles back sharply toward the origin, eventually coalescing with the second bending branch and proceeding out along the speed axis in the usual manner. Meanwhile, the locus of the damping values has crossed the neutral stability axis and proceeded to a speed which is roughly half the zero-damping speed before rising sharply and doubling back to higher speeds. Differences of this magnitude between the zero-damping speed and the minimum speed for unstable solutions are, to say the least, highly unusual and the authors cannot recall ever having encountered such behavior at higher density ratios.

---

*The word meaningless is used here only in the sense that three different values of the same frequency or damping curve obviously cannot exist simultaneously at the same speed.

Flutter Characteristics of A Hydrofoil Strut
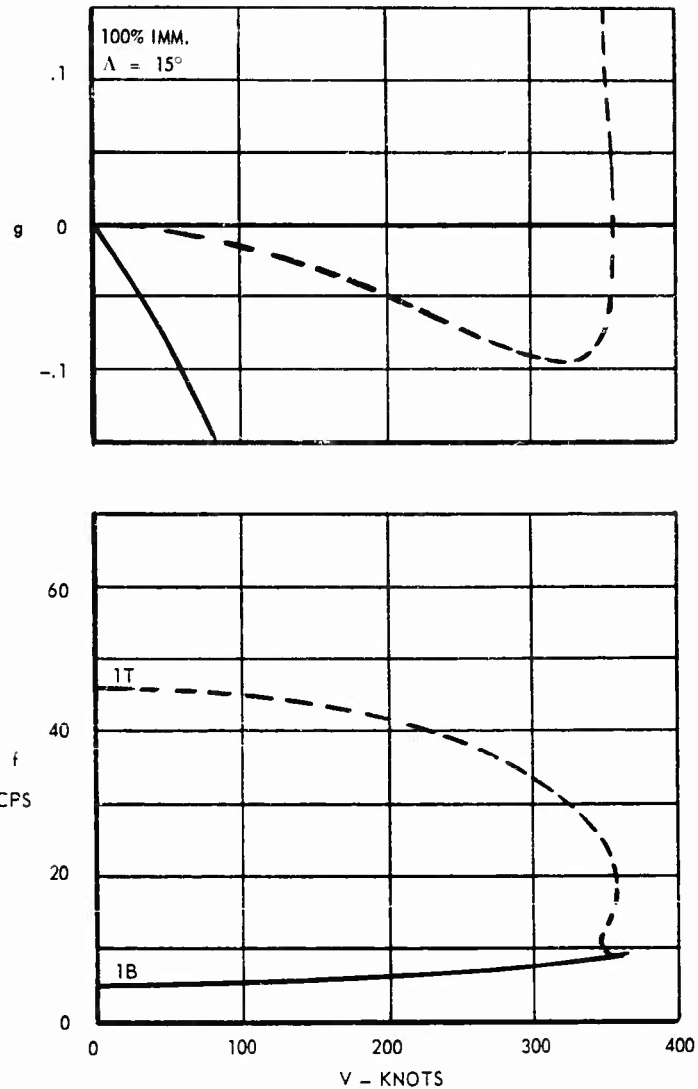
Fig. 11 - μ = 100, First Bending Vs. First Torsion

For mass density ratios slightly less than 0.55 the frequency plot for the torsion branch actually becomes infinite before doubling back toward the origin. That is to say, there exists a small range of reduced frequencies for which this branch yields no real solution. The analysis shown in Fig. 8 exhibits this type of behavior. The disappearance of a root as $V/b\omega$ is increased is not unusual. However, the reappearance of that root for some still higher value of $V/b\omega$ is again a new experience for the authors.
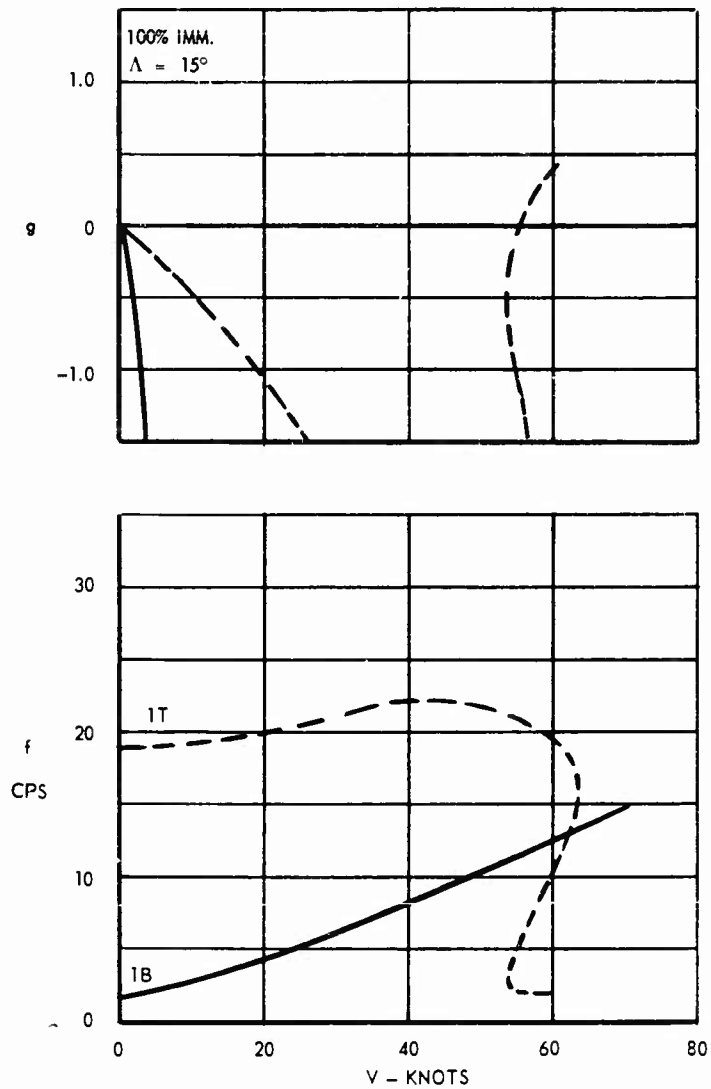
Fig. 12 - μ = 0.1, First Bending Vs. First Torsion

For the particular model under discussion these unusual characteristics were greatiy minimized by the inclusion of additional degrees of freedom (cf. Figs. 8 and 9). Whether or not this result is general or peculiar to this particular model cannot be said with certainty; however, it reinforces an already strong temptation to use something more than a minimum number of modes at low density ratios.

Flutter Characteristics of A Hydrofoil Strut
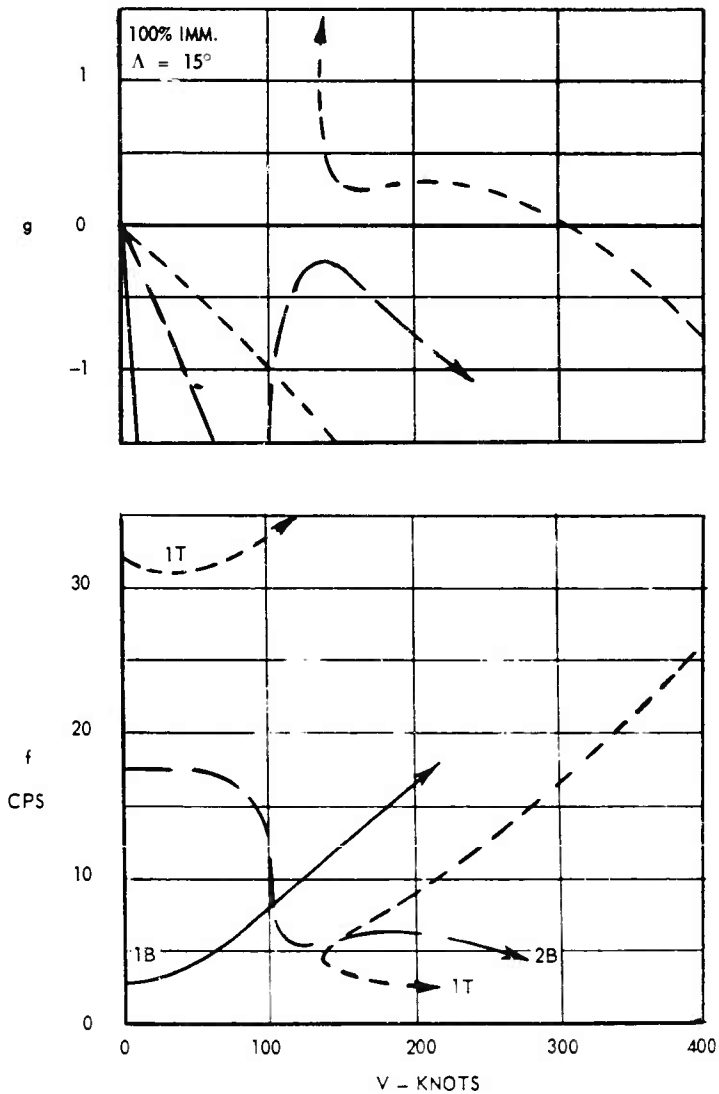
Fig. 13 - ⌣ = .55, Cubic Analysis

IX. Summary Discussion and Conclusions

The investigations reported here have been by no means exhaustive. In particular the behavior of the model in the region of μ_a is still not well understood. It is the intention of the authors to further pursue this particular point, possibly through a study of the changes in flutter mode shape as μ_a is approached from above. A comparison of the modal analysis results with the exact solution of the differential equations of motion might also prove to be enlightening, since the

latter method does not suffer from the convergence problems discussed in Section IV. We remark, however, that this comparison is possible here only because of the uniform nature of the struts being considered; in the analysis of actual working hardware, the analyst is nearly always forced to use modal analysis techniques due to non-uniform mass and stiffness distributions.

With respect to our attempt at gradual transition from the high mass-density-ratio regime to the hydrofoil regime, we must admit only limited success. It would seem, based on the convergence studies reported here, that there is a definite change in the flutter characteristics of the strut as one enters the low-mass-ratio regime, and that the change is in fact abrupt.

Based on our work to date we offer the following conclusions.

1. A modal type of flutter analysis may be used to successfully predict flutter at low-mass-density ratios.

2. The number of modes necessary for a converged solution, i.e., a solution unaffected by the inclusion of additional modes, increases abruptly in the low-mass-density ratio regime.

3. There is some indication that for small problem sizes (quadratic or cubic systems), the use of the natural modes of the model immersed in the fluid yields results superior to those based on the natural or assumed modes in vacuo.

4. The basic unstable mechanism for the model considered appears to be describable by consideration of the primary bending and torsion modes.

5. A local maximum in predicted flutter speed occurs in the region of the so-called critical mass-density ratio.

6. For the very low mass density ratio range the approximate variation in flutter speed as a function of mass ratio is given by $V_F \sim \sqrt{\mu}$.

7. For the range of sweep angles investigated, sweepback is beneficial in increasing the flutter speed.

8. The flutter speed of the strut varies in an inverse manner with percent area immersed.

REFERENCES

1. Baird, E.F., Squires, C.E., Jr., and Caporali, R.L., "An Experimental and Theoretical Investigation of Hydrofoil Flutter," Aerospace Engineering, Vol. 21, No. 2, February 1962.

2. Baird, E.F., Squires, C.E., Jr., and Caporali, R.L., "Investigation of Hydrofoil Flutter - Final Report," Grumman Aircraft Engineering Corporation Report No. DA 10-480.3, February 1962.

3. Henry, C. J., Dugundji, J., and Ashley, H., "Aeroelastic Stability of Lifting Surfaces in High Density Fluids," Journal of Ship Research, Vol. 2, No. 4, March 1959.

4. Herr, Robert W., "A Study of Flutter at Low Mass Ratios With Possible Application to Hydrofoils," NASA TN D-831, May 1961.

5. Theodorsen, Theodore, and Garrick, I.E., "Mechanism of Flutter—A Theoretical and Experimental Investigation of the Flutter Problem," NACA Report 685, 1940.

* * *

COMPARISON OF HYDROFOIL FLUTTER
PHENOMENON AND AIRFOIL FLUTTER THEORY*

Charles J. Henry
Davidson Laboratory
Stevens Institute of Technology
Hoboken, New Jersey

To meet the demand for more effective vehicles, two trends have become apparent in recent designs of naval craft; speeds have increased and structural rigidity has decreased. The effect of the former trend is to increase the hydrodynamic loads acting on the hull and appendages and the effect of the latter is to increase the elastic response of the structure. Each of these trends increases the likelihood of serious hydroelastic problems in ships.

The analogous problems in aircraft design (aeroelasticity) have been investigated thoroughly in order to acquire dependable methods of prediction of aeroelastic phenomenon. Thus, a large amount of knowledge, literature and experience is available to the naval designer concerned with hydroelastic problems, if the dependability of aeroelastic theories carries over to the ranges of parameters of interest to the hydroelastician.

One of the most important problems in hydroelasticity is flutter of hydrofoils, which is a self-excited, oscillatory instability of an elastic lifting surface. To determine whether or not aeroelastic theories could accurately predict hydrofoil flutter conditions, experimental studies were conducted at the Davidson Laboratory and the results were compared with predictions based on aerofoil flutter theory.

Every effort was made to reproduce the theoretical conditions in the experimental configuration. Since the resulting configuration was somewhat idealized, the conclusions of this investigation are limited to deeply submerged, fully-wetted hydrofoils with rectangular planforms in two-dimensional flow and elastically supported in two degrees of freedom. The theoretical and experimental determination of the effects of cavitation, ventilation, free surface, planform geometry, distributed elasticity, more realistic support conditions and three-dimensional flow should be investigated before accurate hydrofoil flutter predictions can be made with assurance. The data presented in this paper, however, indicate that inaccurate predictions may occur in hydrofoil flutter investigations.

761

The model used in these experiments was a symmetric airfoil, 12% thick with a 6-inch chord and 12-inch span (NACA 0012 cross section) and was supported with its chord-plane vertical between large horizontal end-plates. A complete description of the apparatus is given in [1] and [2]. The model was held by a rigid string which was connected to the supporting structure by a flexure balance which provided elastic support in two degrees of freedom in the horizontal plane and rigid support for all other motions of the foil. Thus, the model was elastically restrained in translation perpendicular to the stream direction and rotation about the 1/4 chord axis. Two sets of weights were connected rigidly to the foil and were designed to attain the chosen values of center of gravity location, radius of gyration and natural frequency ratio, while varying the effective foil mass.

The flexure balance was instrumented to give electrical outputs which were proportional to the translational and rotational displacements of the model. A tachometer generator attached to the carriage and driven by a wheel on the carriage rail gave an indication of the instantaneous speed of the apparatus; the measured time for the apparatus to travel a known distance gave an accurate indication of the average speed of the apparatus. The two measurements of the speed agreed and the instantaneous speed was essentially constant during a run. The two displacements and the instantaneous carriage speed were recorded on paper tape.

All motions of the model, other than the two degrees of freedom in the horizontal plane, were rigidly restrained, so that the "assumed modes" method of flutter analysis provided an exact mathematical description of the dynamic system. The appropriate modes of motion were

$$
\left.
\begin{aligned}
h(t) &= h_o b e^{\ell t} \\
\alpha(t) &= \alpha_o e^{\ell t}
\end{aligned}
\right\} \tag{1}
$$

where

$$\ell = -\sigma + i\omega$$

and

$h(t)$ = translational displacement

h_o = dimensionless complex translational amplitude

$\alpha(t)$ = rotational displacement

α_o = complex rotational amplitude

σ = decay rate

ω = circular frequency

b = half chord length

t = time.

The equations of motion for the dynamic system shown in Fig. 1 are

$$m(\ddot{h} - bx_a\ddot{\alpha}) + K_h h = L \tag{2}$$

and

$$I_a\ddot{\alpha} - mbx_a\ddot{h} + K_a\alpha = M \tag{3}$$

where

m = mass of foil plus weights per unit span

x_a = distance from rotational axis to the center of gravity in half chord lengths, positive aft

I_a = mass polar moment of inertia of foil plus weights about the rotational axis per unit span

K_h = translational support stiffness

K_a = rotational support stiffness

L = unsteady hydrodynamic lift per unit span

M = unsteady hydrodynamic moment about the rotational axis, per unit span.

It must be noted, however, in deriving the equations of motion, Eqs. 1 and 2, use was made of the fact that m_h, the mass associated with translational motion, was negligible compared with m_a, associated with rotational motion. (See Fig. 1.) The dots indicate differentiation with respect to time. The system parameters are depicted in Fig. 1 and the sign conventions are indicated in Fig. 2.

Dividing Eq. 2 by $\pi\rho bU^2$ and Eq. 3 by $\pi\rho b^2U^2$ and defining the dimensionless parameters

$\mu = m/\pi\rho b^2$ = density ratio

$r_a^2 = I_a/mb^2$ = radius of gyration

$\Omega_h^2 = K_h b^2/mU^2$ = uncoupled natural frequency in translation in vacuum

$\Omega_a^2 = K_a b^2/I_a U^2$ = uncoupled natural frequency in rotation in vacuum

$$\lambda = \left(\frac{\sigma}{\omega_a} + i\,\frac{\omega}{\omega_a}\right)\frac{\omega_a b}{U}$$
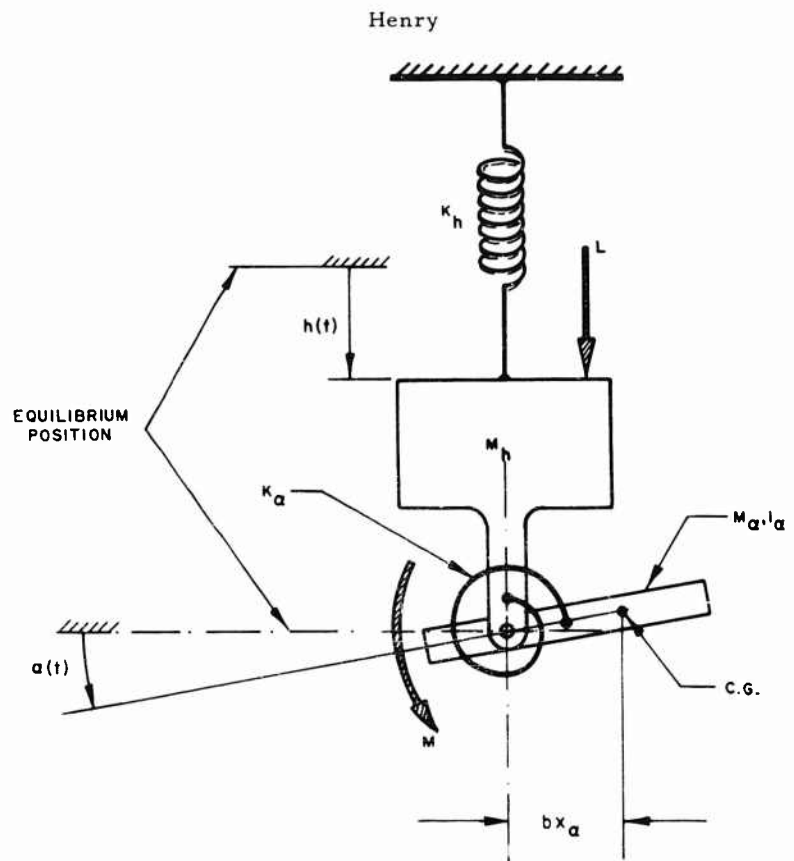
Fig. 1 - Schematic Diagram of System Used for
Dynamic Analysis

and

$$s = Ut/b = \text{dimensionless time,}$$

then the dimensionless responses become

$$\left. \begin{array}{l} h(s) = h_o e^{\lambda s} \\ \\ \alpha(s) = \alpha_o e^{\lambda s} \end{array} \right\} \tag{4}$$

whereas, the equations of motion become

$$\mu h'' - \mu x_\alpha \alpha'' + \mu \Omega_h^2 h = L/\pi \rho b U^2 \tag{5}$$

and

764
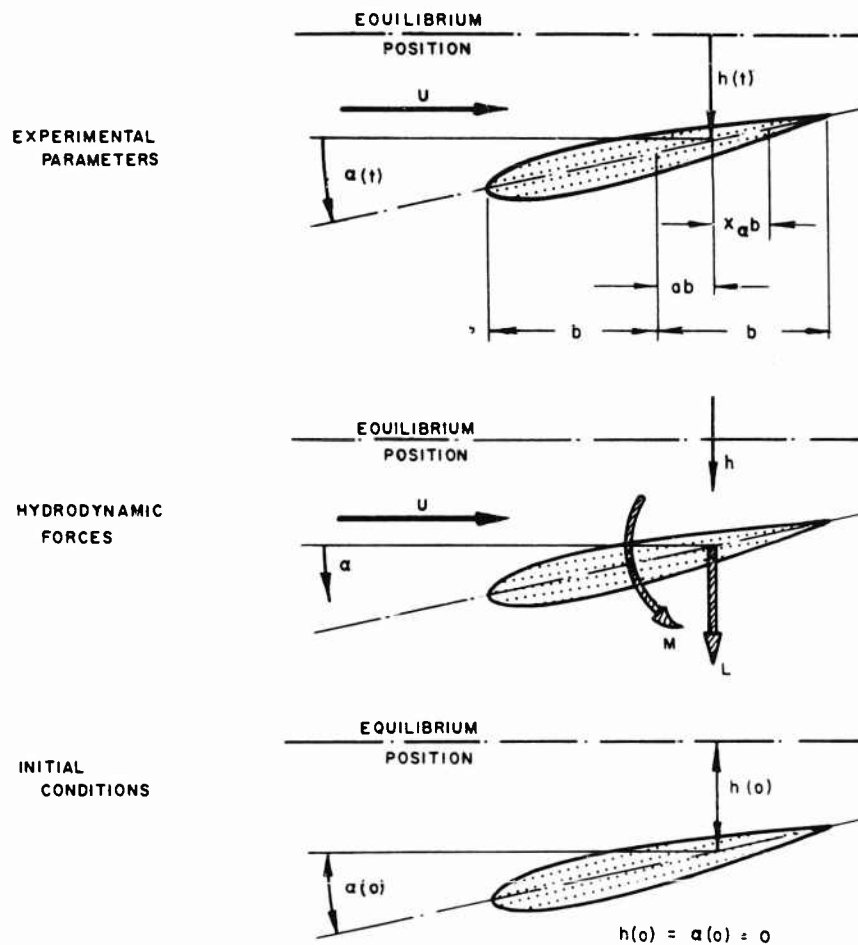
Fig. 2 - Representative Hydrofoil Orientation Showing Nomenclature and Sign Conventions

$$\mu r_a{}^2\alpha'' - \mu x_a h'' + \mu r_a{}^2\Omega_a{}^2\alpha = M/\pi\rho b^2 U^2, \tag{6}$$

where the primes indicate differentiation with respect to s.

To obtain accurate results at speeds below the critical flutter speed, the Wagner description of the circulatory part of the unsteady hydrodynamic force was used, giving

$$L/\pi\rho b U^2 = -h'' + \alpha' - a\alpha'' + 2\left[H'(o)\phi(s) + \int_o^s H''(\psi)\phi(s - \psi)\,d\psi\right] \tag{7}$$

765

and

$$M/\pi\rho b^2 U^2 = -ah'' - \left(\frac{1}{2} - a\right)\alpha' - \left(\frac{1}{8} + a^2\right)\alpha''$$

$$+ 2\left(\frac{1}{2} + a\right)\left[H'(o)\phi(s) + \int_o^s H''(\psi)\phi(s - \psi)\,d\psi\right] \tag{8}$$

where

a = distance from midchord to the rotational axis in half chord lengths, positive aft

$\phi(s)$ = the Wagner function

$H'(s)$ = the vertical velocity of the 3/4 chord point defined by

$$H'(s) = -h' + \alpha + \left(\frac{1}{2} - a\right)\alpha'. \tag{9}$$

The Wagner function as is known represents the indicial circulatory lift response as opposed to the added mass response to the motion given by the first three terms on the right hand side of Eqs. 7 and 8. The following approximate form of the Wagner function given in [3] was used.

$$\phi(s) = 1 - 0.165e^{-0.0455s} - 0.335e^{-0.3s} \tag{10}$$

Equations 5 and 6, in conjunction with Eqs. 7, 8, 9 and 10, were solved using Laplace transform methods, leading to the following responses

$$\left.\begin{array}{l} h(s) = h_1 e^{\lambda_1 s} + h_2 e^{\lambda_2 s} \\[2mm] \alpha(s) = \alpha_1 e^{\lambda_1 s} + \alpha_2 e^{\lambda_2 s} \end{array}\right\} \tag{11}$$

where h_1, h_2, α_1 and α_2 are complex amplitudes and λ_1 and λ_2 are the complex eigenvalues.

In the experiments, the model was held rigidly with an initial angle of attack until the carriage had accelerated to the test speed. The model was then released and the resulting motions were recorded. The speed was increased in each subsequent run until a flutter condition was reached. Tests at speeds slightly above the critical flutter speed were found fruitful and for these cases, the model was started from the equilibrium position. Figure 3a exhibits a typical record taken below the critical flutter speed whereas Fig. 3b shows one above the critical flutter speed.

The responses shown in Fig. 3 contain only one of the predicted modes of vibration, associated with σ_1 and ω_1 since the second mode of vibration, σ_2 and ω_2, was found to be very highly damped as predicted, i.e., $\sigma_2 > \sigma_1$. Thus in the data analysis program, the response was treated as

766
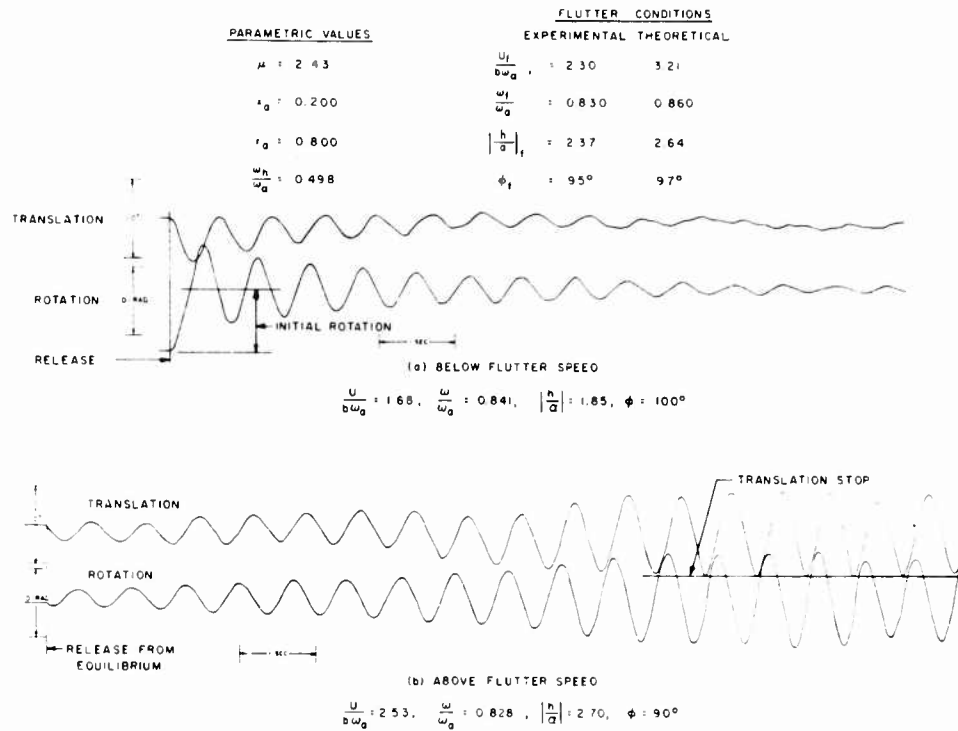
Fig. 3 - Typical Records

$$
\left.
\begin{aligned}
h(s) &= h_1 e^{-\sigma_1 s} \cos \omega_1 s \\[1em]
\alpha(s) &= \alpha_1 e^{-\sigma_1 s} \cos \omega_1 s
\end{aligned}
\right\}
\tag{12}
$$

The decay rate, σ, of the rotational response was measured, whereas, the frequency of response, ω, was measured from both degrees of freedom, as well as the magnitude and argument of the ratio h_1/α_1. The decay rate and response frequency were made dimensionless by dividing by ω_α, the uncoupled natural frequency in rotation, to give the overall damping ratio, σ/ω_α, and the frequency ratio, ω/ω_α. These experimental results are compared with the predicted values in Figs. 4 through 11.

A discrepancy was found between the predicted and measured values of σ/ω_α, whereas predicted and measured values of ω/ω_α and the magnitude and argument of h_1/α_1 agreed in all cases. Calculations showed that appreciable variations of σ/ω_α resulted from systematic changes of the constants in Eq. 10, whereas, the predicted values of ω/ω_α and h_1/α_1 remained essentially unchanged, thus indicating that σ/ω_α is the response characteristic which is most sensitive to the circulatory part of the unsteady lift. Since the discrepancy was found for σ/ω_α, the hypothesis presented in [1] is partially substantiated; i.e.,

767
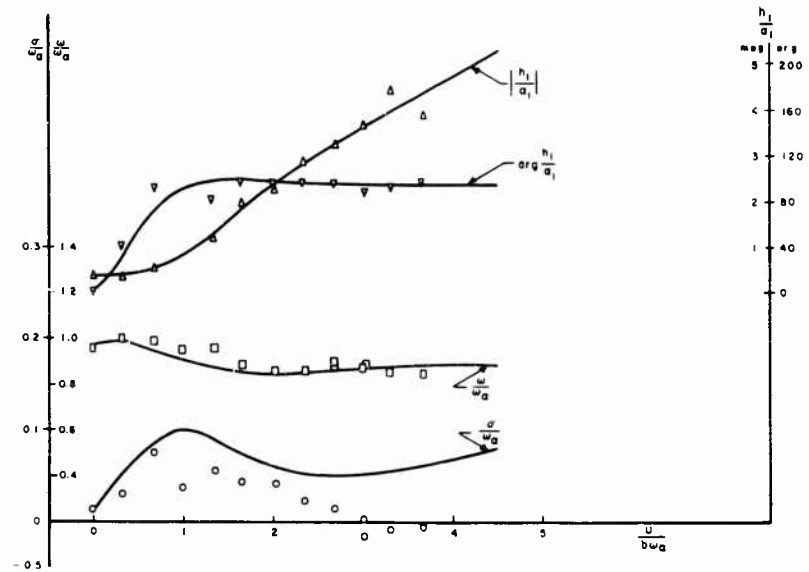
Fig. 4 - Overall Damping Ratio, Frequency Ratio, Amplitude
Ratio and Phase Lag, $\mu = 2.00$, $x_a = 0.2$
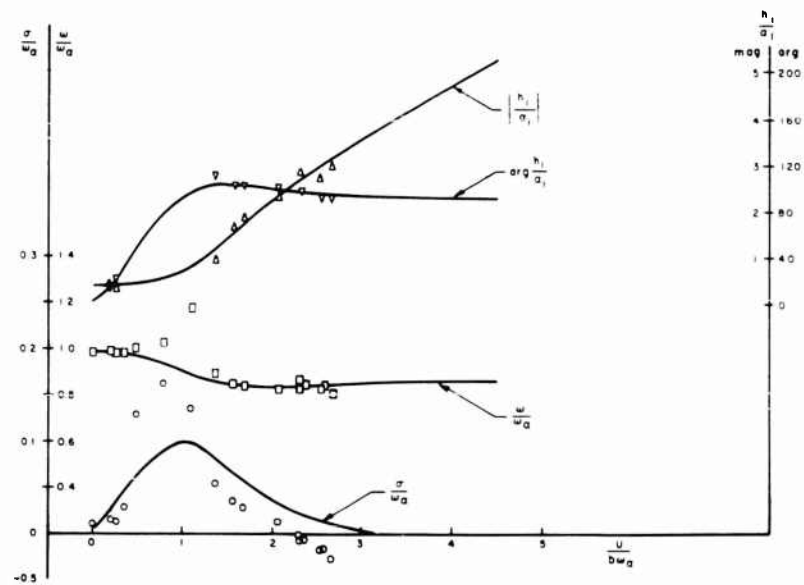
Fig. 5 - Overall Damping Ratio, Frequency Ratio, Amplitude
Ratio and Phase Lag, $\mu = 2.43$, $x_a = 0.2$

768
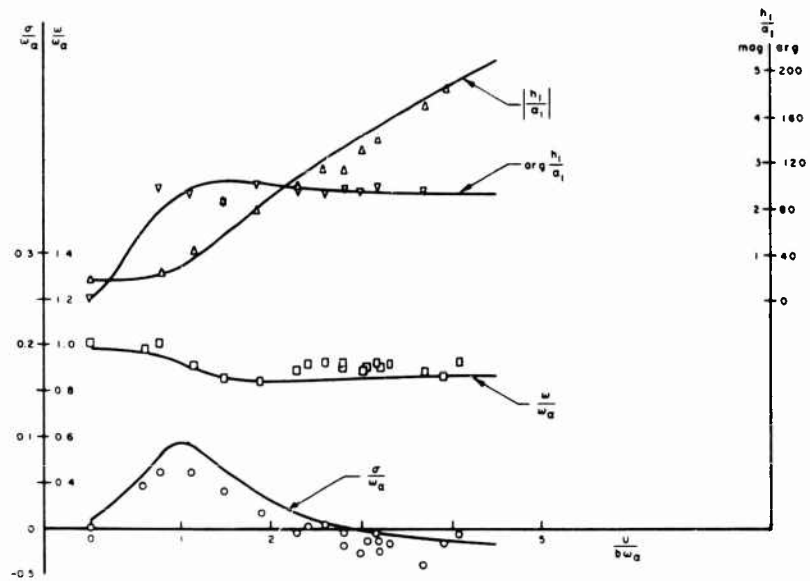
Fig. 6 - Overall Damping Ratio, Frequency Ratio, Amplitude
Ratio and Phase Lag, $\mu = 2.50$, $x_\alpha = 0.2$
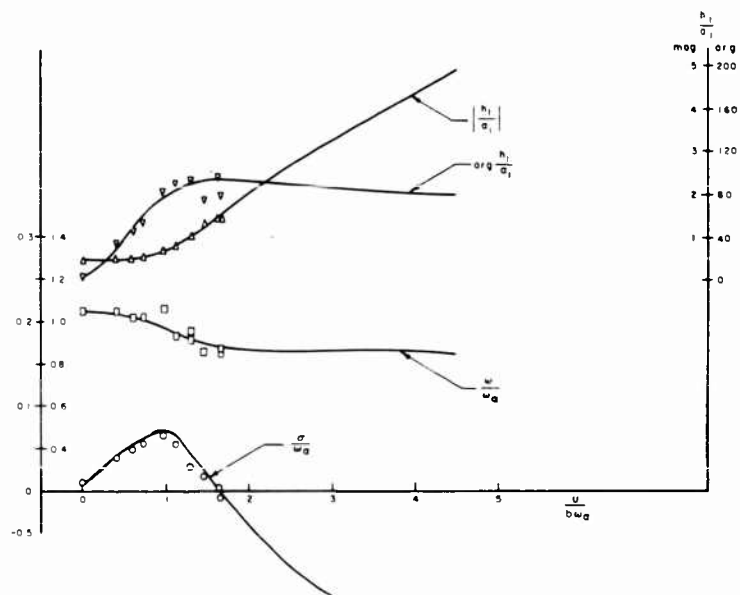
Fig. 7 - Overall Damping Ratio, Frequency Ratio,
Amplitude Ratio and Phase Lag, $\mu = 2.50$, $x_\alpha = 0.3$

769
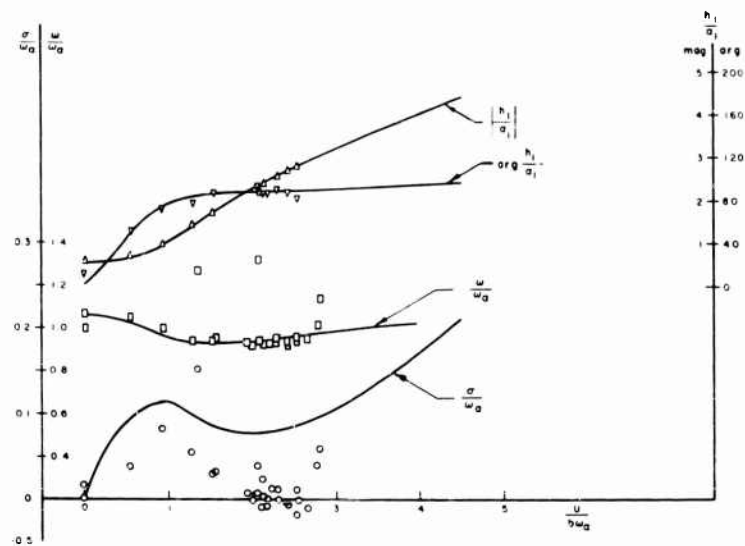
Fig. 8 - Overall Damping Ratio, Frequency Ratio,
Amplitude Ratio and Phase Lag, μ = 0.992, x_α = 0.4
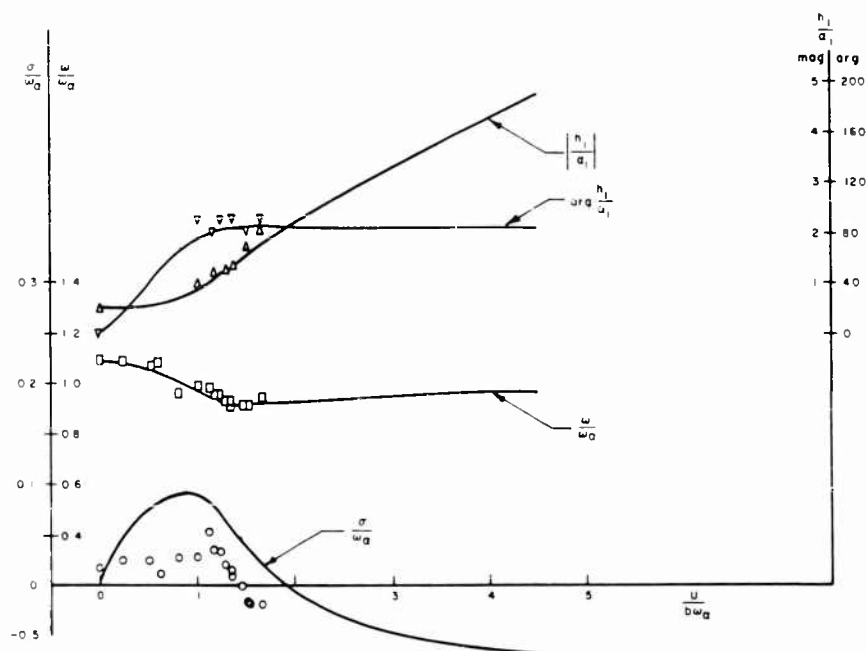
Fig. 9 - Overall Damping Ratio, Frequency Ratio, Amplitude
Ratio and Phase Lag, μ = 1.27, x_α = 0.4

770
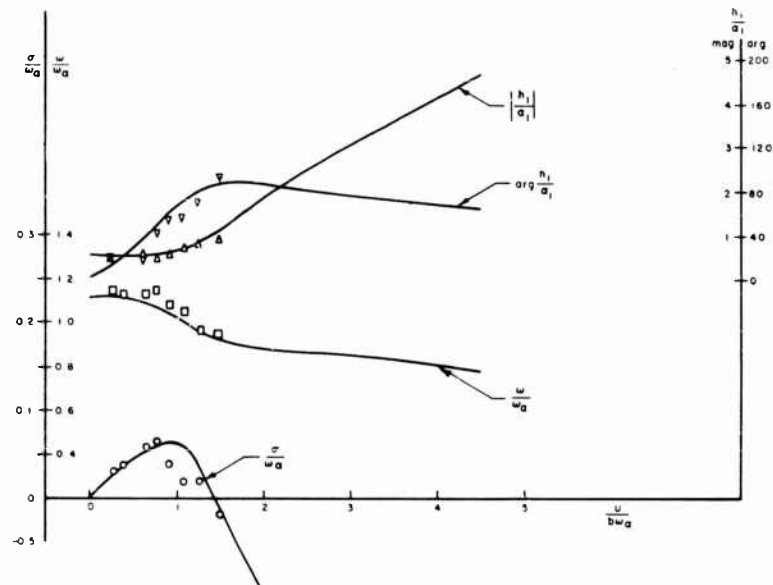
Fig. 10 - Overall Damping Ratio, Frequency Ratio,
Amplitude Ratio and Phase Lag, $\mu = 2.50$, $x_2 = 0.4$
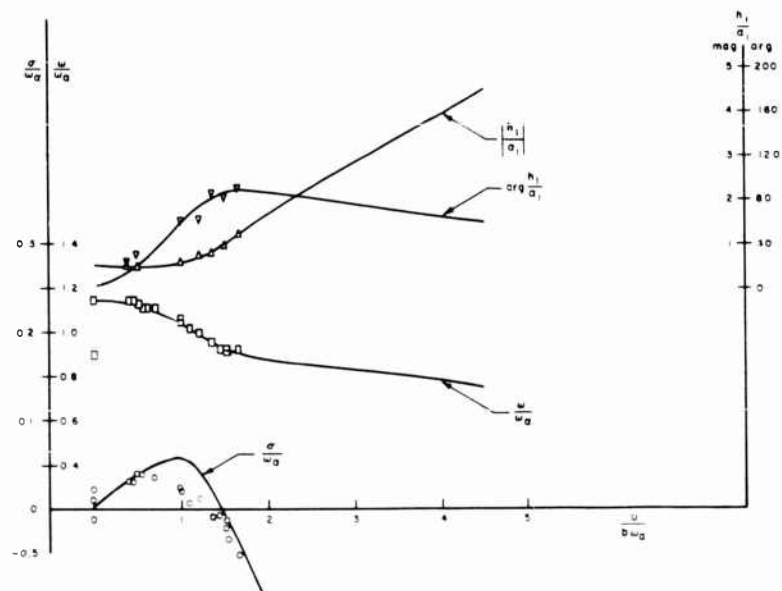
Fig. 11 - Overall Damping Ratio, Frequency Ratio,
Amplitude Ratio and Phase Lag, $\mu = 3.12$, $x_2 = 0.4$

771

the circulatory terms in the theory are less accurate than the added mass terms. It is suggested, therefore, that a new model of the bound and wake vorticity distribution is needed to provide a more accurate representation of the actual flow pattern behind an oscillating foil.

A prediction of flutter speed was obtained from the plots of the overall damping ratio where σ vanishes. These predicted flutter speeds were plotted in Fig. 12 together with those from the experimental results. Flutter speeds for the three center of gravity locations were presented together with those previously obtained. These results show the inadequacy of the theory to predict flutter speeds of the tested configuration, particularly at low values of density ratio. At the high values of μ, the theory gave a conservative estimate of flutter speed which was in agreement with aeroelastic experience. However, the range of μ of practical interest in hydrofoil operation is $0.1 < \mu < 1$, and the discrepancy in this range becomes more dangerous since the theory gives a non-conservative estimate of flutter speed. In fact, flutter was found experimentally within the range of μ for hydrofoil operation where freedom from flutter was predicted at all speeds, thus drastically emphasizing the need for more accurate methods of hydrofoil flutter analysis.

In each case, however, a sharp upward trend in the experimental flutter speed was found as μ decreases. This trend was in agreement with the predicted trend, but the experimental turning-up occurred at a lower density ratio than predicted. This behavior of flutter speed was investigated theoretically in [4] using the quasi-steady representation of the unsteady lift forces. A rather complicated result is obtained except for the limiting case $\omega_h/\omega_\alpha = 0$ when the asymptotic value of density ratio, μ_{CR}, is given by
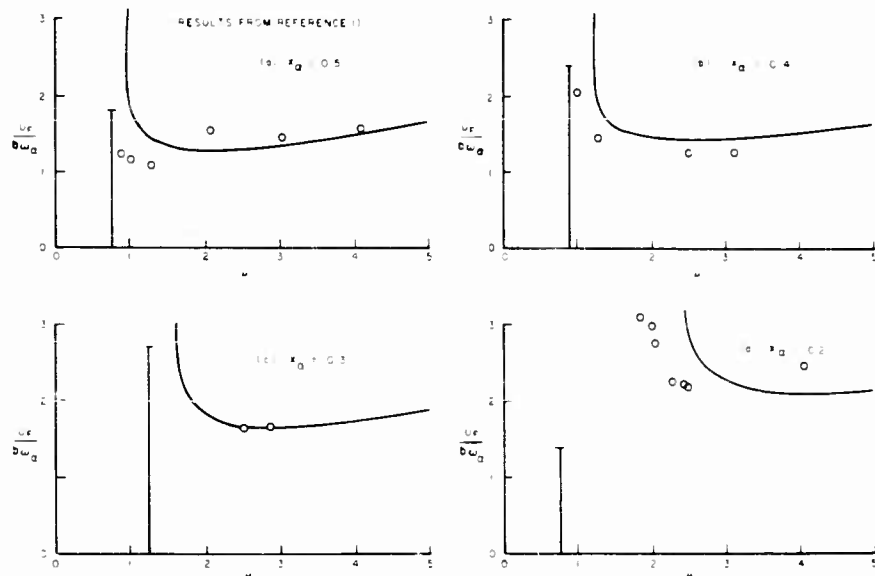
Fig. 12 - Measured and Predicted Flutter Speeds

772

$$\mu_{CR} = \frac{1}{1 + 2(x_a + a)} \tag{13}$$

Equation 13 was plotted in Fig. 13 for comparison with the minimum values of density ratio at which flutter was found experimentally. This comparison shows a constant reduction of 25% in μ_{CR} for the values of $x_a + a$ tested. This quantitative result cannot be generalized for other configurations; in fact, in [5] much larger reductions of μ_{CR} were obtained indicating that the actual flutter stability boundary extends by an unknown amount below the predicted μ_{CR} toward the range of μ for hydrofoils.

In summary, comparison of measured and predicted flutter conditions of a two-degree of freedom system in two-dimensional, fully-wetted flow lead to the following conclusions:

1. The predicted overall damping ratio did not agree with measured values.

2. The measured and predicted values of the frequency ratio and the ratio of complex amplitudes for one mode of vibration were in agreement.
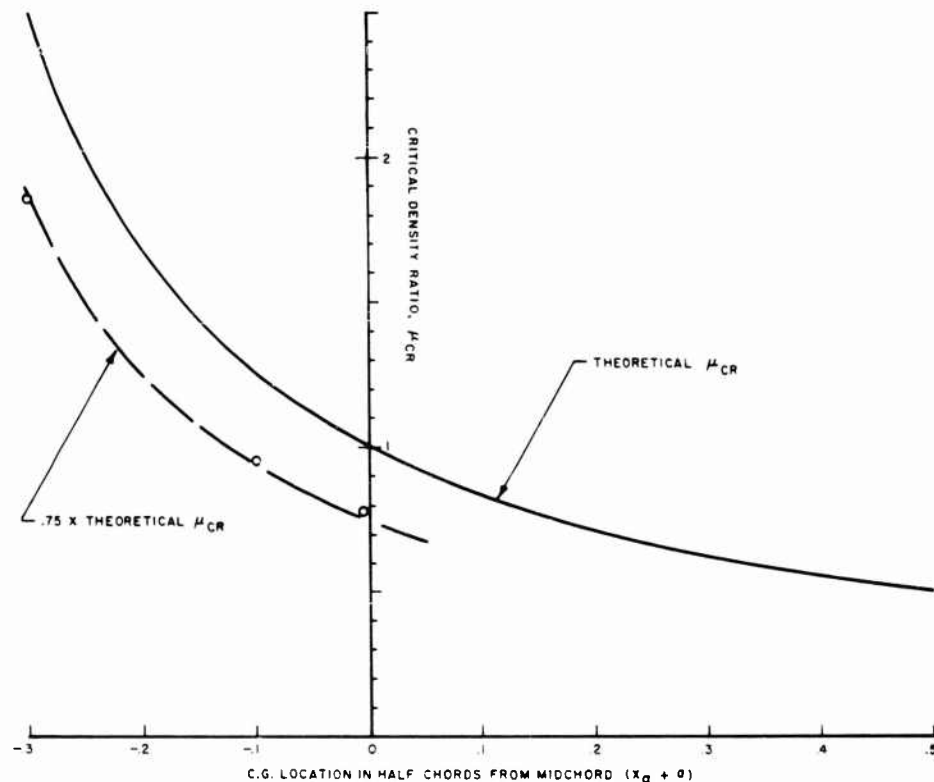
Fig. 13 - Critical Density Ratio

773

3. The predicted flutter speed at high values of density ratio was less than the measured one, a fact which is in agreement with aeroelastic experience.

4. At low values of density ratio, in the range for typical hydrofoils operation, the discrepancy between predicted and measured flutter speeds became non-conservative and thus more dangerous. In addition, flutter was found experimentally in the region of density ratio where freedom from flutter is predicted at all speeds.

5. The predicted upward trend in the flutter speed for decreasing density ratio occurred in the experimental results but at a smaller density ratio.

6. Systematic changes in the circulatory lift terms in the theoretical analysis showed that the overall damping ratio depends strongly on these terms whereas the other response characteristics do not.

Conclusions 1, 2 and 6 give partial substantiation for the hypothesis that the circulatory lift response is less accurately represented than the added mass response in the classical unsteady airfoil theory. It is recommended, therefore, that a more realistic theoretical model is needed for the bound and wake vorticity associated with an oscillating foil.

ACKNOWLEDGMENTS

REFERENCES

1. Henry, C.J., "Hydrofoil Flutter Phenomenon and Airfoil Flutter Theory, Volume I, Density Ratio," Davidson Laboratory Report 856, September 1961.

2. Henry, C.J., "Hydrofoil Flutter Phenomenon and Airfoil Flutter Theory, Volume II, Center of Gravity," Davidson Laboratory Report to be published.

3. Jones, R.T., "The Unsteady Lift on a Wing of Finite Aspect Ratio," NACA Report 681, 1940.

4. Henry, C.J., Dugundji, J. and Ashley, H., "Aeroelastic Stability of Lifting Surfaces in High Density Fluids," Journal of Ship Research, Volume 2, No. 4, March 1959.

5. Woolston, D.S. and Castile, G.E., "Some Effects of Variations in Several Parameters Including Fluid Density on the Flutter of Light Uniform Cantilever Wings," NACA TN 2558, 1951.

*　　*　　*

774

HYDROELASTIC INSTABILITIES OF PARTIALLY CAVITATED HYDROFOILS*

Paul Kaplan
Oceanics, Inc.
Plainview, N. Y.

INTRODUCTION

The present development of hydrofoil craft has been aimed at producing vehicles that can perform effectively at high forward speeds. Subcavitated hydrofoil designs are presently capable of speeds of the order of 50-60 knots, while supercavitating hydrofoil craft are expected to reach 100 knots and higher. One of the problems that face designers of these craft is the possibility of the occurrence of hydroelastic instability (i.e., flutter and/or divergence) at these high speeds. Experience in the aircraft industry has shown that these problems appear as speeds increase and as the structures get thin. Both of these conditions are characteristic of the presently considered classes of hydrofoil craft.

In the past four years, certain theoretical studies have been devoted to the problems of hydroelasticity, for both fully-wetted hydrofoils [1, 2] and for supercavitating hydrofoils with very long cavities [3]. Experimental investigations aimed at determining the hydroelastic characteristics of hydrofoils in fully-wetted flow have only recently been carried out, and some of the results of these studies are being presented at this symposium. The conditions under which flutter and/or divergence occur were determined, in terms of density ratio, speed, natural frequencies, location of center of gravity and elastic axis, etc., in all of these studies. While it appears that flutter may possibly be a problem (in certain instances) for the fully-wetted case, and that divergence is also a practical possibility for that situation, the theoretical results for supercavitating flow [3] show that both flutter and divergence are definite possibilities that must be avoided by proper design.

775

In the various naval applications for which lifting surfaces are utilized, such as propellers, hydrofoil craft wings, control surfaces, etc., there are certain periods of time when a hydrofoil designed for non-cavitated operation will nevertheless experience partial cavitation. This cavitation will be in the form of a cavity extending over a portion of the upper surface of the foil. Even when a foil is designed for supercavitating operation, there are situations that occur wherein it is partially cavitated (e.g., during take-off, slowing down, etc.). Under certain conditions the presence of this partial cavitation may not be too serious with regard to the lift and drag characteristics of the foil, but it is expected that the presence of this particular degree of cavitation will have an important influence on the hydroelastic behavior of the foil. The objective of the present study is the determination of the operating conditions under which hydroelastic instabilities will occur with this particular flow pattern, thereby providing theoretical guidance that will fill the gap between the two cases of fully-wetted flow and supercavitating flow.

HYDRODYNAMIC FORCES AND MOMENTS

The hydrofoil, in steady state, will be oriented at some small angle of attack and the ambient flow conditions are such that the upper surface will have a cavity extending from the leading edge to some point on the foil ahead of the trailing edge. In order to carry out an analysis of the hydroelastic characteristics of foils with such a flow pattern, it is necessary to know the hydrodynamic forces and moments acting on the foil in steady state and also when the foil performs oscillations. The method of analysis will be concerned with the various effects at a representative section of the foil and hence two-dimensional theoretical results for the hydrodynamic effects will be used.

The lift and moment for a partially cavitated foil (flat plate or cambered) in steady state are available in the work of Geurst [4], which contains the most extensive information necessary for the present study. The information presented in [4] related the steady angle of attack, the cavitation number and the cavity length (relative to the chord), thereby defining the range of interest for application to the present problem. A chart exhibiting this relation is shown in Fig. 1, and points out the fact that there are certain multi-valued results for cavity length as a function of angle of attack and cavitation number. The experimental results [5] show that no cavities with a length beyond $3/4$ of the total chord length are stable, and, in addition, further computations show the existence of unrealistic hydrodynamic values at this critical condition. Using the relations given in [4], it can be shown that the static lift rate with angle of attack is given by

$$C_{L_a} = \pi \left(\frac{1 - \sin \frac{\gamma}{2}}{2 \sin \frac{\gamma}{2} - 1} \right) \tag{1}$$

where the angle $\gamma/2$ is defined by

$$\frac{1 + \ell}{2} = \cos^2 \frac{\gamma}{2} \tag{2}$$
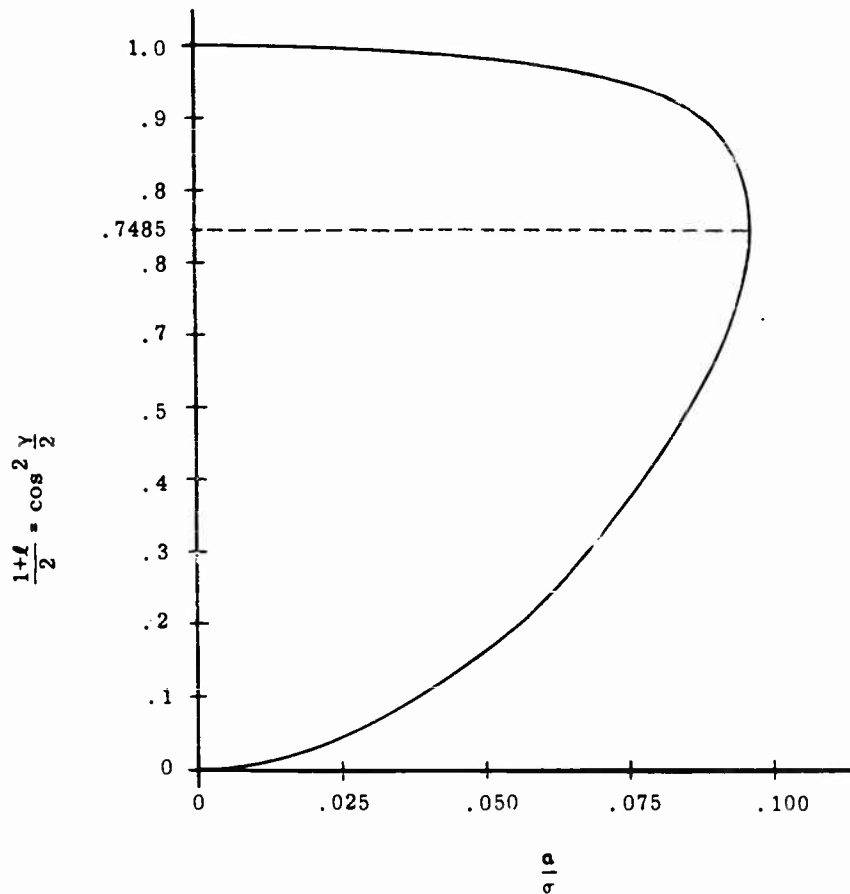
Fig. 1 - Relation between cavity length, steady angle of
attack, and cavitation number

with ℓ the cavity length (in terms of the half-chord b) measured from the mid-chord position, positive for cavities terminating between the mid-chord and the trailing edge of the foil. A plot illustrating the variation of this lift rate is given in Fig. 2, and as associated information, the distance to the center of pressure, d*, (measured from the mid-chord position in terms of the half-chord length, positive for center of pressure aft), for this condition is shown on Fig. 3. All of the results in Figs. 1, 2, and 3 are applied to a flat plate hydrofoil, which will be the configuration of major concern. Much more complicated relations are necessary when the foil is cambered (see [6]), and the results are dependent upon the particular shape of the camber line and the maximum camber ratio.

Examination of the figures shows that the lift rate for a partially cavitated foil exceeds that of a fully-wetted foil, and this result may be ascribed to an effective increase in camber of a flat plate due to the presence of the partial cavity. It also appears that there is not much variation in the position of the center

777
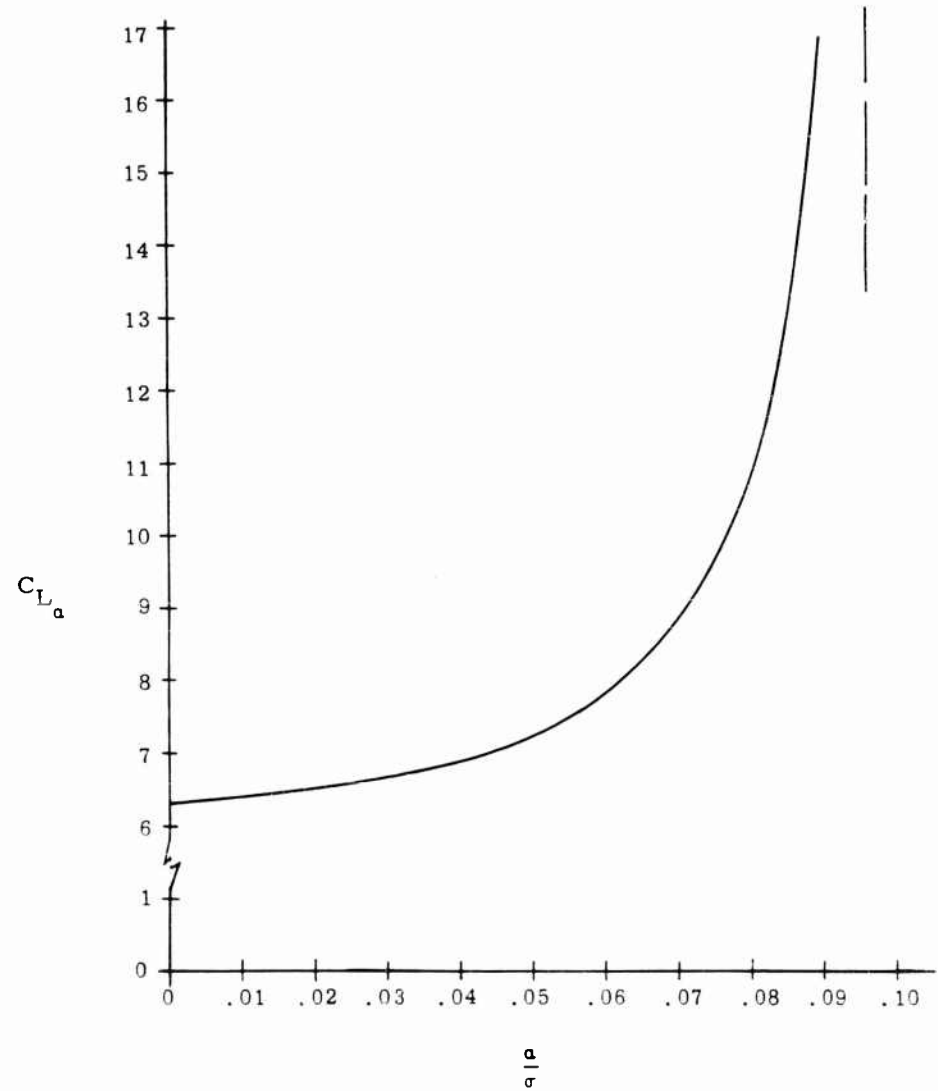
Fig. 2 - Lift slope as a function of angle of attack
and cavitation number

Hydroelastic Instabilities of Partially Cavitated Hydrofoils
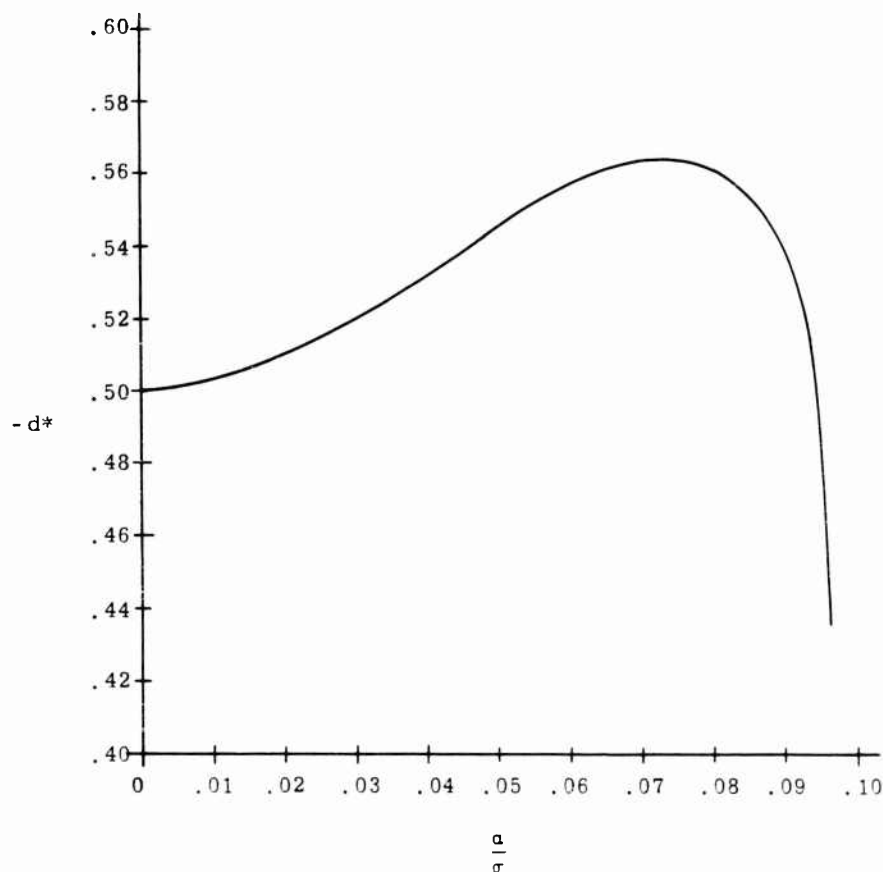
Fig. 3 - Center of pressure position for steady motion

of pressure for this case, in the range of practical cavity lengths of interest. The consequences of these hydrodynamic results for the hydroelastic behavior of partially cavitated foils will be considered in a later section.

In order to consider the dynamic effects in a hydroelastic analysis (i.e., flutter), it is necessary to know the hydrodynamic lift force and pitch moment acting on an oscillating partially cavitated foil, where the degrees of freedom of the oscillations are (essentially) heave and pitch. The heaving motion is the displacement in translation (for the dynamic analysis) and the pitching motion is the displacement in rotation. The translational displacement is defined as positively down, and the rotational displacement is defined as positive for leading edge up, as shown in the illustration of Fig. 4. A formulation of the potential flow problem for determining the lift and moment acting on an oscillating partially cavitated hydrofoil was initially presented by Timman [7], but the solution was not pursued to completion nor was any numerical work presented. Recently, Steinberg and Karp [8] utilized Timman's initial formulation and completely solved

779
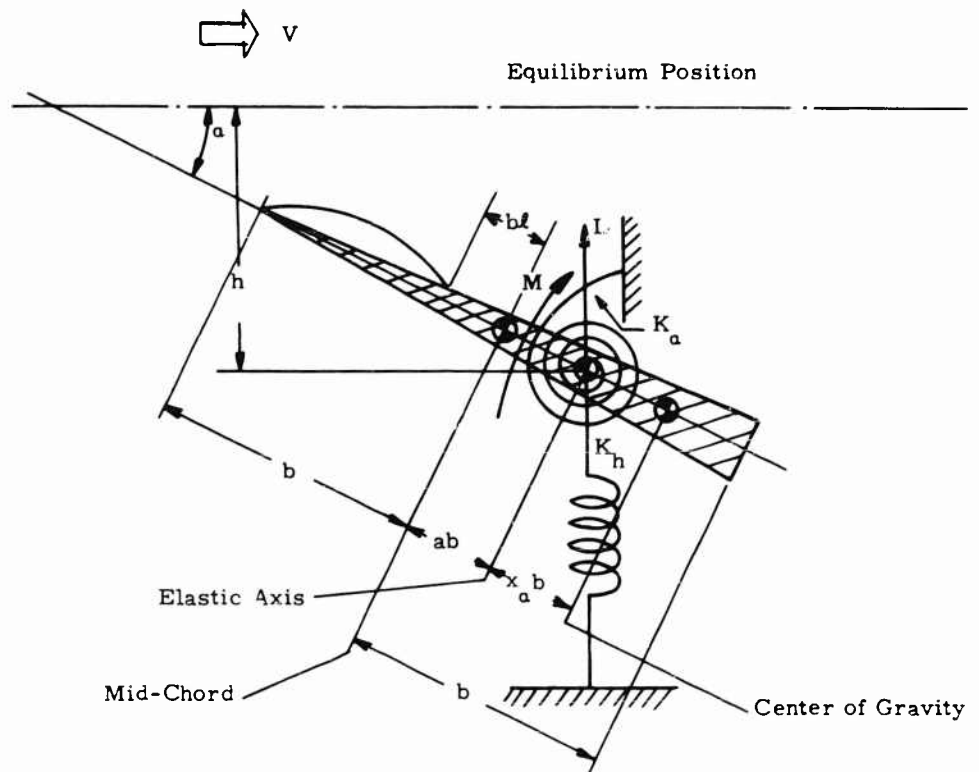
Fig. 4 - Partially cavitated hydrofoil elastically restrained in
translation and rotation, showing nomenclature

the problem including numerical results. The results of that study will be uti-
lized in the determination of the conditions for flutter. The results of [8] can be
arranged in a form that can be directly used in the hydroelastic analysis, where
the lift and moment per unit span at the leading edge are represented by

$$L_o = -\rho b V^2 \left[(f'_{ch} - i f'_{sh}) h_o e^{i\omega t} + (f'_{cp} - i f'_{sp}) \alpha_o e^{i\omega t} \right] \tag{3}$$

and

$$M_o = \rho b^2 V^2 \left[(m'_{ch} - i m'_{sh}) h_o e^{i\omega t} + (m'_{cp} - i m'_{sp}) \alpha_o e^{i\omega t} \right] \tag{4}$$

where

$$h = b h_o e^{i\omega t}, \quad \alpha = \alpha_o e^{i\omega t} \tag{5}$$

are the complex representations of the oscillatory motions in the translational
and rotational degrees of freedom. In Eqs. (3) and (4) the motion α is a rotation

780

of the foil about its mid-chord, and the results in [8] are obtained for that motion. The curves shown in [8] are the quantities denoted as f'_c, f'_s, m'_c, m'_s in the present study (the further subscripts, h or p, represent heave or pitch motion). These terms are functions of the reduced frequency $k = \omega b/V$, and also of α/σ, where α in this instance is the steady-state angle of attack reference condition.

In order to identify the various force and moment quantities in terms of familiar hydrodynamic force terms, a study was made of the form of the force and moment in fully-wetted flow [9] and also supercavitated flow [10]. As an example, the lift force in fully-wetted flow, for oscillations about the foil mid-chord, is represented by

$$L^{(w)} = -\rho b V^2 \left[(\pi k^2 + 2\pi kG) - i 2\pi kF \right] h_o e^{i\omega t}$$

$$-\rho b V^2 \left[(\pi kG - 2\pi F) - i(\pi k + \pi kF + 2\pi G) \right] \alpha_o e^{i\omega t} \tag{6}$$

where $F(k)$ and $G(k)$ are the real and imaginary parts of the complex Theodorsen function $C(k)$, which provides the modification of the forces due to unsteadiness. With this representation as a basis and as a typical example, some identification of the physical quantities associated with f'_{ch}, f'_{sh}, m'_{ch}, etc., for partially cavitated flow, can be made. The following is an outline of the component terms making up these various quantities:

a. f'_{ch} represents the added mass in plunging (heaving) motion, together with the quasi-steady lift force due to vertical velocity, suitably modified by a particular frequency-dependent function. The added mass portion is proportional to k^2 and is the predominant quantity at large values of k, while the remaining part is dependent on k in the form of k times the frequency-dependent modification factor (actually a component of a complex frequency factor, as shown in [9]).

b. f'_{sh} represents the quasi-steady lift due to plunging velocity (effective angle of attack), suitably modified by a frequency-dependent modification factor (this factor is also a function of α/σ, as are all the frequency-dependent factors herein, in the present problem). In the limit of low frequency, this term can be shown to approach the value kC_{L_α} where C_{L_α} is the steady lift rate shown in Fig. 2.

c. f'_{cp} is composed of a term representing the lift due to angle of attack, modified by a frequency-dependent factor; a small added mass term proportional to k^2; and a portion of the lift force due to angular velocity, which is modified by a frequency-dependent factor. In the limit of low frequency this term (i.e., f'_{cp}) can be shown to approach the value $-C_{L_\alpha}$, and hence it is simply related to the low frequency limit of f'_{sh}. This is due to the hydrodynamic equivalence of the flow pattern and resultant lift force arising from an angle of attack and the equivalent effect due to plunging, which gives a spatially uniform distribution of angle of attack.

d. f'_{sp} represents the lift due to angular velocity variations, suitably modified by a frequency-dependent factor; an inertial reaction proportional to angular velocity (probably without a frequency-dependent modification factor); and a portion of the lift due to angle of attack, with a frequency-dependent modification factor.

e. m'_{ch} represents the moment due to the added mass force in plunging motion, together with a portion of the moment due to the vertical velocity which is modified by a frequency-dependent factor. The added mass portion varies as k^2, while the remaining part varies as k times the frequency-dependent factor.

f. m'_{sh} represents the moment due to plunging velocity, modified by a frequency-dependent factor. In the limit of low frequency, this term can be shown to approach the value $(1 + d^*)kC_{L_\alpha} + kC_L d_2^*$, which is simply related to the moment due to steady angle of attack.

g. m'_{cp} is composed of a term representing the moment due to angle of attack, modified by a frequency-dependent factor; an added mass moment proportional to k^2; and a portion of the moment due to angular velocity, which is modified by a frequency-dependent factor. In the limit of low frequency this term can be shown to approach the value $-(1 - d^*)C_{L_\alpha} - C_L d_2^*$, and hence is related to the low frequency limit of m'_{sh}.

h. m'_{sp} is composed of the moment due to angular velocity, modified by a frequency-dependent factor; an inertial moment proportional to angular velocity (probably without a frequency-dependent factor); and a portion of the moment due to angle of attack, with a frequency-dependent modification factor.

The particular frequency-dependent factors are not explicitly represented in the results of [8], but certain judgment can be made as to the limiting values of the different aspects of this frequency factor for low frequencies. Since, as $k \to 0$, the results should be appropriate to quasi-steady values, the different portions of the frequency modification factors can be shown to approach values of 1.0 and 0, depending upon the particular quantity which it modifies. Some discussion of the application of these ideas for analyses appropriate to the limiting condition where $k \to 0$, i.e., for determination of the critical density ratio, will be presented in a later section. Similarly, an outline of further hydrodynamic studies which will lead to representations of the forces and moments in a form that separates the contributions of quasi-steady flow, unsteady flow modifications, inertial effects, etc., will also be presented. These results will allow physical interpretation and identification of the component terms, for both the quasi-steady and unsteady cases, and will aid in interpretation of the major effects that influence the flutter phenomena.

EQUATIONS OF MOTION AND STABILITY ANALYSIS

For the analysis herein the hydrofoil itself is assumed to be rigid but supported elastically in two degrees of freedom. These degrees of freedom, as described previously, are translation normal to the free stream velocity and rotation about an axis, normal to the plane of flow, which is known as the elastic axis. The elastic axis is located at a prescribed position along the foil and the location of the center of gravity and mid-chord position relative to it are defined by certain specific length parameters. An illustration of these various geometrical parameters is shown in Fig. 4, which is the same (except for the particular extent of cavitation) as that used in the investigation of bending-torsion flutter and torsional divergence of rigid foil sections in previous hydroelastic studies.

782

The equations of motion for this system are

$$m\ddot{h} + S_{a}\ddot{a} + K_{h}h = -L \tag{7}$$

and

$$I_{a}\ddot{a} + S_{a}\ddot{h} + K_{a}a = M \tag{8}$$

where

m = mass of hydrofoil section per unit span

S_{a} = first moment of mass per unit span of hydrofoil section about elastic axis

I_{a} = mass polar moment of inertia per unit span of hydrofoil section about elastic axis

K_{h}, K_{a} = spring constants in bending and torsion, respectively

L, M = lift and moment per unit span at elastic axis.

The expressions for L and M in Eqs. (7) and (8) are determined by transforming the results in Eqs. (3) and (4) in order to allow them to be applicable to a reference position at the elastic axis. The results, obtained by transforming in terms of the effective foil displacements relative to the elastic axis position, are given by

$$L = -\rho b V^2 e^{i\omega t} \left\{ (f'_{ch} - i f'_{sh}) h_o - \left[(f'_{cp} - i f'_{sp}) - a(f'_{ch} - i f'_{sh}) \right] a_o \right\} \tag{9}$$

$$M = \rho b^2 V^2 e^{i\omega t} \left\{ \left[(m'_{ch} - i m'_{sh}) - (a-1)(f'_{ch} - i f'_{sh}) \right] h_o \right.$$

$$- \left[(m'_{cp} - i m'_{sp}) - (a-1)(f'_{cp} - i f'_{sp}) - a(m'_{ch} - i m'_{sh}) \right.$$

$$\left. - a(a-1)(f'_{ch} - i f'_{sh}) \right] a_o \right\} \tag{10}$$

for the case where the translational and rotational motions are oscillatory, as in Eq. (5).

The equations of motion given by Eqs. (7) and (8) represent a description of the motions which are departures from the equilibrium position, and the stability of these perturbation displacements is directly determined from the equations. In determining the conditions for divergence, which is a static instability, there are no oscillations (i.e., $\omega = 0$) and also no time-derivative terms appear in the equations of motion. The static instability occurs when the increase in the hydrodynamic moment due to an angular change arising from a structural deformation is greater than the increase in the elastic restoring moment. Hence the equation of concern for studying divergence is the reduced form of Eq. (8), viz.

$$K_{a}a = M = \rho b^2 V^2 (a - d^*) C_L(a). \tag{11}$$

783

This is the simplified approach to the divergence problem and circumvents the necessity of carrying out limiting operations on the various components of the hydrodynamic force and moment. The equation is appropriate to the equilibrium condition as well as when an arbitrary perturbation is considered. With the angle α represented by $\alpha = \alpha_e + \Delta\alpha$, where α_e is the equilibrium value and $\Delta\alpha$ the perturbation, the equation then becomes

$$K_\alpha \left[\alpha_e + \Delta\alpha\right] = M(\alpha_e) + \frac{dM}{d\alpha} \times \Delta\alpha ,\tag{12}$$

where

$$\frac{dM}{d\alpha} = \rho b^2 V^2 \left[(a - d^*)C_{L_\alpha} - C_L d_\alpha^*\right] ,\tag{13}$$

and after subtracting the equilibrium conditions, the resulting equation is

$$K_\alpha \Delta\alpha = \rho b^2 V^2 \left[(a - d^*)C_{L_\alpha} - C_L d_\alpha^*\right] \Delta\alpha .\tag{14}$$

This condition represents the precise balance between the hydrodynamic moment due to an angle of twist and the elastic restoring moment, yielding the particular speed for equilibrium, known as the critical divergence speed. Speeds greater than this value will result in divergence for the foil. Using the definitions

$\mu = m/\pi\rho b^2$ = density ratio

$r_\alpha^2 = I_\alpha/mb^2$ = dimensionless radius of gyration about elastic axis

$\omega_\alpha^2 = K_\alpha/I_\alpha$ = uncoupled rotational natural frequency

Eq. (14) may be rearranged to the form given by

$$\frac{V}{b\omega_\alpha} = \sqrt{\frac{\pi\mu r_\alpha^2}{(a - d^*)C_{L_\alpha} - C_L d_\alpha^*}}\tag{15}$$

which defines the critical divergence speed.

It can be seen, from examination of Eq. (15), that the divergence speeds for the case of partially cavitated foils are usually lower than for fully-wetted foils (for the same elastic and inertial characteristics) as long as the partial cavity length is not too long, since the lift rate C_{L_α} is larger for partially cavitated foils and the quantity d_α^* is negative until the cavity length extends up to about half the chord length. As an illustration of these results, divergence speeds are shown in Figs. 5 and 6 for partially cavitated foils and compared with the results for fully-wetted foils. The results exhibited are appropriate to a condition with a small partial cavity $[(1 - \ell)/2 = .25]$ in Fig. 5 and for a larger partial cavity $[(1 - \ell)/2 = .625]$ in Fig. 6. Analysis shows, for the partially cavitated case $[(1 - \ell)/2 = .625]$ of Fig. 6, that no divergence can occur for $a < -.17$, i.e., as the elastic axis moves further forward of the mid-chord position. Results for the condition where the cavity extends up to the 3/4 chord point on the foil can be
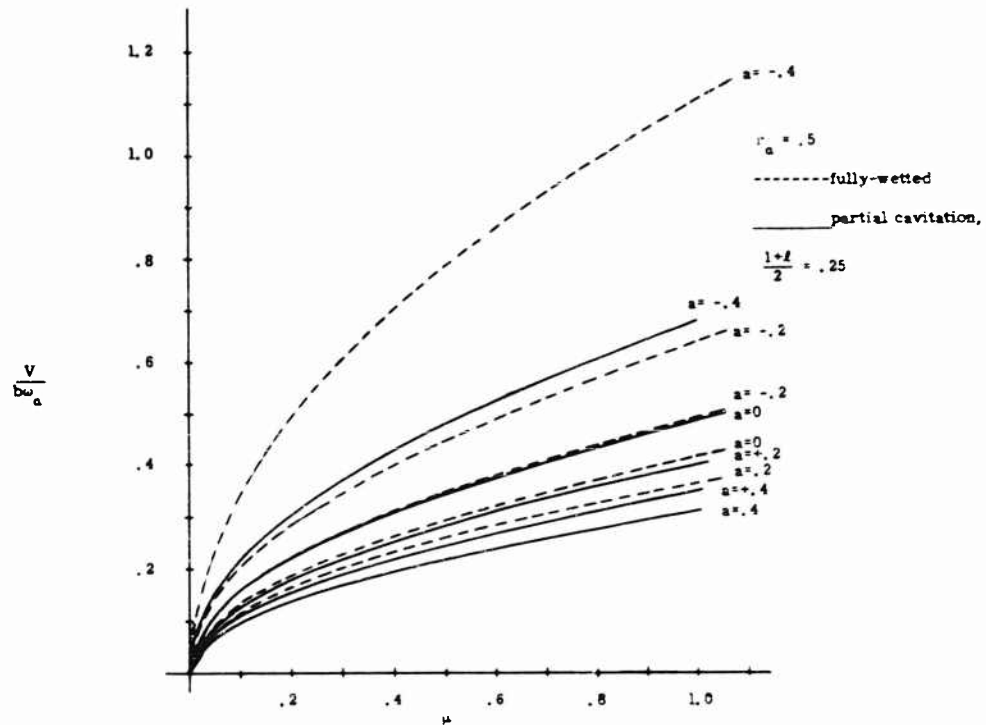
Fig. 5 - Variation of divergence boundary with elastic axis location,
comparing results for fully-wetted and partially cavitated flow

shown to indicate that divergence speed is effectively 0 (theoretically), since the
denominator of Eq. (15) approaches ∞, except for one particular value of the quan-
tity a that determines the elastic axis location. In actual practice such results
will not occur, but they add further emphasis to point out the general flow insta-
bility associated with conditions for cavity lengths extending up to this point and
slightly beyond.

One other important factor with regard to divergence, for the present case
of partially cavitated hydrofoils, is the fact that as the foil increases its angle of
attack due to the "overriding" of the elastic restoring effect, the phenomenon is
accelerated (up to a point) since the lift rate C_{L_α} and the term $-d_i^*$ increase as
α/σ increases. All of these results are appropriate to a flat plate foil since no
computations have been made to include camber effects. If the foil itself is not
completely rigid, but can also undergo chordwise bending, then additional effects
enter since the force and moment differ in that case. The foil will then have
some effective camber, determined from the deflection shape, and hence a new
lift and moment distribution are determined. This in turn determines a new
angle and lift distribution, etc. The obvious behavior of the static hydroelastic
problem as a feedback system is shown by this description, and a process of
successive approximation would be necessary in order to determine the variation
of the stability characteristics associated with these effects. This is rather a

785
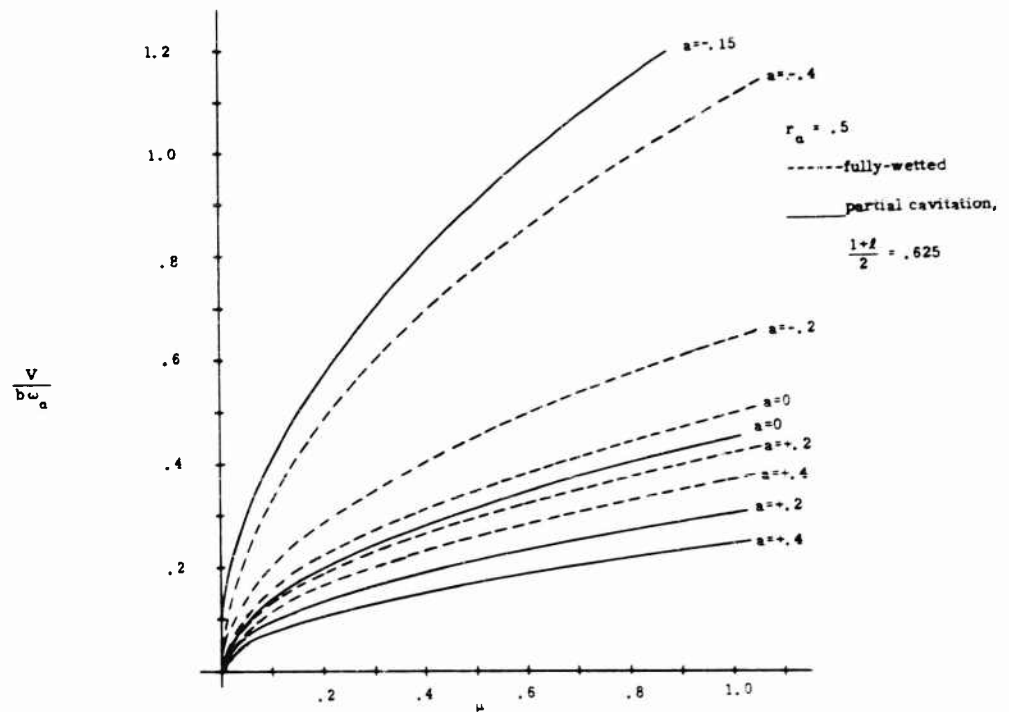
Fig. 6 - Variation of divergence boundary with elastic axis location,
comparing results for fully-wetted and partially cavitated flow

complicated problem, and extends beyond the scope of the present exploratory
study. Nevertheless, for practical purposes of estimation, these effects may be
ignored and the first approximation for critical divergence speeds can be ob-
tained by the simple techniques outlined above.

For the case where dynamic effects are included. the stability of the system
is determined by analyzing the basic equations of motion to determine the condi-
tions under which the perturbation displacements are purely oscillatory. The
conditions under which this occurs are the boundaries of stability, i.e.. they rep-
resent neutral stability. The means of determination of these conditions are
presented below.

The equations of motion are nondimensionalized by dividing Eq. (7) by
$-\pi b^3 \omega^2$ and Eq. (8) by $-\pi b^4 \omega^2$, and cancelling the complex exponential $e^{i\omega t}$ in each
term of the equations. Using the definitions given in the paragraph following Eq.
(14), and also the definitions

$x_a = S_a / mb$ = dimensionless distance between elastic axis and center of
gravity in half-chord lengths, positive when center of gravity
is aft.

$\omega_h^2 = K_h / m$ = uncoupled translational natural frequency.

786

the equations of motion are then represented in the form

$$
h_o \left\{ \mu \left[1 - (1 + ig) \left(\frac{\omega_h}{\omega_a} \right)^2 \left(\frac{\omega_a}{\omega} \right)^2 \right] - \frac{1}{\pi k^2} \left(f'_{ch} - if'_{sh} \right) \right\}
$$

$$
+ \alpha_o \left\{ \mu x_a - \frac{1}{\pi k^2} \left[(f'_{cp} - if'_{sp}) - a(f'_{ch} - if'_{sh}) \right] \right\} = 0 \tag{16}
$$

and

$$
h_o \left\{ \mu x_a - \frac{1}{\pi k^2} \left[(m'_{ch} - im'_{sh}) - (a - 1)(f'_{ch} - if'_{sh}) \right] \right\}
$$

$$
+ \alpha_o \left\{ \mu r_a^2 \left[1 - (1 + ig) \left(\frac{\omega_a}{\omega} \right)^2 \right] - \frac{1}{\pi k^2} (m'_{cp} - im'_{sp}) - \frac{a(a-1)}{\pi k^2} (f'_{ch} - if'_{sh}) \right.
$$

$$
\left. - \frac{(a-1)}{\pi k^2} (f'_{cp} - if'_{sp}) - \frac{a}{\pi k^2} (m'_{ch} - im'_{sh}) \right\} = 0 \tag{17}
$$

A damping force given by

$$
-im \omega_h^2 gh_o
$$

and a damping moment given by

$$
-iI_a \omega_a^2 g\alpha_o
$$

have been included in the equations in order to represent the effect of structural damping. These terms are proportional to the oscillatory amplitude and stiffness of the respective modes of motion, and the dimensionless proportionality factor is the damping coefficient. g. which is assumed equal for both translation and rotation.

Eqs. (16) and (17) obtained above are simultaneous linear homogenous equations with two unknowns, h_o and α_o. A nontrivial solution exists if, and only if, the determinant of the coefficients of the unknowns is zero. The resulting determinantal equation which must be satisfied for the existence of a solution to the equation of motion is then

787

$$\left| \begin{array}{cc} \left\{ \mu \left[1 - \left(\frac{\omega_h}{\omega_a}\right)^2 \left(\frac{\omega_a}{\omega}\right)^2 \right] + \frac{f'_{ch}}{\pi k^2} \right. & \left. \mu x_a + \frac{1}{\pi k^2} \left[m'_{ch} - a f'_{ch} \right] \right\} \\ \left. -i \left[\mu g \left(\frac{\omega_h}{\omega_a}\right)^2 \left(\frac{\omega_a}{\omega}\right)^2 + \frac{f'_{sh}}{\pi k^2} \right] \right\} & \left\{ -\frac{i}{\pi k^2} \left[m'_{sh} - a f'_{sh} \right] \right\} \\ & \\ \left\{ \mu x_a + \frac{1}{\pi k^2} \left[m'_{ch} - (a+1) f'_{ch} \right] \right. & \left\{ \mu r_a^2 \left[1 - \left(\frac{\omega_a}{\omega}\right)^2 \right] + \frac{1}{\pi k^2} \left[m'_{cp} - (a+1) f'_{cp} \right. \right. \\ \left. -\frac{i}{\pi k^2} \left[m'_{sh} - (a+1) f'_{sh} \right] \right\} & - a m'_{ch} + a(a+1) f'_{ch} \Big] \\ & \\ & \left. -\frac{i}{\pi k^2} \left[m'_{sp} - (a+1) f'_{sp} - a m'_{sh} + a(a+1) f'_{sh} \right] \right\} \end{array} \right| = 0$$

(18)

Since the terms in these equations are complex, two sets of equations must be satisfied; one for the real part and one for the imaginary part. The solutions that satisfy this determinantal equation define a neutrally stable motion, to which a particular forward speed is associated. If the speed is less than this critical value the perturbed motion will be convergent (and hence stable), and if the speed is greater than critical the perturbed motion will diverge (unstable). The boundaries between stable and unstable conditions are defined by the solutions of the determinantal Eq. (18), which are the flutter stability boundaries.

The flutter conditions are found from Eq. (18) by setting the damping coefficient $g = 0$ and applying the density variation method [11]. The two equations resulting from expanding the determinant are combined in order to determine the two unknowns, which are the density ratio μ and the frequency ratio ω_a/ω. A quadratic equation is obtained for the quantity $(\omega_a/\omega)^2$, and the quantity μ is determined in terms of the values of $(\omega_a/\omega)^2$ found from the other equation. The only physically meaningful results are those where ω_a/ω and μ are both real and positive. Solutions are obtained at selected values of the reduced frequency k, and a curve of reduced flutter speed $V/b\omega_a$ versus density ratio is obtained from these solutions by means of the relation

$$\frac{V}{b\omega_a} = \frac{1}{k\left(\frac{\omega_a}{\omega}\right)} \cdot$$

(19)

The results of applying this method of solution are shown in Figs. 7 through 12, where the variation of the flutter stability boundaries with cavitation number, elastic axis location, center of gravity location, radius of gyration, and natural frequency ratios are presented.

The results of previous hydroelastic analyses, as well as the appearance of the flutter stability boundaries for the present problem, show that the flutter

$a = .2$

$a = .4$ $a = 0$

$$\frac{1+\ell}{2} = .375$$

$$x_a = .3$$

$$r_a = .3 -----$$

$$r_a = .5 \underline{}$$

$$\frac{\omega_h}{\omega_a} = 0$$

$\dfrac{V}{b\omega_a}$

μ
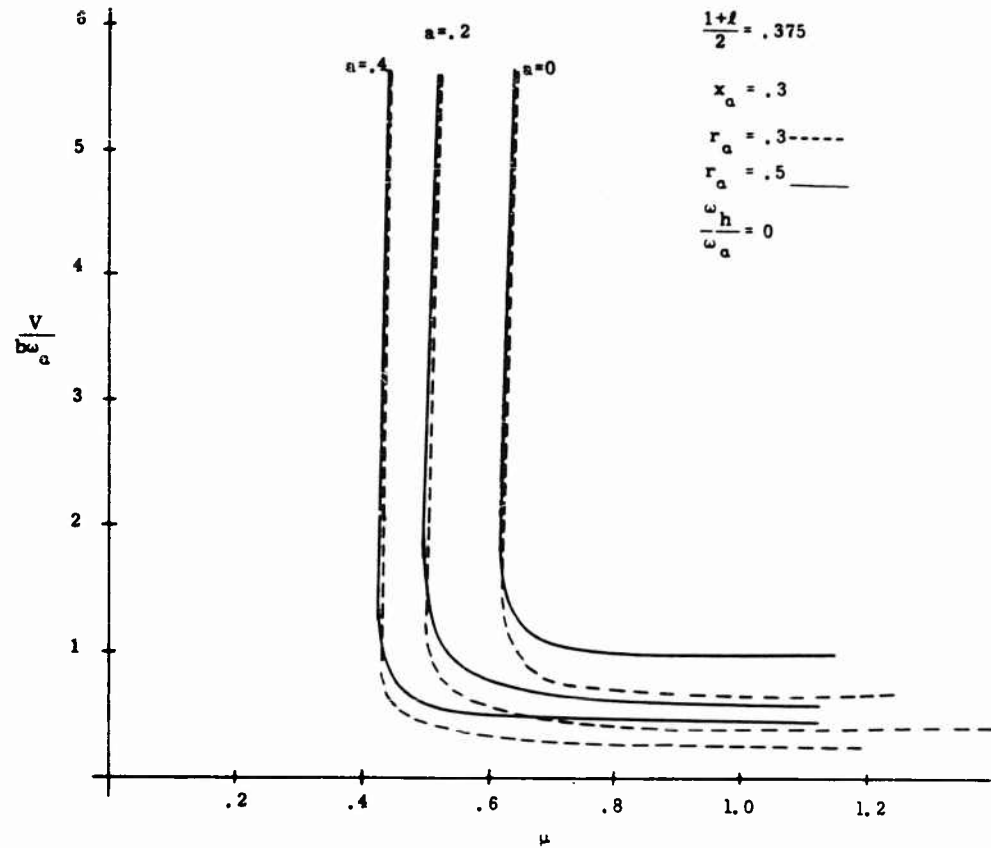
Fig. 7 - Variation of flutter boundary with radius of gyration and
elastic axis location

speed ratio becomes asymptotically infinite at a low value of density ratio.
Along this branch, as $V/b\omega_a \to \infty$, the value of $k \to 0$. The critical μ at which the
asymptote develops can be predicted theoretically, since some of the limiting
values of the hydrodynamic force and moment components as $k \to 0$ are known.
The various frequency-dependent modification factors approach 1 and 0 for the
different hydrodynamic components. Some measure of the behavior of the force
and moment coefficients in the limit as $k \to 0$ is given by the following:

$$f'_{ch} = 0(k^2)$$

$$f'_{sh} = kC_{L_a} = 0(k)$$

$$f'_{cp} = -C_{L_a} = 0(1)$$

$$f'_{sp} = 0(k)$$

$$(20)$$
$$\text{(Cont.)}$$

789
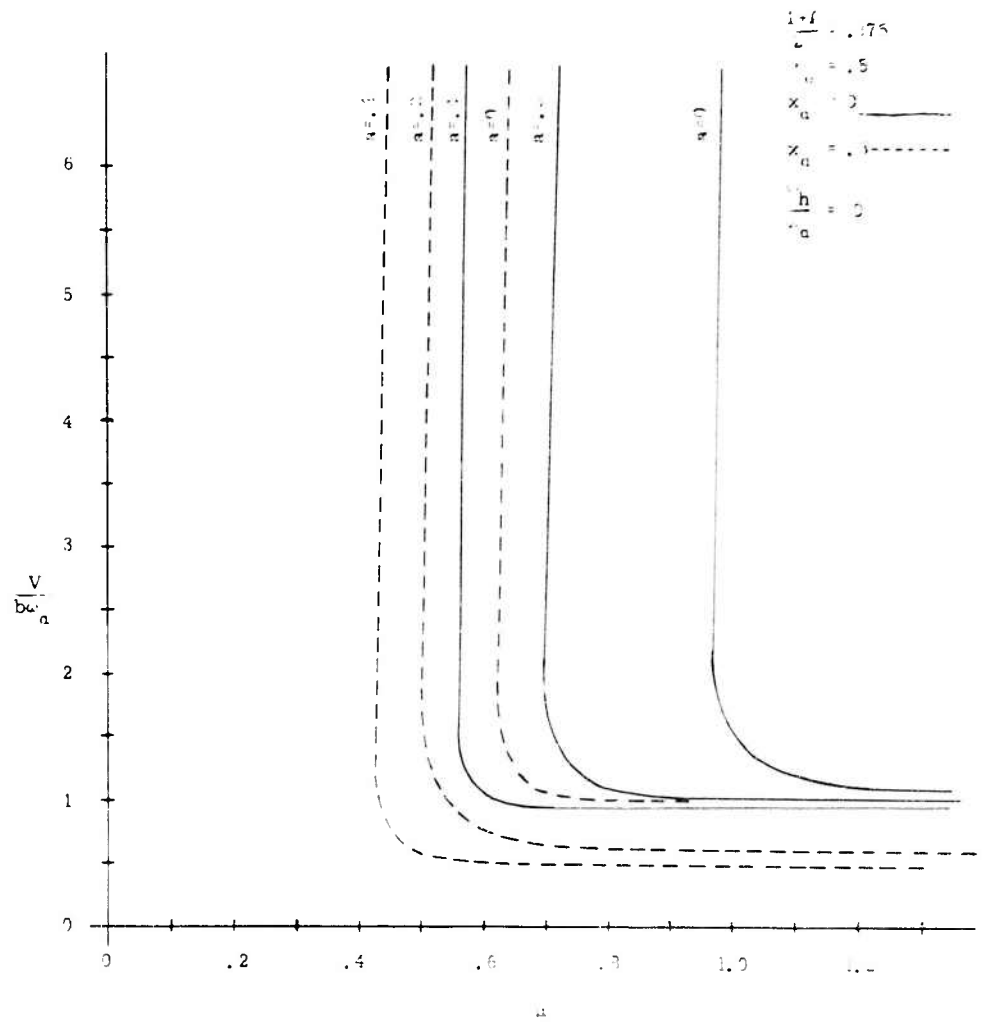
Fig. 8 - Variation of flutter boundaries with center of gravity location
and elastic axis location
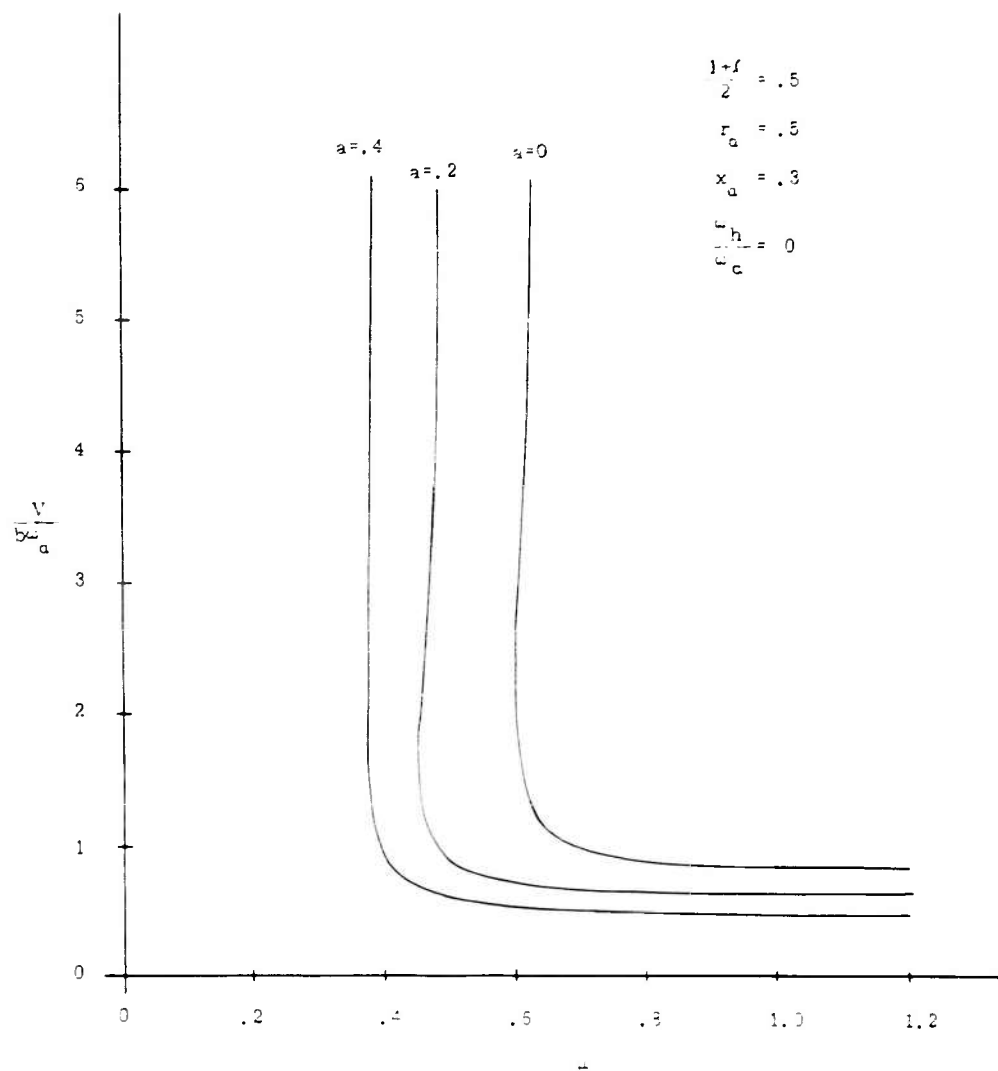
Fig. 9 - Representative flutter boundary variation for a
larger cavity length.
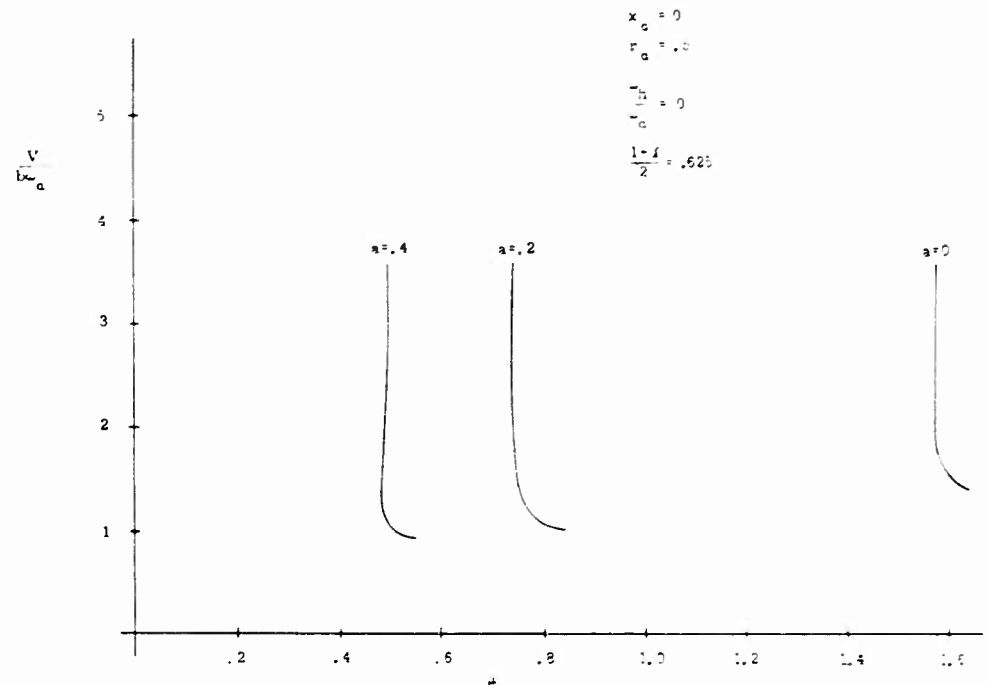
Fig. 10 - Flutter boundaries for greater extent of cavitation, illustrating the effects of center of gravity location

$$m'_{ch} = 0(k^2)$$

$$m'_{sh} = k(1 - d^x) C_{L_z} - kC_L d_z^x = 0(k)$$

$$m'_{cp} = -(1 - d^x) C_{L_z} - C_L d_z^x = 0(1)$$

$$m'_{sp} = 0(k)$$

(20)

The precise form of these relations really requires a determination of the analytical expressions for f'_{ch}, f'_{sp}, m'_{ch}, and m'_{sp} in the quasi-steady sense, including the associated inertial contributions. A technique for determining these quantities for application to the analysis appropriate to $k \to 0$ will be outlined in another section of this paper, but the present results are indicative of the expected overall behavior.

Using the general relations given by Eq. (20) in the determinant of Eq. (18), and collecting the terms of $0(1, k^2)$, the limiting value of the critical $\_$ (when $m_h m_z = \varepsilon = 0$) is obtained in the form

$$\_{cr} = \lim_{k \to 0} \frac{m'_{ch} f'_{cp} - f'_{ch} m'_{cp} - f'_{sh} m'_{sp} - m'_{sh} f'_{sp}}{-k^2 \left[m'_{cp} - (1 - a - x_z) f'_{cp} \right]}$$

(21)

792
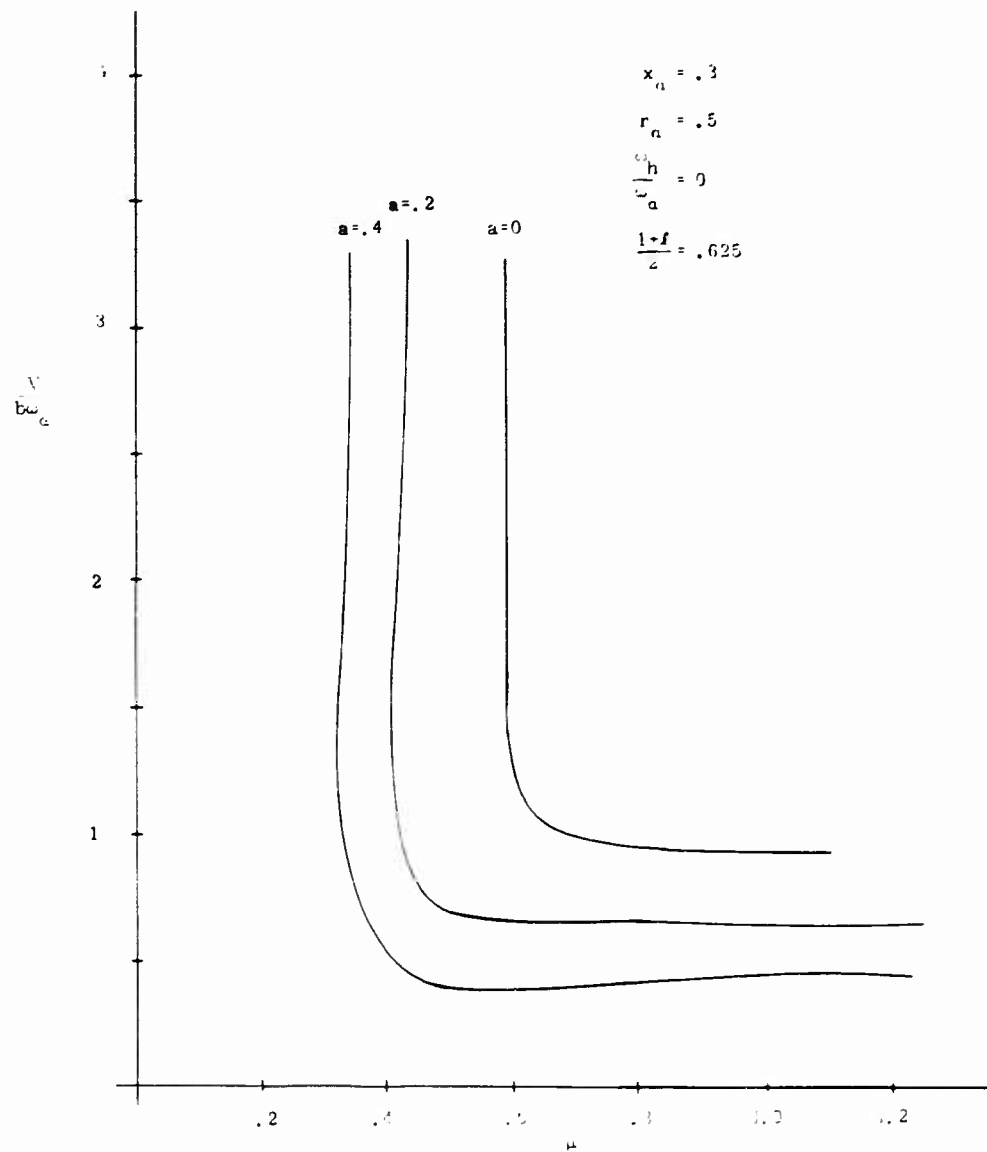
Fig. 11 - Flutter boundaries for greater extent of cavitation, and illustrating the effects of center of gravity location and elastic axis location
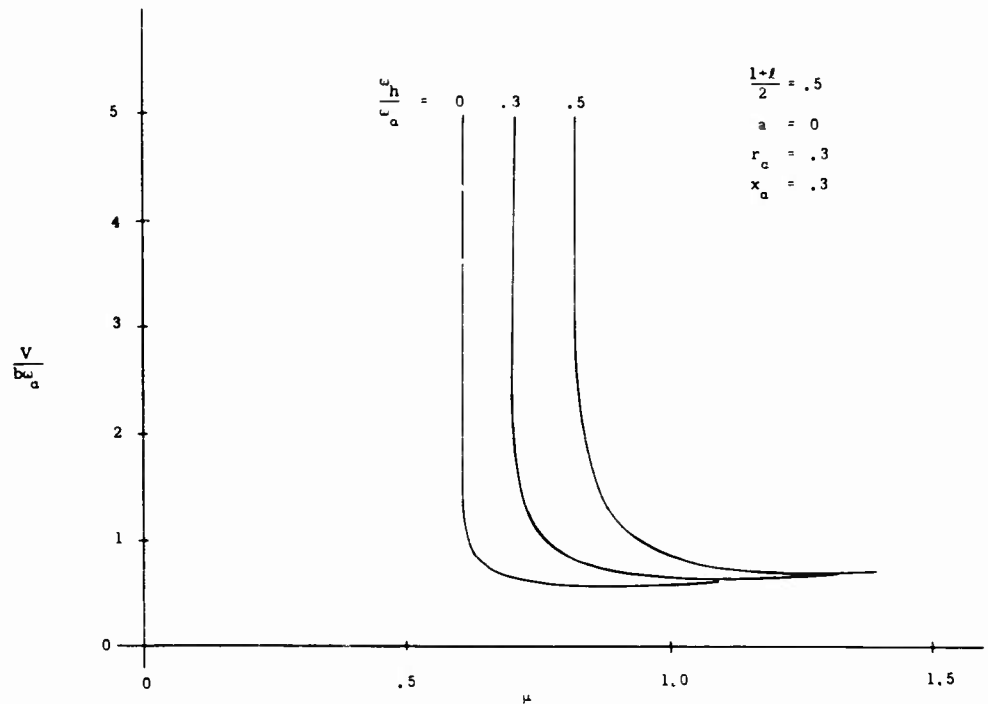
Fig. 12 - Variation of flutter boundaries with natural frequency ratios

No numerical values can be obtained from this result since the explicit forms of some of the hydrodynamic coefficients for this limit case are not precisely known.

DISCUSSION OF RESULTS

In discussing the results of the analysis, it is necessary to bear in mind that these statements apply to foils that are designed for either supercavitating or fully-wetted operation. but which encounter partial cavitating flow conditions. The statements are concerned with the flutter and divergence characteristics of partially cavitated foils. but the foil physical characteristics are those appropriate to the originally intended flow condition. i.e.. either supercavitated or fully-wetted. Emphasis in the present paper is devoted to the supercavitated foil design. since that is the situation which will certainly experience partial cavitation during its operational history. and also because the trend toward higher speed hydrofoil craft will necessitate supercavitating foils.

The application of the theoretical results described in the previous section is illustrated by the curves exhibited in Figs. 5 and 6 for the case of divergence. and in Figs. 7 through 12 for the case of flutter. The range of physical characteristics appropriate to supercavitating hydrofoil sections has been described

previously in [3], and some of the conditions chosen in the present figures were selected to fit within those appropriate ranges. Differences in values of the various geometric and inertial parameters have been selected in order to exhibit the variations in the stability boundaries with changes in these parameters.

Figures 7 and 8 illustrate the effects of changes in radius of gyration, center of gravity position, and elastic axis location on the flutter boundary while similar information with regard to divergence is given in Figs. 5 and 6. The results show that an increase in the radius of gyration results in an increase in the flutter speed ratio, without much change in the value of the critical density ratio. Similarly, an increase in the radius of gyration also increases the divergence speed. Hence a larger value of the radius of gyration decreases the chance of occurrence of both flutter and divergence.

An increase in x_a, i.e., moving the center of gravity aft relative to the elastic axis, results in a lower value of the critical density ratio and also a lower flutter speed. Thus the center of gravity should be as far forward as possible relative to the elastic axis in order to prevent flutter.

An increase in the quantity a, i.e., moving the elastic axis further back from the mid-chord position, leads to a decrease in the value of the critical density ratio, and also a decrease in the flutter speed. Also, an increase in a results in lower divergence speed. Thus a forward elastic axis position decreased the possibility of both flutter and divergence.

Figure 12 illustrates the effect of increasing the ratios of the natural frequencies and it is shown there that an increase in ω_h/ω_a results in a shift in the critical density ratio to higher values.

The results described above as to the effect of changes in the radius of gyration, center of gravity position, elastic axis location, and natural frequency ratio are the same as those obtained in previous studies of hydroelastic instabilities where the flow was fully-wetted [1, 2] or supercavitating [3]. Thus it appears that the same results occur for variations in these geometric and inertial properties whether the flow about the foil is fully-wetted, supercavitated or partially cavitated. Some modification of this latter statement is possible in the case of partial cavitation since the conclusions are only valid up to a certain cavity length, less than the length of the foil chord.

Figures 9, 10 and 11 illustrate the behavior of the flutter boundaries for a larger cavity length than has been considered up to this time in the data presented through Fig. 8. Figure 9 shows the flutter boundary variation for the case where the cavity length extends up to $1/2$ the chord length from the leading edge. Comparison with the results in Figs. 7 and 8 show that there is a tendency toward lower values of the critical density ratio. Similarly, Figs. 10 and 11 exhibit flutter boundaries for larger cavity length conditions, viz., a cavity length of $5/8$ of the chord length, and a shift toward still lower values of the critical density ratio is shown. A trend toward smaller values of flutter speed, all other conditions remaining constant, is seen as the cavity length increases. Results for the case where the cavity length extends up to $3/4$ of the chord length have not been given because of the steady state conditions that indicate infinite

795
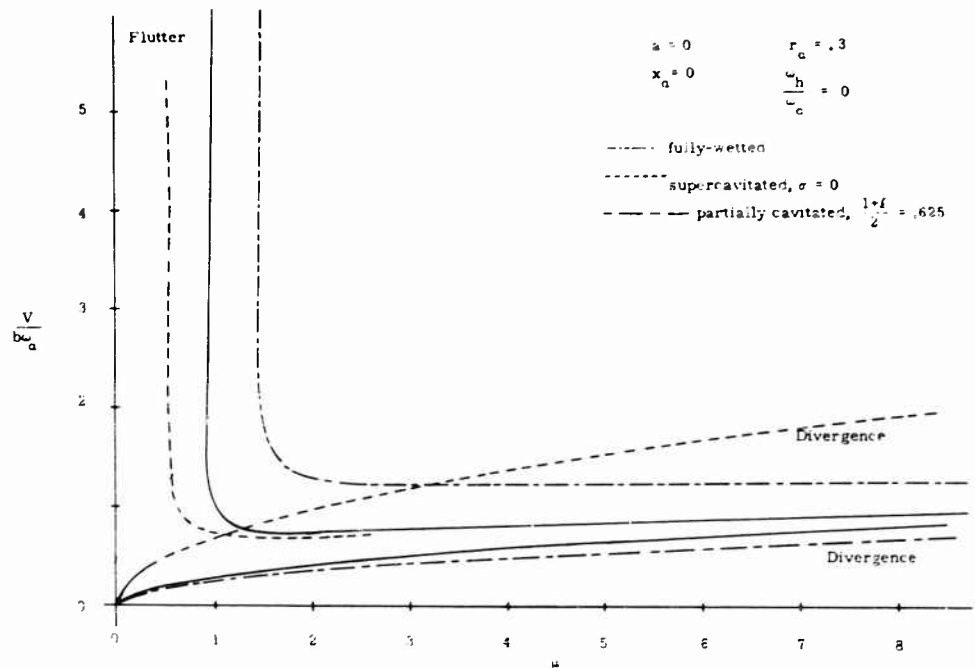
Fig. 13 - Comparison of fully-wetted, partially-cavitated, and super-
cavitating stability boundaries for foils with identical elastic
and inertial properties

behavior in that region. Conditions for flows with cavity length greater than that
length show a flow instability, which caused vibration even when a model was
tested in steady state in a water tunnel [5].

The curves in Fig. 13 compare the different stability boundaries for foils
with identical inertial properties, but with different flow conditions. Unfortu-
nately, the example chosen for illustration is a poor one in that it does not show
much danger for the case of partial cavitation in regard to flutter, but it cer-
tainly points out the difference in regard to the possibilities of failure due to
divergence. This is a definite condition that should be guarded against during
the early stages of design.

The results obtained herein for the case of partially cavitated hydrofoils are
only as valid as the hydrodynamic information available as the input for this
study. Attention should be directed toward proper determination of the hydro-
dynamic reactions on partially cavitated hydrofoils with particular concern for
the region of low reduced frequency. This region is important since it is the re-
duced frequency range where the flutter eigen values were determined. Only a
limited amount of information on the behavior of the hydrodynamic forces in this
range was available and perhaps a quasi-steady analysis method would be ap-
propriate to this particular flow regime. An outline of further theoretical

796

hydrodynamic studies which should be carried out in order to provide a basis for continuing the theoretical work of prediction of flutter is described in the next section.

FURTHER HYDRODYNAMIC STUDIES

As mentioned above, the results of [8] are cast in a numerical form with no separation of the contributions of damping, added mass, unsteadiness, etc. Also the hydrodynamic information presently available for the low-k behavior of the forces and moments is insufficient to determine the critical density ratio, as represented in Eq. (21). It is possible to carry out a hydrodynamic analysis to determine this information, and it will be shown that this only requires proper application of the results of [4] and the extended study [6] based upon it. The quantity f'_{ch}, in the limit as $k \to 0$ (for application to the determination of μ_{cr}), is proportional to the added mass of the partially cavitated foil, and this can be obtained by a simple extension of the results of Geurst [4] for the steady state problem. Expressions are found in [4] for the distribution of the horizontal perturbation velocity on the foil, and this quantity can also be related to the time-dependent pressure component for unsteady motion (see the analysis in [12], where the relation between integrals of the impulsive pressure and integrals of the longitudinal velocity perturbation is exhibited). Thus, if the vertical velocity distribution on the foil is proportional to $\dot{h}$, resulting in the longitudinal perturbation velocity being proportional to h, the added mass force required for f'_{ch} may be determined from the following relation:

$$f'_{ch} \sim \frac{d}{dt} \int_{-1}^{1} (u^+ - u^-)\, x\, dx = \frac{d}{dt}\, \mathrm{Re} \oint wz\, dz \tag{22}$$

where w is the complex perturbation velocity and $z = x + iy$ is the complex variable in the physical plane.

The information presented in [4] is directly applicable to determine this quantity, and in fact, it is found that f'_{ch} is proportional to the moment coefficient C_M determined there. Similarly, the value of m'_{ch}, which may be interpreted for the present application as the moment due to added mass, is also of inertial nature and it can be determined in a similar manner, where it will be necessary to find, as one of the constituent terms, the value of

$$\frac{d}{dt} \int_{-1}^{1} (u^+ - u^-)\, x^2\, dx = \frac{d}{dt}\, \mathrm{Re} \oint wz^2\, dz \tag{23}$$

The procedure followed in [6] will have to be applied to determine this quantity, and it is then necessary to carry out the expansion of the complex velocity perturbation to the next order term (i.e., up to terms of $O(1\ z^3)$).

The term f'_{sp} contains two contributions of the same form, one of which is determined as a quasi-steady force while the other arises from inertial considerations. The inertial term follows in the same manner as given in Eq. (20) above, using the vertical velocity along the foil proportional to z. This results

797

in a term proportional to $\ddot{a}$ which is the required result. The quasi-steady contribution arises from consideration of the vertical velocity along the foil to be proportional to the distance from the leading edge, which is then a linear function of the variable x in the physical plane (i.e., it is of the form $(x + 1)\dot{a}$). The lift force for this distribution of vertical velocity can be obtained by adapting an answer derived for the case of a cambered foil by Geurst [6], where the vertical velocity distribution along the foil was of this particular form. The computations will have to be carried out for that case, recognizing the equivalence of the term in $\dot{a}$ to the camber ratio in that particular study. Similar procedures may be utilized to determine the two components (i.e., inertial and quasi-steady) for the determination of m'_{sp}, and all of the available information needed for that case is also provided by the analytical results in [6] and [12].

While the information on the limiting behavior for the quasi-steady and inertial components of the hydrodynamic forces and moments are of interest, and are also of practical consequence for determining μ_{cr}, it is still required to have a complete unsteady representation of the hydrodynamic forces and moments for analysis of flutter stability conditions. The results given in [8] provide this information numerically, but do not give any information on the nature of the frequency-dependent modification functions. As an example, the representation of lift and moment for oscillating fully-wetted foils, as given in terms of the Theodorsen function [9] with an imposed complex exponential form for the oscillatory motions, allows a simple interpretation of the amplitude and phase modifications brought about by the real and imaginary parts of the Theodorsen function. Similar results are expressed for supercavitating hydrofoils (for $\sigma = 0$), and the form of the complex frequency response function shows the range of frequencies in which important modifications take place. No such function (or functions) are provided by the results of [8], and hence there is no means of determining the modifying effects of unsteadiness, per se. In an effort to obtain the solutions in this form, an alternate method was formulated and is presented in the following discussion. The technique is essentially an application of the Riemman-Hilbert problem for a half-plane, after carrying out a simple auxiliary mapping. The method follows that of Geurst [4] in some aspects, but applied to the unsteady problem. The outline of the analytical procedure to be used for this case is given by the following:

Only the unsteady problem is considered herein, and the boundary conditions in the physical plane are represented by the sketch below

798
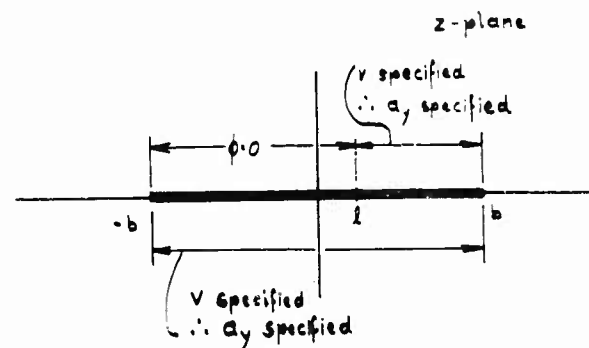
where $F(z) = \phi + i\psi$ is the complex acceleration potential. This plane is mapped to an auxiliary plane by

$$z' = b\sqrt{\frac{b-z}{b+z}}$$

which maps the boundary conditions to the lower half-plane, as shown below
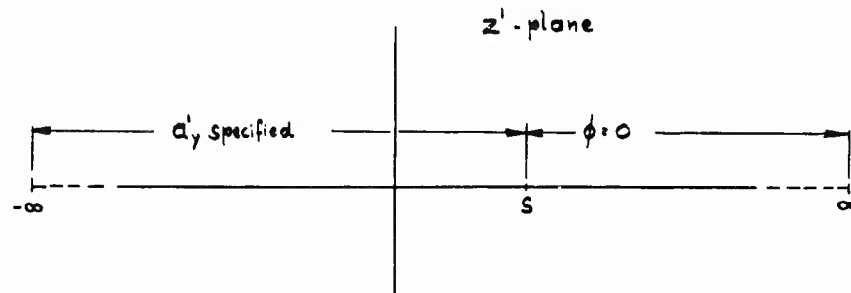
where $s = b\sqrt{\frac{b-\lambda}{b+\lambda}}$

This mixed boundary value problem for ϕ is solved by choosing an appropriate Green's function, which leads to a representation given by:

$$\phi(x',y') = -\frac{1}{2\pi}\frac{\partial}{\partial y'}\int_{-\infty}^{s}\phi(\xi,0)\log\left[(\xi-x')^2 - y'^2\right]d\xi \tag{24}$$

After differentiating with respect to y', applying the definition of the two-dimensional Laplace equation, integrating with respect to x', and then approaching the real axis by allowing $y' \to 0$, there results the singular integral equation

$$c - \int_{-\infty}^{x'}a_y'(t)dt = -\frac{1}{\pi}\int_{-\infty}^{s}\frac{\phi(\xi)}{\xi-x'}d\xi \tag{25}$$

for $\phi(x')$ along the real axis. Rather than solve this particular problem, a different method is utilized, resulting in the equation

$$\psi(x') = \frac{1}{\pi}\int_{-\infty}^{s}\frac{\phi(\xi)}{\xi-x'}d\xi \tag{26}$$

where ϕ and ψ are the real and imaginary parts of the complex function F. Considering the limiting values of F as $y' \to 0-$ or $0-$, denoted as F^+ and F^-, the function F satisfied the relations (after reflection into the upper half-plane by Schwarz's lemma)

799

$$F^+ - F^- = i2 \left[c + \int_{-\infty}^{x'} a_y'(t)dt \right] \quad -\infty < x' < s \quad (27)$$

$$F^+ + F^- = 0 \qquad\qquad s < x' < \infty \quad (28)$$

This is the classic Riemman-Hilbert boundary value problem, and applying the Plemlj formulas leads to

$$F(z') = \frac{\sqrt{s - z'}}{\pi} \int_{-\infty}^{s} \frac{\left[c + \int_{-\infty}^{\xi} a_y'(t)dt \right]}{\sqrt{s - \xi}\,(\xi - z')} \, d\xi + \frac{P(z')}{\sqrt{s - z'}} \quad (29)$$

where the term after the integral represents the homogenous solution, with $P(z')$ a polynomial function. This function, $P(z') \sim z'^n$, where n is chosen such that the pressure (φ) is integrable and has appropriate singular behavior near the leading edge of the plate. Near the leading edge $(z \to -b$ or $z' \to \infty)$,

$$F(z') = 0\left(z'^{\left(n-\frac{1}{2}\right)}\right) = 0\left[(b - z)^{-\left(\frac{n}{2} - \frac{1}{4}\right)}\right] \quad (30)$$

Possible values of n are $n = 1, 2$, but the solution can only be the case where $n = 1$ for the leading edge behavior, in view of the requirement of integrability of pressure and also for the cavity to be on only one side of the plate (see comments by Geurst [6] and Wu [13]). Thus

$$P(z') = Az' - B \quad (31)$$

where A and B are two additional real coefficients to be determined.

An illustrative application is for heaving motion,

$$h = bh_o e^{j\omega t} \quad (32)$$

so that

$$a_y = -\frac{\ddot{h}}{V^2} = \frac{\omega^2 bh_o}{V^2} e^{j\omega t} \quad (33)$$

and

$$a_y' = -4k^2 b^2 h_o e^{j\omega t} \frac{x'}{(b^2 - x'^2)^2} \quad (34)$$

where $k = \omega b / V$ is the reduced frequency. This leads to the representation

$$F(z') = \frac{\sqrt{s-z'}}{\pi} \int_{-\infty}^{s} \frac{\left[c + 2k^2 h_o e^{j\omega t} \frac{b^2}{b^2 + \zeta^2} \right]}{\sqrt{s-\zeta}\ (\zeta-z')}\, d\zeta + \frac{Az' + B}{\sqrt{s-z'}} \tag{35}$$

for the case of heaving motion.

The integral in Eq. (35) can be evaluated by contour integration around a suitable contour, where a branch cut is chosen along the real axis from s to $-\infty$. A circle of radius R surrounds the contour, and a small circle of radius δ surrounds the point $\zeta = s$, joining with the straight line contours of the branch cut.

Taking account of the singularities at $\pm ib$ and z' leads to

$$F(z') = ic + i2k^2 h_o e^{j\omega t} \frac{b^2}{b^2 + z'^2} + \frac{Az' + B}{\sqrt{s-z'}}$$

$$+ k^2 h_o b e^{j\omega t} \left\{ \frac{\sqrt{s-z'}}{\sqrt{s-ib}\ (ib-z')} - \frac{\sqrt{s-z'}}{\sqrt{s+ib}\ (ib-z')} \right\} \tag{36}$$

There are four unknowns, viz., c, s (or ℓ, the cavity length), A, and B. The quantity c is determined by a choice of the value of ψ at ∞. The Kutta condition is satisfied by this solution, and no information can be obtained using that condition. A, B and s are found by use of three additional conditions, such as the limiting value of φ at ∞, given as a constant dependent on σ; the velocity matching condition on the foil; and another condition such as continuity of vertical velocity in the wake, or constant volume, or a singularity free solution, in accordance with the desired physical model (no discussion will be presented herein as to the nature of the proper model for this case). The algebraic manipulations can be carried out to complete this problem, and also similar procedures for the case of pitching motion.

The above procedures are suggested outlines of an approach to determine the hydrodynamic reactions for unsteady partially cavitated flows. Solutions based on these methods will still require extensive computation of specific functions that represent the frequency-dependent modification factors, and there may be some question as to the value of effort to be expended for this case. Nevertheless, the outline is suggested as a means of obtaining a decomposition of the various force and moment components, which is not given in [8]. The completion of the theoretical hydrodynamic studies recommended in the present section for determining the quasi-steady, inertial, and unsteady reactions would then provide all of the necessary tools required for a theoretical analysis of the hydroelastic characteristics of partially cavitated hydrofoils.

CONCLUSIONS

The theoretical results obtained in the present study clearly indicate that there are definite dangers of hydroelastic instabilities occurring in the partially cavitated flow regime on various types of hydrofoils. In view of this result, it is necessary that careful checks be made as to the precise aspects of

these instability possibilities, including both theoretical and experimental studies. A definite recommendation is for the experiments to be carried out in order to ascertain the existence of hydroelastic instabilities in this flow regime by conducting special hydroelastic tests, preferably in a water tunnel. Further theoretical studies should be carried out as well, with emphasis on the low reduced frequency range, with both quasi-steady theory (as outlined in the previous section) and unsteady theory computations being carried out. Furthermore, there should be a back-up program for measurement of the hydrodynamic forces and moments acting on a partially cavitated foil in oscillatory motion, in order to check the results of theory as well as to obtain a better understanding of the mechanisms that contribute to the various types of hydroelastic instabilities.

The theoretical analyses performed in this paper have been carried out for straight, rigid, uniform hydrofoils supported elastically in two degrees of freedom, with only two-dimensional flow concepts utilized in the determination of the hydrodynamic forces. It is possible that three-dimensional effects, together with possible aspects of sweepback, taper, flexibility, etc., may alter some of the conclusions of the present study. Therefore, it is recommended that further experiments and theory be continued in order to ascertain the effects of these additional considerations, and hence to provide basic information for practical design problems.

NOMENCLATURE

a = dimensionless distance between mid-chord and elastic axis, in half-chord lengths, positive when elastic axis is aft

a_y = vertical fluid acceleration on foil

b = half-chord length

C_L = two-dimensional lift coefficients

C_{L_a} = lift coefficient rate of change with angle of attack

$d*$ = dimensionless distance to the center of pressure, measured from mid-chord position in terms of half-chord lengths, positive for center of pressure aft

f_c', f_s' = dimensionless real force coefficients (subscripts h or p indicate either heave or pitch motion, respectively)

F = complex acceleration potential

g = translational displacement, positive down

h_o = dimensionless amplitude of translational oscillation in half-chord lengths

i = $\sqrt{-1}$

I_α = mass polar moment of inertia per unit span of hydrofoil section about the elastic axis

j = $\sqrt{-1}$, $ij \ne -1$

k = reduced frequency, $k = \omega b / V$

K_h, K_α = spring constants in translation and rotation, respectively

ℓ = cavity length, in terms of half-chord, measured from the mid-chord position, positive for cavities terminating between the mid-chord and the trailing edge of the foil

L, M = lift and moment per unit span at the elastic axis

L_o, M_o = lift and moment per unit span at the leading edge

m = mass of hydrofoil section per unit span

m_c', m_s' = dimensionless moments (subscripts h or p indicate either heave or pitch motion, respectively)

P_c = pressure inside cavity

P_∞ = static pressure in fluid at infinity

$\triangle p$ = difference in pressure between static pressure at infinity and constant pressure inside cavity, $\triangle p = P_\infty - P_c$

r_α = dimensionless radius of gyration of hydrofoil section about elastic axis, in half-chord lengths, $r_\alpha^2 = I_\alpha / mb^2$

S_α = first moment of mass per unit span of hydrofoil section about the elastic axis

t = time

u, v = horizontal and vertical fluid velocities components on foil

V = free stream velocity

w = $u - iv$, complex fluid velocity on foil

x_α = dimensionless distance between elastic axis and the center of gravity in half-chord lengths, positive when center of gravity is aft. $x_\alpha = S_\alpha / mb$

x_{cp} = dimensionless distance between elastic axis and center of pressure, in half-chord lengths, positive when the center of pressure is aft

z = $x + iy$, complex coordinate in physical plane

α = rotational displacement, positive when leading edge is up; also steady state of attack

803

Kaplan

α_o = amplitude of rotational oscillation

μ = density ratio, $\mu = m/\rho\pi b^2$

ρ = fluid density

σ = cavitation number, $\sigma = \Delta p / \frac{1}{2}\rho V^2$

ϕ, ψ = real and imaginary parts of complex acceleration potential

ω_h, ω_α = uncoupled translational and rotational natural frequencies respectively; $\omega_h^2 = K_h/m$, $\omega_\alpha^2 = K_\alpha/I_\alpha$

ω = circular oscillation frequency

REFERENCES

1. Henry, C.J., Ashley, H., and Dugundji, J., "Aeroelastic Stability of Lifting Surfaces in High Density Fluids," Journal of Ship Research, Vol. 2, 1959, pp. 10-21.

2. Abramson, H.N. and Chu, Wen-Hwa, "A Discussion of the Flutter of Submerged Hydrofoils," Journal of Ship Research, Vol. 3, 1959.

3. Kaplan, Paul and Henry, C.J., "A Study of the Hydroelastic Instabilities of Supercavitating Hydrofoils," Journal of Ship Research, Vol. 4, No. 3, 1960.

4. Geurst, J.A., "Linearized Theory for Partially Cavitated Hydrofoils," International Shipbuilding Progress, Vol. 6, No. 60, August 1959.

5. Meyer, M.C., "Some Experiments on Partly Cavitated Hydrofoils," International Shipbuilding Progress, Vol. 6, No. 60, August 1959.

6. Geurst, J.A. and Verbrugh, P.J., "A Note on Camber Effects of a Partially Cavitated Hydrofoil," International Shipbuilding Progress, Vol. 6, No. 61, September 1959.

7. Timman, R., "A Generalized Theory for Cavitating Hydrofoils in Nonsteady Flow," Proc., 2nd Symposium on Naval Hydrodynamics, Office of Naval Research, August 1958.

8. Steinberg, H. and Karp, S., "Unsteady Flow Past Partially Cavitated Hydrofoils," Proc., 4th Symposium on Naval Hydrodynamics, Office of Naval Research, August 1962.

9. Theodorsen, Th., "General Theory of Aerodynamic Instability and the Mechanism of Flutter," NACA Rept. 736, 1942.

10. Woods, L.C., "Aerodynamic Forces on an Oscillating Aerofoil Fitted with a Spoiler," Proc. of Royal Soc., Series A, Vol. 239, 1957, pp. 328-337.

11. Bisplinghoff, R.L., Ashley, H., and Halfman, R.L., "Aeroelasticity," Addison-Wesley Publ. Co., Reading. Mass., 1955.

12. Sears, W.R. and von Karman, Th., "Airfoil Theory for Nonuniform Motion," Journal of Aero. Sci., Vol. 5, No. 10, August 1938.

13. Wu, T.Y., Discussion of Reference 7, Proc., 2nd Symposium on Naval Hydrodynamics, Office of Naval Research, August 1958.

*   *   *

COMPARISON OF THEORY AND EXPERIMENT
FOR
MARINE CONTROL-SURFACE FLUTTER

Ralph C. Leibowitz and Donald J. Belz

David Taylor Model Basin

ABSTRACT

Both the Extended Simplified Flutter Analysis and Modified Theodorsen Flutter Analysis, proposed by McGoldrick and Jewell, are applied to the TMB CONTROL SURFACE FLUTTER APPARATUS. Predictions of vibrational stability and instability based on these analyses are compared with stable and unstable (classical flutter) vibrations observed in the apparatus for towing speeds in the range of 0 to 20 knots.

The comparison of predicted and observed values of (1) damping and (2) critical flutter speeds shows that the Modified Theodorsen Analysis gives a consistently better agreement with experimental data than does the Extended Simplified Analysis; moreover, the results of the former analysis are in good agreement with available experimental data, whereas the results of the latter analysis are not.

To extend the range of mass unbalance, speed, and other parameters that show good agreement between theory and experiment, certain studies that will yield refinements to the Modified Theodorsen Analysis are proposed.

INTRODUCTION

The possibility of flutter in marine control surfaces came pointedly to the attention of naval research personnel when sea trials of USS FORREST SHERMAN (DD 931) revealed that severe vibrations were transmitted to the hull by the rudders [1].* This indicated the need for a thorough exploration of the possibility of marine control-surface flutter; for it may be possible that as the speeds of other ships are increased flutter may occur more commonly within the range of operating speeds. For this reason, methods of predicting flutter warrant serious consideration in the field of naval architecture.

---

*References are listed on page 930.

The present comparison of theoretical and experimental results is intended as a help to the researchers under contract to the Bureau of Ships in their search for a suitable method of flutter prediction. Such a method will permit ship designers to establish stability margins of safety from flutter for ships potentially capable of control-surface flutter.

In this report,* the stability of a TMB Control Surface Flutter Apparatus has been analyzed by computing on a digital computer the damping associated with the apparatus; stability predictions based on these computations are compared with available experimental data. These data include the results of tests performed on the flutter apparatus published in [2] and recently published results of similar tests recently performed by the TMB Hydromechanics Laboratory. The recent data are of special interest because, as a result of changes made in certain physical parameters of the apparatus, classical flutter† was observed as a hydroelastic phenomenon.

In addition to the digital computations, an analog solution of the equations of motion [2] used in the analysis of the flutter apparatus was undertaken. Qualitative information on the total motional response was obtained from this solution.

NOTATION

Symbol	Definition	Dimensions
A	Lift constant of the hydrofoil (lift force per unit attack angle per unit velocity squared)	$\dfrac{\text{lb-sec}^2}{\text{in.}^2}$
ab	Distance from midchord to axis of rotation (positive aft of midchord)	in.
B_{10}, B_{11} B_{12}, B_{21} B_{22}	Symbols for coefficients of the hydrofoil equations of motion	varying
b	Semichord length of hydrofoil	in.
C	Linearized damping constant for the translational degree of freedom at zero speed.	lb-sec/in.
C_c	Critical damping constant (general symbol employed for rotational or translational degree of freedom)	in.-lb-sec (rot.) lb-sec/in. (trans.)
$C(k)$	Theodorsen function	Dimensionless
c	Linearized damping constant for the rotational degree of freedom at zero speed	in.-lb-sec

---

*A preliminary report on the present study was published in letter form as [3].
†Classical flutter is a dynamically unstable, self-excited vibration of an oscillatory system immersed in a field of fluid flow [2].

Comparison of Theory and Experiment for Marine Control-Surface Flutter

Symbol	Definition	Dimensions
e	Base of Natural Logarithms (2.718. . .)	Dimensionless
F_L	Oscillatory lift force less the added mass and zero hydrodynamic damping effects	lb
h	Distance from the axis of rotation to the c.g. of the rotating assembly, based on mass plus added mass (positive if c.g. is downstream)	in.
I	Effective mass moment of inertia of the rotating assembly with respect to its axis, including the added mass moment of inertia	in.-lb-sec^2
j	The square root of minus one ($\sqrt{-1}$)	Dimensionless
K	Translational spring constant	lb/in.
k	Torsional spring constant	in.-lb
L	Distance of the center of lift from the axis of rotation (positive if center of lift is forward of the axis)	in.
M	Mass of the apparatus that moves only in translation	lb-sec^2/in.
M_a	Hydrodynamic oscillatory moment exerted on the hydrofoil about the axis of rotation less the added mass and zero speed hydrodynamic damping effects	in.-lb
m	Mass of the hydrofoil including the mass of the entire assembly that rotates with it and the added mass for translation	lb-sec^2/in.
m'	Added mass of the hydrofoil in translation or Y degree of freedom	lb-sec^2/in.
n	Multiplier of t in assumed solution $\delta = e^{nt}$ (See p. in Appendix E)	sec^{-1}
R_{10}, R_{11} R_{12}, R_{20} R_{21}, R_{22}	Symbols for coefficients of the hydrofoil equations of motion	varying
S	Hydrofoil towing speed	in./sec in computations, converted to knots for data presentation

Symbol	Definition	Dimensions
S_a	Moment about the forward quarterpoint of the rotational structural mass	lb-sec ^{2}
T	Period of an oscillation	sec
t	Elapsed time	sec
t_0	Duration of an impulsive force	sec
t_1, t_2	Successive numerical values of elapsed time	sec
Y	Translational displacement of the hydrofoil axis normal to the flow and to the axis of rotation (measured from the equilibrium position)	in.
Y_0	Numerical value of Y at $t = 0$ sec	in.
α_0	Preset angle of attack of hydrofoil	degrees
δ	Logarithmic decrement	dimensionless
β	Rotational displacement of the control surface from the direction of flow	radians
β_0	Numerical value β at $t = 0$ sec	radians
λ	Complex circular frequency of vibration	sec $^{-1}$
λ^*	Complex conjugate of	sec $^{-1}$
ω	Real part of λ indicating the degree of damping	sec $^{-1}$
π	Ratio of circumference to diameter of a circle (3.141. . .)	dimensionless
σ	Phase angle separating Y and β responses	degrees
ω	Circular frequency of vibration (magnitude of imaginary part of λ)	sec $^{-1}$
X_a	The distance of the center of mass aft of the rotational axis.	dimensionless

BACKGROUND

A Control Surface Flutter Apparatus, shown schematically in Fig. 1, was built and tested at the David Taylor Model Basin as a joint effort of the Structural Mechanics and Hydrodynamics Laboratories [2]. Experimental

810

measurements of overall damping* associated with the hydrofoil of the apparatus were made from data obtained while the apparatus was towed with its foil submerged.

In addition, two analytic approaches to the problem of predicting flutter were devised and designated as the Extended Simplified Analysis and the Modified Theodorsen Analysis [2,3,4,5]. The characteristic equation obtained by expansion of the determinant of the coefficients of the differential equations of motion was converted to algebraic form for both approaches, and the Routh discriminant of these characteristic equations was determined in order to predict the stability of the hydrofoil. The results of this study were published in [2].

That reference stated that analytical predictions of instability, based on the Routh criteria alone, were not verified experimentally. However, marked reductions in the damping of stable oscillations were observed. This associated condition

Fig. 1 - Schematic representation of the TMB control surface flutter apparatus

of barely stable vibration was defined as subcritical flutter. Because subcritical flutter is generally not predictable from the Routh criteria, the present study was initiated to compute damping directly in order to furnish a more general prediction of stability for the flutter apparatus.
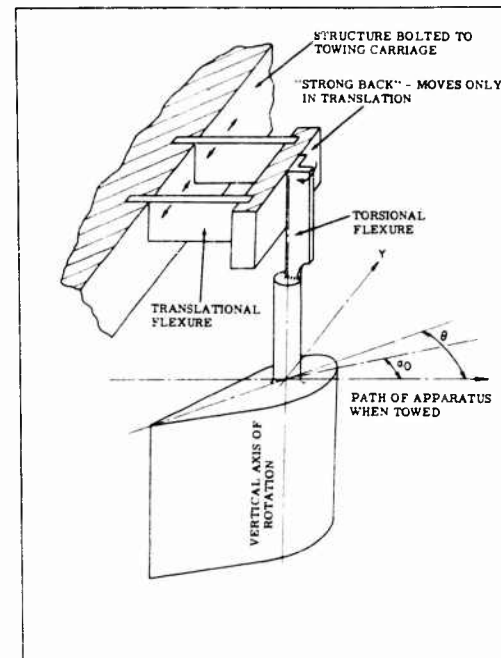
TMB CONTROL SURFACE FLUTTER APPARATUS

The TMB Control Surface Flutter Apparatus† was designed to provide a means of "checking flutter analyses based on various assumptions as to the nature of the oscillatory lift forces and moments"[2].

The mechanism consists of a relatively rigid NACA 0015-section hydrofoil so suspended that it rotates about a vertical axis and translates normal to the path of a towing carriage upon which the Control Surface Flutter Apparatus is mounted. Deflections in the two degrees of freedom, θ (rotation) and Y (translation), of the foil are resisted, respectively, by linear rotational and translational spring forces. In addition, eddy current dampers provide forces for

---

*Overall damping, as defined on page 4 of [2], includes all effects contributing to the rate of decay or buildup of a free vibration.

†A detailed description of this apparatus may be found in [2].

increasing the damping in either or both degrees of freedom. Signals from strain gages mounted on the supporting springs give a continuous indication of displacements, Y and θ, as they vary with time; see Fig. 1.

The foil itself is suspended below a surface plate to eliminate wave effects.

FLUTTER ANALYSIS

Damping ratio,[*] a measure of the rate of decay of oscillations, is used as the criterion for identifying both classical and subcritical flutter. Analytic expressions for damping ratio are obtained from solutions of the equations of motion for the flutter apparatus.

EQUATIONS OF MOTION

Two separate analyses of the response of the flutter apparatus—the Extended Simplified and the Modified Theodorsen Analyses—were proposed by McGoldrick and Jewell in [2].

The Modified Theodorsen Analysis is based on Theodorsen's solution of the stability problem for two-dimensional flow over a plane foil of infinite aspect ratio with no structural damping [2,5]. Modifications of the equations, originally derived by Theodorsen, are explained fully in [2]. Changes were made in expressions for the lift forces and moments and in the inclusion of a steady hydrodynamic moment ascribed to circulation.[†] The equations of motion for the Modified Theodorsen Analysis are:

$$I\ddot{\theta} + \left(c + \frac{1}{2} Ab^2 S\right)\dot{\theta} + \left(k - \frac{1}{2} ALS^2\right)\theta - mh\ddot{Y} = 0$$

$$-mh\ddot{\theta} - AbS\dot{\theta} - \frac{1}{2}AS^2\theta + (M+m)\ddot{Y} + \left(C + \frac{1}{2}AS\right)\dot{Y} + KY = 0,$$

where ($\cdot$) and ($\cdot\cdot$) denote first and second total derivatives with respect to time.[‡]

The equations of motion for the Extended Simplified Analysis are:

$$I\ddot{\theta} + c\dot{\theta} + (k - ALS^2)\theta - mh\ddot{Y} + ALS\dot{Y} = 0$$

$$-mh\ddot{\theta} - AS^2\theta + (M+m)\ddot{Y} + (C+AS)\dot{Y} + KY = 0.$$

For both the Modified Theodorsen Analysis and the Extended Simplified Analysis, the equations of motion are mathematically of the form:

$$B_{12}\ddot{\theta} + B_{11}\dot{\theta} + B_{10}\theta + B_{22}\ddot{Y} + B_{21}\dot{Y} = 0$$

$$R_{12}\ddot{\theta} + R_{11}\dot{\theta} + R_{10}\theta + R_{22}\ddot{Y} + R_{21}\dot{Y} + R_{20}Y = 0.$$

For this reason, the following methods of determining damping ratios may be applied to either of the two analyses by employing the appropriate coefficients.

DIGITAL COMPUTER DETERMINATION OF DAMPING RATIOS

Assumed solutions of the form $\theta = \theta_0 e^{\lambda t}$ and $Y = Y_0 e^{\lambda t}$ (where θ_0, Y_0 and λ are generally complex) are substituted in the equations of motion for both the Extended Simplified and Modified Theodorsen Analyses. Two algebraic equations of the form,

$$(B_{12}\lambda^2 + B_{11}\lambda + B_{10})\,\theta_0 + (B_{22}\lambda^2 + B_{21}\lambda)\,Y_0 = 0$$

$$(R_{12}\lambda^2 + R_{11}\lambda + R_{10})\,\theta_0 + (R_{22}\lambda^2 + R_{21}\lambda + R_{20})\,Y_0 = 0$$

result from this substitution for either analysis. These equations must be satisfied so that the assumed solutions may satisfy the equations of motion.

A nontrivial solution of the preceding equations exists, if, and only if, the determinant of the coefficients vanishes. In other words, the following characteristic equation of fourth degree (frequency quartic) in the generally complex frequency $\lambda = \mu + j\omega$ must be satisfied:

$$(B_{12}R_{22} - R_{12}B_{22})\,\lambda^4 + (B_{11}R_{22} + B_{12}R_{21} - R_{11}B_{22} - R_{12}B_{21})\,\lambda^3$$

$$+ (B_{10}R_{22} + B_{11}R_{21} + B_{12}R_{20} - R_{10}R_{22} - R_{11}B_{21})\,\lambda^2 + (B_{10}R_{21}$$

$$+ B_{11}R_{21} + B_{11}R_{20} - R_{10}B_{21})\,\lambda + B_{10}R_{20} - R_{10}B_{21} = 0.$$

Note that the coefficients of this equation are all real.

The hydrofoil of the flutter apparatus has two degrees of freedom and, consequently, two modes of vibration corresponding, in general, to two distinct natural frequencies. If one of the two modes is considered to predominate in the total motional response, the damping ratio will equal the logarithmic decrement of the response curve θ vs t and/or Y vs t divided by 2π.* For numerical

---

*Logarithmic decrement δ may be considered to be defined by the expression $\delta = 2\pi (c/C_c) \sqrt{1 - (c/C_c)^2}$. When c/C_c is small compared to unity, as is anticipated in the present study, $\delta \approx 2\pi c/C_c$. Damping ratio, defined previously as c/C_c, is then approximately equal to the logarithmic decrement δ divided by 2π.

values of damping ratio that are small compared to unity, damping ratio may also be approximated by $-\mu/\omega$.*

Solutions of the preceding frequency quartic equation, for a given set of coefficients, may occur mathematically as four real roots, two pairs of complex conjugate roots, or as two real roots and one pair of complex conjugate roots.

When solutions occur as two pairs of complex conjugates, two of the roots will be associated with one mode of vibration and the remaining two will be associated with the other mode.

For oscillations in a given mode, no distinction is made between damping in the translational degree of freedom and damping in the rotational degree of freedom. Thus the two roots, $\wedge$, associated with that mode, have identical values of μ and ω, the two roots being complex conjugates.

The sign of the damping ratio, $-\mu/\omega$, is always opposite to the sign of the associated value of damping μ. For, a <u>negative</u> value of μ, indicating <u>stability</u>, is associated with a <u>positive</u> logarithmic decrement and, hence, a <u>positive</u> damping ratio. The <u>converse</u> statement is also true.

When classical, critical, or subcritical flutter occurs, a marked coupling between the two natural modes may be observed [2], depending upon the initial conditions. For the two-degree-of-freedom system, this is mathematically evident from a consideration of the four distinct eigenvalues associated with the equations of motion when solutions of the form $\theta = \theta_o e^{\wedge t}$ and $Y = Y_o e^{\wedge t}$ are assumed. When these four values of $\wedge$ are denoted by subscripts 1 through 4, the total response may be expressed as

$$\theta = \theta_{01}e^{\wedge_1 t} + \theta_{02}e^{\wedge_2 t} + \theta_{03}e^{\wedge_3 t} + \theta_{04}e^{\wedge_4 t}$$

$$Y = Y_{01}e^{\wedge_1 t} + Y_{02}e^{\wedge_2 t} + Y_{03}e^{\wedge_3 t} + Y_{04}e^{\wedge_4 t}$$

If any of the $\wedge_i$ ($i = 1, 2, 3, 4$) contains a positive μ (unstable condition), then, regardless of the initial conditions imposed upon the physical system, the response, θ vs t and Y vs t, must ultimately be unstable for the coupled mode system. That is, the unstable terms in the expression for θ and Y must eventually predominate in the total response.

---

*Consider a response $Y = Y_o e^{\wedge t}$. The logarithmic decrement of the Y vs t curve may be interpreted as the natural logarithm of two successive maximum amplitudes, Y_1 and Y_2, which occur T seconds apart. "T" is therefore the period of oscillation; i.e., $T = 2\pi/\omega$, where ω is the circular frequency of the oscillation. Then

$$\delta = \log_e \frac{R_e(Y_1)}{R_e(Y_2)} = \log_e \frac{Y_0 e^{\mu t_1}}{Y_0 e^{\mu t_2}} = \log_e e^{\mu(t_1 - t_2)} = \log_e e^{-\mu T} = -\mu T = 2\pi\mu/\omega.$$

Thus damping ratio, which is equal to $\delta 2\pi$, may be expressed as $-\mu/\omega$.

Comparison of Theory and Experiment for Marine Control-Surface Flutter

The frequency quartic equation was coded for solution on an IBM 704 electronic data processing machine by the TMB Applied Mathematics Laboratory. A sufficiently wide range of values, for the physical parameters that make up the coefficients of the frequency quartic equation, was employed to correspond to experimental conditions for which damping ratio vs. speed data were available. Solutions, $\lambda_i = \mu_i + j\omega_i$, of the frequency quartic equation were obtained, and for each solution, damping ratio $-\mu/\omega$ and logarithmic decrement δ were computed as part of the program. The results of these digital computations are presented graphically in Appendix A. Figure 2 shows a sample format of the output data. The corresponding input data, together with the coefficients A_0, A_1, A_2, A_3 of the frequency quartic equation, have also been included on this format. Some symbols on the format differ from the notation used throughout this report. Table 1 illustrates the equivalence of these symbols.

Fig. 2 - Sample format of digital computer output data

815

Table 1
Comparison of Notation Used in Fig. 2
with Notation of This Report

Notation Defined on Pages	Notation of Fig. 2
C	CC
c	C
K	KK
k	K
M	MM
m	M
μ/ω	MU/OMEGA
μ	MU
ω	OMEGA
A_0	A-O
A_1	A-1
A_2	A-2
A_3	A-3
mh	MH
L	L
S	S

Note that the results of the computations predict the stability or instability of the system but not the total motional response, because Y_0 and $\dot{\theta}_0$ are not found if the initial conditions are not considered in the solution of the equations of motion.

ANALOG DETERMINATION OF FLUTTER RESPONSE

The equations of motion, whether based on the Extended Simplified Analysis or on the Modified Theodorsen Analysis, may be solved by an electronic differential analyzer to obtain a set of completely predicted response curves, $\theta = \theta(t)$ and $Y = Y(t)$. Four possible general types of response may be obtained; see Fig. 3. These include stable and unstable oscillations, both with one mode predominating and with beating between the two modes to produce either a stable or an unstable condition. "Temporarily suppressed flutter," a special case of the previous classification, occurs when the damping μ is positive (unstable) in one mode, negative (stable) in the other, and when initial conditions are such as to make the stable mode predominate initially in the total response. Eventually, the unstable mode must predominate to produce classical flutter. However, the number of cycles which must pass before the instability is observed will depend upon the physical parameters of the apparatus. Recognition of this phenomenon is of great importance in the use of analog methods of predicting flutter because the number of cycles over which the response curves are recorded may be insufficient to allow the amplitudes due to the unstable mode to reach observable magnitudes. The difficulty may be obviated by obtaining two sets of response
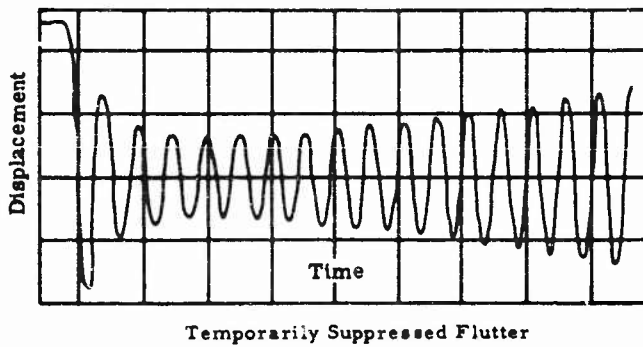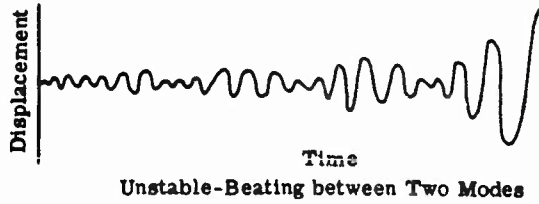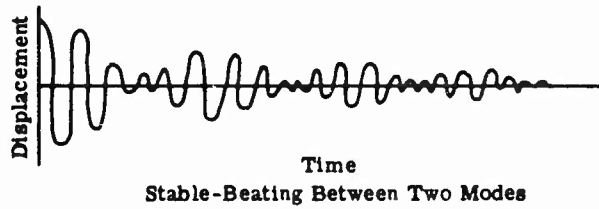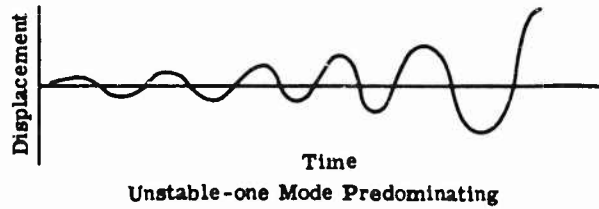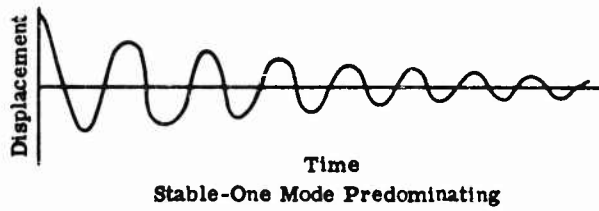
Fig. 3 - Analog response showing stable and
unstable oscillations

817

curves from the analog for each set of parameters, the first with initial conditions to make one mode predominate and the second with initial conditions to make the other mode predominate in the total response. An unstable mode, if it exists, is then easily observed after a few cycles from either of the response curves. An example of "temporarily suppressed flutter" is shown in Fig. 3.

In the present study, the analog approach was used to obtain qualitative information about the general character of the response wave form. However, numerical values of damping ratio may be computed from response curves, in which one mode predominates, by evaluating $\delta/2\pi$, where δ is the logarithmic decrement of these curves.

EXPERIMENTAL WORK

The earliest data obtained from experiments with the TMB Control Surface Flutter Apparatus were presented in [2]. The damping ratios and associated frequencies therein were computed from records of vibrations induced in the apparatus by striking it laterally while underway. In these tests, the vertical axis of rotation was located at the forward quarter-chord position.

A more detailed explanation of the experimental procedure can be found in [2].

Since the publication of [2], the Hydromechanics Laboratory has conducted further tests on the flutter apparatus. The results of those tests have been published in [6] and are included in this study for comparison with the results predicted by the Extended Simplified and Modified Theodorsen Analyses. Table 2 summarizes the various configurations for which the comparison was made. Each configuration corresponds to the different values of the parameters as shown. The most significant changes in these parameters were an increase in the mass of the assembly that rotates with the hydrofoil and the relocation of the center of mass further aft of the vertical axis of rotation.

Classical flutter was observed in tests of Configurations B and D. Experimentally observed damping ratios for these configurations, as well as for the configuration (TMB 1222) used in the study reported in [2], are compared with analytical predictions in the following section.

ANALYTICAL AND EXPERIMENTAL RESULTS

Computations of damping ratio and frequency were made for Configurations B, D, and TMB 1222, based on the Extended Simplified Analysis and the Modified Theodorsen Analysis. Numerical values of the parameters mh, L, S, and τ_0, for which the computations were made, are given in Appendix B. Figures 19 through 86, presented in Appendix A, are plots of computed damping ratio and associated frequency ω vs. speed for both natural modes.

Empirical data published in [2] and more recent data furnished by the TMB Hydromechanics Laboratory [6] are superposed upon these plots to permit the desired comparison between analytical predictions and experimental observations of stability.

818

Table 2

Parameters of the TMB Control Surface Flutter Apparatus for Various Configurations

Parameters			Configurations		
Symbol	Definition	Dimensions	B^*	D^*	TMB 1222†
A	Lift constant of the hydrofoil (lift force per unit angle of attack per unit velocity squared)	lb-sec²/in.²	0.034	0.034	0.034
C	Linearized damping constant for the translational degree of freedom at zero speed	lb-sec/in.	0.63	0.46	0.375
c	Linearized damping constant for the rotational degree of freedom at zero speed	in.-lb-sec	29.0	29.0	22.3
h	Distance from the axis to the c.g. of the rotating assembly, based on mass plus added mass (positive if c.g. is downstream)	in.	Variable	Variable	Variable (max. value 1.64)
I	Effective mass moment of inertia of the rotating assembly with respect to its axis including the added mass moment of inertia	in.-lb-sec²	65.6	65.6	62.3
K	Translational spring constant	lb/in.	867.	867.	867.
k	Torsional spring constant	in.-lb	37,300	37,300	37,300
M	Mass of the apparatus that moves only in translation	lb-sec²/in.	0.30	0.43	0.23
m	Mass of the hydrofoil including the mass of the entire assembly that rotates with it and the added mass for translation	lb-sec²/in.	1.374	1.374	1.23

*Classical flutter obtained for these configurations only.
†See Table 1 of [2].

The most significant information contained in these graphs, for purposes of comparison of theory with experiment, has been reproduced in Figs. 4 through 16. The section, Discussion of Results, gives the reasons for selecting these graphs.

Figures 17 and 18 show the experimentally observed dependence of critical flutter speed on mass unbalance, mh for Configurations B and D, respectively. Superposed on those figures are analytical curves of critical flutter speed vs. mh, based on the Modified Theodorsen Analysis. Note that these curves are based on different values of L even though α_0 =1.88° for all tests conducted for Configurations B and D. The use of values of L not uniquely dependent on α_0 violates the assumption [2] which underlies the Modified Theodorsen and Extended Simplified Analyses; see Discussion of Results and Recommendations.

DISCUSSION OF RESULTS

The data in Figs. 4 through 16 have been selected from Figs. 19 through 86 in Appendix A for convenience in interpreting the comparison of analytical and experimental damping ratios. The following points form the criteria upon which the data of Figs. 4 through 16 were selected:

1. Not all values of L, for which families of damping ratio and frequency vs. speed curves were drawn in Appendix A, correspond to experimental conditions. For Configuration TMB 1222, the observed [2] value of L was 2.8 in., corresponding to $\alpha_0 = 0°$. No experimental measurement of L was obtained for Configurations B and D. Therefore, based on computations, a family of curves for the parameter L was plotted in an attempt to find a correlation between analytical curves for a unique value of L and experimental data. This approach for Configurations B and D is discussed in Point 3.

2. For Configuration TMB 1222, where no classical flutter was observed, the phase angle between Y and θ indicates that the mode of lower frequency predominated in the total response for mh = 0.0 and 0.3 lb-sec²; however, for mh = 2.0 lb-sec² the mode of higher frequency predominated; see Appendix C. Therefore, comparisons of theory and experiment should be made for the lower mode when mh = 0.0 or 0.3 lb-sec² and for the higher mode when mh = 2.0 lb-sec².

3. In Configurations B and D, for all values of mh under consideration, the higher mode consistently gave the best comparison with test data and is therefore postulated to have been the mode predominantly excited in the total response.

4. In Figs. 4 through 16, damping ratio vs. speed is plotted; Figs. 19 through 86 in Appendix A show frequency vs. speed in addition. These frequency curves were omitted in Figs. 4 through 16 not because they are irrelevant but because the major concern in plotting the latter figures was to effect a comparison of stability predictions (damping ratios) and observations. A comparison of analytical frequency predictions with observed frequencies forms an important part of the general comparison of theory with experiment, but does not directly offer a comparison of stability predictions and observations.

Comparison of Theory and Experiment for Marine Control-Surface Flutter
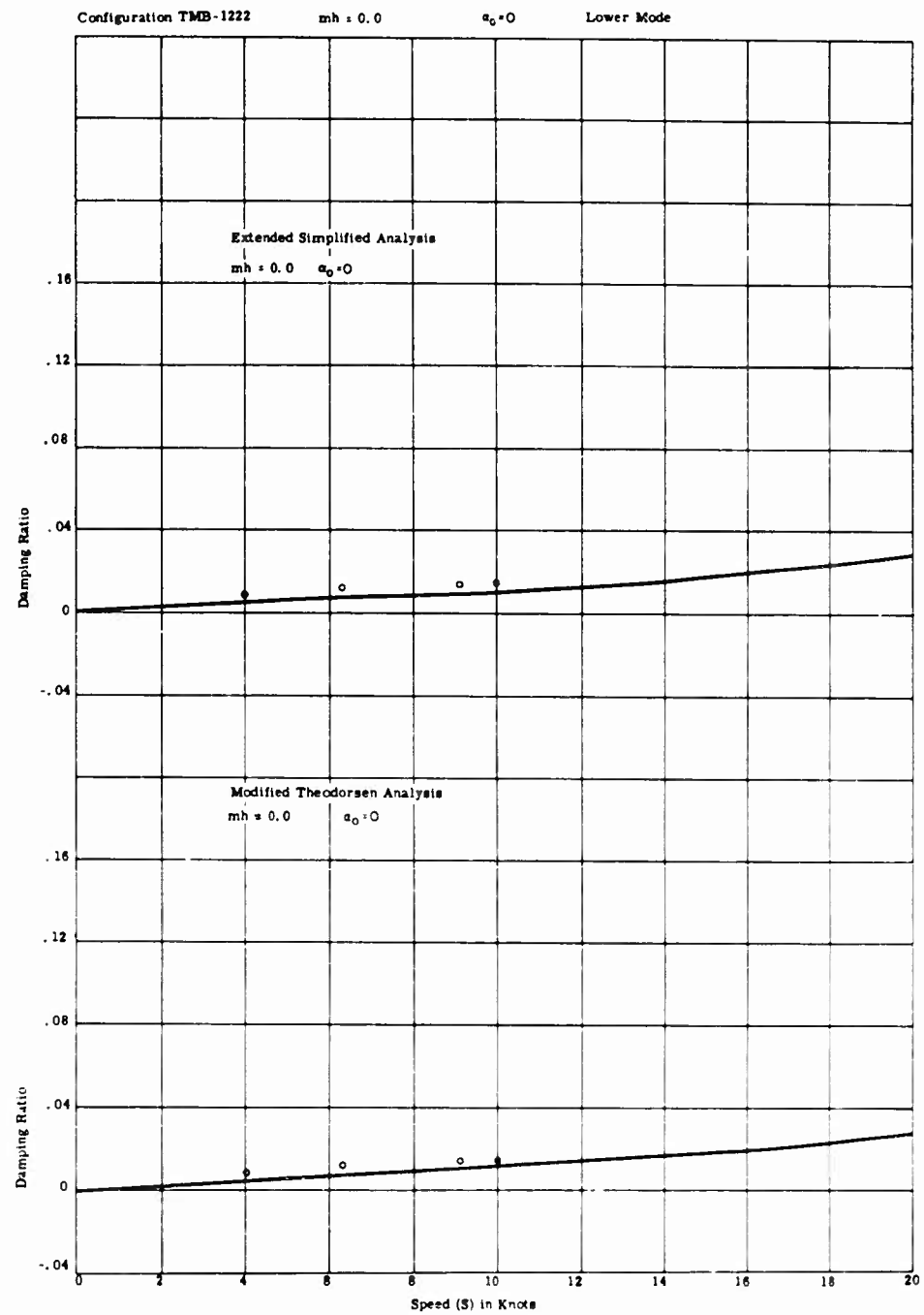
Fig. 4 - Comparison of computed and experimental damping ratios
(Configuration TMB 1222, mh = 0.0 lb-sec^2)
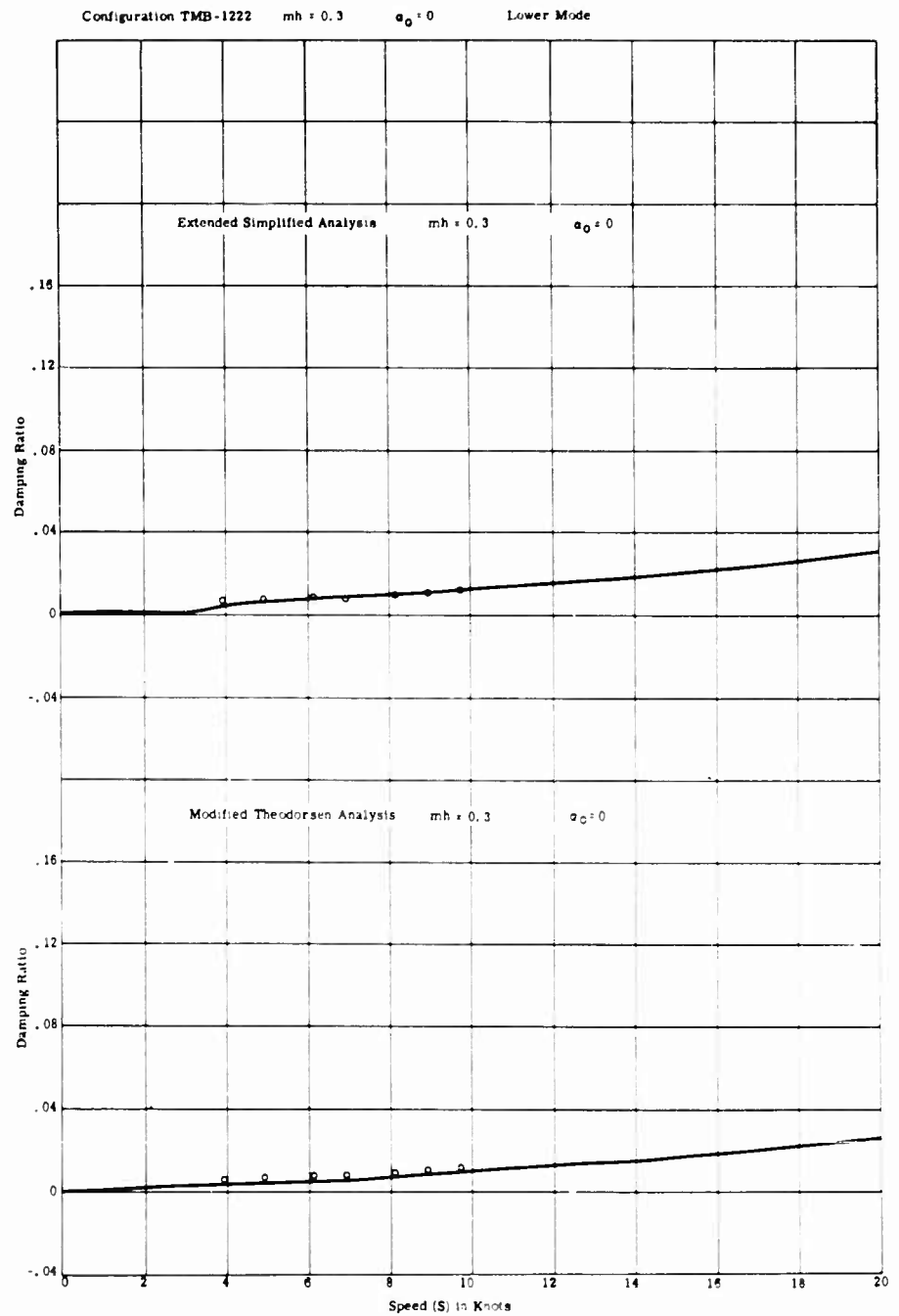
Fig. 5 - Comparison of computed and experimental damping ratios
(Configuration TMB 1222, mh = 0.3 lb-sec^2)
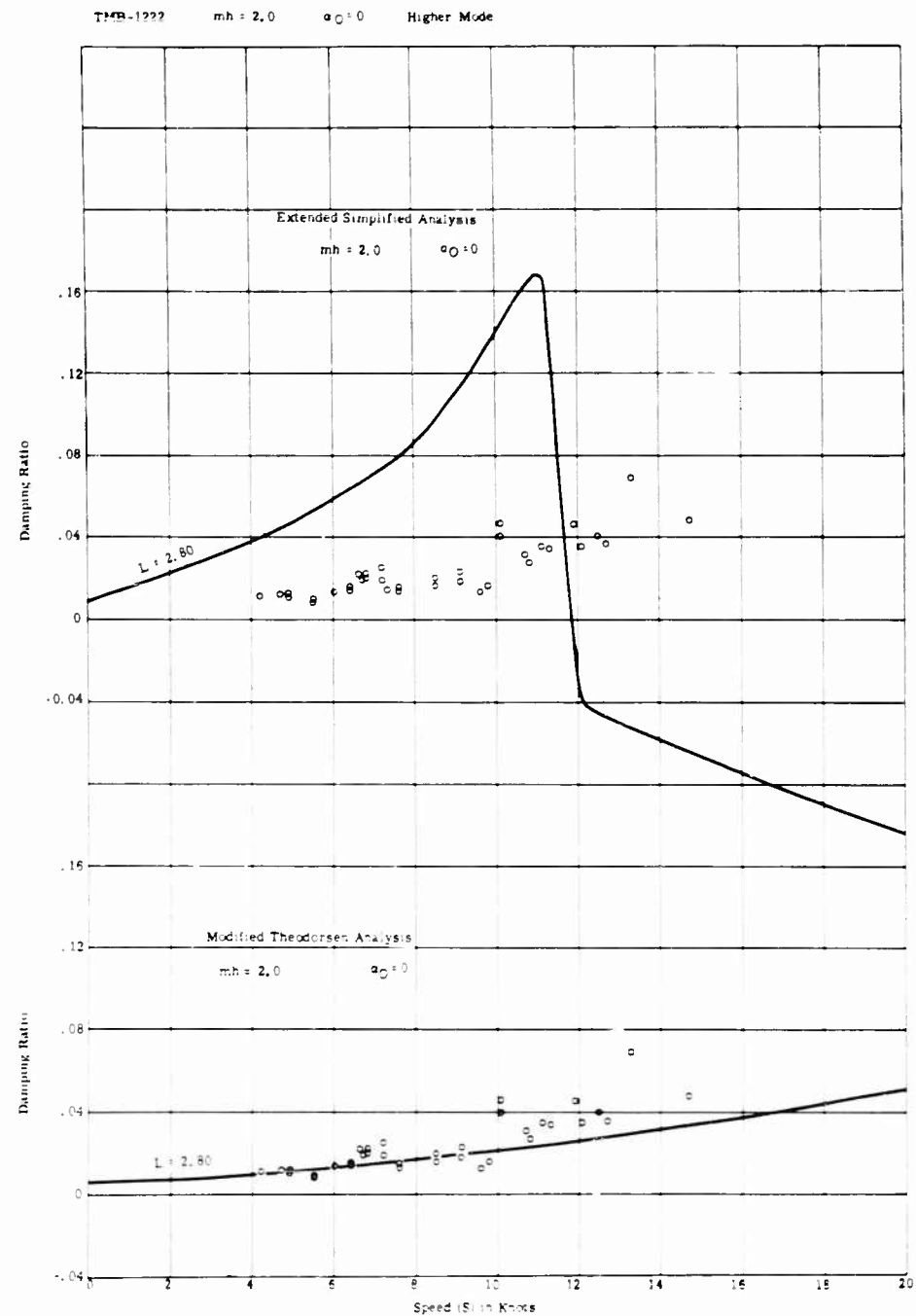
Fig. 6 - Comparison of computed and experimental damping ratios
(Configuration TMB 1222, mh = 2.0 .b-sec²)
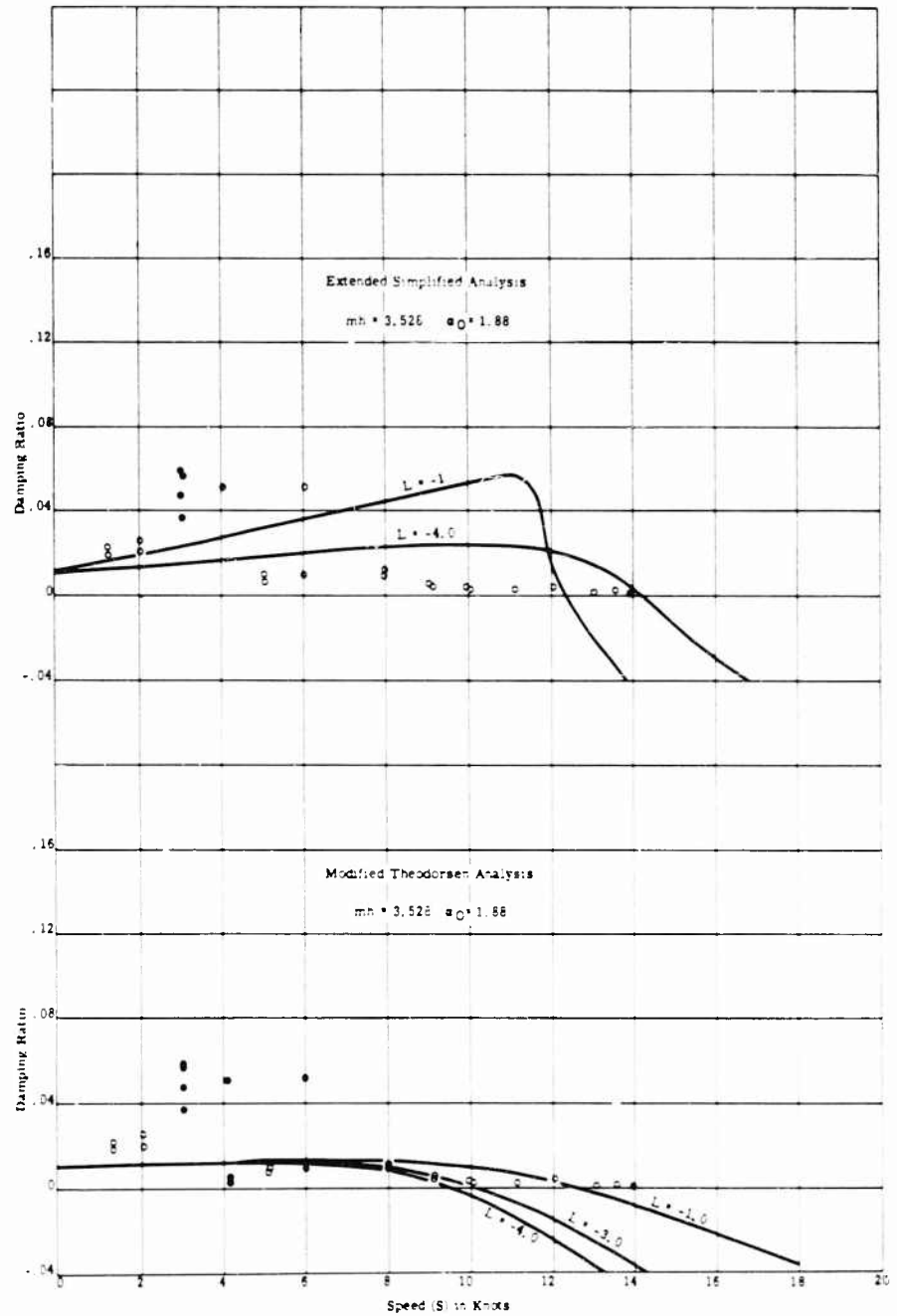
Fig. 7 - Comparison of computed and experimental damping ratios
(Configuration B, mh = 3.53 lb-sec²)
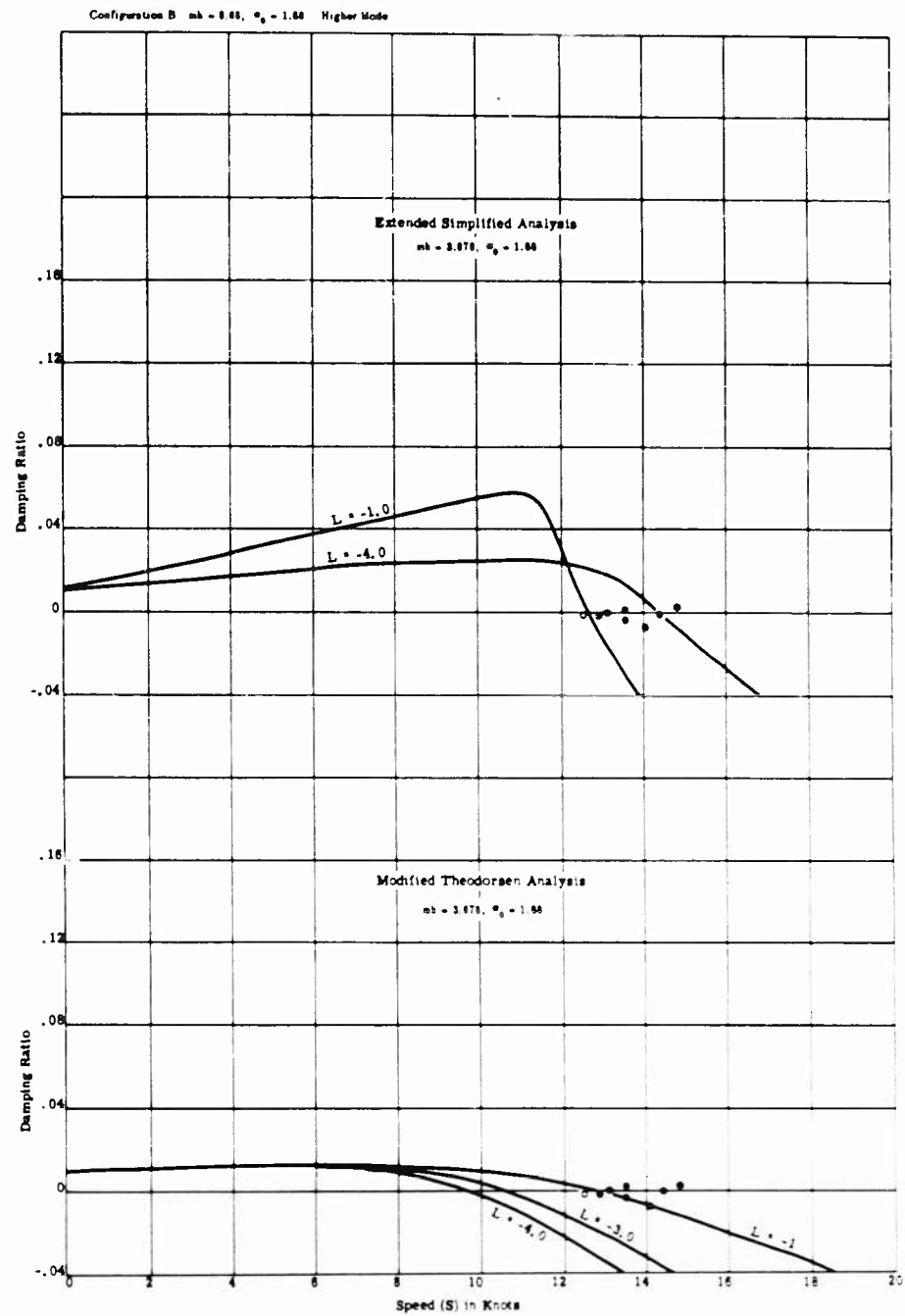
Fig. 8 - Comparison of computed and experimental damping ratios
(Configuration B, mh = 3.68 lb-sec^2)
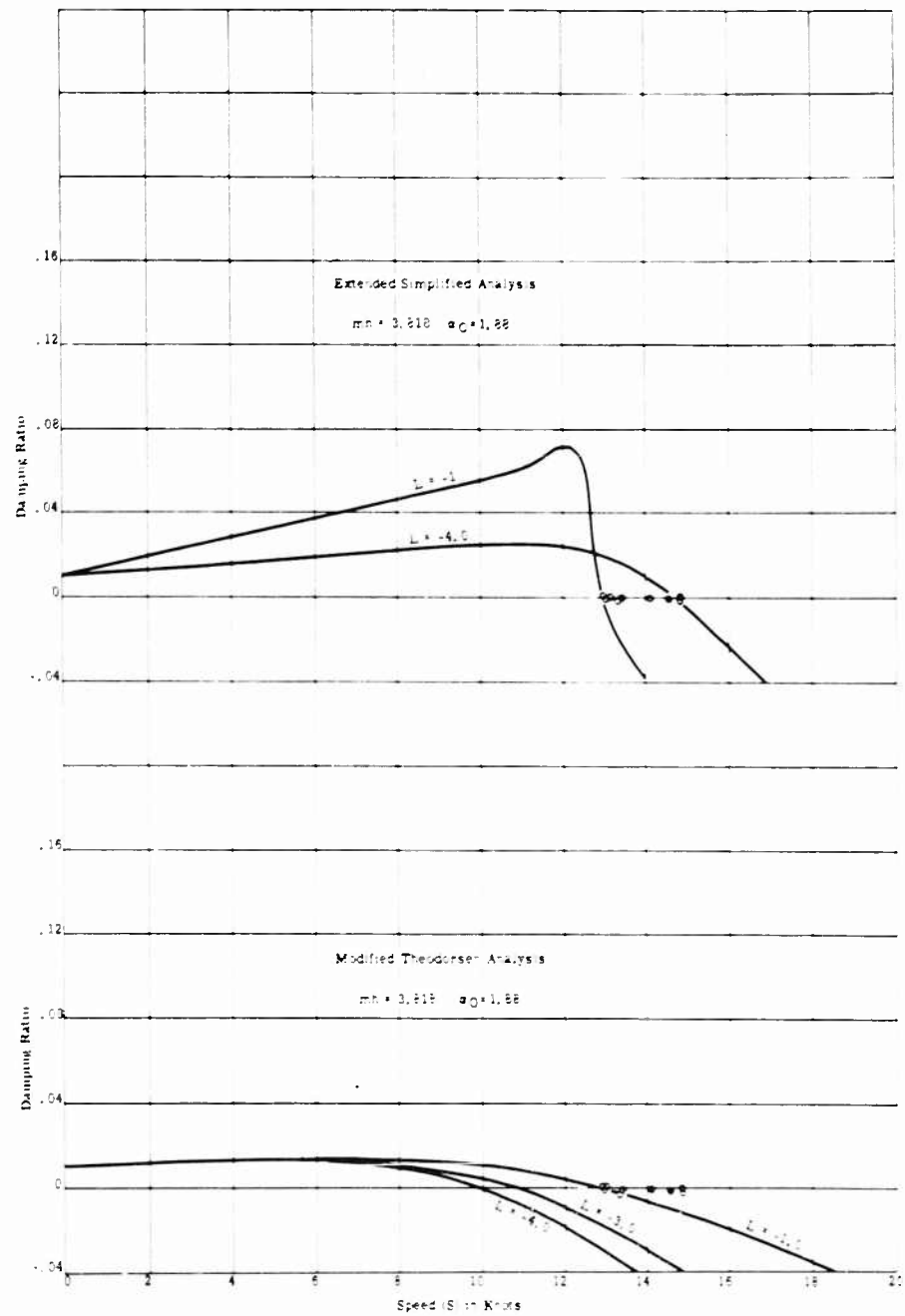
Fig. 9 - Comparison of computed and experimental damping ratios
(Configuration B, mh = 3.82 lb-sec²)
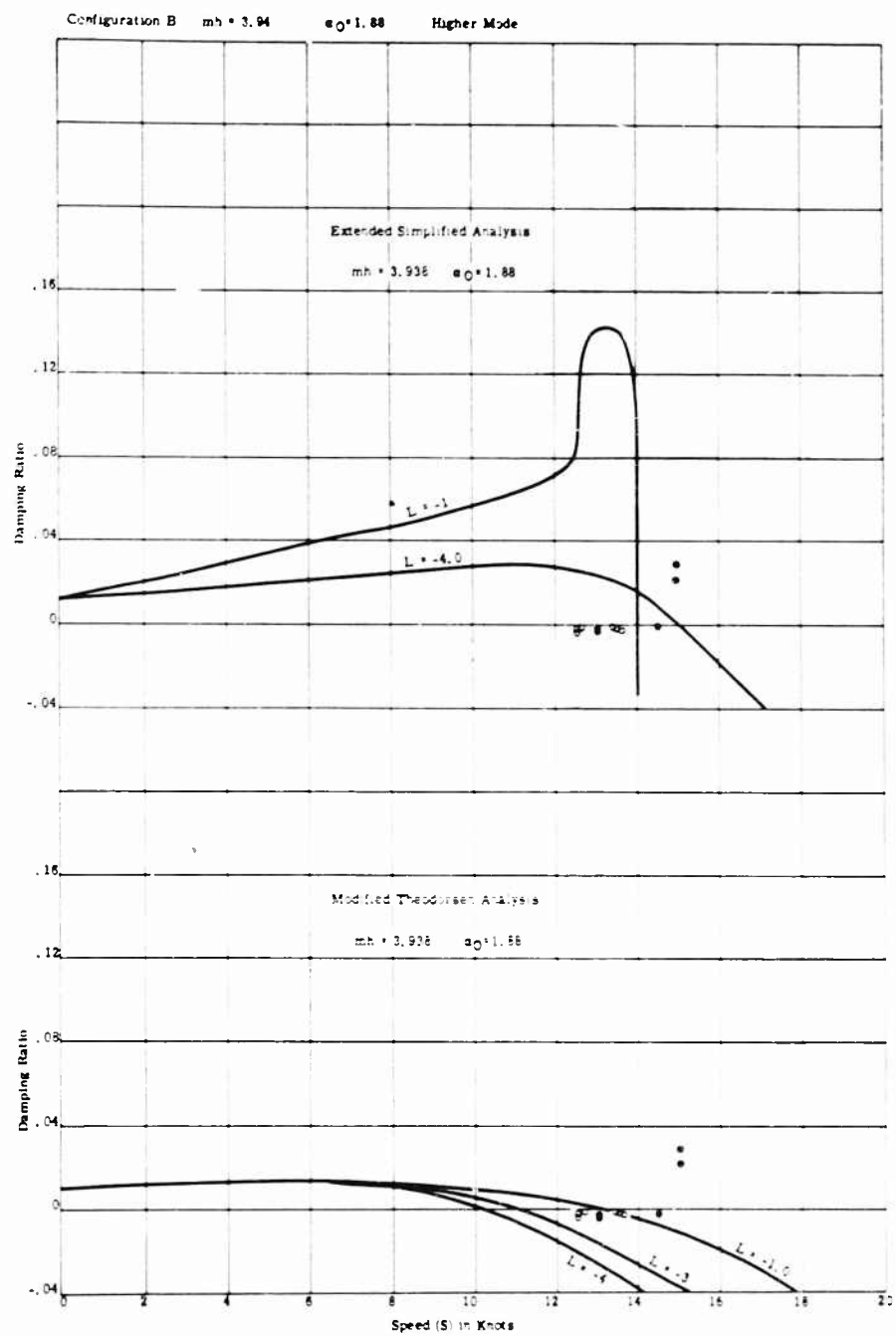
Fig. 10 - Comparison of computed and experimental damping ratios
(Configuration B, mh = 3.94 lb-sec²)

827
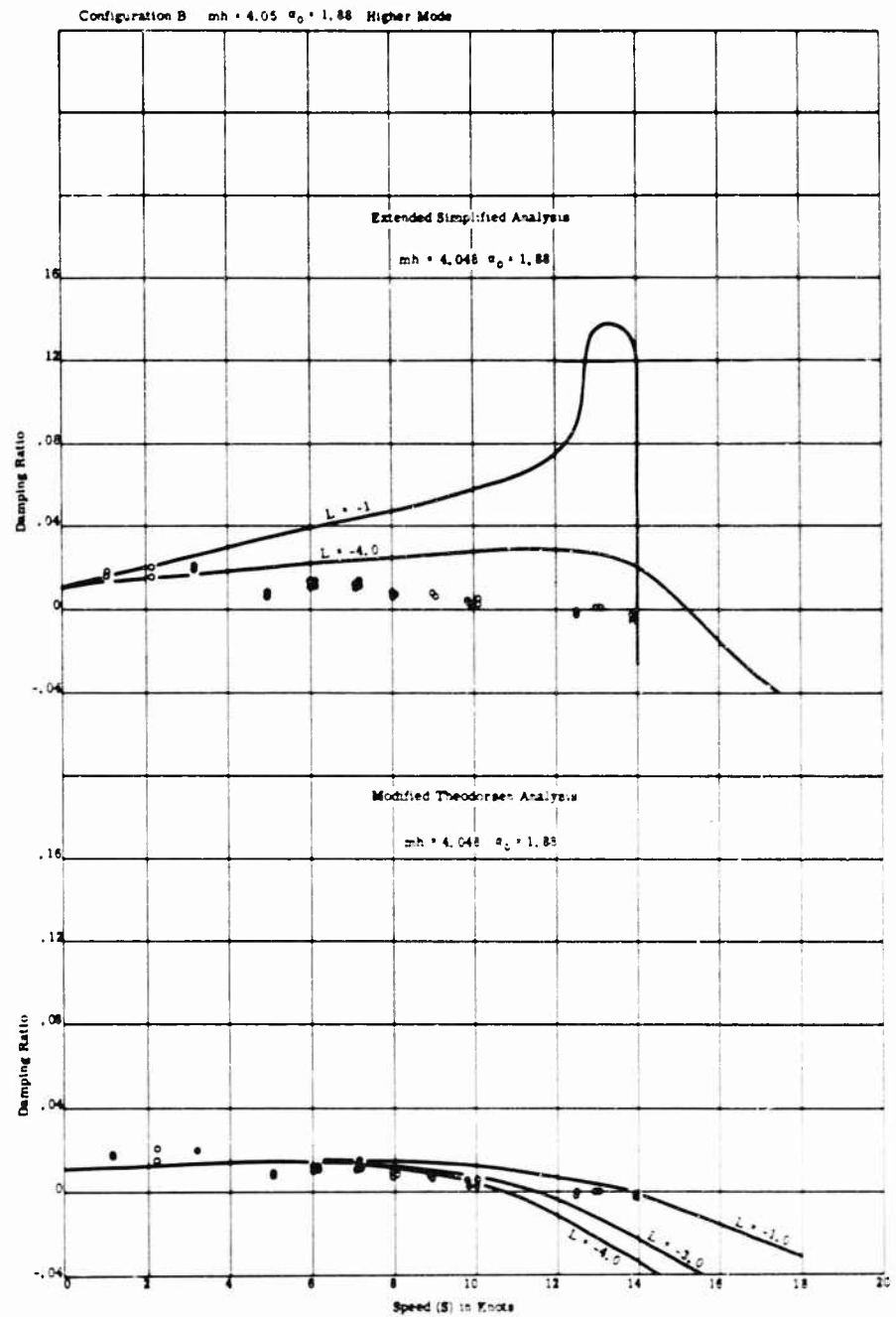
Fig. 11 - Comparison of computed and experimental damping ratios
(Configuration B, mh = 4.05 lb-sec²)

Comparison of Theory and Experiment for Marine Control-Surface Flutter
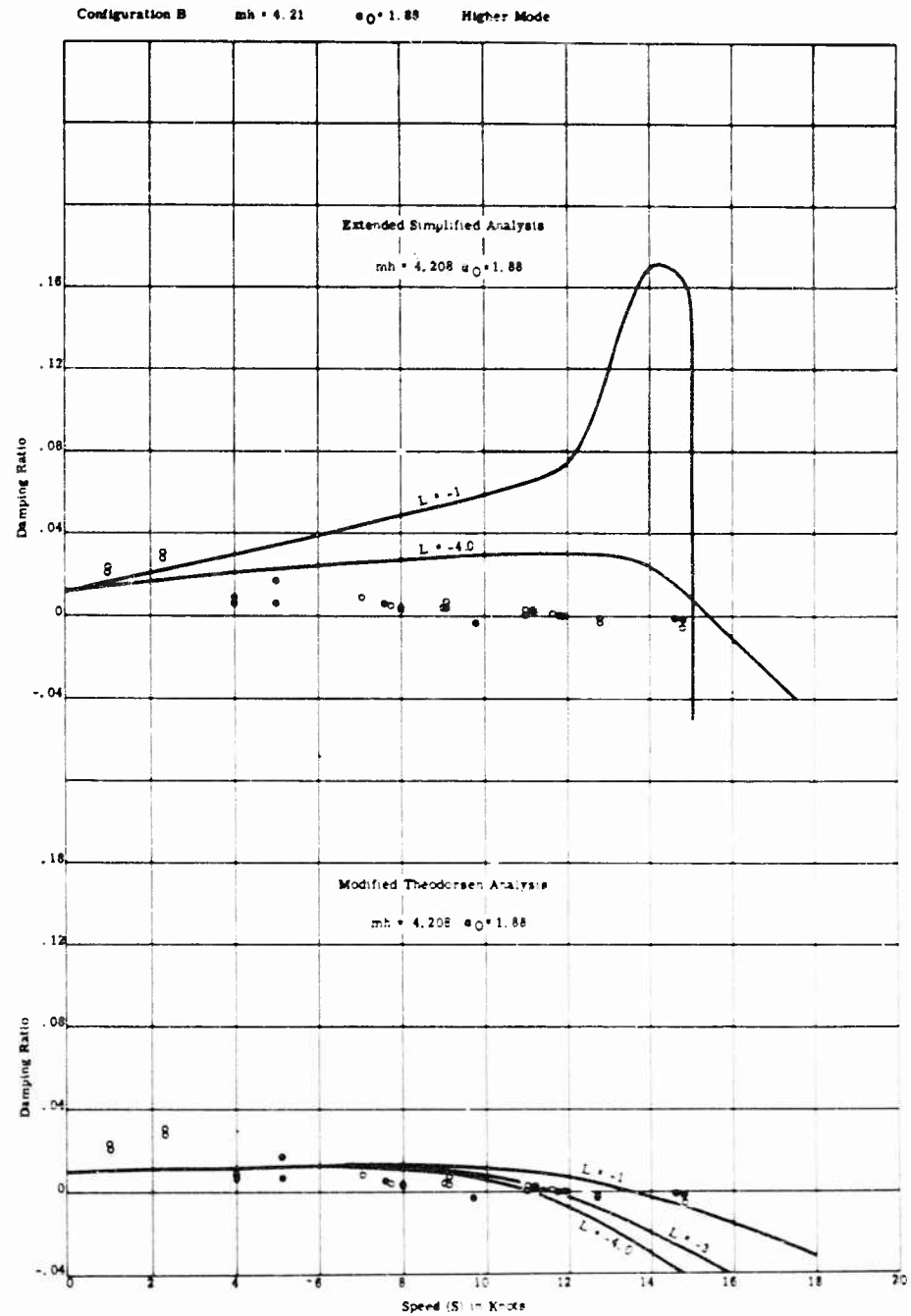
Fig. 12 - Comparison of computed and experimental damping ratios
(Configuration B, mh = 4.21 lb-sec^2)
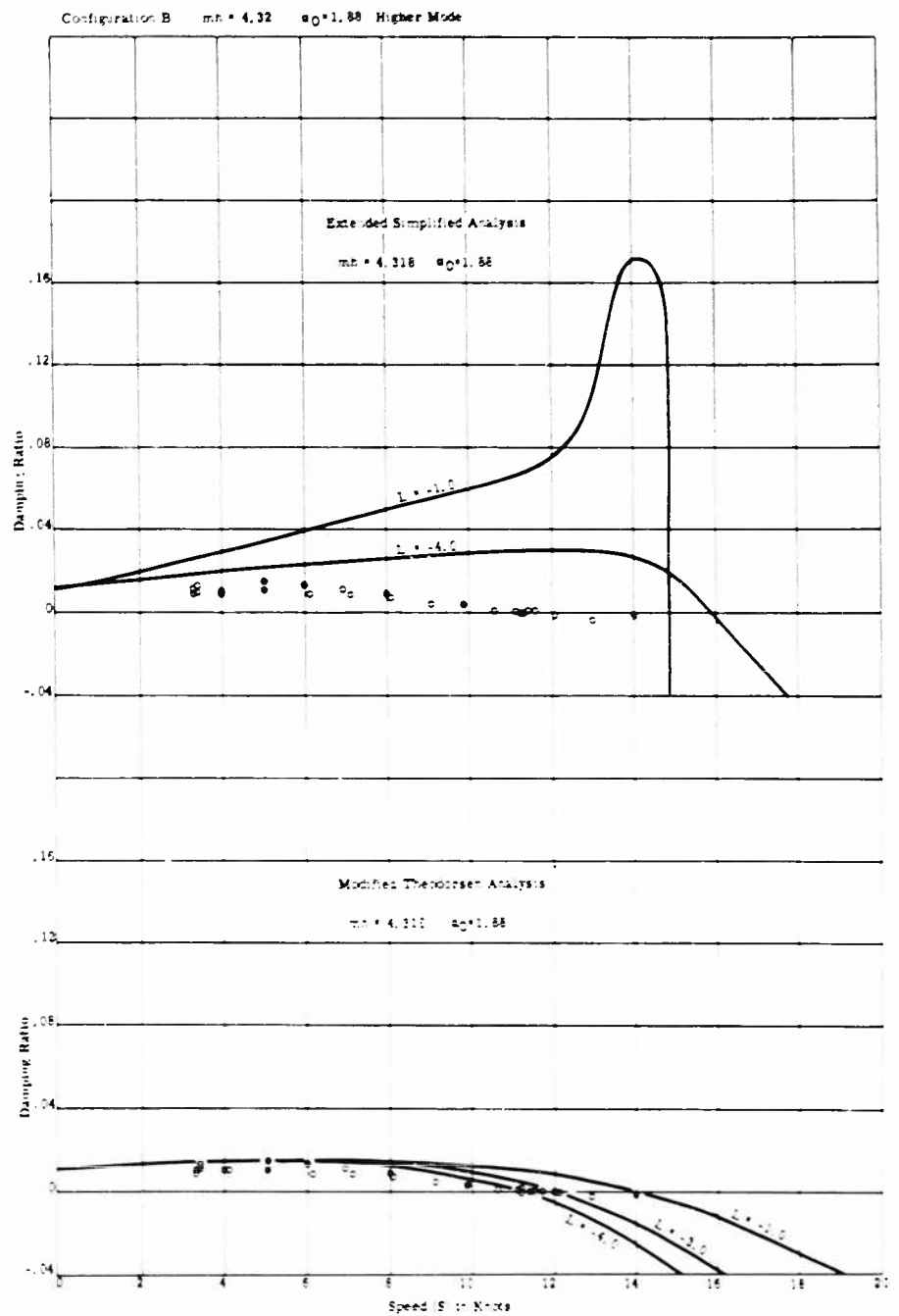
Fig. 13 - Comparison of computed and experimental damping ratios
(Configuration B, mh = 4.32 lb-sec²)
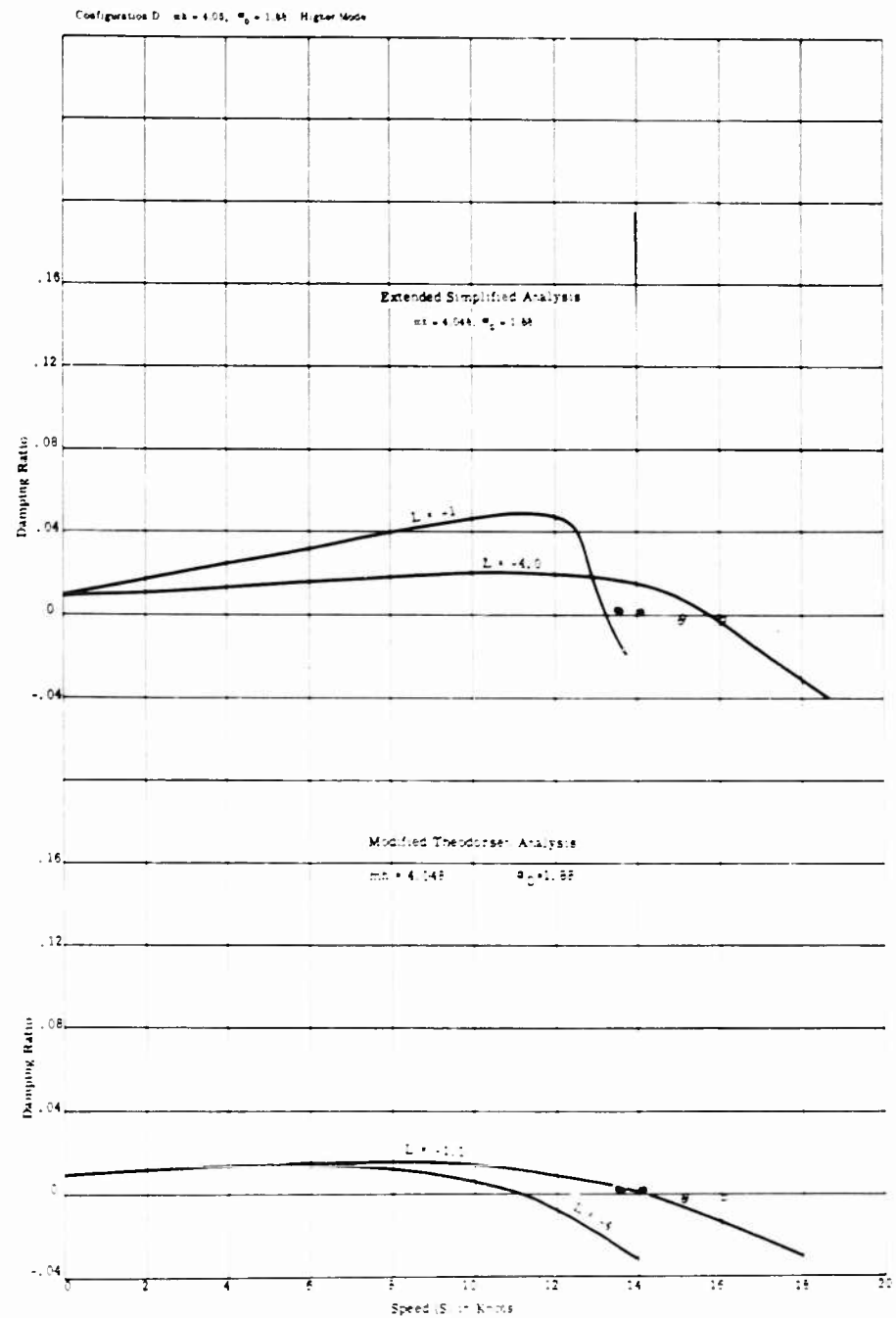
Fig. 14 - Comparison of computed and experimental damping ratios
(Configuration D, mh = 4.05 lb-sec²)
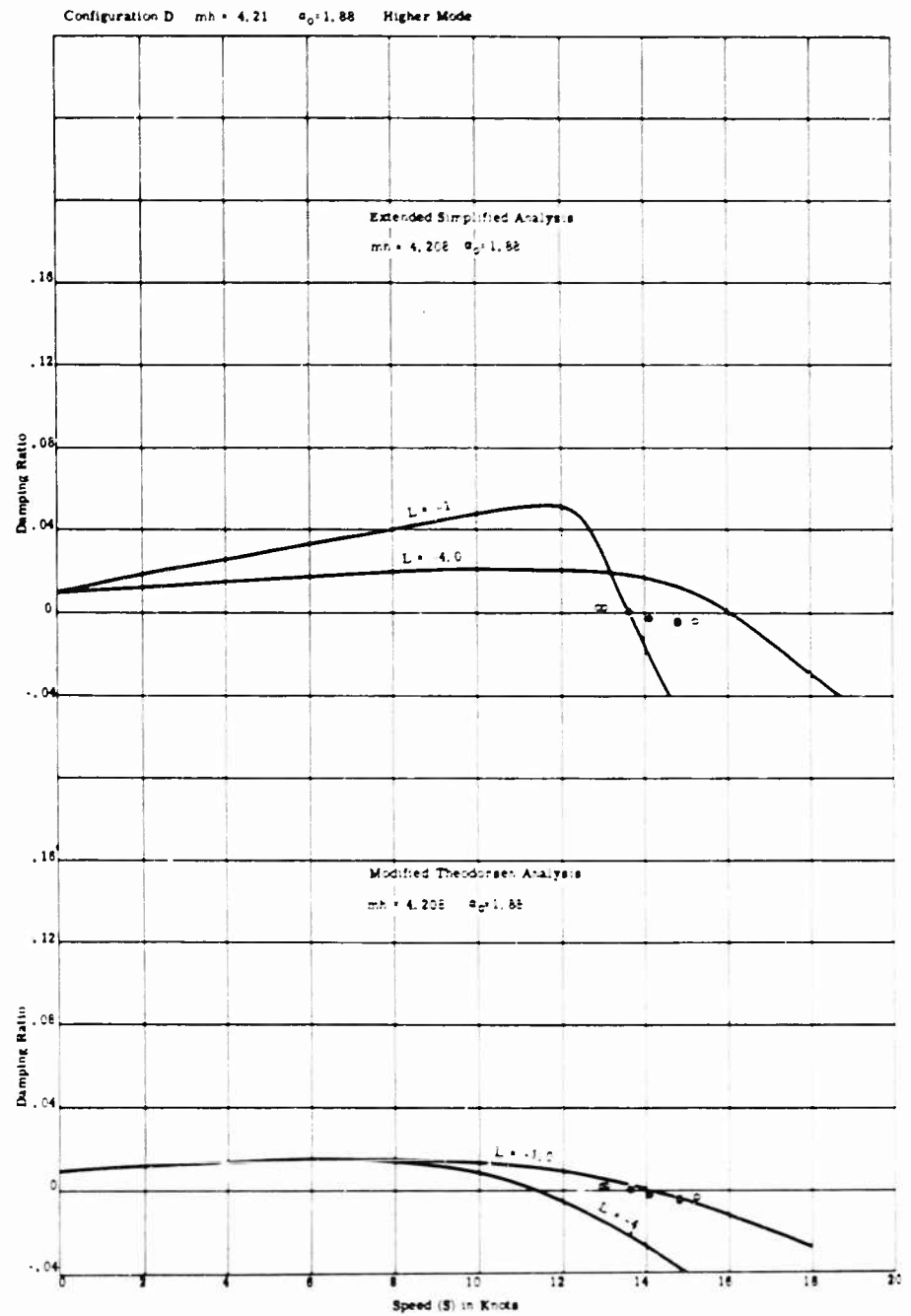
Fig. 15 - Comparison of computed and experimental damping ratios
(Configuration D, mh = 4.21 lb-sec²)

832

Comparison of Theory and Experiment for Marine Control-Surface Flutter
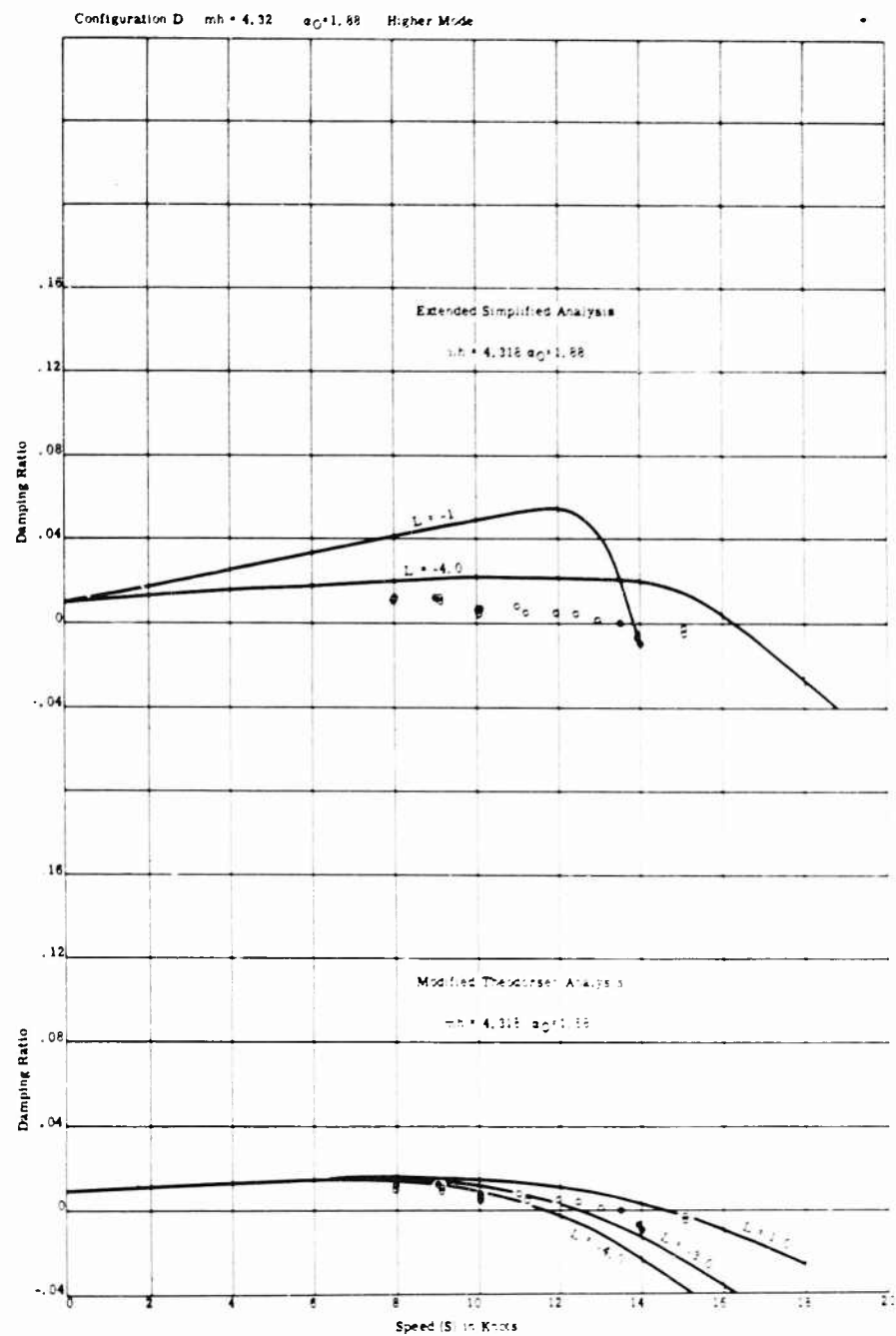
Fig. 16 - Comparison of computed and experimental damping ratios
(Configuration D, mh = 4.32 lb-sec^2)

833
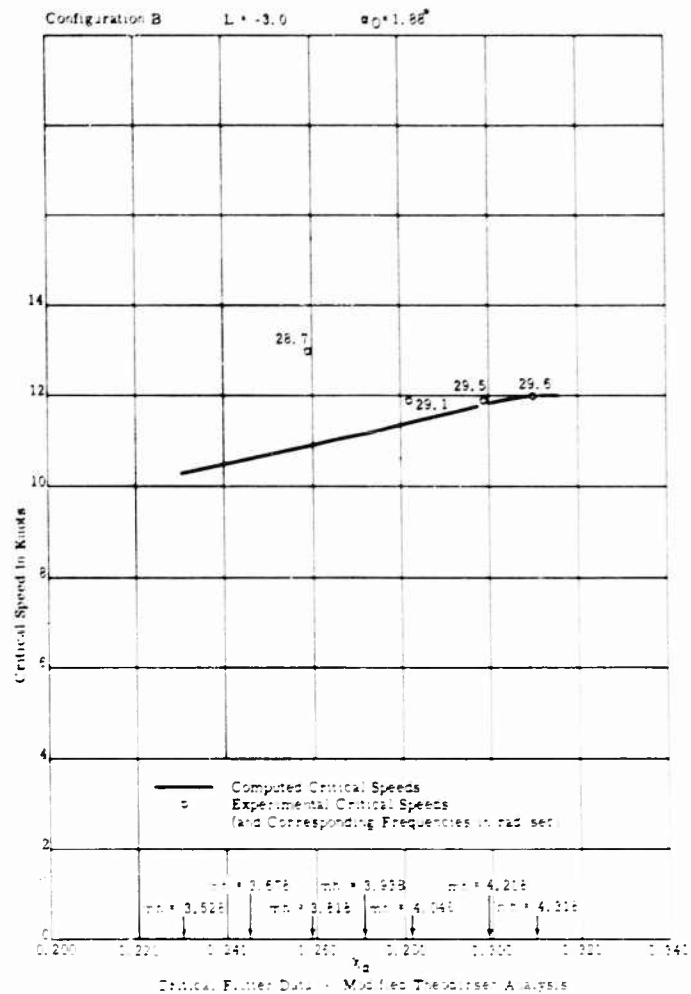
Fig. 17 - Comparison of computed and experimental critical flutter speeds for an assumed value of L (Configuration B)

Figures 4 through 6 furnish convincing evidence that results, based on the Modified Theodorsen Analysis, compare well with test data for the lower range of values of mass unbalance (~h) under consideration.* For the two lowest values of ~h (Figs. 4 and 5), the departure of analytic damping ratio curves from experimental data is generally less than 25 percent of the experimental values. At ~h = 2.0 lb-sec², the scatter of test data is much greater than at the lower ~h values; yet the analytical curve, based on the Modified Theodorsen Analysis, predicts damping ratios near the average of scattered empirical data.

*That is, for ~h = 0.0, 0.5, and 2.0 lb-sec (Configuration TMB ....)
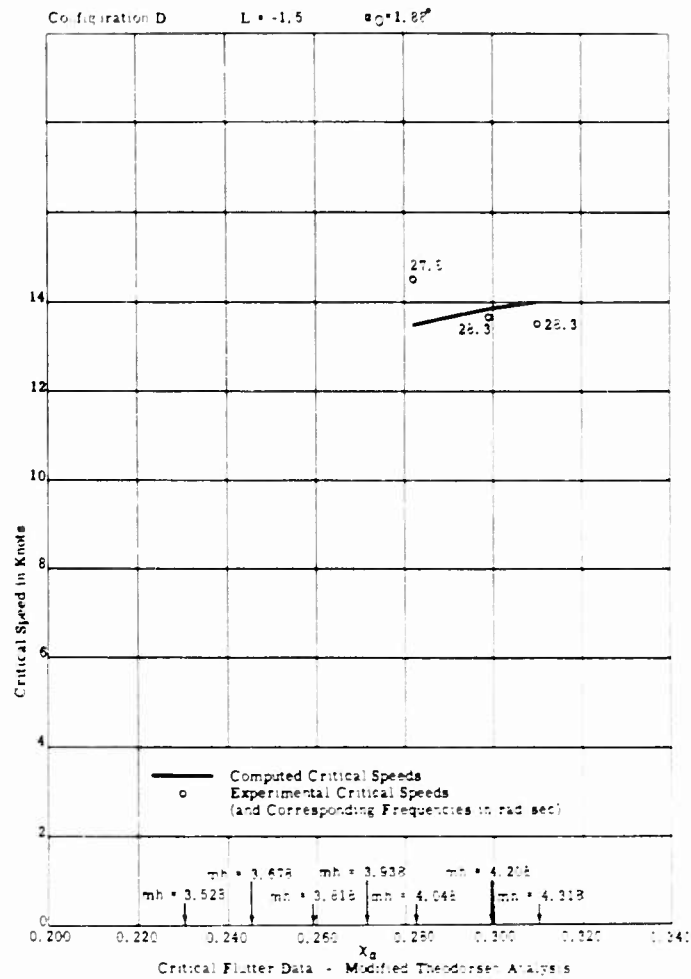
Fig. 15 - Comparison of computed and experimental critical flutter speeds for an assumed value of L (Configuration D)

In the consideration of Figs. 31 through 86, from which Figs. 7 through 16 have been abstracted, no unique value of L provides analytical curves that correlate with test data for Configurations B and D. This lack of correlation is associated with values of mass unbalance (mh) about one and one-half to two times as large as the mh values of Configuration TMB 1222, for which good correlation was obtained between test data and the Modified Theodorsen Analysis. Because experimental estimates of L were, unfortunately, not obtained for Configurations B and D, the correlation considered here is that between the region in which test data fall and a "predicted region," considered to be bounded by two curves of the

835

family of curves for the parameter L.[*] An arbitrary choice of -1 and -4 as values of L provides the bounding curves in which test data generally fall; see curves shown in Figs. 7 through 16. These bounds are associated with a rather narrow range of variation in damping ratio; the differences in ordinates of the damping ratio vs. speed curves based on the Modified Theodorsen Analysis for $L = -1$ and $L = -4$ rarely exceed 0.02 at a given speed below 15 knots. For example, in Fig. 13, the Modified Theodorsen Analysis predicts a damping ratio of 0.004 at a speed of 12.9 knots for $L = -1$ and a damping ratio of -0.014 for $L = -4$ at that speed. The difference in the ordinates for this example is thus 0.018.

Reference 2 reported that at a preset attack angle α_0[†] of zero degrees, both steady lift forces and moments were recorded. One important feature of both the Modified Theodorsen Analysis and the Extended Simplified Analysis is that they include a term for steady hydrodynamic moment due to circulation to account for this experimental observation on the TMB Flutter Apparatus with the axis of the rudder stock at the forward quarter-chord position. The classical Theodorsen analysis [2] predicts zero steady hydrodynamic moment, i.e., hydrodynamic balance when the stock is at this position, thus disagreeing with experimental observation. The presence or absence of hydrodynamic balance makes a marked difference [2] in the overall damping characteristic obtained from the flutter apparatus. It should be recognized that the hydrofoil of the flutter apparatus has an NACA 0015 cross section, i.e., its thickness is 15 percent of the chord length, which may well be a significant departure from the plane foil assumed in the classical theory.

Nevertheless, it has not been conclusively established that the preset attack angle α_0 was actually zero, because mechanical imperfections of the flutter apparatus and its mounting introduce uncertainties as high as 0.5 deg in nominal values of α_0. The values of α_0 considered in this report are small ($\alpha_0 = 0.0$ deg and 1.88 deg). Therefore, uncertainties in α_0 must be considered as a possible explanation of the apparently observed nonzero lift and moment at $\alpha_0 = 0°$.

There is no conclusive evidence, either from experiments or theoretical considerations, to cause one or the other of the preceding explanations to account for the observation of lift forces and moments at $\alpha_0 = 0$ deg, as reported in [2]. For further discussion of the parameter L associated with these moments, see Appendix D.

When applied to the TMB Flutter Apparatus, the classical Theodorsen equations [2,3]:

1. Yield a steady lift force about three times as large as that found experimentally; i.e., the computed force and moment do not converge to the value of

---

the experimental steady lift force and moment at zero frequency. Hence, they cannot predict divergence, which is usually included in a flutter analysis.

2. Show no dependence on the mean angle of attack, whereas the steady moment was found to vary with the mean angle of attack.

3. Show good agreement with observed critical speeds over a limited range of mh [7]. However, this reference gives no information on agreement of predicted frequencies and phase relations. A sound method should check in all respects.

It should be noted that the majority of the conditions explored experimentally and reported in [7] show the "mild flutter" condition in which the inclusion or omission of structural damping can make a relatively large difference in the predicted critical flutter speed.

Analytical curves of damping ratio vs. speed based on the Extended Simplified Analysis do not fall along, or generally near, the experimental data plotted except for the two lowest values of mass unbalance (mh) employed; i.e., mh = 0.0 and 0.3 lb-sec^2; see Figs. 4 through 6.

For analog solutions of the equations of motion, initial conditions imposed on the foil must be taken into consideration. In general, when arbitrary initial conditions are assumed, the solutions $Y(t)$ and $\theta(t)$ of the differential equations of motion for the flutter apparatus represent the superposition of two modes of vibration. The solution can, however, be restricted to represent a single mode of vibration; one of the two modes can be suppressed, if the initial conditions are properly chosen. This will eliminate the possibility of beating between modes, which is the cause of "temporarily suppressed flutter," discussed under Analog Determination of Flutter Response.* Criteria for the proper selection of initial conditions to cause one mode to predominate in the total response are established in Appendix E. For a discussion of initial conditions as they affect the vibration of a ship's rudder, see Appendix F.

In Figs. 17 and 18 the regions in which experimental and analytical data fall are quite close and sometimes overlap. This suggests a strong dependence of critical flutter speed upon the parameters mh and L. Note that a good correlation of observed and analytical critical speeds as functions of mh are possible only by violating the assumption, made in [2], that L is a function of α_0 only. For, in Fig. 17, a value of $L = -3.0$ was assumed to correspond to $\alpha_0 = 1.88$ deg, whereas in Fig. 18, a value of $L = -1.5$ was assumed to correspond to $\alpha_0 = 1.88$ deg. Therefore, the "correlation" between theory and experiment shown in Figs. 17 and 18 has no meaning other than to indicate that L is apparently a function of mh as well as of α_0. (See Recommendation 2.)

---

*This does not imply that "temporarily suppressed flutter" will necessarily occur when two modes beat.

CONCLUSIONS

The preceding comparison of analytical stability predictions with available test data, although quite limited in extent, nevertheless leads to the following conclusions:

1. The Modified Theodorsen Analysis, as compared with the Extended Simplified Analysis, appears to be the most suitable analysis for yielding good predictions of damping ratio and frequency for a given speed and for predicting critical flutter speeds.

2. The Extended Simplified Analysis correlates well with test data for only the two lowest values of mh investigated; i.e., $mh = 0.0$ and 0.3 lb-sec^2. This analysis is therefore considered to be quite limited in its applicability to the problem of predicting flutter.

3. The accuracy of the Modified Theodorsen Analysis apparently improves as mass unbalance mh is decreased. The dependence of L on parameters other than x_0 (such as mh or speed) might be profitably investigated to extend the range of parameters over which the Modified Theodorsen Analysis correlates well with test data (see Recommendation 2).

4. The ship designer requires the simplest analysis that will yield predictions consistent with experimental observations. The results obtained for theoretical and experimental data indicate that the Modified Theodorsen Analysis might yield more realistic predictions for ship control-surface systems than the more elaborate equations used in the classical flutter theory.

RECOMMENDATIONS

To further the development of practical design criteria for avoiding control-surface flutter, the following recommendations are made:

1. A series of hydrofoil towing tests should be conducted to determine

a. the point of application of the hydrodynamic lift force on the foil and

b. whether steady lift and moment do occur at $x_0 = 0$ deg. These tests may not be possible on the existing TMB Control Surface Flutter Apparatus because of the uncertainties in measurements of x_0 that are inherent in the present device. Therefore, in the design of future hydrofoil flutter apparatus, consideration should be given to methods of measuring the chordwise location of center of pressure for variations in x_0; see Recommendation 2. It is recommended at this stage that the value of L, the distance between the axis of rotation and the center of pressure, be determined by taking the ratio of the observed moment and lift force as indicated in [2].

2. If the location of the lift force as determined in accordance with Recommendation 1, is found to depart significantly from the forward quarter-chord position, a series of tests should be carried out to determine the dependence of L on other parameters, as well as on x_0. The result of this recommended

study will be a graphical, or possibly an analytical, relation between L and these parameters. In addition, the assumption that the oscillatory lift and moment follow the steady relations should be investigated. The more realistic expression for L so obtained might then be used in conjunction with the Modified Theodorsen Analysis to extend the range of physical parameters over which that analysis agrees well with experimental findings.

3. A study of the applicability of the classical Theodorsen approach to flutter prediction for model and full-scale rudders should be undertaken along with a continuing study of both the Extended Simplified and Modified Theodorsen Analyses. Investigation of the latter two analyses is particularly stressed because of the relative ease with which they may be applied and because they are formulated in dimensional terms common to present vibrations analysis practice. It would be of value to apply the classical Theodorsen equations to the experimental data published in this report.

A model devised for flutter investigation should be designed so that its experimental operating conditions and (certain) parameter values are similar to those for the full-scale rudder; see Appendix G.

In evaluating the applicability of the classical Theodorsen or other analyses for flutter prediction, it is desirable to experimentally determine the reaction on vibrating rudders and/or rudder models. (In Appendix H an analysis is given for the reduction of the classical Theodorsen results to concrete form. The dependence of the derived formulas on ship parameters is shown, and a discussion is given of the applicability of Theodorsen's results to rudders and the need for measurements of the reactions on the rudder.)

4. The discrepancy between stability predictions based on the Routh discriminant* of the frequency quartic equation, and on solutions of that same equation as reported in the present study, should be resolved.

5. The dependence of critical flutter speed on mass unbalance should be investigated.

6. It is suggested that dimensional notation be used in any hydroelastic analysis made for consistency with existing codes at the Applied Mathematics Laboratory on hull vibration analysis. While dimensionless notation has found wide acceptance by naval architects and aeronautical engineers, it is not widely used in the analysis of mechanical vibration at the present time.

ACKNOWLEDGMENTS

---

*Stability predictions for Configuration TMB 1222, based on the Routh discriminant, can be found in [2], where a discrepancy is also shown to exist between the Routh criteria for stability and experimental results.

They also wish to thank Messrs. L.K. Meals and E.W. Haskins of the TMB Applied Mathematics Laboratory for coding the solution of the frequency quartic equation. Dr. F. Theilheimer of that laboratory contributed substantially to the mathematical analysis given in Appendix E.

Dr. E.H. Kennard made a substantial contribution to the analysis given in Appendix H.

Messrs. D.L. Greenberg, J.W. Church, and F.W. Palmer contributed to the analog study of the equations of motion of the TMB Control Surface Flutter Apparatus.

Appendix A

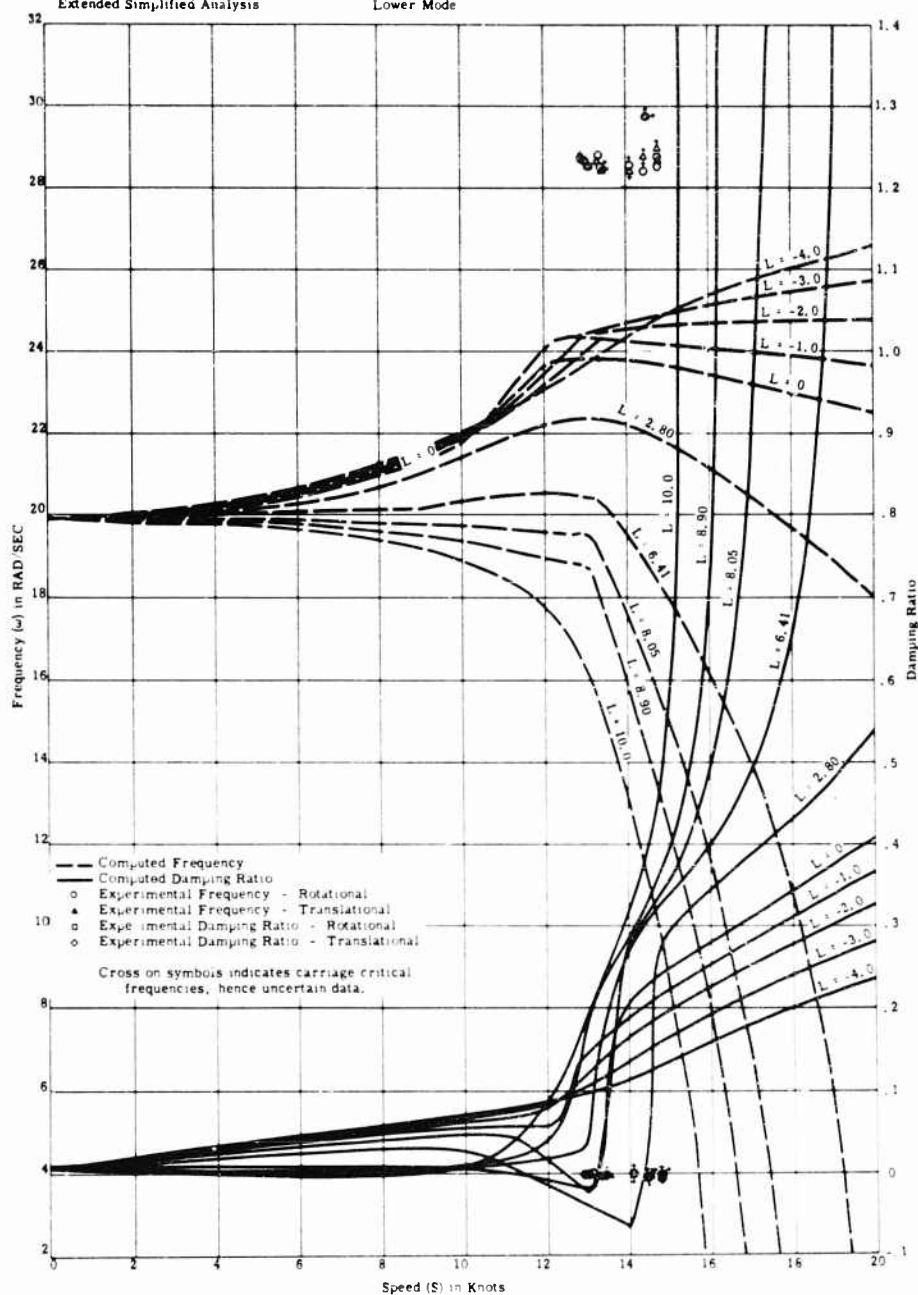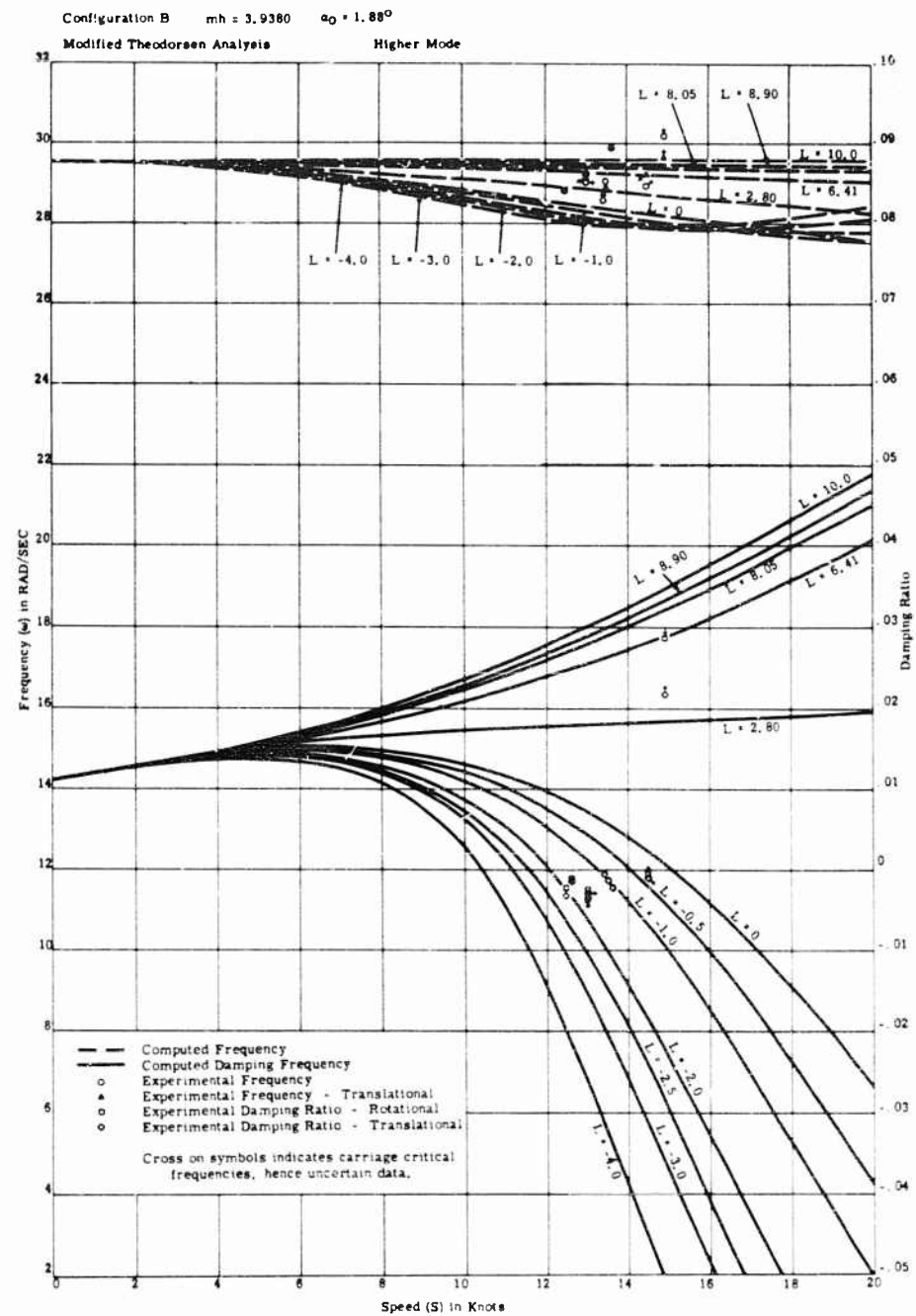### COMPARISON OF PREDICTED AND OBSERVED DAMPING RATIOS AND ASSOCIATED FREQUENCIES FOR THE TMB CONTROL SURFACE FLUTTER APPARATUS

Analytical curves of damping ratio and frequency vs. speed, obtained from digital solutions of the frequency quartic equation based on both the Extended Simplified and Modified Theodorsen Analyses, are presented in Figs. 19 through 86 for combinations of the parameters given in Table 3.

Table 3
Numerical Values of Parameters mh, L, S, and z_0 for which Analytical Frequency and Stability Predictions Have Been Made

Parameters	Dimensions	Numerical Values
		Configuration TMB 1222
mh	lb-sec^2	0.0, 0.3, 2.0
L	inches	0.0, 2.8, 6.41, 8.05, 8.90, 10.0
S	knots*	0.0 to 20.0 in 1-knot increments
z_0	degrees	0.0
		Configurations B and D
mh	lb-sec^2	3.53, 3.68, 3.82, 3.94, 4.05, 4.21, 4.32
L	inches	-4, -3, -2, -1, 0, 2.8, 6.41, 8.05, 8.90, 10.0
S	knots*	0.0 to 20.0 in 1-knot increments
z_0	degrees	1.88

*In performing calculations, S must be in units consistent with those of the other parameters; i.e., in inches per second. For convenience of the reader, speeds are indicated in knots in Figs. 4 through 86. For each configuration, all possible permutations of the above parameters were considered analytically.

Fig. 19 - Comparison of predicted and observed damping
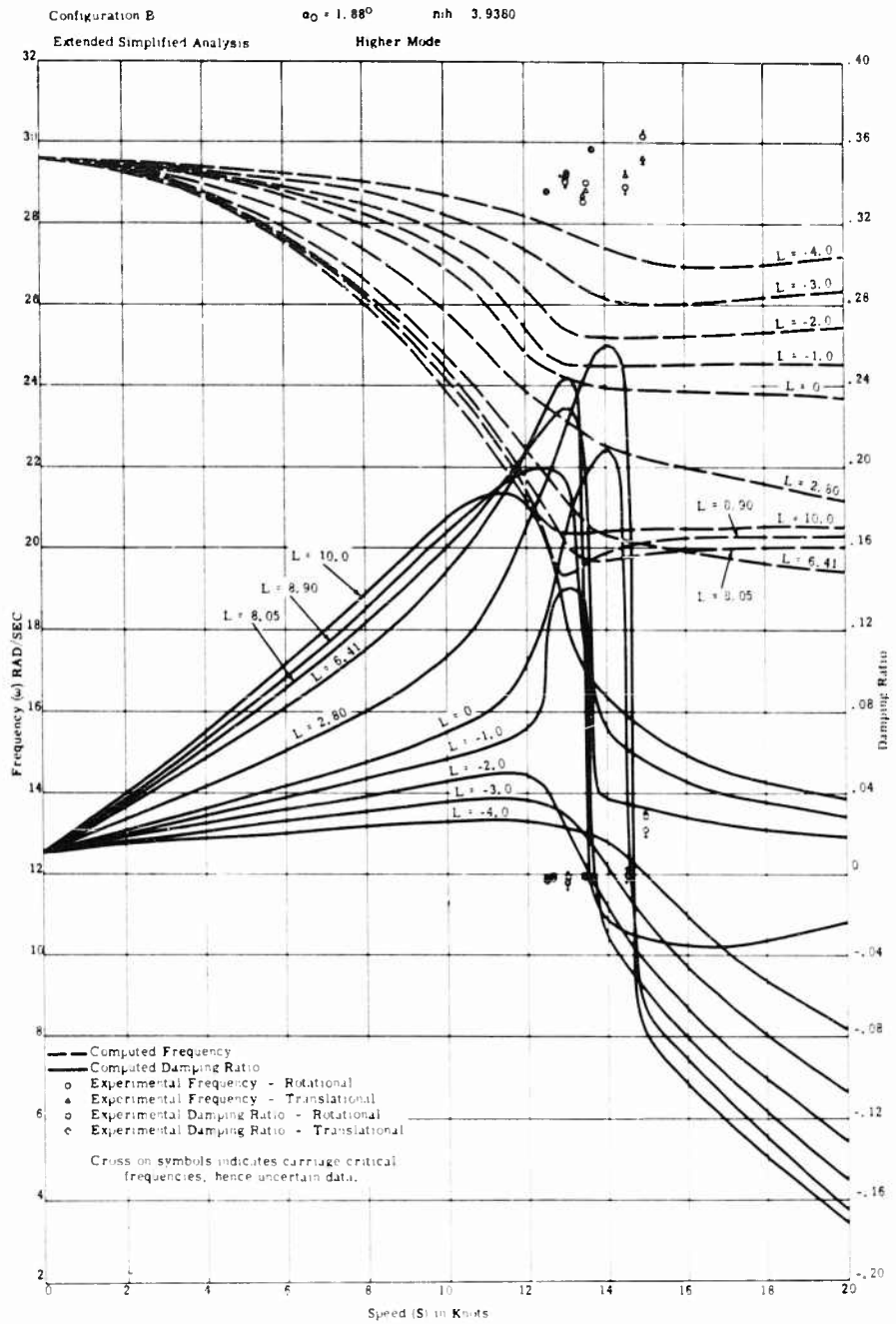ratios and associated frequencies for the TMB control
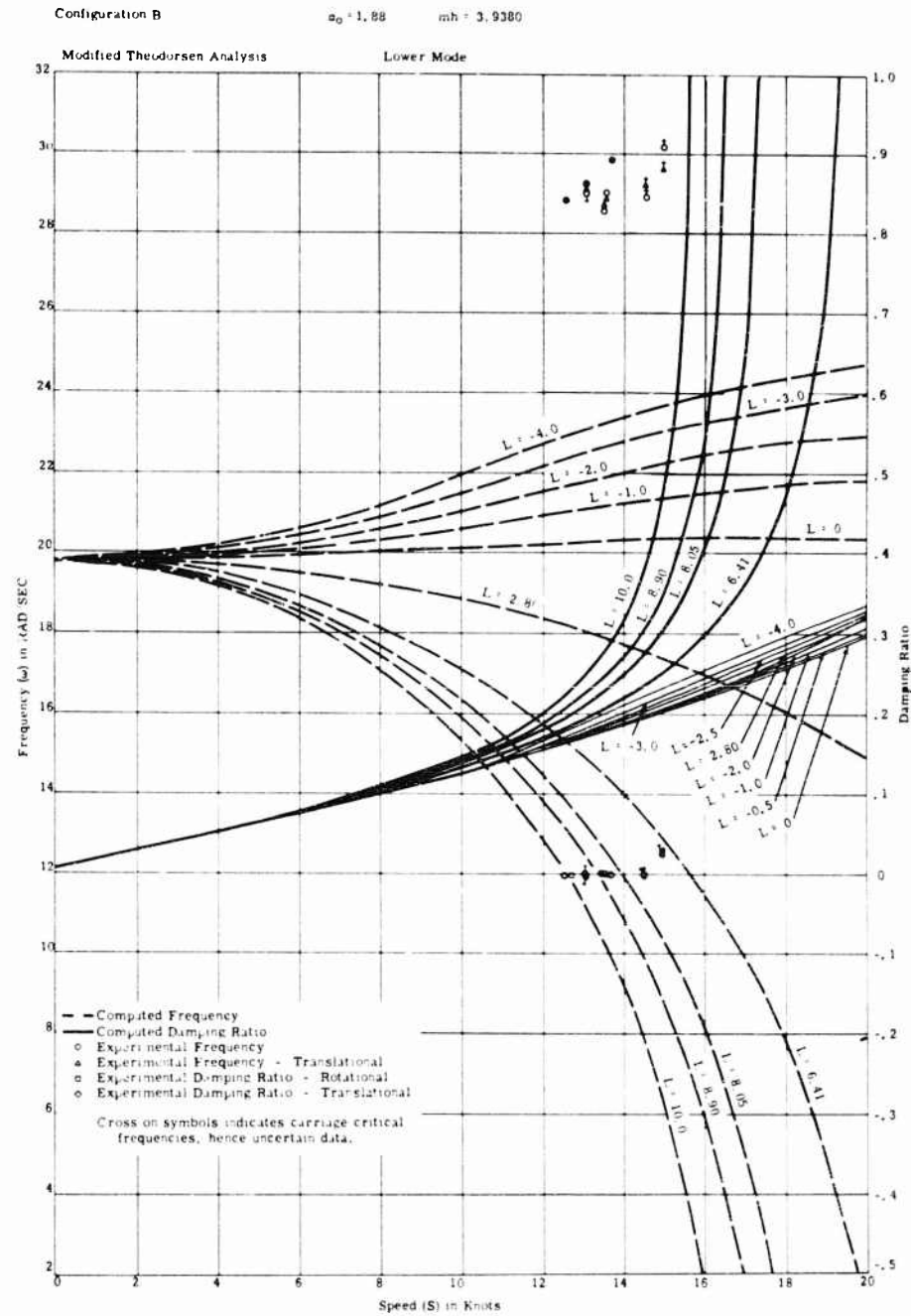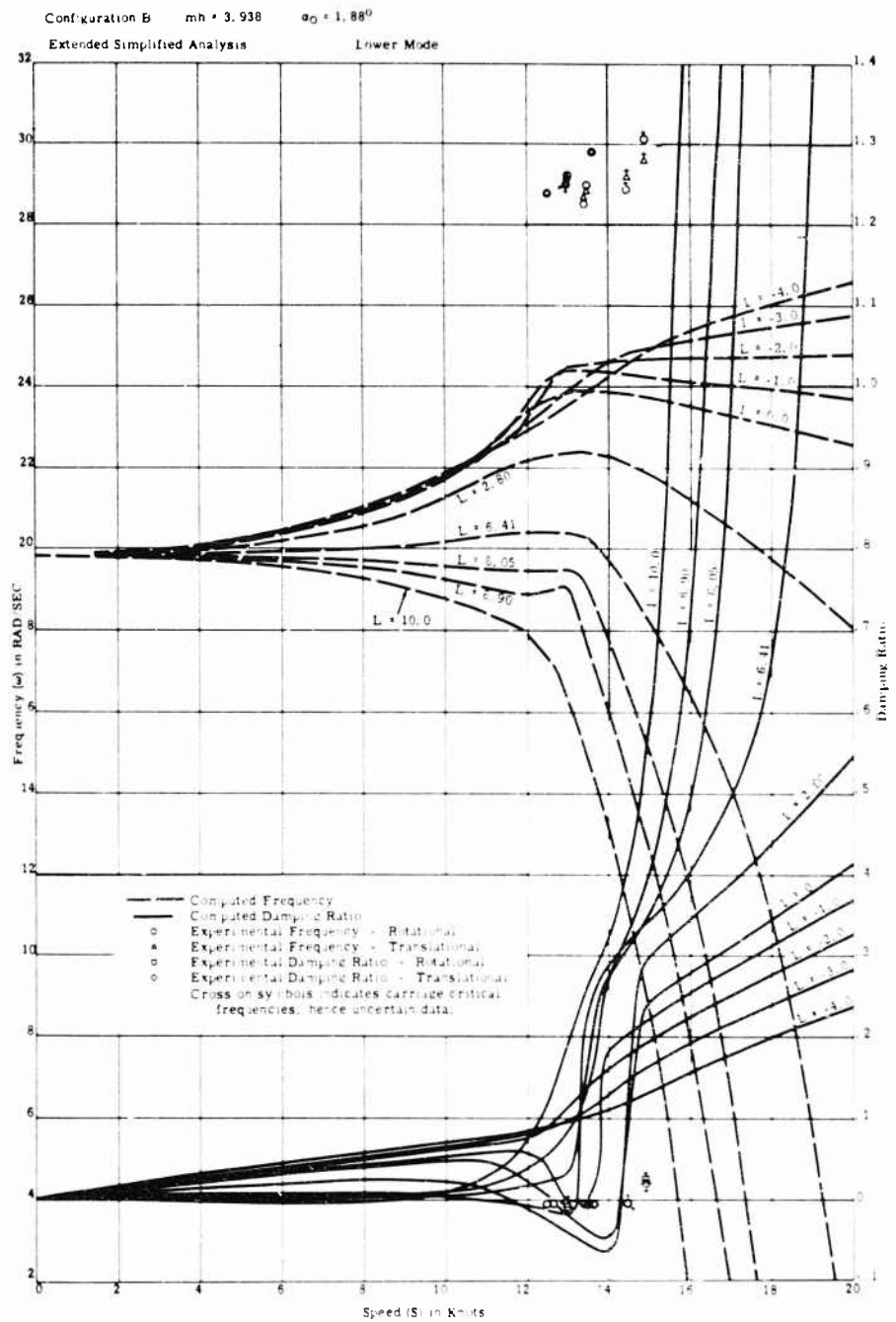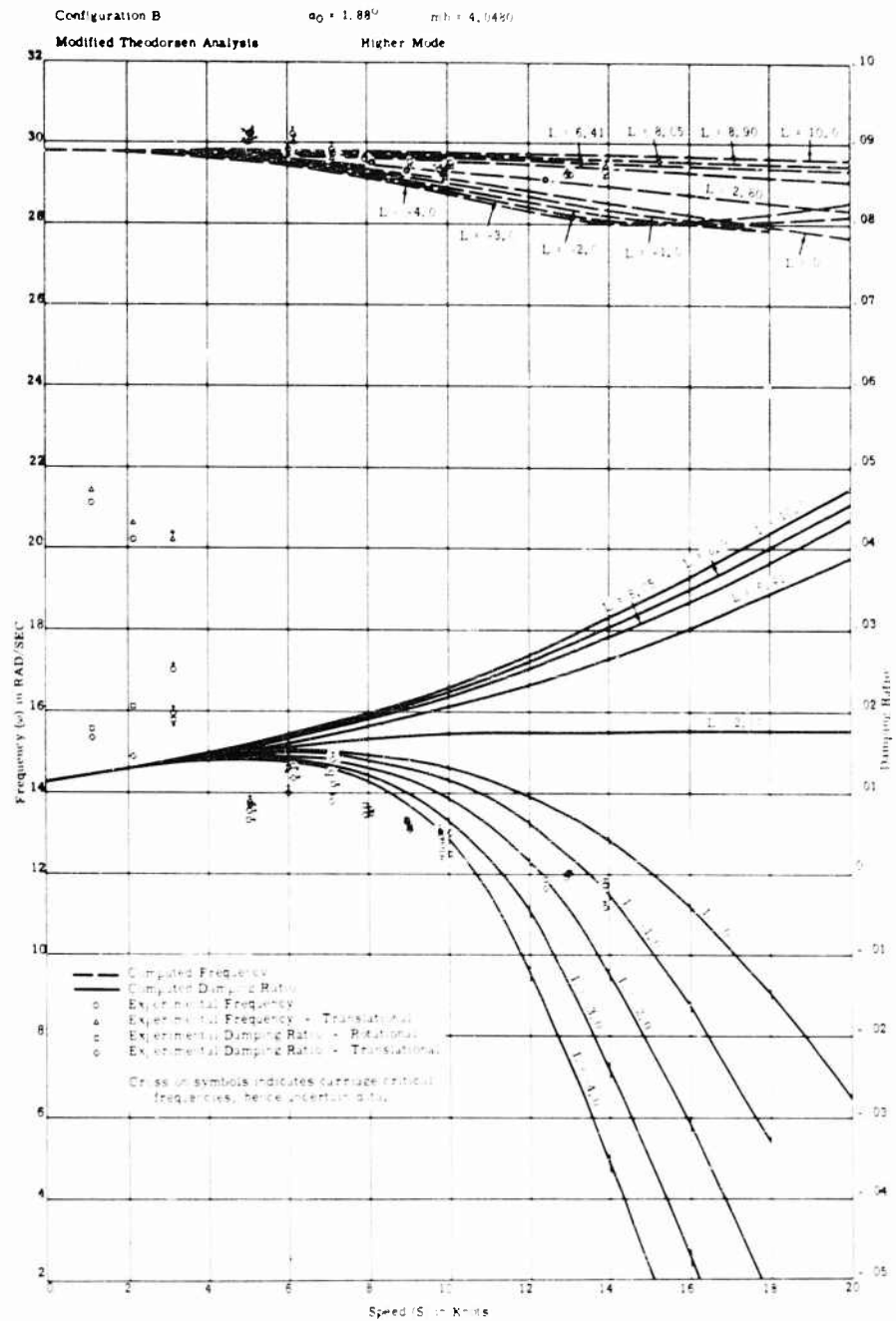surface flutter apparatus

841
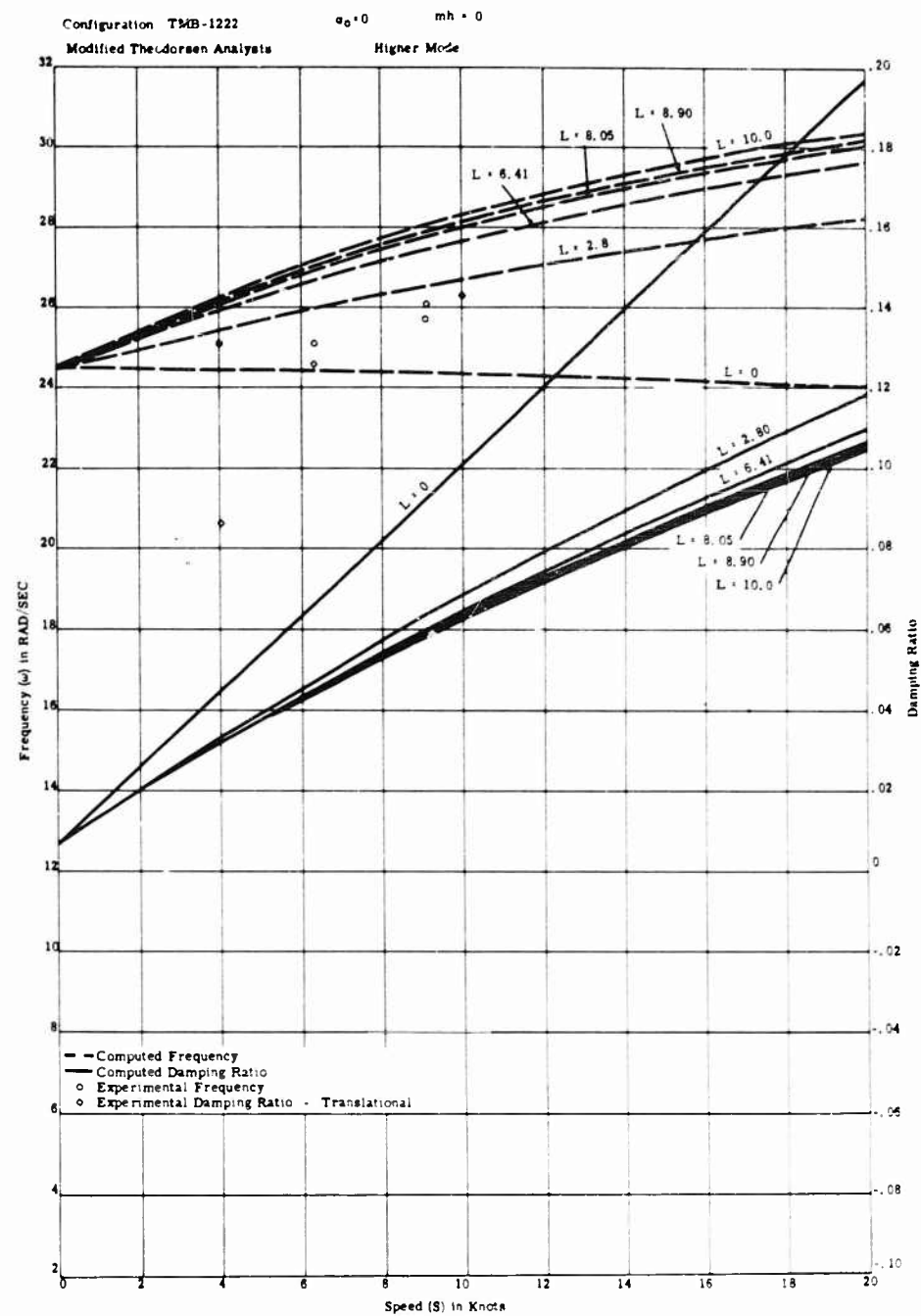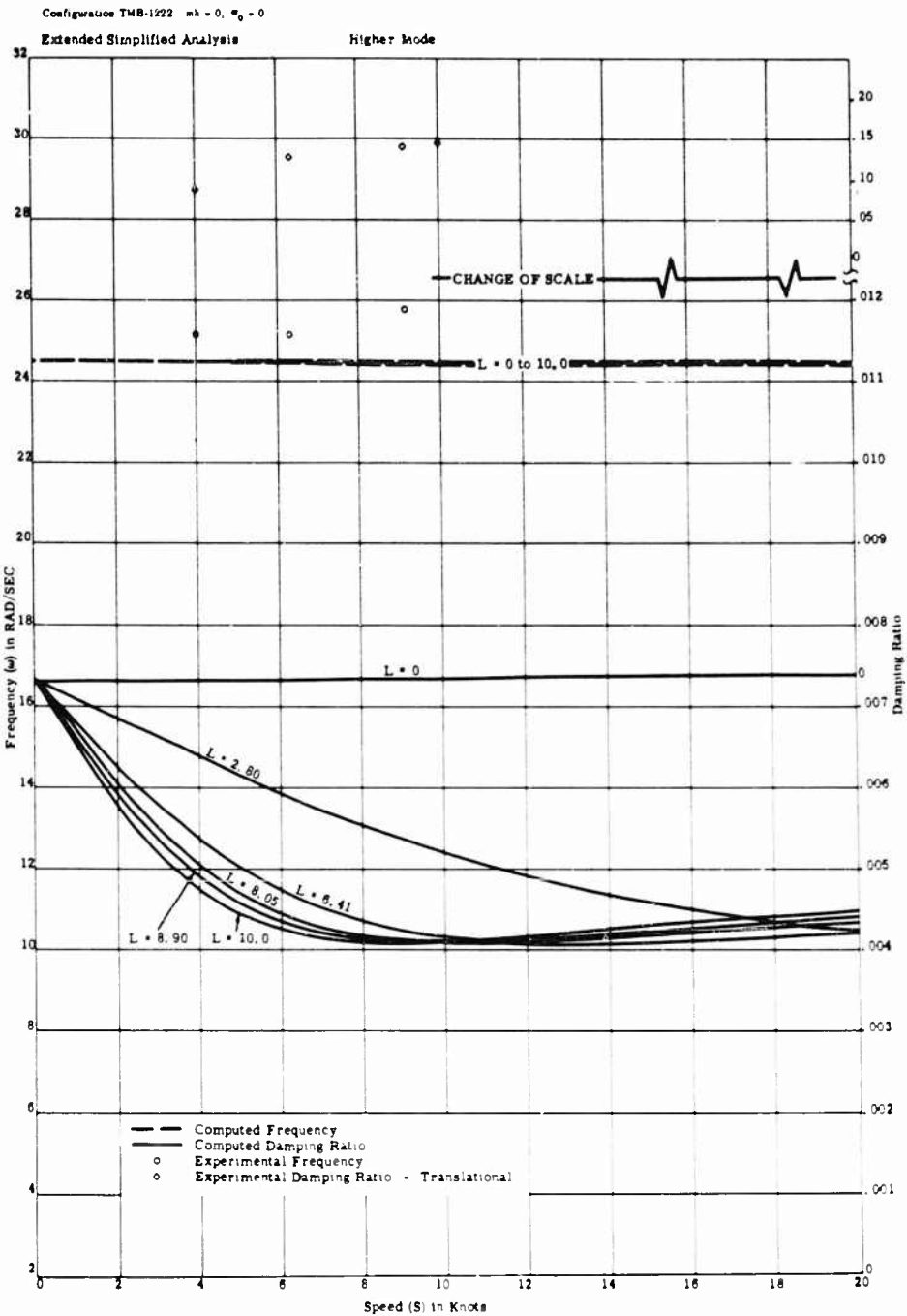
Fig. 20 - Comparison of predicted and observed damping
ratios and associated frequencies for the TMB control
surface flutter apparatus
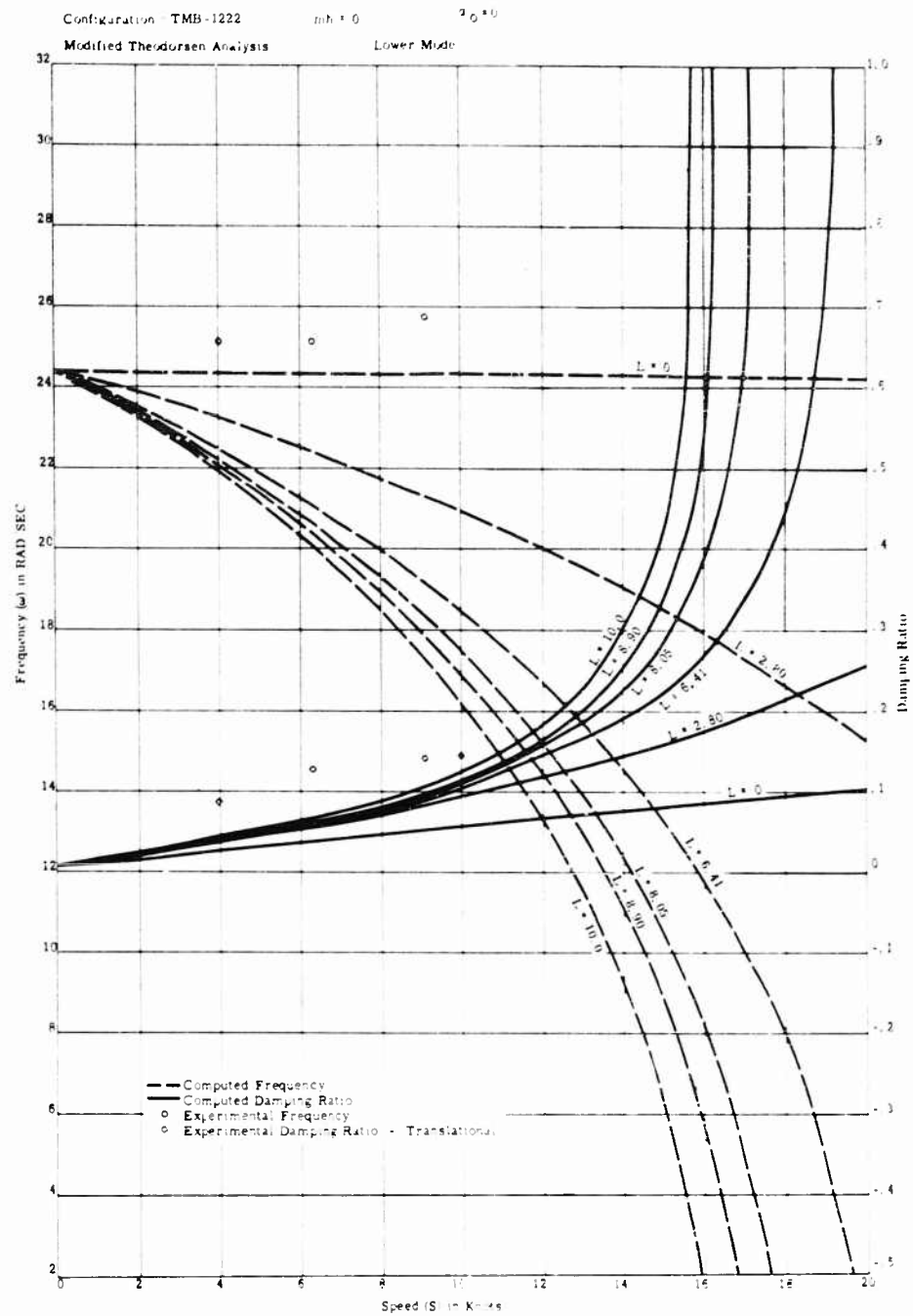
Fig. 21 - Comparison of predicted and observed damping ratios and associated frequencies for the TMB control surface flutter apparatus

843
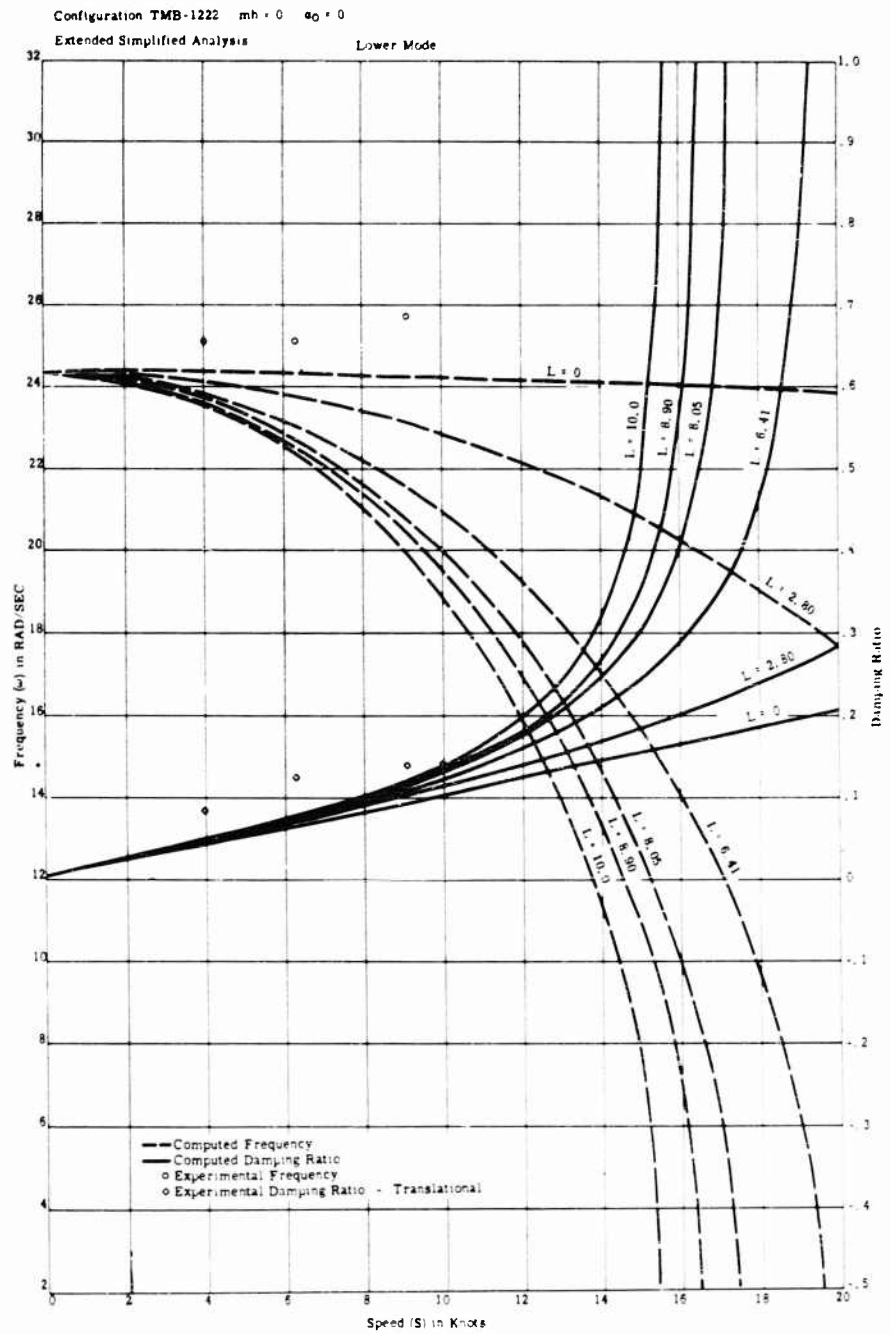
Fig. 22 - Comparison of predicted and observed damping
ratios and associated frequencies for the TMB control
surface flutter apparatus

844

Comparison of Theory and Experiment for Marine Control-Surface Filter
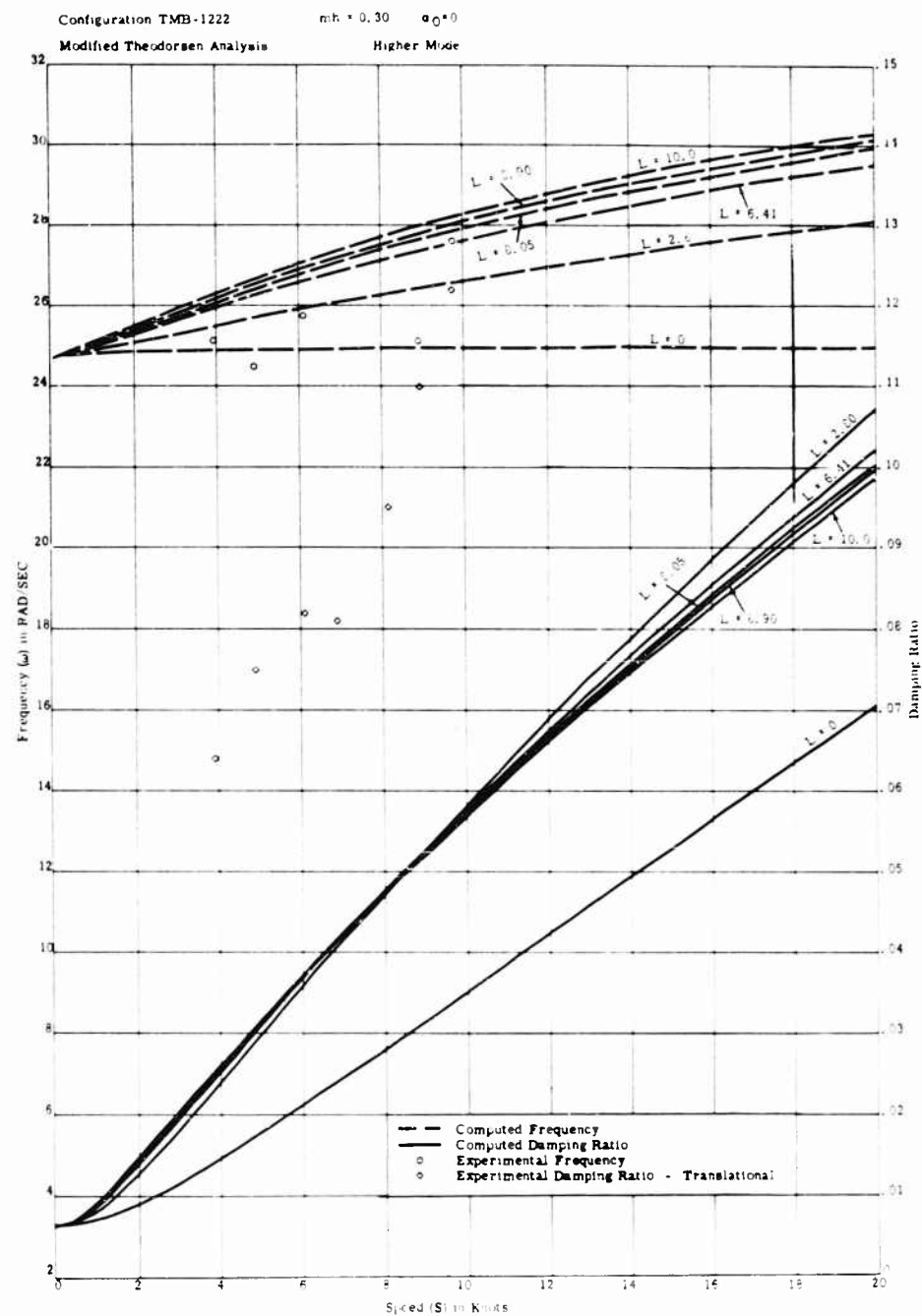
Fig. 23 - Comparison of predicted and observed damping
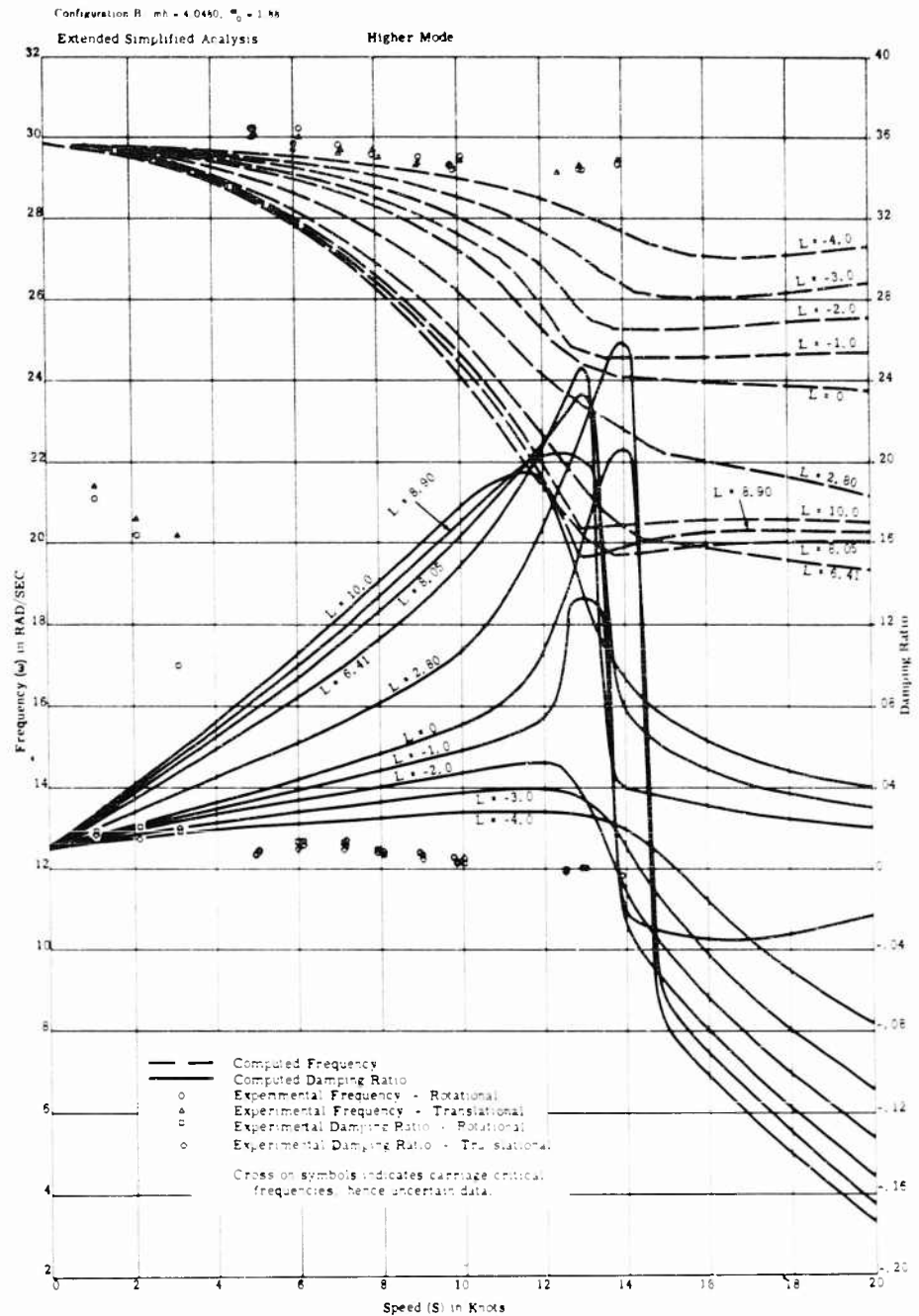ratios and associated frequencies for the TMB control
surface flutter apparatus
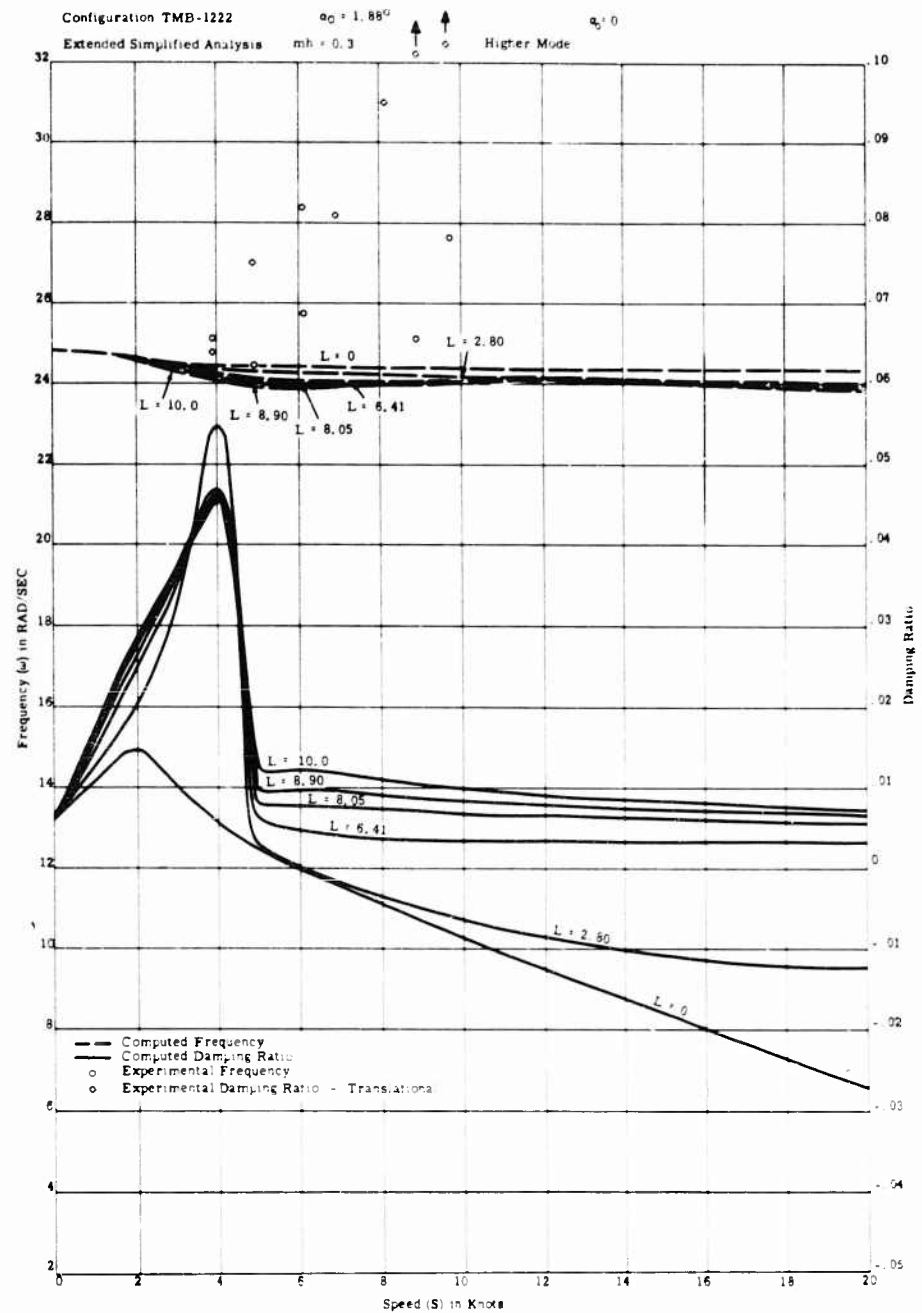
Fig. 24 - Comparison of predicted and observed damping ratios and associated frequencies for the TMB control surface flutter apparatus

846

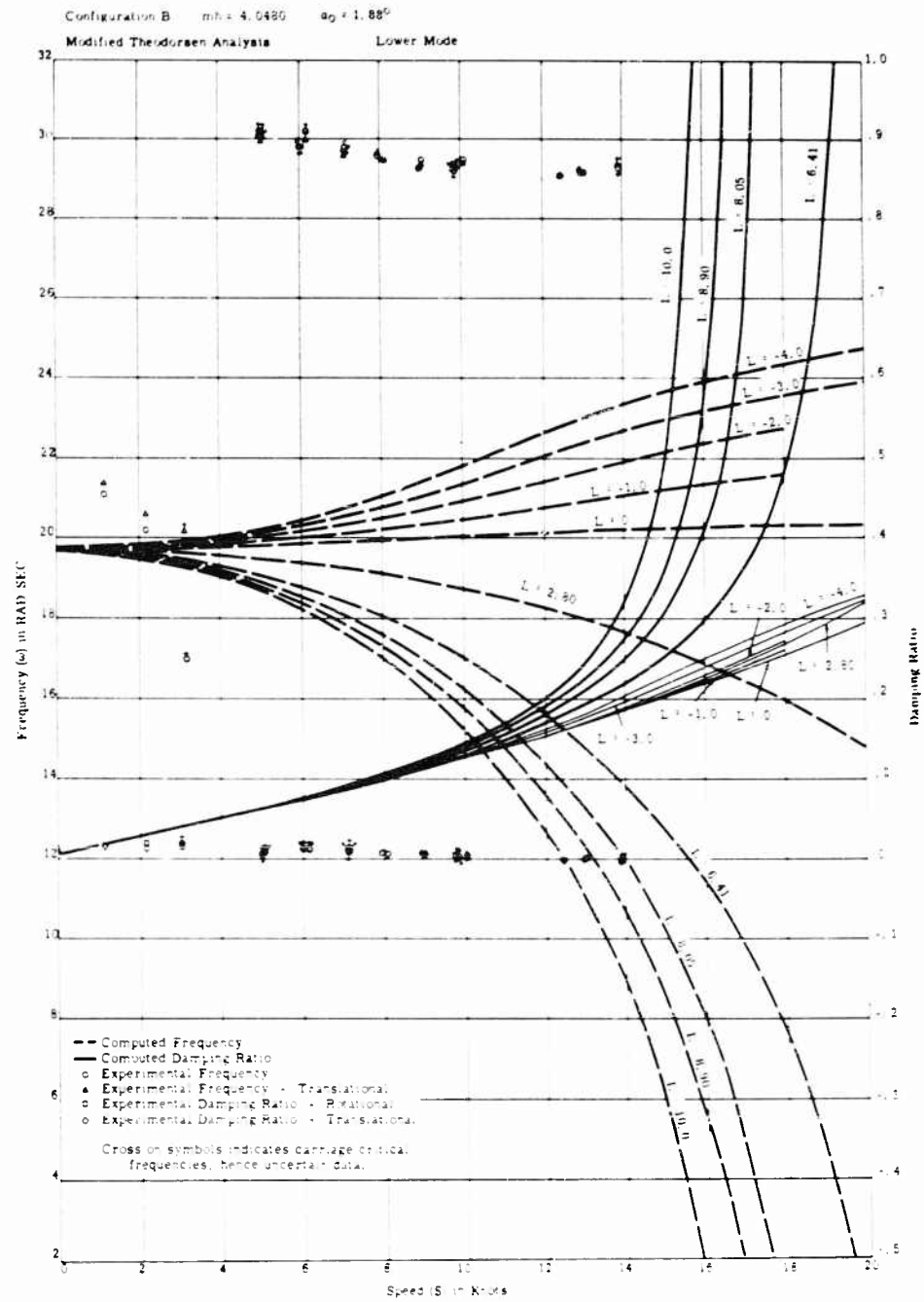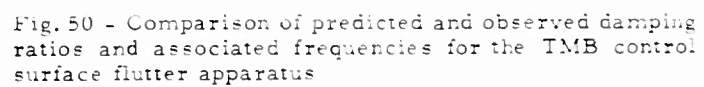Comparison of Theory and Experiment for Marine Control-Surface Flutter
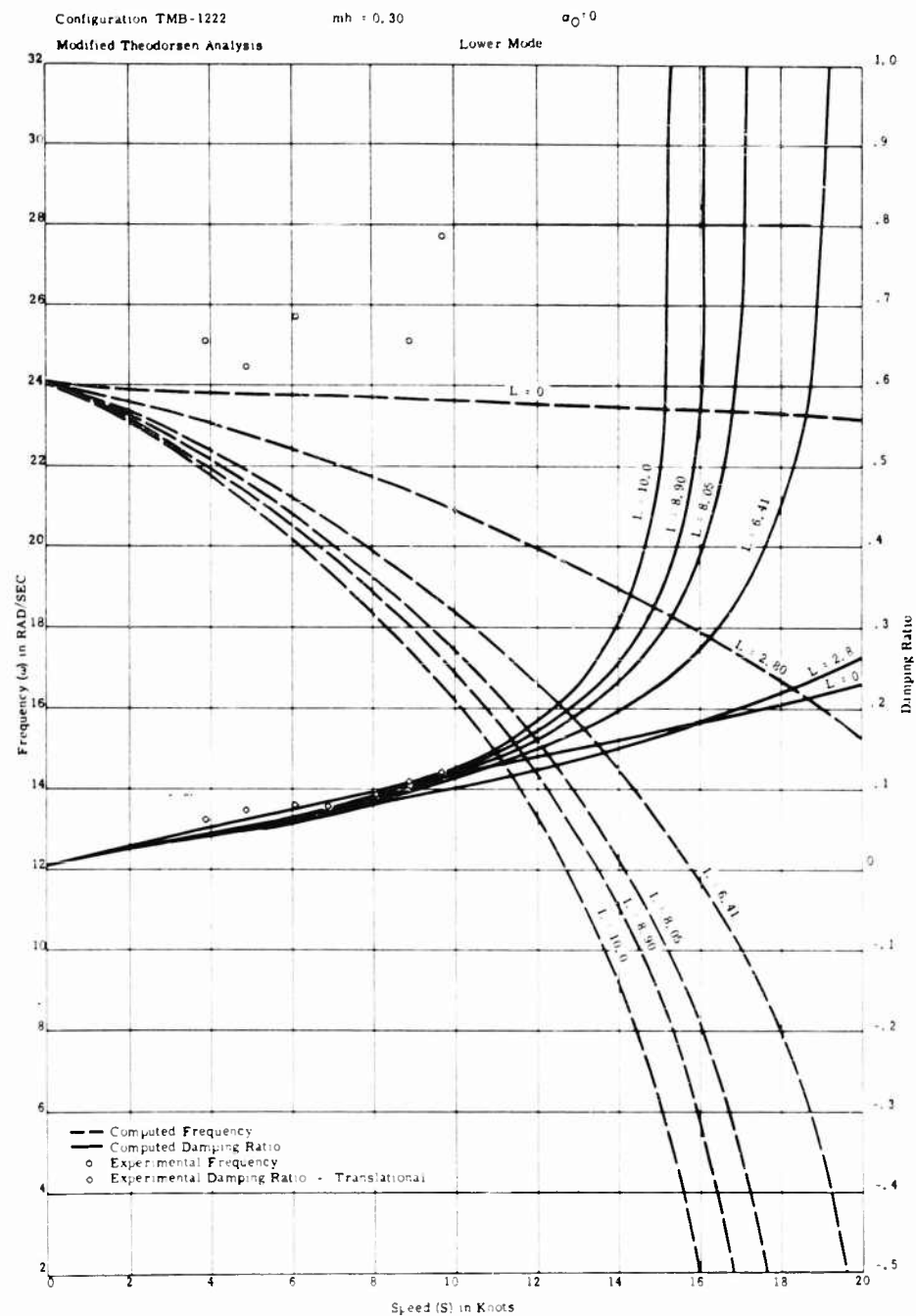
Fig. 25 - Comparison of predicted and observed damping
ratios and associated frequencies for the TMB control
surface flutter apparatus
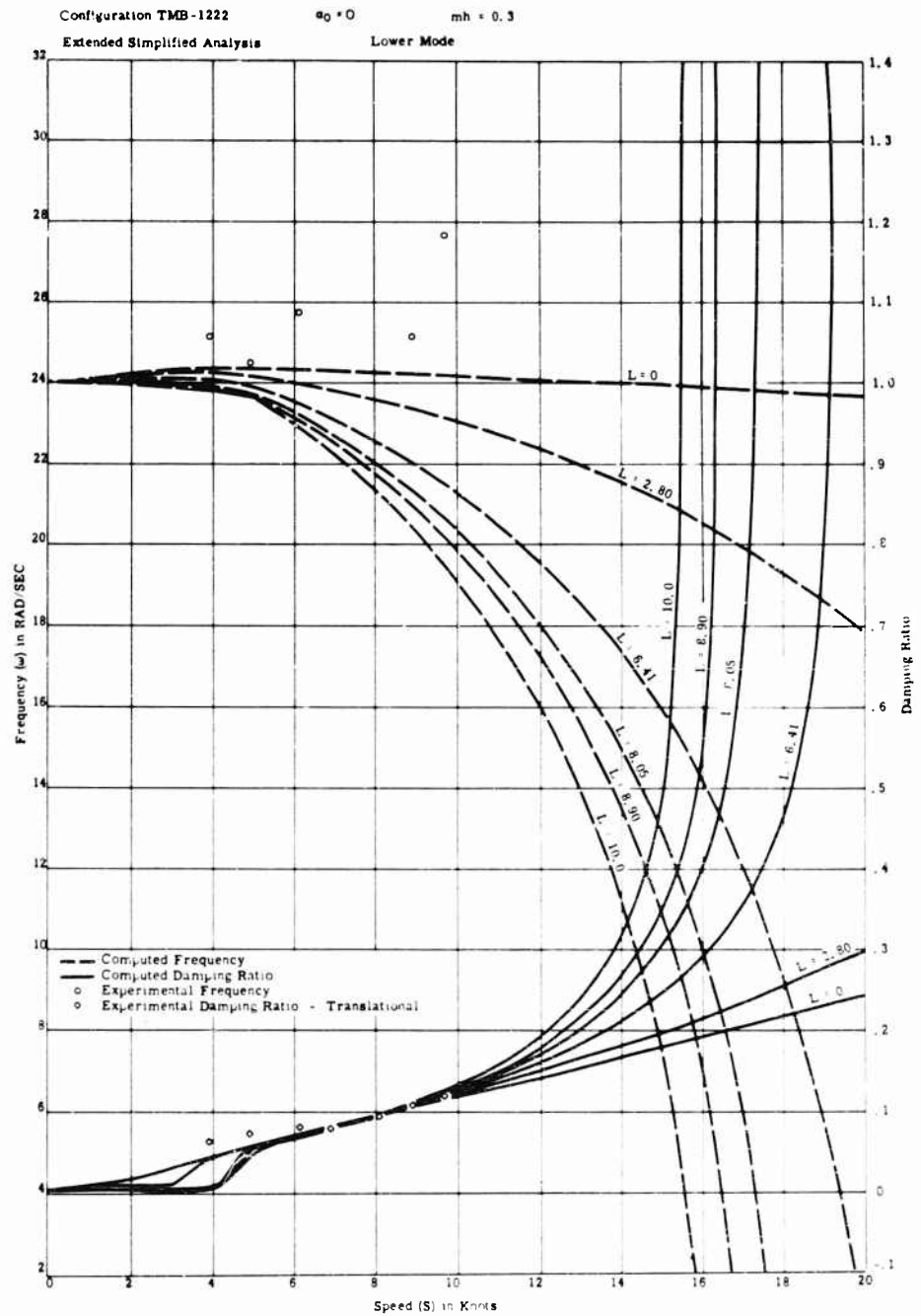
Fig. 26 - Comparison of predicted and observed damping ratios and associated frequencies for the TMB control surface flutter apparatus
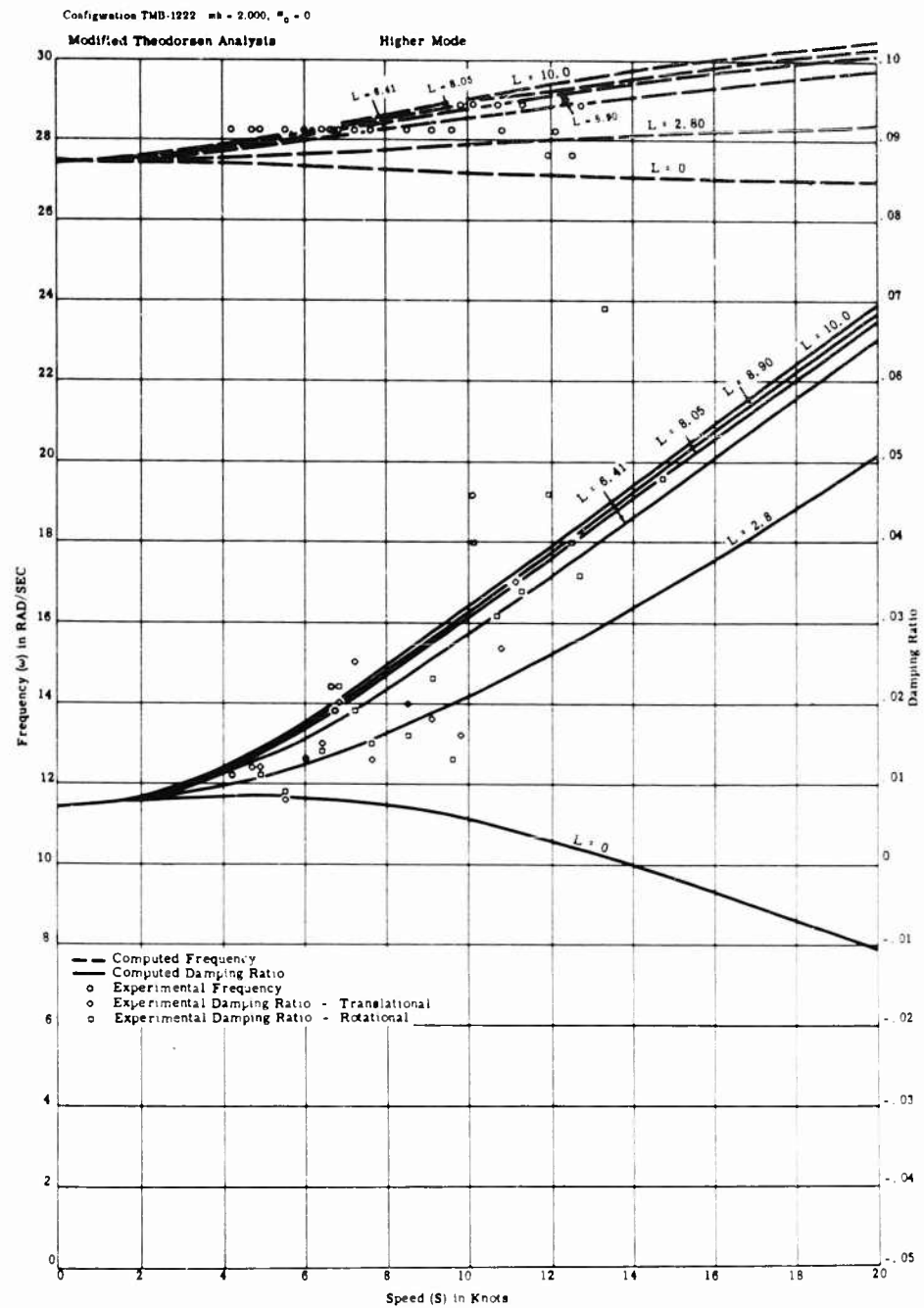
Fig. 27 - Comparison of predicted and observed damping
ratios and associated frequencies for the TMB control
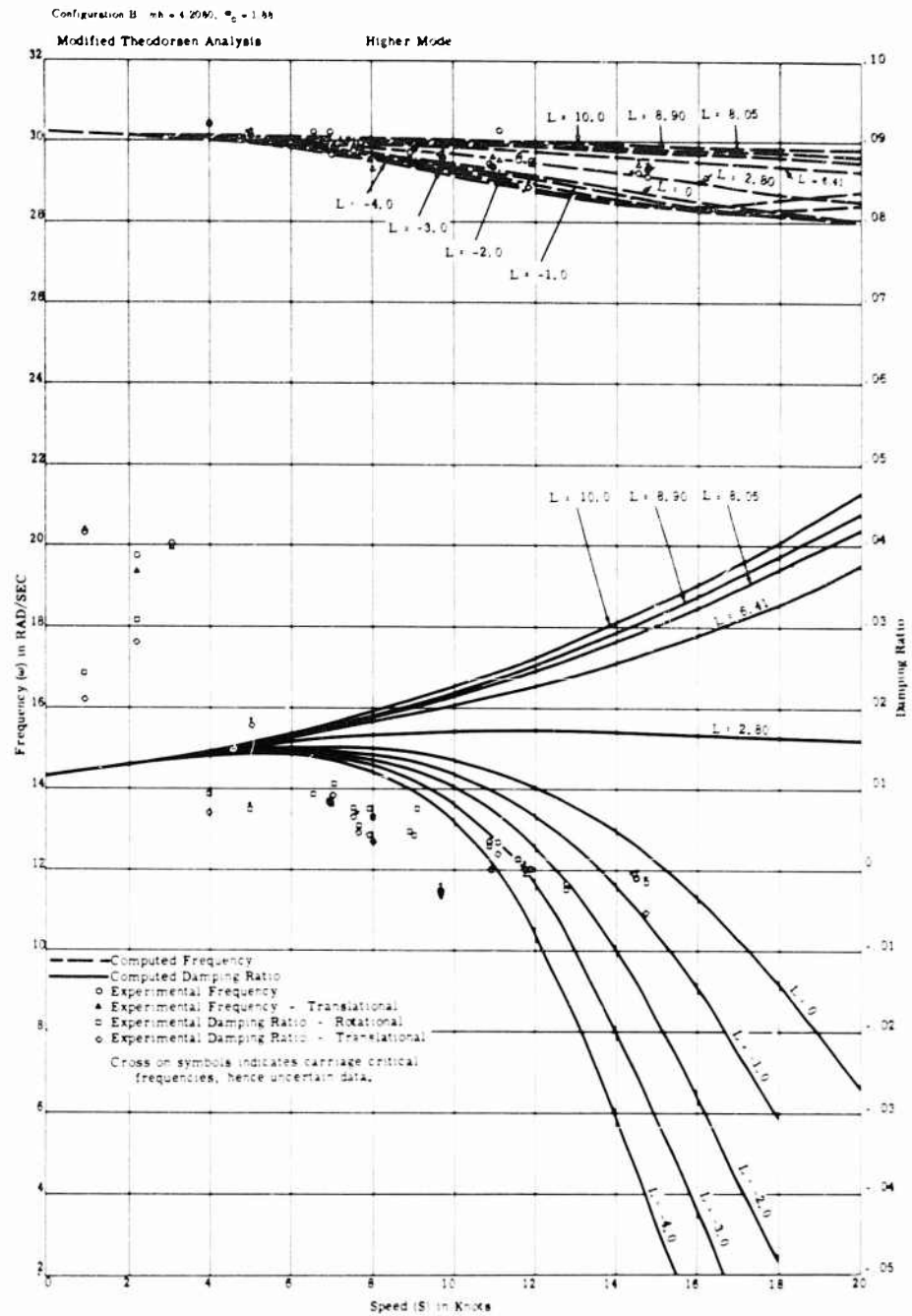surface flutter apparatus

849

Fig. 28 - Comparison of predicted and observed damping
ratios and associated frequencies for the TMB control
surface flutter apparatus
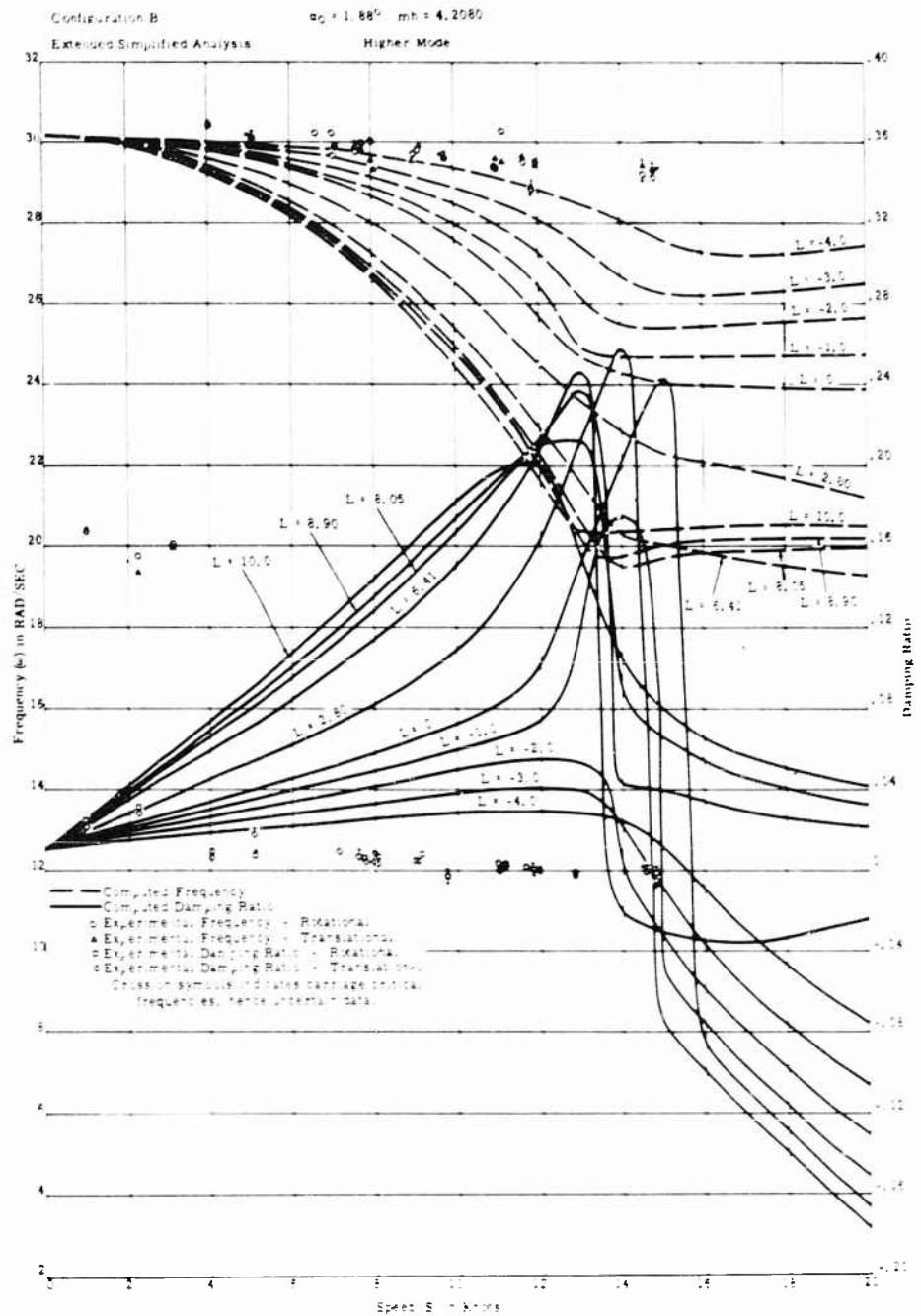
Fig. 29 - Comparison of predicted and observed damping
ratios and associated frequencies for the TMB control
surface flutter apparatus

Fig. 30 - Comparison of predicted and observed damping
ratios and associated frequencies for the TMB control
surface flutter apparatus

Fig. 31 - Comparison of predicted and observed damping ratios and associated frequencies for the TMB control surface flutter apparatus

853

Fig. 32 - Comparison of predicted and observed damping
ratios and associated frequencies for the TMB control
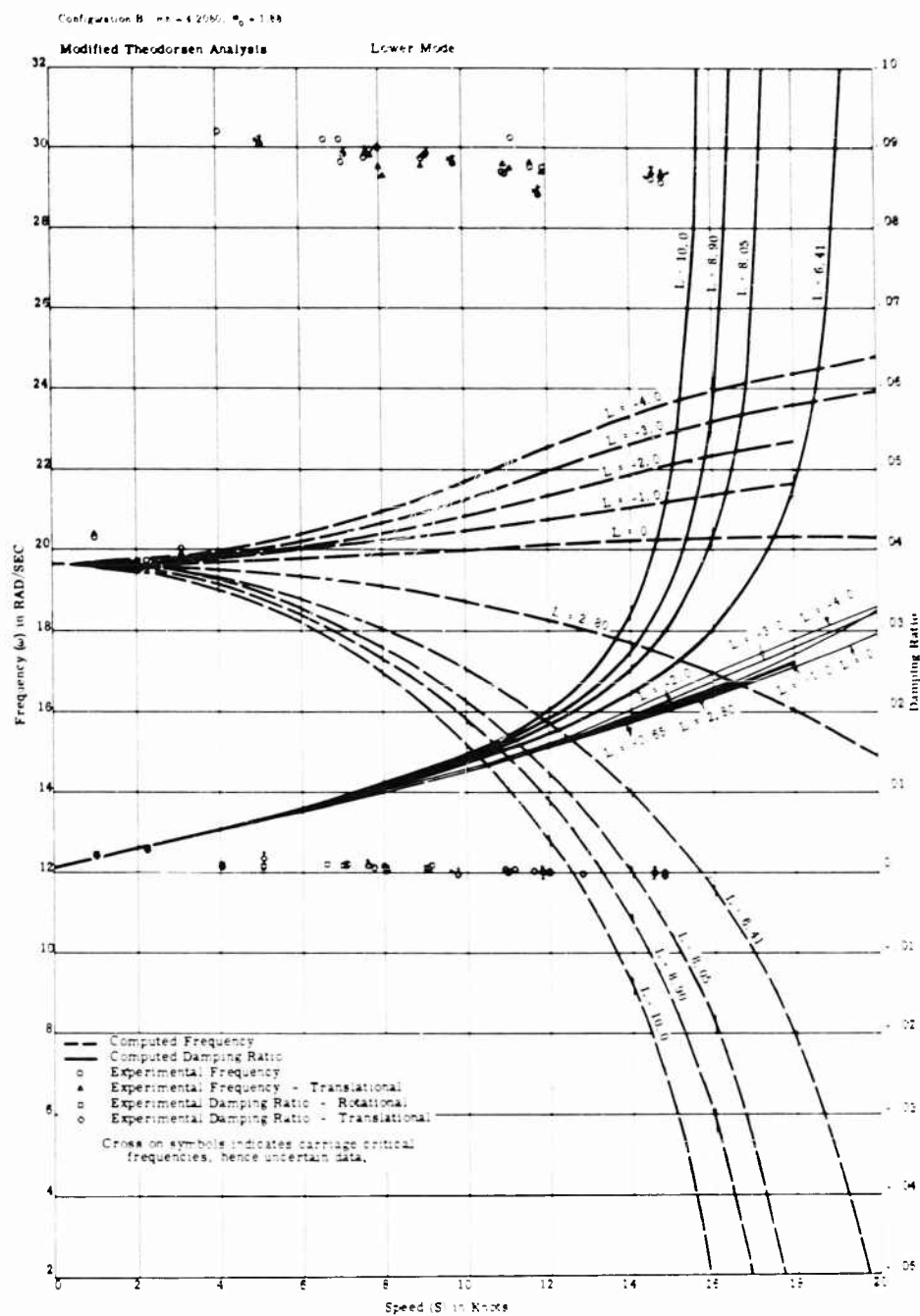surface flutter apparatus

854

Fig. 33 - Comparison of predicted and observed damping
ratios and associated frequencies for the TMB control
surface flutter apparatus

Fig. 34 - Comparison of predicted and observed damping
ratios and associated frequencies for the TMB control
surface flutter apparatus

Fig. 35 - Comparison of predicted and observed damping
ratios and associated frequencies for the TMB control
surface flutter apparatus

857

Fig. 36 - Comparison of predicted and observed damping ratios and associated frequencies for the TMB control surface flutter apparatus

Fig. 37 - Comparison of predicted and observed damping
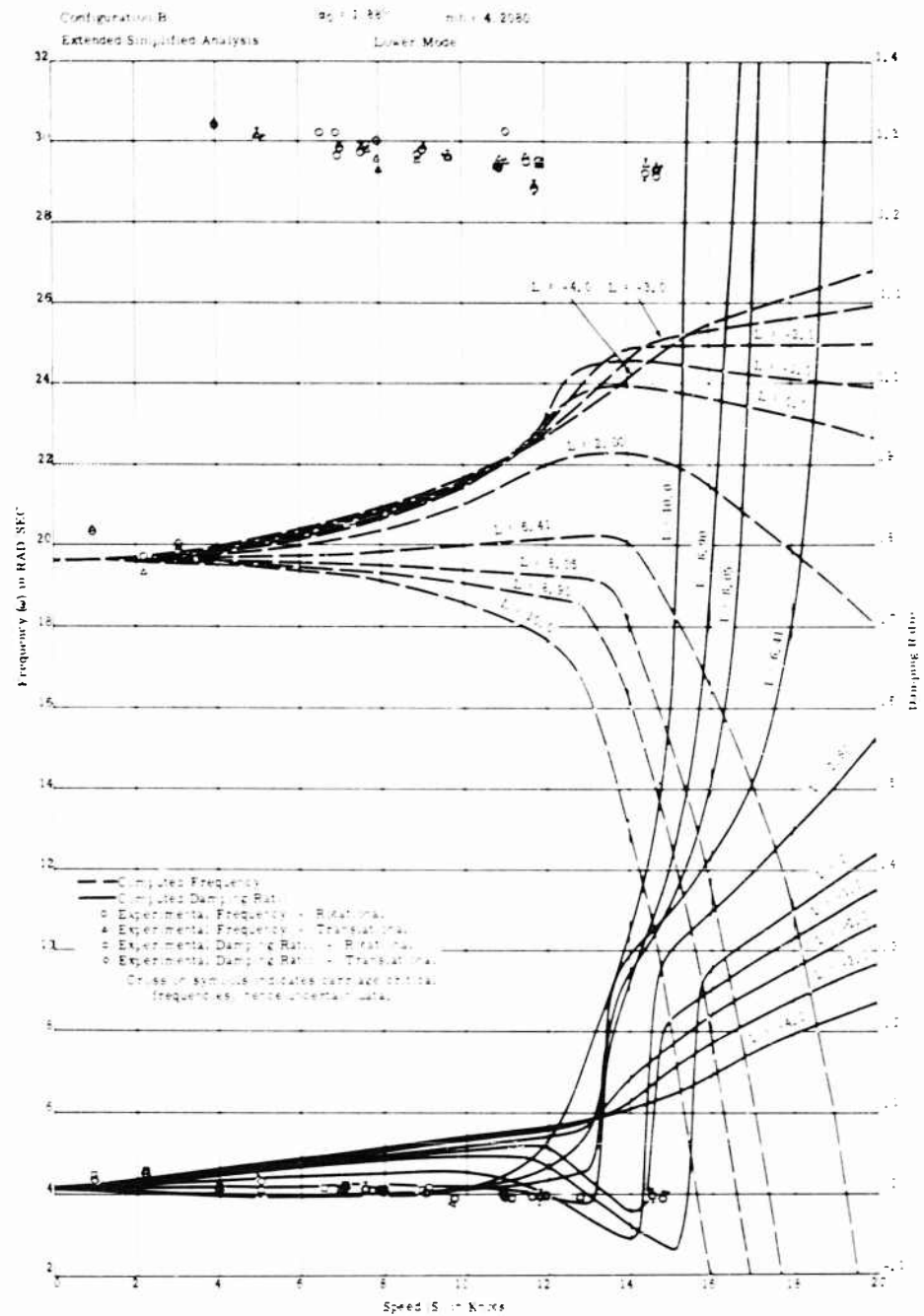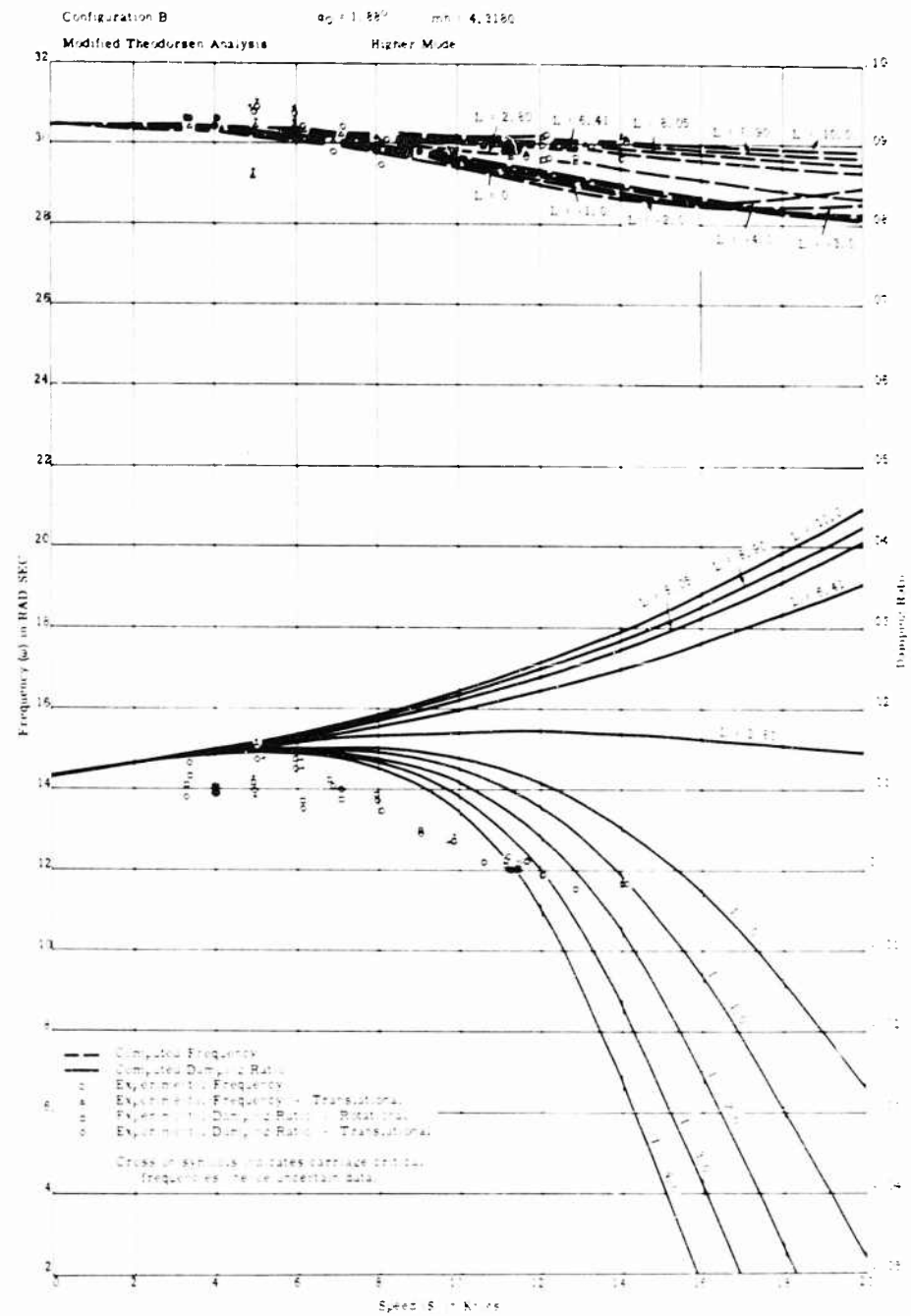ratios and associated frequencies for the TMB control
surface flutter apparatus

Fig. 38 - Comparison of predicted and observed damping ratios and associated frequencies for the TMB control surface flutter apparatus

Fig. 39 - Comparison of predicted and observed damping ratios and associated frequencies for the TMB control surface flutter apparatus
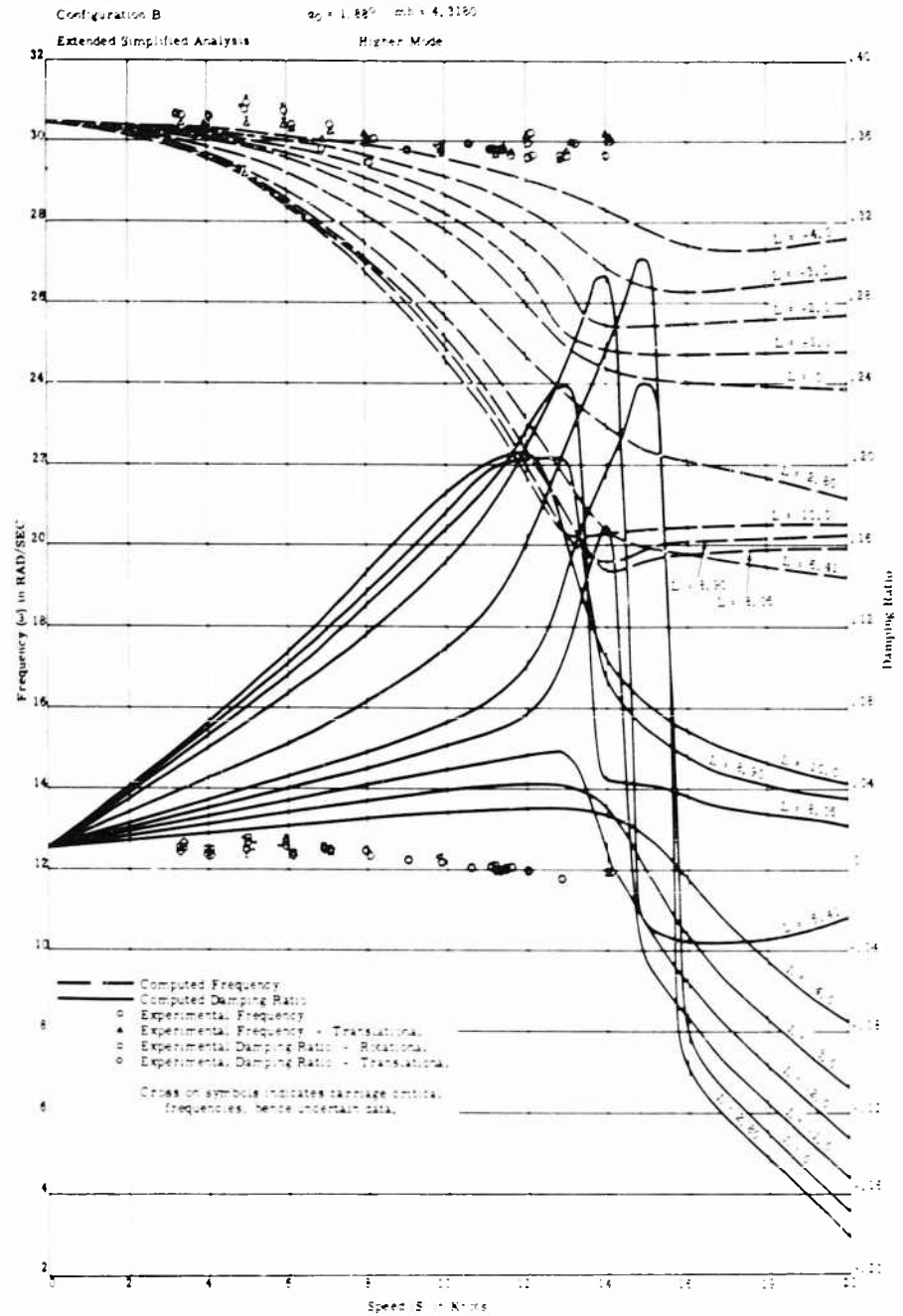
861

Fig. 40 - Comparison of predicted and observed damping
ratios and associated frequencies for the TMB control
surface flutter apparatus

Fig. 41 - Comparison of predicted and observed damping ratios and associated frequencies for the TMB control surface flutter apparatus

863

Fig. 42 – Comparison of predicted and observed damping ratios and associated frequencies for the TMB control surface flutter apparatus

864

Fig. 43 - Comparison of predicted and observed damping ratios and associated frequencies for the TMB control surface flutter apparatus

865

Fig. 44 - Comparison of predicted and observed damping ratios and associated frequencies for the TMB control surface flutter apparatus
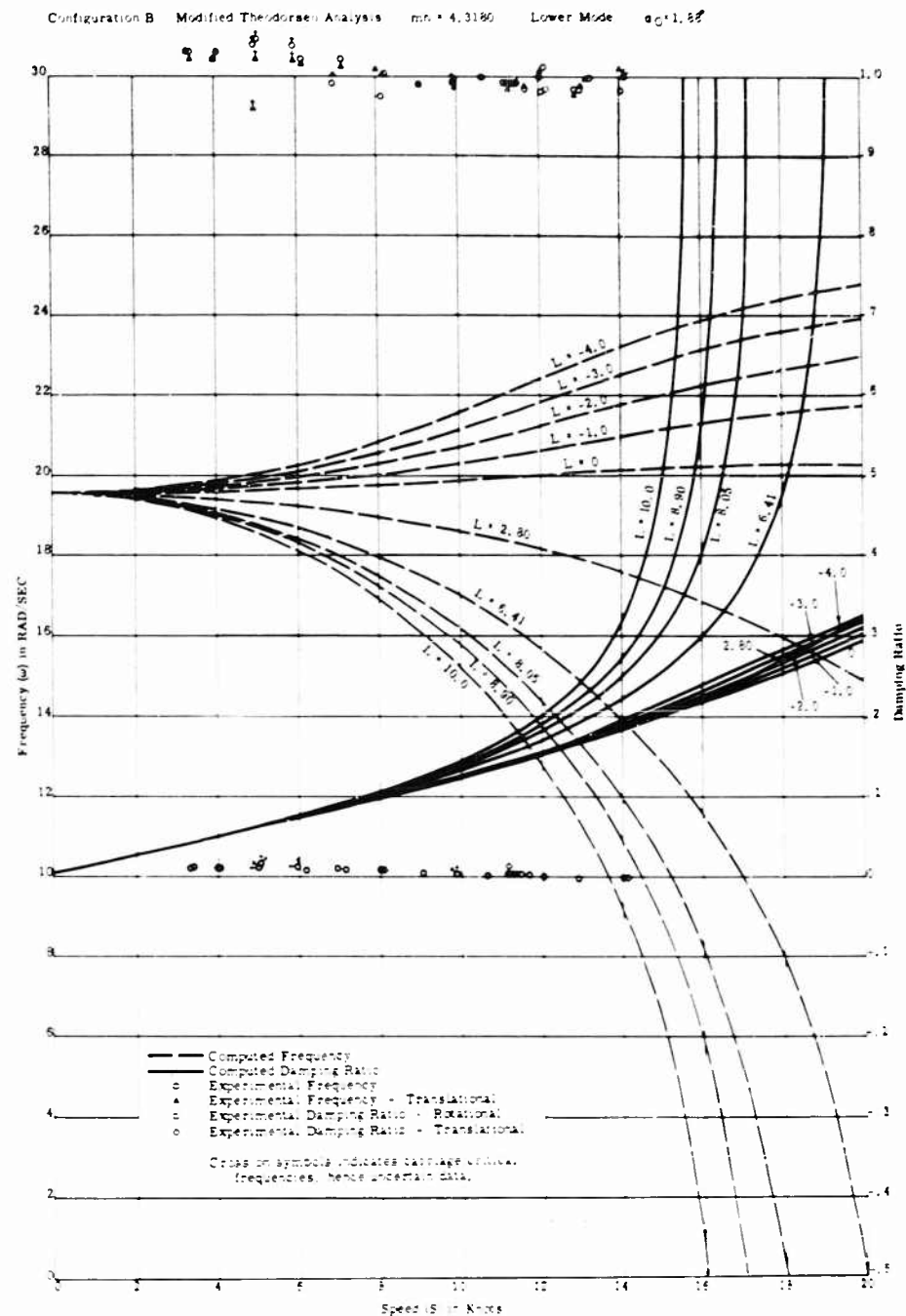
866

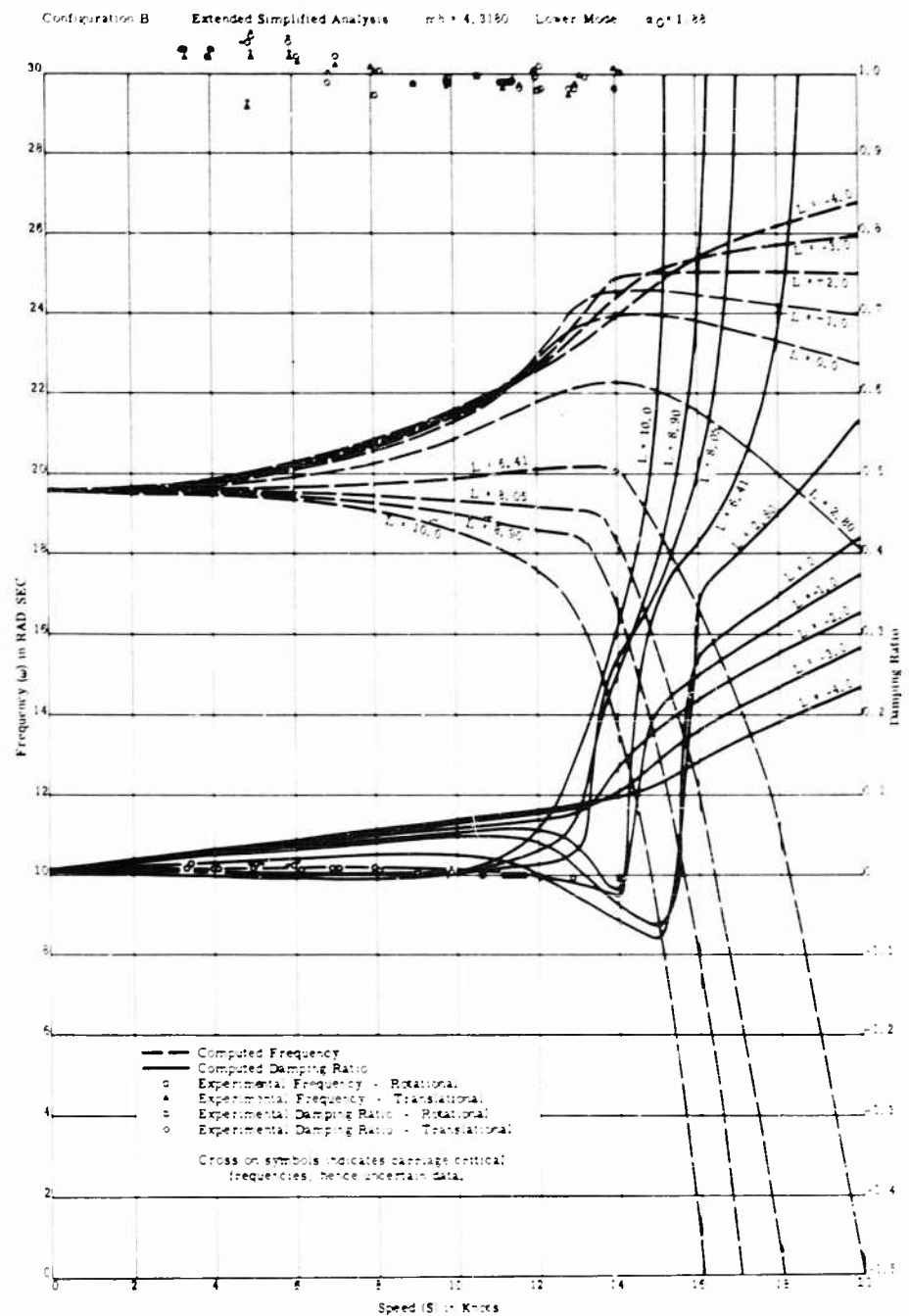Fig. 45 - Comparison of predicted and observed damping
ratios and associated frequencies for the TMB control
surface flutter apparatus

Fig. 46 - Comparison of predicted and observed damping
ratios and associated frequencies for the TMB control
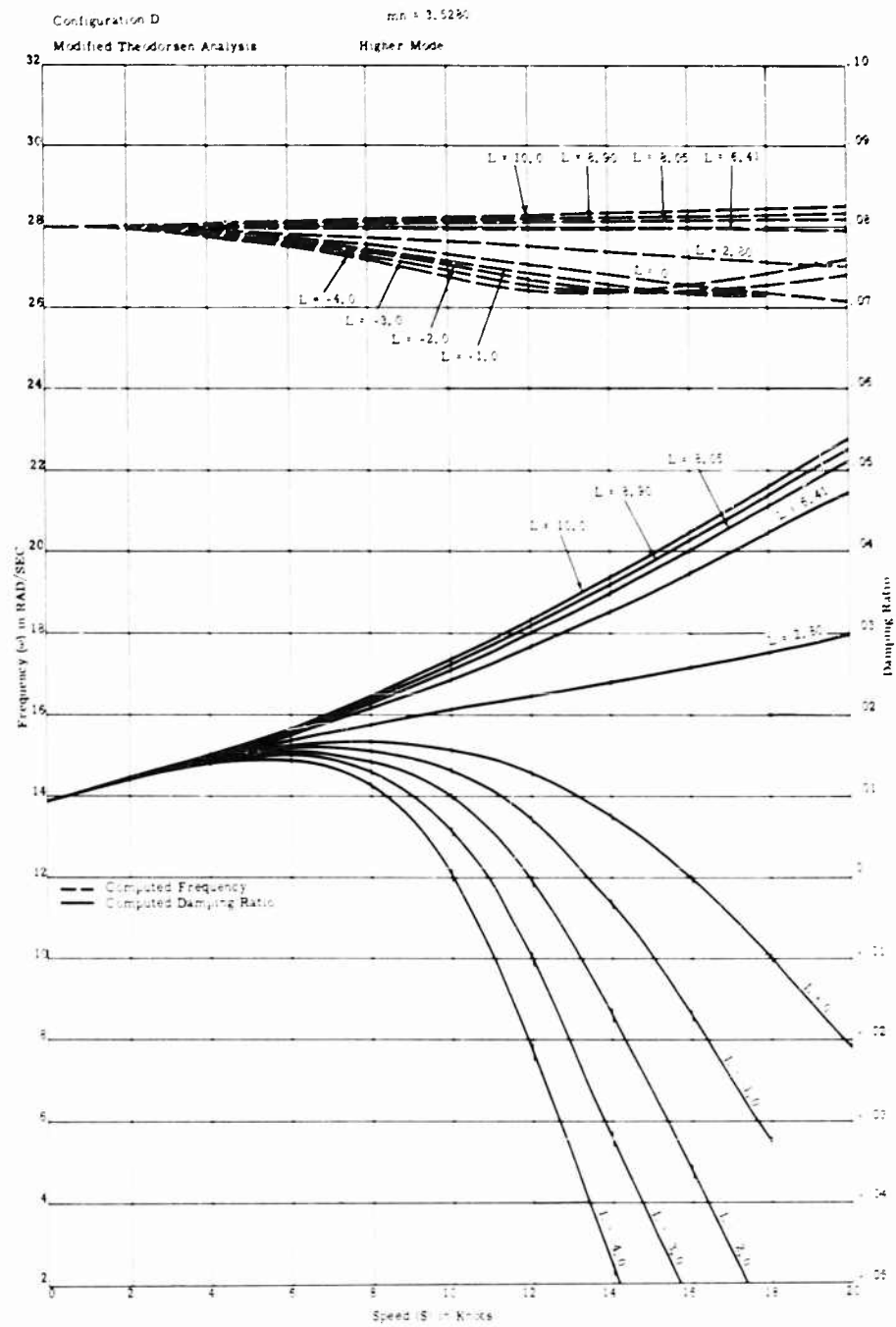surface flutter apparatus

868

Fig. 47 – Comparison of predicted and observed damping ratios and associated frequencies for the TMB control surface flutter apparatus

Fig. 48 - Comparison of predicted and observed damping
ratios and associated frequencies for the TMB control
surface flutter apparatus

870

Fig. 40 - Comparison of predicted and observed damping
ratios and associated frequencies for the TMB control
surface flutter apparatus

871

Fig. 50 - Comparison of predicted and observed damping
ratios and associated frequencies for the TMB control
surface flutter apparatus

Fig. 51 - Comparison of predicted and observed damping
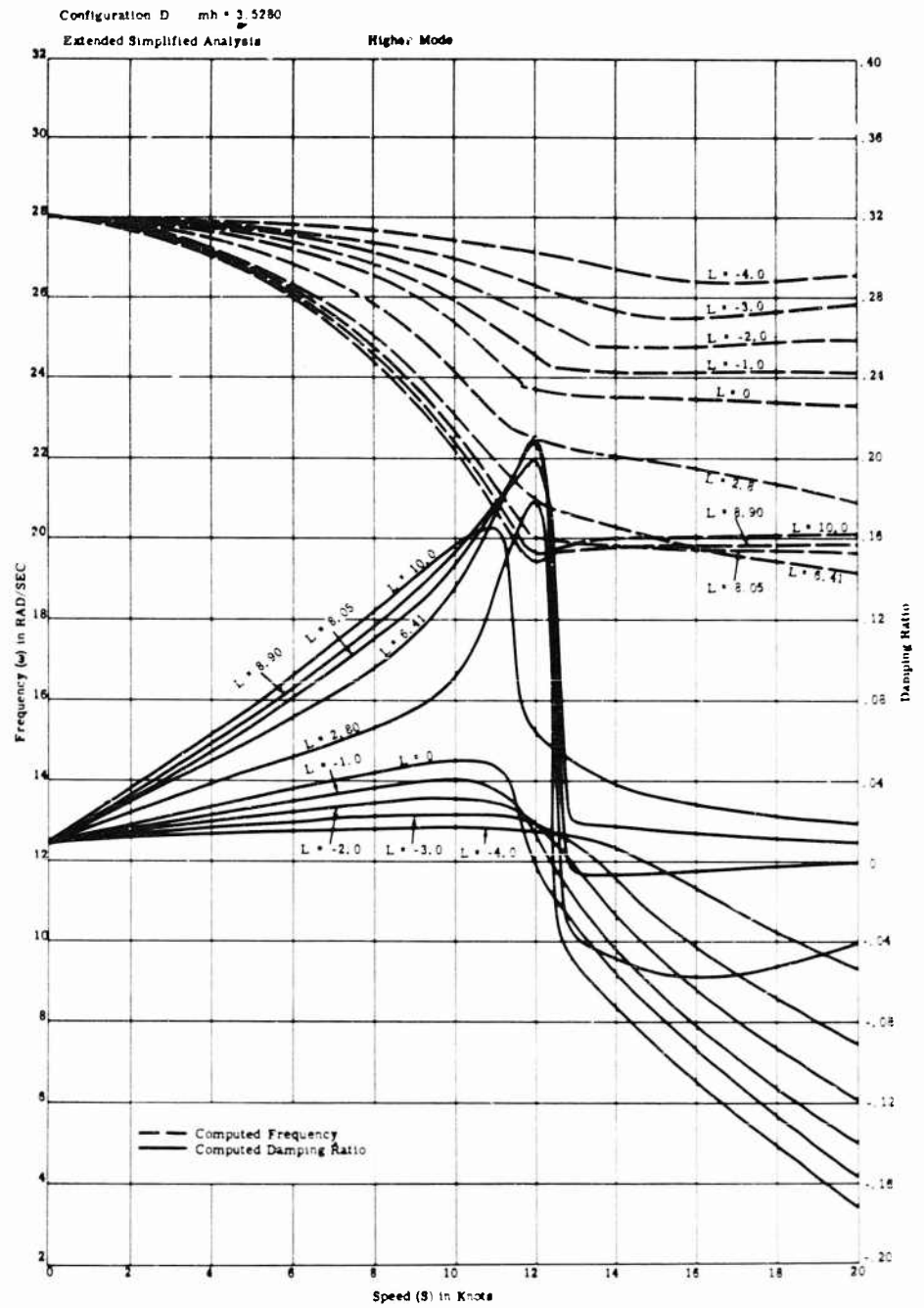ratios and associated frequencies for the TMB control
surface flutter apparatus

873

Fig. 52 - Comparison of predicted and observed damping
ratios and associated frequencies for the TMB control
surface flutter apparatus

874

Fig. 53 - Comparison of predicted and observed damping
ratios and associated frequencies for the TMB control-
surface flutter apparatus

875

Fig. 54 - Comparison of predicted and observed damping ratios and associated frequencies for the TMB control surface flutter apparatus

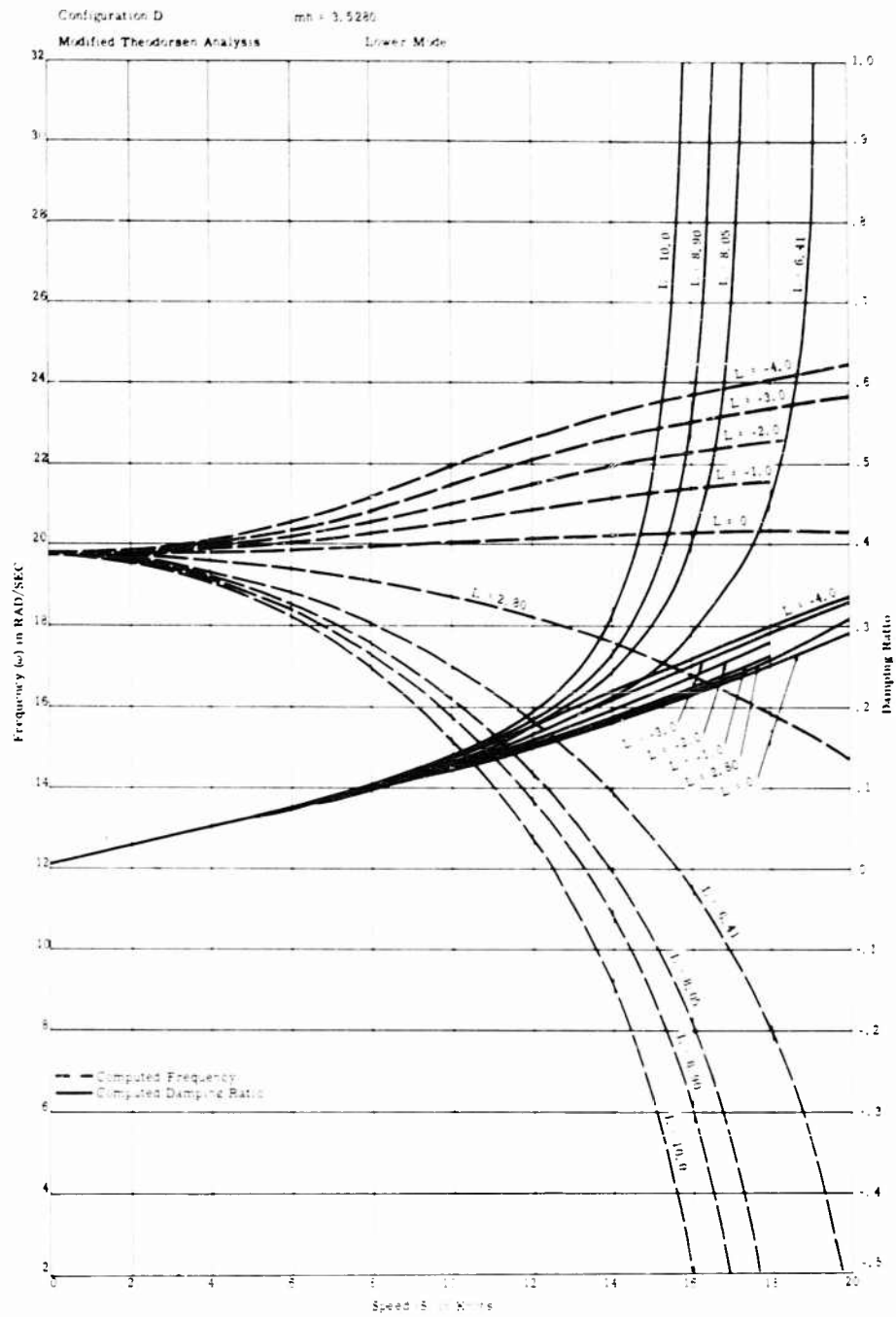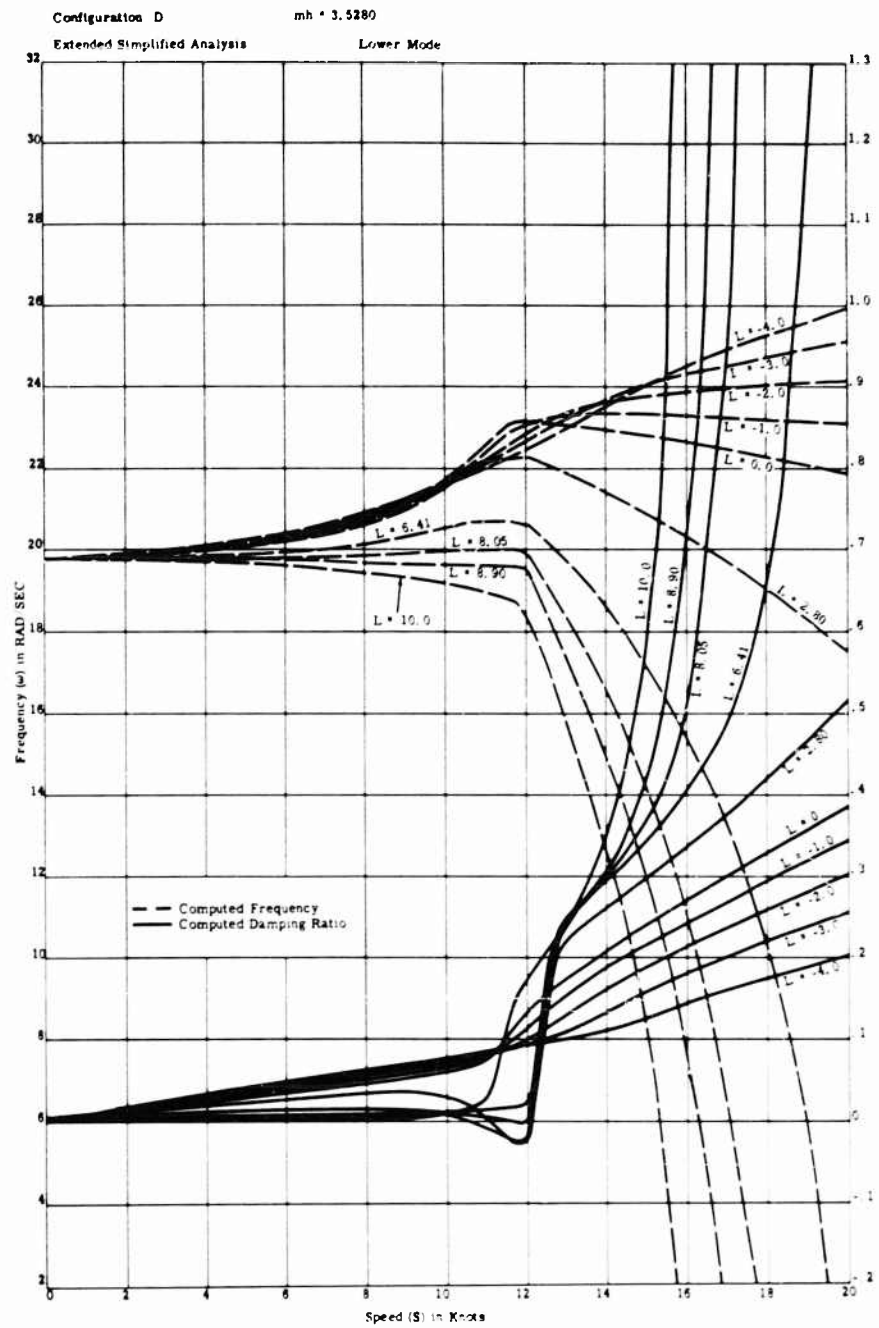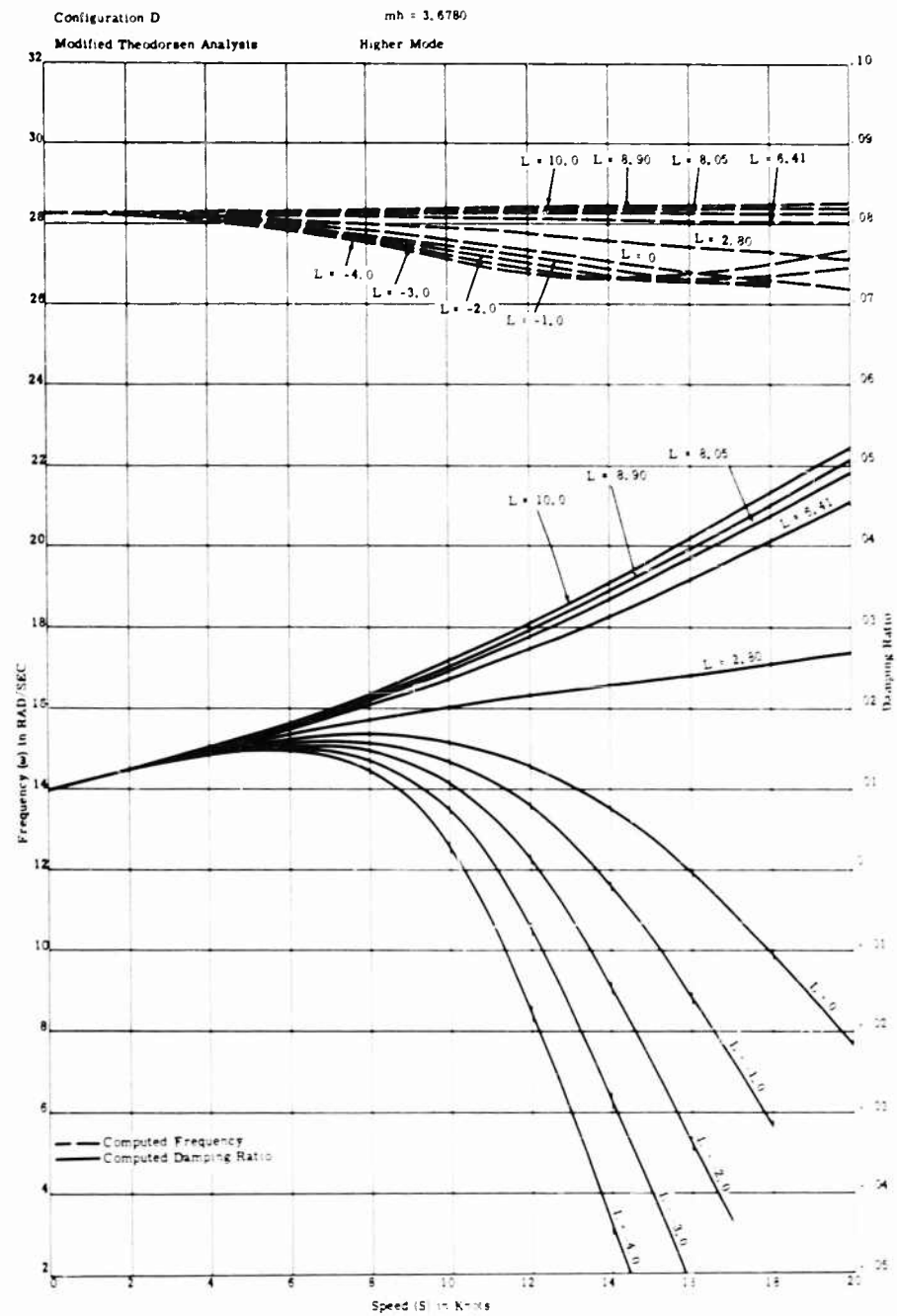Comparison of Theory and Experiment for Marine Control-Surface Flutter

Fig. 55 - Comparison of predicted and observed damping
ratios and associated frequencies for the TMB control
surface flutter apparatus

Fig. 5c - Comparison of predicted and observed damping
ratios and associated frequencies for the TMB control
surface flutter apparatus

Fig. 57 - Comparison of predicted and observed damping ratios and associated frequencies for the TMB control-surface flutter apparatus

Fig. 58 - Comparison of predicted and observed damping ratios and associated frequencies for the TMB control surface flutter apparatus

Fig. 59 - Comparison of predicted and observed damping
ratios and associated frequencies for the TMB control
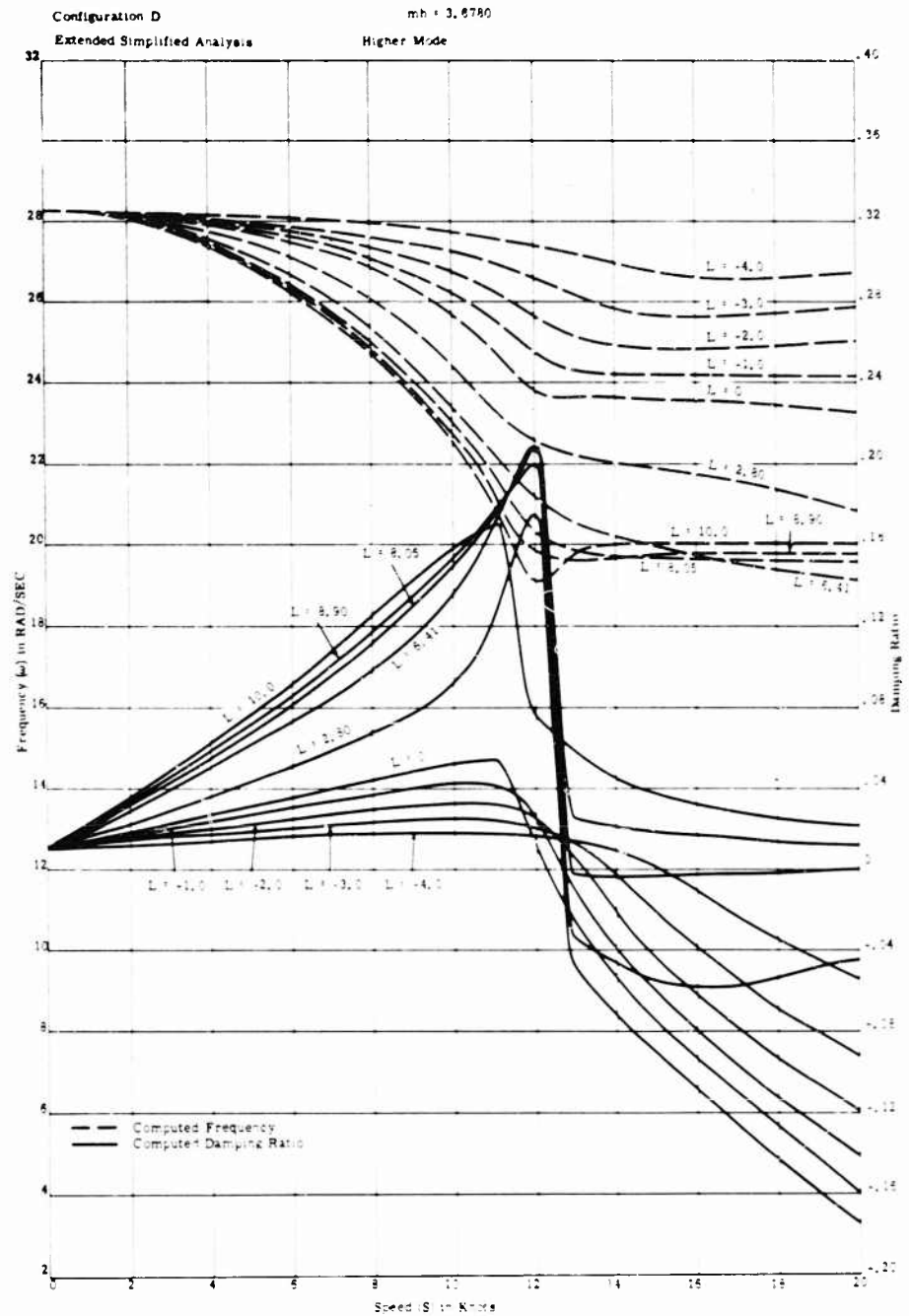surface flutter apparatus

881

Fig. 60 - Comparison of predicted and observed damping ratios and associated frequencies for the TMB control surface flutter apparatus

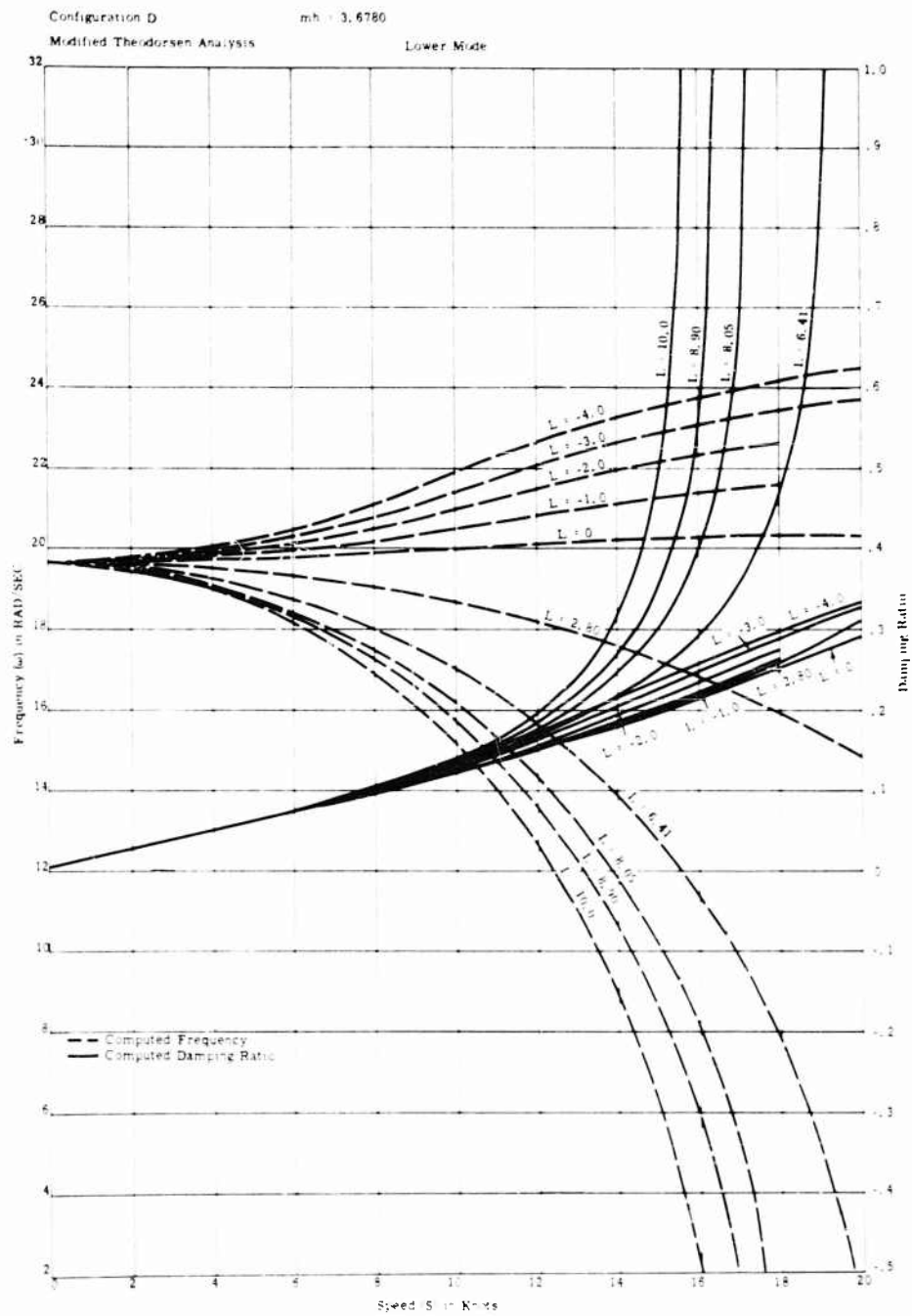Comparison of Theory and Experiment for Marine Control-Surface Flutter

Fig. 61 - Comparison of predicted and observed damping
ratios and associated frequencies for the TMB control
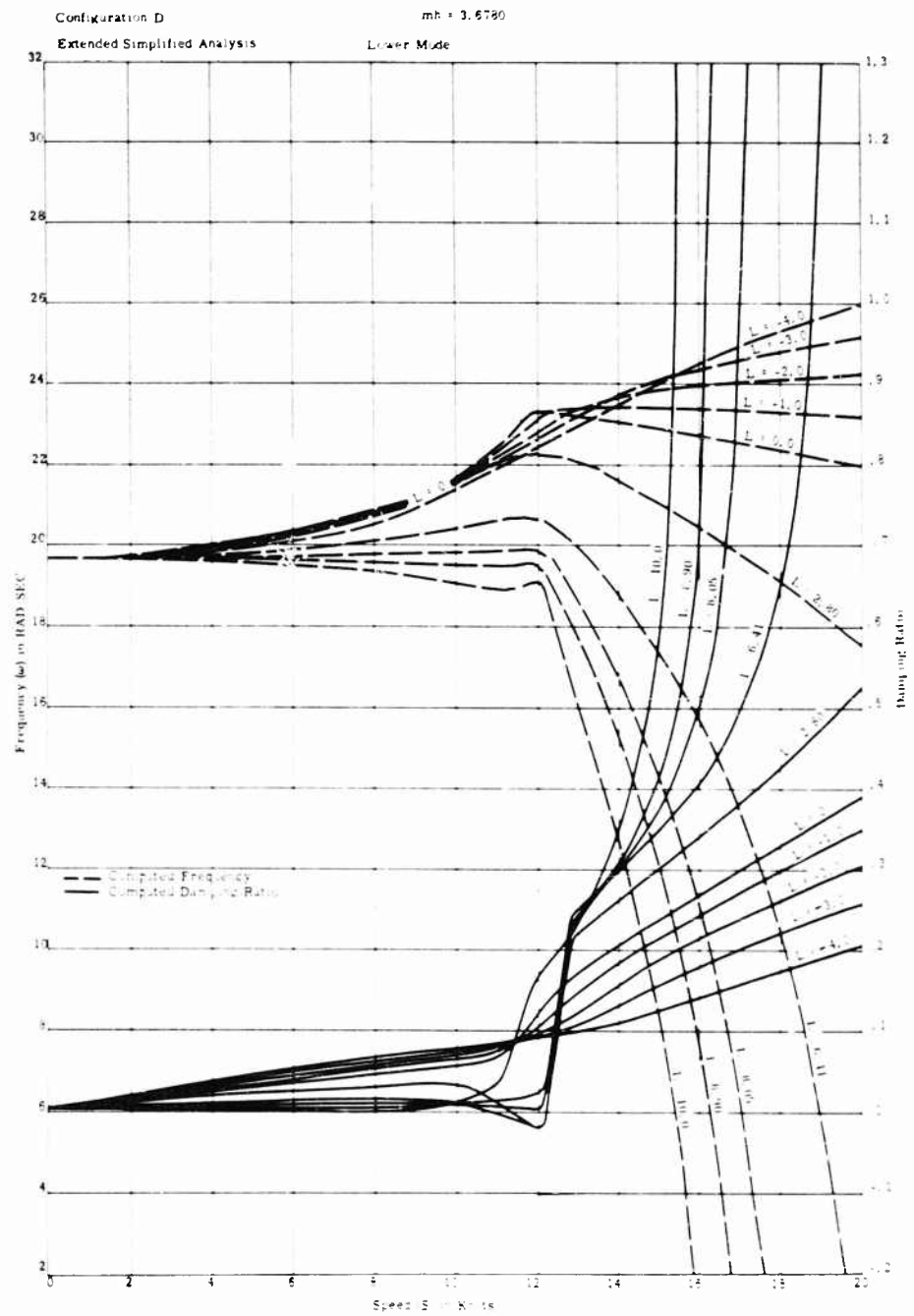surface flutter apparatus

Fig. 62 - Comparison of predicted and observed damping
ratios and associated frequencies for the TMB control
surface flutter apparatus

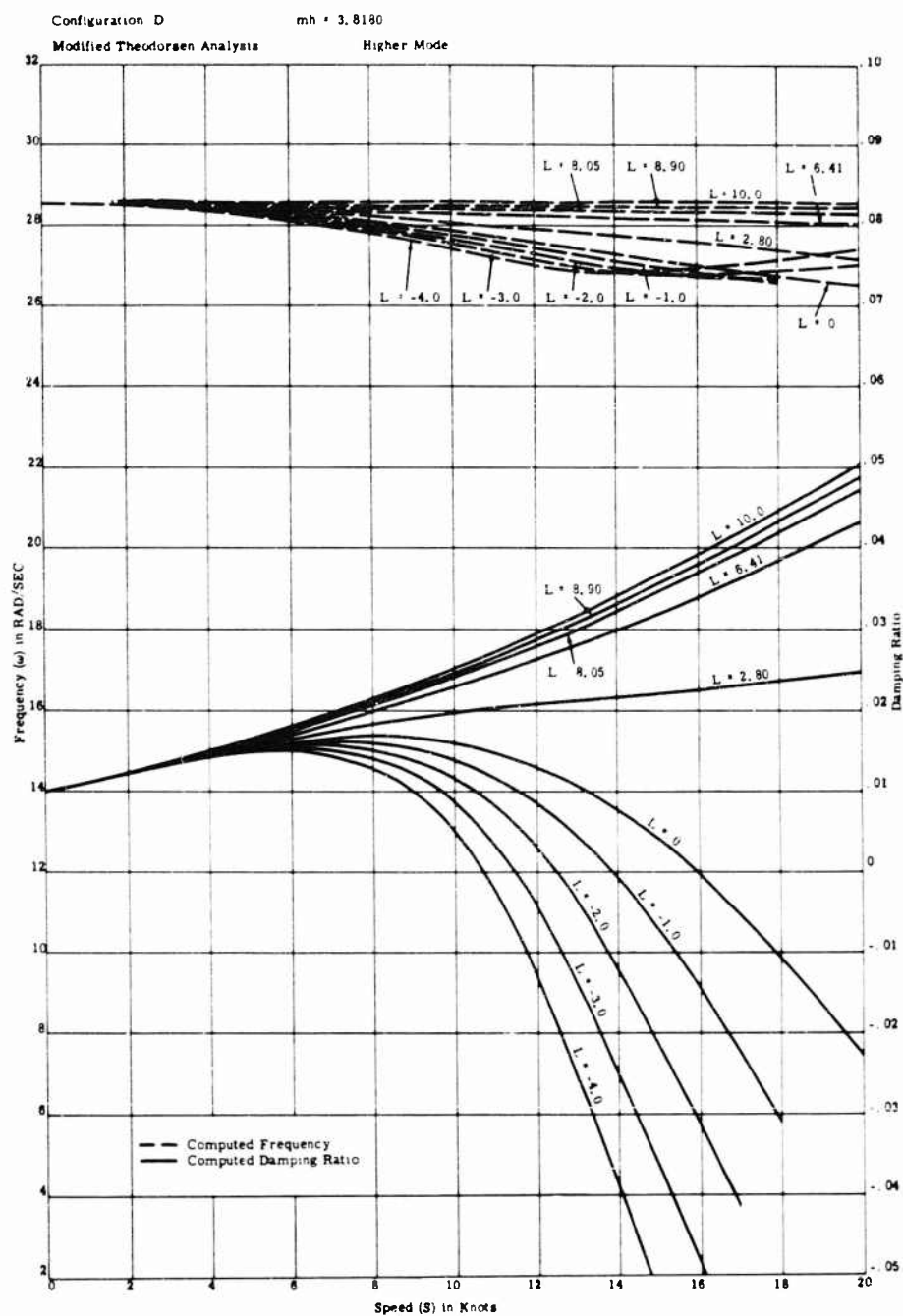Comparison of Theory and Experiment for Marine Control-Surface Flutter

Fig. 63 - Comparison of predicted and observed damping
ratios and associated frequencies for the TMB control
surface flutter apparatus

885

Fig. 64 - Comparison of predicted and observed damping ratios and associated frequencies for the TMB control surface flutter apparatus

Fig. 65 - Comparison of predicted and observed damping
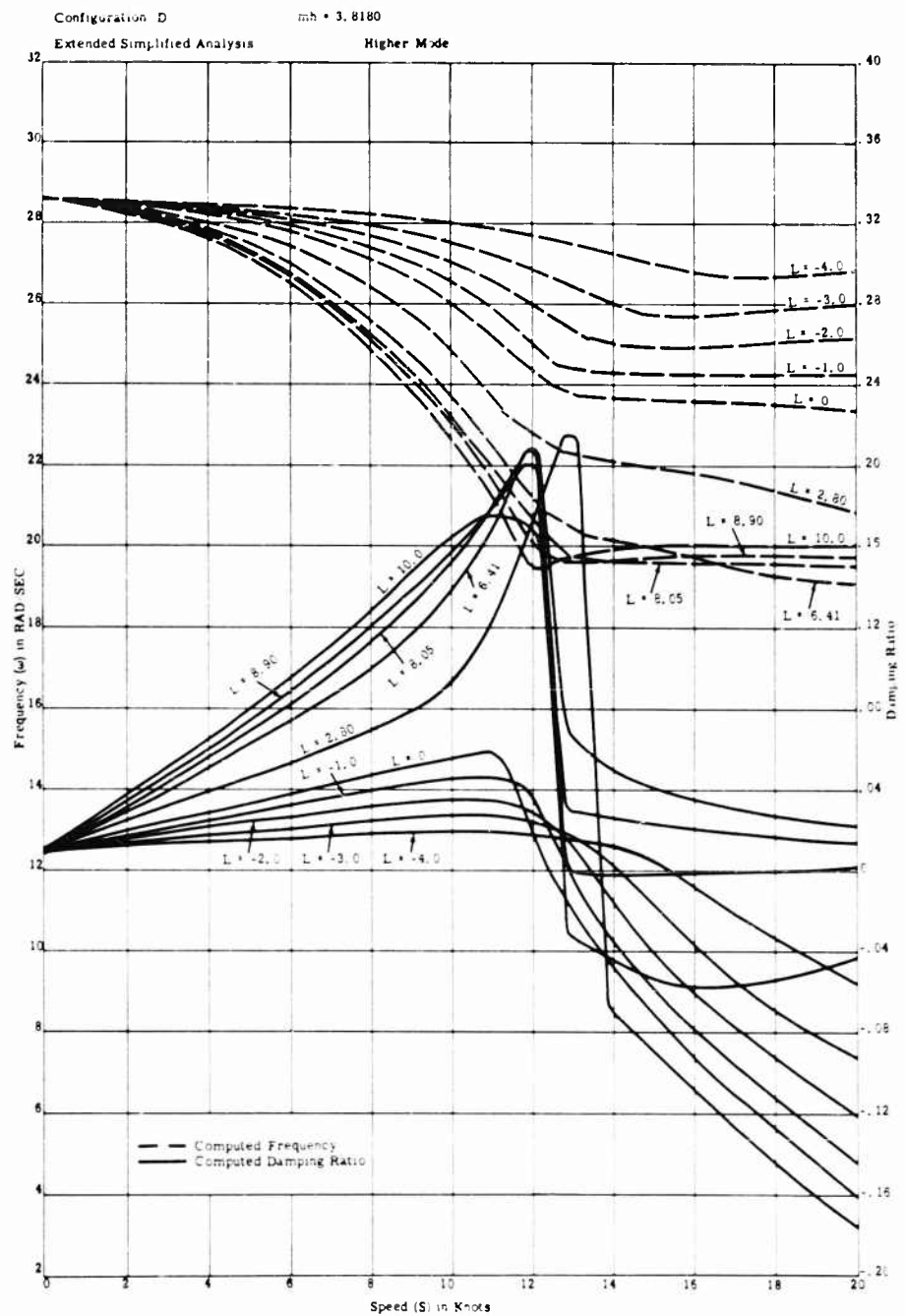ratios and associated frequencies for the TMB control
surface flutter apparatus

887

Fig. 66 - Comparison of predicted and observed damping ratios and associated frequencies for the TMB control surface flutter apparatus

Fig. 67 - Comparison of predicted and observed damping
ratios and associated frequencies for the TMB control
surface flutter apparatus

889

Fig. 68 - Comparison of predicted and observed damping
ratios and associated frequencies for the TMB control
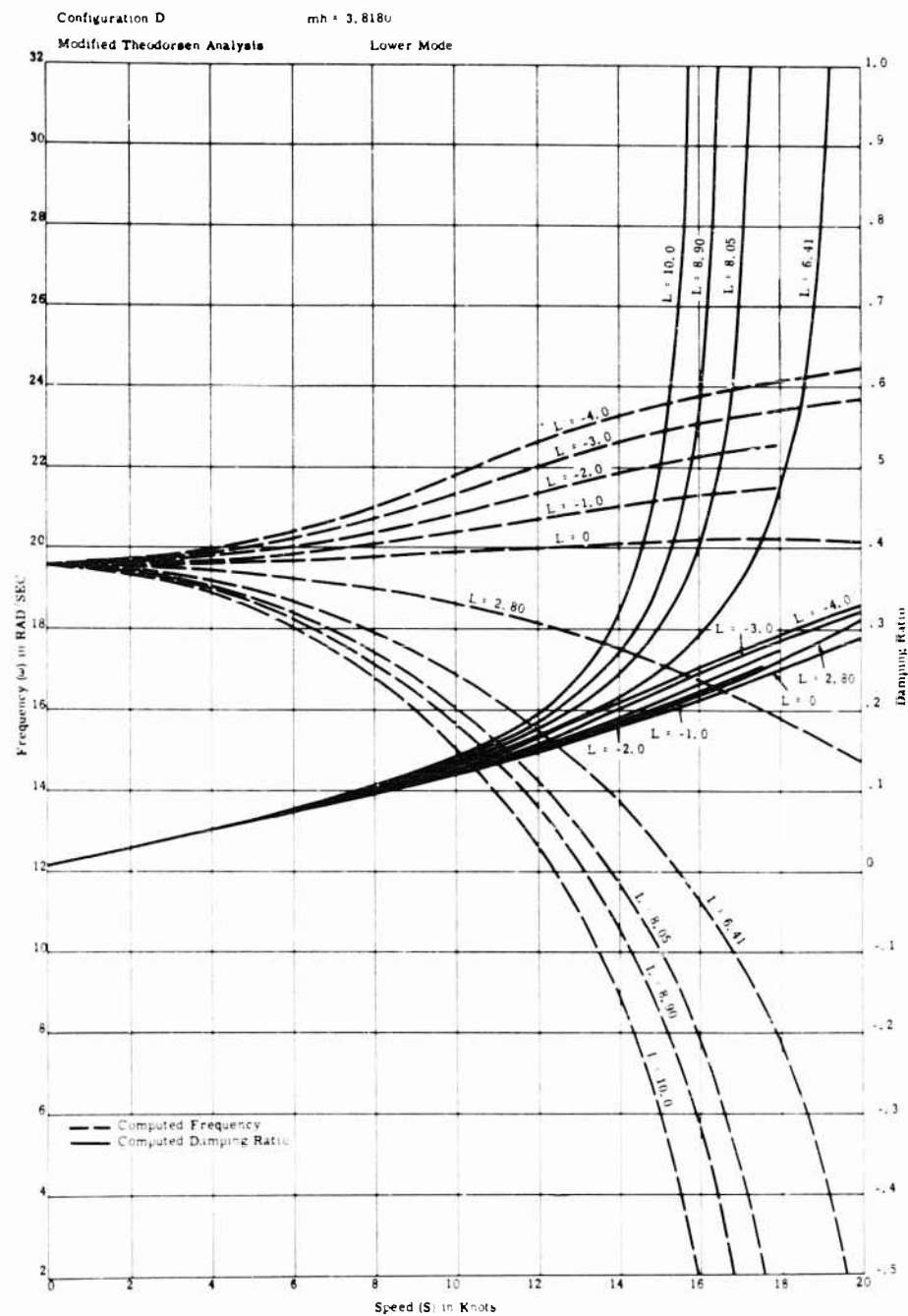surface flutter apparatus

890

Fig. 69 - Comparison of predicted and observed damping ratios and associated frequencies for the TMB control surface flutter apparatus

891

Fig. 70 - Comparison of predicted and observed damping
ratios and associated frequencies for the TMB control
surface flutter apparatus

892

Fig. 71 - Comparison of predicted and observed damping ratios and associated frequencies for the TMB control surface flutter apparatus
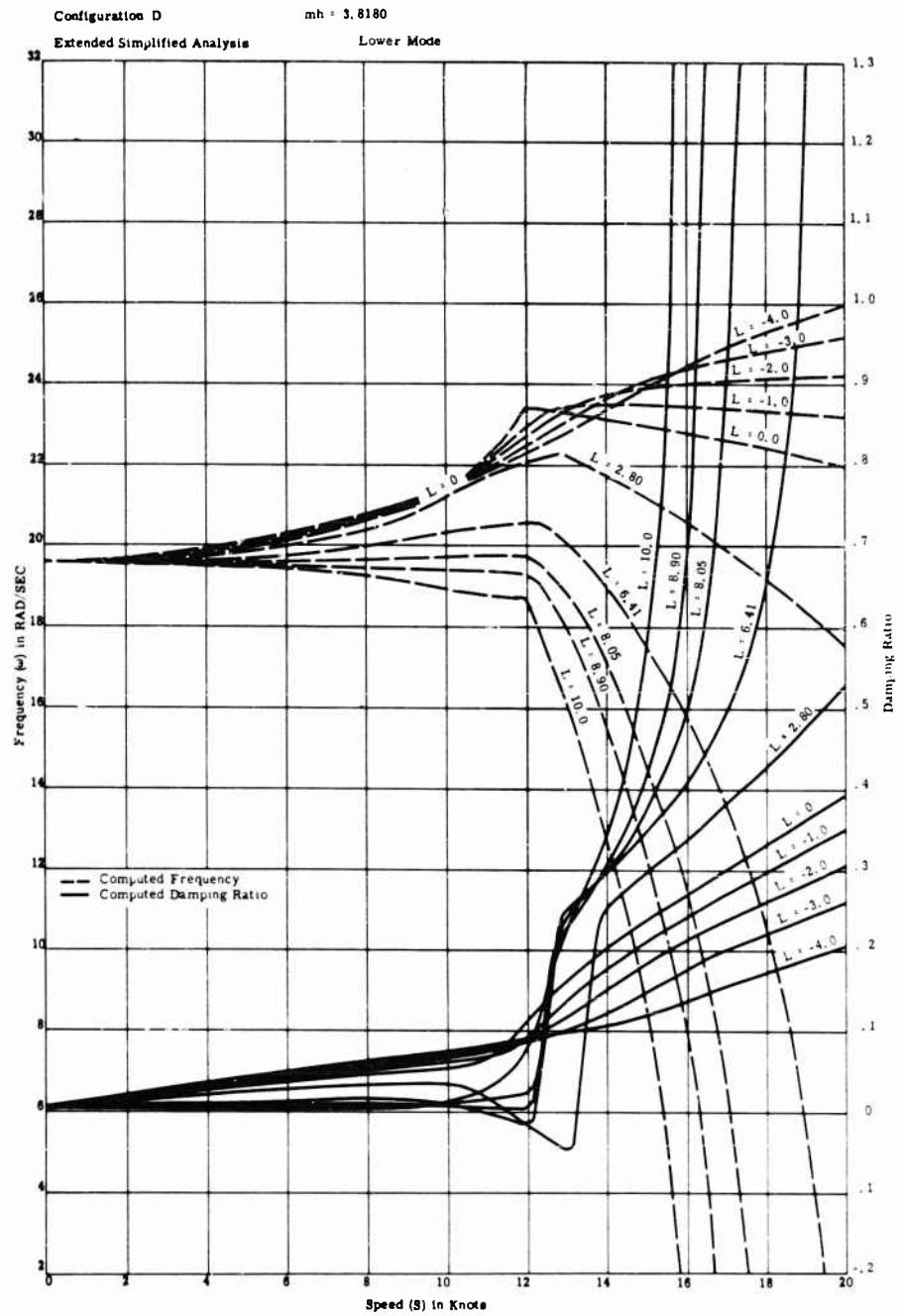
893

Fig. 72 - Comparison of predicted and observed damping
ratios and associated frequencies for the TMB control
surface flutter apparatus

894

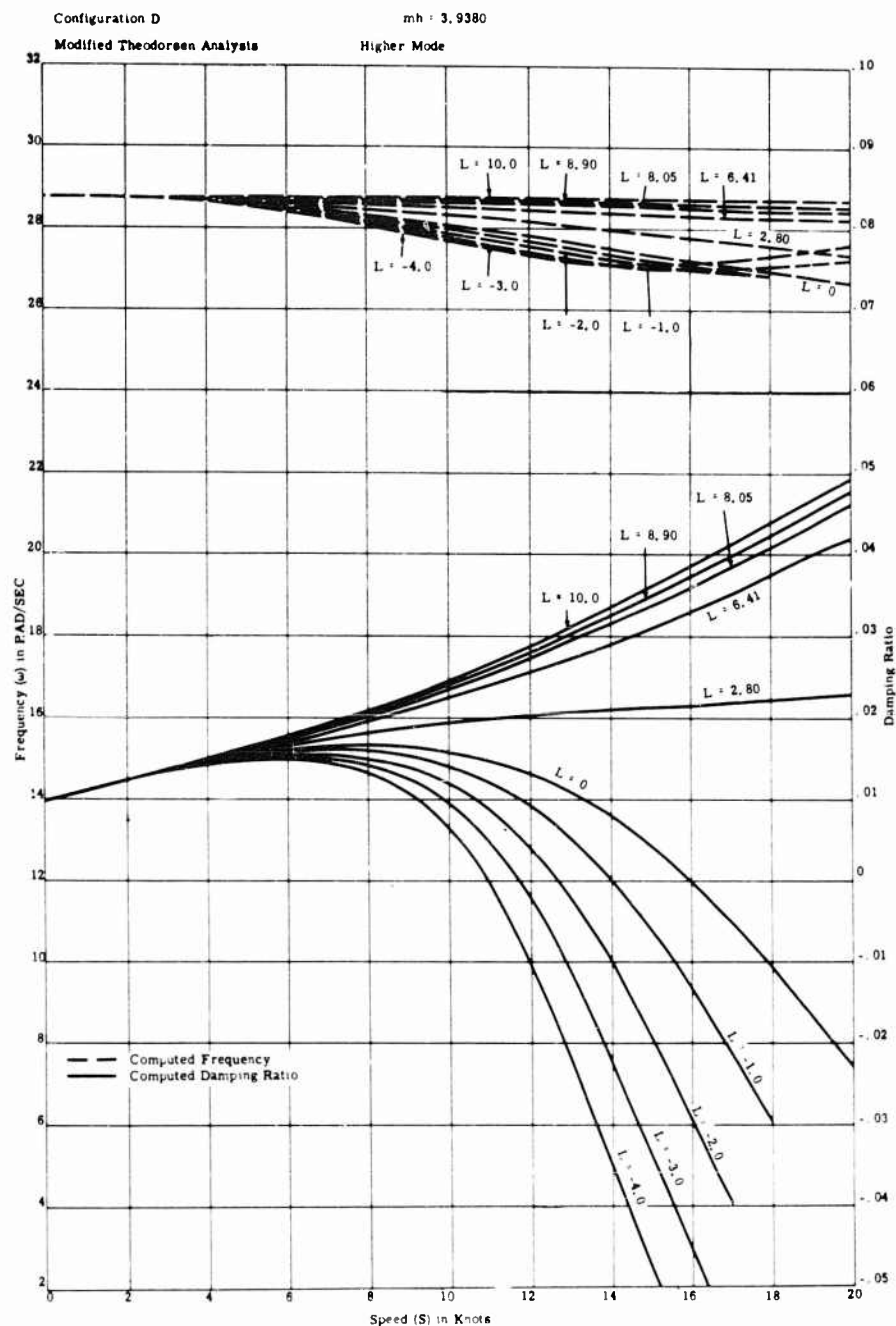Comparison of Theory and Experiment for Marine Control-Surface Flutter

Fig. 73 - Comparison of predicted and observed damping ratios and associated frequencies for the TMB control surface flutter apparatus
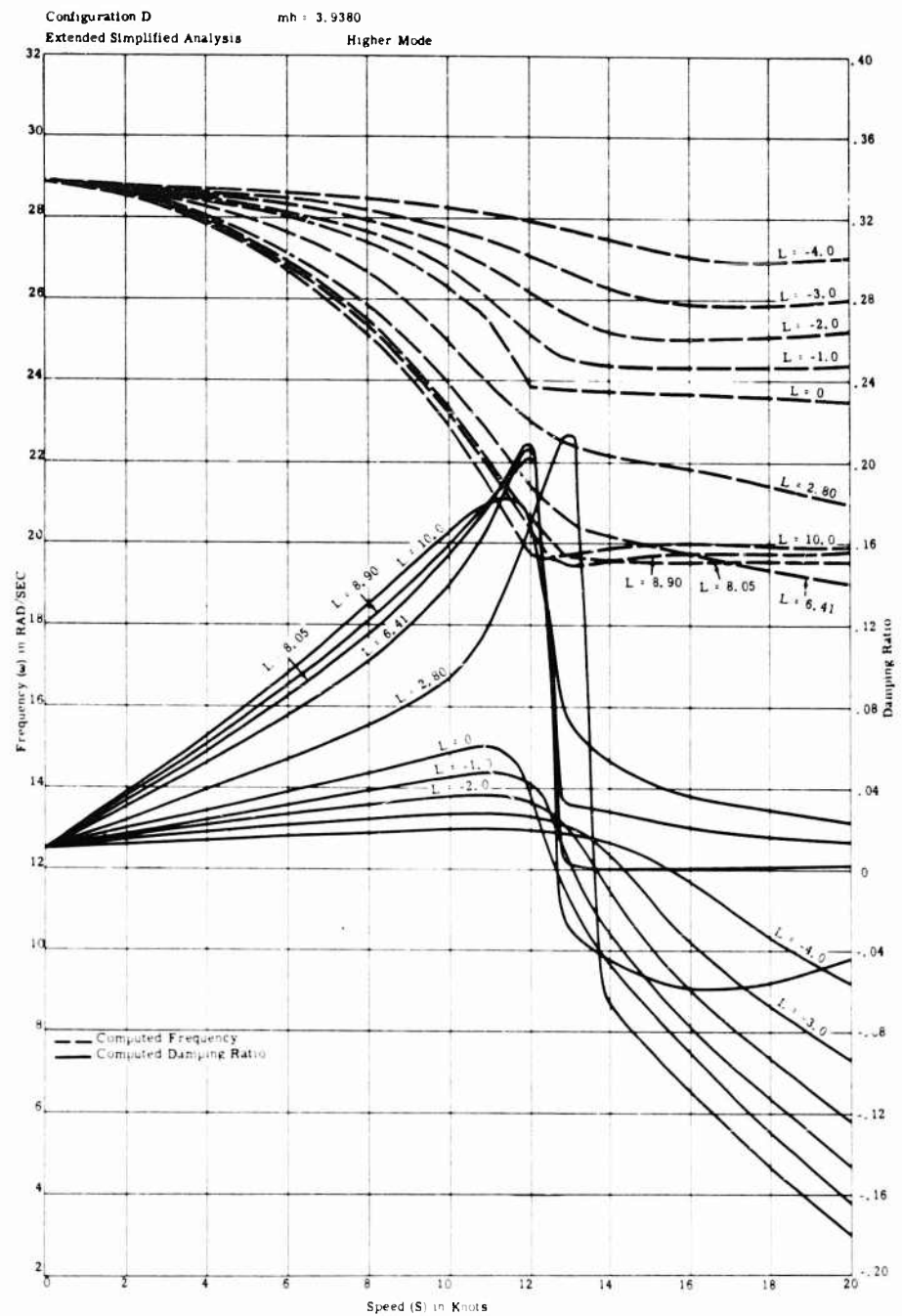
895

Fig. 74 - Comparison of predicted and observed damping
ratios and associated frequencies for the TMB control
surface flutter apparatus

896

Fig. 75 - Comparison of predicted and observed damping
ratios and associated frequencies for the TMB control
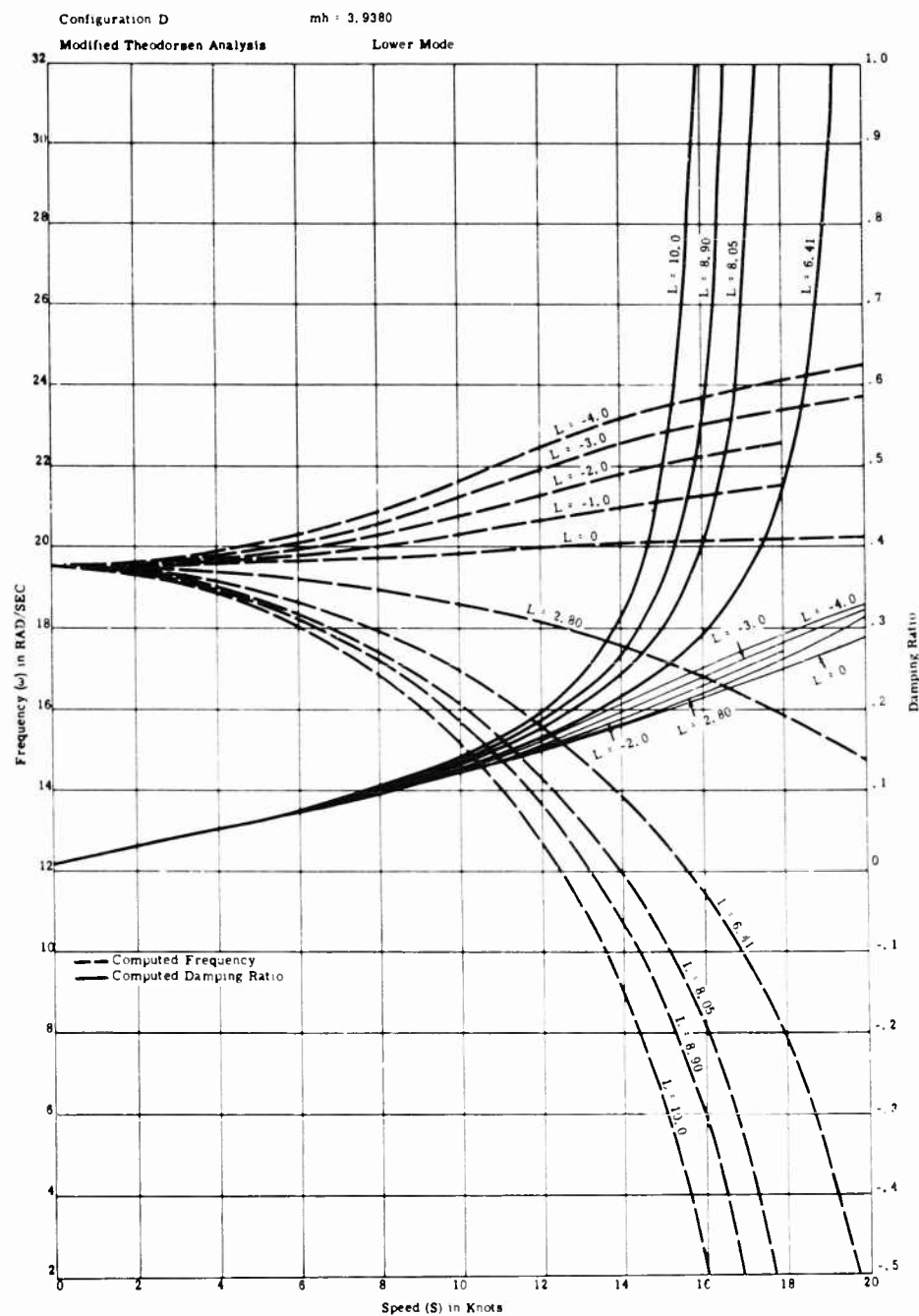surface flutter apparatus

897

Fig. 76 - Comparison of predicted and observed damping
ratios and associated frequencies for the TMB control
surface flutter apparatus

Fig. 77 - Comparison of predicted and observed damping ratios and associated frequencies for the TMB control surface flutter apparatus

899

Fig. 78 - Comparison of predicted and observed damping
ratios and associated frequencies for the TMB control
surface flutter apparatus

900

Comparison of Theory and Experiment for Marine Control-Surface Flutter

Fig. 79 - Comparison of predicted and observed damping ratios and associated frequencies for the TMB control surface flutter apparatus
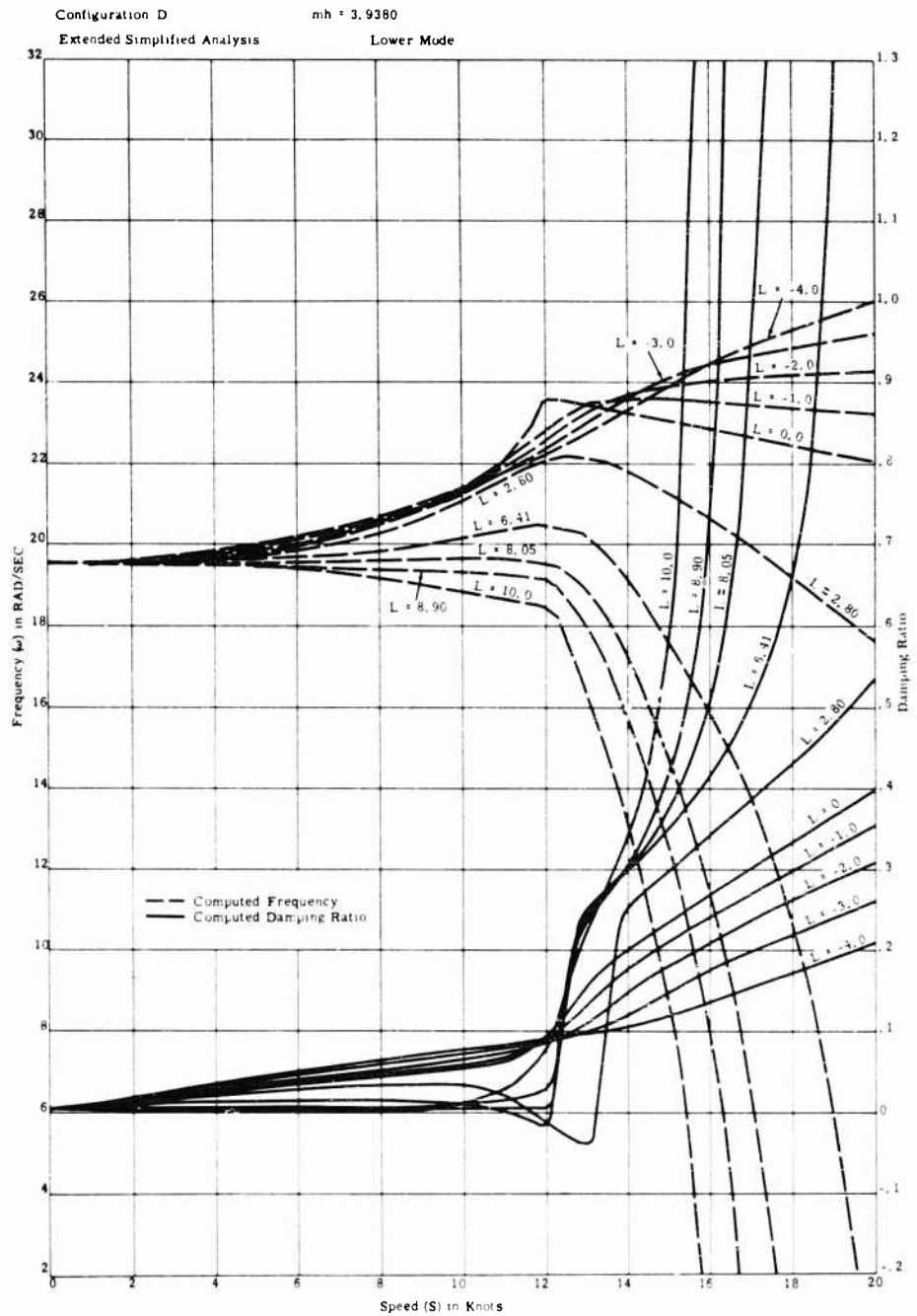
901

Fig. 80 - Comparison of predicted and observed damping
ratios and associated frequencies for the TMB control
surface flutter apparatus

902

Fig. 81 - Comparison of predicted and observed damping ratios and associated frequencies for the TMB control surface flutter apparatus

903

Fig. 82 - Comparison of predicted and observed damping ratios and associated frequencies for the TMB control surface flutter apparatus

904

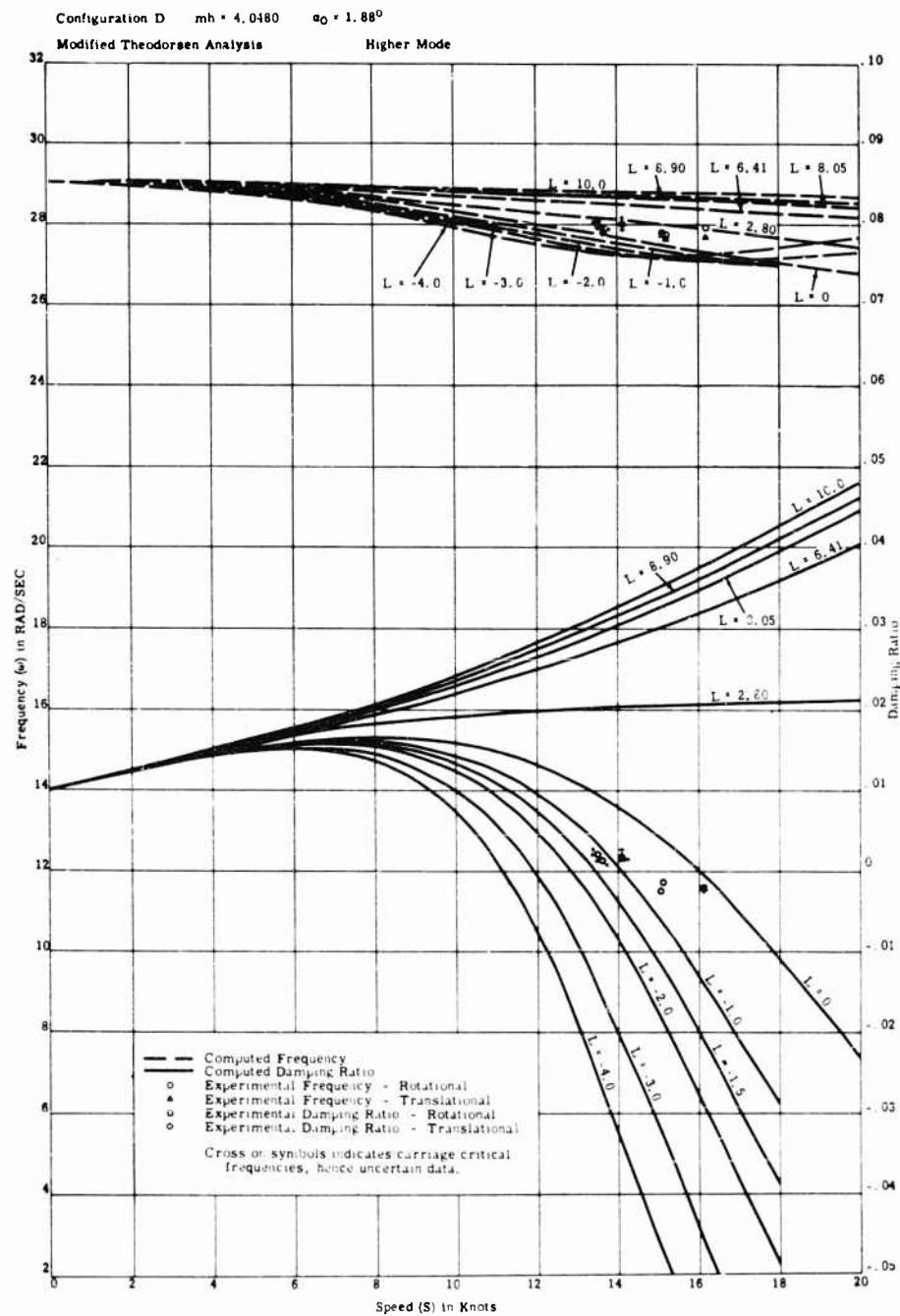Comparison of Theory and Experiment for Marine Control-Surface Flutter

Fig. 83 - Comparison of predicted and observed damping
ratios and associated frequencies for the TMB control
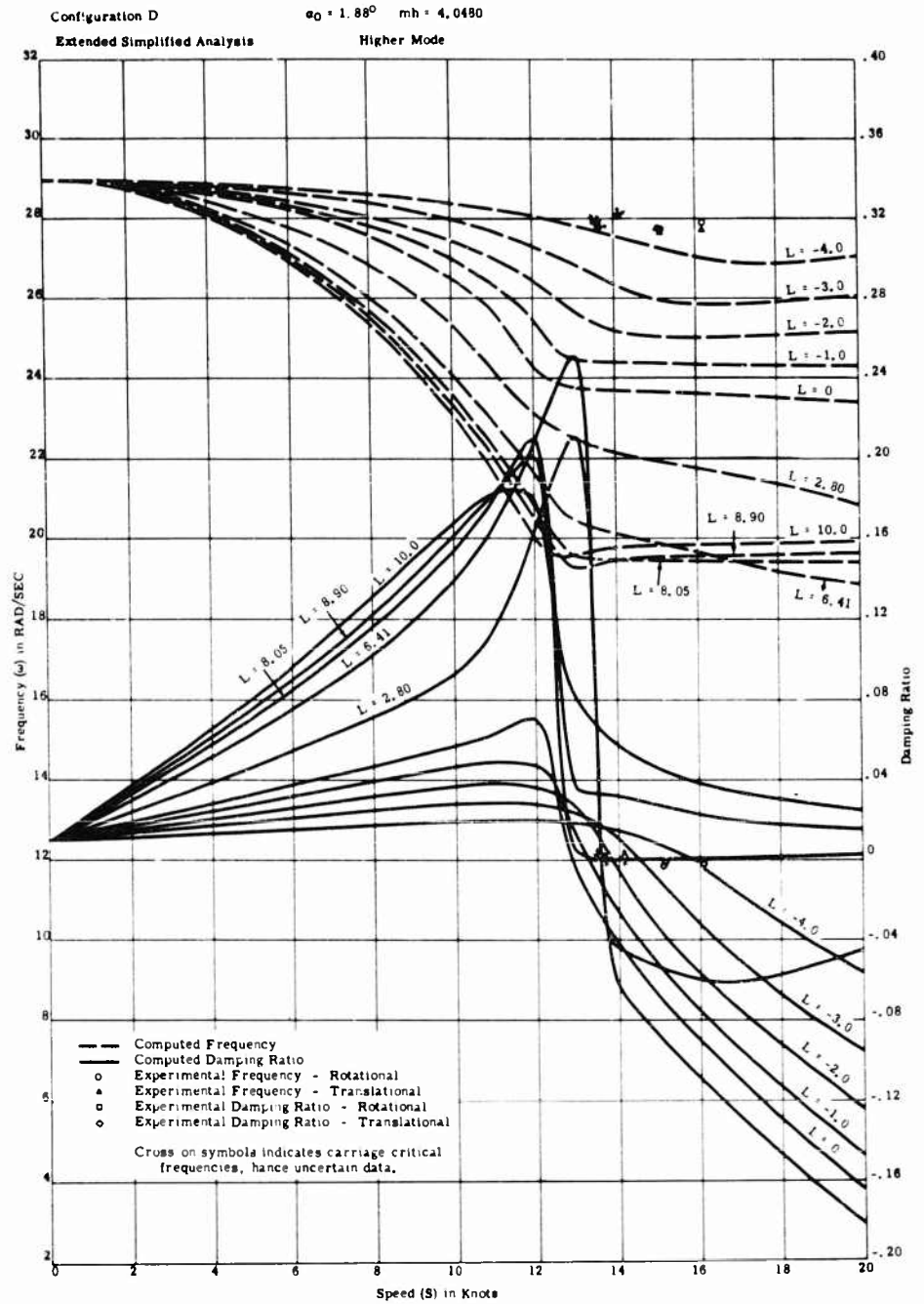surface flutter apparatus

905

Fig. 84 – Comparison of predicted and observed damping
ratios and associated frequencies for the TMB control
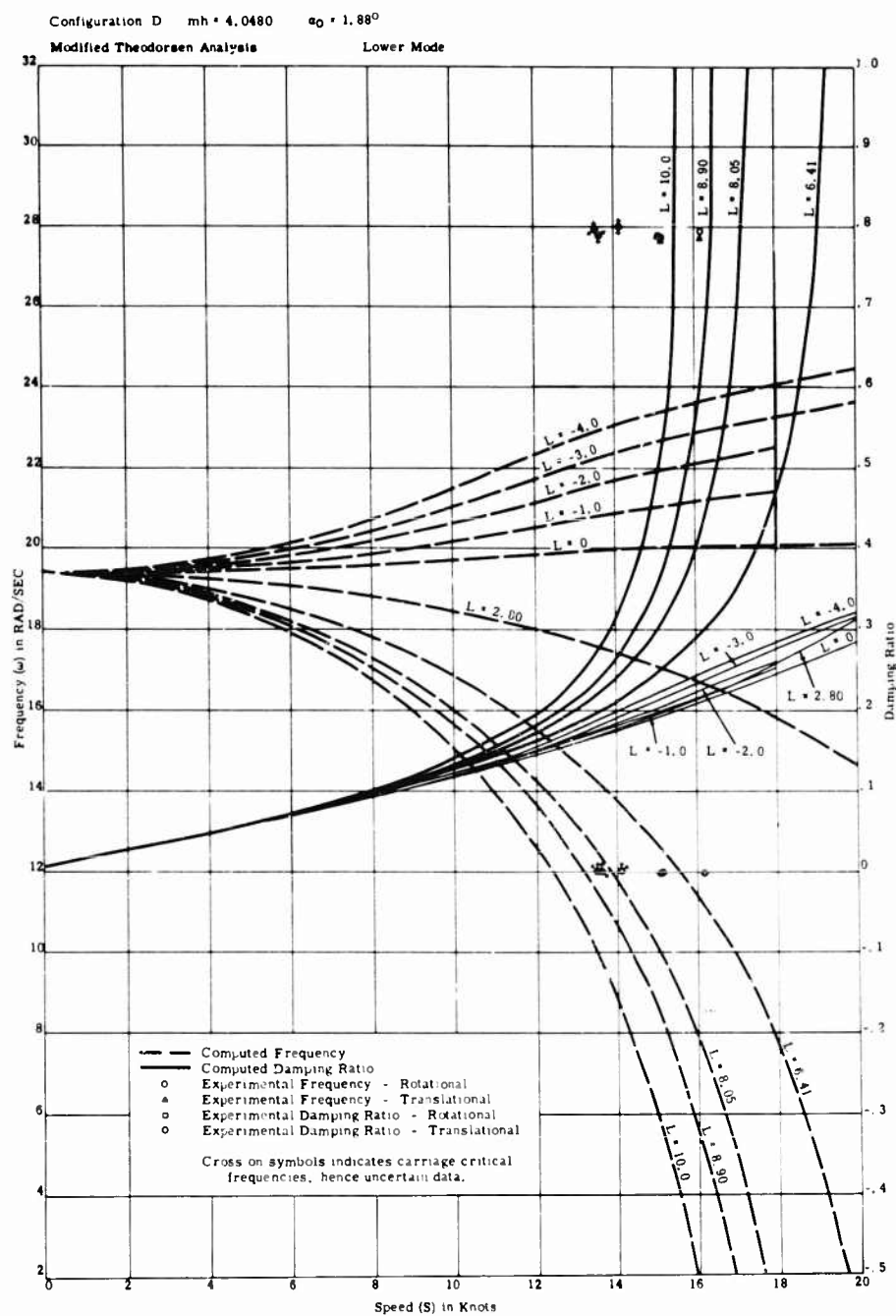surface flutter apparatus

906

Fig. 85 - Comparison of predicted and observed damping ratios and associated frequencies for the TMB control surface flutter apparatus
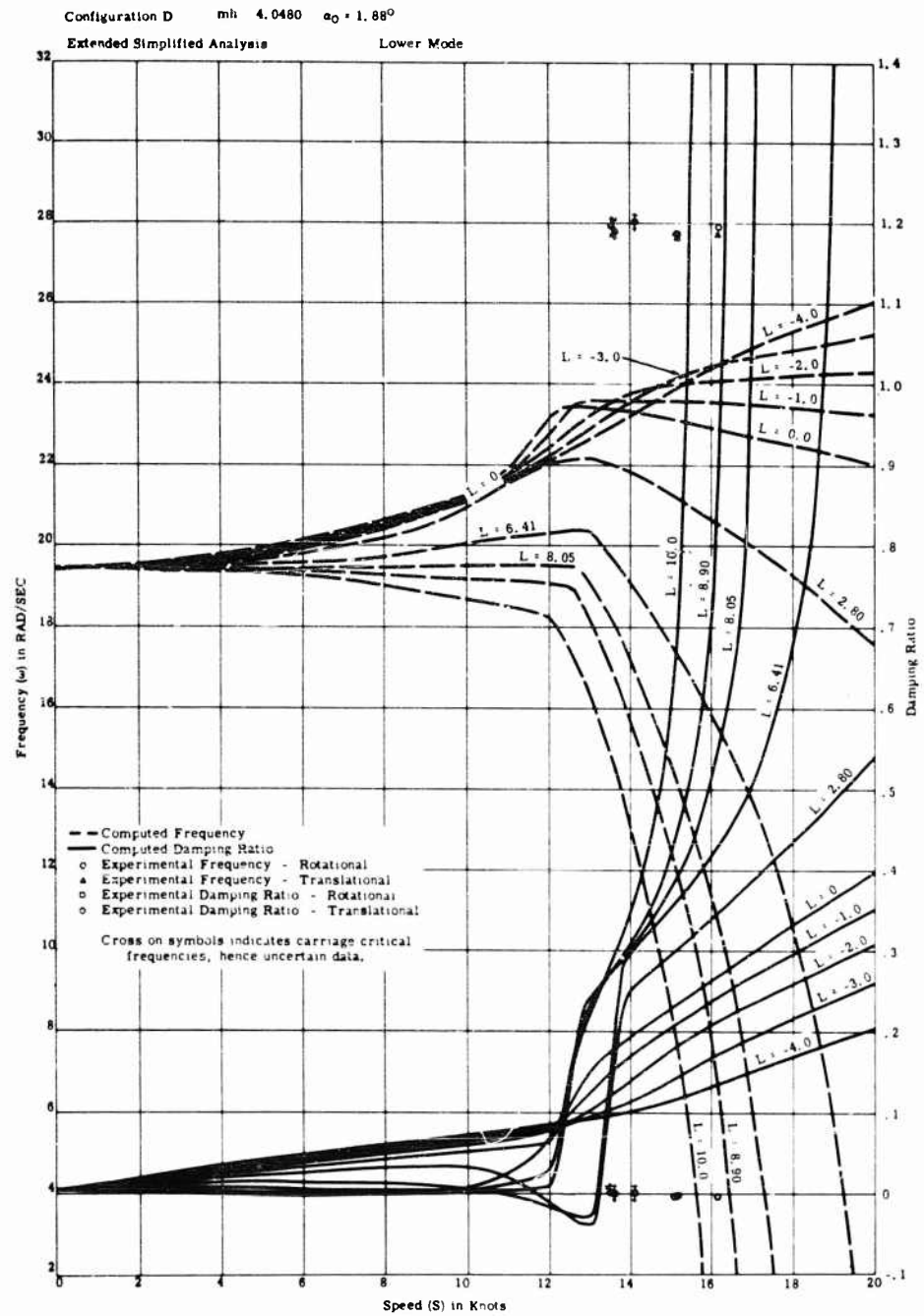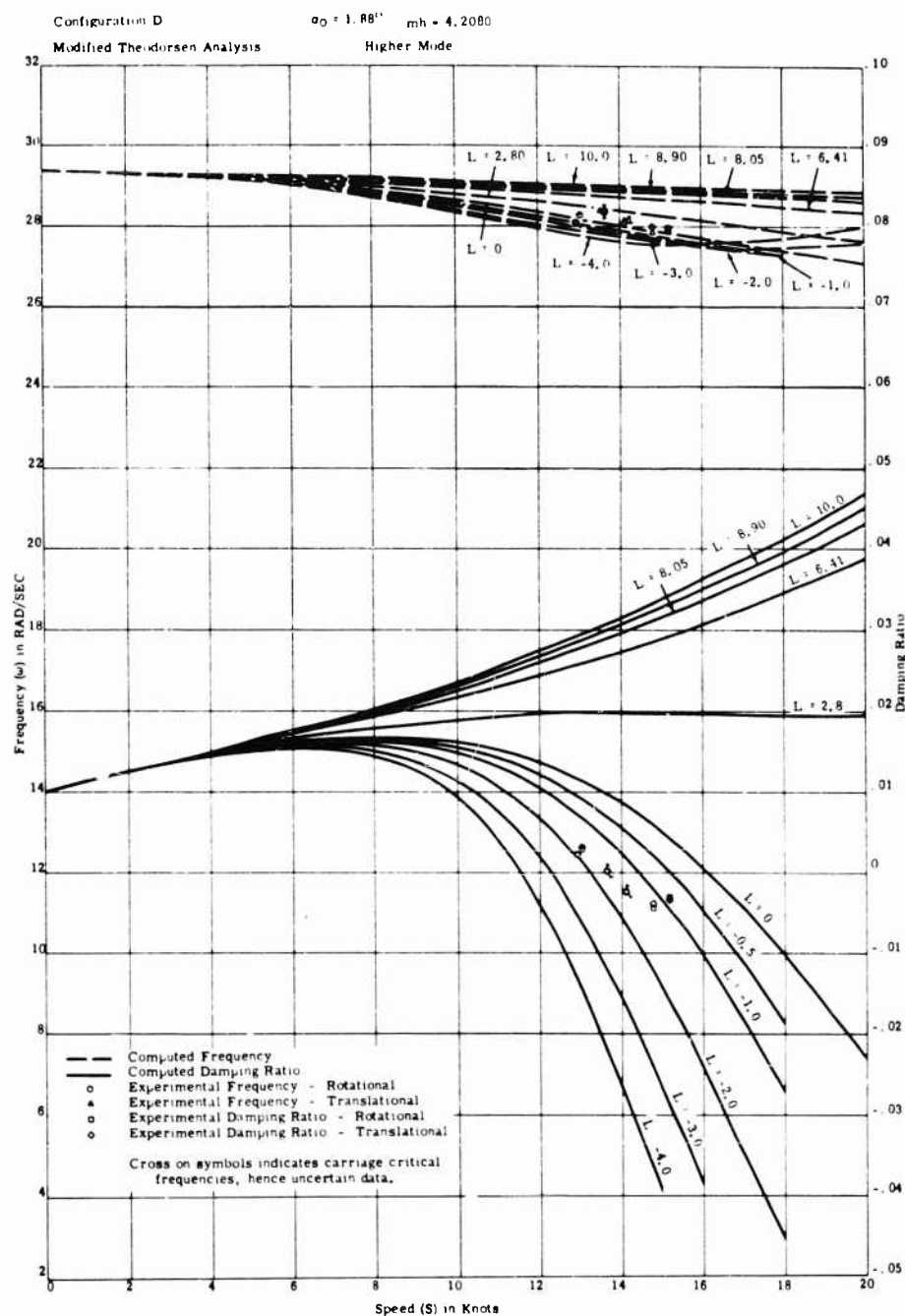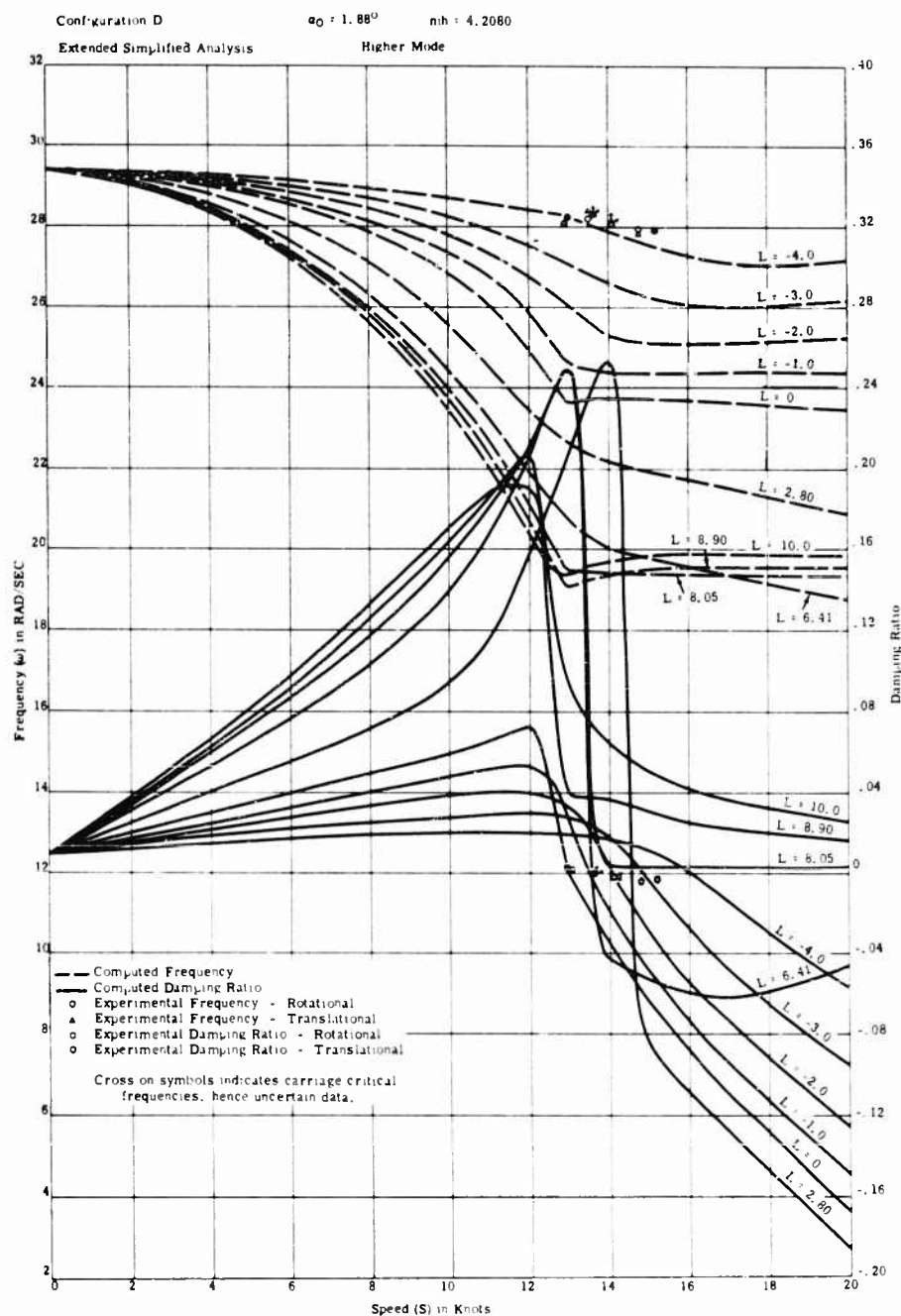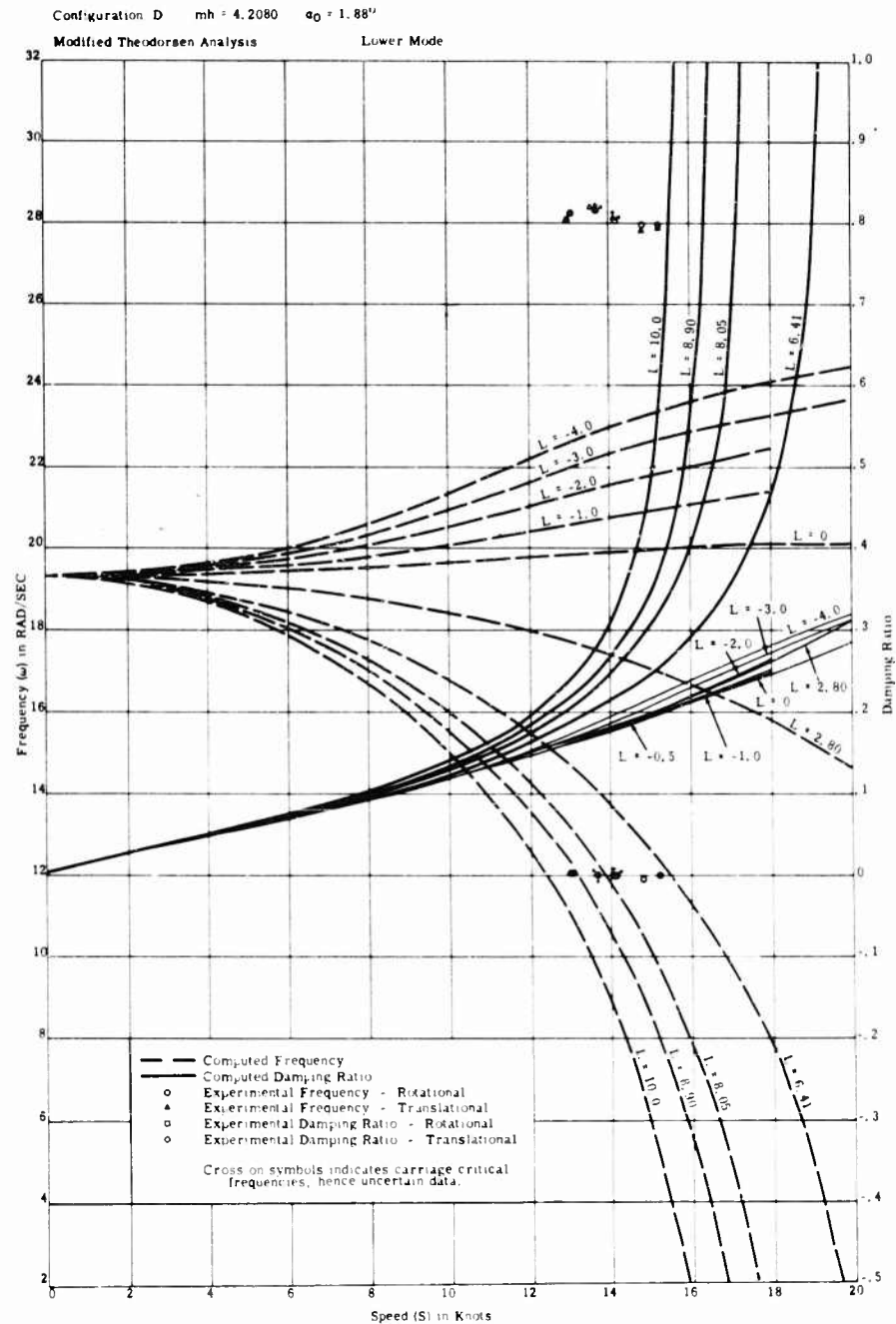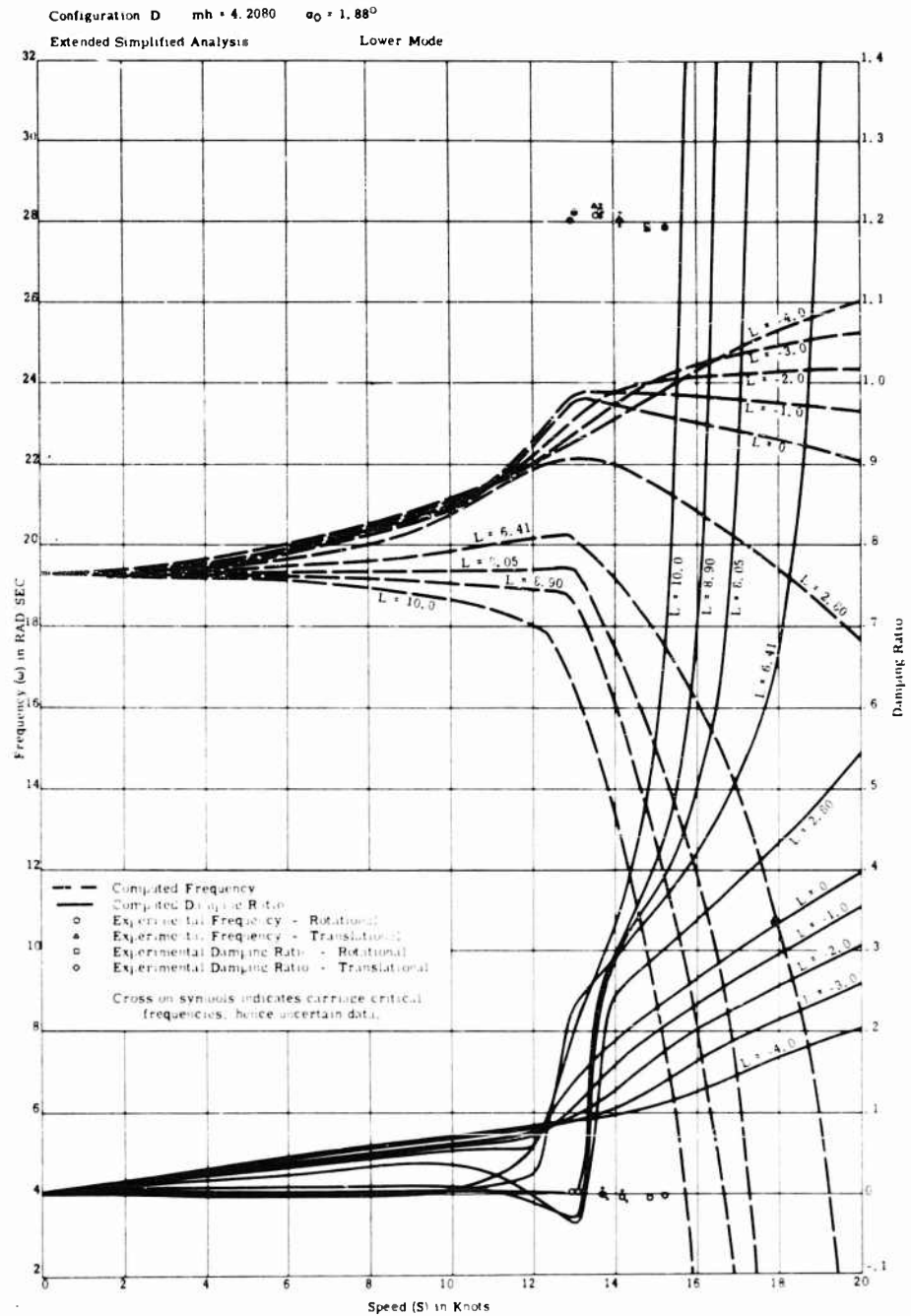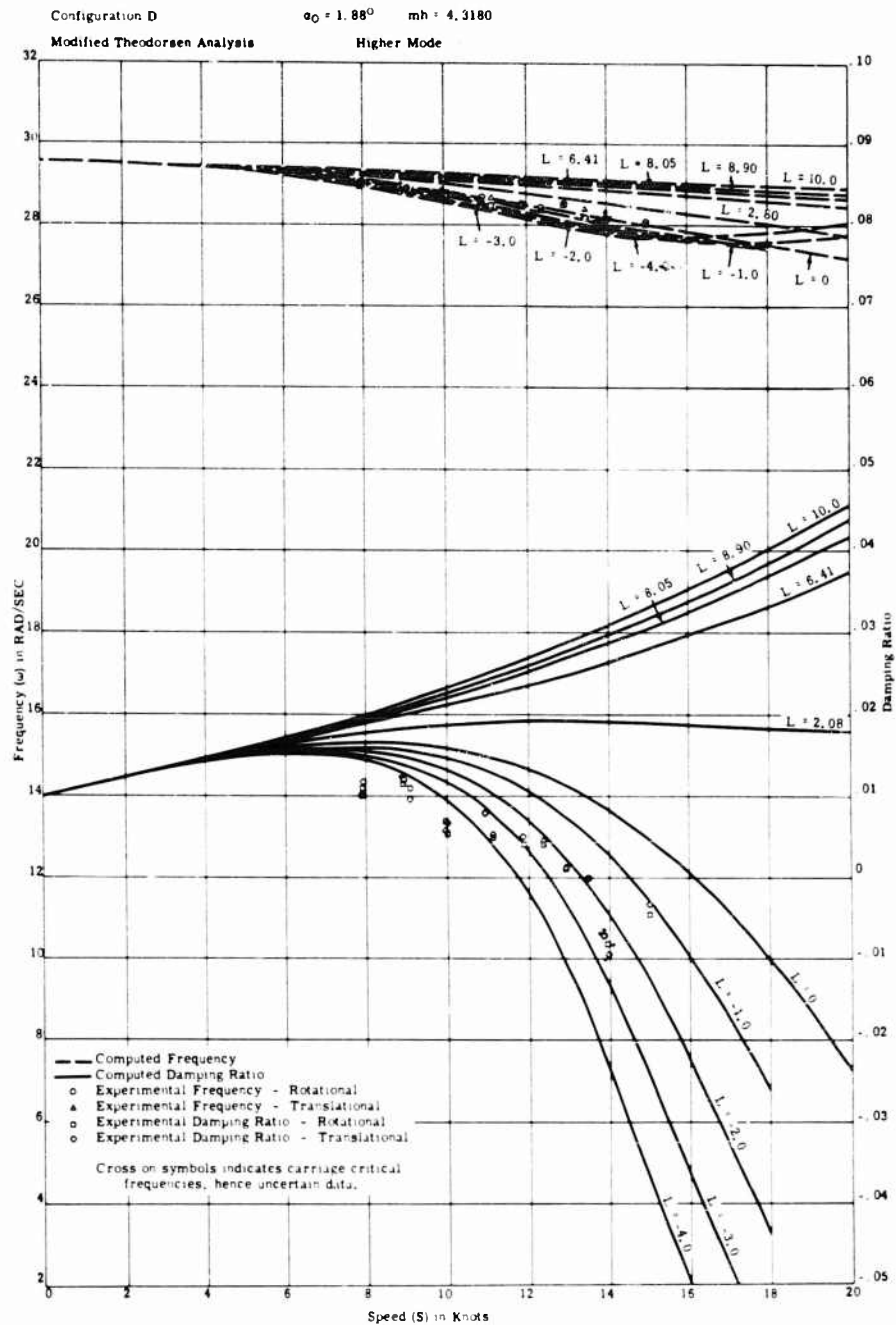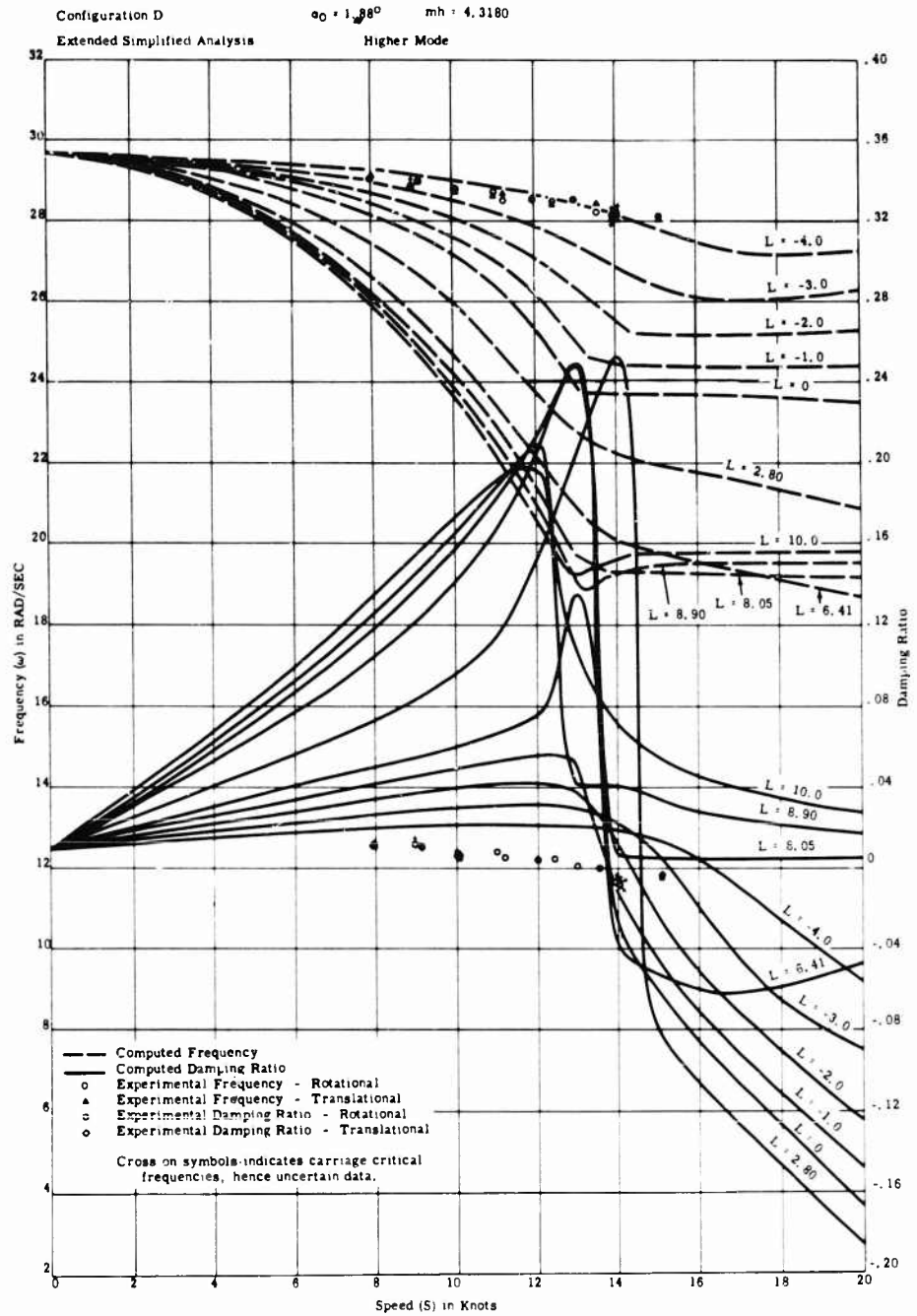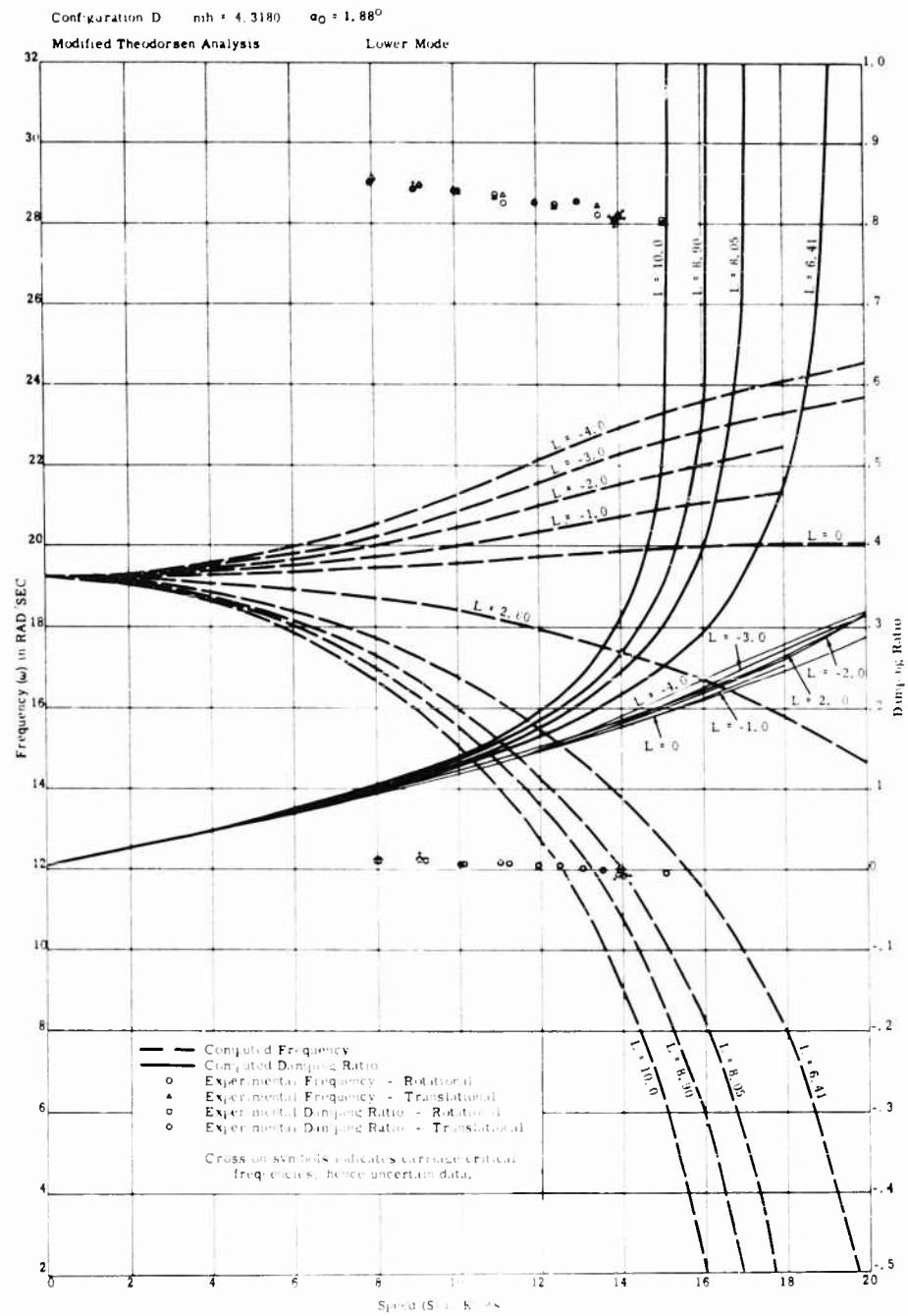
907
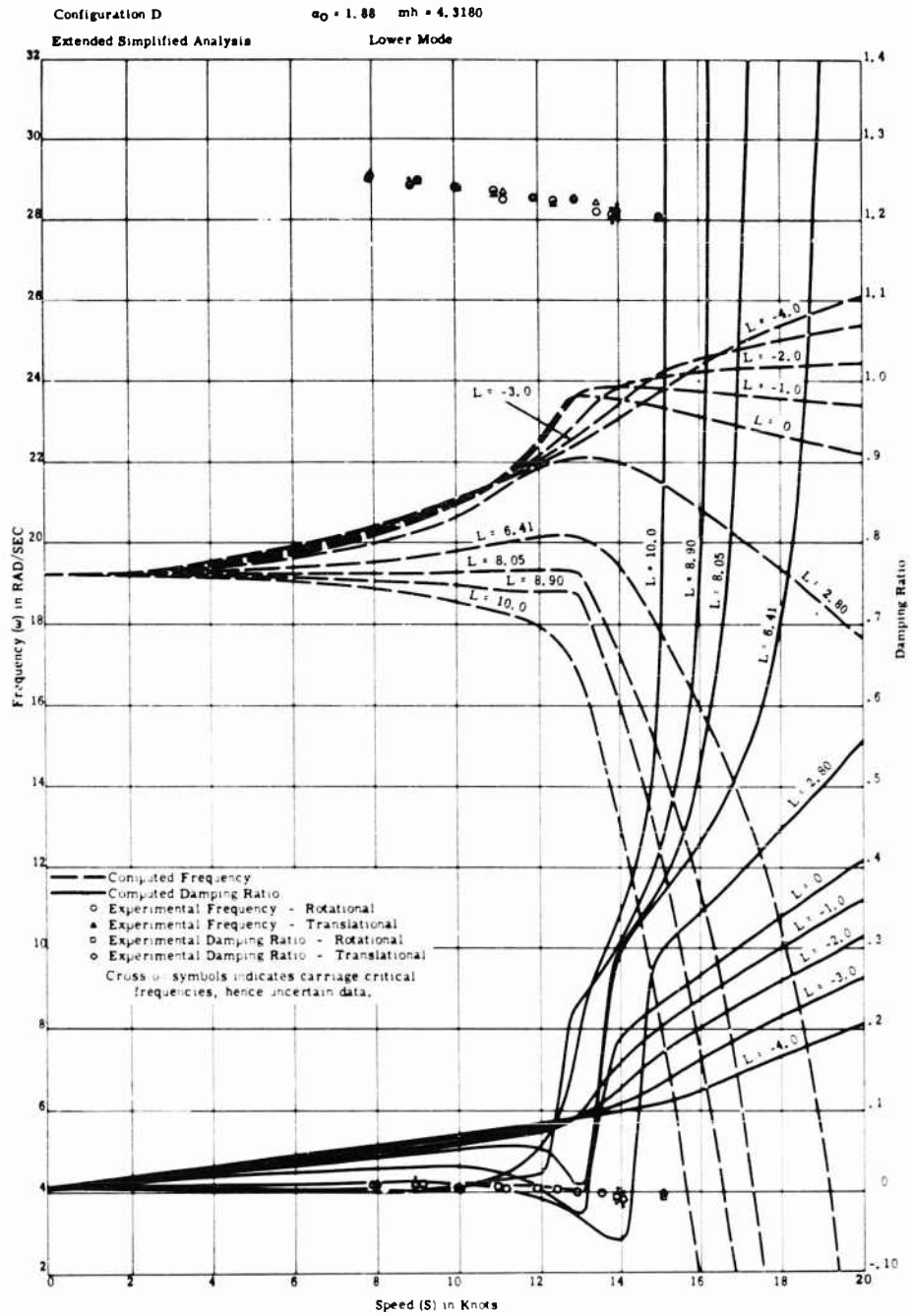
Fig. 86 - Comparison of predicted and observed damping
ratios and associated frequencies for the TMB control
surface flutter apparatus

Superposed on these plots are experimental values of damping ratio and frequency vs. speed. The comparison of theory with experiment should be made in accordance with the points given in the Discussion of Results.

Where experimental data were not available (Figs. 59 through 74), analytical predictions are given to present a qualitative picture of trends, in the computed curves, produced by changes in the parameters mh, L, and S. (Note that in the present analyses, L is a function of a_0 only.)

Appendix B

NUMERICAL VALUES OF THE PARAMETERS mh, L, S, AND a_0

The numerical values of mh, L, S, and a_0, given in Table 3, are those values for which analytical stability predictions were made, based on the Extended Simplified and Modified Theodorsen Analyses.

The mass unbalance (mh) values of Configurations B, D, and TMB 1222 were chosen to correspond to experimental values of mh.

For mh values used in conjunction with Configuration TMB 1222, see [2]. For Configurations B and D, mh values were computed from numerical values of S_a, m', and ab supplied by the Hydromechanics Laboratory. The relation between these quantities is

$$mh = S_a - m'(ab).$$

where ab is the location of the axis of rotation aft of the midchord position, m' is the experimentally observed added mass in translation, and S_a is the moment about the forward quarter-chord point of the rotational structural mass. For both Configurations B and D, ab = -4.5 in. and $m' = 0.284$ lb-sec ^{2}/in. Values of S_a employed experimentally were 2.25, 2.40, 2.54, 2.66, 2.77, 2.93, and 3.04 lb-sec ^{2}.

The values of L listed under Configuration TMB 1222 are all those values for which stability computations based on the Routh discriminant were made in [2]. Experimental measurements reported in that reference showed that L = 2.8 in. was the experimental value to be considered for $a_0 = 0$ deg.

No experimental measurements of L were obtained for Configurations B and D. A range of L corresponding to that employed for Configuration TMB 1222 was used in addition to the negative values, L = -1, -2, -3, -4, which were arbitrarily selected to examine the trends of computed damping ratio and frequency vs. speed curves.

The range of speeds S corresponds to the design range of speeds of the TMB Control Surface Flutter Apparatus (0 to 20 knots).

The a_0's listed in Table 3 are equal to nominal settings of a_0 for which tests were conducted on the flutter apparatus.

Appendix C

RELATIONSHIP OF THE MODEL FREQUENCIES
TO THE PHASE ANGLE BETWEEN Y AND θ

In the ideal two-degree-of-freedom system shown in Fig. 87a, the fundamental or lower frequency is observed when the motions of the two masses are in phase [8]. When the motions are in phase, the algebraic signs of X_1 and X_2 are the same at any instant of time.

When analyzing the motions of the flutter apparatus, the fundamental frequency is also <u>observed</u> when Y and θ have the same signs. However, this condition, for the flutter apparatus, indicates a phase angle ϕ of 180 deg.

This situation is explained by considering the sign conventions employed in the two systems shown in Fig. 87. Table 4 shows the relation between frequency and phase angle for both systems.

Experimental values of phase angle ϕ and frequency are given in Table 4 of [2] for Configuration TMB 1222.
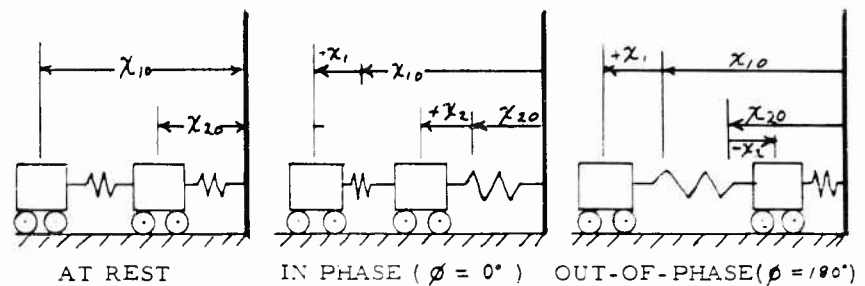
Fig. 87a - Two-mass, two-degree-of-freedom system
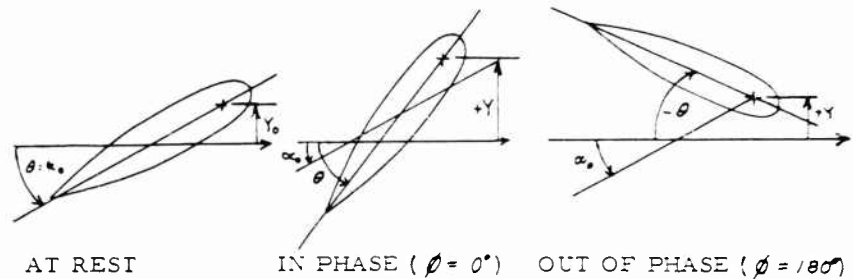
Fig. 87b - Hydrofoil of TMB control surface flutter apparatus

Fig. 87 - Sign convention for two-degree-of-freedom
mass spring system and hydrofoil system

Table 4
Relation Between Frequency and Phase Angle (φ Deg) for Common
Two-Mass System and Hydrofoil of Flutter Apparatus

Two-Mass System (Fig. 87a)			Flutter Apparatus Hydrofoil (Fig. 87b)		
φ Deg	Signs of x_1 and x_2	Frequency	φ Deg (Angle Between Y and σ)	Signs of Y and ς	Frequency
$0°$	Same	Fundamental (Lower)	$\approx 0°$	Same	Higher
$180°$	Opposite	Higher	$\approx 180°$	Opposite	Fundamental

Appendix D

RELATIONSHIP BETWEEN THE PARAMETER L
AND THE ANALYTICAL EXPRESSIONS FOR
HYDRODYNAMIC LIFT AND MOMENT

During constant speed runs of the flutter apparatus with the hydrofoil at a nominal zero preset angle of attack, steady lift forces and moments were observed by the authors of [2].* To account for this observation it was assumed that the center of lift did not coincide with the axis of rotation at the forward quarter-chord position [2]. The observation of steady forces and moments cannot be accounted for by the aerodynamic strip-foil theory used to design the flutter apparatus. Also, the assumption that the center of lift did not coincide with the forward quarter-chord position was made contrary to strip theory.

For both the Extended Simplified and Modified Theodorsen Analyses, it was assumed that the component of oscillatory moment M_ε, due to the oscillatory lift force, follows the steady moment relation; i.e., $M_\varepsilon = L F_L$.

For the Extended Simplified Analysis, the oscillatory lift force is taken to be

$$F_L = AS^2 \left(\tau - \frac{\dot{Y}}{S} \right)$$

which is an expression for the instantaneous oscillatory lift force. The total oscillatory moment was considered to be caused by F_L acting at some point called the center of pressure, not on the axis of rotation. In other words, for the Extended Simplified Analysis,

---

*A great deal of the material contained in this appendix is a restatement of portions of [2]. This material is included here for the reader's convenience.

911

$$M_\theta = LF_1$$

or

$$M_c = ALS^2 \left(\theta - \frac{\dot{Y}}{S} \right)$$

According to the classical Theodorsen analysis, as applied to the flutter apparatus [2], the oscillatory lift forces and moments should be described by the expressions

$$F_L = \frac{1}{2} AS^2\theta - \frac{1}{2} AS\dot{Y} + AbS\dot{\theta}$$

and

$$M_c = -\frac{1}{2} Ab^2 S\dot{\theta}.$$

The Modified Theodorsen Analysis retains the classical expression for F_L. But in describing M_c, both the classical expression $(-1\ 2\ Ab^2 S\dot{\theta})$ and a component to account for the moment due to F_L are considered. Thus

$$M_c = -\frac{1}{2} Ab^2 S\dot{\theta} + LF_L .$$

where F_L is taken to be only the θ dependent terms of the classical expression for F_L. In other words, for the Modified Theodorsen Analysis,

$$F_L = \frac{1}{2} AS^2\theta - \frac{1}{2} AS\dot{Y} - AbS\dot{\theta}$$

and

$$M_c = -\frac{1}{2} Ab^2 S\dot{\theta} + \frac{1}{2} ALS^2\theta .$$

Throughout the derivation of both analyses, L was assumed to depend only on the preset angle of attack α_0, for a given foil section, and to be independent of other parameters such as speed S and mass unbalance mh [2]. In this present study, these analyses, based on this assumption, are used to make computations of damping ratio and frequency of vibration. It is assumed that these computations are reasonably accurate so long as L does not vary widely with parameters other than α_0. (See Discussion of Results and Recommendations.)

Appendix E

CRITERIA FOR SELECTION OF INITIAL CONDITIONS
WHICH ALLOW ONE MODE TO PREDOMINATE
IN THE TOTAL RESPONSE

Two modes of vibration are generally associated with solutions of the equations of motion for the TMB Control Surface Flutter Apparatus. Criteria for the proper selection of initial conditions leading to the suppression of one of the two modes is now derived.

If the equations of motion for either the Extended Simplified or Modified Theodorsen Analyses,

$$B_{12}\ddot{z} + B_{11}\dot{z} + B_{10}z + B_{22}\ddot{Y} + B_{21}\dot{Y} = 0$$

$$R_{12}\ddot{z} + R_{11}\dot{z} + R_{10}z + R_{22}\ddot{Y} + R_{21}\dot{Y} + R_{20}Y = 0$$

have basic solutions of the form

$$z = z_0 e^{\lambda t};\ z_0 e^{\lambda^* t} \quad \text{and} \quad Y = Y_0 e^{\lambda t};\ Y_0 e^{\lambda^* t}.$$

where z_0, Y_0, λ and λ^* are generally complex, then the general solution of the differential equations of motion is

$$z = z_{01}e^{\lambda_1 t} + z_{02}e^{\lambda_1^* t} + z_{03}e^{\lambda_2 t} + z_{04}e^{\lambda_2^* t}$$

$$Y = Y_{01}e^{\lambda_1 t} + Y_{02}e^{\lambda_1^* t} + Y_{03}e^{\lambda_2 t} + Y_{04}e^{\lambda_2^* t}.$$

If the initial conditions are chosen to suppress the λ_2 mode, solutions of the equations of motion representing the λ_1 mode are

$$z = z_{01}e^{\lambda_1 t} + z_{02}e^{\lambda_1^* t}$$

$$Y = Y_{01}e^{\lambda_1 t} + Y_{02}e^{\lambda_1^* t}.$$

These latter solutions for z and Y, with one mode composing the total response, are also solutions of a well known and simpler set of differential equations

$$\ddot{z} + \bar{A}\dot{z} + \bar{B}z = 0$$

$$\ddot{Y} + \bar{C}\dot{Y} + \bar{D}Y = 0.$$

913

To solve these equations for ϕ, assume $\phi = e^{nt}$. Substituting this expression for ϕ, together with its first and second time derivatives, in the simpler differential equation in ϕ yields a quadratic equation,

$$n^2 - \bar{A}n - \bar{B} = 0$$

having roots

$$n_1 = \frac{-\bar{A} - \sqrt{\bar{A}^2 - 4\bar{B}}}{2}$$

and

$$n_2 = \frac{-\bar{A} - \sqrt{\bar{A}^2 - 4\bar{B}}}{2} .$$

With expressions for the roots n_1 and n_2 known, the quadratic equation, $n^2 - \bar{A}n - \bar{B} = 0$ may be written as

$$(n - n_1)(n - n_2) = 0$$

or

$$n^2 - (n_1 - n_2)n - n_1 n_2 = 0 .$$

Comparing this form of the equation with the form originally used shows that

$$\bar{A} = -(n_1 - n_2) \quad \text{and} \quad \bar{B} = n_1 n_2 .$$

The general solution of the equation

$$\ddot{\phi} - \bar{A}\dot{\phi} - \bar{B}\phi = \ddot{\phi} - (n_1 - n_2)\dot{\phi} - n_1 n_2 \phi = 0$$

is

$$\phi = \bar{E}e^{n_1 t} - \bar{F}e^{n_2 t}$$

If $\bar{E}$, $\bar{F}$, n_1 and n_2 are replaced by ϕ_{01}, ϕ_{02}, n_1 and n_2, respectively, then

$$\bar{A} = -(n_1 - n_1) \quad \text{and} \quad \bar{B} = n_1 n_1 .$$

A similar procedure may be followed for γ. When that is done, it is seen that

$$\gamma = \gamma_{01}e^{n_1 t} - \gamma_{02}e^{n_2 t}$$

914

and

$$Y = Y_{01}e^{\lambda_1 t} + Y_{02}e^{\dot{\lambda}_1 t}$$

are solutions of the differential equations

$$\ddot{z} - (\lambda_1 + \dot{\lambda}_1)\dot{z} + \lambda_1\dot{\lambda}_1 z = 0$$

$$\ddot{Y} - (\lambda_1 + \dot{\lambda}_1)\dot{Y} + \lambda_1\dot{\lambda}_1 Y = 0.$$

At this point, note that

$$\lambda_1 + \dot{\lambda}_1 = (\sigma_1 - j\omega_1) + (\sigma_1 - j\omega_1) = 2\sigma_1$$

$$\lambda_1\dot{\lambda}_1 = (\sigma_1 - j\omega_1)(\sigma_1 - j\omega_1) = \sigma_1^2 + \omega_1^2.$$

The preceding differential equations can thus be rewritten as

$$\ddot{z} - 2\sigma_1\dot{z} + (\sigma_1^2 + \omega_1^2)z = 0$$

$$\ddot{Y} - 2\sigma_1\dot{Y} + (\sigma_1^2 + \omega_1^2)Y = 0.$$

The expressions for z and Y with the λ_2 mode suppressed must satisfy both the foregoing simpler differential equations and the equations of motion for the flutter apparatus. Hence, the original equations together with the simpler differential equations may be used to eliminate the second derivatives and to yield a first-order differential equation which must be satisfied by z, Y and $\dot{z}$, $\dot{Y}$. The elimination of the second derivative gives the following set of equations which are the resulting restriction on the initial conditions:

$$(B_{11} - 2\sigma_1 B_{12})\dot{z} + \left[B_{10} - \left(\sigma_1^2 - \omega_1^2\right) B_{12}\right]z$$

$$+ (B_{21} - 2\sigma_1 B_{22})\dot{Y} + \left(\sigma_1^2 - \omega_1^2\right) B_{22}Y = 0$$

$$(R_{11} - 2\sigma_1 R_{12})\dot{z} + \left[R_{10} - \left(\sigma_1^2 - \omega_1^2\right) R_{12}\right]z$$

$$+ (R_{21} - 2\sigma_1 R_{22})\dot{Y} + \left[R_{20} - \left(\sigma_1^2 - \omega_1^2\right) R_{22}\right]Y = 0.$$

These equations enable us to express any two of the quantities $\dot{z}$, z, $\dot{Y}$, or Y in terms of the other two. Because these equations hold at all values of time, they hold at $t = 0$. Thus these two equations constitute the means whereby initial conditions may be chosen to suppress one mode in the total response. That

is, $\dot{Y}_{t=0}$ and $\dot{\theta}_{t=0}$ which may be arbitrarily chosen, and the corresponding values $Y_{t=0}$ and $\theta_{t=0}$ computed from the above equations, are the initial conditions required in solving the original differential equations (practically, by means of an analog or digital computer).[*] There is then no contribution of the θ_2 mode to $\theta(t)$ and $Y(t)$.

Appendix F

THE EFFECT OF INITIAL CONDITIONS ON
THE VIBRATION OF A SHIP'S RUDDER

Solutions $Y(t)$ and $\theta(t)$ of the equations of motion for the flutter apparatus represent the superposition of two modes of vibration when arbitrary initial conditions are assumed. The solution can, however, be restricted to represent a single mode of vibration; i.e., one of the two modes can be suppressed if the initial conditions are properly chosen. This may be seen from the analog solution shown in Fig. 3. Similar solutions can be obtained by the digital method of computation. Criteria for the proper selection of these initial conditions are established in Appendix E.

Similarly, the vibratory response of any point on a rudder or movable control surface of a ship will also depend upon the initial conditions of the rudder[†] in translation and rotation. In actual practice the initial conditions of a rudder vibration may be established by considering an impulsive force of duration τ_i applied at a given point on the rudder at time $t = 0$. The response of the system immediately after the imposition of this force (after $t = \tau_i$) is equivalent to the solution of the homogeneous differential equations of motion for the rudder system with initial conditions the same as the condition of the forced system at $t = \tau_i$.

To obtain the actual initial conditions at time $t = \tau_i$ for the homogeneous equations, it is necessary to solve the inhomogeneous equations of motion which include the impulsive force. Solutions will express the motions of the rudder in translation and rotation as functions of time. The numerical values of these quantities and their time derivatives, evaluated at $t = \tau_i$, are the initial conditions of the vibrating rudder system.

It may be inferred from Table 1 of [9] that the three modes of vibration associated with athwartship motions for an actual rudder system will in general exist simultaneously, unless the initial conditions are specially chosen. Contributions to the displacement of any point on the rudder for each coupled mode are due to the motions in the translational and the two rotational degrees of freedom.

---

[*]This is easily done on the analog computer. Note that all the coefficients are considered as known, ω_i and σ_i having been predetermined on the analog or digital computer as previously explained.

[†]The term rudder will hereafter be used in a broad sense to include rudders and all rudderlike appendages of ships, such as submarine diving planes.

916

The influence of a given set of initial conditions on the vibratory response at different points on the rudder, measured simultaneously, will generally vary because the initial conditions will make different modes (and their associated frequencies) predominate in the vibratory response at different points on the rudder. In other words, different predominant frequencies may be measured at different points on a rudder at the same time. In addition, the relative vibratory response at those same points will vary with changes in the initial conditions, or its equivalent, the point of application of the impulsive force.

Finally, at a given point on a rudder the frequency[*] of a given response curve may vary if an initially predominant mode decays more rapidly than an initially imperceptible mode.

The previous discussion of initial conditions is substantiated by the analysis of the rudder vibration records for ALBACORE presented in [10].

Appendix G

ANALOGY BETWEEN TMB CONTROL SURFACE FLUTTER
APPARATUS AND THE RUDDER CONFIGURATION OF
USS FORREST SHERMAN (DD 931)

The following comments, comparing experimental conditions for the flutter apparatus with trial conditions [1] of FORREST SHERMAN [4] (on which apparent flutter phenomena of the rudders was observed) were made by D.A. Jewell in [7]. These comments are considered to be of great interest in connection with the present study and, because of the concise wording of the original, are quoted here.

"In many ways, the experimental conditions[†] were similar to those on the DD 931. The two degrees of freedom, the natural frequencies, the general rudder configuration, and location of the rotational axis with respect to the rudder were the same in both cases. Two or three experimental parametric values, however, differ significantly from DD 931 values. In dimensionless form, these parameters are:

The mass-density ratio - $\mu = m/\pi \rho b^2$

The distance of the center of mass aft of the rotational axis - X

The frequency - $k = \omega b/v$

where

m is the translational mass,

ρ is the fluid density,

---

b is the rudder semichord,

ℓ is the rudder span length, and

ω is the frequency at speed v.

Values of Three Dimensionless Parameters

Parameter	Experimental	DD 931 Class Ships
μ	≈ 3.0	36
X_a	0.23 to 0.31	0.20
k	≈ 1.0	2.3

The different values of μ and X_a for the ship strongly indicate that the ship's critical flutter speed is much higher than the experimental speeds. For instance, at $X_a = 0.31$, where μ was increased from 3.24 to 3.56 (Configuration B to D), the critical flutter speed increased from approximately 11.5 to 13.5 knots. The effect of the different values of k as an independent parameter cannot yet be evaluated."

The usefulness of the Modified Theodorsen Analysis in predicting the stability of the flutter apparatus can, therefore, reasonably be regarded as an indication of the usefulness of that analysis in predicting ship control-surface flutter, after the refinements suggested in the Recommendations have been made.

Appendix H

THE CLASSICAL THEODORSEN EQUATIONS AND THEIR QUESTIONABLE APPLICABILITY TO RUDDERS

The classical Theodorsen equations are now written for the case of a thin flat foil of width $2b$ and infinite length, inclined at an angle α to a uniform stream of velocity v; see Fig. 88.
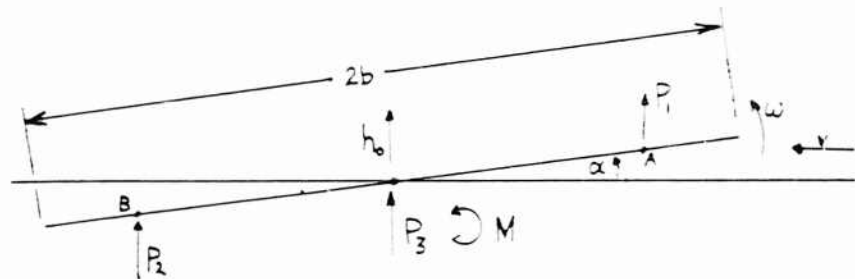
Fig. 88 - Forces and moment on foil moving in a uniform stream

Let h_0 be the displacement of the foil centerline transverse to v and let the foil be stationary or execute small vibrations at circular frequency ω. Then the reactions on the foil are <u>equivalent</u> to three distributed forces and a distributed moment whose respective magnitudes per unit length are:[*]

$$P_1 = 2\pi\rho b v^2 \left(\alpha - \frac{\dot{h}_0}{v}\right) F + \pi\rho b^2 v \left(F + \frac{2}{k} G\right)\dot{\alpha} - 2\pi\rho b^2 \frac{1}{k} G \left(\ddot{h}_0 - \frac{b}{2}\ddot{\alpha}\right)$$

acting along the forward quarterline A,

$$P_2 = \pi\rho b^2 v\dot{\alpha}$$

acting along the rear quarterline B, and

$$P_3 = -\pi\rho b^2 \ddot{h}_0$$

acting along the midchord line, and

$$M = -\frac{1}{8}\pi\rho b^4 \ddot{\alpha}.$$

Here

$$\frac{1}{k} = \frac{v}{b\omega} = \frac{vT}{\pi(2b)} ; \qquad T = \text{period} = \frac{2\pi}{\omega}$$

919

F and G are functions of $1/k$ (see [5], Fig. 4), with F positive and G negative. F rises from $F = 1/2$ at $1/k = 0$ to 1 (?)[a] as $1/k \to \infty$. G decreases from $G = 0$ at $1/k = 0$ to a minimum of -0.20 at about (?) $1/k = 5$ and then slowly increases to 0 (?) as $1/k \to \infty$.

$1/k$ can be visualized as the distance that the stream advances during one period of vibration divided by π times the foil width.

In these formulas, α represents rotation of the foil about the midchord line. It may be preferable to let the rotation α occur about a parallel axis e away, e being positive ahead of midchord. Let h_e denote the displacement of the foil at this new axis; then $h_0 = h_e - e\alpha$. Substitution for h_0 in the formula for P_1 changes the first two terms to P_1' where

$$P_1' = 2\pi b v^2 \left(\alpha - \frac{\dot{h}_e}{v}\right) F - \pi b^2 v \left[\left(1 - 2\frac{e}{b}\right) F - \frac{2}{k} G\right] \dot{\alpha}$$

The individual magnitudes of these terms are thereby changed, but their sum remains the same. It is simplest, however, to let h_0 stand in the third term of P_1 and in P_3 and M. The total turning moment M_e about the new axis of rotation is given by the formula

$$M_e = P_1 \left(\frac{b}{2} - e\right) - P_2 \left(\frac{b}{2} - e\right) - P_3 e - M$$

The forces that give rise to M are distinct from those included in P_1, P_2, or P_3; they add up to a zero resultant but provide a turning moment M, of the magnitude stated, about any axis.

DISCUSSION

The validity of Theodorsen's formulas for rudders is discussed presently. If his formulas are used, it appears probable that the constant $1/k$ will normally be less than unity for ships. When

$$\frac{1}{k} < 1, \qquad \frac{1}{2} = F < 0.55, \qquad -G < 0.05$$

Lift Force. If $\dot{\alpha} = 0$ and $\ddot{h}_e = 0$, only the first term of P_1 remains as the familiar lift force per unit length for steady motion acting along the forward quarter-line. Here $\dot{h}_e$ represents a steady translation and merely alters the steady angle of attack. In this case $\dot{\alpha} = 0$, hence $1/k \to \infty$ and (presumably) $F = 1$.

Virtual Mass. P_3 and M may be regarded as reactions to a distributed virtual mass π_1 along the midchord line and a distributed virtual moment of inertia I along this line. The coefficient of $(\ddot{h}_0 - b/2\ddot{\alpha})$ in P_3 will be denoted by $\bar{M}$. The magnitudes are (per unit length):

[a] These (?) are used because the graphs go only to $1/k = 40$; values at $1/k \to \infty$ have not been verified; or graph is on too small a scale.

920

$$M_\rho = \pi\rho b^2 ; \qquad \overline{M}_\rho = -2\pi\rho b^2 \left(\frac{1}{k}\right) G ; \qquad I_\rho = \frac{1}{8}(\pi\rho b^4) .$$

Note that $\ddot{h}_0 - b/2\ \ddot{\alpha}$ is the acceleration of the rear quarter line and that $G \doteq 0$, so that $\overline{M}_\rho \doteq 0$. Also, $bv/\omega = b^2/k$. The quantities M_ρ and I_ρ have the usual values for a uniform plane strip of infinite length moving transversely.

Significant Terms in P_1. The quantity $\overline{M}_\rho/M_\rho = -(2/k) G \doteq 0$. If $1/k < 2$, $\overline{M}_\rho/M_\rho < 0.6$. As $\omega \to 0$ and $1/k \to \infty$, $\overline{M}_\rho \to \infty$ (?) but less rapidly than $1/\omega$; however, the contribution of the $\overline{M}_\rho$ term to P_1 for given amplitudes of h_0 and α is numerically proportional to $bv\omega G$, and so $\to 0$ as $\omega \to 0$ (since $\ddot{h}_0 = -\omega^2 h_0$, $\ddot{\alpha} = -\omega^2\alpha$). This part of P_1 is not enormously large, as shown by a comparison with the first two F terms in P_1. The terms in $\ddot{h}_0$ and $\dot{h}_0$ differ in phase, but may be compared as to magnitude by introducing the amplitudes $h_{0\ amp}$ = amplitude of h_0, etc.; then $\ddot{h}_{0\ amp} = \omega\dot{h}_{0\ amp}$, etc. Similar comparisons may be made for $\ddot{\alpha}$ and α. Then it is seen that (since $1/k = v/b\omega$):

$$\ddot{h}_0 \text{ ratio} = \frac{2\omega(bv/\omega)(-G)\ \ddot{h}_{amp}}{2\omega bvF\dot{h}_{0\ amp}} = -\frac{G}{F}$$

$$\ddot{\alpha} \text{ ratio} = \frac{2\omega(bv/\omega)(-G)\ 1/2(b\omega^2\ \ddot{\alpha}_{amp})}{2\omega bv^2 F\ddot{\alpha}_{amp}} = \frac{1}{2}\frac{b\omega}{v}\left(\frac{-G}{F}\right) = \frac{1}{2}k\left(\frac{-G}{F}\right) .$$

Here

$$-G/F < 0.35\ (?) : \qquad 1/2\ k/(-G/F) < 0.20\ (?) .$$

Hence for a rough approximation, the

$$G\left(\ddot{h}_0 - \frac{b}{2}\ \ddot{\alpha}\right)$$

term in P perhaps may be ignored in comparison with the first term of P_1.

Damping Terms. Two methods for discussing the foil damping are now presented. In the first method the forces and moments on the foil associated with the $\dot{\alpha}$ terms are considered, whereas in the second method the energy of the foil associated with the $\dot{h}_0$ and $\dot{\alpha}$ terms is treated.

Force-Moment Method. The $\dot{\alpha}$ terms in P_2 and P_1 add to a force P_3 of magnitude

$$P_3 = -\rho b^2 v\left(1 - F - \frac{2}{k} G\right) \dot{\alpha} .$$

Also, these two terms in P_2 and P_1, one acting at $-b/2$ and the other at $-b/2$, give rise to a turning moment M_3 about midchord of magnitude

$$M_3 = \frac{1}{2}\ \rho b^3 v\left(-1 - F - \frac{2}{k} G\right) \dot{\alpha}$$

921

$M_{\dot{a}}/\dot{a} < 0$ since $F < 1$ and $G < 0$. Our equations are valid only for harmonic motion, but we surmise that whatever physical process gives rise to a ratio $M_{\dot{a}}/\dot{a}$ that is negative in all cases of harmonic motion will tend to damp out any motion, i.e., have a positive damping effect. The effect of P_2, however, is not easily seen.

A rough estimate of the quantitative significance of P_2 and M_2 may perhaps be made by comparing these quantities, respectively, with the $\dot{a}$ term in P_1 and with the turning moment about midchord due to this term. Because of a 90 deg difference in phase, the comparison is made most easily in terms of amplitudes by recalling that $\dot{a}_{amp} = \omega a_{amp}$. The algebraic signs are then of minor interest; hence, for convenience $-M_2$ will be used instead of $-M_2$. Denoting the amplitude ratios for P and M by r_p and r_M respectively:

$$r_p = \frac{\pi \rho b^2 v \left(1 - F - \frac{2}{k} G\right) \omega a_{amp}}{2 \pi \rho b v^2 F a_{amp}} = \frac{k}{2}\left(\frac{1}{F} - 1\right) - \frac{G}{F}$$

$$r_M = \frac{\frac{1}{2} \pi \rho b^3 v \left(1 - F - \frac{2}{k} G\right) \omega a_{amp}}{\pi \rho b^2 v^2 F a_{amp}} = \frac{k}{2}\left(\frac{1}{F} - 1\right) - \frac{G}{F}$$

since $b(\omega/v) = k$. Some values calculated from these formulas, using Theodorsen's Fig. 4 for F and G, are:

$1/k$	0	0.25	0.5	1.0	2.0	4.0	10.0	20.0	30.0	40.0	∞
F	.5	0.51	0.52	0.54	0.60	0.70	0.84	0.91	0.94	0.96	1.00
G	0	-0.03	-0.06	-0.10	-0.15	-0.18	-0.16	-0.13	-0.10	0.09	0
r_p	∞	5.9	2.80	1.24	0.42	0.05	-0.08	-0.09	-0.07	-0.07	0
r_M	∞	1.98	1.04	0.61	0.42	0.31	0.20	0.15	0.11	0.09	0

From these values of r_p and r_M, it appears that when $1/k < 0.25$, at least, the $\dot{a}$ terms in P_1 and P_2 may be expected to have large effects in comparison with the $\dot{a}$ term in P_1. Only when $1/k > 5$ do the terms become relatively rather small.

Energy Method. The terms containing $\dot{h}_0$ or $\dot{a}$ in P_1 and P_2 have the form of damping terms. It is worthwhile to ascertain the sign of their net effect upon the energy of the vibrating foil.

Let dW/dt stand for the inflow of energy into the foil due to the components of force represented by the $\dot{h}_0$ and $\dot{a}$ terms. If $dW/dt < 0$, the net energy flow is outward as in ordinary (positive) damping.

922

The value of dW/dt can be found by multiplying each component of force by the velocity of its point of application, and adding these products. The velocity is $\dot{h}_0 + b\dot{\alpha}/2$ for any term of P_1, but $\dot{h}_0 - b\dot{\alpha}/2$ for P_2, which acts along the rear quarter-chord line. Hence (in the case of harmonic motion):

$$\frac{dW}{dt} = -2\pi\rho\, bv \left\{ \left[F\dot{h}_0 - \frac{b}{2}\left(F + \frac{2}{k}G\right)\dot{\alpha}\right] \left(\dot{h}_0 + \frac{b}{2}\dot{\alpha}\right) - \frac{b}{2}\dot{\alpha}\left(\dot{h}_0 - \frac{b}{2}\dot{\alpha}\right)\right\}$$

or

$$\frac{dW}{dt} = -2\pi\rho\, bv\left[F\dot{h}_0^{\,2} - \left(1 + \frac{2}{k}G\right)\dot{h}_0\,\frac{b}{2}\dot{\alpha} + \left(1 - F - \frac{2}{k}G\right)\left(\frac{b}{2}\dot{\alpha}\right)^2\right]$$

The factor enclosed in brackets [ ] in the last equation will be denoted hereafter by the symbol [ ]. The $\dot{h}_0^{\,2}$ and $\dot{\alpha}^2$ terms are positive, since $F < 1$ and $G < 0$, but the sign of the $\dot{h}_0\dot{\alpha}$ term is not fixed. Hence, a numerical investigation is necessary.

Write $b\dot{\alpha}/2 = \zeta\dot{h}_0$ where ζ may have any real value. Then after dividing by $\dot{h}_0^{\,2}$

$$\frac{1}{\dot{h}_0^{\,2}}[\ ] = F - \left(1 + \frac{2}{k}G\right)\zeta + \left(1 - F - \frac{2}{k}G\right)\zeta^2$$

If $\zeta \to \pm\infty$, the ζ^2 term predominates and [ ] must be positive, since $F < 1$ and $G < 0$. Between these extremes, $[\ ]/\dot{h}_0^{\,2}$, regarded as a function of ζ, must have a minimum value and [ ] can become negative only if this minimum is itself negative.

To locate the minimum, set the derivative of $[\ ]/\dot{h}_0^{\,2}$ with respect to ζ equal to zero and solve for ζ, obtaining

$$\zeta = \frac{1 - \frac{2}{k}G}{2\left(1 - F - \frac{2}{k}G\right)}.$$

Substitution of this value of ζ gives as a minimum value

$$\frac{1}{\dot{h}_0^{\,2}}[\ ] = F - \frac{\left(1 - \frac{2}{k}G\right)^2}{4\left(1 - F - \frac{2}{k}G\right)}.$$

Some values calculated with the use of Theodorsen's Fig. 4 are:

$1/k$	0	0.25	0.5	1.0	2.0	4.0	10.0	20.0	30.0	40.0
F	0.50	0.51	0.52	0.54	0.60	0.70	0.84	0.91	0.94	0.96
G	0	-0.03	-0.06	-0.10	-0.15	-0.18	-0.16	-0.13	-0.10	-0.09
$2G/k$	0	-0.02	-0.06	-0.20	-0.60	-1.44	-3.2	-5.2	-6.0	-7.2
$(1+2G/k)^2$	1.0	0.96	0.88	0.64	0.16	0.18	4.84	17.6	25.0	38.4
$1-F-2G/k$	0.50	0.51	0.54	0.66	1.00	1.74	3.36	5.29	6.06	7.24
$[\ ]/\dot{h}_0^2$	0	0.04	0.11	0.30	0.56	0.67	0.48	0.07	-0.09	-0.37

It may be concluded that, at least for $0 \leq 1 k < 21$, $[\ ] > 0$ and hence $dW\ dt < 0$, so that the net effect of the $\dot{h}_0$ and $\dot{\alpha}$ terms in P_1 and P_2 is to withdraw energy from the foil. Thus, if steady flutter occurs with $1\ k$ in the range specified, other terms must provide an equal inflow of energy. At speeds below the lowest speed at which flutter is possible, it may be surmised that the physical processes responsible for the $\dot{h}_0$ and $\dot{\alpha}$ terms in the formulas for the harmonic case will give rise to positive damping.

It would seem that, if the $\dot{h}_0$ term in P_1 is retained, as is usually done, then for consistency the $\dot{\alpha}$ terms should be retained also. In steady motion the $h_0\ v$ term results from a simple cause - namely, a change in the angle of attack - whereas the origin of the $\dot{\alpha}$ terms is not obvious, but this difference scarcely seems to justify retention of the $\dot{h}_0$ term alone.

Simplified Approximations. The following approximations may be useful for some purposes. The steady-motion lift force described on page   is frequently used as an approximation even when α is allowed to vary. It is then necessary to consider whether h_0 should be replaced by the displacement of some point other than the forward quarter-line, and what assumption should be made concerning the effective line of action of the lift. If this line of action is distant L from the axis of rotation, the turning moment about this axis will equal L times the lift force.

For a closer approximation the $\dot{\alpha}$ terms may be retained. So long as $1\ k$ does not exceed 1 or 2, however, the error may not be excessive if all G terms are omitted and F is replaced by $1/2$. This was done in [2] in obtaining the "Modified Theodorsen Analysis." To obtain the results in [2], we assume that the originally specified lines of action for P_1' and P_2 are retained. If $F = 1\ 2$ and $G = 0$, the results for P_1' and P_2 with the axis of rotation distant "e" ahead of midchord are:

$$P_1' = -\pi b v^2 \left(\alpha - \frac{\dot{h}_e}{v} \right) - \pi b^2 v \left(1 - 2\frac{e}{b} \right) \frac{1}{2} \dot{\alpha}$$

$$P_2 = -\pi b^2 v \cdot 1 \cdot \dot{\alpha}.$$

Therefore, the total lift force per unit length on the foil is:

$$P_a = P_1' + P_2 = \pi\rho\, b\, v^2 \left(\alpha - \frac{\dot{h}_e}{v} \right) + \pi\rho\, b^2 v \left(\frac{3}{2} + \frac{e}{b} \right) \dot{\alpha} .$$

We do not try to specify a line of action for P_a as a whole. To calculate the total moment M_a about the axis (exclusive of inertial moment M), it is necessary to split P_a again into its two parts, P_1 acting at $(b/2 - e)$ ahead of the axis and P_2 acting at $(-b/2 - e)$ behind the axis (e is negative if behind mid-chord). Then

$$M_a = P_1'(b/2 - e) + P_a(-b/2 - e) = P_1'(b/2 - e) - P_2(b/2 + e)$$

$$= \pi\rho\, b\, v^2 (\alpha - \dot{h}_e/v)(b/2 - e) + \pi\rho\, b^2 v \dot{\alpha}(1/2 + e/b)(b/2 - e) - \pi\rho\, b^2 v \dot{\alpha}(b/2 + e)$$

$$= -\pi\rho\, b\, v^2 (b/2 - e)(\alpha - \dot{h}_e/v) + \pi\rho\, b^2 v (b/4 + e/2 - e/2 - e^2/b - b/2 - e) \dot{\alpha}$$

$$= \pi\rho\, b\, v^2 (b/2 - e)(\alpha - \dot{h}_e/v) - \pi\rho\, bv(b/2 + e)^2 \dot{\alpha} .$$

In the special case $e = b/2$:

$$P_a = \pi\rho\, bv^2 (\alpha - \dot{h}_e/v) + 2\pi\rho\, b^2 v \dot{\alpha}$$

$$M_a = -\pi\rho\, b^3 v \dot{\alpha} .$$

These values of P_a and M_a agree with those of F_L and M_σ as given in the middle of page 37 of [2], where $S = v$, $Y = h_e$, $\sigma = \alpha$, and $A = 2\pi\rho b1$. The length of the foil 1 occurs in A because F_L and M_σ represent total reactions on the foil, whereas P_a and M_a stand for magnitudes per unit length.

No specific line of action for P_a or F_L is assumed here, since the total turning moment about the α or σ axis is explicitly stated in the second equation. That is, the same distributed forces whose resultant is P_a or F_L give rise to the moment M_a or M_σ. The usual device of replacing the second equation by $M_a = LP_a$ or $M_\sigma = LF_L$ is not available because M_a or M_σ is not proportional to the whole of P_a or F_L. To facilitate thinking, however, it may be desirable to assume that P_a or F_L acts along a line through α or σ axis.

DAMPING COMPUTATIONS FOR ALBACORE RUDDER
AND TMB FLUTTER APPARATUS

A meaningful interpretation of r_p and r_M is strictly valid for the foil described on page ____ and approximately valid for an airplane wing; however, for a structurally damped rudder with finite aspect ratio and thickness, attached at the quarter chord ($e = 0$) through a flexible rudder shaft to a flexible hull, the actual values of r_p and r_M would undoubtedly be different from the theoretical

values found from the equations derived on page   . Moreover, the motions of the top of the rudder stock, at the point of attachment of the rudder stock to the hull, certainly affect the damping of the rudder. Finally, the athwartship vibratory displacements of the rudder consisting of motions in three degrees of freedom, one in translation and two in rotation, further invalidate the use of r_p and r_M in determining the significance of the P_2 and M_2 terms.

For the TMB Flutter Apparatus, the relatively rigid rudder stock (or shaft) is attached at its upper end to a rigid structure and the hydrofoil motions are restricted to two degrees of freedom. However, again $e \neq 0$, the foil is structurally damped and has a finite aspect ratio and thickness.

Nevertheless, it is instructive to show by example how, based on Theodorsen's equations, a value of r_p and r_M can be determined for an actual or rudder model (i.e., rudder plus stock attached to a rigid hull) when the effects of finite aspect ratio and thickness are ignored and when the motions of the rudder in only two degrees of freedom are treated. The motions in these degrees are considered to make the most significant contributions to the vibratory displacement. Although the results here for r_p and r_M hold only for $e = 0$, the procedure for deriving the equations leading to a single calculation for r_p and r_M points the way, for the interested reader, towards deriving just as easily, similar equations for "e" corresponding to a rudder turning about a rudder stock attached at the quarter-chord, i.e., $e = b/2$.

For the rudder of ALBACORE, b may be estimated as 3 ft and the lowest vibration frequency for vY_2 vibrations as 780 cpm.* Thus $\omega = 2\pi \cdot 780/60 = 82$ rad/sec and, if v_{kn} is the speed in knots,

$$1/k = v/b\omega = 1.69 \, v_{kn}/(3 \cdot 82) = v_{kn}/145$$

$$v_{kn} = 10 \quad 20 \quad 30$$

$$1/k = 0.069 \quad 0.138 \quad 0.207.$$

At such speeds the chart on page   indicates that $r_p < 6$, $r_M < 2$. Such values of r_p and r_M discourage omission of the $\ddot{z}$ terms in P_1 and P_2.

For the TMB Flutter Apparatus described in [2], $b = 9$ in. and the frequency is 4 cps, hence

$$1/k = \{1.69 \, v_{kn}/0.75 \, (4 \cdot 2\pi)\} = v_{kn}/11 .$$

Thus at 22 knots, $1/k = 2$ and $r_p = 0.42$, $r_M = 0.42$. Conceivably such values of r_p and r_M justify the suspicion that failure to obtain flutter in the observations might have been due largely to excessive hydrodynamic damping.

Perhaps for airplane wings, low ω and high v make k and, hence, also r_p and r_M much less than 1, so that neglect of the $\ddot{z}$ terms is justified.

---

*As shown in this report, the frequency does not vary much with speed.

APPLICATION OF THE CLASSICAL THEODORSEN
EQUATIONS TO RUDDERS

Theodorsen's results refer to the case of a uniform flat foil of infinite length. In contrast, the aspect ratio of ships' rudders (height over width) is rather small (always between 1 and 3). The forces in this case are likely to be decidedly different from those obtained by direct use of the classical Theodorsen expressions. Recent work described in various reports does, in fact, indicate that this difference is probably large. (See discussion by H.N. Abramson in [4].)

When the foil is locked in rotation ($\dot{\alpha} = \ddot{\alpha} = 0$) at an angle of attack $\alpha = \alpha_0$, then for a constant displacement $h_0(\dot{h}_0 = \ddot{h}_0 = 0)$ the steady lift force ($c(k) = 1$) given by Theodorsen's classical equation is (for a foil of length ℓ):

$$P'_1 = P_1 \ell = 2\pi\rho \, \ell b v^2 \alpha_0$$

whereas the Extended Simplified or Modified Theodorsen Analyses give (In Appendix D let F_L, S, and θ be denoted by P'_1, v, and α respectively)

$$P'_1 = Av^2 \alpha_0 .$$

For the TMB Flutter Apparatus, it was found that the lift force predicted by the classical Theodorsen analysis is approximately three times as large as the lift force found by experiment [2]*; i.e., the lift constant $2\pi\rho \ell b \approx 3A$, where the experimental value for A is 0.034 lb - sec^2/in.^{2} (see Table 2).*

Actually, not much is known so far about the magnitude of the force and moment reactions on a ship's rudder, except, of course, in the case of a steady rudder angle. In other cases, measurement of the reactions is no doubt difficult. Attention should be directed at present toward obtaining actual measurements of the reactions on vibrating rudders or rudder models; such experimental data may lead to the establishment of a reliable method of predicting both steady and unsteady lift force and moment vs. speed relations.

Moreover, as pointed out in the Discussion of Results, the inclusion or omission of structural damping can make a relatively large difference in the predicted critical flutter speed.

Free surface waves and cavitation affect the boundary conditions, thereby causing additional differences between hydroelastic and aeroelastic phenomena.

Further reservations as to the applicability of Theodorsen's equations to ship and/or model rudders are based on analysis and evaluations given in Discussion of Results.

---

*Note that $2\pi\rho\ell b = 6.28 \, (9.34 \times 10^{-5} \text{ lb - sec}^2/\text{in.}^4) \, (18 \text{ in.}) \, (9 \text{ in.}) = 0.094 \text{ lb - sec}^2/\text{in.}^2$.

927

REFERENCES

1. Antkowiak, E.T., "Hull Vibration in the DD 931 Class Destroyer," Boston Naval Shipyard Evaluation Report R-10 (20 Aug. 1956).

2. McGoldrick, R.T., and Jewell, D.A., "A Control-Surface Flutter Study in the Field of Naval Architecture," David Taylor Model Basin Report 1222 (Sep. 1959).

3. David Taylor Model Basin letter 9870-1 (771:RCL:fts)/Ser 7-289 of 28 October 1960 to Chief, Bureau of Ships.

4. McGoldrick, R.T., "Rudder-Excited Hull Vibration on USS FORREST SHERMAN (DD 931) - A Problem in Hydroelasticity," Transactions of Society of Naval Architects and Marine Engineers, Vol. 67 (1959). Also David Taylor Model Basin Report 1431 (June 1960).

5. Theodorsen, T., "General Theory of Aerodynamic Instability and the Mechanism of Flutter," National Advisory Committee for Aeronautics Report 496 (1934).

6. Jewell, D.A., and McCormick, M.E., "Hydroelastic Instability of a Control Surface," David Taylor Model Basin Report 1442 (Dec. 1961).

7. David Taylor Model Basin letter 9870.1 (591:DAJ:mcs) of 25 July 1960 to Chief, Bureau of Ships.

8. Pipes, L.A., "Applied Mathematics for Engineers and Physicists," McGraw-Hill Book Company, Inc., Second Edition, Chapter 8 (1958).

9. Leibowitz, Ralph C., "USS ALBACORE (AG SS 569) Modes of Rudder Vibration," David Taylor Model Basin Report 1540 (Sep. 1961).

10. Leibowitz, R.C., and Kilcullen, A., "Experimental Determination of Structural Damping and Virtual Mass of Control Surfaces," David Taylor Model Basin Report (in preparation).

BIBLIOGRAPHY

1. Abramson, H.N., "An Exploratory Study of the Flutter Characteristics of the Fairwater Planes of SSN 585 (SKIPJACK)," Southwest Research Institute Technical Report 5, Contract Nonr 2470(00), SWRI Project 19-754-2 (Dec. 1959).

2. Abramson, H.N., "Studies of Hydroelasticity," Southwest Research Institute Final Report, Contract Nonr 2470(00), SWRI Project 19-754-2 (Jan. 1960).

3. Abramson, H.N., and Chu, W.H., "A Discussion of the Flutter of Submerged Hydrofoils," Southwest Research Institute Technical Report 1, Contract

Nonr 2470(00), SWRI Project 19-754-2 (Aug. 1958). Also see Journal of Ship Research, Vol. 3, No. 2 (Oct. 1959).

4. Abramson, H.N., and Chu, W.H., "An Alternative Formulation of the Problem of Flutter in Real Fluids," Southwest Research Institute Technical Report 2, Contract Nonr 2470(00), SWRI Project 19-754-2 (Aug. 1958).

5. Abramson, H.N., and Chu, W.H., "A Note on Panel Flutter as a Problem in Hydroelasticity," Southwest Research Institute Technical Report 4, Contract Nonr 2470(00), SWRI Project 19-754-2 (Oct. 1959).

6. Chu, W.H., and Abramson, H.N., "Effect of the Free Surface on the Flutter of Submerged Hydrofoils," Southwest Research Institute Technical Report 3, Contract Nonr 2470(00), SWRI Project 19-754-2 (Sep. 1958). Also see Journal of Ship Research, Vol. 3, No. 1 (June 1959).

7. Abramson, H.N., and Chu, W.H., "Problems of Hydroelasticity," Southwest Research Institute Progress Report 2, Contract Nonr 2470(00), SWRI Project 19-754-2 (June 1958).

8. Campbell, I.J., et al., "Aerodynamic Characteristics of Rectangular Wings of Small Aspect Ratio," (British) Aeronautical Research Council Technical Report 3142 (1960).

9. Chopin, S., "Calculs de Flottement Lorsque Certains Modes Propres Sont Tres Proches Par Leurs Frequences, Sans Que Leurs Masses Generalisees Soient Voisines," La Recherche Aeronautique Bulletin Numero 76 (1960).

10. Dugundji, J., and Crisp, J.D.C., "On the Aeroelastic Characteristics of Low Aspect Ratio Wings with Chordwise Deformations," United States Air Force Office of Scientific Research Technical Note 59-787 (July 1959).

11. Duncan, W.J., "The Fundamentals of Flutter," (British) Aeronautical Research Council Technical Report 2417 (Nov. 1948).

12. Flax, A.H., "Aero-and-Hydro-Elasticity," First Symposium on Naval Structural Mechanics, Stanford University, Stanford, California (August 1958).

13. Harrington, M.C., "Excitation of Cavity Resonance by Air Flow," Meeting of the Division of Fluid Dynamics of the American Physical Society, New York (Jan. - Feb. 1957).

14. Henry, C.J., et al., "Aeroelastic Stability of Lifting Surfaces in High-Density Fluids," Journal of Ship Research, Vol. 2, No. 4 (March 1959).

15. Hilborne, D.V., "The Hydroelastic Stability of Struts," Admiralty Research Laboratory/R1/G/HY/5/3 (Nov. 1958).

16. Jewell, D.A., "A Note on Hydroelasticity," Journal of Ship Research, Vol. 3, No. 4 (March 1960).

929

17. Kaplan, P., and Henry, C.J., "A Study of the Hydroelastic Instabilities of Supercavitating Hydrofoils," Journal of Ship Research, Vol. 4, No. 3 (Dec. 1960).

18. Lankester, S.G., and Wallace, W.D., "Some Investigations into Singing Propellers," North East Coast Institute Transactions, Vol. 71, Part 7 (1955).

19. MacDonough, E.P., "The Minimum Weight Design of Wings for Flutter Conditions," Journal of the Aeronautical Sciences, Vol. 20 (Apr. 1953).

20. MacNeal, R.H., "Unsteady Aerodynamic Forces - Two Dimensional Incompressible Strip Theory," Computer Engineering Associates, Inc., Pasadena, California (Unpublished).

21. Macovsky, M.S., et al., "An Investigation of a Flow-Excited Vibration of the USS FORREST SHERMAN (DD 931)," David Taylor Model Basin Report 1188 (Aug. 1958).

22. Mandel, P., "Some Hydrodynamic Aspects of Appendage Design," Paper Presented at the Annual Meeting of Society of Naval Architects and Marine Engineers (Nov. 1953).

23. Reed, W.H., "Effects of a Time-Varying Test Environment on the Evaluation of Dynamic Stability with Application to Flutter Testing," Paper Presented at the Aeroelasticity-II Session, Twenty-Sixth Annual Meeting, Institute of Aeronautical Sciences, New York (Jan. 1958).

24. Salaun, P., "Structural Damping Matrix in Flutter Calculations," L'Office National D'Etudes et De Recherches Aeronautiques Pub. 69 (Mar. - Apr. 1959).

25. Smith, A.D.N., "The Effect of Various Parameters on Wing-Torsion Aileron-Rotation Flutter," (British) Aeronautical Research Council Technical Report 3168 (1960).

26. Theodorsen, T., and Garrick, I.E., "Mechanism of Flutter - A Theoretical and Experimental Investigation of the Flutter Problem," National Advisory Committee for Aeronautics Report 685 (1940).

27. Wadlin, K.L., and Christopher, K.W., "A Method for Calculation of Hydrodynamic Lift for Submerged and Planing Rectangular Lifting Surfaces," National Aeronautics and Space Administration Report R-14 (1959).

28. Widmayer, E., et al., "Experimental Investigation of the Effect of Aspect Ratio and Mach Number on the Flutter of Cantilever Wings," National Aeronautics and Space Administration Technical Note D-229 (Apr. 1960).

29. Woods, L.C., "Aerodynamic Forces on an Oscillating Aerofoil Fitted with a Spoiler," Proceedings of the Royal Society of London, Series A, Vol. 239 (1957).

30. Woods, L.C., "Unsteady Plane Flow Past Curved Obstacles with Infinite Wakes," Proceedings of the Royal Society of London, Series A, Vol. 229 (1955).

Friday, August 31

Afternoon Session

HYDROELASTICITY

Chairman: J. J. Nachtsheim

Bureau of Ships
Washington, D. C.

EFFECTS OF UNDERWATER EXPLOSIONS
ON ELASTIC STRUCTURES

George Chertock
David Taylor Model Basin
Washington 7, D. C.

INTRODUCTION

Underwater explosions have been in use for 100 years or so, and there has accumulated a considerable store of information on the effects of these explosions on ships and structures. Most of this information is best described as qualitative "know-how", a large part has been condensed into quantitative formulaes based on some empirical data and much speculative data, and a small part of the information has been analyzed mathematically and correlated with fundamental physical theory.

In keeping with the purpose of this symposium I intend to discuss some of this more analytic work, and only with regard to its interest as examples of hydroelasticity, not for its military applications or importance. Special applications of this analysis were published in a series of papers starting about 10 years ago. However, the method has been considerably generalized since then, and I hope that the formalism and point of view will be of value in other hydroelastic problems.

When an underwater explosion acts on a submerged structure there is a very large interaction between the motions of the structure and the pressure field. The structure not only responds to the pressures but substantially modifies them. However, it is possible by a proper choice of generalized coordinates and parameters to separate the analysis of this response into two independent parts, one describing the explosion and its pressure wave without the target, and the other describing the possible motions of the target without the explosion. Thus it makes sense to start by describing the pressure field due to the explosion in a free field with no boundaries.

933

Underwater Explosion Pressure Field

There is a very extensive theoretical and experimental literature on underwater explosion phenomena [1,2] and a good survey was given by Snay at a previous symposium [3]. However, since most of you are probably unfamiliar with the field, I will summarize those features which are of particular importance to our problem.

An explosion is simply a chemical reaction which very quickly converts a solid mass of explosive into an equal mass and volume of gas at high temperature and pressure. The initial gas pressure is typically of the order of a half million psi. In an underwater explosion, this high pressure bubble then expands against the ambient hydrostatic pressure level and pulsates with very large changes in volume and pressure. Thus the pulsing bubble presses on the water and radiates a pressure wave which can be completely determined from the motion of the bubble surface. The initial kick of the bubble generates the high amplitude shock wave which propagates as a steep fronted pulse with exponential decay behind the front. Because of the high amplitude and because of viscosity effects at the front, the amplitude decreases with distance a little faster than $1/r$. The subsequent continuous motion of the bubble generates a pressure wave similar to any low amplitude acoustic pressure which varies in proportion to the volume acceleration of the source. If as in many structural response problems, the response time of the structure is much longer than the duration of the shock wave, then the precise variation of the shock wave pressure is of no consequence and the shock wave can be represented as an impulse. Then the pressure at (r, t) is

$$p(r, t) = \frac{\rho \dot{V}_o}{4\pi r} \delta(t - r/c) + \frac{\rho \ddot{V}(t - r/c)}{4\pi r} .$$ (1)

where $\delta(t - r/c)$ is a delta function of time, $\dot{V}_o$ is the initial volume velocity of the explosion bubble and $\ddot{V}$ is the volume acceleration of the bubble measured at the retarded time $t - r/c$. Thus, the problem of determining the pressure field can be replaced by the problem of determining the history of the bubble volume.

The bubble volume vs time relation is known from a combination of theoretical analysis and experiments on many different scales. A typical $V(t)$ curve is shown in Fig. 1.

The bubble pulses about its equilibrium volume with relatively long slow expansions and short quick contractions. For 1000 lbs of TNT at a depth of 100 ft, the first peak bubble has a diameter of about 50 ft and the first bubble period, i.e., the time to the first contraction is about 0.75 sec. For any other charge size and depth the peak bubble volume is proportional to the weight of charge W divided by the total hydrostatic pressure P at the depth of the explosion, and the first bubble period is proportional to $W^{1/3} P^{5/6}$. When the bubble first contracts, about two thirds of its energy is dissipated in irreversible processes. Hence, the second peak volume of the bubble is about one third as large as the first, and the pulsation period is about 70 percent of the first. There are similar energy losses at every contraction of the bubble and so the amplitude and period of the pulsation progressively decrease. Figure 1 is a representative but simplified history of the explosion bubble. It is modified in detail by the nature of the

934

explosive, by the important effects of migration due to gravity forces and to the presence of nearby surfaces. But for our present purpose the important point is that if the bubble volume is given in units of its maximum value, and if the time is expressed in units of the first bubble period, then the relation between the reduced volume and the reduced time is a universal relation which is applicable with sufficient accuracy to all charge sizes and all depths. This universal curve is simply Fig. 1, with the coordinates of the first maximum set equal to $V/V_m = 1$, $t/T_b = 1/2$.
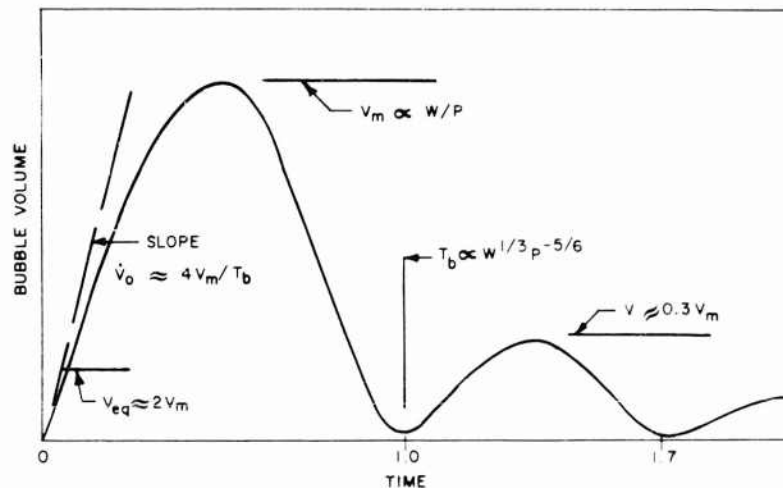
Fig. 1 - Variation of bubble volume with time

The pressure wave generated by the explosion bubble is shown in Fig. 2. Whenever $V < V_{equ}$, then $\ddot{V}$ is positive and a positive pressure signal is generated, and whenever $V > V_{equ}$, which occurs for about 78 percent of the time, then $\ddot{V}$ is negative and a negative pressure signal is radiated. Again to give you a feeling for the others of magnitude involved and again referring to the 1000 lb charge at the 100 ft depth, the shock wave at a 50 foot standoff has a peak pressure of 3000 psi and a time constant of 0.75 millisecond which is only $1/10$ percent of the first bubble period and doesn't even show on the graph. The amplitude of the second positive peak, or first bubble pulse as it is called, can be anything up to 15 to 20 percent of the shock wave peak, typical values are 5 to 10 percent. During the under pressure phase the peak underpressure is typically only $1/2$ percent of the peak shock wave pressure. Despite these relatively low pressures the durations of these later pressures are so much longer that the time constant of the shock wave that they may have a greater influence on structural motions than the shock wave does.

935

Fig. 2 - Variation of pressure with time

STRUCTURAL MOTIONS

In general there are two types of explosion-excited motions which have been amenable to theoretical analysis. Historically the first class of motions to be analysed wa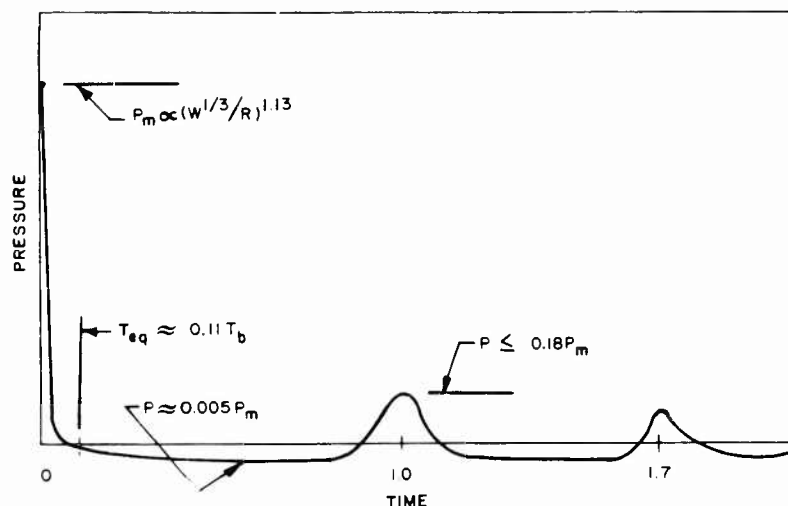s the large plastic deformations of circular steel diaphragms under attack by the shock wave phase of an underwater explosion. It turns out that these motions are very appreciably affected by complex non-linear effects, e.g., strain hardening, strain rate, and delayed yielding effects in the steel, and by cavitation effects in the water, and while most of the features are qualitatively understood a complete theoretical analysis of the process has never been achieved. However, I do not intend to discuss these effects any further, because there has been very little of this type of analysis in the last 10 years, and the older work is adequately described in the now unclassified literature [2].

The types of motion I will discuss are a class of linear elastic motions that appear over the whole outer surface of the hull, and particularly those which can be completely described in terms of normal vibration modes of the surface.

It is a common observation from experience that a structure is capable of sustained vibration in many different characteristic patterns or modes of motion, and that each mode has a characteristic frequency. We will specify the pattern of motion by a mode function $\psi_i(S)$, where ψ_i is the relative displacement in the direction of the normal to the surface at the point S on the surface. The index i labels the modes according to any convenient scheme. As an example of the types of motion, we could consider very general vibration patterns of a submarine hull made up of rigid body motions such as heaving and pitching; beam-like flexural motions or whipping vibrations in which each transverse section of the ship moves as a unit in the direction normal to the longitudinal axis, accordionlike vibrations in which each transverse section moves as a unit

936

in the axial direction and expands or contracts radially, and lobar vibrations in which the perimeter of each transverse section deforms into a wavy pattern. For any particular submarine these mode functions and their associated frequencies can in principle be calculated theoretically by solving an eigenvalue problem, or perhaps they can be measured experimentally. But most of the things I have to say are independent of the particular mode function and depend only on three general properties of these normal modes. First is the fact that these mode functions are mutually orthogonal.

$$\iint \mu \psi_i \, \psi_j \, d\sigma \;=\; M_i \, \delta_{ij} \, , \tag{2}$$

where $\mu(S)$ is the mass per unit area at S divided by the cosine of the angle between the direction of motion and the surface normal, and M_i is the modal mass for mode i. Note that picking M_i is equivalent to normalizing ψ_i. Second is the assumption that the mode functions form a sufficiently complete set, i.e., that any complex vibration history of the surface, whether due to free or forced motion, can be expressed as a superposition of these normal modes

$$f(S, t) \;=\; \sum q_i(t) \, \psi_i(S), \tag{3}$$

where $q_i(t)$ is the normal coordinate which measures the instantaneous amplitudes of excitation. The third property is the equation of motion when any time varying pressure distribution $p(S, t)$ acts on the surface of the body, namely

$$M_i(\ddot{q}_i + z_i^2 \, q_i) \;=\; \iint p \, \psi_i \, d\sigma. \tag{4}$$

where z_i is the circular frequency of that mode (in vacuo) and the right side is the generalized force or modal force in the ith mode. In a real submerged structure, these three relations are only approximations or idealizations of the true situation. For one thing structural damping forces have been neglected. In an actual structure they are not negligible, they are not proportional to the velocity, and they are not distributed in proportion to the mass distribution. Second we have effectively assumed a shell-type structure in which all of the vibrating mass is in the shell or rigidly connected to the shell. In an actual ship or submarine, the greater part of the structure is elastically sprung from the outer shell to a greater or minor degree. This means that for the normal mode of an actual structure the integrations of Eqs. (2) and (4) should be extended over the interior masses as well as the outer surface, and the weighting function in Eq. (2) is more complicated.

These equations are valid approximations whether the structure is vibrating in vacuum, in air, or in water. However, in water the distributed pressures on the surface must include a pressure distribution induced by the motion of the structure, in addition to the externally applied pressures such as those due to an explosion. It is convenient to separate this induced pressure field into contributions due to the separate action in each normal mode.

For the present we consider only low frequency motions of the structure, for which $\omega d / c < 1$, where d is a representative dimension. The pressures

they generate and which act on the surface of the structure are virtually the same as though the water was incompressible and the pressure was transmitted with infinite velocity. Hence we can define an induced modal mass, L_{ij}, as the modal force on the structure in the jth mode due to unit acceleration of the structure in the ith mode.

$$L_{ij} = - \iint p_i \psi_i \, d\sigma / \ddot{q}_i , \tag{5}$$

where $p_j(S,t)$ is the pressure distribution on the surface due solely to the motion $q_i(t) \, \psi_i(S)$. These induced mass coefficients are commonly called the virtual masses, or entrained masses. In general they are independent of the time and they can be calculated theoretically by the solution of a boundary value problem. In terms of these induced mass coefficients the equation of motion is

$$M_i(\ddot{q}_i + \alpha_i^2 q_i) = \iint p_o \psi_i \, d\sigma - \sum_j \ddot{q}_j L_{ij} , \tag{6}$$

where $p(S,t)$ is the pressure distribution on the surface if the structure were rigid and immovable.

In general, unless there is sufficient symmetry for the L_{ij} terms to vanish, all the normal modes are coupled to each other by the induced pressure field. However, under the conditions we are assuming, there exists a real linear transformation to a new set of normal coordinates q_i', mode functions ψ_i', and induced pressures p_i', such that the equations of motion are uncoupled in these transformed variables.

$$M_i'(\ddot{q}_i' + \alpha_i^2 q_i') = \iint p_o \psi_i' \, d\sigma , \tag{7}$$

where the new frequencies

$$\alpha_i = \alpha_i [M_i \, (M_i + L_{ii})] . \tag{8}$$

These new stationary mode shapes are not orthogonal in the sense of Eq. (2). Instead a relation of the form

$$\iint (\psi_i' + p_i' \, \ddot{q}_i) \, \psi_j' = M_i' \, \delta_{ij} \tag{9}$$

is valid. This can be interpreted to show that the rate at which the vibrating structure does work on the fluid in the new stationary mode is proportional to the kinetic energy of the structure in that mode.

A detailed derivation of this transformation of coordinates is given in the appendix of the author's paper [4]. Lax [5] has used a similar analysis in discussing how the radiation pressures modify the vibration modes of a circular diaphragm.

938

RECIPROCITY RELATION FOR THE MODAL FORCE

In our problem the pressure distribution on the surface of the structure is not simply the incident pressure field given by Eq. (1), because it also includes reflected pressures and diffracted pressures due to the presence of the structure. The components due to the motion of the structure have been eliminated. In order to avoid solving a diffraction problem for this pressure distribution, it is possible to express the generalized force term in Eq. (4) as a function of $V(t)$, the volume of the explosion bubble, and $p_i(r,t)$, the pressure, at the vector distance r which locates the center of the explosion, due to a vibration of the structure in the single mode ψ_i. For the case of a nearby explosion, $\omega r/c < 1$, this function has a simple form

$$Q_i(t) = \iint p_o \psi_i \, d\sigma = \rho \phi_i \ddot{V}, \tag{10}$$

where $\phi_i(r)$ is the value of a potential function at r and where $\rho \phi_i \ddot{q}_i = p_i(r,t)$. The function ϕ_i satisfies Laplace's equation in the water and satisfies the boundary condition $\partial \phi_i / \partial n = -\psi_i$ on the surface of the structure.

Equation (10) is a special case of a general reciprocity theorem which relates the radiation field of a surface vibrating in an arbitrary mode to the generalized force which an arbitrary external source with the same time variation exerts in the surface in the same mode. That is, if a simple source at (r,t) varies with time as $V(r,t)$ and exerts a force $F(S,t) = \iint p \psi \, d\sigma$ on S in the pattern $\psi(S)$, and if alternately a vibration of the surface S in a pattern $q(t_o) \psi(S)$ generates a pressure $p(r,t)$ at r, then

$$q(t_o) F(t) = V(t_o) p(t_o) \tag{11}$$

provided only that $q(t_o)$ is proportional to $V(t_o)$. The special case of this theorem given by Eq. (10) was originally proven in [4]. However, the theorem is true in general [6], for an acoustic medium as well as an incompressive medium, and for any time variation including, of course, single frequency vibration.

Thus we have separated the modal force into two factors. the factor $V(t)$ is a known function as previously indicated; the function $\phi_i(r)$ remains to be determined.

PRESSURE FIELD DUE TO VIBRATION IN SINGLE MODE

This latter problem has no easy analytical solution except in cases of high symmetry. But there is a fairly general method which covers a wide range of cases, particularly the low frequency vibrations of a slender shell structure such as a ship or submarine hull. Again we assume that we are in the near field where the pressures are substantially in phase with the instantaneous accelerations,

$$p(r,t) = \rho \ddot{q}_i(t) \phi_i(r)$$

939

and we write $\phi_i(r)$ in the form of a Helmholtz integral

$$\phi_i = \frac{1}{4\pi} \iint \phi_i \frac{\partial}{\partial n} \left(\frac{1}{r}\right) d\sigma - \iint \frac{1}{4\pi r} \frac{\partial \phi}{\partial n} d\sigma , \tag{12}$$

i.e., in terms of the values of ϕ_i and its normal gradient on s. The normal gradient is simply $\psi_i(S)$ so that the second integral can be calculated explicitly. In the first integral, we assume as a plausible approximation that at the surface of S, the local values of ϕ_i are proportional to their gradients and to the mass distribution function $\mu(S)$, i.e.,

$$\rho \phi_i(S) = k_i \mu(S) \psi_i(S) . \tag{13}$$

This would be exact, albeit trivial, if k_i was a function of the position s instead of a constant. However, we note that Eq. (12) requires merely a particular mean value of ϕ_i on S, and the constant k_i can be considered as a mean value of $k_i(S)$, although averaged in a different way. In order to determine k_i, multiply both sides of (13) by ψ_i and integrate over S, whence

$$\rho \iint \phi_i \psi_i d\sigma = k_i \iint \mu \psi_i^2 d\sigma$$

and

$$k_i = L_{ii} / M_i : \tag{14}$$

that is, k_i is simply the ratio of induced mass to modal mass.

Another way [4] to derive this is to expand $\phi_i \mu(S)$ in terms of the complete set of eigenfunctions $\psi_j(S)$

$$\rho \phi_i = \sum_j k_{ij} \mu \psi_j \tag{15}$$

and multiplying by ψ_k and integrating

$$k_{ij} = L_{ij} / M_j . \tag{16}$$

If there was no coupling between the modes, or if the coupling was negligible, then only the k_{ii} term would be important with the same result as Eq. (14).

Hence Eq. (12) becomes

$$\phi_i = \frac{1}{4\pi} \iint \frac{\psi_i}{r} d\sigma + \frac{L_{ii}}{4\pi M_i} \iint \phi_i \frac{\partial}{\partial n} \left(\frac{1}{r}\right) d\sigma . \tag{17}$$

where both integrations can be made explicitly and it remains only to calculate the induced mass L_{ii}. But this is an old problem which has been solved for many motional patterns and many surface shapes. Also, the ratio L_{ii} / M_i can often be measured experimentally. Sometimes as demonstrated by Strasberg [7], the induced mass is negligible and the first integral alone is sufficient in Eq. (17).

This method of calculating the pressure field of a vibrating surface in terms of the induced mass could also be used if the medium is compressible, provided L_{ij} is replaced by a frequency dependent modal impedance coefficient. We are now in the process of testing a computer program for the automatic computation of the pressure field of a slender body vibrating in an arbitrary pattern with a single frequency. This will be described in a forthcoming report.

However, I can show you some general formulas that apply to the types of motion we have been considering, namely the vibration modes of slender bodies in an acoustic medium. First consider pure axial vibrations in which each transverse section moves without deformations in the axial or x direction with axial velocity $q(t) \psi_i(x)$. Then

$$\Phi_i = -\frac{1}{4\pi} \int \frac{[\dot{q}]}{r} \psi_i \frac{dA}{dx} dx + \frac{L_{ii}}{4\pi M_i} \int \psi_i \frac{A \partial[\dot{q}]}{\partial x r} dx \tag{18}$$

where Φ_i is defined by $p_i = \rho \ddot{\Phi}_i$, $[\dot{q}]$ means that q is to be evaluated at the retarded time $t - r/c$, r is the distance from the field point to the section at x, and $A(x)$ is the sectional area at x. This is easily interpreted as the field of a linear array of monopoles and a linear array of axially oriented dipoles, both with specified strength. Since L_i/M_i is negligible for slender enough bodies, the first term predominates.

Now consider pure transverse vibrations of a slender body, including radial breathing motions, whipping motions, and lobar vibrations. For the breathing motion, where the radial transverse velocity at each section is $q_i(t) \psi_i(x) \csc \beta$, and β is the angle between the normal to the surface and the longitudinal axis,

$$4\pi\Phi_i = \int \frac{[\dot{q}]}{r} \psi_i \tan \beta \frac{dA}{dx} dx + \frac{L_{ii}}{M_i} \int \frac{\psi_i A}{\tan \beta} \frac{\partial}{\partial x} \frac{[\dot{q}]}{r} dx . \tag{19}$$

In this case L_{ii} is the induced mass for the transverse motion, not the axial motion of the previous case. L_{ii}/M_i can be greater than unity, and the second term might dominate over the first.

For the whipping motions of the slender body where each transverse section moves with a velocity $q_i(t) \psi_i(x)$ in the vertical or z direction

$$4\pi\Phi_i = \frac{M_i + L_{ii}}{M_i} \int \psi_i A \frac{\partial}{\partial z} \frac{[\dot{q}]}{r} dx . \tag{20}$$

The field is the same as from a linear array of vertically oriented dipoles with the dipole strength of each sectional segment increased in the ratio $(M_i + L_i)/M_i$.

The last case to be considered is the general lobar vibration of a slender body. Here the perimeter of each section deforms into a wavy pattern, $\cos n\epsilon$, where ϵ is the angle about the longitudinal axis. It turns out that to the level of approximation used here $\Phi = 0$ for $n \geq 2$. Note that $n = 0$ is the breathing motion previously considered while $n = 1$ is the whipping motion.

There are other methods available for calculating the pressure field. If the surface of the structure is sufficiently close to the shape of a prolate spheroid, obtained by rotating an ellipse about its major axis, then the complete field due to any vibration pattern can be calculated by the use of spheroidal wave functions [8]. If the surface differs somewhat from the prolate spheroid, the spheroidal function analysis might be used only to estimate the induced mass, and then Eq. (17) could be used.

SOLUTIONS OF THE EQUATIONS OF MOTION

Now to summarize this method. We calculate the motion in any single specified mode at a time by solving the differential equation of motion, which for a nearby explosion has the form

$$(M_i + L_{ii})\ (\ddot{q}_i + \omega_i^2 q_i) = -\rho \phi_i \ddot{V} \tag{21}$$

and we must first know the mode shape, its frequency in water, and the pressure field it generates, and the last can be calculated if the induced mass is known. Also we must know the peak volume of the explosion bubble and its first pulsation period in order to completely specify the V term.

It is evident from the form of this equation that the shape of the solution $q_i(t)$ depends only on the value of $\omega_i T_b$. The other parameters merely multiply the amplitude scale and the time scale. There are two extreme cases. First a very high frequency motion for which $\omega_i T_b \to \infty$. In this case $q(t) \propto \ddot{V}(t) \propto p_b(t)$ and the normal coordinate varies in the same way as the pressure-time curve of Fig. 2. An example of this might be the breathing mode of a stiff submarine hull. The mean compression of the hull is nearly proportional to the mean pressure on the hull. It is a maximum during the shock wave phase and is unaffected by the bubble pulses. The other extreme is a low frequency motion for which $\omega_i T_b \to 0$. In that case $q(t) \propto V(t)$, and the normal coordinate varies in the same way as the volume-time curve of Fig. 1. For example the mean bodily translation of a submarine as a whole is simply proportional to the volume of the explosion bubble (not the radius!). The displacement is a maximum at half the bubble period, and is relatively unaffected by the shock wave.

The most interesting cases occur when $\omega_i T_b \approx 1$ for then we get synchronization effects between the vibration of the structure and the pulsation of the explosion bubble. This is demonstrated in Fig. 3 which is a plot of several solutions to the reduced differential equation

$$\frac{d^2 u}{d\tau^2} + (2\pi n)^2 u = \frac{d^2 v}{d\tau^2} \ . \tag{22}$$

where

$$u = (M_i + L_{ii})\ q_i / \rho \phi_i V_o$$

$$v = V/V_o ; \quad \tau = t/T_b ; \quad n = \omega_i T_b / 2\pi .$$
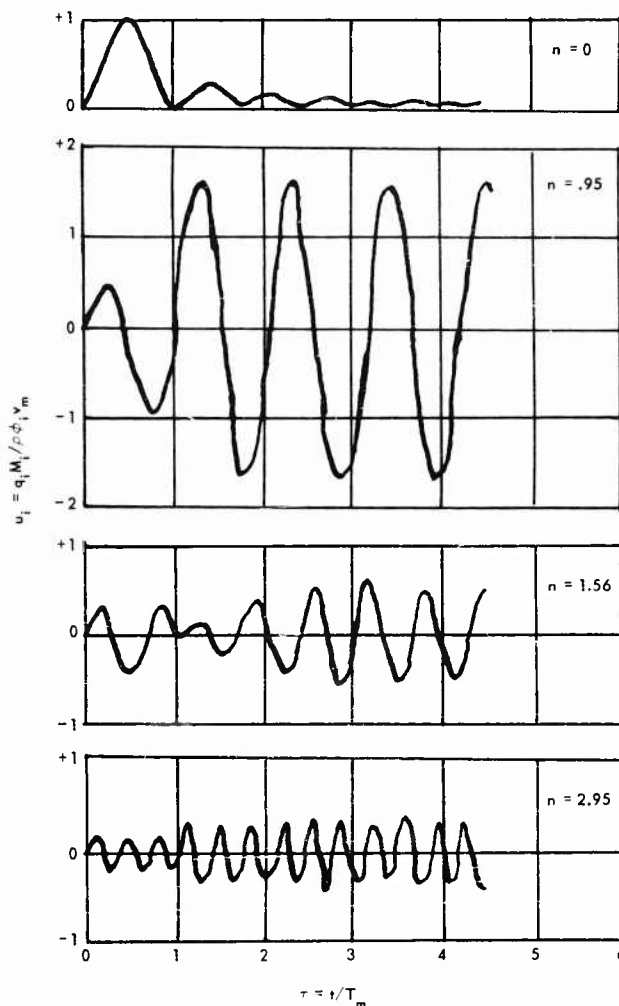
942

Fig. 3 - Solutions to Eq. (21) with selected
values of period ratio n

The upper curve in Fig. 3 applies when $n = 0$, whence $u(t) = v(t)$. For $n = 0.95$, the bubble period is about equal to the vibration period. The first swing of the target, due mostly to the shock wave impulse, is increased by about 50 percent on the second swing because of the underpressure phase, and is subsequently increased to four times its initial peak by the bubble pulses. When $n = 1.56$, the first bubble pulse hits the target out of phase with the target motion and actually reverses the motion.

The previous discussion of the nature of the solutions to the equations of motion applies only when the explosion is in the "near" field of the target so

that the generalized force is independent of the sound velocity. However if the explosion is sufficiently distant, the dominant term in the generalized force will be of the form $f(t)/rc$. It turns out that in these cases $f(t)$ is proportional to a first or higher time derivative of $\ddot{V}$, i.e., to a first or higher time derivative of the incident pressure. Since these derivatives are of appreciable magnitude only during the shock wave it follows that the bubble pulsation pressures have no effect on the motion from a distant explosion.

There is one last theoretical point I want to mention and that is the technique for accounting for the presence of the free surface, particularly when the target is floating. To the approximation used here, the free surface is a surface of zero excess pressure. This is taken into account by the usual assumption that the target is exposed to the simultaneous action of the actual explosion and its negative image in the free surface. If the structure is floating, the image part of the structure is a reflection of the underwater portion of the real structure, where the motion of the upper part is the negative of the motion of the lower part.

CONCLUSION

I have described a general method of analyzing the interaction between an elastic structure and an underwater explosion, which depends upon specifying the motion in terms of the stationary vibration modes in water, and in specifying the explosion forces in terms of their influence on each separate mode. The time pattern of the response in any such mode then depends only on the ratio of the modal vibration period to the pulsation period of the explosion bubble. I hope that this general technique can be of use in other hydroelastic problems.

However, lest I leave you with the impression that all problems have been solved I want to conclude by mentioning some of the many problems which are still awaiting detailed analysis:

1. There is the enormous class of problems where the difficulties are not due to the nature of the explosive pressures or to the interaction with the water but simply to the complexity of the vibration mode, or to the complexity of the deformation pattern, or to the non-linearity of the deformation. This is true of all but the simplest vibration modes, and all cases with plastic deformation.

2. There are many cases where the relief pressures generated by the response of the structure is so large and negative that the net pressure in the water falls below some critical value and the water cavitates. The same cavitation can occur when the pressure wave is reflected from the free surface with a change in phase. This cavitation constitutes a non-linear process in the water which can only be treated in a qualitative manner.

3. The third problem is the transmission of mechanical shock through a ships structure when hit by an underwater explosion. The ship is a very complex system with very many degrees of freedom. It should be possible to analyze the statistical properties of the shock transmitted to some interior point in the ship in terms of some statistical transfer function and the statistical properties of the explosion attacks on the hull.

944

REFERENCES

1. Cole, R.H., "Underwater Explosions," Princeton University Press (1948).

2. "Underwater Explosion Research," Vols. I, II, III, Washington:Office of Naval Research (1950).

3. Snay, H.G., "Hydrodynamics of Underwater Explosions," Naval Hydrodynamics, Publication 515, National Academy of Sciences, 1957.

4. Chertock, G., J. Appl. Phys., 24, 192 (1953).

5. Lax, M., J. Acous. Soc. Am., 16, 5 (1944).

6. Chertock, G., J. Acous. Soc. Am., July 1962.

7. Strasberg, M., Fourth International Congress on Acoustics, Copenhagen, August 1962.

8. Chertock, G., J. Acous. Soc. Am., 33, 871 (1961).

*   *   *

COMPUTER MODELING OF THE ELASTIC RESPONSE OF SHIPS TO SEA LOADS

J. W. Church
David Taylor Model Basin
Washington, D. C.

INTRODUCTION

We are aware that the ship in heavy seas can experience severe impact-type loadings and can develop elastic motions which produce appreciable stresses in the hull girder. The effects of bottom impact forces on the ship have been discussed by Dr. Szebehely, Dr. Ochi and others. Such treatment has not been given for the slamming impact produced by the immersion of a flared bow and the resultant rapid increase in hydrodynamic forces.

This lack of information plus the substantial whipping response demonstrated on the aircraft carrier USS ESSEX prompted Dr. Norman Jasper to initiate studies to develop and verify a method of computer modeling of the sea loads, the rigid body and elastic motions, and the hull girder stresses of ships with appreciable bow flare in heavy seas. It was hoped that the speed and flexibility of the computer might be used to study the response of ships while still on the drawing boards for the many different combinations of parameters that describe the characteristics of the ship and the state of the sea.

At the Model Basin, therefore, a mathematical model was developed. Based on this model, studies were made under contract with the Model Basin on a passive element analog computer operated by Computer Engineering Associates under the direction of Dr. R. H. MacNeal. The computer model resulting from these studies has been referred to as the "Seaworthiness Analog Computer."

The paper presented to this Symposium describes the mathematical model used in the development, the computer model and some applications of the model to studies of the elastic response of the ship to the loads of the sea. Much of the material presented in the paper originated with Dr. Jasper, Mr. McGoldrick and many others at the Model Basin, with Mr. Ed Hoyt of Taggert Associates, and with Dr. MacNeal and Mr. R. G. Schwendler of C.E.A. Since the model development is continuing, however, this information has received rather limited distribution. The purpose of this paper, therefore, is to acquaint other researchers with the Model Basin efforts in this area.

It must also be noted that such opinions as are expressed herein do not necessarily represent the views of the Navy Department.

BACKGROUND

In studies of vibratory characteristics of ship hulls, the Structural Mechanics Laboratory has for several years represented the ship as a free-free, non-uniform beam with three principal types of elastic motion: bending, shearing, and torsional. McGoldrick has discussed the conversion of the ship into an equivalent lumped system in which the inertias are concentrated at certain points and the elastic properties are assigned to massless elastic members joining these lumped elements [1]*. One of the several methods used to obtain the natural frequencies of elastic motion is by means of an analog computer.

In this computer, passive networks model the inertial and elastic properties of the hull. The circuitry of analog is set up so that in a part of coupled transmission lines, the current represents either the shearing force in the hull or the bending moment. Voltages are analogous to mechanical translational velocities or angular velocities. The natural frequencies of the circuit are found by applying continuous excitation by means of an oscillator until the condition corresponding to resonance in the mechanical system has been obtained. When the external voltages are removed, only transient oscillations remain. These eventually die out just as the vibrations of a structure die out after the exciting force is removed.

In this way, the network has been used successfully to predict the natural frequencies of flexural vibration and the corresponding normal mode shapes of the hull. These results help the ship designer to avoid the possibility of vibration in the fundamental mode due to machinery unbalance. In general, however, this analog cannot be used to determine the elastic motions and associated stresses induced in ships at sea.

The structural response of the ship under slamming loads is considered to consist of the elastic motions of the hull, the "whipping" stress induced by the impact loading, and the "wave-induced" stresses of lower frequency corresponding to ordinary wave encounter. The whipping may be generated by bottom slamming, (the immersion of the bow and subsequent impact), by bow flare slamming, (the immersion of the bow) having an appreciable flare and resultant rapid increase in hydrodynamic forces), and by pounding, (the impact of the wave against the forward quarter at the ship side).

These elastic motions and associated stresses may be simulated by testing a structurally scaled model in a towing basin. Such a model is under construction now by the Davidson Laboratory. When completed, it will be used to study the effects of slamming on the elastic motions and on bending stresses as well as on the rigid body motions. However, Korvin-Kroukovsky has suggested that such a study might not permit a complete prediction of the dynamic stresses in a ship's hull because of the difficulty in securing similarity in shear rigidity;

---

*References are listed on page 991.

948

and the dependence of structural damping on the vibration frequency [2]. If this is found to be so, computer studies may be indica⁺ed to correlate the model data with the full scale motions.

The mathematical model used in the vibration studies was extended and programmed for solution by high-speed digital computers available at the Applied Mathematics Laboratory. This program required as inputs, the time history of the hydrodynamic forces resulting from rigid body ship motions and the ocean waves, and the mass-elastic parameters representing the hull as a composite of 20 equi-length sections.

Andrews has shown by comparison of calculations of ship motions and stresses with full scale measured values of ESSEX that the method could be employed to compute wave-induced and whipping stress [3]. However, changes in hull and sea parameters could not be made easily and the requirement to hand-compute the hydrodynamic forces prior to computer solution was undesirable. In particular, the requirement for a prior knowledge of ship motions severely limited the model for purposes of design evaluation. These considerations prompted further development of the mathematical model.

Hoyt, under a Model Basin contract with Reed Research. Inc., derived a mathematical model in which the forces exerted upon a ship by waves could be simulated on an analog computer without prior knowledge of ship motion [4]. Lee obtained hydrodynamic damping terms from experimental values for two-dimensional shapes appropriate to each segment. The values thus obtained were frequency dependent [5].

Based on these results MacNeal developed the "Seaworthiness Analog Computer" and with Schwendler, conducted two studies to determine the applicability of their model and to obtain some insight into the structural response of ships at sea [6, 7].

It is noted that the "Seaworthiness Analog Computer" is not a particular piece of hardware or a special purpose computer. The name refers to the specific arrangement of electrical and electronic elements of a general purpose computer which was used to model the ship-sea system.

Concerning the notation in the paper: McGoldrick in one of his latest writings finds it impossible to adhere strictly either to standards of naval architecture or of mechanical vibrations in his notation usage [8]. Adoption of a nomenclature more in keeping with other studies in dynamics would be of considerable value but would also be a considerable task. So, I have tried herein simply to reduce inconsistencies in symbols between the several sources of the material presented. It will be noted that the "stations" for the computer model shown continue to be numbered from stern to stem!

Concerning the subject matter for the second part of the Symposium: hydroelasticity has been defined as the science which studies the mutual interaction between hydrodynamic forces and elastic responses and the influence of this interaction on design. In that sense, the material presented hereafter is not hydroelasticity at all! For although we consider herein the elasticity of the ship structure, we do not consider the effects of the secondary hydrodynamic forces

generated by this elasticity (the hydroelastic forces). This omission is probably of negligible consequence for hull girder studies but may be crucial in studies of local stiffness and secondary tertiary bending.

MATHEMATICAL MODEL

In the mathematical model of the elastic ship in the seaway, the ship is represented as a non-uniform beam, free in space (in the sense that neither end of the beam is "fixed") and with elastic and inertial properties per unit length. Further, the ship-beam is approximated by system with discrete segments of equal length, each having the appropriate elastic and inertial properties. Each segment can be considered as represented by equations of motion and as related to adjacent segments through the beam equations. Figure 1 shows the principal elements which make up the model of the ship-sea system.
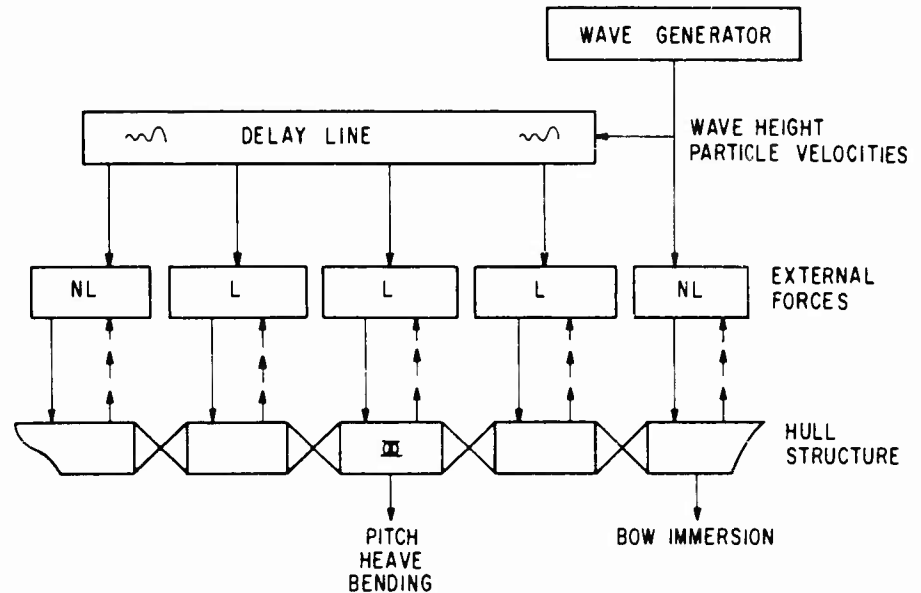

Fig. 1 - Schematic Diagram of Ship-Sea Model

The sea is represented by wave profiles which pass along the length of the ship. The hydrodynamic forces are computed from the relative motions of the ship and the sea at selected points along the hull and are applied to the ship at these points. Non-linear forces were computed only for segments near the bow and near the stern. The motions of the ship include both rigid body motions and elastic deformations. However, in this study motions were limited to the vertical plane and to head seas.

It should be noted that the developers of a mathematical model to determine the elastic response of the ship to the sea must consider not only the seaway and the ship but also the manner in which the mathematical model will be used. For example, while differential equations of motion can be solved on one type of analog computer, solution by the analog computer described herein, (or solution by numerical methods or by digital computer) requires that some of the differential equations be approximated by difference equations. Hence, familiar expressions may be written in disguised forms.

Environment

The mathematical models of the environment included the modeling of a sinusoidal wave, a discrete wave train, and a sea composed of random waves having specified statistical properties. The height of the wave (surface profile), the horizontal and vertical fluid particle velocities, the vertical fluid particle accelerations and the wave propagation velocity were generated as outputs. The surface profile was represented at the bow and was considered to pass along the ship length without change in form at a constant propagation velocity. For the segmented ship-beam, this passage was approximated by a delay line that caused the signal to appear at points along the ship with a time delay equal to the distance from the bow divided by the velocity of the wave. The following relations between deep water wave characteristics are provided for convenient reference in considering wave propagation velocity, c, and circular frequency, ω.

$$c = \frac{\lambda}{T_w} = \frac{g}{\omega} = \frac{g\lambda}{2\pi} \tag{1}$$

$$\omega = \frac{2\pi}{T_w} = \frac{2\pi c}{\lambda} \tag{2}$$

where: λ is the wave length,

T_w is the wave period, and

g is the acceleration of gravity.

The velocity of propagation of the surface of the sea was assumed to be constant for all components.

For the sinusoidal sea model, y_w, the amplitude of the wave relative to the mean water line may be given by the following equation:

$$y_w = \frac{h}{2} \cos \frac{2\pi c}{\lambda} \tag{3}$$

where: h is the wave height, trough to crest, and is twice the maximum amplitude of the sinusoidal wave.

In addition to the height, the velocity and vertical acceleration of the water particle at the surface were required as inputs into the hydrodynamic forces. The components of particle velocity and acceleration may be obtained by differentiating the formulae for infinitesimal sinusoidal waves in deep water. The horizontal component of the particle velocity is

$$u = -\frac{h}{2} e^{-\frac{2\pi Y}{\lambda}} \frac{2\pi c}{\lambda} \cos \frac{2\pi c}{\lambda} t \ , \tag{4}$$

the vertical component of velocity is

$$v = \frac{h}{2} e^{-\frac{2\pi Y}{\lambda}} \frac{2\pi c}{\lambda} \sin \frac{2\pi c}{\lambda} t \ , \tag{5}$$

and the vertical acceleration of the fluid particle is

$$\dot{v} = -\frac{h}{2} e^{-\frac{2\pi Y}{\lambda}} \left(\frac{2\pi c}{\lambda}\right)^2 \cos \frac{2\pi c}{\lambda} t \ , \tag{6}$$

where: Y is the mean depth below the mean water surface.

The relative propagation velocity of a sea wave, c_r, is also required. For a head sea in deep water the velocity of well-formed waves of specified wave length relative to the whip, and the relative frequency of encounter, ω_r, are given by:

$$c_r = c + U = \frac{g}{\omega} + U \tag{7}$$

$$\omega_r = \frac{2\pi}{\lambda} (c + U) = \omega \left(1 + \frac{U}{c}\right) \tag{8}$$

where: U is the ship velocity, positive in the opposite sense to c.

The wave height, and particle velocities and accelerations, based on ship-fixed coordinates are therefore given by:

$$y_w = \frac{h}{2} \left[\cos \frac{2\pi\xi}{\lambda} \cos \frac{2\pi c_r t}{\lambda} - \sin \frac{2\pi\xi}{\lambda} \sin \frac{2\pi c_r t}{\lambda}\right] \tag{9}$$

$$u = -\frac{\pi h c}{\lambda} \left[\cos \frac{2\pi\xi}{\lambda} \cos \frac{2\pi c_r t}{\lambda} - \sin \frac{2\pi\xi}{\lambda} \sin \frac{2\pi c_r t}{\lambda}\right] \tag{10}$$

$$v = \frac{\pi h c}{\lambda} \left[\sin \frac{2\pi\xi}{\lambda} \cos \frac{2\pi c_r t}{\lambda} + \cos \frac{2\pi\xi}{\lambda} \sin \frac{2\pi c_r t}{\lambda}\right] \tag{11}$$

$$\dot{v} = -\frac{h}{2} \left(\frac{2\pi c}{\lambda}\right)^2 \left[\cos \frac{2\pi\xi}{\lambda} \cos \frac{2\pi c_r t}{\lambda} - \sin \frac{2\pi\xi}{\lambda} \sin \frac{2\pi c_r t}{\lambda}\right] \tag{12}$$

where: ξ is the distance to the station of interest from the midpoint of the ship.

It is noted that in deriving Eq. (9) from Eq. (3), the angular frequency was replaced by a relative frequency, a phase angle, $2\pi\xi/\lambda$, was added, and, for

952

convenience in representation, the trigonometric function of two angles were replaced by the sum of the products of functions of a single angle.

For the discrete wave train model, the surface of the sea was represented as a train of waves with specified time history preceded by a long period of calm. The shape of the wave train was taken from a portion of an oscillogram trace obtained from full scale trial data of ESSEX at a time when severe whipping stresses were recorded [9]. This wave trace is shown in Fig. 2. Inspection of the oscillogram from which this record was taken indicated that the whipping
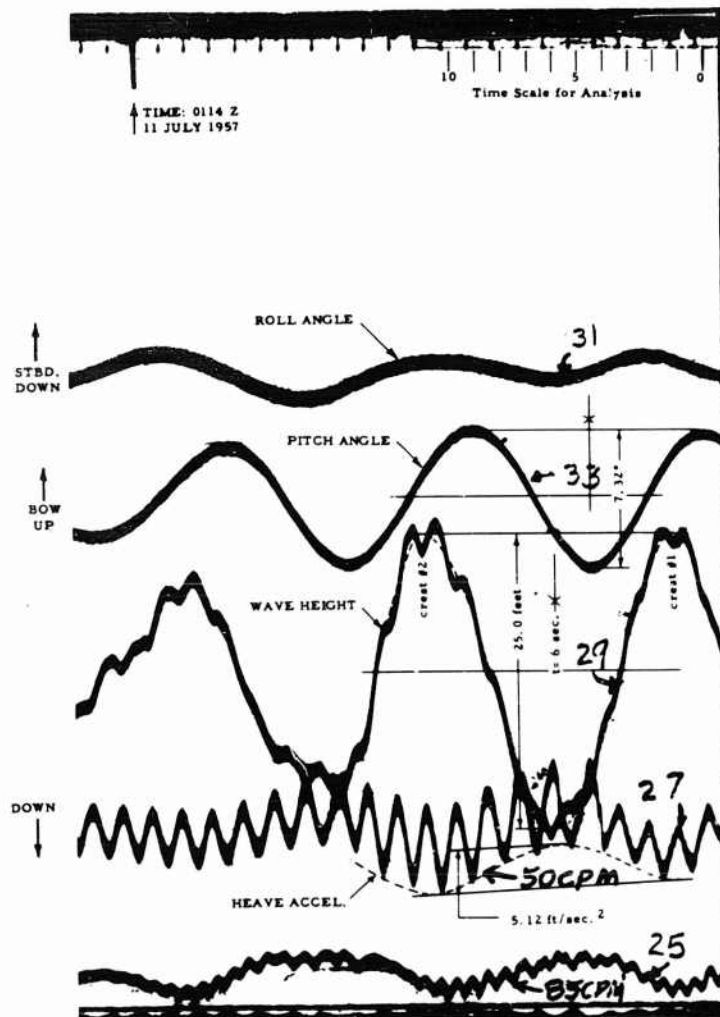

Fig. 2 - Oscillogram Taken on ESSEX at Time
of Severe Whipping Stresses

was excited by forces generated by the entrance of the bow into the wave crest marked number 2. At this time the crest number 1 was approximately at the stern of the ship and therefore the wave length-ship length ratio approached unity. The wave height is seen to be about 25 feet. An arbitrary time scale was placed on the chart and the relative propagation velocity for a ship speed of 16 knots was found to be about 86 ft/sec [10].

By using this trace as an excitation function, the pitch angle and bending moment obtained from the analog computer analysis could be compared with corresponding full scale traces. An important advantage of the use of a discrete wave train over the use of a statistically random wave train is that it provides a simple means for comparing solutions when the parameters describing the system are varied.

For the random sea, the surface was represented as a randomly varying profile with specified statistical properties similar, for example, to those deduced for ESSEX environment or for those associated with a fully-developed Neumann sea as generated by a 30 knot or a 50 knot wind. The rms value of wave height, $(y_w)_{RMS}$, was computed from the formula

$$(y_w)_{RMS} = \sqrt{E} \tag{13}$$

where E is the integral of the power spectral density function. The mean value of peak-to-peak wave height is approximately equal to 2.8 times the rms value. For the sea state corresponding to the full scale data (shown in Fig. 3), the contribution to the integral for values of ω below 0.25 was ignored.

The velocity of propagation of sea waves was an important parameter in the development. The propagation speed, c, was assumed to be about 2/3 of the value associated with the period, T_w, of a well-formed wave in deep water. Thus

$$c = \frac{2}{3} \frac{g}{2\pi} T_w = 3.5 \, T_w \tag{14}$$

The value of c was used to design the delay line wherein the relative propagation velocity, c_r (phase velocity), was given by Eq. (7) as before. In addition, the frequency scale of a sea-fixed power spectral distribution is increased by the factor $1 + U/c$ and the magnitude of the function decreased by the factor $1/(1 + U/c)$ when expressed in ship-fixed coordinates. The wave velocity for a particular sea state was chosen to correspond to the frequency at the peak of the power spectral density function.

Hull Structure

The mathematical model of the hull structure for elastic and rigid body motions in a single plane has been represented by a set of five differential equations: a vertical force-per-unit-length equation; a moment-per-unit-length equation, a geometrical relation and two fundamental beam equations relating bending moment and bending rigidity and shear force and shearing rigidity.

954
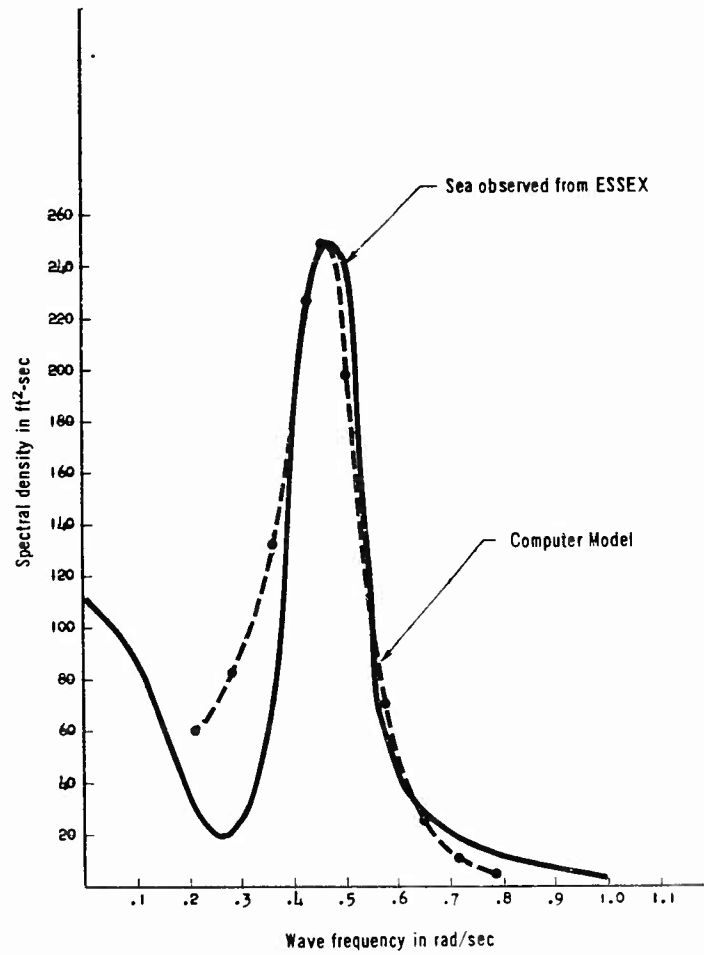
Fig. 3 - Power Spectrum of Sea and Computer Model

$$\mu\, \frac{\partial^2 y}{\partial t^2} \;+\; c_d\, \frac{\partial y}{\partial t} \;=\; \frac{\partial V}{\partial x} \;+\; P(x,t)$$

inertia   structural   internal   external
            damping   forces   forces

(15)

$$I_\mu\, \frac{\partial^2 \gamma}{\partial t^2} \;=\; \frac{\partial M}{\partial x} \;-\; V$$

rotary   bending   shear
inertia   moment "moment"

(16)

955

$$\frac{\partial y}{\partial x} \cong \gamma_b + \psi - \beta$$

beam   angle   pitch   shear
deflection   due to   angle   strain
slope   curvature   angle   (17)

$$M = EI \times \frac{\partial \gamma_b}{\partial x}$$

bending   bending   beam
moment   rigidity   curvature   (18)

$$V = -KAG \times \beta$$

shear   shearing   shear
force   rigidity   strain
           angle   (19)

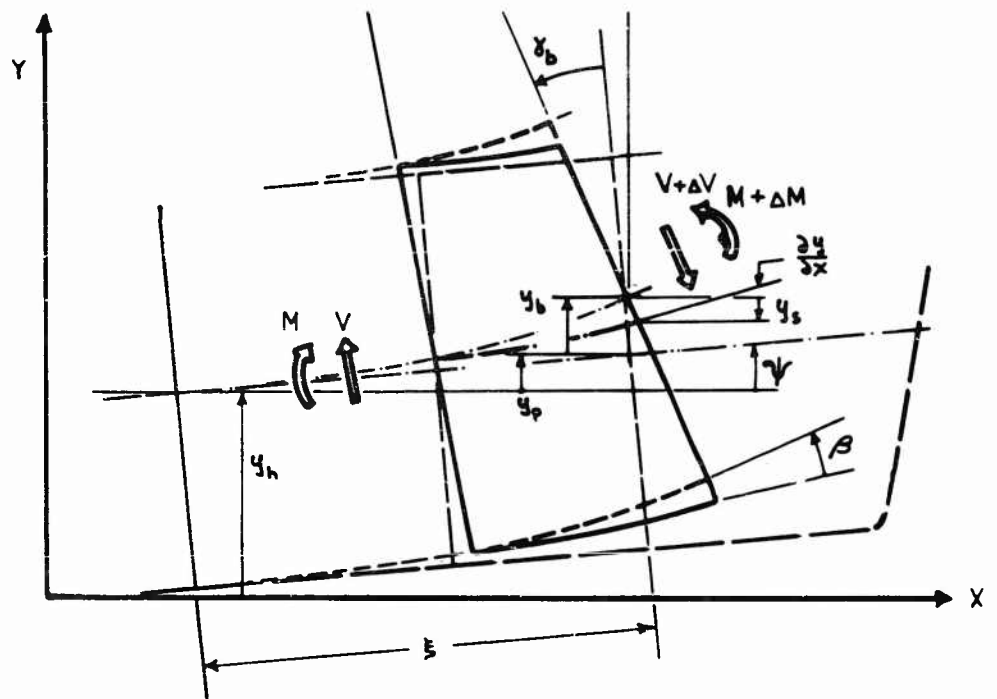The coordinate system used for the equations and some of the variables are illustrated in Fig. 4.

Fig. 4 - Ship Segment Showing Bending and Shear Deflections

The following symbol definitions are somewhat more detailed than would be required for the vibration engineer.

μ is the mass per unit length. The mass of a segment of length would be Δx. The total ship mass would be $\mu \Delta x$.

c_d is the structural damping coefficient per unit length per unit velocity.

V   is the internal shearing force at any cross-section. Hence, $\partial V/\partial x$ is the rate of change in shearing force from one face of a segment to the other, i.e., from station to station.

$P(x,t)$ is an external force per unit length which is the resultant of the vertical force acting on the ship at the segment midpoint or along the segment. It includes ship weight, virtual mass, buoyancy and hydrodynamic damping as well as wave excitation.

y is the vertical displacement of the center of mass of the segment from a reference line fixed in still water.

I_μ is the moment of inertia or rotary inertia per unit length about a transverse axis parallel to the Z-axis through the center of mass.

γ is defined as the angle of rotation of a cross-section about the neutral (transverse) axis. As indicated in Fig. 4, it is composed of an angle γ_b and a second angle which by inspection is found equivalent to the pitch angle ψ. It is not considered to contain the shear strain angle β.

γ_b is defined as the angle between the radius of curvature of the longitudinal axis a section and a perpendicular to the original, non-curved longitudinal axis at that section. The derivative $\partial \gamma_b/\partial x$ is the beam curvature. The angle γ_b may be considered as the angle of rotation of a cross-section about a transverse (neutral) axis due to beam bending. This angle therefore measures the longitudinal deformation in the fibres of the segment due to curvature and is the appropriate angle in the beam deflection equation. In the absence of a pitch angle, γ_b equals γ, and in the absence of shear, γ_b may be approximated by $\partial y/\partial x$.

β is defined as the shear strain angle, i.e., the angle whose tangent is the shear strain divided by the segment length. In effect, this is the angle between the longitudinal axis without shear deformation and the longitudinal axis with shear deformation. The effects of shear deformation are not considered to change the angle of rotation of the cross-section but are considered to produce an incremental change in the slope of the longitudinal axis.

M   is the bending moment at any cross-section. Hence, $\partial M/\partial x$ is the change in bending moment across the segment.

957

$\partial y/\partial x$ is the beam deflection, i.e., the slope of the neutral axis of the ship at any cross-section or station with reference to the horizontal reference, x. For the midstation, this value is equal to the pitch angle, ψ.

E is the modulus of elasticity at any cross-section.

I is the moment of inertia of any cross-section about the transverse axis.

K is a pseudo-empirical constant used to relate the shear force per area and the shear stress.

A is the total cross-sectional area of the section.

G is the shear modulus of rigidity.

It is noted that Eq. (16) has been referred to as the "pitching moment" equation. This designation can create problems in understanding for those who are accustomed to associate pitch angle with rigid body motions. It may also be noted that in Eq. (16) when the rotary inertia is neglected, the shear force is seen to be the first derivative of the bending moment as would be expected.

The above equations are differential equations, as distinct from difference equations to be presented later in this section.

To be compatible with the computer model, further revisions of these equations are required. The velocities which will appear as outputs in the computer are represented by the dot notation; Eqs. (17) and (19) are combined and then differentiated with respect to time; Eq. (18) is also differentiated with respect to time; the space derivative $\partial \gamma_b/\partial x$ is replaced by the space derivative $\partial \gamma/\partial x$ since the space derivative of the other component of γ, i.e., $\partial \gamma_s/\partial x$ is zero, and the terms are rearranged:

$$\mu \frac{\partial \dot{y}}{\partial t} - c_d \dot{y} - \frac{\partial V}{\partial x} = P(x, t) \tag{20}$$

$$\frac{\partial M}{\partial x} - I_{-z} \frac{\partial \dot{y}}{\partial t} - V = 0 \tag{21}$$

$$\frac{\partial \dot{y}}{\partial x} - \frac{\dot{V}}{KAG} - \dot{\gamma} = 0 \tag{22}$$

$$\frac{\partial M}{\partial t} - EI \frac{\partial \dot{\gamma}}{\partial x} = 0 \tag{23}$$

It is also necessary to approximate the space derivatives in Eqs. (20) through (23) by the following finite differences. The subscripts indicate the stations where values of the variables are taken and applied.

958

$$\left(\frac{\partial V}{\partial x}\right)_{n+\frac{1}{2}} = \frac{V_{n+1} - V_n}{\Delta x} \tag{24}$$

$$\left(\frac{\partial M}{\partial x}\right)_n = \frac{M_{n+\frac{1}{2}} - M_{n-\frac{1}{2}}}{\Delta x} \tag{25}$$

$$\left(\frac{\partial \dot{y}}{\partial x}\right)_n = \frac{\dot{y}_{n+\frac{1}{2}} - \dot{y}_{n-\frac{1}{2}}}{\Delta x} \tag{26}$$

$$\left(\frac{\partial \dot{\gamma}}{\partial x}\right)_{n+\frac{1}{2}} = \frac{\dot{\gamma}_{n+1} - \dot{\gamma}_n}{\Delta x} \tag{27}$$

Thus, the differential equations of motion are replaced, after multiplication by Δx, by the following set of mixed difference differential equations.

$$(\mu \Delta x)_{n+\frac{1}{2}} \frac{d}{dt}(\dot{y})_{n+\frac{1}{2}} + (c_d \Delta x)_{n+\frac{1}{2}}(\dot{y})_{n-\frac{1}{2}} - V_{n+1} - V_n = \Delta x \dot{P}_{n-\frac{1}{2}} \tag{28}$$

$$\dot{y}_{n+\frac{1}{2}} - \dot{y}_{n-\frac{1}{2}} - \left(\frac{\Delta x}{KAG}\right)_n \left(\frac{dV}{dt}\right)_n - \Delta x \dot{\gamma} = 0 \tag{29}$$

$$M_{n+\frac{1}{2}} - M_{n-\frac{1}{2}} - (I_{-z} \Delta x)_n \left(\frac{d\dot{\gamma}}{dt}\right)_n - \Delta x V_n = 0 \tag{30}$$

$$\left(\frac{\Delta x}{EI}\right)_{n-\frac{1}{2}} \left(\frac{dM}{dt}\right)_{n-\frac{1}{2}} - (\dot{\gamma}_{n-1} - \dot{\gamma}_n) = 0 \tag{31}$$

The hull characteristics of ESSEX are shown in Table 1. The mass and stiffness of ESSEX are shown in Table 2. As shown in Fig. 5, the masses of the ship were lumped at all of the 21 stations. (A station interval was 41 feet.) The bending stiffness was evaluated at these same points and the shear stiffness and rotary inertia were evaluated at points midway between the stations.

Table 1
Hull Characteristics of USS ESSEX

LBP	Length between Perpendiculars in feet-inches	820-0
Δ	Displacement in tons	39,503
H	Draft, Design, in feet-inches	28-6
B	Beam, in feet-inches	103-0
A_ϕ	Area of the Midship Section in square feet	2880
C_ϕ	Midship Section Coefficient	0.981
Cp	Prismatic Coefficient	0.586
Cb	Block Coefficient	0.574
Cwp	Water Plane Coefficient	0.724

959

Table 2
Elastic Properties of ESSEX

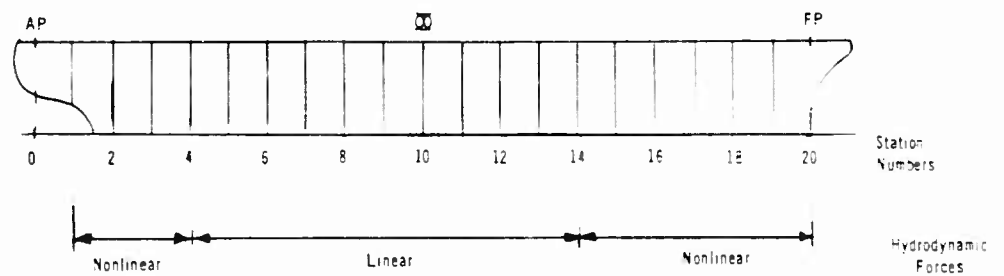| Station	Mass m_s	Bending Stiffness $EI \times 10^{-9}$	Station	Moment of Inertia $I_{mz} \times 10^{-3}$	Shear Stiffness $KAG \times 10^{-5}$
	ton-sec^2/ft	ton-ft^2		ton-sec^2/ft	tons
0	10.17	—			
1	27.12	5.70	0.5	7.28	14.88
2	33.89	9.83	1.5	13.55	20.61
3	35.59	14.80	2.5	20.81	30.08
4	57.30	21.81	3.5	29.67	41.51
5	82.30	32.28	4.5	38.46	54.13
6	90.14	41.62	5.5	44.82	66.00
7	90.56	46.86	6.5	50.07	74.54
8	85.37	52.50	7.5	53.89	77.98
9	86.43	57.83	8.5	55.77	76.09
10	85.90	59.68	9.5	54.21	73.45
11	82.09	58.32	10.5	51.65	70.74
12	81.34	43.02	11.5	49.59	69.94
13	77.96	31.93	12.5	46.27	72.75
14	74.04	34.48	13.5	40.78	78.40
15	70.75	34.48	14.5	33.87	77.36
16	64.93	22.80	15.5	26.52	56.61
17	46.39	15.74	16.5	18.33	32.27
18	25.00	11.56	17.5	10.74	21.55
19	19.38	8.09	18.5	5.97	16.43
20	10.48	—	19.5	4.71	13.50

Fig. 5 - Ship Stations Used in Finite Difference Beam Analogy

Hydrodynamic Forces

"Hydrodynamic" forces of three types were considered: hydrostatic forces, including an approximation to the Smith Correction; damping forces; and a virtual mass force. It may be noted that in the representation the forces of the sea are included in these hydrodynamic forces. In other models it is common and convenient to represent the wave forces independently. It should also be noted that the "forces" used in the computer study are generally forces per unit length and therefore have dimensions of pounds per foot rather than pounds.

The external "hydrodynamic" force per unit length, $P(x,t)$, includes both the hydrodynamic and hydrostatic forces and may be represented by the following equation.

$$P = P_1 + P_2 - P_3 \tag{32}$$

where

$$P_1 = -\frac{d}{dt'} (m_v V_r) \tag{33}$$

is the apparent mass term,

$$P_2 = \rho A \left(g + \frac{dV_r}{dt'} \right) - \rho g A_o \tag{34}$$

is the buoyancy term, and

$$\bar{P}_3 = -B(p) \bar{V}_r \tag{35}$$

is the Laplace transform of the hydrodynamic damping term. For the relative vertical velocity we have

$$V_r = \frac{d}{dt'} \left(Y_h - Y_w \right) = \frac{d}{dt'} (Y_T) \tag{36}$$

where Y_h is the vertical displacement of the ship and Y_w is the vertical displacement of the sea surface. The force P_1 and the velocity V_r in the above equations are expressed in terms of a coordinate system moving longitudinally in an oscillatory manner with a fluid lamina. This force is expressed in terms of a coordinate system fixed in the ship by the following transformation.

$$X = (U - u) t - \xi$$
$$t' = t \tag{37}$$

or

961

$$\xi = X - (U - u) t'$$
$$t = t'$$
(38)

Here U and u are the horizontal velocities of the ship and water particle respectively. Note that u is not the wave speed, c.

Transforming, assuming u negligible, and rewriting Eqs. (33) through (36) we obtain,

$$P_1 = - \frac{\partial}{\partial t} (m_v V_r) - U \frac{\partial}{\partial \xi} (m_v V_r)$$
(39)

$$P_2 = \rho g (A - A_o) - \rho A_o \left(\frac{c}{c - U} \right)^2 \frac{\partial^2 Y_w}{\partial t^2}$$
(40)

$$\bar{P}_3 = - \left[C(\omega) - i D(\omega) \right] \bar{V}_r$$
(41)

$$V_r = \frac{\partial Y_r}{\partial t} - U \frac{\partial Y_r}{\partial \xi}$$
(42)

where: m_v is the apparent mass,
  A is the area of the submerged portion of the ship, and
  A_o is the area at the still waterline.

For convenience of analog simulation, the buoyancy and virtual mass forces given by Eqs. (39) and (40) are regrouped into a sum of linear terms, P_p, and a sum of non-linear terms, P_a. These two sums are

$$P_p = - m_o \frac{\partial^2 Y_r}{\partial t^2} - \rho A_o \left(\frac{c}{c - U} \right) \frac{\partial^2 Y_w}{\partial t^2}$$
(43)

$$P_a = m_o U \frac{\partial^2 Y_r}{\partial t \partial \xi} - \frac{\partial}{\partial t} \rho V_r - U \frac{\partial}{\partial \xi} m_o V_r - \rho V_r - \rho g \bar{A} - b_1 Y_r$$
(44)

where:

$$m_v = m_o - \rho$$
(45)

$$A = A_o - b_1 Y_r - \bar{A}$$
(46)

The term m_o is the added mass associated with the still waterline and ρ is the time varying portion of the added mass. The term $b_1 Y_r$ is the rectangular area measured from the still waterline to the actual waterline where Y_r is the distance from the still waterline to the actual waterline, and $\bar{A}$ is the dynamic or non-linear portion of the buoyancy force.

962

The term $\bar{m}$ is defined by the following relationships:

$$\bar{m} = m_1 \quad \text{for } V_r > 0 \tag{47}$$

$$\bar{m} = m_2 \quad \text{for } V_r < 0 \tag{48}$$

Figure 6 illustrates the non-linear portion of the virtual mass term as a function of the immersion. Station 19 is 41 feet aft of the forward perpendicular. The displacement y is from the mean waterline. The curve on the left side indicates the bow going down into the water. The level portion indicates submergence of the carrier flight deck. The curve on the right side indicates the bow emerging from the water. Termination of the curve at about 28.5 feet corresponds to the keel breaking clear of the water surface at that station. Also shown is the computer approximation to the mathematical representation.

Figure 7 illustrates the non-linear portion of the buoyancy term.

Bow Fins

For some parts of the study the effects of a set of rigid anti-slamming fins were represented. Each fin was assumed to have a planform area, S, of 750 square feet with a mean chord, c_m, of 41 feet (to fit segment length conveniently), and a span of about 18 feet from the centerline. The fins were assumed to be located with the quarter-chord about 0.05 L aft of the bow (station 19) and sufficiently near the keel so as to be submerged at all times.

The hydrodynamic force exerted by the fins was assumed to act at the quarter-chord and to be composed of a lift force, P_{4a}, resulting from the effective angle of attack at the fin and a virtual mass force, P_{4b}. The lift force was given by

$$P_{4a} = \frac{1}{2} \rho u_r^2 \left[2 - SC_p \alpha_e - \frac{-Sc_m}{2u_r} \dot{\alpha} \right] \tag{49}$$

where: ρ is the mass density of water,

u_r is the relative velocity of ship and wave particle,

C_p is a Theodorsen function, and

α_e is the effective angle of attack.

The effective angle of attack is given by

$$\alpha_e = \alpha_b - \frac{c_m}{2} \dot{\alpha}_b - \frac{\dot{y}_r}{u_r} \tag{50}$$

where α_b is the local pitch angle of the bow fins, i.e., the angle between the fixed bow fins and the horizontal reference, X. It will be noted that the contribution to the angle of attack from ship motion was represented in part by $c_m \dot{\alpha}_b/2u_r$ and in part by a portion of the term $\dot{y}_r/u_r$.
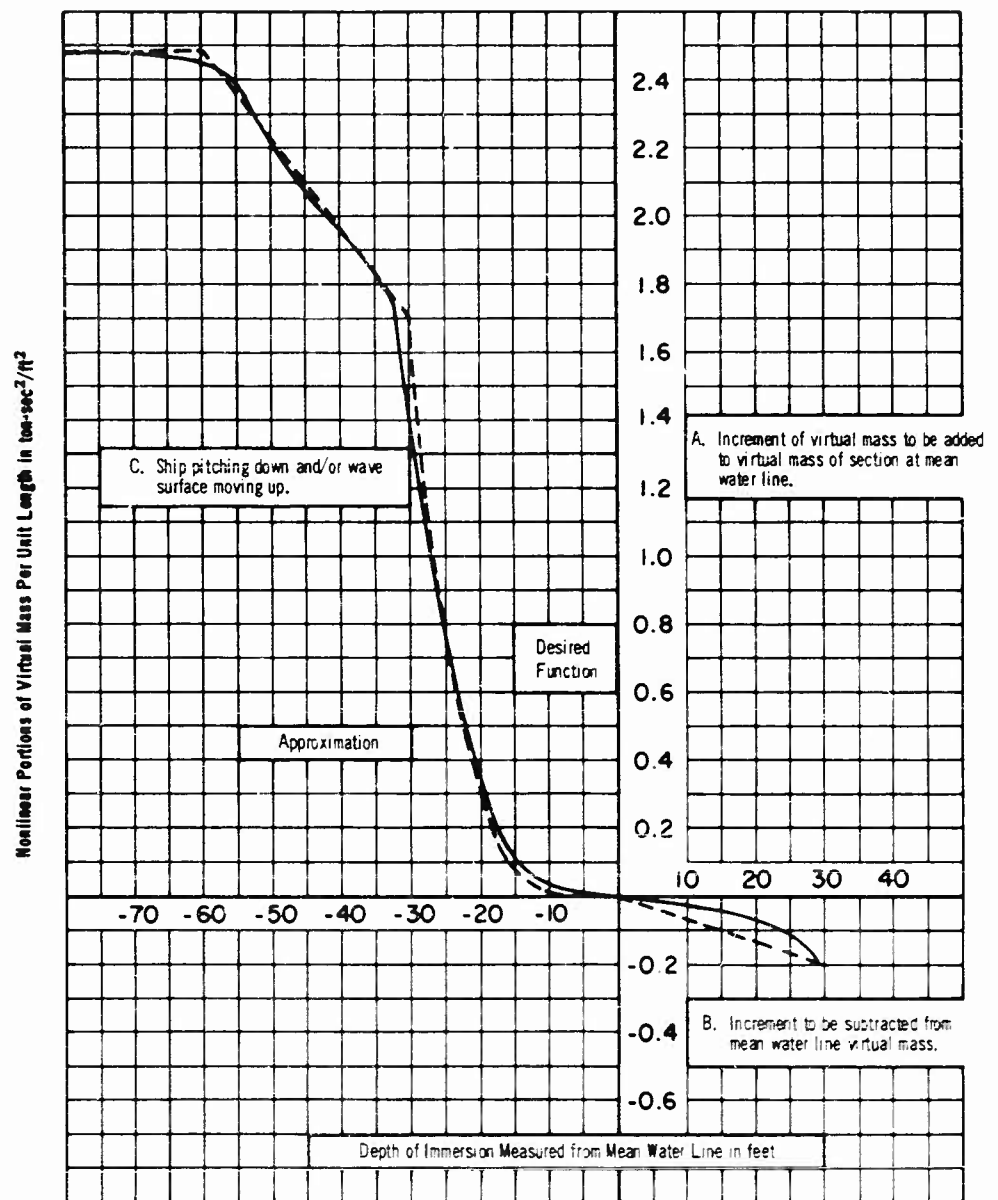
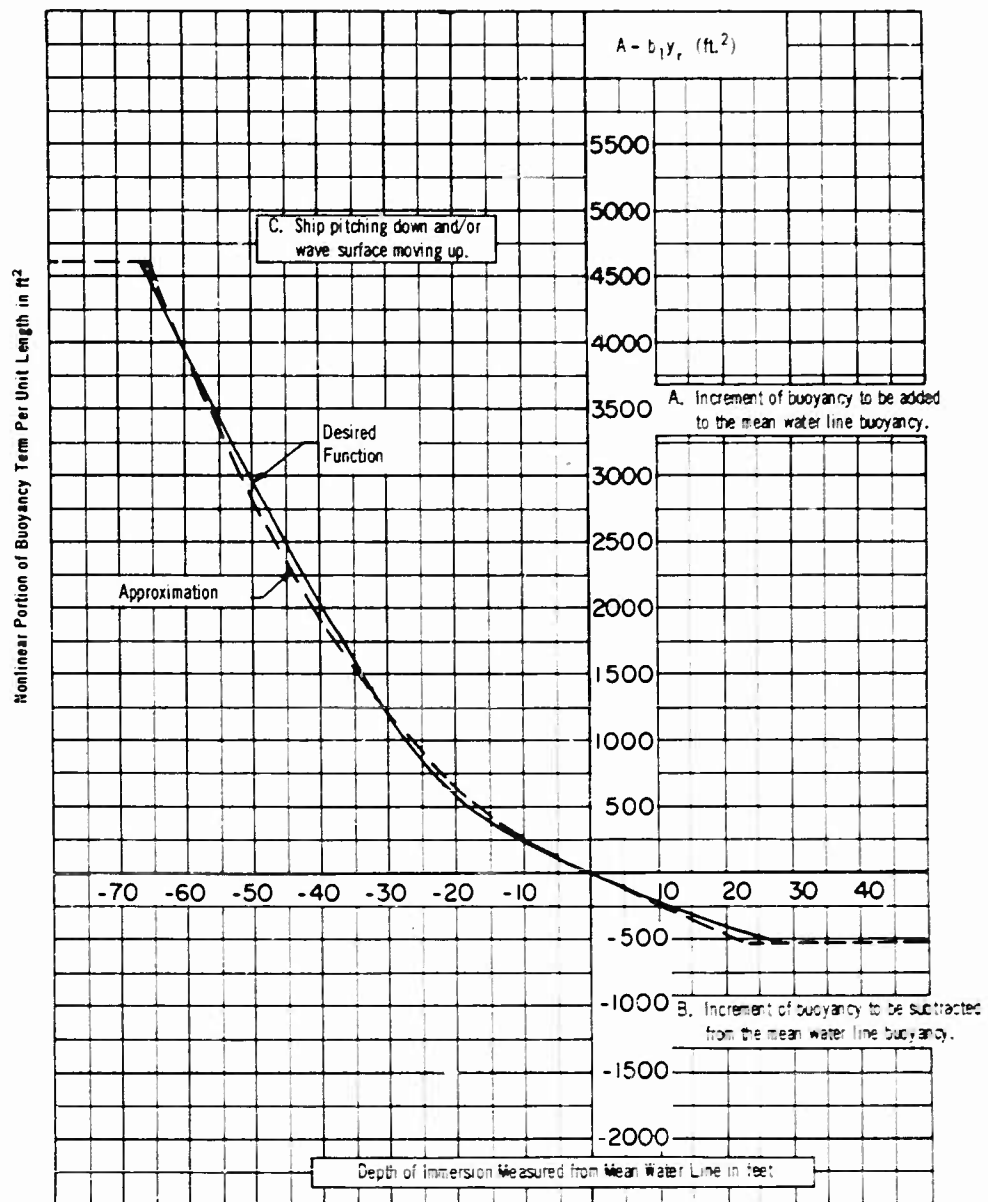Fig. 6 - Representation of Nonlinear Portion of Virtual Mass
Term at Station 18

Fig. 7 - Representation of Nonlinear Portion of
Buoyancy Term at Station 18

The virtual mass force was given by approximating the mass of a cylinder of revolution.

$$P_{4b} = -\rho \frac{\pi}{4} c_m S \frac{d\dot{y}_r}{dt} \tag{51}$$

The total hydrodynamic force representing the effect of the bow fins was therefore given by

$$\bar{P}_4 = \frac{1}{2}\rho u_r^2\left[2\pi S C_p\left(\theta + \frac{c_m}{2u_r}\dot{\theta} - \frac{1}{u_r}\dot{y}_r\right) + \pi S \frac{c_m}{2u_r}\dot{\theta}\right] - \frac{\pi}{4}\rho c_m S \ddot{y}_r \tag{52}$$

Assumptions

The assumptions made in deriving the mathematical model are the following:

1. Continuous differential operators are replaced by finite difference operators.

2. The ship hull and surrounding water may be approximated by a free-free beam with bending and shear and may be loaded by arbitrary forcing functions.

3. There is no coupling between the vertical motion and horizontal or torsional motion, elastic or rigid body modes.

4. The effects of local flexibility, structural discontinuities, concentrated mass, hatch openings and large superstructures may be ignored.

5. Structural damping has a Raleigh distribution; that is, it is proportional to mass and velocity.

6. The fluid particle velocity does not decrease with depth.

7. The fluid lamina at a station or cross-section remains plane and vertical, containing always the same fluid particle at the surface; thus permitting the assumption of two-dimensional flow.

COMPUTER MODEL

An important distinction is to be made between those analog computing devices that perform purely mathematical operations such as integration and differentiation and those in which a physical analogy exists between the currents or voltages of various branches of a circuit and the amplitudes of vibration or forces in the corresponding mechanical system. The former are called operational analogs, active element computers or electronic differential analyzers, and the latter are termed network analyzers, passive element computers or direct analogy computers.

Proponents of the passive network computers point out that analysis can be simplified and questionable mathematical relations bypassed by using direct correspondence between elements of electrical networks and elements of the mechanical system. Proponents of the active element computers maintain that adjustable passive elements are very costly, that the study results are much more dependent upon the characteristics of the computer, and that while the primary property of an element in a physical system may be ideally analogous to the primary property of an element in an electrical network, secondary effects in the two supposedly analogous elements may depart from the ideal in radically different ways.

Much of the rigid body motion studies which have been performed, have been conducted using operational analog computers. Most of the elastic motion studies including vibration surveys have been conducted on passive networks.

The Computer Engineering Associates, Inc., have developed a passive network computer to which has been added a considerable amount of operational amplifier units.

Environment

The computer model of the environment consisted primarily of a "wave-maker" circuit and a delay line.

The wave-maker circuit provides for three different types of signals: steady state sine waves, a wave train with specified time history, and a random signal with specified statistical properties. A simple wave-maker circuit is shown in Fig. 8.

The steady state sine waves are generated by an audio oscillator with manual frequency control. In the previous section it was seen that computation of the displacement and hydrodynamic forces requires the height of the wave surface profile, the horizontal and vertical components of the fluid particle velocities and the vertical accelerations of the particle. From Eqs. (9) through (12) we see that these quantities can be obtained as the sum of sine and cosine components at the appropriate frequencies.

The discrete wave train is generated by a photoformer which is a device for generating a voltage signal of any desired form in a finite interval of time. The photoformer makes use of a cathode ray oscilloscope and a mask on which the desired function is drawn. Since the input to the delay line is the time derivative of wave height, a differentiator was placed between the output of the photoformer and the input to the delay line. The transfer function of the differentiator has the form $p(1 - tp)$, where t is chosen to reduce the magnitude of high frequency components. It was necessary to use fairly large values of t to prevent a spurious excitation of the lowest fundamental mode.

The basic component in the simulation of a random sea is a random noise generator. This device produces a voltage signal with a constant power spectral density over a very broad spectrum (from 20 cps to 20,000 cps in the model used in the analysis), and a Gaussian distribution. The desired power spectrum is
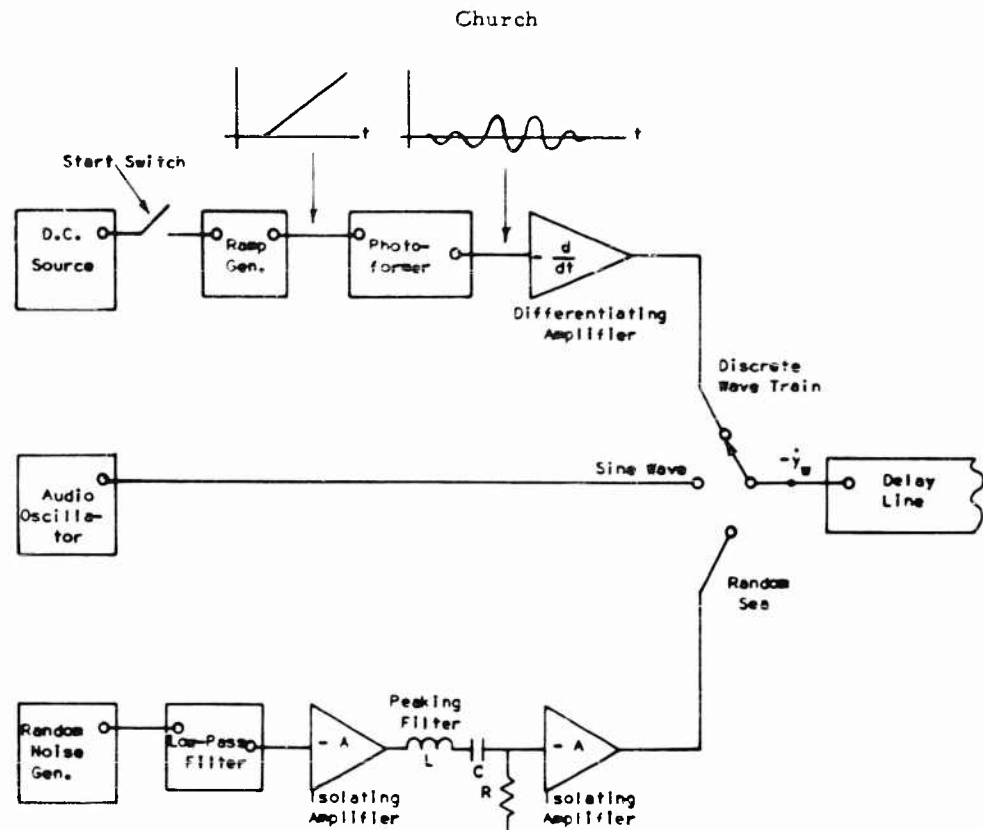
Fig. 8 - Wave Maker Circuit

then produced by connecting the noise generator to an electrical filter. The power spectral density of the output of the filter is related to the power spectral density of the input as follows:

$$\sigma_0(\omega) = |A(i\omega)|^2 \, \sigma_1(\omega) \tag{53}$$

where $|A(i\omega)|$ is the absolute value of the filter's transfer function for $p = i\omega$. Since $\sigma_1(\omega)$ is a constant, Eq. (54) gives the design equation of the filter.

$$|A(i\omega)| = \sqrt{\sigma_0(\omega)} \tag{54}$$

The power spectral density functions (such as is shown in Fig. 3) display a single relatively narrow peak, similar to the transfer function of the simple L-R-C circuit shown in Fig. 8. The peak response of such a filter occurs near $\omega = 1/\sqrt{LC}$, and the band width between half-power points is $\Delta\omega = R\sqrt{C/L}$. In each case a peaking filter having the correct peak frequency and band width was set up on the computer and tested. Adjustments were then made to the constants

968

in the peaking filter and in the accompanying low-pass filter so as to satisfy Eq. (54) experimentally. A typical comparison of the square of the filter transfer functions with the desired power spectral density functions is shown in Fig. 3. The main purpose of the low-pass filter is to attenuate frequency components near the bending modes of the ship. As for the discrete wave train, large attenuation is required in order to prevent a spurious excitation of the lowest fundamental mode at high frequencies. The ratio of peak power spectral density to the power spectral density at the first bending mode was made equal to 10^6, with satisfactory results.

The purpose of the delay line is to represent the passage of the wave crest from stem to stern. The wiring diagram for the delay line is shown in Fig. 9 (Fig. 15 of [7]). At low frequencies the delay line produces a uniform time delay between modes without appreciable attenuation or distortion. The time delay per section is equal to $\sqrt{LC}$. In order to prevent reflections the line is terminated at both ends with resistors whose value $R = \sqrt{L/C}$. L and C are computed as follows:

$$L = \frac{\triangle x}{Nu_r} \times R \tag{55}$$

$$C = \frac{\triangle x}{Nu_r} \frac{1}{R} \tag{56}$$

where: N is a scale factor equal to the ratio of electrical frequency to mechanical frequency.
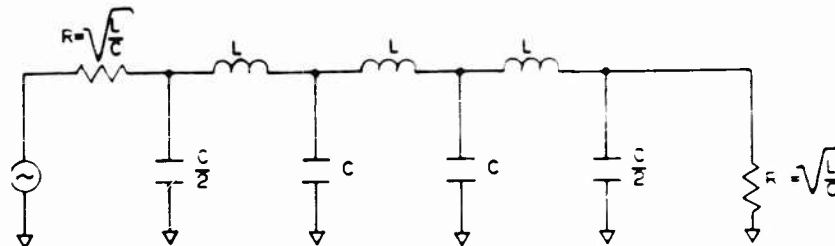
Time Delay Per Section $= \sqrt{LC}$

Fig. 9 - Simple Delay Line

The delay line has a cut-off frequency in mechanical units equal to $2u_r/\triangle x$. Signals at frequencies above this limit are severely attenuated and signals at frequencies near the limit are severely distorted. At each output station along the delay line an amplifier is employed as an output transducer to prevent loading of the delay line by the remainder of the circuit.

In the present analysis considerable attention was given to the selection of the frequency scale factor, N, defined above. In a conventional vibration analysis, the electrical frequency of the lowest bending mode would be chosen to occur near 100 cps since this gives optimum values of inductors and capacitors. This selection would be poor in the present analysis because the peak in the power spectrum of the sea occurs at a frequency roughly equal to 1/10th of the lowest bending mode of the ship. The corresponding electrical frequency would be 10 cps which is well below the range of good computer accuracy.

The frequency scale factor was made equal to 628 which converts a mechanical frequency of 1 rad/sec into an electrical frequency of 100 cps. With this scaling the lowest bending mode occurs near 470 cps and the peak of the power spectrum of the sea occurs near 50 cps. The rigid pitch and heave frequencies of the ship occur near 80 cps.

The simulation of a dispersive wave propagation was attempted but was found unworkable because the number of electrical elements required for good simulation appeared to be prohibitive and knowledge of the proper method of terminating such a delay line was lacking.

Hull Structure

Two models of the ship structure were studied, the conventional finite difference beam analogy using 20 segments and a Russell beam analogy using 9 segments. Equations (28) through (31) presented in the previous section to represent the ship structure are shown in Fig. 10 together with the analogous electrical circuit equations for the finite difference beam analogy. In this particular system, mass is analogous to capacitance and the network is termed a "Mobility Analog." The relation between the circuit elements and the mechanical properties are shown in Table 3.

Table 3
Relations between Mechanical and Electrical Systems

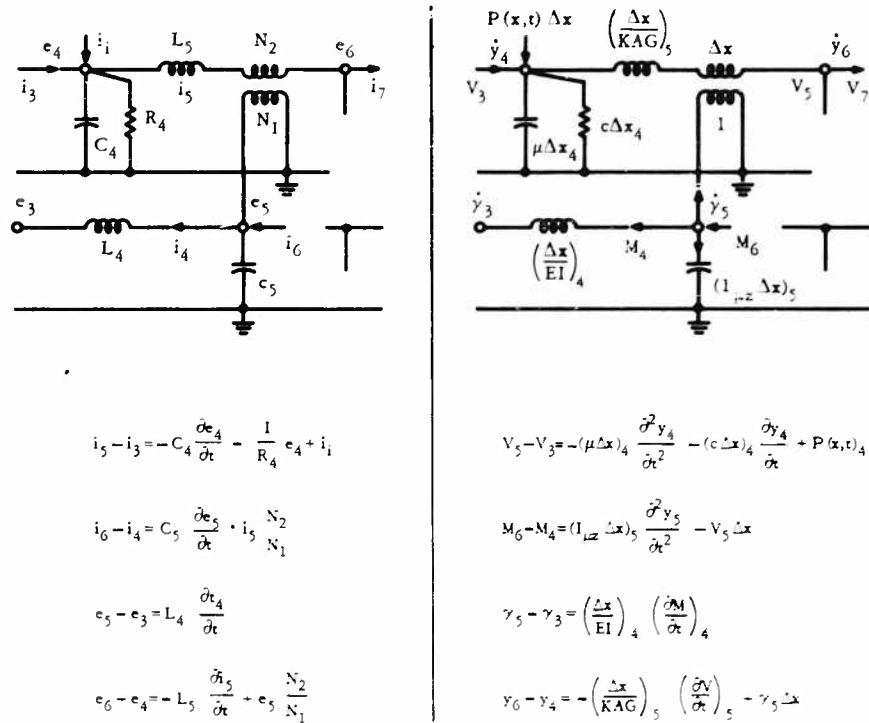| Mechanical System					Electric Analog	
Translational		Rotational			Mobility	
Force	(F)	Torque or Moment		(M)	Current	i
Velocity	$\left(v, \frac{dy}{dt}\right)$	Angular Velocity		$(\dot{\cdot})$	Voltage	e
Mass	$(m, \ddot{x})$	Rotational Inertia		(I_{z})	Capacitance	C
Compliance	$\left(\frac{\cdot x}{KAG}\right)$	Rotational Compliance		$\left(\frac{\cdot x}{EI}\right)$	Inductance	L
Damping	$(c\dot{x})$	Rotational Damping		$(c'\dot{\cdot})$	Conductance	$\frac{1}{R}$

970

Fig. 10 - Electrical and Mechanical Representation of Ship Structure

Figure 10 shows two stations of the complete 20 station analog. Equation (1) of this figure (Eq. (28) in the paper) can be considered as a node current equation. Thus the difference in currents at the two ends of the upper or "shear" transmission line must equal the current flowing from the shear line to ground. Equation (2) can also be considered a node current equation. In the moment line, four currents, M_6, M_4, V_5 (through the transformer winding which is coupled to the shear line) and $\dot{\gamma}_5 (I_\mu \Delta x)_5$ through the capacitance, must equate to zero at the node. Equation (3) gives the voltage drop between adjacent node pairs, i.e., the voltage drop in the inductance is equal to the inductance times the rate of change of current. Equation (4) also gives the voltage drop between adjacent node pairs. Since the voltage drop in the winding of the transformer in the shear line is Δx times the voltage across the other winding, γ, and since the voltage drop in the inductance is equal to $(\Delta x/KAG)\dot{V}$, Eq. (4) is represented.

In order that the boundary conditions of the free-free hull are satisfied in the analog, the shear and moment lines are isolated at the ends to make $V = M = 0$ at these points.

The driving force, $P(x_1 t)\Delta x$, must be inserted at the node marked as a current. Greenberg points out that it is advantageous to have this current relatively independent of the load. The outputs are vertical velocities represented by the

971

voltage at the node $\dot{y}_4$, $\dot{y}_6$. These velocities are used in the calculation of the hydrodynamic forces. The velocities may also be integrated to determine the elevation of each station from the equilibrium. Other outputs are shear force and bending moments as currents.

The proportionality between the analog and mu anical quantities can be varied by a ratio of 100 to 1 in time. The scale factor ratio between beam slope and translation was chosen so that the transformer ratio for a 41 foot section is 5.0. A large ratio such as this tends to increase the values of the inductors in the beam bending circuit.

Other scale factors were selected so that:

> 1 mass unit (ton-sec ^{2}/ft) → 0.005 microfarad
> 1 unit of bending flexibility → 0.02131 × 10^9 henries
> 507.1 tons of force → 1 milliampere
> 1 ft/sec translational velocity → 0.028 volts
> 104,000 ft-tons, bending moment → 1 milliampere

The scale factors gave reasonable values of passive electrical elements and good signal levels throughout the system.

The Russell beam analogy used, shown in Fig. 11, is identical in appearance to the finite difference analogy used in [1] but differs in the magnitudes of the inductors. The advantage of the Russell beam analogy over the finite difference analogy is that the Russell rigorously defines the elastic behavior of the beam when loads are applied only at the ends of the beam segments.
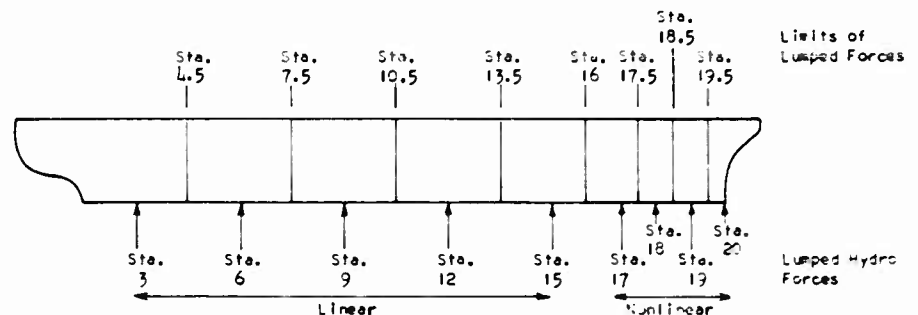

Fig. 11 - Ship Stations Used in Russell Beam Analogy

By using the Russell beam analogy it was possible to represent the ship by a 9 segment beam rather than by the 20 segment finite difference beam representation. The chief advantage of using fewer cells lies in the ability to obtain lower equivalent structural damping in the passive analogy. The pitching inertia capacitors were not included in the analogy because they were found to be of negligible magnitudes.

Generation of Hydrodynamic Forces

The buoyancy and virtual mass force expressions were combined for convenience into a sum of linear terms, P_p, given by Eq. (43) and a sum of nonlinear terms, P_a, given by Eq. (44).

In the force, P_p, the linear virtual mass force at a particular station was generated by a capacitor and the Smith correction was obtained by a transformer.

The force, P_a, is generated by operational amplifiers. Three amplifiers, one an integrator, are required per segment. Changes in speed require an adjustment of the potentiometers. The terms are combined by means of a summing current generator circuit and are inserted into the hull structure as a reversed current flow through a transformer.

The hydrodynamic damping force from Eq. (41) may be written as

$$P_3 = \left[C(\omega) + iD(\omega) \right] \bar{V}_r = v_{rn} \frac{\tau_2 s}{\tau_2 s + (1 + \tau_1 s)} = v_o \tag{57}$$

The circuit equations are:

$$i = i_1 + i_2 \tag{58}$$

$$v_i = \frac{1}{c_{1i}} \int i \, dt + i R_{11} - i_2 R_{12} \tag{59}$$

$$v_o = i_2 R_{12} = \frac{1}{c_{12}} \int i_1 \, dt \tag{60}$$

The Laplacians of these equations are

$$I = I_1 + I_2 \tag{61}$$

$$v_i = \frac{I + I s C_{11} R_{11} - I_2 s C_{11} R_{12}}{s C_{11}} \tag{52}$$

$$v_o = I_2 R_2 = \frac{I_1}{s C_{12}} \tag{63}$$

thus

$$\frac{v_o}{v_i} = \frac{s R_{12} C_{11}}{R_{12} C_{11} s + (1 + R_{11} C_{11} s)(1 + R_{12} C_{12} s)} \tag{64}$$

973

now let

$$R_{11}C_{11} = R_{12}C_{12} = \tau_1$$

and

$$R_{12}C_{11} = \tau_2$$

therefore

$$\frac{v_o}{v_i} = \frac{\tau_2 s}{\tau_2 s (1 + \tau_1 s)^2} = \frac{v_o}{v_{rn}} \tag{65}$$

which agrees with Eq. (57).

Bow Fins

Before simulating the bow fin hydrodynamic force, P_4, shown in Eq. (52), the investigators multiplied the last term in Eq. (52) by the Theodorsen function, C_p. The bow fin force was represented as a total force acting at station 19 and given by

$$P_4 = \frac{1}{4} \rho u_r^2 \left[2\pi S C_p \left(\phi + \frac{3}{4} \frac{c_m}{u_r} \dot{\phi} - \frac{1}{u_r} \dot{y}_r \right) \right] - \frac{\pi}{4} \rho c_m S \ddot{y}_r \tag{66}$$

The first term of Eq. (66) was simulated by means of a circuit containing operational amplifiers. The last term was simulated passively by means of a capacitor.

Assumptions

The assumptions made in deriving the mathematical model have been listed in the previous section. The approximations that were made in deriving the analog model of these equations are the following.

1. The horizontal particle velocity, u, is assumed to be zero.

2. The surface of the sea is represented by a wave train all of whose frequency components travel with the same velocity; in general, the velocity of a wave component is inversely proportional to its frequency. For the simulation of a random sea, the velocity of propagation is chosen to correspond to the frequency at which the power spectral density is a maximum.

3. Non-linear virtual mass and buoyancy terms are approximated by quadratic and cubic functions of the relative displacement, y_r. The coefficients in these approximations are, in general, different for y_r positive and y_r negative. The dependence of the virtual mass upon the direction of the relative velocity is obtained by assuming that

Computer Modeling of the Elastic Response of Ships to Sea Loads

$$m_i = m_1 (y)_r \quad \text{for} \quad \dot{y}_r > 0 \tag{67}$$

$$m_i = m_2 (y)_r \quad \text{for} \quad \dot{y}_r < 0 \tag{68}$$

4. Hydrodynamic damping is represented by the following Laplace transform operator

$$P = -B(D) \dot{y}_r \tag{69}$$

The real part of the transfer function for $p = i\omega$ is the damping coefficient. It is approximated by an analytical function so as to give a good approximation to the damping curves described previously. It should be noted that the imaginary part of the transfer function gives a force that is out of phase with the relative velocity. This out-of-phase component cannot be eliminated in an electrical circuit representation and for minimum reactance networks is uniquely determined by the real part.

MODEL CHECKS AND MODIFICATIONS

Computations were made for the rigid body and elastic response of ESSEX to four types of excitation: a simple harmonic driving force to obtain the normal modes, a sinusoidal sea wave, a discrete wave train modeled from a measured wave history, and a random sea which specified statistical properties.

The basic information obtained for harmonic and sinusoidal inputs were amplitude and phase measurements at the various stations as read on an oscilloscope. Photographs were taken of the oscilloscope screen for analysis of transient and non-linear responses and peak values and rms values were obtained. An electronic counter was also used to measure frequency, phase angle and time increments. Rigid body motions were represented by the vertical acceleration at station 11 (heave) and the "deflection" angle at station 10 (pitch). The midship bending moment was determined at station 10.

Normal Modes

The response of the ship to a simple harmonic driving force of varying frequency was used to determine the vibratory modes. These modes were determined primarily for the purpose of checking the linear portions of the ship model. The completeness of the linear model examined is indicated by Tables 4 and 5. For the cases where buoyancy and hydrodynamic damping were omitted, but virtual mass was included, MacNeal reports that the frequency of the lowest structural mode was checked to within 1 percent by an energy method. However, when the 20 segment finite difference beam analogy was used, the frequency was about 12 percent lower than the response of ESSEX during sea trials, and a comcomputer-induced damping was observed. This computer-imposed damping was about twice as high in the non-damping case as that evidenced in ESSEX sea trials. When the 9 segment Russell beam analogy was used, the scaling changes made possible by the reduced number of segments accomplished a reduction in

975

Table 4
Natural Frequencies from Finite Beam Analogy

Case	Mode No	Frequency (cps)	Damping (% Critical)	Buoyancy Force	Hydro. Damping
1	1 2 3	0.734 1.37 2.07	2.0 2.0 2.2	No	No
2	Heave Pitch 1 2 3	0.128 0.144 0.744 1.37 2.07	1.2 1.1 1.6 1.7 2.3	Yes	No
3	Heave Pitch 1 2 3	0.139 0.158 0.750 1.37 2.08	21.2 22.5 1.9 1.9 2.3	Yes	Yes
ESSEX	Heave Pitch 1	0.105 0.11 0.87		Yes	Yes

the inherent damping. However, the computer-induced damping for the first
mode of the no-damping case was still about as large as that exhibited by ESSEX
(with damping, of course).

The inclusion of buoyancy forces produced little change in the lowest struc-
tural mode but produced rigid body heave and pitch. One of the properties of sig-
nificance in the normal mode treatment is that of orthogonality. The orthogonal-
ity of the heave and pitch modes was checked both with regard to kinetic energy
and with regard to potential energy. The heave mode was observed to include a
considerable amount of pitching motion, and the mode shape was found to be very
sensitive to small changes in the relative locations of the total buoyancy force
and the center of mass of the ship.

The inclusion of hydrodynamic damping was found to have little effect on the
elastic modes of the ship although the rigid body modes were substantially
damped. For the 20 segment model, heave and pitch frequencies of 0.139 and
0.158 cps were obtained. For the 9 segment model, frequencies of 0.123 and
0.138 were obtained. This appears to be an improvement for the ship structure
since estimated natural heaving and pitching frequencies of ESSEX are 0.105 and
0.11 cps. However, the differences produced by going from one model to the
other are larger than the change in natural frequency produced by the inclusion
of the damping term!

976

Table 4
Natural Frequencies from Finite Beam Analogy

Case	Mode No	Frequency (cps)	Damping (% Critical)	Buoyancy Force	Hydro. Damping
1	1 2 3	0.734 1.37 2.07	2.0 2.0 2.2	No	No
2	Heave Pitch 1 2 3	0.128 0.144 0.744 1.37 2.07	1.2 1.1 1.6 1.7 2.3	Yes	No
3	Heave Pitch 1 2 3	0.139 0.158 0.750 1.37 2.08	21.2 22.5 1.9 1.9 2.3	Yes	Yes
ESSEX	Heave Pitch 1	0.105 0.11 0.87		Yes	Yes

the inherent damping. However, the computer-induced damping for the first mode of the no-damping case was still about as large as that exhibited by ESSEX (with damping, of course).

The inclusion of buoyancy forces produced little change in the lowest structural mode but produced rigid body heave and pitch. One of the properties of significance in the normal mode treatment is that of orthogonality. The orthogonality of the heave and pitch modes was checked both with regard to kinetic energy and with regard to potential energy. The heave mode was observed to include a considerable amount of pitching motion, and the mode shape was found to be very sensitive to small changes in the relative locations of the total buoyancy force and the center of mass of the ship.

The inclusion of hydrodynamic damping was found to have little effect on the elastic modes of the ship although the rigid body modes were substantially damped. For the 20 segment model, heave and pitch frequencies of 0.139 and 0.158 cps were obtained. For the 9 segment model, frequencies of 0.123 and 0.138 were obtained. This appears to be an improvement for the ship structure since estimated natural heaving and pitching frequencies of ESSEX are 0.105 and 0.11 cps. However, the differences produced by going from one model to the other are larger than the change in natural frequency produced by the inclusion of the damping term!

Table 5
Natural Frequencies from Russell Beam Analogy

Case	Mode No	Frequency (cps)	Damping (% Critical)	Bow Fin	Buoyancy Force	Hydro. Damping
1	1 2 3	0.709 1.27 1.80	1.1 1.4 1.5	No	No	No
2	1 2 3	0.636 1.18 1.72	1.2 1.2 1.2	Yes	No	No
3	Heave Pitch 1 2 3	0.123 0.138 0.714 1.27 1.80	0.4 0.6 1.0 1.2 1.4	No	Yes	No
4	Heave Pitch 1 2 3	0.117 0.133 0.644 1.18 1.72	0.7 0.7 0.8 1.4 1.2	Yes	Yes	No
5	Heave Pitch 1 2 3	0.140 0.156 0.719 1.27 1.80	24.0 20.0 1.3 1.3 1.3	No	Yes	Yes
6	Heave Pitch 1 2 3	0.130 0.149 0.648 1.18 1.72	24.2 21.0 1.4 1.2 1.2	Yes	Yes	Yes

Sinusoidal Inputs

The response of the ship to a steady state sinusoidal sea was obtained to further check the linear model of the ship and in particular, the delay line, and to examine the conditions associated with large bow immersions and the effects of methods of slam reduction.

A comparison of the magnitude of the wave height, y_w, at segments 3, 11, and 19 is a measure of the proper functioning of the delay line. The results in Table 6 showed that the delay line functioned well for frequencies (in sea-fixed coordinates) up to about 0.70 rad/sec for ship speed of 16 knots. The band width of satisfactory performance of the delay line was larger when the ship's speed was higher.

977

Table 6
Ship Response to Sinusoidal Excitation

Case			4		5	
ω			0.46		0.25	
ω'			0.6376		0.3025	
Quantity	Segment	Units	Mag.	Phase Angle (Lagging)	Mag.	Phase Angle (Lagging)
Y_w	3 11 19	ft	9.80 9.95 10.30	257 125 0	9.76 10.0 9.97	90 51 0
Y_r	3 7 11 15 17 19	ft	4.20 4.95 3.20 7.46 15.00 22.80	184 355 320 143 128 116	0.71 0.33 0.34 0.598 1.60 2.77	73 245 241 57 50 47
$\dfrac{\ddot{Y}_h}{\theta}$	11 10.5	g's degrees	0.0905 2.67	300 78	0.0283 1.33	236 316
Hydro. Force	2.5 15.5 17.5 19.5	tons	517.00 614.00 674.00 273.00	351 289 289 276	94.3 72.5 86.2 44.6	244 224 218 212
Bend Moment	4 8 10 12 16	ft-tons	86.3×10^3 279.0×10^3 304.0×10^3 260.0×10^3 66.0×10^3	324 310 302 293 282	9.88×10^3 32.8×10^3 35.5×10^3 31.4×10^3 11.5×10^3	262 233 226 221 196

Introduction of non-linear terms showed a significant increase in amplitude of the elastic modes; however, this was found to be caused by a resonance of the lowest elastic mode due again to the inherent computer characteristics.

The effect of removing the mass-transport terms in the expression for virtual mass was found to be small for ship speed of 16 knots. A larger effect was observed at a higher speed.

Discrete Wave Train

The response of ESSEX to a train of waves with a specified time history and preceded by a long period of calm was computed to check the complete model as

978

well as to provide another method of determining the effects of changes in system parameters. The discrete wave train is shown in Fig. 12.

The two sets of curves show a remarkable but somewhat misleading agreement in magnitude and character. In order to obtain agreement in magnitude shown for the pitch angles, MacNeal found it necessary to use peak-to-peak wave height of 33 feet rather than the 25 feet measured in [8] and suggested that measurement of wave heights at sea are relatively inaccurate. As noted previously, the wave profile also had to be smoothed in order to get the right magnitude of
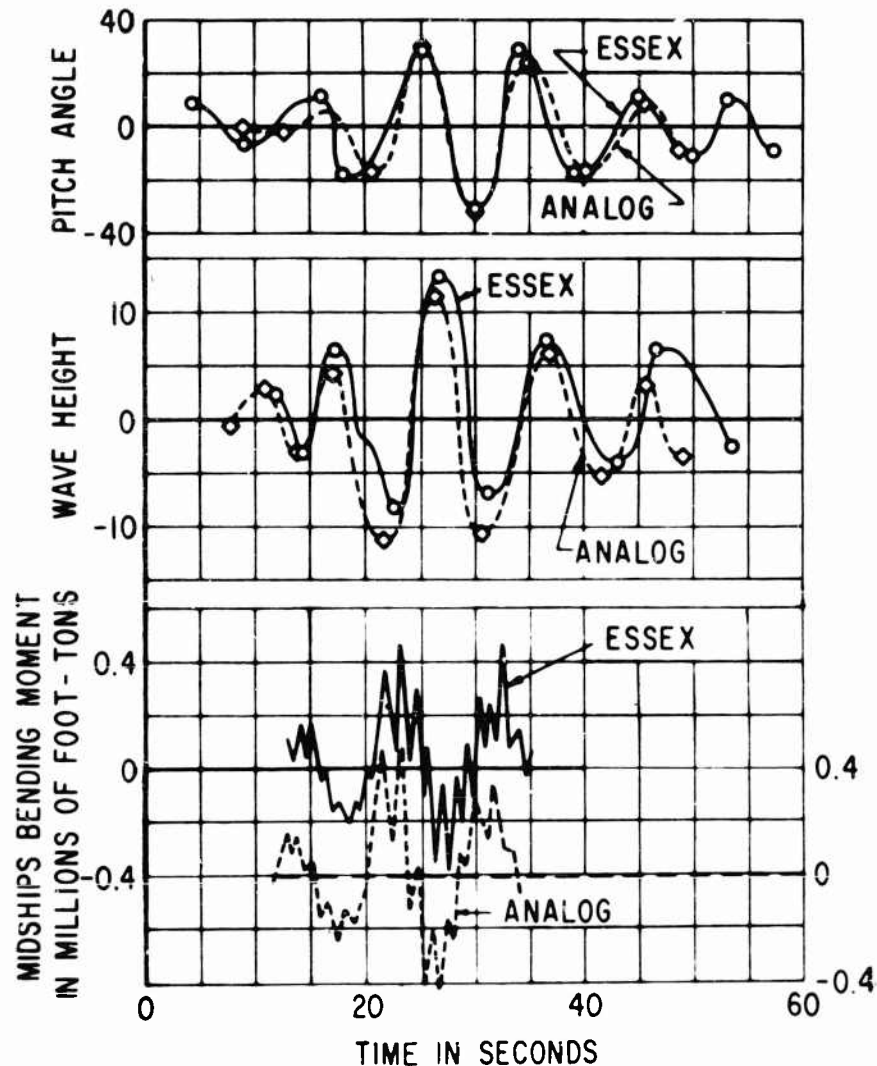
Fig. 12 - Comparison or Analog with Experimental Results

979

the bending moment. For the purposes of comparison, therefore, the ordinates of the analog wave height were multiplied by 0.07 before being plotted in Fig. 12. Apparently the severe slamming pulses at the bow occur at a lower value of wave height for the actual ship than they do for the analog computer model. MacNeal suggests that a possible explanation of this discrepancy is that the slamming pulses are significant for only about the first ten percent of the length of the ship. And since only one analog computer cell is located in this region, at a point five percent aft of the forward perpendicular, therefore the slamming effect is underestimated and perhaps somewhat blunted because of the bow overhang.

Notwithstanding these adjustments, the general agreement in magnitude and, in particular, in the frequency of the bending moment is considered a significant correlation between computer and full scale, using only the measured sea as an input.

THE ELASTIC RESPONSE OF SHIPS TO SEA LOADS

Although the main objectives of the study were to develop and verify a method for analog computer simulation of the motions and stresses at sea, exploratory studies were also made to learn more about the elastic response of ships like ESSEX to sea loads. Interesting information was obtained on the nature of bow flare slamming, on the effects or lack of effects resulting from bow fins, and on relations between bow immersion, wave crest height and wave-induced and whipping components of the bending moment.

A small portion of the results obtained in the studies are presented for the purpose of illustrating the usefulness of the computer model when fully developed.

Nature of Bow Flare Slamming

One result of the investigations of ship response concerned the nature of the mechanism of bow flare slamming. The high values of bending moment observed in bow flare slams on ESSEX apparently were the results of a double resonance. One resonance occurs between a "triplet" pulse representing the unsteady pressure forces accompanying bow immersion, and the lowest elastic mode of the ship, about 52 cpm.

Figure 13 illustrates this triplet pulse. The shape of the pulse was derived from an elementary consideration of the form of the non-linear virtual mass expression used in the model. As may be seen, the velocity of bow immersion is the time derivative of the immersion. The non-linear portion of the virtual mass is represented as shown. The discontinuity indicates that the virtual mass term used herein depends upon the direction of flow as well as the ship form. This to some extent reflects the rise of water on the hull accompanying emergence. The virtual momentum is of course the product of the velocity and the "mass." Finally, the time derivative of the momentum yields a force which reflects the non-linear portion of the virtual mass and which has a triplet pulse shape. As stated previously, the period of this pulse was found to approach the lowest elastic period of ESSEX and thereby to approach resonance.
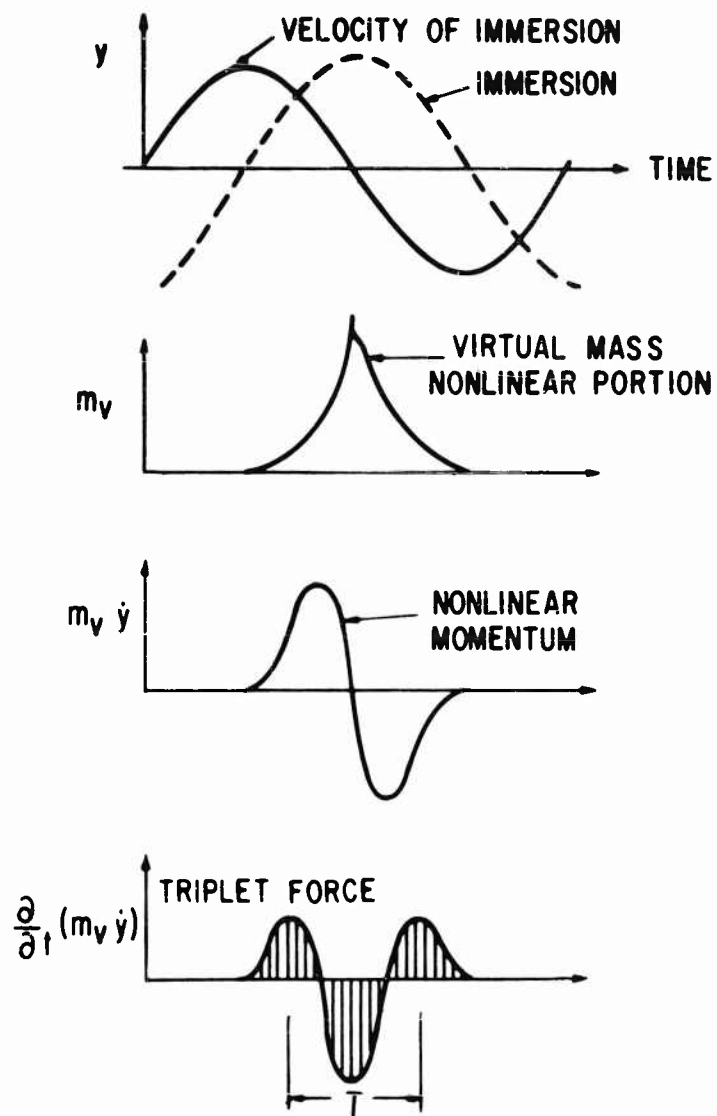
Fig. 13 - Triplet Pulse Associated with Bow
Flare Slamming

The second resonance occurs between the motions of the surface of the sea and the heaving and pitching motions of the ship as reflected in the immersion of the bow.

Figure 14 shows the immersion amplification factor (the ratio of bow immersion to wave height) for the ESSEX model versus the frequency of steady state sinusoidal seas. The lower frequency corresponds to a ship length-wave length ratio of about unity for ESSEX. The higher frequency corresponds approximately to the ship natural pitching frequency. It can be seen that large values of the bow
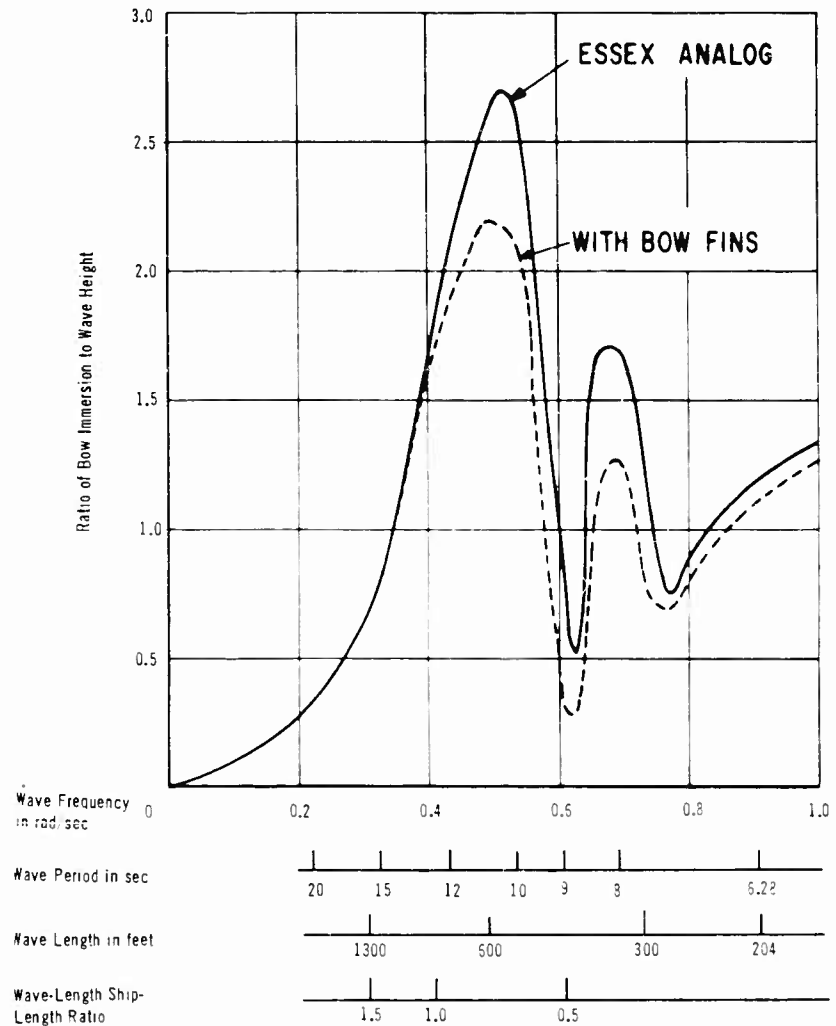
Fig. 14 - Immersion Complication Factor

immersion amplification factor lie within a narrow frequency range. Unfortunately for ESSEX, this same range of wave frequencies also appears to be the significant frequency range for State 6 seas and higher, e.g., periods of from 4 to 15 seconds for State 6 and 5 to 20 seconds for State 7.

This resonance combined with the resonance of the virtual inertia force with lowest elastic mode are considered to produce the large bending moments experienced on ESSEX.

Response to Random Waves

The simulation of ESSEX in a random sea was used to study the correlation which exists, during 30 minute periods, between the following quantities:

1. Bow immersion and wave crest height.

2. Bow emersion and wave crest height.

3. Total midship bending moment and bow immersion.

4. Wave induced component of bending moment and bow immersion.

5. Whipping component of bending moment and bow immersion.

The data points recorded are peak values of the functions experienced in independent 30 minute intervals in a stationary random sea of specified statistical properties and rms wave height. Data points were taken at 3 rms values of wave height, 8.0, 5.7, and 3.4 feet, corresponding to States 6, 5 and 4.

Figures 15 through 18 present data taken using a random sea with the power spectral density function representing ESSEX environment.

Each data point of Fig. 15 presents a comparison of the peak bending moment experienced in a 30 minute period with the peak bow immersion experienced in the same 30 minute period. Figure 15 includes 100 data points at each of the three indicated rms levels of wave height. The results recorded in this figure therefore represent a total of 150 hours at sea.

The scatter band of data points in Fig. 15 is quite narrow and therefore peak bending moment can probably be predicted reasonably well from knowledge of the peak bow immersion. Also of note in Fig. 15 is the rather large variation in observed peak values for a single rms level of wave height. The maximum and minimum peak values observed are summarized below.

Table 7
Maximum and Minimum Peak Values of Ship Response

rms Wave Height (ft)	Peak Bending Moment (10^6 ft-tons)		Peak Bow Immersion (ft)	
	Max.	Min.	Max.	Min.
8.0	1.7	0.83	58	39
5.7	1.2	0.52	44	28
3.4	0.36	0.18	26	16
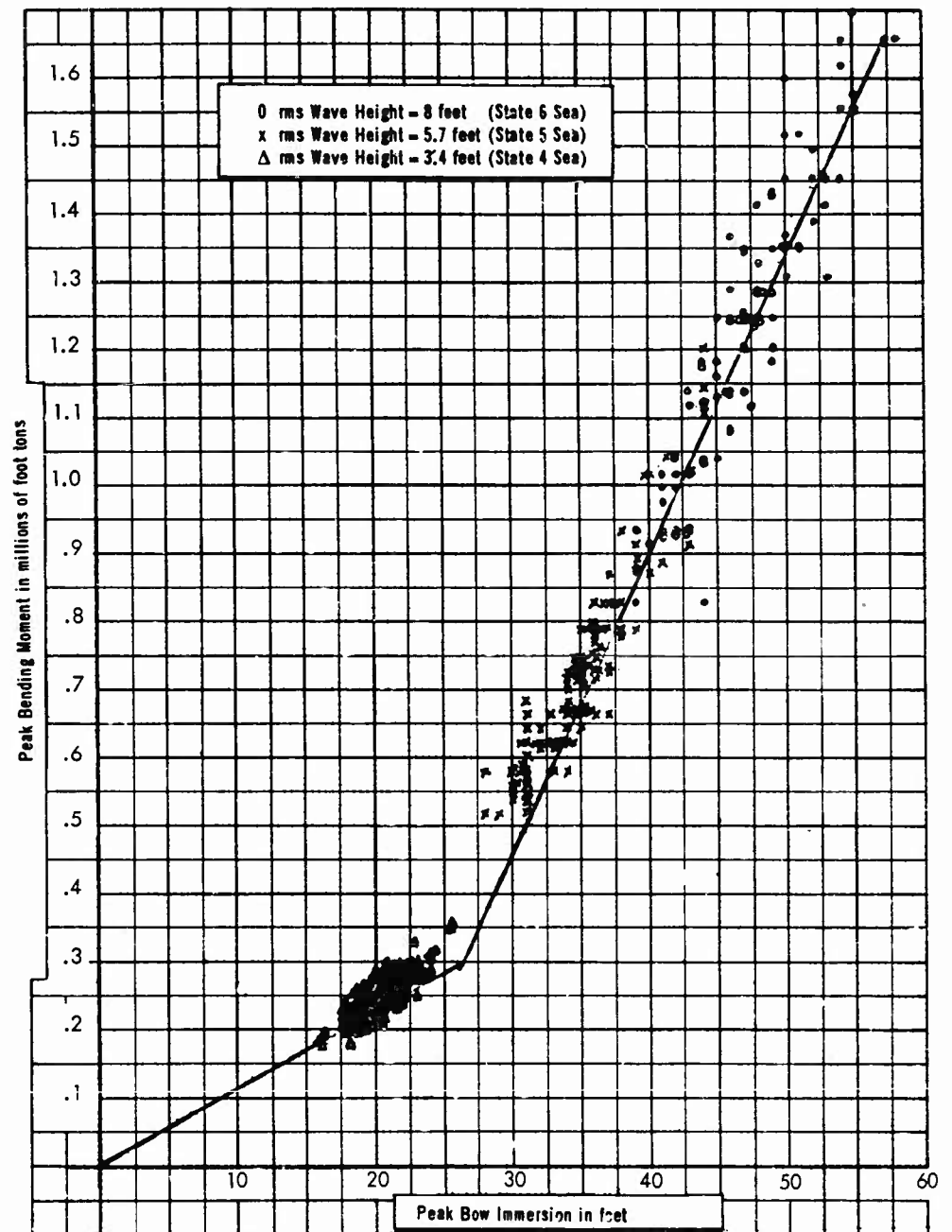
Fig. 15 - Peak Bending Moment versus Bow Immersion during
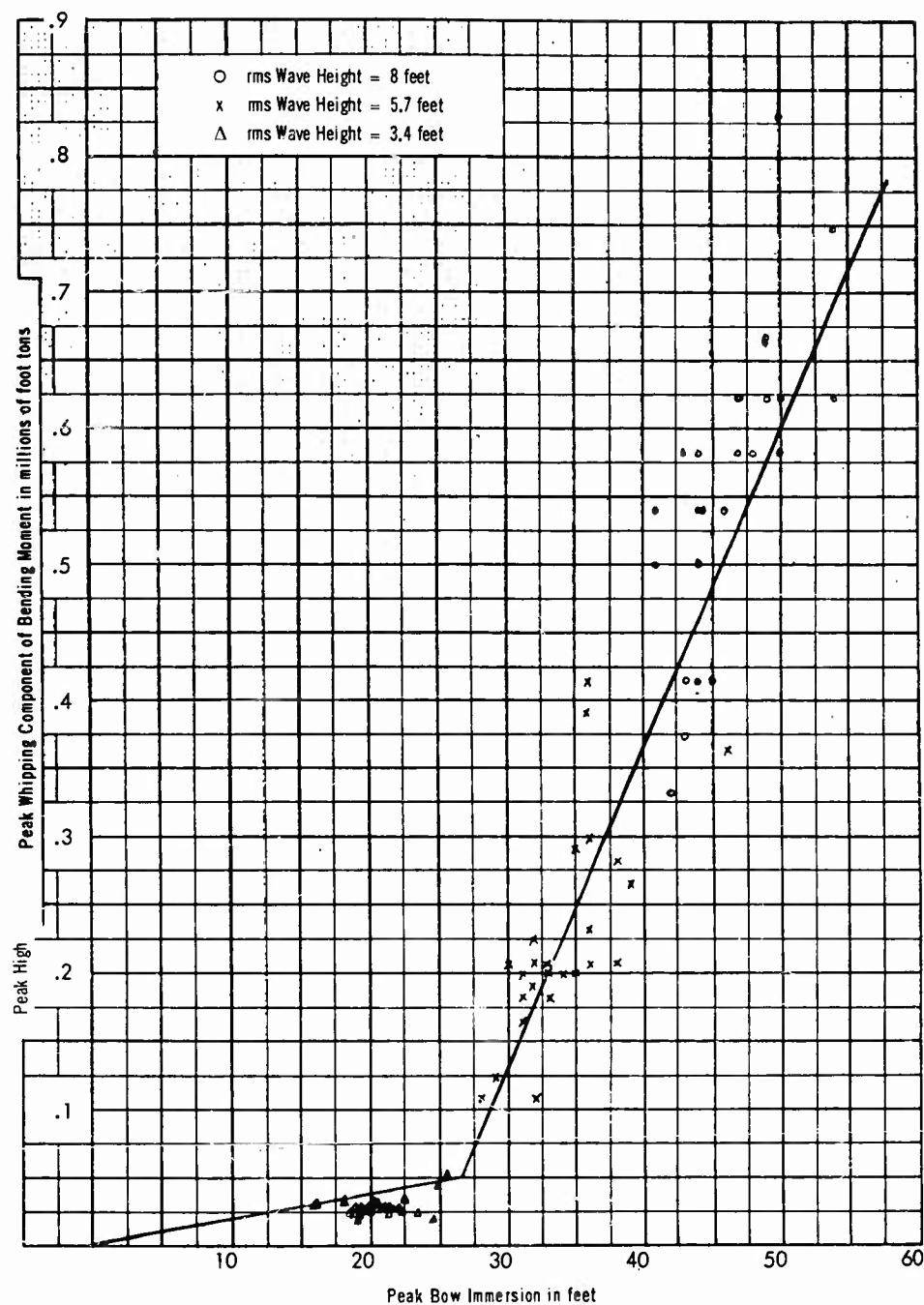30 Minute Periods

984

Fig. 16 - Peak Whipping Component of Bending Moment versus
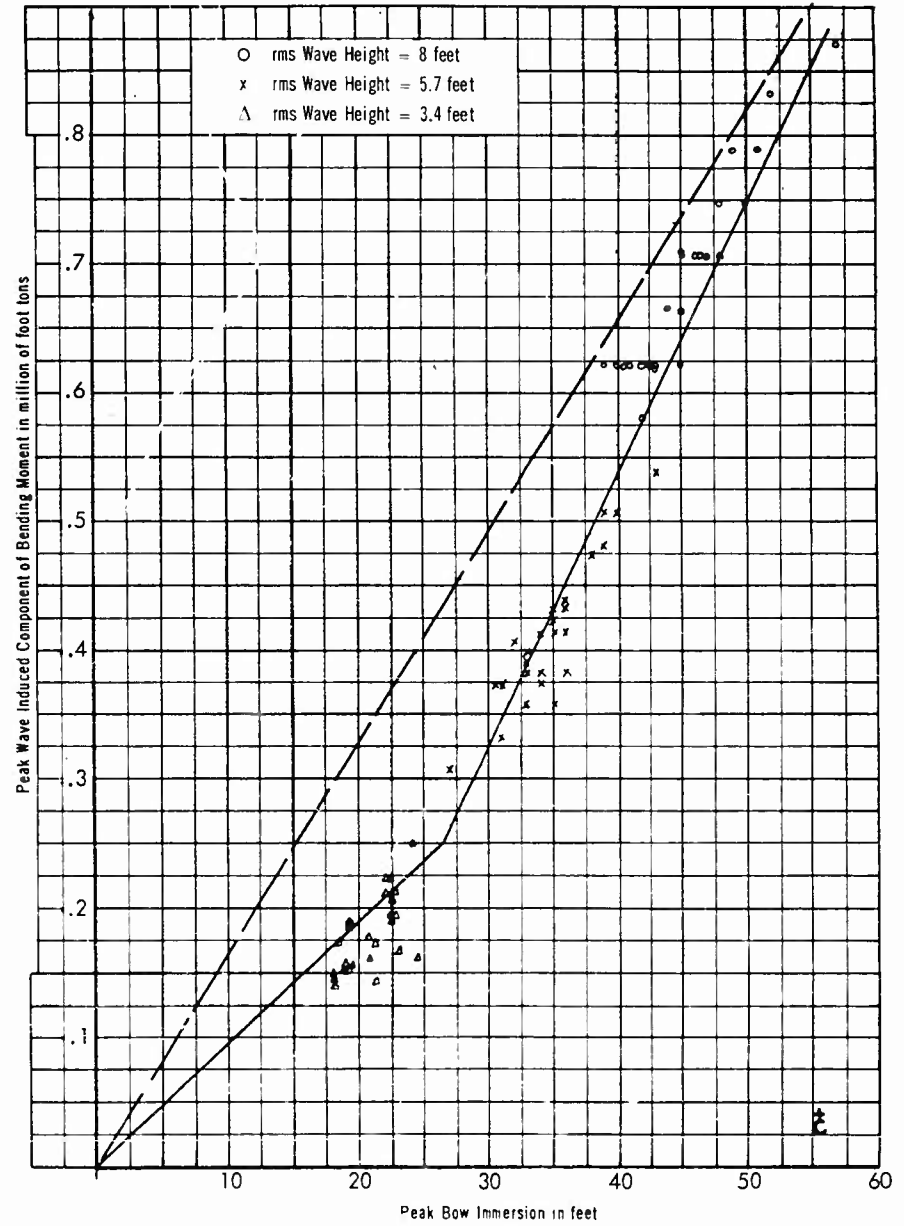Bow Immersion during 30 Minute Periods

985

Fig. 17 - Peak Wave Induced Component of Bending Moment versus
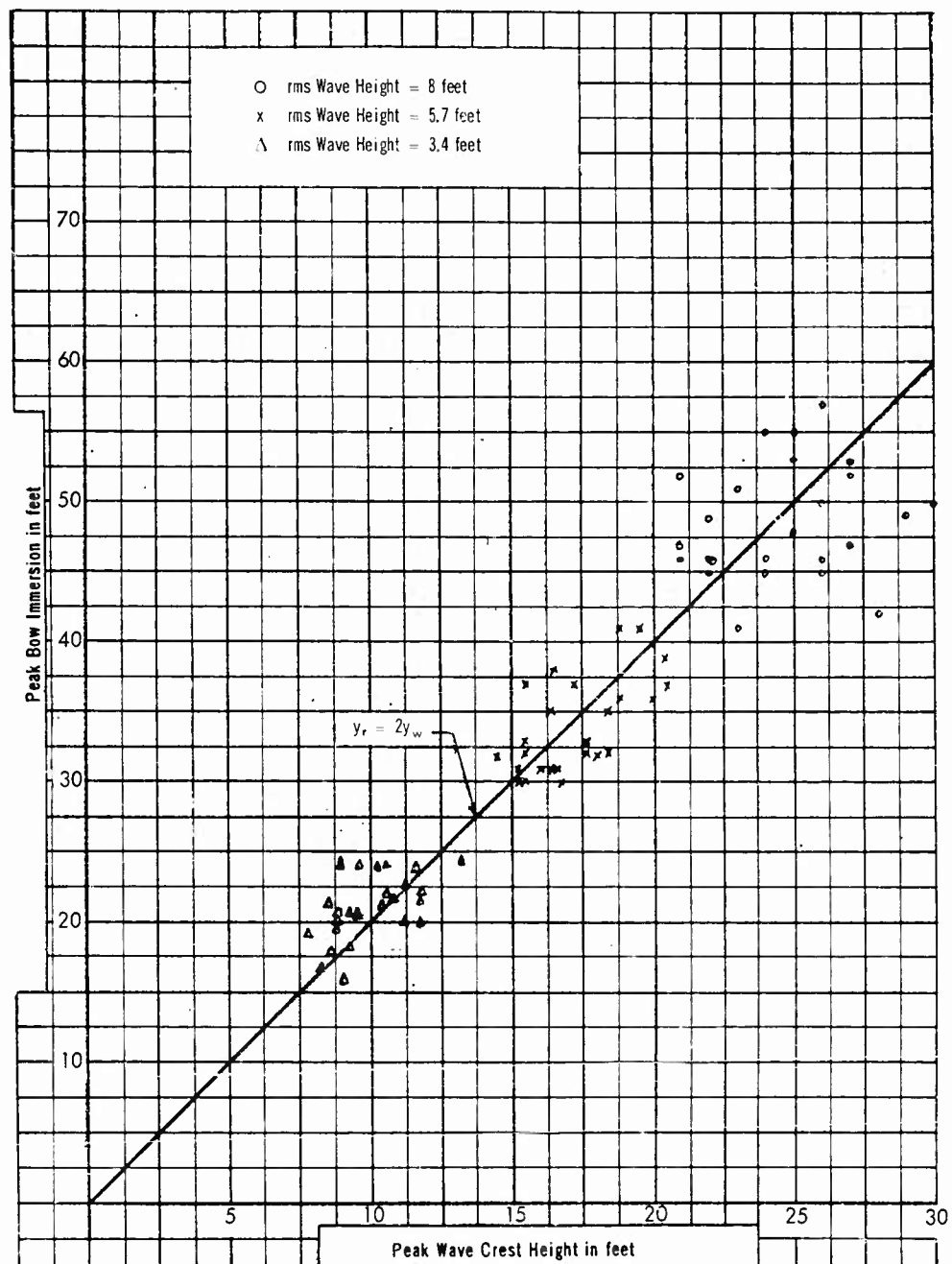Bow Immersion during 30 Minute Periods

Fig. 18 - Peak Bow Immersion versus Wave Crest Height
during 30 Minute Periods

987

These large variations in peak values indicate that although the 30 minute periods used in these studies may be generally considered ample for ordinary wave observations, they appear to be insufficient for extreme values. The standard deviation of these samples is quite large.

Figures 16 and 17 present comparisons of peak bow immersion with peak whipping component of bending moment and peak wave-induced component of bending moment during 30 minute intervals. These components of bending moment were separated by filtering the electrical signal corresponding to total bending moment with, respectively, a high-pass and low-pass filter. The wide frequency separation of the whipping and wave-induced components (17 cps vs 0.1 cps) makes this method of separation practical. Both figures show reasonable correlation by virtue of rather narrow scatter band. Data points taken from the discrete wave train analyses are shown in both figures to fall within the scatter bands.

Of particular interest in Fig. 16 is the negligible high frequency bending moment component at values of bow immersion less than about 25 feet. This phenomenon is easily explained by the fact that the non-linear virtual mass at the bow is negligibly small for values of immersion below 25 feet.

Of interest in Fig. 17 is the relatively small amount of non-linearity in the relationship between wave-induced bending moment and bow immersion. The frequency of the peak of the filter (see Fig. 3) approximates the frequencies of the peaks of both the bow immersion amplification factor and the bending moment factor. Assuming a linear relationship we may divide the peak factor of the bending moment by the peak factor of the bow immersion to obtain a value of 0.0163×10^6 ft-tons of bending moment per foot of bow immersion. The dashed line of Fig. 17 corresponds to this value derived from the linear solution.

Figure 18 shows a comparison of peak bow immersion with peak wave crest height in 30 minute intervals. The peak bow immersion amplification factor predicted by the linear solution gives a reasonable approximation to the relationship shown in Fig. 18.

Bow Fins

Studies of the bow fin effectiveness were made using steady state sinusoidal waves and a discrete wave train. The addition of the bow fin representation to the computer model was found to reduce all the natural frequencies. The lowest elastic mode was reduced by about 10 percent. The heave period was increased by 8 percent and the pitch period increased by 5 percent. As an aid in comparing these changes in values with those of real ships, an effective thin area ratio is defined as the planform area of the fins to the water plan area of the ship. For ESSEX this ratio is 0.0245. Pournaras has conducted model studies on Mariner type ships with anti-pitching fins, having an effective area ratio of 0.022 [11]. He found that the addition of the anti-pitching fins increased the pitching period by about 10 percent.

Figure 14 shows the rigid body response to a sinusoidal input. It is seen that the bow fins will reduce bow immersion by about 20 percent at the condition of resonance. MacNeal notes, however, that this is insufficient to prevent bow flare slamming. Pournaras also found that the primary effect of his fins was seen at the resonant condition and little effect was observed for other combinations of ship length and effective wave length. However, he obtained much greater reductions in bow motion than is seen in Fig. 14, and he observed that the anti-pitching fins would prevent bottom slamming.

The response of the ship to the discrete wave train showed that the maximum peak-to-peak bending moment was reduced by about 9 percent when bow fins were introduced. The whipping component, however, appears to have been reduced by about 25 percent. These values are probably influenced considerably by the amounts of reduction in natural frequency obtained when the bow planes were added.

FUTURE USEFULNESS

The model described in this paper shows remarkable promise for yielding the rigid body motions, the first few modes of elastic motions and the associated hull stresses for ships in a sea wave. The future usefulness of this model, however, will be determined by the direction of further development. And many more correlations with experimental data must be made before this technique will influence the design at the drafting board.

Studies can be made now of bow flare problems but the computation of the required mass and elastic parameters is tedious and time consuming. Therefore, a method of mechanizing the computation of these parameters is required.

A workable expression for bow flare slamming has been found, but a similar expression for bottom slamming is required to complete the representation of the vertical elastic motions of the ship in the sea wave. Suitable representations for the hull structure and hydrodynamic forces for transverse and torsional modes must also be developed.

As indicated previously, many more correlations between the computer results and full scale data and between computer results and model data for different types of ships are required. This is not so much to establish confidence on the part of the researcher as to convince those who have the immediate responsibility for the design of a ship that the computer results are reliable.

In addition, the computer results should point towards the development of:

a. simple empirical-analytic expressions which can be used in the preliminary design state, and

b. "on-line" procedures to be used in development of the final design.

Finally, to realize the objectives of the Model Basin in developing this technique, a facility comprising passive networks and operational amplifiers should be

developed within the Bureau of Ships area since the future usefulness of this "slide rule" will depend upon its convenience to the ship designer and the researcher as well as its capacity for handling varied problems and its demonstrated reliability.

CONCLUSIONS

The development presented demonstrates that a finite beam representation of the ship structure, a determination of "hydrodynamic" forces by strip theory methods and the representation of the environment as a water profile having a constant form along the ship length gives real promise as a satisfactory representation of the ship-sea system for rigid and elastic motions and structural response.

It is not clear whether substantial improvements in correlation with sea trial data can be attained by better modeling of the hull contour or by other refinements in the modeling of the hydrodynamic forces, or whether instead, the shortcomings should be attributable to the lack of physically mathematical description of the hydrodynamic forces, particularly those associated with virtual mass.

Although the ship had been represented as a finite difference beam with 21 stations, only three degrees of freedom were found important to the slamming problem, the rigid body pitch and heave modes and the lowest elastic mode. And the role of the lowest elastic mode was passive in that it did not contribute appreciably to the hydrodynamic forces but merely responded to these forces, i.e., no hydroelastic forces were generated. Therefore, the main advantage in setting up the analog computer as a 20 segment beam was not that it provided additional degrees of freedom, but rather that it provided means for measuring applied forces, displacements and internal loads at many points along the ship length.

Some terms in the model were found to contribute little to the response. The non-linear representations of the hydrodynamic forces were important only in the forward 20 percent of the ship, the structural damping term was relatively unimportant for studies primarily of transient excitation, and the mass transport terms were relatively unimportant at moderate ship speeds.

Examination of the computed ship responses to various inputs indicates that the parametric and design studies concerned with bow flare slamming may be made with the existing computer model and the results accepted with a reasonable degree of confidence. Some such results are:

a. The high values of bending moment observed in bow flare slams are the result of a double resonance. The first resonance occurs between the immersion of the bow and the surface of the sea, and is based on an unfavorable ship length-wave length relationship found for large ships in heavy seas. The second resonance occurs between a "triplet" pulse, representing the unsteady pressure forces accompanying bow immersion, and the lowest elastic mode of the ship.

b. Bow fins of a reasonable size gave no appreciable reduction in bow flare slamming except near resonance.

990

c. The peak value of the bending moment for a given ship design can be expressed as a function of the peak bow immersion, that the peak value of the bending moment can be expressed as the sum of the peak magnitudes of a high frequency component (the result of a slamming event) and of a low frequency component, and that the peak bow immersion can be estimated as a linear function of the peak wave crest height.

However, several improvements appear indicated in the computer and several additional correlations are required before the Seaworthiness Analog Computer becomes an effective design tool for general studies of the elastic response of ships to loads of the sea.

REFERENCES

1. McGoldrick, R.T., et al., "Recent Developments in the Theory of Ship Vibration," David Taylor Model Basin Report 739, October 1953.

2. Korvin-Kroukovsky, V.B., "Some Similarity Relationships for Towing Tank Models Used in Combined Ship Structural and Hydrodynamic Experiments," Davidson Laboratory Note 631, August 1961.

3. Andrews, J.N., "A Method for Computing the Response of a Ship to a Transient Force," David Taylor Model Basin Report 1544 (in publication).

4. "Simulation of the Sea and Analog Computation of the Forces on a Ship in Waves," Reed Research Report on Project RR-1458-N, November 1959.

5. Lee, S.E., "Problem Summary on the Seaworthiness Analog Computer," Structural Mechanics Laboratory Technical Note SML-760-36, September 1962.

6. MacNeal, R.H., "Analog Computer Analysis of the Bow Slamming Problem for the USS ESSEX," Computer Engineering Associates Report on Project ESD172, January 1961.

7. Schwendler, R.G., "Improved Analog Computer Analysis of the Bow Slamming Problem," Computer Engineering Associates Report on Project ES178, April 1962.

8. McGoldrick, R.T., "Ship Vibration," David Taylor Model Basin Report 1451, December 1960.

9. Jasper, N.H. and Birmingham, J.T., "Strains and Motions of USS ESSEX (CVA 9) During Storms near Cape Horn," David Taylor Model Basin Report 1216, August 1958.

10. "Calculation of Forces due to Wave Encounter," Reed Research Report on Project RR-1458-G, October 1958.

11. Pournaras, V.A., "A Study of the Sea Behavior of a Mariner-Class Ship Equipped with Anti-pitching Bow Fins," David Taylor Model Basin Report 1084, October 1958.

HYDRODYNAMIC IMPACT WITH
APPLICATION TO SHIP SLAMMING

K. M. Ochi and M. D. Bledsoe
David Taylor Model Basin
Washington, D. C.

ABSTRACT

This paper presents the results of a theoretical and experimental study of the added mass and impact pressures and force on a ship's bottom during slamming.

The theory, based on hydrodynamic considerations, utilizes Lewis' mathematical formulation for ship form which enables it to be applied to almost any practical ship forebody section. The theory was applied to three different ship forms ranging from extreme U to extreme V. Pressures, forces and impulse are compared for the three forms.

The two-dimensional drop tests were carried out using a model representing an extreme V form section. Pressures, velocities and accelerations were measured and piled up water obtained photographically.

A comparison of theory and experiment showed some discrepancies in the pressures and forces. However, a comparison of the total impulse showed good agreement during the period critical for slamming.

INTRODUCTION

Numerous theoretical treatises of a body impacting a flat water surface have appeared in the literature during recent years. For the most part these theories are based on the earlier work of von Karman, [1] later extended by Wagner [2]. Their work essentially involved the wedge entry problem. The basic idea of von Karman was that during impact, the momentum of the dropping body is imparted to the momentum of an apparent mass of water, assumed to be that associated with a flat plate having the dimensions of the wedge at the intersection of the water surface. Wagner introduced the concept of piled-up water. That is, when

993

body penetrates a water surface the displaced water produces an elevation of the surface around the body. According to Wagner the contribution of this piled-up water should also be considered in evaluating the added mass. A further refinement due to Wagner was the consideration of the effect of finite deadrise on added mass where von Karman had considered flow about a flat plate only.

Based on these fundamental ideas are the works of Milwitzky, [3], [4] Mayo [5], Bisplinghoff [6], Fabula [7], Szebehely [8] et al and Ochi [9]. The work of Bisplinghoff, Mayo and Milwitzky dealt primarily with the impact of wedges as applied to sea plane hulls while Fabula and Ochi treated elliptical shapes. Szebehely was among the first to apply the theories of von Karman and Wagner to the specific problem of ship slamming. However his theory, which essentially applies to a wedge-shaped body with no flat bottom, has the basic deficiency that it is not applicable at the instant of impact, a time most critical for ship slamming.

The theories of the previous investigators all suffered from the lack of sufficient generality to permit universal application to any ship bow form. For example, while the wedge theory may be applicable to an extreme V-form ship section with no flat bottom, it is not applicable to a more blunt U-form section. Similarly, the ellipse fitting method is not applicable to an extreme V-form section. Since the form of a ship bow section shows a wide variation from extreme U to extreme V, depending on the type of ship, a more generalized theory which is applicable to any sectional form is desirable. Fortunately, the mathematical representation of ship form presented by Lewis [10] permits coverage of the practical range of ship forms by proper selection of parameters. The present paper utilizes the Lewis forms and develops a theory for evaluating piled-up water, added mass and the hydrodynamic impact force associated with slamming so that the results may be applicable to realistic ship sections.

The paper is divided into two parts. In Part I the theory is developed and applied to ship sections ranging from extreme V to extreme U. Comparative merits of these three forms are evaluated. Part II presents a description of experiments carried out using a two-dimensional V-form model. The model was allowed to strike a still water surface at an impact velocity which is considered to be realistic. Accelerations, velocity and impact pressures were measured and piled-up water obtained photographically. The results are analyzed and correlations with theory are made of pressure, total force and impulse.

PART I. THEORETICAL STUDY OF IMPACT DURING SHIP SLAMMING

MATHEMATICAL PRESENTATION OF SHIP FORWARD SECTION AND VELOCITY POTENTIAL

In order to evaluate the piled-up water and added mass associated with impact of a body on a water surface and thereby obtain the force acting on the body, the velocity potential must be established. This necessitates that the shape of the body be expressed by a proper mathematical formulation. For this

purpose, a cylinder which represents the shape of a forward ship section is considered. This cylinder expands with immersion so that its shape adequately represents the submerged portion of ship section. It is particularly important that the cylinder represents the lower part of the ship section well, since ship bottom form greatly influences the severity of the slamming.

Among the various fitting methods used in the past for expressing a ship forward section by a simple mathematical form are the wedge [8], and ellipse [7] [9] [11]. However, neither of these methods is applicable over the entire range of ship forebody sections which vary from extreme-U to extreme-V in form. In addition, the existence of a flat bottom makes it difficult to express the given shape by a simple mathematical form.

It is well known that ship form can be represented approximately by the following equation.

$$\frac{z}{U} = e^{\zeta} + \sum_{n=1}^{n} C_{2n-1} e^{-(2n-1)\zeta} , \tag{I.1}$$

where $z = x + iy$, $\zeta = \xi + i\eta$, C_{2n-1} is a coefficient determined from the given form, and U is a unit length. This equation reduces an ellipse when $n = 1$. It yields the Lewis forms when $n = 1$ and 2 [10] and the Prohaska forms when $n = 1$ and 3, $n = 1$ and 5, etc. [12].

Attempts were made to fit the lower part of a ship's forward sections by Eq. (I.1) using several combinations of values for n. The results showed that the combination of $n = 1$ and 2 (Lewis forms) adequately represented the lower part of the sections. Examples of the fitting are shown in Fig. I.1. Included also in the figure for comparison, are the results obtained by the ellipse fitting method. In preparing Fig. I.1, the section at Station $3\text{-}1/2$ (17.5 percent of the length aft of the forward perpendicular) of the MARINER was selected.

This form was modified to an extreme U-form and extreme V-form keeping the area under the load-water-line constant.* As can be seen in the figure, the substitution of Lewis forms for these given ship sections provides a reasonable approximation at all immersions considered to be significant for slamming. On the basis of this result, the Lewis forms will be used in the present analysis. A brief description of Lewis forms is given in the Appendix I.

First, the complex potential for the Lewis forms will be obtained. The complex potential discussed here is that for the irrotational two-dimensional motion of a cylinder in an infinite fluid moving with a velocity V. The application of the concept of complex potential in an infinite fluid to impact phenomena on the free surface is justified, since the associated high velocities permit the conditions of zero potential on the free surface to be satisfied [8] [13]. Now, take $n = 2$ in Eq. (I.1),

---

*The modification was made by members of the HS-2 Panel, Hull Structure Committee of the Society of Naval Architects & Marine Engineers.

$$x = U \left\{ (e^{\xi} + C_1 e^{-\xi}) \cos \eta + C_3 e^{-3\xi} \cos 3\eta \right\}$$
$$y = U \left\{ (e^{\xi} - C_1 e^{-\xi}) \sin \eta - C_3 e^{-3\xi} \sin 3\eta \right\} ,$$

(I.2)

where, ξ varies from 0 to ∞, and varies from 0 to $\pm \pi$. Then, $\xi = 0$ gives the Lewis form.

Consider the case of a vertical flow with velocity, v, as shown in Fig. I.2. The boundary condition on the surface of the body is,

$$\left| \frac{\partial \phi}{\partial \xi} \right|_{\xi=0} = V \left| \frac{\partial y}{\partial \xi} \right|_{\xi=0}$$

(I.3)

Another boundary condition is that the velocity potential, ϕ, must become 0 for $\xi \to \infty$.
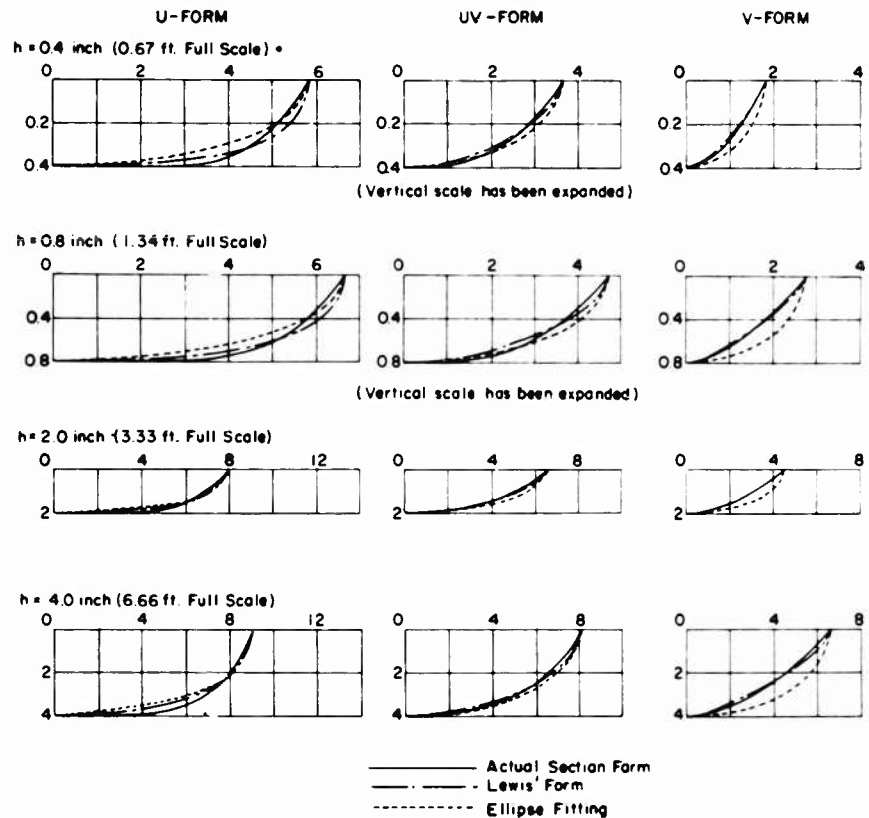
Fig. I.1 - Examples of fitting methods by Lewis' form and ellipse (1/20 scale model of a 520 ft ship)

996

Hydrodynamic Impact with Application to Ship Slamming
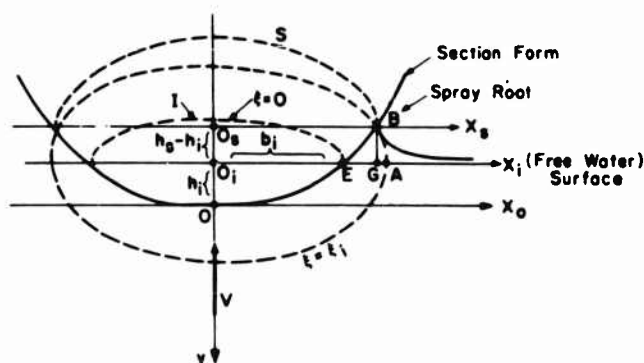
Fig. I.2 - Sectional form showing piled-up
water and wetted width

From Eqs. (I.2) and (I.3),

$$\left|\frac{\partial y}{\partial \xi}\right|_{\xi=0} = U \left\{ (1+C_1) \sin \eta + 3C_3 \sin 3\eta \right\}. \tag{I.4}$$

The complex potential will take the following general form;

$$w = -i V U \sum_m (A_m + iB_m) e^{-m\zeta}. \tag{I.5}$$

Then, the following equation can be derived.

$$\left|\frac{\partial \phi}{\partial \xi}\right|_{\xi=0} = VU (A_1 \sin \eta - B_1 \cos \eta + 3A_3 \sin \eta - 3B_3 \cos \eta). \tag{I.6}$$

From Eqs. (I.3) (I.4) and (I.6), B_1 and B_3 are zero, and $A_1 = 1 + C_1$, $A_3 = C_3$. Then, the complex potential and the velocity potential are simply obtained as follows:

$$w = -iVU \left\{ (1+C_1) e^{-\zeta} + C_3 e^{-3\zeta} \right\} \tag{I.7}$$

$$\phi = -VU \left\{ (1+C_1) \sin \eta \times e^{-\xi} + C_3 \sin 3\eta \times e^{-3\xi} \right\}. \tag{I.8}$$

PILED-UP WATER AT IMPACT

When a body penetrates the water surface, the displaced water produces an elevation of the surface around the body. This phenomenon is referred to as a piling-up of water and the amount has been believed to be appreciable even at the initial stage of impact. Figure I.2 shows a pictorial sketch of the piled-up water around a body at a time when its instantaneous immersion is h_i. The

997

section form for this immersion is expressed by a cylinder, I, having parameters with subscript i, such as C_{1i}, etc. When the piled-up water surface arises and meets the section at a point B, called the spray root, there exists another cylinder, S, called the spray-root or equivalent cylinder. This cylinder has parameters with subscript s, such as C_{1s}, etc. If the ratio of the semi-major axes of both cylinders, b_s/b_i, is obtained, the amount of piled-up water is estimated.

Referring to the original cylinder, I, the complex velocity for a given flow is

$$
\nu = u - iv = -\frac{dw}{d\zeta} \times \frac{d\zeta}{dz}
$$

$$
= -iV \frac{(1 + C_{1i}) e^{-\zeta} + 3C_{3i} e^{-3\zeta}}{e^{\zeta} - C_{1i} e^{-\zeta} - 3C_{3i} e^{-3\zeta}} .
$$

(I.9)

The above equation gives the vertical velocity outside of the cylinder on the free surface ($\eta = 0$). That is,

$$
v_n = V \frac{(1 + C_{1i}) e^{-\xi} - 3C_{3i} e^{-3\xi}}{e^{\xi} - C_{1i} e^{-\xi} - 3C_{3i} e^{-3\xi}} .
$$

(I.10)

Consider a water particle outside of the cylinder located at a point A. This point lies on a cylinder represented by ξ_i which has a common axis with the original cylinder. The normal velocity of this particle is obtained from Eq. (I.10) as,

$$
v_n = V \frac{(1 - C_{1i}) e^{-\xi_i} + 3C_{3i} e^{-3\xi_i}}{e^{\xi_i} - C_{1i} e^{-\xi_i} - 3C_{3i} e^{-3\xi_i}} .
$$

(I.11)

The time integral of Eq. (I.11) gives the elevation of a fluid particle above the undisturbed surface, and a water particle initially located at a point A touches the body surface after a time t. This is the point B in the figure. In the strict meaning, a water particle located at a point G moves to a point B since BG is vertical to the water surface. However, this assumption may be acceptable because of the fact that the width of the bottom increases gradually. Thus, the following equation is obtained.

$$
\int_0^t V(t) \frac{(1 - C_{1i}) e^{-\xi_i} - 3C_{3i} e^{-3\xi_i}}{e^{\xi_i} - C_{1i} e^{-\xi_i} - 3C_{3i} e^{-3\xi_i}} dt = h_s .
$$

(I.12)

Where h_s satisfies the relation shown in Eq. (I.2), since the point B lies on the actual section of the body. Equation (I.12) is the one which gives the relation between the original and the equivalent cylinders.

In order to solve Eq. (I.12), the following relation is introduced

$$\frac{V(t)}{\frac{d\alpha_i}{dt}} = \frac{dh_i}{d\alpha_i} = \lambda(\alpha_i),$$ (I.13)

where

$$\alpha_i = \frac{h_i}{b_i}.$$

Then, Eq. (I.12) becomes

$$\int_0^{\alpha_i} \lambda(\alpha_i) \; \frac{(1+C_{1i}) \, e^{-\xi_i} + 3C_{3i} \, e^{-3\xi_i}}{e^{\xi_i} - C_{1i} \, e^{-\xi_i} - 3C_{3i} \, e^{-3\xi_i}} \; d\alpha_i = h_s.$$ (I.14)

In Eq. (I.14) $C_{3i} e^{-3\xi_i}$ can be neglected in comparison with $C_{1i} e^{-\xi_i}$, since $C_{3i} \ll C_{1i}$ and $\xi_i > 0$. This means physically that, in the evaluation of the piled-up water, an elliptic cylinder may be substituted for the cylinder represented by Eq. (I.2). It is noted that, even though $C_{3i} e^{-3\xi_i}$ is neglected in Eq. (I.14), the terms which contain $C_3 e^{-3\xi}$ in Eq. (I.2) cannot be neglected since these terms are multiplied by $\cos 3\tau$ or $\sin 3\tau$-components. By using these assumptions, Eq. (I.12) is written as,

$$\int_0^{\alpha_i} \lambda(\alpha_i) \; \frac{(1+C_{1i}) \, e^{-\xi_i}}{e^{\xi_i} - C_{1i} \, e^{-\xi_i}} \; d\alpha_i = h_s.$$ (I.15)

Now referring to the point B in the figure, there are the two following relations,

$$O_s B = b_s = O_i G = O_i A$$

$$O_s O_i = h_s - h_i.$$

These relations can be expressed by the following equations,

$$U_i \left\{ \left(e^{\xi_i} + C_{1i} \, e^{-\xi_i} \right) \cos \tau_i - C_{3i} \, e^{-3\xi_i} \cos 3\tau_i \right\} = b_s$$ (I.16)

$$U_i \left\{ \left(e^{\xi_i} - C_{1i} \, e^{-\xi_i} \right) \sin \tau_i - C_{3i} \, e^{-3\xi_i} \sin 3\tau_i \right\} = h_s - h_i.$$ (I.17)

The third term in the above equations may again be neglected since experimental results have shown that the magnitude of τ_i is small (less than $\pi/16$), and since $C \ll C$, $\xi_i > 0$. Results of numerical calculations made for possible values of ξ_i and τ_i showed that the effect of neglecting the 3rd term in the equations is less than 2 percent. Then, the following equation can be derived from Eqs. (I.16) and (I.17).

$$e^{\xi_i} = \frac{1}{2}\left\{\frac{b_s}{U_i} + \sqrt{\left(\frac{b_s}{U_i}\right)^2 - 4C_{1i}}\right\}.$$

and

$$\eta = \sin^{-1}\frac{\left(\dfrac{h_s - h_i}{U_i}\right)}{\sqrt{\left(\dfrac{h_s - h_i}{U_i}\right)^2 - 4C_{1i}}}, \tag{I.18}$$

where

$$U_i = b_i k_i.$$

Hence, Eq. (I.15) yields

$$\int_0^{a_i} \lambda(a_i)\left(\frac{1+C_{1i}}{2C_{1i}}\right)\left\{\frac{\left(\dfrac{b_s}{b_i}\right)}{\sqrt{\left(\dfrac{b_s}{b_i}\right)^2 - 4C_{1i}k_i^2}} - 1\right\}da_i = h_s. \tag{I.19}$$

The above integral equation is quite difficult to solve. However, the equation is greatly simplified and can be solved approximately by introducing the following expression for C_{1i} and k_i (see Appendix I).

$$C_{1i} \approx \frac{1 - a_i}{1 + 2\ell a_i}$$

$$k_i \approx \frac{1 + 2\ell a_i}{2} \tag{I.20}$$

Where, ℓ is a constant which depends on ship sectional form. It is noted that the above approximation holds up to $a_i = 0.6$ which corresponds approximately to 8 ft immersion of forward sections for a 520-ft ship. Since slamming impact is completely over before the ship section has a submergence of about 4 ft, the approximation given in Eq. (I.20) can safely be used in the present analysis.

Substituting Eq. (I.20) into Eq. (I.19), and by differentiating Eq. (I.19) with respect to a_i, the following equation may be derived.

$$\left\{\frac{2 + (2\ell - 1)a_i}{2(1 - a_i)}\right\}\left\{\frac{\left(\dfrac{b_s}{b_i}\right)}{\sqrt{\left(\dfrac{b_s}{b_i}\right)^2 - (1 - a_i)(1 + 2\ell a_i)}} - 1\right\} = \frac{dh_s}{dh_i}. \tag{I.21}$$

1000

The right-hand side of Eq. (I.21) is the ratio of the velocities for immersions h_i and h_s. On the other hand, the velocity for an arbitrary immersion of a body during the impact process can be written from the momentum theorem as follows:

$$V = \frac{M}{M+m} V_o ,$$ (I.22)

where

V = velocity at a time t, after impact

V_o = initial velocity

M = mass of a body

m = added mass at a time, t, after impact.

Also, the added mass can approximately be written as (see next section),

$$m = \frac{\rho \pi}{2} b_s^2 = \frac{\rho \pi}{2} (b_i x)^2 ,$$ (I.23)

where

b_s = half of wetted width

b_i = half of actual width of a body at time, t

x = ratio of wetted width to actual width; that is b_s/b_i.

By using the relations given in Eqs. (I.22) and (I.23), Eq. (I.21) may be expressed as

$$\left\{ \frac{2 + (2\ell - 1) a_i}{2(1 - a_i)} \right\} \left\{ \frac{x}{\sqrt{x^2 - (1 - a_i)(1 + 2\ell a_i)}} - 1 \right\} = \frac{M + \frac{\rho \pi}{2} b_i^2 x^2}{M + \frac{\rho \pi}{2} b_i^2 x^4} .$$ (I.24)

where

$$x = \frac{b_s}{b_i}$$

The above equation gives the ratio of the wetted width to the actual width and thereby the piled-up water for an arbitrary immersion can be obtained. In a practical evaluation of the value x from Eq. (I.24), it will be the simplest to compute both sides of the equation for various values of x, respectively, and obtain the answer graphically. However, since two parameters a_i and b_i are involved in Eq. (I.24), it may be convenient to express Eq. (I.24) by a single parameter. For this, the following method is given.

Divide the breadth of a given section into two parts: that associated with the flat portion, b_*, and that associated with the curved portion Δb (see Fig. I.3). Take the ratio of immersion, h, and Δb, and define a new parameter z'. That is,

$$b = b_* - \Delta b$$

$$z' = h/\Delta b .$$

(I.25)

where

b_* = half-breadth of flat bottom

h = immersion.
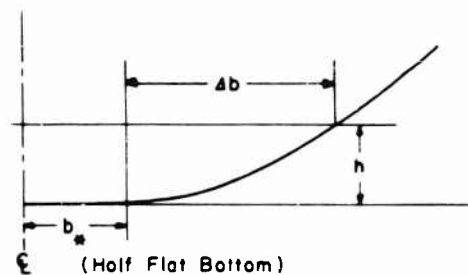
Fig. I.3 - Sketch showing section segmention used in theory

Furthermore, express the immersion h, as a function of the parameter, z', approximately. That is,

$$h = c z'^n .$$

(I.26)

where, c and n are constants dependent on ship form and size (c has the dimension of length). It should be mentioned that the simple expression given in Eq. (I.26) is permissible up to certain immersions. The limiting immersions would be 3 ft at Station 2, 5 ft at Station 3-1 2, and 10 ft at Station 5 for a 520-ship. As mentioned earlier, a maximum of 4 ft immersion of a body is sufficient for consideration for slamming problem: therefore the approximation given in Eq. (I.26) may be acceptable. As an example, the values of c, n, and b_* for Station 3-1 2 of the model and ship are as follows:

	c		n	b_*	
	Model (in.)	520-ft Ship (ft)		Model (in.)	520-ft Ship (ft)
U-Form	11.2	18.7	1.80	3.35	5.58
UV-Form (MARINER)	14.2	23.7	1.98	1.20	2.00
V-Form	21.0	35.0	3.00	0.28	0.47

1002

Hydrodynamic Impact with Application to Ship Slamming

Now, from relations given in Eqs. (I.25) and (I.26), α_i and b_i in Eq. (I.24) can be written by a single parameter, α_i',

$$b_i = b_* + c(\alpha_i')^{n-1}$$

$$\alpha_i = \frac{c(\alpha_i')^{n-1}}{b_* + c(\alpha_i')^{n-1}} .$$

(I.27)

Numerical calculation of piled-up water was made for three different forms, (U, UV, V) and the results are shown in Fig. I.4. As can be seen in the figure, the magnitude of piled-up water is much less than that found in [2] and [8]. Comparison of the values computed by the present theory with those obtained in the experiment have shown good agreement for the UV-Form, but some difference was observed for the V-Form model (1.18 as compared to 1.44 from the experiments).

Fig. I.4 - Ratio of wetted breadth to breadth at undisturbed water level versus immersion (1/20 scale model)
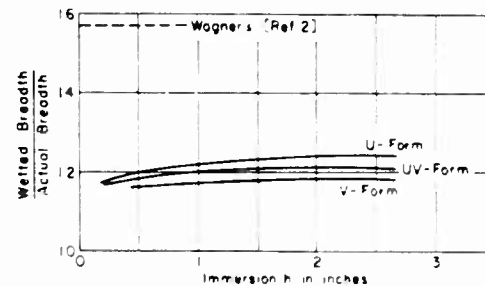
ADDED MASS

Earlier investigations have assumption that the added mass associated with impact for a body having a wetted width, b_s, is $c \sim 2 b_s^2$ [2] [8] [14]. The result is applicable to plate, circular and elliptic cylinder. However, the added mass for a body of an arbitrary form will not be the same as that for a plate, circular cylinder, etc. In order to obtain the added mass for a body of an arbitrary form, the theory of added mass of two-dimensional forms oscillating in a free surface developed by Landweber and de Macagno [15] is applied here. Since the boundary conditions used in their theory and in the present study are the same, the added mass for a body oscillating in a free water surface can be applied to the impact problem also.

The kinetic energy of an irrotational fluid in an infinite field of potential flow is given by,

$$T = \frac{\rho}{2} \int_v (\nabla \phi)(\nabla \phi) dv .$$

(I.28)

1003

By applying Green's theorem and by taking the continuity condition into consideration, the above equation becomes,

$$T = -\frac{\rho}{2} \int_v \varphi \nabla^2 \varphi \, dv - \frac{\rho}{2} \int_S \varphi \frac{\partial \varphi}{\partial n} \, dS = -\frac{\rho}{2} \int_S \varphi \frac{\partial \varphi}{\partial n} \, dS.$$ (I.29)

The interation is to be taken over the boundary of a cylinder. Since $\partial n = h \, \partial \xi$, $\partial s = h \, \partial \eta$, and

$$h = \sqrt{\left(\frac{\partial x}{\partial \xi}\right)^2 + \left(\frac{\partial x}{\partial \eta}\right)^2}$$ (I.30)

$$\frac{\partial x}{\partial \xi} = \frac{\partial y}{\partial \eta}, \qquad \frac{\partial x}{\partial \eta} = -\frac{\partial y}{\partial \xi}.$$

Then, Eq. (I.29) can be written as

$$T = -\frac{\rho}{2} \int_{-\pi}^{\pi} \left| \varphi \frac{\partial \varphi}{\partial \xi} \right|_{\xi=0} \partial \eta.$$ (I.31)

The velocity potential, φ, is given in Eq. (I.8). However, since added mass is to be considered for an equivalent cylinder (spray-root cylinder), coefficients U_s, C_{1s}, etc., must be substituted for U, C_1, etc., in Eq. (I.8). The result of integration in Eq. (I.31) gives,

$$T = \frac{\rho \pi}{2} V^2 U_s^2 \left\{ (1 - C_{1s})^2 - 3C_{3s}^2 \right\}.$$ (I.32)

Furthermore, the kinetic energy may be expressed in terms of added mass by,

$$T = \frac{1}{2} mV^2.$$ (I.33)

From these two equations, the added mass is obtained as follows:

$$m = \rho \pi U_s^2 \left\{ (1 + C_{1s})^2 - 3C_{3s}^2 \right\}.$$ (I.34)

It is sufficient to consider half of the above added mass since only half of its volume is submerged in the case under study. Then, the added mass of a cylinder becomes,

$$m = \frac{\rho \pi}{2} U_s^2 \left\{ (1 - C_{1s})^2 - 3C_{3s}^2 \right\}.$$ (I.35)

Since $U_s = b_s k_s$, Eq. (I.35) is written as

$$m = \frac{\rho \pi}{2} b_s^2 \, \textcircled{C}.$$ (I.36)

where

$$\textcircled{C} = k_s^2 \left\{ (1+C_{1s})^2 + 3C_{3s}^2 \right\} .$$

As was mentioned earlier, the added mass of an ellipse having a wetted width, b_s, is $(\rho\pi/2)b_s^2$. This is the formula which has been conventionally used in the estimation of added mass associated with slamming. Then, the coefficient, $\textcircled{C}$, given in Eq. (I.36) is the modification factor of the added mass for a ship-like section as compared with that for a plate or circular cylinder. It may be said that if $\textcircled{C} > 1$ the conventionally used formula gives an underestimation, and if $\textcircled{C} < 1$, the conventionally used formula gives an overestimation.

Inasmuch as the coefficients, k_s, C_{1s}, etc., in Eq. (I.36) can be expressed by a single parameter, a_s (see Appendix), the modification factor, $\textcircled{C}$, is written simply as,

$$\textcircled{C} = \left\{ 1 + \left(\frac{2\ell - 1}{2} \right) a_s \right\}^2 . \tag{I.37}$$

In the derivation of this formula, terms of higher order of small values are neglected. Since a_s in the above equation is a parameter for the spray-root cylinder, a_s must be expressed as a function of a_i or a_i' for the original cylinder so that the modification factor, $\textcircled{C}$, can be directly computed for a given cylinder. For this, the relations given in Eqs. (I.25) and (I.26) are again used.

From Eq. (I.26) the following relation is established

$$a_s = \frac{h_s}{b_s} = \frac{\epsilon(a_s')^n}{x b_i} . \tag{I.38}$$

While, from Eq. (I.25),

$$\frac{b_s}{b_i} = x = \frac{b_* + \epsilon(a_s')^{n-1}}{b_* + \epsilon(a_i')^{n-1}} . \tag{I.39}$$

From the above two equations, a_s can be expressed as a function of a_i'. That is,

$$a_s = \frac{\epsilon \left\{ \left(\frac{x-1}{\epsilon} \right) b_* - x(a_i')^{n-1} \right\}^{n \; n-1}}{x \left\{ b_* - \epsilon(a_i')^{n-1} \right\}} . \tag{I.40}$$

Hence, the modification factor, $\textcircled{C}$, can be written as,

$$\textcircled{C} = \left[1 - \left(\frac{2\ell - 1}{2} \right) \frac{\epsilon \left\{ \left(\frac{x-1}{\epsilon} \right) b_* - x(a_i')^{n-1} \right\}^{n \; n-1}}{x \left\{ b_* - \epsilon(a_i')^{n-1} \right\}} \right]^2 . \tag{I.41}$$

1005
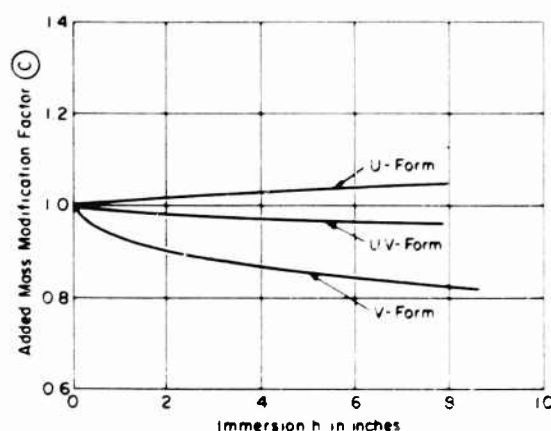
Fig. I.5 - Added mass modi-
fication factor versus im-
mersion (1/20 scale model)

The modification factor, ⓒ, for the three different forms was computed at
various immersions of the bodies, and the results are shown in Fig. I.5. As
can be seen in the figure, the modification factor for the U and for the UV-
Forms is approximately 1. This means that the conventionally used formula
for evaluating the added mass is sufficient for these forms. However, the
added mass estimated by the conventionally used formula is somewhat over-
estimated for the V-Form as can be seen in the figure.

UNSTEADY HYDRODYNAMIC IMPACT FORCE

The piled-up water and added mass associated with impact of a body on a
water surface have been discussed in the previous sections. The unsteady
hydrodynamic force due to impact is derived from a consideration of the time
rate of change of momentum of the added mass.

If the forces due to buoyancy, gravity and friction acting on the body are
assumed to be negligibly small in comparison with the unsteady hydrodynamic
impact force, the equation describing the motion of the system may be written
as.*

$$M\dot{V} - \frac{d}{dt} - V = 0 \tag{I.42}$$

where

M = mass of body per unit length

~ = added mass of body per unit length

V = velocity.

*Effect of gravity on impact force is discussed in Appendix A. Effect of gravity
on added mass is discussed in Part II.

The velocity, V, is obtained from the momentum theorem as,

$$V = \frac{M}{M+m} V_o . \tag{I.43}$$

where V_o = initial velocity.

Then, the unsteady hydrodynamic impact force, F, can be written as

$$F = \left(\frac{M}{M+m}\right)^2 V_o \left(\frac{dm}{dt}\right) . \tag{I.44}$$

The time rate of change of added mass involved in this equation is obtained from Eq. (I.36). That is,

$$\frac{dm}{dt} = \pi \, \textcircled{C} \, b_s \frac{db_s}{dt} \tag{I.45}$$

While, the wetted half-breadth, b_s, is equal to xb_i, and b_i is given in Eq. (I.27). Then,

$$\frac{db_s}{dt} = \frac{d}{dt} \left[x \left(b_* + c(z_i')^{n+1} \right) \right]$$

$$= x c (n+1)(z_i')^{n-2} \left(\frac{dz_i'}{dt}\right) . \tag{I.46}$$

In the above equation, x is considered as a constant for simplicity, since the results of the numerical computation of x indicate that it is relatively time invariant (See Fig. I.4). On the other hand, from Eq. (I.26),

$$\frac{dz_i'}{dt} = \frac{db_i}{dt} \frac{dt}{c(n+1)z_i'^{n+1}} = \frac{V}{cn(z_i')^{n+1}} . \tag{I.47}$$

Substitute Eq. (I.43) into Eq. (I.47),

$$\frac{dz_i'}{dt} = \frac{MV_o}{cn(z_i')^{n+1}(M+m)} = \frac{MV_o}{cn(z_i')^{n+1}\left(M + \frac{\pi}{2} \textcircled{C} b_s^2\right)} . \tag{I.48}$$

While from Eq. (I.27),

$$b_s = xb_i = x \left(b_* + c z_i'^{n+1} \right) . \tag{I.49}$$

Then, dz_i'/dt can be written as follows:

$$\frac{dz_i'}{dt} = \frac{MV_o}{cn(z_i')^{n+1}\left[M + \frac{\pi}{2} \textcircled{C} x^2 \left(b_* + c z_i'^{n+1} \right)^2 \right]} \tag{I.50}$$

1007

Next, substituting Eqs. (I.45) (I.46) (I.50) into Eq. (I.44) the unsteady hydro-dynamic force, F, is obtained as a function of z_i'. That is,

$$F = \rho\pi \, \copyright \, x^2 \left(\frac{n-1}{n}\right) V_o^2 \left(\frac{1}{z_i'}\right) \left\{b_* + \epsilon(z_i')^{n-1}\right\}$$

$$\times \left[\frac{M}{M + \frac{\rho\pi}{2} \copyright \, x^2 \left\{b_* + \epsilon(z_i')^{n-1}\right\}^2}\right]^3 \qquad (I.51)$$

It is of interest to obtain the hydrodynamic impact force as a function of time. For this, the following relation derived from Eqs. (I.43), (I.26) and (I.27) will be used.

$$MV_o t = (M+m)h_i = \left[M + \frac{\rho\pi}{2} \copyright \, x^2 \left\{b_* + \epsilon(z_i')^{n-1}\right\}^2\right] \epsilon(z_i')^n. \qquad (I.52)$$

Numerical calculations of the above equation were made for the U and V-Form and the results are shown in Fig. I.6. As an approximation, only the 1st term of the equation was taken and the result is shown in the figure also. As can be seen in the figure, the 2nd term of the right-hand side of Eq. (I.52) can be neglected at the earlier stages of impact. Since the results of experiments on the V-Form have shown that the significant impact is over after 0.03 sec. from impact (See Part II), only the 1st term of the right-hand side of Eq. (I.52) need be taken if an error of a maximum of 10 percent is permissible. Some discrepancy can be seen between the exact and approximate values for the U-Form. However, the above statement may still apply since the duration of the critical period for impact may be significantly less for the U-Form than for the V-Form. To evaluate the exact magnitude of the impact force at some later time, both terms of Eq. (I.52) should be taken.
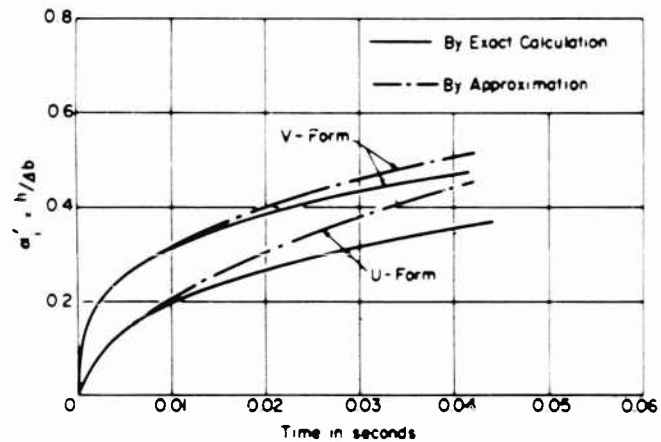
Fig. I.6 - Coefficient z_i' as a function of time (1/20 scale model), $V_o = 5.02$ ft/sec

1008

Now, if the 1st term of Eq. (I.52) is taken, z_i' can simply be expressed by a function of time. That is,

$$z_i' = \left(\frac{V_o t}{\varepsilon}\right)^{1/n}. \tag{I.53}$$

Then, the impact force given in Eq. (I.51) can be written as a function of time.

$$F = \rho\pi \copyright x^2 \left(\frac{n-1}{n}\right) \left\{ b_* \varepsilon^{\frac{1}{n}} V_o^{2-\frac{1}{n}} t^{-\frac{1}{n}} - \varepsilon^{\frac{2}{n}} V_o^{3-\frac{2}{n}} t^{1-\frac{1}{n}} \right\}$$

$$\times \left[\frac{1}{1 - \frac{\rho\pi}{2M} \copyright x^2 \left\{ b_* - \varepsilon^{\frac{1}{n}} V_o^{1-\frac{1}{n}} t^{1-\frac{1}{n}} \right\}^2} \right]^3. \tag{I.54}$$

The average magnitude of impact pressure can be obtained by dividing the impact force by the wetted breadth of the body. That is,

$$P_{ave} = \frac{\rho\pi}{2} \copyright x \left(\frac{n-1}{n}\right) V_o^2 \left(\frac{1}{z_i'}\right) \left[\frac{M}{M - \frac{\rho\pi}{2} \copyright x^2 \left\{ b_* - \varepsilon (z_i')^{n-1} \right\}^2} \right]^3. \tag{I.55}$$

If the approximation given in Eq. (I.53) is used, the above equation again can be written as a function of time.

$$P_{ave} = \frac{\rho\pi}{2} \copyright x \left(\frac{n-1}{n}\right) \varepsilon^{\frac{1}{n}} V_o^{2-\frac{1}{n}} t^{-\frac{1}{n}}$$

$$\times \left[\frac{1}{1 - \frac{\rho\pi}{2M} \copyright x^2 \left\{ b_* - \varepsilon^{\frac{1}{n}} V_o^{1-\frac{1}{n}} t^{1-\frac{1}{n}} \right\}^2} \right]^3. \tag{I.56}$$

DISCUSSION OF NUMERICAL EXAMPLE

In order to evaluate the effect of form of a ship's forward sections on slamming impact, it may be well to give a discussion on the basis of the results of a numerical example. For this, numerical calculations of the hydrodynamic impact force and impulse were made for three models representing the U, UV, and V-Forms (See Fig. I.1). The comparison was made for the same impact velocity, namely, $V_o = 5.62$ ft/sec, on all three models. This magnitude of the impact velocity corresponds to 25.1 ft/sec for a full scale ship, a relative velocity between wave and ship forward section quite typical of those experienced by ships at sea. A mass per unit length of 0.019 lbs-sec^2/in.^{2} was used in the computation. This magnitude corresponds to a light draft condition (45 percent loading condition) of a 1/20 scale model. Two-dimensional drop tests of 1/20 scale models were carried out under the same conditions, thereby the theoretically obtained results can be compared directly with the

1009

experimental results. Analysis of the experiments on the V-Form model was completed, and the results are given in Part II of this paper. A discussion of the theoretically obtained results is given here.

The impact forces acting on the three different forms will be treated first. Prior to a comparison of the magnitude of impact force it may be of interest to discuss the nature of the impact force given in Eqs. (I.51) or (I.54) in more detail. It is recognized in these equations that the hydrodynamic impact force consists of two parts. That is, the 1st term of the Eq. (I.51) is related to the flat bottom of the body, and the 2nd term is related to the curved portion just above the base line. It is of interest, therefore to compare the contribution of these two terms to the magnitude of the total impact force. For this, the ratio of the forces contributed by the 1st and the 2nd terms was obtained and is shown in Fig. 1.7. As can be seen in the figure, the ratio is quite large at the very early stages of impact for all three forms. Particularly, the ratio remains large longer for the U-Form than for the other two forms. Hence, it may be said that an impact force applied to the U-Form is primarily related to the flat bottom while an impact force applied to the V-Form is mainly related to the body shape itself in the area just above the base-line. A very sharp impact
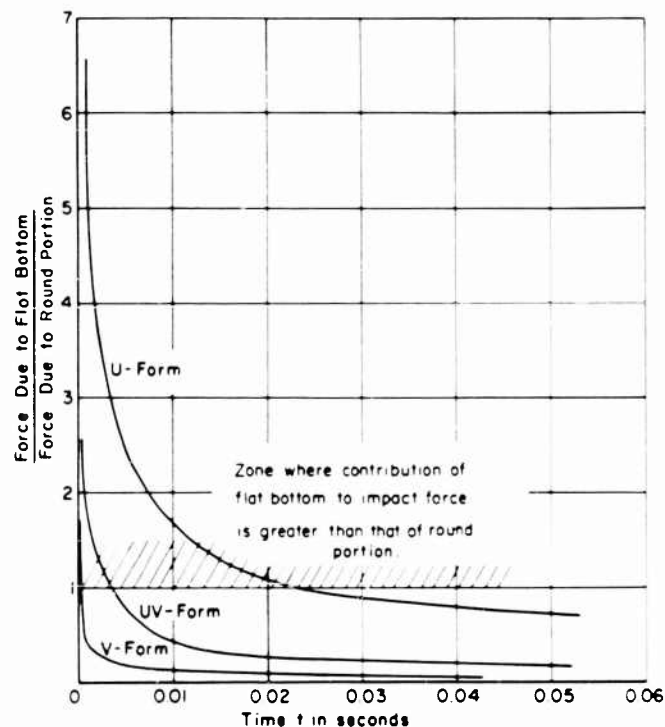
Fig. I.7 - Ratio of impact force due to flat bottom and that due to round portion (1/20 scale model), $V_o = 5.02$ ft/sec

1010

force is noticeable at the very early stage of impact on the V-Form model. This is due to impact of the small flat bottom of the V-Form; however, it will not be significant since it's time duration is extremely short.

The resultant forces due to flat bottom and body shape for the three forms were computed and the results are shown in Fig. I.8. As can be seen in the figure, a very large force is observed on the U-Form for a relatively short time, while an impact force of moderate magnitude is observed on the V-Form and the time duration of loading is longer than that for the U and UV-Form. This remarkable difference in tendency between the V-Form and the other two forms is apparently due to the differences in shape of the lower part of the sections, in other words, the differences are primarily attributable to the 2nd term of Eqs. (I.51) or (I.54). Let us examine the 2nd term of Eq. (I.54) in more
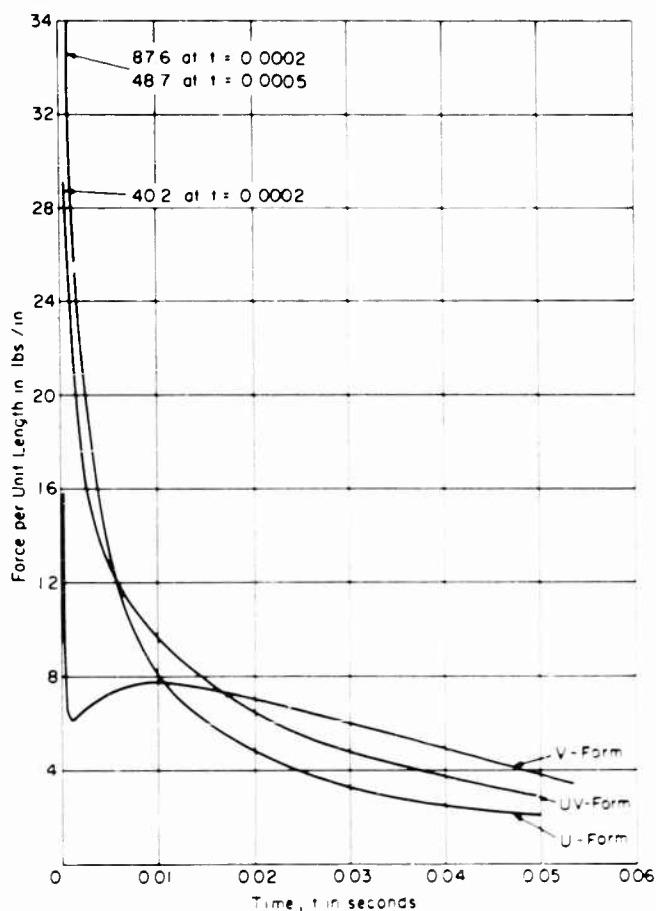
Fig. I.8 - Time history of impact force (1/20 scale model), V_0 = 5.02 ft/sec

detail. In the case $n < 2$, the 2nd term of Eq. (I.51) shows a tendency to de-crease with time, and this is the case of the U and UV-Form. While, in the case of the U and UV-Form. While, in the case $n > 2$, the term shows a tend-ency to increase with time (the term becomes 0 at $t = 0$), and this is the case of the V-Form. Since sharp impact does not appear when $n > 2$, the V-Form may be beneficial for slamming impact.

It is of importance to mention here that the impact forces become infinite at the instant of impact ($t = 0$) as can be seen in Fig. I.8. This is due to the fact that the present theory has been developed for an incompressible fluid. In order to obtain a finite pressure or force at the instant of impact, an impact theory of a flat bottom for a compressible fluid is required.*

It is of interest to mention that the average pressure (Impact force/Wetted breadth) at a specific time is not necessarily proportional to the square of the impact velocity but is dependent on sectional form. As can be seen in Eq. (I.56), the pressure at a specific time of a given form is proportional to the initial ve-locity to the $(2 - 1/n)$ power. Since n is a function of sectional form, the pres-sure magnitude is dependent on form.

Next, let us consider the impulse associated with the impact force. The impulse is the time integral of the impact force, and is considered to be a very important measure of the intensity of slamming. For example, even if the
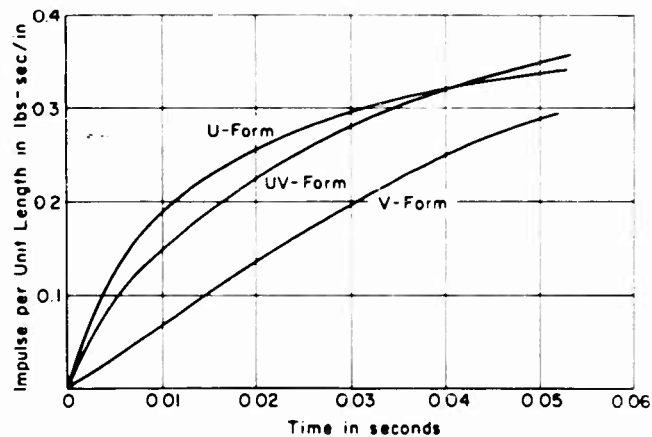
Fig. I.9 - Time history of impulse (1/20 scale model), V_o = 5.62 ft/sec

---

*At the suggestion of Professor Timman, University of Technology, Delft, Netherland, one of the authors has evaluated the pressure of a flat bottom when it impacts the surface of a compressible fluid. A finite pressure of cV^2 was obtained at the instant of impact for the two-dimensional case. (c = speed of sound in water). This becomes to cV for the one-dimensional case as found by von Karman.

magnitude of the force is large, structural damage would not occur if the loading is sufficiently short. Figure I.9 shows the impulses for the three different forms obtained from Fig. I.8. A comparison between theoretical and experimental results of the magnitude of impulse on the V-Form is shown in Part II of this paper. As can be seen in Fig. I.9, the impulse for the U-Form is a slightly larger than for the UV-Form, and the impulse for the V-Form is appreciably smaller than that for either the U or UV-Form. This results again indicates the V-Form to be superior from the slamming point of view.

PART II. AN EXPERIMENTAL STUDY OF THE TWO-DIMENSIONAL WATER IMPACT OF A SHIP FOREBODY SECTION

GENERAL

Presently existing theories for estimating impact forces and pressures due to slamming are based on the two-dimensional unsteady potential flow in the vicinity of a body in an infinite fluid. Application to the realistic three-dimensional problem is attempted through aspect ratio corrections. Checks for the theories have been made for the most part through carefully designed three-dimensional experiments, however, such experiments are not appropriate for evaluating the fundamental aspects of the problem.

For the purpose of evaluating the adequacy of the present theory, comparisons are made with the results of two-dimensional drop tests of a V-form model ship section. The results presented here are part of a much larger effort directed toward establishing the exact impact pressure-velocity relationship as a function of ship form by dropping various two-dimensional forms covering the practical range of ship forebody sections. This work was carried out at the Model Basin with partial support from the HS-2 Panel of the Society of Naval Architects and Marine Engineers. It is with the Panel's permission that partial results of this overall program are included here.

DESCRIPTION OF MODEL AND TESTS

The cross-section of the model used in the present tests is shown in Fig. II.1. It represents a 1:20 scale model of the MARINER section at 17.5 percent of the length aft of the forward perpendicular, which has been modified to a V-form. This modification was effected by keeping the area beneath the design waterline constant and equal to that of the MARINER. The constant section model was 26.5 inches in length with a maximum beam of 42 inches and a depth of almost 30 inches. The model was made of pine with a hull thickness of 2.5 inches normal to the surface. The model ends were closed with 3/4 inch plates. It was ballasted to a weight of 190 pounds which corresponds approximately to a 45 percent loading condition for the MARINER.

The tests consisted essentially of dropping the model vertically from elevated positions and recording pressures, accelerations and velocities resulting from impact with the smooth water surface. The height of drop was varied so that five different impact velocities were obtained covering the range
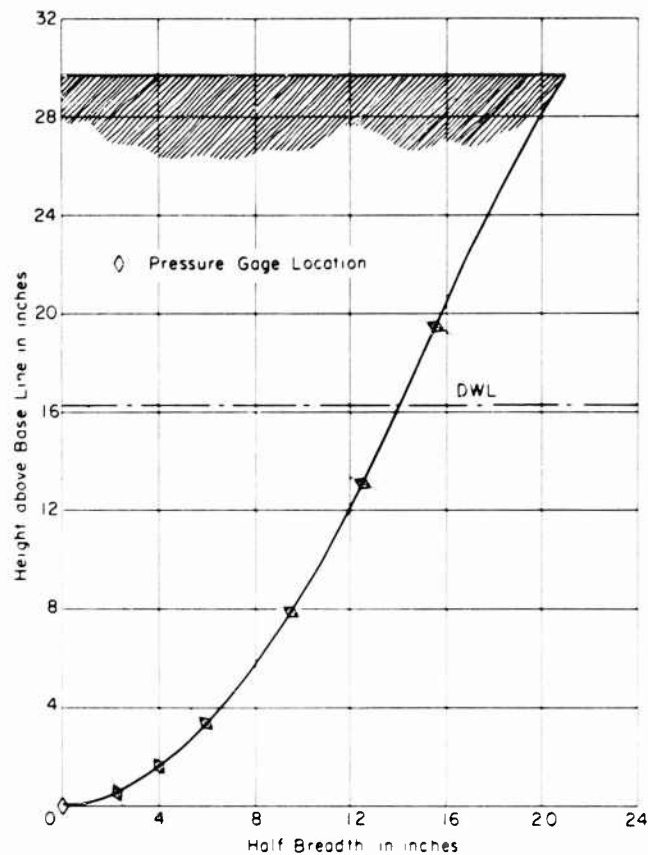
Fig. II.1 - Offsets of V-form model and
pressure gage locations

up to 10 ft per sec. This upper limit corresponds to an impact velocity of about 50 ft per sec for a 520-ft ship. In addition to recording the quantities mentioned above, high speed movies of the piled-up water during impact were also taken.

DESCRIPTION OF TEST APPARATUS

The facility used for the tests was a large rectangular tank 25 · 15 feet with a water depth of 8.5 feet. To duplicate two-dimensional flow conditions a special test section was fabricated by constructing two rigid walls which spanned the length of the tank and extended the full tank depth. The walls were parallel and rigidly connected to the tank floor and sides. They were separated by a distance equal to the model length plus a small amount to permit unrestricted movement of the model between the walls. This gap was kept to a minimum to insure two dimensional flow.

The support and guide system for the model rested on channels spanning the test section. The system consisted of a frame at the mid-section of the channel comprised of two vertical members which were connected by a horizontal member at the top. Connected to the vertical members were guide posts on which a box type beam was free to travel with minimal friction. The model was attached to this beam and the desired impact velocity was obtained by proper positioning of this beam. The system was designed so that maximum rotation of the model in any plane was limited to 0.25 degrees.

The releasing mechanism consisted of a solenoid attached to the horizontal member of the frame structure. This solenoid was equipped with a pin which was inserted in a bracket attached to the beam. When the solenoid was activated the pin was instantaneously released and the beam and model were free to fall.

A photograph of the apparatus and model is shown in Fig. II.2.

INSTRUMENTATION

Commercial Dynisco transducers were used for the pressure measurements. These are diaphragm type instruments, 0.5 inches in diameter, in which the sensing device consists of unbonded strain gages connected in a four arm bridge. The displacement of the diaphragm produced by the pressure results in an unbalance of the bridge. The capacity of the gages ranged from 15 to 50 psi, and their natural frequencies were around 7000 cps.
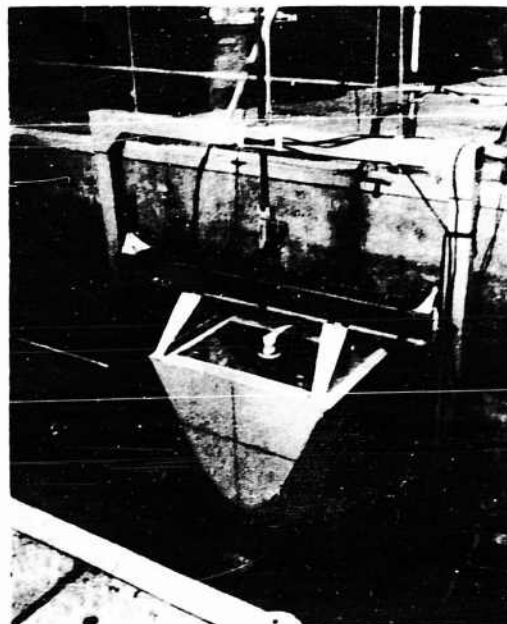
Fig. II.2 - Photograph showing drop mechanism and V-form model

Gages were located around the girth of the model at its midsection at the positions shown in Fig. II.1. At one location (6-inch half-breadth) gages were located on both the port and starboard sides. Since the pressures for a vertical impact should be symmetric with respect to the keel, the outputs of these gages provide a measure of any deviation from the vertical, should it occur.

100 g and 50 g Statham accelerometers with natural frequencies of 700 cps were used to measure acceleration and velocity respectively. The accelerometers were rigidly attached to the inside of the base of the model. The output of the 50 g accelerometer was electrically integrated to yield the velocity.

The displacement (immersion) of the model was measured from the instant of impact to a full submergence of 28 inches. This was accomplished by mounting a geared rack on the posts which guided the beam in its fall. Attached to the beam was a matching pinion which travelled on this rack and in its travel activated a potentiometer. Two duplicate systems were used, one for the full travel of 28 inches with 0.1 inch accuracy and a second one for measuring displacement from keel impact to 4-inch immersion with 0.01 inch accuracy.

The outputs of all transducers were fed through Consolidated carrier amplifiers and recorded on a consolidated string oscillograph. Type 1-118 carrier amplifier with a natural frequency of 3 kc was used for all sensors except the keel pressure gage. The gavonometer natural frequency was 600 cps. For the keel gage, a CEC Type 1-127 amplifier was used with a 20 kc frequency response. The string galvonometer response was 3 kc in this case. All recordings were made at a paper speed of 40 inches per sec.

An Eastman high speed movie camera was used for measuring the piled-up water. Movies were taken at 3000 frames per sec using a wide angle lens. Sufficient time was allowed for the camera to get up to speed before a drop was initiated. Standard 16mm Tri-X film was used. Lighting consisted of six photo bulbs located in front of the model and five to the model side. In order that the instant of impact could be clearly identified in the film, a light source was appropriately arranged so that it would be activated when the model first contacted the water surface, thereby marking the film.

PRESENTATION AND DISCUSSION OF RESULTS

Background

Prior to a discussion of the results and correlation with theory, it may be well to restate the basic principle on which the theory is derived. That is, that during water entry the change in momentum of the dropping body is the time integral of forces acting on the body. This can be expressed mathematically as

$$(M + m) V - MV_o = \int_0^t \sum F_n \, dt \, . \tag{II.1}$$

where

M = mass of body

m = apparent mass of water

V_o = impact velocity

V = velocity at time t

F_n = forces acting on the system in the vertical direction.

In the case of slamming, the impact is considered as an impulse and the assumption is made that gravity can be neglected in comparison with the unsteady hydrodynamic force. Then the conservation of momentum principle applies and Eq (II.1) reduces to:

$$(M + m) V = MV_o . \tag{II.2}$$

The velocity at any time can then be expressed as

$$V = \frac{V_o}{1 - \_} . \tag{II.3}$$

where

$$\_ = \frac{m}{M} .$$

The unsteady hydrodynamic impact force is

$$F = \frac{d}{dt} (mV) . \tag{II.4}$$

Utilizing Eq (II.3) the force may be expressed as

$$F = - M\dot{V} = \frac{V_o}{(1 - \_)^2} \cdot \frac{d\_}{dt} . \tag{II.5}$$

From Eq (II.5) the impulse at any time $-$ can be expressed as:

$$I_\_ = \int_{.0}^{-} F \, dt - V_o \int_0^{-} \frac{d\_}{(1 - \_)^2} . \tag{II.6}$$

Integrating and substituting the initial conditions that when $t = 0$, $- = 0$ we obtain

$$I_\_ = MV_o \left[\frac{\_}{1 - \_} \right]_\_ . \tag{II.7}$$

If the effect of gravity acting on the body is included in Eq. (II.1), then Eq. (II.2) becomes

$$(M + m) V - MV_o = Mgt .$$ (II.8)

In this case the unsteady hydrodynamic impact force is expressed as

$$F = -M\dot{V} + Mg \cdot = \frac{V_o + gt}{(1 + \_)^2} \frac{dm}{dt} + \frac{Mg\_}{1 + \_} .$$ (II.9)

where $\dot{V}$ is obtained from Eq. (II.8).

Equations (II.1) through (II.7) are the fundamental relations on which the previous investigators have based their work, including that of Part I of the present paper. These relations will also be utilized in the analysis of experimental data for estimating added mass, pressure, force and impulse. The significance of gravity will be evaluated using Eqs. (II.8) and (II.9).

Relationship of Pressure to Impact Velocity

In the tests several drops were made at each of five different heights. The peak pressures for each of the gages were determined and the results for each height (impact velocity) averaged. The repeatability of impact velocity for each height of drop was excellent as was the repeatability of pressures for the outboard gages. Some scatter however, appeared in the keel gage measurements, sometimes amounting to as much as 10 percent. A plot of these pressures, as a function of impact velocity, is shown in Fig. II.3 for four different locations on the model. The most outboard gage which registered any impact pressure was the gage located 6 inches outboard from the keel.

Since the data for each gage falls on a straight line when plotted on logarithmic scale the pressures may be simply expressed in the form of $p = C v_o^{\_}$. The slope of the straight lines gives the exponent of the velocity while the proportionality constants are determined by the intersection of the lines at an impact velocity of 1. These values are given in the figure. It is seen that the power of the velocity varies from about 1.62 at the keel to 2.43 at the most outboard location. In the theory presented in Part I, the average pressure was shown to be proportional to the velocity with the exponent 1.67 for the V-Form section (See Eq. I.56, Part I). Since the values given in Fig. II.3 pertain to peak pressures (not average) a comparison with theory is meaningful only for the keel gage where the average pressure is most nearly equivalent to the peak pressure. On the basis of the experimental results for this case it appears that the theoretically obtained value of 1.67 is highly realistic.

Velocity — Time History

Studies of ship motions and their relation to slamming have indicated a relative velocity between ship and wave of 25 ft per sec to be highly significant from the slamming point of view. Therefore in the following sections added
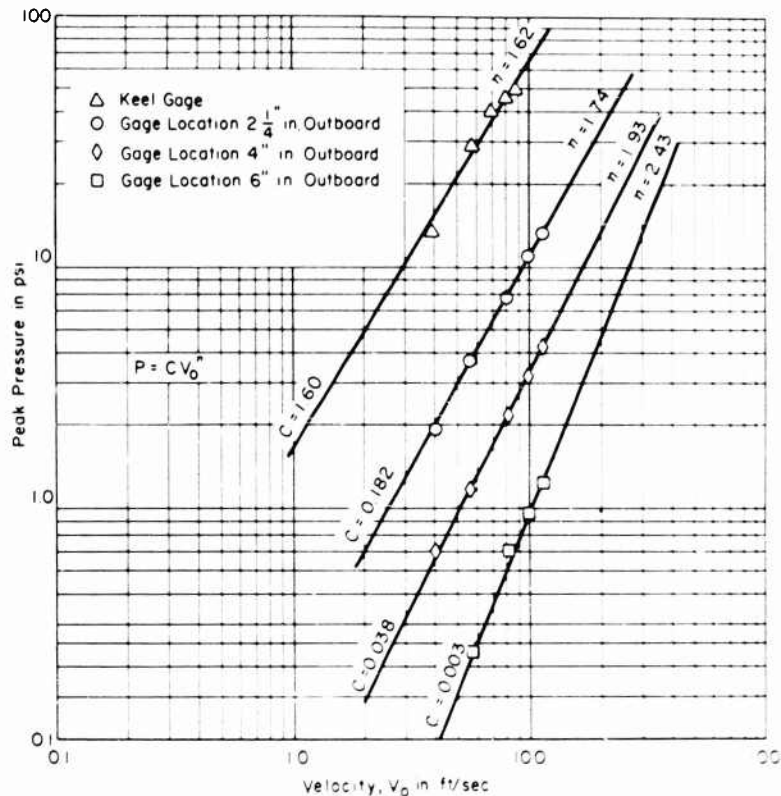
Fig. II.3 - Peak pressure as a function of impact velocity

mass, piled-up water, force and impulse will be discussed for this initial velocity.

In the present tests this scaled velocity was obtained for the 6-inch drop. The time history of velocity from the instant of model release until it reached its maximum submergence is shown in Fig. II.4. Shown also is the immersion from instant of impact until full submergence of 19.5 inches. So that the reader may have an understanding of the critical period for impact, the time required for all gages to register peak pressures is indicated in the figure as well as the interval during which any impact pressure acts. It can be seen that all pressures had reached a maximum by the time the model had obtained a 2-inch submergence. Remarkably little decrease in velocity occurred during this time - about 2 percent. The immersion trace shows that this decrease was so small and of such short duration that the model's motion was virtually unaffected. Even at 0.07 sec when all impact pressures were over, the velocity decrease amounted to only 4 percent. It is interesting to note that after the model had attained an immersion of 12 inches, the velocity decreased almost
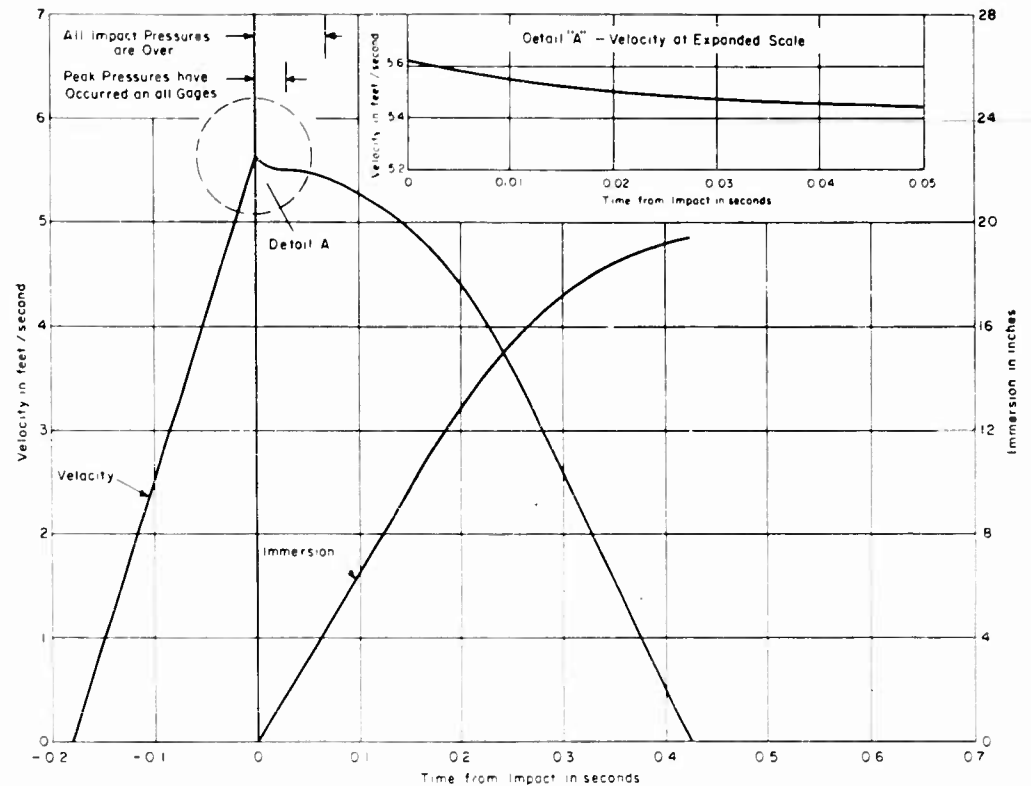
Fig. II.4 - Time history of velocity and immersion for
an impact velocity of 5.62 ft/sec

linearly with time. This immersion corresponds to the draft of the model for the 190-lb ballast condition.

Piled-up Water

The shape of the free-water surface was obtained from the high speed movies. For this purpose, the 16 mm film was read on a Bausch and Lomb Comparator using a magnification of 25 so that the outline of the body and piled-up water would be easily discernible. The film showed that at the instant of impact sizeable spray was generated but the earliest time at which any piled-up water could be clearly identified was 0.0057 sec after impact. As submergence increased, the water surface near the model continued to rise along the boundary of the body. After about 0.08 sec the piled-up water began separating from the body resulting in a decrease in the model's wetted breadth. This separation process continued and by 0.20 sec generated a clearly discernible wave. At successively later times, this wave continued propogating away from the model and the water level at the model's boundary returned to its original position.

1020

The shape of the free surface is shown for several times during the critical impact period in Fig. II.5a. Indicated also is the still waterline for these times. The point at which the water surface meets the section is called the spray-root. The half-breadth of the model at this point (referred to as wetted half-breadth) is used in the theory for estimation of added mass, therefore it is of interest to compare the experimental results with theoretical predictions. For this purpose the ratio of the wetted width associated with the free water surface to actual width (width at the still waterline) is plotted in Fig. II.5b as a function of time. The ratio remained constant throughout the first 0.08 sec at a value of 1.44. Since piled-up water could not be observed at times earlier than 0.0057 sec this portion of the curve is dashed. The dot-dash curve shows the value predicted by Eq. I.24 of the present paper. While the theory maintains the trend found experimentally, some difference is observed in the magnitudes. A similar comparison between experiment and theory for the U-V Form, however, showed excellent agreement, (1.20 as compared to 1.22 from experiment). Included also in the figure is the value $(\pi/2)$ found by Wagner to be applicable for a wedge.
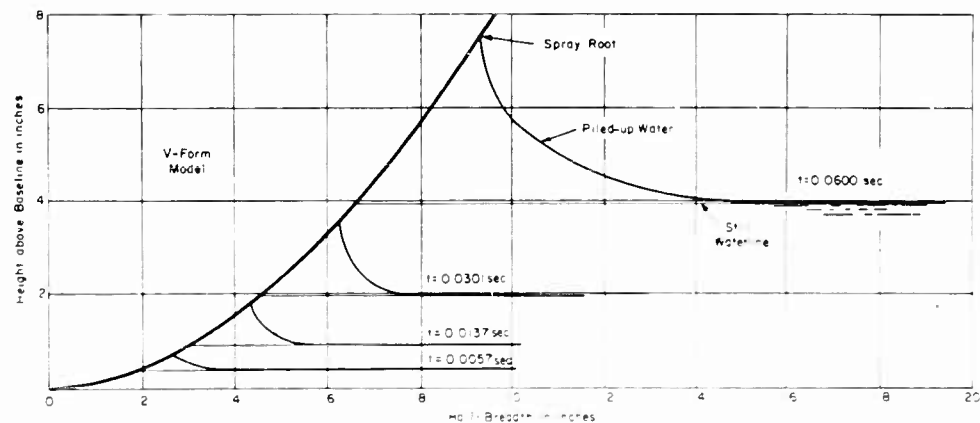
Fig. II.5a - Piled-up water for various times during impact
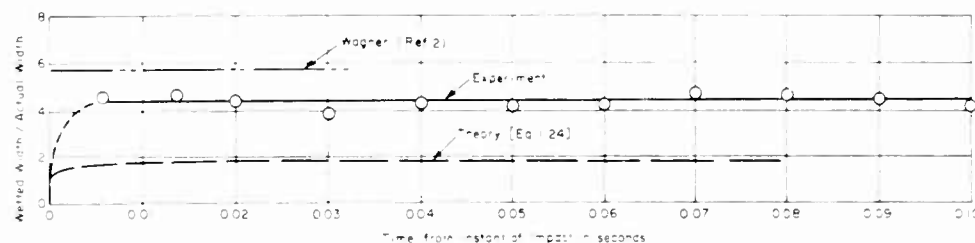
Fig. II.5b - Ratio of wetted width to width at still water surface

Pressure Distribution

The pressure distribution on the model was determined for appropriate
times after impact. These results are shown in Fig. II.6. The instants selected
for these evaluations are those times at which peak pressures were measured
on each of the four gages. For example, at $t = 0.0004$ sec, the peak pressure
occurred at the keel, when $t = 0.0057$ sec, the gage located 2-1/4 inches out-
board registered maximum pressure, etc. In preparing the figures the pres-
sures were plotted normal to the hull at the point of measurement. The curve
connecting these points shows the envelop of pressures acting at those particular
times. The end points of the envelop were established by using the spray-root
of the piled-up water which existed at these times (see Fig. II.5a). It can be
clearly seen in the figure that the significant pressures have dissipated by the
time $t = 0.030$ sec. Thus we may say that for this model the critical period
for slamming is of the order of 0.03 sec. The pressure rise time and duration
(time for pressure rise to peak and return to zero) varied with locations.
These times are summarized in the following table:

Gage	Time from Impact to Start of Pressure Rise (sec)	Rise Time (sec.)	Duration (sec)
Keel	0	0.0004	0.0150
2-1/4-inch Outboard	0.0040	0.0017	0.0260
4-inch Outboard	0.0106	0.0031	0.0258
6-inch Outboard	0.0248	0.0053	0.0458

It may be of interest to discuss these data in terms of their significance for
a 520-ft ship. Using a linear conversion for the pressure magnitudes, the keel
pressure measured here would correspond to about 570 psi with a duration of
.067 sec for the full scale. The pressure measured at 2-1/4 inches outboard
(3.75 ft full scale) converts to 64 psi with a duration of 0.116 sec. The critical
period for slamming for the full scale would be about 0.134 sec with a total
duration of pressures of about 0.32 sec.

This pressure of 570 psi does not appear to be unrealistic. Results from
full scale trials of the USCGC UNIMAK [16] shows pressures of about 300 psi
on the keel plate. The measuring system used in the full scale trials was
limited to a frequency response of 600 cps. During the exploratory phase of
the present tests two measuring systems were used, one with a frequency re-
sponse of 600 cps and the other with a frequency capability of 3000 cps. It was
found that the keel pressure was significantly different with the two systems.
In the low frequency response system (600 cps), keel pressures of the order of
270 psi (full scale) were measured. While use of the 3000 cps system resulted
in the pressure (570 psi) reported herein. Therefore, it may be expected that
much higher pressures would have been obtained in the UNIMAK tests had a
system having a higher frequency response been used.

Average Pressure, Force and Impulse

The average pressure acting on the section was obtained by integration of the pressures in Fig. II.6 and dividing by the wetted breadth. These results are shown for various times in Fig. II.7. Included also are the theoretical predictions. Since the theory estimates vertical force (not normal) the vertical component of the pressures in Fig. II.6 was used for a more meaningful comparison. The agreement of theory with experiment is good during the early stages of impact, however at later times the theory predicts higher pressures than actually measured.

The impulse was also obtained by time integration of the force. A comparison of the theoretical and experimental results is shown in Fig. II.8. While there is some variation between the two approaches for any particular instant, the total impulse during the time critical for slamming (0.03 sec) shows reasonable agreement.

Added Mass

In an analytical treatment of the impact problem perhaps the most important yet most difficult parameter to estimate is the added mass. This is especially true for an arbitrary ship section which cannot be expressed by a simple mathematical formulation. The technique used by theoretical investigators is to approximate the actual ship section by some mathematical shape such as the wedge, ellipse, etc. The accuracy of the theory then is limited by the extent to which this approximation permits a realistic evaluation of added mass and its time rate of change. In the present theory this parameter is derived for an expanding cylinder and is given by Eqs. (I.36) and (I.41) in Part I.

Experimental evaluation of added mass neglecting gravity may be obtained either by use of the impulse equation or from the conversation of momentum principle. In the first approach, since the mass of the body and impact velocity are known, it is only necessary to obtain the impulse by a time and space integration of the measured pressures. The second approach requires that a very exact time history of the velocity after impact be obtained. A difficulty in use of the conservation of momentum principle is that it is subject to greater error. This results from the fact that it requires differencing numbers which may be of the same order of magnitude, (impact velocity minus velocity after impact) and then computing a quotient where the numerator and denominator may not be of proper relative order. Thus a small error in velocity measurement could result in a larger error in the evaluation of added mass.

Added mass was evaluated by both of the methods mentioned above and the results are shown in Fig. II.9. In the figure these two curves are identified by the equation used for analysis, i.e., Eq. (II.7) and Eq. (II.2) indicating the impulse and conservation of momentum principles respectively. A significant difference in the experimental results derived by the two approaches is observed. The discrepancy is so great that it cannot be fully ascribed to be inherent inaccuracies involved in use of the conservation of momentum principle. For example, for the conservation of momentum principle to yield added mass comparable to that obtained from the impulse equation, a velocity decrease
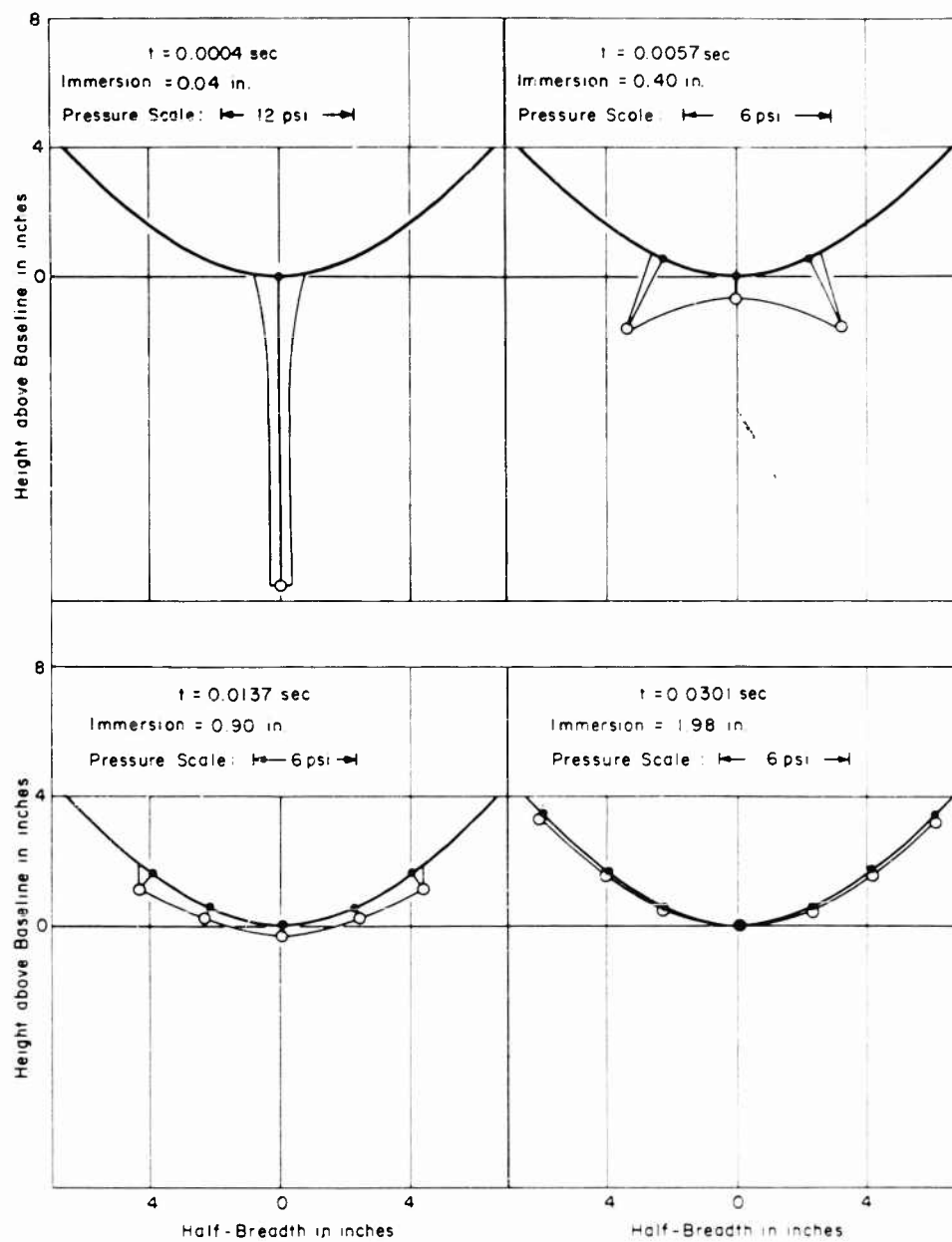
Fig. II.6 - Pressure distribution at various times during impact
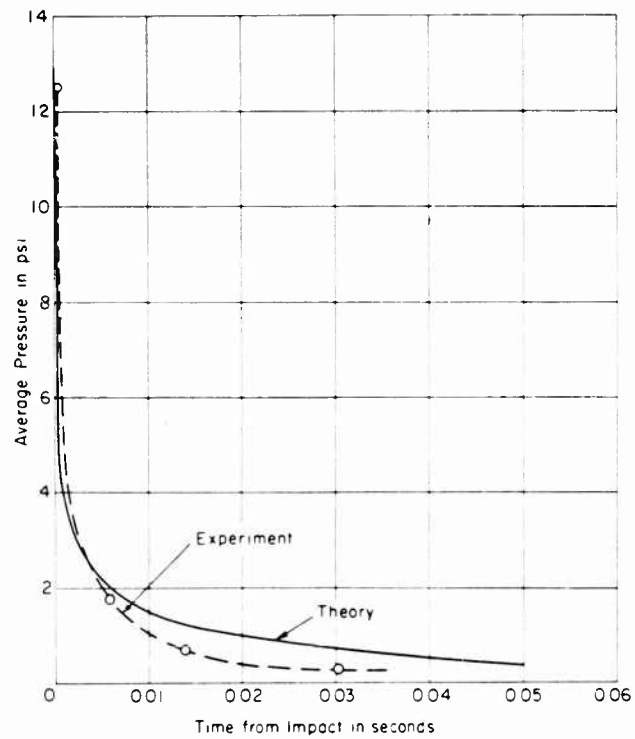
Fig. II.7 - Comparison of theoretical and ex-
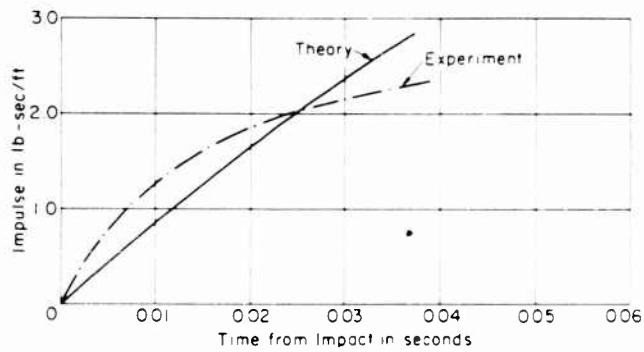perimental average pressures during impact

Fig. II.8 - Comparison of theoretical and
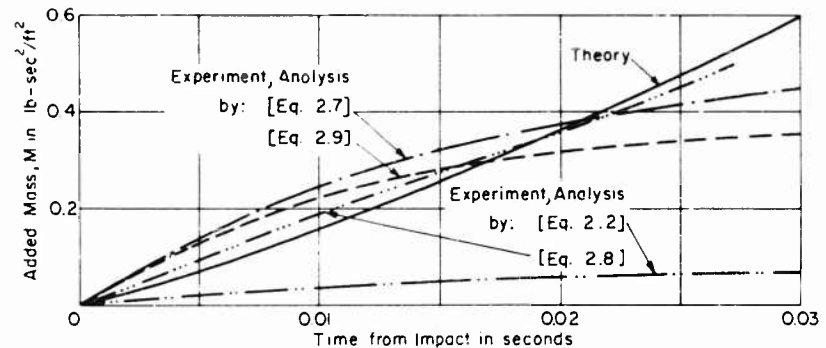experimental impulse

Fig. II.9 - Variation of added mass during impact

of 13 percent during the first 0.03 sec would be required. Yet, three independent measurement systems from which the velocity could be evaluated (acceleration, velocity and displacement) were in good agreement and none indicated such a large velocity decrease during this time. However, it is to be noted that if the velocity which the body would have attained in this additional 0.03 sec (had it not impacted the water surface) is considered, then a 13 percent decrease in velocity due to impact is obtained. This indicates that gravity does significantly affect the motion of the body and must therefore be included in the momentum equation. On this basis added mass was also computed using the momentum equation modified for gravity Eq. (II.8). Computations were also made using Eq. (II.9) to determine the effect on added mass of introducing gravity into the force equation. These results are also included in Fig. II.9 and the curves are again identified by the equation used for the analysis. It is apparent in the figure that, with this correction for gravity, added mass as determined from the momentum of the body is in good agreement with that evaluated from the measured pressures during the early stages of impact. The results are also in substantial agreement with the theoretically calculated values using the concept of kinetic energy of a fluid in an infinite field of potential flow. After about 0.02 sec, the theory as well as the experimental results evaluated by the momentum principle show a deviation from that obtained from the measured pressures. This suggests that other factors (e.g., buoyancy, gravity effect on the displaced water, etc.), may become important at this later stage. These factors were not investigated here since the experimental results showed an 85 percent decrease in the force at $t = 0.02$ sec, indicating that later times were not significant as far as the impact process is concerned.

In summary, a most interesting observation can be made from Fig. II.9 concerning gravity effect. That is, though gravity must necessarily be included in the momentum equation when deriving added mass, its effect is comparatively unimportant when the force equation is considered. This somewhat paradoxial result indicates that though gravity does affect the motion of the body, the theoretical "no external force" assumption in deriving the impact forces is reasonally correct.

CONCLUSIONS

On the basis of the results of this combined theoretical and experimental study the following conclusions may be drawn:

1. The ratio of wetted width to a actual width associated with slamming impact appears to be less than the value $(\pi/2)$ given by Wagner for a flat plate. The theoretically obtained value for the UV-Form shows agreement with experimental results; however, some difference was observed for the V-Form.

2. Gravity significantly influences added mass evaluated from the momentum equation; however, it has a relatively minor effect in the impulse equation. The theoretical added mass obtained from the kinetic energy concept is in substantial agreement with experimental results from the impulse equation as well as the momentum equation when gravity is included. Thus, the conventionally used expression for added mass $(\rho \pi b_s^2/2)$ was found to be adequate; however, it results in an overestimation of added mass for the V-Form of about 10 percent.

3. The pressure magnitude is not necessarily proportional to the square of the impact velocity but is dependent on sectional form.

4. Forces resulting from slamming consist of two parts, one related to the flat bottom and the other related to the curved portion of the body. The former is the primary source of the force for the U-Form, while the latter is the main contributor for the V-Form. Effect of gravity on impact force appears to be not significant.

5. The impulse resulting from the slamming is largest for the U-Form and smallest for the V-Form during the critical impact period. Thus the V-Form is more beneficial from the slamming point of view.

ACKNOWLEDGMENTS

REFERENCES

1. von Karman, T., "The Impact of Seaplane Floats during Landing," NACA TN 321, 1929.

2. Wagner, H., "Über die Landung von Seeflugzeugen," Zeitschrift für Flugtechnik and Motorluftschiffart, Vol 22, No. 1, 1931.

3. Milwitzky, B., "A Theoretical Investigation of Hydrodynamic Impact Loads on Scalloped - Bottom Seaplanes and Comparisons with Experiment," NACA Report No. 867, 1947.

4. Milwitzky, B., "Generalized Theory for Seaplane Impact," NACA Report No. 1103, 1952.

5. Mayo, W. L., "Analysis and Modification of Theory for Impact of Seaplanes on Water," NACA Report No. 810, 1945.

6. Bisplinghoff, R. L. and Doherty, C. S., "A Two-Dimensional Study of the Impact of Wedges on a Water Surface," prepared for Bureau of Aeronautics under Contract No. NOa(s) - 9921, 1950.

7. Fabula, A. G., "Ellipse-Fitting Approximation of Two-Dimensional, Normal Symmetric Impact of Rigid Bodies or. Water, Proceedings of the Fifth Mid-western Conference on Fluid Mechanics, 1957.

8. Szebehely, V. G., "Hydrodynamics of Slamming of Ships," David Taylor Model Basin Report No. 823, July 1952.

9. Ochi, K. M. and Bledsoe, M. D., "Theoretical Consideration of Impact Pressure During Ship Slamming," David Taylor Model Basin Preliminary Report No. 1321, 1960.

10. Lewis, F. M., "The Inertia of the Water Surrounding a Vibrating Ship," Transactions of the Society of Naval Architects and Marine Engineers, Vol 37, 1929.

11. Chu, W. H. and Abramson, H. N., "Hydrodynamics Theory of Ship Slamming Review and Extension," Southwest Research Institute Tech Report No. 1, Contract No. Nonr 2729(00), 1959.

12. Probaska, C. W., "Vibrations Verticales du Navire," Association Technique Maritime et Aeronautique, Vol 46, 1947.

13. Weinblum, G. P., "On Hydrodynamic Masses," David Taylor Model Basin Report No. 809, 1952.

14. Lamb, H., "Hydrodynamics," Cambridge University Press, Sixth Edition, 1932.

15. Landweber, L. and de Macagno, M. C., "Added Mass of Two-Dimensional Forms Oscillating in a Free Surface," Journal of Ship Research, Vol 1, No. 3, 1957.

16. Greenspon, G. E., "Sea Tests of the USCGC UNIMAK, Part 3, Pressures, Strains, and Deflections of the Bottom Plating Incident to Slamming," David Taylor Model Basin Report No. 978, 1956.

APPENDIX A - OUTLINE OF LEWIS FORM

An outstanding mathematical   first pre-
sented by F. M. Lewis in 1929   which is
used in various fields of naval
paper to represent the ship forward

the section. The results have shown that the method adequately repr $\quad$ nts the sections as illustrated in Fig. I.1.

In Lewis' method, the following conformal transformation is us

$$x = U \left\{ (e^{\xi} + C_1 e^{-\xi}) \cos \eta + C_3 e^{-3\xi} \cos 3\beta \right\}$$

$$y = U \left\{ (e^{\xi} - C_1 e^{-\xi}) \sin \eta - C_3 e^{-3\xi} \sin 3 \right\} \qquad (A.1)$$

where

$\quad$ U = unit which gives the size

C_1 and C_3 = coefficients

$\quad \xi$ = from 0 to ∞

$\quad \eta$ = from 0 to $\pm \pi$.

A ship section is given for $\xi = 0$ in Eq. (A.1). That is

$$x = U \left\{ (1 + C_1) \cos \eta + C_3 \cos 3\eta \right\}$$

$$y = U \left\{ (1 - C_1) \sin \eta - C_3 \sin 3\eta \right\} . \qquad (A.2)$$

The two coefficients C_1 and C_3 involved in the above equati $\quad$ ar $\quad$ function $\quad$ f the parameters draft-beam ratio and section area coefficient.

These are,

$$C_1 = \frac{1 - \sigma}{2k}$$

$$\qquad (A.3)$$

$$C_3 = \frac{1 + \sigma}{2k} - 1 .$$

where

$\quad \sigma$ = draft-beam ratio, h/b

$$k = \frac{U}{b} = \frac{3(1 + \sigma) - \sqrt{(1 + \sigma)^2 + 8\sigma(1 - 4\sigma)}}{4}$$

$\quad \sigma$ = section-area coefficient = $\dfrac{\text{sectional area}}{2bh}$

$\quad h$ = draft

$\quad b$ = half breadth at draft, h

Since C_1 and C_3 can be computed for any given ship section, the section form can be expressed by Eq. (A.2).

Although Eq. (A.3) gives the exact value for the coefficients C_1 and C_3 for a given ship section, the following approximation is used in the present analysis. That is, the coefficients C_1, C_3, and k are expressed by a single parameter,

$$C_1 \approx \frac{1 - a}{1 + 2\ell a}$$

$$C_3 \approx \frac{(1 - 2\ell) a}{1 + 2\ell a} \tag{A.4}$$

$$k \approx \frac{1 + 2\ell a}{2} ,$$

where ℓ is a constant depending on sectional form. For example, ℓ is 0.52 for station 3-1/2 of the U-Form, 0.48 for the UV-Form, and 0.40 for the V-Form shown in Fig. I.1. It should be mentioned that this approximation is limited to a certain extent of ship draft. For example, the approximation is permissible for drafts of 8 ft and less for a 520-ft ship. Since slamming impact is completed before the section attains an immersion of 4 ft, the approximation is acceptable for the analysis under study.

APPENDIX B - EFFECT OF GRAVITY ON IMPACT FORCE

The theory given in Part I of this paper was developed neglecting the effect of gravity acting on a body, since it has been assumed that this effect is not significant at the early stage of impact. However, in order to determine the extent to which this assumption is valid, the following analysis will be made.

If the gravitational force on the body is taken into consideration in the impact problem under study, the impact force equation given in Eq. (I.44) becomes:

$$F = -M\dot{V} + Mg \tag{B.1}$$

while, the velocity given in Eq. (I.43) becomes,

$$V = \frac{M}{M + m} (V_o + gt) . \tag{B.2}$$

Hence, the acceleration, $\dot{V}$, becomes,

$$\dot{V} = -\frac{M(V_o + gt)}{(M + m)^2} \times \frac{dm}{dt} + \frac{Mg}{M + m} . \tag{B.3}$$

Substituting Eq. (B.3) into Eq. (B.1),

Hydrodynamic Impact with Application to Ship Slamming

$$F = \left(\frac{M}{M+m}\right)^2 V_o \frac{dm}{dt} - \left(\frac{M}{M+m}\right)^2 g \left\{\frac{dm}{dt} \times t + \left(\frac{M+m}{M}\right) m\right\}. \tag{B.4}$$

In the above equation, the last two terms give the effect of gravity. (dm/dt) included in the equation is given as

$$\frac{dm}{dt} = \rho\pi \, \text{C} \, x^2 \left(\frac{n-1}{n}\right)\left(\frac{1}{z_i'}\right)\left\{b_* + \epsilon(z_i')^{n-1}\right\}$$

$$\times \left[\frac{M}{M + \frac{\rho\pi}{2} \, \text{C} \, x^2 \left\{b_* + \epsilon(z_i')^{n-1}\right\}^2}\right](V_o + gt). \tag{B.5}$$

where

$$z_i' = \left\{\frac{(V_o + gt)t}{\epsilon}\right\}^{1/n}. \tag{B.6}$$

A numerical calculation was made on the V-Form model for V_o = 5.62 ft/sec (same velocity as shown in Fig. I.8). The result shows that the gravitational force on the body increases the impact force by 2.6 percent at t = 0.005 sec, 5.5 percent at t = 0.01 sec, 13.2 percent at t = 0.02 sec, and 22.3 percent at t = 0.03 sec. Since the impact force has significantly dissipated at t = 0.03 sec for the V-Form, it may safely be said that the effect of gravity on the impact force is not significant.

*   *   *

PULSATION OF TWO-DIMENSIONAL CAVITIES

C. S. Song
University of Minnesota
Minneapolis, Minnesota

INTRODUCTION

It has been known for a long time that the characteristics of cavitating flows under steady conditions are mainly functions of the cavitation number. Under natural conditions, the cavity pressure of a fully developed cavity is approximately equal to the vapor pressure of the liquid and the cavitation number is determined mainly by the ambient condition. However, by introducing gas into the cavity region, whether the cavity originally existed or not, it is possible to increase the cavity pressure at will, decreasing the cavitation number and producing a "ventilated" cavity. To maintain such a cavity gas supply must be continually maintained.

A typical curve relating cavitation number and air supply rate measured in the free jet tunnel at the St. Anthony Falls Hydraulic Laboratory published in [1] is reproduced in Fig. 1. Two distinct regimes, a reentrant jet regime and a pulsating cavity regime, are indicated. Within the reentrant jet regime, the air supply rate is roughly proportional to the decrease in cavitation number and cavity appears very similar to a natural cavity with the same cavitation number. Detailed discussion of the flow in this regime can be found elsewhere. See [2].

This paper is devoted to a report on the experimental findings and the theoretical explanation and prediction of the flow in the pulsating cavity regime. The air supply rate in this regime is no longer a function of cavitation number as shown in Fig. 1 and the flow condition is remarkably different from that of a natural cavity. Visually, the cavity walls begin to vibrate violently, the cavity changing its length and width periodically, and the reentrant jet disappears for a part of the cycle. Figure 2, reproduced from [1] illustrates two cycles of the vibration as seen by a high-speed motion-picture camera. It was found that the flow can be adjusted so that any number of waves can be made to appear on the cavity walls. Pulsating cavities were then classified into "n-stage" cavities according to the number of waves, n, appearing on the surface. There

1033
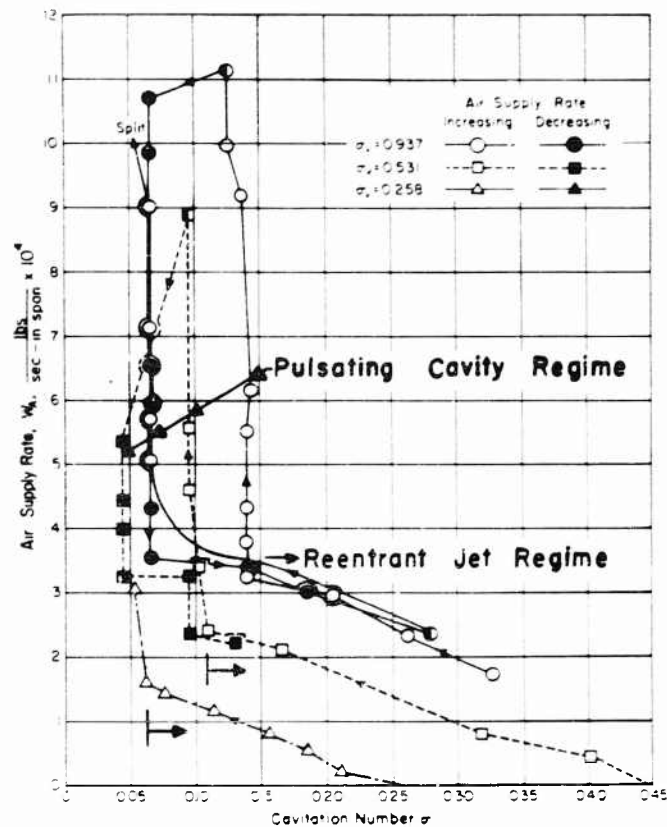
Fig. 1 - Air supply rate as a function
of Cavitation Number

is a fixed average cavitation number corresponding to each stage cavity as
shown in Fig. 1. Photographs in Fig. 3 illustrate how different stage cavities
look. As a result of the cavity wall vibration, the cavity pressure changes
periodically and radiates sound waves in all directions: these can be heard from
outside the water tunnel. Another consequence of the pulsation is that an un-
steady force acts on the body: this results in variable lift and drag which can be
measured by a sensitive dynamometer. Figure 4 illustrates variable pressure
and drag measured by a pressure transducer and a dynamometer respectively.

Pulsation may occur when the flow is bounded by one or two free surfaces.
A good example of the pulsation under one free surface can be found in [2].
However, the discussion here will be limited to the case with two free bound-
aries. In formulating the theory, it will be further assumed that gravitation is
nonexistent, thus ruling out the possibility of the trailing vortex phenomenon
reported in [3] and [4].

1034
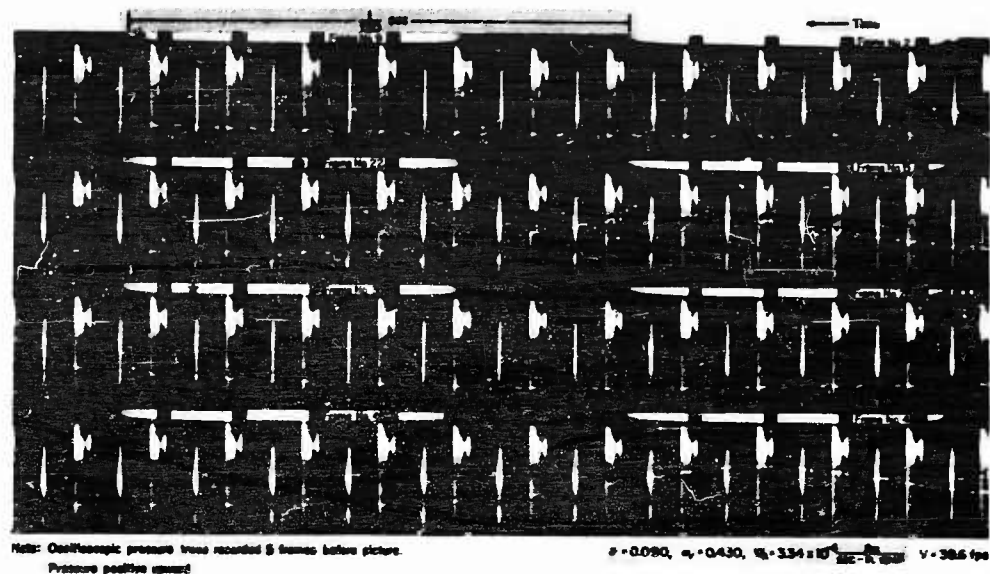
Fig. 2 - Consecutive motion picture frames for a pulsating cavity
(two-dimensional, 1/8-in. normal plate in 10-in. jet)

MECHANISM OF PULSATING CAVITIES

As reported in [1], it was experimentally observed that pulsation occurs only when a cavity is ventilated. It was also found that the phenomenon is independent of the air supply system. The size and length of the air pipe, the location and distribution of the air entrance to the cavity, or any other possible change in the air supply system did not seem to affect the pulsation. It was also observed that for each stage of pulsation there existed a unique relationship between the average cavitation number of the cavity and the cavitation number based upon vapor pressure. That is, for each stage of pulsation there is a unique relationship between the five variables: P_z, P_c, P_v, ε, and t suggesting that the phenomenon is an interaction of pressure and momentum forces. (Here the symbols mean the pressure of the undisturbed flow, the cavity pressure, the vapor pressure, the water density, and the speed of the undisturbed flow.) Furthermore, it was demonstrated experimentally that the above statements were true for bodies of different shapes and sizes.

The experimental facts stated above lead to the suggestion that pulsation is a resonance phenomenon of the gas-liquid (cavity-jet) system. The traveling surface wave on the cavity walls causes the cavity volume to change periodically, hence changing the cavity pressure periodically. The pulsating cavity pressure sets the bounding liquid into radial motion, creating new disturbances at the body and new surface waves. In order for the pulsation to be self-sustaining, the frequency of the volume change due to the moving surface waves must be equal to the natural dynamic frequency of the gas-liquid system.

1035

$\bar{\sigma} = 0.0735, \ \sigma_v = 0.372, \ W_A = 4.60 \times 10^{-4} \frac{lbs}{sec - in \ span} \quad V = 41.5 \ fps, \ f = 26.0 \ cps$

a. First Stage

$\bar{\sigma} = 0.0612, \ \sigma_v = 0.985, \ W_A = 6.50 \times 10^{-4} \frac{lbs}{sec - in \ span} \quad V = 35.6 \ fps, \ f = 41.5 \ cps$

b. Second Stage

$\bar{\sigma} = 0.0665, \ \sigma_v = 2.225, \ W_A = 740 \times 10^{-4} \frac{lbs}{sec - in \ span} \quad V = 27.2 \ fps, \ f = 49.0 \ cps$

c. Third Stage

$\bar{\sigma} = 0.0668, \ \sigma_v = 3.710, \ W_A = 7.60 \times 10^{-4} \frac{lbs}{sec - in \ span} \quad V = 22.0 \ fps, \ f = 48.0 \ cps$

d. Fourth Stage

$\bar{\sigma} = 0.0726, \ \sigma_v = 6.440, \ W_A = 3.28 \times 10^{-4} \frac{lbs}{sec - in \ span} \quad V = 17.0 \ fps, \ f = 52.5 \ cps$

e. Fifth Stage
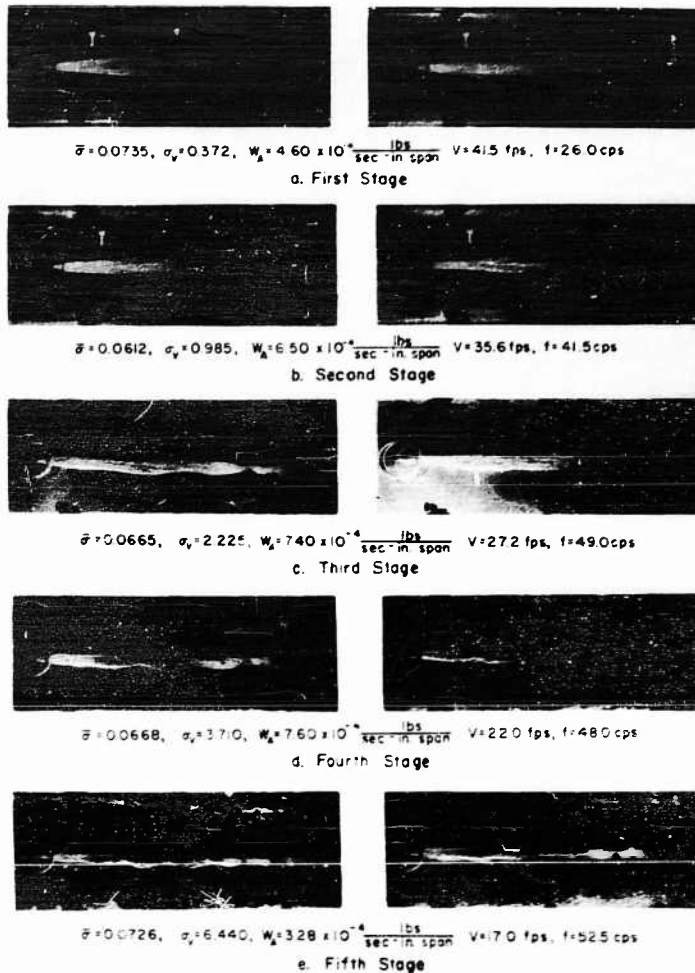
Fig. 3 - Several pulsating cavities for
two-dimensional bodies

Three steps are required to solve the pulsation problem theoretically. The first step is to consider the kinematics of the motion and thus derive the frequency of pulsation due to the surface waves. The next step is to find the natural frequency of the gas-liquid system and to equate this to the frequency obtained by the kinematic consideration. In this way, the condition of pulsation may be derived. Knowing the pressure amplitude and frequency of the pulsation, the unsteady force acting on the body may be found by using a linear theory for unsteady supercavitating flows. These steps are outlined in more detail and compared with experiment in the remainder of this paper.

(a) 1-in. Wedge, $2\gamma = 30°$
10-in. jet, $b = 10$

(b) 2-in. Wedge, $2\gamma = 15°$
6-in. jet, $b = 3$
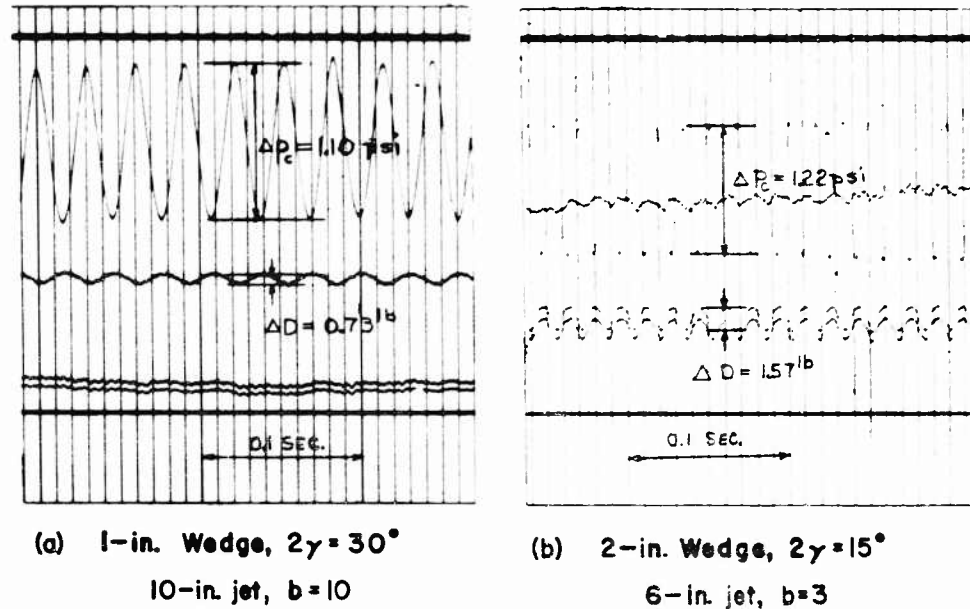
Fig. 4 - Typical pressure and drag records

KINEMATICS OF PULSATING CAVITIES

Consider a steady cavity profile as shown in Fig. 5(a). The cavity is assumed to be so long that the length of the solid body may be neglected, and the cavity is assumed to start from the leading edge. Consider, next, a moving wave of constant amplitude and wavelength as shown in Fig. 5(b). For simplicity, first consider a single-stage pulsation of which the wavelength is equal to the average cavity length ℓ. Superimposition of the wave profiles on the steady cavity profile will create a new profile which changes with time.

Since the boundary condition at the leading edge requires that the cavity width at the leading edge be constant throughout a period of pulsation, the wave profiles to be superimposed on the steady cavity profile do not allow a finite amplitude at the leading edge. This means that waves with growing amplitudes along the direction of flow are necessary. Wave profiles sketched in Fig. 5(c) meet this requirement. Superimposition of (c) on (a) results in new profiles as shown in Fig. 5(d). These cavity shapes resemble the actual cavity shapes as shown by the motion pictures in Fig. 2. Because of the variable amplitude of the wave to be superimposed on the steady cavity profile, the resulting cavity will have variable cross-sectional area as indicated in Fig. 5(d). The period of the area pulsation of the cavity is seen to be equal to the period of the traveling wave. This leads to the following formulas:

$$T = \ell\,c \quad \text{or} \quad f\ell\,c = 1 \tag{1}$$

1037
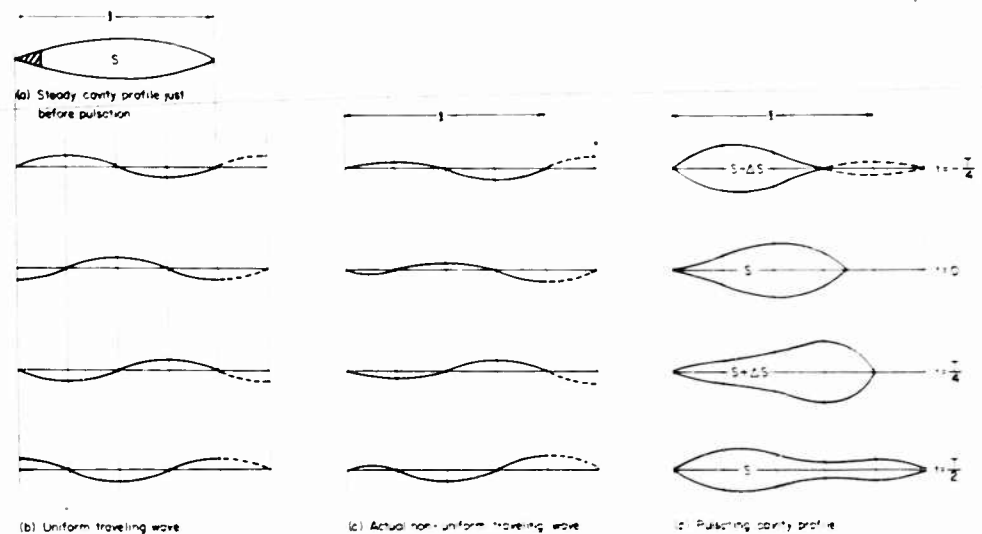
Fig. 5 - Kinematics of first-stage pulsating cavity

where

T = the period of the traveling wave,

f = the frequency of cavity pulsation = $1\,T$, and

c = phase speed of the wave.

Similar argument for n-stage pulsating cavities will lead to the following formulas:

$$T = i\ nc \quad or \quad fi\ c = n. \tag{1a}$$

Since a cavity wall is made up of the water particles passing a fixed point (the separation point) and moving with speed q_c, the phase speed c must be equal to q_c (measured relative to the fixed bodies). A more detailed argument relative to this point is given in [5]. The average phase speeds have been measured by means of motion pictures for different stages of pulsations and in all cases confirmed the present statement.

Equation (1a) may now be replaced by

$$fi\ q_c = n \tag{1b}$$

Some data supporting the validity of Eq. (1b) published in [5] is reproduced in Fig. 6. There are many more data similar to those shown in Fig. 6 covering many different test bodies over a wide range of flow conditions, and all agree with Eq. (1b) with reasonable accuracy. It is thus believed that Eq. (1b) is universally applicable. It should be noted, however, that the definition of the
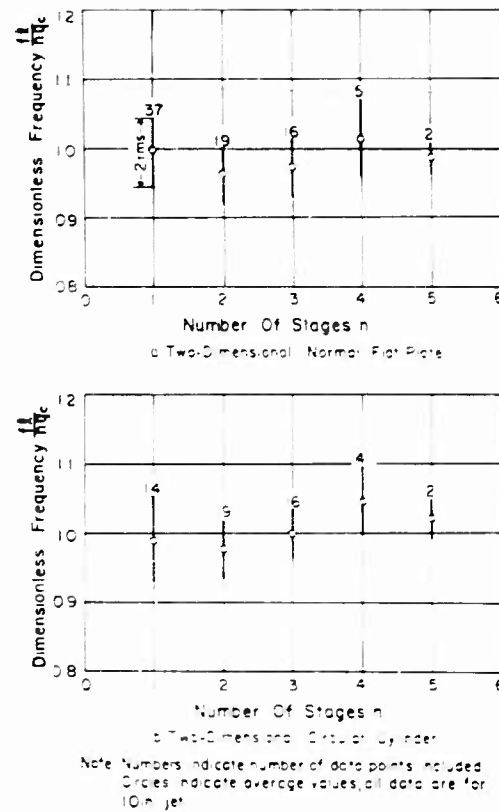
Fig. 6 - Experimental data showing
reduced frequency as a function of
stage

cavity length ℓ, as well as its actual measurement, are rather difficult: hence, considerable scatter is inevitable in comparing experiment with the formula.

THE RESONANCE MODEL AND ITS SOLUTION

Resonance Model

Instead of attempting to find the natural frequency of the real dynamic system as shown in Fig. 7(a), a simple static model as shown in Fig. 7(d) will be considered as an approximation. The model consists of an annulus of water bounded by two cylindrical free surfaces of radius R_0 and r_0 surrounded by air of pressure P_a. The problem is then reduced to finding the natural frequency of the annulus undergoing a pure radial oscillation. The reasoning leading to the adoption of the model is given in the following paragraph.

1039
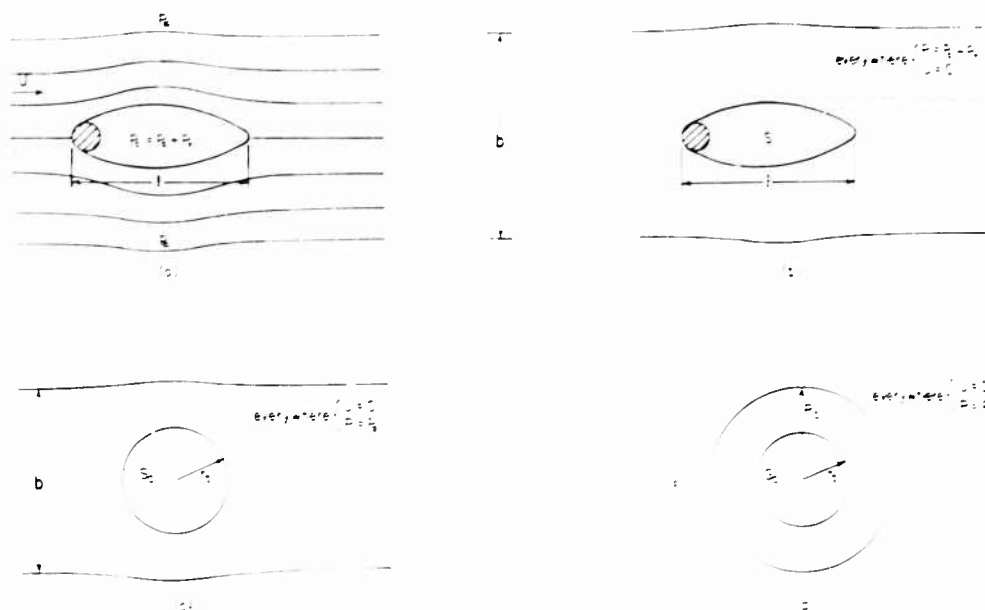
Fig. 7 - Resonance model of a pulsating cavity

Under a steady flow condition as shown in Fig. 7(a), the pressure difference $P_z - p_c$ is balanced in every direction by the centrifugal force created by the flow of water along curved streamlines. If the velocity everywhere is reduced to zero and the pressure everywhere is reduced to p_c, as shown in Fig. 7(b), equilibrium can still be maintained. Of course, under the static condition a real cavity will be a circle because of the surface tension effect. Fortunately, the natural frequency of the volume pulsation of a gas cavity is nearly independent of its shape [6] and the cavity in Fig. 7(b) may be replaced by a circular cavity of equal area without causing too much error.

In reality, a cavity is filled not only with air but also with water vapor and water particles. Since the water within the cavity plays no part in pressure change, the part of the area occupied by water must be left out of consideration. Furthermore, for relatively low frequency pulsation, the process of evaporation and condensation may safely be assumed as instantaneous. This means that the water vapor may also be left out of consideration. The model (b) can now be replaced by model (c) in Fig. 7; here, the total cavity area s has been reduced to S_o by subtracting the internal area occupied by water and water vapor. Finally, the two walls of the free jet are replaced by a circle of radius R_o and, hence, model (d) is obtained.

Natural Frequency of the Gas-Liquid System

Let us now disturb the equilibrium condition by applying a small change to the cavity area s due to radial motion. This will destroy the equilibrium and the system will start an oscillatory motion.

1040

Lagrange's equation of motion in a general coordinate system for an irrotational motion is [7]

$$\frac{d}{dt}\left(\frac{\partial L}{\partial \dot{s}_i}\right) - \frac{\partial L}{\partial s_i} = Q_i \tag{2}$$

where

s_i = general coordinates,

L = Lagrangian = kinetic energy - pote. ..l energy, and

Q_i = forces not arising from a potential.

Here it is convenient to take the change of cavity area, s, as the single generalized coordinate.

The potential energy of the bubble with reference to the equilibrium condition, assuming an adiabatic process, can be shown to be

$$P. \ E. \ = \frac{kP_a}{2S_o} s^2 - O(s^3) \tag{3}$$

where P_a is the partial pressure due to air in the cavity and k is a gas constant.

Assuming incompressibility, the potential energy of the water is equal to zero. Since the density of air is so small compared with the density of water, the kinetic energy of the air in the bubble may be neglected. By considering the continuity requirement, the speed of radial flow, q, on a circle of radius r is

$$q = \dot{s} \ 2\pi r. \tag{4}$$

The kinetic energy of the water is then:

$$K. \ E. \ = \frac{\rho \dot{s}^2}{4\pi} \ln \frac{R_o}{r_o} \cdot \tag{5}$$

Now, the Lagrangian of the system, up to the second order terms, is

$$L = \frac{\rho \dot{s}^2}{4\pi} \ln \frac{R_o}{r_o} - \frac{kP_a}{2S_o} s^2. \tag{6}$$

Since in this case the nonconservative force Q_i may be set equal to zero, Lagrange's equation of motion is reduced to

$$\left(\frac{\rho}{2\pi} \ln \frac{R_o}{r_o}\right) \ddot{s} - \frac{kP_a}{2S_o} s = 0. \tag{7}$$

Equation (7) is the equation of a vibrating spring without damping and excitation. The frequency of vibration is

1041

$$f = \frac{1}{2\pi} \sqrt{\frac{2\pi k P_a}{\rho \, S_o \ell n \frac{R_o}{r_o}}} \cdot \tag{8}$$

The factor $S_o \ell n \, R_o/r_o$ is an unknown quantity which should depend, among other variables, upon the jet width b and the cavity length ℓ. Equation (8) then may be written in the following dimensionless form.

$$\frac{fd}{a} = P_n \left(\frac{\ell}{b}, \; \frac{d}{b} \right) \tag{9}$$

where

$a = \sqrt{\frac{kP_a}{\rho}}$ = reference speed (analogous to sound speed),

b = jet width, and

d = characteristic dimension of body.

The function P_n is a reduced frequency. Since P_n is a characteristic number of the pulsating cavity, it will be referred to as the "pulsation number" hereafter. The functional form of P_n can not be determined by this simplified theory. Experimental frequency data shown in Fig. 5 of [5] are replotted in Fig. 8 as a family of curves, P_n as a function of ℓ/b with d/b as a parameter. Graph (a) shows the data for a $1/8$-in. normal plate in a 10-in. jet and graph (b) shows the data for two circular cylinders, $1/4$-in. diameter and $1/8$-inch. diameter in three different size jets. All data points seem to form a family of parallel straight lines indicating the pulsation number is a linear function of the dimensionless cavity length ℓ/b.

Average Cavitation Number of Pulsating Cavities

By virtue of Bernoulli's equation and the definition of cavitation number, Eq. (1b) may be written as

$$f\ell/U = n\sqrt{1 - \bar{\sigma}} \tag{10}$$

where U is the undisturbed stream velocity and $\bar{\sigma}$ is the average cavitation number defined as

$$\bar{\sigma} = \frac{P_\infty - \bar{P}_c}{1/2 \rho U^2} \cdot$$

The combination of Eqs. (8) and (10) leads to the following formula:

$$\frac{P_a}{1/2 \rho U^2} = 4\pi^2 \, (1 - \bar{\sigma}) \, \frac{S_o}{k\ell^2} \, \ell n \, \frac{R_o}{r_o} \cdot \tag{11}$$

1042
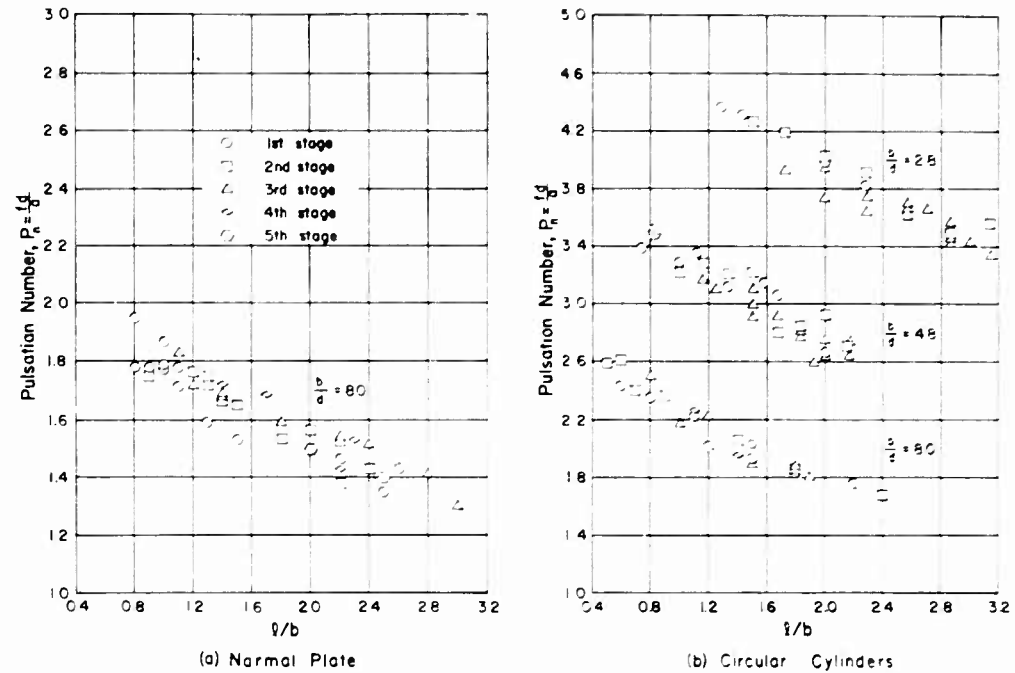
Fig. 8 - Pulsation number as a function of cavity length and jet width

If we assume that S_o is proportional to S and note that, for a slender cavity, S/ℓ^2 is approximately proportional to σ [8], then Eq. (11) may be written as

$$\frac{P_a}{1/2 \rho U^2} = K n^2 (1 - \sigma) \sigma . \tag{11a}$$

Here all uncertain factors are included in K. Equation (11a) can, finally, be written in the following form:

$$\sigma_v = (1 - Kn^2) \sigma - K n^2 \sigma^2 \tag{12}$$

where σ_v is the reference cavitation number defined as

$$\sigma_v = \frac{P_z - P_v}{1/2 \rho U^2} .$$

The parameter K may depend on many dimensionless numbers, such as the pulsation number, the Reynolds number and the Froude number. Within the range of the experiments reported in [1] and [5], the constant $K = 3.45$ seems to fit the data fairly well. The comparison of the data and the semi-empirical formula (12) with $K = 3.45$ is presented in Fig. 9.
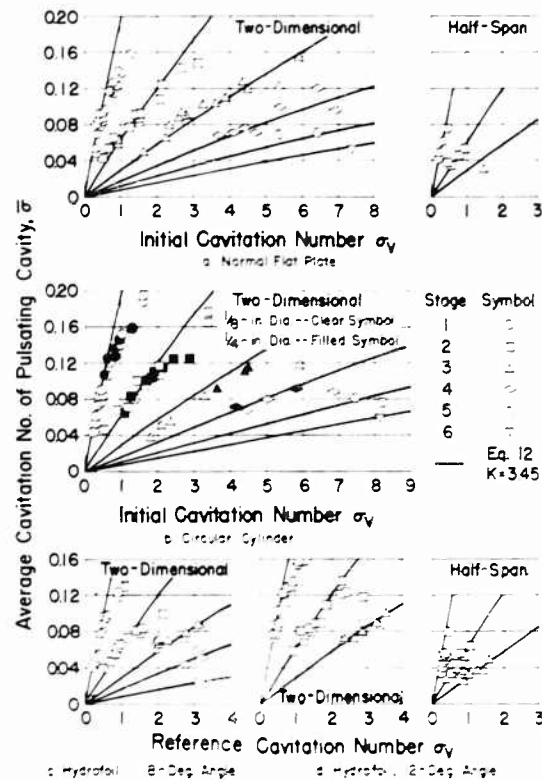
Fig. 9 - Average cavitation number for each pulsating stage as a function of the reference cavitation number

It has been observed experimentally that there is a maximum possible σ or σ_v corresponding to each stage of pulsation. (These maximums are given by the data points of largest σ in Fig. 9.) This is equivalent to saying that there is a minimum cavity length below which pulsation cannot occur. The cause and exact magnitude of the limit are still uncertain. The available data seem to indicate that the minimum ℓ is about 32 diameters in the case of circular cylinders and about 64 chords in the case of normal plates. It seems that there is no lower bound for σ and σ_v nor upper bound for ℓ. (The lowest data points in Fig. 9 correspond to the maximum cavity length which could be physically produced in the free jet tunnel without splitting the cavity. In other words, the limitation in Fig. 9 is due to tunnel size rather than to pulsation.)

Another important characteristic of a pulsating cavity should be mentioned. As long as a cavity is below an upper bound of σ and σ_v, it may pulsate at the stage to which the bound applies or at any higher stage. That is, for a given flow condition, a cavity may pulsate at one stage or another or even change its stage with no apparent reason. It may be stated, therefore, that pulsating cavities are neutrally stable.

1044

Amplitude of Pulsation and Maximum Air Supply Rate

So far, computations have been based on the average air pressure in the cavity P_a. The true air pressure fluctuates, however, and varies between the limits $P_a \pm \angle P_a/2$. To estimate the amplitude of pressure pulsation, reference will be made to the sketches of Fig. 5. It may be observed that the main source of the cavity area change has been attributed to the assumption that the wave to be superimposed on a steady cavity has zero amplitude near the leading edge and increasing amplitude downstream. The maximum area change of a first-stage cavity is given by integrating the upper wave of Fig. 5(c);

$$s_{max} = \int_0^\ell y \, dx = \alpha S_o$$

where α is an unknown parameter, presumably a function of cavity size and air supply rate. In the case of a multi-stage cavity, the change of cavity area may be assumed to occur mainly within the first wavelength as may be deduced by examination of Fig. 3. This concept leads to the following expression for a cavity at any stage n:

$$s_{max} = \frac{\alpha S_o}{n} \, . \tag{13}$$

Assuming the air supply rate is in equilibrium with the average rate at which air is being carried out of the cavity, so that the amount remaining in the cavity is constant, it can be shown by using the adiabatic gas law that

$$\frac{\angle P_a}{P_a} = \left(\frac{n}{n - \alpha} \right)^\kappa - \left(\frac{n}{n + \alpha} \right)^\kappa \tag{14}$$

where

$$\angle P_a = P_{a\,max} - P_{a\,min}.$$

Neglecting the part of the air carried out by turbulent diffusion across cavity walls, the only way the air can escape from the cavity is through the final wavelength (indicated by dotted lines in the upper sketch of Fig. 5(d), which breaks and separates from the main cavity. For the ideal case of zero air exchange, this final wavelength which may be called the "residual cavity" must have zero volume. The residual cavity grows with the air supply rate. This is why there is no unique air supply rate for a pulsating cavity as indicated by Fig. 1. The maximum size of the residual cavity, however, cannot exceed the original wave size. Therefore, it can be concluded that each pulsating cavity must have its maximum air carrying capacity given by the following formula:

$$\frac{W_A}{L} = g \, \varsigma_a S_o \, n \tag{15}$$

where W_A, L, ς_a are weight rate of air supply, span length and air density in the cavity respectively.

Using Eq. (10) and the fact that for a slender cavity [8]

$$S \propto \sigma^{-3}, \quad \ell \propto \sigma^{-2} .$$

Equation (15) may be written in the following dimensionless form:

$$\bar{\sigma} C_W = K' \sqrt{1 + \bar{\sigma}}$$

or for small $\bar{\sigma}$

$$\bar{\sigma} C_W \approx K' \tag{16}$$

where C_W is an air supply coefficient defined as

$$C_W = \frac{W_A}{dLg \rho \, aU} .$$

Here the constant K' includes various proportionality factors which change with reentrant jet and cavity size. It is therefore clear that K' is not a universal constant, but rather a parameter varying with some dimensionless numbers.

The measured dimensionless amplitude $\Delta P_a / P_a$ is plotted against the air supply coefficient C_W for a number of different stages in Fig. 10. Solid lines are from Eq. (14) with $\alpha = 0.18$. It is seen that with this empirical value of α the experimental data can be made to approach the theoretical values as C_W
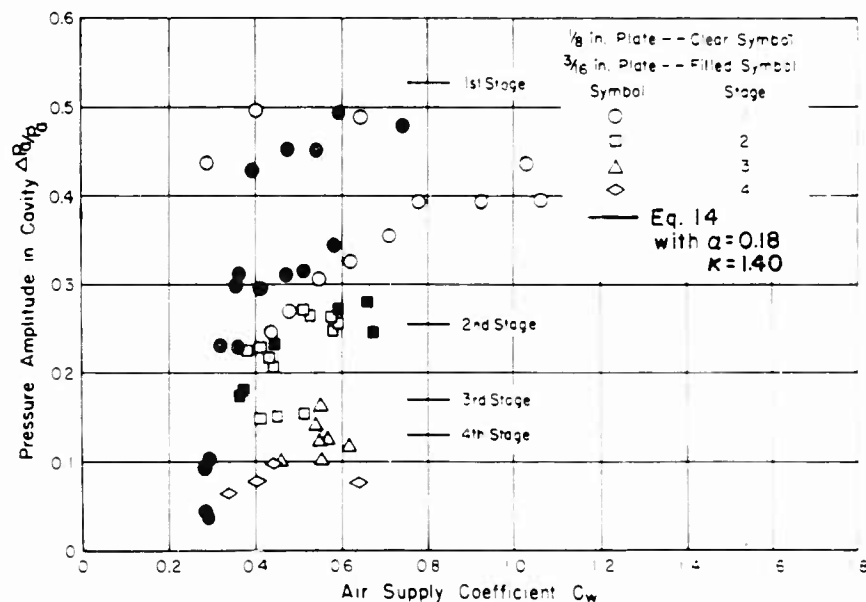
Fig. 10 - Amplitude of pressure pulsation in cavities

1046

increases for each stage. With the limited amount of data available, the parameter K' still cannot be determined with certainty. More data on maximum air supply rate under various flow conditions are required.

UNSTEADY DRAG DUE TO PULSATION

A question of considerable importance in practice concerns the unsteady force due to pulsation. Since the dimensionless pressure amplitude as shown in Fig. 10 can be as high as 0.5, the unsteady part of the drag could be very large. Indeed, continuous records of forces measured by a sensitive dynamometer indicated variable forces almost in phase with the variable cavity pressures. (See Fig. 4.) Drag on a symmetrical wedge with pulsating cavities will be analyzed by a method similar to the method used in [9] and [10]. The theoretical result will then be compared with the experimental data.

It is known that if flow is incompressible and irrotational, then there exists an acceleration potential. Furthermore, for a slightly disturbed flow (the non-uniform flow field is produced by a small disturbance to the undisturbed, uniform flow) the acceleration potential satisfies the Laplace equation up to the first order of smallness. This implies that there exists a complex acceleration potential which is an analytic function of the space variable, $z = x + iy$. Hereafter, all the linear dimensions will be normalized with respect to the chord length.

In dimensionless form, the Euler equation of motion may be written as (without external forces)

$$\frac{\vec{a}}{\bar{q}_c^2} = \text{grad } \sigma \tag{17}$$

where

$$\sigma = \frac{P_\infty - p}{\sigma \bar{q}_c^2} = \text{acceleration potential}, \tag{18}$$

$\vec{a}$ = acceleration vector, and

$\bar{q}_c$ = average speed on cavity walls.

The complex acceleration potential is

$$F(z, t) = \sigma(x, y, t) - i \tau(x, y, t) \tag{19}$$

where σ and τ are related to each other by Cauchy-Riemann equations.

By using the Bernoulli equation for steady flow, it can be shown that

$$\bar{q}_c = U\sqrt{1 - \sigma} \tag{20}$$

1047

Assuming a slender cavity, the velocity vector $\vec{q}$ may be written in terms of the perturbation velocity components as

$$\vec{q} = \bar{q}_c(1 - u, \; v) \tag{21}$$

and

$$u \ll 1, \quad v \ll 1.$$

In terms of the perturbation velocity components defined by Eq. (21), the Euler equation of motion, Eq. (17) is reduced to

$$\sigma_x = -y = u_t \bar{q}_c - u_x, \quad \sigma_y = -\cdot x = v_t \bar{q}_c - v_x. \tag{22}$$

The problem is now reduced to finding the analytic function $F(z, t)$ which satisfies given boundary conditions listed below. (The real and linearized physical planes are shown in Fig. 11.)

(i) On the free surfaces, $p = P_z$, hence

$$\sigma = 0.$$

(ii) On the cavity boundary, $p = p_c(t)$, hence

$$\sigma = \frac{\sigma}{2\sqrt{1 - \sigma}}$$

where σ is the instantaneous cavitation number.

(iii) On the parts of the centerline of the jet, oc and ef, $v = 0$, hence by Eq. (22)

$$\sigma = 0.$$

Here the constant of integration is set equal to zero on account of the condition at ∞ where flow is steady.

(iv) If the wedge angle is 2ϵ, then the wedge profile may be written as

$$h = \epsilon x$$

and, by Eq. (22), it can be shown that

$$\sigma = \sigma_1 t = \text{on the wedge.}$$

The unknown quantity σ_1 may be evaluated by using the general integral of Eq. (22) which satisfies the condition at infinity:

$$v = -\int_{-\infty}^{x} \sigma_{-x}\left(\sigma, \; y, \; t - \frac{x}{\bar{q}_c} - \frac{\sigma}{\bar{q}_c}\right) d\sigma. \tag{23}$$
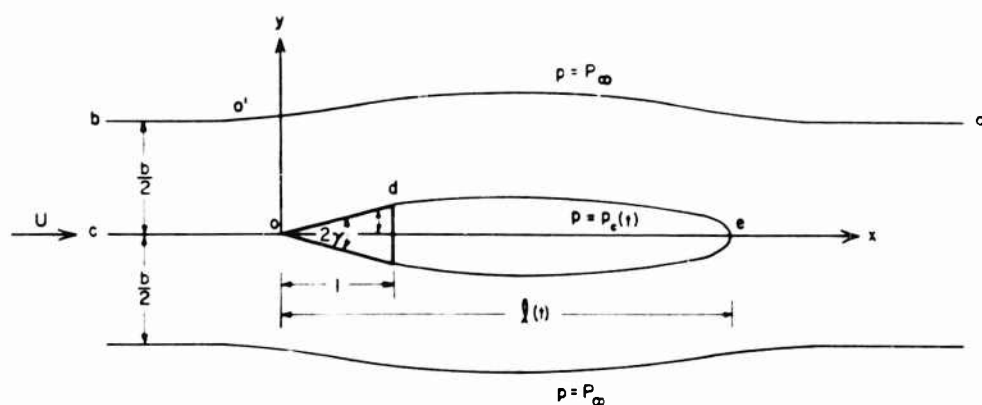
(a) True   z - Plane
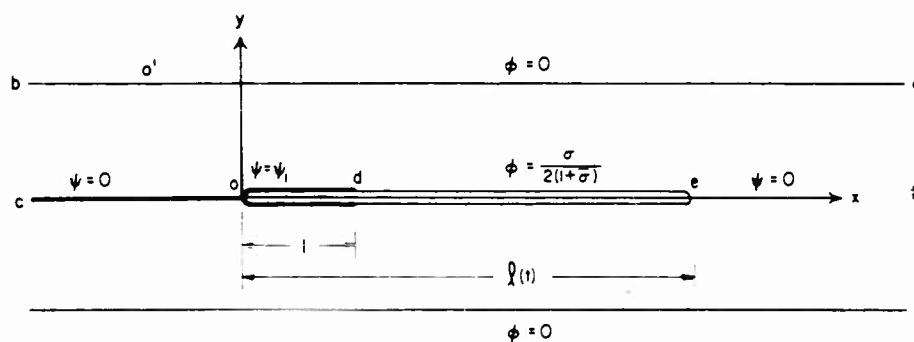
(b) Linearized   z - Plane

Fig. 11 - Real and linearized physical planes

In particular, when the variable pressure $p_c(t)$ is sinusoidal, which is the case considered here, then $\sim$ is also sinusoidal and Eq. (23) reduces to

$$v = - \exp\left(-j\,\frac{\sim x}{\overline{q}_c}\right)\int_{-\infty}^{x} \exp\left(j\,\frac{\sim\sim}{\overline{q}_c}\right)\frac{\sim\sim}{\sim\sim}d-. \tag{23a}$$

Integrating Eq. (23a) by parts and noting that $\sim = 0$ on the line oc, Eq. (23a) leads to

$$v\,(\text{wedge}) = -\,\_\,(\text{wedge}) = -\,\sim_1. \tag{24}$$

This means, within the accuracy of the linearization

$$\psi_1 = -\gamma. \tag{25}$$

Since the flow is symmetrical with respect to the centerline, only the upper half of the flow region needs to be considered. The following transformation formula is used to transform the upper half of the linearized z-plane into the upper half of ζ-plane shown in Fig. 12.

$$z = \frac{b}{2\pi} \ln (1 + \zeta/x_o) \tag{26}$$

where

$$x_o = \left(\exp \frac{2\pi}{b} - 1\right)^{-1} \tag{27}$$

It is readily seen that Eq. (26) transforms the point at $-\infty$ to $(-x_o, 0)$, the nose of the wedge to $(0, 0)$ and the tail of the cavity to $(\ell', 0)$. Here ℓ' is related to ℓ by

$$\ell' = x_o\left(\exp \frac{2\pi \ell}{b} - 1\right). \tag{28}$$

Following the method used in [9] and [10], the solution of the mixed boundary value problem is the ζ-plane as shown in Fig. 12 with finite pressure everywhere is

$$F(\zeta) = \frac{1}{\pi} H(\zeta) \left[-\gamma \int_0^1 \frac{d\tau}{H(\tau)(\tau - \zeta)} \right.$$

$$\left. - \frac{\sigma}{2(1 + \bar{\sigma})} \int_1^{\ell'} \frac{d\tau}{\sqrt{(\tau + x_o)(\tau - 1)(\ell' - \tau)(\tau - \zeta)}} \right] \tag{29}$$

where

$$H(\zeta) = \sqrt{(\zeta + x_o)(\zeta - 1)(\zeta - \ell')} \tag{30}$$

provided the following equation is also satisfied:

$$-\gamma \int_0^1 \frac{d\tau}{H(\tau)} - \frac{\sigma}{2(1 + \bar{\sigma})} \int_1^{\ell'} \frac{d\tau}{(\tau + x_o)(\tau - 1)(\ell' - \tau)} = 0 \tag{31}$$

performing the integrations, Eq. (31) is reduced to

$$\frac{\sigma}{2\gamma(1 + \bar{\sigma})} = \frac{F(\varphi, k)}{K(k_1)} \tag{32}$$
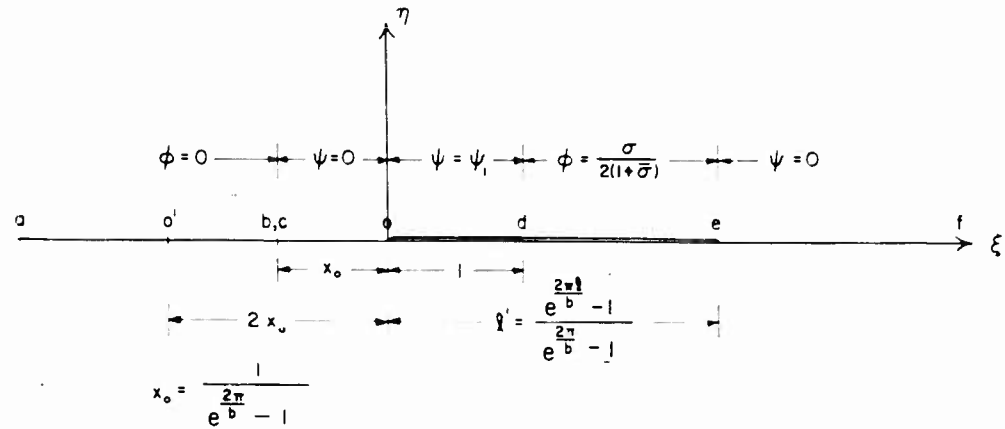
Fig. 12 - Boundary Conditions on ξ-Plane

where

$F(z, k)$ = incomplete elliptic integral of first kind,

$K(k_1)$ = complete elliptic integral of first kind,

$$z = \arcsin \sqrt{\frac{x_o - \ell'}{\ell'(1 - x_o)}} = \text{argument},$$

$$k = \sqrt{\frac{1 - x_o}{\ell' - x_o}} = \text{modulus, and}$$

$$k_1 = \sqrt{\frac{\ell' - 1}{\ell' - x_o}} = \text{modulus.}$$

Equation (32) may be used to determine the cavity length as function of other variables. The right-hand side of Eq. (32) is a function of ℓ and b only and is plotted in Fig. 13.

The drag coefficient is, by definition,

$$C_D = \frac{2}{U^2} \int_0^1 (P - P_c) \, dx. \tag{33}$$

By using the definition of the acceleration potential and the solution given by Eq. (29), it can be shown that

$$C_D = \frac{4}{\ell} (1 - \ell) L_o - \ell L_2 \tag{34}$$

1051
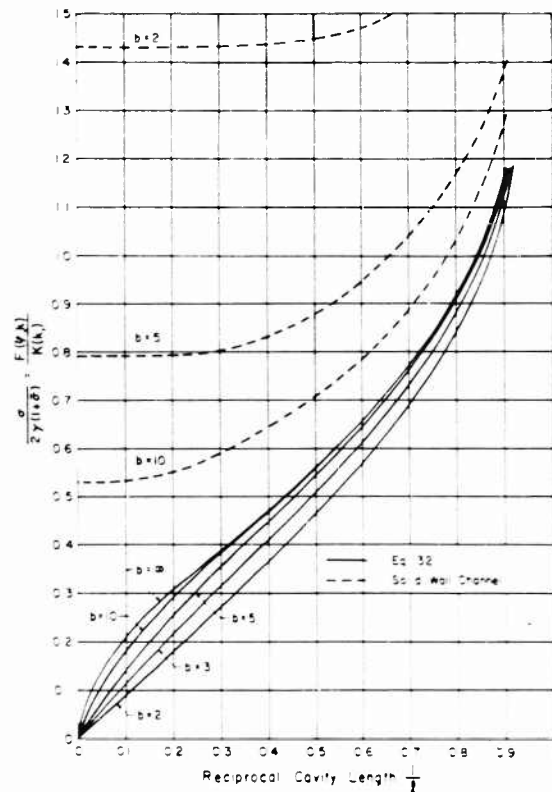
Fig. 13 - Cavity length as a function of
cavitation number and jet width

where

$$L_0 = \frac{b}{4\pi} \text{Re} \int_0^1 \frac{H(\xi)d\xi}{\xi - x_0} \int_0^1 \frac{d\tau}{H(\tau)(\tau - \xi)} \tag{35}$$

$$L_2 = 1 - \frac{b}{2\pi^2} \text{Re} \int_0^1 \frac{H(\xi)d\xi}{\xi - x_0} \int_1^{\ell'} \frac{d\tau}{\sqrt{(\tau - x_0)(\tau - 1)(\tau - \ell')(\tau - \xi)}} \tag{36}$$

The functions L_0 and L_2 are identical to the functions appearing in [9] with the same symbols. After performing the necessary integrations they are reduced to

$$L_0 = \frac{b}{2\pi} F(\tau, k) \left[2E(\tau, k) - \frac{\ell' - 1}{\ell' - x_0} F(\tau, k) - \sqrt{\frac{x_0}{\ell'(\ell' - x_0)}} \right] \tag{35a}$$

1052

$$L_2 = 1 - \frac{b}{\pi} \int_{\beta}^{\pi/2} \triangle_o(\theta, k_1) \cot \theta \, d\theta \tag{36a}$$

where

$E(\phi, k)$ = incomplete elliptic integral of second kind,

$\triangle_o(\theta, k_1)$ = Heuman's lambda function,

β = arc $\sin\sqrt{\frac{x_o}{1+x_o}}$, and

θ = variable of integration.

The functions L_0 and L_2 plotted in [9] are reproduced in Fig. 14. (The corresponding function, L_0, for the flow in solid walled channels as reported in [10] is indicated by dotted lines.)

Using bars to denote average values, it can be shown from Eq. (34) that

$$\bar{C}_D = \frac{4\gamma}{\pi} (1 + \bar{\sigma}) \bar{L}_0 - \bar{\sigma} \bar{L}_2 \tag{34a}$$

(a) L_o (b) L_2
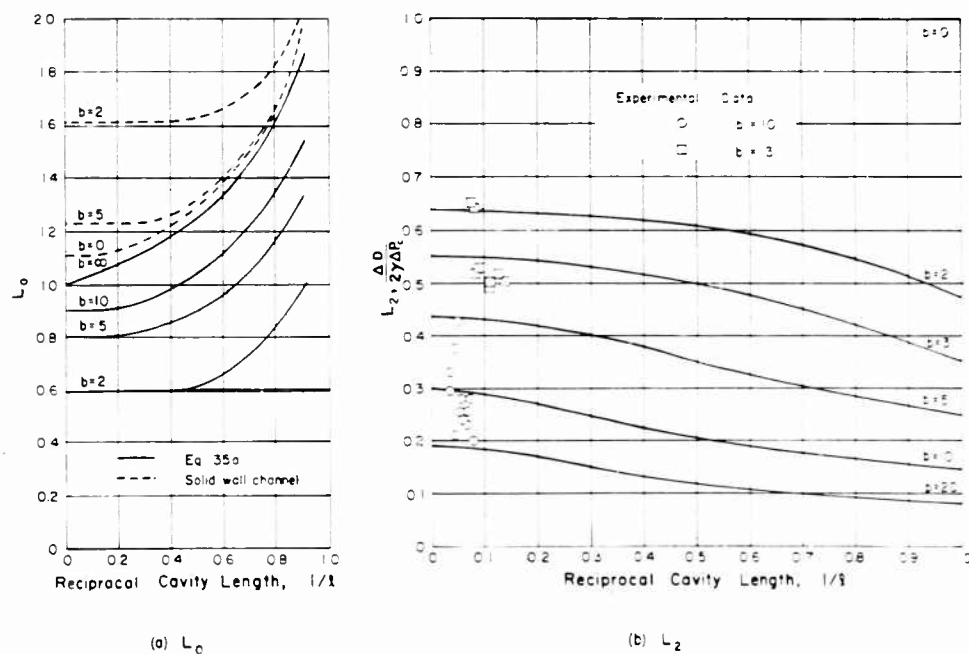
Fig. 14 - The drag functions L_0 and L_2

1053

$$\angle C_D = \frac{4\gamma}{\pi} (1 + \bar{\sigma}) \angle L_0 + \bar{L}_2 \angle \sigma + \bar{\sigma} \angle L_2 + \angle \sigma \angle L_2 \tag{34b}$$

where $\angle C_D$ is the change in C_D produced by a change from $\bar{\sigma}$ to $\bar{\sigma} + \angle \sigma$. It is readily seen from Fig. 14 that, for a large ℓ, the changes in L_0 and L_2 are very small. In fact, it may be shown that $\angle L_0$ and $\angle L_2$ are, at most, of order of $\bar{\sigma}\angle\sigma$. This means, for large ℓ or small $\bar{\sigma}$, the second term on the right-hand side of Eq. (34b) predominates over all other terms and the equation may be simplified to

$$\frac{\angle C_D}{\angle \sigma} = \frac{\angle D}{2\gamma \angle P_c} = \bar{L}_2 \tag{37}$$

where D is the drag. Since $2\gamma\angle P_c$ is the force on the wedge base due to the fluctuating cavity pressure, $\angle D/2\gamma\angle P_c$ or $\bar{L}_2$ indicates the fraction of the fluctuating pressure being transmitted to the body as drag. The function L_2 was called the "pressure function" in [9].

It is noteworthy that L_2 is unity when $b = 0$ and approaches zero as b is increased indefinitely. Furthermore, the corresponding function for the flow in solid walled channels as reported in [10] is zero for any channel width. It is now clear that L_2 is a characteristic function of flows with free surfaces.

Two wedges ($\gamma = 15$ degrees and $\gamma = 7.5$ degrees) were tested for the purpose of measuring the unsteady drag due to the pulsation. The measured $\angle D/2\gamma \angle P_c$ values for $b = 10$ and $b = 3$ cases are plotted in Fig. 14(b). The data plotted in Fig. 14(b) covered the first three stages of pulsating cavities. It should be noted that the order of magnitude of the drag amplitude, $\angle D$, measured in this experiment was between 0.5 lb and 1.5 lb, which is not very much above the sensitivity of the dynamometer. This is probably why the data shown in Fig. 14(b) have considerable scatter. It can nevertheless be concluded that, as an average, the agreement between data and theory is satisfactory.

CONCLUSIONS

An artificial or ventilated cavity may be created by supplying air to the wake of a moving body. There are two distinct regimes of ventilated cavities in a gravitation-free field with free boundaries. One regime may be called reentrant jet and the other pulsating. A cavity with reentrant jet occurs at the smaller air flow rates and is similar to a natural cavity in many respects. A pulsating cavity is formed when too much air is added to the cavity: that is, when the cavitation number is reduced below a certain critical value.

A pulsating cavity has a wavy surface, a periodically variable length, and a periodically fluctuating pressure field which causes the net force acting on the body to fluctuate about its mean value. The result of the analysis and the experimental data have proved the validity of the assumption that the pulsation of ventilated cavities is a peculiar phenomenon of mechanical resonance of the air-water system which occurs when one or more free surfaces exist. It is the motion of surface waves on the cavity walls which causes the cavity to change its volume periodically. This periodical volume change is accompanied

1054

by a vibratory motion of the surrounding water and a pressure pulsation in the cavity. The pulsation is possible only when the natural frequency of the air-water system agrees with the frequency of the surface waves.

There may be any integral number of surface waves appearing on a cavity wall, from one to infinity. Hence, pulsating cavities may be classified according to the number of waves and called first-stage, second-stage, and so on. By a purely kinematical consideration, it was shown that the frequency of the pulsation must be such that the reduced frequency should be equal to the number of stages as indicated by Eq. (1b). By considering the dynamics of the system, it was further shown that the pulsation number defined by Eq. (9) is a function of the dimensionless cavity length and the dimensionless jet width. Furthermore, it was shown that, up to a constant which was determined experimentally, there exists a unique relationship between the average cavitation number, the reference cavitation number and the number of stages. It is also noteworthy that to each stage there corresponds a maximum amplitude of pulsation and air-carrying capacity.

Finally, by using the linearized acceleration potential theory, it was shown that the unsteady part of the dimensionless drag normalized with the unsteady part of the cavity pressure depends mainly on the jet width. It is interesting to note that the unsteady part of the drag due to pressure pulsation in the cavity is negligible in infinite fluid or in a finite fluid bounded by solid walls.

ACKNOWLEDGMENT

REFERENCES

1. Silberman, E. and Song, C. S., "Instability of Ventilated Cavities," Journal of Ship Research, Vol 5, No. 1, pp. 13-33, June 1961.

2. Schiebe, F. R. and Wetzel, J. M., Ventilated Cavities on Submerged Three-Dimensional Hydrofoils, University of Minnesota, St. Anthony Falls Hydraulic Laboratory Technical Paper No. 36, Series B, December 1961.

3. Cox, R. N. and Clayden, W. A., "Air Entrainment at the Rear of a Steady Cavity," Proceedings of the N. P. L. Symposium on Cavitation in Hydrodynamics, London, England, Paper No. 12, 1955.

4. Campbell, I. J. and Hilborn, D. V., "Air Entrainment Behind Artificially Inflated Cavities," Second Symposium on Naval Hydrodynamics, Washington, D.C., August 1958.

5. Song, C. S., "Pulsation of Ventilated Cavities," Journal of Ship Research, Vol 5, No. 4, pp. 8-20, March 1962.

6. Strasberg, N., "The Pulsation Frequency of Nonspherical Gas Bubbles in Liquid," Journal of the Acoustical Society of America, Vol 25, p. 536, 1953.

7. Goldstein, H., Classical Mechanics, Addison-Wesley Publishing Company, Inc., Cambridge, p. 21, 1953.

8. Wu, T. Yao-Tsu, A Simple Method for Calculating the Drag in the Linear Theory of Cavity Flows, California Institute of Technology, Engineering Division Report No. 85-5, August 1957.

9. Song, C. S., Unsteady, Symmetrical, Supercavitating Flows Past a Thin Wedge in a Jet, University of Minnesota, St. Anthony Falls Hydraulic Laboratory Technical Paper No. 34, Series B, January 1962.

10. Song, C. S. and Tsai, F., Unsteady, Symmetrical, Supercavitating Flows Past a Thin Wedge in a Solid Wall Channel. University of Minnesota, St. Anthony Falls Hydraulic Laboratory Technical Paper No. 38, Series B, May 1962.

*　　*　　*

FLOW-INDUCED CAVITY RESONANCE IN VISCOUS COMPRESSIBLE AND INCOMPRESSIBLE FLUIDS

William H. Dunham
David Taylor Model Basin
Carderock, Maryland

ABSTRACT

Oscillations induced into ship structures by high-speed flow of water past immersed openings leading to internal cavities, such as sea chests for condensation of steam, have caused serious structural failures. Flows of this type have been studied in both air and water to determine the physical mechanism of excitation. The studies in air were carried out in the low turbulence wind tunnel at the David Taylor Model Basin. Frequencies, peak to peak pressures, mean pressures, and flow velocities were measured. Also, photographs were made of the individual pressure wave forms projected onto an oscilloscope screen. Flow visualization experiments in water, using dye techniques and high-speed smoke tunnel motion pictures, taken by Professor F.N.M. Brown and Brian Quinn, were used to determine the streamline pattern caused by the fluctuating velocity fields normal and tangential to the cavity mouth. The vortices appear to be controlled by, or coupled to, the natural frequency of the cavity by the combined normal and tangential flow in and out of the cavity mouth, and the positive pressure gradient which exists over the after portion of the cavity opening.

INTRODUCTION

Unstable time dependent flows have become extremely important due to the possible excitation of structural oscillation and failure. These flows, many times self-excited, represent a serious problem to the designer of immersed bodies at high speed. Many times in the past, when the dynamic pressure due to forward motion was sufficiently high, self-excited wing oscillations in aircraft have caused structural failure. Cavity oscillations in aircraft, traveling at high speeds, have indicated the existence of sound fields of 160 db at 20,000 to 40,000 cps, but no structural damage resulted due to the difference between the

1057

exciting frequency and the resonant frequency of the structure. This has not been the case in water immersed cavities.

The elastic modulus of water is of the same order of magnitude as that of steel and, therefore, upon excitation of cavity oscillation, transmits almost all of the pressure energy to the surrounding air-backed structure (see Fig. 1). The structure then responds, depending upon its resonant frequency and dampening, to the oscillating driving pressure in the mouth of the cavity. Serious structural failures have resulted from cases where the forcing frequency excited the natural resonant frequency of the air-backed structure.
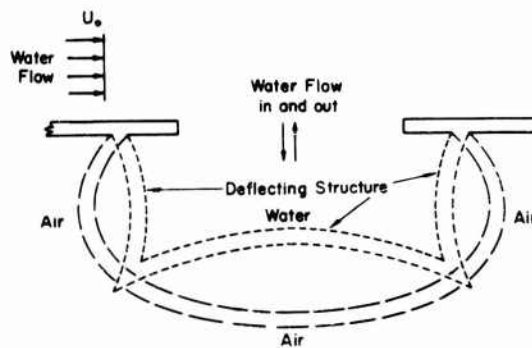
Fig. 1 - Schematic drawing of an oscillating air backed cavity open to the freestream velocity of an incompressible fluid

Historically, Helmholtz cavity resonance was discovered by Herman Ludwig F. Helmholtz, 1821-1894, a German mathematician who worked out analytical expressions for this phenomenon. Rayleigh [1,2]* later extended his work based on energy relations which allowed end corrections to be made for different mouth geometries. His analysis was based upon a compressible fluid which oscillated an effective mass of fluid in the cavity mouth. Rayleigh postulated that the kinetic energy of the oscillating fluid in the mouth is stored in the compression pressure of the fluid in the cavity base. This produced an equivalent spring mass oscillating system.

Further work on flow-excited systems of cavity resonance was not continued until the early 1950's when Blokhintsev, Roshko, Krishnamurty, Harrington [3,4, 5,6,7] and others began to look into the problem. Little was known of boundary layer flow stability at the time of Helmholtz and Rayleigh. It was generally assumed by later workers that this field of study could be advanced again by the simple application of viscous flow theory. However, this was not the case. Great difficulty was experienced in obtaining visual photographs of the cavity

---

*Numbers in brackets refer to the References listed on page 1080.

oscillations. Also, analytical attempts to explain the phenomena without experimental boundary conditions showed a great deal of mathematical complexities which could not be resolved.

D.I. Blokhintsev of the Physical Institute, Academy of Science, USSR, developed a simple empirical theory based on his experimental work. He assumed that there were two independent vibrating systems: one driving frequency and one resonating or reinforcing frequency. He believed that the driving frequency obeyed the edge tone Strouhal number relation with an amplitude proportional to $1/2 \rho U^2$. The Strouhal relation consisted of a constant multiplied by the product of the frequency and the freestream velocity and divided by the streamwise length of the cavity mouth opening. Frequency expressed by the Strouhal relationship is as follows:

$$f_D = \frac{SV}{L}$$

where

f_D is the driving frequency,

S is the nondivisional Strouhal numbers varying between 0.2 and 0.83,

V is the velocity, and

L is the length of the cavity mouth in the flow direction.

The second oscillating system involved is the reinforcing or natural frequency of the cavity, which was found by Rayleigh to be:

$$f_C = \frac{A^{1/4}}{2\pi} \left[\frac{1}{\frac{\partial V}{\partial P} (0.8c)} \right]^{1/2}$$

where

f_C is the reinforcing frequency of the cavity,

A is the area of the cavity mouth,

$\partial V/\partial P$ is the rate of volume change with pressure, and

c is the density of air.

Note: The constant 0.8 arises from geometrical consideration for a Helmholtz resonator which has its mouth in a thin sheet [7].

Resonance between the two systems occurred when $f_D \approx f_C$ and continued over a small range of freestream velocities. During the experiments conducted by Blokhintsev, frequencies were observed to pull off from a linear relationship, indicating that some coupling existed between the cavity oscillating system and the linear driving frequency. Further work by Harrington reinforced the results of Blokhintsev.

1059

The present work is an attempt to determine the physical mechanism of cavity resonance by a combination of two techniques, flow visualization and the measurement of important flow parameters. The flow visualization technique led to the design of an experiment in which high-speed motion pictures were taken, in water, of dye streamers flowing past the mouth of a mechanically driven oscillating cavity. Wind tunnel tests were also conducted in order to make quantitative the flow visualization information. Data taken included mean pressures, peak to peak pressures, pressure wave forms and frequencies. These data were, in turn, taken as a function of fluid velocities, cavity volume, mouth size, and mouth configuration.

EXPERIMENTAL EQUIPMENT AND TECHNIQUE

Two experiments were conducted at the David Taylor Model Basin, the purpose of which was to determine the physical mechanism of flow-excited cavity resonance. The first experiment was to visualize the streamline patterns of the oscillating flow near the mouth of a mechanically oscillating cavity located in the DTMB miniature water channel. The second experiment was quantitative in nature, using the 2 ft × 4 ft low turbulence wind tunnel facility to produce 0 to 120 ft/sec wind velocities over an open variable volume cavity.

The flow visualization experiment required the design and construction of a 12 in. × 8 in. transparent test section with a boxlike cavity, also with transparent sides, located in its floor (see Fig. 2). The mouth of the cavity was constructed flush with the test section floor, and made removable in order to change the mouth dimensions during the experiment. A series of cavity mouth inserts were made, as shown in Fig. 3.

Cavity oscillation was simulated by a 3 in. reciprocating cylinder delivering alternating air pressure to an air pocket behind a rubber diaphragm comprising
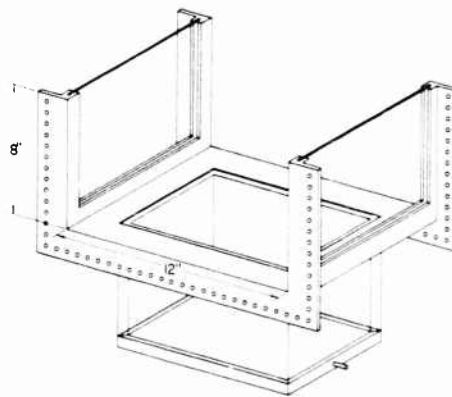
Fig. 2 - Transparent sided test section for the miniature water channel
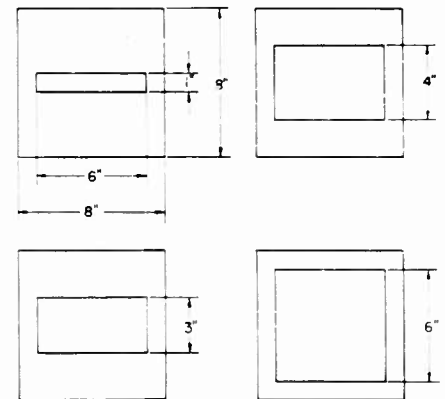
Fig. 3 - Cavity mouth inserts for the test section shown in Fig. 2
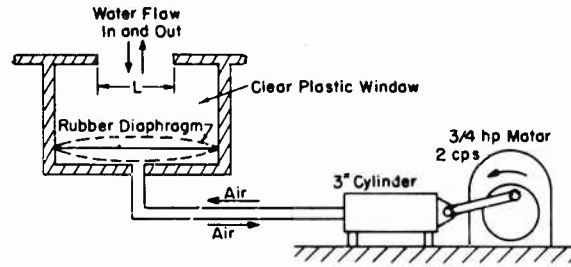
Fig. 4 - Schematic drawing of the mechan-
ically oscillated water channel cavity

the cavity floor (see Fig. 4). The vertically oscillating diaphragm in the base
caused an alternating flow, in and out of the cavity mouth.

Since the purpose of the flow visualization experiment was to determine the
physical mechanism by which the freestream fluid transfers energy into the
oscillating cavity system, it was necessary to simulate resonant conditions dur-
ing the experiment. From the literature [7], Strouhal numbers for resonance
conditions were known to be about 0.43 and 0.80. By allowing the driving fre-
quency to remain constant at 1.5 cps, a table of velocities (see Table 1) which
would produce resonant conditions was computed from the relation

$$U = \frac{fL}{S}$$

where

      S is the Strouhal number,

      U is the freestream velocity,

      f is the frequency, and

      L is the length of the mouth in the stream direction.

Table 1

Length of Mouth	Frequency	Velocities in ft/sec	
		For Strouhal No. 43	For Strouhal No. 80
0.083 ft	1.5	0.29 ft/sec	0.16 ft/sec
0.250 ft	1.5	0.87 ft/sec	0.47 ft/sec
0.330 ft	1.5	1.16 ft/sec	0.62 ft/sec
0.500 ft	1.5	1.74 ft/sec	0.94 ft/sec

By adjusting the freestream velocity to correspond with the mouth sizes and frequencies, shown in Table 1, it was possible to simulate a streamline pattern for resonant conditions [8].

Flow visualization was accomplished by injecting dye into the boundary layers upstream of the cavity mouth and simultaneously taking high-speed motion pictures, from 64 fps to 600 fps, through the transparent sides of the cavity and test section.

The second experiment was designed to measure the important properties of the oscillating cavity in air as a function of cavity geometry. To accomplish this, an 8 in. round metal cylinder was designed to fit into the top of the 2 ft x 4 ft low turbulence wind tunnel, as shown in Fig. 5. The cylinder was equipped with an aluminum airtight piston which allowed the volume to be varied from 0 to 0.518 ft^3 (see Fig. 6). Six separate mouth inserts with square openings of various sizes were constructed to change the frequency range. Also, a series of three steps were made to elevate the upstream lip of the cavity a varying height over the downstream lip, as shown in Fig. 7.
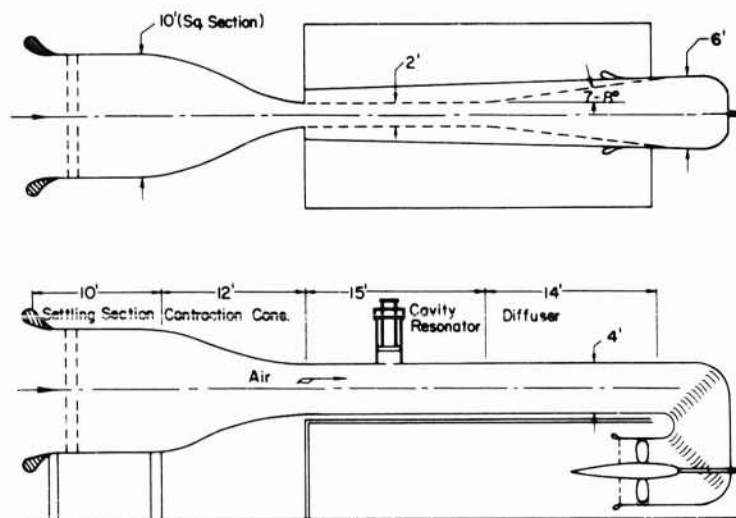
Fig. 5 - Low-turbulence wind tunnel with adjustable cavity mounted on top

Two Dynisco pressure measuring transducers of the strain gauge diaphragm type, rated from 0 to 1 psi, were placed in the center of the movable piston at the end of the cavity, and on the wall of the cavity near the downstream lip (see Fig. 5).

The pressure transducers were calibrated statically for both positive and negative gauge pressures by comparing the combined response of both the transducer and Sanborn 350-1100 Amplifier to the change in level of an alcohol
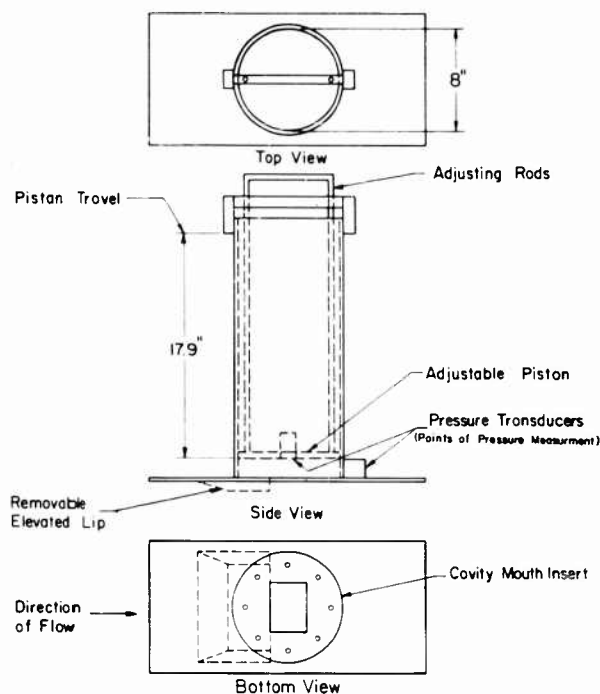
Fig. 6 – Adjustable cavity for wind tunnel
mounting with mouth insert and removable
elevated upstream lip

monometer. The response of this type transducer is apparently linear from 0
to 2000 cps and, therefore, no correction was necessary on its output in the
range of frequencies from 0 to 300 cps.

A general schematic of the electrical arrangement for the measurement of
pressures and frequencies is shown in Fig. 8. The AC component of the pressure
signal output was read directly on a dual beam oscilloscope. The DC component
was read on a sensitive 100,000 ohms/volt meter. The frequency was deter-
mined by measuring the output pulses on an electronic counter and checked by
Lissajous figures formed by combining the pressure signal with the output of a
low range audio frequency oscillator. Phase relations between the two pressure
signals were observed by superimposing both signals simultaneously on the
screen of the dual beam oscilloscope.

THEORY OF THE PHYSICAL MECHANISM BY WHICH
FLOW-INDUCED OSCILLATIONS OCCUR

The qualitative discussion which will follow is based on the results of the
author's water channel and wind tunnel work, as well as the work of Professor
F.M.N. Brown, Department Head, Department of Aeronautical Engineering of

1063
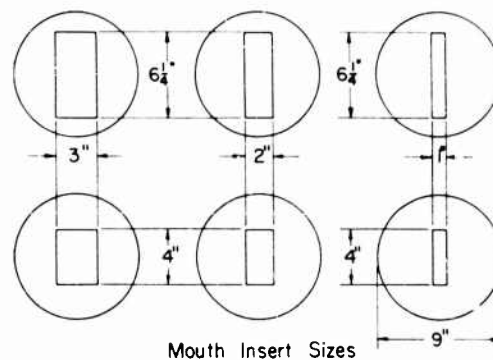
Mouth Insert Sizes

Fig. 7 - Cavity mouth inserts
and elevated upstream lips

Side View

Top View
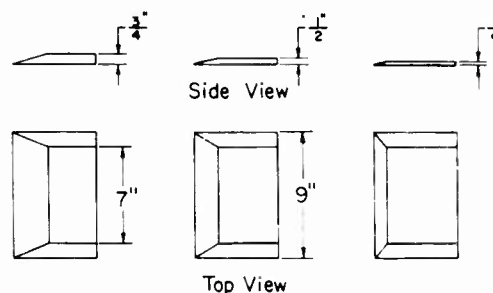
Notre Dame University, and his assistant Brian Quinn. The smoke tunnel still photographs, high-speed motion pictures (3000 fps), and data, as yet unpublished, provided by Professor Brown, have been of great assistance in developing the flow theory.

The results of the smoke tunnel, water channel motion pictures, and wind tunnel data, indicate a series of flow patterns which seem to repeat during each cycle of cavity oscillation. These patterns are as follows:

1. The flow visualization motion pictures taken in the smoke tunnel and water channel are similar in appearance (see Figs. 9 and 10).

2. For wind velocities over 30 ft per second, one and possibly two vortices appear in the mouth of the cavity during one oscillation (see Figs. 15 and 18).

3. The formed vortices are partially destroyed when they strike the downstream lip.

4. The water channel photographs indicate that the vortices are created during the inflow or compression portion of the cavity oscillation cycle.

5. The position of vortices forming in the water channel could be moved back and forth in the cavity mouth by changing the freestream velocity.

1064

Flow-Induced Cavity Resonance in Viscous Fluids
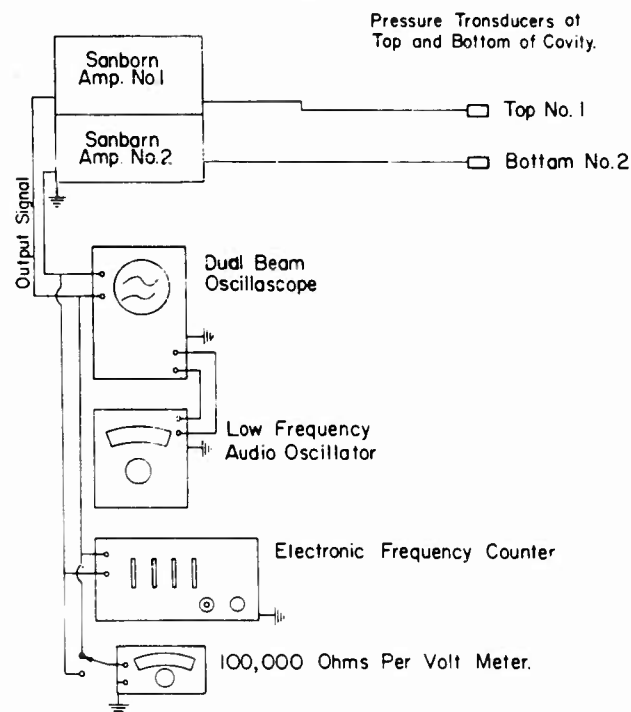
Fig. 8 - Schematic drawing of the
instrument arrangement for fre-
quency and pressure measurement

6. For the water channel test, the freestream velocity agreed with resonant conditions when the vortices formed in the middle portion of the cavity mouth.

7. For the water channel experiment, the resonant conditions of the Strouhal number of 0.43 represented one vortex in the center of the cavity mouth. The resonant conditions for the Strouhal number at 0.80 represented two vortices in the cavity mouth.

8. The number of vortices in the water channel mouth apparently was a function of the velocity in the water mouth and the frequency of the driven cavity oscillation.

9. Smoke tunnel photographs indicate that the instability in the mouth formed after a period of smooth flow over the cavity mouth.

10. The smoke tunnel photographs indicate that the normal displacement of the streamlines during cavity oscillation is small relative to the length of the cavity mouth.

11. During the smoke tunnel test, fluid from the freestream did not seem to enter the cavity base.

1065
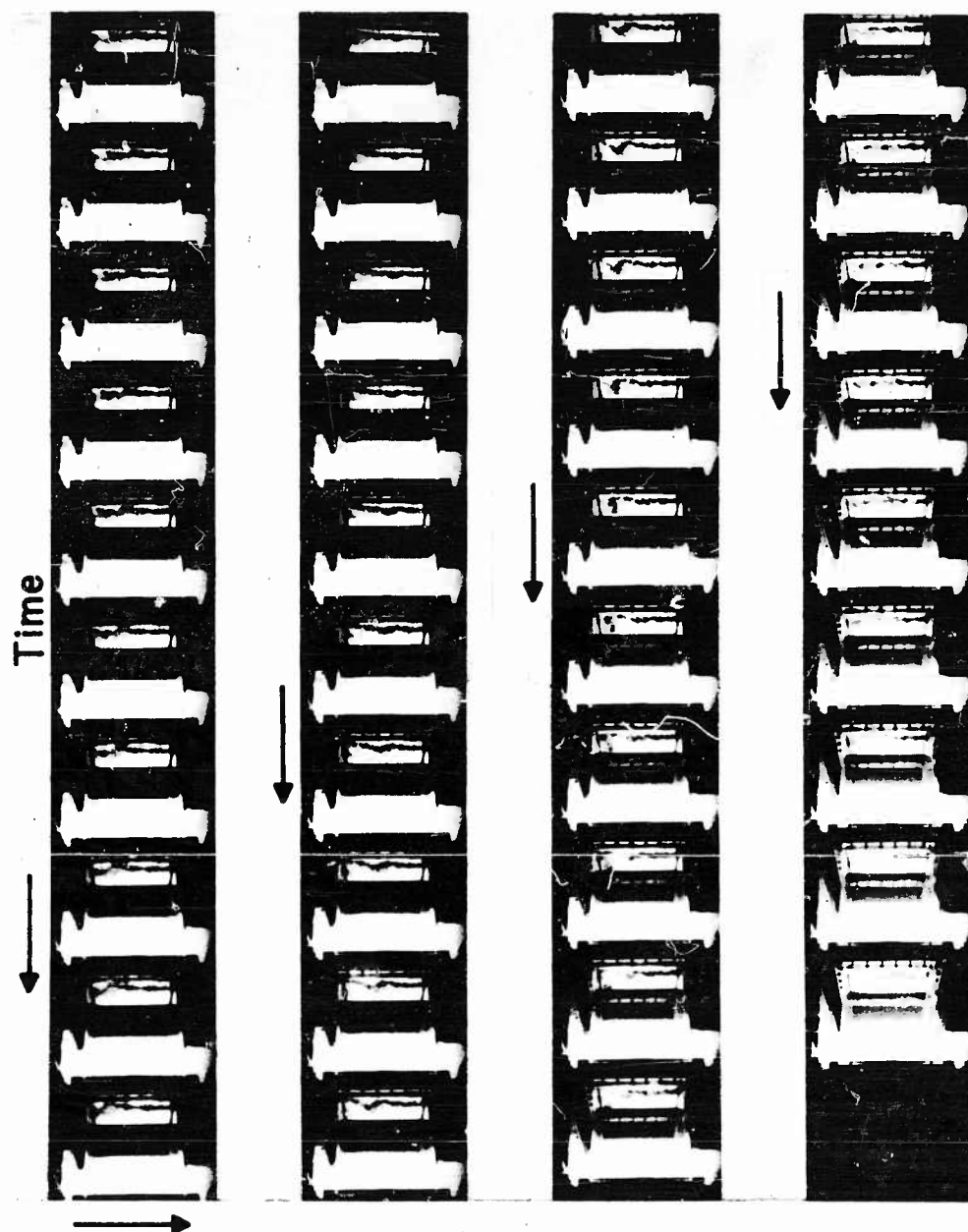
Fig. 9 - Sequence from the water channel flow visualization motion picture
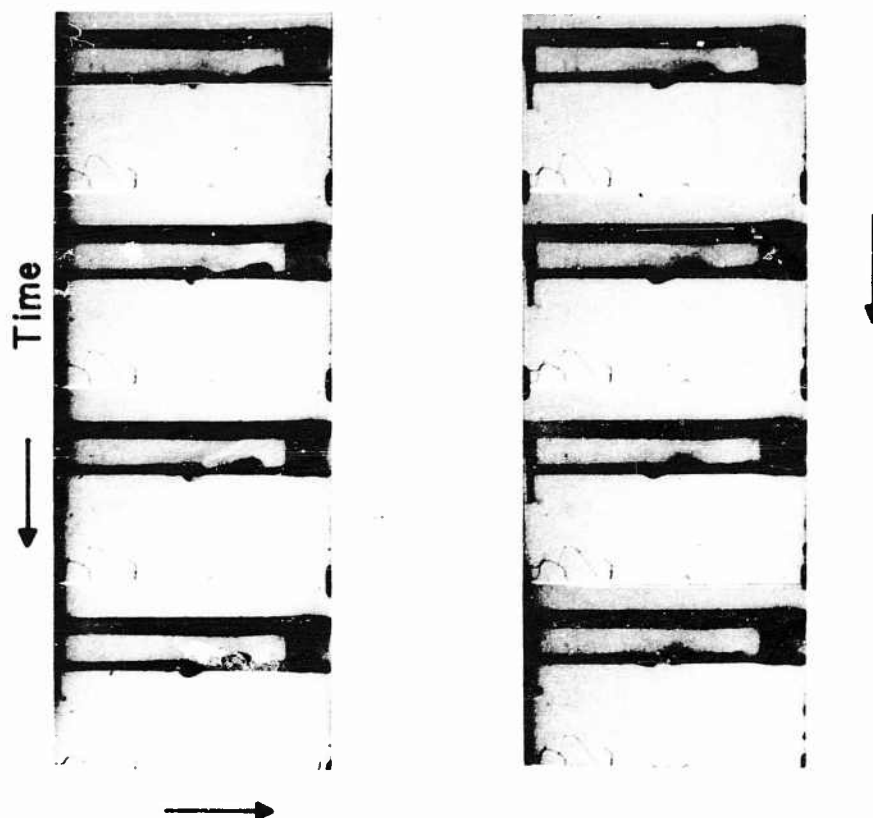
Fig. 10 - Sequence from smoke tunnel motion picture
of Brown and Quinn

The above streamline patterns imply that the mechanism of energy transfer from the freestream to the oscillating cavity system is the formation of flow separation vortices in the cavity mouth. The vortex velocity field, consequently, directs the high energy freestream fluid into and out of the cavity mouth without exchanging fluid within the cavity. This hypothesis is borne out by the high-speed photographs of Professor Brown and by the literature concerning the stability of boundary layers during turbulent and laminar mixing of fluids of different velocities.

The early works of Tollmien and others [9,10] indicate that the velocity distribution of a mixing zone, whether laminar or turbulent, has an inflection point. This type of velocity distribution in a boundary layer is unstable in nature, and when forced to flow into a positive pressure gradient, causes separation at the point where $\partial U / \partial y_{y=0}$ vanishes [10]. This condition appears in the cavity mouth, shown in Fig. 11, and suggests a possible means of activating cavity oscillation.
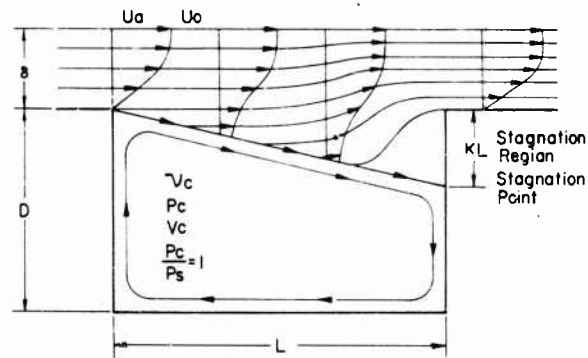
Fig. 11 - Streamline pattern of cavity flow
before oscillation occurs

The following discussion will attempt to describe a possible model of cavity oscillation. If the freestream velocity is increased over a flush mouth cavity, the static pressure inside the cavity will drop slightly below freestream value, and a positive pressure gradient will form over the after portion of the cavity mouth in front of the stagnation region on the downstream lip. At some distance λ from the downstream lip of the cavity mouth, a vortex will form caused by separation of the flow at a point $\delta\lambda$ upstream of the vortex (see Fig. 12). Fluid is directed into the cavity by the vortex velocity field from the freestream and from the boundary layer downstream of the cavity mouth, causing a pressure increase in the cavity base. After the formation of the vortex, the positive pressure gradient in the after portion of the cavity mouth is destroyed and the vortex moves with the velocity u_v over the distance λ to the downstream lip. When the vortex
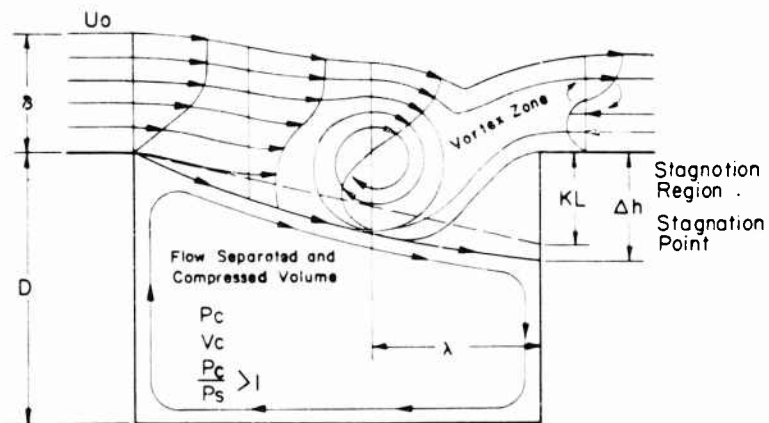
Fig. 12 - Streamline pattern of cavity flow during the
formation of the vortex in the cavity mouth and the
compression portion of the cycle

1068

strikes the downstream edge, the inward portion of the velocity field is redirected into the downstream boundary layer (see Fig. 13). The outward portion of the vortex velocity field entrains fluid in the cavity mouth and causes a pressure reduction over the downstream lip of the cavity and also reduces pressure inside the cavity base. Once the vortex has passed into the boundary layer downstream of the cavity, the flow returns to a smooth streamline pattern, and begins to build up a positive pressure gradient, as shown in Fig. 14. During the entire oscillation, the cavity below the stagnation streamline does not gain or lose fluid. This mass of air apparently is compressed by the gain of fluid in the cavity mouth, and expanded by the loss of fluid from the cavity mouth during oscillation.
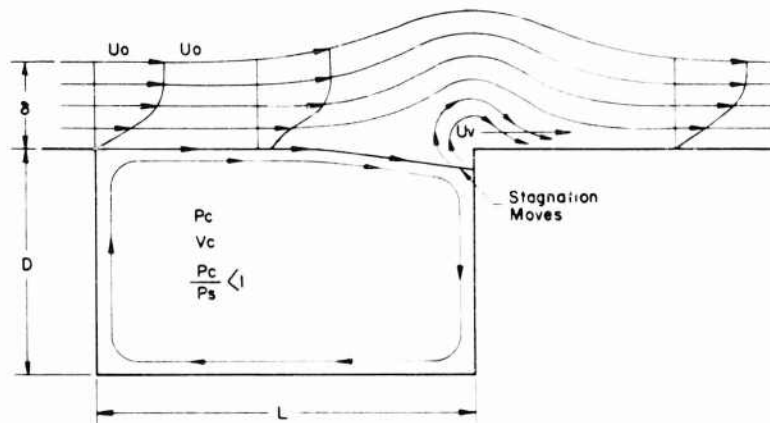
Fig. 13 - The streamline pattern of the vortex velocity field as it strikes the downstream lip
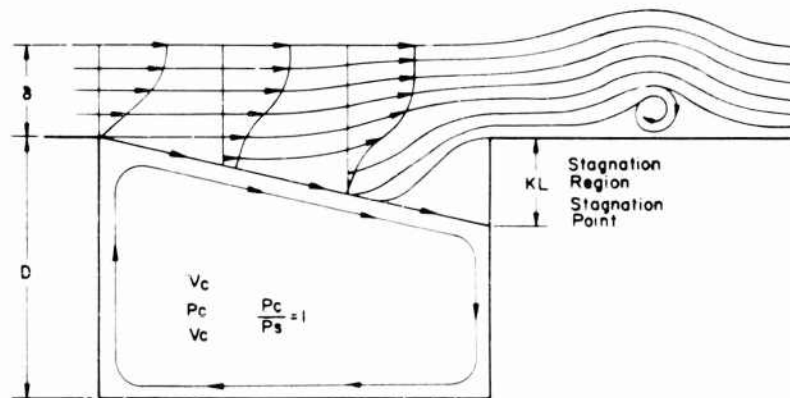
Fig. 14 - Flow returns to a smooth pattern, with the positive pressure gradient building up in front of the downstream lip

Once oscillation has started, flow separation in the cavity mouth is locked into phase with the cavity oscillation by the combination of normal and tangential velocity components caused by the cavity oscillation. When the velocity normal to the plane of the cavity mouth is in an inward direction, the angle of diffusion is increased, causing an earlier than normal flow separation to occur.

The cavity flow model just described, and shown in Figs. 11 through 14, does not have protruding lips as is the case with the experimental water tunnel cavities and some of the wind tunnel cavities. However, the observed streamline patterns seem identical in both cases, as shown in the wind tunnel photographs in Figs. 15 and 16. It is reasonable to assume, therefore, that the mechanism of activation is similar in nature. Qualitative verification of the flow patterns shown in Figs. 11 through 14 is shown in Figs. 15 through 19.

Fig. 15 - Smoke tunnel still photograph by Brown and Quinn of the compression portion of the oscillation cycle. (Note: The downstream lip is square and does not protrude.)

CONCLUSIONS FROM THE SIMPLIFIED FLOW MODEL

The simplified flow model just described leads to some expressions which have been used empirically in the past for frequency prediction. If it is assumed that the passage of separation vortices over the distance λ in the cavity mouth (see Fig. 11) to the downstream lip causes the cavity oscillation, then the following relations hold true:

$$f_D = n \frac{\bar{u}_v}{\lambda} \tag{1}$$
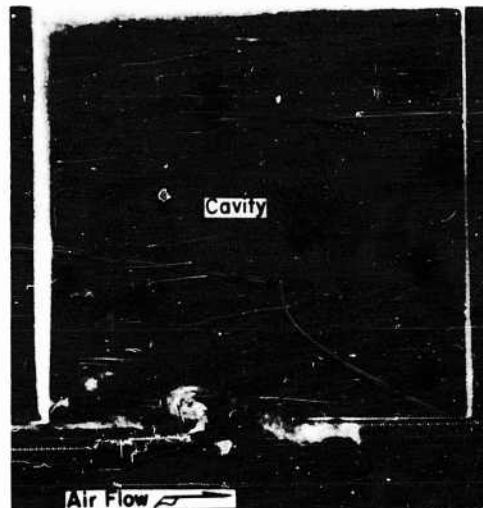
Fig. 16 - Smoke tunnel still photo-
graph by Brown and Quinn of the
compression portion of the oscillation
cycle. (Note: The downstream lip
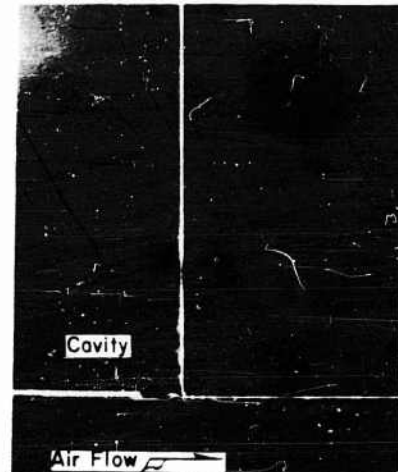protrudes upstream from the wall.)

Fig. 17 - Smoke tunnel
still photograph by Brown
and Quinn of the com-
pression portion of the
oscillation cycle, show-
ing the history of vortex
formations in the bound-
ary layer

where

$\bar{u}_v$ is the average vortex velocity over the period T,

λ is the distance from the origin of the vortex to the downstream lip, and

n represents the number of vortices in the distance λ during time T.

Since the cavity responds at but one frequency, the number of velocities
which can produce this frequency is limited by integer multiples of the number
of vortices passing over the distance λ. The requirement of integer values for
c is caused by the necessity of having vortices formed in the mouth pass the
downstream lip in single or multiple groups.

From the simplified model and boundary layer theory, it is assumed that
some degree of similarity exists between velocity profiles taken across the
cavity mouth at the same time during cycle. If this is true then the non-
dimensional velocity ratio

$$\frac{u_v}{U_o}\bigg|_{at\ time\ T} = constant$$

1071
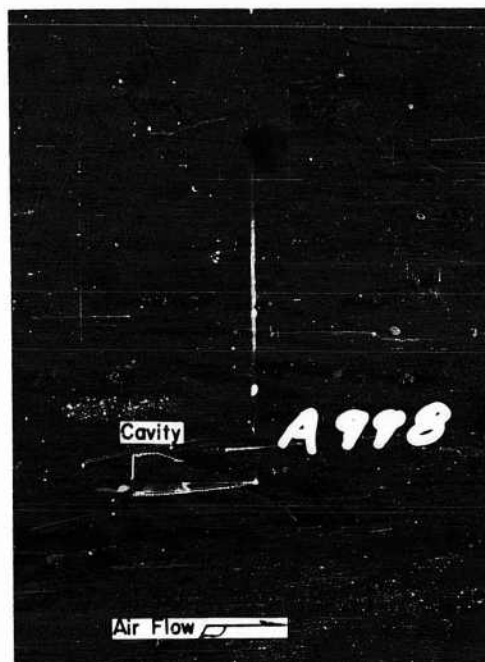
Fig. 18 - Smoke tunnel still photograph by Brown and Quinn of multiple vortices in the cavity mouth

and that

$$\frac{u_v}{U_o} = \frac{1}{T} \int_o^T \frac{u_v}{U_o}(t)\, dt$$

We can now say that $\bar{u}_v$ is averaged over time T and is proportional to U_o or

$$\bar{u}_v = KU_o \tag{2}$$

Substituting Eq. (2) into Eq. (1), we obtain the following relation:

$$f_D = \frac{nKU_o}{\cdot}$$

To evaluate the function , we must consider the effect of the changing amplitude of cavity oscillation on the point of flow separation in the cavity mouth. The function remains constant for non-resonating regions of the cavity, as can be seen from Fig. 20. When the cavity oscillates, the diffusion angle increases upon the inward position of the cavity, causing an earlier separation of the fluid and an increase in the magnitude of , which presumably could explain the nonlinear frequency velocity variation during resonance.

If we now assume non-resonance of the cavity, the ratio of L is constant or

1072

Fig. 19 - Smoke tunnel still photograph by Brown and Quinn of the low speed vortex in the base of a cavity where the height to length ratio approaches one
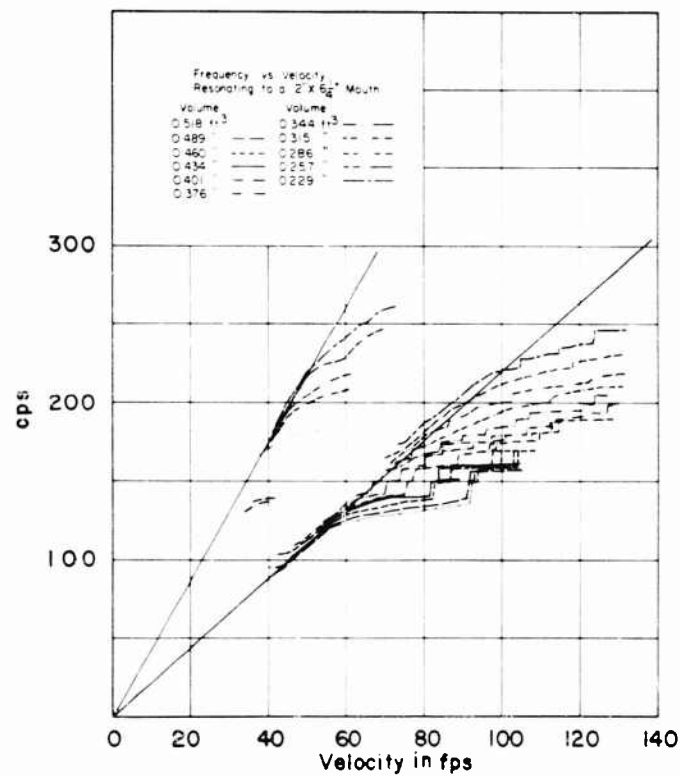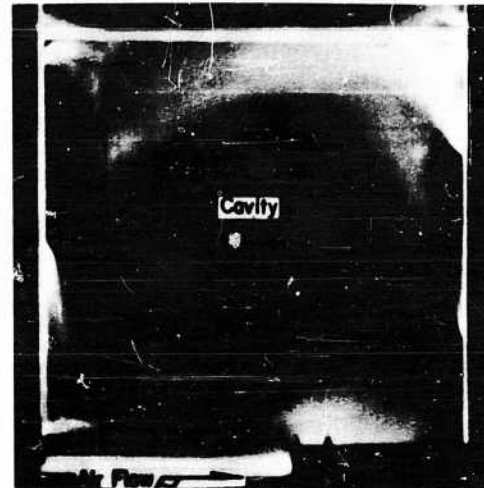
Fig. 20 - Frequency vs velocity for various cavity volumes resonating to a 2" × 6-1/4" mouth. (Note: The 2" dimension is in the streamwise direction.)

1073

$$\frac{\wedge}{L} = C \tag{3}$$

Substituting this value for $\wedge$ in Eq. (2), we obtain

$$f_D = \frac{nK}{C} \frac{U_o}{L} \tag{4}$$

By letting

$$\frac{K}{C} = S$$

we obtain the well-known non-dimensional Strouhal number

$$S = \frac{f_D L}{nU_o} \tag{5}$$

Equation (5) has been determined to be true for Helmholtz resonance by experimental means and n found to have values about 1 and 2.

Based on the above analysis, Strouhal number can be defined as a function of the separation point and boundary layer velocity distribution. Referring to Eqs. (1) and (2), we redefine S as

$$S = \frac{L}{\wedge} \frac{\bar{u}_v}{U_o} \tag{6}$$

Equation (6) indicates that Strouhal number is not a simple constant but a function of the boundary layer velocity distribution in the mouth of the cavity, and the point of flow separation in the cavity mouth.

As a matter of side interest, Eq. (6) can be obtained by equating the frequencies of the following fundamental relations:

$$f_{D,C} = \frac{n\bar{u}_v}{\wedge} = \frac{nSU_o}{L} \quad \text{or} \quad S = \left(\frac{L}{\wedge}\right)\left(\frac{\bar{u}_v}{U_o}\right)$$

THE FORCING FUNCTION FOR CAVITY RESONANCE
AND ITS EFFECT ON THE MAGNITUDE OF n

The response of an open cavity to a forcing function of the frequency $f_D = nSU_o/L$ at several different freestream velocities (see Fig. 19); i.e., $n = 1$ and 2, leads to the question, why doesn't $n = 4$ and 6 represent values of n? Assuming that the flow model described is an accurate description of the oscillation, the question can be resolved by examining the coupling between n and the amplitude of the forcing function, as well as the dampening of the system.

Blokhintsev [3] suggested that the driving frequency had an amplitude proportional to $1/2\,\rho U^2$. The degree of proportionality apparently is a function of the boundary layer thickness δ or δ/L. The proportionality constant probably

approaches 1 as $\delta/L \to 0$. If Blokhintsev's assumption is modified so that the boundary layer effect is compensated for, the forcing function can be expressed as follows:

$$\text{Forcing Function Amplitude} = f\left\{\frac{\delta}{L}\right\}\frac{1}{2}\rho U_o^2 \sin 2\pi n\left(\frac{SU_o}{L}\right)t \tag{7}$$

It can be seen that a coupling now exists between n and the amplitude of the forcing function by eliminating the velocity between the magnitude of Eq. (7) and the relation $f_D = nSU_o/L$. The following equation defines the modulus of n in terms of the absolute value forcing function amplitude, the remaining values of $f\{\delta/L\}L$ and ρ are constant.

$$n\,\Big|_{\substack{\text{evaluated as} \\ \text{integer values}}} = \frac{f_D L}{S\sqrt{\dfrac{2|\text{Forcing Function Amplitude}|}{f\left\{\frac{\delta}{L}\right\}\rho}}} \tag{8}$$

As can be seen from Eq. (8), the amplitude of the forcing functions must be reduced for n to grow in magnitude. The upper limit on the value of n depends upon how much the amplitude of the forcing function can be reduced and still maintain oscillation. This upper limit has been found experimentally by the author to be $n = 2$. Work done by Harrington at the David Taylor Model Basin indicates the existence of a weak oscillation at $n = 3$. The geometric conditions of Harrington's experiment were different, in that cavity and mouth sizes were much larger than the author's apparatus.

ANALYSIS OF THE DATA

Representative data obtained during the wind tunnel tests of the adjustable resonating cavity, shown in Fig. 5, are shown in Figs. 20 through 25. The data include frequency and pressure measurements as a function of freestream velocity, cavity volume, relative heights of the cavity mouth lips and the streamwise length of the cavity mouth.

The frequency measurements shown in Fig. 20 verify the results found by others [3,7]. The driving frequency appears linear with freestream velocity as the theory predicted and continuous throughout a wide range of volume variations. The variation from the linear relation is apparently caused by the cavity controlling the time of flow separation. Since the cavity has only one excitation frequency in this velocity range, it either retards the vortex velocity or lengthens the path over which the vortex must travel. The result is a lower frequency than predicted by the Strouhal relation. This continues until the driving frequency is too far out of phase with the cavity for the coupling between the cavity and the driving frequency to maintain oscillation. At some point, as seen in Fig. 20, the organized oscillation ceases until the second Strouhal number occurs. Figure 20 also illustrates the effect of changing volumes while holding the cavity mouth a constant size. Each cavity volume apparently has its own excitation frequency and cut-off points. However, all curves seem to be similar in nature and do not appear below 30 ft/sec. Strouhal number remains relatively constant for the same experimental conditions, as can be seen from Fig. 21.

However, there is an effect of geometry which appears. Higher Strouhal numbers are restricted to larger cavity mouth lengths. For example, in Fig. 21, at no time was a Strouhal number found over 0.36 for a cavity length of 1 in., but Strouhal numbers 0.36 - 0.40 and 0.76 - 0.80 were common in mouth lengths over 2 in. This observation fits well into the hypothesis of higher Strouhal numbers being caused by multiple vortices in the cavity mouth. No attempt was made to vary boundary layer thickness or velocity distribution effects. These factors may have an appreciable effect and would be worth investigating.
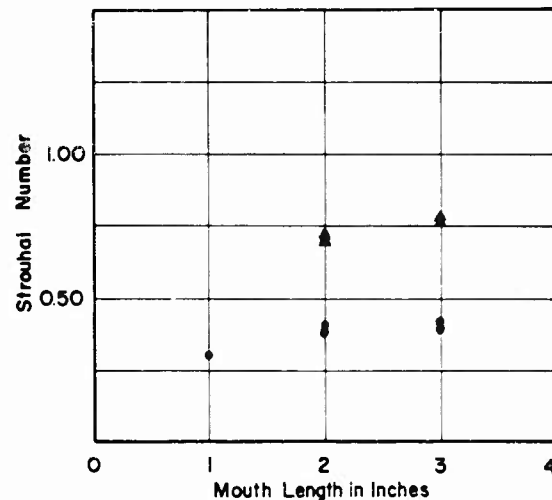
Fig. 21 - Strouhal number vs cavity length

Pressure measurements were made in an attempt to determine a method of computing the amplitude of pressure fluctuations with time during cavity oscillation. It was also hoped that, during the experimental investigation, a method would be discovered, by increasing the damping in the system or removing some vital part of its activation, which would prevent flow-excited oscillation.

Mean pressures were measured as a function of freestream velocity, cavity volume, cavity mouth length, and the relative heights of the mouth lips. The results are shown in Figs. 22 and 23. The mean pressure was found to be slightly below that of the freestream for a flush mouth and still farther below freestream when the upstream lip was raised, as shown in Fig. 23. A surprising result was observed in the regions of resonance. Contrary to some reports of high mean pressures during resonance, the mean pressure curve remained smooth through resonance and remained, at all times, below freestream static pressure. This result was further borne out by the wave forms of pressure variation with time, as shown in Fig. 24. These pressure wave forms indicate that the pressures at the mouth and base of the cavity were in phase, and that the wave forms were symmetrical about the zero amplitude axis. The elevated lip configuration, shown in Fig. 23, indicated a marked drop in mean pressure
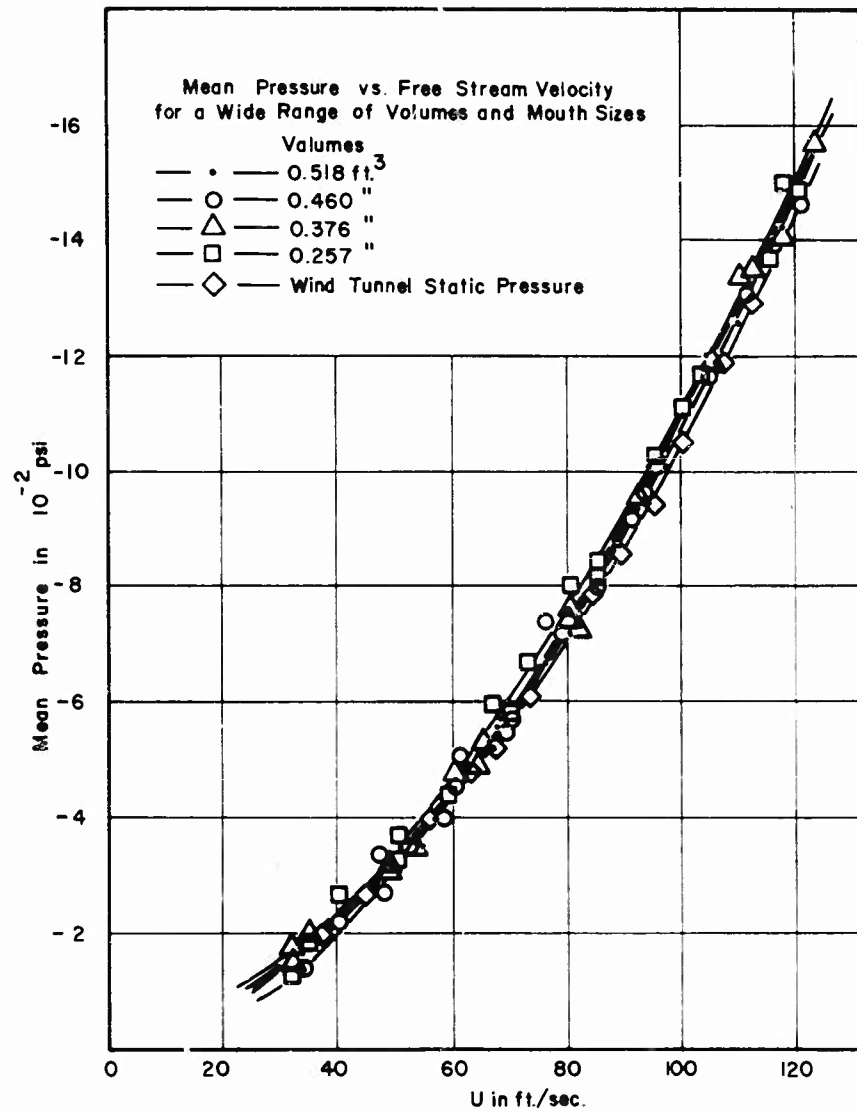
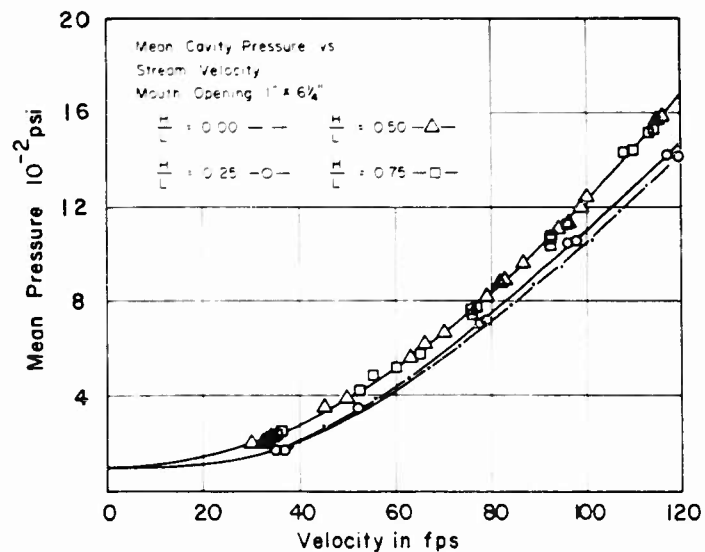Fig. 22 - Mean pressure vs velocity for a wide range of volumes

Fig. 23 - Mean cavity pressure vs velocity
for different ratios of cavity to streamwise
mouth length

between the relative lip height to cavity mouth length ratio (H L) between 0.0
and 0.25. Further increases in this height to length ratio caused much smaller
pressure reductions.

The most dramatic reaction to any configuration change occurred in Fig.
25. The raising at the upstream lip eliminated cavity oscillation completely.
This observation again falls in line with the theoretical prediction that a posi-
tive pressure gradient over the downstream portion at the cavity mouth is nec-
essary to activate and maintain cavity oscillation. This rapid attenuation of
pressure fluctuations apparently occurs because of the elimination of the

Fig. 24 - Variation of pressure with
time inside an oscillating cavity of
frequency 140 cps and peak to peak
pressures of 5 inches of water
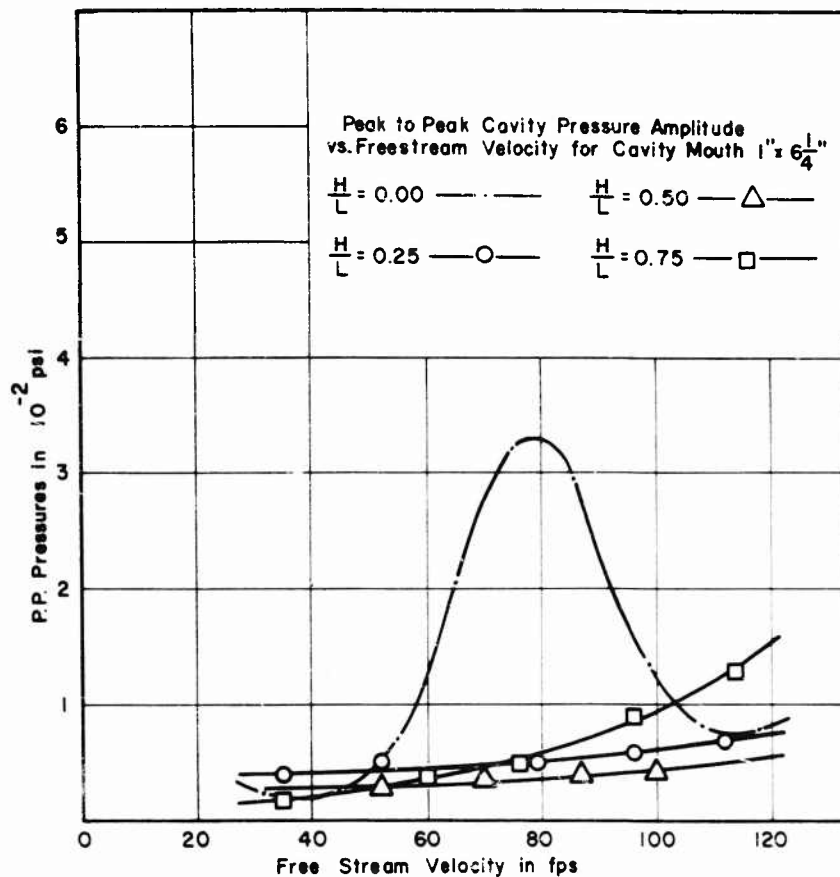
Fig. 25 - Peak to peak cavity pressure amplitude vs free-stream velocity for different ratios of cavity heights to stream-wise mouth lengths. (Note: The 1-in. dimension is in the streamwise direction.)

stagnation point on the downstream lip or edge. When the H L ratio was increased over 0.5, a tendency toward oscillation at a much higher velocity was observed. Flow visualization experiments have not yet been done to evaluate this phenomenon. However, a possibility exists that as H L → 1, a vortex forms above the cavity causing a reversal of flow against the elevated step.

CONCLUSIONS

1. Flow-induced cavity oscillations are caused by flow separation vortices in the mouth of the cavity which are, in turn, caused by:

a. The unstable velocity distribution in the mixing zone of the cavity mouth.

1079

b. The positive pressure gradient over the after portion of the cavity mouth.

2. Flow-induced cavity oscillation can be reduced and some cases eliminated by:

a. Increasing the dampening of the system by making long narrow rectangular mouth openings.

b. Mismatching the streamwise hole length and velocity range with the cavity response.

c. Eliminating the positive pressure gradient in the cavity mouth by raising the upstream lip until the H/L ratio lies greater than 0.25 but less than 0.50.

REFERENCES

1. Strutt, J.W. (Lord Rayleigh), "On the Theory of Resonance," Philosophical Transactions of the Royal Society of London, Vol. 161, Part I, pp. 77-118 (1871).

2. Rayleigh, J.W.S., "The Theory of Sound," MacMillan Company, Ltd., Vol. 2, pp. 412-414, 170-235 (1896).

3. Blokhintsev, D.I., "Excitation of Resonance by Air Flow," SLA Translation Pool No. 270(ONR) from ZATF Vol. 15, pp. 63-70 (1945).

4. Kirshnamurty, K., "Sound Radiation from Surface Cutouts in High Speed Flow," Thesis California Institute of Technology, Pasadena, California (1956).

5. Kirshnamurty, K., "Acoustic Radiation from Two Dimensional Rectangular Cutouts in Aerodynamic Surfaces," NACA TM 3487 (Aug 1955).

6. Roshko, Anatol, "Some Measurements of Flow in a Rectangular Cutout," NACA TM 3488 (Aug 1955).

7. Harrington, M C., "Excitation of Cavity Resonance by Air Flow," American Physical Society Division of Fluid Dynamics, New York, 30 Jan - 2 Feb 1957.

8. Harrington, M.C. and Dunham, Wm. H., "Studies of the Mechanism for Flow-Induced Cavity Resonances," Journal Acoustical Society of America, Vol. 32, p. 921 (Jul 1960).

9. Tollmien, Walter, "Zeitschrift fur Angewandte Mathematik und Mechanik," Vol. 6 (1926). Translation and Report NACA TM 1085 (Sep 1945).

10. Prandtl, L., "The Mechanics of Viscous Fluids," Division G in W.F. Durand, "Aerodynamic Theory," III, pp. 112-118 (1935).

11. Shvets, M.E., "Method of Successive Approximations for the Solution of Certain Problems in Aerodynamics," NACA TM 1268 (1951).

12. Charwat, A.F., Roos, J.N., Dewey, F.C., and Hitz, J.A., "An Investigation of Separated Flows," Part I, Journal of Aerospace Sciences, Vol. 28, No. 6, pp. 457-470 (Jun 1962).

13. Charwat, A.F., Dewey, C.F., Roos, J.N., and Hitz, J.A., "An Investigation of Separated Flows," Part II, Journal of Aerospace Sciences, Vol. 28, No. 7, pp. 513-527 (Jul 1961).

*   *   *

AUTHOR INDEX